LOAN DOCUMENT

PHOTOGRAPH THIS SHEET

AD-A267 970

DTIC ACCESSION NUMBER

LEVEL

1

INVENTORY

AFOSR-TR-93-0532

DOCUMENT IDENTIFICATION

19 Dec 89

DISTRIBUTION STATEMENT A
Approved for public release
Distribution Unlimited

DISTRIBUTION STATEMENT

HANDLE WITH CARE

ACCESSION FOR
NTIS GRA&I ☑
DTIC TRAC ☐
UNANNOUNCED ☐
JUSTIFICATION

BY

DISTRIBUTION/

AVAILABILITY CODES

DISTRIBUTION	AVAILABILITY AND/OR SPECIAL	
A-1		

DISTRIBUTION STAMP

DTIC
ELECTE
AUG 9 1993
S C D

DATE ACCESSIONED

DTIC QUALITY INSPECTED 3

DATE RETURNED

93 8 06 147

93-18096

DATE RECEIVED IN DTIC

REGISTERED OR CERTIFIED NUMBER

PHOTOGRAPH THIS SHEET AND RETURN TO DTIC-FDAC

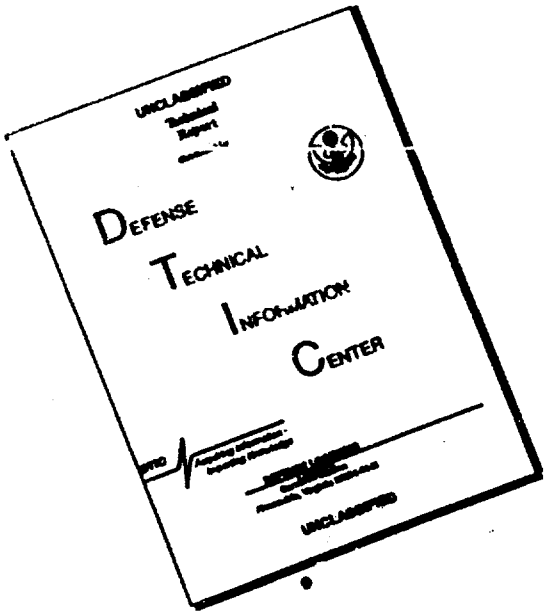
DTIC FORM 70A
JAN 89

DOCUMENT PROCESSING SHEET

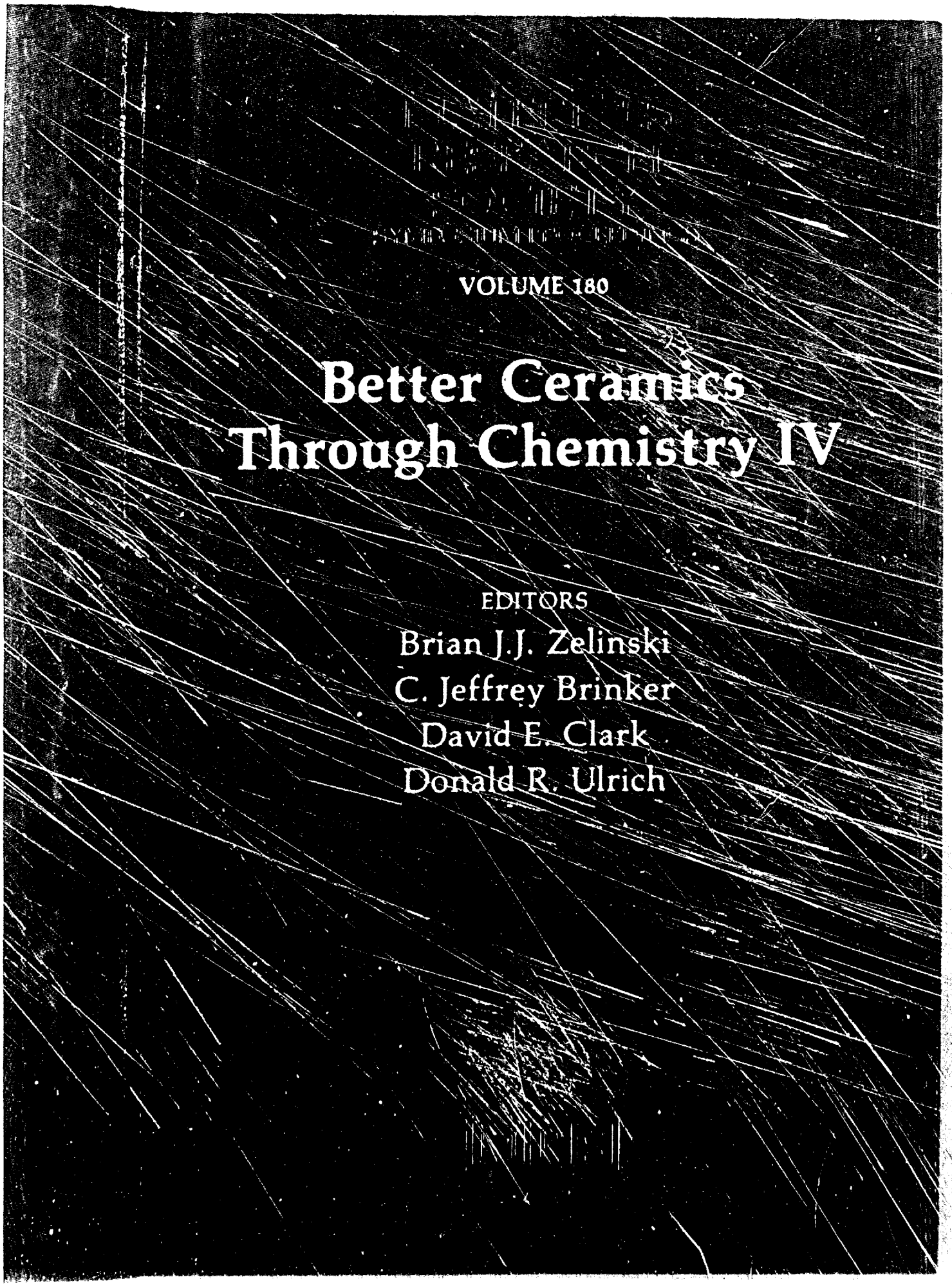
PREVIOUS EDITIONS MAY BE USED UNTIL STOCK IS EXHAUSTED.

LOAN DOCUMENT

DISCLAIMER NOTICE



THIS DOCUMENT IS BEST QUALITY AVAILABLE. THE COPY FURNISHED TO DTIC CONTAINED A SIGNIFICANT NUMBER OF PAGES WHICH DO NOT REPRODUCE LEGIBLY.


VOLUME 180
Better Ceramics Through Chemistry IV
EDITORS
Brian J.J. Zelinski
C. Jeffrey Brinker
David E. Clark
Donald R. Ulrich

Better Ceramics Through Chemistry IV

UNCLASSIFIED
SECURITY CLASSIFICATION OF THIS PAGE

REPORT DOCUMENTATION PAGE

Form Approved
OMB No. 0704-0188

1a. REPORT SECURITY CLASSIFICATION UNCLASSIFIED	1b. RESTRICTIVE MARKINGS
2a. SECURITY CLASSIFICATION AUTHORITY	3. DISTRIBUTION / AVAILABILITY OF REPORT Approved for public release; distribution is unlimited.
2b. DECLASSIFICATION / DOWNGRADING SCHEDULE	
4. PERFORMING ORGANIZATION REPORT NUMBER(S)	5. MONITORING ORGANIZATION REPORT NUMBER(S) AFOSR-TR- 93 0532
6a. NAME OF PERFORMING ORGANIZATION Johns Hopkins Univ	6b. OFFICE SYMBOL (If applicable)
7a. NAME OF MONITORING ORGANIZATION AFOSR/NC	
6c. ADDRESS (City, State, and ZIP Code) Baltimore, MD 21218	7b. ADDRESS (City, State, and ZIP Code) Building 410, Bolling AFB DC 20332-6448
8a. NAME OF FUNDING / SPONSORING ORGANIZATION AFOSR	8b. OFFICE SYMBOL (If applicable) NC
9. PROCUREMENT INSTRUMENT IDENTIFICATION NUMBER AFOSR-86-0110	
8c. ADDRESS (City, State, and ZIP Code) Building 410, Bolling AFB DC 20332-6448	10. SOURCE OF FUNDING NUMBERS

PROGRAM ELEMENT NO.	PROJECT NO.	TASK NO.	WORK UNIT ACCESSION NO.
61102F	2303	B3	

11. TITLE (Include Security Classification)
See Back

12. PERSONAL AUTHOR(S)
David R. Yarkony

13a. TYPE OF REPORT	13b. TIME COVERED	14. DATE OF REPORT (Year, Month, Day)	15. PAGE COUNT
Reprint	FROM _____ TO _____	1989 December 18	13

16. SUPPLEMENTARY NOTATION
J. Chem. Phys., Vol. 91, No. 8, 15 October 1989, pg 4745-4757

17. COSATI CODES			18. SUBJECT TERMS (Continue on reverse if necessary and identify by block number)
FIELD	GROUP	SUB-GROUP	

19. ABSTRACT (Continue on reverse if necessary and identify by block number)

In this work the fine structure splitting of the $X^3\Sigma^-$ state of NH together with the spin-forbidden dipole-allowed radiative transitions $(b^1\Sigma^+, a^1\Delta) \rightarrow X^3\Sigma^-$ in that system are considered. In addition the spin-allowed $A^3\Pi \rightarrow X^3\Sigma^-$ and $c^1\Pi \rightarrow (b^1\Sigma^+, a^1\Delta)$ transitions which provide valuable optical probes of the NH radical are studied. Symbolic matrix methods permit the use of large configuration state function (CSF) spaces ($170–280 \times 10^3$ CSF's) in characterizing these effects. The fine structure splitting and spin-forbidden decay are described within the context of the Breit-Pauli approximation. In the determination of the fine structure splitting both $\hat{H}^{so}$, the full microscopic spin-

20. DISTRIBUTION / AVAILABILITY OF ABSTRACT	21. ABSTRACT SECURITY CLASSIFICATION
☐ UNCLASSIFIED/UNLIMITED ☐ SAME AS RPT. ☐ DTIC USERS	UNCLASSIFIED
NAME OF RESPONSIBLE INDIVIDUAL L. P. DAVIS, MAJOR, USAF	22b. TELEPHONE (Include Area Code) (202) 767-4963
	22c. OFFICE SYMBOL AFOSR/NC

DD Form 1473, JUN 86 Previous editions are obsolete. SECURITY CLASSIFICATION OF THIS PAGE

UNCLASSIFIED

11. **On the electronic structure of the NH radical. The fine structure splitting of the $X\,^3\Sigma^-$ state and the spin-forbidden ($b\,^1\Sigma^+, a\,^1\Delta$)$\rightarrow X\,^3\Sigma^-$, and the spin-allowed $A\,^3\Pi \rightarrow X\,^3\Sigma^-$ and $c\,^1\Pi \rightarrow (b\,^1\Sigma^+, a\,^1\Delta)$, radiative transitions**

AFOSR-TR- 93 0532

orbit and spin-other-orbit operator and $\hat{H}^{ss}$, the dipolar spin-spin operator, are considered through second order in perturbation theory. The completely *ab initio* determination of $\lambda_0 \equiv [E(X^3\Sigma_1^-, v = 0) - E(X^3\Sigma_{0+}^-, v = 0)]/2$, presented here gives $\lambda_0 = 0.903$ (0.9198) cm^{-1} in good accord with the experimental value given parenthetically. The predicted radiative lifetimes for the v=n level of the $A^3\Pi$ state $\tau_n(A^3\Pi)$ (corresponding to $A^3\Pi$, v=n $\rightarrow X^3\Sigma^-$) are $\tau_0(A^3\Pi) = 392[418\pm8, 453\pm10]$ns and $\tau_1(A^3\Pi) = 438[420\pm35, 488\pm10]$ in good agreement with the experimental values given parenthetically. The predicted radiative rate for the v=0 level of the $c^1\Pi$ state is somewhat slower than the total decay rate measured experimentally suggesting predissociation of even the lowest rotational levels. The radiative lifetime for the v = 0 level of the $a^1\Delta$ state, $\tau_0(a^1\Delta)$ corresponding to the spin-forbidden dipole-allowed transition $a^1\Delta_2 \rightarrow X^3\Sigma_1^-$ was found to be $\tau_0(a^1\Delta) = 2.18(>1.9)$s which compares favorably with the lower bound determined from matrix isolation experiments given parenthetically. For the $b^1\Sigma^+ \rightarrow X^3\Sigma^-(0,0)$ transition the ratio of the parallel to the perpendicular transition moment was found to be $\mu_\parallel/\mu_\perp = -0.30(-0.35 \pm 0.05)$ which again compares favorably with the experimental result given parenthetically. This result is qualitatively different from that in the isovalent systems NF, NCl and NBr for which $\mu_\parallel/\mu_\perp > 1$. A partial explanation for this result in terms of molecular dipole moments is offered. The predicted radiative lifetime for the $b^1\Sigma^+$, v=0$\rightarrow$ $X^3\Sigma^-$ transition $\tau_0(b^1\Sigma^+) = 100$ms, which is in excellent agreement with the independent theoretical determination $\tau_0(b^1\Sigma^+) = 97$ms of Marian and Klotz, is significantly longer than the most recent gas phase measurement $\tau_0(b^1\Sigma^+) = 53\binom{+17}{-13}$ms.

MATERIALS RESEARCH SOCIETY SYMPOSIUM PROCEEDINGS VOLUME 180

Better Ceramics Through Chemistry IV

Symposium held April 16-20, 1990, San Francisco, California, U.S.A.

EDITORS:

Brian J.J. Zelinski
University of Arizona, Tucson, Arizona, U.S.A.

C. Jeffrey Brinker
Sandia National Laboratories, Albuquerque, New Mexico, U.S.A.

David E. Clark
University of Florida, Gainesville, Florida, U.S.A.

Donald R. Ulrich
Air Force Office of Scientific Research, Washington, D.C., U.S.A.

MRS MATERIALS RESEARCH SOCIETY
Pittsburgh, Pennsylvania

This work was supported largely by the Air Force Office of Scientific Research under Grant Number AFOSR 90-0196.

Single article reprints from this publication are available through University Microfilms Inc., 300 North Zeeb Road, Ann Arbor, Michigan 48106

CODEN: MRSPDH

Copyright 1990 by Materials Research Society.
All rights reserved.

This book has been registered with Copyright Clearance Center, Inc. For further information, please contact the Copyright Clearance Center, Salem, Massachusetts.

Published by:

Materials Research Society
9800 McKnight Road
Pittsburgh, Pennsylvania 15237
Telephone (412) 367-3003
Fax (412) 367-4373

Library of Congress Cataloging in Publication Data

Better ceramics through chemistry IV : symposium held April 16-20, 1990, San Francisco, California, U.S.A. / editors, Brian J.J. Zelinski, C. Jeffrey Brinker, David E. Clark and Donald R. Ulrich.

p. cm. — (Materials Research Society symposium proceedings : ISSN 0272-9172 ; v. 180)

Proceedings of the Fourth Materials Research Society Symposium on Better Ceramics Through Chemistry, April 16-20, 1990.

Includes bibliographical references and index.

ISBN 1-55899-069-0

1. Ceramics—Chemistry. I. Zelinski, Brian J.J. II. Materials Research Society. III. Materials Research Society Symposium on Better Ceramics Through Chemistry (4th : 1990 : San Francisco, Calif.) IV. Title: Better ceramics through chemistry 4. V. Title: Better ceramics through chemistry four. VI. Series: Materials Research Society symposium proceedings : v. 180.

TP786.B4852 1990 90-13520
666—dc20 CIP

Manufactured in the United States of America

Contents

DEDICATION xviii

PREFACE xix

ACKNOWLEDGMENTS xxi

MATERIALS RESEARCH SOCIETY SYMPOSIUM PROCEEDINGS xxii

PART I: REACTION MECHANISMS AND KINETICS

*SOL-GEL CHEMISTRY OF HYDROGENOSILICONATES: THE ROLE OF HYPERVALENT SILICON SPECIES 3
V. Belot, R. Corriu, C. Guerin, B. Henner, D. Leclercq, H. Mutin, A. Vioux, and Q. Wang

HIGH PRESSURE RAMAN STUDY OF THE HYDROLYSIS REACTION OF TMOS AND TEOS 15
G. Hoang, J. Watson, and T.W. Zerda

*CURRENT ISSUES IN SOL-GEL REACTION KINETICS 21
Roger A. Assink and Bruce D. Kay

*MOLECULAR ARCHITECTURE AND ITS ROLE IN SILICA SOL-GEL POLYMERIZATION 29
P.C. Cagle, W.G. Klemperer, and C.A. Simmons

SYNTHETIC AND STRUCTURAL STUDIES OF BISMUTH/COPPER ALKOXIDES 39
William J. Evans and John H. Hain, Jr.

PART II: PRECURSOR EFFECTS AND AQUEOUS CHEMISTRY

*MOLECULAR STRUCTURE OF METAL ALKOXIDE PRECURSORS 47
C. Sanchez, P. Toledano, and F. Ribot

*MOLECULAR ROUTES TO TIN OXIDES 61
T.A. Wark, E.A. Gulliver, L.C. Jones, M.J. Hampden-Smith, A.L. Rheingold, and J.C. Huffman

TAILORED MOLECULAR PRECURSORS OF YTTRIUM OXIDE USING FUNCTIONAL ALCOHOLS AND ACETYLACETONE AS MODIFIERS 73
Liliane G. Hubert-Pfalzgraf, Olivier Poncelet, and Jean-Claude Daran

NMR SPECTROSCOPIC INVESTIGATIONS OF $PbTiO_3$ SOL-GEL PROCESSING 79
S.D. Ramamurthi and D.A. Payne

*Invited Paper

*REVIEW OF HYDROLYSIS BEHAVIOR OF IONS IN AQUEOUS SOLUTIONS 85
R.E. Mesmer and C.F. Baes, Jr.

*HYDROLYSIS OF ALUMINUM - ARE ALL GELS CREATED EQUAL? 97
T.E. Wood, A. Siedle, J.R. Hill, R.P Skarjune, and C.J. Goodbrake

SMALL-ANGLE NEUTRON SCATTERING AND 27AL NMR STUDIES ON THE MICROSTRUCTURE AND COMPOSITION OF ALUMINA SOL-GELS 117
L.F. Nazar, D.G. Napier, D. Lapham, and E. Epperson

SMALL ANGLE X-RAY SCATTERING STUDIES OF POLYMERIC ZIRCONIUM SPECIES IN AQUEOUS SOLUTION 123
J.A. Jutson, R.M. Richardson, S.L. Jones, and C. Norman

PART III: PROCESSING SCIENCE I: AGGREGATION, PARTICLE GROWTH AND CONCENTRATED DISPERSION

*PRECIPITATION OF UNIFORM PARTICLES: THE ROLE OF AGGREGATION 131
C.F. Zukoski, M.K. Chow, G.H. Bogush, and J-L. Look

*SIMPLE MODELS FOR PARTICLE AGGREGATION, DEPOSITION AND SEGREGATION 141
Paul Meakin

MECHANISMS OF SILICA AND TITANIA COLLOIDAL PARTICLE FORMATION FROM METAL ALKOXIDES 153
Joseph K. Bailey and Martha L. Mecartney

*SHEAR INDUCED ORDER OF CONCENTRATED DISPERSIONS 159
Bruce J. Ackerson and T.A. Morris

CONSOLIDATION OF COLLOIDAL SUSPENSIONS 167
Wei-Heng Shih, Seong Il Kim, Wan Y. Shih, Christopher H. Schilling, and Ilhan A. Aksay

*RHEOLOGY AND MICROSTRUCTURE OF CONCENTRATED SUSPENSIONS 173
Lisa A. Mondy and Alan L. Graham

RHEOLOGICAL AND RELATED COLLOIDAL ASPECTS OF AQUEOUS PROCESSING THAT AFFECT THE DEVELOPMENT OF MICROSTRUCTURE 185
Alan Bleier and C. Gary Westmoreland

PREPARATION OF MULTICOMPONENT CERAMIC POWDERS BY SOL-GEL PROCESSING 191
J.R. Bartlett and J.L. Woolfrey

PART IV: PROCESSING SCIENCE II: GELATION, AGING AND DRYING

*FRACTAL STRUCTURE AND FRACTAL TIME IN SILICA SOL-GELS 199
James E. Martin and Jess Wilcoxon

*Invited Paper

^{29}Si NMR STUDY OF SILICON ALKOXIDES: FROM THE CONDENSATION KINETICS IN SOLUTION TO THE DETERMINATION OF THE FRACTAL DIMENSION IN AEROGELS 211
F. Devreux, J.P. Boilot, F. Chaput, and A. Lecomte

LOW WAVENUMBER RAMAN SCATTERING IN SILICA AND SILICOPHOSPHATE AEROGELS 217
Barbara L. Walden, Else Breval, and William B. White

BASE-CATALYZED SILICA GELS: STRUCTURE AND CHEMISTRY 223
Garry J. Garvey and Bruce E. Smith

SOLUTION CHEMISTRY IN THE Al_2O_3-SiO_2 SYSTEM 229
W.G. Fahrenholtz, S.L. Hietala, D.M. Smith, A.J. Hurd, C.J. Brinker, and W.L. Earl

*IN-SITU PORE STRUCTURE ANALYSIS DURING AGING AND DRYING OF GELS 235
Douglas M. Smith, Pamela J. Davis, and C. Jeffrey Brinker

RELATIONSHIP BETWEEN STRAINED SILICON-OXYGEN BONDS AND RADIATION INDUCED PARAMAGNETIC POINT DEFECTS IN SILICON DIOXIDE 247
W.L. Warren, P.M. Lenahan, C.J. Brinker, and C.S. Ashley

MOLECULAR ORBITAL MODELING OF WATER ADSORPTION ON A TETRASILOXANE RING 255
J.K. West and S. Wallace

PART V: POSTER SESSION: SOLUTION CHEMISTRY, PROCESSING SCIENCE, ELECTRICAL AND OPTICAL PROPERTIES, THIN FILMS AND FIBERS

CATALYTIC CONTROL OF SiO_2 SOL-GEL KINETICS - A MECHANISTIC STUDY OF BASES 263
Jorge Sanchez, Mary Reese, and Alon McCormick

ORGANIC CATALYSTS IN THE SILICA SOL-GEL SYSTEM 269
T.A. Gallo, B.L. Simms, and V.T. Brice

THE INFLUENCE OF CATIONS ON GROWTH KINETICS OF SILICA AGGREGATES 273
Theo P.M. Beelen, Peter W.J.G. Wijnen, Kees P.J. Rummens, and Rutger A. van Santen

SOLVENT SELECTION AND THE CONTROL OF SOL-GEL REACTIONS 277
K. Jones, J.M. Boulton, and H.G. Emblem

INVESTIGATION OF THE SILICA NETWORK DURING THE SOL TO GEL TRANSITION AND FINAL XEROGEL PROPERTIES 283
Paul R. Soskey, Randall E. Nikles, George F. Fattman, Robert M. Mininni, and Deborah A. Gerenza

*Invited Paper

FORMATION OF SPINEL IRON OXIDE IN SOLUTION 289
Jean Pierre Jolivet, Elisabeth Tronc, Philippe Belleville, and Jacques Livage

RELIABLE ELECTROKINETIC CHARACTERIZATION PROCEDURES FOR CERAMIC POWDERS 293
Jiun-Fang Wang, Richard E. Riman, and Daniel J. Shanefield

FRACTAL CONCEPTS AND AGGREGATION OF IRON OXIDES 299
R. Amal, J.A. Raper, and T.D. Waite

S.A.N.S. STUDY OF FRACTAL ALUMINO-SILICATE AEROGELS 305
F. Chaput, J.P. Boilot, A. Dauger, F. Devreux, and A. de Geyer

CHARACTERIZATION OF PARTIALLY CONDENSED SILICA FORMED FROM THE PARTIAL HYDROLYSIS OF TMOS 309
T.M. Tillotson and L.W. Hrubesh

CHARACTERIZATION OF ULTRALOW-DENSITY SILICA AEROGELS MADE FROM A CONDENSED SILICA PRECURSOR 315
Lawrence W. Hrubesh, Thomas M. Tillotson, and John F. Poco

MICROSTRUCTURAL DEPENDENCE OF AEROGEL MECHANICAL PROPERTIES 321
J.D. LeMay, T.M. Tillotson, L.W. Hrubesh, and R.W. Pekala

POSITRONIUM DECAY IN SILICA SOL-GELS 325
B. Hopkins, C.A. Quarles, and T.W. Zerda

A COMPARISON OF TiO_2-SiO_2 AEROGELS AND XEROGELS 329
G. Cogliati, M. Guglielmi, T.M. Che, and T.J. Clark

THE EFFECTS OF HYDROLYSIS CONDITIONS, AND ACID AND BASE ADDITIONS, ON THE GEL-TO-CERAMIC CONVERSION IN SOL-GEL DERIVED $PbTiO_3$ 335
Robert W. Schwartz, C.D.E. Lakeman, and D.A. Payne

EFFECTS OF TRIOXANE ON SILICA GEL 341
Xiaoming Li and P.F. Johnson

EFFECT OF DOPANTS ON THE CRYSTALLIZATION OF ZIRCON FROM ZIRCONIUM SILICATE GELS 347
J.D. Barrie and M.J. Meshishnek

EFFECT OF SnO_2 ON THE MECHANICAL PROPERTIES OF SiO_2/SnO_2 GEL-DERIVED COMPOSITES 351
R. Dal Maschio, S. Dire', R. Campostrini, G.D. Soraru, and G. Carturan

CRYSTALLIZATION AND PHASE TRANSFORMATION OF ZrO_2-SiO_2 GELS 355
Xiaoming Li and P.F. Johnson

PREPARATION OF THE POROUS SUPPORTS WITH SiO_2-ZrO_2-Na_2O COMPOSITION 361
Y. Tsurita and K. Wada

STUDIES IN THE Ba-Ca-Al-O SYSTEM CHEMICAL MODIFICATION OF ALUMINUM ALKOXIDE BY PROPIONIC ACID 365
V. Hebert, S. Vilminot, and D. Brion

SOL-GEL SYNTHESIS OF THIN FILMS FOR USE AS PLANAR WAVEGUIDES 371
G.W. Dale, H.H. Fox, Brian J.J. Zelinski, and Laura Weller-Brophy

PROCESSING OF SiO_2-TiO_2 THIN FILM WAVEGUIDES 377
L. Weisenbach, T.L. Davis, B.J.J. Zelinski, R.L. Roncone, and L.A. Weller-Brophy

OPTICAL INTERFERENCE FILTERS BY SOL-GEL PROCESSING 383
J.L. Keddie and E.P. Giannelis

TITANIA/SILICA SOL-GEL FILMS: COMPARISON OF TECHNIQUES FOR THIN FILM THICKNESS MEASUREMENT 387
S.M. Melpolder, A.W. West, M.P. Cunningham, and R. Sharma

HETEROMETALLIC ALKOXIDES AS PRECURSORS TO MULTICOMPONENT OXIDES 393
Liliane G. Hubert-Pfalzgraf, Renee Papiernik, Marie-Cecile Massiani, and Bernard Septe

STABILIZATION, CHARACTERIZATION AND OPTICAL APPLICATIONS OF NIOBIUM AND TANTALUM OXIDE SOLS PREPARED VIA ALKOXIDE ROUTES 397
Stephen Parraud, Liliane G. Hubert-Pfalzgraf, and Herve Floch

MICROWAVE PROCESSING OF SOL-GEL DERIVED POTASSIUM NIOBATE 401
Z. Fathi, I. Ahmad, and D.E. Clark

DIELECTRIC CHARACTERIZATION OF POLYCERAM FILMS 407
G. Teowee, J.M. Boulton, H.H. Fox, A. Koussa, T. Gudgel, and D.R. Uhlmann

SOL-GEL THIN FILM ELECTRONIC PROPERTIES 413
W.L. Warren, P.M. Lenahan, C.J. Brinker, G.R. Shaffer, C.S. Ashley, and S.T. Reed

SOL-GEL SYNTHESIS OF LEAD TITANATE FIBRES FOR USE IN THE FABRICATION OF PIEZOCERAMIC-POLYMER COMPOSITES 421
H. Janusson, C.E. Millar, and S.J. Milne

MICROSTRUCTURAL EVOLUTION OF TiO_2 SOL-GEL THIN FILMS 425
J.L. Keddie and E.P. Giannelis

ELECTRON DIFFRACTION ANALYSIS OF THE STRUCTURE OF SiO_2 GEL-FILM 429
Hisashi Ohsaki, Michel A. Aegerter, and Takaki Shichiri

PROPERTIES OF FILMS PREPARED FROM LOW SURFACE AREA/ DENSITY ALUMINA-SILICA 433
S.L. Hietala, D.M. Smith, V.M. Hietala, G.C. Frye, A.J. Hurd, and C.J. Brinker

THIN ANISOTROPIC COATINGS BASED ON SOL-GEL TECHNOLOGY 439
S. Randall Holmes-Farley and Lynn C. Yanyo

PARTICLE GROWTH AND DEVELOPMENT DURING THE IN-SITU PRECIPITATION OF SILICA IN A POLYMERIC MATRIX 445
Ping Xu, Shuhong Wang, and James E. Mark

SOL-GEL DEPOSITION OF ELECTRONIC CERAMIC FILMS 453
J.M. Bell, B. Ben-Nissan, M. Anast, B.O. West, L. Spiccia, J. Cullen, I. Watkins, D. deVilliers, and G. Johnston

THE FORMATION OF THIN FILMS AND FIBERS OF TiC FROM A POLYMERIC TITANATE PRECURSOR 457
S-J. Ting, C-J. Chu, E. Limatta, J.D. Mackenzie, T. Getman, and M.F. Hawthorne

CERAMIC FIBER COATING BY A NON-AQUEOUS SOL-GEL PROCESS 461
F.C. Montgomery, H.H. Streckert, R.O. Harrington, J.L. Kaae, S.P. Paguio, and D.R. Wall

IMPROVEMENT OF BUILDING MATERIALS PERFORMANCE BY SOL-GEL DERIVED COATINGS 467
Wolfram Beier and Ivan Odler

GLASSES AND MULTI-COMPONENT SOL-GELS FOR USE AS HIGH-TEMPERATURE PROTECTIVE COATINGS 473
Lauri J. DeVore and Nora R. Osborne

CHARACTERIZATION OF CERIA STABILIZED ZIRCONIA COATINGS ON METAL SUBSTRATES 481
Rosa Di Maggio, Paolo Scardi, and Andrea Tomasi

SOL-GEL PROCESSING OF $PbTiO_3$ FIBERS 485
S.I. Aoki, S.C. Choi, D.A. Payne, and H. Yanagida

EVOLUTION OF SURFACE AREA DURING THE CONTROLLED GROWTH OF SILICA SPHERES 491
Gregory H. Bogush, C.J. Brinker, P.D. Majors, and D.M. Smith

PART VI: PROCESSING SCIENCE III: DRYING, DENSIFICATION AND CRYSTALLIZATION

THE CRACKING OF SOL-GEL FILMS DURING DRYING 497
Terry J. Garino

*EFFECT OF INCLUSIONS ON SHRINKAGE 503
George W. Scherer

*Invited Paper

*HYBRID GELS DESIGNED FOR MULLITE NUCLEATION AND CRYSTALLIZATION CONTROL 515
Jeffrey C. Huling and Gary L. Messing

MOLECULARLY MODIFIED ALKOXIDE PRECURSORS FOR SYNTHESIS OF DIELECTRIC CERAMICS 527
Pradeep P. Phule and Farida Khairulla

EFFECT OF PRECURSORS ON LITHIUM INFILTRATED SILICA GELS STUDIED BY XPS 533
S.F. Ho and L.C. Klein

PHASE TRANSFORMATIONS IN ZrO_2-SiO_2 GELS 541
J. Campaniello, E.M. Rabinovich, P. Berthet, A. Revcolevschi, and Nonna A. Kopylov

CRYSTALLIZATION OF IN-SITU SiC-MULLITE COMPOSITES FROM MULTICOMPONENT ALUMINA-SILICA GELS 547
S. Jagota and A. Parvizi-Majidi

PART VII: THIN FILMS AND FIBERS

*RHEOLOGY FOR BETTER SOL-GEL FIBER AND FILM FORMATION 555
C.W. Macosko, M.L. Mecartney, and L.E. Scriven

THE PROCESS OF GEL FIBER FORMATION 569
N. Taneda, T. Kawaguchi, D. Arai, and K. Matsuzaki

*SOL-GEL FILM FORMATION BY DIP COATING 575
Alan J. Hurd and C. Jeffrey Brinker

*SOL-GEL COATINGS ON ACOUSTIC WAVE DEVICES: THIN FILM CHARACTERIZATION AND CHEMICAL SENSOR DEVELOPMENT 583
Gregory C. Frye, C. Jeffrey Brinker, Antonio J. Ricco, Stephen J. Martin, Janice Hilliard, and Daniel H. Doughty

*OXOMETALATE-GLASS COMPOSITES AND THIN FILMS 595
Karin Moller, Thomas Bein, and C. Jeffrey Brinker

INHOMOGENEITIES IN SOL-GEL COATINGS 605
B.D. Fabes, D.L. Klein, and L.J. Raymond

DENSIFICATION AND CRYSTALLIZATION OF THIN TRANSITION METAL OXIDE COATINGS FROM METAL ALKOXIDES 611
H. Hirashima, R. Muratake, T. Yamashita, and T. Chiba

PART VIII: CERAMIC PROCESSING OF NATURAL SYSTEMS

*BIOMIMETIC CERAMICS 619
Paul Calvert

*BIOMIMETIC PROCESSING OF CERAMICS AND CERAMIC-METAL COMPOSITES 625
M. Yasrebi, G.H. Kim, K.E. Gunnison, D.L. Milius, M. Sarikaya, and I.A. Aksay

*Invited Paper

*SYNTHESIS OF NANOCERAMIC PARTICLES BY INTRAVESICULAR PRECIPITATION 637
Suhas Bhandarkar, Iskandar Yaacob, and Arijit Bose

PART IX: STRUCTURE/PROPERTIES I: ELECTRICAL

*WET CHEMICAL DERIVED FILMS FOR ELECTRICAL APPLICATIONS 645
D.R. Uhlmann, G. Teowee, J.M. Boulton, and B.J.J. Zelinski

CRYSTALLIZATION KINETICS OF METALLO-ORGANICS DERIVED PZT THIN FILM 663
K.C. Chen and J.D. Mackenzie

EVOLUTION OF MOLECULAR STRUCTURE IN ALKOXIDE-DERIVED LITHIUM NIOBATE 669
Dennis J. Eichorst and D.A. Payne

PREPARATION OF SINGLE-PHASE $KNbO_3$ USING BIMETALLIC ALKOXIDES 675
Mostafa M. Amini and Michael D. Sacks

*INTERCALATION CHEMISTRY: A NOVEL APPROACH TO MATERIALS DESIGN 685
E.P. Giannelis, V. Mehrotra, and M.W. Russell

PREPARATION OF COPPER AND COPPER-BARIUM-YTTRIUM SOLS FROM METAL 2-(2-ETHOXYETHOXY)ETHOXIDES AND CONVERSION OF COPPER-BARIUM-YTTRIUM ALKOXIDE PRECURSORS TO $Ba_2YCu_3O_{7-\delta}$ 697
Mary Rose Scozzafava, Wendell E. Rhine, and Michael J. Cima

ION-IMPLANTATION EFFECTS ON SPIN-ON-GLASS (SOL-GEL) SiO_2 FILMS 703
Y. Shacham-Diamand, N. Moriya, and R. Kalish

CHEMICAL SYNTHESIS OF ALUMINUM NITRIDE POWDERS 709
Phillip R. Coffman, William T. Petuskey, and Sandwip K. Dey

PART X: STRUCTURE/PROPERTIES II: OPTICAL

*GRIN ROD OF LARGE DIAMETER AND LARGE DELTA-N 717
Masayuki Yamane, Atsuo Yasumori, Mitsunobu Iwasaki, and Kazutaka Hayashi

STUDIES ON THE REPRODUCIBLE PRODUCTION OF GRIN (GRADIENT INDEX) GLASS RODS BY A SOL-GEL PROCESS 727
J. Brian Caldwell, Tessie M. Che, Richard W. Cruse, Robert M. Mininni, Randall E. Nikles, Victor N. Warden, and Mark A. Banash

*Invited Paper

LIGHT HARVESTING MOLECULAR ASSEMBLIES IN THE DESIGN OF HIGHLY LUMINESCENT SOL-GEL DERIVED GLASSES 733
Joel I. Dulebohn, Béatrice Van Vlierberge, Kris A. Berglund, Ronald B. Lessard, Jeong-a Yu, and Daniel G. Nocera

*SOL-GEL PROCESSED INORGANIC AND ORGANICALLY MODIFIED COMPOSITES FOR NONLINEAR OPTICS AND PHOTONICS 741
Paras N. Prasad

INCORPORATION OF POLYANILINE INTO A SILICA GEL VIA THE SOL-GEL TECHNIQUE 747
F. Nishida, B. Dunn, E.T. Knobbe, P.D. Fuqua, R.B. Kaner, and B.R. Mattes

OPTICAL SWITCHES BASED ON VANADIUM DIOXIDE FILMS GROWN BY THE SOL-GEL PROCESS 753
Richard S. Potember and Kenneth R. Speck

VANADIUM PENTOXIDE GELS: STRUCTURAL DEVELOPMENT AND RHEOLOGICAL PROPERTIES 759
J.K. Bailey, T. Nagase, G.A. Pozarnsky, and M.L. Mecartney

PART XI: POSTER SESSION: NOVEL PROCESSING, SUPERCONDUCTORS

PREPARATION OF PHENYLSILOXANE FILMS VIA SOLUTION DEPOSITION TECHNIQUES 767
E.W. Burkhardt, R.R. Burford, and J.H. Deatcher

SYNTHESIS AND STRUCTURAL CHARACTERISTICS OF POLYCERAMS 773
J.M. Boulton, H.H. Fox, G.F. Neilson, and D.R. Uhlmann

POLYMERIZATIONS OF ALKENYLSILANES USING EARLY TRANSITION METAL CATALYSTS 779
John Masnovi, Xin Y. Bu, Paula Conroy, A. Harry Andrist, Frances I. Hurwitz, and Doug Miller

HIGH RESOLUTION TEM OF ORGANIC AEROGELS AND INORGANIC AEROGELS 785
George C. Ruben and Richard W. Pekala

A NEW SYNTHETIC ROUTE TO ORGANIC AEROGELS 791
R.W. Pekala and C.T. Alviso

CRYSTALLIZATION OF PYROLYZED POLYSILAZANES 797
Roger L.K. Matsumoto

PRE-RESONANCE RAMAN CHARACTERIZATION OF METAL-ORGANIC FILMS FROM TITANIUM ALKOXIDE CARBOXYLATE COMPLEXES 801
Charles D. Gagliardi, Dilum Dunuwila, and Kris A. Berglund

*Invited Paper

STABILITY OF BORON NITRIDE COATINGS ON CERAMIC SUBSTRATES 807
Abhaya K. Datye, Xiaomei Qui, Theodore T. Borek, Robert T. Paine, and Lawrence F. Allard

XPS CHARACTERIZATION OF MIXED CARBIDES OBTAINED FROM POLYMER PRECURSORS 811
Gaetano Granozzi, Antonella Glisenti, and Gian D. Soraru

MIXED CARBIDES VIA POLYMER ROUTE 815
Gian D. Soraru, Florence Babonneau, and John D. Mackenzie

LASER DENSIFICATION MODELING 819
Taipau Chia, L.L. Hench, Chaobin Qin, and C.K. Hsieh

THE USE OF SOLUBLE METAL-POLYSELENIDE COMPLEXES AS PRECURSORS TO BINARY AND TERNARY SOLID METAL SELENIDES 825
S. Dhingra and M.G. Kanatzidis

CHEMICALLY DERIVED YTTRIA-STABILIZED ZIRCONIA FOR PLASMA-SPRAYING 831
Fawzy G. Sherif and H. Herman

EMULSION PRECIPITATION AND CHARACTERIZATION OF ZIRCONIA 837
Lieh-Jiun Shyu and Frank M. Cambria

TRANSPIRATION COOLED POROUS TYPE VI SILICA ROCKET WINDOWS 843
Albert G. Fosmoe II and Larry L. Hench

PLASMA SYNTHESIS OF FINE CERAMIC POWDERS BY A NOVEL COUNTER-FLOW LIQUID INJECTION METHOD 849
P. Kong, T.W. Or, L. Stachowicz, and E. Pfender

MORPHOLOGY CONTROL IN PRECURSOR CERAMIC POWDER PRODUCTION BY THE ELECTRICAL DISPERSION REACTOR 853
Michael T. Harris, Timothy C. Scott, Osman A. Basaran, and Charles H. Byers

DC PLASMA SYNTHESIS OF ALUMINUM NITRIDE CERAMIC POWDERS 857
Z.P. Lu and E. Pfender

EFFECT OF NITROUS OXIDE GAS ON CVD DIAMOND FILM DEPOSITION 861
H. Koinuma, M. Yoshimoto, Y. Takagi, A.B. Sawaoka, T. Hashimoto, T. Nagai, and T. Shiraishi

SUPERCONDUCTING FIBERS FROM ANHYDROUS METAL CARBOXYLATES 865
Richard M. Laine, Kay A. Youngdahl, Richard A. Kennish, Martin L. Hoppe, Zhi-Fan Zhang, and D. Jean Ray

FABRICATION OF SUPERCONDUCTING Bi-Sr-Ca-Cu-O OXIDE FILMS USING THE METAL ALKOXIDE METHOD 873
Shingo Katayama and Masahiro Sekine

POLYFUNCTIONAL CARBOXYLIC ACIDS AS COPRECIPITATING AGENTS FOR BARIUM, YTTRIUM, AND COPPER 877
Robert B. Hallock, P.O. Rexer, M.S. Jolly, W.E. Rhine, and M.J. Cima

SYNTHESIS OF SUPERCONDUCTING THIN FILMS BY ORGANOMETALLIC DECOMPOSITION 883
Christophe Barbe and Terry A. Ring

CHEMICAL PREPARATION OF SUPERCONDUCTING OXIDES USING CONVENTIONAL CHELATING AGENTS 889
Cyril Chiang and C.Y. Shei

SYNTHESIS OF SUPERCONDUCTING PEROVSKITE BY COPRECIPITATION OF HYDROXIDES 893
I. Valente-Campion, P. Barboux, L. Mazerolles, D. Michel, R. Morineau, and J. Livage

SUPERCONDUCTING $YBa_2Cu_3O_{7-x}$ FIBERS FABRICATED BY THE SOL-GEL METHOD USING METAL ALKOXIDES 897
Shingo Katayama and Masahiro Sekine

SOL-GEL PROCESSING OF THE $Tl_2Ca_1Ba_2Cu_2O_{8+x}$ HIGH Tc SUPERCONDUCTING PHASE 901
M.R. Teepe, D.S. Kenzer, G.A. Moore, and G. Kordas

PREPARATION OF SUPERCONDUCTING $YBa_2Cu_3O_{7-x}$ COMPOUNDS BY WATER EXTRACTION VARIANT OF SOL-GEL PROCESS 907
A. Deptuła, W. Łada, T. Olczak, T. Żółtowski, and A. Di Bartolomeo

METALLO-ORGANICS DERIVED TRACTABLE RESINS FOR YBCO SUPERCONDUCTING FIBER FABRICATION 913
K.C. Chen, A.Y. Chen, and K.S. Mazdiyasni

PREPARATION OF Bi-Pb-Sr-Ca-Cu-O SUPERCONDUCTOR BY THERMAL DECOMPOSITION OF AN EDTA COLLOID 917
H.S. Koo, C.K. Chiang, Y.T. Huang, and G.C. Tu

SOLUBLE AND VOLATILE PRECURSORS FOR THE PREPARATION OF SUPERCONDUCTING FILMS 921
Nancy N. Sauer, Eduardo Garcia, and Robert R. Ryan

KINETIC STUDY OF HIGH Tc Bi-Pb-Sr-Ca-Cu-O SYSTEM 925
W.-M. Hurng, Y.T. Huang, C.Y. Shei, C. Chiang, H.S. Koo, S.F. Wu, and P.T. Wu

SOLUTION-DERIVED $YBa_2Cu_3O_{7-\delta}$ THIN FILMS AND BARRIER LAYERS 929
G.E. Whitwell, J.H. Wandass, F.M. Cambria, and M.F. Antezzo

PREPARATION, THERMAL PROCESSING BEHAVIOR AND CHARACTERIZATION OF POWDERED AND BULK $YBa_2Cu_3O_{7-x}$ FROM FREEZE DRIED NITRATE SOLUTIONS 935
N. Coppa, A. Bura, J.W. Schwegler, R.E. Salomon, G.H. Myer, and J.E. Crow

TEN MINUTE PREPARATION OF $YBa_2Cu_3O_{7-x}$ USING BARIUM HYDROXIDE 941
N. Coppa, A. Kebede, J.W. Schwegler, I. Perez, R.E. Salomon, G.H. Myer, and J.E. Crow

EVALUATION OF $YBa_2Cu_3O_{7-\delta}$ SOL-GEL DERIVED FILMS ON SAPPHIRE SUBSTRATES PRODUCED FROM DIFFERENT Cu(II) ALKOXIDE GROUPS 947
D.S. Kenzer, M.R. Teepe, G.A. Moore, and G. Kordas

CHARACTERIZATION OF AMORPHOUS GEL TO SUPERCONDUCTING OXIDE CONVERSION FOR SOL-GEL PRODUCED $Y_1Ba_2Cu_3O_{7-x}$ 953
G.A. Moore, D. Kenzer, M. Teepe, and G. Kordas

PART XII: NOVEL PROCESSING I

*ASPECTS OF CHEMISTRY AND CHEMICAL PROCESSING OF ORGANICALLY MODIFIED CERAMICS 961
Helmut K. Schmidt

ARYL-BRIDGED POLYSILSESQUIOXANES - NEW MICROPOROUS MATERIALS 975
Kenneth J. Shea, Owen Webster, and Douglas A. Loy

RUBBERY ORMOSILS 981
Young J. Chung, Su-Jen Ting, and John D. Mackenzie

NON-LINEAR ORGANIC DYES IN POLYCERAM HOSTS 987
J.M. Boulton, J. Thompson, H.H. Fox, I. Gorodisher, G. Teowee, P.D. Calvert, and D.R. Uhlmann

INORGANIC-ORGANIC COMPOSITES (ORMOCERs) AS STRUCTURED LAYERS FOR MICROELECTRONICS 995
Michael Popall, Henning Meyer, Helmut Schmidt, and Jochen Schulz

RAPID THERMAL PROCESSING OF HIGH TEMPERATURE SUPERCONDUCTING FIBER 1003
J.W. Halloran, M.J. Neal, D.S. Ginley, E.L. Venturini, J.F. Kwak, R.J. Baughman, M.A. Mitchell, B. Morosin, S.N. Basu, and T.E. Mitchell

PREPARATION OF POROUS OXIDE BEADS USING POLYMERIC BEADS TO CONTROL BEAD SIZE AND SHAPE 1009
Anne B. Hardy, Wendell E. Rhine, and H. Kent Bowen

PART XIII: NOVEL PROCESSING II

*NEW CHEMICAL ROUTES TO METAL NITRIDES 1017
Wayne L. Gladfelter, Jen-Wei Hwang, John F. Evans, Scott A. Hanson, Klavs F. Jensen, and Kwok-Lun Ho

*Invited Paper

BORON NITRIDE AND COMPOSITE AEROGELS FROM BORAZINE BASED POLYMERS 1029
David A. Lindquist, Douglas M. Smith, Abhaya K. Datye, Gregory P. Johnston, Theodore T. Borek, Riley Schaeffer, and Robert T. Paine

SPECTROSCOPIC CHARACTERIZATION OF A PRE-CERAMIC POLYMER FOR SiC/TiC SYSTEM 1035
Florence Babonneau, Patrice Barre, Jacques Livage, and Michel Verdaguer

CHEMICAL REACTIONS DURING THE THERMAL PROCESSING OF BORAZENE POLYMERS 1041
R.R. Rye, T.T. Borek, D.A. Lindquist, and R.T. Paine

LASER DENSIFICATION OF SOL-GEL COATINGS 1047
D.J. Taylor, B.D. Fabes, and M.G. Steinthal

*ELECTRODEPOSITION OF NANOMODULATED CERAMIC THIN FILMS 1053
Jay A. Switzer, Michael J. Shane, and Richard J. Phillips

*THE CHEMICAL PROCESSING OF SILICATES FOR BIOLOGICAL APPLICATIONS - A REVIEW 1061
L.L. Hench and June Wilson

PART XIV: LATE PAPERS ACCEPTED

MAGNETIC RESONANCE AS A STRUCTURAL PROBE OF A URANIUM (VI) SOL-GEL PROCESS 1075
Charles M. King, R. Bruce King, A. Ronald Garber, Major C. Thompson, and Bruce R. Buchanan

OXYGEN-17 NMR STUDIES OF URANIUM (VI) HYDROLYSIS AND GELATION 1083
R. Bruce King, Charles M. King, and A. Ronald Garber

*MECHANICAL PROPERTIES OF SILICA ALCOGELS AND AEROGELS 1087
T. Woignier, J. Phalippou, H. Hdach, and G.W. Scherer

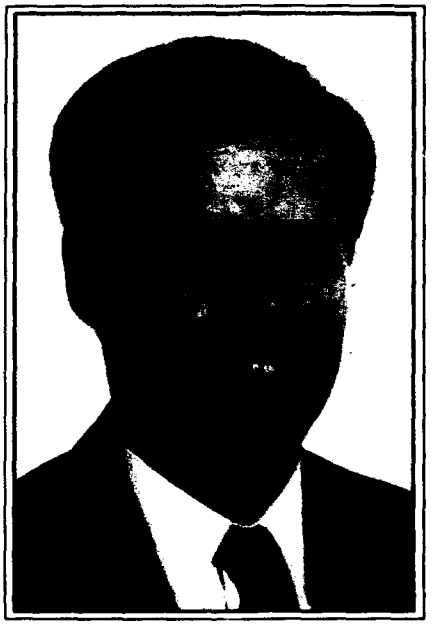
AUTHOR INDEX 1101

SUBJECT INDEX 1107

MATERIALS RESEARCH SOCIETY SYMPOSIUM PROCEEDINGS 1113

*Invited Paper

Dedication



Dr. Donald R. Ulrich
1936 - 1990

The entire scientific community is saddened by the tragic death of our colleague, co-editor of this volume, Dr. Donald R. Ulrich. Don was instrumental in establishing and nurturing research into the area of chemical synthesis of ceramics. Through his vision and imagination he supported the efforts of scientists from around the world and provided them with a forum for discussion of the progress and promise of this exciting field. The explosive rate of scientific achievement and technological development experienced by this field during the last decade was due, in large part, to his efforts. His leadership and support played a critical role in the development and success of this symposium series. In recognition of his many efforts to promote **Better Ceramics Through Chemistry**, this volume is dedicated to him.

Preface

The fourth meeting of the Materials Research Society Symposium on Better Ceramics Through Chemistry was held in San Francisco, California, April 16-20, 1990. This volume contains a majority of the papers presented at that meeting. The symposium is held biennially and the proceedings of previous meetings appear as Volumes 32, 73, and 121 of the MRS Symposium Proceedings Series. The Better Ceramics Through Chemistry Symposium Series is funded by the Air Force Office of Scientific Research. This year, additional funding was provided by Gelest Inc.

As in past years, the intention of this symposium was to provide a forum for scientists and engineers from a diversity of backgrounds to discuss sol-gel, solution processing and other synthetic chemical techniques for engineering new or improved ceramics on a molecular level. The appropriateness of this interdisciplinary approach to research on chemically engineered ceramics is validated by the steady and vigorous growth in symposium participation. Each successive Better Ceramics Through Chemistry Symposium has experienced an increase of between 30 and 60 in the number of papers presented at the meeting.

At this year's meeting, research into the area of reaction mechanisms and kinetics of silicon species remained strong, while significant advances in the area of structure and properties of modified and unmodified metal alkoxide species were reported. The complementary area of processing in water based systems also received considerable attention with emphasis being placed on the hydrolysis behavior of ions in solution. The nature of particle/aggregate growth was also a major topic of discussion with papers being presented on the role of aggregation in particle growth and on the nature and rheology of concentrated suspensions. Important developments in the area of mechanical properties of aerogels, fibers and films were presented as well as research into techniques for in situ monitoring of films during dip coating. Continued advances in applications which utilize solution derived ceramics were also reported. These applications included GRIN lenses, planar waveguides, optical filters and switches, transpiration cooled windows, dye-polymer composites for nonlinear optics, dielectrics and electrooptic materials including PLZT's and the niobates, and chemical sensors. Finally, one of the meeting highlights was a special evening session on biomimetics: ceramic processing in natural systems.

One hundred ninety-one papers were presented either orally or as posters. One hundred fifty-nine of the presented papers appear here. All papers were subjected to a peer review after which the authors had an opportunity to respond to the reviewer's comments. Because a primary goal of the editors was rapid publication, the revised papers were accepted without

further revision. Thus the papers which comprise this volume reflect the views and standards of the authors and not necessarily those of the editors.

Brian J.J. Zelinski
C. Jeffrey Brinker
David E. Clark
Donald R. Ulrich

August 21, 1990

Acknowledgments

We wish to express our appreciation to all of the symposium contributors. In particular, the invited speakers presented excellent papers which formed the nuclei for discussions of the various topics covered at this symposium.

Successful presentation of the program was due in large part to the efforts of our session chairs including: Paul Calvert, Ilhan Aksay, George W. Scherer, Jon K. West, Emmanuel P. Giannelis, George Kordas, Sharon M. Melpolder, Douglas M. Smith and Brian D. Fabes. Many thanks to these individuals for their assistance.

Also, the invaluable help provided by the entire staff of the Materials Research Society with respect to the financial, technical, operational and publication aspects of preparing a symposium and proceedings of this size is much appreciated. Also, the help of Geri Champagne and Pat Broyles of the Department of Materials Science and Engineering at the University of Arizona in preparing this manuscript is gratefully acknowledged.

One of the organizers, Brian J.J. Zelinski, would like to thank the remaining symposium chairs for the guidance and support he received from them during his involvement with this symposium.

Finally, the organizers gratefully acknowledge the financial support of the Air Force Office of Scientific Research and Gelest Inc.

MATERIALS RESEARCH SOCIETY SYMPOSIUM PROCEEDINGS

Recent Materials Research Society Symposium Proceedings

Volume 157—Beam-Solid Interactions: Physical Phenomena, J.A. Knapp, P. Borgesen, R.A. Zuhr, 1989, ISBN 1-55899-045-3

Volume 158—In-Situ Patterning: Selective Area Deposition and Etching, R. Rosenberg, A.F. Bernhardt, J.G. Black, 1989, ISBN 1-55899-046-1

Volume 159—Atomic Scale Structure of Interfaces, R.D. Bringans, R.M. Feenstra, J.M. Gibson, 1989, ISBN 1-55899-047-X

Volume 160—Layered Structures: Heteroepitaxy, Superlattices, Strain, and Metastability, B.W. Dodson, L.J. Schowalter, J.E. Cunningham, F.H. Pollak, 1989, ISBN 1-55899-048-8

Volume 161—Properties of II-VI Semiconductors: Bulk Crystals, Epitaxial Films, Quantum Well Structures and Dilute Magnetic Systems, J.F. Schetzina, F.J. Bartoli, Jr., H.F. Schaake, 1989, ISBN 1-55899-049-6

Volume 162—Diamond, Boron Nitride, Silicon Carbide and Related Wide Bandgap Semiconductors, J.T. Glass, R.F. Messier, N. Fujimori, 1989, ISBN 1-55899-050-X

Volume 163—Impurities, Defects and Diffusion in Semiconductors: Bulk and Layered Structures, J. Bernholc, E.E. Haller, D.J. Wolford, 1989, ISBN 1-55899-051-8

Volume 164—Materials Issues in Microcrystalline Semiconductors, P.M. Fauchet, C.C. Tsai, K. Tanaka, 1989, ISBN 1-55899-052-6

Volume 165—Characterization of Plasma-Enhanced CVD Processes, G. Lucovsky, D.E. Ibbotson, D.W. Hess, 1989, ISBN 1-55899-053-4

Volume 166—Neutron Scattering for Materials Science, S.M. Shapiro, S.C. Moss, J.D. Jorgensen, 1989, ISBN 1-55899-054-2

Volume 167—Advanced Electronic Packaging Materials, A. Barfknecht, J. Partridge, C-Y. Li, C.J. Chen, 1989, ISBN 1-55899-055-0

Volume 168—Chemical Vapor Deposition of Refractory Metals and Ceramics, T.M. Besmann, B.M. Gallois, 1989, ISBN 1-55899-056-9

Volume 169—High Temperature Superconductors: Fundamental Properties and Novel Materials Processing, J. Narayan, C.W. Chu, L.F. Schneemeyer, D.K. Christen, 1989, ISBN 1-55899-057-7

Volume 170—Tailored Interfaces in Composite Materials, C.G. Pantano, E.J.H. Chen, 1989, ISBN 1-55899-058-5

Volume 171—Polymer Based Molecular Composites, D.W. Schaefer, J.E. Mark, 1989, ISBN 1-55899-059-3

Volume 172—Optical Fiber Materials and Processing, J.W. Fleming, G.H. Sigel, S. Takahashi, P.W. France, 1989, ISBN 1-55899-060-7

Volume 173—Electrical, Optical and Magnetic Properties of Organic Solid-State Materials, L.Y. Chiang, D.O. Cowan, P. Chaikin, 1989, ISBN 1-55899-061-5

Volume 174—Materials Synthesis Utilizing Biological Processes, M. Alper, P.D. Calvert, P.C. Rieke, 1989, ISBN 1-55899-062-3

Volume 175—Multi-Functional Materials, D.R. Ulrich, F.E. Karasz, A.J. Buckley, G. Gallagher-Daggitt, 1989, ISBN 1-55899-063-1

Volume 176—Scientific Basis for Nuclear Waste Management XIII, V.M. Oversby, P.W. Brown, 1989, ISBN 1-55899-064-X

Volume 177—Macromolecular Liquids, C.R. Safinya, S.A. Safran, P.A. Pincus, 1989, ISBN 1-55899-065-8

Volume 178—Fly Ash and Coal Conversion By-Products: Characterization, Utilization and Disposal VI, F.P. Glasser, R.L. Day, 1989, ISBN 1-55899-066-6

MATERIALS RESEARCH SOCIETY SYMPOSIUM PROCEEDINGS

Volume 179—Specialty Cements with Advanced Properties, H. Jennings, A.G. Landers, B.E. Scheetz, I. Odler, 1989, ISBN 1-55899-067-4

Volume 180—Better Ceramics Through Chemistry IV, C.J. Brinker, D.E. Clark, D.R. Ulrich, B.J.J. Zelinsky, 1990, ISBN: 1-55899-069-0

Volume 181—Advanced Metallizations in Microelectronics, A. Katz, S.P. Murarka, A. Appelbaum, 1990, ISBN: 1-55899-070-4

Volume 182—Polysilicon Thin Films and Interfaces, B. Raicu, T.Kamins, C.V. Thompson, 1990, ISBN: 1-55899-071-2

Volume 183—High-Resolution Electron Microscopy of Defects in Materials, R. Sinclair, D.J. Smith, U. Dahmen, 1990, ISBN: 1-55899-072-0

Volume 184—Degradation Mechanisms in III-V Compound Semiconductor Devices and Structures, V. Swaminathan, S.J. Pearton, O. Manasreh, 1990, ISBN: 1-55899-073-9

Volume 185—Materials Issues in Art and Archaeology II, J.R. Druzik, P.B. Vandiver, G. Wheeler, 1990, ISBN: 1-55899-074-7

Volume 186—Alloy Phase Stability and Design, G.M. Stocks, D.P. Pope, A.F. Giamei, 1990, ISBN: 1-55899-075-5

Volume 187—Thin Film Structures and Phase Stability, B.M. Clemens, W.L. Johnson, 1990, ISBN: 1-55899-076-3

Volume 188—Thin Films: Stresses and Mechanical Properties II, W.C. Oliver, M. Doerner, G.M. Pharr, F.R. Brotzen, 1990, ISBN: 1-55899-077-1

Volume 189—Microwave Processing of Materials II, W.B. Snyder, W.H. Sutton, D.L. Johnson, M.F. Iskander, 1990, ISBN: 1-55899-078-X

Volume 190—Plasma Processing and Synthesis of Materials III, D. Apelian, J. Szekely, 1990, ISBN: 1-55899-079-8

Volume 191—Laser Ablation for Materials Synthesis, D.C. Paine, J.C. Bravman, 1990, ISBN: 1-55899-080-1

Volume 192—Amorphous Silicon Technology, P.C. Taylor, M.J. Thompson, P.G. LeComber, Y. Hamakawa, A. Madan, 1990, ISBN: 1-55899-081-X

Volume 193—Atomic Scale Calculations of Structure in Materials, M.A. Schluter, M.S. Daw, 1990, ISBN: 1-55899-082-8

Volume 194—Intermetallic Matrix Composites, D.L. Anton, R. McMeeking, D. Miracle, P. Martin, 1990, ISBN: 1-55899-083-6

Volume 195—Physical Phenomena in Granular Materials, T.H. Geballe, P. Sheng, G.D. Cody, 1990, ISBN: 1-55899-084-4

Volume 196—Superplasticity in Metals, Ceramics, and Intermetallics, M.J. Mayo, J. Wadsworth, M. Kobayashi, A.K. Mukherjee, 1990, ISBN: 1-55899-085-2

Volume 197—Materials Interactions Relevant to the Pulp, Paper, and Wood Industries, J.D. Passaretti, D. Caulfield, R. Roy, V. Setterholm, 1990, ISBN: 1-55899-086-0

Volume 198—Epitaxial Heterostructures, D.W. Shaw, J.C. Bean, V.G. Keramidas, P.S. Peercy, 1990, ISBN: 1-55899-087-9

Volume 199—Workshop on Specimen Preparation for Transmission Electron Microscopy of Materials II, R. Anderson, 1990, ISBN: 1-55899-088-7

Volume 200—Ferroelectric Thin Films, A.I. Kingon, E.R. Myers, 1990, ISBN: 1-55899-089-5

Earlier Materials Research Society Symposium Proceedings listed in the back.

PART I

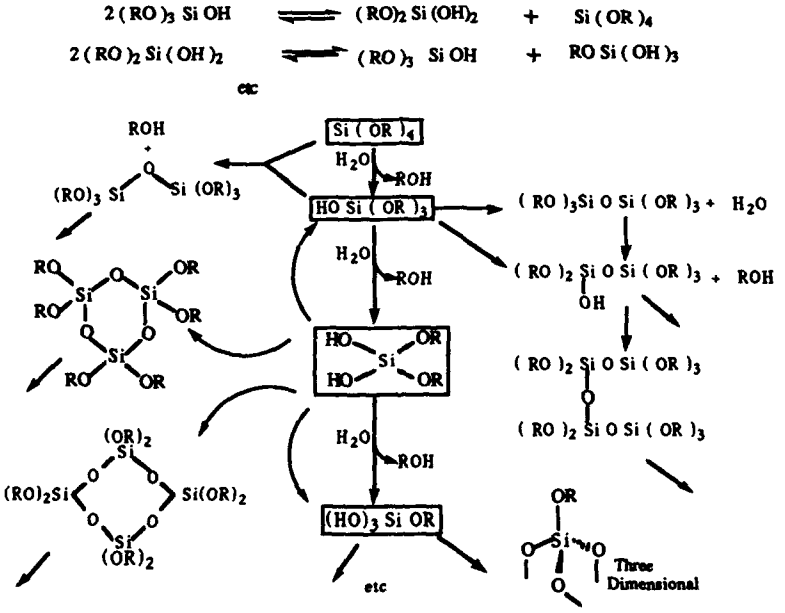
Reaction Mechanisms and Kinetics

SOL-GEL CHEMISTRY OF HYDROGENOSILICONATES:THE ROLE OF HYPERVALENT SILICON SPECIES

V.BELOT, R. CORRIU, C. GUERIN, B. HENNER, D. LECLERCQ, H. MUTIN, A. VIOUX, Q.WANG

Unité Mixte CNRS, Rhône Poulenc, USTL n° 44 Université de Montpellier II Place E. Bataillon 34095 Montpellier Cedex 05

The hydrolysis of organic silicates (mainly $Si(OEt)_4$: [TEOS] and $Si(OMe)_4$: [TMOS]) is the key reaction in sol gel process for preparation of silica. The mechanism of this reaction is not well known because of the competition taking place between hydrolysis itself and condensation reactions (homo or heterocondensations) but also because of redistribution reactions which take place competitively. Furthermore the competition between these steps depends also on the catalysis (acid,basic or nucleophilic) [1, 3] .



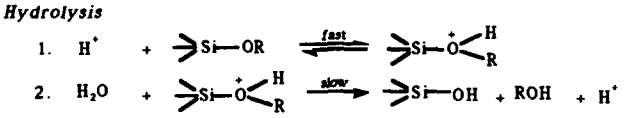
The lack of kinetic studies originates from the great difficulty to have an accurate measure of the concentration of the species which are formed at each step.

Concerning the nature of the intermediates formed during the first step in basic or acidic conditions, some indications can be obtained from previous studies performed in the field of organosilicon- chemistry in the case of mono and dialkoxysilanes [4]. Both acid and basic catalysis involve the nucleophilic attack of water on the electrophilic silicon. This is commonly accepted by organosilicon chemists and the experimental facts

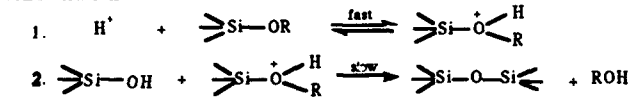
Mat. Res. Soc. Symp. Proc. Vol. 180. ©1990 Materials Research Society

obtained by AELION [2] in the hydrolysis of silicates as well as those obtained by GRUBB [3] concerning siloxanes are in agreement with this mechanism.

Hydrolysis

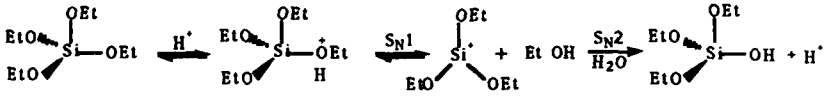


Condensation

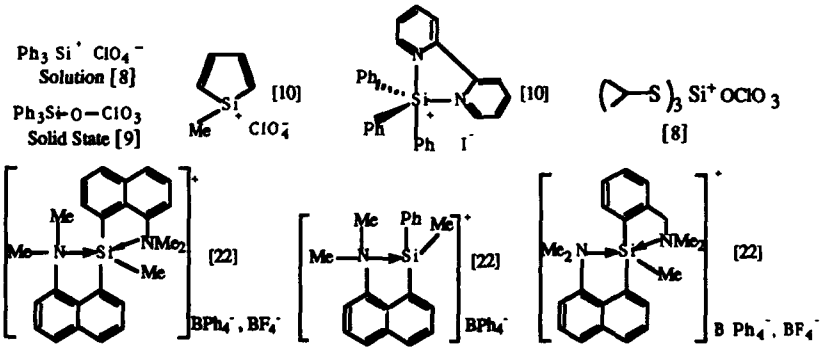


In acid catalysis the first step is a fast and reversible protonation of the alkoxy group which increases the capability of this group to be displaced by nucleophilic reagent. This S_N2 type reaction in acid catalysis is well illustrated by EABORN [5] who observed a racemisation rate two times faster than the exchange rate in labelling exchange reactions of optically active alkoxysilanes.

Some authors have proposed the possibility of an S_N1 reaction involving tricoordinate silicenium ions $(RO)_3Si^+$ [6].



This proposition cannot be eliminated *stricto sensu* because of the lack of experimental studies on tetraalkoxysilanes. However it is unlikely in view of the general literature of organosilicon chemistry [7-10]. Silicenium ions have been unambiguously observed in the gas phase but they have been reported only in very rare and particular cases in solution [8, 10]. Very recently triphenylsilyl perchlorate has been shown to be covalent in the solid state [9]. However the dissociation into a closed ionic pair in solution has been postulated [8]. Furthermore many organosilicon chemists have attempted to isolate this species without any success [7] and even in super acidic conditions it was not posssible to isolate and identify silicenium ions [10].



From this consideration and taking into account the weak acid conditions used in sol gel chemistry, the most probable mechanism for the hydrolysis of Si-OR bond appears to be the S_N2 type .

In basic conditions, the first step can be considered as a pure nucleophilic displacement at silicon in which the increase of the rate due to the catalyst corresponds to an increase of the nucleophilicity of the reagent: OH^- instead of H_2O.

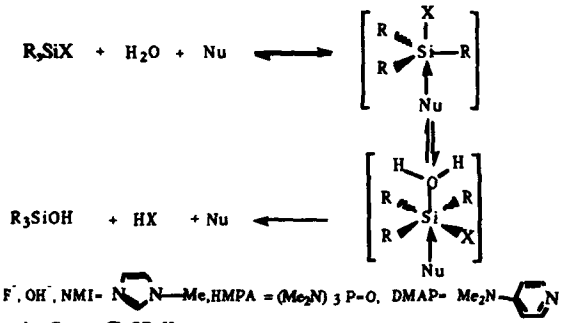
Hydrolysis

1. $OH^- + \equiv Si-OR \xrightarrow{slow} \equiv Si-OH + OR^-$
2. $OR^- + H_2O \xrightarrow{fast} ROH + OH^-$

Condensation

1. $\equiv Si-OH + OH^- \xrightarrow{fast} \equiv Si-O^- + H_2O$
2. $\equiv Si-O^- + \equiv Si-OR \xrightarrow{slow} \equiv Si-O-Si \equiv + OR^-$

However another possible explanation could be the nucleophilic activation taking place through hypervalent silicon species[11].



In this process the first step is the coordination of the base at silicon with formation of a pentacoordinated anionic silicate which reacts faster with water than the starting tetracoordinate silane [12, 13]. Experimental evidence has been supplied that hypervalent anionic species react towards nucleophiles faster than the corresponding tetracoordinated ones [13].

In the case of the sol gel process nucleophilic activation has been shown to be very efficient for the hydrolysis of silicates : anionic agents like F- ions, but also neutral donors like N-methylimidazole(NMI), dimethylaminopyridine (DMAP) or hexamethylphosphotriamide (HMPA) have been observed to be more efficient than the classical bases NaOH or KOH [14]. Thus it is particularly attractive to consider that OH^- could react as a nucleophile in the course of the hydrolysis of silicates.

The consideration of basic catalysis as a nucleophilic activation working through pentacoordinated silicon species has been supported by chemical theoretical calculations [15] which have shown that the formation of pentahydroxysilicates is a favorable process.

The same conclusions have been reached by calculations concerning the adducts of fluoride ion to silicic acid which have been found very stable , corresponding to a

high affinity of F^- towards silicates [16] in agreement with experiments previously reported in the activation of gelation process by F^- [14-17].

In order to test the hypothesis of pentacoordinated ionic species in basic catalysis we have prepared pentacoordinated siliconates using the DAMRAUER process [18]. Potassium alcoholates can be added to tetraalkoxysilanes in presence of 18 crown -6 ether. The following compounds have been obtained:

$$Si(OR)_4 + RO^-K^+/18\text{-crown-6} \longrightarrow Si(OR)_5^- K^+/18\text{ crown-6}$$
(R=Me, Et, Ph, iPr)

As an example, $Si(OEt)_5^- K^+$/18 crown-6 has been hydrolysed with neutral H_2O and we observe a very easy hydrolysis taking place with a gelation time only 11 minutes shorter than the time usually observed (a few hours).

The observation is in ageement with the mechanism involving extension of coordination at silicon. However in order to discriminate one of the groups during the hydrolysis reaction, and since the Si-H bond is a functional group, we have studied the hydroalkoxysilanes: $HSi(OR)_3$. The study of these precursors is interesting for the following aspects :

1- During the hydrolysis, the cleavage of the Si-H bond leads to the evolution of H_2 . In this way the hydrolysis of one functional group at silicon can be followed.

2- The Si-H bond is easily identified in solution and in the solid state by IR and NMR spectroscopy.

3- It is also interesting to prepare silica gels with functional groups Si-H still present in solid state. This gel could be used for chemical transformations on the solid itself.

In view of the possibility for pentacoordinated siliconates to be involved as intermediates during the basic catalysis, we have prepared hydridotetraalkoxysiliconates. The preparation of these compounds has been performed by addition of KOR on hydrotrialkoxysilanes[21]. The following adducts have been isolated and identified:

$$HSi(OR)_3 + ROK \longrightarrow H(Si\,OR)_4^- K^+ \quad (R=Me, Et, Ph, iPr)$$

Table I

^{29}Si NMR Spectral Data (THF as solvent)

Compound	δ ppm (d)	J (^1H-^{29}Si) Hz	Compound	δ ppm (d)	J (^1H-^{29}Si) Hz
$HSi(OMe)_3$	- 62, 6	290	$HSi(OPh)_3$	- 71, 3	320
$[HSi(OMe)_4]^-$	- 82, 5	223	$[HSi(OPh)_4]^-$	- 112, 6	296
$HSi(OEt)_3$	- 59, 1	285	$HSi(OiPr)_3$	- 63, 4	285
$[HSi(OEt)_4]^-$	- 86, 2	218	$[HSi(OiPr)_4]^-$	- 90, 5	215

We have studied the hydrolysis of these hypervalent siliconates. A very fast evolution of hydrogen takes place in presence of water and without any catalyst. The main results are listed table II.

Table II

$$[H\,Si\,(OR)_4]^-\,K^+ \;+\; 2\,H_2O \xrightarrow{THF} \text{Gel}$$

R	[C] M/l	Temp.	t Gel	Product
OMe	0.25	room T.	*	White Powder
	0.10	room T.	*	
		0°C		
	0.05	room T.	*	
		0°C		
OEt	0.50	room T.	*	White Powder
	0.25	room T.	≃5mn	Gel
	0.10	room T.	≃13mn	
OPh	0.10	room T.	*	Gel
	0.05	room T.	≃ 3mn	
OiPr	0.10	room T.	- 30h	Gel

*:Reaction occurs instantly IR spectroscopy shows no SiH bond in any of the products

The main observations are the following :

1- The gelation times observed for hypervalent species are always faster than the gelation times of the tetracoordinated trialkoxysilanes $H\,Si(OR)_3$.

2- The hydrolysis of $[HSi(OMe)_4]^-K^+$ is very fast even at low temperature and whatever the concentration of reagents. A viscous sol is formed at first which precipitates into white powder after a while.

3 - $[HSi(OEt)_4]^-K^+$ gives gels at low concentration : however at higher concentration only powder can be obtained.

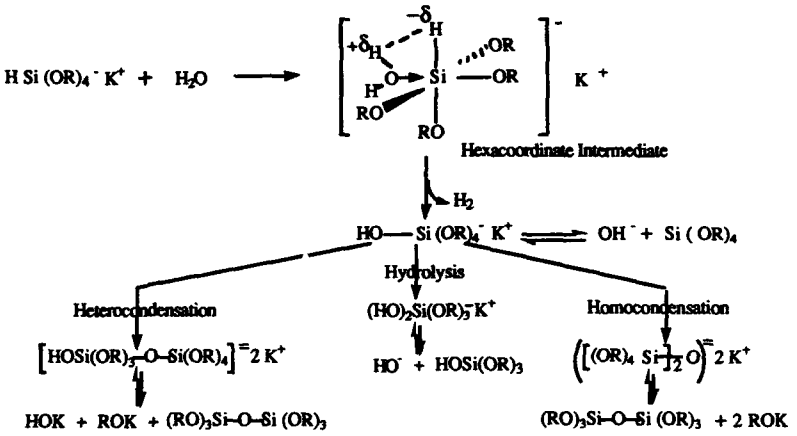
4 - $[HSi(OPh)_4]^-\,K^+$ is hydrolysed faster than $Si(OEt)_4$ leading to a gel. The high rate is certainly due to the better aptitude of Si-OPh as leaving group.

5- The case of $[HSi(OiPr)_4]^-K^+$ is more interesting since the evolution of H_2 takes place at first without any formation of neither a gel nor a powder. A monolithic gel is slowly formed after 30 hours.We can interpret this fact by a fast attack of water on the hypervalent siliconate taking place with displacement of the Si-H bond leading to a hydroxytetraalkoxysiliconate. Because of the steric hindrance of the isopropyl group, the hydrolysis of the Si - O iPr bond is slower and leads to a monolithic gel. In the case of the other hypervalent compounds, the competition between Si-H and Si-O displacement by water results in non monolithic gels since the evolution of H_2 is not complete when the gelation process occurs.

$$H\,Si\,(OR)_4^-\,K^+ + H_2O \longrightarrow HO\,Si\,(OR)_4^-K^+ + H_2\uparrow$$
$$H\,Si\,(OR)_4^-\,K^+ + H_2O \longrightarrow H\,Si(OR)_3(OH)^-K^+ + ROH$$

6- In all cases the infrared spectra of the gels obtained are similar : they contain free O-H groups and the Si-H absorption in the range of 2300 cm^{-1} is completely absent.Thus, the first step appears to be the nucleophilic attack of H_2O at silicon leading to an hydroxysiliconate with evolution of H_2 through an hexacoordinated intermediate in which the Si-O and the H-H bonds are formed . Interestingly this hydroxysiliconate corresponds to the possible intermediate [11-14] involved in the basic catalysis which has

been calculated as highly probable by Davies [15-16]. This hydroxysiliconate can undergo homo or heterocondensation or hydrolysis leading to the gel. All the anionic compounds proposed are in equilibrium with neutral species.



In order to identify the first step, we have studied the alcoholysis of the hydrogenosiliconates. The alcoholysis permits the stopping of the reaction after the first step since the condensation step is no longer possible.The reactions studied are the following :

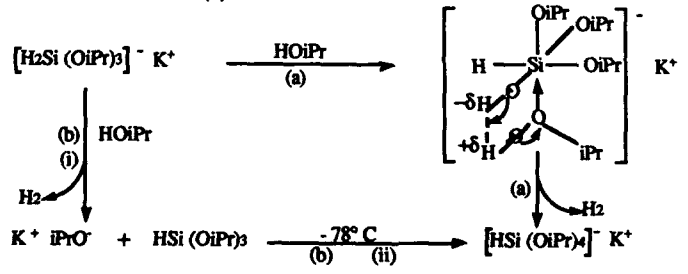
$$[H\text{-}Si(OR)_4]^- K^+ + ROH \xrightarrow[(R= Me, Et, Ph)]{18\text{-crown-}6} [Si(OR)5]^- K^+ / 18\text{-crown 6} + H_2\uparrow$$

In all cases we have observed the substitution of the Si- H bond by alcohol leading to pentacoordinated siliconates, $Si(OR)_5^- K^+$/18 - crown 6 from the starting hydridotetraalkoxysiliconates. This nucleophilic displacement at pentacoordinated silicon can also take place through a hexacoordinated intermediate. Evolution of H_2 is also observed with R = iPr. In order to study more in details this case, we have prepared $[H_2Si(OiPr)_3]^- K^+$ by addition of KH to $HSi(OiPr)_3$.

$$HSi(OiPr)_3 + KH \longrightarrow [H_2Si(OiPr)_3]^- K^+$$

The reaction with isopropanol leads to $[HSi(OiPr)_4]^- K^+$ with evolution of H_2. This reaction proceeds slowly at -78°C.

(a) Direct Substitution (b) Acid-Base Reaction



These results show that the mechanism proceeds through a direct substitution at silicon (path a), involving an hexacoordinate intermediate (or transition state). Indeed the alternative acid-base mechanism (path b) should proceed via two very fast steps: a deprotonation (i) and the subsequent coordination of RO^- to silicon (ii) . This step (ii) performed separately has been demonstrated to be very fast at - 78°C.Since the overall reaction observed with alcohol is slow, these results show that the mechanism proceeds through direct substitution at silicon (a).

In conclusion we have shown that hydrolysis of pentacoordinated compounds takes place via nucleophilic attack of water (or alcohols) on pentacoordinated silicon. This conclusion supports clearly the possible role of pentacoordinated species during the basic catalysis of hydrolysis of silicates .

It is also interesting to point out that the nucleophilic activation corroborates this observation : indeed F^-, formamide, NMI or DMAP which are very active catalysts in nucleophilic processes leading to the elimination of hydrogen in the reaction with HSi(OR)3 in presence of water [19].

Table

Time of gelation of $HSi(OR)_3$

Solvent	Methanol	Ethanol	Acetone		Dioxane	
Nature of R	CH_3	C_2H_5	CH_3	C_2H_5	CH_3	C_2H_5
Catalysts						
Without	4mn	16h	12h	24h	8h	48h
HCl	18mn	40h	55mn	16h	1h	16h
NH_4OH	1mn	↑	↑	↑	↑	↑
NH_4F	2h	↑	↑	↑	↑	↑

[Catalyst] = 0,2 x 10^{-6} mole/mole $HSi(OR)_3$ H_2O/ $HSi(OR)_3$ = 4

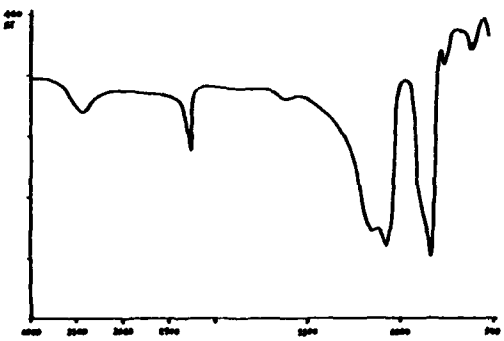
The arrow indicate the presence of hydrogen bubles in the solution.

The gelation of $HSi(OR)_3$ has been performed in different experimental conditions. Both basic catalysis (NH_4 OH) and nucleophilic catalysis (NH_4 F) provide evolution of H_2 in all cases with TEOS and only with dioxan as solvent for TMOS. The evolution of H_2 is in agreement with nucleophilic attack on a pentacoordinated intermediate, as developed previously. However neutral or acidic conditions permit the gelation of HSi(OR)3 without breaking of the Si-H bond.

The table illustrates the good parallel between nucleophilic and basic catalysis for displacement of the Si-H bond in the hydrolysis of $HSi(OR)_3$. The process corresponding to nucleophilic activation is well established as a mechanism involving extension of coordination at silicon followed by attack by nucleophiles (water in the case of sol-gel) on the pentacoordinated intermediate.This parallel supports the possibility of nucleophilic activation during the catalysis by bases.

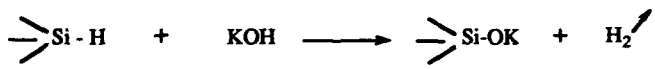
In acetone or dioxane as solvent it is possible to obtain monolithic gels. The gelation times are much faster than those observed with $Si(OR)_4$: for instance in neutral conditions, $HSi(OMe)_3$ gives a gel after 5 minutes instead of 30 days for $Si(OMe)_4$. The fact can be explained by the higher electrophilicity and lower steric hindrance of $HSi(OMe)_3$. The gels obtained contain H- Si bonds as illustrated by IR spectroscopy which exhibits absorptions at 2250 cm^{-1} for Si - H and at 830 cm^{-1} for Si- O (this absorption is at 800 cm^{-1} for $Si O_2$).

IR spectrum of $HSiO_{1.5}$



Interestingly the gels are hydrophobic illustrated by a very poor capacity to absorb water vapour. This capacity appears to be 25 time less than the absorption observed on silicagels: at 0.6 bar adsorption is 0,8% for $HSiO_{3/2}$ instead of 20% for silica.

The proportion of Si-H was quantitavely analysed by attack of the gel with KOH and measure of the volume of H_2 formed.



The results confirmed that the hydrolysis does not affect the Si-H bonds which remain present in the gel (theoretically: 1, 88 % ; found: 1,74 - 1,88 %)

The specific surface is always high (490 to 940 m^2/g) depending on the experimental conditions (solvent, catalysis, ratio of water) (conf. table). It is also interesting to point out the narrow porosity centered around 40 A°.

Table Surfaces $HSiO_{1.5}$

$HSi(OEt)_3 + H_2O$ (1.5 eq)

Solvent	[HSi(OR)3] mole/l	S m^2/g	% SiH (a)
Et OH	2.38	490	1.78 / 1.88
	4.84	640	1.65 /1.88
$(CH_3)_2CO$	2.38	870	1.3 /1.88
THF	2.38	900	1.34 /1.88

a) Percentage of SiH present in the gel determined by measure of H_2 obtained by alkaline attack

The solid state NMR exhibits a ^{29}Si resonance at - 86ppm.The T8H compound which has been prepared [20] as a model exhibits a ^{29}Si resonance absorption at - 85,3 ppm .This ^{29}Si NMR spectrum is completely different from the spectrum observed for SiO_2 (-110 ppm). All the analytical and spectroscopic data illustrate the formation of a solid having the stoichiometry $HSiO_{3/2}$ and containing the Si-H functionality at silicon .

Some preliminary studies concerning the chemical behaviour of the $HSiO_{3/2}$ gel have been performed. The Si-H bond which is a functional group for chemistry performed in solution, appears also to be very reactive in the solid state. This reactivity is displayed in the course of thermal treatment performed under argon or NH_3 and also during oxidation reactions.

1 - Thermal treatment under argon [24]

During the thermal treatment under argon an evolution of Si H_4 is observed between 350 and 480°C by Mass Spectroscopy coupled with TGA.The TGA curve exhibits two steps: one corresponds to the elimination of SiH_4,the second one concerns the evolution of H_2 between 400°and 700°C (cf. figure 1) [24]

The evolution of SiH_4 is an interesting phenomenon highly dependent on the conditions of preparation of the gel(solvent, catalysis drying method,):the weight of SiH_4 eliminated varies from 0,5% to 6 %.The elimination of SiH_4 can easily be explained by redistribution reactions which are very common processes in organosilicon chemistry. For instance H Si $(OR)_3$ undergoes redistribution with elimination of SiH_4 and formation of Si $(OR)_4$ in presence of either acids or bases.

$$2\ H\,Si(OR)_3 \rightleftharpoons H_2\,Si(OR)_2 + Si(OR)_4$$

$$H\,Si(OR)_3 + H_2\,Si(OR)_2 \rightleftharpoons H_3SiOR + Si(OR)_4$$

$$H\,Si(OR)_3 + H_3Si(OR) \rightleftharpoons Si\,H_4 + Si(OR)_4$$

The proof of occurence of this redistribution in the solid state is afforded by solid state NMR which exhibits the signals of H_2SiO and SiO_2 besides the signal of $HSiO_{3/2}$ (Figure 2)

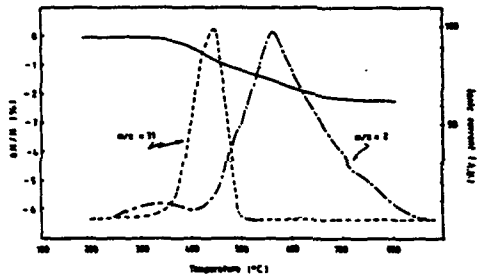
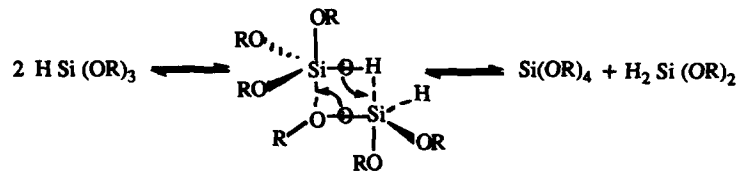
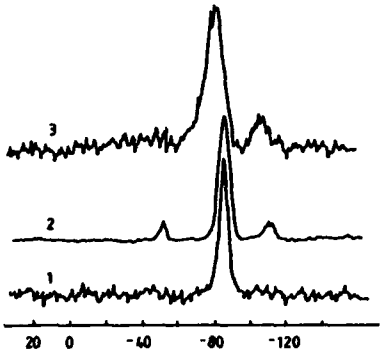


fig. 1 : TG-MS analysis of a gel $HSiO_{1.5}$ under argon at 10°C/min . —— : TGA trace, ... SiH_4 evolution, – . – H_2 evolution

The redistribution is known to be a bimolecular reaction in solution, involving pentacoordinated silicon atoms.



It is interesting to point out : (1) the possible formation of such intermediates in solid state where the molecular movements are restricted; (2) the importance of the preparation conditions, since evolution of 6% SiH_4 corresponds to a loss of 24 % of Si - H bonds in the gel.



(Figure 2)
^{29}Si solid state NMR spectra of gel $HSiO_{1.5}$. [23]

1: non heated
2: heated 20mn at 405°C
3: heated 20mn at 665°C

- 110 ppm SiO_2
- 85 ppm $HSiO_{3/2}$
- 45 ppm H_2SiO

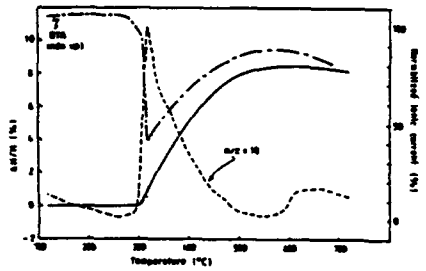


fig. 3 : TG.MS analysis of a gel $HSiO_{1.5}$ under air at 10°C/mn
— : TGA trace, —. — DTA trace, ... : H_2O evolution

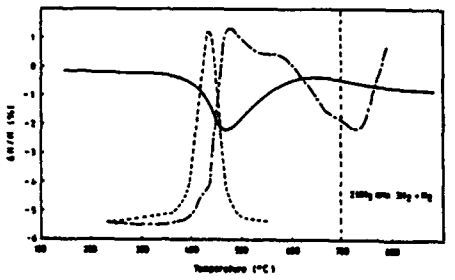


fig. 4 : TG.MS analysis of a gel $SiO_{1.5}$ under NH_3 . — TGA trace
--- SiH_4 evolution, — . — H_2 evolution

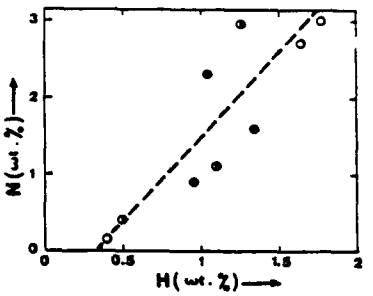


fig. 5 : Variation of nitrogen content with hydrogen content of the starting xerogel

2 - Oxidation reactions

The reactivity towards oxygen is very high as expected because of the high affinity of silicon towards oxygen. The thermal treatment has been carried out in air[19]. The TGA curve exhibits two oxidation steps at 400°C and 500°C each of them corresponds to an exothermic reaction as shown by TDA . At the same temperatures much evolution of water is observed by Mass Spectroscopy.(Figure 3)

The highly exothermic reaction observed at 400°C corresponds to the oxidation of SiH_4, the evolution of which was observed under inert atmosphere at the same temperature (cf fig 1) and which is immediately oxidized in air

$$Si\,H_4 + 2\,O_2 \longrightarrow 2\,H_2O + Si\,O_2$$

At 500° the exothermic reaction corresponds to the oxidation of Si-H bond.

$$\gtrless Si-H + O_2 \longrightarrow \gtrless Si-O-Si\lessgtr + H_2O$$

$$2 \gtrless Si-O-H \longrightarrow \gtrless Si-O-Si\lessgtr + H_2O$$

In fact this oxidation takes place between 350° and 700° as observed by evolution of H_2 during the thermal treatment under inert conditions and also by the TGA curve which exhibits an increase in weight of 8% between 350° and 700°. The oxidation of SiH starts even before the evolution of SiH_4, illustrating the very high reactivity of this functional gel towards oxygen.

3 - Thermal treatment under NH3

When the gel is heated under NH_3 silicon oxynitride is formed due to the high reactivity of theSi-H bond towards NH_3. The Fig 4 shows the TGA curve and the mass spectroscopic analysis of the gases formed during the reaction.

At 400°C,the TGA curve exhibits a loss of weight of 1,5% corresponding to the evolution of $Si\,H_4$. At the same temperature the evolution of H_2 starts and continues until 700°. In the TGA curve between 450° and 600°, we observed an increase of weight about 2% corresponding to the formation of Si-N bonds. From 700°C a small weight loss (0,2%) is observed.

The increase in weight observed in spite of the evolution of H_2 corresponds to the nitruration and can be determined by chemical analysis.The percentage of nitrogen in the gel,determined by chemical analysis following the Kjeldahl Method, depends on the percentage of SiH bond initially included in the gel and remaining after evolution of SiH_4 (fig. 5).

The amination reaction can be explained by the following reactions:

$$O_{3/2}\,Si-H + NH_3 \longrightarrow O_{3/2}\,Si-NH_2 + 1/2\,H_2\uparrow$$

$$O_{3/2}\,Si-NH2 + HSiO_{3/2} \longrightarrow O_{3/2}\,Si-NH-SiO_{3/2} + 1/2\,H_2\uparrow$$

In the last step the small loss of weight observed above 700°C can be explained by the formation of trisilylated amine by transamination reactions which implies evolution of NH_3.

$$2\,O_{3/2}\,Si-NH-SiO_{3/2} \longrightarrow (O_{3/2}\,Si)_3-N + SiO_{3/2}-NH_2$$

$$O_{3/2}\,Si-NH-SiO_{3/2} + O_{3/2}\,Si-NH_2 \longrightarrow (O_{3/2}\,Si)_3-N + NH_3\uparrow$$

In conclusion we have illustrated the possible occurrence of pentacoordinate intermediates during the hydrolysis of silicates catalysed by bases. We have also found a way to obtain silica gels containing the functional Si - H bond.This functionality allows the reaction of the gels with oxygen and NH_3, and also some rearrangements in the solid state.

REFERENCES

1 - C. Eaborn, Organosilicon compounds, (Butterworths, London) 1960 ; D. W. Scott J. Am. Chem. Soc. 68, 2294 (1946) ; S.W. Kantor, W.T. Grubb, R.C. Osthoff, ibid.

74, 5190 (1954) ; R.K. Iler ; The chemistry of Silica, (Wiley, New-York) 1979.
2 - R. Aelion, A. Loebel, F. Heirich, Rec. Trav. Chim. 69, 61 (1950) ; J. Am. Chem. Soc. 72, 5705 (1950).
3 - W.T. Grubb, J. Am. Chem. Soc. 76, 3408 (1954).
4 - H. Schmidt, A. Kaiser, Glastechn. Ber. 54, 338 (1981) ; H. Schmidt, H. Scholze, A. Kaiser, J. Non Cryst. Solids 48, 65 (1981) ; I.G. Khaskin, Dokl. Akad. Nauk. SSSR 85, 129 (1952) ; C.G. Swain, R.M. Esteve Jr., R.H. Jones, J. Amer. Chem. Soc. 71, 965 (1949) ; L.H. Sommer, C.F. Frye and al., J. Amer. Chem. Soc. 83, 2210 (1961) ; ibid 82, 3796 (1960).
5 - R. Baker, R.W. Bott, C. Eaborn, P.W. Jones, J. Organomet. Chem. 1, 37 (1963)./
6 - S.S. Jada, J. Am. Ceram. Soc. 70, C 298 (1987).
7 - L.D. David, J. Am. Ceram. Soc. 71, C 412 (1988).
8 - J.B. Lambert in the Chemistry of Organic Silicon Compounds - Part 1 - Ed. by S. Patai and Z. Rappoport (John Wiley and Sons Publishers) 1989, p. 1007 and ref. therein ; J. Am. Chem. Soc. 110, 2201 (1988).
9 - G.K. Suryaprakash, S. Keyaniyan, R. Aniszfeld, L. Heiliger, G.A. Olah, R.C. Stevens, H-K Choi, R. Bau, J. Am. Chem. Soc. 109, 5123 (1987).
10 - R. Corriu, M. Henner, J. Organomet. Chem. 74, 1 (1974) and ref. therein ; J.B. Lambert, H. nSun, J. Am. Chem. Soc. 98, 5611 (1976) ; T.J. Barton, A.K. Hovland, C.R. Tully, ibid. 98, 5695 (1976) ; G.A. Olah, L.D. Field, Organometallics 1, 1485 (1982) ; J.Y. Corey, R. West, J. Amer. Chem Soc. 85, 4034 (1963); A. Balasingam, P. Boudjouk, 8e Int. Symp. Organosi Chem. St Louis, Missouri June 1987, Abstract PAB 21 p. 178 ; G.A. Olah, D.H. O'Brien, ; C.Y. Lui, J. Am. Chem. Soc. 91, 701 (1969).
11 - R.J.P. Corriu, G. Dabosi, M. Martineau, J. Organomet. Chem. 150, 27 (1978) ; 154, 33 (1978) 186, 256 (1980).
12 - S.E. Johnson, J.A. Deiters, R.O. Day , R.R. Holmes, J. Am. Chem. Soc. 111, 3250 (1989).
13 - R.J.P. Corriu, C. Guérin, B.J.L. Henner, W.W.C. Wong Chi Man, Organometallics 7 237 (1988).
14 - R.J.P. Corriu, D. Leclercq, A. Vioux, M. Pauthe, J. Phalippou in Ultrastructure Processing of Advanced Ceramics ed. by J.D. Mackenzie, D.R. Ulrich (John Wiley and sons Publishers 1988) p. 113.
15 - L.P. Davis, L.W. Burgraf in Ultrastructure Processing of Advanced Ceramics ed. by . J.D. Mackenzie, D.R Ulrich (John Wiley and Sons Publishers 1988) p. 367 ; L.W. Burgraf, L.P. Davis, M.S. Gordon Topics in Physical Organometallic Chem. 3 (1990) in press and ref. therein.
16 - L.P.Davis, L.W. Burgraf, M.S. Gordon, K.K. Baldridge, J. Am. Chem. Soc. 107, 4415 (1985).
17 - E.M. Rabinovich, D.L. Wood, Mater. Res. Soc. 73, 251 (1986) ; E.J.A. Pope, J.D. Mackenzie, J. Non-Cryst. Solids. 87, 185 (1986) ; C. Caslouska, P. Gron, Caries Res. 18, 354 (1984).
18 - R. Damrauer, S.E. Danahey, Organometallics 5, 1490 (1986).
19 - M. Pauthe, J. Phalippou, R. Corriu, D. Leclercq, A. Vioux, Journal of Non-Cryst. Solids 113, 21 (1989).
20 - C.L. Frye, W.T. Collins, J. Am. Chem. Soc. 92, 5586 (1970).
21 - B. Becker, R. Corriu, C. Guérin, B. Henner, Q. Wang, J. Organomet. Chem. 359, C33-C35- (1989) ; R. Corriu, C. Guérin, B. Henner, Q. Wang, J. Organomet. Chem. 365, C7- C10 (1989) ; B. Becker, R. Corriu, C. Guérin, B. Henner, Q. Wang, J. Organomet. Chem. 368 (1989) C25-C28.
22 - C. Brelière, R. Corriu, G. Royo, W.W.C. Wong Chi Man, J. Zwecker, J. Organomet. Chem. (submitted for publication).
23 - D.Seyferth, C. Prud'Homme, C.H. Wiseman, Inorg. Chem. 22, 2163 (1983) ; H.G. Horn, H.C. Marsmann, Makromol. Chem. 162, 255 (1972).
24 - R.J.P. Corriu, D. Leclercq, H. Mutin, A. Vioux, J. Mater-Sci Letters (in press) ; M. Pauthe, J. Phalippou, V. Belot, R. Corriu, D. Leclercq, A. Vioux, J. Non-Cryst. Solids (submitted for publication)

HIGH PRESSURE RAMAN STUDY OF THE HYDROLYSIS REACTION OF TMOS AND TEOS

G. HOANG, J. WATSON and T. W. ZERDA
Physics Department, Texas Christian University, Fort Worth, TX 76129

ABSTRACT

High pressure Raman spectroscopy is used to monitor the hydrolysis reaction of TMOS in solutions with methanol, acetonitrile, acetone, dioxane and formamide, and of TEOS as a function of pH and the catalyst used. The rate constants for various solvents, temperatures and pressures are experimentally determined from the time dependence of Raman band intensities. It is shown that the reaction is slow in dioxane and fast in methanol or formamide. The volume of activation is found from the pressure dependence of the rate constant. The volume of activation, the dielectric constant, dipole moments and hydrogen bonding properties and their role in the hydrolysis reaction are discussed. It is shown that solvents which can form hydrogen bonding with Si-OR groups can increase the rate of the reaction.

INTRODUCTION

The hydrolysis reaction, the first step of the sol-gel processing, has been studied both theoretically [1,2] and experimentally. Different experimental techniques, such as NMR [3-5], Raman [3,6,7], UV absorption [8], and chromatography [9] have been used. It is now generally accepted that hydrolysis proceeds by bimolecular nucleophilic displacement reactions (S_N2 reactions) involving pentacoordinate intermediates [10]. However, there are still unanswered questions relating the details of the role of the solvents.

Previously, we studied the effects of pH of water, temperature, pressure, and solvent on the hydrolysis reaction of TMOS [6,7]. Using high pressure Raman spectroscopy we determined the volume of activation, and we provided evidence for the pentavalent intermediate. In this report, we examine the effect of the dielectric constant, dipole moment and hydrogen bonding on the reaction rate.

The overall hydrolysis reaction of alkoxide can be written as:

$$Si(OR)_4 + nH_2O \rightarrow Si(OR)_{4-n}(OH)_n + nROH \qquad (1)$$

where n varies from 1 to 4, and OR represents an alkoxide group. We studied the band due to Si-OR vibrations located at about 645 cm^{-1} for TMOS and at about 656 cm^{-1} for TEOS. The intensity of the Raman band is proportional to the concentration of the molecules in the system. The decay in time of the Si-OR vibrational band, due to the consumption of alkoxides by water molecules, can be used to characterize the reaction rate. For a system with an excess of water, one may assume that reaction (1) is a quasi-first order reaction and the rate, k, can be found from

$$\ln I(t) = - kt + \text{const.} \qquad (2)$$

where I is the intensity of the Si-OR band, and t is time elapsed.

When only a small amount of water is used, alcohol producing condensation may decrease the the number of silicon alkoxides in the system [5]. In order to find the reaction rate, the concentrations of water have to be known at a given time, then it can be found from the intensity of the C-O band of alcohol. The rate is then found from the second order kinetics.

The rate constant increases with pressure, and from that dependence, one can find the volume of activation [6,11]

$$\Delta V^{\#} = - \lim_{p \rightarrow 0} RT(d \ln k / dp) \qquad (3)$$

The volume of activation is defined as the difference between the volume of the reactants and the volume of the intermediate state, and the data on $\Delta V^{\#}$ can be used to provide a mechanistic model for the reaction. Typically, the reaction rates are known for a limited number of pressures; so to improve the accuracy of the value of $\Delta V^{\#}$, the dependence of ln k(p) is approximated by an empirical function. A number of empirical functions have been proposed; they all lead to similar results. In this study we used the Asano function [11]:

$$\ln(k_p/k_0) = ap + b\{\ln(1 + cp)\} \qquad (4)$$

Mat. Res. Soc. Symp. Proc. Vol. 180. ©1990 Materials Research Society

where a, b, and c are constants, and k_p and k_o are the rate constants at pressure p and at normal pressure, respectively. The data for the volume of activation reported in this paper were obtained from Eq. 3, where the ln k was approximated by the Asano formula.

EXPERIMENTAL

Throughout the experiment, the samples of sol-gels were prepared by adding a premixed water/alcohol solution drop by drop to the solution of TEOS/ ethanol under vigorous stirring. In the first set of experiments, the effects of molar ratios of TEOS: ethanol: water were examined by comparing reaction rates for the ratios 1:7.5:10 and 1:1.4:1. Also the effect of the pH of water was examined by comparing reaction rates for water of pH 2.54 versus pH 4.9. The pH of water was adjusted by using HF or HCl and was measured using a Hach free-flowing reference junction electrode with accuracy better than 0.01.

In another series of experiments, we compared rate constants obtained for the samples prepared at the same pH values and adjusted by the same acid, but for different silicon alkoxides. Tetramethylorthosilicate, TMOS, was premixed with methanol and added to the water/methanol mixture of pH = 4.9, and the results obtained for this mixture were compared with those obtained for TEOS mixed with ethanol and water at pH ≈ 4.9.

In order to investigate the effects of additives on the reaction, we added acetone, acetonitrile, dioxane or formamide to mixtures of TMOS, methanol and water. For experimental reasons, this set of measurements was done at pH of water equal to 6.0.

After preparation, the samples were immediately placed in a scattering cell, and Raman spectra were recorded at equal time intervals. Raman spectra were taken using an argon ion laser operating at 488 nm at a power of 600 mW and a Spex 14018 double monochromator with a photo-counting system. An IBM computer was used for data acquisition and instrument control. No polarizer or analyzer was used; only non-polarized spectra were recorded by the monochromator.

To avoid interactions with metal walls of the scattering chamber, the solutions were placed inside glass inserts closed with a movable piston. The pressure was transmitted into the cell by an alcohol which pushed the piston into the insert. A constant temperature was maintained inside the cell to avoid temperature fluctuations that can affect the hydrolysis reaction. The high pressure measurements were taken at temperatures of 298 or 280 K. All the measurements were repeated at least four times. The details of the experimental setup are provided in Ref. 6.

The dielectric constant was measured using a stainless steel precision capacitor and a Hewlett-Packard 4268 universal bridge. Accuracy of dielectric constant measurements was better than 5%.

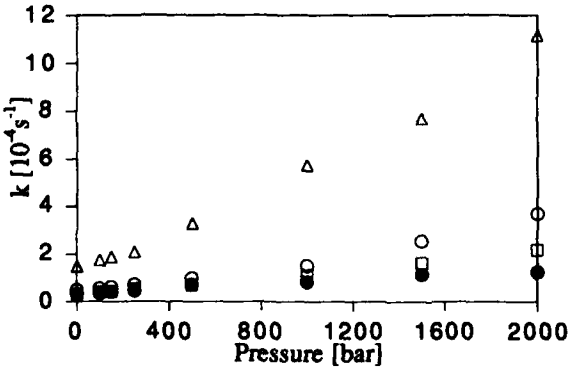


Fig. 1. Pressure dependence of rate constants for TMOS in solutions with dioxane ●, methanol O formamide Δ, acetone □. Molar ratio of TMOS:water:solvent was 1:7.5:10. pH = 6.0.

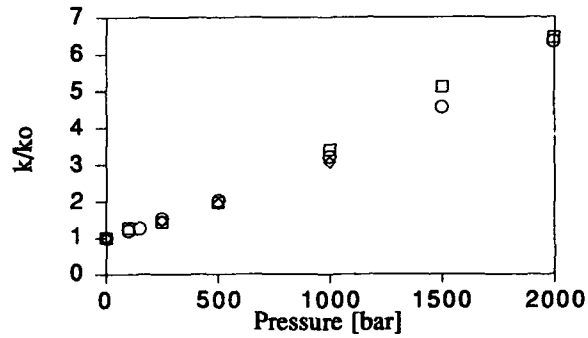


Fig. 2. Reduced rate constants for hydrolysis of TMOS (squares) and TEOS (circles and diamonds). pH = 2.54 was adjusted using HCl (squares and diamonds) and HF (circles).

RESULTS

The pressure dependence of the hydrolysis rate for TMOS in different solutions is illustrated in Fig. 1. It is seen that the fastest reaction occurs in formamide, and the slowest rate is observed in dioxane. Our finding that formamide accelerates the hydrolysis reaction is consistent with that previously reported by Artaki et al.[3,11] and Orcel [12], who reported their findings on the reduced time scale. Dioxane is miscible with TMOS and water at any concentration, and it is possible to study the reaction rate in the solution containing only TMOS, water and dioxane. For this mixture, we observed the lowest reaction rate of 3.89×10^{-6} s^{-1}. As dioxane is replaced by methanol, the rate of the reaction increases to 27.2×10^{-6} s^{-1}.

As expected, for the same solvent and identical molar ratio of water to alkoxide, and using water of the same pH, the speed of the hydrolysis reaction of TEOS was found to be about 50 times slower than that of TMOS. For example, the rate is 6.1×10^{-5} s^{-1} for TEOS and 1.42×10^{-3} for TMOS when the alkoxide to alcohol to water molar ratio is 1:7.5:10. As explained by Aelion et al. [13], the difference in reaction rates is the results of steric hindrance effects, which are stronger in TEOS than in TMOS. In Fig. 2 we have plotted normalized rates, k/k_o, for both TEOS and TMOS as a function of pressure. It is seen that the pressure dependence of rate constants obtained with different acids and alkoxides are similar. The pressure dependence of the rate constant enabled finding the volume of activation, which for TEOS was found to be independent of catalysts used and equal -45 cm^3/mol. The data on the volume of activation are summarized in Table 1.

Table 1. The volume of activation for hydrolysis reaction of TMOS in different solvents

	TMOS					TEOS
	Methanol	Methanol+ Acetone	Methanol+ Acetonitrile	Methanol+ Dioxane	Methanol+ Formamide	Ethanol
$\Delta V^{\#}$	-42.1±5	-39.8±2	-45.4±2	-40.8±2	-43.5±2	-45.3±4

DISCUSSION

We found that there is no correlation between the dipole moment and the reaction rate. For dioxane, a molecule with no dipole moment, the reaction is very slow, and for formamide, a solvent with large dipole moment of 3.73 Debye, the reaction is relatively fast. It seems reasonable to expect that for acetonitrile, a molecule of a large dipole moment (μ=3.92 D)

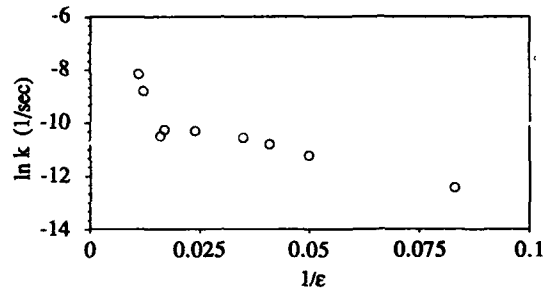


Fig. 3. Hydrolysis rate versus dielectric constant.

comparable to that of formamide, the reaction also should be fast, but in contrast, the experimental results show that the reaction is slow, and is even slower than that observed in acetone of smaller dipole moment, μ= 2.88 D; moreover, it is also slower than in methanol of a dipole moment μ= 1.70 D. Although the role of the dipole moment cannot be ignored, it does not seem likely that dipolar forces play an important role in the hydrolysis reaction.

Rate of reactions between neutral molecules and ions may be estimated from a simple electrostatic theory [14] as

$$\ln k = \ln k_o + \frac{A}{\varepsilon} \qquad (5)$$

where A is a constant that depends on electrostatic charges and radii of ions and activated complexes, and ε is the dielectric constant of the medium. For the hydrolysis of TMOS, the radius of the intermediate complex is greater than the radius of the ion (OH^- or H_3O^+) and the constant A is positive [15], which means that the rate should be greater in a medium of lower dielectric constant. In Fig. 3, we plot the observed reaction rates as a function of the dielectric constant of the solvents. Clearly, there is a correlation between those two quantities, but it is exactly opposite to that predicted by the electrostatic model. This finding suggests that specific solvent effects and the spatial charge distribution within the TMOS molecule are important, and both may produce larger effects than those of the dielectric constant.

Additional arguments that electrostatic effects are not dominant in the hydrolysis reaction are provided by the analysis of the volume of activation. We found the volume of activation to be practically independent of the solvent, catalyst, and pH, and within experimental error equal to -42 cm^3/mol (compare to Table 1). Since the volume of activation measures the difference between the total volume of the reactants and the volume of the intermediate complex, we expected that $\Delta V^{\#}$ should reflect specific interactions between reactants and solvent molecules. Different shielding of the reacting molecules by solvent molecules, the size of the anion, the extent of local order of the solvent, the strength of hydrogen bonding network, all may affect the solvation, and thus, should change the volume of activation.

Reaction (1) does not involve the formation of new charges, and the solvational part of the volume of activation may originate from the redistribution of charge in the activated complex. Whalley [18] studied the effect of pressure on solvation of an intermediate state with dipole and quadrupole moments in a cavity in a dielectric. He found that in aqueous solutions the electrostriction originating from the quadrupole moment of the activated complex is greater than that due to the dipole moment, but both contributions are usually less than 10 cm^3/mol, a value too small to explain the observed $\Delta V^{\#}$. Besides, if the electrostriction were important, then when more polar solvents were added into solutions, the volume of activation should become less negative, and the reaction should proceed at a slower rate. A similar conclusion was reached by Dack [16] who analyzed cohesive forces and internal pressure during the reaction and offered the following explanation: in the absence of specific interactions, concentration of polar molecules about ions is greater than in the proximity of the intermediate state. Consequently, the volume of the reactants is smaller than that of the transition state, and the volume of activation becomes more positive while the reaction is slower. Our results do not follow that trend,

indicating that electrostatic interactions alone cannot explain the mechanism of the hydrolysis reaction. This conclusion is in agreement with the discussion accompanying Fig. 3.

We found that the volume of activation does not depend on the amount of water used to hydrolyze silicon alkoxide and was the same when 10 moles or 1 mole of water was used per each mole of TMOS. In addition, similar values of $\Delta V^{\#}$ were found for TEOS hydrolysis prepared at pH = 2.54 with different acids used to adjust the pH. This means that different anions present in the solution had little effect on the volume of activation. In the following section we will examine effects other than solvation that may determine the value of $\Delta V^{\#}$.

The increased pressure may also affect the volume of the intermediate complex. We suggest, after Whalley [18], that the dominating factor in the volume of activation is due to contraction of the intermediate complex. Although we showed that the contribution due to electrostriction is relatively small, it is impossible to evaluate, and to separate it from the contribution due to complex contraction. Thus, at the present time, it is impossible to estimate the pressure induced changes in the intermediate state.

Although the mechanism of the hydrolysis reaction is similar for TEOS and TMOS, and is not altered by different solvents or catalysts used, the speed of the reaction varies substantially; in this study, we observed changes by more than two orders of magnitude. The changes caused by the solvent can be partially attributed to different molecular structures of the solutions. Under acidic conditions, the reaction is H^+ catalyzed, and the transport of this ion depends on the connectivity between water molecules [6]. But even in water-dioxane mixtures, the sponge-like structure of the solution enables rapid transfer of the ion.

In this section, we will examine the specific interactions between the solvents and silicon alkoxides. The geometry of the transition state can be approximated by a deformed trigonal bipyramid in which the donor site occupies an axial site. Three methoxy groups are in equatorial sites, and the fourth group is at the site opposite to the hydroxyl. Usually the axial bonds are significantly longer than the equatorial bonds [17], and consequently they are weaker, and it is expected that the methoxy group opposite the attacking hydroxyl group will leave the system. When a molecule capable of forming a strong hydrogen bond, such as formamide, is coupled to an Si-OR group, this interaction may weaken the Si-O bond by shifting the electron cloud toward formamide, thus enabling more pronounced changes in bond lengths and angles that are necessary to accommodate the additional bond in the transition state. Also, by protonating the OCH_3 group, the hydrogen bond interaction improves the quality of the leaving group, and thus the reaction may proceed faster. Acetone, dioxane, and acetonitrile are all aprotic and lack protons capable of hydrogen bonding to TMOS, but sol-gels prepared with those solvents contained water and/or methanol. Because both water and methanol may interact specifically with TMOS, it is not surprising that the reaction rates in those systems are similar, with the reaction rate being the fastest for the sol containing pure methanol.

This hypothesis is further supported by Raman studies of pressure induced band shift and band broadening. Oxygen atoms of TMOS are easily accessible to water or other proton donating molecules and may form hydrogen bonds. The Si-O-C mode at 645 cm^{-1} is a bending vibration. It is known that the frequency of bending vibrations, as well as the band width, increase when a hydrogen bond is formed. The band widths and frequencies are listed in Table 2. In the mixture of TMOS, water, and dioxane, we found a small, positive frequency shift (blue shift), which we explain as due to hydrogen bonding between TMOS and water. Significantly larger blue shifts and broader bands were measured in water-methanol and even larger ones in formamide-water

Table 2. Frequency shift and band broadening of the Si-O-C mode of TMOS for different solvents as a function of pressure.

Pressure [bar]	Frequency shift [cm^{-1}]			Bandwidth [cm^{-1}]		
	Formamide	Methanol	Dioxane	Formamide	Methanol	Dioxane
1	4.0	3.6	2.0	8.2	7.2	6.3
100	4.5	3.7	2.1	8.2	7.4	6.5
250	4.9	4.1	2.3	8.3	7.5	6.6
500	5.2	4.4	2.4	8.4	7.6	6.7
1000	5.5	5.0	2.7	8.6	7.6	6.8
1500	6.3	5.7	3.5	8.9	7.7	6.8
2000	6.9	6.3	3.9	9.0	7.9	7.0

mixtures. With increased pressure, intermolecular distances decrease, H-bond interactions become stronger and the changes in the band shapes are more pronounced.

CONCLUSION

The rate of hydrolysis reaction depends on the properties of the solvent added to the reaction, and it is shown that solvents capable of forming strong hydrogen bonds with oxygen atom of silicon alkoxide accelerate the reaction. Volume of activation is practically independent of solvent properties, concentrations of water and solvent, the pH and the alkoxide used. Volume of activation can be separated into two components, first component is due to the change in the volume of the solvation, and the other due to the change in the volume of the solute. We estimate that the compression of the solvent (electrostriction) is smaller than the compression of the reactants. This conclusion does not depend on the size of the reactant, but rather on its compressibility.

ACKNOWLEDGEMENTS

Acknowledgement is made to the donors of The Petroleum Research Fund, administrated by the ACS, and to the Air Force Office of Scientific Research, grant 90-0165, for partial support of this research.

REFERENCES

1. L. P. Davis and L. Burggraf, in Science of Ceramic Chemical Processing, Eds. L. L Hench and D.R. Ulrich (J. Wiley, New York, 1986)
2. L. Burggraf, L. P. Davis and M. Gordon, J. Non-Crystal. Solids, in press
3. I. Artaki, T. W. Zerda, M. Bradley and J. Jonas, J. Phys. Chem. 89, 4399 (1985).
4. A. R. Grimmer, H. Rosenberger, H. Burger and W. Volgel, J. Non-Crysrtal. Solids 99, 371 (1988).
5. R. A. Assink and B. D. Key, J. Non-Cryst. Solids 99, 359 (1988)
6. T. W. Zerda and G. Hoang, J. Non-Cryst. Solids 109, 9 (1989).
7. G. Hoang and T. W. Zerda, Chem. Mat., submitted
8. K. J. McNeil, J. A. Dicaprio, D. A. Walsh and R. F. Pratt, J. Am. Chem. Soc. 102, 1859 (1980).
9. J. C. Ro and I. J. Chung, J. Non-Cryst. Solid 110, 26 (1989).
10. E. R. Pohl and F. D. Osterholtz, in Molecular Characterization of Composite Interfaces, Eds. H. Ishida and G. Kumar (Plenum, New York 1985)
11. H. Kelm and D. A. Palmer, High Pressure Chemistry, Ed. H. Kelm (Reidel Publishing Company, Boston, 1978).
12. G. Orcel and L. L. Hench, J. Non-Cryst. Solids 79, 177 (1986)
13. R. Aelion, A. Loebel and F. Eirich, J. Am. Chem. Soc. 72, 5705 (1950)
14. W. F. K. Wynne-Jones and H. Eyring, Ann. N. Y. Acad. Sci., 39, 492 (1935).
15. J. W. Moor and R. G. Pearson, Kinetics and Mechanism, (J. Wiley, New York, 1981)
16. M. R. J. Dack, Chem. Soc. Rev., 4, 231 (1975)
17. G. Åkerlof and O. A. Short, J. Am. Chem. Soc. 58, 1241 (1936).
18. E. Whalley, J. Chem. Phys., 38, 1400 (1963)
19. R. J. P. Corriu and J. C. Young, in The Chemistry of Organic Silicon Compounds, Eds. S. Patai and Z. Rappoport, (J. Wiley, New York, 1989)

CURRENT ISSUES IN SOL-GEL REACTION KINETICS

Roger A. Assink and Bruce D. Kay
Sandia National Laboratories
Albuquerque, NM 87185

ABSTRACT

This paper surveys a few of the current issues in sol-gel reaction kinetics. Many times seemingly modest changes in reactants or reaction conditions can lead to substantial differences in the overall reaction rates and pathways. For example, qualitative features of the reaction kinetics can depend on catalyst concentration. At very high acid-catalyst concentrations, reverse reactions are significant for TMOS sol-gels, while for moderate acid-catalyst concentrations, reverse reactions are substantially reduced. The reaction kinetics of two similar tetraalkoxysilanes: tetramethoxysilane (TMOS) and tetraethoxysilane (TEOS), can be markedly different under identical reaction conditions. Under acid-catalyzed reaction conditions, a TMOS sol-gel undergoes both water- and alcohol-producing condensation reactions while a TEOS sol-gel undergoes only water-producing condensation. The early time hydrolysis and condensation reactions of a TMOS sol-gel are statistical in nature and can be quantitatively described by a few simple reaction rate constants while the reaction behavior of a TEOS sol-gel is markedly nonstatistical. A comprehensive theory of sol-gel kinetics must address these diverse experimental findings.

INTRODUCTION

There have been many studies of the reaction kinetics of acid-catalyzed tetraalkoxysilanes. The experimental techniques used to study the chemical reaction kinetics include ^{1}H and ^{29}Si NMR spectroscopy [1,2], capillary gas chromatography [3]and infrared and Raman spectroscopy [4]. Most of these studies have investigated a single tetraalkoxysilane under very specific conditions. These conditions include acid-catalyst concentration, silane concentration, water to silane ratio and even a specific time regime. Very often one wishes to extend the conclusions reached for a single system under specific conditions to sol-gel systems in general. This paper will attempt to show that one must be careful in making such extrapolations.

We will examine three areas which have been the subject of

This work performed at Sandia National Laboratories, supported by the U. S. Department of Energy under contract number DE-AC04-76DP00789.

recent study. These areas are: (1) the relative importance of thermodynamic versus kinetic factors in governing the product distribution of sol-gels, (2) the existence of both water- and alcohol-producing condensation pathways, and (3) the statistical (or nonstatistical) behavior of the hydrolysis and condensation reactions.

RESULTS AND DISCUSSION

Thermodynamic vs Kinetic Control

Recently Klemperer and Ramamurthi demonstrated the importance of thermodynamic factors in determining the final product distribution in an acid-catalyzed TMOS sol-gel [3]. Using capillary gas chromatography they were able to show that in three days the species distribution of an acid-catalyzed 3 M TMOS monomer with 1.5 M H_2O sol-gel was the same, within experimental error, as that of an acid catalyzed 1.5 M TMOS dimer sol-gel. Thus, thermodynamic factors had driven the two systems to the same equilibrium state. In contrast to this study, we previously used ^{29}Si NMR spectroscopy to study the kinetics of an acid-catalyzed TMOS sol-gel [5]. The early time product distribution of species could be accurately modelled using only two functional group condensation rate constants and appropriate statistical factors. The authors of each study would like to generalize their results and state that thermodynamic (or kinetic) factors dominate the chemical kinetics of all sol-gels. Obviously, one of these conclusions cannot be correct.

Our interpretation of these two seemingly disparate results [3,5] is that the authors were investigating similar sol-gel systems under quite different reaction conditions. The two most obvious differences in the studies are the unequal catalyst concentrations used and the different time domains investigated. In order to compare the importance of thermodynamic and kinetic factors under the same reaction conditions, Assink and Brinker [6] used ^{29}Si NMR spectroscopy to investigate the reaction kinetics of TMOS monomer and the redistribution kinetics of TMOS dimer for both short and long times for each of the catalyst concentrations used in the two previous studies [3,5].

Figure 1 shows the ^{29}Si NMR spectra of TMOS monomer and TMOS dimer after 24 hours at a nominal pH of 1.3 . This pH is the same as that used by Klemperer and Ramamurthi [3]. The

resonances are labelled by the usual Q^n nomenclature where n refers to the number of silicon-oxygen-silicon bonds about the observed silicon. We see that TMOS monomer and dimer have reached the same state in this very short time. Spectra taken after 1 week are similar, indicating that the reaction has attained equilibrium.

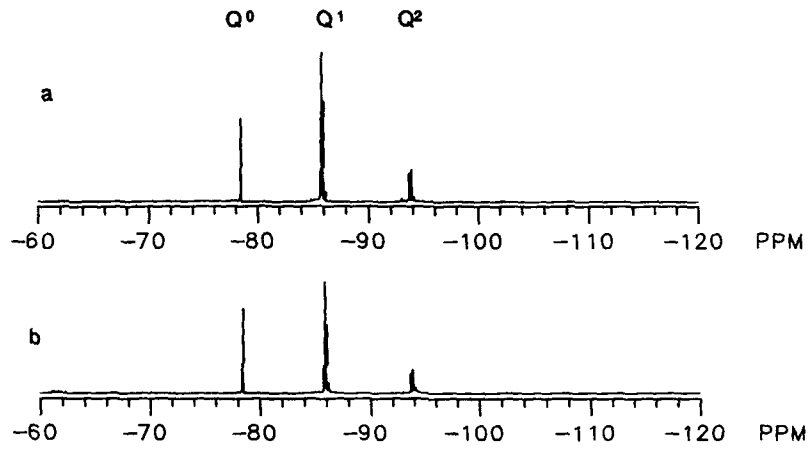


Fig.1 The ^{29}Si NMR spectra of (a) TMOS monomer reacted at pH=1.3 for 24 hours and (b) TMOS dimer reacted at pH=1.3 for 24 hours.

Figure 2 shows the ^{29}Si NMR spectra of TMOS monomer and TMOS dimer after 24 hours at a nominal pH of 2.8 . This acid concentration is the same as that used by Assink and Kay [5]. The species distributions are obviously quite different. After 1 week, the relative Q^0, Q^1 and Q^2 distributions become more similar. Howeve., detailed investigation of the Q^2 and Q^3 region show that even after 1 week there are significant differences between the monomer and dimer derived sol-gels. In particular, the TMOS monomer derived sol-gel contains many more cyclic species and many more branching species (Q^3's) than does the TMOS dimer derived sol-gel.

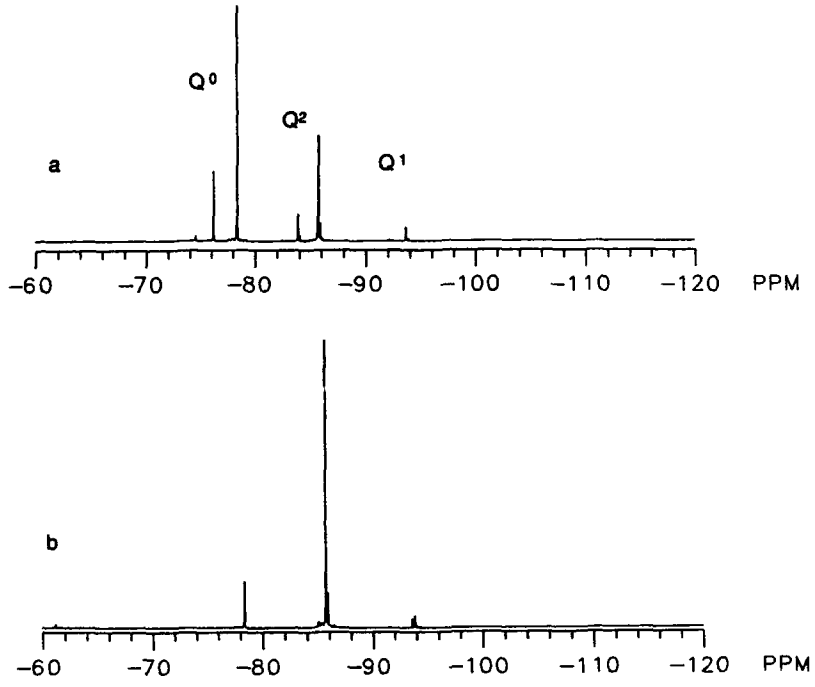


Fig.2 The ^{29}Si NMR spectra of (a) TMOS monomer reacted at pH=2.8 for 24 hours and (b) TMOS dimer reacted at pH=2.8 for 24 hours.

Thus, we conclude that thermodynamic factors dominate at pH=1.3 for both relatively short and long times. Kinetic factors tend to dominate at pH=2.8 at short times and even appear to exert considerable influence on the product distribution for long times. Our findings strongly suggest that the rate constants for the reverse reactions increase with decreasing pH.

Condensation Pathways

Earlier we found that TMOS reacts via two condensation pathways [7]. Condensation of two silanols to form water and an Si-O-Si bond is termed water-producing condensation while condensation of a silanol with a methoxy group to form an alcohol and an Si-O-Si bond is termed alcohol-producing condensation.

Alcohol-producing condensation is an important reaction pathway at low water to silicon ratios while water-producing condensation is an important reaction pathway at high water to silicon ratios. Both pathways were necessary in order to describe the reaction kinetics accurately over a range of water to silicon ratios. Pouxviel and Boilot studied the reaction kinetics of TEOS [8]. They were able to model the time evolution of species using hydrolysis, water-producing condensation and reesterification reactions. They did not need to include alcohol-producing condensation reactions in their model in order to achieve an accurate fit of their data.

Their are several differences between the sol-gel system which we investigated [7] and the sol-gel system which Pouxviel and Boilot investigated [8]. A major difference is the much higher water to silicon ratios used by Pouxviel and Boilot. Our TMOS results indicate that alcohol-producing condensation becomes less important for high water to silicon ratios. A second major difference between the two studies is the use of TMOS in our work and the use of TEOS in the work of Pouxviel and Boilot. Minor differences include moderately lower silicon and acid concentrations in the TEOS sol-gel.

In order to understand the reason for the different condensation pathways in the two systems we investigated the condensation kinetics of TEOS under conditions identical to those used in our prior investigation of TMOS. Previously we derived the relationship [7]:

$$\frac{d[(SiO)\text{-}Si]/dt}{<[SiOH]>} = (k_{CW} - k_{CA})<[SiOH]> + k_{CA}[SiOR]_0 \quad (1)$$

By measuring the initial condensation rate, d[(SiO)-Si]/dt, as a function of the average silanol concentration, <[SiOH]>, we were able to determine the relative importance of the two condensation pathways having rate constants k_{CW} for water-producing condensation and k_{CA} for alcohol-producing condensation. The results of the study are shown in Figure 3. Within experimental error, the intercept is zero indicating that the second term in eq(1) and hence k_{CA} is zero. Thus, for otherwise identical experimental conditions, TMOS undergoes significant alcohol-producing condensation while TEOS does not.

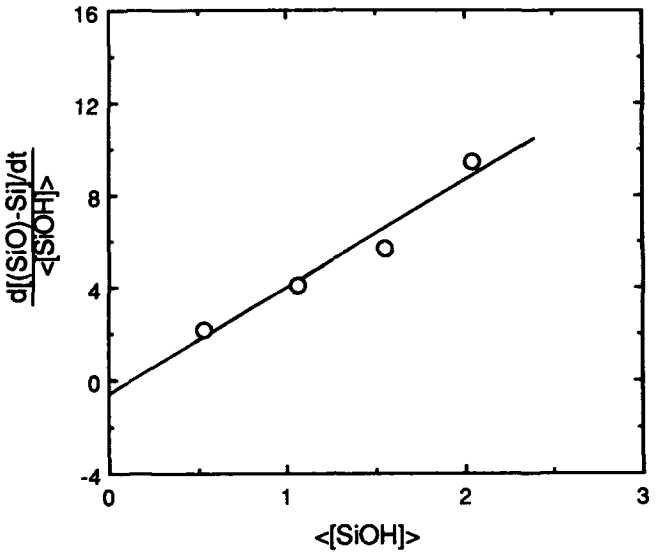


Fig.3 A plot of eq.(1) for acid-catalyzed TEOS. An intercept near zero indicates that the alcohol-producing condensation pathway is insignificant.

Statistical Reaction Behavior

In a previous study we found that we could accurately predict the time evolution of the many product species in a sol-gel by using the two functional group condensation rate constants and appropriate statistical factors [9]. The sol-gel was based on TMOS and only early reaction times were investigated. Pouxviel and Boilot studied the time evolution of a TEOS sol-gel [8] and followed the system for longer times. Their analysis employed distinct reaction rate constants for reactions between each of several species. A detailed analysis of their data using appropriate statistical factors shows that although the condensation reactions could reasonably be expressed in terms of an overall functional group rate constant and appropriate statistical factors, this simplification was not possible for the hydrolysis reactions. As discussed in the previous section, the two studies differed in several aspects: (1) the use of TMOS versus TEOS, (2) the use of different water to silicon ratios and (3) analysis of the system over different time regimes.

We investigated the reaction kinetics of the various species of TEOS under conditions otherwise identical to those used in our previous TMOS studies [9]. Table I compares the early time distribution of hydrolyzed TMOS and TEOS monomers for an initial [H_2O] to [Si] ratio of 0.5. The first column lists the various monomeric species where the first digit in parenthesis corresponds to the number of alkoxy groups, the second digit corresponds to the number of silanol groups, and the final digit corresponds to the number of Si-O-Si bonds (zero for

HYDROLYSIS PRODUCTS

H_2O : TEOS = 1/2 : 1

MONOMER	THEORY	TMOS (5 MIN)	TEOS (4 MIN)
(400)	58.9	57.2	77.5
(310)	33.4	36.6	12.5
(220)	7.0	4.6	7.2
(130)	0.6	----	2.9
(040)	0.0	----	----

these monomeric species). The second column shows the expected distribution of species if statistical reaction behavior is assumed and the initial water is consumed by hydrolysis on a time scale fast compared to the generation of water by subsequent water-producing condensation reactions [9]. The third column shows the measured distribution of species for a TMOS sol-gel which has reacted for 5 minutes. Approximately 92% of the water has been consumed and the TMOS distribution agrees very well with the statistical distribution. The last column shows the distribution of species for a TEOS sol-gel which has reacted for

4 minutes. After 4 minutes, only 71% of the water has been consumed. The (400) concentration is still much larger than the statistical value, however, both the (220) and (130) concentrations have already reached or exceeded their statistical values. These observations mean that the first hydrolysis rate constant is much smaller than the second hydrolysis rate constant which is much smaller than the third hydrolysis rate constant. This trend is the same as that observed by Pouxviel and Boilot [8]. Thus the different results of the two studies does not appear to be related to the unequal water to silicon ratios or to the different time frames observed, but rather to the distinct chemical reaction rates of the monomeric species used.

CONCLUSION

We have seen qualitatively diverse behavior in the reaction kinetics of sol-gels prepared under different experimental conditions. The acid-catalyst concentration can dramatically influence the relative importance of thermodynamic and kinetic factors. TMOS and TEOS, although seemingly very similar monomers, can react along different condensation pathways and react in a predominately statistical (TMOS) or markedly nonstatistical (TEOS) fashion.

REFERENCES

1. R. A. Assink and B. D. Kay in Better Ceramics through Chemistry, edited by C. J. Brinker, D. E. Clark, and D. R. Ulrich (Mater. Res. Soc. Proc. 32, Elsevier Science, NY, 1984) p. 301.

2. L. W. Kelts, N. J. Effinger, and S. M. Melpolder, J. Non-Cryst. Solids 83, 353 (1986).

3. W. G. Klemperer and S. D. Ramamurthi in Better Ceramics through Chemistry III, edited by C. J. Brinker, D. E. Clark, and D. R. Ulrich (Mater. Res. Soc. Proc. 121, Mater. Res. Soc., Pittsburgh, Pennsylvania, 1988) p. 1.

4. C. A. Balfe, K. J. Ward, D. R. Tallant and S. L. Martinez in Better Ceramics through Chemistry II, edited by C. J. Brinker, D. E. Clark, and D. R. Ulrich (Mater. Res. Soc. Proc. 73, Mater. Res. Soc., Pittsburgh, Pennsylvania, 1988) p. 619.

5. R. A. Assink and B. D. Kay, J. Non-Cryst. Solids 107, 35 (1988).

6. R. A. Assink and C. J. Brinker, unpublished results.

7. R. A. Assink and B. D. Kay, J. Non-Cryst. Solids 99, 359 (1988).

8. J. C. Pouxviel and J. P. Boilot, J. Non-Cryst. Solids 94, 374 (1987).

9. B. D. Kay and R. A. Assink, J. Non-Cryst. Solids 104, 112 (1988).

MOLECULAR ARCHITECTURE AND ITS ROLE IN SILICA SOL-GEL POLYMERIZATION

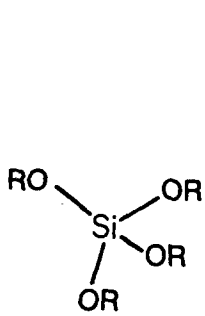
P. C. CAGLE, W. G. KLEMPERER AND C. A. SIMMONS
School of Chemical Sciences and Materials Research Laboratory, University of Illinois, Urbana, IL 61801

ABSTRACT

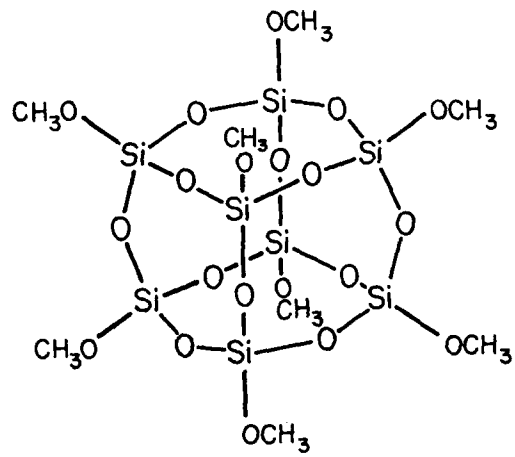
Sol-gel polymerization of $[Si_8O_{12}](OCH_3)_8$ in CH_3CN under neutral conditions yields very high surface area ($S_{BET} > 900\ m^2/g$) xerogels. This property is seen to result from the structure of the gel on the molecular level. According to N_2 adsorption studies, model studies, and TEM studies, the large size and rigidity of the cubic $[Si_8O_{12}]$ core structure leads to polymers whose rigidity inhibits extensive crosslinking of the type observed in orthosilicate derived xerogels.

I. INTRODUCTION

An enormous body of research has been devoted to optimizing silica sol-gel polymerization conditions for the processing of films, fibers, monoliths, and aerogels by controlling the conditions of tetralkylorthosilicate, $Si(OR)_4$ (**a**), hydrolysis/condensation [1,2]. Relatively little attention has been devoted, however, to the architecture of sol-gel derived silica on the molecular size scale. We have recently addressed this issue through the synthesis of the cubic octamethyl octasilicate $[Si_8O_{12}](OCH_3)_8$ (**b**), with the hope that sol-gel polymerization of



a



b

Mat. Res. Soc. Symp. Proc. Vol. 180. ©1990 Materials Research Society

this species might proceed with retention of the cubic $[Si_8O_{12}]$ core [3]. Given the rigidity of the $[Si_8O_{12}]$ core and the relative sizes of the $Si(OR)_4$ and $[Si_8O_{12}](OR)_8$ monomers, even a simple beads-on-a-string model predicts a more rigid silicate framework in octasilicate oligomers than in orthosilicate oligomers. As illustrated below, the relative sizes of the repeat distances in $Si(OR)_4$ polymers (up to 3Å) and $[Si_8O_{12}](OCH_3)_8$ polymers (up to 9Å) should generate very different materials on a molecular size scale:



c



d

Moreover, the rigidity of the polymerized octasilicates, **d**, should inhibit extensive crosslinking and thus generate porous materials with very high surface areas, as is seen to be the case below.

This paper is concerned with demonstrating the role that molecular architecture can play in silica sol-gel polymerization through a comparative study of $Si(OCH_3)_4$ and $[Si_8O_{12}](OCH_3)_8$ hydrolysis/condensation. The paper is divided into three sections. The first section is concerned with demonstrating the high surface area of $[Si_8O_{12}](OCH_3)_8$-derived xerogels relative to $Si(OCH_3)_4$-derived xerogels, and showing that the different properties of the two types of gels can be accounted for in terms of the different flexibilities of the polymer chains involved. In the second section, model studies are reported that support the contention that the $[Si_8O_{12}]$ framework of the $[Si_8O_{12}](OCH_3)_8$ monomer is substantially retained during polymerization. The final section provides electron microscopic evidence that the high surface area of $[Si_8O_{12}](OCH_3)_8$-derived xerogels is in fact due to a low degree of crosslinking between polymer chains in the structure.

II. SURFACE AREA AND POROSITY OF $Si(OCH_3)_4$- AND $[Si_8O_{12}](OCH_3)_8$-DERIVED XEROGELS

Data recorded in Table I were obtained from cylindrical xerogel monoliths prepared as follows. Solutions of $Si(OCH_3)_4$ and $[Si_8O_{12}](OCH_3)_8$ in CH_3CN were prepared at 60° C with [Si] = 1.08 M and $[H_2O]$ = 5.40 M and 7.78 M for $Si(OCH_3)_4$ and $[Si_8O_{12}](OCH_3)_8$,

TABLE I. SURFACE AREA AND POROSITY DATA FOR $Si(OCH_3)_4$- AND $[Si_8O_{12}](OCH_3)_8$-DERIVED XEROGELS[a]

$Si(OCH_3)_4$

	S_{BET}[b] (m^2/g)	Density[c] (g/cm^3)	V_{pore}[d] (cm^3/g)	D_{pore}[e] (Å)
acid	427 (34, 83, 9)	1.43 (4, 6, 8)	0.24 (2, 5, 9)	22.3 (3, 9, 8)
neutral	510 (20, 44, 10)	0.55 (1, 4, 10)	1.35 (2, 4, 10)	106 (5, 8, 10)
base	354 (2, 5, 5)	0.53 (2, 9, 5)	1.48 (8, 12, 5)	167 (10, 15, 5)

$[Si_8O_{12}](OCH_3)_8$

	S_{BET} (m^2/g)	Density (g/cm^3)	V_{pore} (cm^3/g)	D_{pore} (Å)
acid	604 (24, 45, 8)	1.16 (3, 6, 8)	0.42 (2, 3, 8)	27.9 (2, 4, 8)
neutral	919 (31, 42, 5)	0.88 (1, 3, 5)	0.68 (3, 4, 5)	29.8 (6, 12, 5)
base	750 (42, 82, 8)	0.617 (7, 10, 7)	1.21 (2, 6, 8)	65 (3, 7, 8)

[a]See text for details of sample preparation. All data are averaged values of measurements made from independently-prepared samples. The first number in parenthesis following an average value is the average deviation from the average value, the second number is the maximum deviation from the average value, and the third number is the number of individual measurements that are included in the average value.

[b]BET surface area from multipoint analysis of N_2 adsorption isotherm.

[c]Bulk density calculated from weight and volume measurements of cylindrical monoliths.

[d]Pore volume is calculated from plateau in N_2 adsorption isotherm, and includes volume of pores less than about 500 Å in diameter.

[e]Average pore diameter calculated asssuming cylindrical pores by dividing $4V_{pore}$ by S_{BET}.

respectively, such that the total amount of non-alkoxide oxygen (H_2O, SiOH, plus SiOSi oxygen) per silicon was the same in each system, namely, five:

$$8\ Si(OCH_3)_4 + 40\ H_2O = [Si_8O_{12}](OCH_3)_8 + 24\ CH_3OH + 28\ H_2O \qquad (1)$$

Basic and acidic solutions were prepared by addition of NaOH [0.002 M for $Si(OCH_3)_4$ and 0.005 M for $[Si_8O_{12}](OCH_3)_8$] and HCl [0.05 M], respectively. Each 12 mL sample was allowed to gel and age in a sealed 15 mm diameter polypropylene test tube for 12 days at 60°C, was dried for 10 days at 60°C and 2 days at ambient temperature, and finally was heated at 110°C for 48 hours. The conditions just described were dictated in part by solubility considerations. The $[Si_8O_{12}](OCH_3)_8$ molecule has a low solubility in CH_3OH, the solvent traditionally employed for $Si(OCH_3)_4$ hydrolysis/condensation. It has a better but nonetheless low solubility in CH_3CN, the solvent employed in the present study. The increased solubility of $[Si_8O_{12}](OCH_3)_8$ in CH_3CN at elevated temperatures dictated the processing temperature.

TABLE II. SURFACE AREA AND POROSITY DATA FOR $Si(OCH_3)_4$-DERIVED XEROGELS[a]

Gelation Conditions[b] [Si]; °C	S_{BET} (m^2/g)		Density (g/cm^3)		V_{pore} (cm^3/g)		D_{pore} (Å)	
1M; 60°C	510	(20, 44, 10)	0.55	(1, 4, 10)	1.35	(2, 4, 10)	106	(5, 8, 10)
1M; 25°C	693	(8, 10, 4)	0.78	(1, 3, 4)	0.84	(2, 3, 4)	48	(1, 1, 4)
2M; 60°C	778	(4, 9, 4)	0.93	(2, 4, 4)	0.68	(1, 2, 4)	35	(7, 10, 4)
2M; 25°C	765	(25, 49, 4)	1.12	(3, 6, 4)	0.53	(4, 5, 4)	28	(1, 3, 4)

[a]See text for details of sample preparation, and Table I for explanation of symbols.
[b]No acid or base catalyst was employed.

The effects of Si concentration and elevated temperature were probed by preparing neutral $Si(OCH_3)_4$ solutions with $[H_2O]/[Si] = 5$ and [Si] = 1.08 or 2.15 M, carrying out gelation and aging at either 25°C or 60°C as described above, and drying as described above. The properties of these xerogels are recorded in Table II.

Comparison of BET surface areas given in Table I for xerogels prepared under neutral conditions shows the $[Si_8O_{12}](OCH_3)_8$-derived gels ("cube gels") to have extraordinarily high surface areas of 919 m^2/g, a value much higher than the more typical value of 510 m^2/g observed for the $Si(OCH_3)_4$-derived gels ("TMOS gels") [4]. Gels processed under acidic or basic conditions display lower surface areas both in the case of cube gels and TMOS gels, but the cube gels consistently show higher surface areas. Density, pore volume, and average pore diameter data given in Table I also reveal consistent differences between TMOS and cube gels. In both systems, acid gels have higher densities than base gels, by a factor of 2.7 for TMOS gels and 1.9 for cube gels. Base gels consistently display larger pore volumes than acid gels, by a factor of 6.2 for TMOS gels but only 2.9 for cube gels. Average pore diameters are also higher for base gels than for acid gels, by a factor of 7.5 for TMOS gels but only 2.3 for cube gels. In short, TMOS and cube gels respond in a similar fashion to changes in solution pH, but the response is attenuated in the case of the cube gels.

The trends just noted can be explained in terms of the greater rigidity proposed above for cube polymers derived from $[Si_8O_{12}](OCH_3)_8$ relative to orthosilicate polymers derived from TMOS. According to TEM studies of gels [5] and xerogels [6], base gels obtained by alkylorthosilicate sol-gel polymerization are particulate whereas acid gels have a continuous, homogeneous microstructure. The continuous, dense nature of acid gels accounts for their low porosity, and the particulate nature of base gels accounts for their high pore volume. The gross differences between acid and base gels can be accounted for by the fundamentally different polymer growth pathways involved. Under acidic conditions, predominantly linear polymer chains crosslink to form a continuous network gel [7,8]. Under basic conditions, highly branched polymer chains collapse to particles that aggregate to form a particulate gel [9]. According to this picture, the flexible orthosilicate polymer chains are free to undergo extensive crosslinking in a continuous network or collapse to particles but the rigidity of the cube

polymers hinders chain crosslinking and chain collapse. As a result, the effect of acid and base is less pronounced in cube polymerization than in orthosilicate polymerization.

In the above discussions, we have deliberately avoided discussion of details such as electrophilic vs. nucleophilic substitution mechanisms [10], hydrolysis vs. condensation rates [11], and thermodynamic versus kinetic growth models [12]. These topics have been avoided because the difference between the "acid" pathway (crosslinking of linear polymers to a continuous network) and the "base" pathway (collapse of branched polymers to particles) is far more fundamental and general than the specific kinetic and thermodynamic consequences of pH change. Under acid conditions, hydrolysis/condensation is relatively selective and occurs preferentially at sterically uncongested sites, thus generating relatively linear polymers [13,7,8]. Under basic conditions, hydrolysis/condensation is relatively unselective and does not avoid sterically crowded sites to the same extent, thus generating more highly branched silicate polymers [13,7,8]. Variation of pH, however, is only one specific way in which reaction selectivity can be controlled. Another way is through temperature variation, which causes selectivity to increase as temperature decreases. Increased selectivity might therefore account for the differences in density, pore volume, and average pore diameter between 1M; 60°C and 1M; 25°C as well as 2M; 60°C and 2M; 25°C orthosilicate xerogels (see Table II). In both cases, lower temperature yields more "acidic" properties: higher density, lower pore volume, and smaller average pore size. Manipulation of hydrolysis/condensation selectivity is also only one way in which the overall course of orthosilicate polymerization can be influenced. The linear polymerization/cross-linking pathway ("acid" pathway) and the branched polymerization/collapse pathway ("base" pathway) differ on a more fundamental level in that polymer crosslinking is predominantly an intermolecular process whereas polymer collapse is an intramolecular process. Dilution should therefore favor the "base" pathway, a prediction supported by data in Table II, specifically, comparison of 2M; 60°C and 1M; 60°C as well as 2M; 25°C and 1M; 25°C density, pore volume, and average pore diameter data.

III. MODELING THE $[Si_8O_{12}](OCH_3)_8$ SOL-GEL POLYMERIZATION REACTION

In the previous section, it was implicitly assumed that linkage of octamethyl octasilicate cubes by hydrolysis/condensation proceeds with retention of the cubic $[Si_8O_{12}]$ core structure as in equation (2):

$$2\,[Si_8O_{12}](OCH_3)_8 + H_2O \longrightarrow (CH_3O)_7[Si_8O_{12}]O[Si_8O_{12}](OCH_3)_7 + 2CH_3OH \qquad (2)$$

The $[Si_8O_{12}]$ cube contains twenty-four siloxane (Si-O) bonds, and cleavage of any one of these by water, alcohol, or a silicic acid (SiOH) group would correspond to opening up of a cube edge. Although small amounts of $[Si_8O_{12}]$ degradation would not affect the rigidity of

cube polymers, extensive degradation would of course have an adverse effect.

Condensation is sufficiently slow relative to hydrolysis in the neutral $[Si_8O_{12}](OCH_3)_8$-/CH_3CN system such that hydrolysis products can be observed by $^{29}Si\{^1H\}$ NMR spectroscopy [3]. These observations indicate that Si-OCH_3 hydrolysis is much faster than Si-O-Si hydrolysis, and that as a result, no $[Si_8O_{12}]$ core degradation is observed during $[Si_8O_{12}](OCH_3)_8$ hydrolysis. It has been far more difficult to determine whether silicic acid condensation is accompanied by $[Si_8O_{12}]$ core degradation. GC/MS techniques that have been successfully applied to orthosilicate polymerization [7] have only limited utility in the $[Si_8O_{12}](OCH_3)_8$ system, due to the very high molecular weights involved; only the cube dimer $(CH_3O)_7[Si_8O_{12}]O[Si_8O_{12}](OCH_3)_7$ can be monitored by GC/MS. Furthermore, this dimer is observed in low concentration (ca. 5% total silicon) since the cube monomer is octafunctional and Flory-Stockmayer statistics consequently generate a very dispersed molecular size distribution [8]. The degree of $[Si_8O_{12}]$ core degradation that accompanies cube condensation has therefore not been evaluated by direct observation.

Given the difficulty of characterizing the molecular structures of cube condensation products in the sol-gel polymerization of $[Si_8O_{12}](OCH_3)_8$, a model system has been synthesized in which seven of the reactive $[Si_8O_{12}]$ cube vertex sites are occupied by inert trimethylsilyl groups and the eighth is occupied by a hydroxyl group. This compound, $(Me_3SiO)_7[Si_8O_{12}]OH$, was prepared from $[Si_8O_{12}]H_8$ [14] as follows:

$$[Si_8O_{12}]H_8 \xrightarrow{Me_3NOSiMe_3Cl\ [15]} (Me_3SiO)_7[Si_8O_{12}]H \qquad (3)$$

$$(Me_3SiO)_7[Si_8O_{12}]H \xrightarrow{Me_3SnOH} (Me_3SiO)_7[Si_8O_{12}]OSnMe_3 \qquad (4)$$

$$(Me_3SiO)_7[Si_8O_{12}]OSnMe_3 \xrightarrow{HCl(aq)} (Me_3SiO)_7[Si_8O_{12}]OH \qquad (5)$$

In the presence of $(C_2H_5)_3N$ in benzene solution, it undergoes self-condensation according to equation (6) without any measurable degradation of the $[Si_8O_{12}]$ core structure according to

$$2(Me_3SiO)_7[Si_8O_{12}]OH \rightarrow (Me_3SiO)_7[Si_8O_{12}]O[Si_8O_{12}](OSiMe_3)_7 + H_2O \qquad (6)$$

GC/MS and $^{29}Si\{^1H\}$ NMR spectroscopic data. The computer-generated structure of the condensation product shown in Figure 1 illustrates in a realistic fashion the large dimensions of cube oligomers.

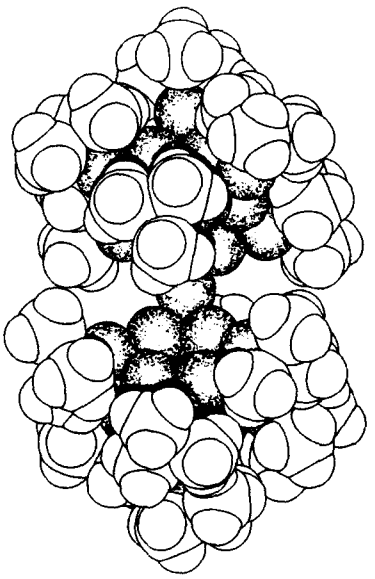


Figure 1. Computer-generated, space-filling model of $(Me_3SiO)_7[Si_8O_{12}]O[Si_8O_{12}](OSiMe_3)_7$. Oxygen atoms are represented by shaded van der Waals spheres, carbon and hydrogen atoms are represented by unshaded van der Waals spheres, and silicon atoms have been omitted. Bond lengths and angles are those observed in $[Si_8O_{12}](OSiMe_3)_8$ [16], except the intercube siloxane Si-O-Si angle which was arbitrarily set at 180°.

IV. TRANSMISSION ELECTRON MICROSCOPIC STUDIES

Ruben has recently reported transmission electron micrographs of platinum-carbon replicated xerogels prepared from $[Si_8O_{12}](OCH_3)_8$ and $Si(OCH_3)_4$ at ambient temperature under neutral conditions (see Figure 2a-c) [17]. In Figure 2a-c, silica structures appear as white images and the pores appear as black background. The micrograph in Figure 2d was obtained from a flat mica surface and its features thus illustrate the background "noise" level. The Pt-C coated images of the cube xerogel structure are approximately 16Å thick and subtraction of 6Å for the Pt-C coating gives an approximate value of 10Å for the cube chain diameter. In contrast to the images of the cube gel that show individual cube chains, images of the TMOS gel show thicker (ca. 18Å) silica structures corresponding not to individual chains but to aggregates of presumably crosslinked chains. The electron micrographs thus support the proposal articulated above that the rigidity of cube polymers inhibits extensive crosslinking and thus generates high surface area xerogels.

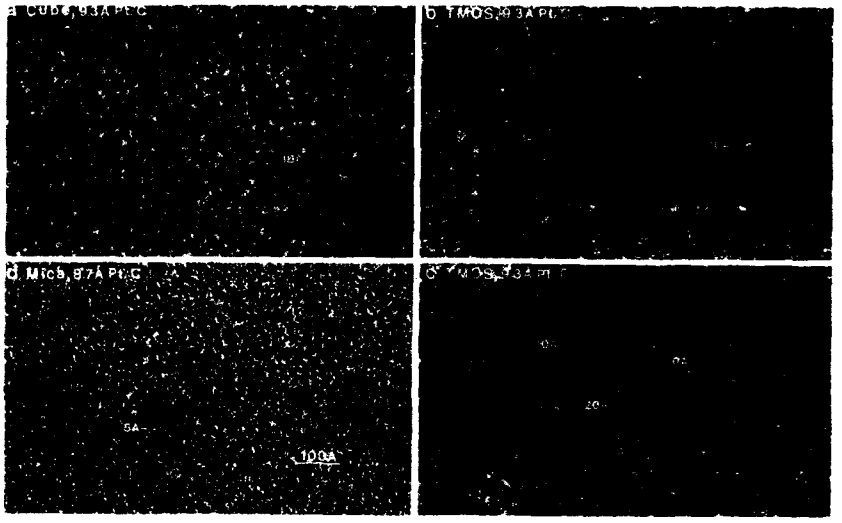


Figure 2. Transmission electron micrographs of platinum replicated (a) $[Si_8O_{12}](OCH_3)_8$-derived xerogel, (b)/(c) $Si(OCH_3)_4$-derived xerogel, and (d) mica surfaces. For details, see reference [17]. Used with permission.

ACKNOWLEDGMENT

This research was supported by the United States Department of Energy, Division of Materials Science, under Contract DE-AC02-76ER01198. The facilities of the Center for Cement Composite Materials at the University of Illinois were used to measure and analyze N_2 adsorption isotherms.

Dr. Dean Millar played a key role in early stages of the research reported above. We are grateful to Professor Charles Zukoski for helpful discussions. Dr. Thomas Bier provided invaluable assistance with N_2 adsorption measurements.

REFERENCES

1. I. Strawbridge, in Chemistry of Glasses, edited by A. Paul, 2nd Ed (Chapman and Hall, New York, 1990), pp 51-85.

2. C. J. Brinker, and G. W. Scherer, Sol-Gel Science, the Physics and Chemistry of Sol-Gel Processing, (Academic Press, Inc., Boston, 1990).

3. V. W. Day, W. G. Klemperer, V. V. Mainz, and D. M. Millar, J. Am Chem. Soc. 107, 8262 (1985).

4. a) A. D. Irwin, J. S. Holmgren, and J. Jonas, Mat. Lett. 6, 25 (1987); b) M. Yamane, S. Aso, S. Okano, and T. Sakaino, J. Mat. Sci. 14, 607 (1979); c) M. Yamane, S. Aso, and T. Sakaino, J. Mat. Sci. 13, 865 (1978).

5. J. K. Bailey, T. Nagase, S. M. Broberg, and M. L. Mecartney, J. Non-Cryst. Sol. 109, 198 (1989).

6. a) M. Nogami and Y. Moriya, J. Non-Cryst. Sol. 37, 191 (1980); b) C. J. Brinker, K. D. Keefer, D. W. Schaefer, and C. S. Ashley, J. Non-Cryst. Sol. 48, 47 (1982).

7. W. G. Klemperer and S. D. Ramamurthi in Better Ceramics Through Chemistry III, edited by C. J. Brinker, D. E. Clark, D. R. Ulrich (Mater. Res. Soc. Symp. Proc. 121, Pittsburgh, PA 1988) pp. 1-13.

8. W. G. Klemperer and S. D. Ramamurthi, J. Non-Cryst. Sol., in press.

9. C. F. Zukoski, M. K. Chow, G. H. Bogush, and J. L. Look, these proceedings.

10. D. W. Schaefer, MRS Bull. 13, 22 (1988).

11. K. D. Keefer in Silicon-Based Polymer Science: A Comprehensive Resource, edited by J. M. Zeigler and F. W. Gordon (Adv. Chem. Ser. 224; Am. Chem. Soc., Washington, DC 1990) pp. 228-240.

12. D. W. Schaefer, Science 243, 1023 (1989).

13. L. W. Kelts, N. J. Effinger, and S. M. Melpoder, J. Non-Cryst. Sol. 83, 353 (1986).

14. C. L. Frye and W. T. Collins, J. Am. Chem. Soc. 92, 5586 (1970).

15. P. A. Agaskar, V. W. Day, and W. G. Klemperer, J. Am. Chem. Soc. 109, 5554 (1987).

16. Yu. I. Smolin, Yu. F. Shepelev, and R. Pomes, Khim. Silik. Oksidov 1982, 68.

17. G. C. Ruben, J. Electron Microsc. Tech., 13, 335 (1989).

SYNTHETIC AND STRUCTURAL STUDIES OF BISMUTH/COPPER ALKOXIDES

WILLIAM J. EVANS* AND JOHN H. HAIN, JR.
Department of Chemistry, University of California-Irvine, Irvine, California 92717

ABSTRACT

The reaction of $Bi[OC(CH_3)_3]_3$ with $[Cu(\mu\text{-}O_2CCH_3)_2]_2$ has been investigated as a possible route to mixed-metal materials containing bismuth and copper. The product distribution obtained from this reaction depends not only upon the stoichiometry, but also upon the method of product isolation. Products containing bismuth and copper are obtainable as well as an unusual, soluble hexametallic copper(II) alkoxide acetate complex, $Cu_6[OC(CH_3)_3]_6(O_2C\text{-}CH_3)_6$. The mixed-metal products were examined by differential scanning calorimetry, and thermolyzed and hydrolyzed samples of these products were compared by scanning electron microscopy.

INTRODUCTION

The recent discovery that mixed-metal oxides such as $YBa_2Cu_3O_{7-x}$ [1], $Bi_2Sr_2Ca_2Cu_3O_{10}$ [2] and $TlBa_2Ca_3Cu_4O_{11}$ [3] are superconducting at temperatures above 90 K has stimulated research on the preparation of high purity samples of these materials [4,5]. Hydrolysis of heteropolymetallic alkoxides via sol-gel processes offers one route to high purity oxides [6,7], but utilization of this approach is hindered by insufficient synthetic and structural information on mixed-metal alkoxide precursors. In fact, only limited data are available even on single metal alkoxide precursors. For example, we only recently obtained the first X-ray crystallographic data on bismuth alkoxides, $Bi(OR)_3$ ($R = C(CH_3)_3$ and $C_6H_4(CH_3)_2$-2,6) [8]. These data showed that these bismuth alkoxides are monomeric in the solid-state and that $Bi(OC_6H_4Me_2\text{-}2,6)_3$ has a pyramidal structure presumably due to a stereochemically active lone pair of electrons on bismuth. We have now investigated the utility of these bismuth complexes for the preparation of mixed-metal compounds containing copper. We describe here our results using the bimetallic copper(II) complex $[Cu(\mu\text{-}O_2CCH_3)_2]_2$.

EXPERIMENTAL

$Bi(OCMe_3)_3$, prepared as previously described [8], and commercially available anhydrous $[Cu(O_2CMe)_2]_2$ (Alfa) were reacted in the stoichiometries described in the following sections in THF dried over sodium benzophenone ketyl in an inert atmosphere glove box.

Mat. Res. Soc. Symp. Proc. Vol. 180. ©1990 Materials Research Society

The 1:1 $[Cu_2(O_2CMe)_2]_2$:$Bi(OCMe_3)_3$ Reaction

$Bi(OCMe_3)_3$ (0.729 mmol) was added to a blue, stirred solution of $[Cu(O_2CMe)_2]_2$ (0.729 mmol) in 20 mL of THF. The solution immediately became forest green. After 6 hours, THF was removed by rotary evaporation to leave a green solid. The solid was extracted with hexane to form a blue-green solution, A, which was separated from the remaining blue solid, B, by centrifugation. Removal of hexane from solution A left a solid which contained primarily $Cu_6(O_2CMe)_6(OCMe_3)_6$, 1, (46% yield based on copper) with a small amount of a bismuth contaminant present. Recrystallization from THF/hexane at -34°C generated pure $Cu_6(\mu\text{-}OCMe_3)_6(\mu\text{-}O_2CMe)_4(\mu_4\text{-}O_2CMe)_2$, isolated as blue crystals. ^1H NMR (THF-d_8, ppm): 12.5 (O_2CMe), 9.6 ($OCMe_3$). The complex was identified by X-ray crystallography. 1 crystallizes in space group $P2_1/n$ with a = 13.149(2) Å, b = 9.7566(15) Å, c = 19.535(3) Å, β = 90.580(11)°, V = 2506.0(6) Å^3 and D_{calcd} = 1.556 g cm^{-3} for Z = 2. Least-squares refinement of the model based on 3027 reflections ($F^2 > 3.0\sigma(F^2)$) converged to a final R_F = 5.2%.

THF extraction of the blue solid B from the above reaction and removal of the THF left a copper bismuth complex, 2, which had a complete elemental analysis consistent with the formula $[Cu(O_2CMe)_2]_2[Bi(OCMe_3)_2(O_2CMe)]_2$. Calcd: Bi, 35.10; Cu, 10.66; C, 28.21; H, 4.53. Found: Bi, 34.99; Cu, 10.09; C, 26.59; H, 3.95 (yield 42% based on copper). ^1H NMR (THF-d_8): 12.7 (CuO_2CMe), 1.41 (BiO_2CMe), 1.35 ($OCMe_3$).

The 1:2 $[Cu(O_2CMe)_2]_2$:$Bi(OCMe_3)_3$ Reaction

Addition of $Bi(OCMe_3)_3$ (0.42 mmol) to a blue solution of $[Cu(O_2CMe)_2]_2$ (0.21 mmol) in 12 mL of THF also generated a forest green solution. Immediate removal of solvent gave a forest green solid, 3. Samples of 3 in THF-d_8 were found to be unstable by ^1H NMR spectroscopy and resonances consistent with the formation of 1 and $Bi(OCMe_3)_2(O_2CMe)$ were observed.

Hydrolysis and Thermolysis Reactions

A sample of 3 (60 mg, 0.049 mmol) was placed in one side of an H-shaped tube and dissolved in benzene. The apparatus was attached to a high vacuum line and the solution was degassed. Degassed water was condensed into the other side of the apparatus and both sides were warmed to room temperature. The benzene solution of 3 formed a gel in approximately 15 minutes. The solvent was removed and the gel was dried under vacuum (10^{-5} torr). Final weight of gel: 43 mg. Elemental analysis: Calcd for "$[Cu(O_2CMe)_2]_2[Bi(OH)_3]_2$": Bi, 47.33; Cu, 14.38; C, 10.87; H, 1.74. Found: Bi, 49.79; Cu, 15.39; C, 11.39; H, 1.74. Thermolysis reactions were conducted on a high vacuum line (10^{-5} torr) using a tube furnace.

RESULTS AND DISCUSSION

$Bi(OCMe_3)_3$ reacts instantaneously with blue THF solutions of anhydrous $[Cu(O_2CMe)_2]_2$ to generate green products. If a base adduct of the

type known for $[Cu(O_2CMe)_2]_2L_2$ (where L = H_2O, pyridine, etc.) is formed in this reaction (i.e., L = $Bi(OCMe_3)_3$), it is not very stable. Ligand redistribution products can be identified in this system even if the reaction mixture is analyzed immediately following mixing. This is consistent with the weak basicity of bismuth compounds in general. Although this reaction system is difficult to fully analyze by NMR spectroscopy due to the paramagnetism of the copper complexes, by varying the reaction stoichiometry and the isolation procedures, definitive identification of some products was possible.

The reaction of $[Cu(O_2CMe)_2]_2$ and $Bi(OCMe_3)_3$ in a 1:1 molar ratio was most informative in this regard. In this case, after six hours of reaction time, two main products could be isolated. The product most definitively characterized is the unusual hexametallic copper(II) alkoxide acetate complex, $Cu_6(\mu\text{-}OCMe_3)_6(\mu\text{-}O_2CMe)_4(\mu_4\text{-}O_2CMe)_2$, 1, shown in Figure 1. This complex shows that tert-butoxide ligands from the bismuth reagent have migrated to the copper centers and indicates that ligand exchange reactions are alternative reaction pathways in this system.

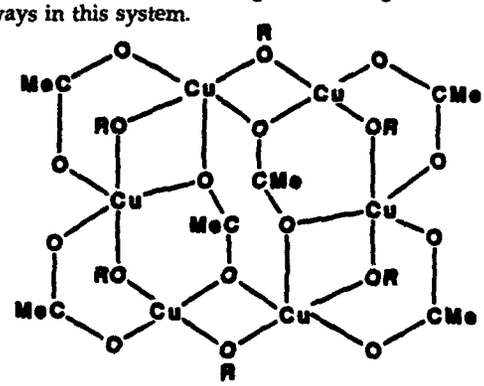


Figure 1. The molecular structure of $Cu_6(\mu\text{-}OCMe_3)_6(\mu\text{-}O_2CMe)_4(\mu_4\text{-}O_2CMe)_2$.

Complex 1 was fully characterized by single crystal X-ray crystallography. The six copper atoms are linked by six bridging tert-butoxide ligands to form a hexagonal substructure in which the copper atoms lie along the edges. The copper atoms are planar to within 0.01 Å. The copper atoms are futher linked around the periphery of the hexagon by four bridging acetate groups. The final connection between the copper atoms occurs via quadruply-bridging acetate ligands. Four of the copper sites are surrounded by five oxygen atoms which have a very distorted square pyramidal geometry. The remaining two copper sites are ligated by four oxygen atoms which have an irregular geometry. The complex is soluble in THF and as such it is one of the few soluble copper(II) alkoxide complexes [9]. Isopiestic molecular weight studies in THF indicated that the compound oligomerized over time to a THF-soluble material of much higher molecular weight. Complex 1 does not readily form from the direct reaction of $[Cu(O_2CMe)_2]_2$ with $NaOCMe_3$.

The bismuth containing product of the 1:1 reaction, 2, has an elemental composition consistent with the formulation $[Cu(O_2CMe)_2]_2[Bi(OCMe_3)_2(O_2CMe)]_2$. The NMR spectrum of 2 is also consistent with, although not definitive for, this formulation. The existence of bismuth units containing acetate is consistent with the observation that tert-butoxide ligands are

attached to copper in 1. The overall 1:1 reaction can best be represented by the following equation.

$$6\ Bi(OCMe_3)_3 + 6\ [Cu(O_2CMe)_2]_2 \rightarrow Cu_6(OCMe_3)_6(O_2CMe)_6 + 3\ [Cu(O_2CMe)_2]_2[Bi(OCMe_3)_2(O_2CMe)]_2 \quad (1)$$

Compounds 1 and 2 are obtained in amounts which together account for a yield of over 80% based on copper.

The reaction of $[Cu(O_2CMe)_2]_2$ and $Bi(OCMe_3)_3$ in a 1:2 molar ratio was examined in efforts to see if the di-bismuth base adduct, $[Cu(O_2CMe)_2]_2[Bi(OCMe_3)_3]_2$, could be isolated. The reaction solution again immediately changed from blue to green upon mixing. To minimize ligand exchange reactions leading to 1 and 2, the reaction solvent was immediately removed and the product, 3, was isolated. Hexane extraction of 3 gave a mixed-metal product (37.52% bismuth and 8.32% copper) which differed from 2 in that it was hexane soluble. However, this hexane soluble product was not very stable and decomposed to 1 and hexane insoluble bismuth complexes upon removal of hexane. To avoid decomposition of the product of the 1:2 reaction, solid 3, isolated immediately upon solvent removal prior to extraction, was used in subsequent studies.

The mixed-metal products 2 and 3 were analyzed by differential scanning calorimetry (DSC) and found to be distinct from each other and from the starting materials. No evidence for 1 was observed by DSC. Thermolysis of 2 and 3 at 280°C generated gases which were analyzed by GC-MS. Evidence for CO_2, acetone, tert-butanol, 2-methylpropene and 1,1-dimethylethylacetate was observed. At this thermolysis temperature, red and white products containing bismuth (by spot tests) sublimed separately and a grey-black material was left behind.

Scanning electron micrographs of the residue left after thermolysis of 3 are shown in Figure 2. Solid particles ranging in size from 1 to 20 microns were observed. In contrast, SEM photographs of hydrolyzed samples of 3 revealed stacks of plate-like particles with sizes up to 20 x 50 microns (Figure 3). X-ray analysis of these plates showed some surfaces and edges to be rich in bismuth, while other regions appeared to have a more even distribution of copper and bismuth. Greater magnification showed the presence of numerous, small, oblong particles of approximate dimension 1.5 x 0.2 microns (Figure 3). SEM analysis of the product obtained by thermolysis of 2 showed large flakes of porous material with a honeycomb topology (Figure 4).



Figure 2. Scanning electron micrograph of a sample of 3 heated to 280°C.



Figure 3. Scanning electron micrographs of a hydrolyzed sample of 3.

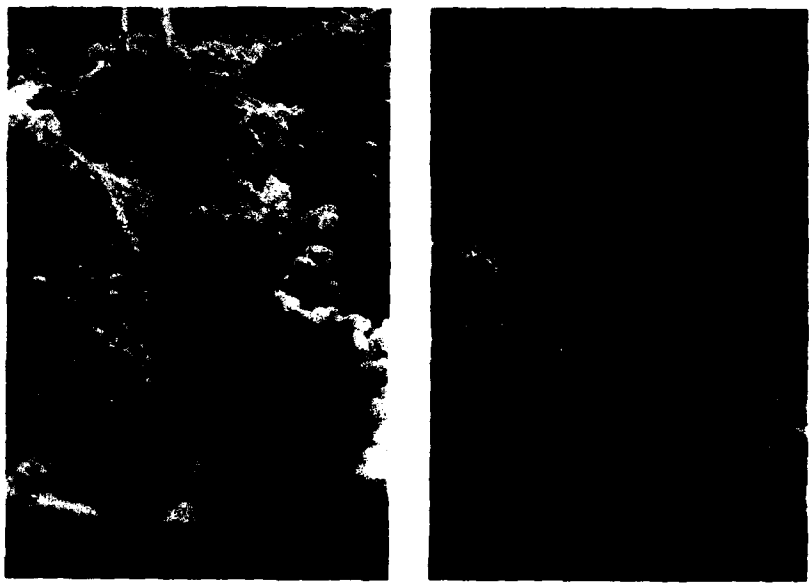


Figure 4. Scanning electron micrographs of a sample of 2 heated to 280°C.

Upon greater magnification, the surface was found to be speckled with small spheres in two size ranges (Figure 4). The large spheres were found to be copper by qualitative X-ray analysis, the small spheres were found to be bismuth, and the remaining material was a mixture of these metals.

CONCLUSION

$Bi(OCMe_3)_3$ readily reacts with $[Cu(O_2CMe)_2]_2$ to form mixed-metal bismuth copper species. Ligand exchange occurs in this system to form the hexametallic copper complex $Cu_6(\mu\text{-}OCMe_3)_6(\mu\text{-}O_2CMe)_4(\mu_4\text{-}O_2CMe)_2$. Neither thermolysis nor hydrolysis of the mixed-metal products gives materials containing homogeneous distributions of bismuth and copper, but hydrolysis seems to give a more uniform morphology.

ACKNOWLEDGMENT

We thank the Division of Chemical Sciences of the Office of Basic Energy Sciences of the Department of Energy for support of this research.

REFERENCES

1. J. G. Bednorz, K. A. Muller, and M. Takashige, Science (Washington, DC) 236, 73 (1987).

2. H. Maeda, Y. Tanaka, M. Fukutomi, and T. Asano, Jpn. J. Appl. Phys. 27, L209 (1988).

3. Z. Z. Sheng and A. M. Hermann, Nature (London) 332, 138 (1988).

4. Better Ceramics Through Chemistry II, edited by C. J. Brinker, D. E. Clark, and D. R. Ulrich (Mat. Res. Soc. Symp. Proc. 73, and references therein.

5. H. S. Horowitz, S. J. McLain, A. W. Sleight, J. D. Druliner, P. L. Gai, M. J. VanKavelaar, J. L. Wagner, B. D. Biggs, and S. J. Poon, Science 243, 66 (1989).

6. L. G. Hubert-Pfalzgraf, New J. Chem. 11, 663 (1987) and references therein.

7. J. Livage, M. Henry, and C. Sanchez, Prog. Solid St. Chem. 18, 259 (1988).

8. W. J. Evans, J. H. Hain, Jr., and J. W. Ziller, J. Chem. Soc., Chem. Commun. 1628 (1989).

9. S. C. Goel, K. S. Kramer, P. C. Gibbons, and W. E. Buhro, Inorg. Chem. 28, 3619 (1989) and references therein.

PART II

Precursor Effects and Aqueous Chemistry

MOLECULAR STRUCTURE OF METAL ALKOXIDE PRECURSORS

C. SANCHEZ, P. TOLEDANO AND F. RIBOT
Laboratoire de Chimie de la Matière Condensée URA 302
Université Pierre et Marie Curie
4 place Jussieu 75252 Paris France

ABSTRACT

Oxo-alkoxides and allied derivatives are the organic counter part of polyanions and polycations. Most of them do not lead to further polymerization and are therefore dead endswhich are grnerally not directly involved in the formation of macromolecular oxide networks. However their well defined structure make them good models for the basic understanding of the first steps of hydrolysis- condensation reactions. The structural characterization of a new metal oxo species $Ce_6(\mu_3\text{-}O)_4(\mu_3\text{-}OH)_4(acac)_{12}$ obtained via the hydrolysis of acetylacetone modified cerium isopropoxide is presented. Possible mechanisms of formation of this compound as well as for some other titanium $Ti_6(\mu_2\text{-}O)_2(\mu_3\text{-}O)_2(\mu_2\text{-}OAc)_4(\mu_2\text{-}OPr^i)_6(OPr^i)_6$ and niobium $Nb_8O_{10}(OEt)_{20}$ based oxo-alkoxides will be discussed.

INTRODUCTION

Sol-gel chemistry offers unique advantages for making monodispersed powders, multicomponent ceramics, coatings, fibers or even completely new mixed organic-inorganic materials [1,2,3]. It is based on inorganic polymerization reactions. An oxide network can be obtained via hydrolysis and condensation of molecular precursors such as metal alkoxides. This chemistry is controled by parameters such as the hydrolysis ratio, catalysis or molecular structures of precursors [4,5,6]. This latter can be simply modified by oligomerization, solvolysis or addition of nucleophilic chemical additives such as organic acids, β-diketones or allied derivatives which lead to a tayloring of the coordination shell of the metal. The sol gel chemistry of transition metal alkoxides is very different from that of silicon precursors. Main differences arise from the fact that most of the transition metal atoms exhibit a higher electrophilic character and can have several coordination numbers. Consequently transition metal alkoxides can easily present different molecular structures which depend on the nature of the metal (size, electonegativity, d^n or f^n configuration, oxidation state) and on the nature of the ligands. Such differences in the structure of the molecular precursors can drastically change their reactivity. The morphology of TiO_2 powders strongly depends on the nature of the alkoxy group. Spherical monodispersed TiO_2 particles can be obtained via controled hydrolysis of dilute ethanolic solutions of trimeric titanium ethoxide $Ti(OEt)_4$ [7] while polydispersed particles of irregular shape are obtained from monomeric titanium isopropoxide $Ti(OPr^i)_4$ [8]. Oligomerization provides a nice way to promote decoupling between nucleation and growth steps [9].

One of the main parameter that can be easily adjusted is the hydrolysis ratio defined as $h = H_2O/M$. It does not only affect the mean size of macromolecular species, but also their

Mat. Res. Soc. Symp. Proc. Vol. 180. ©1990 Materials Research Society

structure, texture and physical properties. For small h values, condensation is mainly governed by alkoxy bridging, oxolation and in some cases olation reactions. Under such conditions the functionality of precursors towards oxolation and olation is small. As a consequence an infinite network is seldom obtained. Gelation or precipitation cannot occur as long as hydrolysis remains carefully controled (no local excess of water). Both processes, alkoxy bridging and oxolation, lead to molecular oxo-alkoxides. One of the main drawback of transition metal alkoxides is their high reactivity towards water, only few oxo-alkoxides ($Ti_7O_4(OEt)_{20}$[10], $Nb_8O_{10}(OEt)_{20}$ [11], $Zr_{13}O_8(OMe)_{36}$ [12], $Ti_{16}O_{10}(OEt)_{32}$ [13], $Al_{10}O_4(OEt)_{22}$ [14], $Y_5O(OPr^i)_{13}$ [15]) have been isolated as single crystals. Complexation of alkoxides by organic acids, β-diketones and allied derivatives can be used to stabilize such molecular crystals. Most oxo-alkoxides are chemical culs de sac which in most cases are not directly involved in the polymerization of sols and gels. However their well defined molecular structures make them good references for the basic understanding of hydrolysis and condensation mechanisms. This is an aera of research we would like to comment. This paper addresses the structural characterization of some modified oxo-alkoxides and the possible mechanism for their formation.

RESULTS AND DISCUSSION

The synthesis of crystalline oxo-alkoxides (and modified oxo-alkoxides) is governed by the same parameters that control sol-gel chemistry [6]. Three parameters seem to be of first importance: the hydrolysis ratio, the nature of the organic groups (alkoxy, acylate or β-diketonate) and the nature of the metallic center. These three points will be illustrated with different examples choosen in the chemistry of niobium, titanium and cerium alkoxides.

Chemistry of Niobium alkoxides.

Niobium alkoxide chemistry give a good example of the role of the hydrolysis ratio. Niobium(V) has a strong preference for octahedral coordination. In the solid state niobium methoxide is a dimer $Nb_2(\mu_2\text{-}OMe)_2(OMe)_8$. It is made of two edge sharing octahedra with methoxy bridges[16]. In the liquid state cryoscopic measurements and ^1H NMR experiments performed at low temperature (200K) show the presence of several well defined resonances assigned to terminal (axial and equatorial) and bridging methoxy groups [17]. Integration of these peaks agrees with the dimeric structure found in the solid state [17]. ^1H NMR experiments performed at 220K in our laboratory on niobium ethoxide and pentoxide show similar results. However the equilibrium between oligomeric species can be modified in such measurements performed at temperatures lower than room temperature. ^{93}Nb NMR experiments carried out at room temperature on niobium ethoxide diluted in dry ethanol give two broad resonances about 170 ppm apart. Their respective intensities depend on concentration. Such a behavior suggests the presence at room temperature of two solute species probably a dimer $Nb_2(\mu_2\text{-}OEt)_2(OEt)_8$ and solvated monomers $Nb(OEt)_5$,(HOEt) (fig 1a). This assignment agrees with Bradley's results showning that upon hydrolysis primary niobium alkoxides follow a polymerization process based on dimers and solvated monomers [18]. Substoichiometric hydrolysis of niobium ethoxide in ethanol leads to the formation of $Nb_8O_{10}(OEt)_{20}$ single crystals [11]. Their structure

is shown in figure 1c. They are probably formed via Nb_3O_{13} trigonal units built from three edge sharing octahedra (fig 1b). This entity could be formed through the condensation (oxolation) of partially hydrolyzed dimers $Nb_2(OEt)_8(OH)_2$ and monomers $Nb(OEt)_4(OH)_1(HOEt)$. Once such trimeric units are formed they cannot condense together to form compact structures such as hexaniobate (fig 5) or decaniobiate polyanions (fig 1d). The μ_3-oxo ligand cannot be a leaving group in a neutral or acidic medium, and alkoxo ligands increase the steric hindrance preventing the approach of Nb_3O_{13} moieties. Direct condensation between Nb_3O_{13} units is not possible: $Nb_8O_{10}(OEt)_{20}$ crystals are preferentially formed via condensation of Nb_3O_{13} units and monomeric hydrolyzed species that acts as steric spacers. On the other hand the complete hydrolysis of the same niobium ethoxide in the presence of an organic base (NMe_4OH) leads to the formation of a compact decaniobiate polyanion $[Nb_{10}O_{28}(NMe_4)_6, 6H_2O]$ [19] isostructural with the decavanadate $(V_{10}O_{28})^{6-}$ anion. The complete "peeling off " of all organic ligands allows the obtention of a compact structure (fig 2d). Such results can be also obtained with vanadium(V) and tungsten(VI) alkoxides. When hydrolyzed in similar conditions $VO(OBu^t)_3$ leads to the decavanadate $(V_{10}O_{28})^{6-}$ polyanion while $WO(OEt)_4$ leads to $(W_6O_{19})^{3-}$ with the well known Lindqvist structure (fig 5) [20]. Decavanadate $(V_{10}O_{28})^{6-}$ and hexatungstate $(W_6O_{19})^{3-}$ polyanions can also be prepared by acidification of inorganic aqueous precursors [20].

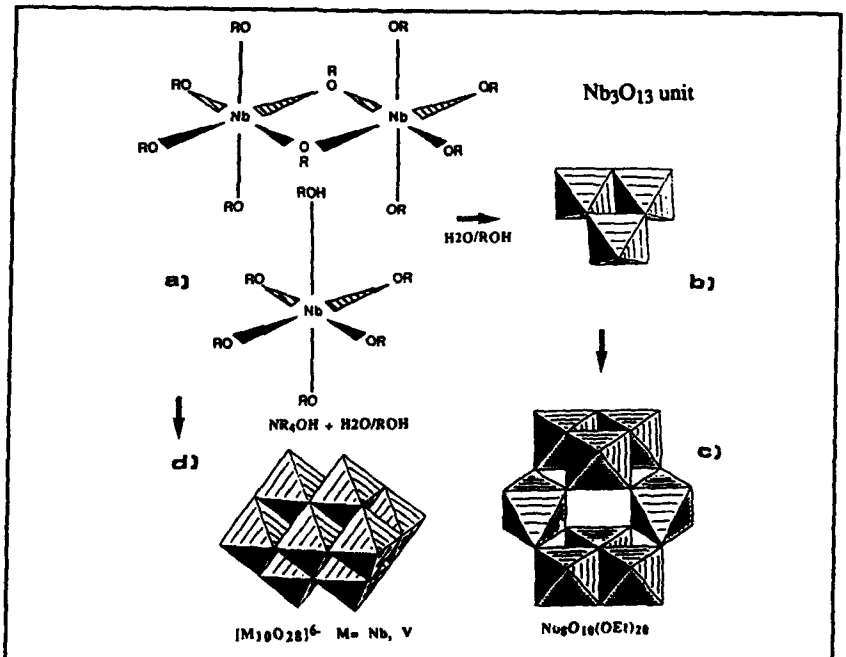


Fig1. molecular structures related to niobium alkoxides chemistry

Chemistry of Titanium alkoxides

Titanium alkoxides with primary alkoxy groups are trimeric species with a pentacoordinated metal atom while those with secondary or tertiary alkoxy groups are monomers with titanium in a tetrahedral environment as shown by cryoscopy [21] and XANES-EXAFS experiments [22,23]. Bradley et al [18,21] carefully studied the hydrolysis of a large number of alkoxides. They showed that the molecular structure of alkoxides has to be taken into account to describe their chemical reactivity. Different models were proposed to account for the hydrolysis behavior of transition metal alkoxides (Ti, Zr, Nb, Ce). For each model the molecular complexity deduced from ebullioscopic experiments was related to the hydrolysis ratio. A sixfold coordination was assumed for metal atoms and the molecular precursor was not supposed to be modified upon hydrolysis and condensation of oligomerized species.

The hydrolysis model of primary titanium alkoxides was based on non solvated trimeric units $Ti_3(OR)_{12}$ while that of titanium alkoxides with bulky alkoxy groups was based on the condensation of solvated monomers $Ti(OR)_4(ROH)_2$. However hydrolysis of monomeric $Ti(OPr^i)_4$ seems also to fit the model based on condensation of trimeric units [18,21]. Moreover quantitative predictions based on solution measurements also show some discrepancies with the molecular stucture found in the solid state by X-ray diffraction. The first hydrolysis product predicted from Bradley's model, $Ti_6O_4(OEt)_{16}$, does not correspond to X-ray data on single crystals giving $Ti_7O_4(OEt)_{20}$ [10].

Hydrolysis and condensation reaction of $Ti(OR)_4$ ($OR=OPr^i$, OBu^n) are strongly modified in the presence of acetic acid (AcOH) [4, 24]. This is due to the complexing ability of acetate ligands. Moreover a detailed analysis of hydrolysis-condensation reactions in the presence of acetic acid can provide information about the chemical role of the acetate group. It also gives some clues on the origin of the discrepancies previously mentionned. X-ray absorption experiments (XANES), performed before and after acetic acid addition, show that the coordination number of Ti increases up to 6. ^{13}C and ^1H NMR show that acetate groups are bonded to titaniufn while one alcohol molecule is released in the solution. The exothermic reaction occuring for a one to one molar ratio can be written as follows :

$$Ti(OR)_4 + AcOH \longrightarrow Ti(OR)_3OAc + ROH$$

Infrared experiments show that acetates behave mainly as bridging bidentate ligands [25]. Moreover EXAFS experiments indicate the presence of Ti-Ti correlations located at about 3.1Å suggesting oligomeric structures for the modified precursors[22,25]. Because of steric hindrance of OPr^i groups, titanium is only fourfold coordinated in monomeric $Ti(OPr^i)_4$ alkoxides. Substitution of OPr^i groups by acetate ligands decreases the steric hindrance and allows the formation of oligomeric species. Molecular structures based on dimers $Ti_2(OR)_6(OAc)_2$ and/ or trimers $Ti_3(OR)_9(OAc)_3$ can be proposed (fig 2a): they are made of edge sharing octahedral $Ti(OR)_3OAc$ units bonded together by both (OR) and (OAc) bridges. Upon ageing in a closed vessel the formation of ester (butyl acetate or isopropyl acetate) is detected by infrared ($\nu(C=O)=1740\ cm^{-1}$).When titanium isopropoxide is used as a precursor this solution leads to the formation of single crystals corresponding to $Ti_6(\mu_2\text{-}O)_2(\mu_3\text{-}O)_2(\mu_2\text{-}OAc)_4$

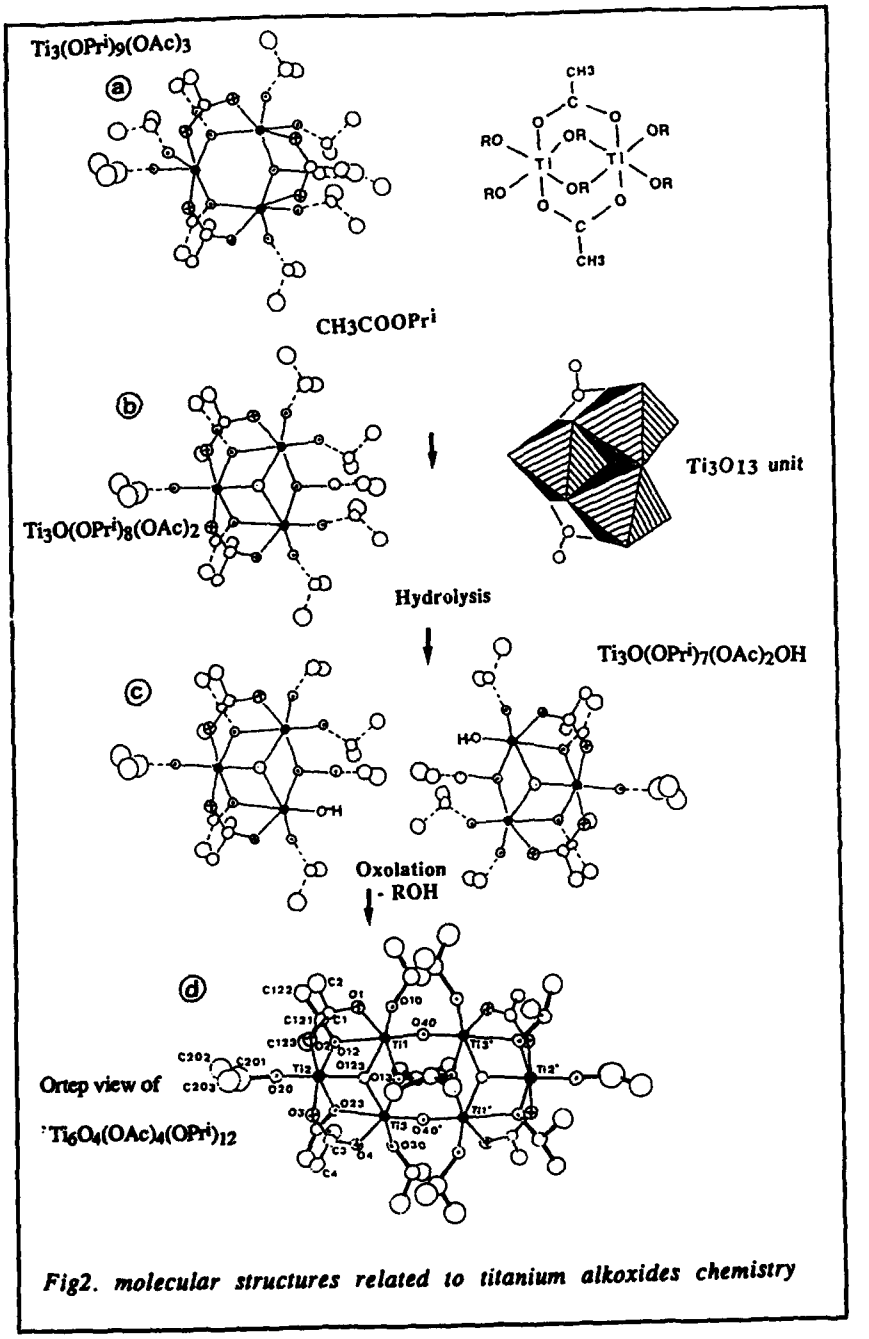


Fig2. molecular structures related to titanium alkoxides chemistry

$(\mu_2\text{-OPr}^i)_6(\text{OPr}^i)_6$. Their structure resolved by X-ray diffraction [26] is presented in figure 2d. It is made of an hexameric titanium cluster in which titanium is in a distorted octahedron. All acetate groups act as bridging ligands. The coordination sphere of each titanium is satisfied with bridging μ-oxo, μ-acetato, as well as terminal and bridging μ-isopropoxy groups. Their obtention probably first involved the formation of the trigonal edge sharing $Ti_3(\mu_3\text{-O})(\mu_2\text{-OAc})_2(\mu_2\text{-OPr}^i)_3(\text{OPr}^i)_3$ species shown in figure 2b. Such trigonal M_3O_{11} units are thermodynamically favored by the presence of a stable μ_3-oxo bridge (enthalpy) and by the removal of two organic ligands (entropy). They are commonly found as building blocks in the framework of the discrete structures of many polyanions and polycations. Two mechanisms can account for the formation of the μ_3-O bridge in Ti_3O_{11} units:

- direct esterification within the trimer $Ti_3(OR)_9(OAc)_3$ (figure 2a) via a template effect. This is a well known mechanism in homogeneous catalysis, already mentionned for alkoxoacylates by Mehrotra et al [27] . Water is virtually provided via this inner shell mechanism and thus oxolation can be performed.
- Esterification in the solution between slowly exchanged organic acid (as suggested by ^{1}H NMR linewidths) and ROH molecules. Such an esterification reaction provides water in-situ leading to homogeneous hydrolysis and then to condensation.

Once $Ti_3(\mu_3\text{-O})(\mu_2\text{-OAc})_2(\mu_2\text{-OPr}^i)_3(\text{OPr}^i)_3$ species are formed hydrolysis of one terminal isopropoxy group leads to $Ti_3(\mu_3\text{-O})(\mu_2\text{-OAc})_2(\mu_2\text{-OPr}^i)_3(\text{OPr}^i)_2\text{OH}$ (fig 2c). Hexamers (fig 2d) can thus simply be obtained via oxolation (elimination of HOPr^i) between two hydrolyzed trimeric units.

Hexamers with different structures can be obtained for an AcOH/Ti ratio of about 2. They correspond to $Ti_6(\mu_2\text{-O})_2(\mu_3\text{-O})_2(\mu_2\text{-OAc})_8(\mu_2\text{-OR})_2(\text{OR})_6$ (with OR=OEt, OBu^n) [28,29]. They are also based on Ti_3O_{11} units but fittings between octahedra are different.

It is interesting to point out that for each of these three compounds the composition $Ti_6O_4(\text{OR}')_{16}$ with OR'= (OR+ OAc) fits perfectly the product $Ti_6O_4(\text{OR})_{16}$ predicted from Bradley's model based on condensation of trimeric units. Bridging acetate groups probably play a double role: it strengthens trimeric units and prevents the formation of a more compact structure such as those of the $Ti_7O_4(\text{OEt})_{20}$. Moreover the presence in all these structures of trigonal Ti_3O_{11}units with a bridging μ_3-O ligand suggest that its formation is the thermodynamically favored step.

When terminal non hydrolyzable chelates such as acetylacetone are added to titanium alkoxide monomeric species, $Ti(\text{OR})_2(\text{acac})_2$ where titanium is in octahedral coordination are formed. Upon ageing those solutions lead via hydrolysis and condensation to dimers $Ti_2(\mu_2\text{-O})\ (\text{acac})_2$ whose stucture was resolved by X-ray diffraction [31]. Condensation is therefore limited by the two functionnality lockers (acac) and by the fact that titanium has already satisfied its sixfold coordination.

Chemistry of Cerium alkoxides.

Modified Cerium(IV) alkoxides provide a nice example where all conditions (nature of the organic ligands, hydrolysis ratio, large orbital extension of the metal) are fulfilled to obtain discrete structures directly related to those obtained in aqueous media .

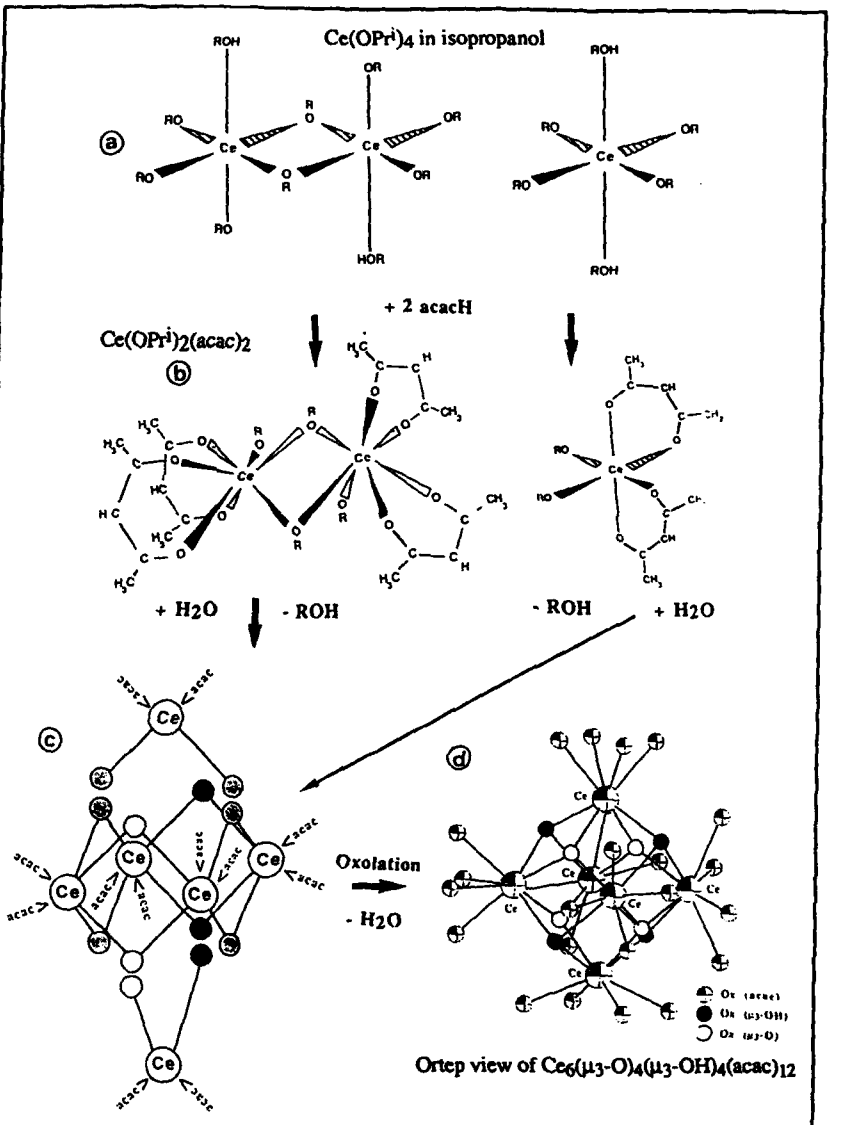


Fig.3 molecular structures related to cerium alkoxides chemistry

The hydrolysis of cerium isopropoxide even with diluted water, readily leads to the precipitation of cerium oxide-based materials. Spontaneous precipitation can be avoided when acetylacetone is added prior to hydrolysis. Sols and gels can be obtained when the acac/Ce ratio is smaller than one, while for a ratio of two, hydrolysis and condensation lead to red single crystals. They correspond to hexameric $Ce_6(\mu_3\text{-}O)_4(\mu_3\text{-}OH)_4(acac)_{12}$ clusters whose structure is shown in figure 3d. It is interesting to point out that such an hexamer is isostructural with the polycation $[Ce_6(\mu_4\text{-}O)_4(\mu_3\text{-}OH)_4(H_2O)_{24}]^{12+}$ [32] obtained in acidic aqueous media. Cerium atoms are in an eight fold coordinated oxygen ligand field (antiprism). Acac groups act as a bidentate ligand located outside the cerium oxo-hydroxo core. Ce-Ce=3.77Å, Ce-O(μ_3-OH)=2.46Å, Ce-O(μ_3-O)=2.21Å, Ce-O(acac)=2.40Å and 2.34Å are the typical distances found in this structure.

A detailed analysis of the chemical reactions involved all along the synthetic route of these crystals was undertaken to provide information about their formation. The structure of cerium isopropoxide was recently resolved by X-ray diffraction[33]. It is made of dimeric molecules (fig 3a), where each cerium is octahedrally coordinated. This coordination is satisfied via isopropoxy bridging and solvate formation. Dimers correspond to $Ce_2(\mu_2\text{-}OPr^i)_2(OPr^i)_6(HOPr^i)_2$. The following mean distances were obtained: Ce-Ce= 3.74Å, four Ce-O=2.32Å and two Ce-O=2.04Å.

^1H NMR experiments performed in solution at RT (in presence of one mole of isopropanol per mole of cerium) showed only one set of resonances characterized by the following chemical shifts: δCH_3 = 1.318ppm, δCH = 4.9 ppm. However such resonances are broad and result from different isopropoxy groups whose resonances are averaged by chemical exchange. This was confirmed by ^1H NMR at 223K which clearly shows the presence of three different sets of resonances located at δCH_3 = 1.49ppm, δCH_3 = 1.27 ppm, δCH_3 = 1.16ppm, δCH = 5.49 ppm, δCH = 4.96 ppm, δCH = 4.6ppm. They can be assigned to terminal and bridging isopropoxy groups and solvating isopropanol molecules. The Fourier transform of the EXAFS signal of cerium isopropoxide in isopropanol is shown in figure 4a. The best fit of the EXAFS signal leads to a mean coordination number of six with three Ce-O distances at 2.13Å, 2.32Å and 2.82Å in a ratio 2:3:1. They can be assigned to terminal, bridging isopropoxy and solvating isopropanol ligands. Moreover a cerium-cerium correlation was observed corresponding to a Ce-Ce distance of 3.78Å.

In agreement with ebullioscopic measurements in isopropanol [18], all these spectroscopic data confirm that the dimeric structure shown in figure 3a is mostly conserved in solution. However as reported by Bradley [18] the variation of the degree of polymerisation with the hydrolysis ratio does not fit perfectly a model based on the unique condensation of dimeric solvated species. A best fit was obtained when a small amount of monomeric solvated species was considered. As a consequence, as for niobium alkoxides, an equilibrium between both dimeric and monomeric solvated species is a more realistic picture of the molecular structure of cerium isopropoxide in isopropanol (fig 3a).

The ^1H NMR spectra of acetylacetone modified precursor exhibits two new resonances located at 1.92ppm and 5.42ppm assigned respectively to δCH_3 and δCH chemical shifts of acetylacetonate ligand bonded to a cerium atom.

Infrared spectrum of a solution where 2 acac groups were added to one $Ce(OPr^i)_4$ molecule show the presence of several vibrations (ν (C-O + C=C) = 1620, 1520 cm^{-1}) indicating that acac group behaves as a bidentate chelating ligand. The reaction is stoichiometric and can be described as follows: $Ce(OPr^i)_4 + 2\ acacH$ ---------> $Ce(OPr^i)_2(acac)_2 + 2\ HOPr^i$.

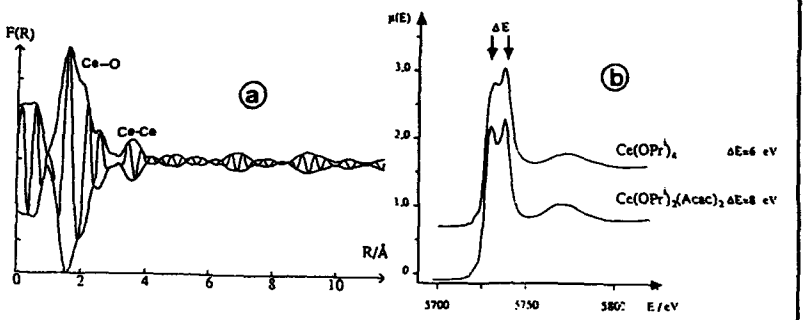


Fig.4 Ce L_{III} edge (a) Fourier transform of the EXAFS of $Ce(OPr^i)_4$ in isopropanol; b) XANES of $Ce(OPr^i)_4$ and $Ce(OPr^i)_2(acac)_2$

X-ray absorption experiments performed before and after acac addition show a variation of the intensity and of the splitting ΔE of the two transitions located on top of the absorption edge (figure 4b). These changes in the XANES spectra suggest that cerium coordination shell is modified upon acetylacetone addition. This was confirmed by EXAFS. The best fit for $Ce(OPr^i)_2(acac)_2$ in isopropanol leads to three Ce-O distances respectively at 2.18Å, 2.34Å and 2.77Å in a 3/4/1 ratio assigned to terminal, bridging isopropoxy ligands and Ce-O (acac) and Ce-O (solvate) distances. Moreover a Ce-Ce correlation was observed corresponding to a distance of 3.71Å. According to these spectroscopic data molecular structures of $Ce(OPr^i)_2(acac)_2$ shown in figure 3b can be proposed,assuming an equilibium between oligomeric species. The infra-red spectrum shows that all the isopropoxy groups are removed upon hydrolysis of $Ce(OPr^i)_2(acac)_2$ (ν (C-O-Ce) = 985 cm^{-1} vibrations have disapeared) while the characteristic vibrations of free acacH (ν (C=O) and ν (C=C) = 1620 cm^{-1}) are not observed. On the basis of our experimental data, a mechanism for the formation of the hexameric $Ce_6(\mu_4\text{-}O)_4(\mu_3\text{-}OH)_4(acac)_{12}$ can be proposed. For h=2 all metal isopropoxy bonds are cleaved leading to fully hydrolyzed modified precursors (fig 3c). Two hydrolyzed dimers can condense via an olation mechanism to form a cyclic tetramer $Ce_4(\mu_2\text{-}OH)_8(acac)_{12}$. Nucleophilic addition occurs as cerium coordination is not fully satisfied. In this tetramer, cerium atoms are in eightfold coordination (antiprism) and bonded together via double hydroxo bridges (fig 3c). Such cyclic tetramers are highly favored thermodynamically (maximum of OH bridges per cerium atom).

They are similar to $[Zr_4(\mu_2\text{-}OH)_8(H_2O)_{16}]^{8+}$ [34] polycations isolated in the aqueous chemistry of zirconium. Finally two hydrolyzed monomers condense with a cerium tetramer via oxolation (elimination of H_2O is the limiting step) to form the hexamer. Eight fold coordination of the cerium atoms belonging to monomers is satisfied through olation (nucleophilic addition).

CONCLUSION

Oxo-alkoxides are the organic counter part of polyanions and polycations which can be obtained in aqueous solutions under a careful control of pH. They can be obtained in both organic and inorganic media because some ligands acts as functionnality lockers for condensation. Such ligands are located outside the oxide rich part of the core. Alkoxy groups and more particularly non hydrolyzable acac ligands play such a role in oxo-alkoxides. Similarly short M=O bonds arising from the metal oxygen π-bonding, typical in tungsten, vanadium and molybdenum chemistry are essentially non basic. They prevent extensive protonation and further polymerization. They play a key role in the formation of discrete polyoxoanions. Polycations are olated clusters, therefore presenting a higher reactivity. Consequently some of them cannot be considered only as dead ends but could be directly involved in the formation of oxide networks[35].

The structure of oxo-alkoxides clusters is close to their inorganic analogs. $Ti_7O_4(OEt)_{20}$ is isostructural with heptamolybdate anion $(Mo_7O_{24})^{6-}$ and $Nb_8O_{10}(OEt)_{20}$ is made of the same structural units as paratungstate $[H_2W_{12}O_{42}]^{10-}$. A question arises when we consider all these discrete structures. Cyclic oligomers with μ-oxo or μ–OH bridges (M_3O_{13}, $M_4(OH)_8L_x$) are always present probably because their formation minimizes free energy. Differences in the end fittings between such small building blocks should be related to the strong differences between hydrolysis and condensation when they occur in organic or in aqueous media. Water has a high dielectric constant, it is a rather good σ donor ligand and act as both a reagent and solvent. Hydrolysis is performed via pH variations. As a consequence inorganic precursors are present as ionic charged species, where the metal coordination is at its maximum value (aquo ions) at least in neutral or acidic media. Organic solvents (usually alcohols) exibit low dielectric constants and weak ligand ability. Water is just added as a reagent. Thus a detailed comparison of similarities and differences between discrete structures (polyanions, polycations, oxo-alkoxides) seems difficult to discuss. However, a parallel can be roughly drawn. Cluster formation can also be driven via metal-metal interactions. They can arise from minimization of electrostatic repulsions or via metal-metal bonding. The former effect arises for large cations with empty orbitals (Ce^{IV}, f^0), while the latter effect is strongly enhanced by a partial filling of valence orbitals. This latter interaction is typical of molybdenum and tungsten oxo-alkoxides in their lower valence state (Mo^V, Mo^{IV}, W^V, W^{IV}). Their chemistry is mainly controlled by metal-metal interactions [36] which decrease W-W or Mo-Mo distances by about 0.7Å-1.2Å. Such interactions can be so strong that compact trigonal clusters such as $Mo_3(\mu_3\text{-}O)(OR)_{10}$ made with three face sharing octahedra can be formed [36].

However main differences between organic and aqueous chemistry are related to the nature and the amount of organic ligands still bonded to the metal, and thus to the hydrolysis ratio. Organic ligands play an important role in oxo-alkoxide formation:

- The ability of oxo-alkoxides to crystallize usually decreases with increasing the bulkiness of alkoxy groups. Most of the reported X-ray structures were carried out in the presence of small OR groups such as methoxy or ethoxy .
- Alkoxy ligands being strong π-donors, transition metal alkoxides are usually neutral species in which maximum metal coordination is generally not satisfied. Consequently during the first steps of hydrolysis and condensation reactions, large cations (Zr, Y, Hf, Ce) are prone to nucleophilic additions (olation, alkoxy-bridging) leading to the formation of oxo-alkoxide structures.
- The location of different ligands inside molecular structures can be different. Some of them prefere bridging positions (acetic acid), while others act in most cases as terminal ligands (acetylacetone). Alkoxy groups can act both as bridging or terminal ligands.
-Alkoxy groups, bidentate ligands (organic acids) and strong chelating agents (β-diketones) present strong differences in their reactivity towards hydrolysis (β-diketones<acetic acid<alkoxy groups). However even bridging and terminal alkoxy groups can present a slightly different reactivity.

The hydrolysis ratio controls the number of organic ligands still bonded to the metal. However, their final number strongly depends on their reactivity and consequently on their nature. It is one of the most important external parameter. It corresponds directly to the amount of water added to the alkoxide precursor or to the OH/ metal ratio obtained by pH adjustement of the aqueous solution of the inorganic precursor. It is interesting to point out that increasing the hydrolysis ratio avoids steric hindrance created by the OR groups and allows the formation of more compact discrete structures. Substoichiometric hydrolysis of niobium ethoxide leads to $Nb_8O_{10}OEt_{20}$ while complete hydrolysis leads to the decaniobate anion. In the same way discrete polyoxovanadate and polyoxotungstate increase their compacity when the pH decreases i.e by forcing oxygen protonation and allowing condensation. As shown in figure 5 more compact polyanions are formed when the pH decreases [20] :

$(H_2W_{12}O_{42})^{10-}$ (Z=1.1) --> $(H_2W_{12}O_{42})^{6-}$ (Z=1.5) -->$(W_{10}O_{32})^{4-}$ (Z=1.5) -->$(W_6O_{19})^{2-}$(Z= 1.67) (Z= p/n number of protons/ number of metallic centers).

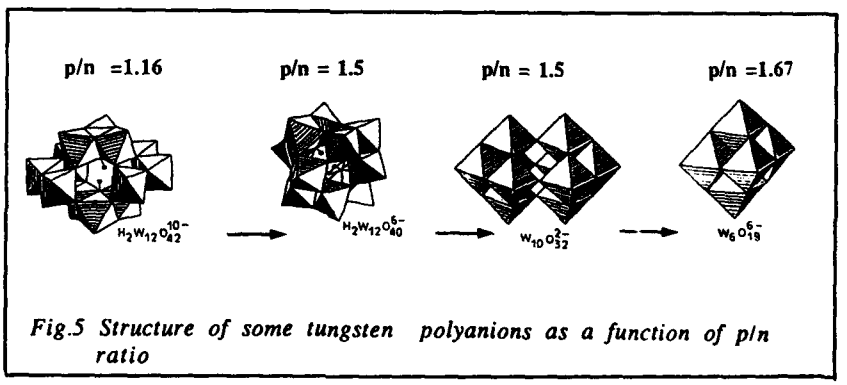


Fig.5 Structure of some tungsten polyanions as a function of p/n ratio

In a similar way hydrolysis of a molar solution of $VO(OPr^n)_3$ in n-propanol with different amounts of water leads to different compounds[37]. For h =3 transparent orange monolithic gels made of a highly branched alkoxo-oxide polymeric network are obtained within a few seconds while thixotropic red vanadium pentoxide based gels made of flat ribbons are obtained within a few hours when h becomes larger than 100. These latter gels are also obtained upon acidification of an aqueous solution of metavanadate.

In conclusion this paper shows that for a given metal, identical clusters can be obtained in both aqueous $(Ce_6(\mu_3\text{-}O)_4(\mu_3\text{-}OH)_4(H_2O)_{24})^{12+}$ and organic $Ce_6(\mu_3\text{-}O)_4(\mu_3\text{-}OH)_4(acac)_{12}$ media when all the following chemical parameters are fulfilled.

- Terminal non hydrolyzable ligands can stop extensive condensation (acac). An acac/Ce ratio of two is needed to sufficiently decrease the functionnality of the precursor towards hydrolysis.
- Hydrolysis is strongly differentiated: for h = 2 all alkoxy groups have been removed while all acac groups are still bonded to Ce atoms.
-Cerium IV is a large cation favoring cluster formation.

AKNOWLEDGEMENTS: A. Michalowicz is gratefully acknowledged for the use of his performing EXAFS programms. Rhône Poulenc S.A. is also aknowledged for the financial support of one of the authors.

REFERENCES:

1. B.J.J. Zelinski. and D.R. Ulhmann, J. Phys. Chem. Solids 45, 1069 (1984).
2. H. Dislich and P. Hinz, J. Non-Cryst. Solids 48, 110 (1982).
3. C.J. Brinker and G. Scherrer , in Sol-Gel Science, the physics and chemistry of sol-gel processing, (Academic Press, Harcourt Brace Jovanovich, Pubs, 1989).
4. C. Sanchez, J. Livage, M. Henry and F. Babonneau, J. Non-Cryst. Solids 100, 650 (1988).
5. J. Livage, M. Henry and C. Sanchez, Progress in Solid State Chemistry 18, 259, (1988).
6. (a) C. Sanchez, J. Livage , New J. of Chem., in print (1990); (b) M. Nabavi , S. Doeuff, C. Sanchez and J. Livage, J. Non-Cryst. Solids (in print)
7. E.A. Barringer and H.K. Bowen, Langmuir 1, 23 (1985).
8. E.A. Barringer and H.K. Bowen, J. Amer. Ceram. Soc. 65, C199 (1982).
9. J. Livage, M. Henry, J.P. Jolivet and C. Sanchez, MRS bulletin XV(1) 18 (1990).
10. K. Watenpaugh and C.N. Caughlan, Chem. Comm, 76 (1967).
11. D.C. Bradley, M.B. Hurthouse and P.F. Rodesiler, Chem. Comm, 1112 (1968).
12. B. Morosin, Acta Cryst B 33, 303 (1977).
13. A. Mosset and J. Galy, C. R. Acad. Sci. Paris 307, 1747 (1988).
14. A.I. Yanovskii, N.Y. Turova, N.I. Kozlova, and Y. Stychkov, Koord. Khim. 13 (2) 242, (1987).
15. O. Poncelet, W.J. Sartrain, L.G. Hubert-Pfalzgraf, K. Folting and K.G. Caulton, Inorg. Chem. 28, 263 (1989).
16. A.A. Pinkerton, D. Schwarzenbach, L.G. Hubert-Pfalgraf, and J.G. Riess, Inorg. Chem. 15, 1196 (1976).
17. (a) J.G. Riess, and L.G. Hubert-Pfalzgraf, Chimia 30, 481 (1976); (b) L.G. Hubert-Pfalzgraf, New J. of Chem. 11, 663 (1987).
18. D.C. Bradley, Coord. Chem. Review 2, 299 (1967).
19. E.J. Graeber and B. Morrison, Acta Cryst. B 33, 2136, (1977).

20. M.T. Pope, in Heteropoly and Isopoly Oxometalates, Inorg. chem. concepts 8, (Springer Verlag, Berlin 1983).
21. D.C. Bradley , R.C. Mehrotra and D.P. Gaur, in Metal Alkoxides, (Academic Press, New York, 1978).
22. C. Sanchez, F. Babonneau, S. Doeuff and A. Leaustic, in Ultrastructure processing of Advanced Ceramics, edited by J.D. Mackenzie and D.R. Ulrich (Wiley, New-York, 1988) p. 77.
23. F. Babonneau, S. Doeuff, A. Leaustic, C. Sanchez, C. Cartier and M. Verdaguer , Inorg. Chem. 27, 3166 (1988).
24. S. Doeuff, M. Henry, C. Sanchez and J. Livage, J. Non-Cryst. Solids 89, 206, (1987).
25. J. Livage, C. Sanchez, M. Henry and S. Doeuff, Solid State Ionics 32-33, 633 (1989).
26. S. Doeuff, Y. Dromzee and C. Sanchez, C. R. Acad. Sci. II 309, 531 (1989).
27. R.C. Mehrotra and R. Bohra, in Metal Carboxylates, (Academic Press, London, 1983)
28. I. Luneau-Gautier, A. Mosset and J. Galy , Zeit. Krist. 180, 83 (1987).
29. S. Doeuff ,Y. Dromzee, F. Taulelle and C. Sanchez, Inorg. Chem. 28, 4439 (1989).
30. R.C. Mehrotra, R. Bohra and D.P. Gaur, in Metal β-diketonates and allied derivatives, (Academic Press, London, 1978).
31. G.D. Smith, C.N. Caughlan and J.A. Campbell, Inorg. Chem. 11(12) 2989 (1972).
32. G. Lungren, Rec. Trav. Chim. 75, 585 (1956).
33. (a) P. Toledano, F. Ribot and C. Sanchez , Acta Cryst., (in print, 1990).
    (b) B.Vaartstra, J.C. Daran, P.S. Gradeff, L.G. Hubert-Pfalzgraf, J.C. Parraud, K. Yunlu, and K.G. Caulton, Inorg. Chem., (in print, 1990)
34. A. Clearfield and P.A. Vaughan, Acta Cryst. 9, 555 (1956).
35. M. Henry, J.P. Jolivet and J. Livage, Stucture and Bonding, (in print, 1990).
36. M. H. Chilsholm, Polyhedron 2, 681 (1983).
37. C. Sanchez, M. Nabavi and F. Taulelle, Better Ceramics Through Chemistry III, Brinker C.J., Clark D.E. and Ulrich D.R. Eds (Mater. Res. Soc. Proc. 121 1988) p. 82.

MOLECULAR ROUTES TO TIN OXIDES

T.A. WARK*, E.A. GULLIVER*, L.C. JONES*, M.J. HAMPDEN-SMITH*, A.L. RHEINGOLD** AND J.C. HUFFMAN***

*Department of Chemistry and Center for Micro-Engineered Ceramics, University of New Mexico, Albuquerque, NM 87131.

**Department of Chemistry, University of Delaware, Newark, DE 19716.

***Molecular Structure Center, Indiana University, Bloomington, IN 47405.

ABSTRACT

A general route to low temperature synthesis of ternary metal tin oxides with controlled stoichiometries from single component molecular metal alkoxide precursors is described. The solid state and solution structures of homoleptic tin(IV) alkoxide compounds have been investigated to establish criteria for the determination of their solution structure. Tin alkoxide compounds suitable for metathesis reactions have been synthesized and used to prepare the mixed metal alkoxide compounds $[ZnSn(OEt)_6]$ and $[((COD)Rh)_2Sn(OEt)_6]$ (where Et = ethyl and COD = 1,5-cyclooctadiene). Hydrolysis of $[ZnSn(OEt)_6]$ at neutral pH results in the formation of a high surface area, mainly amorphous hydrous oxide powder which forms Zn_2SnO_4 and SnO_2 on heating to 600°C and $ZnSnO_3$ on heating to 1000°C.Thermolysis of $[\{(COD)Rh\}_2Sn(OEt)_6]$ results in formation of rhodium and tin(IV) oxide (cassiterite phase).

INTRODUCTION

The preparation of metal oxide ceramics is currently an area of intense scientific and industrial interest. In particular, complex metal oxides such as superconducting phases [1] and ferroelectric materials [2] have received much attention. Significant advances in this area are likely to arise from new synthetic strategies [3], new processing techniques [4] and a better understanding of condensation phenomena [5]. The work described here is aimed at developing a systematic synthetic approach for preparing multicomponent metal oxides and investigating condensation processes.

For many years, metal alkoxide compounds have been used as precursors for the formation of metal oxides by sol-gel type hydrolytic condensation [3,6]. The potential advantages of this method over other methods include lower processing temperatures, better homogeneity, controlled stoichiometry and flexibility of processing to form dense monoliths, thin films or high surface area powders, for example. A number of different approaches have been taken to synthesize mixed metal oxides. In most studies, solutions containing mixtures of different metal alkoxide compounds have been hydrolytically condensed [7], while there are

Mat. Res. Soc. Symp. Proc. Vol. 180. ©1990 Materials Research Society

relatively few studies in which discrete, molecular mixed metal alkoxide species have been hydrolyzed [8]. A potential advantage of using a single component molecular precursor is that stoichiometry should be controlled on the molecular level.

As part of our studies to prepare mixed metal oxides with controlled stoichiometries, we are developing a systematic approach centered on tin(IV) alkoxide chemistry as shown below,

$$\underset{\mathbf{A}}{nMOR} + \underset{\mathbf{A}}{Sn(OR)_4} \text{ --------> } \underset{\mathbf{B}}{M_nSn(OR)_{4+n}} \quad (1)$$

$$\underset{\mathbf{B}}{M_nSn(OR)_{4+n}} + M'X_m \text{ --------> } \underset{\mathbf{C}}{M'[Sn(OR)_{4+n}]_m} + mMX \quad (2)$$

$$\underset{\mathbf{C}}{M'[Sn(OR)_{4+n}]_m} \xrightarrow{-H_2O} \underset{\mathbf{D}}{condensation} \text{ ---> } \underset{\mathbf{E}}{M'Sn_mO_{m(4+n)/2}} \quad (3)$$

where M represents an exchangeable cation that is replaced by a different metal (M') in the second step to form the molecular mixed metal alkoxide precursor with the desired M:Sn ratio [9]. This metal alkoxide is subsequently hydrolyzed to form a mixed metal hydrous oxide that is thermally dehydrated to form the final mixed metal oxide. Particular points of focus for this work are (i) synthetic routes to **B**-**E** with systematically varied stoichiometries, (ii) characterization of the solid state and solution structures of **A**-**D** and (iii) the phase transformations of **D**-**E**. These aspects are discussed here for homoleptic tin(IV) alkoxide compounds, metastable tin(IV) alkoxide compounds and for the formation of bimetallic systems.

A possible limitation of this approach to the formation of metastable phases of mixed metal oxides is the temperature required for the final dehyrdration step which, if too high, may result in separation of thermodynamically stable phases. As a result, we are also seeking alternative approaches to hydrolytic/thermal condensation for the conversion of metal alkoxide compounds to metal oxides. One approach discussed here is transition metal induced thermolysis of alkoxide ligands.

1. EXPERIMENTAL

All manipulations were carried out under an atmosphere of dry (molecular sieves) and deoxygenated (MnO) dinitrogen [10]. All hydrocarbon and ethereal solvents were dried and distilled from sodium benzophenone ketyl. Alcohols were dried by distillation from magnesium turnings [11]. NMR solvents were dried over 4A molecular sieves and stored under N_2. Sn(O-t-Bu)$_4$ was prepared by a method analogous to that published by Chandler et al. [12]. Elemental

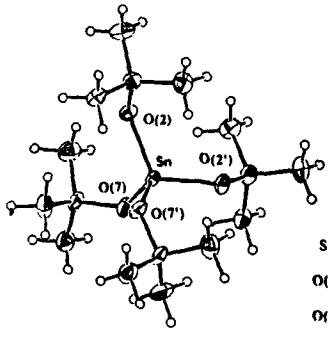
analyses were performed by Oneida Research Services. NMR data were recorded on a Bruker AC-250P NMR spectrometer using the protio impurities of deuterated solvents as references for ^{1}H NMR spectroscopy and the ^{13}C NMR resonances of the solvents as references for ^{13}C NMR spectroscopy. Temperatures were calibrated with either ethylene glycol or methanol. Infra-red spectra were recorded on a Perkin-Elmer 1620 FTIR. Molecular weights were determined *cryoscopically* at two different concentrations by freezing point depression of benzene [13].

Detailed synthetic procedures, spectroscopic and X-ray structural data are being published elsewhere.

2. SOLID STATE AND SOLUTION STRUCTURAL CHARACTERIZATION OF HOMOLEPTIC TIN(IV) ALKOXIDE COMPOUNDS.

While the synthesis of many homoleptic tin(IV)alkoxide compounds has been published [14], there is little solid state or solution structural data available. As a starting point, we have studied some simple examples in order to develop criteria for the basis of solution structural assignment. In the solid state, $Sn(O\text{-}t\text{-}Bu)_4$, **E**, (Figure 1) and $[Sn(O\text{-}i\text{-}Pr)_4.HO\text{-}i\text{-}Pr]_2$, **G**, (Figure 2) are monomeric and dimeric, respectively [15].

$Sn(O\text{-}t\text{-}Bu)_4$ possesses terminal alkoxide ligands and exhibits a distorted tetrahedral tin environment, *probably as a result of the steric* conjestion caused by the t-butyl groups. $[Sn(O\text{-}i\text{-}Pr)_4.HO\text{-}i\text{-}Pr]_2$ adopts an edge-shared bioctahedral structure similar to that proposed by Bradley and coworkers for the analogous zirconium compound [16]. The Sn-O distances increase in the order $Sn\text{-}OR_{terminal} < Sn\text{-}OR_{bridging} < Sn\cdots HOR$ as expected. The coordinated alcohol ligands can clearly be distinguished in the solid state by their long Sn····O distances and the distortion of the axial terminal alkoxide ligands is a result of an asymmetric hydrogen bonding interaction.



Sn-O(2) = 1.946(2) Sn-O(7) = 1.949(2)
O(2)-Sn-O(2') = 115° O(2)-Sn-O(7') = 105°
O(7)-Sn-O(7') = 115° Sn-O(2)-C(3) = 125°

Figure 1: The molecular structure of $Sn(O\text{-}t\text{-}Bu)_4$

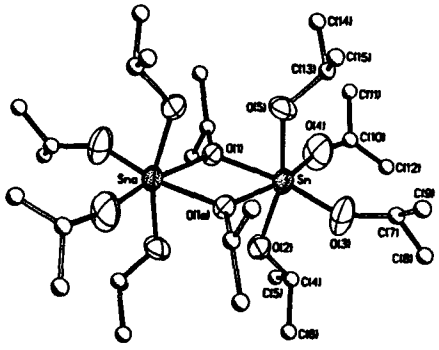
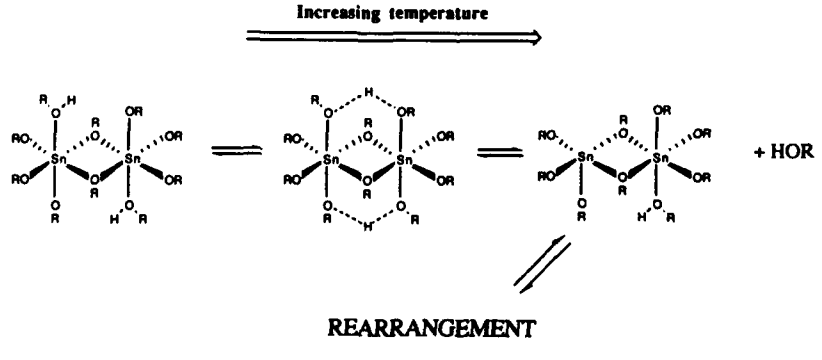


Figure 2: The molecular stucture of $[Sn(O\text{-}i\text{-}Pr)_4.HO\text{-}i\text{-}Pr]_2$

$Sn(O\text{-}t\text{-}Bu)_4$ was chosen for study since it contains only terminal alkoxide ligands. In the solid state, the position of $\nu(Sn\text{-}OR_{terminal}) = 605cm^{-1}$ can be unambiguously established by comparison to the per-deuterated compound $Sn(O\text{-}t\text{-}Bu\text{-}d_9)_4$ in which $\nu(Sn\text{-}OR^*_{terminal}) = 568$ cm^{-1} (where OR* = O-t-Bu-d_9), close to the calculated value [17]. In solution, $Sn(O\text{-}t\text{-}Bu)_4$ is monomeric and exhibits a ^{119}Sn NMR resonance at -375ppm. In the ^{13}C NMR spectrum, the terminal $^2J_{IC\text{-}SnI} = 45Hz$ and $^3J_{IC\text{-}SnI} = 27Hz$ coupling constants are observed. These values can be compared to the analogous coupling constants in tin alkoxide compounds containing doubly bridging alkoxide ligands such as $[Tl_2Sn(OEt)_6]$ [18], **H**, and $[\{(COD)Rh\}_3Sn(OEt)_6]^+ PF_6^-$ [19] for which $^2J_{IC\text{-}SnI} = 27Hz$ and 25Hz, respectively. We have not yet developed a system for the unambiguous measurement of $^2J_{IC\text{-}SnI}$ in triply bridging alkoxide systems.

In solution at room temperature $[Sn(O\text{-}i\text{-}Pr)_4.HO\text{-}i\text{-}Pr]$ has a molecular complexity of 1.6-1.8, and exhibits only one type of O-i-Pr environment as determined by ^1H and ^{13}C NMR spectroscopy. At lower temperatures, four types of O-i-Pr resonances are observed in a 1:2:1:1 ratio. Details of the variable temperature ^{13}C and ^1H NMR data will be published elsewhere, and are consistent with a dynamic solution process as described by Scheme 1.



Scheme 1: Proposed mechanism for dynamic solution behavior of **G**.

At room temperature, a facile alcohol exchange process occurs which results in scrambling of the alkoxide ligands via a five coordinate intermediate, while at -60°C, the alcohol ligands are coordinated to tin, but the protons exchange rapidly between the axial oxygen atoms. Further evidence for this mechanism comes from the observation that the isopropoxide ligands of $[Sn(O\text{-}i\text{-}Pr)_4.HO\text{-}i\text{-}Pr]_2$ exchange rapidly with added isopropanol at room temperature, but separate resonances for the added isopropanol are observed below -50°C.

3. SYNTHESIS OF METAL TIN ALKOXIDE COMPOUNDS FOR METATHESIS REACTIONS.

In our first experiments in this area we have prepared $[Tl_2Sn(OEt)_6]$, **II**, by the reactions shown in equations 4 and 5 below [18].

$$Sn(O\text{-}t\text{-}Bu)_4 + \text{excess } HOEt \text{ -----> } [Sn(OEt)_4] + 4HO\text{-}t\text{-}Bu \quad (4)$$

$$2TlOEt + [Sn(OEt)_4] \text{ -----> } [Tl_2Sn(OEt)_6] \quad (5)$$

It is important to note that the addition of one equivalent of TlOEt to $Sn(OEt)_4$ results in the isolation of half an equivalent of $[Tl_2Sn(OEt)_6]$, and not $[TlSn(OEt)_5]$. Thallium was chosen as the exchangeable cation due to the extremely low solubility of thallium halides which contributes to the thermodynamic driving force for subsequent metathesis reactions.

In the solid state $[Tl_2Sn(OEt)_6]$ exists as a one-dimensional infinite polymer as shown in Figure 3, but is monomeric in benzene solution. The solution spectroscopic characterization data are consistent with the structure shown below in Figure 4 which is analogous to the solid state structure of $SrSn_2(O\text{-}t\text{-}Bu)_6$ [20].

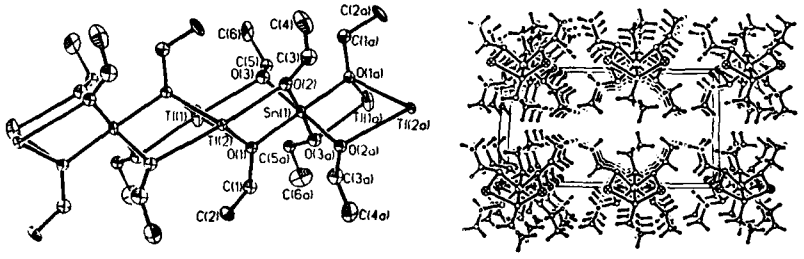


Figure 3: Solid state structure of $[Tl_2Sn(OEt)_6]$

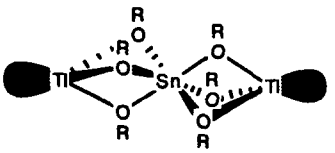


Figure 4: Proposed solution structure of $[Tl_2Sn(OEt)_6]$

These observations emphasize the need for both solid state and solution structural characterization of these species.

Sources of $[Sn(OR)_5]^-$ are also being developed including $[KSn(O\text{-}t\text{-}Bu)_5]$, **J**, and $[LiSn(OEt)_5]$, **J** [21]. $[KSn(O\text{-}t\text{-}Bu)_5]$ possesses one type of alkoxide ligand in solution as determined by ^1H and ^{13}C NMR spectroscopy in the temperature range +23°C to -90°C. In the ^{13}C NMR spectrum, the two bond $^2J_{C\text{-}Sn} = 47Hz$ is consistent with the presence of terminal alkoxide ligands in solution. $[LiSn(OEt)_5]$ is tetrameric in benzene solution and exhibits two types of ethoxide ligands at room temperature (by ^1H NMR spectroscopy). It is noteworthy that the ^{119}Sn NMR chemical shifts of these species are significantly shielded compared to the parent neutral complex. For example, the ^{119}Sn NMR chemical shift of $[KSn(O\text{-}t\text{-}Bu)_5]$ is 214.8 ppm further *upfield* than that of $Sn(O\text{-}t\text{-}Bu)_4$, consistent with a significant increase in negative charge located at the tin center. The solid state and solution structures of these species have not yet been unambiguously determined.

4. METATHESIS REACTIONS

$[Tl_2Sn(OEt)_6]$ acts as a source of $[Sn(OEt)_6]^{2-}$ as demonstrated by its reactions with a number of metal halides. Two examples will be discussed here, the preparation of $[ZnSn(OEt)_6]$ and $[\{(COD)Rh\}_2Sn(OEt)_6]$, according to the reactions of equations 6 and 7.

$$\underset{\mathbf{H}}{[Tl_2Sn(OEt)_6]} + ZnCl_2 \text{ --------> } \underset{\mathbf{K}}{[ZnSn(OEt)_6]} + 2TlCl \qquad (6)$$

$$\underset{\mathbf{H}}{[Tl_2Sn(OEt)_6]} + [(COD)RhCl]_2 \text{ ---> } \underset{\mathbf{L}}{[\{(COD)Rh\}_2Sn(OEt)_6]} + 2TlCl \qquad (7)$$

Compound **K** is isolated as a glassy solid, which exhibits a single type of alkoxide ligand as determined by NMR spectroscopy, even at -90°C. Compound **L** is monomeric both in benzene solution and in the solid state and exhibits only one type of ethoxide and cyclooctadiene ligand according to ^1H and ^{13}C NMR spectroscopy at room temperature. On cooling to -90°C in

toluene-d_8 solution, the ^1H NMR resonances broaden, but the low temperature limiting spectrum could not be obtained in this solvent.

The solid state structure of **I** is shown in Figure 5 and consists of a distorted $Sn(OEt)_6^{2-}$ octahedron with two pairs of ethoxide ligands coordinated to two $\{(COD)Rh\}^+$ moities in a *cis* fashion leaving two terminal ethoxide ligands [19].

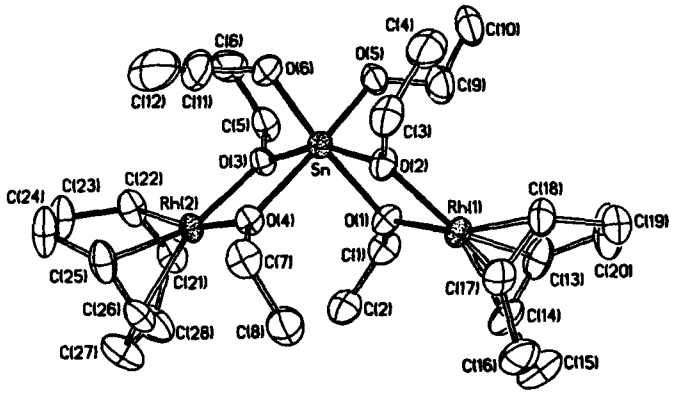


Figure 5: Solid state molecular structure of $[\{(COD)Rh\}_2Sn(OEt)_6]$

The COD ligands can be replaced by reaction with carbon monoxide to form $[\{(CO)_2Rh\}_2Sn(OEt)_6]$. We believe that in solution, rapid intramolecular rearrangement occurs on the NMR timescale. This is consistent with the solution spectroscopic data, including the retention of $^2J_{IC\text{-}SnI}$ and $^3J_{IC\text{-}SnI}$ coupling constants in the ethoxide ligands and $^1J_{IC\text{-}RhI}$ coupling constants of the COD ligand in $[\{(COD)Rh\}_2Sn(OEt)_6]$, and the coupling between ^{13}CO and ^{119}Sn in $[\{(CO)_2Rh\}_2Sn(OEt)_6]$ during the fast exchange limit.

5. HYDROLYTIC CONDENSATION OF $[ZnSn(OEt)_6]$

Hydrolysis of toluene solutions of $[ZnSn(OEt)_6]$ at room temperature results in formation of a fine white powder. The material is mainly amorphous (as determined by X-ray powder diffraction) and its IR spectrum has broad absorptions at 3400, 900 and 600 cm^{-1}. No evidence was found for residual C-H bonds. However, combustion elemental analysis indicated the presence of both C (2.60%) and H (1.64%) and atomic absorption spectroscopy indicated that the Zn (17.0 weight%) to Sn (30.8 weight%) ratio of 1:1 had been retained. Thermogravimetric analysis of the powder demonstrated three major weight losses between 50-400°C (13%), 400-

500°C (1%) and 550-900°C (10%) to give a total weight loss of approximately 24% up to 1000°C. The surface area of the hydrolyzed material was measured by nitrogen absorption to be 261m^2/g. On successive heating to 200°C, 400°C and 600°C, the surface area changed to 250m^2/g, 61m^2/g and 24m^2/g, respectively. An unidentified crystalline phase (or phases) was formed on hydrolysis, however, on heating to 600°C, two crystalline phases are formed, Zn_2SnO_4 (inverse spinel) and SnO_2 (cassiterite). Further heating to 1000°C results in formation of crystalline $ZnSnO_3$.

6. CONDENSATION OF METAL ALKOXIDE COMPOUNDS BY NON-HYDROLYTIC PROCESSES

The thermogravimetric analysis of $[\{(COD)Rh\}_2Sn(OEt)_6]$ under a nitrogen atmosphere is shown in Figure 6 below.

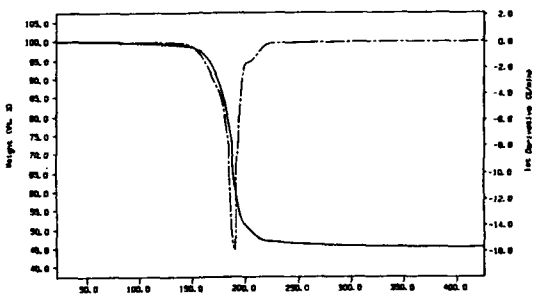
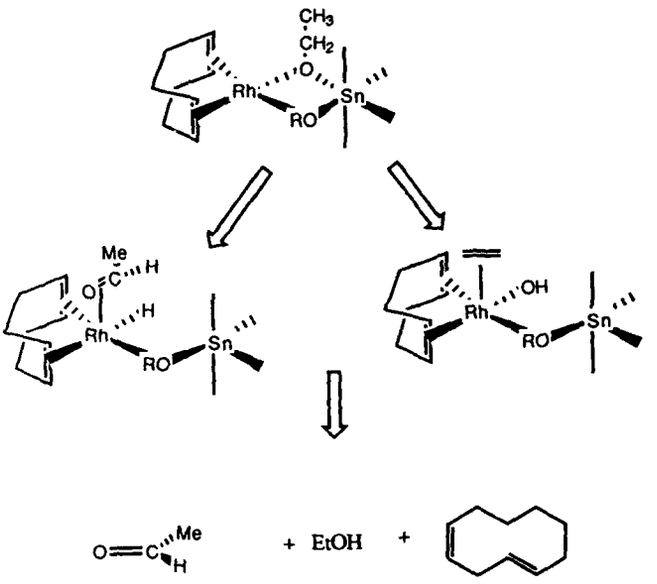


Figure 6: Thermogravimetric analysis of $[\{(COD)Rh\}_2Sn(OEt)_6]$

The onset of significant weight loss occurs at about 150°C and is complete by approximately 220°C. Yellow crystals of $[\{(COD)Rh\}_2Sn(OEt)_6]$ melt at 82-84°C to form a yellow liquid which begins to turn black at 150°C. The observed weight change corresponds to the loss of all the organic fragments and consistent with a residue of composition "Rh_2SnO_3". There is no further detectable weight change on heating this sample to 1039°C. An X-ray powder diffraction experiment revealed that this black powder residue (after heating the 1039°C) contained only Rh metal and SnO_2 (cassiterite), as crystalline phases.

To investigate this system further, a large scale thermal decomposition experiment was conducted under dry nitrogen (1 atm) and the evolved volatile by-products were trapped at -196°C. Two major components were observed: ethanol and a cyclooctadiene derivative, together with trace amounts of other components including acetaldehyde. Surprisingly, no evidence for ethylene was observed [22]. The volatile by-products were then fractionated under vacuum and the

cyclooctadiene derivative separated. ^{1}H and ^{13}C NMR data together with IR and Mass spectral data are consistent with the formation of an organic fragment with the empirical formula $C_{10}H_{16}$ - formally derived from the addition of COD and ethylene. The spectroscopic evidence for $C_{10}H_{16}$ is consistent with the structure *cis,trans*-1,4-cyclodecadiene[23]. These reaction products can be accounted for by activation of C-H bonds by the coordinatively unsaturated 16 electron rhodium(I) center according to Scheme 2.



Scheme 2: Proposed thermal decomposition pathways for $[\{(COD)Rh\}_2Sn(OEt)_6]$.

We are currrently conducting isotope labelling experiments to investigate this hypothesis.

X-ray diffraction data on the powder that had been heated to 300°C is consistent with the presence of mainly amorphous material with some evidence for crystalline rhodium metal. Nitrogen absorption measurements indicate that this powder has a very low surface area of 4 m^2/g.

7. CONCLUSIONS

The solid state and solution structures of homoleptic tin(IV) and mixed metal tin(IV) alkoxide compounds are being investigated and mechanisms for dynamic solution rearrangements have been proposed. It is envisaged that a better understanding of these solution structures will lead

to greater control over hydrolytic condensation. The mixed metal alkoxide [$ZnSn(OEt)_6$] has been prepared and on hydrolytic condensation fromed an as yet unidentified crystalline phase together with amorphous material. Heating resulted in crystallization of Zn_2SnO_4 and SnO_2, initially and subsequently $ZnSnO_3$. The thermal decomposition of [$\{(COD)Rh\}_2Sn(OEt)_6$] has been studied and evidence has been presented that the rhodium center is involved in decomposition of the ethoxide ligands.

8. ACKNOWLEDGEMENTS

This work is supported by the UNM/NSF Center for Micro-Engineered Ceramics and Sandia National Laboratories. We thank NSF for the purchase of an NMR spectrometer under the Chemical Instrumentation program, Greg Johnston for surface area measurements, Shirley Weaver for SEM data, Ted Borek for help in obtaining some of the X-ray diffraction data and the Johnson-Matthey precious metals loan program.

8. REFERENCES

1. a. H.M. Hsu, I. Yee, J. DeLuca, C. Hilbert, R.F. Miralky and N.L. Smith, *Appl. Phys. Lett.*, 54, 957, **1989**: b. A. Gupta, E.I. Cooper, R. Jagannathan and E.A. Geiss, ACS symposium series No. 377, *"Chemistry of High T_c Superconductors"*, T.T. George and D.L. Nelson Eds.: c. *"Better Ceramics Through Chemistry III"* Part IV, C.J. Brinker, D.E. Clark and D.R. Ulrich, Eds., MRS symposium proceedings, **1988**: d. S.C. Goel, K.S. Kramer, P.C. Gibbons and W.E. Buhro, *Inorg. Chem.*, 28, 3619, **1989**.

2. a. J.C. Debsikerdar, *J. Mat. Sci.*, 20, 4454, **1985**: b. J.B. Blum and S.R. Gurkovich, *J. Mat. Sci.*, 20, 4479, **1985**: c. J.L. Rehspringer, S. El Hagigui, S. Vilminot, P. Poix and J.C. Beringer in *"Ultrastructure Processing of Advanced Ceramics"*, J.D. Mackenzie D.R. Ulrich, Eds, Wiley, **1988**: d. D.R. Ulrich, *J. Non-cryst. Solids*, 100, 174, **1988**: e. J. Mackenzie, *J. Non-cryst. Solids*, 100, 162, **1988**: f. E. Wu, K.C. Chen and J.D. Mackenzie in *"Better Ceramics Through Chemistry"* , C.J. Brinker, D.E. Clark and D.R. Ulrich, Eds., MRS symposium proceedings, **1984**.

3. a. D.C. Bradley, *Chem. Rev.*, 89, 1317, **1989**: b. L.G. Hubert-Pfaltzgraf, *New J. Chem.*, 11, 663, **1987**.

4. H. Anderson, T.T. Kodas and D.M. Smith, *Cer. Bull.*, , 68, 996, **1989**.

5. *"Better Ceramics Through Chemistry III"* , C.J. Brinker, D.E. Clark and D.R. Ulrich, Eds., MRS symposium proceedings, **1988**.

6. a. D.C. Bradley, R.C. Mehrotra and D.P. Gaur in *"Metal Alkoxides"* Academic press, **1978**: b. W.G. Klemperer, V.V. Mainz, S.D. Ramanmurti and F.S. Rosenburg, in *"Better Ceramics Through Chemistry III"* , C.J. Brinker, D.E. Clark and D.R. Ulrich, Eds., MRS symposium proceedings, **1988**: c. R.E. Riman, D.M. Haaland, C.J.M. Northrup, H.K. Bowen and A. Bleier, *Mat. Res. Soc. Symp. Proc.*, Vol. 32, 233, **1984**:.d. J. Fukushima, K. Kodaira, T.

Matsushita, *Ceramic Bulletin*, 55, 1064, **1976**: e. F. Kirbir and H. Komiyama, *Chem. Lett.*, 791, **1988**: F. M. Shiota, *J. Mat. Sci.*, 23, 1718, **1988**.

7. J.S. Smith, R.T. Dollof and K.S. Mazdiyasni, *J. Am. Cer. Soc.*, 91, 53, **1970**.

8. a. M.I. Yanovskaya, E.P. Turevskaya, A.P. Leonov, S.A. Ivanov, M.V. Kolganova, S.Y. Stefanovich, N.Y. Turiva and Y.N. Venevtsev, *J. Mat. Sci.*, 23, 395, **1988**: b. A. Rousett, F. Chassagneux and J. Paris, *J. Mat. Sci.*, 21, 3111, **1986**: c. D.C. Bradley and A.K. Patel in reference 3.

9. It has been demonstrated that tin(IV) alkoxide compounds can be used as precursors for the formation of high purity SnO_2 powders, I.M. Thomas, U.S. patent 3,946,056, July 25th, **1974**. Tin(IV) oxide is commonly prepared by hydrolysis of $SnCl_4$ in aqueous ammonia, but the retention of halide impurities often plague this method, P.G. Harrison and B.M. Maunders, *J. Chem. Soc., Faraday Trans.*, 80, 1341, **1984**, and references therein.

10. D.F. Shriver and M.A. Dresden, "*The Manipulation of Air Sensitive Compounds*" 2nd Edition, Wiley Interscience, **1986**, p78.

11. D.R. Burfield and R.H. Smithers, *J. Org. Chem.*, 48, 2420, **1983**.

12. C.D. Chandler, G.D. Fallon, A.J. Koplick and B.O. West, *Aust. J. Chem.*, 40, 1427, **1987**.

13. D.P. Shoemaker, C.W. Garland and J.I. Steinfield, "*Experiments in Physical Chemistry*" 3rd Ed., McGraw-Hill Book Company, p174-185, **1974**.

14. a. D.C. Bradley, E.A.V. Caldwell and W. Wardlaw, *J. Chem. Soc., A.*, 4775, **1957**: b. I.M. Thomas, *Can. J. Chem.*, 39, 1386, **1961**.

15. M.J. Hampden-Smith, T.A. Wark , A.L. Rheingold and J.C. Huffman, *Can. J. Chem.*, submitted for publication.

16. a. D.C. Bradley, R.C. Mehrotra, J.D. Swanwick and W. Wardlaw, *J. Chem. Soc.*, 5020, **1952**.: b. K.G. Caulton private communication.

17. Using a simplified "diatomic molecule" approach, the ν(Sn-O) stretching frequency was calculated to be 580 cm^{-1} by treating labelled and unlabelled tertiary butoxide groups as point masses of 82 and 73, respectively. This assumption has previously yielded satisfactory results in analogous ^{18}O labelling experiments. D.C. Bradley and A.H. Westlake, "*Proc. Symp. Coord. Chem.*," Tihany, Hungary, published by the Hungarian Acad. Sci., Budapest, 309, **1965**, referred to in reference 6a.

18. M.J. Hampden-Smith, D.E. Smith and E.N. Duesler, *Inorg. Chem.*, 28, 339, **1989**.

19. T.A. Wark, E.A. Gulliver, M.J. Hampden-Smith and A.L. Rheingold, *Inorg. Chem.*, submitted for publication.

20.a. M. Veith and R. Rosler, *Z. Naturforsch*, 41b, 1017, **1986**: b. M. Veith and R. Rosler, *Angew. Chem., Int. Ed., Engl.*, 21, 858, **1982**.

21. T.A. Wark and M.J. Hampden-Smith, unpublished results. We note that similar compounds have previously been prepared, e.g. $LiSn_2(OR)_9$, see ref. 6a.

22. It has previously been reported that thermal decomposition of metal alkoxide compounds results in formation of alcohol and alkene, D.C. Bradley and M.M. Faktor, *Trans. Faraday Soc.*, 55, 2117, **1959**: D.C. Bradley and M.M. Faktor, *J. Appl. Chem.*, 9, 435, **1959**: H.A. Stecher, A. Sen and A.L. Rheingold, *Inorg. Chem.*, 28, 3280, **1989**. An exception has recently been reported, P.M. Jeffries and G.S. Girolami, *Chem. Mat.*, 1, 8, **1989**.

23. Similar cyclodecadienes have been prepared by Wilke et al. at nickel centers, see e.g. P. Heimbach and G. Wilke, *Liebigs Ann. Chem.* 727, 183, **1969** and 727, 194,**1969**: G. Wilke, *Angew. Chem., Int. Ed. Engl.*, 2, 105, **1963**.

TAILORED MOLECULAR PRECURSORS OF YTTRIUM OXIDE USING FUNCTIONAL ALCOHOLS AND ACETYLACETONE AS MODIFIERS

LILIANE G. HUBERT-PFALZGRAF*, OLIVIER PONCELET* AND JEAN-CLAUDE DARAN**

*Laboratoire de Chimie Moléculaire, Associé au CNRS, Université de Nice-Sophia Antipolis, Parc Valrose, 06034 Nice, France

**Laboratoire de Chimie des Métaux de Transition, Place Jussieu, 75230 Paris, France

ABSTRACT

Yttrium is involved as oxide in a variety of advanced materials. Hydrolysis of its most common alkoxide, yttrium oxoisopropoxide $Y_5O(O^iPr)_{13}$, is difficult to control as a result of the high electropositivity of the metal. Functional alcohols such as 2-methoxyethanol and acetylacetone have thus been used as modifiers. These tailored precursors have been fully characterized (single crystal X-Ray diffraction, IR, NMR, ...). The tendency of methoxyethanol to act as a bridging ligand and to stabilize high oligomers - $Y(OC_2H_4OMe)_3$ is a decamer - gives some insight into its behavior as "network builder". The unexpected cleavage of acetylacetone offers a route to an interesting acetatoacetylacetonate derivative, $Y_2(OAc)_2(acac)_4(H_2O)_2$, but also suggest that this classical "modifier" could be affected by the hydrolysis-polycondensation reactions of the metallic species during the sol-gel process. Comparison of the hydrolysis behavior of the different precursors was performed.

INTRODUCTION

The importance of chemistry in the development of high performance ceramics is well established, and the sol-gel processing of glasses and ceramics has gained scientific as well as technological interest during the last decade [1]. Yttrium is involved as oxide in various materials such as yttrium-iron garnets (YIG), high Tc superconductors, fast sodium-ion conducting glass-ceramics (NASICON), and in the stabilization of thermomechanical ceramics [2]. Molecular precursors, especially metal alkoxides, are as versatile and thus attractive precursors of oxides [3].

This paper reports the synthesis of yttrium oxoisopropoxide $Y_5O(O^iPr)_{13}$ and of the 2-methoxyethoxide $[Y(OC_2H_4OMe)_3]_{10}$, their chemical modification in the presence of acetylacetone, and finally a comparison of their behavior towards hydrolysis.

EXPERIMENTAL

All syntheses were carried out under inert atmosphere, using Schlenk tube techniques. Spectroscopic characterization was done as published previously [4].

Mat. Res. Soc. Symp. Proc. Vol. 180. ©1990 Materials Research Society

Controlled Hydrolysis

Hydrolysis of the different precursors was achieved in 0,05 M solutions in isopropanol or acetone. Water was added as a solution in the same solvent. Gelification was considered achieved when the sample could be inverted. All experiments were performed in the same glass vessel and with the same total volume.

RESULTS AND DISCUSSION

Synthesis and Characterization of Precursors

Among the various types of molecular precursors of oxide, metal alkoxides $M(OR)_n$ or oxoalkoxides $MO(OR)_n$ display attractive features [3] such as :

- high purity;
- ability to form homogeneous solutions in a large variety of conditions and for multicomponent systems via heterometallic (double) alkoxides;
- easy transformation into oxides with formation of volatile by-products.

Various synthetic routes have been explored for acceding to yttrium and/or lanthanide alkoxides. By contrast with the classical transition metals, halide substitution reactions, either by alcohol in basic conditions (NH_3) or by an alkali metal alkoxide, lack selectivity.

A convenient route to yttrium and lanthanide trisisopropoxides, the products being characterized by microanalysis and infra-red, was shown by Maszdiyasni [5] to be the attack of the metal by isopropanol, according to eq. 1 :

$$Y + {}^{i}PrOH \xrightarrow{HgCl_2} Y(O^{i}Pr)_3 + H_2 \qquad (1)$$

Reinvestigation of this reaction offered, after crystallization or sublimation, a solid whose infra-red was identical to the product reported to be $Y(O^{i}Pr)_3$, but whose other spectral data (e.g. ^{1}H, ^{13}C or ^{89}Y NMR) were not in agreement with a tetranuclear structure analogous to that of $[Al(O^{i}Pr)_3]_4$ as suggested in the literature. For instance, although the ^{89}Y NMR spectrum displayed two resonances (Fig. 1), the small (<5 ppm) difference in their chemical shifts suggests a similar coordination number for the two types of non-equivalent metals.

The identity of the compound isolated from reaction 1 was established by single crystal X-ray diffraction to be in fact an oxoalkoxide of formula $Y_5O(O^{i}Pr)_{13}$, 1, whose structure is represented in Figure 2 and in which the metal is hexacoordinated [5].

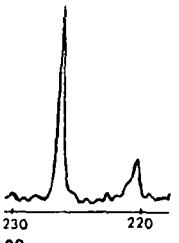


Fig. 1. ^{89}Y NMR spectrum of 1

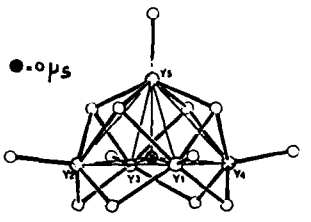
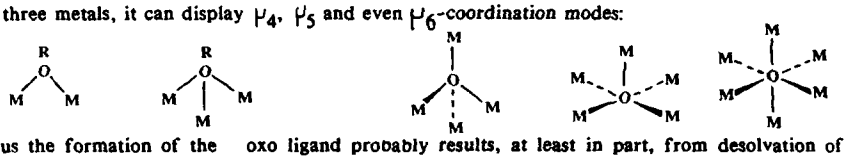


Fig. 2. The Y_5O_{14} framework of 1

The oxo O^{2-} ligand represents a means for a trivalent metal to attain hexacoordination in the absence of neutral ligands, since, while an alkoxo group OR can accommodate only two or three metals, it can display μ_4, μ_5 and even μ_6-coordination modes:



Thus the formation of the oxo ligand probably results, at least in part, from desolvation of $[Y(O^iPr)_3,x^iPrOH]_m$ species.[6]

Although $Y_5O(O^iPr)_{13}$ is an oxoalkoxide, it still displays a high sensitivity to moisture. The nucleophilic attack of water is favored by the high electropositivity of yttrium, and its possibility of expanding its coordination numbers (Y is often 8-coordinated); furthermore, the isopropoxide group represents a secondary alkoxide, and as such is relatively susceptible to hydrolysis.

Several alternatives stand open in order to slow down hydrolysis rates: [3,7]

- changing the nature of the organic group R;
- decreasing the functionality of the precursor by chemical modifiers such as acetylacetone.

Alcoholysis reactions are widely used for the synthesis of metal alkoxides. Functional alcohols such as alkoxyalcohols or alkanolamines are often used in material science as additives during the sol-gel process, and we therefore investigated the reactivity of an excess of 2-methoxyethanol towards $Y_5O(O^iPr)_{13}$ as well as yttrium chips. Both reactions offered the same product, characterized by X-ray diffraction to be a non-oxoalkoxide $[Y(OC_2H_4OMe)_3]_{10}$, 2 [8].

The remarkable feature of this compound is a high solubility, even in non-polar solvents such as petroleum ether. On the other hand, the increase in the coordination number of the metal, which is now seven-coordinated as a result of the chelating behavior of the bridging 2-methoxyethoxide and the involvement of the ether OMe functionality (fig 3) decreases its sensitivity to atmospheric moisture, which in turn leads to an easier manipulation. The tendency of the 2-methoxyethoxide to form bridges also leads to the largest oligomer (a cyclic decamer) known so far for a homoleptic alkoxide.

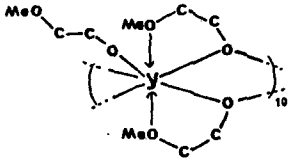


Fig. 3. Environment of yttrium in $[Y(OC_2H_4OMe)_3]_{10}$

Modification of the functionality has mostly been achieved so far by acetylacetone $CH_3COCH_2COCH_3$ (acacH). Our choice of this chelating ligand was motivated by its use as modifier in the sol-gel process as well as for its ability to increase the volatility of the

derivatives and thus their potential use in MOCVD techniques. It was also particularly interesting to estimate whether the 2-methoxyethoxide ligand was labile despite its bridging chelating coordination mode.

Addition of acetylacetone leads in all cases to a decrease in the nuclearity of the precursor of and an increase in the coordination number of the metal, as established by X-ray diffraction.

Addition of acetylacetone to the oxoisopropoxide 1 in toluene at room temperature gave a crystalline material, whose ^1H NMR spectrum was puzzling. It was characterized as a dinuclear ß-diketonatoacetato derivative $Y_2(OAc)_2(acac)_4(H_2O)_2$, 3; the salient feature is the unexpected presence of the acetato ligands which bridge the two metals. These groups can only originate from the cleavage of the acetylacetone ligand in a retro-Claisen reaction, which is probably induced by the water resulting from the reactivity of the oxo ligand [9]. Indeed the reaction between $[Y(O^iPr)_3,{}^iPrOH]_m$ and acetylacetone led to the classical yttrium trisacetylacetonate $Y(acac)_3$. Acetylacetone is a chemical modifier, commonly used in the sol-gel process with formation of acetylacetonato alkoxides $M('OR)_{n-x}(acac)_x$. By hydrolysis, the OR group is removed first and condensation occurs by formation of M-O-M bonds and thus oxo groups [10]. Our results show that reactions involving acetylacetone modifiers may be much more complex when metal oxo groups are involved and thus during hydrolysis even at room temperature as the chemical modifier might be modified as well.

Metal acetylacetonates are sometimes used as metal oxide precursors in the sol-gel when the alkoxide is not easily available [11]; it was therefore interesting to obtain more insight into such reactions at a molecular level. We thus considered the reaction between tris(2-methoxyethoxide)yttrium and copper(II) acetylacetonate, since soluble copper(II) alkoxides remain scarce [12].

Complex redistribution reactions occur even in inert solvents such as toluene and at room temperature. The isolated products correspond to homometallic mixed species, with alkoxide as well as acetylacetonate in the coordination sphere (eq. 2).

$$Y(OR)_3 + Cu(acac)_2 \longrightarrow Y_3(OR)_5(acac)_4 + [Cu(OR)(acac)]_m + \ldots \quad (2)$$
$$R = C_2H_4OMe$$

These products were separated by their solubility properties and fully characterized. Comparable reactions are observed between $Y_5O(O^iPr)_{13}$ and $Cu(acac)_2$ even in pentane, but the products are much more air-sensitive. Since no reaction is observed between $Cu(acac)_2$ and an alcohol - isopropanol or 2-methoxyethanol in similar conditions - these ligand exchange reactions proceed via unstable heterometallic species. It therefore appears that ß-diketones are ligands which have a tendency to destabilize heterometallic species. Obtention of multimetallic systems, homogeneous at a molecular level, is therefore much more questionable than for mixing only alkoxides. However, it should be emphasized that mixing alkoxides and ß-diketonates of different metals can be a means of increasing the solubility of ß-diketonates by synthesizing

new soluble and hydrolysable precursors. This seems particularly valuable here: Copper(II) acetylacetonate is non-hydrolysable, as commonly observed for metal ß-diketonates. Copper(II) 2-methoxyethoxide is an insoluble polymer; the mixed species **5**, however, is largely soluble and can be hydrolysed.

Hydrolysis

Hydrolysis of the various precursors was achieved in comparable conditions in isopropanol or acetone solutions. The results are summarized in Table I. They show that the chemical modification has a strong influence on the hydrolysis product as well as on the hydrolysis rate. Hydrolysis always proceeds very rapidly when acetone is used as a solvent, but this precludes the obtaining of homogeneous gels.

Table I: Hydrolysis behavior of the various precursors

Compound	coordination number	Hydrolysis ratio h = $[H_2O]/M$			Ligand removed (IR evidence)
		0.13	10	15	
1	6	crystalline precipitate	amorphous precipitate	amorphous precipitate	O^iPr
2	7	no effect	transparent gel (t=15mn)	transparent gel (t=15mn)	OC_2H_4OMe
3	8	no effect	no precipitation	acidic catalysis (precipitation)	acac first then OAc
4	8	no effect	no precipitation	fibers after ≈ 7 days	OC_2H_4OMe

As expected, the oxoisopropoxide **1** is the most sensitive, and precipitation starts already for very small amounts of water (h ≈ 0.01). The methoxyethoxide derivative undergoes hydrolysis, giving very homogeneous and stable gels. The tendency of this alcohol to display a bridging chelating behaviour, as established for **2**, is indeed a favorable feature for building polymeric networks. Despite its high hydrolytic sensitivity, **1** can be used as a precursor for obtaining multicomponent oxide materials, since hypercritical conditions can be used as a way to overcome mismatched hydrolysis rates [13] and pure $YBa_2Cu_3O_{7-x}$ can thus be obtained. Introduction of acetylacetone in the coordination sphere of the metal results in the increase of the coordination number of the metal and in drastic decrease of the hydrolysis rate. In fact, water is already present as a ligand for compound **3**, and interacts by hydrogen bonding with acetylacetonate groups. This favors spontaneous hydrolysis (without additional water) with elimination of acetylacetone and formation of Y-OH bonds, but the resulting product $[Y(OH)(OAc)(acac)]_m$ remains soluble in isopropanol and acidic catalysis is required to proceed to further hydrolysis at a reasonable rate, since the acetate and the ß-diketonate ligands are both poor leaving groups [14]. The presence of free acetic acid (in the infra-red spectra (νCO_2

= 1717 cm^{-1}) shows that hydrolysis occurs at the acetate groups. The presence of the poorly hydrolysable acac ligand in 4 prevents the tendency of 2-methoxyethoxide to form gels and the differential hydrolysis leads to the slow formation of fibers.

CONCLUSION

Yttrium alkoxides or oxoalkoxides can be prepared easily in high yields by direct reaction of the alcohol on yttrium chips. Oligomerization and/or spontaneous formation of oxo O^{2-} ligands is required in order for the metal to achieve a coordination number of 6 or 7. Addition of a chemical modifier such as acetylacetone always tends to a diminution of the oligomerization (of the nuclearity of the precursor) as well as to an increase (up to 8) of the coordination number of the metal. This generally decreases the solubility properties, but also slows down hydrolysis rates. It should also be emphasized that chemical transformation (cleavage of C-C bond) of acetylacetone can occur under very mild conditions (room temperature, inert solvent) when metal oxo linkages are present, a situation which occurs during hydrolysis reactions.

REFERENCES

1. D.R. Ulrich, Chem. Eng. News, 1990, 28. ; H.J. Sanders, ibid., 1984, 26.
2. K. Yamashita, T. Nojimi, T. Umegaki and T. Kamazawa, Solid State Ionics 35, 299 (1989).
3. L.G. Hubert-Pfalzgraf, New J. Chem. 11, 663 (1987).
4. O. Poncelet, W.J. Sartain, L.G. Hubert-Pfalzgraf, K. Folting and K.G. Caulton, Inorg. Chem. 28, 263 (1989).
5. L.M. Brown and K.S. Mazdiasni, Inorg. Chem. 9, 783 (1970).
6. x = 1, m = 4 in the case of neodymium, as established by X-ray diffraction studies.
7. J. Livage, M. Henry and C. Sanchez, Progress in Solid State Chem. 18, 259 (1988).
8. O. Poncelet, L.G. Hubert-Pfalzgraf and J.C. Daran, J. Chem. Soc. Chem. Commun. 1989, 1846 .
9. O. Poncelet, L.G. Hubert-Pfalzgraf and J.C. Daran, Polyhedron, in the press.
12. O. Poncelet, L.G. Hubert-Pfalzgraf and J.C. Daran, Inorg. Chem., in the press.
10. A. Leaustic, F. Babonneau and J. Livage, Chem. of Mater. 1, 240; 248 (1989).
11. T. Nanao and T. Eguchi, Patent EP 84/104 194 840413, CA 102 ,099 762.
12. S.C. Goel, K.S. Kramer, P.C. Gibbon and W.E. Buhro, Inorg. Chem. 28, 3619 (1989).
13. N. El Khokh, R. Papiernik, L.G. Hubert-Pfalzgraf, F. Chaput and J.P. Boilot, J. Mater. Sci. Lett. 8, 762 (1989).
14. C. Sanchez, J. Livage, M. Henry and F. Babonneau, J. Non-Cryst. Solids 100, 65, (1988).

NMR SPECTROSCOPIC INVESTIGATIONS OF $PbTiO_3$ SOL-GEL PROCESSING*

S.D. RAMAMURTHI* AND D.A. PAYNE**
* Battelle, 505 King Ave., Columbus, OH 43201
**Department of Material Science and Engineering, University of Illinois at Urbana-Champaign, 105 S. Goodwin Ave., Urbana, IL 61801.

ABSTRACT

Lead titanate gels were prepared by sol-gel processing from lead acetate and titanium isopropoxide in methoxyethanol. In the present study, ^{1}H, and ^{13}C FTNMR spectroscopic and mass spectrometric techniques were used to identify the structures of lead and titanium precursors formed by refluxing lead acetate and titanium isopropoxide in methoxyethanol, respectively. Lead acetate was found to be partially alkoxylated, whereas, the titanium precursor was identified as a dimer with complete alkoxy group exchange. Similar procedures were applied to identify the lead titanium complex formed from lead and titanium precursors.

INTRODUCTION

Interest in the properties of ferroelectric materials has lead to the development of new chemical routes for the preparation of materials in a variety of forms, including, monoliths, films, fibers, and powders[1]. One of these chemical methods is sol-gel processing, which normally involves hydrolysis and condensation of metal alkoxides in an alcoholic media. As polymerization proceeds, the viscosity of the solution increases and the solution eventually gels. The sol-gel process generally offers advantages over conventional methods of ceramic processing by providing homogeneity, purity, stoichiometric control, and low temperature processing[2]. Lead titanate in particular has been synthesized from lead acetate and titanium isopropoxide in methoxyethanol[1b,3]. The procedure used can be summarized by the following equations:

$$Pb(OOCH_3)_2.3H_2O + CH_3OCH_2CH_2OH \xrightarrow[\text{Dehydrate}]{\text{Reflux, Distill}} X \text{ (Lead Precursor)} \quad (1)$$

$$Ti(OiPr)_4 + CH_3OCH_2CH_2OH \xrightarrow[\text{Distill}]{\text{Reflux}} Y \text{ (Titanium precursor)} \quad (2)$$

$$X + Y \xrightarrow[\text{Reflux, Distill}]{CH_3OCH_2CH_2OH} Z \text{ (Lead titanium Precursor)} \quad (3)$$

$$Z + xH_2O \xrightarrow{CH_3OCH_2CH_2OH} PbTiO_3 \quad (4)$$

---

* This research was carried out at the University of Illinois at Urbana-Champaign, IL.

Mat. Res. Soc. Symp. Proc. Vol. 180. ©1990 Materials Research Society

Limited studies using FTIR and Raman spectroscopic techniques[4] have attempted to identify lead titanate precursors (X, Y, and Z) and hydrolysis/condensation products in situ. These studies have provided only a limited understanding of the system due to the presence of overlapping and unresolved peaks in the spectra. Other studies[3,5] have primarily studied the by-products of reactions 1 through 4. In the present study, however, the X, Y, and Z precursors were isolated and characterized by FTNMR and mass spectrometric methods[6].

EXPERIMENTAL PROCEDURE

Lead and titanium precursor solutions were prepared by methods originally reported by Budd et al.[1b]. Lead (X), titanium (Y), and lead titanium precursor (Z) precursors were isolated by removing the volatiles under reduced pressure at 1 torr from their 1 molar solutions in methoxyethanol. The clear and viscous liquids were dissolved in deuterated benzene for NMR spectroscopy experiments. ^{1}H NMR experiments were carried out to verify the complete removal of methoxyethanol and other volatiles from the samples.

^{1}H and ^{13}C FTNMR[7] experiments were used to identify the structures of the precursors isolated. Chemical shifts were internally referenced to tetramethyl silane. ^{207}Pb FTNMR shifts were referenced to $Pb(OOCH_3)_2.xH_2O$ solution in D_2O. Mass spectrometry[7] in chemical ionization (CI) mode was used to determine the molecular formulae for X, Y, and Z precursors.

RESULTS AND DISCUSSIONS

Mass spectrometric experiments were first conducted to obtain the molecular formulae for the precursors. NMR spectrometry was later used to determine the structures of these precursors.

Lead Precursor (X): Mass spectrum of X in CI mode produced a molecular ion peak at 343 amu (atomic mass unit) corresponding to the molecular formula, $Pb(OOCH_3)(OCH_2CH_2OCH_3)$ plus a proton[6]. In addition, it indicated fragmentation along two paths, one, where an acetate group was lost and the other where a methoxyethoxy group was lost, giving rise to ions at 283 and 267 amu, respectively.

^{207}Pb NMR of X indicated that it was no longer a simple lead diacetate species, since an upfield shift was observed for X in D_2O. The $^{13}C\{^{1}H\}$ NMR experiments were carried out to verify the above analysis. First, a $^{13}C\{^{1}H\}$ NMR (decoupled) spectrum of $CH_3OCH_2CH_2OH$ (inset in Figure 1) was obtained as reference. The remaining spectra were analyzed by comparison. The $^{13}C\{^{1}H\}$ NMR of X given in Figure 1 indicated two additional peaks. This suggested the presence of both acetate and methoxyethoxy groups in the sample, supporting the mass spectrum analyses discussed above. The nomenclature used for the peak assignments in Figure 1 are given over leaf:

$$\underset{\quad a}{HO - CH_2} - \underset{\quad b}{CH_2} - \underset{\quad c}{OCH_3}$$

$$\underset{\quad e}{H_3C} - \underset{\quad d}{COO} - Pb - \underset{\quad a'}{OCH_2} - \underset{\quad b}{CH_2} - \underset{\quad c}{OCH_3}$$

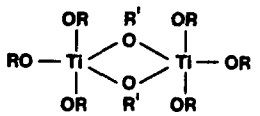
From a simple ^{13}C NMR spectrum of X the ratio of acetate group to methoxyethoxy group was calculated to be approximately 1:1. The ^1H NMR spectrum of X verified the above analysis and indicated the presence of <0.5 moles of H_2O per mole of lead in the sample. The above analyses suggested the structure of X to be:

$$(H_3CCOO - Pb - OCH_2CH_2OCH_3)\ .xH_2O, \qquad \text{where } x<0.5.$$

(X)

Titanium Precursor (Y): The CI mass spectrum of Y exhibited peaks at 696, 621, and 273 amu which correspond to molecular ion formula $[Ti_2(OC_2H_4OCH_3)_8]^+$; and ion formulae $[Ti_2(OC_2H_4OCH_3)_7]^+$ and $[Ti(OC_2H_4OCH_3)_3]^+$, respectively. Based on similar mass spectrometric studies by Ramamurthi[8], the present analysis indicated the molecular formula of Y to be $[Ti_2(OC_2H_4OCH_3)_8]$, where peaks at 621 and 276 resulted from the loss of methoxyethanol and titanium tetramethoxyethoxide groups, respectively.

Based on the mass spectrometric analysis, the $^{13}C\{^1H\}$ NMR of Y should be identical to inset in Figure 1, except for peaks due to carbon centers a_1' and a_2' (see nomenclature below), since they are closest to titanium.



(Y)

$$R = \underset{\quad a_1'}{CH_2} - \underset{\quad b}{CH_2} - \underset{\quad c}{OCH_3}$$

$$R' = \underset{\quad a_2'}{CH_2} - \underset{\quad b}{CH_2} - \underset{\quad c}{OCH_3}$$

At room temperature a single peak (73.54 ppm) for both a_1' and a_2' carbon centers was observed due to rapid alkoxy group exchange[8]. Two peaks in the $^{13}C\{^1H\}$ NMR spectrum were resolved when the temperature was lowered to -40°C (see Figure 2). Resonances due to carbon centers, b, in R and R' groups also started to resolve at -40°C (Figure 2). These analyses clearly indicate Y to be dimeric in nature with the structure shown above.

Lead Titanium Precursor (Z): The lead titanium alkoxide precursor could have at least three possible compositions:

1) A simple mixture of lead (X) and titanium (Y) precursors.
2) A double metal alkoxide complex with -Pb-O-Ti- or -Pb-OR-Ti- bonds, where R = $CH_2CH_2OCH_3$.
3) A simple mixture of titanium alkoxide polymer and a lead polymer.

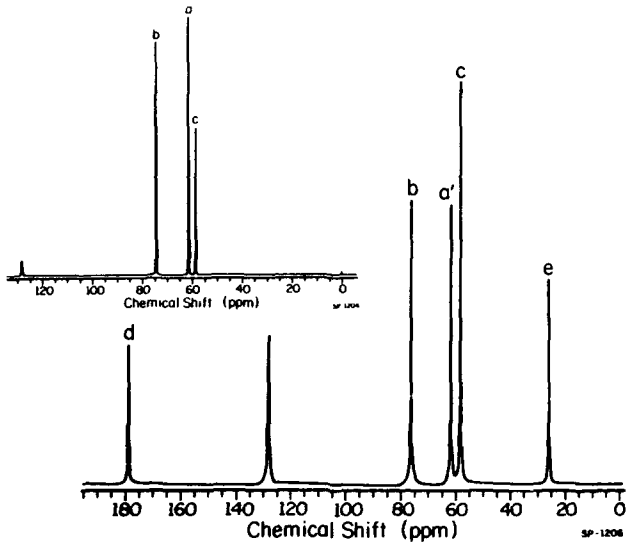


Figure 1. $^{13}C\{^1H\}$ NMR spectra (decoupled) of 2-methoxyethanol (inset) and X in C_6D_6. Chemical shifts were referenced to TMS and peaks at ≈128 ppm are due to C_6D_6. For peak nomenclature see text.

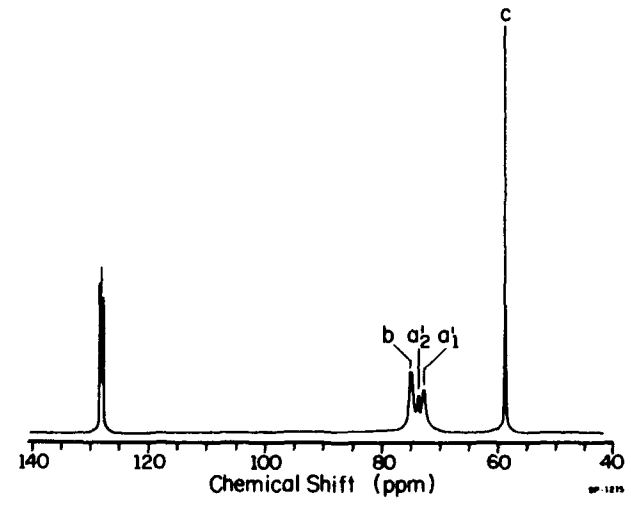
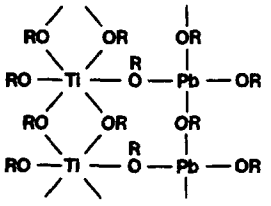


Figure 2. $^{13}C\{^1H\}$ NMR spectrum (decoupled) of Y in C_6D_6 at -40°C. For peak nomenclature see text.

The first possibility was ruled out due to an absence of molecular ions of X and Y in the CI spectrum of Z. The third possibility of independent polymers was considered unlikely, also due to an absence of appropriate ions of the repeating units of titanium and lead polymers in the CI mass spectrum. The CI mass spectrum of Z exhibited peaks at 621 and 790 amu. The $^{13}C\{^1H\}$ NMR spectrum of Z given in Figure 3 also indicated more than three peaks in a region. Based on the above data, the following structure for Z was proposed, where the peaks in the mass spectrum at 621 and 790 amu could correspond to $[Ti_2(OC_2H_4OCH_3)_7]^+$ and a lead fragment of the structure shown below,



where R = $C_2H_4OCH_3$.

$^{13}C\{^1H\}$ NMR and ^1H NMR spectra of Z indicated the presence of only residual amounts of acetate groups in the compound. Studies by Eichorst et al.[9a] on the crystal structure of lithium niobium alkoxide polymer, and by Leaustic et al.[9b] on the structure of modified titanium alkoxide, support the presence of bridging alkoxy groups in metal alkoxide polymers.

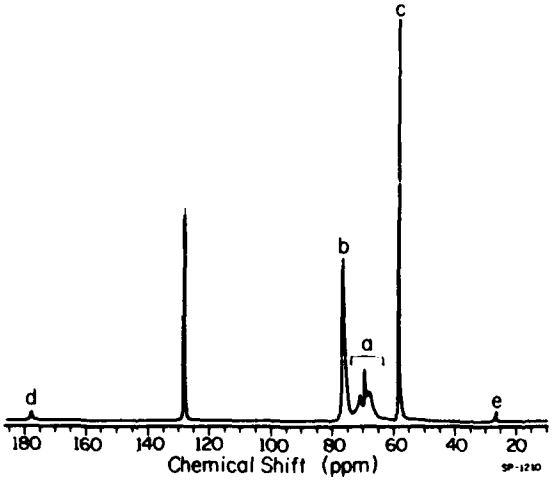


Figure 3. $^{13}C\{^1H\}$ NMR spectrum (decoupled) of Z in C_6D_6 at room temperature. For peak nomenclature see text.

In conclusion, this study identified the structure of prehydrolysed precursors used in the sol-gel processing of $PbTiO_3$. Lead precursor, X was determined to be partially alkoxylated with the formula, $Pb(OOCH_3)(OC_2H_4OCH_3).xH_2O$, where $x<0.5$. Titanium precursor, Y, was determined to be dimeric in nature with the formula, $Ti_2(OC_2H_4OCH_3)_4$ and with a trigonal bipyramidal type of geometry around titanium. A double alkoxide structure[10] was proposed for Z where linear titanium and lead polymers were interlinked in a parallel manner.

ACKNOWLEDGMENT

The research was supported by DOE DMR under project number DE-AC0Z-76ER01198 at the University of Illinois. Discussions with L.F.Francis, R.W.Schwartz, and D.H.Eichorst are acknowledged. Battelle (Columbus) is acknowledged for the support and assistance in the presentation and preparation of this paper.

REFERENCES

1a. K.D. Budd, S.K. Dey, D.A. Payne, Brit. Ceram. Proc., 36, 107 (1985).
b. J.B. Blum, S.R. Gurkovich, J. Mat. Sci., 22, 2655 (1987).
c. K.D. Budd, S.K. Dey , D.A. Payne, Mat. Res. Soc. Symp. Proc., 73, 711(1986).

2. For recent studies see:
a. Mat. Res. Soc. Symp. Proc., Edited by C.J. Brinker, D.E. Clark, D.H. Ulrich, 73(1986); *ibid*, 121(1988).
b. Ultrastructure and Processing of Advanced Ceramics, Edited by J.D. MacKenzie, D.R. Ulrich, (John Wiley & Sons, New York, 1988).

3. K.D. Budd, Ph.D. Thesis, University of Illinois at Urbana-Champaign, IL, (1986).

4. S. Li, R.A. Condrate, R.M. Spriggs, Spect. Lett., 21[9 & 10], 969(1988).

5. T.W. Dekleva, J.M. Hayes, L.E. Cross, G. Geoffory, J. Am. Ceram. Soc., 71[5], c280 (1988).

6. S.D. Ramamurthi and D.A Payne, accepted for publication in J. Am. Ceram. Soc., Feb. (1990).

7. A.G. Harrison, Chemical Ionization Mass Spectrometry, (CRC Press, Boca Raton, FL, 1983).

8. S.D. Ramamurthi, Ph.D. Thesis, University of Illinois at Urbana-Champaign, IL, (1990).

9a. A. Leaustic, F. Babonneau, J. Livage, Chem. Mater., 1, 240, (1989).
b. D.J. Eichorst, K.E. Howard, D.A. Payne, S.R. Wilson, accepted for publication in Inorg. Chem, Feb. (1990).

10. K. Kezuka, Y. Hayashi, T. Yamaguchi, J. Am. Ceram. Soc., 72[9], 1660 (1989).

REVIEW OF HYDROLYSIS BEHAVIOR OF IONS IN AQUEOUS SOLUTIONS*

R. E. MESMER AND C. F. BAES, JR.
Chemistry Division, Oak Ridge National Laboratory, Oak Ridge, TN 37831

ABSTRACT

The word "hydrolysis," literally "water splitting," refers here to those reactions of metallic ions with water that liberate protons and produce hydroxy or oxy complexes in solution and precipitate hydroxide or oxide solids. Over the wide range of pH available in water, the strong tendency of hydroxide to bond to and bridge among cations leads to a multitude of species for many of the metals. Properties of the metal ion such as "hardness" and, especially, charge and size, determine the strength of these interactions and the species formed by each. Over 200 mononuclear species have been identified that predominate in dilute solutions across the pH scale. It is the stability of these species that largely determines the pH dependence of the solubility of the oxide or hydroxide solid formed. Both the tendency of the variety of polynuclear species (those containing more than one metal ion) to form and the solubility of the hydrolytic solid correlate with the stability of the first mononuclear species. Other correlations allow one to predict the enthalpy and entropy of a variety of hydrolysis reactions, and therefore the dependence of the stability of hydrolysis products on temperature.

INTRODUCTION

In this paper we will review the hydrolysis behavior of the ions drawing principally on two sources: the book Hydrolysis of Cations [1] and our review article on the thermodynamics of hydrolysis reactions [2]. The word "hydrolysis" is used here to represent reactions of ions, especially metal ions, in which the water molecule is split causing the liberation of protons and the formation of hydroxy or oxy complexes in solution. When saturation is reached the precipitation of a hydroxide or mixed hydroxide-oxide solid occurs. These reactions are common to most cations because of the wide range of hydroxide concentrations accessible in water ($< 10^{-14}$ m to > 1 m) as a result of the small dissociation constant of water ($\sim 10^{-14}$ at 25°C). Because of the tendency of the hydroxide and oxide to act as bridging ligands with certain metal ions, often several polynuclear species form, i.e., $M_x(OH)_y^{(xz-y)+}$ where x is greater than one. These species can form in the presence of several mononuclear species of the type, $M(OH)_y^{(z-y)+}$. Hydrolysis reactions are important in chemistry because they determine such behavior as: (1) the solubility of the metal ion (in the absence of other ligands), (2) the species actually present in solution and therefore the interactions with other complexing ligands or with solids, (3) the tendency for coagulation of colloids and other surface phenomena, (4) the oxidizability or reducibility of the metal to other valence states, (5) the transport and deposition of the metal in natural systems and technological applications, and (6) the toxicity of the element to organisms.

The general reaction in solution is

$$xM(H_2O)_a^{z+} + (y+b-ax)H_2O = M_x(H_2O)_b(OH)_y^{(xz-y)+} + yH^+ \qquad (1)$$

Since we know little about the hydration of complex species in solution the reaction is more appropriately written simply as

$$xM^{z+} + yH_2O = M_x(OH)_y^{(xz-y)+} + yH^+ \qquad (2)$$

---

*Research sponsored by the Division of Chemical Sciences, Office of Basic Energy Sciences of the U. S. Department of Energy under contract DE-AC05-84OR21400 with Martin Marietta Energy Systems, Inc.

The equilibrium quotient for this reaction Q_{xy} is

$$Q_{xy} = [M_x(OH)_y^{(xz-y)+}][H^+]^y/[M^{z+}]^x \quad (3)$$

where the brackets represent concentrations and the equilibrium constant referring to infinite dilution standard states, is given by

$$K_{xy} = Q_{xy}\, g_{xy} g_{H^+}{}^y / g_{M^{z+}}{}^x a_{H_2O}{}^y \quad (4)$$

where g's represents specie activity coefficients and a_{H_2O} is the activity of the solvent.

If the saturating solid phase is a hydroxide, the equilibria with the hydrolysis species in solution are represented by

$$xM(OH)_z(cr) + (xz-y)H^+ = M_x(OH)_y^{(xz-y)+} + (xz-y)H_2O \quad (5)$$

for which the quotient Q_{sxy} is $[M_x(OH)_y^{(xz-y)+}]/[H^+]^{(xz-y)}$ and the corresponding equilibrium constant is K_{sxy}. The simplest example of reaction (5) is that involving the unhydrolyzed cation with the quotient, Q_{s10}.

In general the order of preference for ligands is $H_2O < OH^- < O^{2-}$ with increasing charge-to-radius ratio of the cation. The following sequences in the order of increasing y/x, are examples of this trend for the z values of +2 to +6:

+2: $Mg(H_2O)_6^{2+}$, $Mg(H_2O)_5(OH)^+$
+3: $Al(H_2O)_6^{3+}$, $Al(H_2O)_5(OH)^{2+}$, [a] $Al_{13}O_4(OH)_{24}(H_2O)_{12}^{7+}$, $Al(OH)_4^-$
+4: [b] $Zr_4(OH)_8(H_2O)_{16}X_8$
+5: $Si(OH)_4$, $SiO(OH)_3^-$, $SiO_2(OH)_2^{2-}$
+6 $UO_2(H_2O)_6^{2+}$, $UO_2(H_2O)_5(OH)^+$, $(UO_2)_2(OH)_2X_2(H_2O)_4$

where X is chloride or other halide, and a and b refer respectively to Refs. [3] and [4].

Another trend which occurs as y/x increases is the tendency toward tetrahedral species as the anionic condition is approached. Rarely is there detailed structural information indicating where the transition from the geometry of the unhydrolyzed cation (often octahedral [5]) converts to the lower coordination geometry of the anion.

MONONUCLEAR HYDROLYSIS REACTIONS

In most cases metal ions hydrolyze to form mononuclear species in dilute solutions ($\leq 10^{-4}$ m). The first one is represented by reaction (2) where x=1 and y=1 and is usually the best determined. The reasons for that will become apparent in subsequent discussion.

Because of their low stability the species formed from alkali metal ions may well be outer sphere complexes as suggested by Robinson and Harned [6]. Other mononuclear complexes are formed by the removal of a proton from a hydrating water molecule, a process that occurs very rapidly. As already noted, with further steps of hydrolysis, there can also be a loss of water molecules. This can be seen in the series of mononuclear hydrolysis products of $Al(H_2O)_6^{3+}$, which begins with $Al(H_2O)_5OH^{2+}$ and ends with $Al(OH)_4^-$. Small, highly charged cations produce ions such as $SO_3(OH)^-$ (bisulfate), which form by the loss of protons from OH groups. The data available for the stability of fluoride complexes has suggested [7,8] the use of functions involving charge and radius for correlations of the behavior. These results also suggest a regularity of about a log unit decrease in successive stepwise formation constants. There is too little solid evidence, however, to support the occurrence of such a regular trend for successive hydrolysis species, even though data of varying quality suggest the existence of about 200 mononuclear species, listed in Ref [1].

First Hydrolysis Step

The values of log K_{11} for the cations of the same type can be well represented by a linear variation with z/d where d is the M-O interatomic distance (the atomic radius of M^{2+} plus ∿ 1.38 Å) as given by Shannon and Prewitt [9]. This correlation for 25°C is shown in Figure 1 wherein the cations are grouped according to their A values in the expression

$$\log K_{11} = A + 11.0\ z/d. \qquad (6)$$

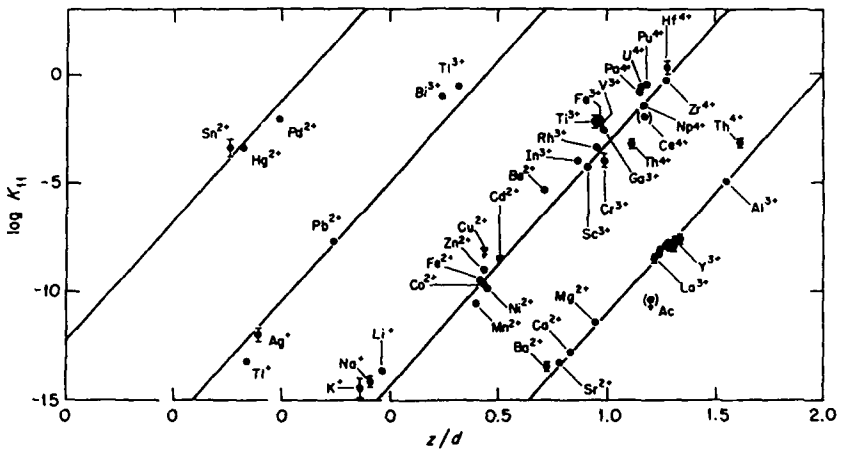


Figure 1. The linear dependence of log K_{11} on the ratio of the charge to the M-O distance for four groups of cations (Ref. [1]).

The first group (A = -22) includes the "hard" pre-transition metal cations including the rare earths with their outer electron configurations of the rare gases. The second group (A = -20) includes the transition metal cations and the alkali metal ions. The third group (A = -16) contains most of the "soft" stable post-transition elements with filled d shells. The last group (A = -12) contains the most readily hydrolyzed "soft" ions Sn^{2+}, Pd^{2+}, and Hg^{2+}.

For very high z/d ratios, where covalent character is favored, hydrolysis species with stabilities to the left of the Sn^{2+}, Hg^{2+}, Pb^{2} line in Figure 1 are expected. For z equal to or greater than four, the z/d ratio is greater than 2, which indicates that these cations would have already hydrolyzed (possibly several steps) in a solution even as acidic as 1 m H^{+}. For example, some species present in 1 m H^{+} for various charges are: (+4): $Si(OH)_4$, $Ge(OH)_4$, VO^{2+}; (+5): $PO(OH)_3$, VO_2^{+}; (+6): UO_2^{2+}, $SO_3(OH)^{-}$.

The first hydrolysis reaction reflects the tendency of the metal to hydrolyze and, as will be shown, is related to polynuclear species formation and precipitation of the solid hydroxide. The enthalpy change [2] for this reaction, ΔH_{11}, is positive and often close to the enthalpy of dissociation for water (13.3 kcal/mole). Hence the tendency of cations to hydrolyze increases with temperature. The post-transition metal ions with the strongest tendency to hydrolyze exhibit the least positive values (as low as 7 kcal/mole). The positive enthalpy opposes hydrolysis and the $T\Delta S$ term favors hydrolysis.

The temperature dependence for the first hydrolysis step is represented in Figure 2. Here ΔH_{11} is assumed to be independent of T, an approximation known to be good for reactions involving only ions of the same sign. A similar result is obtained using the Criss-Cobble approach for estimating ΔCp_{11} [2]. The -log

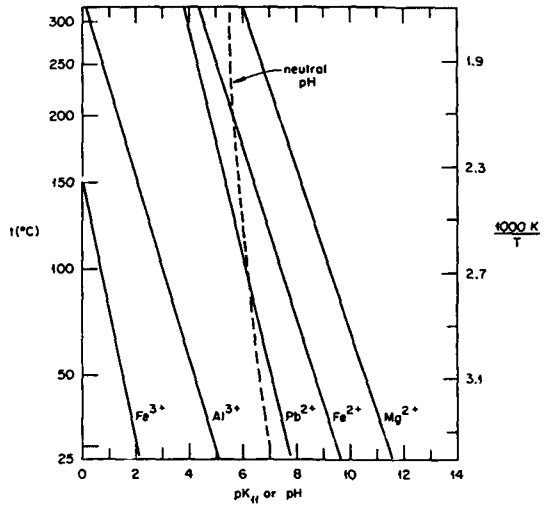


Figure 2. Dependence of log K_{11} on temperature for five cations. pK_{11} equals pH for dilute solutions with equal concentrations of $[M^{z+}]$ and $[MOH^{(z-1)+}]$. The dashed line represents the neutral pH given by 0.5 log K_w.

K_{11} is equal to the pH when the two concentrations $[MOH^{(z-1)}]$ and $[M^{z+}]$ are equal in dilute solutions. The log K_{11} shifts by several units toward greater hydrolysis (lower pH) by 200°C for all the ions represented here (Fe^{3+}, Al^{3+}, Pb^{2+}, Fe^{2+}, Mg^{2+}) and the slopes are nearly equal. The quantity (0.5 log K_w) is shown as a dashed line to indicate the "neutral" pH for comparison (where K_w is the dissociation constant for water).

SOLUBILITY OF HYDROXIDES (OR OXIDES)

Hydrolysis chemistry in solution is limited by the precipitation of solid phases that are variously hydroxides, oxyhydroxides, or oxides. Because such phases are generally quite insoluble and, probably because of the bridging characteristics of the oxygen containing ligands, amorphous phases often form either lacking order or sufficient crystallite size to exhibit diffraction of x-rays. Based on the ideas of Enüstün and Tunkevich (1960) [10], it can be shown that the solubility of a solid should increase linearly with 1/d (the reciprocal of the average particle size). The change in free energy for a reaction such as

$$M(OH)_3(cr,A) = M(OH)_3(cr,A=0) \qquad (7)$$

involving the growth of a hydroxide phase with surface area A to form large particles (A = 0) is equal to

$$\Delta G = -2/3\ \bar{\gamma}A = -\ RT\ln[K_{S10}(A)/K_{S10}(0)] \qquad (8)$$

where $\bar{\gamma}$ is the mean surface energy per unit area of the solid and A is the surface area per mole of the hydroxide. The surface area A is equal to $M\alpha/(\rho d)$ where M is the molecular weight, ρ is the density, and α is a geometrical factor determined by particle shape (e.g., 6 for a cube or a sphere).

For example, Schindler [11] has reported for ZnO

$$\log K_{S10} = 12.18 + 50/d \qquad (9)$$

with d in Angstroms, giving $\bar{\gamma} = 770$ erg cm^{-2}. Even though there are five polymorphs of $Zn(OH)_2$ more soluble than ZnO, there are particle sizes of ZnO below which the oxide is more soluble than each of the hydroxide phases. Therefore, as nuclei of ZnO grow, five other phases are more stable before the size is reached beyond which only ZnO spontaneously crystallizes. In most cases an amorphous solid will form ahead of a crystalline phase for this reason suggesting that the heterogeneous nucleation or growth on seeds is a route to the stable crystalline form.

A remarkable correlation exists between the solubility equilibrium constant K_{S10} and the first mononuclear hydrolysis constant K_{11} for 47 oxides, oxyhydroxides, and hydroxides as first shown in Ref. [1]. This is shown in Figure 3, where the negative slope of the lines is equal to the charge on the unhydrolyzed metal ion. These plots are combined in the relationship

$$K_{11}{}^{z}K_{S10} = 10^{-5.6} = [MOH^{(z-1)+}]^{z}/[M^{z+}]^{(z-1)} \qquad (10)$$

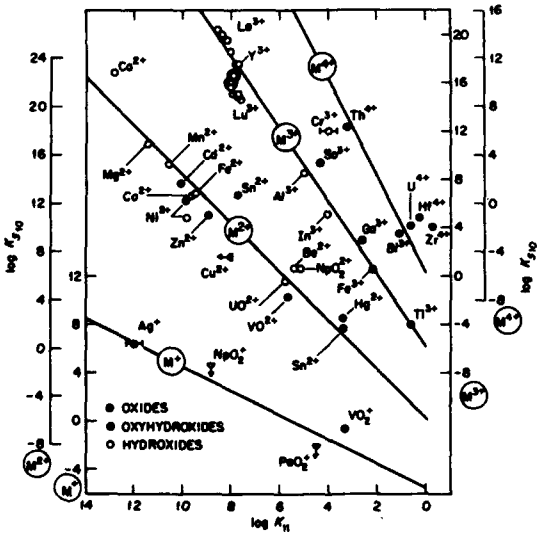


Figure 3. The correlation of the solubility product K_{S10} (reaction 5) with the first hydrolysis constant K_{11} for M^{+}, M^{2+}, M^{3+}, and M^{4+} cations. The lines have slopes of $-z = -1$, -2, -3, and -4 (Ref. [1]).

Half the observed values fall within 1.6 log units and ninety percent fall within 3 log units--a remarkably tight fit considering the wide range of K_{11} and K_{S10} values covered. This product is the equilibrium constant for the

reaction of the solid with the unhydrolyzed metal ion to produce z moles of $MOH^{(z-1)+}$.

$$M(OH)_z(cr) + (z-1)M^{z+} \rightleftharpoons zMOH^{(z-1)+} \qquad (11)$$

For the case of $[M^{z+}] = [MOH^{(z-1)}]$, both concentrations equal $\sim 10^{-5.6}$ m. In other words, to a good approximation all metal ions form only about 2.5×10^{-6} m of the first hydrolysis product in a solution containing 5×10^{-6} m total metal before saturation with respect to the solid occurs, assuming no polynuclear species are formed at this dilution. The low value of $K_{11}^z K_{S10}$ reflects the general tendency of cations to precipitate shortly after hydrolysis begins unless the concentration of M^{z+} is quite low. Also, for divalent metal ions this indicates that in equilibrium with the solid only $\sim$ 0.16% of the M^{2+} in a 1 m solution is hydrolyzed to MOH^+ and $\sim$ 1.6% is hydrolyzed in a 0.01 m solution. This also indicates why it is so difficult to obtain good information on the mononuclear species. Fortunately supersaturation is commonly attained making it possible to obtain such information. Correspondingly, lesser amounts of the other subsequent mononuclear hydrolysis species are formed.

The effect of electrolyte concentration or ionic strength ($\Sigma z_i^2 m_i/2$) on the equilibrium constant for equation (11) increases rapidly with charge on the metal ion. At ionic strength of 1 m, $\log(Q_{11}^z/Q_{S10})$ is more negative than $\log(K_{11}^z/K_{S10})$ by about 0.5, 1.50, and 3.0 log units for $z = +2$, +3, and +4 respectively at 25°C.

A correlation has been found for a number of divalent ions (Be^{2+}, Mn^{2+}, Fe^{2+}, Zn^{2+}, Cd^{2+}, Pb^{2+}), which relates K_{S13} with K_{11} at 25°C as follows

$$\log K_{S13} = -9 + \log K_{11} \quad (\pm 2 \text{ log units}) \qquad (12)$$

Combining this with equation (10) allows one to estimate the minimum solubility of divalent hydroxides (assuming only MOH^+ and $M(OH)_3^-$ are the important solution species) at $\sim 10^{-7}$ m, occurring at pH $\approx$ (1.7 - log K_{11})

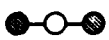
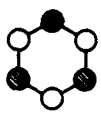
POLYNUCLEAR SPECIES

Many ions in water hydrolyze to form species containing more than one cation, $M_x(OH)_y^{(xz-y)+}$, and sometimes both x and y are quite large. There are many methods [1,13] for studying such cases but all lack sufficient resolution to precisely define the formulae as the x and y values become greater than about six and especially when several species coexist over a range of solution composition. Of all the methods, the potentiometric method, in which measurement of H^+ concentrations are generally made by glass or hydrogen electrodes has provided the greatest share of the useful hydrolysis information, largely because of the high precision of the data that is achievable and the ease of broad variation of compositions.

Often supersaturation with respect to the hydrolytic solid permits the formation of the polynuclear species and their study. Little information exits on the formation of polynuclear species at concentrations greater than about 1 molal especially at concentrations that lead to a deficiency of solvent for solvation of ions ($\geq$ 4 m). Here, undoubtedly, network structures are produced and although these conditions are sometimes relevant to synthesis of materials, they remain poorly described. In the concentration range 0.01 to 1 molal, a region of considerable practical interest, many cations are known to produce a limited number of species, two-to-six, and where these are sufficiently separated in composition they have been well characterized principally by EMF, ultracentrifugation, light scattering, and in a few cases by X-ray diffraction.

The occurrence and structure of some polynuclear hydrolysis products is summarized in Table I. The most favored configurations seem to be symmetrical ones and most have six or fewer cations. For example, the $M_2(OH)_2^{(2z-2)+}$ species has been reported for 12 different cations with z values from +2 to

Table I. Occurrence and structure of polynuclear hydrolysis products [1]

Species	Cation (source)	Probable structure ● = M^{z+}, o = OH^-
M_2OH^{3+}	Be^{2+}, Mn^{2+}, Co^{2+}, Ni^{2+}, Zn^{2+}, Cd^{2+}, Hg^{2+}, Pb^{2+}	
$M_2(OH)_2^{(2z-2)+}$	Cu^{2+}, Sn^{2+}, UO_2^{2+} (1), NpO_2^{2+}, PuO_2^{2+}, VO^{2+}, Al^{3+} (2), Sc^{3+}, Ln^{3+}, Ti^{3+}, Cr^{3+}, Th^{4+} (3)	
$M_3(OH)_3^{3+}$	Be^{2+}, Hg^{2+}	
$M_3(OH)_4^{(3z-4)+}$	Sn^{2+}, Pb^{2+}, Al^{3+}, Cr^{3+}, Fe^{3+}, In^{3+}	
$M_3(OH)_5^{(3z-5)+}$	UO_2^{2+}, NpO_2^{2+}, PuO_2^{2+}, Sc^{3+}, Y^{3+}, Ln^{3+}	
$M_4(OH)_4^{4+}$	Mg^{2+}, Co^{2+}, Ni^{2+}, Cd^{2+}, Pb^{2+} (4, 5)	
$M_4(OH)_8^{8+}$	Zr^{4+} (6, 7), Th^{4+}	M_4 square with two OH^- ions centered over and under each edge.
$M_6(OH)_8^{4+}$	Be^{2+}, Pb^{2+}	M_6 octahedron with eight OH^- ions centered on faces.
$M_6(OH)_{12}^{6+}$	Bi^{3+} (8)	M_6 octahedron with 12 OH^- ions centered along edges.

Sources: (1) Aberg (1970); (2) Johansson (1962); (3) Johansson (1968*b*); (4) Johansson and Olin (1968); (5) Maroni and Spiro (1967, 1968*a*; 1968*b*); (6) Muha and Vaughan (1960); (7) Clearfield and Vaughan (1956); (8) Levy et al. (1959). (These citations come from Ref. [1].)

+4. The symmetrical ring $M_3(OH)_3^{3+}$ has been reported for Be^{2+} and Hg^{2+} only. Not shown in the table is the most polymerized cation formed for Al^{3+} in solution, $Al_{13}(OH)_{32}^{7+}$ (actually $Al_{13}O_4(OH)_{24}(H_2O)_{12}^{7+}$, as observed in crystals of basic aluminum sulfate by Johansson [3]). In that structure 12 aluminum atoms are 6-coordinate and one 4-coordinate; all OH groups are 2-coordinate and the oxygens are 4-coordinate.

An interesting factor in determining the stability of polynuclear species seems to be that the quantity $\Delta z_{xy}^2/y$ (where $\Delta z_{xy}^2/y$ is the change in the squared charges for reaction (2)) is as low as possible for the given z and x. This is shown [1] to be the case to a very good approximation for the most definitively known species. The $\Delta z_{xy}^2/y$ is generally in the range +2 to -1.5, and an electrostatic argument is given for the stability of complexes being favored by small or negative values.

Reaction (13) reflects the tendency of the initial hydrolysis product to polymerize.

$$M(OH)^{(z-1)+} = 1/y\ M_x(OH)_y^{(xz-y)+} + (1-x/y)M^{2+}. \quad (13)$$

The three species can be shown to be at equal concentrations at values generally less than 0.01 m and often less than 0.001 m from the relationship $(K_{11}^y/K_{xy})^{(1/(x-1))}$ which gives this species concentration. This shows that polynuclear species remain prominent among the hydrolysis products of many metals down to very low concentrations.

SOLUBILITY AND DISTRIBUTION PLOTS

The solubility of hydroxides is usefully represented by log-log plots of concentration of metal (or species) vs pH. For example, Figure 4 shows the solubility of gibbsite at 25°C as a function of pH from Ref. [1]. The light lines represent equilibrium concentrations of species labeled by their (x,y) values; i.e., (2,2) represents $Al_2(OH)_2^{4+}$, etc. The slopes of the lines are equal to minus the charge on the species, (y-zx); cations have negative slopes and anions positive slopes. The bold curve sums the metal concentration and is the total solubility of the solid phase. In Ref. [1] such plots are most commonly shown for the condition 1 m (ionic strength) and 25°C. Clearly measurements of solubility as a function of pH can provide information on

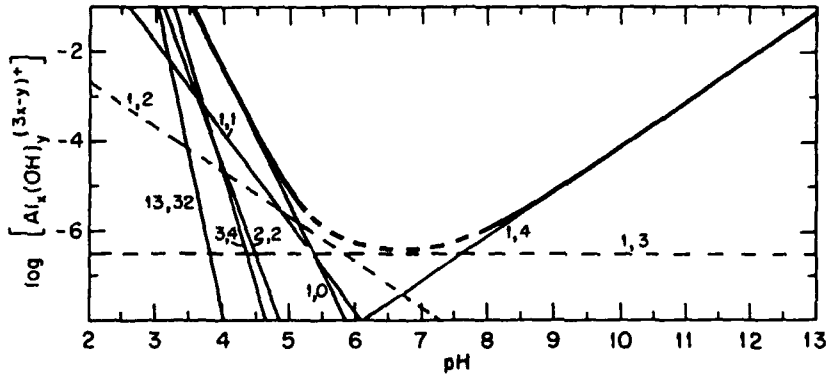


Figure 4. Concentrations of hydrolysis products (x,y) of Al(III) at I = 1 m and 25° in solutions saturated with $\alpha(Al(OH)_3$ (gibbsite). The heavy curve is the total concentration of Al(III) and x,y values mark the lines (Ref. [1]). The stability of the 1,3 and 1,2 species of aluminum(III) are in doubt (dashed lines) [13].

species charge and equilibrium quotients while no information on polynuclearity can be derived. Generally this method has not been successful, however, because of (a) the difficulty of obtaining well crystallized phases, (b) the low concentrations, and (c) the relatively unbuffered conditions encountered. Recently detailed studies on gibbsite have been carried out at ORNL by Palmer and Wesolowski [13] in the best application of this approach to date. In other experiments on aluminum, solutions from 60° to 125°C [14] could be studied which were quite supersatuated with respect to gibbsite or boehmite, AlO(OH). The ratio of hydroxide complexed in hydrolyzed species to the total aluminum in solution reached values of 1.0 at 150°C, 1.8 at 125°C, 2.2 at 100°C [14] and 2.4 at 25°C [15]. Even at 125°C several hours was required for equilibrium in the region where the large polynuclear species $Al_{13}(OH)_{32}^{7+}$ was found.

The distribution of species (two of which are in some doubt [13]) in two solutions containing 0.1 m and 10^{-5} m total aluminum in 1 m electrolyte, are shown in Figure 5 as a function of pH. The ordinate gives the percent of the metal in the form indicated by the x,y values. Most of the curves are dashed to reflect supersaturation with respect of gibbsite.

Another important form of presentation for hydrolysis species occurrence is the predominance diagram in which boundaries representing conditions for equal concentrations of two species are plotted, and formulas are shown in regions for which that species is the predominant (not the only) species. As an example, the predominance diagram for V(V) is shown in Figure 6 at an ionic strength of 1 m. The boundaries are straight lines where only two species are significant but curvature occurs as intersections involving additional species are approached. In the dilute solutions, $<10^{-5}$ m, only mononuclear species are dominant. Decavanadates and metavanadates predominate in the concentrated solutions.

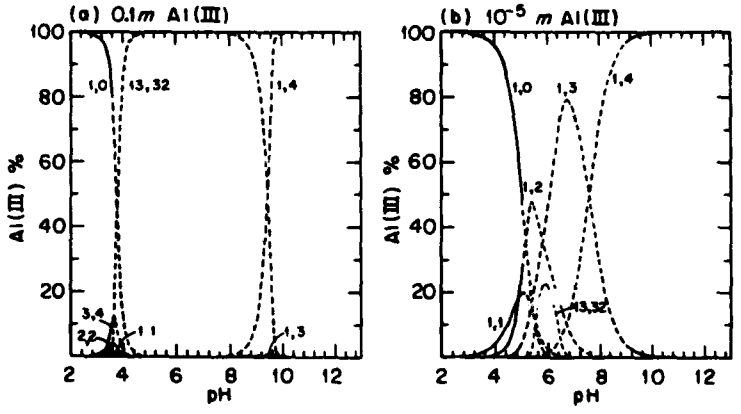


Figure 5. Distribution of hydrolysis products of Al(III) in solutions containing 0.1 m and 10^{-5} m Al(III). Dashed regions are supersaturated with gibbsite (Ref. [1]).

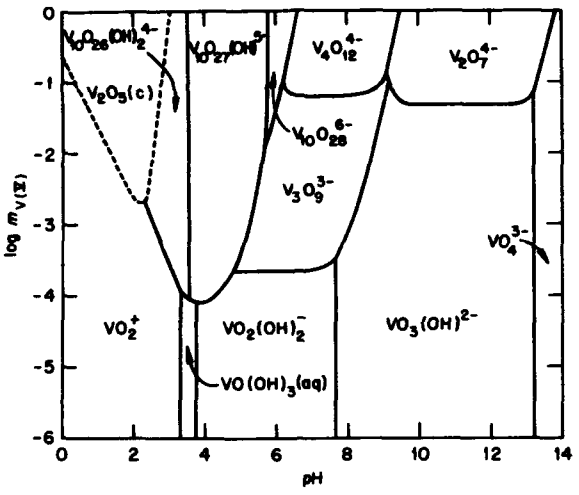


Figure 6. Predominance diagram for V(V)-OH^- species at 25° and I = 1 m. The solid lines represent conditions under which the predominant species in adjacent regions contain equal amounts of V(V). The dashed lines represent the solubility of V_2O_5 (Ref. [1]).

OTHER TEMPERATURE EFFECTS

Temperature effects on the hydrolysis reactions have been reviewed in Ref. 2. The correlations observed are summarized in Table II and are represented for a typical cation in Figure 7. The important observations for hydrolysis reactions beyond the first step are as follows:

1. The enthalpy ΔH_{S10} for the solubility reaction to form the unhydrolyzed cation is negative and therefore with increasing temperature the solid oxide or hydroxide shows a decreasing solubility in acid. Also, there is a correlation between ΔH_{S10} and ΔH_{11}.
2. The enthalpy of the reaction (11) to form the first hydrolysis species from the solid and the unhydrolyzed cation is related to ΔH_{11} and is slightly positive. Accordingly, the pH of the intersection $M(OH)_z(cr)/M^{z+}/MOH^{(z-1)+}$ in Figure 7 decreases with temperature.
3. The enthalpy of reaction of the $MOH^{(z-1)+}$ to polymerize to form a polynuclear species (13) is in the range -2.6 to -7.5 kcal/mole and therefore the intersection $M^{z+}/MOH^{(z-1)+}/M_x(OH)_y^{(xz-y)+}$ in Figure 7 rises to higher metal concentration with increasing temperature reflecting a decreasing stability of polynuclear species.
4. From a consideration of the first hydrolysis step for cations and the ionization reactions of acids of groups IV-to-VI, the enthalpy of each stepwise hydrolysis should decrease and the pH range of each successive mononuclear species should increase with temperature.
5. The solubility of the solid to produce the neutral species $M(OH)_z$ contributes to the minimum in the solubility and generally decreases with increasing charge on the cation and increases with temperature, the enthalpy of the reaction being small and usually positive.
6. The tendency of the solid to react with basic solutions to produce the anion $M(OH)_{z+1}^-$ is expected to have a very small temperature dependence.
7. The heat capacity changes are expected to be small for stepwise hydrolysis reactions except for those producing anions.

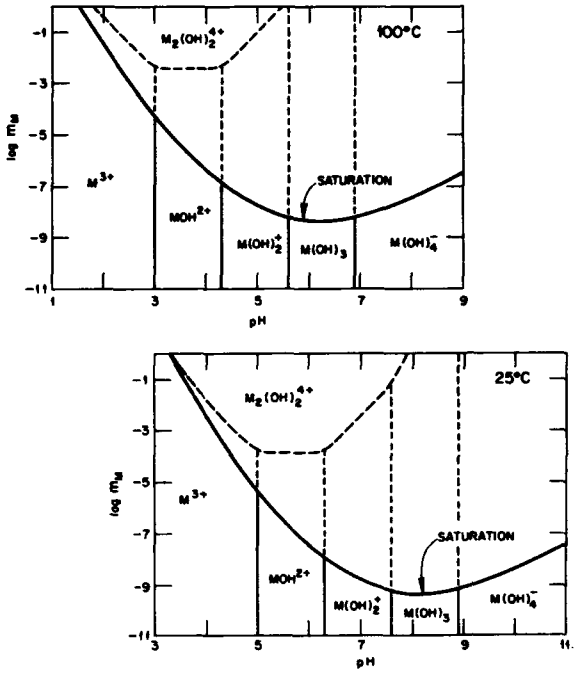


Figure 7. Regions of dominance of the hydrolysis products in solution at 25° and 100°C for a hypothetical trivalent cation. The curve represents the solubility limit of the hydroxide solid phase. This figure was constructed assuming only values for K_{11} and a spacing of 1.3 log units per each mononuclear hydrolysis step. The other boundaries were inferred from correlations described in Ref. [2].

Table II. Summary of important correlations at 25°C [1,2].*

	Remarks
$\log(Q_{xy}^{1/y}/Q_{11}) \approx 2.8 - (x-1)/y \log 55.5$	$I \sim 1$ m.
$\Delta S_{xy}/y \approx -17.5 + 16.2\ z/d + [(1+y-x)/y]\ R \ln 55.5$	
$\Delta H_{xy}/y - \Delta H_{11} \approx -6.6 - 0.53 \log K_{11} - 0.9(z/d)$	
$\Delta S_{11} = 1.772 \log K_{11} + 19.12(z/d)$	
$\Delta H_{11} = -0.836 \log K_{11} + 5.70(z/d)$	
$\Delta H_{S10} = z\ (9.30 - 1.588\ \Delta H_{11})$	
$\Delta H_{1,y+1} - \Delta H_{1y} = -1.36 \log(K_{1,y+1}/K_{1y}) - 5.3 + 3.64\ (z-y)$	
$\log K_{Siz} \approx -5.6 - 0.5\ z(z-1)B$	Stepwise constants decrease by B.
$\log K_{1z} \approx z \log K_{11} - 0.5\ z(z-1)B$	

*Q_{xy} and K_{xy} are defined by equations 3 and 4, respectively. The subscript sxy refers to reaction (5).

The effect of temperature on the solubility of a hypothetical trivalent cation [2] based on the above correlations is shown in Figure 8. On the acid side the solubility falls rapidly with increasing temperature. At the solubility minimum the temperature dependence is very small. On the alkaline side where anions appear the small positive temperature coefficient of solubility is reduced and finally reversed by the heat capacity effect as the temperature above about 150°C.

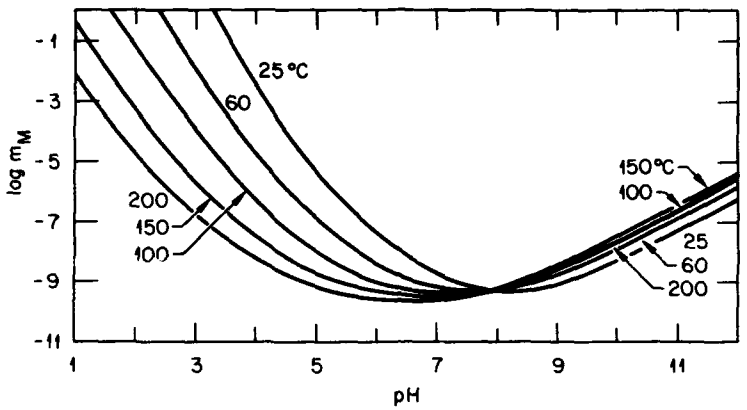


Figure 8. Solubility of the hydroxide solid phase from Figure 7 as a function of temperature (Ref. [2]).

REFERENCES

1. C. F. Baes, Jr. and R. E. Mesmer, The Hydrolysis of Cations, (John Wiley and Sons, New York, 1976; second printing, Robert E. Krieger, Malabar, FL, 1986).
2. C. F. Baes, Jr. and R. E. Mesmer, Am. J. Science, 281, 935 (1981).
3. G. Johansson, Acta Chem. Scand., 14, 771 (1960).
4. G. M. Muha and P. A. Vaughan, J. Chem. Phys., 33, 194 (1960).
5. J. E. Enderby, S. Cummings, G. J. Herdman, G. W. Nielson, P. S. Salmon, and N. Skipper, J. Phys. Chem., 91, 5851 (1987).
6. R. A. Robinson and H. A. Harned, Chem. Rev., 28, 419 (1941).
7. R. E. Mesmer and C. F. Baes, Jr., Inorg. Chem., 8, 618 (1969).
8. A. M. Bond and G. T. Hefter, IUPAC Chem. Data Ser. 27, 1 (1980).
9. R. D. Shannon and C. T. Prewitt, Acta Cryst., B25, 925 (1969).
10. B. V. Enüstün and J. Turkevich, J. Amer. Chem. Soc., 82, 4502 (1960).
11. P. Schindler, "Heterogeneous Equilibria Involving Oxides, Hydroxides, Carbonates, and Hydroxide Carbonates," Advances in Chemistry Series No. 67, p 196 (1967).
12. L. G. Sillen, "Polynuclear Complexes in Solution," in Coordination Chemistry, ed. A. E. Martell, Vol. 1, 491-541 (1971).
13. D. A. Palmer and D. J. Wesolowski, "The Solubility of Gibbsite in Aqueous Sodium Chloride Solutins, "Proceedings of the 11th International Conference on the Properties of Steam, Prague, Czechoslovakia (1989).
14. R. E. Mesmer and C. F. Baes, Jr., Inorg. Chem. 10, 2290 (1971).
15. J. Aveston, J. Chem. Soc., 4438 (1965).

HYDROLYSIS OF ALUMINUM - ARE ALL GELS CREATED EQUAL?

T. E. Wood, A. R. Siedle, J. R. Hill, R. P. Skarjune and C. J. Goodbrake
Ceramic Technology Center, Science Research Laboratory, and Analytical and Properties Research Laboratory, Building 201-4N-01, 3M Center, St. Paul, MN 55144

ABSTRACT

The nuclearity and structure of aluminum cations generated by the hydrolysis of aluminum salt solutions depends markedly on the method of preparation. This speciation affects not only the thermochemistry of processes leading to ceramics, but the microstructures of the ceramics themselves. A brief review of aluminum ion hydrolysis is presented along with a study of the thermal evolution of gels derived from aluminum salt solutions via several different hydrolysis methods. The observation of 5 - coordinate aluminum in a bulk transition alumina by MAS-NMR is reported. A new, high defect precursor of η-alumina dubbed "high-5 alumina" is described and the far reaching implications of this discovery are discussed.

INTRODUCTION

Hydrolyzed aluminum solutions and gels are used industrially as precursors to ceramic fibers, powders, and binders [1]. Of particular interest to the ceramist is how differences in the aluminum cation speciation affect the thermal evolution of the derived alumina towards the final ceramic product. Unfortunately, aqueous aluminum chemistry is exceedingly complex and poorly understood. A holistic interpretation of the voluminous data that exists is complicated by the fact that aluminum cation speciation depends strongly on the method of preparation. The diversity of aluminum cation speciation, described below, well illustrates the formidable nature of the aluminum hydrolysis problem. Yet to the ceramist this diversity is also indicative of the tremendous potential and flexibility the polynuclear aluminum cation solutions possess as ceramic precursors.

In a sol-gel process, the nature of the aluminum cations in a ceramic precursor sol determines the molecular structure of the basic unit of the resulting gel and the packing of such units in the gel. Therefore, some soluble relationship should exist between the cation speciation in the precursor sol and the thermal evolution of the resulting gel. While the differences between molecular and colloidal approaches to sol-gel synthesis have received considerable attention [2], to our knowledge, a detailed study of the effects of cation speciation on the development of alumina phases has not been reported. In order to begin to elucidate a relationship, we have prepared several gel alumina precursors from aluminum salt solutions by different techniques and examined their thermal behavior. Although the exact identity of most of the complex cations in the precursor sols is not known, solution state ^{27}Al NMR can be used to "fingerprint" such sols so that a systematic comparison of thermal evolution can be made. Differences in structure and nuclearity of these cationic aluminum precursors will be shown to persist and propagate through ambient to high temperature processing regimes notwithstanding the addition of substantial thermal energy. These differences

Mat. Res. Soc. Symp. Proc. Vol. 180. ©1990 Materials Research Society

are thus associated with significant kinetic effects in ceramic synthesis [3].

An important implication of this study is that control of speciation may enable substantial control of phase formation, crystal perfection and microstructure of sol-gel derived alumina. In addition, we report the first observation of 5-coordinate aluminum in a bulk transition alumina by MAS-NMR along with the discovery of a super-high defect precursor of η-alumina.

HYDROLYSIS OF ALUMINUM

A brief review of the hydrolysis of the aluminum ion is presented to illustrate the complexity and diversity of aluminum cation speciation.

Aluminum exists in aqueous solution solely as monomeric $[Al(OH_2)_6]^{3+}$ below pH 3 and, above pH 11, as the $[Al(OH)_4]^-$ ion. Between a pH of 3 and 11, at least a portion of the aluminum is hydrolyzed to form polynuclear ions. Regardless of the method of preparation, hydrolyzed aluminum solutions slowly change with time, and the aging behavior is also dependent on aluminum cation speciation and the identity of the counterions and heterospecies which may be present. In general, hydrolyzed aluminum solutions or gels maintained under acidic conditions will slowly convert to pseudo-boehmite or boehmite, AlOOH; neutral or basic gels are unstable with respect to precipitation of aluminum hydroxide. The initial stages of the hydrolysis of aluminum are rapid, but as the polynuclear cations grow in size, the intercluster condensation reactions become slow so that metastable solutions are obtained which can be analyzed and used as precursors to ceramics [4].

Attempts to unravel this complex chemistry have included studies using potentiometry [5], light and X-ray scattering [6], ultracentrifugation [7], coagulation studies [8], colorimetric techniques [9], Raman and infrared spectroscopy [10] and ^{27}Al NMR [11-16]. Reviews of the hydrolysis and the water chemistry of aluminum exist [17], but recent results using ^{27}Al NMR spectroscopy has cast doubt on some conclusions drawn from earlier work.

Studies utilizing ^{27}Al NMR spectroscopy to establish speciation have been pioneered by Akitt et al [11,12] and notable contributions have been made by Bottero [13], Bersch [14], Oldfield [15], and others [16]. Aluminum has a quadrupolar nucleus ($I = 5/2$, $Q = 0.149 \times 10^{-29} M^2$) with 100% natural abundance. Although a sensitive nucleus for NMR, it is subject to quadrupolar line broadening effects when the nucleus is in an asymmetric electric field gradient. The chemical shifts and the linewidths for Al are known [18] to be dependent on ligand type, coordination number, ligand field symmetry, and the rate of chemical exchange. In aqueous solution, hydrolyzed octahedral aluminum species usually resonate between about 0 and 25 ppm [11,16]. Aluminum in a tetrahedral environment generally resonates at lower field, between 50 and 85 ppm for aqueous solutions, although resonances as high as 221 ppm and as low as -28 ppm have been observed for organic complexes [19].

Solutions containing hydrolyzed aluminum complexes can be prepared by several different methods. For example, solutions can be hydrolyzed to m = 2.5 (where m =

moles Al/moles base added) without precipitation of insoluble phases by the drop-wise addition of a base to an aluminum salt solution (chloride or nitrate counterion) [11]. Using high resolution ^{27}Al NMR and gel permeation chromatography, Akitt and others [11-16] have shown that when carefully carried out, reactions of this type initially generate a small, polynuclear cation at low m values which gives rise to a resonance at 3.3 ppm (figure 1). This species along with the monomer, $[Al(OH_2)_6]^{3+}$, are both consumed with continued base addition to generate almost exclusively the "Al13" ion, $[AlO_4\ Al_{12}(OH)_{24}\ (OH_2)_{12}]^{7+}$. The structure of this tridecamer has been determined to be Keggin-like (figure 2) by X-ray studies of sulfate and selenate derivatives [20]. Low angle X-ray and light scattering [6], ^{27}Al NMR [11], and Raman spectroscopic measurements [10] have demonstrated unequivocally that this species is present in solutions of hydrolyzed aluminum salts in the presence of non-coordinating anions. The tetrahedral aluminum at the center of the Al_{13} ion gives rise to a sharp, characteristic resonance at 63.5 ppm (figure 1). The 3.3 ppm resonance has historically been attributed to the dimer, $[Al_2(OH)_2(OH_2)_8]^{4+}$, whose single crystal structure as a sulfate salt has been reported [21]. This assignment has recently come into question due to the anomalously high amount of base consumed in the formation of this species [22].

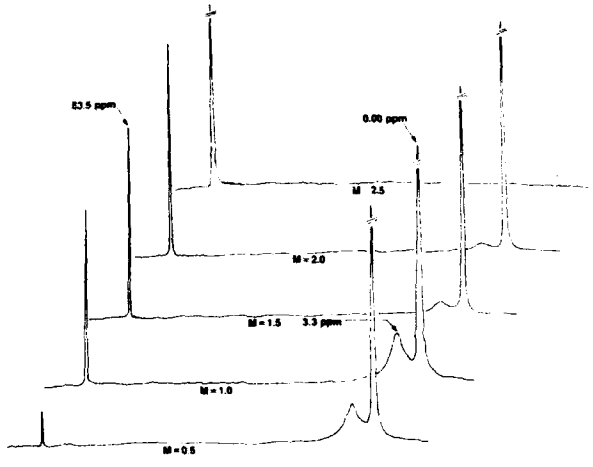


Figure 1. ^{27}Al NMR spectra of 0.25M Al^{3+} solutions hydrolyzed by the drop-wise addition of aqueous bicarbonate [16].

Akitt and others have shown [11,16] that at low concentrations (< 0.025 - 0.05 M Al), the monomer hydrolyzes directly to Al_{13} regardless of the ionic strength and temperature. As the concentration of the aluminum in these reactions is raised, the 3.3 ppm species begins to be formed and increases in concentration until a hydrolysis ratio of 0.5 - 1.0 is reached. With continued addition of base, the 3.3 ppm species is

consumed to form the tridecamer. The implication is that 3.3 ppm species is a highly hydrolyzed precursor of the Al_{13} ion and indeed may be a recognizable Al_{13} cluster fragment or subunit.

When base is added to the metal salt solution rapidly or the concentration of the base solution is high, a mixture of oligomers is formed in addition to the tridecamer as evidenced by a broad asymmetric resonance centered at 10 ppm [16]. These species are not consumed on further base addition to form Al_{13}.

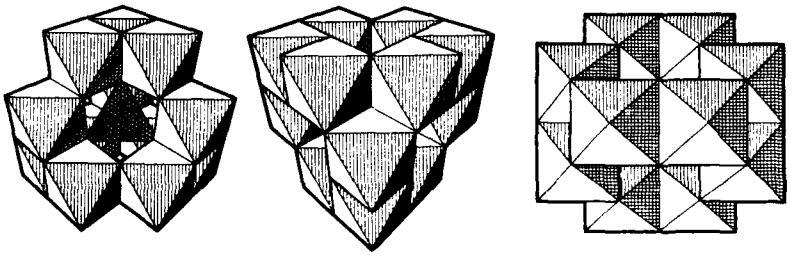


Figure 2. Three different views of the $[AlO_4\,Al_{12}(OH)_{24}\,(OH_2)_{12}]^{7+}$ ion.

The hydrolysis of alkoxides is also a convenient method of preparing hydrolyzed aluminum solutions that can be used as precursors to ceramics [23]. The hydrolysis of aluminum sec-butoxide was shown by Olson and Bauer to generate solutions and gels which contained mainly octahedral aluminum when the acid/Al ratio was low [24]. Komarneni et al using ^{27}MAS-NMR confirmed that such gels contained predominantly octahedral aluminum [2]. Like boehmite derived gels, these gels dehydrate to form γ-alumina [2]. Nazar and Klein found that at higher acid/Al ratios a speciation is obtained similar to that generated by the drop-wise addition of a base to an aluminum salt solution with the exception that a new species characterized by a 7.6 ppm NMR signal is observed [25].

The digestion of aluminum metal in an acid solution is used on an industrial scale [26] to prepare basic aluminum salt solutions which are used in the production of ceramic fibers [27]. Akitt and coworkers have shown that the hydrolysis of aluminum metal produces a very complex, concentration dependent cation speciation [12]. The digestion of aluminum in dilute aluminum chloride solution ($m = 2.5$) produces a mixture of monomer, Al_{13}, and oligomers which give broad resonances at 4, 12, and 70 ppm. The amount of aluminum observed in the NMR experiment decreases sharply with increasing value of m as, presumably, species having very broad, unobservable ^{27}Al signals are formed. When concentrated aluminum chloride is used, a new, resonance for an octahedral aluminum oligomer appears at 9 - 10 ppm, along with new broad resonances at 50, - 9 and - 50 ppm. Clearly, a complex combination of species possessing a variety of polynuclear structures are present.

The hydrolysis of aluminum driven by the in situ generation of a base, a process which is used to generate alumina powders [28] and highly active alumina catalysts [29], has also been studied [16]. In this process, a substance such as urea or hexamethylenetetramine (HMTA) is homogeneously mixed with an aluminum salt solution and thermally decomposed to controllably promote aluminum hydrolysis. The distribution of cations generated by these reactions depends on the concentration of aluminum, temperature, reaction time, and the concentration and identity of the base generator. When the concentration of aluminum is low (<0.5 M), hydrolysis using a stoichiometric amount of base generated by the thermal decomposition of either HMTA or urea produces oligomers which contain octahedral and at least two forms of tetrahedral aluminum [16]. The NMR spectra of these solutions (figure 3) appear similar to that described for aged solutions of Al_{13} [30]. In general, these solutions also contain a small amount of the tridecamer. Solutions of this type were used to prepare the gels whose thermal evolution are described in the experimental section.

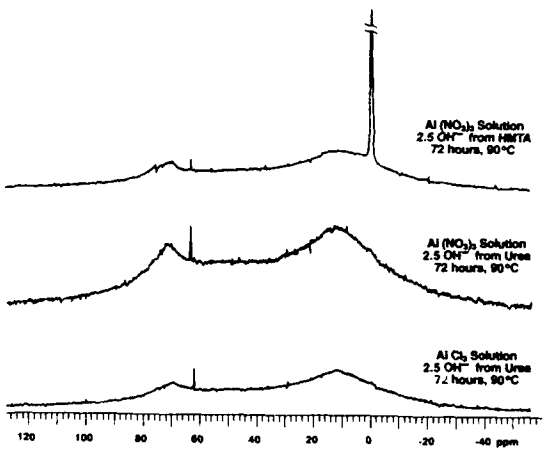


Figure 3. ^{27}Al NMR spectra of 0.25M Al^{3+} solutions hydrolyzed by the in situ generation of a base [16].

As the aluminum concentration is raised, the system becomes much more complex. The ^{27}Al NMR spectra in figure 4 were obtained from hydrolyzed aluminum solutions generated by the reactions of a) 2M aluminum nitrate with an excess of HMTA and b) 2M aluminum nitrate with an excess of urea, both under reflux conditions. The amount of aluminum observed by NMR represents about 24% of the total aluminum in the HMTA reaction and 40% of the total aluminum in the urea reaction because the ^{27}Al signal intensity decreased as the reaction progressed. The speciation produced by the thermal degredation of HMTA in the presence of aluminum nitrate is very similar to that reported by Akitt [12] for concentrated metal-hydrolyzed aluminum salt solutions with several notable exceptions. The symmetry and the line width of the resonance in the 8 - 12 ppm range seems to indicate the presence of only one species.

In addition, a new broad resonance centered at about -1 ppm has emerged, and the broad resonance at -9 ppm is noticably absent. There are clearly at least two different resonances in the tetrahedral region, a broad resonance at about 70 ppm and a more narrow, but lower intensity resonance at 56 ppm.

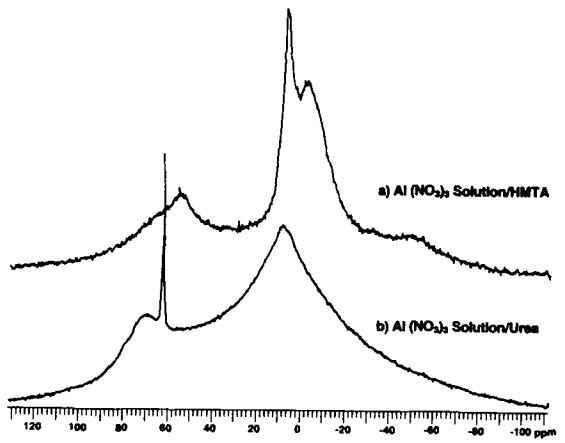


Figure 4. ^{27}Al NMR spectra of 2M Al^{3+} solutions hydrolyzed by the in situ generation of a base under reflux conditions using a) HMTA as a base generator and b) urea as a base generator [16].

When urea is used as the base source (figure 4b), the speciation seems to be similar to what Akitt has described [12] for the low concentration metal hydrolyzed salt solutions. Besides the tridecamer, an oligomer or mixture of oligomers is evidenced by broad resonances at about 10 ppm and 70 ppm.

One universal feature of all the methods of aluminum hydrolysis is the ease with which the tridecamer is formed. With the exception of the low acid/alkoxide hydrolysis, the majority of the large oligomers observed in the other cases may prove to be derivatives of Al_{13} or condensation products of this ubiquitous ion. Indeed, Nazar has provided evidence that the tridecamer dimerizes as the initial step in aging [30].

To test the the influence the nature of the aluminum cations has on thermal evolution of a sol-gel system, four gels were prepared from hydrolyzed aluminum solutions having either different aluminum cations or different counterions (nitrate or chloride ion). One precursor solution contained predominantly the Al_{13} ion; the others were prepared by the in situ hydrolysis method. The hydrolyzed aluminum sols were gelled in an identical fashion. The sol precursors were examined by solution NMR; further, the thermal evolution of the gels into more thermodynamically stable forms of alumina was characterized by DTA, XRD, and ^{27}Al MAS-NMR. Notable differences are observed which appear to be linked to the cation speciation.

EXPERIMENTAL

A flow chart for the experimental procedure is shown in figure 5. The Al_{13} gel precursor was prepared by the drop-wise addition of an ammonium bicarbonate solution to a rapidly stirred 0.38M aluminum nitrate solution held at 90° C. After 2.5 equivalents of base were added, an aliquot was withdrawn and examined by ^{27}Al NMR to confirm the formation of the tridecamer. The final concentration of aluminum was 0.25M. Three additional gel precursor solutions were prepared by aging at 90° C for 72 hours 0.25M Al solutions containing 2.5 equivalents of base in the form of either urea or hexamethylenetetramine. The mixtures examined consisted of aluminum nitrate/urea (gel B), aluminum chloride/urea (gel C), and aluminum nitrate/HMTA (gel D). The gels were formed by the addition of an ammonium bicarbonate solution to the precursor solution in a blender under high shear. The final hydrolysis ratio was 3.0. The resulting gels were immediately washed three times with 500 ml deionized water by centrifugation (5000 RPM)/decantation. Between separations the gels were well mixed in the wash water using a blender . The gels were dried at 85° C and the thermal evolution of the samples was studied by examining calcined samples (0.5 hour at temperature) using solid state ^{27}Al NMR, DTA, TGA, XRD, and IR spectroscopy.

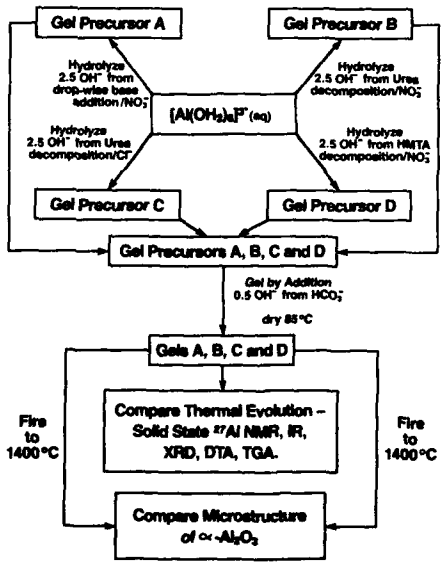


Figure 5. Flow chart for the experimental procedure.

The solution-state ^{27}Al NMR spectra were acquired at 104 MHz on a Varian XL-

400 with D_2O added as a deuterium lock. Single-pulse excitation with proton decoupling was used to acquire data over a spectral width of 50 kHz. About 300 - 400 transients were accumulated at 0.4 s intervals. Solid-state ^{27}Al NMR spectra were acquired at 52.1 MHz on a Varian XL-200 modified for solids operation. The powders were loaded into 7 mm cylindrical zirconia rotors and spun at the magic angle at rates from 3 - 4 KHz in a Doty probe (Doty Scientific, Inc., Columbia, SC). Single pulse excitation using 10 microsecond 90^o pulses was used. *Chemical shifts* were established by using a seperate sample of $[Al(OH_2)_6](ClO_4)_3$ in D_2O solution and assigning its resonance as 0 ppm. Positive chemical shifts were downfield of the reference, and chemical shifts were assigned from peak maxima (not the true isotropic shift).

RESULTS AND DISCUSSION

Three of the aluminum solutions used to generate the gels were hydrolyzed by the in situ generation of a base (gels B, C, and D). The general features of the solution ^{27}Al NMR of these solutions, with the exception of the small amount of unreacted monomer in the HMTA case, are very similar (figure 3) suggesting similar speciation. The thermal decomposition of HMTA seemed to initially proceed more rapidly than the decomposition of urea, but the HMTA reactions were difficult to drive to completion as evidenced by the presence of unreacted $[Al(OH_2)_6]^{3+}$ in the hydrolyzed solutions. The absence of a sharp resonance for $[Al(OH_2)_5urea]^{3+}$ at -2.7 ppm in the urea reactions indicated that the majority of the urea had decomposed.

The ^{27}Al NMR spectrum of the Al_{13} solution, used to prepare gel A, consisted of a single sharp resonance at 63.5 ppm indicating that the tridecamer was the major component.

The addition of 0.5 equivalents of base (HCO_3^-) was used to induce gelation of the hydrolyzed aluminum solutions. The yield of gel recovered was consistently higher for the tridecamer sol than for the sols generated by the in situ hydrolysis. The HMTA hydrolyzed sol had the lowest yield, possibly as a result of the incomplete thermal decomposition of the HMTA. The slight turbidity of the wash solutions indicated the colloidal nature of the hydrolyzed aluminum that was lost.

After drying at 85^o C, the gels were hard, brittle, and clear to turbid white in appearance. All four dried gels react slowly with weak acid to form solutions which contain the tridecamer ion. An infrared spectroscopic study of the calcination of these gels revealed that the samples prepared from aluminum nitrate contained a small amount of nitrate ion which slowly decomposed above 300^o C. The 200 - 1200 cm^{-1} region was essentially identical for all the samples consisting of a broad absorption envelope with poorly defined features. This broad envelope collapsed above 1100^o C with the emergence of the sharp absorptions characteristic of alpha alumina.

The percent fired solids of these gels as determined by TGA was as follows: gel A - 64.1%, gel B - 53.9%, gel C - 65.7%, and gel D - 42.3%. The TGA of these dried gels also reveals very dissimilar, complex weight loss patterns (figure 6). Since these

400 with D_2O added as a deuterium lock. Single-pulse excitation with proton decoupling was used to acquire data over a spectral width of 50 kHz. About 300 - 400 transients were accumulated at 0.4 s intervals. Solid-state ^{27}Al NMR spectra were acquired at 52.1 MHz on a Varian XL-200 modified for solids operation. The powders were loaded into 7 mm cylindrical zirconia rotors and spun at the magic angle at rates from 3 - 4 KHz in a Doty probe (Doty Scientific, Inc., Columbia, SC). Single pulse excitation using 10 microsecond 90° pulses was used. Chemical shifts were established by using a separate sample of $[Al(OH_2)_6](ClO_4)_3$ in D_2O solution and assigning its resonance as 0 ppm. Positive chemical shifts were downfield of the reference, and chemical shifts were assigned from peak maxima (not the true isotropic shift).

RESULTS AND DISCUSSION

Three of the aluminum solutions used to generate the gels were hydrolyzed by the in situ generation of a base (gels B, C, and D). The general features of the solution ^{27}Al NMR of these solutions, with the exception of the small amount of unreacted monomer in the HMTA case, are very similar (figure 3) suggesting similar speciation. The thermal decomposition of HMTA seemed to initially proceed more rapidly than the decomposition of urea, but the HMTA reactions were difficult to drive to completion as evidenced by the presence of unreacted $[Al(OH_2)_6]^{3+}$ in the hydrolyzed solutions. The absence of a sharp resonance for $[Al(OH_2)_5urea]^{3+}$ at -2.7 ppm in the urea reactions indicated that the majority of the urea had decomposed.

The ^{27}Al NMR spectrum of the Al_{13} solution, used to prepare gel A, consisted of a single sharp resonance at 63.5 ppm indicating that the tridecamer was the major component.

The addition of 0.5 equivalents of base (HCO_3^-) was used to induce gelation of the hydrolyzed aluminum solutions. The yield of gel recovered was consistently higher for the tridecamer sol than for the sols generated by the in situ hydrolysis. The HMTA hydrolyzed sol had the lowest yield, possibly as a result of the incomplete thermal decomposition of the HMTA. The slight turbidity of the wash solutions indicated the colloidal nature of the hydrolyzed aluminum that was lost.

After drying at 85° C, the gels were hard, brittle, and clear to turbid white in appearance. All four dried gels react slowly with weak acid to form solutions which contain the tridecamer ion. An infrared spectroscopic study of the calcination of these gels revealed that the samples prepared from aluminum nitrate contained a small amount of nitrate ion which slowly decomposed above 300° C. The 200 - 1200 cm^{-1} region was essentially identical for all the samples consisting of a broad absorption envelope with poorly defined features. This broad envelope collapsed above 1100° C with the emergence of the sharp absorptions characteristic of alpha alumina.

The percent fired solids of these gels as determined by TGA was as follows: gel A - 64.1%, gel B - 53.9%, gel C - 65.7%, and gel D - 42.3%. The TGA of these dried gels also reveals very dissimilar, complex weight loss patterns (figure 6). Since these

gels were well washed, the majority of the weight loss which is observed is due to loss of water. Gel A, which was prepared from the tridecamer sol, begins to appreciably lose weight at about 140° C, with the maximum rate of weight loss occuring at about 200° C. The rate of weight loss decreases gradually with increasing temperature with additional small increases in rate of weight loss occuring at 300° C, 360° C, and 420 - 450° C. By 550° C, the majority of the weight loss was complete.

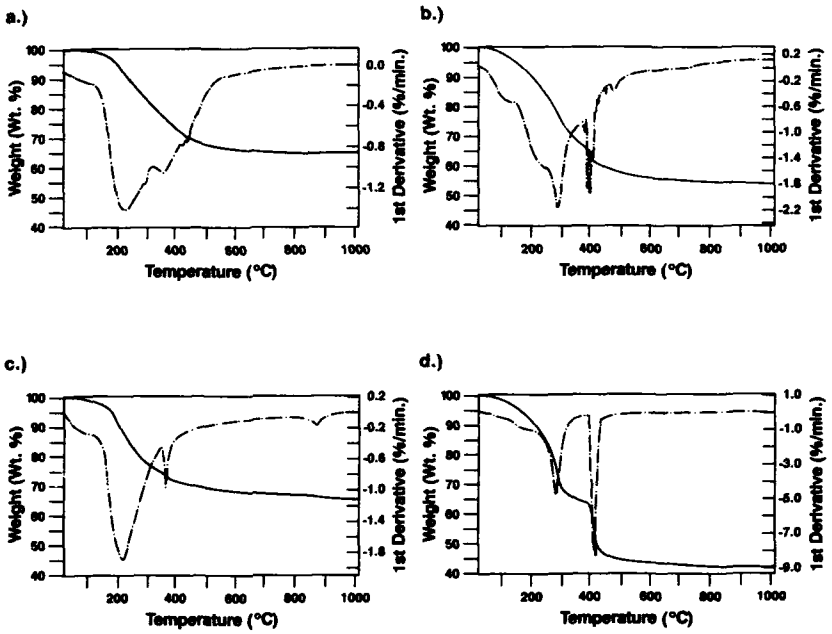


Figure 6. TGA of dried gels (heating rate 10° C/min.)

Despite the fact that the ^{27}Al NMR spectra of the hydrolyzed aluminum solutions which were used to prepare gels B, C, and D appeared very similar, the gels dehydrate in a very dissimilar fashion. Sample B, prepared from aluminum nitrate hydrolyzed in situ with urea, shows a step-wise weight loss pattern which reaches a maximum rate of weight loss at about 290° C, followed by a rapid decrease in rate of weight loss and a series of very rapid ejections of small quantities of volatiles around 400° C. The TGA of sample C, which was prepared using aluminum chloride as the aluminum source, indicates that most of the volatiles in this gel are lost between about 180 and 300° C. Peaks corresponding to weight losses are also observed at 350° C and 860° C. This latter weight loss, which is only observed for the sample containing Cl^-, may correspond to volatilization of HCl. The sample prepared using HMTA as the in situ base generator, gel D, contained the lowest percent fired solids (42.3%). This gel lost the majority of its volatiles rapidly in two steps. As in the case of gel C, the loss of

volatiles was for the most part complete by 450°C.

The DTA traces for these gels (figure 7) indicate endothermic transformations in most regions where weight loss was observed by TGA. A notable exception is the small loss in weight at 860° C in the AlCl3/urea system, gel C. This weight loss, which we surmise is due to loss of HCl, precedes a sharp exothermic transformation at 875° C which represents the appearance of a more ordered transition alumina phase. This exothermic transformation is also observed for the other gels. The intensity of this peak scales in the order AlCl3/urea > Al(NO3)3/HMTA > Al(NO3)3/urea > Al13 derived gel. The peak temperature is slightly higher for the more exothermic transformations. Assuming that this peak represents a transformation to the same phase in all these gels, as is indicated by the XRD results, it can be concluded that the Al13 gel and the AlCl3/urea gel initially calcine to form the lowest and highest energy defect phases, respectively.

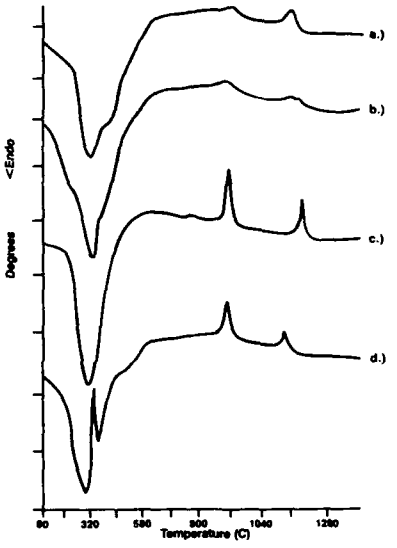


Figure 7. DTA of dried gels (heating rate = 10° C/min.)
a) Al_{13} gel
b) $Al(NO_3)_3$/urea gel
c) $AlCl_3$/urea gel
d) $Al(NO_3)_3$/HMTA gel

This conclusion is supported in striking fashion by the ^{27}Al MAS-NMR spectra of the heat treated samples (figure 8). As prepared, the gels all contain octahedral and tetrahedral aluminum in a ratio very close to that found for an Al13 ion. Upon heating, a third component, which gives rise to a resonance at 35 ppm, develops in differing amounts in the calcined gels. This aluminum species is particularly prominent in the samples B, C, and D, whose precursors had been prepared by the in situ hydrolysis method. In these samples, the 35 ppm peak and the 60 - 65 ppm peak increase with heat treatment at the expense of the octahedral aluminum resonance (0 ppm) up to about 500° C. This trend reverses somewhat on heating to 700° C, although the 35 ppm species remains a prominent feature of the spectra particularly in the case of the AlCl3/urea sample. Clearly, the coordination number of the aluminum is changing dramatically during calcining.

The chemical shift of this newly identified third component is similar to those reported for 5-coordinate aluminum [31]. The 35 ppm resonance is well separated

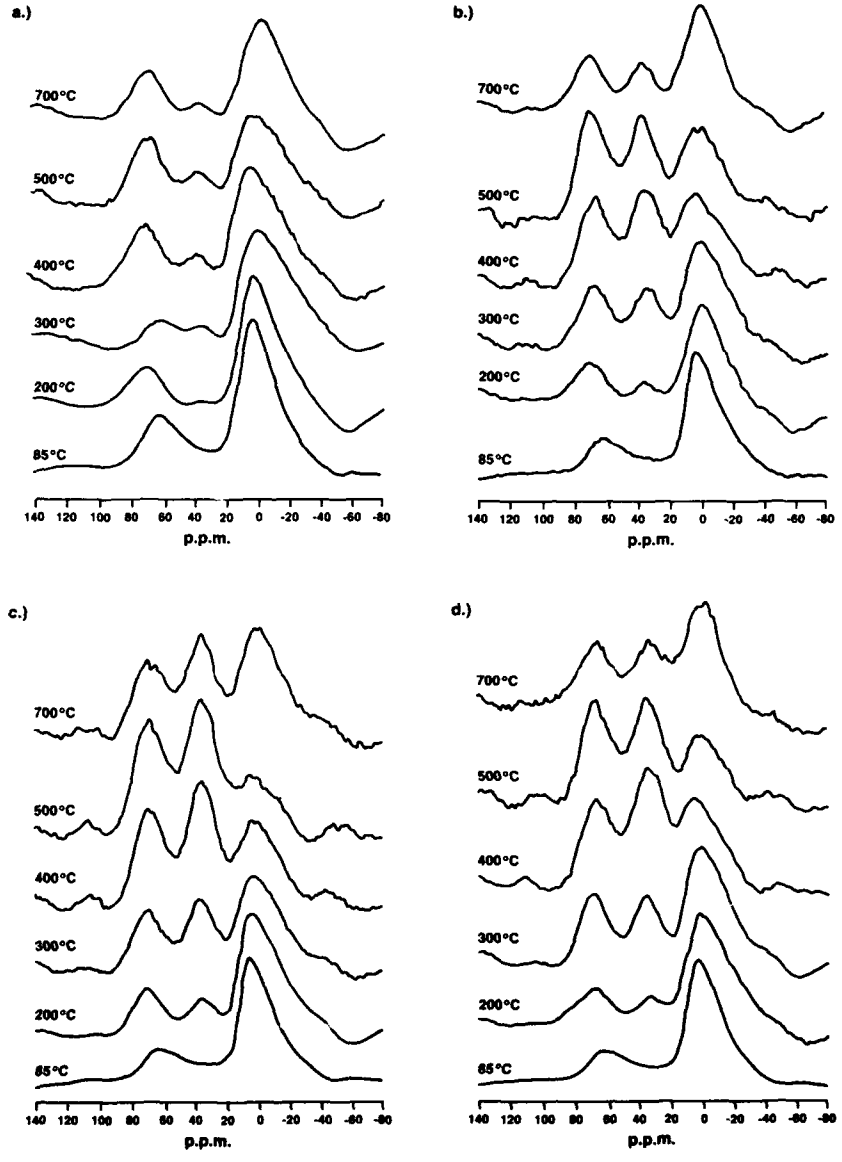


Figure 8. ^{27}Al MAS-NMR of heat treated samples showing octahedral (0 ppm), tetrahedral (60 - 70 ppm) and 5-coordinate (35 ppm) aluminum.

from the octahedral and tetrahedral resonances and its appearance and growth coincides with a decrease in the intensity of the octahedral aluminum resonance. Thus we assign this resonance as arising from 5-coordinate aluminum. As such, this constitutes the first observation of 5-coordinate aluminum by MAS-NMR in a bulk aluminum oxide in the absence of hetero-elements such as P or Si. The MAS-NMR of other transition aluminas has been reported [32], but the signal from the small amount of the 5-coordinate species which may have been present would have been obscured by the presence of spinning side bands.

The η-alumina structure is a defect spinel having a cubic close packed oxygen anion lattice and aluminum vacancies primarily in octahedral sites [33]. The 5-coordination in this η-alumina precursor is probably attained by aluminum cations in octahedral sites of the defect spinel adjacent to oxygen anion vacancies. Between 200 and 500° C, the percentage of both 4- and 5-coordinate aluminum increase with concomitant decrease of aluminum in 6-coordination. The driving force for the creation of oxygen anion vacancies adjacent to occupied octahedral cation sites thus seems to be linked to the movement of aluminum ions from octahedral to tetrahedral sites. The population of these tetrahedral sites demands that the supporting anion framework for tetrahedral coordination be intact. Hence, in order for an aluminum which is in an octahedral site to shift into a tetrahedral site which is anion deficient, an oxygen must shift along with the aluminum to complete the tetrahedral anion cage. Depending on the number of adjacent octahedral sites which are occupied, one oxygen anion vacancy can produce as many as three 5-coordinate aluminum sites. In the case where an aluminum shifts along with an oxygen into an adjacent tetrahedral site, two 5-coordinate sites will result from the oxygen anion vacancy. Regardless of the oxygen vacancy/5-coordinate aluminum ratio, every anion vacancy demands 2/3 cation vacancy, so the large percentage of aluminum of this coordination number indicates a very high energy, defect alumina. Interestingly, the highest levels of 5-coordination were obtained on the samples prepared by the in situ hydrolysis method. The 5-coordinate species is only a minor component in the calcination products of the Al_{13} gel, whereas in the $AlCl_3$/urea derived aluminas it is the major component in samples calcined at 400 or 500° C. After calcining at 500° C, this sample was composed almost entirely of 5- and 4-coordinate aluminum in a ratio of about 1.2 : 1. This material also retained the highest percentage of 5-coordinate aluminum after firing to 700° C. This fact supports the previous illation from the DTA data that inferred that the calcined $AlCl_3$/urea gel had the highest energy structure. The residual chloride ion in this sample may in some way stabilize this metastable structure. The low amount of 5-coordinate aluminum in the calcined Al_{13} derived gel suggests that this material dehydrates to form the most ordered, low energy structure. After conversion to η-alumina by heating at 900° C for 0.5 hour, the $AlCl_3$/urea sample still contained a small amount of 5-coordinate aluminum whereas no 5-coordinate aluminum was observed by ^{27}Al MAS-NMR in the η-alumina derived from the Al_{13} gel.

Examination of the dried and calcined gels by TEM (figure 9) revealed that the dried and calcined gels all possessed a similar, fine, porous structure. Selected area diffraction generated a weak pattern consistent with η-alumina, but the materials slowly became more crystalline on electron beam irradiation. Dark field imaging showed that the smallest crystallites were about 10 A in diameter. This value corresponds to the approximate diameter of a tridecamer cluster.

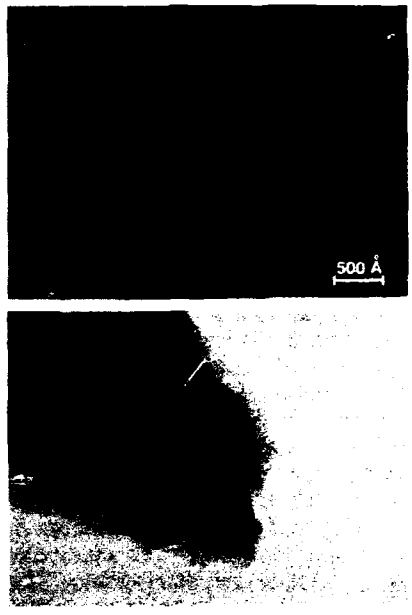


Figure 9. TEM of calcined (400° C)
a) Al_{13} gel and
b) Al(NO3)3/urea gel

The XRD of the thermally treated samples (figure 10) indicates that all the gels initially dehydrate to form amorphous alumina. The thermal development of these amorphous aluminas is dependent on the method of preparation of the parent sol and the presence of chloride ion. After calcining to 400° C all appear to develop an oxygen anion lattice approximating cubic close packing as evidenced by the broad reflections coincident with η-alumina lines. However, by 700° C, it is clearly apparent that sample A is relaxing to an ordered structure more rapidly than the other samples. Sample C, derived from the AlCl3/urea solution, is the most sluggish in thermal evolution. The diffractograms of sample C remain essentially unchanged for calcination temperatures between 200 and 700° C. After firing to 1000° C for 30 minutes, a substantial amount of samples A and D and a portion of sample B have been converted to the alpha phase, whereas sample C contains only a trace of alpha alumina.

The alpha alumina peak transformation temperatures, as determined by high temperature DTA (figure 7), further illustrates differences in the thermal evolution of these samples. The highest peak transformation temperature, 1166°, was observed for the AlCl3/urea sample. It is possible that residual chloride ion in this sample retarded

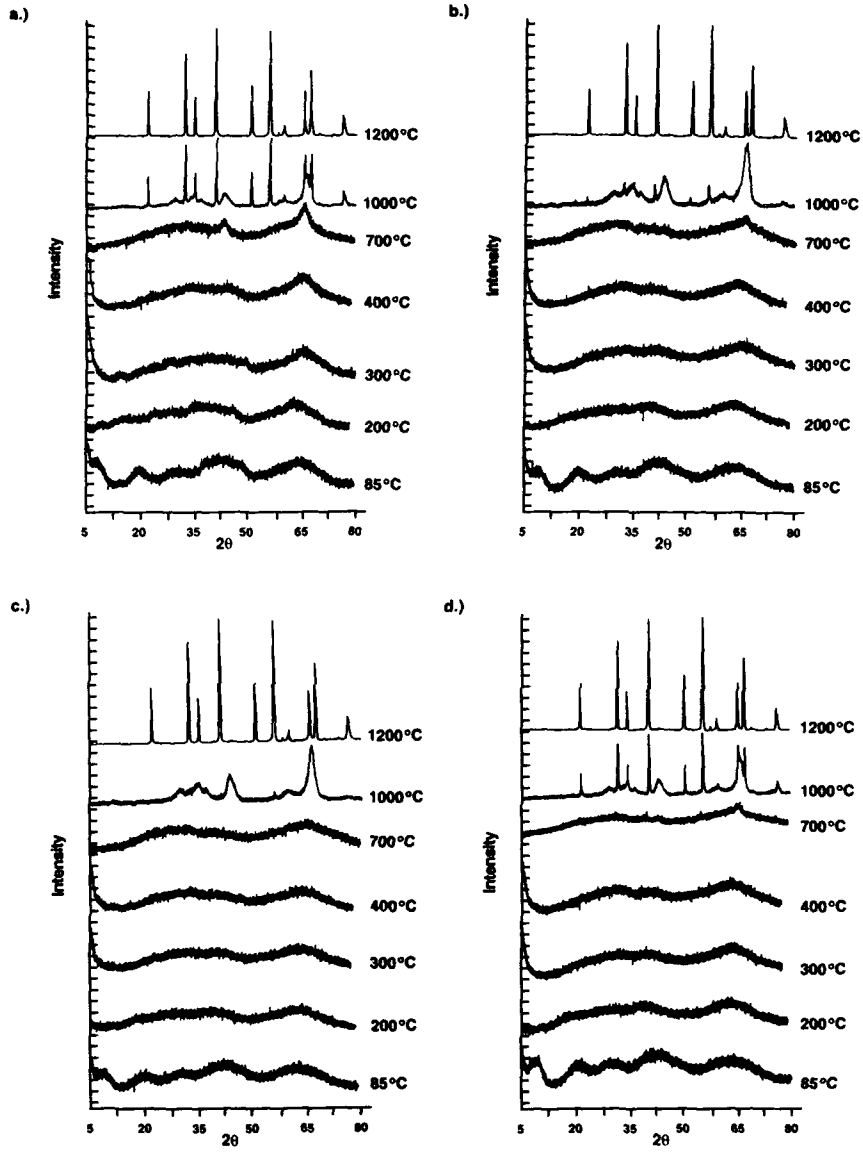


Figure 10. XRD of the heat treated samples a) Al_{13} gel, b) $Al(NO_3)_3$/urea gel c) $AlCl_3$/urea gel d) $Al(NO_3)_3$/HMTA gel

the alpha transformation. e Al_{13} derived material and the $Al(NO_3)_3$/HMTA sample exhibited peak transfor ıation temperatures of 1113° C and 1095° C, respectively. The DTA trace of the $Al(NO_3)_3$/urea sample reproducibly displayed two transformation peaks at 1105° and 1140° C. The reason for this double transformation is unknown.

The four samples were converted to alpha alumina by firing at 1400° C for 5 minutes. Optical microscopy (figure 11) revealed that the alumina derived from the tridecamer sol possessed a much finer grain size than the alumina obtained from solutions hydrolyzed by the in situ generation of a base. An SEM examination of fracture surfaces confirmed this finding and showed that all the samples consisted of porous, vermicular grains (figure 12). Sample A, derived from the Al_{13} sol, had an average grain size of about 2 microns with the smallest grains being slightly sub-micron. The alumina derived from the solutions hydrolyzed by the in situ generation of the base all had coarser structures with average grain sizes of greater than 5 microns. Interestingly, despite the fact that sample A and sample D transformed to alpha alumina at about the same temperature, sample A possessed a much finer microstructure. The majority of the fracture in samples A and C was transgranular whereas the fracture in samples B and D occured primarily in an intergranular fashion.

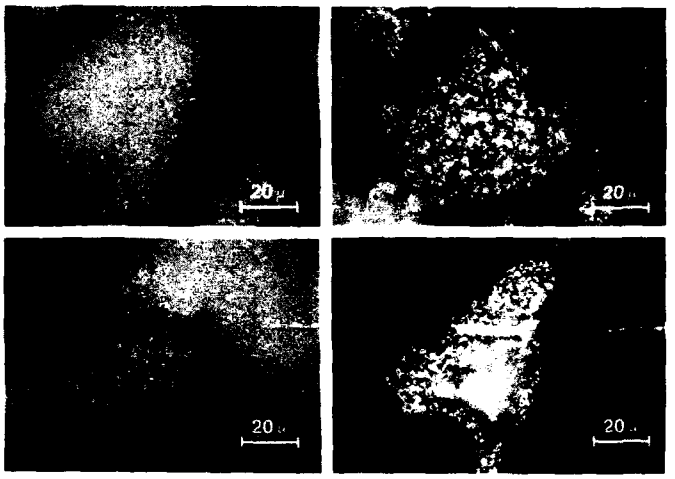


Figure 11. Photomicrographs (cross-polarized light) of microstructures of α-Al_2O_3 formed by heating gels to 1400° C. Note finer microstructure of alumina derived from the Al_{13} gel (upper left). $Al(NO_3)_3$/urea sample is upper right, $AlCl_3$/urea sample lower left, and $Al(NO_3)_3$/HMTA sample is lower right.

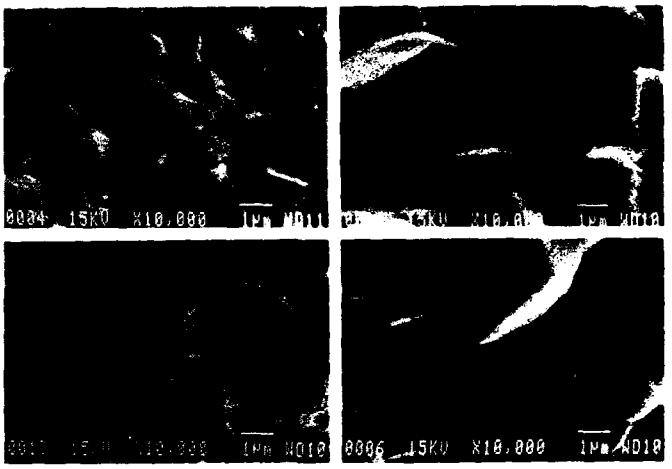


Figure 12. Scanning electron micrographs of fracture surfaces of α-Al_2O_3 formed from gels heated to 1400° C.

Because of the large amounts of 5-coordinate aluminum in the calcined gels prepared by the in situ hydrolysis, we have dubbed this family of materials "high-5 aluminas". Materials prepared in a similar fashion have been shown to be very active catalysts for isomerization reactions [29]. In the case of the $AlCl_3$/urea sample, a portion of the 5-coordinate aluminum is retained after conversion to η-alumina. A study of the effect of 5-coordinate content on catalyst activity would certainly appear worthwhile.

From these studies, several important conclusions can be drawn. In the case where basic aluminum salt solutions are used as precursors in sol-gel processes, all gels are not "created equal". There is a distinct connection between the level of the 5-coordinate aluminum in the calcined intermediate and the method of preparation of the parent sol. Since the method of inducing gelation was identical for all the samples, we surmise that the differences in the 5-coordinate aluminum content derives from the differences in the nuclearity and structure of the aluminum cations in the parent sols. Hydrolysis by the in situ generation of a base produces an aluminum cation or distribution of cations that either possess structures or form structures upon gelation (molecular structures or pore structures) that give rise to 5-coordinate aluminum after calcination. The presence of chloride ion stabilizes this defect structure. The material derived from the Al13 sol contained less 5-coordinate aluminum during calcination, converted to alpha alumina at a lower temperature, and formed alpha alumina with a markedly finer grain size than the materials obtained from the in situ hydolysis method. It is readily apparent, that manipulation of aluminum ion hydrolysis can be used to establish a substantial degree of control of phase formation, crystal perfection, and microstructure of sol-gel derived ceramics.

ACKNOWLEDGEMENTS

The authors gratefully acknowledge the support of 3M and the assistance of Walt Thatcher, Ernesto Cabarga, and Willi Conway of the Analytical and Properties Research Lab, 3M, Paul Jakubowski of the Ceramic Technology Center, 3M, and Randy Bunde, Visual Graphics, 3M.

REFERENCES

1. J. D. Birchall in Fabrication Science 3, edited by D. Taylor (Brit. Ceram. Soc. 33, Shelton, Stoke-on-Trent, England 1983) pp 51 - 62; M. D. Sacks, T. Tseng, and S. Y. Lee, Am. Ceram. Soc. Bull. 63 (2), 301 -310 (1984); J. E. Blendell, H. K. Bowen, and R. L. Coble, ibid., 63 (6), 797- 802 (1984); G. W. Ritter, II, U. S. Patent No. 4 512 913 (23 April 1985); J. C. Hayes, D. Mcgrath, and V. Haensel, U. S. Patent 3 340 205 (5 September 1967).

2. S. Komarneni, R. Roy, C. Fyfe, and G. J. Kennedy, J. Am. Ceram. Soc. 68, C-243 - C-245 (1985).

3. A. R. Siedle, T. E. Wood, M. L. Brostrom, D. C. Koskenmaki, B. Montez, and E. Oldfield, J. Amer. Chem. Soc. 111, 1665 (1989).

4. D. D. Johnson and H. G. Sowman, in Engineered Materials Handbook Volume1, edited by C. A. Dostal (ASM International, Metals Park, Ohio, 1987), pp. 60 -65.

5. P. L. Brown, R. N. Sylva, G. E. Batley, and J. Ellis, J. Chem. Soc. Dalton Trans. 1985, 1967; J. Aveston, J. Chem. Soc. 1965, 4438; C. Brosset, G. Biedermann, and L. G. Sillen, Acta Chem. Scand. 8, 1917 (1954).

6. W. V. Rausch and H. D. Bale, J. Chem. Phys. 40, 3391 (1964); J. K. Ruff and S. Y. Tyree, J. Amer. Chem. Soc. 80, 1523 (1958); J. Y. Bottero, D. Tchoubar, J. M. Cases, and F. Flessinger, J. Phys. Chem. 86, 3667 (1982).

7. J. Aveston, J. Chem. Soc. 1965, 4438.

8. E. Matijevic, K. G. Mathai, R. H. Ottewill, and M. Kerker, J. Phys. Chem. 65, 826 (1961).

9. P. M. Bertsch, W. J. Layton, and R. I. Barnhisel, Soil Sci. Soc. Am. J. 50, 1449 (1986); R. C. Turner, Can. J. Chem. 54, 1910 (1976); ibid., 47, 2521 (1969).

10. D. N. Waters and M. S. Henty, J. Chem. Soc. Dalton 1977, 243.

11. J. W. Akitt and J. M. Elders, J. Chem. Soc. Dalton Trans. 1988, 1347; J. W. Akitt, N. N. Greenwood, and G. D. Lester, J. Chem. Soc. (A) 1969, 803; J. W. Akitt and A. Farthing, J. Magn. Reson. 32, 345 (1978); J. W. Akitt and B. E. Mann, ibid., 44, 584 (1981); J. W. Akitt and A. Farthing, J. Chem. Soc. Dalton

1981, 1617; J. W. Akitt, N. N. Greenwood, B. L. Khandelwal, and G. D. Lester, ibid., 1972, 604; J. W. Akitt and A. Farthing, ibid., 1981, 1606.

12. J. W. Akitt and A. Farthing, J. Chem Soc. Dalton 1981, 1624; J. W. Akitt, J. M. Elders, X. L. R. Fontaine, and A. K. Kundu, ibid., 1989, 1889.

13. J. Y. Bottero, J. M. Cases, F. Fiessinger, and J. E. Poirier, J. Phys. Chem. 84, 2933 (1980).

14. P. M. Bertch, R. I. Barnhisel, G. W. Thomas, W. J. Layton, and S. L. Smith, Anal. Chem. 58, 2583 (1986); P. M. Bertsch, W. J. Layton, and R. I. Barnhisel, Soil Sci. Soc. Am. J. 50, 1449 (1986); P. M. Bertsch, G. W. Thomas, and R. I. Barnhisel, ibid., 50, 825 (1986).

15. A. R. Thompson, A. C. Kunwar, H. S. Gutowsky, and E. Oldfield, J. Chem. Soc. Dalton Trans. 1987, 2317.

16. T. E. Wood, J. R. Hill, L. Bergmark, and R. P. Skarjune, presented at the Third International Conference on Ultrastructure Processing of Ceramics, Glasses and Composites, San Diego, CA (unpublished) and the 1989 International Chemical Congress of Pacific Basin Societies, Honolulu, Hawaii, 1989 (unpublished).

17. C. F. Baes, Jr. and R. E. Mesmer, The Hydrolysis of Cations, (John Wiley and Sons, Inc., New York, 1976), pp.112 - 123; R. S. Alwitt, in Oxides and Oxide Films Volume 4, edited by J. W. Diggle and A. K. Vijh (Marcel Dekker, Inc., New York, 1976), pp.168 - 254.

18. S. J. Karlik, E. Tarien, G. A. Elgavish, and G. L. Eichhorn, Inorg. Chem. 22, 525 (1983) and references therein.

19. J. F. Hinton, and R. W. Briggs, in NMR and the Periodic Table, edited by R. K. Harris and B. E. Mann (Academic Press, New York, 1978), pp. 279 - 285.

20. G. Johansson, G. Lundgren, L. G. Sillen, and R. Soderquist, Acta Chem. Scand. 14, 769 (1960); G. Johansson, ibid., 14, 771 (1960).

21. G. Johansson, Acta Chem. Scand. 16, 403 (1962).

22. J. W. Akitt and J. M. Enders, J. Chem. Soc. Dalton Trans. 1988, 1347.

23. B. E. Yoldas, Am. Ceram. Soc. Bull. 54 286 (1975); J. Mater. Sci. 10 1856 (1975); ibid., 14 1843 (1979); D. W. Johnson, Jr., Am. Ceram. Soc. Bull. 64 1597 (1985).

24. W. L. Olson and L. J. Bauer, in Better Ceramics Through Chemistry II, edited by C. J. Brinker, D. E. Clark, and D. R. Ulrich (Mater. Res. Soc. Prac. 73, Pittsburgh, PA 1986) pp. 187 - 193.

25. L. F. Nazar and L. C. Klein, J. Am. Ceram. Soc. 71, C-85 (1988).

26. A. Bellan and K. Deneke, U. S. Patent No. 3 891 745 (24 June 1975).

27. J. D. Birchall, Trans. J. Brit. Ceram. Soc. 82, 143 (1983); L. E. Seufert, U. S. Patent No. 3 808 015 (30 April 1974).

28. R. Brace and E. Matijevic, J. Inorg. Nucl. Chem. 35, 3691 (1973); E. Kato, K. Daimon, and M. Nanbu, J. Am. Ceram. Soc. 64, 436 (1981).

29. M. Utiyama, H. Hattori, and K. Tanabe, Bull. Chem. Soc. Jpn. 54, 2521 (1981).

30. L. Nazar, presented at the 1989 International Chemical Congress of Pacific Basin Societies, Honolulu, Hawaii, 1989 (unpublished).

31. L. B. Alemany and G. W. Kirker, J. Amer. Chem. Soc. 108, 6158 (1986); A. D. Irwin, J. S. Holmgren, and J. Jonas, J. Mater. Sci. 23, 2908 (1988).

32. V. M. Mastikhin, O. P. Krivoruchko, B. P. Zolotovskii, and R. A. Buyanov, React. Kinet. Catal. Lett. 18, 117 (1981); N. S. Kotsarenko, V. M. Mastikhin, I. L. Mudrakovskii, and V. P. Shmachkova, React. Kinet. Catal. Lett. 30, 375 (1986); T. H. Walter and E. Oldfield, J. Phys. Chem. 93, 6744 (1989).

33. E. J. W. Verwey, Z. Krist. 91, 65 (1935); H. Zagodzinski and H. Saalfeld, Z. Krist. 110, 197 (1958).

SMALL-ANGLE NEUTRON SCATTERING AND 27AL NMR STUDIES ON THE MICROSTRUCTURE AND COMPOSITION OF ALUMINA SOL-GELS

*L. F. NAZAR, *D. G. NAPIER, *D. LAPHAM AND [a]E. EPPERSON
* University of Waterloo, Department of Chemistry, Waterloo, Ontario, Canada
[a] Argonne National Laboratories, Materials Science Division

ABSTRACT

We have used small angle neutron scattering, static light scattering and ^{27}Al NMR to examine the structure and composition of alumina sol-gels formed by the hydrolysis of aluminum alkoxides. For LT sols at low acid concentrations, and HT gels over a wide range of acid concentration, ^{27}Al solution NMR suggests, by the dearth of spectral resonances, that high molecular weight species are being formed. Analysis of the small angle neutron scattering data in the Porod regime indicates these sol-gels exhibit a power-law dependence consistent with mass fractal dimensions ranging from 1.45 to 1.8. These fractal dimensions are consistent with models based on diffusion limited cluster aggregation. The fractal dimensions do not differ significantly between LT and HT sols at the same acid concentration. However, for both temperature regimes, the fractal dimension increases with increasing acid concentration, suggesting a progression to a more compact network. Static light scattering measurements indicate the Guiner radii of the cluster aggregates vary from 600 to 2000Å.

INTRODUCTION

Alumina sol-gel processing is thought to have an important future in fiber manufacture, coatings, porous ceramic membranes, and in the formation of ceramic precursors. In comparison to silica sol-gel processing by alkoxide hydrolysis, the analogous alumina chemistry is notably different, but not as well understood. One of the major differences is in the relative rate of hydrolysis, which is very fast in alumina, but comparatively slow for silica. For silica sols at acid or neutral pH, this results in the formation of polymeric fractal structures, which crosslink into a rigid gel structure [1]. For alumina sols, on the other hand, the processes have not been elucidated, but appear to result in "colloidal" sol-gels. Figure 1 briefly outlines some previous results which describe the effects of various processing conditions on the composition of alumina sol-gels. The physical

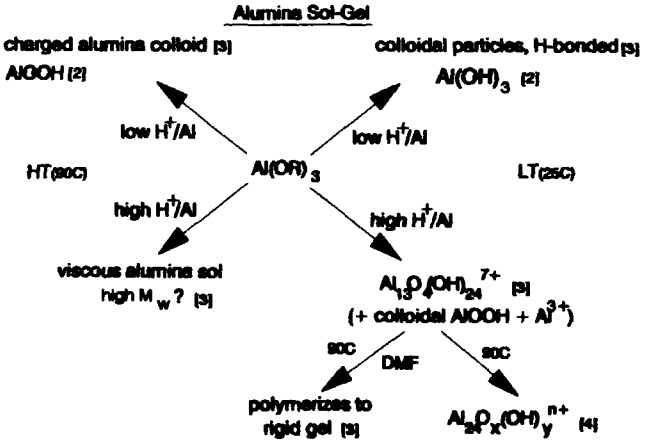


Figure 1. Outline showing the effects of acid/Al ratio and processing temperature on alumina sol-gel compositions.

Mat. Res. Soc. Symp. Proc. Vol. 180. ©1990 Materials Research Society

and chemical nature of the sol can be modified by changes in temperature, electrolyte concentration and the addition of solvent in the initial stages of hydrolysis. In many cases, these effects are not readily reversible.

At low acid concentrations (<0.4 H+/Al mole ratio), hydrolysis at room temperature (LT) leads to the formation of hydrated-colloidal precipitates [2], which solution NMR studies indicate contain very small amounts of well defined aluminum hydroxyoxide cluster cations, with the remainder of the Al in solution being undetectable due to molecular weight and/or quadrupole broadening [3]. The small cluster cations have the formulation $Al_{13}O_4(OH)_{24}(H_2O)_{12}^{7+}$ ("Al_{13}"). At higher acid levels (>0.4 H^+/Al), these species dominate in the sol, together with $Al(H_2O)_6^{3+}$ (monomer) [3]. Aging these LT sols at 90°C leads to the condensation of the Al_{13} clusters to form dimers (or trimers) [4].

Hydrolysis at 90°C (HT) leads to translucent sols whose viscosity increases rapidly with increasing acid concentration. For both LT and HT sols, the total number of small, mobile Al_xO_y cations (Al_1, Al_2, Al_{13}, etc) increases as the acid concentration increases [3,5].

In this paper, we present our results of small-angle neutron scattering and light scattering studies on some sols obtained over range of different processing conditions, in which the pH and temperature were varied and solid-state NMR studies on the resulting gels. These probes are ideally suited to determining sol composition and structure over a wide range of length scales: ^{27}Al NMR yields information on the local atomic enviroment (very small length scales); SANS can provide information on the average structure of complex colloid/polymer networks in the region of 10-500Å (generally NMR-invisible); and light scattering is an effective probe at longer length scales, in the vicinity of 500-2000Å. Complementary information about the microstructure of sol-gels hydrolyzed at both low and high temperature has been obtained from a combination of the techniques.

EXPERIMENTAL

SANS and light scattering studies were performed on five sol-gel compositions prepared from aluminum sec-butoxide: three sols hydrolyzed at 90°C with 100 moles H_2O/Al at the following H^+/Al molar ratios: 0.07 (HT007); 0.3 (HT03); 0.6 HT(06); and two were hydrolyzed at room temperature at the latter two ratios, 0.3 (LT03) and 0.6 (LT06). The Al sol concentration was approximately 0.5M. Samples for SANS were prepared using a 75% D_2O/25% H_2O solution for hydrolysis, as this D/H ratio was experimentally found to optimize the scattering intensity, while minimizing the incoherent scattering. The experiments were performed using the SAD instrument at the Intense Pulsed Neutron Source (IPNS) at Argonne National Laboratory. The data were collected in 1mm quartz cells, and are calibrated to absolute intensity. The Q range [$Q=(4\pi/\lambda)\sin(\theta/2)$] covered by the instrument is 0.005 - 0.35$Å^{-1}$. The data in the high Q-range was supplemented by scattering measurements carried out at the Chalk River Neutron Laboratories (CRNL).

Static light scattering (SLS) measurements were carried out on a Model 5000 Light Scattering Monophotometer. The solutions were filtered with a 0.2μ PTFE filter and capped in quartz cells. For each sample, intensities were collected by running 1/4, 1/8, 1/12, 1/16, and 1/24 dilutions at 10 different scattering angles.

^{27}Al NMR solution and solid state magic-angle spinning (MAS) measurements were carried out on a Bruker AM-500 spectrometer, operating at 130.12 MHz. NMR shifts are reported relative to $Al(H_2O)_6^{3+}$, which was used as an external standard.

RESULTS AND DISCUSSION

Small angle neutron scattering and static light scattering

There are two regimes in the small-angle scattering curve that are used in determining structure on the scale of colloid dimensions: the Guinier and Porod regions. The Q-range that determines these regions is dependent on the size of the aggregrates or particles. In the Guinier region, which occurs at low Q where $Q < R_g^{-1}$, (R_g = radius of gyration), the scattering intensity is approximated by [6]:

$$I(Q) = m[1 - Q^2R_g^2/3] + \ldots \qquad (1)$$

R_g (or the Guinier radius) is related to the size of the particles in a dilute colloidal solution or the correlation length in systems where there are overlapping or interacting chains of molecules, such as in this case.

The Porod regime occurs at larger Q, where $R_g^{-1} << Q < a^{-1}$ (a is the primary subunit length): this region can reveal information on the microstructure of the alumina network. In this region the approximation $I(Q) \propto Q^{-4}$ holds for compact (non-fractal) particles in the limit of very large Q, although in general it can be shown that

$$I(Q) = AQ^{-n} \qquad (2)$$

The power-law exponent, n, is related to the fractal dimension, D, of the particle [6,7]. For mass fractals of dimension $1 < D < 3$, D=n [6]. The concept of fractal geometry has proven to be a useful, and natural method of describing the average structure of many colloidal/sol-gel systems. D has been calculated by theoretical modelling for various reaction schemes involving particle or cluster aggregation mechanisms [7]. Hence, measurement of D, (from a ln-ln plot of I(Q) vs Q) can reveal mass distribution within the particle. This, in turn, tells us something about how the particle was formed, and how its subunits are interconnected.

Figure 2 shows the combined light scattering and neutron scattering data for a representative sol, HT-06, as a Porod (ln-ln) plot. The SLS and SANS data were matched in intensity by a shift factor so that a smooth curve was obtained. The scattering plot shows behavior of the type expected for colloidal aggregrates with a fractal structure. The SLS data in the low Q, or Guinier region ($Q < R_g^{-1}$), for sols at the highest dilutions (usually 1/24th) gave excellent fits to equation (1), using an exponential approximation for $1-(R_gQ)^2/3$. Since the particle size distribution is not monodisperse, the R_g values obtained represent a root-mean-square radius of gyration of the aggregates. There was no detectable light scattering from sol LT-06.

The data in the Porod region were fit to equation (2), to determine the power-law dependence, D. In each sample, a constant power-law dependence is observed over a more than a decade of the scattering vector, down to Q= 0.1. The slopes for the individual samples for which scattering was observed (HT sols, and LT-03) fell in the range of 1.4 to 1.8. This is consistent with the presence of large aggregrates (600 - >2000Å) with a mass fractal structure which is maintained down to small length scales. The curves all deviate from a straight line at small Q (Guiner region), and at large Q, (Q=0.1), where D begins to approach the Porod limit of Q^{-4}: this correlates to a subunit size of 10-20Å. These data are qualitatively quite similar to those obtained for alumina colloids generated by other methods

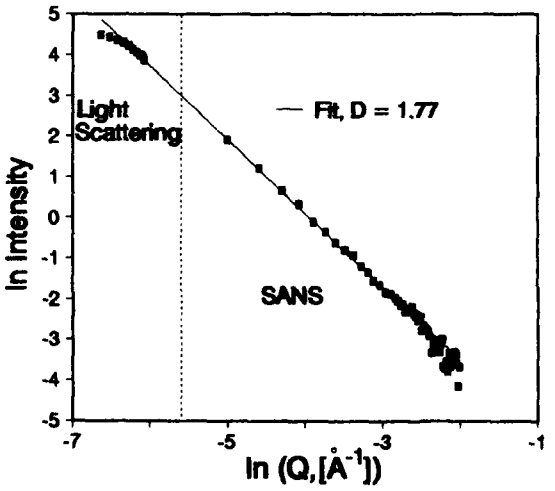


Figure 2. Combined light scattering and SANS curve for a representative sol-gel sample, HT-06. The light scattering data cover the small-Q regime and the SANS data cover the high Q region.

(*vide infra*). The fractal dimension was found to be independent of the D_2O/H_2O ratio, and insensitive to a two-fold increase in Al concentration: hence, interference from multiple scattering can be ruled out.

The results for all of the samples are summarized below in Table I .

TABLE I - Combined SLS and SANS data

Temp	$\%D_2O$	H+/Al	Fractal Dim.(D)	Source	R_g
HT	75	0.07	1.46	IPNS	[a]
HT	75	0.3	1.53	IPNS	2000Å
HT	75	0.6	1.79	IPNS	720Å
HT	25	0.6	1.76	IPNS	-
HT	0	0.6	1.77	CRNL	-
LT	75	0.3	1.79	IPNS	600Å
LT	75	0.6	-	IPNS	[b]

[a] Not measured
[b] Sol did not scatter light; the SANS scattering was also extremely weak (see text)

Several observations can be made from the data. Firstly, for the same acid concentration, the HT sols have larger aggregate particles than the LT sols. This is not surprizing, given the physical appearance of the sols, and is also consistent with ^{27}Al NMR data [3]. Secondly, in the LT-06 sols, the lack of SLS and the SANS data confirm that the particles are very small. SANS scattering for this sol was extremely weak. A Guinier plot gave a very poor fit to the data, and indicated that there is no simple radius of gyration to be obtained from the data, except possibly at very small Q (a value of 80Å or less was obtained from a fit to four data points). This is consistent with ^{27}Al NMR data which indicate that 70% of the sol contains non-interacting Al_{13}^{+7} clusters ($R_g \approx 4Å$) and some monomer, with the remaining 20-30% not being visible by solution NMR [3,5]. The latter species are probably present as somewhat larger clusters, which may be giving rise to most of the scattering in the SANS experiment. The SAS intensity is proportional to the square of the particle volume, and hence in a polydisperse system, the smallest clusters (ie, Al_{13}) contribute much less to the scattering.

The most interesting observations come from examination of the change in fractal dimension, D. Comparison of D for the sols HT-007, HT-03 and HT-06 shows a progression from 1.45 -> 1.53 -> 1.78. This implies formation of a more compact structure as the acid concentration increases, especially as this trend is concurrent with a decrease in particle size. (Note -the change of D with aggregate size is also apparent in comparing the R_g of HT-03 with LT-03, in which R_g decreases from 2000 to 600Å, concomitant with a increase in D from 1.53 -> 1.79). The decrease in aggregate size, however, could also be due to an actual decrease in the molecular weight by the loss of subunits. Without accurate measurement of M_w (which was not possible here), it is difficult to distinguish between the two. However, as previous studies have shown that the number of small, mobile species increases with increasing acid concentration for both LT and HT sols[3], we conclude that both factors are probably responsible.

The D = 1.77 $\pm$0.03 determined for the HT-06 and LT-03 sols agrees very well with models based on diffusion limited cluster aggregation (DLCA) [7]. D values of 1.78 are calculated for 3 dimensional aggregation of clusters with a small repulsive barrier, which represents a relatively rapid aggregation process. The predicted value of D increases up to 2.04 in the case of large repulsive barriers. As mentioned above, fractal dimensions similar to these, in the range of 1.4-2.0, have been recently observed for other alumina colloid systems generated by reaction of $Al(H_2O)_6^{3+}$ with OH^- at OH/Al ratios of 2.5. Early SAXS studies on these colloids found a power-law dependence of 2, which the authors suggested arose from non-fractal sheet-like platelets of pseudoboehmite [8]. Schaefer et al. also observed the slope of -2.0 in their SAXS studies on 0.1M colloids, which on dilution, decreased to -1.4. The fractal dimension of 2 was interpreted as a lattice animal structure

Fractal Dimensions Based on Simulations of Some Aggregation Models [10]

Model	Fractal Dimension, D
Diffusion-Limited Monomer-Cluster Aggregation	2.50
Diffusion-Limited Cluster Aggregation (2D)	1.42
Diffusion-Limited Cluster Aggregation (3D) (rapid aggregation)	1.75 - 1.80
DLCA - Cluster Polarizability (3D)	1.44
Diffusion-Limited Cluster Aggregation (3D) (slow aggregation/chemically limited)	1.98 - 2.04

Figure 3.

which swelled and fragmented with the addition of water[9]. Axelos and Bottero observed a slope of -1.4 for .1M colloids at very early stages of aggregration, and postulated that this could be due to a 2-dimensional DLCA process [10]. A summary of some calculated mass fractal dimensions based on computer simulations of differing aggregation models is shown in Figure 3, above (from reference 10).

We believe that the fractal structures are being formed by a DLCA process in all of the sols (except LT-06), and the differences in the fractal dimension are due to modification of the aggregation process by charge on the clusters in some of the sols. Recently, it has been shown that lowered fractal dimensions in 2D and 3D aggregation models can be explained by invoking polarizablity effects in the aggregation scheme [10]. Effectively, two colliding clusters develop opposite charges on their neighboring tips, thus biasing their relative motion. This model gives a modified D = 1.42 in three dimensions, in good agreement with the values for HT-03 and HT-007. In accordance with this model, we observe the D values of 1.77 in sols where rheology measurements by Klein *et al.* have shown that shear thinning occurs (suggestive of a network connected by weak H-bonds), whereas D values of 1.4 - 1.5 are observed in sols which display shear thickening, suggestive of highly charged alumina species [3b,5].

The existence of the fractal structure down to very small length scales suggests that the subunits of the aggregate are very small. It is tempting to propose the Al_{13} cluster as the subunit on this basis, as other authors have done for the alumina colloids discussed above. However, this can be ruled out in this system, on the basis of NMR evidence. ^{27}Al solution NMR would not be able to detect the tetrahedral resonance in Al_{13} if the cluster were highly agglomerated, but it would be visible in a solid state spectrum of a gel derived from such a sol. Figure 4 shows the MAS-^{27}Al NMR spectrum of gels HT-06 and LT-06. As can be seen, the tetrahedral resonance of the Al_{13} clusters in the LT-06 gel is clearly visible at 62.9ppm in Figure 4a, but is absent in the HT-06 gel in Figure 4b. The latter contains only octahedrally-coordinated aluminum in two sites, with chemical shifts of 0.4 ppm and 7.8 ppm, corresponding to monomer, and a boehmite-like species.

CONCLUSIONS

In summary, our combined small-angle scattering results on alumina sol-gels formed by alkoxide hydrolysis show that the microstructure of the HT sols, and the low-acid LT sol, LT-03, are best described by mass fractals over length scales down to 10-20Å. The internal structure of the aggregates change as a function of acid concentration, such that more compact, and smaller aggregates form at higher acid concentrations for both LT and HT sols. At high acid concentrations in the LT sols, large colloidal aggregate scattering disappears, consistent with NMR observations of the formation of Al_{13} clusters under these conditions. Particle formation is well described by a diffusion limited cluster aggregation model, in

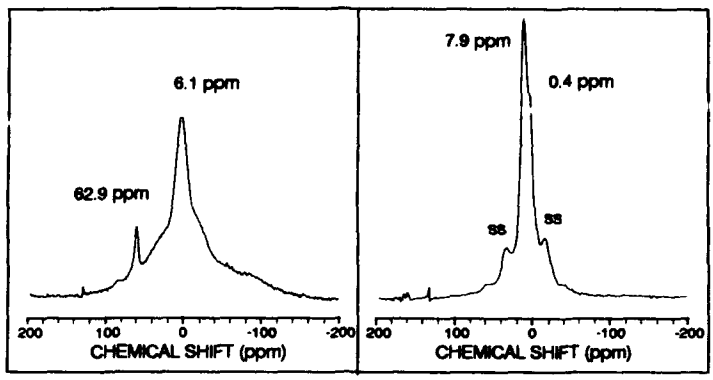


Figure 4. 27Al MAS solid state NMR spectra: a) LT-06; b) HT-06. The chemical shifts are reported relative to $Al(H_2O)_6^{3+}$ (external standard).

which the fractal dimension of 1.8 is lowered to 1.4 by a cluster-polarizability effect in the case of charged subunit clusters. These data correlate well with previous rheology measurements on these sols. The subunits, in the case of the HT sols, do not appear to be Al_{13} clusters, based on ^{27}Al MAS-NMR results.

ACKNOWLEDGMENTS

The authors would like to thank Prof. Bruce Gaulin, Mr. John Avelar of MacMaster University, and Dr. John Root at the Chalk River Nuclear Labs for their advice and assistance and support during various stages of this work. The authors also wish to thank Prof. L.C. Klein of Rutgers University for her collaboration on the rheology and NMR aspects of the project, and Prof. J. Berlinsky at MacMaster University for his encouragement. This work was supported by the Ontario Centre for Materials Research, and the National Sciences and Engineering Council of Canada Strategic Grant.

REFERENCES

1. D.W. Schaefer and K.D. Keefer, Mat. Res. Soc. Symp. Proc., 73, 277 (1986); C.J. Brinker, J. Non-Cryst. Solids, 100, 31 (1988).

2. B.E. Yoldas, J. Appl. Chem. Biotechnol., 23, 803 (1973).

3. L.F. Nazar and L.C. Klein, J. Am. Ceram. Soc., 71, C85 (1988); L.F. Nazar, L.C. Klein and D.C. Napier, Mat. Res. Soc. Symp. Proc., 121, 133 (1988).

4. L.F. Nazar, G.Fu and A.D. Bain, in preparation.

5. L.F. Nazar, L.C. Klein, G. Fu, A.D. Bain and D.C. Napier, in preparation.

6. D.W. Schaefer, Science, 243, 1023 (1989); and references therein.

7. R. Jullien and R. Botet, Aggregation and Fractal Aggregates, World Scientific Publishing, Singapore, 1987.

8. W.V. Rausch and H.D. Bale, J. Chem. Phys., 40, 3391 (1964).

9. D.W. Schaefer, R.A. Shelleman, K.D. Keefer and J.E. Martin, Physica, 140A, 105 (1986).

10. M. Axelos, D. Tchoubar, J.Y. Bottero and F. Flessinger, J. Physique, 46, 1587 (1985).

SMALL ANGLE X–RAY SCATTERING STUDIES OF POLYMERIC ZIRCONIUM SPECIES IN AQUEOUS SOLUTION

J.A. JUTSON*, R.M. RICHARDSON*, S.L. JONES** AND C. NORMAN**
*University of Bristol, Department of Physical Chemistry, Cantock's Close, Bristol BS8 1TS, United Kingdom.
** Alcan Chemicals Ltd., Chalfont Park, Gerrards Cross, Buckinghamshire SL9 OQB, United Kingdom.

ABSTRACT

Small angle X–ray scattering techniques have been used to investigate the shape and size distribution of Zr(IV) species in aqueous solution. This study has shown that when zirconyl chloride solutions, containing the zirconyl tetramer, are subjected to various treatments polymerisation occurs. While ageing and addition of base produces an increase in particle size the shape remains globular. Refluxing the solutions produces "rod" like particles of varying length but constant cross sectional radius.

INTRODUCTION

Zirconium chemicals have a wide range of applications from ceramics manufacture to water repellants, catalysts and paint additives. Treatment of the zirconium ores produces an acidic solution which is used to manufacture pure zirconium compounds. When the acid used is hydrochloric acid, zirconyl chloride is formed and in concentrated solutions this is present as the tetramer $[Zr_4(OH)_{12}(H_2O)_{12}]^{4+}$. This tetramer is known to polymerise with ageing, heating or reduction of solution acidity, but the size distribution of the polymeric (ZrIV) species formed has not been widely studied.

In this work small angle X–ray scattering (SAXS) has been used to study the shape and size distribution of these polymeric species in solutions of zirconyl chloride which have been diluted, aged, refluxed or treated with base.

SMALL ANGLE X–RAY SCATTERING (SAXS)

Small angle X–ray scattering techniques can be used to study the structural features of particles of colloidal dimensions. The particle size is large (10–1000 Å) compared with the wavelength of the radiation used (λ = 1.54 Å) and there is an inverse relationship between particle size and scattering angle. The intensity of the scattering data is measured as a function of scattering vector Q, where

$$Q = \frac{4\pi \sin\theta}{\lambda} \qquad (1)$$

and 2θ is the scattering angle.

For an isolated particle scattering arises from the constructive interference of X–rays scattered from electrons within the particle and the intensity is therefore dependent on electron density. The scattering at low Q is not sensitive to short range inhomogeneities in the electron density (i.e. $< \frac{2\pi}{Q}$). The particles may therefore be treated as if they had a uniform electron density distribution.

For dissolved particles the scattered intensity is proportional to the square of the electron density difference between solute and solvent. The radius of gyration (R_g), which intuitively relates to the spacial extension of the particle, can be obtained from the scattering data. A plot of LnI vs Q^2 (Guinier plot) [1], as shown in figure 1 will give a straight line of slope $R_g^2/3$ in the region $Q<1/R_g$ i.e.

Mat. Res. Soc. Symp. Proc. Vol. 180. ©1990 Materials Research Society

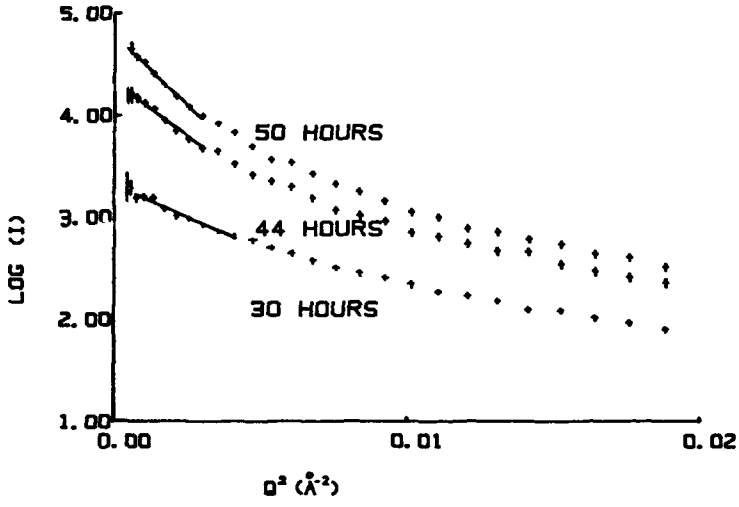


Figure 1. Guinier plots for 0.5 M $ZrOCl_2$ refluxed for up to 50 hours.

$$I(Q) \simeq I(0)\exp - \left[\frac{Q^2 R_g^2}{3}\right] \qquad (2)$$

where I(0) is the scattered intensity at zero scattering angle and I(Q) is the intensity for the vector Q. The radius of gyration is related to the particle dimensions. For spherical particles the radius of the sphere (R_s) is given by

$$R_s = \sqrt{\frac{5}{3}} R_g \qquad (3)$$

For long thin rods, the length (L) is given by

$$L \simeq \sqrt{12}\, R_g \qquad (4)$$

Information on the cross section of elongated particles may be obtained from a "longrods" plot [2] of Ln(Q.I(Q)) vs.Q^2 which will give a straight line plot in the region $\frac{2\pi}{L} < Q < \frac{1}{R_c}$ i.e.

$$Q.I(Q) \propto \exp - \left[\frac{Q^2 R_c^2}{2}\right] \qquad (5)$$

where L is the length of the particle and R_c is the radius of gyration of the cross section (figure 2). For a cylinder

$$R_{cyl} = \sqrt{2}\, R_c \qquad (6)$$

INTERPRETATION OF SCATTERING DATA

A curved Guinier plot is an indication that the solution investigated is either polydisperse or that the particles present are not isometric. Where a plot of Ln(I) vs. Q^2 gave a line with single slope it was assumed that the particle shape was essentially isometric and we will refer to such particles as "spherical". Where this plot was a curve and a "longrods" plot did not give a straight line attempts were made to fit values for maximum and minimum R_g values.

PARTICLE SIZE DISTRIBUTION

In a polydisperse system large particles dominate the scattering at low Q and the smaller particles dominate at high Q. As a result the R_g value obtained from a Guinier plot is biased towards the largest particle size. The scattering function of such a system is determined by the shape and size distribution of the particles and it is not possible to determine both directly. However, it is possible to assume one and determine the other using a suitable modelling programme.

Particle size distribution p(r) for a solution can, in principle, be obtained from the inversion of its scattering curve. Generally the experimental data available is limited in two respects; there are only a finite number of observations and these are subject to experimental error. Thus it is impossible to obtain a unique solution for the continuous function p(r). The maximum entropy method developed by Potton and Daniell [3] has been used in this study and has the advantage that no assumptions are made with regard to absent data.

If the particles are assumed to be spherical, the method will produce the "maximum entropy" distribution of radii that is consistent with the data. If the

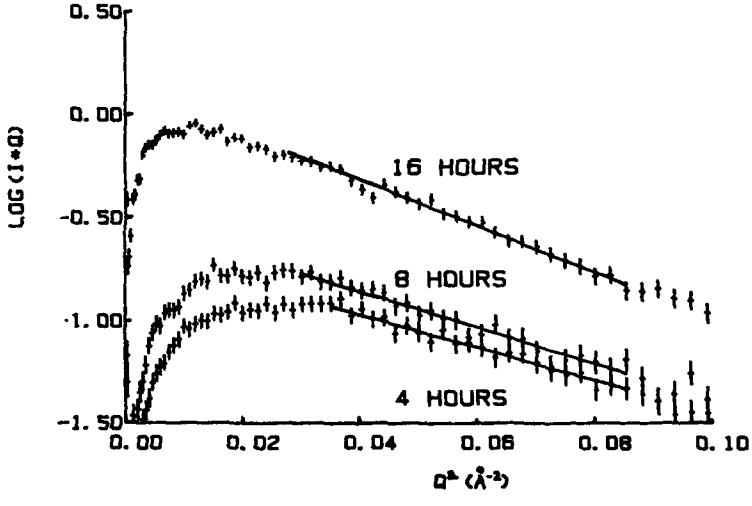


Figure 2. "Longrods" plots for 0.5 M $ZrOCl_2$ refluxed for up to 16 hours.

particles are believed to be rods, we have assumed a value for their length and used the method to produce the "maximum entropy" distribution for the cylinder radius. The fixed values of the length were obtained from the Guinier plots. The maximum entropy method was found to be a useful tool in that it gave a thorough test of the consistency of a model with the data and gave an "unbiased" estimate of the particle dimension.

EXPERIMENTAL

A two dimensional X–ray imaging system was used to detect CuKα X–rays scattered by transmission through the solutions under investigation [4,5]. Aqueous solutions of zirconyl chloride were contained in 1 mm thick cells with thin mica windows. Small angle X–ray scattering from these solutions was measured when they were first prepared and after ageing, refluxing and the addition of ammonia. In addition, solutions of varying acidity were prepared by adding hydrochloric acid to basic zirconium carbonate.

RESULTS AND DISCUSSION

Zirconyl chloride solutions which had not been treated in any way exhibited a small apparent increase in particle size with dilution due to the effect of interparticle interference in the most concentrated solutions. These particles were essentially spherical in shape. Extrapolation of R_g values to zero concentration gave a value of 4 Å, in agreement with the calculated R_g value for a tetramer of 3.96 Å. When these solutions were allowed to age polymerisation of the more dilute solutions occurred but the particle shape remained spherical.

More extensive polymerisation of these solutions occurred when they were refluxed for up to 50 hours and with the exception of the 1 molar solution, which was the highest concentration studied, the particles formed appeared to be rodlike in that they gave a straight section in a "longrods" plot as shown in figure 2. The radius of cross section of R_{cyl} derived from these plots was found to remain at 6.5 Å –7.5 Å (figures 3 and 4), while the length (derived from the initial slope of Guinier plots) increased with reflux time to around 100 Å as shown in figure 3. The particle length

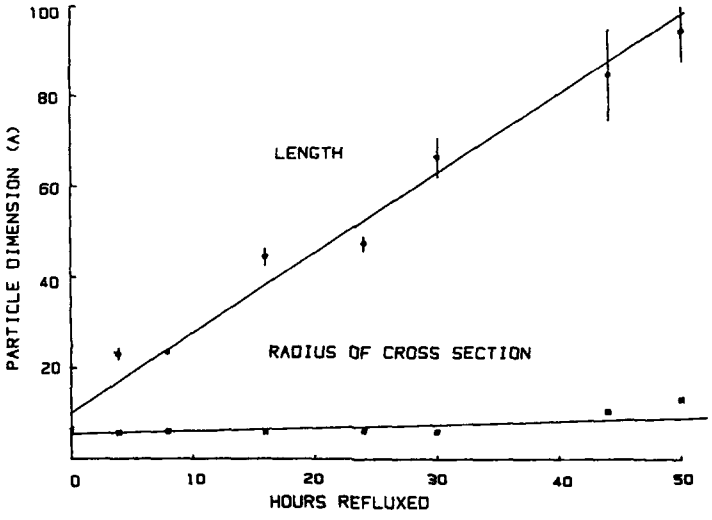


Figure 3. Plot of particle dimension vs. reflux time for a 0.5 M $ZrOCl_2$ solution.

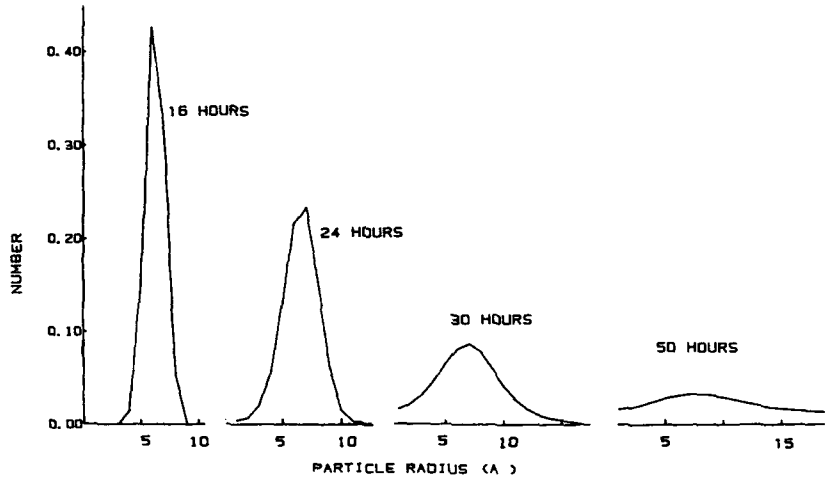


Figure 4. Distribution of cross sectional radius for polymeric particles produced when 0.5 M $ZrOCl_2$ refluxed for up to 50 hours (derived using maximum entropy method).

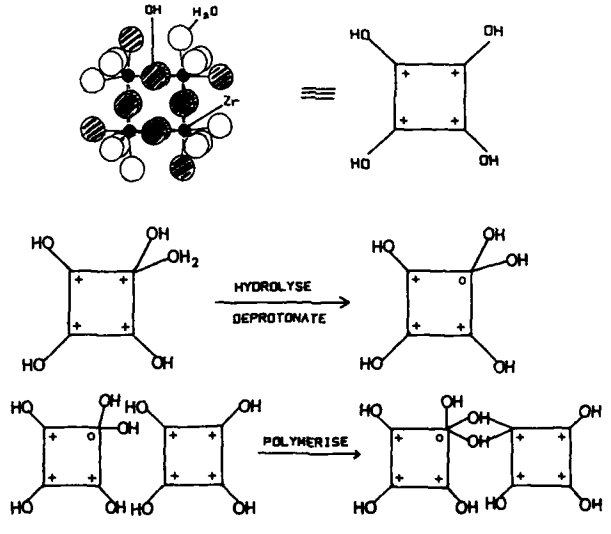


Figure 5. Polymerisation scheme for the zirconyl chloride tetramer.

also increased with dilution and there was a small increase in radius of cross section to about 9 Å –10 Å.

Previous work [4] has indicated that while small angle scattering showed particles similar in size and shape to that found in this study, in aqueous solutions of Zr(IV), other methods of analysis did not substantiate this. Instead, it was demonstrated that larger, more globular, particles were present. This apparent discrepancy may have two possible explanations. It is conceivable that the tetramers polymerise to form large randomly coiled polymer chains and the "length" measured by SAXS is the mean length of the straight section. Alternately, if "rod" shaped particles are present they may aggregate into larger particles, possibly held together by hydrogen bonds between OH groups on adjoining chains. Figure 5 shows the structure of a tetramer in aqueous solution and a possible scheme for polymerisation. The consistency in radius of cross section and the size of the tetramer implies that the polymer is made up from a series of stacked tetramers linked together by OH groups.

The addition of ammonia to $ZrOCl_2.8H_2O$, to give solutions with NH_3:Zr molar ratio of 1:1, resulted in little polymerisation and the particles remained spherical in shape. Even when these solutions were subsequently refluxed polymerisation was less extensive than that found for solutions which had been refluxed without base. When solutions of varying acidity were prepared using basic zirconium carbonate (ZBC) and HCl as the starting point the results obtained were as expected. With ZBC:HCl ratios of 1:2 the solutions behaved as a solution of $ZrOCL_2$.

As the acid content of the solutions was reduced the particle size became bigger and the shape less spherical. This effect was more pronounced in the most dilute solutions. While the solutions were polydisperse in nature, the peak radius of cross section was found to be 6.5 Å – 7.5 Å and peak length of around 25 Å – 30 Å. For solutions with less acid than that required to produce the tetramer (ZBC:HCl 1:<2) the breakdown of the carbonate molecule is incomplete and the persistence of particles of similar size suggests that the molecule has a backbone which is resistant to acid attack.

SUMMARY

The data obtained from this study have shown that polymerisation of tetramer by ageing alone is greatest for the most dilute solutions of $ZrOCl_2$ and that under these conditions the particles remain essentially spherical in shape. Refluxing of solutions produces "rod" like particles which increase in length with dilution and reflux time. The cross sectional radius remains fairly constant with reflux time but increases slightly with dilution.

Changing the solution acidity by the addition of ammonia only produces a small increase in particle size and the shape remains spherical. Varying the acidity by using ZBC and HCL as the starting point gives a persistent particle size which indicates that the carbonate molecule has a backbone which is particularly resistant to acid attack.

ACKNOWLEDGEMENTS

This work was carried out at the University of Bristol with the financial support of Alcan Chemicals Ltd. and S.E.R.C.

REFERENCES

1. A. Guinier, Ann.Phys.12, 161 (1939).
2. B. Porod, in Small Angle X-Ray Scattering, edited by O. Glatter and O. Kratky (Academic Press Inc. (London) Ltd., 1982), p.32.
3. J.A. Potton, G.J.Daniel and B.D. Rainford, Inst.Phys.Conf.Ser. 81, (1986).
4. S. Swanton, Ph. D. Thesis, University of Bristol, U.K., 1989.
5. J.E. Bateman, J.F. Conolly, R.Stephenson, A.C. Flesher, C.J. Bryant, A.D. Lincoln, P.A. Tucker and S.Swanton, Nucl. Inst. and Meth., A257, 506(1986).

PART III

Processing Science I: Aggregation, Particle Growth and Concentrated Dispersions

Precipitation of Uniform Particles: The Role of Aggregation

C.F. Zukoski, M. K. Chow, G.H. Bogush, and J-L. Look
Department of Chemical Engineering, University of Illinois, Urbana, Il 61801

I. Introduction

The conventional mechanism developed by LaMer (1) is often considered as the most relevant model for describing the precipitation of uniform particles. In this model, the concentration of a species is slowly increased above its equilibrium value until a critical concentration is reached and nucleation occurs. The resulting particles consume soluble species and the supersaturation level is reduced until there is a balance between particle growth and the generation of reactive species. At this point nucleation stops. Particle growth then continues by molecular addition of soluble species to the growing particles. Uniformity is achieved through a short nucleation time and a particle growth mechanism where the small particles grow more rapidly than the large particles.

In studies of the preparation of uniform particles, the LaMer mechanism is often invoked. Additional proposed mechanisms include precipitation and redissolution through an Ostwald ripening process (2), thermodynamic limits where a single particle size has the lowest free energy (3), and nucleation followed by aggregation (4-11). Distinguishing between these mechanisms has taken on added importance as methods of scaling-up precipitation technologies are sought. While it is unlikely that a single mechanism will be at the heart of all precipitation chemistries, the classes of precipitation mechanisms that result in uniformity must meet common underlying conditions. Among these are that the final solids be colloidally stable. If irreversible aggregation occurs at an appreciable rate, the number density of particles in the suspension will continuously decrease and the average particle size will grow. A second condition that is closely related to the need for colloidal stability is that a constant number density of stable, growing particles be established at some point in the precipitation reaction.

These necessary conditions can be used to compare and contrast various proposed mechanisms for uniform particle formation. In the Ostwald ripening model developed by Lifshitz and Slyozou (12), a constant number density of particles is never reached and standard deviations in particle size distribution reach greater than 50 % of the average diameter. In typical precipitation reactions, once formed, the particle size is found to be stable for extremely long periods of time (months to years) and size distributions considerably narrower than those expected from Ostwald ripening are routinely reported. Consequently, Ostwald ripening alone is unlikely to result in uniformity. In the thermodynamic limitation model, particle size distribution narrows to the particle size with the lowest free energy and a constant number density of particles need not be reached until the end of the reaction. As currently developed, the thermodynamic model of Feenstra and Debruyn (4) suggests that for a given surface potential and solid characteristics a unique particle size will result. As a consequence if more reagent is added to the suspension and solution conditions (primarily those controlling the particle surface potential) do not change, the number density of particles should grow but the average size should not increase. In many systems, average particle sizes can be

Mat. Res. Soc. Symp. Proc. Vol. 180. ©1990 Materials Research Society

increased after an initial precipitation by the addition of more reagent. As a result, the universality of the thermodynamic model is brought into question. This is particularly true for the case of silica particles precipitated from alcohol solutions containing silicon alkoxides, ammonia and water. Here final particle surface potential is observed to be independent of solution composition for a range of final particle diameters.

The LaMer model meets the conditions discussed above for achieving uniformity by reaching a constant number density of colloidally stable particles during the nucleation period. Thus, each nucleus acts like a seed and survives as a particle at the end of the precipitation reaction. Extensive calculations have shown, however, that small particles are very difficult to stabilize against aggregation (13,14). Indeed, in later studies (15) of the sulfur system used by LaMer and Dinager (1) to develop their precipitation model, particle number density is found to pass through a maximum during the reaction. A decrease in number density is difficult to rationalize within the LaMer model but is very suggestive of a growth mechanism where aggregation occurs. These results, and several studies on a wide variety of precipitation chemistries (4-11,13), indicate that while colloidal stability is clearly needed at the end of the reaction, aggregation can also play an important role in establishing a constant number density of growing particles early in the precipitation process.

In this paper we present recent results supporting the aggregation mechanism for the formation of uniform particles from the hydrolysis and condensation of silicon and titanium alkoxides.

II. Aggregation Kinetics

Particles interact through a variety of interparticle forces. These include solvation, electrostatic and van der Waals interactions. Extensive studies have shown that incorporation of these forces into descriptions of the dynamics of colloidal suspensions captures the essential features of suspension behavior: in particular rates of aggregation (16,17). Within this formalism, the rate of aggregation of particles of size i and j can be written

$$\beta(i,j)\, n_j\, n_i \qquad (1)$$

where $\beta(i,j)$ is the aggregation rate constant which depends of the particle interaction potentials and n_i is the number density of particles of size i. Classical colloid stabiltiy theory suggests that $\beta(i,j)$ has the form

$$\beta(i,j) = 2kT(r_i+r_j)^2/[3\eta r_i r_j W_{ij}] \qquad (2)$$

where the stability ratio W_{ij} is written

$$W_{ij} = (2r_i)\int_{2r_i}^{\infty} dr\, \exp(-V_T/kT)/r^2$$

$$W_{ij} \simeq W_{11} \exp Jr_{11} (r_{ij}/r_{11}-1) \quad (3)$$

Here V_T is the total particle interaction potential which can be decomposed into a sum of repulsive electrostatic, attractive van der Waals attractive, and repulsive solvation, potentials and $r_{ij} = 2r_ir_j/(r_i+r_j)$.

Jr_{11} is found from the slope of a plot of $\ln(W_{ij}/W_{11})$ vs $(r_{ij}/r_{11}-1)$. Jr_{11} is a measure of how fast the maximum in V_T increases as the particle size grows. J can be calculated in a straight forward manner if particle surface potentials and Hamaker constants are known (13,14). Neglected are hydrodynamic interactions that play an insignificant role in the agruments made here (15). kT is the product of Boltzmann's constant and the absolute temperature, r is the pair center to center separation and η is the continuous phase viscosity.

If one starts with a number density of particles N at time t=0 and allows aggregation to take place, the time required to reach a number density of particles of N/2 is given by (16,17):

$$t_{1/2} = \frac{3\eta W_{ij}}{4kTN} \quad (4)$$

where η is the viscosity of the continuous phase. If W_{ij} is approximated as $\exp(4\pi\varepsilon_o\varepsilon_c a\psi_o^2/kT)$ for particles with surface potentials ψ_o, of 12 mV, and radius a of 5 nm, a half life of 0.1 s is calculated. Here $\varepsilon_o\varepsilon_c$ is the product of the permitivity of free space and the continuous phase dielectric constant. However a particle of diameter 50 nm has a half life of 40 hrs. Under conditions typical for alkoxide precipitations, surface potentials of 12 mV are often encountered. If the first solid particles formed are smaller than approximately 25 nm, aggregation is expected to occur on a time scale comparable to that of the precipitation reaction. As a result, aggregation is expected early in the precipitation reaction. As W_{ij} grows with aggregate size, however, interaction potentials will play a key role in determining if a constant number density of particles is established.

These ideas have been combined into a model for the precipitation of silicon and titanium alkoxides where particle growth occurs primarily by aggregation and molecular addition of soluble species to particle surfaces is neglected. While this is clearly an extreme position to take, as shown below, surpisingly good agreement between measured and predicted particle size distributions can be achieved. The aggregation model is based on the assumption that reactions between soluble species result in the formation of primary particles and these reactions proceed independently of the presence of an insoluble (colloidal) phase. As a result, particle growth can be written as being due solely to aggregation where, upon aggregating, the particles coalesce. With these assumptions, the size distribution of precipitated particles is controlled by the size dependence of $\beta(i,j)$ and the rate of generation of primary particles and can be found from a solution to Smoluchowski's aggregation equation

$$\frac{\partial n(k,t)}{\partial t} = 1/2 \sum_{i=1}^{k-1} \beta(i,k-i)n(i,t)n(k-i,t) - n(k,t) \sum_{i=1}^{\infty} \beta(i,k)n(i,t) + \delta_{k,1}g(t) \qquad (5)$$

where n(j,t) is the number density of particles containing j primary particles at time t and g(t) is the rate of generation of the primary particles. By assuming that g(t) has the form (13,15)

$$g(t) = g_o [\exp(-k_1 t) - \exp(-k_2 t)] \qquad (6)$$

numerical solutions to eqn. (5) have been generated for a range of colloidal interaction parameters and generation rate constants that are found for precipitation reactions involving alkoxides. The results of these calculations suggest that final average particle diameters, <D>, and standard deviations in particle size distributions, d, can be found from:

$$\langle D \rangle = 2r_1[3v([C]_o - [C]_e)/(4\pi r_1^3 n_o N_{STB})]^{1/3} \qquad (7)$$

where N_{STB} = dimensionless number of colloidally stable particles = $2.4 \times 10^{-2}(Jr_1)^3$
and

$$\frac{d}{\langle D \rangle} = 5 \times 10^{-2} (Jr_1)^{4/5} \left[\frac{k_1 k_2 t_o}{k_2 - k_1}\right]^{1/10} \qquad (8)$$

where v is the molar volume of the precipitated material, $[C]_o$ is the initial concentration of the source material and $[C]_e$ is the equilibrium concentration. These correlations are valid for conditions where $Jr_1 > 1.4$. For smaller values of Jr_1, as are found by lowering the surface potential below 12 mV, the correlations fail. The number density scale n_o is $(g_o/\beta_o)^{1/2}$ and the time scale is $t_o = (g_o\beta_o)^{-1/2}$. Here $\beta_o = 2kT/3\eta W_{11}$ and
$g_o = 3v\,([C]_o - [C]_e)/(4\pi r_1^3(1/k_1 - 1/k_2))$.

These numerical results suggest that from a knowledge of the colloidal interaction potentials, rate constants required for g(t) and the primary particle size, r_1, absolute final particle diameters and the standard deviations in size distribution can be predicted. Few systems have been studied in sufficient detail to provide adequate estimates of these parameters and thus test the model predictions. Recently we have carried out extensive studies of precipitation reactions involving silicon and titanium alkoxides where rate constants and particle interaction potentials have been measured over a wide range of reagent concentrations. Below we present a comparison of model predictions and experimental results. First, however, we briefly review the assumptions of the aggregation model in light of what is known about the detailed chemistry of alkoxide precipitation systems.

III. Alkoxide Hydrolysis and Condensation Chemistry and the Aggregation Model

The hydrolysis and condensation of silicon alkoxides have seen extensive study. Recent detailed studies of the initial stages of these reactions suggest that under basic conditions, silicon alkoxides react as if they were monomers with 3-4 reactive sites and follow the predictions of Flory-Stockmayer theory (18,23). In this model of polymerization reactions, the molecular weight distribution is determined under the assumptions that all reactive sites have the same reactivity and that there is no internal cross linking within a growing molecule. For monomers with 3-4 reactive sites, the predicted molecular weight distribution remains peaked at the monomer up to the point of gellation. Klemperer and Ramamurthi (22,23) have shown that silicon alkoxides follow this polymerization pathway with the assumption of no internal cross linking becoming an increasingly poor assumption as the reaction proceeds. However, the molecular weight distribution remains peaked at the monomer up to the point of gelation.

The molecular weight distribution predicted by Flory-Stockmayer theory suggests that a low concentration of large molecular weight species is generated early in the reaction. If at some point, these species become insoluble and precipitate, primary particles can be formed that can grow either by molecular addition or by aggregation with other molecular species. Flory-Huggins polymer solubility theory (18) suggests that if a polymer is growing in a poor solvent, a critical molecular weight is reached where the polymer is no longer soluble and undergoes a phase transition. In a similar manner, Tanaka and co-workers (24) have shown that as the cross-link density is increased in a gel that contains a poor solvent, the gel will collapse at a critical cross-link density. If either of these processes occurs in the alkoxide system, collapse will occur first in the largest molecules. Due to the low concentration of large molecular weight species, such a phase transition may involve a small number of unstable molecules resulting in a "gel" phase that can grow by coalescence with other bits of the "gel" phase. Thus aggregation can be looked upon as the first stages of a transition from a homogeneous system to one containing polymer rich and a polymer poor phases. Due to accelerated internal cross-linking that will occur on formation of the "gel" phase and the resulting loss of reactive sites, molecular addition to the new gel phase is expected to occur at a rate that is substantially lower than molecular addition to soluble species. As a result growth of the "gel" or particulate phase may occur primarily by aggregation with freshly formed "gel" phase rather than by molecular addition of soluble species.

Recent experiments involving silicon and titanium alkoxides confirm that the rates of loss of soluble titania and silica species are independent of the size or density of particles in solution (13). These experiments were carried out in seeded growth experiments where the rate of loss of soluble metal species and rates of particle growth were measured first in the formation of the seed particles and then in the presence of different number densities of seed particles. If molecular addition to the particle surfaces is a primary growth mechansim, the rates of loss of hydrolyzed alkoxide species should depend on particle size and density. In the experiments involving silicon and titanium alkoxides, the concentration and rate of loss of hydrolyzed species was found to be independent of size or number density of the seed particles and to be equal to the rates found in the homogeneous reactions.

A similar decoupling of reaction rates from the presence of a solid phase have been found

for the hydrolysis and condensation of titanium alkoxides. Such results are not in keeping with the LaMer model or the recently published molecular addition model of Matsoukas and Gulari (29), but are in keeping with the aggregation model where rates of reactions between reactive species are linked to the presence of a solid phase.

IV Comparisons of Predicted and Measured Particle Size Distributions

If k_1 and k_2 are extracted from conductivity data for the precipitation of silica (13,25) eqns. (7) and (8) can be used to predict final particle size distributions. If the parameter J is estimated from measured surface potentials, estimates of solvation interaction prameters and Hamaker coefficients, the aggregation model has a single remaining adjustable parameter, the size of the primary particle. While adjustable r_1 must fall within realistic limits and is expected be on the order of 1-10 nm. On the other hand, if r_1 is chosen such that eqn. (7) predicts the measured <D>, the same r_1 can be used in prediction of d/<D> with no futher adjustable parameters. Such a comparison is given in Table I.

Note primarily that the r_1's required to give a quantative fit to the measured final particle diameters fall within a physically acceptable range. Secondly, the standard deviations predicted with no asjustable parameters, while being systematically low, follow the correct trends (i.e., standard deviations are largest for the smallest particles) despite an order of magnitude change in k_1 and k_2. Due to the changing solution contitions and the dynamic state of the growing particle surfaces, estimation of surface potentials, Hamaker coefficients and solvation interaction parameters is difficult. In addition, accurate determination of particle size distributions is tedious and as only 200 particles were used in determination of d/<D>, considerable uncertainity exists in the mesaured values. Reasonable estimates of colloidal interaction parameters along with measured rates of reactions between soluble species have been used in generating the predictions presented in Table I. As a result, we feel Table I represents a surprisingly good correspondence between predicted and measured parameters and suggests that the aggregation model may represent the initial stages of development of a quantitative model for the precipitation of uniform particles. Origins of the variation in r_1 with solvent conditions are discussed elsewhere (13).

The success of the aggregation model in predicting the trends observed in the silica system suggests that when attempting to control the morphology of precipitates, instead of focussing on the length of the nucleation time as is done in the LaMer model, attention should be paid to the colloidal interactions of growing particles. In essence, this was the conclusion reached by Jean and Ring (26,27) in studies of the formation of uniform titania particles through the hydrolysis and condensation of titanium alkoxides. These authors suggested that a polymeric stabilizer, hydroxypropyl cellulose (HPC), could be used to control particle size distribution. Later studies have indicated that the particles prepared by this technique are very porous and have poor sintering charateristics (28).

The origin of the large porousity in the titania particles precipitated in the presence of HPC has not been fully explained. However, a second method of controlling the stabiltiy of particles is to increase the charge on the particle surface. In the case of titania, this can be accomplished through the addition of acid to the precipitation medium. As shown in Fig. 1, the electrophoretic mobility of titania particles suspended in ethanol containing

Table I. Kinetic Parameters and Final Sizes or Particles Precipitated from 0.17M TEOS at 25°C

$[H_2O]$ M	$[NH_3]$ M	<D>[a] nm	d/<D>[b]	k_1[c] $s^{-1}x10^4$	k_2[c] $s^{-1}x10^3$	r_1[d] nm	d_{sg}/<D>[e]
3.8	1.0	392	0.06	1.5±0.5	3.2±0.3	4.0	0.03
6.8	1.0	531	0.03	3.2±0.3	5.7±0.6	2.1	0.02
9.5	1.0	412	0.05	5.0±0.5	8.3±0.8	2.6	0.02
15.0	1.0	343	0.06	9.5±1	17±2	3.0	0.02

a) Average final particle diameter
b) Standard deviation in particle size distribution relative to average diameter
c) Rate constants determined from conductivity measurements. k_2 is also the rate constant for particle growth as found from determinations of particle size (see references 13 and 25)
d) Primary particle size required to give <D> using J = 0.35 in eqn. (7). W_{11} used in the calculation was 1.6.
e) Ratio of standard deviation in particle size distribution to final average diameter as predicted from eqn. (8)

water at concentrations used in precipitations of titanium alkoxides increases from a small value at low acid concentration to a value of ~$0.7x10^{-8}m^2/Vs$. At concentrations above ~10^{-3}M, no precipitate is observed. At low concentrations of HCl, and high water concentrations (>0.3M) the particle size distribution is broad and the particles have irregular shapes. For all water and acid concentrations such that the mobility is above a value of $0.2x10^{-8}m^2/Vs$, uniform particles are precipitated. Examples are shown in Fig. 2. Changes in rates of reaction can be ruled out as the source of the uniformity. Measurements of the rate of loss of soluble titanium indicate that the psuedo-first order rate constant for the loss of titanium is $2.5\pm0.2x10^{-5}s^{-1}$, with no HCl added as well as at an HCl concentration of 10^{-4} M. Finally, the effect of acid shown in Table I is not limited to HCl as similar results have been observed for H_2SO_4 and acetic acid. We conclude that, in keeping with the predictions of the aggregation model, the uniformity associated with increasing acid concentration is due to an increase in particle surface charge.

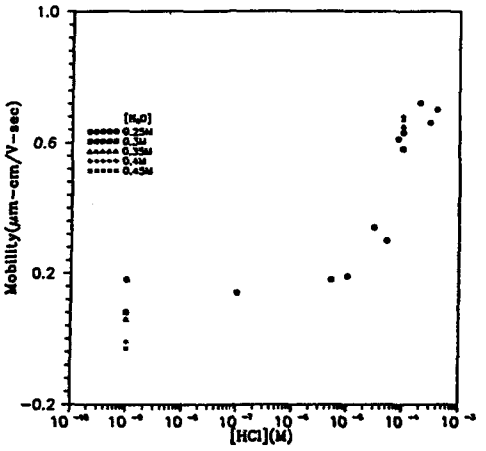


Fig. 1 Electrophoretic mobility of titania particles suspended in ethanol containing 0.25 M H_2O as a function of HCl concentration. Particles were precipitated in-situ from 0.05 M tetraethylortho titanate.

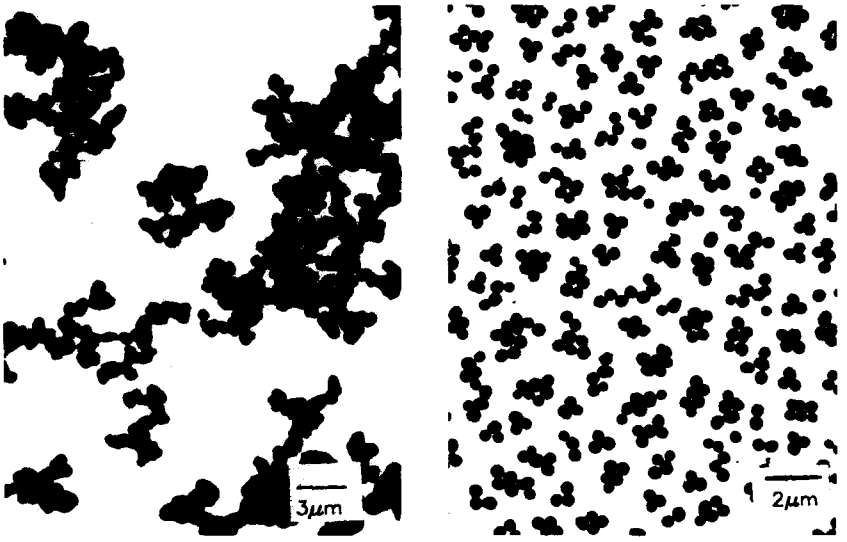


Fig. 2 Particles precipitated from 0.05 M tetraethylortho titanate in ethanol containing a) 0.4 M H_2O and no acid and b) 0.25 M H_2O and 10^{-4} M [HC].

V. Examples Where Aggregation Has Been Implicated During Particle Growth.

Aggregation as a mechanism for the formation of uniform precipitates has been suggested for a wide variety of chemical systems. Among these are metallic gold (7), (where we find that final particle size increases with electrolyte concentration), FeOOH (4-6), and TiO_2 precipitated from $TiCl_4$. The precipitates in these systems are crystalline and, in the case of gold and iron hydroxide, the resulting particles are observed to have facets. Such a result suggests that aggregation can occur with a preferred orientation giving rise to what appear to be single crystals.

Perhaps the best studied system where uniform particles are precipitated is that of polymer latexes prepared by emulsion polymerization. Here extensive studies indicate that a constant density of particles is established by aggregation of small primary particles composed of sytrene oligimers that have grown to a size where they are insoluble in the aqueous phase (9-11).

Finally we note that large biological and inorganic molecules are commonly crystallized from solution for structural studies. Molecular sizes on the order of 2-10 *nm* are not uncommon in such studies. The resulting solids are crystalline in nature but are clearly composed of well defined structural subunits. At this level, the distinction between soluble and insoluble becomes blurred and discussions of crystal growth can occur in classical molecular terms or with aggregation theory where reaction rates are governed by electrostatic, van der Waals and solvation forces. The distinction between growth of crystals from preformed molecules and those where the solid is formed through reactions between soluble species is one of time scale. In precipitation reactions the solids that undergo aggregation are formed in-situ. In the crystallization of large biomolecules or inorganic molecules, the subunits are formed via previous reactions and, rather than growing to a size that is insoluble, these molecules are rendered insoluble through changes in solution conditions. From this perspective, we see no reason that small silica or titania particles may not have interaction potentials similar to biological molecules undergoing crystallization and aggregate to form dense, nonfractal flocs or, in the case of FeOOH and Au, to form faceted crystallites.

Acknowledgements:

The authors would like to thank Elizabeth Lestan and Paul Carus for their help in defining the conditions for the precipitation of uniform titania precipitation and W.G. Klemperer for insightful discussions on sol-gel reaction chemistry. This work has been supported through a grant from the International Fine Particle Research Institute and the US Department of Energy through grant number DOE DEAC02-76ER01198.

References:

(1) LaMer, V. K., and Dinegar, R. H., J. Am. Chem. Soc. 72, 4847 (1950).
(2) Keefer, K. P., in "Better Ceramics Through Chemistry II", eds., Brinker, C. J., Clark, D. E., and Ulrich, D. R., Mat. Res. Soc., Pittsburgh, Pa., 1986, 295-304.
(3) Feenstra, T. P. and deBruyn, P. L., J. Colloid Interface Sci. 84, 66 (1981).

(4) Murphy, P. J., Posner, A. M., and Quirk, J. P., J. Colloid Interface Sci. 56, 270, 284, 298, 312 (1976).
(5) Van der Woude, J. H. A., Rijnbout, J.B., and deBruyn, P.L., Colloids and Surfaces 11, 391 (1984).
(6) Van der Woude, J. H. A. and deBruyn, P. L., Colloids and Surfaces 12, 179 (1984).
(7) Ugeda, N., Nishino, M., and Suito, E., J. Colloid Interface Sci. 43, 264 (1973).
(8) Santacesaria, E., Tonell, M., Storti, G., Pace, R. C., and Carra, S., J. Colloid Interface Sci. 111, 44 (1986).
(9) Fitch, R. M., Palmgren, T. H., Aoyagi, T., and Zuikov, A., Die Agnew and Malcromolekulwe Chemie 123/124, 261 (1984).
(10) Lichti, G., Gilbert, R. G., Gilbert and Napper, D. H., J. Polymer Sci 21, 269 (1983).
(11) Feeney, P. J., Napper, D. H., and Gilbert, R. G., Macromolecules 17, 2570 (1984).
(12) Lifshitz, I. M., and Sglozov, V. V., Chem. Solids, 19, 35 (1961).
(13) Bogush, G. H., and Zukoski, C. F., submitted to J. Colloid Interface Sci. 1990.
(14) Kim, S., and Zukoski, C. F., accepted to J. Colloid Interface Sci. 1990.
(15) Kerkez, M. Daby, E., Cohen, G. L., Krabhril, J. P., and Matijevic, E., J. Am. Chem. Soc. 67, 2105 (1963).
(16) Hunter, R. J., Foundations of Colloid Science Vol. I, Clarendon Press, Oxford (1987).
(17) Russel, W. B., Saville, D. A., and Schowalter, W.R., Colloidal Dispersions, Oxford University Press, Oxford 1989.
(18) Flory, P. J., Principals of Polymer Chemistry, Cornell University Press, Ithaca, 1953.
(19) Flory, P. J., J. Am. Chem. Soc. 58, 1977 (1936).
(20) Stockmayer, J., J. Chem. Phys. 11, 45 (1943).
(21) Stockmayer, J., in Adv. in Chemistry I. High Polymers, Reinhold Press, New York 1945, pp 61.
(22) Klemperer, W. K., and Ramamurthi, S. D., in Better Ceramics Through Chemistry III, eds., Brinker, C. J., Clark, D. E. and Ulrich, D. R., Mat. Res. Soc. Symp. 121 (1988).
(23) Klemperer, W. K., and Ramamurthi, S. D., to appear in J. Noncrystalline Solics, 1990.
(24) Tanaka, T., Ishiwara, S., and Ishimuto, C., Phy. Rev. Lett 38, 771 (1977).
(25) Bogush, G. H., Dickstein, G. L., Lee, P. K. D., and Zukoski C. F., M.R.S. Symposium Series 121, 57 (1988).
(26) Jean, J., and Ring, T. A., Langmuir 2, 251 (1986).
(27) Jean, J., and Ring, T. A., Colloids and Surfaces 29, 273 (1988).
(28) Edelson, L. H., and Glaeser, A. M., J. Am. Ceramic. Soc. 71, 225 (1988).
(29) Matsoukas, T., and Gulari, E., J. Colloid Interface Sci. 124, 252 (1988) and 132, 13 (1989).

SIMPLE MODELS FOR PARTICLE AGGREGATION, DEPOSITION AND SEGREGATION

PAUL MEAKIN
E. I. du Pont de Nemours and Company, Central Research and Development Department, Wilmington, DE 19880-0356

ABSTRACT

Most conventional and experimental methods for the formation of ceramic objects involve the manipulation of small particles and/or structures comprised of these particles. Consequently, a better understanding of the physics and chemistry of small particles could contribute to the development of better ceramics. Here the results of some recent computer simulation studies of processes such as particle aggregation, deposition and segregation are surveyed. More realistic models are needed to represent accurately the behavior of most real systems.

INTRODUCTION

Many of the most promising approaches to the manufacture of ceramics with superior mechanical properties involve the manipulation of small particles. Phenomena such as aggregation, segregation, packing, sedimentation, sintering and fragmentation are an integral and unavoidable part of many of these processes. Consequently, the development of improved ceramics can be facilitated by a better understanding of the behavior of large assemblies of small particles. The continual increase in the power, availability and convenience of digital computers has stimulated the development of a variety of simple models for the behavior of small article systems. Despite their unrealistic simplicity, these models frequently lead to structures and kinetic behavior that resemble quite closely those observed in real systems. The objective of this short survey is to describe some of the recent progress in this direction.

AGGREGATION

The aggregation of small particles to form extended structures is a ubiquitous process that has important implications for ceramic processing. It is an essential part of processes such as sol-gel processing [1] and can be a major impediment to the achievement of high densities in compaction processes. The use of computer models to study particle aggregation has a relatively long history [2,3]. However, most of the recent work in this area appears to have been stimulated by the introduction of the diffusion-limited aggregation (DLA) model by Witten and Sander [4] in 1981. In this model particles are added, one at a time, to a growing cluster or aggregate of particles via random walk trajectories. When a particle contacts the growing cluster, it is joined irreversibly to the cluster at its contact position. This model leads to the formation of random ramified structures that have a fractal dimensionality [5], D, that is distinctly smaller than that of the space or lattice in which the simulation process is embedded. Under some circumstances, this model can be used to describe fluid-fluid displacement during the drying of ceramic powders [6], but it does not provide a basis for understanding most colloidal aggregation processes.

During recent years a variety of models have been developed to represent the aggregation of small particles to form tenuous random flocs. The most simple of these models provide limiting scenarios that

Mat. Res. Soc. Symp. Proc. Vol. 180. ©1990 Materials Research Society

can be compared with experiments. In most cases real systems have been found that come quite close to satisfying the conditions assumed in these models. However, many important aggregation processes cannot be understood in terms of simple models and this has motivated the development of more realistic models that recognize in a more complete way the complex physical and chemical phenomena associated with most colloidal aggregation processes.

Simple Cluster-Cluster Aggregation Models

A simple diffusion-limited cluster-cluster aggregation model was developed simultaneously by Meakin [7] and by Kolb et al. [8]. This model results in the formation of clusters that have a much smaller fractal dimensionality ($D \simeq 1.78$) than that associated with the three dimensional DLA model ($D \simeq 2.50$). This model appears to provide a quite satisfactory description of the structure and kinetics associated with a variety of fast aggregation processes in dense fluids [2,3,9].

If instead of following random walk or Brownian trajectories, the particles or clusters follow linear or ballistic paths, then the resulting clusters have a fractal dimensionality of about 1.95 [2,3,10,11]. This model is relevant to the early stages of aggregation of small particles generated in flames and processes such as the aggregation of ceramic "nanoparticles" in gases at reduced pressure.

The most simple, and one of the most important, cluster-cluster aggregation models is the reaction-limited cluster-cluster aggregation model in which the particles and clusters can be considered to follow zero dimensional trajectories [12,13]. Both the structure and kinetics of reaction-limited cluster-cluster aggregation can be represented by a model that proceeds by the following steps starting with a large number of single particles [14-16]: (1) A pair of particles is selected at random from the system and the time is increased by a small constant amount

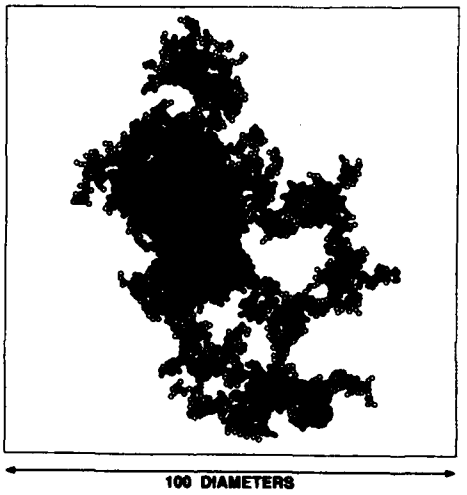


Fig. 1. A projection of a 10,000 particle cluster generated by a three dimensional off-lattice reaction-limited cluster-cluster aggregation model.

(δt). (2) If the selected particles belong to different clusters, the two particles are placed in contact with each other after rotating the clusters to which they belong to random orientations. (3) The two clusters to which the randomly selected particles belong are tested for overlap and if no overlap is found, they are combined irreversibly in the contacting configuration to form a larger structure. Steps (1)-(3) are repeated many times until a preselected mean cluster size or maximum cluster size is reached. Using both cubic lattice and off-lattice models clusters with a fractal dimensionality of about 2.10 are formed [2-3,17]. The simulations also indicate an exponential growth in the mean cluster size and a power law cluster size distribution given by

$$N_S(t) \sim s^{-\tau} f(s/S) \qquad (1)$$

Here $N_S(t)$ is the number of clusters of size s at time t and S is the mean cluster size. The cut-off function f(x) has the form f(x) ≈ const. for $x \ll 1$ and $f(x) \ll 1$ (a rapidly decreasing function of x) for $x \gg 1$. The exponential growth in S is in accord with theoretical arguments [18], but the value of the exponent τ found in the simulations is somewhat larger ($\tau \simeq 1.7$) than the theoretical value of 1.5. It is not known at present if this discrepancy represents a fundamental difference between theory and simulation or is a consequence of finite times and sizes in the simulations. It appears that the slow aggregation of small particles in a liquid can often be described quite well by the reaction-limited cluster-cluster aggregation model [2,3,17,19]. Figure 1 shows a "typical" 10,000 particle cluster generated during a three-dimensional off-lattice simulation of reaction- limited cluster-cluster aggregation.

Towards More Realistic Models

Although the simple models discussed in the previous section provide a basis for understanding a wide range of aggregation processes, many other processes cannot be described in terms of these models. The fractal dimensionalities of the clusters may be significantly outside of the rather narrow range of $1.75 \leq D \leq 2.15$ covered by the simple models and addditional discrepancies may be revealed by the aggregation kinetics. For example, Kim and Brock [20,21] have found effective fractal dimensionalities of 1.34 and 1.72 respectively for the aggregation of (large magnetic moment) iron particles and (small magnetic moment) cobalt particles respectively. It appears that results consistent with these observations can be obtained by including long range magnetic dipole-dipole interactions in the standard cluster-cluster aggregation models [22].

In most aggregation models the inclusion of attractive or repulsive interactions requires very large amounts of computer time and only very small scale simulations can be carried out. A partial exception to this is the reaction-limited cluster-cluster aggregation. In this case the algorithm must be modified to select potential bonding configurations with probabilities proportional to the Boltzman factor given by

$$P_{ij}(\Omega) \propto e^{-E_{ij}(\Omega)} \qquad (2)$$

where Pij is the probability of selecting the bonding configuration given by the coordinates Ω between the two contacting clusters (i and j). The random selection of bonding configurations with probabilities given by equation (2) is reasonable provided that attractive interactions do not overwhelm the short range repulsive interactions associated with reaction-limited aggregation. Both two [23] and three [24] dimensional simulations have been carried out using models of this type in which the interaction energy Eij is assumed to be the sum of pairwise particle-particle interactions.

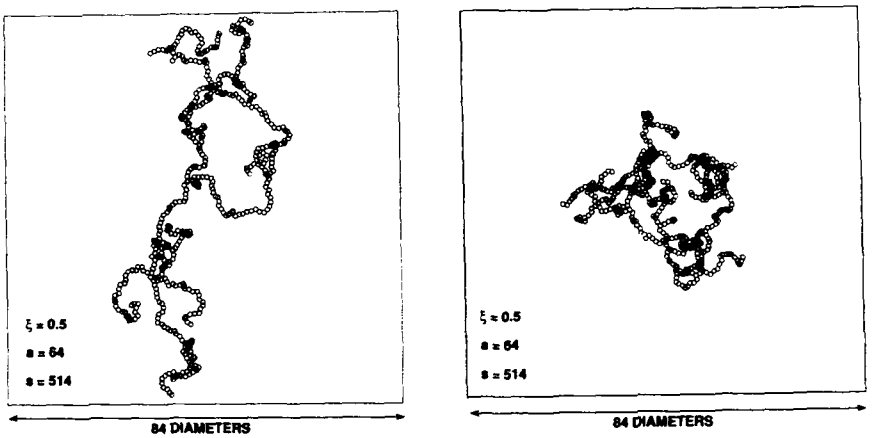


Fig. 2. A cluster of 514 particles generated using a three dimensional off-lattice reaction-limited cluster-cluster aggregation model with a short range pairwise particle-particle repulsive interaction with the form $e_{k\ell} = (a/r_{k\ell})e^{-r_{k\ell}/\xi}$ with the parameters a = 64kT and $\xi = d_o/2$ where d_o is the particle diameter. Two mutually perpendicular projections of the clusters are shown.

$$Eij = \sum_{k=1}^{i} \sum_{\ell=1}^{j} e_{k\ell} \qquad (3)$$

where $e_{k\ell}$ is a simple function of the distance $r_{k\ell}$ between the center of particle k in cluster i and particle ℓ in cluster j. Figure 2 shows a cluster generated using a three dimension reaction-limited cluster-cluster aggregation model with an interaction energy given by

$$e_{k\ell} = \frac{a}{r_{k\ell}} e^{-(r_{k\ell}/\xi)} \qquad (4)$$

The parameters a and ξ were set to values of 64 (in units of k_BT where k_B is the Boltzman constant) and 1/2 (in units of the particle diameter) respectively. This is an example of a short range repulsive interaction. The short range structure is influenced dramatically, but the asymptotic (long length scale) fractal dimensionality is not changed [23,24].

One of the most drastic assumptions associated with simple cluster-cluster aggregation models is the irreversible combination of rigid clusters in the configuration in which they first contact each other. In many cases it seems quite likely that the initial bonding between pairs of clusters will be quite flexible permitting reorganization to a more rigid structure. Figure 3 illustrates a model for such structural reorganization that proceeds in three stages called bending (Figure 3a), folding (Figure 3b) and twisting (Figure 3c) [25, 26]. These reorganization processes increase the number of contacts between aggregating pairs of clusters and increase their fractal dimensionalities.

Figure 4 shows clusters of similar sizes generated using an off-lattice diffusion-limited cluster-cluster aggregation model with four restructuring models (no restructuring (IR = 0) in Figure 4a, bending (IR = 1) in Figure 4b, bending and folding (IR = 2) in Figure 4c and complete restructuring (bending, folding and twisting, IR = 3 in Figure 4d). Table I shows the fractal dimensionalities obtained from polydisperse diffusion-

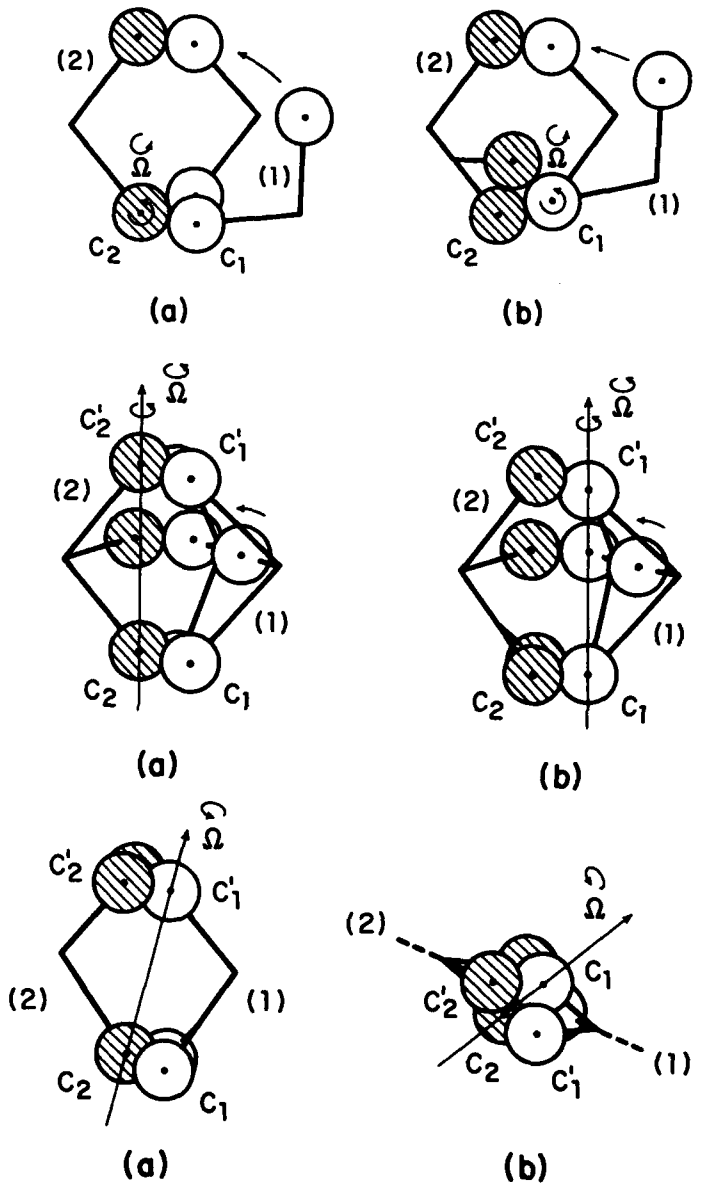


Fig. 3. Simple restructuring mechanisms that can be incorporated into cluster-cluster aggregation models. The two (rigid) clusters are distinguished by shaded and empty circles. Figure 3a illustrates the "bending" process stage that involves rotation of one cluster about the center of the contacting particle in the other cluster to form an additional contact. Figure 3b illustrates the "folding" process in which one of the clusters is

rotated about an axis passing through a pair of contacting particles in the other cluster. The "twisting" stage (Figure 3c) involves rotation about an axis passing through the centers of two particles in different clusters. In all stages the "rotations" are stopped when an additional contact between the two clusters has been found.

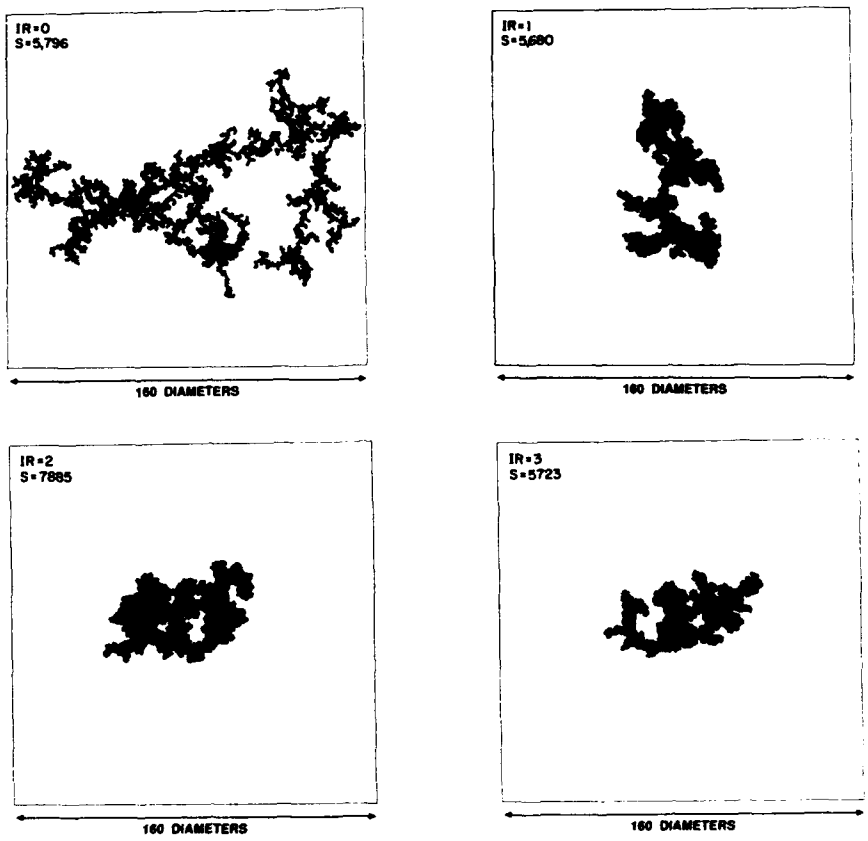


Fig. 4. Projections of clusters generated using a three dimensional off-lattice diffusion-limited cluster-cluster aggregation model without restructuring (IR = 0) and with the three restructuring processes illustrated in Figure 3. (IR = 1, 2 and 3).

limited, ballistic and reaction-limited cluster-cluster aggregation models using these restructuring mechanisms. In each case the smallest of the two possible rotation angles leading to additional contacts between the two "aggregating" clusters was always selected.

TABLE I

Fractal dimensionalities obtained from three dimensional cluster-cluster aggregation models with restructuring.

Model	Number of Restructuring Stages			
	0	1	2	3
Diffusion-Limited	1.80	2.09	2.17	2.18
Ballistic	1.95	2.13	2.18	2.19
Reaction-Limited	2.09	2.18	2.24	2.25

MODELS FOR PARTICLE DEPOSITION AND SEGREGATION

Like the aggregation models described above, simple models for particle deposition have a relatively long history. The recent interest in particle deposition models was stimulated by work on closely related aggregation models [2,3] and by the discovery by Family and Vicsek [27] that for the ballistic deposition model [3] the dependence of the width ξ characterizing the surface of deposits growing in a strip or channel of width L (with periodic boundary conditions in the lateral direction(s)) could be described by the scaling form

$$\xi(t,L) \sim L^{\alpha} f(t/L^{\alpha/\beta}) \qquad (5)$$

where t is the deposition time (mean deposit thickness). The scaling function f(x) has the form $f(x) = x^{\beta}$ for $x<<1$ and f(x) saturates to a constant value for $x>>L^{\alpha/\beta}$. This means that $\xi \sim t^{\beta}$ for $t<<L^{\alpha/\beta}$ and $\xi \sim L^{\alpha}$ for $t>>L^{\alpha/\beta}$. The width ξ is a correlation length describing the fluctuations in the surfce height in a direction perpendicular to the smooth substrate from which the deposit has grown. A second correlation length $\xi_{||}$ describes the lateral distance over which the height fluctuations persist. For the ballistic deposition model equation (5) implies that $\xi_{||}$ grows algebraically with increasing time

$$\xi_{||} \sim t^{\beta/\alpha} \qquad (6)$$

so that the correlation lengths $\xi_{||}$ and ξ ($\xi_{\perp}$) are related by

$$\xi_{\perp} \sim \xi_{||}^{\alpha} \qquad (7)$$

The exponent α is the Hurst exponent [5] that describes the self-affine fractal scaling properties associated with surfaces generated using the ballistic deposition model [28] and other simple surface growth models such as the Eden [29] model.

Most recent surface growth simulations have been carried out using lattice models. The simplicity of these models allows very large scale simulations to be carried out that are suitable for exploring the asymptotic geometric scaling associated with the growth of rough surfaces. However, the short length scale structure generated by these models is not realistic and they cannot readily be used to investigate processes such as particle size segregation. Figure 5 illustrates a family of three dimensional off-lattice ballistic deposition models [30]. In these models spherical particles are "dropped" onto a growing deposit of equal particles. In some versions of the model the particles may follow a path of steepest descent on the surface after the initial contact has been made. In this case the motion of the center of mass of the deposited particle

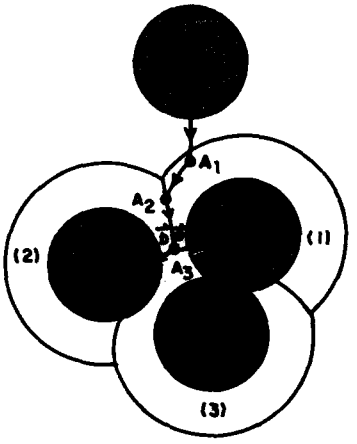


Fig. 5. Three dimensional off-lattice models for the deposition of spherical particles of equal size. The deposited particle will stop and be incorporated into the deposit when its center reaches positions A_1, A_2 or A_3 in models I, II and III respectively. In model IV the deposited particle continues to follow a path of steepest descent on the surface until a local minimum has been reached.

may be represented as the motion of a point on the surface of a deposit in which the radius of each particle has been doubled. In model I the particle stops at the position at which it first contacts the cluster (with its center at position A_1, in Figure 5). This corresponds to the standard off-lattice ballistic deposition model first investigated by Vold [31]. In model II the particle follows the path of steepest descent until a second particle is contacted (position A_2, in Figure 5) and the particle is irreversibly incorporated into the growing deposit at this position. In model III the particle follows the path of steepest descent until it simultaneously contacts three particles in the deposit. In model IV the particle continues to follow the path of steepest descent until it reaches a local minimum in the surface.

Figure 6 shows the results of small scale simulations carried out using all four of these models. The density of the deposits increases from about 0.147 for model I to 0.582 for model IV. The value of 0.582 lies within (but to the low side) of the range of densities found in a variety of random packing models ($0.57 \leq \rho \leq 0.63$). The dependence of the surface width (ξ) on the deposition time appears to be algebraic for model I ($\beta \simeq 0.2$) but is logarithmic for model IV ($\xi \sim (\log(t))^{1/2}$) in accord with the theoretical work of Edwards and Wilkinson [32]. Models similar to version IV of the off-lattice ballistic deposition model (ballistic deposition with complete restructuring) have been used to simulate the segregation of particles of different sizes [33,34]. Figure 7 shows a two dimensional version of this model. After contacting the surface, the particle follows a path of steepest descent consisting of "rolling" and "falling" stages until a local minimum is reached. Figure 8 shows the results of simulations carried out using a three dimensional version of this model in which particles of different sizes (selected at random) are deposited along the axis of a vertical cylindrical "container". After contacting the deposit the particles follow a path like that illustrated in Figure 7 until they reach the floor of the container, reach a local minimum in the deposit surface or

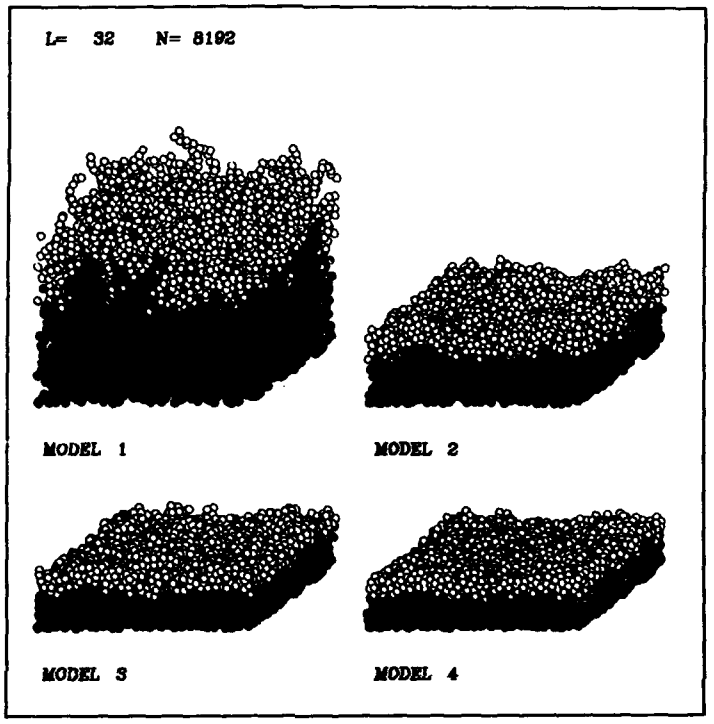


Fig. 6. Small scale deposits generated using all four of the off-lattice ballistic deposition models illustrated in Figure 5. Each deposit contains the same number of particles.

reach a minimum in contact with the inner wall of the container. Figure 8 show results obtained using a size ratio, R, of 2 where $R = R_1/R_2$ and $R_1 > R_2$). The results of a similar simulation with R = 4 is shown in Figure 9. In general, the degree of segregation increases as the radius ratio (R) is increased and as the fraction of small particles increases.

In this model segregation is a consequence of the ability of large particles to roll over small particles while small particles cannot easily roll over large ones. Size segregation is a very common phenomena and there are many mechanisms contributing to it.

SUMMARY

Simple models for the behavior of multiparticle systems provide a basis for understanding more complex phenomena occurring in ceramic processing. They provide a sound basis for the development of the more complex and realistic models that will be needed to accurately represent the rich phenomenology associated with the development of practical ceramics. Some progress has been made in this direction, but we are still a long way from the development of general models that can be used to guide experimental work.

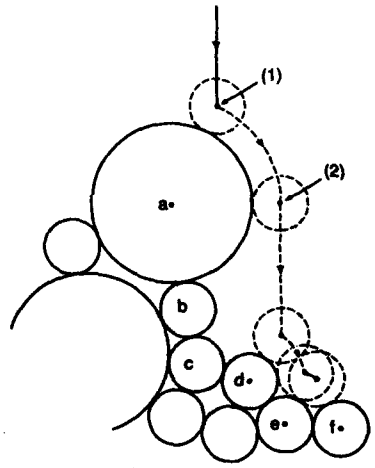


Fig. 7. A two dimensional ballistic deposition model used to simulate the segregation of particles of different sizes. After contacting the surface (at position 1) the particle follows a path of steepest descent on the surface until it reaches a local minimum. However, if the particle reaches a position (such as position 2) at which it no longer contacts particles in the deposit with centers at a lower height, it falls freely until the deposit is again contacted.

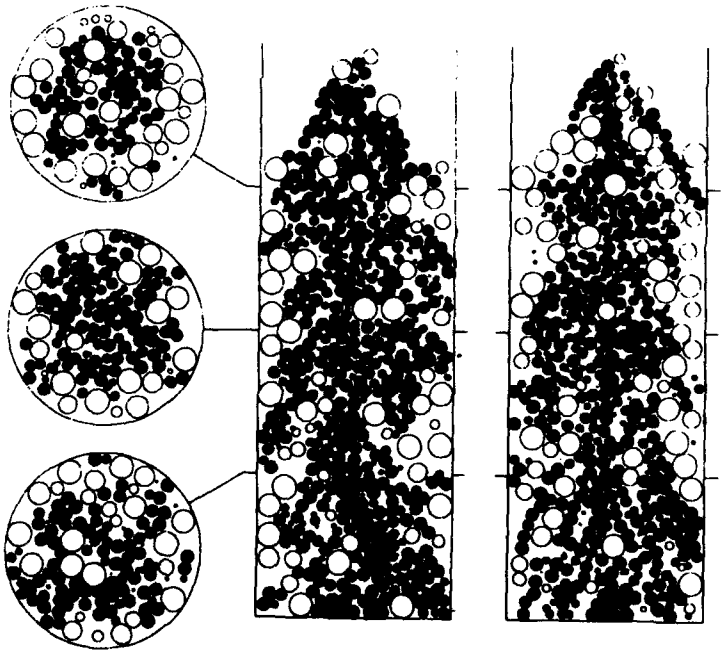


Fig. 8. Cross-sections through a three dimensional deposit formed by adding large particles (open) with a diameter of 1.0 and small particles (filled) with diameter 1/2 according to the algorithm illustrated in Figure 7 along the axis of a cylinder with a diameter of 8.0.

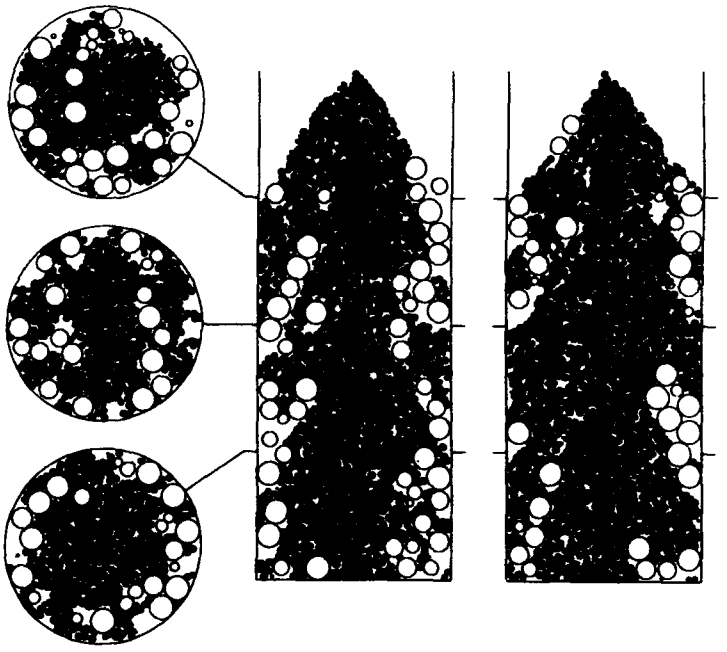


Fig. 9. Cross-sections through a three dimensional deposit formed by adding large particles with a diameter of 1.0 and small particles with diameter 1/4 according to the algorithm illustrated in Figure 7 along the axis of a cylinder with a diameter of 8.0. In both Figures 8 and 9 the wall particles are represented by fitted circles and the large particles by open circles. In Figure 8 the fraction of large spheres is 0.1 and in Figure 9 this fraction is 0.01. The deposit in Figure 8 contains 4818 particles and that shown in Figure 9 contains 40206 particles.

ACKNOWLEDGMENT

Most of the work described here was carried out in collaboration with R. Jullien. Important contributions were also made by F. Family and M. Muthukumar.

REFERENCES

1. C. J. Brinker and G. W. Scherer, Sol-Gel Science: The Physics and Chemistry of Sol-Gel Processing, Academic (1990).
2. R. Jullien and R. Botet, Aggregation and Fractal Aggregates, World Scientific, Singapore (1987).
3. P. Meakin in "Phase Transition and Critical Phenomena", C. Domb and J. L. Lebowitz, eds., Academic, New York (1988) p. 335.
4. T. A. Witten and L. M. Sander, Phys.Rev. Lett. 47, 1400 (1981).
5. B. B. Mandelbrot "The Fractal Geometry of Nature", W. H. Freeman and Company, New York (1982).

6. T. M. Shaw, Phys. Rev. Lett. 59, 1671 (1987).
7. P. Meakin, Phys. Rev. Lett. 51, 1119 (1983).
8. M. Kolb, R. Botet and R. Jullien, Phys. Rev. Lett. 51, 1123 (1983).
9. M. Y. Lin, H. M. Lindsay, D. A. Weitz, R. C. Ball, R. Klein and P. Meakin, Proc. Roy. Soc. (London), A423, 72 (1989).
10. D. N. Sutherland, J. Colloid Interface Sci., 25, 373 (1967).
11. P. Meakin, Ann. Rev. Phys. Chem. 39, 237 (1988).
12. M. Kolb and R. Jullien, J. Physique Lett. 45, L977 (1984).
13. R. Jullien and M. Kolb, J. Phys. A27, L639 (1984).
14. F. Leyvraz, private communication.
15. W. D. Brown and R. C. Ball, J. Phys. A18, L517 (1985).
16. P. Meakin and F. Family, Phys. Rev. A36, 5498 (1987).
17. P. Meakin, Advances in Colloid and Interface Sci., 28, 249 (1988).
18. R. C. Ball, D. A. Weitz, T. A. Witten and F. Leyvraz, Phys. Rev. Lett. 58, 274 (1987)
19. M. Y. Lin, H. M. Lindsay, D. A. Weitz, R. C. Ball, R. Klein and P. Meakin, Nature 339, 6223 (1989).
20. S. G. Kim and J. R. Brock, J. Applied Phys. 60, 509 (1986).
21. S. G. Kim and J. R. Brock, J. Colloid Interface Sci., 116, 431 (1987).
22. P. M. Mors, R. Botet and R. Jullien, J. Phys. A20, L975 (1987).
23. P. Meakin and M. Muthukumar, J. Chem. Phys. 91, 3215 (1989).
24. P. Meakin, J. Colloid Interface Sci. 134, 235 (1989).
25. R. Jullien and P. Meakin, J. Colloid Interface Sci, 127, 265 (1989).
26. P. Meakin and R. Jullien, J. Chem. Phys. 89, 246 (1988).
27. F. Family and T. Vicsek, Phys. Rev. A28, L75 (1985).
28. P. Meakin, CRC Critical Reviews in Solid State and Materials Science, 13, 143 (1987).
29. M. Eden, Proceedings of the Fourth Berkeley Symposium on Mathematics, Statistics and Probability, F. Neyman, ed., University of California Press, Berkeley (1961).
30. R. Jullien and P. Meakin, Europhys. Lett. 4, 1285 (1987).
31. M. J. Vold, J. Colloid Sci. 14, 168 (1959).
32. S. F. Edwards and D. R Wilkinson, Proc. Roy. Soc. London Ser A381, 17 (1982).
33. P. Meakin, Physica A163, 733 (1990).
34. R. Jullien and P. Meakin, Nature, 334, 425 (1990).

MECHANISMS OF SILICA AND TITANIA COLLOIDAL PARTICLE FORMATION FROM METAL ALKOXIDES

JOSEPH K. BAILEY AND MARTHA L. MECARTNEY
Department of Chemical Engineering and Materials Science, University of Minnesota, Minneapolis, Minnesota 55455

ABSTRACT

Control of the preparation of monodisperse particles for green body formation can be achieved by understanding the growth mechanism. Growth processes for colloidal silica and titania were followed by cryo-TEM, which allows direct observation of the particles in the liquid state. Structural development was tracked by quenching samples at successive reaction times. The preparation of silica particles involved the formation of ramified species which subsequently collapsed after reaching a certain size. In the titania system, initially small dense nuclei are observed which eventually form uniformly textured homogeneous particles.

INTRODUCTION

High quality advanced ceramic materials can be prepared by using unagglomerated monodisperse powders; therefore, there is incentive to understand methods of producing monodisperse unagglomerated. Stober et al. [1] first showed that monodisperse silica particles can be derived from silicon alkoxides, and Bogush et al. [2] demonstrated that control over particle size and mass fraction can be obtained. In these processes, a solution of silicon alkoxide monomers undergoes hydrolysis and condensation to form the particles. Barringer and Bowen [4] demonstrated that an analogous preparation of titania particles was feasible.

In order to understand the growth mechanism that produces monodisperse silica particles, Bogush and Zukoski performed kinetic and structural investigations on the silica system [3]. They inferred that nucleation of particles was occurring throughout the reaction, and discredited the idea of a traditional nucleation and growth mechanism. They proposed a nucleation and aggregation mechanism whereby small particles nucleate and then aggregate until reaching a colloidally stable size. These larger, colloidally stable particles diffuse through the solution aggregating with small particles which are continuing to nucleate. The rate at which the particles add onto the colloids is sufficient to prevent any of the smaller particles from growing to a colloidally stable size, thus ensuring monodispersity. A similarly intensive study has not yet been performed on the titania, however, microscopic investigations on the final dried titania particles indicate that they appear to be comprised of many small particles [5].

In order to understand the influence of the processing conditions on the morphology of the particles, the growth mechanism needs to be understood. This paper describes an comparative investigation of the structural development in silica and titania colloids by cryo-TEM.

Mat. Res. Soc. Symp. Proc. Vol. 180. ©1990 Materials Research Society

EXPERIMENTAL

Silica colloids were prepared from a solution of 0.17M tetraethoxysilane, 1.0-1.3M NH_3, and 1.0M to 3.8M H_2O in n-propanol solvent [1,3]. Titania colloids were prepared from a solution of 0.1M Titanium isopropoxide and 0.3-1.0M H_2O in n-propanol [5]. Normal propanol was used in these studies since it is relatively resistant to electron damage in the TEM. After mixing the solutions, the titanium colloids were allowed to stand while the reaction occurred,while the silica solutions were stirred with a magnetic stirrer during the reaction.

TEM samples were prepared while the reaction proceeded as described fully in reference [6]. At a given time in the reaction, a drop of solution was taken from the reaction vessel and was placed on a holey carbon grid suspended in a controlled environment chamber. The grid was blotted to produce thin liquid films in the grid holes. The grid was then rapidly plunged into liquid ethane which vitrified the solvent. The frozen specimens were transferred to the TEM, where the structures present in the fast-frozen liquid films were directly observed.

RESULTS

The growth of silica colloids at 1.0M water concentration is shown in Figures 1a-f. This solution took 36 minutes to first show turbidity. Figure 1a shows the cryo-fixed sol at 6 minutes of reaction. This solution contains no visible particles and is featureless. In comparison a dried sample was prepared similar to [2] at the same reaction time: the dried silica particles of average size 14nm are shown in Figure 1b. Cryo-TEM of sols at 16 minutes (Figure 1c) show that there are low contrast particles in solution with an average size of 26nm. The low contrast is due to low density of the particles. At 24 minutes of reaction, high contrast, dense particles can be seen in the cryo-fixed solution (Figure 1d). These particles have a rough texture and an average size of 20nm. In this micrograph some low density particles are also visible. If a solution is dried at this reaction time, high contrast particles are seen (Figure 1e) which have an average size of 30nm at 25 minutes. In addition to the large particles in Figure 1e, smaller distinct particles are seen, some of which have attached to the larger particles. Cryo-TEM micrographs taken after this point in the reaction show only high density particles, and no low density particles can be seen. Figure 1f shows particles at 186 minutes into the reaction. In this figure the particles, average size = 72nm, are supported on the carbon grid, since particles this large break the surface tension of the thin liquid films. In Figure 1f, small bridging particles are seen connecting the larger colloids. The silica colloids grow to an average size of 200nm in 24 hours.

Figure 2 shows the silica solution with 2.0M H_2O 75s into the reaction. This solution first showed turbidity at 4 minutes. Low density particles are seen similar to Figure 1c. This solution also contained higher density particles later in the reaction, however the distinct colloids had a smoother texture than the 1.0M water solutions. Cryo-TEM experiments indicated that no samples of 2.0 or 3.8M water content viewed at reaction times less than two-thirds of the time to

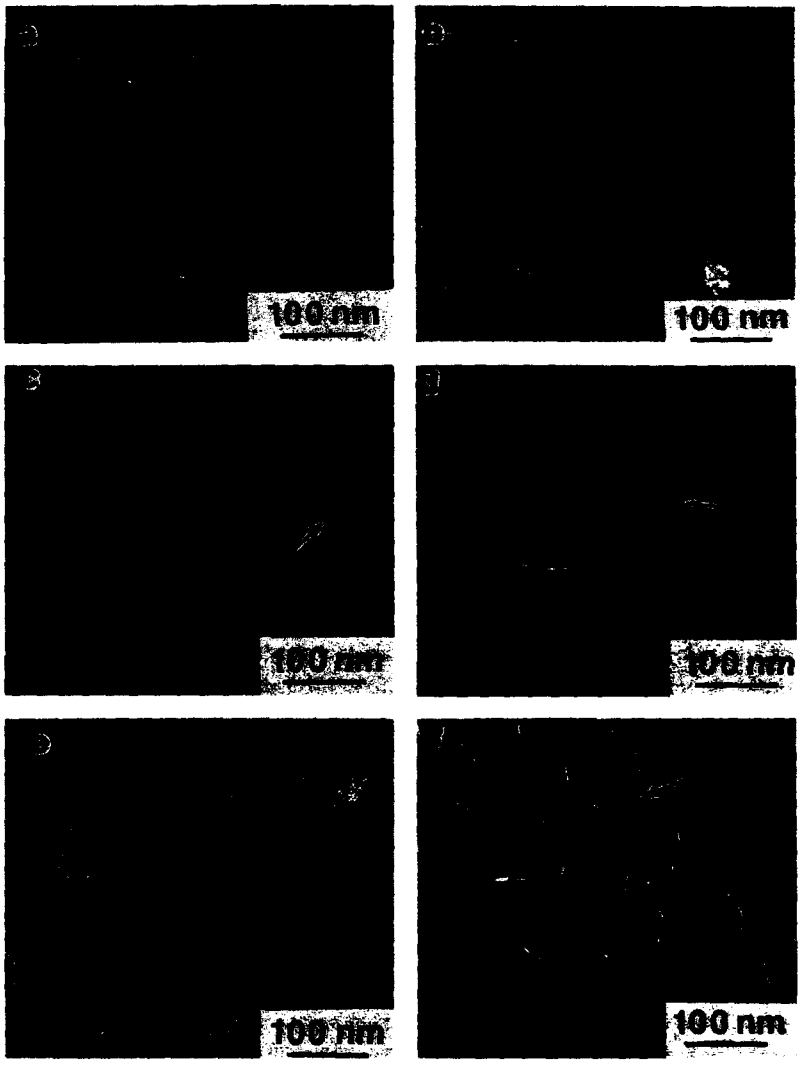


Figure 1: Stages in the growth of silica particles with 1.0M water concentration.
(a) Cryo-TEM of fast-frozen solution after 6 minutes.
(b) Dried sample after 6 minutes of reaction.
(c) Cryo-TEM of fast-frozen solution after 16 minutes; arrow denotes low density particle.
(d) Cryo-TEM of fast-frozen solution after 24 minutes; arrow denotes high contrast textured particle.
(e) Dried sample after 25 minutes of reaction.
(f) Dried sample after 186 minutes of reaction; arrow denotes bridge between particles.

the onset of turbidity showed high density particles. (time to turbidity onset = t_r)

Figure 3a-c shows the development of structure for titania. The sol at $t/t_r = 0.3$ is featureless, similar to Figure 1a. At $t/t_r \approx 0.4$, Figure 3b shows rough graininess, indicating that small dense particles in solution, the largest of which are ≈ 2-3 nm in size. Figure 3c shows the structures observed when a solution at $t/t_r = 0.3$ is dried on a carbon support grid; again, a rough graininess is evident. Figure 3c shows particles at $t/t_r = 0.8$ where agglomerates of large uniformly textured particles are visible with smooth necks between the particles.

DISCUSSION

The most noticeable feature from the cryo-TEM micrographs is that early in the reaction, there are no dense colloidal particles in solution. In the liquid phase, one sees that there are low density, i.e. ramified particles present. Previous work using the cryo-TEM technique has been able to resolve silica clusters of 4nm diameter in solution in a base catalyzed TEOS gel [7], so if there were small, dense, particles of this size present in the colloidal growth process, they would be visible. Upon drying; however, the low density particles collapse and can be seen by TEM. The earliest time that dense particles are present in the micrographs is 24 minutes, and prior to this time, no dense silica particles are seen. It is also evident from Figure 1d, that solutions which contain dense particles may also contain low density particles indicating that not all particles are at the same stage in their growth. The mechanism for structural development in these silica systems is postulated to be the growth of ramified, low density particles, which at a critical point in their growth collapse and densify. This collapse is expected to be a function of the size and degree of ionization of the particle, or the local solvent composition. The collapse may be similar to phase separation in organic polymers, where the thermodynamic solvent quality is a function of the molecular weight [8]. The molecular weight increases until the self attraction of the molecule overcomes the entropic solvation forces and the particle collapses.

Small particles are seen attached to larger particles in Figure 1d and small bridging particles are seen in Figure 1e, both dried samples. However, distinct small particles are not seen in the liquid state at these times by cryo-microscopy indicating that the small particles are densified by drying. These observations combined with the analysis of Bogush and Zukoski [3] lead us to hypothesize that the dense colloids are colloidally stable with respect to each other, however they can react with the smaller ramified species. We speculate that ramified particles collapse onto the surface of the colloids during growth, allowing the particles to remain spherical.

In contrast to the silica, the titania does form small dense particles in solution. Unlike silica, one can see (Figure 3a) small dense TiO_2 particles approximately 2-3nm embedded in the solvent, producing a rough grainy texture. Also unlike silica, titania solution dried on a grid (Figure 3b) show a structure that is similar to that seen in solution by cryo-TEM. The dried sample has a rough graininess and upon close inspection, individual particles can be identified.

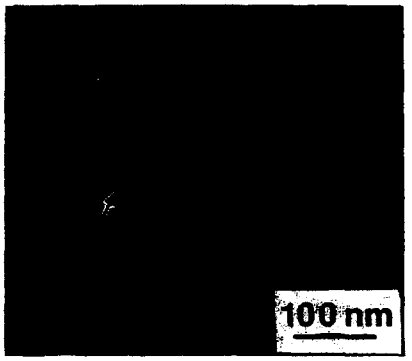


Figure 2: Cryo-TEM of silica solution with 2.0M water concentration 75s into the reaction. Arrow denotes low density particle.

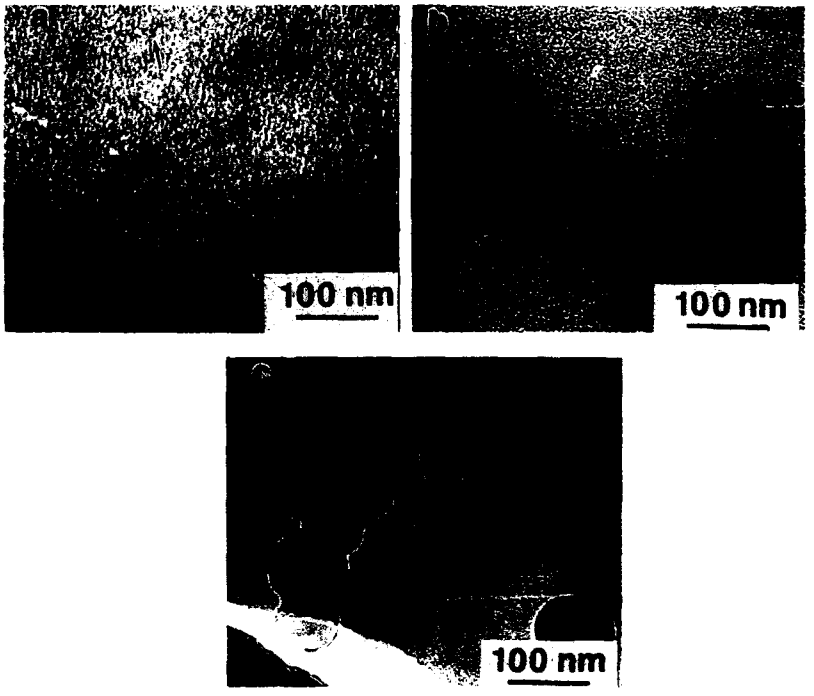


Figure 3: Stages in the growth of titania particles.
(a) Cryo-TEM of fast-frozen solution at t/tr = 0.4; arrow denotes 3nm dense particle.
(b) dried sample at t/tr = 0.3
(c) Cryo-TEM of solution at t/tr = 0.8

At later times in the reaction, Figure 3c, the titania particles are dense and uniformly textured, unlike the rough textured silica particles. There is also aggregation of the large particles, which was not seen in the silica system. The aggregates of the particles have well developed necks between the particles. From the DLVO theory of colloidal stabilization [9], it is assumed that small particles are less stable towards aggregation than large particles, thus it is expected that the smaller particles seen in Figure 3a have aggregated to form the larger particles.

CONCLUSIONS

For the growth of colloidal silica produced from alkoxides, there is no evidence of small dense particles forming early in the reaction. Highly ramified silica structures form and then undergo collapse after reaching a critical size to form small dense particles. Little evidence for aggregation of these particles was found. We postulate that these dense particles are colloidally stable and that particle growth is by the addition of small ramified structures, of too low density to be seen in the TEM, which collapse onto the surface of the particle when they attach. For the titania system studied, nucleation of small particles and aggregation of particles was noted.

ACKNOWLEDGMENTS

This work was supported by Sandia National Laboratories, contract 05-3976. Informative and aiding discussions with C.J. Brinker are acknowledged. Professors H.T. Davis and L.E. Scriven are thanked for the use of the controlled environment vitrification system.

REFERENCES

1. W. Stöber, A. Fink, and E. Bohn, J. Coll. Inf. Sci. 26, 62 (1968).
2. G.H. Bogush, M.A. Tracy, and C.F. Zukoski IV, J. Non-Crystal. Sol. 104 95 (1988).
3. G.H. Bogush and C.F. Zukoski IV, in Ultrastructure Processing of Advanced Ceramics, eds. J.D. Mackenzie and D.R. Ulrich, (John Wiley & Sons, New York, 1989) p. 477.
4. B. Barringer and H.K. Bowen, J. Amer. Ceram. Soc. 65, C-199 (1982).
5. M.I. Diaz-Guemes, T. Gonzalez Carreno, C.J. Serna, and J.M. Palacios, J. Mater. Sci. Lett. 7, 671 (1988).
6. J.K. Bailey, J. Bellare, and M.L. Mecartney, in Specimen Preparation for Transmission Electron Microscopy of Materials, eds. J.C. Bravman, R.M. Anderson, and M.L. McDonald (Mat. Res. Soc. Proc. 115, Pittsburgh, 1988) p. 69.
7. J.K. Bailey and M.L. Mecartney, J. Non-crystal. Sol. 109, 198 (1989).
8. P.C. Heimenz, Polymer Chemistry (Marcel Dekker, New York 1984) p. 529.
9. J.N. Israelachvili, Intermolecular and Surface Forces (Academic Press, London, 1985) p. 187.

SHEAR INDUCED ORDER OF CONCENTRATED DISPERSIONS

BRUCE J. ACKERSON AND T. A. MORRIS
Department of Physics, Oklahoma State University, Stillwater, OK 74078

ABSTRACT

The microstructure or interparticle ordering in concentrated dispersions of colloidal PMMA (polymethylmethacrylate) particles in a mixture of tetralin and decalin have been monitored using light scattering techniques. These sterically stabilized, uniformly sized, nearly hard, colloidal spheres are observed to exhibit an equilibrium phase transition from a liquid-like ordering to a crystal-like ordering of suspended particles as the volume fraction of solids increases. The crystals have a close packed - random stacked structure. At the largest volume fractions a nonequilibrium glassy phase results.

Samples at different volume fractions are subjected to steady and oscillatory shear flow. Four basic structures are observed to exist: liquid or distorted liquid-like, string-like, sliding or randomly stacked layers, and face centered cubic (FCC) structures. Oscillatory shear studies will be reported here and are made as a function of strain amplitude and shear history, in addition to volume fraction. Generally, oscillatory shear is effective in ordering samples. For example, an unstable FCC ordering can be induced in an equilibrium liquid-like sample.

INTRODUCTION

The microstructure of particles in a packed powder is an important factor in determining the strength of a ceramic body. Defects in an otherwise uniform microstructure concentrate stress and lead to mechanical failure. Therefore, a large amount of work has been directed at understanding and controlling microstructure. Many years ago Bernal and Scott investigated the microstructural properties of an ideal "powder" made from uniformly sized ball bearings. It was found in repeated experiments that, when ball bearings are poured into a container, the volume fraction occupied by the spheres is $\phi = 0.637$[1]. This is less than the maximum volume fraction of 0.74 when these hard spheres are arranged in a cubic close packed crystalline structure (either face centered cubic FCC or hexagonal close packed HCP[2]). Investigation of the ball bearing microstructure revealed a random arrangement of the spheres similar to that found for the atomic arrangement in pure liquids and glasses[3]. Thus this structure is now referred to as the Bernal close packed glass or Bernal glass.

These Bernal glasses have been subjected to oscillatory shear deformations in rectangular containers having hinged corners[4]. When the shear deformation is near unity [wall motion parallel to itself equal to the wall separation], the volume fraction of spheres was observed to increase to 0.66. For smaller or larger shear deformations the volume fraction remained near the Bernal glass value. Investigation of the microstructure of sheared glasses revealed local islands of cubic close packed crystalline structures[5]. Evidently, the shear oscillations are most effective at moving the spheres into a more close packed structure at a shear deformation of unity. Smaller deformations do not provide enough motion and larger deformations move particles out of close packed

Mat. Res. Soc. Symp. Proc. Vol. 190. ©1990 Materials Research Society

registration sites again. The close packed structures are not complete, as observed macroscopically in the volume fraction measurements or in the microstructure.

In this paper experimental results are presented for the microstructure induced in model hard sphere suspensions undergoing oscillatory shear flow. These results are given as a function of particle volume fraction and strain amplitude. A simple geometric model of a strained face centered cubic lattice is developed to interpret and understand the oscillatory shear induced ordering. These experimental results and model calculations, along with scattering diffraction patterns, steady shear flow measurements and equilibrium phase behavior, will be presented in more detail elsewhere[6]. Furthermore, this work was presented at the 3rd International Conference on Ceramic Powder Processing Science, and this manuscript is largely a reproduction of those proceedings (Ceramic Powder Science - III.).

While there are similarities with powder systems [e.g. the interparticle interaction is hard], there are also important differences. Because the particles are suspended in a solvent, there are hydrodynamic interactions between particles in nonequilibrium and shear flow conditions. Because the particles are colloidal, the volume of the sample is set by the solvent-particle mixture and need not change under its own weight like the ball bearing systems described above. Because the particle execute vigorous Brownian motion, the suspended particles are not stuck in a particular configuration but evolve towards an equilibrium microstructure. Such model hard sphere systems are expected to have an amorphous or liquid-like microstructure at low volume fraction of particles and a transition to a close packed crystalline structure with increasing volume fraction[7]. Specifically, at a sample volume fraction of $\phi = 0.494$ an equilibrium fluid state begins to freeze. At a sample volume fraction of $\phi = 0.545$ the melting line is reached and the sample is fully crystalline, presumably with an FCC microstructure.

EXPERIMENTAL DETAILS AND RESULTS

The colloidal particles used in these experiments are 0.99um diameter polymethylmethacrylate (PMMA) spheres which are suspended in a mixture of tetralin and decalin. The particles are stabilized against aggregation by a surface coating layer of poly (12- hydroxystearic acid) which produces a short ranged repulsive force approximating the model hard sphere interaction, which is infinitely repulsive when the center to center separation is equal to a particle diameter and zero for larger separations. Thus these model hard sphere systems are expected to undergo an equilibrium liquid-like to crystal phase transition with increasing particle volume fraction.

The relative standard deviation of the particle radius to the mean is 0.05, such that polydispersity effects should not interfere with the crystallization process[8]. Indeed, an order-disorder phase transition is observed in these samples as a function of volume fraction. Because the particles settle during the equilibration process, care must be taken in determining the volume fractions where melting and freezing occur[6,9]. It is found for these samples that the freezing point is at $\phi = 0.47$ and the melting point is at $\phi = 0.52$. These values of the volume fraction at the phase boundaries are at variance with the model hard sphere values quoted above. However, these volume fractions are determined by drying and weighing. If some of the solvent is absorbed into the particle stabilizing layer effectively increasing the particle radius, then this is not properly included when drying and weighing. Pusey and van Megen[10] have made similar observations for smaller diameter PMMA spheres with the same steric stabilizer coating in a solvent mixture of decalin and carbon disulphide. The shift of the phase boundaries is even larger than observed here. To

compare with hard spheres, they simply scale their volume fractions such that the value at freezing corresponds to the hard sphere freezing transition. We follow the same procedure and multiply our measured values by 1.04 to obtain the scaled values quoted hereafter. The scaling parameters used and the trend with particle size are consistent with absorbed solvent but could also indicate some softness in the interparticle interaction.

Tetralin and decalin have indices of refraction 1.54 and 1.48, respectively, and are mixed in a ratio such that the average solvent index of refraction matches the particle refractive index (n_p = 1.51). In this way samples with high solids content (greater than 0.70 volume fraction) are rendered transparent. Thus light scattering, similar to x-ray scattering from pure atomic liquids and crystals[11], may be used to determine the particle microstructure of the suspension. The scattered intensity evidences a diffuse Debye-Scherrer ring concentric with the incident beam for samples having a liquid-like microstructure and localized intensity maxima for other structures having crystalline or layer structures. Scattering from the equilibrium crystalline phase gives a crystal powder pattern indicating the existence of randomly oriented polycrystals. The scattered intensity pattern evidences both intense narrow and broad diffuse rings concentric with the incident beam, a pattern consistent with a registered but random stacking of hexagonal close packed layers of particles in each crystallite[12]. The intense narrow rings correspond to Bragg scattering from the regularly spaced (111) layers, while the diffuse scattering results from a random registration of these same layers. Such a structure might be expected for hard sphere interactions which have neither long range attractive interactions, leading to an HCP ordering, or long range repulsive interactions, leading to FCC (or even body centered cubic) ordering. For charge stabilized colloidal particle suspensions having long range repulsive interactions, the microstructure is indeed face centered cubic[13].

Several parameters are important for characterizing the rheology of hard sphere suspensions[14]. These include the particle volume fraction ϕ, reduced stress or Peclet number Pe, solvent to particle density ratio, the Reynolds number, strain amplitude and experimental run time. The solvent to particle density ratio (0.75) is not considered an important parameter for the experiments discussed, because insignificant sedimentation occurs for the duration of the shear experiments. Shear rates are kept sufficiently low that turbulence and inertial effects are negligible, and thus the Reynolds number is not important. The Pe number which is the product of the shear rate and a Brownian relaxation time, $\tau = R^2/(k_BT/\eta_E R)$, is expected to be important. Here R is the particle radius, k_BT is the thermal energy, and η_E is the solvent viscosity at the shear rate $\dot{\gamma}$. For small Pe values Brownian motion dominates and the microstructure should be little disturbed from equilibrium. For large Pe values hydrodynamic convection dominates the particle microstructure. The role of particle volume fraction has been shown to be significant in determining equilibrium order and is expected to remain an important parameter at large Pe values. Given the results for oscillatory shear of the Bernal glass, the strain amplitude is expected to be a critical parameter in these studies. Finally the experimental run time is an important parameter because equilibrium microstructure may influence nonequilibrium microstructure[15], and a certain period of time is required to nucleate and grow equilibrium crystallites.

To determine the importance of the experimental run time in oscillatory shear experiments, measurements have been made of the dimensionless growth rate of crystals following a procedure similar to Aastuen et. al[16]. Here a sample in the coexisting liquid and crystal region or in the crystal region is shear melted by tumbling. The sample cell is then placed on a metallurgical microscope and illuminated by white light at an angle such that there is Bragg scattering into the objective of

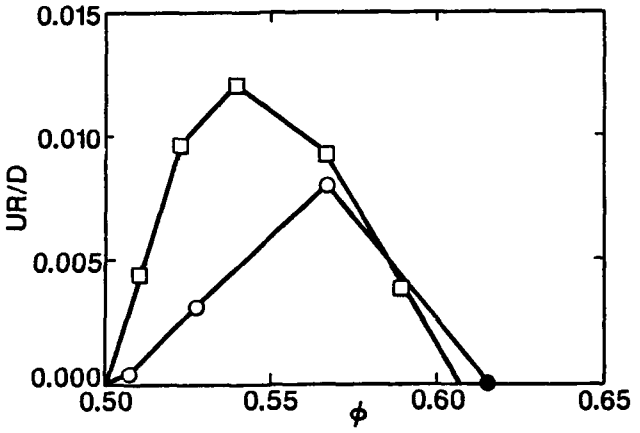


FIGURE 1. Dimensionless growth rate, UR/D, as a function of particle volume fraction. The symbols correspond to ○ data for the equilibrium coexisting phase or crystal phase samples, ● datum for the glass phase sample, and □ data from Pusey and van Megen as reduced in reference 17.

the microscope by the (111) planes of properly oriented crystallites. The size of these crystals, which form and grow near the bottom surface of the sample cell, are monitored. Figure 1 gives the dimensionless growth rate results for three different volume fractions greater than the freezing value. Here U is an average linear growth velocity of the crystals for the period of observation, before growth is hindered by the presence of other growing crystallites. D is the Stokes-Einstein diffusion constant for a single particle of radius R in the solvent. Stated differently, to achieve a linear crystallite dimension of 50um requires a time of 2600, 380 and 140 minutes for sample volume fractions 0.507, 0.527, and 0.565, respectively. Because the oscillatory shear experimental run times are only a few minutes, equilibrium crystal growth mechanisms will not produce crystals of macroscopic dimension during these experiments.

These dimensionless growth rate results agree qualitatively with more crude measurements made by Pusey and van Megen using smaller PMMA spheres suspended in decalin and carbon disulphide. These results[17] are also shown in figure 1. While our data increase with volume fraction due to the greater degree of supersaturation, it is suggested[17] that the growth rate should have a maximum and decrease due to the increase viscosity with volume fraction. Indeed, a sample with volume fraction 0.615 showed no evidence of crystallization for several months, and a zero growth rate is indicated for this sample by a ● in figure 1. However, this is misleading because there may be a large growth rate but failure to nucleate crystallites in this sample. It also should be mentioned that crystals of macroscopic dimension (50um) are observed more quickly after the first nucleation of crystallites in a given sample. Evidently, crystallites are not completely broken up by the shear melting process and serve as nuclei for subsequent growth. This is also indicated in our growth data which do not extrapolate to zero crystal radius at zero time. The larger growth rate values of Pusey and van Megen also are consistent with having finite size crystal nuclei at zero time, since the growth rate is determined from the time needed to produce a 50um crystal assuming zero crystal radius at

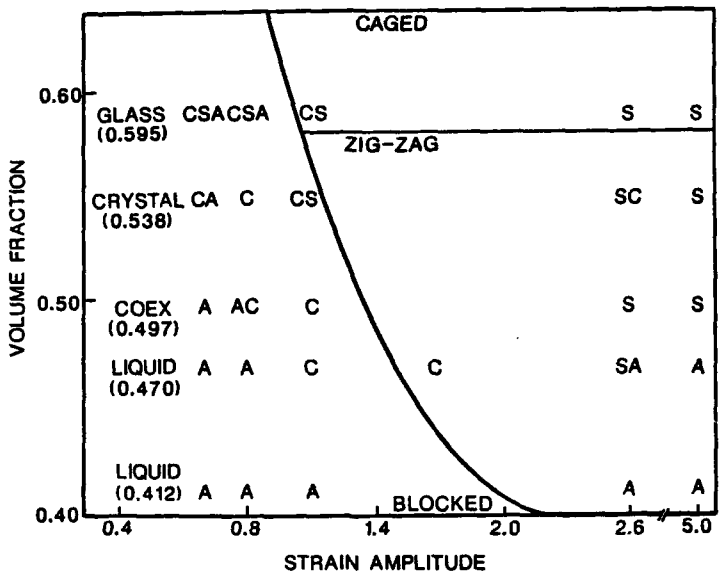


FIGURE 2. Shear oscillation microstructure phase diagram as a function of volume fraction and strain amplitude at 3.3 Hz. Here the symbols correspond to C - face centered cubic order, S - layer ordering, and A - amorphous order. The first symbol in a grouping indicates the predominant ordering observed. A face centered cubic order is allowed by the FCC model to the left of the nearly vertical solid line, while to the right a layer ordering is expected. Also indicated are the FCC model predictions for caging, blocking and zig-zag motion. (Reproduced from reference 6.)

zero time. Finally, we note that the growth rate for PMMA "hard" spheres is an order of magnitude greater than the growth rate for silica "hard" spheres[17]. It is not clear why this is so, but the PMMA particles may be slightly soft giving the greater growth rate.

For oscillatory shear studies[6] a concentric cylinder couette cell is used, which has a diameter of 2cm and a gap of 250um. A gap of up to 1mm was also used to check for gap size effects. None were observed. Because the sample is index matched and has an index of refraction nearly equal to that of glass, a laser beam [wavelength 442nm] may be directed through the sample at a variety of angles with respect to the local shear and velocity directions in the sample. Thus a large range of reciprocal space[11] [k-space] may be explored to aid in microstructure determination. A sample with a given volume fraction is injected into the cell and, before each oscillatory experiment, randomized to have a scattering pattern characteristic of amorphous microstructure. Each experiment consists of selecting a strain amplitude and oscillating the inner shear cell rotor at 3.3 Hz for a minute before making any observations of the scattered intensity patterns, which are videotaped for further analysis. The oscillation is continued up to about five minutes. While the pattern may sharpen in time, there seem to be no gross changes in the microstructure.

The results of the oscillatory experiments are presented in figure 2. At the smallest volume fraction $\phi = 0.412$ the equilibrium state has a

liquid microstructure and evidences a liquid or distorted liquid microstructure for all strain amplitudes applied in this experiment. The next larger volume fraction $\phi = 0.47_0$ is within a few per cent of the freezing value, and the sample has a liquid microstructure in equilibrium. At small strain amplitudes the microstructure has a distorted liquid order but evidences localized and temporally periodic intensity maxima which index to an FCC ordering and its twin for strain amplitudes near 1.5. The orientation of one of these twins is shown in the top of figure 3. At larger strain amplitudes stationary localized intensity maxima appear which correspond to a sliding layer structure also shown in figure 3. At even larger strain amplitudes the microstructure is again liquid-like. It is interesting to note that the crystalline FCC structures will melt away with the cessation of the oscillatory shear. At volume fraction $\phi = 0.49_7$, there are coexisting crystal and liquid phases in equilibrium. The dependence on strain amplitude is similar to the $\phi = 0.47_0$ volume fraction sample, except that the FCC structures are observed at smaller strain amplitudes and the layer structure extends to larger strain amplitudes. The $\phi = 0.53_8$ volume fraction sample has a polycrystalline structure in equilibrium but shows the oriented FCC structure at the smallest strain amplitudes. The transition to the layer structure occurs at even smaller strain amplitudes than the lower volume fraction samples. The glass sample, which has volume fraction $\phi = 0.595$, evidences a liquid or amorphous microstructure for months, if left undisturbed. However, small amplitude shear oscillations produce coexisting amorphous, layer, and FCC structures. Large amplitude strains produce a layer structure.

DISCUSSION AND INTERPRETATION

Layer microstructures have been observed in other concentrated particle suspensions undergoing steady shear flow[18,19]. Hoffman[20] has described this structure as hexagonal close packed planes of particles, where the planes are regularly spaced with respect to one another but randomly positioned parallel to the gap separating them. As the volume fraction increases, the gap separating the planes narrows until a volume fraction of 0.60 is reached, when the planes touch. Our data indicate less random positioning of the layers and a lower particle concentration in the layers than that suggested by Hoffman. A simple packing model[6] based on a sheared FCC lattice provides insight into the phenomena observed in our experiments. An FCC lattice is shown in figure 3a. The open circles represent a (111) hexagonal close packed layer. Another layer, the x's, are placed on this layer in one of two possible registration positions formed by the dips between particles in the open circle layer. To form an FCC structure, the third layer [the closed square] must be placed at a registration position on the x's over a hole in the open circle layer. If it is placed over a circle, then an HCP crystal structure results. When a shear flow is applied as shown in the figure, each layer shifts to the right to a new registration site in the layer below to produce an FCC twin structure. These FCC structures are the ones observed in our experiments.

The ability to move the layers in the fashion described above depends on the space available. The available space depends on the volume fraction occupied by the particles. If the volume fraction is less than 0.40, the model predicts that layers may slide freely over one another without hindrance. This is probably the reason that no induced FCC structure is observed in our lowest volume fraction sample. There is simply not enough restriction to force the particles into the FCC order. Between volume fraction 0.40 and 0.64 the model predicts that motion is restricted to oscillations between the two FCC twins with the degree of allowed strain being reduced with increasing volume fraction. The maximum strain value allowed by this model is shown in figure 2 as a line which extends from 2.1 at a volume fraction of 0.40 to 0.9 at a volume fraction of 0.64. The

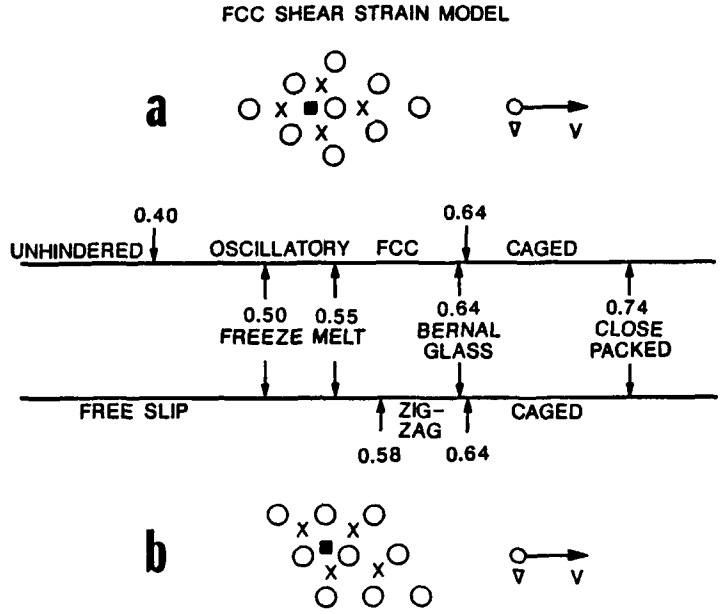


FIGURE 3. FCC model results showing the allowed shear strain motion at different volume fractions for two orientations of this closest packed crystal. (Reproduced from reference 6.)

experimentally observed FCC structures are largely to the left of this line in the allowed strain range. For the small volume fractions and the small strain amplitudes, the amorphous microstructure is observed. Here the Pe number is near unity and may not be large enough to produce the FCC structure described above. For volume fractions greater than 0.64, the particles become trapped in a cage of nearest neighbors and the conveyance of the layers to different registration sites is not allowed. Finally at a volume fraction of 0.74, the particles are touching and no motion is allowed.

For strains larger than that allowed by the oscillating FCC structure, a new particle microstructure is required to accommodate the flow. This is shown in figure 3b, where thehexagonal close packed layers have become oriented with respect to the velocity to allow more easy slippage of layers over one another. If rows of particles aligned parallel to the velocity are centered between corresponding rows in neighboring layers, then the layers may slip over one another without hindrance up to a volume fraction of 0.58. Above this volume fraction a zig-zag motion of layers is necessary. Again at a volume fraction of 0.64 particles become trapped in a cage of nearest neighbors and flow is hindered. These sliding layer structures are observed experimentally to replace the FCC structures for the large strain amplitudes in figure 2. The glass sample does evidence a tortured erratic motion at small steady shear flows, suggesting a zig-zag motion of layers. However, this becomes a smooth motion at large steady

shear flows before dilatant behavior is observed as an instability in the sample air interface. Thus, in general, the geometric model gives a reasonable explanation of the phenomena observed.

In terms of possible processing applications it should be noted that the observed FCC structures and layer structures appear homogeneous and uniform throughout the sample. While a sample may have a polycrystalline equilibrium structure, the oscillatory shear produces a single crystal which fills the whole sample volume. The scattered intensity maxima are broad indicating little long range order, but there is a large degree of orientational order. This is similar to the order proposed for the hexatic phase[21]. It is not known how perfect a long range order can be achieved in these samples by a sustained oscillatory shear or in an equilibrium polycrystalline sample, which has been processed by oscillation for a period of time and then left to anneal. The effect of oscillatory shear on mixtures of different particle sizes and on sedimenting samples remains to be investigated.

The authors wish to thank P. N. Pusey for helpful discussions and the Department of Energy for support of this work through grant DE/FG05/88ER45349.

REFERENCES

1. G.D. Scott, Nature 188, 908 (1960).
2. C. Kittel, Introduction to Solid State Physics, 5th ed. (Wiley, New York, 1976), chapter 1.
3. J.D. Bernal, Nature 183, 141 (1959).
4. G.D. Scott, A.M. Charlesworth, and M.K. Mak, J. Chem. Phys. 40, 611 (1964).
5. J.D. Bernal, Proc. Roy. Soc. 280, 299 (1962).
6. B.J. Ackerson, J. Rheol. (to be published).
7. W.G. Hoover and F.H. Ree, J. Chem. Phys. 49, 3609 (1968).
8. P.N. Pusey, J. Phys. (Paris) 48, 709 (1987).
9. S.E. Paulin and B.J. Ackerson, (submitted to the Physical Review Letters).
10. P.N. Pusey, W. van Megen, Nature 320, 340 (1986).
11. C. Kittel, Introduction to Solid State Physics, 5th ed. (Wiley, New York, 1976), chap. 2.
12. P.N. Pusey, W. van Megen, P. Bartlett, B.J. Ackerson, J.G. Rarity, and S.M. Underwood, Phy. Rev. Lett. 63, 2753 (1989).
13. B.J. Ackerson, J.B. Hayter, N.A. Clark, and L. Cotter, J. Chem. Phys. 84, 2344 (1986); P. Pieranski, Contemp. Phys. 24, 25 (1983).
14. I.M. Krieger, Adv. Coll. Interface Sci. 3, 111 (1972).
15. L.V. Woodcock, Phys. Rev. Lett. 54, 1513 (1985).
16. D.J.W. Aastuen, N.A. Clark, L.K. Cotter, and B.J. Ackerson, Phys. Rev. Lett. 57, 1733 (1986).
17. W.B. Russel, Phase Transitions, (to be published).
18. R. Patzold, Rheol. Acta. 19, 322 (1980).
19. R.L. Hoffman, Trans. Soc. Rheol. 16, 155 (1972).
20. R.L. Hoffman, J. Coll. Interface Sci. 46, 491 (1974).
21. D.R. Nelson and B.I. Halperin, Phys. Rev. B19, 2457 (1979); A.P. Young, Phys. Rev. B19, 1855 (1979); L.T. Shi and W. Krakow, Phys. Rev. B34, 7407 (1986).

CONSOLIDATION OF COLLOIDAL SUSPENSIONS

WEI-HENG SHIH,* SEONG IL KIM,* WAN Y. SHIH,* CHRISTOPHER H. SCHILLING,*† and ILHAN A. AKSAY*

*Department of Materials Science and Engineering; and
Advanced Materials Technology Center, Washington Technology Centers,
University of Washington, Seattle, WA 98195
†Pacific Northwest Laboratory,[1] Richland, WA 99352

INTRODUCTION

A key step in the processing of ceramics is the consolidation of powders into engineered shapes. Colloidal processing uses solvents (usually water) and dispersants to break up powder agglomerates in suspension and thereby reduce the pore size in a consolidated compact. However, agglomeration and particle rearrangement leading to pore enlargement can still occur during drying. Therefore, it is beneficial to consolidate the compact as densely as possible during the suspension stage. The consolidation techniques of pressure filtration and centrifugation were studied and the results are reported in this paper. In particular, the steady-state pressure-density relationship was studied, and information was obtained regarding the consolidation process, the microstructure, and the average density profile of consolidated cakes. We found that the compaction processes in these two consolidation methods are quite different. In general, a consolidated cake is a particulate network made up of many structural units which are fractal objects formed during aggregation in the suspension. In pressure filtration, compaction is a process of breaking up the fractal structural units in the particulate network by applied pressure; the resulting particle rearrangement is produced by overcoming energetic barriers which are related to the packing density of the compact. Recently, we performed Monte Carlo simulations on a cluster-cluster aggregation model with restructuring,[1] and found the exponential relationship between pressure and density is indeed the result of the breaking up of the fractal structural units.[2] On the other hand, in centrifugation, compaction involves the rearrangement of the fractal structural units without breaking them so that the self-similar nature of the aggregates is preserved. Furthermore, we calculated density profiles from the bottom to the top of the consolidated cakes by solving the local static force balance equation in the continuum particulate network. In pressure filtration of alumina and boehmite, the cakes are predicted to have uniform density. The results of γ-ray densitometry[3] on a pressure-filtrated alumina cake confirmed this prediction. In contrast, in centrifugation, the density profiles are predicted to show significant variation for cakes on the order of one centimeter high. Moreover, the pressure-filtered boehmite cakes showed no cracking during drying. This indicated that pressure filtration is a good consolidation technique for nanometer-sized particles such as boehmite. The improved drying property is probably a result of a minimal shrinkage due to the formation of higher packing densities during filtration.

PRESSURE FILTRATION

Pressure filtration of a colloidal suspension involves filtration of a fluid and compaction of a particulate network. The filtration part is described by the well-known Darcy's Law,[4] whereas the compaction of the solid part is less understood. During the early stages of filtration, pressure is applied to the suspension by means of a piston. At the final stage of filtration, the piston contacts the cake, and the cake is compressed (expression[4]). When the piston no longer moves and fluid no longer comes out of the filtrator, the system reaches

---

1 Pacific Northwest Laboratory is operated for the U. S. Department of Energy by Battelle Memorial Institute under Contract DE-AC06-76RLO 1830.

a steady state. We measured the cake density at the steady state by comparing the cake height to that of the initial suspension. The steady-state density as a function of applied pressure is shown in Figure 1 for both alumina and boehmite suspensions at various pH values. The Sumitomo AKP-30 alumina powders have a median diameter of 0.4 μm. The Vista Catapal-D boehmite powders are plate-like and have an approximate diameter of 50-100 Å and a thickness of 10-20 Å. The density was found to be a logarithmic function of the applied pressure:[5,6]

$$\varphi = A\ln(P / P_0) + \varphi_0 \tag{1}$$

where φ is the packing density (volume fraction) of solid particles, P is the applied pressure, φ_0 is a reference density, P_0 is the pressure at the reference density, and A is the slope. The reference density is chosen to be the packing density of the dispersed state, which is 0.65 for alumina.

The exponential relationship between pressure and density is the result of the compaction process and implies the breaking up of the fractal structural units in the particulate network due to the applied pressure. Resulting densification involves particles overcoming energetic barriers that are related to packing density. Here, we present an argument explaining how the exponential relationship may come about. The change in density $\Delta\varphi$ due to an increment in pressure ΔP, $\Delta\varphi / \Delta P$, is proportional to the probability of overcoming an energetic barrier for rearrangement, $\exp(-\alpha\varphi)$, where α is a constant. Here, it is implicitly assumed that the barrier height is proportional to the density. Therefore, we have $\Delta\varphi / \Delta P = \exp(-\alpha\varphi)$ which gives the exponential relationship between the pressure and the density after integration.

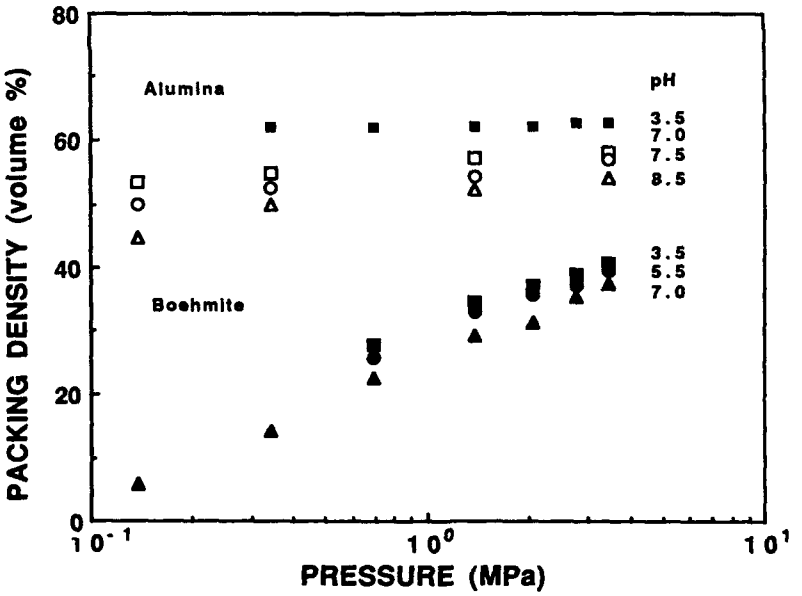


Figure 1 Packing density at steady state by pressure filtration as a function of applied pressure for micrometer-sized alumina and nanometer sized boehmite suspensions at various pH values.

The pressure-filtered boehmite cakes studied showed no cracking after drying for several days. However, a mullite-precursor gel made up of boehmite and silica particles needed to be dried very slowly over a few months' time in order to avoid cracking. The improved drying behavior is due to less shrinkage in pressure-filtered cakes. For the boehmite cakes we studied, typical shrinkage is around 10% compared with the typical 50% shrinkage of boehmite gels.[7] Less shrinkage produces less stress in the cakes and reduces the possibility of cracking.

CENTRIFUGATION

Centrifugation speeds up the sedimentation process of a suspension. However, the accelerating force is not uniform throughout the suspension and depends on the distance from the center of rotation. Buscall[8] showed that one can use an approximate mean force to describe the forces exerted on the sediment, provided the cake height is much smaller than the distance from the rotor center. We adopted Buscall's approach and estimated the mean pressure $\bar{P}$ as $\bar{P} = \omega^2(R - H_e)\varphi_0 H_0 \Delta\rho/2$ where ω is the angular velocity, R is the distance from the rotor center to the bottom of the cake, H_e is the cake height, φ_0 and H_0 are the initial concentration and suspension height respectively, and $\Delta\rho$ is the mass density difference between the particle and the solvent. The density as a function of the mean pressure is shown in Figure 2 for both alumina and boehmite suspensions. The pressure-density relationship can be described by a power law:

$$P = \beta\varphi^n \,. \tag{2}$$

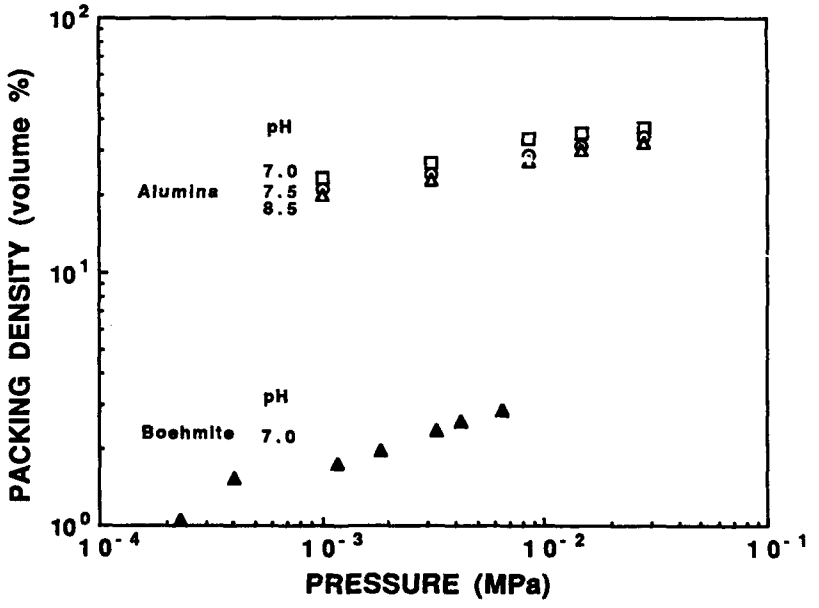


Figure 2 Packing density at steady state by centrifugation as a function of the mean pressure for micrometer-sized and nanometer-sized boehmite suspensions.

We can define an irreversible bulk modulus, K, as $K = -dP/d\ln V \sim dP/d\ln\varphi$ where V is the volume of a given cake.[9] Thereby, the irreversible bulk modulus behaves as $K = B\varphi^n$, where B is a constant. For boehmite cakes at pH = 7.0, results of Figure 2 can be used to calculate $K = 3.024\times10^{10}\varphi^{3.68}$ (dyne/cm^2). Previously we measured the storage moduli of boehmite gels at pH = 5.5 using a rheometer in the dynamic mode,[10] and the results are $G' = 4\times10^{9}\varphi^{4.1}$(dyne/cm^2). Similar power-law behavior for yield stress as a function of φ was also found in polystyrene latex suspensions by Buscall[11] with an exponent of 4.31.

We have developed a scaling theory[10] to relate K and φ, and results indicate that power-law behavior is attributed to the elastic deformation of fractal structures within the particulate network. Power-law behavior shown in Figure 2 indicates that the fractal structures formed during aggregation in the suspension may be preserved in the centrifuged cake. There appears to be very little restructuring, which is in direct contrast to the behavior observed in pressure filtration. The results for centrifuged alumina cakes can also be fitted to the form of equation (2) with $n \sim 8$ (Figure 2).

DENSITY PROFILE

With the results of the pressure-density relationship available (Figure 1), we can calculate the density profile from the bottom to the top of a consolidated cake. Based on local static force balance, Tiller et al.[4] have derived an equation for the pressure gradient within the solid network as

$$\frac{dP}{dZ} = -g\Delta\rho\varphi - \frac{\eta\varphi_l}{k}\left(\frac{q_l}{\varphi_l} - \frac{q_s}{\varphi}\right) \tag{3}$$

where Z denotes the distance from the bottom of the cake, g is the acceleration of gravity, $\Delta\rho$ is the mass density difference between the solid and the fluid, η is the viscosity of the fluid, k is the permeability of the cake, φ_l is the volume fraction of liquid, and q_l and q_s are the flux of the fluid and solid, respectively. In the final steady state, q_l and q_s are zero and we can ignore the second term on the right-hand side. Now we can substitute the empirical relationship between density and pressure, equation (1), in equation (3) to obtain a differential equation for the density profile. After integration, we obtain

$$Ei(\varphi/A) = Ei(\varphi_{max}/A) - \frac{\Delta\rho gA}{P_0}\exp(\varphi_0/A)Z \tag{4}$$

where $Ei(x)$ is the exponential integral

$$Ei(x) = \int_{-\infty}^{x}\frac{e^t}{t}dt\ . \tag{5}$$

In equation (4), the argument of the exponential integral is $x = \varphi/A$. The values of $Ei(x)$ are tabulated in mathematical tables. It should be noted that equation (4) describes the behavior of density profile when the packing density at the bottom of a cake φ_{max} is given. The present approach does not predict the value of φ_{max}. With the experimental data of A, P_0, φ_0, and φ_{max} for a particular material, the density profile can be calculated. For alumina at pH = 8.5, with $\varphi_{max} = 0.5$, we get $Ei(\varphi/A) = 352.5 - 8.2\times10^{-3}Z$, provided Z is measured in cm. This indicates that the density profile is constant since the first term on the right-hand side is much larger than the second term. Similarly, for boehmite cakes at pH = 3.5, with $\varphi_{max} = 0.3$, we get $Ei(\varphi/A) = 3.8 - 0.4\times10^{-4}Z$. Therefore for pressure filtration, the consolidated cake is predicted to have a uniform density profile from the bottom to the top of the cake. Recently, we measured the density profile of pressure-filtered cake using γ-ray densitometry.[3] For alumina at pH = 8.5, the density profiles are shown in Figure 3. As is clear, in the final steady state, the density profile is uniform. Therefore, our prediction

based on the empirical pressure-density relationship is in good agreement with the direct density profile measurement.

The density profile of centrifuged cakes can be calculated similarly. There are two differences, however, from the pressure filtration calculations. First, the acceleration of gravity, g, should be changed to the corresponding effective acceleration of gravity, $g_e = \omega^2 R$, assuming $H_e << R$. Second, the pressure-density relationship is changed to a power-law behavior, equation (2). Incorporating these two changes, we obtain the equation of the density profile for centrifugation:

$$\varphi^{n-1} = \varphi_{max}{}^{n-1} - \frac{(n-1)}{\beta n} \Delta\rho g_e Z \ . \tag{6}$$

For alumina with pH = 8.5, $\varphi_{max} = 0.4$, and $g_e = 824g$, we have $\varphi^{7.27} = 1.3\text{x}10^{-3} - 2.57\text{x}10^{-4}Z$. Whereas for boehmite at pH = 7.0, $\varphi_{max} = 0.03$, and $g_e = 824g$, we have $\varphi^{2.68} = 8.29\text{x}10^{-5} - 2\text{x}10^{-6}Z$. Based on these equations, it can be seen that for a typical cake height of 1 cm, there will be significant density variations with elevation. The density profile of flocculated alumina at pH = 8.5 in gravitational sedimentation has been studied by γ-ray densitometry.[3] The density profile showed sharp decreases from the maximum density at the bottom, in qualitative agreement with our prediction.

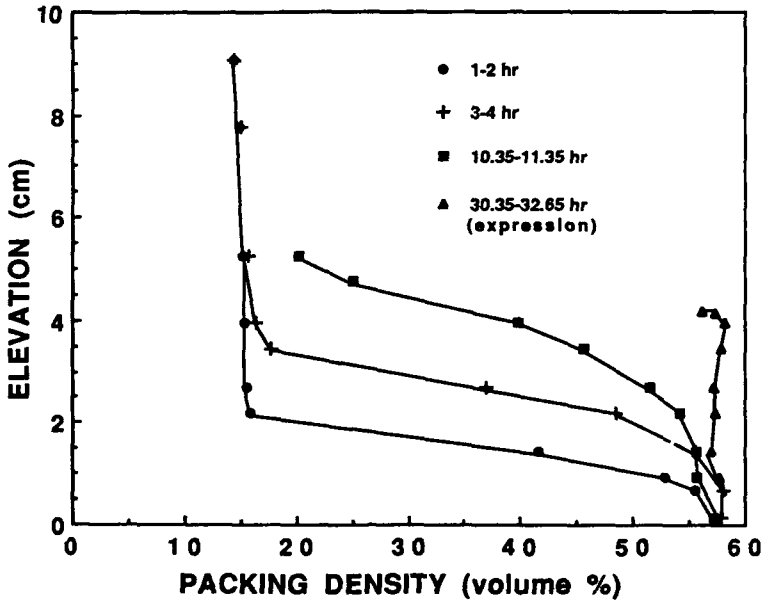


Figure 3 Density profiles of a pressure-filtered alumina cake (pH = 8.5) at various time steps, based on γ-ray densitometry. The density profile at steady state (expression) is uniform with elevation.

SUMMARY AND DISCUSSION

Two consolidation techniques, pressure filtration and centrifugation, were studied and the steady-state pressure-density relationships obtained. It was found that for pressure filtration the pressure-density relationship has an exponential form. The exponential form implies that compaction is a restructuring process where the movement of particles requires overcoming energetic barriers which are proportional to packing density. For centrifugation, the pressure-density relationship exhibits a power-law behavior. Power-law scaling suggests that the centrifuged cakes contain fractal aggregates which were formed during aggregation. The two consolidation techniques involve different compaction processes, resulting in different structures within each cake. Furthermore, we calculated the density profile within the cake, using the empirical pressure-density relationship. The pressure-filtered cakes are predicted to have uniform density profiles. The constant density profile was confirmed by the results of γ-ray densitometry on a pressure-filtered alumina cake. On the other hand, centrifuged cakes are predicted to show density variations for cakes a few centimeters in thickness. Previous γ-ray densitometry results on sedimented alumina cakes showed significant density variations, in qualitative agreement with the prediction.

Finally, we comment on the validity of equation (2). The data in Figure 2 can also be fitted to the form of equation (1) due to the finite number of data points. However, when the data is fitted to equation (1), the irreversible modulus is too large to be physically reasonable. For instance, for boehmite cakes with pH = 7.0 at $\varphi = 0.1$, the power-law fit gives $K = 6.3 \times 10^{6}$(dyne/cm^2), whereas when fitted to the logarithmic form of equation (1), it gives 1.3×10^{11}(dyne/cm^2). Therefore, the power-law behavior of equation (2) is indeed more appropriate for description of the centrifuged cakes.

ACKNOWLEDGMENTS

This work was supported by the Air Force Office of Scientific Research (AFOSR) and the Defense Advanced Research Projects Agency (DARPA) under Grant No. AFOSR-87-0114 and the Office of Basic Energy Sciences, U.S. Department of Energy, through a subcontract by Pacific Northwest Laboratory under Contract No. 063961-A-F1.

REFERENCES

1. W. Y. Shih, I. A. Aksay, and R. Kikuchi, *Phys. Rev. A*, **36**, 5015 (1987).
2. W. Y. Shih, W.-H. Shih, and I. A. Aksay, in ***Physical Phenomena in Granular Materials, MRS Symp. Proc.***, Vol. 195, edited by T. H. Geballe, P. Sheng, and G. D. Cody (Materials Research Society, Pittsburgh, PA, 1990), submitted.
3. C. H. Schilling, G. L. Graff, W. D. Samuels, and I. A. Aksay, in ***Atomic and Molecular Processing of Electronic and Ceramic Materials: Preparation, Characterization, and Properties, MRS Conf. Proc.***, edited by I. A. Aksay, G. L. McVay, T. G. Stoebe, and J. F. Wager (Materials Research Society, Pittsburgh, PA, 1988), p. 239.
4. F. M. Tiller, C. S. Yeh, C. D. Tsai, and W. Chen, *Filtration & Separation*, **24**, 121 (1987).
5. W.-H. Shih, J. Liu, W. Y. Shih, S. I. Kim, M. Sarikaya, and I. A. Aksay, in ***Processing Science of Advanced Ceramics, MRS Symp. Proc.***, Vol. 155, edited by I. A. Aksav, G. L. McVay, and D. R. Ulrich (Materials Research Society, Pittsburgh, PA, 1989), p. 83.
6. F. Lange and K. T. Miller, *Am. Ceram. Soc. Bull.*, **66**, 1498 (1987).
7. D. S. Horn and G. L. Messing, *J. Am. Ceram. Soc.*, **72** (9) 1719 (1989).
8. R. Buscall, *Colloids and Surfaces*, **5**, 269 (1982).
9. T. J. Fennelly and J. S. Reed, *J. Am. Ceram. Soc.*, **55** (8) 381 (1972).
10. W.-H. Shih, W. Y. Shih, S. I. Kim, J. Liu, and I. A. Aksay, *Phys. Rev. A*, submitted.
11. R. Buscall, I. J. McGowan, P. D. A. Mills, R. F. Stewart, D. Sutton, L. R. White, and G. E. Yates, *J. Non-Newtonian Fluid Mech.*, **24**, 183 (1987).

RHEOLOGY AND MICROSTRUCTURE OF CONCENTRATED SUSPENSIONS

LISA A. MONDY* AND ALAN L. GRAHAM**
*Sandia National Laboratories, Division 1511, Albuquerque, New Mexico 87185
**Los Alamos National Laboratory, MEE-4, Los Alamos, New Mexico 87545

ABSTRACT

We give an overview of some of the experiments currently underway to study the coupling of the microstructure and rheology of concentrated suspensions. Nuclear magnetic resonance imaging, real-time x-ray radiography, and refractive index matching allow the viewing of particles in concentrated suspensions. Both shear flow experiments and falling ball rheometry are reviewed. In the slow flow of these suspensions of large, hard, particles in a viscous Newtonian fluid, colloidal forces are negligible and hydrodynamic forces dominate.

Large local concentration changes are shown to occur rapidly in suspensions of uniform spheres subjected to flow between concentric rotating cylinders. Suspensions of spheres with a bimodal size distribution not only show similar phenomena, but also exhibit particle separation according to size. In addition, the large particles in the bimodal suspension migrate into ordered, concentric, cylindrical sheets, parallel to the axis of the cylinders. These sheets of particles rotate relative to each other. The particle migration and structure formation induced by this inhomogeneous shear flow is believed to be responsible for torque reductions and other anomalous behavior witnessed during the rheological testing of concentrated suspensions reported in the literature. Thus, suspensions may not always be characterized by a viscosity that is a scalar material property.

Suspensions of fibers also show markedly different rheological properties when the particles are aligned by flow. Falling ball rheometry is shown to be an effective tool to determine the bulk viscosity of a suspension while only slightly influencing the microstructure. This is illustrated by showing that falling ball rheometry can isolate the effect of orientation on the viscosity of a suspension of fibers.

INTRODUCTION

The microstructure of a concentrated suspension influences the macroscopic flow properties of that suspension and, therefore, affects such processes as injection molding of ceramics or the incorporation of reinforcing fibers into ceramics. In turn, the flow of the suspension influences the microstructure in a tightly coupled process.

Migration and ordering of suspended particles have been hypothesized to cause viscosity measurements that vary with total strain of a sample.[1,2] Microstructural changes in the shear flow of colloidal suspensions of both spheres and fibers have been inferred via light scattering techniques.[3,4] We observe similar phenomena in suspensions of large spheres (600 μm < diameter < 3.2 mm) using nuclear magnetic resonance (NMR) imaging. This noninvasive technique has recently shown great potential in the study of two-phase flow.[5] The experiments discussed in this paper were performed in collaboration with Drs. S. A. Altobelli and Eiichi Fukushima of Lovelace Medical Foundation.

We show that NMR imaging allows the study of flow-induced particle migration in concentrated (solids volume fraction $\geq$ 0.50) suspensions. Concentration profiles are easily determined, and good spatial resolution obtained. When subjected to flow between

Mat. Res. Soc. Symp. Proc. Vol. 180. ©1990 Materials Research Society

rotating concentric cylinders, neutrally buoyant particles migrate away from the inner rotating rod toward the outer fixed cylinder. This migration occurs in suspensions of monodisperse and bidisperse spheres. The monodisperse spheres migrate until the region of lowest shear rate (near the outer wall) contains approximately the maximum concentration of spheres possible for random packing. A similar migration occurs in suspensions of bidisperse spheres. Furthermore, in these bimodal suspensions, concentric bands of larger particles form after shearing. Visual observations of opaque particles in bands near the outer wall of the apparatus show that the larger spheres are arranged in two-dimensional hexagonal close-packed (hcp) sheets that rotate relative to each other.

This is a dramatic illustration of shear-induced formation of structure in suspensions. If such phenomena are caused by shearing a suspension, then one must confront the need to determine the viscosity of a suspension without *changing* the suspension viscosity through the very act of *measuring* it. Conventional viscometers all employ flow fields that tend to influence the microstructure of the suspension. For example, suspended fibers, if not subject to strong, randomizing, rotary Brownian forces, will tend to align in shearing flow; hence, the measurements will be performed on suspensions having flow-induced anisotropy.

We show that falling ball rheometry may be used to determine the bulk viscosity of a suspension with little effect on the microstructure of the suspension. If the size of the probe (the falling ball) is of the order of the characteristic length of the suspended particles, the ball disturbs the original microstructure of the quiescent suspension only slightly as it falls. We discuss experiments, performed in collaboration with Dr. R. L. Powell of University of California–Davis and Dr. M. Gottlieb of Ben Gurion University, Israel, which illustrate the use of falling ball rheometry to determine the viscosity of suspensions both of randomly oriented rods and of approximately aligned rods. We find that the viscosity in the direction of the aligned rod axes is significantly lower than that with the rods randomly oriented. Furthermore, the viscosity of the oriented rods agrees well with the viscosity measured with rotational rheometers, implying that the rod alignment we set may mimic that induced by shear flow.

NMR imaging experiments showing shear-induced ordering of suspensions of spheres will be detailed in the following section. The third section will discuss real-time radiography and index-matching techniques that allow falling ball rheometry in suspensions of both spheres and fibers. Here, we will discuss falling ball rheometry as a tool to explore the effect of microstructure on the bulk viscosity.

SHEAR-INDUCED DIFFUSION AND CRYSTALLIZATION IN SUSPENSIONS OF SPHERES

NMR Imaging

The distribution of particles and suspending fluid in concentrated suspensions is difficult to measure because observation of the interior of a flow field is obstructed by the high particle density. Most suspensions are opaque even at relatively low particle concentrations. However, the noninvasive method of NMR imaging does allow analysis of the particle distribution profiles in such suspensions. Background material on basic NMR phenomena can be found in standard NMR textbooks.[6,7] Some details of our specific use of NMR imaging techniques will be given in the following paragraphs.

Experiments involving the flow of concentrated suspensions between rotating concentric cylinders currently are being performed in collaboration with Drs. Steve Altobelli and Eichii Fukushima at Lovelace Medical Foundation. They have developed the capability of imaging suspensions using a horizontal bore, superconducting, 1.9 T magnet controlled by a NALORAC, Inc. (Martinez, CA) imaging/spectrometer system. The precisely timed sequence of gradient and rf pulses and data acquisitions used is an adaption of a "spin-warp" technique.[7] A single 100-mm "birdcage" type rf coil[8] generates the rf pulses and detects the NMR signal in these experiments. The signal is extracted from the spectrometer and is processed offline. The original time-domain data are acquired in quadrature and images are calculated from these data by two-dimensional Fourier transformation. Each time-domain data set is a 128 by 128 complex array obtained by averaging the results of four to eight phase-cycled image acquisition sequences to optimize the signal-to-noise ratio. The modulus of each resulting picture element of the image is mapped to intensity or color for display.

The fluid in the imaged slice of sample gives a full-intensity signal and the particles give no signal. The normalized value of the image intensity is proportional to the density of the liquid phase protons in a volume element. The NMR image then can not only provide visualization of the particle structure but also quantitative information about the concentration of particles as a function of location.

The Couette Flow Experiments

We will discuss the results obtained when two highly concentrated, model suspensions were subjected to wide-gap, annular, Couette flow. Both suspensions consisted of polymethyl methacrylate (PMMA) spheres in a Newtonian oil. The spheres in the first suspension were approximately monodisperse with a mean diameter of 600 μm. The spheres in the second suspension were a mixture of 720-μm-mean-diameter spheres and individually ground, 3.175-mm-diameter spheres (Clifton Plastics Company) to form a bimodal size distribution. Thirty-five percent by volume of the particles in this suspension were the small spheres and 65% by volume were the large spheres. Total solids contents of the two suspensions were 50 vol% and 60 vol% for the suspensions with monomodal and bimodal size distributions, respectively.

The Newtonian suspending liquid used is discussed in detail in the section entitled "Refractive Index Matching to Produce Transparent Suspensions". This composition was chosen to match the density of the PMMA spheres at 21.5°C (1.185 g/cm^3). Although the temperature of each suspension was controlled only by the room air conditioner, no settling of the suspended particles was detected over the duration of the experiments. This liquid has been used in our laboratory in experiments based on optical techniques because it also matches the refractive index of the PMMA; however, this property is not necessary when using the NMR technique. The viscosity of the suspending liquid was 4.95 Pa·s at 21.5°C.

Two concentric cylinder (Couette) devices were built. Each consisted of a rotating solid PMMA cylinder concentric in a fixed outer PMMA tube capped with solid PMMA disks. These were wide-gap Couette devices designed to produce an inhomogeneous shear field in the gap. The gap sizes used corresponded to about 32 times the diameter of the particles in the monomodal suspension and about 7 times the diameter of the large spheres in the bimodal suspension. The inner rod was turned at approximately 48 rpm by a variable speed motor. This gave shear rates from about 1 to 10 sec^{-1} (assuming a Newtonian fluid response) across the gap of either apparatus.

The motor was stopped periodically and NMR images were taken of the resulting particle structure. Because buouyancy, Brownian, and surface forces were negligible in these suspensions, no particle movement was expected to occur in the few minutes it took to collect an NMR image. End effects were minimized by making the length-to-diameter ratio of the device sufficiently large and examining each sample specimen near its center. Images were taken of a cross section of the Couette, perpendicular to the Couette axis, about midway along the apparatus. This slice was 24 mm thick in the axial direction.

For each image the centroid of the image was computed, corresponding to the Couette axis. Then the average values of the image intensity in concentric annuli about the centroid were computed. These values were normalized so that the average intensity of the image depicting the initial state matched the known fluid fraction. Thus, with this relative calibration we could estimate the fluid fraction in each concentric annuli of each image, giving the fluid fraction as a function of radius and time (or strain).

The resulting information on fluid fraction as a function of radial distance from the axis of the device showed that substantial particle migration away from the inner rod began to happen immediately upon rotation of the inner rod. With the monomodal suspension, the inner rod was stopped for the first time after 10 revolutions and NMR images were taken. The fluid fraction near the inner rod increased noticeably after only 10 revolutions of the inner rod. The radial distribution of particles did not appear to change substantially after 2500 revolutions. The data taken at this point, apparently at steady state, indicate that the fluid fraction had reached a low of about 0.40 at the outer cylinder. This corresponds to a solids fraction of about 0.60, a value near the maximum value for random packing of monodisperse spheres (0.63). A reviewer pointed out that closest packed (hcp) layers of spheres randomly stacked upon one another, but free to slip, occupy a volume fraction of 0.60. However, details of the packing structure for monodisperse spheres will have to wait for the results of experiments currently underway using higher resolution NMR imaging on suspensions of larger monodisperse particles.

After steady state was obtained with clockwise revolutions of the inner rod, the motor was reversed and the inner rod was rotated counterclockwise for approximately the same number of revolutions. The data remained unchanged with the reverse rotation, and, therefore, the particle-concentration distribution remained at the steady-state value. This irreversibility is consistent with the proposed mechanisms of shear-induced migration of particles or "hydrodynamic diffusion" down a shear-field gradient.[1,9]

The particle migration occurred almost entirely in the radial direction. No significant axial migration of colored marker particles was detected in the bimodal suspension. Furthermore, NMR images taken near the ends of the Couette device were not noticeably different from those taken at the center of the device.

For the suspension of spheres with a bimodal size distribution, changes in the concentration profile of the suspension were again seen very quickly upon rotating the inner rod. The initial and final images are shown in Figure 1, with the light areas indicating the presence of liquid. Individual large spheres can almost be distinguished, although the thickness of the imaged volume results in a blurring of the particles. The initial state looks relatively uniform with the particles dispersed randomly. In the final image, the bright area near the inner cylinder represents a higher fluid fraction, indicating that the fluid fraction is significantly higher near the inner rod (the region of highest shear rate) and lower near the outer cylinder. In addition, definite indications of structure can be seen as the fluid fraction oscillates rather than decreases monotonically with radial position. We can see distinct bands of larger spheres interspersed with fluid and smaller spheres. From visual observations of the band near the outer wall of the apparatus, the larger spheres in this layer appear to be hexagonal close-packed. Although individual small spheres cannot

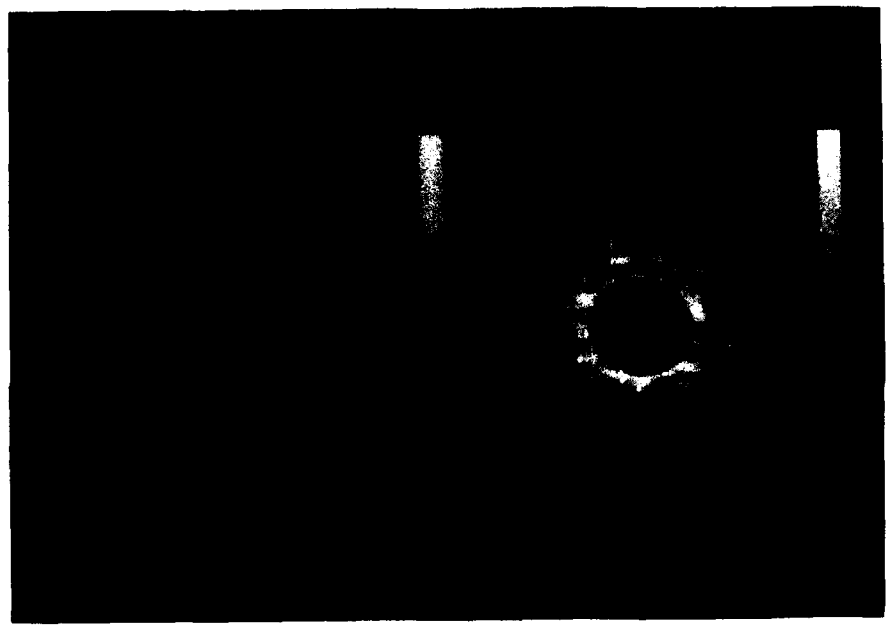


Figure 1. NMR images of a cross section of the suspension of 60 vol% bidisperse spheres between concentric cylinders. The image on the left represents the initially well dispersed state of the suspension. The image on the right was taken after rotating the inner cylinder until steady state was achieved.

be distinguished at this resolution, we infer from the concentration data that the smaller particles are interspersed throughout the suspension but are predominantly in the regions between the outermost layers of large spheres. One way to look at this phenomenon is to consider the concentric shells to be formed in order to minimize the force necessary to turn the center rod. This conjecture is corroborated by our observation that the torque required to turn the center rod decreases with increasing number of rotations until steady state is achieved.

FALLING BALL RHEOMETRY IN CONCENTRATED SUSPENSIONS

Real-Time X-Ray Radiography

Radiography using penetrating radiation such as x rays is another method to image opaque suspensions. If the imaging is on a fluor, the image may be electronically amplified, observed by a video camera, and recorded on videotape. This technique allows the tracking of high-Z-number tracer particles within the suspension.

We have used a variety of x-ray generators in this technique. Most commonly we use a fixed x-ray generator, manufactured by Philips, to produce a beam with a 150 kV constant potential, a 20 mA current, and a 1.2 mm focal spot size. The beam is collimated to limit the radiation beam to the area of inspection, minimizing unwanted, scattered radiation that could interact with the fluor and degrade the image. A high-energy x-ray image intensifier, manufactured by Science Application Inc., is used to convert the x-rays to light. This system offers a choice of three sizes (100, 150, or 230 mm diameter) for the x-ray field of view. Once formed, the radiographic image is viewed by a video camera placed at the output of the image intensifier. Video recording of the image allows immediate playback of the event.

The use of two complete x-ray systems focused on the same point provides a stereo view of the tracer particles for three-dimensional tracking. The video system can support two cameras simultaneously. The use of split-screen recording ensures the synchronization of the two images. With this stereo view, we obtain four screen coordinates to determine three spatial coordinates of the centroid. This is an overdetermined systems problem that lends itself to linear regression analysis. In collaboration with Prof. Howard Brenner and Mr. James R. Abbott, both of M.I.T., we have used the process described by Walton[10] to determine the laboratory-fixed coordinates from the camera coordinates.

The accuracy in laboratory space depends on the field of view, determined by the needs of the particular experiment. In the experiments on model suspensions, discussed in the following subsections, an area about 150 × 75 mm is imaged on each split screen. This implies that the accuracy in the measured position of the particle is within 0.02 cm. (However, note that with an x-ray microfocus, a typical field of view is only 10 mm × 10 mm, and very small particles can be tracked accurately. We have successfully tracked steel balls with diameters of 432 μm, both while they were settling in a propellant simulant and while they were moving with the simulant in capillary flow.[11])

Refractive Index Matching to Produce Transparent Suspensions

Although real-time radiography has the distinct advantage that it can be used with any opaque suspension, the tracking of tracer particles can be accomplished optically in a transparent suspension. We have developed the three-component, Newtonian liquid, mentioned previously, that matches both the refractive index and the density of PMMA. Therefore, transparent suspensions of neutrally buoyant PMMA particles can be made.

This suspending liquid is a solution of practical grade 1,1,2,2 tetrabromoethane (TBE) from Eastman Kodak (14.07% by weight); UCON oil (H-90,000), a polyalkylene glycol made by Union Carbide (35.66% by weight); and Triton X-100, an alkylaryl polyether alcohol from J. T. Baker (50.27% by weight). A small amount (about 0.1% of the weight of TBE) of Tinuvin 328, made by Ciba-Giegy, is dissolved in the TBE before mixing to prevent the breakdown of TBE when it is subjected to UV radiation. Similar solutions with various viscosities can be made by using different UCON oils, which can be purchased in a wide range of viscosities.

Failing Ball Experiments and Suspensions of Spheres

Both of the methods discussed above have been used by us and by our coworkers to track the path of a dense sphere settling slowly through a quiescent suspension. In a single-phase Newtonian liquid, the terminal velocity of the sphere is directly related to the liquid viscosity by Stokes' law,[12] corrected, if needed, for the increased drag on the sphere that occurs because of the presence of the container walls.[13] In a suspension an apparent viscosity can be measured as if the suspension were representable as a hypothetical Newtonian liquid.[14]

We have measured the viscosities of suspensions of 5% to 55% by volume of uniform PMMA spheres in various density-matched Newtonian liquids, usually a mixture of UCON oil and TBE. Suspended spheres from 3.18 mm to 12.7 mm in diameter have been used. A ball composed of any metal such as brass, nickel, or tungsten carbide is a sufficient x-ray attenuator, relative to the liquid, the suspended particles, and the container, to produce an x-ray image that can be tracked as the ball falls through the suspension. Balls of opaque plastic, glass, aluminum, and corrundum have also been used in transparent suspensions. Typically, we use balls of a size fairly close to that of the suspended spheres. The suspensions are held in temperature-controlled cylindrical columns and are stirred before each experiment to achieve a uniform distribution of suspended particles.

The discrete nature of the suspension is readily apparent in falling ball experiments. We observe that a large ball falls smoothly through a suspension of smaller particles and its velocity appears fairly constant. Passage of a ball of the same diameter as the suspended particles is extremely erratic. Periods of almost no motion, as the falling ball approaches and "rolls off" suspended particles, alternate with periods of almost free fall in the interstices between suspended spheres. However, a statistical analysis reveals that the *average* terminal velocity of the ball, measured over a distance (usually between 100 and 1000 suspended particle diameters), is reproducible.

Furthermore, if this terminal velocity, corrected for Newtonian wall effects, is translated into a viscosity, this viscosity is independent of the size of the falling ball relative to the diameter of the suspended spheres over a wide range of falling ball sizes. (Anomalous behavior can occur with very small or very large balls, though.[15,16]) For moderately concentrated suspensions (below about 30% solids), the average relative viscosity (η_r, the viscosity of the suspension normalized by the suspending fluid viscosity), agrees with independent measurements taken in shear and capillary rheometers[17] (Figure 2). These rheometers generally indicate that moderately concentrated suspensions of spheres behave as Newtonian fluids, without the anomalous strain-dependent results of the higher concentrations. Therefore, the falling balls experience the same average resistance to motion that they would experience if the effects of the numerous surrounding spheres were replaced by a hypothetical, Newtonian, one-phase fluid, characterized by the suspension viscosity.

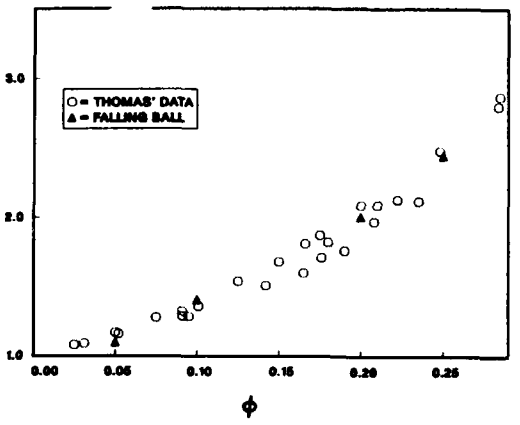


Figure 2. Comparison among the relative viscosities of spherical particle suspensions measured using falling ball rheometry and those measured using shear and capillary rheometers.[17]

Falling ball rheometry, using relatively small balls, then can determine the bulk shear viscosity of a suspension *while only slightly modifying the suspended particle distribution.* In collaboration with Professor Brenner and Mr. Abbott, we are exploring the possibility of using the fluctuations in the terminal velocity, as the ball interacts with individual suspended particles or clusters of suspended particles, to give information about the suspension microstructure.

Falling Ball Experiments and Suspensions of Rods

An illustration of the use of falling ball rheometry as a tool to measure viscosity without unduly influencing the microstructure of the suspension can be found in recent work with suspensions of rodlike particles.[18–20] For suspensions of non-Brownian rods in Newtonian fluids, viscometric and elongational flows, the usual tools of rheologists, induce an alignment of the rods. With falling ball rheometry the initial orientational distribution of the rods can be controlled and fiber-aligning effects of the flow field are minimal.

Experiments were performed in collaboration with Drs. W. J. Milliken, R. L. Powell, and M. Gottlieb to determine the macroscopic viscosity of suspensions of randomly oriented rods.[18,19] Large rods (typically 1.596-mm diameter) were suspended in density-matched Newtonian liquids. The particles were well characterized, and suspensions with various particle aspect ratios and concentrations were tested. As in the tests with suspension of spheres, the suspensions were placed in temperature-controlled cylindrical columns and were stirred before each experiment to achieve a random distribution of particles. The average viscosity given by a ball of specific size was determined by measuring the terminal velocity of at least 10 or 20 identical balls. Again, balls of various sizes all yielded the same average viscosity.

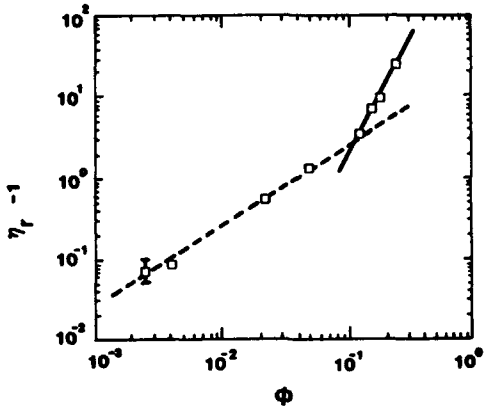


Figure 3. Specific viscosity (measured with falling ball rheometry) of suspensions with various volume fractions (ϕ) of randomly oriented, aspect-ratio-19.83 rods. The equations representing the least-squares fits (the dashed and solid lines) to the data are $\eta_r - 1 = 28.5\phi^{1.01}$ for $\phi < 0.125$ and $\eta_r - 1 = 2040\phi^{3.01}$ for $\phi > 0.125$.

The principal results of experiments using suspended rods with aspect ratio of 19.83 are shown in terms of the specific viscosity ($\eta_r - 1$) in Figure 3. The viscosities of the suspensions vary linearly with solids volume fraction below a volume fraction of about 0.125. Therefore, linear behavior is observed at volume fractions much higher than previously expected and considerably higher than is found with suspensions of spherical particles. However, this critical volume fraction where the transition between dilute (linear) and (semi)concentrated behavior occurs is remarkably similar to that predicted for solutions of rodlike macromolecules, as is the dependence of the specific viscosity on the cube of the concentration after this transition.[21-23] Steric effects, present both in the solutions of macromolecules and the suspensions, may account for the similarity in behavior.

Unlike with suspensions of spherical particles, here we cannot compare the falling ball measurements with shear flow measurements because the latter measurements cannot be done on a similar suspension of *random'y distributed* rods. The flow necessarily sets up a different structure of particles in the suspension. However, theoretical predictions by Brenner exist for suspensions of rods subject to strong Brownian motion.[24] Furthermore, the work by Haber and Brenner shows that these suspensions of Brownian rods behave in shear flow exactly as would suspensions with sustained random distributions of particles.[25] Therefore, we can compare these experiments at large Peclet numbers with the theory for Brownian particles. The intrinsic viscosity predicted by Brenner for suspensions of rods of this aspect ratio is 29.2, and the experimental results of 27.6 differ from this by only 5.8%. Further experiments with other aspect ratio rods also show very good agreement with theory.[19,26]

In these falling ball measurements, the suspensions were stirred before each experiment to ensure that the suspensions were isotropic. In a following series of experiments, the suspended rods were approximately aligned before each measurement so that the suspensions were anisotropic.[20] The large, neutrally buoyant rods were oriented hydrodynamically by passing a fixture through the suspension. This produced a local flow that tended to align the particles along the axis of the column containing the suspension. Here,

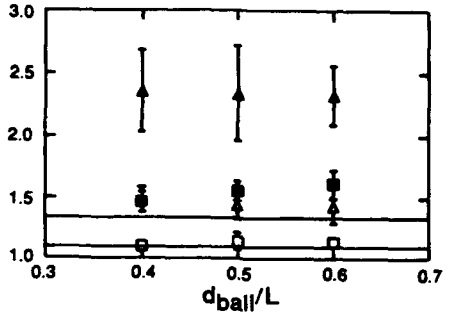


Figure 4. The relative viscosity vs. dimensionless ball diameter (diameter of the falling ball divided by the length of the suspended rods) for suspensions of aligned rods as measured using falling ball rheometry. Suspensions of various volume fractions are represented: $\phi = 0.02$ ( ), $\phi = 0.05$ ( ). Also shown are the relative viscosities of suspensions of randomly oriented rods: $\phi = 0.02$ ( ), $\phi = 0.05$ ( ), and lines representing data obtained in shearing flows.

the falling ball measurements yielded an apparent viscosity (in the direction parallel to the axis of the cylinder) that was substantially less than that for a suspension having the same volume fraction of the same rods in a random configuration. The results are shown in Figure 4. In addition, the viscosities measured for the suspension of aligned rods closely correlated with the viscosities of suspensions of short fibers (having similar aspect ratios and concentrations) measured in shearing flows.[27] This implied that such alignment may mimic the flow-induced orientation found in rotational rheometers. These results showed the possibility of using falling ball rheometry to determine a viscosity dependent on the measurement direction (a viscosity *tensor*) for anisotropic suspensions.

CONCLUSIONS

With techniques such as NMR imaging, real-time radiography and refractive-index matching, we have been able to view the movement of particles in concentrated suspensions. Experiments using these techniques have shown that suspensions may not always be characterized by a scalar material property such as the term "viscosity" implies. Instead, flow may induce particle arrangements that affect the bulk flow properties of the suspension. In other words, the suspension would yield different measured macroscopic viscosities in different flow fields. We have presented here an illustration of flow-induced structure in the form of NMR images taken of a concentrated suspension undergoing inhomogeneous shear in a wide-gap Couette apparatus. The measurements of viscosity taken in such a flow field would depend on the total strain and, hence, on the time of the measurement, until a steady-state particle arrangement formed.

In contrast, falling ball measurements show that a *homogeneous isotropic* suspension often behaves as would a single-phase Newtonian liquid. These measurements, however, have little effect on the structure of the suspension because the probe (the falling ball) size is fairly small compared with the size of the suspended particles. Experiments using suspensions of rods illustrate that falling ball rheometry may be a useful tool to isolate the effects of particle orientation on the bulk viscosity and, furthermore, to probe the relationship between the suspension microstructure and its macroscopic properties.

ACKNOWLEDGMENTS

Many colleagues not explicitly mentioned in the text were also involved in various aspects of the work presented here. In chronological order they were Ms. Julie Jensen, Mr. Larry Bryant, Jr., Ms. Laura Price, Mr. T. G. Morrison, Dr. Thomas S. Stephens, Lt. Wayne J. Tetlow, Lt. James E. Breck, and Mr. Raffy Mor.

This work was sponsored by the U. S. Department of Energy, at Los Alamos National Laboratory under Contract W-7405-ENG-36 with the University of California and at Sandia National Laboratories under Contract DE-AC04-76DP00789. The authors would like gratefully to acknowledge partial support for this work by the U.S. Department of Energy, Division of Engineering and Geosciences, Office of Basic Energy Sciences. Work at Los Alamos National Laboratory was also partially supported by the Air Force Astronautics Laboratory, Edwards AFB, CA.

REFERENCES

1. D. Leighton and A. Acrivos, *J. Fluid Mech.*, **181**, 415 (1987).

2. R. D. Surovec, D. M. Husband, T. S. Stephens, and A. L. Graham, "Reproducibility in Measuring Rheology of Highly Concentrated Suspensions," JANNAF Propellant Development Characterization Subcommittee 1989 Annual Meeting, Laurel, Maryland, 1989.

3. A. J. Salem and G. G. Fuller, *J. Colloid Interface Sci.*, **108**, 149 (1985).

4. B. J. Ackerson and P. N. Pusey, *Phys. Rev. Lett.*, **61**, 1033 (1988).

5. P. D. Majors, R. C. Givler, and E. Fukushima, *J. Magnetic Resonance*, **85**, 235 (1989).

6. P. G. Morris, *Nuclear Magnetic Resonance Imaging in Medicine and Biology*, Clarendon Press, Oxford, 1986.

7. A. Abragam, *The Principles of Nuclear Magnetism*, Clarendon Press, Oxford, 1961.

8. J. C. Watkins and E. Fukushima, *Rev. Sci. Instrum.*, **59**, 926 (1988).

9. D. L. Koch, *Phys. Fluids A*, **1**, 1742 (1989).

10. J. S. Walton, "Close-Range Cine-Photogrammetry," Thesis, Penn State University (1981).

11. A. L. Graham, L. A. Mondy, and R. L. Powell, "Applications of Real-Time Radiography to Rheological Characterization and Processing Dynamics," JANNAF Propellant Development Characterization Subcommittee 1987 Annual Meeting, Laurel, Maryland, 1987.

12. R. B. Bird, W. E. Stewart, and E. N. Lightfoot, *Transport Phenomena* (John Wiley & Sons, New York, 1960), p. 59.

13. T. Bohlin, *Trans. R. Inst. Tech. (Stockholm)*, No. 155.

14. L. A. Mondy, A. L. Graham, and J. L. Jensen, *J. Rheol.*, **30**, 1031 (1986).

15. W. J. Milliken, L. A. Mondy, M. Gottlieb, A. L. Graham, and R. L. Powell, *PCH PhysicoChemical Hydrodynamics*, **11**, 341 (1989).

16. L. A. Mondy, A. L. Graham, and M. Gottlieb, "Microrheological Observations on the Onset of Non-Newtonian Behavior in Suspensions," Xth International Congress on Rheology, Sydney, Australia, August 1988.

17. D. G. Thomas, *J. Colloid Sci.*, **20**, 267 (1965).

18. W. J. Milliken, M. Gottlieb, A. L. Graham, L. A. Mondy, and R. L. Powell, *J. Fluid Mech.*, **202**, 217 (1989).

19. R. L. Powell, L. A. Mondy, G. G. Stoker, W. J. Milliken, and A. L. Graham, *J. Rheol.*, **33**, 1173 (1989).

20. L. A. Mondy, T. G. Morrison, A. L. Graham, and R. L. Powell, *Int. J. Multiphase Flow*, (in press 1990).

21. M. Doi and S. F. Edwards, *J. Chem. Soc. Faraday Trans. II*, **74**, 918 (1978).

22. G. T. Keep and R. Pecora, *Macromol.*,**18**, 1167 (1985).

23. J. J. Magda, H. T. Davis, and M. Tirrell, *J. Chem. Phys.*, **85**, 6674 (1986).

24. H. Brenner, *Intl. J. Multiphase Flow*, **1**, 195 (1974).

25. S. Haber and H. Brenner, *J. Colloid Interface Sci.*, **97**, 496 (1984).

26. Morrison, T. G., M.S. thesis, University of California - Davis, 1989.

27. E. Ganani and R. J. Powell, *J. Rheol*, **30**, 995 (1986).

RHEOLOGICAL AND RELATED COLLOIDAL ASPECTS OF AQUEOUS PROCESSING THAT AFFECT THE DEVELOPMENT OF MICROSTRUCTURE

Alan Bleier and C. Gary Westmoreland
Oak Ridge National Laboratory, Metals and Ceramics Division, P. O. Box 2008, Oak Ridge, TN 37831-6068

ABSTRACT

Shear flow in α-Al_2O_3 suspensions having a volume fraction of solids (ϕ) in the range between 0.17 and 0.50 was investigated between pH 4 and 12. It is Newtonian if the magnitude of the zeta potential exceeds a critical value which depends on ϕ; its value is 39 mV if $\phi = 0.40$ and 74 mV if $\phi = 0.50$. If this potential is less than the critical value, shear flow is pseudoplastic; its yield value markedly changes (e.g., 0 to >100 Pa) in a slightly ϕ-dependent, narrow pH range (<0.5 units). If a second oxide, t-ZrO_2, is present, its pH-dependent colloidal behavior governs the overall rheology, though its concentration may be only 11 % that of α-Al_2O_3. Scanning electron microscopy of composite pieces indicates that a detrimental, rheologically detectable interaction between α-Al_2O_3 and t-ZrO_2 can be avoided and the distribution of t-ZrO_2 can be optimized during pressure casting by control of pH. Best conditions correspond to either Newtonian flow or pseudoplastic flow with a very low yield value.

INTRODUCTION

Some recent processing studies [1-4] have focussed on the particulate interactions that affect the development of a uniform distribution of monoclinic zirconia (m-ZrO_2) in alpha alumina (α-Al_2O_3) and the use of polyacrylic acid (PAA) as a deflocculant in this system. This research showed that, since the densities differ greatly for the two oxides, their relative particle size determines the degree to which differential sedimentation is detrimental to the ZrO_2-distribution in the final microstructure. The data of Baik et al. [1] suggested, however, that the ratio of zeta potentials (ζ) for the two oxides, denoted herein as R_ζ, is a useful guide for predicting conditions under which reversible association of ZrO_2 and Al_2O_3 occurs and overcomes problems derived from sedimentation. Bleier and Westmoreland [2] explored this ratio further and clearly demonstrated, using experiments in which an alumina-like electrostatic charge was imparted to m-ZrO_2, that differential sedimentation and uniformity of the final microstructure worsen as the two oxides become more electrostatically similar ($R_\zeta \rightarrow 1$) when each possesses the same sign of charge ($R_\zeta > 0$). These researchers extended the study to the effects of PAA on the processing of α-Al_2O_3:m-ZrO_2 composites [3] and found that the stabilizing force when PAA is present is electrostatic. The presence of this polymer requires pH conditions differing from those for the PAA-free case if the association of m-ZrO_2 and α-Al_2O_3 is to occur. Colloidal forces that effect a net attraction exceeding ~8 kT when $R_\zeta > 1$ underpin the association process. [4]

The present study also examines the processing of α-Al_2O_3:ZrO_2 composites but focuses on the use of tetragonal ZrO_2 containing ceria (CeO_2) as the crystallographic stabilizer and the rheological behavior of binary suspensions used to prepare pellets by colloidal filtration. Other data include sedimentation and electrokinetic properties; density measurements and scanning electron microscopy are used to evaluate sintered pellets.

Mat. Res. Soc. Symp. Proc. Vol. 180. ©1990 Materials Research Society

EXPERIMENTAL MATERIALS AND PROCEDURES

Materials

Alumina and Zirconia. Table I summarizes the physical properties of these powders, after fractionation by size [1]. Concentration is expressed herein as volume fraction (ϕ and ϕ_T for unary and binary systems, respectively).

Other Chemicals. HCl and NaOH were used to adjust pH and NaCl was used to maintain ionic strength at 0.01 mol dm^{-3}; these chemicals were of analytical grade (Fisher Scientific). Lastly, distilled deionized water was used.

Procedures

Powder Characterization. Electrophoretic mobility, μ_E, was measured ($\phi \sim 8 \times 10^{-5}$) at 20° C using an automated analyzer (Pen Kem, Model 3000); samples were subjected to ultrasonication prior to measurement. Zeta potential (ζ) was calculated from mobility following Henry [6] and the guidelines given by Smith [6b]; thus, experimentally derived ζ-values are denoted as ζ_H.

$$\zeta_H(\text{in mV; } 20\,^{\circ}\text{C}) = 21.12\,\mu_E / f_H(\kappa a) \quad . \tag{1}$$

The term, f_H, depends [6] on ionic strength, via the Debye-Hückel reciprocal length parameter (κ), and particle radius (a). Its values were calculated [6b] to be 1.437 for α-Al_2O_3 and 1.422 for t-ZrO_2 in 0.01 mol dm^{-3} NaCl.

Slurry Preparation and Evaluation. The concentration of α-Al_2O_3 was varied, such that $0.17 \leq \phi \leq 0.50$ in unary suspensions; the volume-based ratio of concentrations (t-ZrO_2:α-Al_2O_3) was either 1:9 or 1:4 in binary systems.

Relative suspension height (R.S.H.) was evaluated with quiescent unary α-Al_2O_3 ($\phi = 0.05$) and t-ZrO_2 ($\phi = 0.03$) systems at desired ages up to two weeks after their preparation.

For quantitative rheological evaluation, slurry components were mixed at ambient room temperature for 1 d using a reciprocal shaker and subjected to ultrasonication just prior to use. Shear stress (τ) was measured at desired shear rates ($\dot{\gamma}$) with a parallel-plate viscometer (Rheometrics, Model 8400) in the thixotropic loop mode at 24° C; this mode consisted of the following stages: (1) 60 s at 300 s^{-1}, (2) 180 s to reduce $\dot{\gamma}$ to 0 s^{-1}, (3) 180 s to increase it to 300 s^{-1}, and (4) 180 s to reduce it again to 0 s^{-1}. This procedure ensured evaluation of five properties: (i) apparent viscosity ($\eta^{app} = \tau/\dot{\gamma}$), (ii) Bingham plastic flow with yield stress (τ_B) and constant differential viscosity ($\eta^{dif} = d\tau/d\dot{\gamma}$) when $\tau \geq \tau_B$, (iii) pseudoplastic flow (η^{app} and η^{dif} decrease regularly with increasing $\dot{\gamma}$), (iv) hysteresis ($\tau_3 \neq \tau_4$, subscripts specify stages), and (v) thixotropy (time-dependent τ). [7] Owing to the quantity of solid required for these measurements, as-received powders were used for obtaining most rheological data but these were checked with desired size-fractionated

Table I: Properties of Size-Fractionated Powders.

Property	Characterization		Method
Type	Alumina	Zirconia	
Supplier, Designation	Sumitomo, AKP-30	Tosoh, TZ-12Ce	
Composition	α-Al_2O_3	t-ZrO_2	XRD[a]
Density, g cm^{-3}	3.98 [5a]	6.25 [5b]	
Surface Area, m^2 g^{-1}	6.21[b]	11.6[b]	BET[c]
Diameter, μm	0.37 (0.39[b])	0.29 (0.68[b])	SED[d]
Isoelectric Point, pH	8.5	6.9	EM[e]

[a]X-Ray Diffraction; [b]Prior to size fractionation; [c]Gas Adsorption; [d]Sedimentation (Horiba, Model 500); [e]Electrophoretic Mobility.

material when necessary. Finally, fluidity was qualitatively assessed when rheology differed greatly for systems with similar composition.

Pellet Fabrication. Cylindrical pellets with diameter and thickness of 24 and 2 to 5 mm, respectively, were prepared by pressure filtration (0.2-μm filter) at 20 psi Ar(g) using slurries in which $\phi = 0.17$. Pellets were kept under pressure for 18 h, after which time they were removed, air-dried while uncovered for 1 d, and then placed for 18 to 24 h in a vacuum oven at 60° C. Specimens from pellets were thinly coated with paraffin (Fisher Scientific) prior to the measurement of density (ρ_g) by Archimedes' method [1,3].

Microstructure Evaluation. Pellets were heated from room temperature to 200° C over a 3-h period, after which the temperature was raised to 1500° C over the next 2 h and ultimately held at this value for 1 h. Temperature was then lowered to 1000° C over a 3-h period and to room temperature over the next 4 h. Density of sintered pellets (ρ_s), without a paraffin coating, was also determined by Archimedes' method. Sintered pellets were fractured, polished, and examined by scanning electron microscopy (SEM).

RESULTS AND DISCUSSION

Experimental Results. Figure 1A summarizes the stability of α-Al_2O_3, as evaluated by R.S.H.-values. α-Al_2O_3 settles rapidly (2-h data) and packs least efficiently (high R.S.H.; 334-h data) between pH 6.7 and 11.3. Outside this range, which can be defined by the pH_{trans}-values that are noted in the figure, it is colloidally stable. Evidently, stable, positively ($\zeta_H > 0$) and negatively ($\zeta_H < 0$) charged α-Al_2O_3 systems exist in Regions I and III, respectively. Unstable ones of low charge ($|\zeta_H| \to 0$ near pH 8.5) are in Region II (hatching). Analogously, Figure 1B shows that the pH values defining Regions I, II, and III for t-ZrO_2 are 5.5 and 10.8.

Figure 2A gives typical rheological data for α-Al_2O_3 ($\phi = 0.40$) within the regions just identified, while Figure 2B summarizes τ_y-data as a function of pH for four concentrations of α-Al_2O_3 in the ϕ-range, 0.20 to 0.50. Shear flow

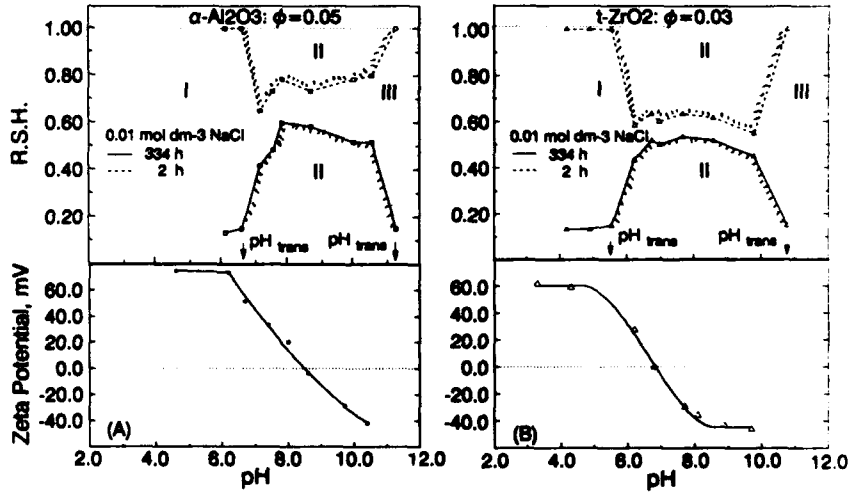


Figure 1: Relative sedimentation height (R.S.H.) after 2 and 334 h and zeta potential (ζ_H) as functions of pH for (A) α-Al_2O_3 ($\phi = 0.05$) and (B) t-ZrO_2 ($\phi = 0.03$) suspensions in 0.01 mol dm^{-3} NaCl. Stability exists in Regions I and III that are characterized by the borderline stable systems denoted as pH_{trans}; colloidal instability (hatching) occurs in Region II.

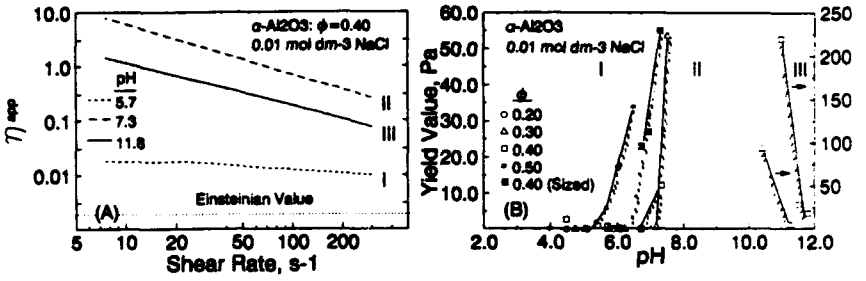


Figure 2: (A) Logarithm of apparent viscosity (η^{app}) for α-Al_2O_3 systems as a function of logarithm of shear rate ($\dot{\gamma}$) for pH values representing Regions I, II, and III in Figure 1A; (B) Bingham plastic yield (τ_B) of α-Al_2O_3 as a function of pH identifying these regions for various concentrations of solid (ϕ).

is virtually Newtonian ($d\eta^{app}/d\dot{\gamma} \sim 0$) in Region I and pseudoplastic (power-law behavior [7b]) in Regions II and III. The η^{app}-values in Region III are less than those in Region II but clearly exceed the ones in Region I. Note that η^{app}-values in Region I, in turn, greatly exceed the Einsteinian value [8] for suspensions of noninteracting, spherical particles for which $\phi = 0.40$. The value of η^{dif} was nearly constant in each system, including binary suspensions, for most of the $\dot{\gamma}$-range investigated [9], justifying treatment of these systems as Bingham-like fluids [7b,c] and use of a yield value to quantify rheological behavior. Lastly, hysteresis and thixotropy are absent or nil when τ_B is low. [9]

Figure 3A shows the effect of a second phase, t-ZrO_2, on the pH-dependence of τ_B at various values of ϕ_T for two binary ratios. The rheologically detected value of pH_{trans} separating Regions I and II, is lower in the presence of t-ZrO_2 than in its absence (Figure 2B). However, this pH does not seem to depend on the concentration of t-ZrO_2 (ϕ_{Zr}) for the ϕ_{Zr}-range examined. Hysteresis and thixotropy are similarly absent or nil in these mixtures when τ_B is low. [9] Finally, Figure 3B gives SEM data demonstrating that the degree of clustering of t-ZrO_2 in Region I ($pH < pH_{trans}$) is less that in Region II ($pH > pH_{trans}$).

Discussion. It is noteworthy that the data in Figure 2 relate well to the previously gathered ones [3] for a similar alumina which also exhibited regions analogous to those denoted herein as I, II, and III. The rheological changes defining the transitions between II and either I or III and depicted in Figure 2B are determined by the ζ_H-values of α-Al_2O_3 (Figure 1A), values which also relate to changes in the R.S.H.-pH profile.

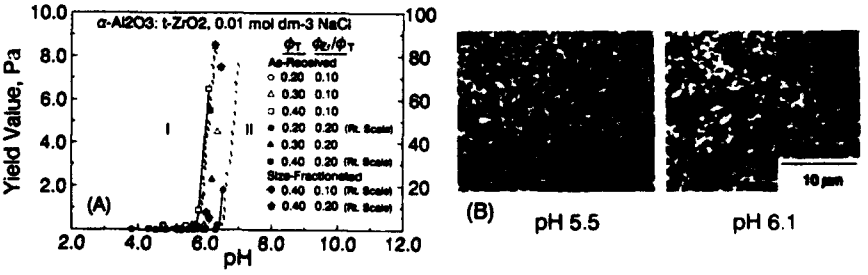


Figure 3: (A) Similar to Figure 2B but for binary systems ($0.20 \leq \phi_T \leq 0.40$); (B) SEM micrographs showing polished interior surfaces of composite pellets prepared in Regions I and II, respectively, at pH 5.5 [$R_\zeta = 1.5$; $\rho_{B(s)} = 0.61(1.00)$] and 6.1 [$R_\zeta = 2.7$; $\rho_{B(s)} = 0.55(0.94)$] with size-fractionated powders ($\phi_T = 0.17$; $\phi_{Zr} = 0.20\phi_T$); white areas are grains of ZrO_2.

Table II: Summary of Rheological Transitions.

Powder Type	ϕ_T	ϕ_{Al}[a,b]	ϕ_{Zr}[a,b]	N_{Al}[b,c]	N_{Zr}[b,c]	pH_{trans}	R_ζ[d] (ζ_H[e])
Size-Fractionated	0.40	1.00	-	1.00	-	6.4	- (64.3)
		0.90	0.10	0.81	0.19	6.1	2.5 (28.8)
		0.80	0.20	0.66	0.34	6.0	2.3 (31.7)
As-Received[f]	0.50	1.00	-	1.00	-	5.5	- (73.9)
	0.40	1.00	-	1.00	-	6.7	- (54.5)
						11.7	- (-57.5)
		0.90	0.10	0.98	0.02	5.8	1.8 (40.4)
		0.80	0.20	0.95	0.05	5.8	1.8 (40.2)
	0.30	1.00	-	1.00	-	7.2	- (39.1)
						11.3	- (-53.8)
		0.90	0.10	0.98	0.02	6.0	2.2 (33.8)
		0.80	0.20	0.95	0.05	6.2	2.9 (25.0)
	0.20	1.00	-	1.00	-	>6.1[g]	- (-)
		0.90	0.10	0.98	0.02	>6.3[g]	>3.3 ($\leq$20.9)
		0.80	0.20	0.95	0.05	6.3	3.4 (20.4)

[a]Fraction of ϕ_T; [b]Subscript $Al(Zr)$ designates the oxide by its metal; [c]Particle number fraction; [d]$R_\zeta \geq 1$; [e]α-Al_2O_3 in unary systems, t-ZrO_2 in binary ones; [f]Not fractionated by size; [g]Highest pH examined in Region I.

Table II summarizes the data in Figures 2 and 3, stressing binary systems. The pH range to which the transition between Regions I and II is shifted in Figure 3A, relative to its location in Figure 2B, seems to be set by the comparative instability of t-ZrO_2 (Figure 1B). The low ζ_N-values of t-ZrO_2 near pH 6 govern the stability of not only this solid, but also that of the overall suspension. Interestingly, this influence occurs when $\phi_{Zr} \leq 0.2\phi_T$ and is rheologically detectable, involving phenomena that theoretically depend primarily on volume fraction and secondarily on ζ-potential [7].

Conclusions. Based on the foregoing data and considerations we conclude that desirable characteristics can be achieved and that uniformity of binary phase distributions can be realized in green and sintered components by control of particle interactions. The findings show:

1. Transitions in colloidal stability for α-Al_2O_3 suspensions, identified as pH_{trans}, are detectable rheologically (τ_B) and by sedimentation behavior (R.S.H.); similar transitions for mixtures of α-Al_2O_3 and t-ZrO_2 are discernible rheologically.

2. Rheological transitions in stability for α-Al_2O_3 suspensions with $\phi \leq 0.40$ relate well to those detected by R.S.H. values for dilute systems; this correspondence is valid for positively charged systems ($\zeta_H > 0$) and negatively charged ones ($\zeta_H < 0$).

3. Shear flow in α-Al_2O_3 suspensions is nearly Newtonian in Region I and pseudoplastic in Regions II and III; viscosity in these regions increases according to the sequence: I $\ll$ III < II.

4. The values of pH and, therefore, the magnitude of ζ_N that correspond to the rheological transitions in stability of α-Al_2O_3 depend on ϕ when this value exceeds the range 0.20 to 0.30; a minimum ζ_N-value at pH_{trans} is on the order of 39 mV for $\phi = 0.30$, whereas it may be as great as 74 mV for higher ϕ-values.

5. The presence of t-ZrO_2 lowers pH_{trans} between Regions I and II.

6. The value of pH_{trans} between Regions I and II seems to be independent of the concentration of t-ZrO_2 in the range, $0.10\phi_T \leq \phi_{Zr} \leq 0.20\phi_T$; this finding suggests that (i) interactions between the two oxides occur near pH 6, a region in which t-ZrO_2 is the less stable component (Figure 1) and $R_t > 1$ (Table II) and (ii) since N_{Zr}-values of 0.02 to 0.05 do not seriously affect pH_{trans} (Table II), these interactions depend more on the presence of t-ZrO_2 than on its concentration.

7. The interaction between the oxides, inferred from the rheological data and supported theoretically [1,2,4], is detrimental to green and sintered densities at pH > pH_{trans}, viz. pH 6.1 (Figure 3B), but has been shown [1-4] to be beneficial to the distribution of ZrO_2 under conditions slightly more acidic than pH_{trans} between Regions I and II, without affecting these values.

ACKNOWLEDGEMENTS

Research sponsored by the Division of Materials Sciences, U.S. Department of Energy, under contract DE-AC05-840R21400 with Martin Marietta Energy Systems, Inc. The authors thank Drs. H. T. Lin, A. C. Young, and P. F. Becher for reviewing the manuscript and are grateful for their comments.

REFERENCES

1. S. Baik, A. Bleier, and P. F. Becher, in Better Ceramics Through Chemistry II, edited by C. J. Brinker, D. E. Clark, and D. R. Ulrich (*Mater. Res. Soc. Proc.* 73, Pittsburgh, PA, 1986), pp. 791-800.
2. A. Bleier and C. G. Westmoreland, in Better Ceramics Through Chemistry III, edited by C. J. Brinker, D. E. Clark, and D. R. Ulrich (Mater. Res. Soc. Symp. Proc. 121, Pittsburgh, PA, 1988), pp. 145-154.
3. A. Bleier and C. G. Westmoreland, in Interfacial Phenomena in Biotechnology and Materials Processing, edited by B. Moudgil and Y. A. Attia (Elsevier Science, New York, 1988), pp. 217-236.
4. (a) A. Bleier, P. F. Becher, S. Baik, and C. G. Westmoreland, in Abstracts of the 89th Annual Meeting (Am. Ceram. Soc., Westerville, OH, 1987), p. 37; (b) A. Bleier, in Abstracts of the 61st Colloid and Surface Science Symposium (Am. Chem. Soc., Ann Arbor, MI, 1987), Paper No. 64; in Abstracts of the *Symposium on Particle Deposition at the Solid-Liquid Interface* (Soc. Chem. Ind., London, 1988), Paper No. 9; submitted for publication, Colloids Surfaces; (c) A. Bleier and C. G. Westmoreland, to be submitted for publication (Am. Ceram. Soc., Westerville, OH).
5. (a) J. F. Lynch, Ed., Engineering Property Data on Selected Ceramics, Vol. III. Single Oxides, Battelle Columbus Labs, Columbus, OH, 1981, p. 5.4.1.-1; (b) P. F. Becher (private communication).
6. (a) D. C. Henry, Proc. R. Soc. Lond. A133, 106 (1931); (b) A. L. Smith, in Dispersion of Powders in Liquids, 3rd Ed., edited by G. D. Parfitt (Applied Science, London, 1981), pp. 99-148; (c) R. J. Hunter, Zeta Potential in Colloid Science (Academic, London, 1981), p. 71.
7. (a) R. J. Hunter, Foundations of Colloid Science, Vol. I (Clarendon, Oxford, 1987), pp. 76-89; (b) R. J. Hunter, Foundations of Colloid Science, Vol. II (Clarendon, Oxford, 1989), pp. 992-1052; (c) Th. G. M. van de Ven, Colloidal Hydrodynamics (Academic, London, 1989), 582 p.
8. A. Einstein, Investigations on the Theory of the Brownian Movement (Dover, New York, 1956), pp. 36-62.
9. A. Bleier and C. G. Westmoreland, unpublished results.

PREPARATION OF MULTICOMPONENT CERAMIC POWDERS BY SOL-GEL PROCESSING

J.R. Bartlett and J.L. Woolfrey
Advanced Materials Program, Australian Nuclear Science and Technology Organisation, Private Mail Bag No. 1, Menai, N.S.W. 2234. Australia.

ABSTRACT

Sol-gel methods have been applied to the production of the multicomponent ceramic, Synroc B. These techniques involved the hydrolysis of a mixture of Ti and Zr, alkoxides peptising to form a sol and subsequent sorption of Al^{3+}, Ba^{2+} and Ca^{2+} cations under acidic conditions. Powder properties were examined by a variety of techniques, including electron microscopy, x-ray diffraction, N_2 sorption, and differential thermal analysis. The effects of processing conditions on the physical properties of the powders are discussed.

1. INTRODUCTION

Synroc B is a complex, multiphase, titanate ceramic, designed to immobilise High Level Wastes (HLW) from nuclear fuel reprocessing plants [1]. The Synroc concept involves immobilising the elements present in HLW within a series of thermodynamically stable mineral phases (hollandite, zirconolite, and perovskite). These minerals are formed during ceramic processing of a precursor powder containing TiO_2, ZrO_2, Al_2O_3, BaO, and CaO in relative mass abundances of (70.4 to 76.4), (5.5 to 8.5), (3.5 to 5.5), (4.6 to 6.6) and (10.1 to 12.1) percent, respectively.

Synroc B precursor powders are routinely produced by alkoxide hydrolysis and simultaneous sorption of Ca^{2+} and Ba^{2+} cations [2]. This paper discusses the preparation of Synroc using an alternative sol-gel process and compares the physical characteristics of precursor powders produced by the two different routes.

2. EXPERIMENTAL

2.1 Preparation of Sols and Powders

2.1.1 Synthesis of TiO_2 sol. Titanium tetra(iso-propoxide) (TPT) was added to a large excess of hot water (70 to 80 °C, 40 to 100 moles of water per mole of TPT). The aqueous phase was rapidly stirred during addition, and the resulting hydrolysate consisted of relatively large, weakly agglomerated flocs. The hydrolysate was peptised with HNO_3 (approximately 0.1 moles H^+ per mole of TPT), and the total volume of the sol was gradually reduced by evaporation at 40 to 60 °C. The solids content (oxide basis) of the final TiO_2 sol, which exhibited a shelf life of at least 6 months, generally exceeded 600 g dm^{-3}.

2.1.2 Synthesis of AlOOH sol. Boehmite sols were prepared by a procedure similar to that described by Yoldas [3]. Aluminium tri (sec-butoxide) (ASB) was added to a large excess of hot water (75 to 85 °C, 100 moles of water per mole of ASB), and the resulting hydrolysate was peptised with HNO_3 (0.07 moles H^+ per mole ASB). The colloidal solution was aged at 90 °C for at least 48 hours before use. The solids content of the sol was generally maintained at approximately 30 to 40 g dm^{-3} (oxide basis) to obtain a shelf life exceeding 4 months. Solids contents as high as 200 g dm^{-3} could also be achieved, although the shelf life of these concentrated sols was typically less than 48 hours.

2.1.3 Synthesis of TiO_2/ZrO_2 sol. A mixture of TPT and zirconium tetra (n-butoxide) (TBZ) was hydrolysed, peptised and concentrated, as described above for the pure TiO_2 system. The solids content of the concentrated TiO_2/ZrO_2 sol generally exceeded 1100 g dm^{-3}, and the sols were stable over intervals exceeding 4 months.

2.1.4 Synthesis of TiO_2/ZrO_2/AlOOH sols. A mixture of TPT, TBZ and ASB was hydrolysed according to the procedure described above for the TiO_2 system. The resulting hydrolysate could not be peptised under the conditions used to obtain TiO_2, TiO_2/ZrO_2 or AlOOH sols, and the solutions typically gelled during heating.

2.1.5 Synthesis of sol-gel-route Synroc. Three different procedures were used to prepare Synroc B powders from the above sols.

(i) Appropriate quantities of the TiO_2/ZrO_2 and AlOOH colloidal solutions were mixed to form a metastable

TiO_2/ZrO_2-AlOOH solution with a shelf life of less than 48 hours, and a solids content exceeding 600 g dm^{-3}. An aqueous solution of $Ba(NO_3)_2$ and $Ca(NO_3)_2$ was then slowly added to the stirred colloidal solution. The viscosity of the solution increased rapidly during addition of the cations, and gelation occurred well before complete mixing was obtained, leading to potential component segregation. Consequently, no further work was undertaken on this system.

(ii) The concentrated TiO_2/ZrO_2 sol was added drop-wise to a hot aqueous solution containing appropriate quantities of $Al(NO_3)_3$, $Ba(NO_3)_2$ and $Ca(NO_3)_2$. The sol rapidly flocculated during addition, and the resulting slurry was heated to a thick paste with stirring, and then dried at 110 °C. Synroc B powders produced by this route will be referred to as S_{SG1}.

(iii) The concentrated TiO_2/ZrO_2 sol was spray-dried at 160 °C to yield a free-flowing powder. The powder was heated at 100 to 200 °C, and an aqueous solution containing appropriate quantities of $Al(NO_3)_3$, $Ca(NO_3)_2$ and $Ba(NO_3)_2$ was quickly added. The resulting yellow/green slurry was heated to form a thick viscous paste with stirring, and then dried at 110 °C. Synroc B powder produced by this method will be referred to S_{SG2}.

Small quantities of TiO_2/ZrO_2-AlOOH powder were also produced by spray-drying the metastable TiO_2/ZrO_2-AlOOH sol. However, the sol consistently gelled within the fine nozzles of the spray-dryer, and hence, no additional work was undertaken on this system.

2.2 Powder Characterisation.

The specific surface area, pore surface area, pore volume (Micromeritics ASAP 2400), scanning electron micrographs (JEOL JXA-840), transmission electron micrographs (TEM, JEOL JEM 2000FX II), x-ray diffraction (XRD) patterns (Siemens Kristalloflex D500), particle size distribution (Malvern Autosizer IIC) and skeletal density (Micromeritics Autopore 9220) of selected sols and powders were obtained. Differential thermal analyses (DTA, Setaram TAG 24) of selected powders were also obtained using a heating rate of 10 °C min^{-1} in air.

3. RESULTS

The XRD patterns of as-dried TiO_2 and TiO_2/ZrO_2 are shown in Fig. 1. Both the TiO_2 and TiO_2/ZrO_2 powders contained anatase and minor quantities of brookite (TiO_2), and no crystalline phases containing Zr(IV) species were evident. In contrast, Synroc powder prepared by the standard alkoxide route (S_{HR}) [2] was amorphous.

The pore volume distributions of the spray-dried TiO_2 and TiO_2/ZrO_2 powders both exhibited maxima below 1.7 nm, Fig. 2, consistent with the presence of micropores in the powder agglomerates. In contrast, S_{SG1} and S_{SG2} powders exhibited maxima at pore apertures of 3 to 4 and 6 to 7 nm, respectively. The total pore volume and BET surface area of the amorphous S_{HR} powder are both significantly higher than those of the crystalline S_{SG1}, S_{SG2}, TiO_2 and TiO_2/ZrO_2 powders (Table 1).

The results of DTA characterisation of TiO_2, TiO_2/ZrO_2, S_{HR}, S_{SG1} and S_{SG2} are given in Fig. 3. The spray-dried TiO_2 powder (anatase) transformed to rutile at 595±5 °C, whereas the corresponding transformation for the TiO_2/ZrO_2 powder was observed at 930±5 °C. S_{HR}, S_{SG1} and S_{SG2} powders exhibited exotherms above 750 °C associated with crystallisation of the key Synroc phases [4]. The powders also exhibited several endotherms below 600 °C, which were associated with desorption and/or decomposition of H_2O, $[OH]^-$ and

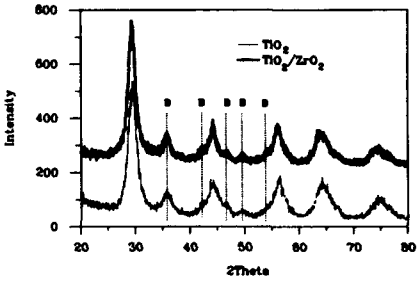


Fig. 1. XRD patterns of spray-dried TiO_2 and TiO_2/ZrO_2. Labelled peaks arise from brookite. Remaining peaks are due primarily to anatase.

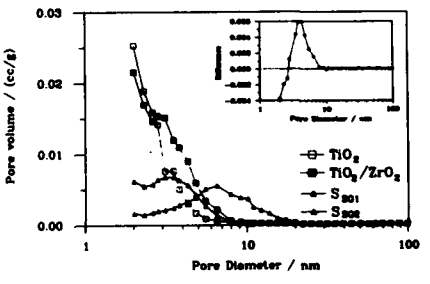


Fig. 2. Pore volume distribution of TiO_2, TiO_2/ZrO_2, S_{SG1} and S_{SG2}. Inset : Difference between TiO_2 and TiO_2/ZrO_2 distributions.

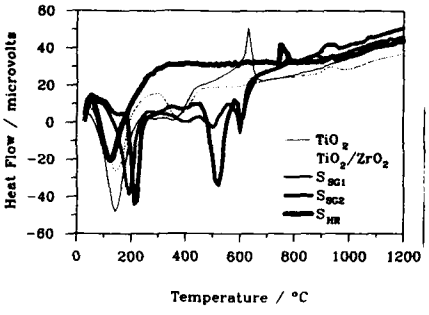


Fig. 3. DTA of TiO_2, TiO_2/ZrO_2, S_{SG1}, S_{SG2} and S_{HR}.

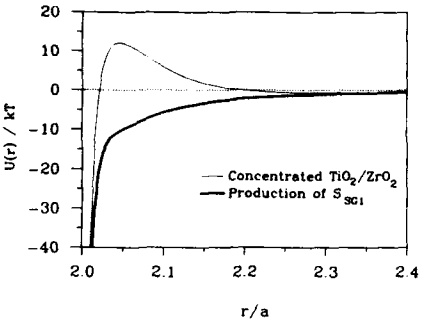


Fig. 4. Potential energy of TiO_2/ZrO_2 colloids as a function of separation distance during preparation of TiO_2/ZrO_2 and S_{SG1}.

$[NO_3]^-$. Selected physical properties of the powders are summarised in Table 1. The agglomerate and crystallite size of S_{SG1} and S_{SG2} could not be measured, since the $Al(NO_3)_3$, $Ca(NO_3)_2$ and $Ba(NO_3)_2$ components of these powders are soluble in the solvents typically used to prepare samples for light scattering and TEM analysis (i.e. water and alcohol).

4. DISCUSSION

4.1 Stability of concentrated sols and preparation of Synroc B

The potential energy barrier to aggregation in colloidal systems, which influences both the stability and, indirectly, the maximum solids concentration that can be achieved, may be evaluated from the theory of Derjaguin, Landau, Verwey and Overbeek (DLVO theory) [5]. The net potential energy between particle pairs is given by [6]

$$U(r) = U_R(r) + U_A(r)$$

where $U_R(r)$ is the screened Coulombic repulsion, $U_A(r)$ the van der Waals attraction and r the centre-to-centre separation of the particles. $U_R(r)$ and $U_A(r)$ (unretarded form) are given by

$$U_R(r) = 2\pi\varepsilon_r\varepsilon_0 a\psi_0^2 \ln[1+\exp(-\kappa(r-2a))]$$

$$U_A(r) = -(A_H/12)[4a^2/(r^2-4a^2) + (2a/r)^2 + 2\ln(1-(2a/r)^2)]$$

$$\kappa^2 = 2e^2 I N_A/\varepsilon_r\varepsilon_0 kT$$

where ε_r is the relative dielectric constant of the medium, ε_0 the permittivity of free space, κ^{-1} the Debye length, I the ionic strength, a the particle radius, N_A Avagadro's number, and A_H the effective Hamaker constant of the particles in a given medium. Accurate values for A_H are generally unavailable for the majority of aqueous colloidal metal oxide systems, although Hiemenz [7] and Bijsterbosch [8] have presented limited compilations for selected systems. Nominal values of $A_H = 5 \times 10^{-20}$ J and $\psi_0 = 70$mV have been used for the TiO_2/ZrO_2 system in the discussion below. This approach has been found to predict qualitatively the properties of the sols during preparation of the key powder systems.

4.1.1 Production of TiO_2/ZrO_2. The DLVO potential energy diagram for the concentrated TiO_2/ZrO_2 system is given in Fig. 4. The ionic strength ($I=0.14$ mole dm^{-3}) was estimated by assuming that the only source of electrolyte was the HNO_3 used to peptise the hydrolysate (approximately 0.1 moles HNO_3 per mole TiO_2/ZrO_2). Under these conditions, the calculated barrier to aggregation is 12kT, which is consistent with the long shelf life of the sol.

Table 1. Selected properties of TiO_2, Ti/ZrO_2, S_{SC1}, S_{SC2} and S_{HR}.

	TiO_2	TiO_2/ZrO_2	Synroc B		
			S_{SC1}	S_{SC2}	S_{HR}
Agglomerate Size /nm*	22	30	N/A	N/A	10,000
Pore Volume (N_2) /$cm^3\ g^{-1}$	0.11	0.13	0.05	0.06	0.18
Total BET Surface Area /$m^2\ g^{-1}$	255	213	37	66	409
BJH Surface Area of Pores /$m^2 g^{-1}$	153	179	43	74	251
BJH/BET Ratio	0.60	0.84	1.2	1.1	0.61
Skeletal Density (Hg) /gcm^{-3}	2.72	2.86	2.87	2.31	1.93
Crystalline phases present in dried powder	Anatase Brookite	Anatase Brookite	Anatase Brookite	Anatase Brookite	Amorphous
**Transformation temperatures /°C (DTA)	595 (s)	930 (m)	780 (w) 880 (w)	780 (w) 935 (w)	750 (s) 940 (w)

N/A, Not available
*Determined by light scattering
**Letters in parenthesis refer to peak heights : s, strong; m, medium; w, weak.

During spray-drying, small droplets of the sol are rapidly concentrated as water is evaporated, leading to an increase in electrolyte (HNO_3) concentration (assuming no loss of electrolyte), and the higher ionic strength produces a corresponding decrease in the barrier to aggregation. However, the calculated barrier never falls below 7kT, even for solids concentrations (and associated ionic strengths) exceeding 60 volume %. Under these conditions, it would be anticipated that the particles would be tightly packed in the spray-dried powder agglomerates. Indeed, the measured skeletal density of the TiO_2/ZrO_2 powder was 2.86 gcm^{-3}, which is equivalent to 74 % of the theoretical density of anatase [9]. The dense particle packing in this system was also clearly evident in TEM images of the spray-dried powder.

4.1.2 Production of S_{SC1}. The S_{SC1} powders were prepared by dropwise addition of the well-dispersed TiO_2/ZrO_2 sol into a heated solution of $Al(NO_3)_3$, $Ca(NO_3)_2$ and $Ba(NO_3)_2$ (I = 1.3 mole dm^{-3}). The DLVO potential energy diagram for this system, Fig. 4, indicates that the calculated potential energy is always attractive (i.e. no barrier to aggregation), thus favouring rapid aggregation of the colloidal TiO_2/ZrO_2 particles. In accord with this prediction, the TiO_2/ZrO_2 sol droplets rapidly flocculated on contacting the ionic solution, and formed large, loosely packed agglomerates.

4.1.3 Aggregation and gelation in TiO_2/ZrO_2-AlOOH mixed sols. The relatively high rate of aggregation and gelation in the mixed TiO_2/ZrO_2-AlOOH system (see Section 2.1.5) may result from two separate processes :-

(a) Partial dissolution of the AlOOH species in the concentrated acidic TiO_2/ZrO_2 solution would lead to an increase in the ionic strength of the medium, and to an associated decrease in the zeta potential and barrier to aggregation. In particular, for a solids concentration of 600 g dm^{-3}, dissolution of the AlOOH particles would lead to an Al^{3+} concentration of up to 0.6 mole dm^{-3}, and an associated ionic strength of up to 3 mole dm^{-3}. DLVO theory predicts that there is no barrier to aggregation for this system when $I \geq 0.45$ mole dm^{-3}, and hence, even partial dissolution of the AlOOH particles would promote gelation.

(b) Since the magnitude of $U_A(r)$ is proportional to A_H, the barrier to aggregation may be reduced if the presence of the AlOOH particles were to increase the effective Hamaker constant of the system. However, there is no experimental evidence to support such an increase.

The TiO_2/ZrO_2 sol was chosen as the precursor from which to prepare Synroc B powders in this study, since the stability of the mixed TiO_2/ZrO_2-AlOOH sol at high solids concentrations appeared to be unacceptably low.

4.2 Powder Properties

4.2.1 TiO_2 and TiO_2/ZrO_2 powders

The properties of the TiO_2 and TiO_2/ZrO_2 powders are substantially different, even though the abundance of ZrO_2 is less than 10 wt. % (oxide basis) in the latter system. These differences are discussed below.

(i) Surface area and pore volume distribution. The distribution of pores below 10 nm for the TiO_2 powder is significantly different from that of the TiO_2/ZrO_2 powder, Fig. 2. The TiO_2/ZrO_2 powder contains a larger number of pores with apertures of 4 to 6 nm, whereas the TiO_2 powder contains significantly more 2 to 3 nm pores (see inset to Fig. 2). These differences correlate with the sizes of the colloidal particles from which the spray-dried agglomerates were formed, since the apertures of interparticle pores formed in a close-packed array of 30 nm particles would be expected to be larger than those formed from 20 nm particles. The BET surface area of the TiO_2/ZrO_2 powder (213 m^2g^{-1}) is in good agreement with the calculated "hard sphere" surface area of the ~10 nm crystallites observed by TEM in the powder agglomerates (210 m^2g^{-1}.)

(ii) DTA. Both powders exhibit well-defined endotherms and associated weight losses at 140 °C and 350 to 400 °C, which are attributed to desorption of H_2O, $[NO_3]^-$ and/or $[OH]^-$ species, respectively (Fig. 3). The TiO_2 powder also exhibits a sharp exotherm at 595 °C, which is attributed to the anatase→ rutile transformation, on the basis of XRD data. In contrast, the anatase→rutile transformation for the TiO_2/ZrO_2 powder occurs at 930 °C, and the associated exotherm is much broader than that of the TiO_2 powder. These data indicate that the multicomponent powder is very homogeneous, and that the anatase→rutile transformation is inhibited by the presence of the Zr(IV) species. A heterogeneous mixture would be expected to exhibit an exotherm much closer to that of the pure TiO_2 powder, and a second exotherm associated with crystallisation of a Zr(IV) oxide phase. Barksdale [10] has reported that oxides such as Na_2O and WO_3 also inhibited the anatase→rutile transformation, whereas ZnO, Sb_2O_3, MgO and Li_2O enhanced the transformation.

4.2.2 S_{SG1} and S_{SG2} Powders

(i) Surface area and pore volume distribution. Addition of $Al(NO_3)_3$, $Ca(NO_3)_2$ and $Ba(NO_3)_2$ to the spray-dried TiO_2/ZrO_2 powder during production of S_{SG2} significantly alters the total surface area, the total pore volume and the distribution of pores within the powder (Fig. 2 and Table 1). A comparison of the pore volume distributions of the S_{SG2} and TiO_2/ZrO_2 powders indicates that S_{SG2} contains substantially fewer pores with apertures less than 5 nm, suggesting that the Al^{3+}, Ca^{2+}, and Ba^{2+} cations are sorbed preferentially within these small pores, leading to the observed changes in surface properties.

The pore volume distribution of S_{SG1} is also different to that of S_{SG2}, Fig. 2, although both materials were prepared from the same TiO_2/ZrO_2 precursor sol. The S_{SG2} distribution exhibits a maximum at 3 to 4 nm, whereas the S_{SG1} distribution exhibits a much broader maximum at 6 to 7 nm, reflecting differences in particle packing in the respective powder agglomerates. Since the TiO_2/ZrO_2 powder is prepared by spray-drying a well dispersed colloidal solution (with a low "sticking probability" [6]), the agglomerates in the S_{SG2} powder should be tightly packed. In contrast, S_{SG1} agglomerates are prepared under conditions where rapid, chaotic aggregation will occur (high "sticking probability" [6]), which will yield loosely packed clusters with larger, poorly defined interparticle pores [11]. Hence, the distribution of pores in the Synroc powders can be easily manipulated by varying the conditions under which the powder agglomerates are produced.

(ii) DTA. The DTA curves of S_{SG1} and S_{SG2} are substantially different to those of S_{HR} and the TiO_2 and TiO_2/ZrO_2 powders, Fig. 3. The S_{SG1} and S_{SG2} powders both exhibit multiple endotherms at or below 600 °C, which are assigned to desorption or decomposition of H_2O, $[OH]^-$ and $[NO_3]^-$ species. As expected, S_{HR} powder only exhibits a single endotherm in this region due to desorption of H_2O, since there are no $[NO_3]^-$ species associated with this latter powder.

The exotherms observed above 700 °C for the Synroc B samples correspond to the onset of crystallisation of the key Synroc phases, namely barium hollandite ($Ba_{1.14}Al_{2.28}Ti_{5.71}O_{16}$), zirconolite ($CaZrTi_2O_7$), perovskite ($CaTiO_3$) and rutile ($TiO_2$), Table 1 and Fig. 3. XRD data confirmed that the standard Synroc B phases were formed in all cases, although the S_{HR} transitions were much stronger and sharper than those of the S_{SG1} and S_{SG2}

powders. The key difference between the S_{HR} and sol-gel route precursor powders is that the S_{HR} powder is amorphous until 600 °C, whereas S_{SG1} and S_{SG2} are crystalline after drying at 100 °C (Table 1). Consequently, the formation of the Synroc mineral phases would be expected to occur via fundamentally different reaction sequences in the two powder systems.

In the S_{HR} system, the exothermic peak at 750 °C is associated with the initial crystallisation of the amorphous material to form metastable, intermediate $(Ca,Ti)(O,OH)_2$ and $CaTi_2(O,OH)_5$ phases [4], which then transform to the stable Synroc phases. In contrast, these crystallisation reactions occur in discrete, well defined stages in the S_{SG1} and S_{SG2} powders. XRD data revealed that the first exotherm is associated with the formation of perovskite, while the second represents the transformation of anatase to rutile and the crystallisation of hollandite. The formation of zirconolite also occurs between approximately 950 and 1200 °C. The fabrication characteristics of the S_{SG1} and S_{SG2} powders are currently being evaluated for comparison with standard reference route Synroc (S_{HR}).

5. CONCLUSIONS

(1) TiO_2 and TiO_2/ZrO_2 sols with oxide concentrations in excess of 1100 g dm^{-3} were prepared from alkoxide precursors. These sols were subsequently mixed with colloidal and/or ionic Al(III), Ba(II) and Ca(II) species to produce the multicomponent titanate ceramic powder, Synroc B.

(2) The potential energy barrier to aggregation in these systems was evaluated using DLVO theory :
- Concentrated TiO_2/ZrO_2 sols (up to 1100 g dm^{-3}, oxide basis) were very stable (high DLVO barrier to aggregation), and exhibited shelf lives in excess of four months.
- In contrast, the shelf life of mixed TiO_2/ZrO_2-AlOOH sols, with solids concentrations of only 650 g dm^{-3} was typically less than 48 hours (there being no barrier to aggregation).

(3) The porosity of the Synroc powders varied with the processing conditions used. Powders prepared under high ionic strength conditions (low barrier to aggregation) exhibited relatively large pores, consistent with loose particle packing in the agglomerates. Conversely, powders prepared under conditions involving a high barrier to aggregation exhibited much smaller pores, consistent with tighter particle packing in the latter agglomerates

(4) DTA revealed that the formation of the key Synroc crystal phases from the crystalline sol-gel derived powders followed a substantially different reaction sequence to that of amorphous precursor powders.

6. ACKNOWLEDGMENTS

The authors gratefully acknowledge the assistance of Dr K.L. Smith, D. Cassidy, P. Bendeich, P. Angel and G. Thorogood in obtaining data for this paper.

7. REFERENCES

1. A.E. Ringwood, S.E. Kesson, K.D. Reeve, D.M. Levins and E.J. Ramm, in "Radioactive Waste Forms of the Future", edited by W. Lutze and R.C. Ewing (Elsevier Science Publishers B.V., 1988), Chapter 4.
2. J.L. Woolfrey, J.R. Bartlett and W.J. Buykx, in "Proceedings of the 2nd International Conference on Ceramic Powder Processing Science", (Berchtesgaden, FRG, OCT 12-14, 1988), in Press.
3. B.E. Yoldas, Bull. Amer. Ceram. Soc. 54, 289-290 (1975).
4. E.R. Vance, D.J. Cassidy, K.L. Smith and J.L. Woolfrey in "Proceedings of the 4th International Symposium on Ceramics in Nuclear Waste Management", (Indianapolis, USA, April 23-27, 1989), in press.
5. E.J.W. Verwey and J.Th.G. Overbeek, "Theory of Stability of Lyophobic Colloids", Elsevier, Amsterdam, 1948.
6. G.C. Ansell and E. Dickinson, J. Chem. Phys., 85, 4079 (1986).
7. P.C. Hiemenz, "Principles of Colloids and Surface Chemistry", 2nd Edition, (Marcel Dekker, New York, 1986).
8. B.H. Bijsterbosch in "Solid/Liquid Dispersions", edited by Th.F. Tadros, (Academic Press, London, 1987), Chapter 4.
9. "Handbook of Physics and Chemistry", 64th Edition, edited by R.C. Weast, (CRC Press, Boca Raton, 1984).
10. J. Barksdale, "Titanium. Its Occurrence, Chemistry, and Technology", 2nd Edition, (The Ronald Press Company, NY, 1966).
11. T.A. Ring, ChemTech, 60 (January, 1988).

PART IV

Processing Science II: Gelation, Aging and Drying

FRACTAL STRUCTURE AND FRACTAL TIME IN SILICA SOL-GELS

JAMES E. MARTIN AND JESS WILCOXON
Sandia National Laboratories, Albuquerque, NM 87185

ABSTRACT

Near the gel point, light scattering studies of silica sol-gels reveal fractal clusters whose size diverges as a power law, in accord with the predictions of percolation theory. More surprising is the appearance of a fractal time description of the dynamics of these clusters. This novel dynamics has recently been revealed by quasielastic light scattering from the density fluctuations that occur at the sol-gel transition. Since the relaxation of fluctuations in these branched polymer systems is self-similar, decay processes occur on all time scales (fractal time), and average decay times diverge. An interpretation of this observation will be presented that relies on a length-scale-dependent viscosity and the geometrical self-similarity of the sol-gel transition. The scattering theory is extended to the calculation of time- and frequency-dependent viscoelastic properties, as well as mechanical properties such as the shear modulus, steady state creep compliance, and viscosity. The viscoelastic predictions are found to be in good agreement with experimental data.

INTRODUCTION

Silica gels are technologically important materials with a rich chemistry, yet relatively little is known about the evolution of structure of these complex materials. In part, the complexity of silica gels arises from the wealth of synthetic routes used to produce them. A typical synthetic process depends on such parameters as the pH, concentration of monomer, water, catalyst, salt etc., and these parameters are usually varied in an empirical fashion to produce a suitable gel time, gel density and so forth. That the evolution of structure in these gels is so poorly understood is partially due to the fact that researchers are unable to agree on exactly what is meant by structure. Once a suitable definition of structure is adopted, one might then ask some very basic questions, such as "What structural characteristics are strongly affected by the chemistry and what properties are largely immutable?" Since the most dramatic physical changes occur in the vicinity of the sol-gel transition, this regime would seem to offer the most fruitful initial avenue of investigation.

The investigations we have made on the sol-gel transition include relatively

Mat. Res. Soc. Symp. Proc. Vol. 180. ©1990 Materials Research Society

The investigations we have made on the sol-gel transition include relatively straightforward static structure measurements as well as more complex determinations of dynamical properties. To interpret these measurements we have used the well known analogy [1-4] between the sol-gel transition and a second-order thermodynamic phase transition to develop theories of the elastic and inelastic light scattering behavior, and viscoelastic phenomena. In this article we give a overview of the various aspects of the sol-gel transition in silica, and briefly discuss the less universal aspects of growth that occur at early times.

THE SOL-GEL TRANSITION

Length Scales

At the gel point many physical properties have the value o or ∞: for example, the shear modulus is 0, the viscosity is ∞, the gel fraction is 0 and the average cluster mass is ∞. One way to quantify structure is to ascertain exactly how things come to be 0 or ∞. This *critical point* approach to gelation produces a family of exponents that can then be understood in terms of a model of growth that predicts a length scale divergence at a finite time. The obvious practical question thus becomes whether this family of exponents can be affected by the choice of chemistry - the standard lore of critical phenomena would suggest that chemistry is irrelevent. However, the sol-gel transition is more complex than a thermodynamic phase transition and in the presence of solvent there are *two* length scales [5]. One of these length scales, the *spatial* correlation length, is sensitive to chemistry and the other length scale, associated with the connectivity divergence, is not. The spatial correlation length is finite and arises from the aggregation phase of growth that occurs at early time, whereas the connectivity correlation diverges at the gel point.

In a chemical gel bond energies are large compared to kT, so it is not obvious that the *quenched* randomness of the resulting structures can be described by an equilibrium model. However, if the bonding between neighboring monomers is completely random, the structure of the gel will be described by the bond percolation model. As applied to gelation, percolation may be thought of as a kinetic model that generates a frozen equilibrium ensemble. We will consistently use the percolation model as a basis for comparison of our data.

Fractal Dimensions and Scattering

Near the gel point, the percolation model generates a self-similar ensemble of branched polymers. Any single polymer has a fractal dimension [1] D=2.5, i.e. the radius R scales with the mass M as $M \sim R^{2.5}$. However, the distribution of cluster masses is also self-similar, in the sense that the mean separation distance between polymers of radius R is proportional to R for all R, implying an ever increasing number of smaller clusters. It is easily shown [6] that the number of clusters of mass M is $N(M)=M^{\tau}$ where the *polydispersity exponent*

$$\tau=1+3/D=2.2 \qquad (1)$$

Since this relates a critical exponent to the dimension of space (in eq. 1 d=3), it is known as a *hyperscaling relation* [1]. A light or x-ray scattering experiment allows us to probe the *net* self-similarity of this *twice fractal* ensemble, which is a combination of the self-similarity of a single cluster and the self-similarity of the size distribution. The combined effects give [7,8]

$$I \sim q^{-D(3-\tau)} \qquad (2)$$

where I denotes the scattered intensity and q is the scattering wavevector [$q=4\pi\sin(\theta/2)/\lambda$, where θ is the scattering angle and λ is the wavelength in the scattering medium]. The dimension $D(3-\tau)$ is called the *ensemble fractal dimension* and is a distinct concept from the fractal dimension D of a single cluster. This point is not universally appreciated and some investigators [9] have incorrectly assumed that the standard mass fractal scattering behavior $I \sim q^{-D}$ applies near the gel point.

In making comparisons to experiment there is an additional subtlety; gelation is a transition in *connectivity*, and in order to probe the connectivity scattering measurements must be done on diluted samples. Otherwise, the self-similar packing of clusters cancels the scattering. As explained below, clusters swell upon dilution [10,11], reducing the single cluster fractal dimension D from 2.5 to 2. Thus the anticipated scattering behavior from a dilute bath of percolation clusters is $I \sim q^{-1.6}$, since $D(3-\tau)=2(3-2.2)=1.6$. Our light scattering experiments [12,13] on tetramethoxysilicon (TMOS) gels, catalyzed by either acids, bases, or with fluoride ion, give $I \sim q^{-1.60\pm0.06}$ in excellent agreement with percolation. Similar results were obtained on TEOS gels, indicating that this aspect of the structure is insensitive to the chemistry.

The structural evolution that occurs far before the gel point is controlled

by aggregation and is therefore much more sensitive to chemistry. By carefully controlling pH and ionic strength a wide variety of structures can be produced, and growth rates can easily be changed over 8 orders of magnitude. In fact, it is possible to observe [5] the exponential growth associated with *reaction-limited aggregation*, as well as the power-law growth [14] associated with *diffusion-limited aggregation*. However, no matter how complex and chemistry-dependent the initial growth is, near the gel point the aggregates percolate to create a universal sol-gel transition.

Polydispersity

An important aspect of the critical approach to the sol-gel transition is the prediction that the polydispersity exponent $\tau=1+3/D$ is greater than 2. In fact, $\tau>2$ is absolutely essential if one is to have a gel point in finite time. The reason is clear enough; at the gel point the average cluster radius diverges to infinity, yet clusters of comparable size cannot overlap. Thus if all clusters were more or less the same size, they would tend to occupy an infinite volume at the gel point. Of course, in reality the volume of the gel doesn't diverge at the gel point. It turns out that the only way in which the average radius can diverge without the total volume diverging is to have the polydispersity algebraically decay as $N(M)\sim M^{-\tau}$ with $\tau=1+3/D$. From lineshape analysis of the intensity correlation autocorrelation function, we have determined [15] $\tau=2.3\pm.15$, in accord with the critical point analogy of the the sol-gel transtion.

Divergence of the Cluster Size

Let us now return to our original point of how things come to be 0 or ∞. In short, all divergences are due in one way or another to the divergence of the average cluster mass, i.e. the appearance of an infinite cluster at the gel point. In the percolation model divergences follow standard critical point formulae [1] $A\sim\varepsilon^{\alpha}$, where in practical measurements ε is the time from the gel point and the critical exponent α may be positive or negative. For example, the percolation model predicts that the average cluster radius and mass diverge as

$$R_z\sim\varepsilon^{-\nu(.9)} \qquad M_w\sim\varepsilon^{-\gamma(1.76)} \tag{3}$$

respectively, where the numerical value of the exponent is in parenthesis. Using quasielastic and elastic light scattering we found that [16] $R_z\sim\varepsilon^{-1.1\pm0.06}$

(exponent corrected for swelling) and $M_w \sim \varepsilon^{-2.7\pm0.3}$, in excellent support of the critical point analogy, but only in qualitative agreement with percolation. Data on organic systems are in better agreement with percolation exponents.

These light scattering measurements demonstrate that ~10 min before a gel time of ~170 min, silica cluster radii were already well over 10,000 Å. This observation is in conflict with previous small angle x-ray scattering measurements on TEOS gels [9]. In these measurements the so-called 'Guinier' radius (i.e. R_z) was reported to be only ~200 Å just 1 min before a gel point of ~500 min. Further, a critical divergence of R_z was not found, implying that the system never gels. These unexpected measurements appear to be an artifact of the 200 Å resolution of the Kratky SAXS camera. In short, when scattering measurements are made in the intermediate regime where $qR_z>>1$, the scattering is described by the *length scale independent* form $I \sim q^{-\alpha}$, and no information about the cluster radius can be obtained (a direct result of mass conservation.) Thus although the 'Guinier' analysis can be erroneously applied to intermediate scattering data, it does not yield the cluster radius, but simply measures the smallest scattering wavevector available on the instrument - the instrumental resolution.

Swelling of Clusters (Linear Polymers?)

Since the growth that gives rise to branched polymers is a continuous divergence in connectivity, it is not possible to determine the structure in the reaction bath by using techniques that probe spatial correlations (e.g. scattering). Thus we can only measure the ensemble fractal dimension of the branched polymers after significant dilution. In practice it has been necessary to dilute clusters as much as 1000:1.

Theories of branched polymers predict a dramatic swelling upon dilution from the bulk state into a good solvent. In fact, the fractal dimension of a branched polymer is predicted to change from 2.5 to 2 upon dilution [10,11] Since this change cannot be determined directly, we have adopted indirect methods of determining the change in fractal dimension ΔD. The first method is to measure the divergence of the intrinsic viscosity $[\eta]$ near t_{gel}. In terms of the typical cluster mass M_z this divergence depends on ΔD through [2,17]

$$[\eta] \sim M_z^{3\Delta D/D_s} \qquad (4)$$

where D_s is the swollen dimension. Thus if the fractal dimension doesn't change upon dilution the viscosity does not diverge as a power law. Using percolation exponents, eq. 4 can be expressed in terms of the weight average cluster mass as

$[\eta]\sim M_w^{3/8}$. Preliminary experiments show that the intrinsic viscosity diverges, but that ΔD only changes by about 2/3 of its theoretically predicted value of 0.5. *A technical note: in the silica literature the intrinsic viscosity is sometimes expressed in terms of the number average molecular weight as $[\eta]\sim M_n^a$. This is correct for linear polymers, but for branched polymers formed near the sol-gel transition this relation is incorrect, since M_n does not diverge at the gel point. In other words, formally the exponent $a=\infty$.*

ΔD can also be determined by using light scattering to measure the concentration dependence of the spatial correlation length ξ which may be thought of as an apparent cluster size in solution (it has nothing to do with the real cluster size, but is merely the radius that is measured in a scattering experiment.) In the reaction bath ξ is small, typically ~200 Å, but when the system is diluted, ξ increases rapidly, eventually becoming the true cluster size (10^4 - 10^5 Å) in the limit of infinite dilution. Physically, the correlation length is the length scale beneath which the solution is essentially dilute. In any case, it can be shown that ξ increases with dilution according to [18,19]

$$\xi\sim c^{-D/3\Delta D} \qquad (5)$$

Using percolation exponents and the predicted swelling of $\Delta D=0.5$ gives $\xi\sim c^{-5/3}$. Light scattering measurements [19] on successively diluted silica clusters formed very close to the gel point give $\xi\sim c^{-2.0\pm0.3}$ for both acid- and base-catalyzed TMOS sols, in substantial agreement with eq. 5. It is important to note that the observed concentration dependence is strong and independent of the method of catalysis.

This observation conflicts with earlier studies [9] of silica that attempted to determine whether acid or base catalysis forms linear or branched polymers. In these SAXS studies, samples formed very close to the gel point were diluted and the change in the 'Guinier' radius was determined. Two errors led to the conjecture of linear polymers. First, the 200 Å resolution of the Kratky camera made it seem that in the base-catalyzed samples the Guinier radius did not change upon dilution, whereas light scattering measurements, with a resolution of ~10,000 Å, demonstrate a large change in the correlation length. Second, in this work it was argued that a Guinier radius that does not increase with concentration indicates branched polymers, since branched polymers do not overlap, whereas a Guinier radius that does increase with concentration indicates linear polymers. This led to the conjecture that acid-catalyzed gels are linear-like and base-catalyzed gels are branched. In fact, when the effects of polydispersity and swelling are properly accounted for one obtains eq. 5, showing that the concentration dependence of the Guinier radius of branched

polymers is actually much *stronger* than in linear polymers. For linear polymers in good solvents the correlation length only diverges [4] as $\xi \sim c^{-3/4}$; thus upon a 10-fold dilution the correlation length of branched polymers increases by ~100, whereas for linear polymers it increases by only ~5.

These observations are further supported by ^{29}Si NMR studies [20] that show that the Q-distributions observed under conditions of acid catalysis are consistent with the binomial distributions expected from percolation (the Statistical Reaction Model [21] is a percolative system). Percolation clusters are highly branched, having a *topological dimension* [22] of ~1.8 (versus 1 for linear structures and 2 for sheets) so the notion of linear chain formation in acid catalyzed gels is in conflict with extant experimental evidence.

Viscoelasticity

Perhaps the most striking aspect of the sol-gel transition is the transformation of a viscous liquid into a rubbery solid. Prior to t_{gel} the viscosity of the sol diverges as $\eta \sim \varepsilon^{-k}$ and beyond t_{gel} the shear or tensile modulus grows as $E \sim \varepsilon^{z}$ [3,4]. The growth in the elastic modulus is related to the appearance of a *gel fraction* - the fractional mass belonging to the infinite network - which is given by yet another power law, $G \sim \varepsilon^{\beta}$.

A less obvious aspect of the fluid near the sol-gel transition is the appearance of dramatic viscoelastic properties [23,24]. An anomalous power law frequency dependence of the complex viscosity is observed near t_{gel}, which results in a slow, power law decay of stress with time. By taking advantage of the concept of self-similarity in the *time* domain, we have developed a dynamical scaling approach to the calculation of normal modes in branched polymers. By summing over these normal modes a complete description of the linear viscoelastic properties can be obtained [24]. For example, at the gel point the shear relaxation modulus decays algebraically in time according to

$$G(t) \sim t^{-3/(2+D)} \qquad (6)$$

Using D=2.5 gives the percolation prediction $G(t) \sim t^{-2/3}$. Since the frequency-dependent complex shear modulus $G(\omega) = G'(\omega) + iG''(\omega)$ is a transform of G(t), the same gel point power law behavior is observed,

$$G'(\omega) \sim G''(\omega) \sim \omega^{3/(2+D)} \qquad (7)$$

Here $G'(\omega)$ is the storage component and $G''(\omega)$ is the loss component of the modulus. Dividing by frequency then gives the percolation prediction for the

complex viscosity $\eta'(\omega)\sim\eta''(\omega)\sim\omega^{-1/3}$. Experimental data taken for the TMOS system at the gel point, shown in figure 1, are in good agreement with this prediction, as are data for many organic gels [24,25].

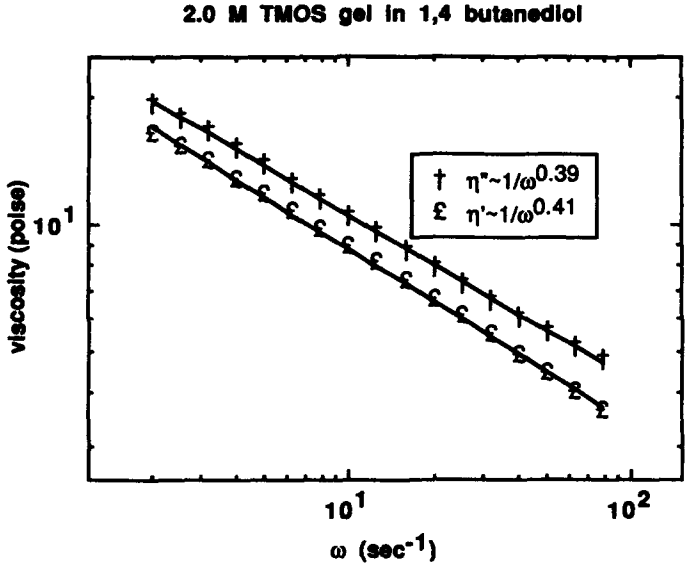


Fig. 1: The complex viscosity for a 2.0 M base cataylzed gel at the gel point shows a power law frequency dependence in accordance with the percolation prediction $\eta'(\omega)\sim\eta''(\omega)\sim\omega^{-1/3}$.

It turns out that these relations for the dynamical properties imply that beyond t_{gel} both the equilibrium shear and tensile moduli scale as [24]

$$E\sim kT/R_z^3 \qquad (8)$$

where R_z is the radius of a typical branched polymer in the reaction bath (above t_{gel} this is just the mesh size of the infinite network.) Thus the modulus, an energy density, is a statement of equipartition - in a unit shear deformation kT is stored per elastic cell of volume R_z^3. Since R_z decreases beyond the gel point, the modulus increases as $E\sim kT/\varepsilon^{8/3}$; this has been experimentally verified in organic resins [25], but not yet in silica gels.

Finally, the steady state shear viscosity diverges as

$$\eta\sim R_z^{2-d_c} \qquad (9)$$

where the *codimension* d_c=3-D. This leads to the percolation prediction $\eta \sim R_z^{3/2} \sim \varepsilon^{-1.4}$. From the light scattering measurements described below, we have determined $\eta \sim \varepsilon^{-1.5\pm0.1}$ for base catalyzed 1M TMOS gels. Direct viscosity measurements on organic resins are in excellent agreement with eq. 9.

Shear Modulus

The last topic we address is the dependence of the shear elastic modulus on the initial monomer concentration, this having more to do with aggregation than gelation. At the start of the reaction a dilute solution of silica monomers is activated by a catalyst. In order to react, these monomers must first diffuse together, colliding many times before reacting if the activation energy is large. This diffusion process is not described percolation, but may be thought of as an aggregation process in which clusters grow exponentially in time [5,26] until the entire volume of the solution is filled. The situation is then much like a huge container filled with tumbleweeds- the mass fraction is very small, but the bushes occupy the entire volume of the container. At this point the aggregates act as huge 'monomers' that then percolate to form a gel. The radius of these monomers is a second, nondivergent length scale that is sensitive to the reaction conditions. For example, the radius at cluster overlap is concentration dependent, becoming large at low monomer concentrations. If ϕ_o is the initial monomer volume fraction, cluster overlap will occur at an aggregate radius of

$$\xi_s \equiv b\phi_o^{-1/(3-D)} \qquad (10)$$

where D is now the fractal dimension of the aggregates and b is the silica monomer radius.

Light scattering experiments [5] on TMOS gels grown under dilute conditions give D=2.3, so the radius $\xi_s \sim \phi_o^{-1.4}$. At this critical radius the system crosses over to gelation, passes through the sol-gel transition and cures into a more-or-less firm gel. However, being an inherently nonequilibrium structure, the final gel maintains the remnants of the early stage of growth, and *far beyond the gel point* the elastic modulus is dictated by the aggregation that occurred at the earliest times! If we accept the aforementioned equipartition of energy as a general rule, the shear modulus of the fully cured gel will be $E \sim kT/\xi_s^3 \sim kT\phi_o^{4.2}$. Thus the final gel shows a strong sensitivity to the reaction conditions. In fact, it is possible to maintain the initial monomer concentration and vary the spatial correlation by an order of magnitude by modifying the pH and ionic strength. This also has a large effect on the rigidity of the final gel.

Critical Dynamics

Reaction bath

It has long been known that when a laser beam is directed through a gel, a grainy pattern is discerned, indicating inhomogeneities in the gel. These structural inhomogeneities have been dignified with the term *microsyneresis* [4]. It is commonly believed that these irregularities arise from microphase separation and therefore would not occur in a perfectly compatible system. However, in quasielastic light scattering investigations [6,26] of the dynamics of the silica sol-gel transition, we have demonstrated that these inhomogeneities are a fundamental part of the physics of chemical gels, being a natural manifestation of the breaking of ergodicity at the gel point.

The scattering of light is due to spontaneous, thermally driven concentration fluctuations. These fluctuations typically have a very short lifetime ($1\text{-}10^4$ μsec) so the eye only sees a time-averaged, apparently homogeneous, emission from the sample. However, in a gel these fluctuations become very slow so that the human eye can easily resolve the motion. To quantify exactly how fluctuations slow down when a gel is formed, we used quasielastic light scattering (QELS) to measure the decay of a concentration fluctuation of wavevector q. We found that as the sol approaches the gel point, the relaxation time of a concentration fluctuation diverges to ∞ in a proper critical point fashion [6], as

$$\langle\tau\rangle \sim \varepsilon^{-1.9\pm0.1} \tag{11}$$

This *critical slowing down* of microscopic density fluctuations before t_{gel} forshadows the frozen inhomogeneities so commonly observed in gels.

More perplexing is the observed form of the relaxation of fluctuations. Most relaxation processes decay exponentially in time, or nearly so, but at the gel point, measurements of TMOS gels indicate that fluctuations relax via the ultra-slow power-law decay [6]

$$S(q,t) \sim t^{-0.27} \tag{12}$$

where S(q,t) is the *homodyne*, or self-beating, dynamic structure factor, which is proportional to the relaxing part of the intensity autocorrelation function. This power law decay is novel, being found only in gelling systems at or beyond the gel point, and implies that the detected scattered photons break time into a fractal set of dimension D=1-0.27=0.73. This fractal time set may be thought of

as a kind of random Cantor set [27].

To explain these dynamical phenomena we developed a theory that describes this system as a *heirarchically constrained dynamics* where the relaxation time of any mode is dependent only on the relaxation of faster modes, not on the relaxation of slower modes. Physically, this implies the existence of a length-scale-dependent viscosity: that is, at the gel point, where the bulk viscosity is ∞, a probe of radius R feels a finite viscosity that scales as $R^{\kappa/\nu}$. This theory of the dynamics of concentration fluctuations correctly predicts a homodyne power law decay of

$$S(q,t) \sim t^{-d_c/(3-d_c)} \qquad (13)$$

along with the critical point divergence of *two* distinct relaxation times. The net result is that QELS beneath the gel point allows determination of the viscosity exponent in $\eta \sim \varepsilon^{-k}$ and the gel fraction exponent in $G \sim \varepsilon^{\beta}$. Numerically, we find $k=1.5$, in good agreement with eq. 7, and $\beta=0.35$, in agreement with the percolation prediction of $\beta=0.39$.

Dilute solution

The relaxation of concentration fluctuations may also be studied in dilute solutions of the sol. In this case the observed relaxations are due to the translational and configurational diffusion of the polydisperse ensemble of branched polymers, and the observed dynamics [12,13,28] is analogous to critical slowing down at consolute points in binary fluids. In this case, *Kawasaki-Ferrel* dynamics is expected [7,28] wherein the relaxation time τ of a concentration fluctuation of wavevector q scales as $\tau \sim 1/q^3$. This result is consistent with self-similarity of the sol, and further justifies the critical point approach to the sol-gel transition. However, internal modes of monodisperse branched polymers can also give $\tau \sim 1/q^3$, so this result is not definitive.

Conclusions

The growth, structure, and dynamics of silica gels is well described by the critical point analogy, and reasonable agreement with percolation exponents is found. This implies that the chemistry is to a large degree an irrelevent aspect near the sol-gel transition. The notion of linear-like polymers in acid catalyzed gels conflicts with experimental evidence and proper theoretical analysis. The early time growth of silica is a nonuniversal aggregation process and accounts for many of the differences in the fully formed silica gels.

References

1. D. Stauffer, *Introduction to Percolation Theory* (Taylor & Francis, London, 1985).
2. M. Daoud and J. E. Martin, in *The Fractal Approach to the Chemistry of Disordered Systems: Polymers, Colloids, Surfaces*, edited by D. Avnir.
3. D. Stauffer, A. Coniglio and M. Adam, in *Advances in Polymer Science 44* (Springer-Verlag, Berlin, 1982).
4. P. G. de Gennes, *Scaling Concepts in Polymer Physics* , (Cornell, New York, 1979).
5. J. E. Martin and J. P. Wilcoxon, Phys. Rev A **39**, 252 (1989).
6. J. E. Martin and J. P. Wilcoxon, Phys. Rev. Lett. **61**, 373 (1988).
7. J. E. Martin and B. J. Ackerson, Phys. Rev. A **31**, 1180 (1985).
8. J. E. Martin, J. Appl. Cryst.**19**, 25 (1986); *also* J. E. Martin and A. J. Hurd, J. Appl. Cryst. **20**, 61 (1986).
9. D. W. Schaefer and K. D. Keefer, Phys. Rev. Lett. **53**, 1383 (1984).
10. J. Isaacson and T. C. Lubensky, J. Phys. (Paris) **41**, L469 (1980).
11. P. -G. de Gennes, C. R. Acad. Sci. Paris **291**, 17 (1980).
12. J. E. Martin, in *Time Dependent Effects in Disordered Materials*, edited by R. Pynn and Tormod Riste, NATO ASI Series, Physics Vol. 167 (Plenum, New York, 1987).
13. J. E. Martin and K. D. Keefer, Phys. Rev. A **34**, 4988 (1986).
14. J. E. Martin, J. P. Wilcoxon, and J. Odinek, to appear in Phys. Rev. A.
15. J. E. Martin, J. Sullivan and J. P. Wilcoxon, unpublished results.
16. J. E. Martin, J. P. Wilcoxon and D. Adolf, Phys. Rev. A **36** 1803 (1987).
17. M. Daoud, F. Family and G. Jannink, J. Physique Lett. **45**, 199 (1984).
18. M. Daoud and L. Leibler, Macromol. **21**, 1497 (1988).
19. J. E. Martin and J. Odinek, preprint.
20. R. A. Assink and B. D. Kay, J. Non-Cryst. Solids **107**, 35 (1988).
21. B. D. Kay and R. A. Assink, J. Non-Cryst. Solids **104**, 112 (1988).
22. J. E. Martin, J. Phys. A: Math. Gen. **18**, L207 (1985).
23. F. Chambon and H. H. Winter, Polym. Bull. **13**, 499 (1985); *also* H. H. Winter, P. Morganelli and R. Chambon, Macromol. **21**, 532 (1988).
24. J. E. Martin, D. Adolf, and J. P. Wilcoxon, Phys. Rev. Lett. **61**, 2620 (1988); *also* J. E. Martin, D. Adolf, and J. P. Wilcoxon, Phys. Rev. A **39**, 1325 (1989).
26. J. E. Martin, in *Atomic and Molecular Processing of Electronic and Ceramic Materials*, Proc. of the Twenty-Third Conference on Ceramic Science, editors I. Aksay, T. Stoebe, G. McVay and J. Wager, Mats. Res. Soc. (1987).
27. B. B. Mandelbrot, in *The Fractal Geometry of Nature*, pg. 247 (Freeman, New York, 1983).
28. J. E. Martin and F. Leyvraz, Phys. Rev. A **34**, 2346 (1986).

^{29}Si NMR STUDY OF SILICON ALKOXIDES: FROM THE CONDENSATION KINETICS IN SOLUTION TO THE DETERMINATION OF THE FRACTAL DIMENSION IN AEROGELS

F.DEVREUX*, J.P.BOILOT*, F.CHAPUT*,AND A.LECOMTE**
*Laboratoire de Physique de la Matière Condensée, URA CNRS 1254, Ecole Polytechnique, 91128 Palaiseau Cédex (FRANCE)
**Ecole Nationale Supérieure de Céramique Industrielle, 87065 Limoges Cédex (FRANCE)

ABSTRACT

The complete condensation kinetics of three silicon alkoxides have been studied by ^{29}Si NMR in the conditions of rapid hydrolysis (acidic medium, water in excess). The gelation of the tetravalent TEOS takes several weeks, whereas the trivalent MTEOS and VTEOS do not form gels. From a quantitative data analysis, we deduce that the first steps of the condensation proceed by progressive formation of small organized units. This accounts for the occurence of highly condensed agglomerates, the absence of gelation in trivalent systems and the very slow kinetics (logarithmic function of time). For the tetravalent TEOS, this is followed by an aggregation phase, which leads to gelation. After the gel time, the transformation of the sol fraction into gel has been followed by observing the broadening of the static NMR spectra. Moreover, the structures of the aerogels obtained by hypercritical drying and of the densified materials resulting from further sintering are characterized by MAS NMR. In particular, measurements of the nuclear relaxation in samples doped with paramagnetic impurities give directly the fractal dimension D of the silicate lattice. The measured value is in agreement with that obtained by the SAXS technique in aerogels ($D\approx2.2$) and is close to $D=3$ for the densified materials.

INTRODUCTION

Besides its possible interest for the preparation of homogeneous glasses and ceramics, sol-gel condensation of silicon alkoxides offers the unique possibility to build in a more or less controlled way randomized objects, which are believed to be a physical realization of fractal geometry [1,2]. In the present communication, we show that ^{29}Si NMR can be used profitably in the whole condensation process and may provide information on both the polymerization kinetics and the structure of the condensed objects.

EXPERIMENTAL

Three silicon alkoxides have been studied: the well known tetraethoxy-silane ($Si(OC_2H_5)_4$ or TEOS) to which a large number of studies have been already devoted and two new systems having three -instead of four- branching possibilities, methyl-triethoxy-silane (CH_3-$Si(OC_2H_5)_3$ or MTEOS) and vinyl-triethoxy-silane (CH_2=CH-$Si(OC_2H_5)_3$ or VTEOS). The polymerization process was initiated by adding acidic water to a solution of alkoxide and ethanol. The alkoxide:ethanol:water concentration ratios were

Mat. Res. Soc. Symp. Proc. Vol. 180. ©1990 Materials Research Society

1:6:10 and the pH of the added water solution was fixed to 2.5. The chemical conditions (water in excess, acidic medium) were chosen in such a way that nearly complete hydrolysis of the alkoxides occurs in a few minutes. This allows to study separately the condensation kinetics which result from the formation of siloxane bridges between the hydrolyzed species.In acidic media , this condensation process is very slow and the gelation -when it occurs- may require several weeks. The samples were kept at a constant temperature of 21°C throughout the experiment. A concentration of 8.10^{-3} M/l of chromium nitrate $Cr(NO_3)_3 9H_2O$ was added in the polymerization solution to enhance the nuclear relaxation.

NMR spectra were recorded at 71.54 MHz with a BRUKER MSL 360 spectrometer, using a home-made silicon-free probe for the liquid state and a Doty MAS probe for the gel state. The repetition time was chosen as a compromise between nuclear relaxation and kinetics: long enough to allow nuclear magnetization recovery, short enough to avoid excessive averaging of the kinetics.

CONDENSATION KINETICS UP TO THE GEL TIME

Figure 1 shows typical ^{29}Si NMR spectra as a function of time for MTEOS, VTEOS and TEOS systems. For MTEOS and VTEOS, the hydrolysis is almost completed within the time necessary to record the first spectrum, that is about ten minutes. For TEOS, a small fraction (less than 10 per cent) of species with one non-substituted ethoxyl group may remain after an hour. This quasi-absence of partially hydrolyzed species leads to quite simple spectra, from which the contribution of silicon atoms with 0, 1, 2, 3, or 4 siloxane bridges, which are conventionally denoted as Q^0, Q^1, Q^2, Q^3 or Q^4, can be accurately obtained. The complete evolution is quantified in figure 2, which displays the relative concentration q_i of the Q^i species as a function of the logarithm of the time. Also shown is the evolution of the degree of condensation, defined as: $c = \Sigma_i \, i * q_i / f$, with f being the connectivity of the monomer (f=3 for MTEOS and VTEOS and f=4 for TEOS). This degree of condensation characterizes the progress of the condensation reactions as a whole[3].

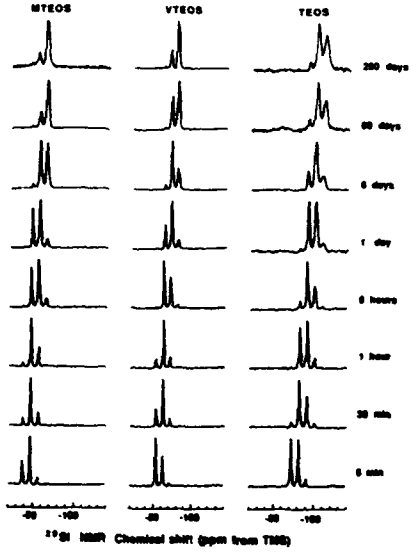


Figure 1: ^{29}Si NMR spectra at different times during the condensation of MTEOS, VTEOS and TEOS. The last two spectra for TEOS have been obtained using Magic Angle Spinning in the gel state.

There are several indications that the beginning of the condensation process in our rapidly hydrolyzed systems corresponds to the formation of small units. First of all, it is seen in figure 2 that the degrees of condensation reach

very high values: 0.95 without gelation for the trivalent systems and 0.81 at the gel point for TEOS. This indicates highly condensed agglomerates, which is not consistent with a simple random polymerization of monomer units. Neglecting intra-cluster condensation, the maximum value for c would be 2/f, i.e. 0.67 for MTEOS and VTEOS and 0.5 for TEOS. Moreover, according to the classical Flory theory [4], the gelation is expected to occur for 1/(f-1), i.e. 0.5 for MTEOS and VTEOS and 0.33 for TEOS. To explain the observed values of c, it is necessary to assume either that the polymerization involves considerable intra-cluster condensation at each step or that the primary units which polymerize are already highly condensed objects. As the first explanation is not consistent with the fractal structure observed for the final aggregates (see below), we favor the second one. Actually, if we assume for simplicity that the starting units are uniform and made of n silicon atoms with a degree of condensation c_0, the final degree of condensation will be $c_\infty = c_0 + 2/(nf)$. In the case f=4 (TEOS), this will give $c_0=1/2$ and $c_\infty=5/8=0.63$ for a 4-membered cycle (n=4) and $c_0=3/4$ and $c_\infty=13/16=0.81$ for an 8-membered cube (n=8). This hypothesis is supported by high resolution NMR studies, which point out the role of cyclic and polyhedral stucture in the condensation process [5,6] and by the absence of gelation in trivalent compounds, where the degree of condensation is as high as 0.95.

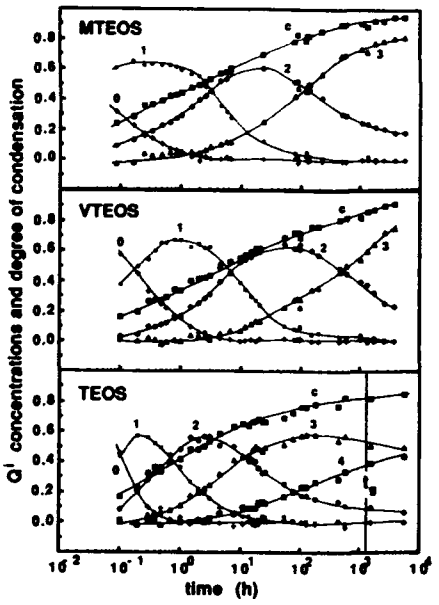


Figure 2: Time evolution of the concentration of the different Q^i species (i=0 to 4) and of the degree of condensation c for MTEOS, VTEOS and TEOS.

On the other hand, a noteworthy feature in figure 2 is that the degree of condensation increases as the logarithm of the time in a large part of the kinetics: almost up to the saturation for the trivalent MTEOS and VTEOS and up to c=0.6 for TEOS. This functional dependence is much slower than those usually expected for first and second order kinetics, c~1-exp(-t) and c~t /(1+t), respectively. The logarithmic law corresponds rather to a kinetic equation of the form: dc/dt ~exp(-c). In fact, such an equation is not unexpected according to the above structural considerations. The mentioned step by step condensation would require bond deformations and possible bond breakings and reformings. In any case, this process should involve an energy barrier which is expected to be proportional to the mean number of already formed siloxane bridges per silicon atom: this may explain that the kinetic constant contains a thermally activated term with an activation energy proportional to c.

SOL-GEL TRANSFORMATION AFTER THE GEL TIME

As recently observed by Vega and Sherer [7], the main effect of gelation is a progressive broadening of the NMR lines due to a slowing down of the molecular motion, which becomes unable to average the anisotropic chemical shift and the dipolar coupling with the protons. This effect can be pointed out by comparing static and MAS spectra. Figure 3 shows spectra recorded with and without rotation at $t = t_g$, 1.4 t_g and 4.1 t_g. MAS spectra show only a small evolution which reflects the slow condensation process. On the other hand, the static spectra display a dramatic broadening due to the progressive freezing of the molecular rotational motion. At $t = 4.1\ t_g$ the static spectrum looks like the one which is expected for a non-averaged anisotropic chemical shift powder distribution. At $t = t_g$ and $t = 1.4\ t_g$, the spectra could be regarded as the superposition of two contributions: a rigid-lattice signal similar to the static spectrum at $t = 4.1\ t_g$ and a motional-narrowed signal similar to the MAS spectrum. The first contribution would correspond to the gel fraction and the second one to the sol fraction. These results are consistent with viewing the gel transition as resulting of the formation of a large scale percolation cluster (the gel phase), coexisting with smaller aggregates (the sol phase). After t_g, the small clusters are progressively connected to the large one. This leads to a small increase of the condensation rate, but to a strong decrease of the motional-narrowed contribution to the static NMR spectrum.

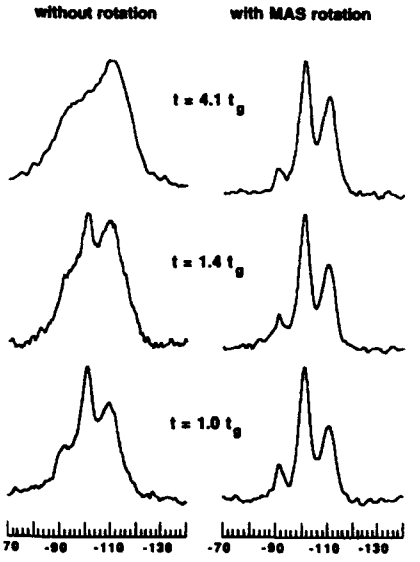


Figure 3: Comparison of ^{29}Si NMR spectra of condensed TEOS without and with MAS rotation at different times after t_g.

HYPERCRITICAL DRYING AND SINTERING

By evacuating the solvant under hypercritical conditions (T= 255°C and p = 75 bars), the alcogel is transformed into an aerogel, whose density (0.17 g/cm^3 in the present case) is controlled by the monomer concentration in the initial solution. Then, the aerogels can be sintered. Heating at 1000°C leads to an amorphous material whose density is about 1.6 g/cm^3 and heating above 1200°C gives the cristobalite phase of the silica with a density 2.3 g/cm^3 .

Figure 4 shows the spectra of these different forms of silica. In the alcogel and in the aerogel, the three broad lines

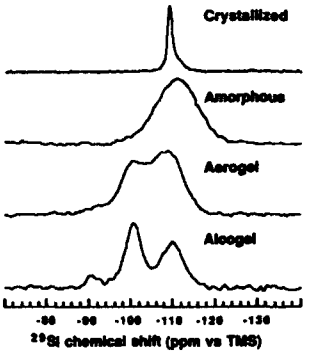


Figure 4: ^{29}Si MAS NMR spectra for different forms of silica.

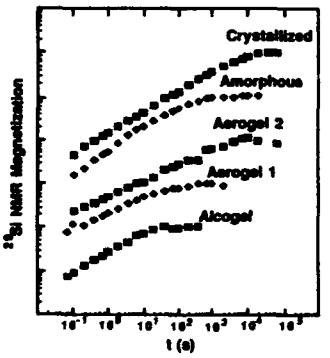


Figure 5: Time dependence of the ^{29}Si magnetization recovery after saturation.

Q^2, Q^3 and Q^4 reflects the lacunar structure of these systems. In the densified materials, it only remains the line of four-coordinated Q^4 silicon. As a result of the random or ordered environment of the silicon atoms, the line is broad for the amorphous compound and sharp for the crystallized one.

FRACTAL DIMENSION IN AEROGELS

Finally, we present a new method to determine the fractal dimension in these systems. It is based upon the nuclear relaxation induced by the paramagnetic impurities diluted in the lattice [8]. Contrary to the diffusion techniques which involve an analysis of the scattered intensity in reciprocal space, the present method gives directly the mass-to-distance relation in real space: $M(r) \sim r^D$, with D being the fractal dimension. Actually, if one applies a saturation comb to kill the ^{29}Si spin magnetization, the recovery of this magnetization will reflect the spatial repartition of the nuclear spins which relax to their equilibrium polarization by dipolar flipping with the dilute magnetic ions. Since the time constant for the dipolar coupling relaxation increases with the distance as r^6, the recovered magnetization at time t after saturation will be that of the spins which are contained in a sphere of radius $r \sim t^{1/6}$ and therefore, it will retain a time dependence as: $m(t) \sim t^{D/6}$.

Figure 5 shows the recovery of the ^{29}Si magnetization after a saturation comb in five compounds: an alcogel, two aerogels with different paramagnetic impurity concentrations, an amorphous and a crystallized sample. The chromium to silicon ratio has been measured by ESR: It was 6×10^{-3} for the alcogel and the first aerogel, 6×10^{-4} for the second aerogel, 3×10^{-4} for the amorphous and 9×10^{-5} for the polycrystalline powder. The relaxation is strongly non-exponential for all the studied samples. From the log-log plot in figure 2, it turns out that the time dependence of the magnetization recovery follows a power law $m(t) \sim t^{\alpha}$ in an extended time range, before reaching a saturation plateau.

The values of the exponent α are obtained by fitting the

power law regimes in figure 5 up to the point where the magnetization is half of its saturation value. This gave D values * of 2.85 for the alcogel, 2.3 and 2.1 for the aerogels, 3.1 for the amorphous and 2.85 for the crystal. Finding values near D=3 for the densified materials is quite satisfactory and provides a good reliability test. For the aerogels, the NMR results are quite consistent with those of small angle X-ray scattering (SAXS) experiments performed on the same samples which give D=2.3. On the other hand, the SAXS result is D=2.0 for the alcogel. This disagreement is easily explained by remarking that the relation $M(r) \sim r^{D}$, from which the NMR D is deduced, describes the mass distribution around the magnetic impurities. Since the chromium spins can be everywhere in the alcogel solution, the NMR relaxation does not reflect any more the spatial correlations on the silica polymer, but the mass repartition in the gelled solution which has no reason to be different from a regular tri-dimensional one.

Actually, it is quite unusual to observe a power law for such a long time range, because the direct dipolar coupling between nuclear and electronic spins is generally relayed at long distances by the nuclear spin diffusion, which gives rise to an exponential recovery [9]. However,this short cut is avoided in the present experiments because of different effects. Firstly, in the aerogels, the fractal geometry imposes a tortuous path to the magnetization leading to a slow anomalous diffusion.Secondly, in both the aerogel and amorphous samples, the structural disorder may cause considerable shifts of the NMR lines of neighbouring spins making the dipolar flipping quite inefficient.Finally, in all samples, the magic angle spinning which averages the secular part of the dipolar coupling between nuclear spins inhibits the flip-flop transitions between neighbouring ^{29}Si and quenches the nuclear spin diffusion process.

* Note here that $D = 6\alpha$

REFERENCES

1.D.W. Schaefer and K.D. Keefer, Phys. Rev. Lett., 56, 2199 (1986)

2.R. Vacher, T. Woignier, J. Pelous and E. Courtens, Phys. Rev. B, 37, 6500 (1988)

3.F. Devreux, J.P. Boilot, F. Chaput and A. Lecomte, Phys. Rev. A, to be published

4.P.J. Flory,Principles of Polymer Chemistry (Cornell Univ. Press, New York, 1953)

5.J.C. Pouxviel, J.P. Boilot, J.C. Beloeil and J.Y. Lallemand, J. Non Cryst. Solids, 89, 345 (1987)

6.L.W. Kelts and N.J. Armstrong, J.Mat.Res.,4, 423 (1989).

7.A.J. Vega and G.W. Sherer, J. Non Cryst. Sol., 111, 153 (1989)

8.F.Devreux, J.P. Boilot, F. Chaput and B. Sapoval, submitted

9. W.E. Blumberg, Phys. Rev., 119, 79 (1960)

LOW WAVENUMBER RAMAN SCATTERING IN SILICA AND SILICOPHOSPHATE AEROGELS

BARBARA L. WALDEN, ELSE BREVAL, AND WILLIAM B. WHITE
Materials Research Laboratory, The Pennsylvania State University,
University Park, PA 16802

ABSTRACT

Raman spectra, measured on silica and silicophosphate aerogels in the range of 5 to 70 cm^{-1}, revealed a "particle band" that arises from the discrete particulate character of the gels at very small size scales. TEM measurements of the nanoscale structure in the gels correlate with the location of the particle band maximum.

INTRODUCTION

Raman spectroscopy has proved a useful tool in the study of disordered materials. In particular, the low frequency regions (below 100 cm^{-1}) is sensitive to structural features with characteristic lengths of one to tens of nanometers, intermediate in scale between the atomic and bulk regimes. Glasses, for example, exhibit density fluctuations over this range and as a consequence display features in their low frequency Raman spectra not seen in well ordered crystals. Recently Duval and his coworkers [1] discovered that very small crystallites in glassy matrices would give rise to a distinct "particle band" at very low wavenumbers. Since then similar findings have been reported for silica aerogels [2-5]. These low frequency bands are thought to arise from torsional and spherical acoustic modes of the small particulates which make up the aerogel. The wavenumber of the particle band is inversely related to particle size and has values in the range of 5 - 30 cm^{-1}.

The present investigation was designed to first reexamine the particle bands in silica aerogels and then to extend the measurements to aerogels containing phosphorus as a second component. All of the studies thus far reported have dealt exclusively with the SiO_2 composition. It would be of interest to know if the addition of other network-forming components modifies the aerogels at the nanostructural scale.

EXPERIMENTAL METHODS

Gels were prepared by the hydrolysis and condensation of a solution of tetraethylorthosilicate (TEOS), ethanol, and water, aided by either HCl (acid catalyzed gels) or NH_4OH (base catalyzed gels). Orthophosphoric acid both provided the source of phosphorus and acted as an additional catalyst for the silicophosphate gels. The ratio of phosphorus to silica ranged from 0.0005 to 0.01. Other compositional parameters varied were pH and the amount of water.

Once gelled, the alcogels were allowed to age for times ranging from a few hours to more than 1000 hours. They then immersed in ethanol inside a pressure vessel which was heated to bring the temperature and pressure close to the critical point of water. Pressure was slowly bled off to eliminate the solvent and dry the gel. This procedure helps preserve the gel structure by eliminating the internal capillary stresses which distort and shatter gels dried under atmospheric pressure. The dried aerogels were baked out at about 500 C for 1-2 hours to drive off the remaining organic components. In many samples, an additional heat treatment at 500 to 700 C was necessary to quench a ubiquitous fluorescence which would otherwise overwhelm the Raman scattering. At these temperatures the internal

Mat. Res. Soc. Symp. Proc. Vol. 180. ©1990 Materials Research Society

surfaces of the gel become smoother [2,6] but the nanostructure undergoes no significant changes [3].

The final aerogels varied in appearance from hard and glassy for the acid catalyzed gels to typically bluish yet still transparent for base catalyzed aerogels. Two of the base catalyzed silicophosphate gels (PB170 and PB330) developed macroscopic crystals, and of these PB330 also formed a precipitate which settled out before the solution gelled. The sample notation incorporates the preparation conditions and the density: e.g. SA360. S = silica aerogel (P = silicophosphate aerogel) A = acid catalyzed (B = base catalyzed), 360 = density in kg/m^3. The bulk density of the gels was determined by mercury displacement and varied from 170 to 550 kg/m^3.

Raman measurements were obtained with a Spex model 1401 double monochromator using the 514.5 nm line of an argon ion laser as an excitation source. All spectra were measured without a polarization analyzer. The resolution was 2 cm^{-1} for silica and acid catalyzed silicophosphate gels and 3 cm^{-1} for base catalyzed silicophosphate gels. The spectroscopic range investigated, 5 to 70 cm^{-1}, places all features of interest very close to the laser line, making it difficult to separate desired signals from stray light. To assist in stray light discrimination, an iodine filter was used. One of the very sharp absorption lines of iodine happens to lie within the gain curve of the 514.5 nm line and by using an etalon to force the laser into single mode oscillation, the laser output can be tuned to precisely coincide with this resonance [7]. The filter consisted of an evacuated optical cell which contained a few crystals of iodine which could be heated to increase the iodine vapor pressure. When placed between the scattering sample and the entrance slit it strongly attenuated the elastic contribution to the scattered light, leaving the inelastic component relatively unaffected. At a typical operating temperature of 95 C, the cell attenuated elastically scattered laser light by a factor of 10^3 to 10^4 while reducing the Raman intensity by only a factor of two The iodine filter does impart a noticeable waviness to the Raman spectrum, however, and in order to extract spectra with correct lineshapes it was necessary to ratio the raw Raman data to a white light spectrum taken under identical experimental conditions. This was done for all spectra shown here.

Transmission electron microscope (TEM) images were obtained using a Philips EM420 instrument with an acceleration voltage of 120 kV. Sample preparation proved to be difficult, and for those images shown here, the gels were crushed, the powder distributed on a carbon-coated grid, then re-coated with carbon. The magnification was set at 105,000 to avoid the beam damage which occurred at high magnifications. A representative set of TEM images is shown in Figs. 1-4. The images show a distinct granularity at a scale of 2 to 10 nm and these granules are considered "particles" for the purpose of analysis. However, they are strongly interconnected, as shown particularly well in Fig. 1, and are not "particles" in the strict sense of the word. Particle size was measured for each aerogel by simply measuring the diameters of about 20 of the "particles" shown on each TEM image and calculating the mean.

LOW WAVENUMBER RAMAN SCATTERING

Spectra for acid catalyzed silica aerogels are shown in Fig. 5 and for base catalyzed silica aerogels in Fig. 6. The observed Raman scattering intensity was corrected both for the average dark current and for absorption by the iodine cell. The remainder was taken to be the count rate due to Raman scattering and was divided by the usual population factor to obtain the spectra shown in the figures.



Fig. 1 TEM image of acid-catalyzed aerogel SA360. Scale bar = 50 nm.

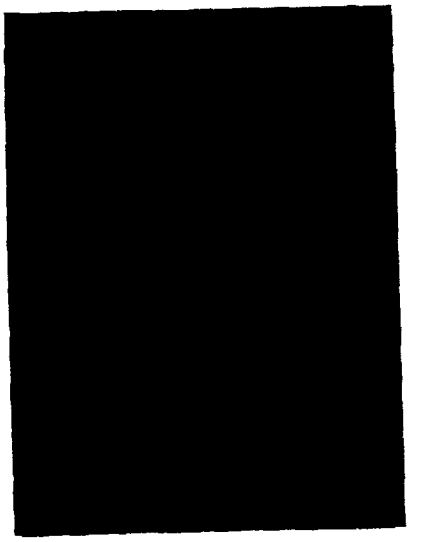


Fig. 2 TEM image of base catalyzed aerogel SB240. Scale bar = 50 nm.

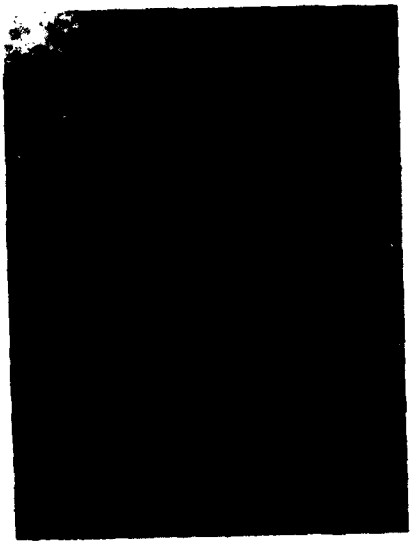


Fig. 3 TEM image of acid catalyzed silicophosphate aerogel PA420. Scale bar = 50 nm.

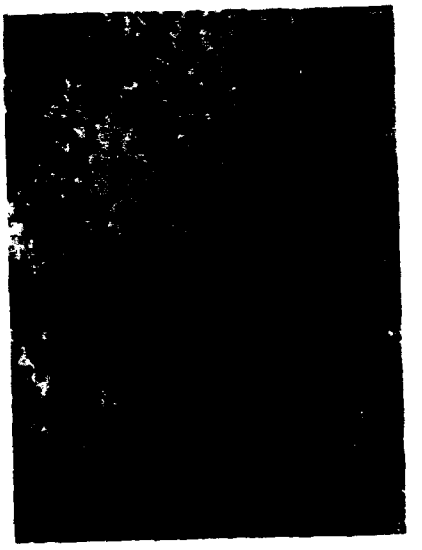


Fig. 4 TEM image of base catalyzed silicophosphate aerogel PB170. Scale bar = 50 nm.

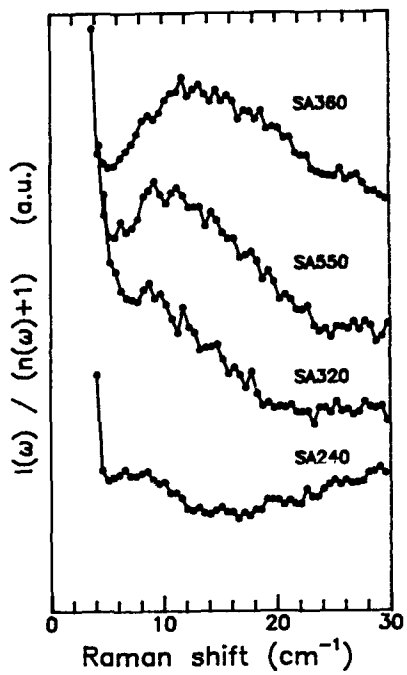


Fig. 5 Raman spectra of acid catalyzed silica aerogels.

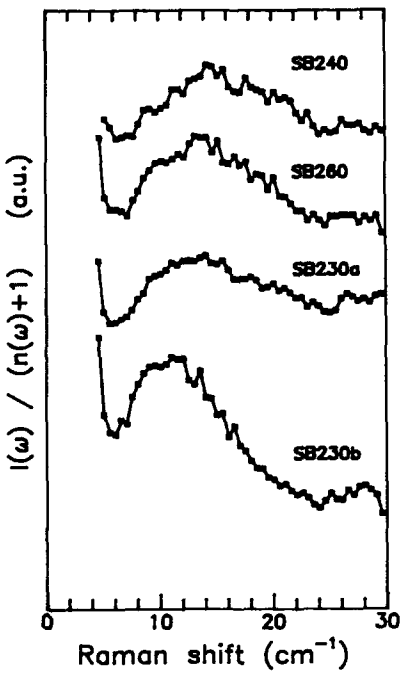


Fig. 6 Raman spectra of base catalyzed silica aerogels.

The spectra agree with spectra of silica aerogels reported in the literature [2-5]. Most show a distinct broad band with a maximum near 10 cm^{-1}, though peaks in the spectra of two of the acid catalyzed aerogels are less well defined, having partially disappeared into the laser line.

Raman spectra of the silicophosphate aerogels are shown in Figs. 7 and 8. The processing of the intensity data was the same as for the silica aerogels. These spectra show that the addition of very small amounts of phosphorus causes a substantial difference in the scattering behavior. The particle band in the silicophosphate aerogels is typically much broader and less well defined than in the silica aerogels, making it necessary to extend the scan range up to at least 60 cm^{-1}. In this region the additional Raman scattering from air trapped in the pore spaces of the aerogel becomes most apparent. This is especially noticeable in the base catalyzed silicophosphate aerogels (Fig. 8) and responsible for the "fine structure" seen between 30 and 60 cm^{-1}. The spectrum of air is shown for comparison at the bottom of the figure. This interference makes it extremely difficult to assign "peak" positions in any but a very rough way.

DISCUSSION AND CONCLUSIONS

The main effect of phosphorus is a general reduction in the size of the fundamental particles (Figs 3 and 4). The smallest particles were obtained at the lowest phosphorus concentrations (Fig. 9).

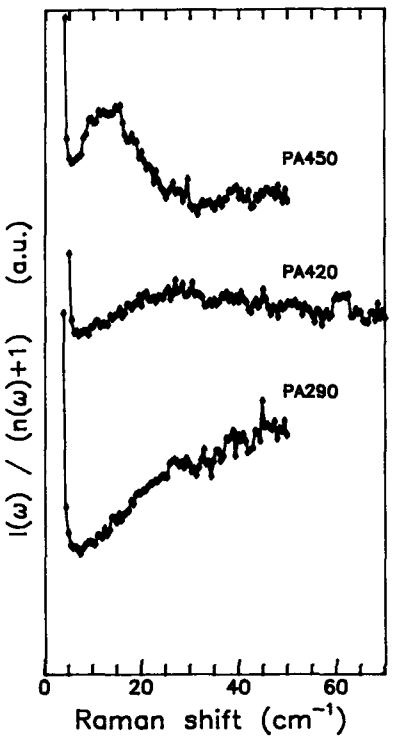


Fig. 7 Raman spectra of acid catalyzed silicophosphate aerogels.

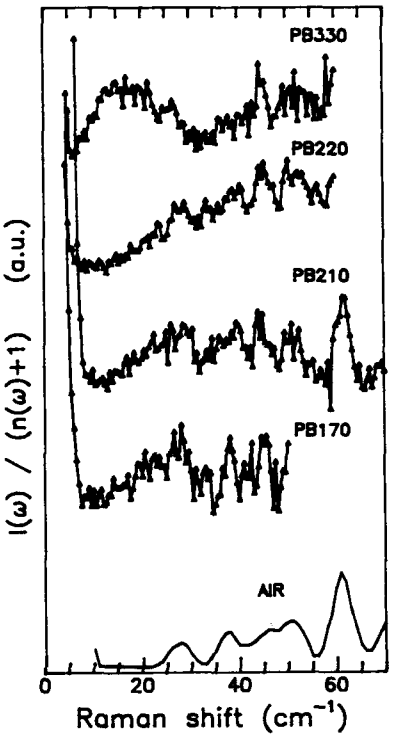


Fig. 8 Raman spectra of base catalyzed silicophosphate aerogels

The particle band was originally interpreted as a surface mode of small spherical crystallites separated from a glassy matrix [1]. This interpretation was carried over to the particle-like small structures that appear in aerogels [2-5]. As such there is a relationship between the frequency of the particle band and the particle size

$$\omega = 0.8\ v/2ac \qquad (1)$$

where ω = band wavenumber in cm^{-1}, v = sound velocity in m/sec, 2a = particle diameter in m, and c = velocity of light in m/sec. The numerical factor of 0.8 is a geometrical factor associated with spherical particles.

Figure 10 shows a plot of the "particle size" as measured from the TEM images as a function of the measured particle band wavenumber. A linear trend is apparent. Previous workers [2-4] have taken 4000 m/sec as the sound velocity, a value which is close to the average sound velocity in silica glass. If this value of v is substituted into the particle mode formula, the result is the straight line plotted in Fig. 10. Although there is some scatter in the data, the fit is quite good. Estimated error for both wavenumber and particle diameters is shown on the figure by open rectangles; dots next to data points indicate additional uncertainty. The fact that the particle bands for both silica and silicophosphate aerogels fall on the same trend line supports the hypothesis that these bands are due to surface modes dependent only on particle size.

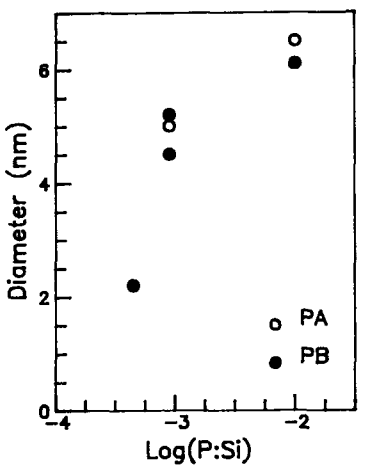


Fig. 9 Relation between particle size and P/Si ratio.

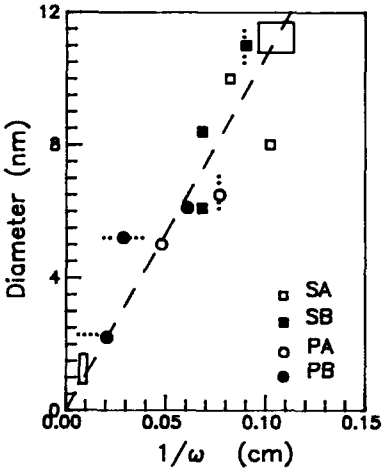


Fig. 10 Relation of particle size to particle band wavenumber.

It appears that the particle band is a useful probe of gel structure at size scales up to about 20 nm. The particle band for larger size structures becomes lost in the tail of the laser line. This procedure has already been used to monitor the growth of silica particulates during thermal densification of aerogels [3,5]. This is a nondestructive technique which involves minimal sample preparation, a clear advantage over TEM when semiquantitative measurements of particle size are desired.

Acknowledgements

This work was supported by the National Science Foundation under Grant No. DMR-8812824.

References

1. E. Duval, A.Boukenter, and B. Champagnon, Phys. Rev. Lett. 56, 2052 (1986).
2. A. Boukenter, B. Champagnon, E. Duval, J.L. Rousset, J. Dumas, and J. Serughetti, J. Phys. C 21, L1097 (1988).
3. J.L. Rousset, E. Duval, A. Boukenter, B. Champagnon, A. Monteil, J. Serughetti and J. Dumas, J. Non-Cryst. Solids 107, 27 (1988).
4. A. Boukenter, B.C. Champagnon, E. Duval, J.L. Rousset, Phil. Mag. B 59, 125 (1989).
5. J. Pelous, J.L. Sauvajol, T. Woignier and R. Vacher, Physica A 157, 625 (1989).
6. Y. Tsujimi, E. Courtens, J. Perlous, and R. Vacher, Phys. Rev. Lett. 60, 2757 (1988).
7. G.E. Devlin, J.L. Davis, L. Chase, and S. Geshwind, Appl. Phys. Lett 19, 138 (1971).

BASE-CATALYZED SILICA GELS: STRUCTURE AND CHEMISTRY

GARRY J. GARVEY and BRUCE E. SMITH
AKZO Chemicals Inc., Livingstone Ave., Dobbs Ferry, NY 10522.

ABSTRACT

The chemical and physical properties of two base-catalyzed silica gels systems were characterized. The sol-gel transition was studied by titration, rheometry, and NMR. Pyrolysis behavior was monitored by TGA and mass spectroscopy. Many characteristics were strikingly similar for the two base-catalyzed systems. However ammonium hydroxide additions resulted in heterogeneities at lower concentrations than ammonium carbonate. Ammonium carbonate enhanced oxidation on pyrolysis.

INTRODUCTION

Gelation of hydrolyzed tetraethyl orthosilicate (TEOS) sols can be induced by addition of aqueous bases, which under some circumstances results in heterogeneous gelation due to localized regions of high pH. This commonly occurs for highly concentrated ammonium hydroxide additions. The problem can be avoided by using an equal normality of a weaker base such as ammonium carbonate. The current study is a comparison between silica gels prepared using these two bases.

The two-step process of gel formation is an excellent method of rapidly producing a silica gel. First, aqueous acid catalysis of TEOS produces rapid and nearly complete hydrolysis. Second, base catalysis of the hydrolyzed sol promotes rapid polymerization and gel formation. This process has been well characterized [1] and chemical mechanisms have been proposed [2,3]. Ion specific effects have been noted [4].

The conditions under which this two step process occurs affect the gel structure. The mechanical properties of the sol-gel transition have been studied by shear rheometry [5]. The evolution of gel structure over long time periods has been investigated by transverse loading of cast gel bars [6,7]. Gel structure has also been characterized by NMR [8,9]. The surface area, residue hydroxyl, and carbon contents of TEOS-derived dry gels have been investigated [10]. The effects of chemistry on the pyrolysis and densification of dry gels were addressed [11].

The current study seeks to apply several of these approaches to define differences generated by two bases, ammonium hydroxide and ammonium carbonate. This study follows the evolution of some chemical and physical properties from solution to calcined silica gel in an attempt to identify these differences.

PROCEDURE

A clear sol was prepared from TEOS, [AKZO, Silbond Pure ®] using 1N nitric acid (Fisher, ACS reagent), ethanol (Quantum, U.

Mat. Res. Soc. Symp. Proc. Vol. 180. ©1990 Materials Research Society

S. P.) and deionized water (18 MΩ) and refluxed for ten minutes. The sol composition was 1 mole TEOS, 2.7 moles water, 0.05 moles ethanol at 0.0125 N nitric acid concentration. The sol sample was analyzed by capillary GC (HP-5890 with a 30m x 0.25mm DB5 column). Hydrolysis was more than 80 % complete as determined by ethanol peak intensity. No unreacted monomer was detected.

The hydrolyzed TEOS sols, thermostated to 25°C, were titrated using each base catalyst (0.1N). A titration rate of one ml/min was continued until gelation. PH was monitored using the Beckman Select-Ion 2000 Analyzer.

Using the above ion analyzer and fluoride electrode (Orion, 94-09), the fluoride content was found to be <0.2 ppm for all raw materials except the ammonium carbonate solution with 0.3 ppm.

A test was performed to determine the maximum concentration of aqueous base that could be homogeneously added to the sol. A series of sols were catalyzed by base additions. For each sol the base concentration was increased incrementally. The resultant series of gels was evaluated by light scattering intensity measured at 90° to incidence. Scatter intensity was plotted against concentration. An abrupt increase in scattering was interpreted as the onset of heterogeneity.

In all subsequent experiments 0.1 N base additions were magnetically mixed with the sol in a volumetric ratio of 1:9.

Rheometry was performed on the base catalyzed sols using a Rheometrics RMS-800 with a couette test fixture. Dodecane was floated on top of the sample prior to each measurement to prevent sample evaporation. The following conditions were observed; dynamic mode at 20 radians/second, torque between 0.1 and 0.13 g·cm, and strain was minimized but maintained > 0.025%. During measurement, the temperature was ramped from 25°C to 60°C in 10 minutes then maintained at 60°C.

NMR measurements were performed with a Varian, XL-300 at 20°C. The NMR tube contained a capillary of 5% hexamethyl disiloxane in benzene for standardization with 30 ppm Cr acetylacetonate relaxation agent. Samples were prepared by mixing 0.1 N base with the sol. After sample measurement, the outer tube was emptied, cleaned, and scanned with the standard capillary. This scan was subtracted from all sample spectra.

Effluent gas analysis was performed using a VG TRIO-3 mass spectrometer with EI impact and a heated solid probe. Samples were dried in air at 150°C for 16 hours. The samples were loaded into the spectrometer and heated in a vacuum to 150°C and held for 1 minute for outgassing. Heating continued at 20°C/minute to 520°C, the instrument's maximum temperature.

Thermal gravimetric analysis was performed using a Dupont 951 TGA under argon at a heating rate of 20°C/minute. Samples were prepared for TGA by drying for 16 hours in air at 150°C.

Dry silica grain samples (200 µm diameter) were heated in a mullite tube furnace at a rate of 20°C/minute to 1350°C, held for one hour then cooled to 25°C under flowing oxygen (<3 ppm water). Samples were analyzed for trace carbon by Leco Analytical Labs.

RESULTS AND DISCUSSION

The first phase of this study describes the effects of base addition on the pH and gelation of the sol. Before discussing these results, it is worth considering the effect of titrating acidic solutions with the individual bases. When a strong acid

is titrated with ammonium hydroxide solution, an abrupt jump in pH occurs from ~1.8 to ~7.7 through the single equivalence point. If ammonium carbonate is used, the pH of the solution jumps from ~1.8 to ~4.9 through the first equivalence point. This is followed by a gradual rise in pH to ~6.8 where the second abrupt pH jump to ~7.7 occurs through the second equivalence point.

This information helps interpret the behavior of base titration of the acid-catalyzed sol presented in Figure 1. For ammonium hydroxide titration, the pH of the sol rises gradually in the initial stage. Then there is a rapid rise in the pH at the equivalence point of ammonium hydroxide. This pH rise ends when at a gel point of pH 6.2.

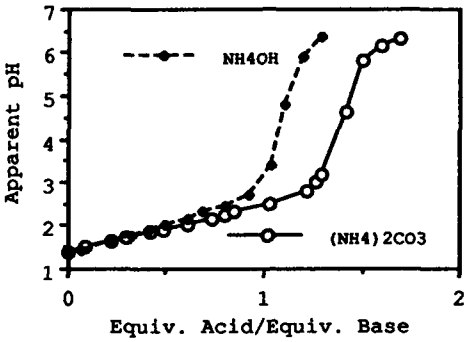


Figure 1: Titration of acid-hydrolyzed TEOS sols with two bases.

As with ammonium hydroxide, there is a gradual rise in pH as the sol is titrated with ammonium carbonate solution. There is an abrupt rise in pH through the first equivalence point of ammonium carbonate to somewhat above pH 5. At this point, as with the pure electrolyte, there begins a gradual increase in pH toward the second equivalence point. This rise continues to the pH of gelation, 6.2.

Two points should be noted. First, the pH of gelation is the same for both bases. This would suggest that gelation is more dependent on pH (more accurately on pOH) than on the concentration of secondary ions in this study (i.e. CO_3^{2-}). Second, more equivalents of ammonium carbonate are required to reach the pH of gelation. This is because the first equivalence is complete at pH 5, which is below the gel point. More ammonium carbonate is needed to reach the gel point of pH 6.2.

The maximum concentration of each base that could added homogeneously as determined by light scattering was 0.3 N ammonium hydroxide and greater than 1.0 N ammonium carbonate. These result represent a clear advantage of using the carbonate over the hydroxide as greater compositional range is possible.

Figures 2a and 2b report changes in sol viscosity and elasticity with time for ammonium hydroxide and ammonium carbonate solution additions, respectively. The plots are nearly identical. Each plot reflects an initial dip in G" (viscous) due to sample heating from 25°C to 60°C. Each plot reveals increases in G' (elastic) and G" at the gel point at similar times. Each plot also indicates that the levels to which G' and G" rise after

gelling are very similar. These data imply that these two bases produce gels of similar structure.

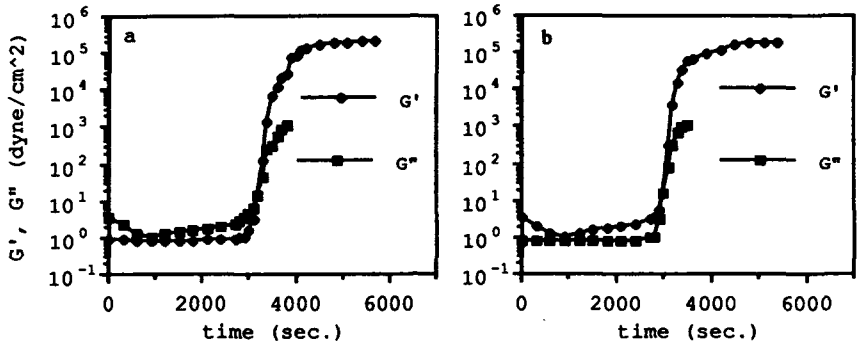


Figure 2: Rheology of TEOS sols over time after the addition of base; a) ammonium hydroxide b) ammonium carbonate. [G'= storage modulus (elastic); G"= loss modulus (viscous)].

This conclusion is corroborated by NMR results. Figures 3a and 3b compare the different silicon species which evolve during polymerization through gelling. Q2 (linear siloxane) and Q3 (branched siloxane) decrease monotonically with time while Q4 (network) increases with time. The rate of change and the final values are very similar. For equal base additions, the ammonium hydroxide catalyzed sol crosslinks and gels more rapidly than the ammonium carbonate catalyzed sol. Gelation occurs at about the same Q2:Q3:Q4 ratio for the two sols. There is slightly less crosslinking (i.e. Q_4) in the final ammonium carbonate catalyzed gel, due to lower pH for equal base concentration. Despite these similarities, chemical differences may exist between gels catalyzed with different bases.

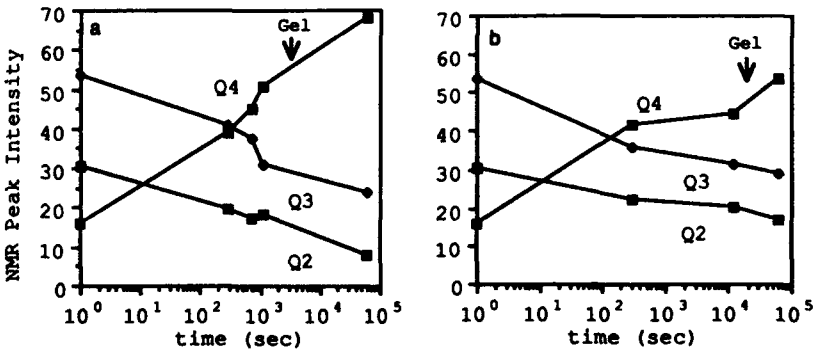


Figure 3: Structural evolution of base catalyzed gels as determined by NMR; a) ammonium hydroxide; b) ammonium carbonate. [Q2 = $Si^*(OR)_2(O\text{-}Si)_2$; Q3 = $Si^*(OR)(O\text{-}Si)_3$; Q4 = $Si^*(OSi)_4$] Only silicon marked with * is defined.

Effluent gas analysis can differentiate chemical changes during firing. Figure 4 presents mass spectroscopy data of two silica gel samples. High abundance ions are plotted as a function of temperature. Assignments have been made for these ions based on secondary ion intensities found in the mass spectra. Assignments are as follows: 18 a.m.u. = water, 28 a.m.u. = CO, 44 a.m.u. = CO_2, and 45 a.m.u. = ethoxy.

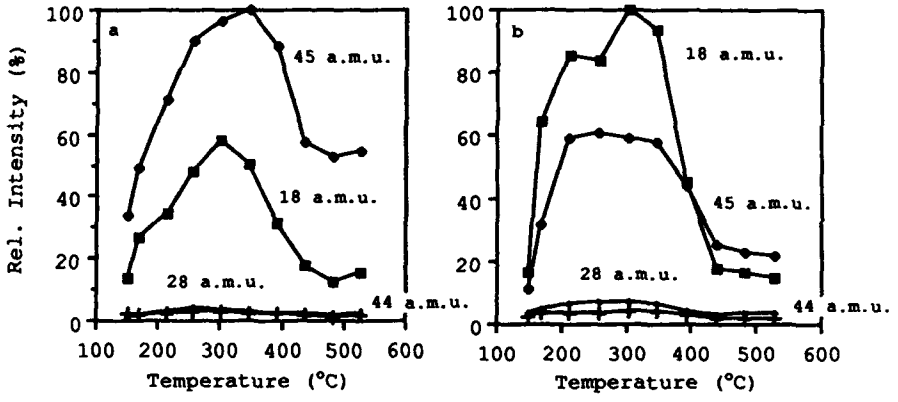


Figure 4: Effluent analysis during pyrolysis as determined by heated solid probe sampling mass spectroscopy: a) ammonium hydroxide b) ammonium carbonate.

In comparing figures 4a (ammonium hydroxide-catalyzed gel) with 4b (ammonium carbonate-catalyzed gel), a significant difference is noted. For the ammonium hydroxide gel, the intensity of the ethoxy evolution is much greater than the intensity of the water evolution. In the case of ammonium carbonate gel, the situation is reversed. These data imply that ammonium carbonate gel effluent is more highly oxidized than the ammonium hydroxide gel effluent.

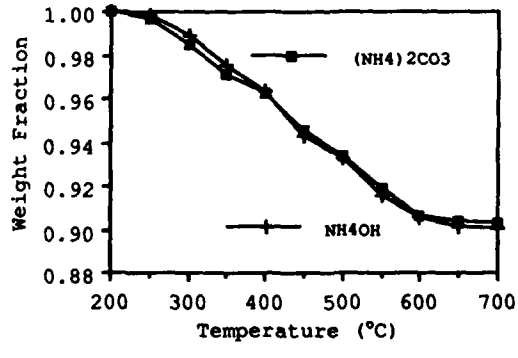


Figure 5: Thermal gravimetric analysis (TGA) of base catalyzed silica gels; a) ammonium hydroxide gel (closed symbol), b) ammonium carbonate gel (open symbol).

Despite the substantial differences in vacuum pyrolysis behavior, the TGA data for these dry gels reveal nearly identical behavior. Figure 5 illustrates these similarities.

The high temperature pyrolysis treatment to 1350°C of both base catalyzed silica grain samples resulted in identical carbon contents of 15 +/- 5 ppm.

Differences in pyrolysis behavior among the three thermal treatments in this study may be attributed to differences in atmosphere and the relative insensitivity of TGA and batch pyrolysis to identify chemical changes during firing. The chemical pyrolysis effects identified by mass spectroscopy are substantial and may have significance for critical processes such as thin film coating. More work is required.

SUMMARY

The effects of two bases, ammonium hydroxide and ammonium carbonate, on the chemistry and physical properties of TEOS-derived silica gels were studied. Based on identical gelation pH, it was concluded that the pH had a greater effect on gelling than the specific ions in this study.

The gels prepared with either catalyst had remarkably similar structures as determined by rheometry and NMR analysis.

The presence of carbonate during pyrolysis enhanced the oxidation of residual organic groups in vacuum at intermediate temperatures. The thermal gravimetric behavior and the post-high temperature calcination carbon contents of the two dry gels were identical.

ACKNOWLEDGEMENTS

The authors thank V. Brice, B. Lynn, C. Peterson, B. Simms, R. Spirn, B-M. Su, and R. Valluzzi. Thanks are also extented to AKZO Corporate Research Labs and J. Vleggaar for support in rheometric measurements.

REFERENCES

1. C.J. Brinker, et.al., J. Non-Cryst. Sol., 63 45 (1984).
2. C.J. Brinker, J. Non-Cryst. Sol., 100, 31-50 (1988).
3. E.J.A. Pope and J.D. Mackenzie, J. Non-Cryst. Sol., 101, 198-202 (1984).
4. E.J.A. Pope and J.D. Mackenzie, J. Non-Cryst. Sol., 87, 185-198 (1986).
5. M.D. Sacks and R.S. Sheu, J. Non-Cryst. Sol., 92, 383-396 (1987).
6. G.W. Scherer, et.al., J. Non-Cryst. Sol., 107, 14 (1988).
7. G.W. Scherer, J. Non-Cryst. Sol., 108, 28-36 (1989).
8. W.G. Klemperer, V.V. Mainz, and D.M. Millar, MRS Symposia Proc., 73, 15-25 (1986).
9. C.C. Lin and J.D. Basil, MRS Symposia Proc., 73, 585-590
10. L.C. Klein and G.J. Garvey, Better Ceramics Through Chemistry, MRS Symposia Proc., 32, 33-39 (1984).
11. T.A. Gallo, C.J. Brinker, L.C. Klein, and G.W. Scherer, MRS Symposia Proc., 32, 85-90 (1984).

SOLUTION CHEMISTRY IN THE Al_2O_3-SiO_2 SYSTEM

W.G. FAHRENHOLTZ*, S.L. HIETALA*, D.M. SMITH*, A.J. HURD**, C.J. BRINKER**, AND W.L. EARL***

* UNM/NSF Center for Micro-Engineered Ceramics, University of New Mexico, Albuquerque, NM 87131
** Sandia National Laboratories, P.O. Box 5800, Albuquerque, NM 87185
*** Los Alamos National Laboratory, Los Alamos, NM 87545

ABSTRACT

In the alumina-silica system, the surface area of gels exhibit dependence upon both composition and the fluid in the pores during drying. Under controlled conditions, an anomalous drop in both the surface area and skeletal density of identically prepared gels occurs at a composition of 47% alumina. An effort has been made to understand the reasons for this phenomenon. The effect of various solution precursor systems has been investigated. Precursors that contain boehmite, or other colloidal species, do not exhibit low surface area/density at 47% alumina. Data from light scattering, infrared spectroscopy, and solution NMR will be discussed for the precursor system used to prepare low surface area gels. Data will be interpreted to determine the effect of solution structure on gel characteristics.

INTRODUCTION

Materials in the alumina-silica system are of general interest in ceramics due to their ubiquity as well as favorable thermal, mechanical, and electrical properties [1]. These materials also find application in heterogeneous catalysis because of chemical durability and a controlled number of active surface sites [2]. Generally, catalyst supports have been prepared by co-precipitation techniques, but more recently a great deal of effort has gone into the gel-forming of aluminosilicates [3,4].

As part of an effort to prepare Al_2O_3-SiO_2 catalyst supports with compositions ranging from pure alumina to pure silica, it was discovered that the surface area and density of these materials was dependent upon certain washing procedures [5]. Typically, the surface area of powders was decreased by washing in water, but a large anomalous drop in both surface area and skeletal density was discovered at a composition of 47 weight percent alumina. Results from this study are detailed in Figure 1. It is thought that this effect occurs during the drying process due to the formation of closed porosity. Surface area and density have been shown to vary with the surface tension of the washing fluid, with high surface tension liquids giving low surface area powders. In order to better understand the low surface area/density phenomenon, the effect of precursor chemistry has been studied. Originally, powders were prepared by mixing a solution of TEOS/water/HCl with a saturated aluminum nitrate solution. Recently, it was shown that the same effect is possible using a TEOS/aluminum sec-butoxide/ethanol solution gelled by the addition of excess water. Solution characterization has focused on the latter precursors. Other precursors investigated include colloidal silica (Cab-o-sil) and a boehmite sol prepared by the hydrolysis of aluminum sec-butoxide (ASB) in water. Discussion in this paper will be limited to compositions of 47 weight percent alumina.

Mat. Res. Soc. Symp. Proc. Vol. 180. ©1990 Materials Research Society

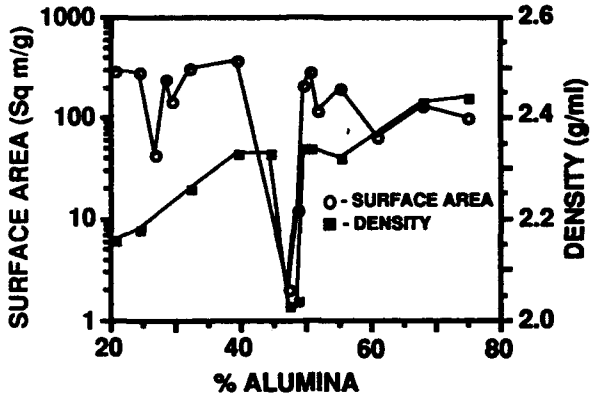


FIG. 1. *Variation of surface area and density with composition [5].*

EXPERIMENTAL

Solutions and gels in this study were prepared from tetraethylorthosilicate (TEOS) and aluminum sec-butoxide (ASB). First, TEOS was diluted with an equal amount of ethanol. Hydrochloric acid diluted 1 part to 2 with ethanol was then added. The amount of acid was one mole acid per mole TEOS. After stirring, ASB diluted one part to ten by volume with ethanol was mixed with the previous solution. For a final composition of 47 weight percent alumina, the precursor solution consisted of TEOS, ASB, and HCl in a molar ratio of approximately 1:1:1. Many other compositions have been prepared by simply varying the TEOS/ASB ratio. After the addition of the ASB, the mixture was diluted to a concentration of 2 weight percent solids, based on SiO_2 and Al_2O_3, with ethanol. The reaction flask was fitted with a condensor and the solution was refluxed for 24 hours. Solutions prepared in this manner could be stored indefinitely without gelation, although the gel time did increase with aging. Gels were formed from these solutions by the addition of excess water. For low surface area gels, water was added to produce a water/Si molar ratio of 100. After gelation, samples were dried at 100°C for 24 hours. Powders were prepared from dried gels by lightly grinding in an alumina mortar and pestal.

RESULTS AND DISCUSSION

Gelation of solutions prepared from ethanol solutions was monitored by quasi-elastic light scattering. Water, in the amount of 100 moles H_2O/mole Si, was added at time equal zero and polymer size was recorded as a function of time. As shown in Figure 2, little change occurs in polymer size before t = 6000 sec (100 min). After this time polymer growth was rapid until the gel point, about t = 10,000 sec (300 min). Although little information is gained as to the exact structure of the solution species, information of this sort is extremely valuable in the preparation of coatings from solution. In film preparation, it is advantageous to have completely hydrolyzed species in solution of a minimum size [7]. Such a solution would allow for the preparation of coatings that contain a minimum of chemically bound organics in addition to a minimum of crosslinking between polymers. Reduction of bound organics reduces film shrinkage during heat treatment while an increase in crosslinking could inhibit

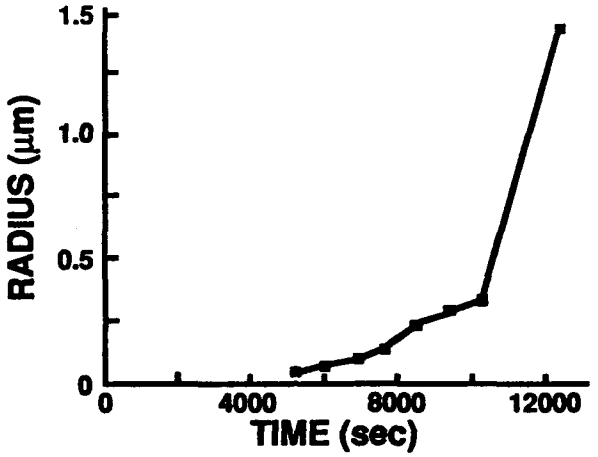


FIG. 2. Growth of polymers in solution as a function of time.

densification and structural rearrangement during the formation process. From this data, it can be seen that polymer growth is limited below t = 6000 sec.

Results from infrared spectroscopy are presented in Figure 3. IR spectra were collected at various times during the gelation process. After the addition of water ($t/t_g > 0$), a large, broad peak developed near 1650 cm^{-1}. This absorption was caused by an HOH bending mode in free water. This peak should be expected after addition of the large excess of water used for gelation. From this data it can be shown that no appreciable quantities of boehmite were formed during any portion of the gelation process. Boehmite has strong absorptions at 1016.2, 975.6, and 776.4 cm^{-1} [8].

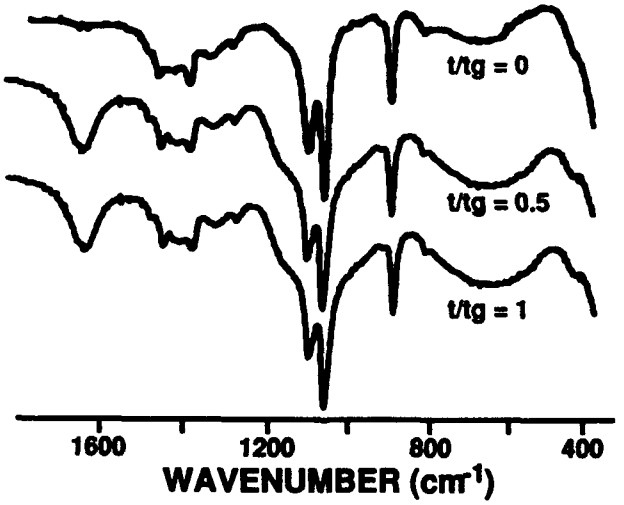


FIG. 3. IR spectra before ($t/t_g = 0$) and after water addition.

These absorptions were never seen in spectra of the ethanol-based precursor solutions, before or after the addition of water. The lack of boehmite, as well as other colloidal species, seems to be one criteria for the formation of the low surface area gels. Gels prepared by mixing an aqueous TEOS/HCl sol and a colloidal boehmite sol (prepared by the method of Yoldas [9]) did not exhibit the same surface area phenomena as gels prepared from ethanol-based solutions or from aqueous TEOS, HCl, and aluminum nitrate. The assignment of IR peaks is summarized in Table I.

Precursor solutions exhibited a drastic increase in gel time after aging. In addition, a small but significant increase in the surface area of dried gels prepared from aged solutions was noticed. Gels prepared from fresh solutions typically had surface areas of approximately 2 m^2/g while gels prepared from aged solutions had surface areas greater than 10 m^2/g. Figure 4 illustrates ^{27}Al NMR spectra of a solution aged for 3 months and a freshly prepared solution. The fresh solution showed two distinct, broad resonances. The peak extending from 80 ppm to 20 ppm ($\delta = 0$ for hexa-aquoaluminum) is due to Al–O tetrahedra bound to various numbers of Si–O tetrahedra and alkoxy ligands.[12] The presence of Al–O–Si bonds causes an upfield shift in the tetrahedral aluminum resonance.[13] The peak extending from 10 ppm to 0 ppm is due to 6 coordinate Al.[13] The aged solution shows a decrease in the number of tetrahedrally coordinated Al atoms. This rearrangement could be caused by the formation of 6 coordinate aluminum complexes.[14] The stability of these complexes would lead to an increase in the time required for gelation and would decrease the homogeneity of the gel since large Al–O clusters are formed. Formation of such complexes would account for the change in gelation time and might explain the observed increase in surface area.

Upon addition of water, as illustrated in Figure 5, peaks developed and grew at 0 ppm and 65 ppm. After 35 minutes of hydrolysis, only these two peaks were present. The peak at 0 ppm can be assigned to hexa-aquoaluminum. The other resonance is not easily assigned. The 65 ppm peak is in the region attributed to the presence of a tetrahedrally coordinated aluminum complex.[13] For a network consisting solely of Al–O tetrahedra, this peak would appear at 80 ppm.[12] The upfield shift could be due coordination with Si (through O) or to the formation of a hydrated oligomeric aluminum species.[12] Investigation via ^{29}Si NMR could confirm the presence of Al–O–Si complexes In addition, the total integrated peak area decreases with time, but the area of the peak at 0 ppm remains constant after 35 min. Combining these

TABLE I. IR peak assignments from Figure 3.

PEAK	ASSIGNMENT	PEAK	ASSIGNMENT
420 (sm)	Si–O–Si Bend [10]	1090 (l)	Si–O–R Stretch [11]
~700 (b)	O–H Bend [11]		C–O Stretch [11]
	Al–O Bend [10]	1270 (sm)	C–H Stretch [11]
810 (sm)	O–Si–O Bend [10]	1320 (b)	O–H Bend [11]
880 (m)	Si–OH Stretch [11]	1380 (sm)	C–H Bend [11]
	C–C Stretch [11]	1450 (sm)	C–H Bend [11]
1050 (l)	Si–O Stretch [10]	1650 (b)	H–O–H Bend [10]

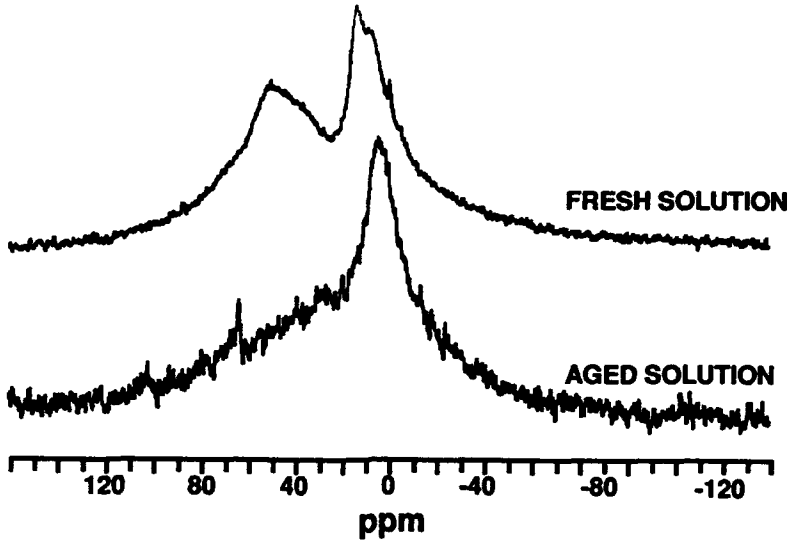


FIG. 4. ^{27}Al NMR of aged and fresh 47% Al_2O_3-SiO_2 solutions before water addition.

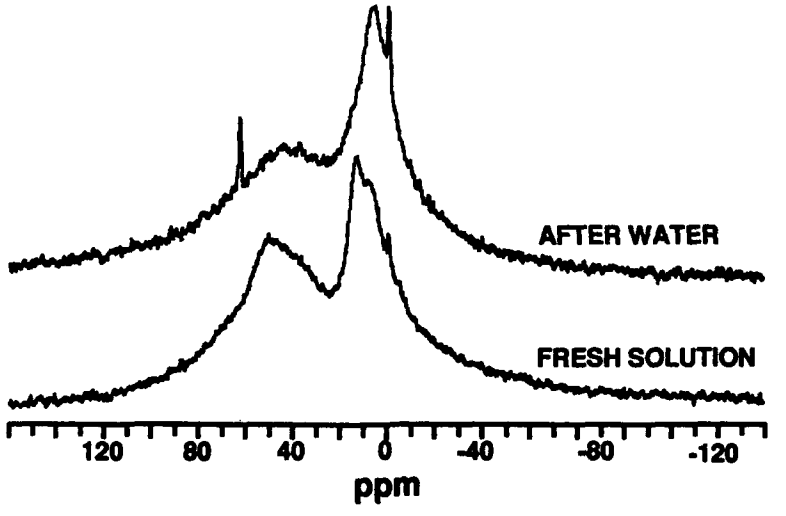


FIG. 5. ^{27}Al NMR of 47% Al_2O_3-SiO_2 solutions before and 4 minutes after H_2O addition.

observations leads to the conclusion that part of the aluminum is forming a stable 6 coordinate hydrate, while the remainder of the aluminum remains reactive and participates in network formation.

CONCLUSIONS

Formation of low surface area/density powders depends upon the homogeneity of the precursor solution, as well as composition and preparation conditions. Precursor solutions containing colloidal species did not form low surface area/density products. From IR data, no colloidal species appeared to form in the ethanol-based solutions. Results from light scattering and NMR showed that the initial period after water addition was dominated by the hydrolysis of solution species. Light scattering determined that there was little polymer growth, but NMR showed drastic chemical changes were occurring. ^{27}Al NMR data indicates that aluminum was present in both tetrahedral and octahedral coordination. Addition of water lead to the formation of both four and six coordinate aluminum species. Results from NMR also proved that the loss of reactivity in aged solutions was due to changes in the solution chemistry.

REFERENCES

1. R.K. Iler, The Chemistry of Silica, (Wiley, New York, 1979).
2. C.L. Thomas, Ind. Eng. Chem. 41 (11), 2564 (1949).
3. A.J. Léonard, P. Ratnasamy, F.D. Declerk, and J.J. Fripiat, Disc. Farad. Soc. 52 98 (1971).
4. J.C. Pouxviel, J.P. Boilot, A. Lecomte, and A. Dauger, J. Phys. 48 921 (1987).
5. S.L. Hietala, D.M. Smith, J.L. Golden, and C.J. Brinker, J. Amer. Ceram. Soc. 72 (12), 2354 (1989).
6. S.L. Hietala, D.M. Smith, V. Hietala, G.C. Frye, A.J. Hurd, and C.J. Brinker, "Properties of Films Prepared from Low Surface Area/Density Silica-Alumina, these proceedings.
7. C.J. Brinker, A.J. Hurd, and K.J. Ward, in Ultrastructure Processing of Advanced Ceramics, edited by J.D. Mackenzie and D.R. Ulrich (John Wiley and Sons, New York, 1987).
8. K. Wefers and C. Misra, Oxides and Hydroxides of Aluminum, (ALCOA, 1987).
9. B.E. Yoldas, J. Appl. Chem. Biotechnol. 23, 803 (1973).
10. M.L. Hair, Infrared Spectroscopy in Surface Chemistry, (Marcel Dekker, Inc., New York, 1967).
11. R.M. Silverstien, G.C. Bassler, and T.C. Morrill, Spectrometric Identification of Organic Compounds, (John Wiley and Sons, New York, 1981).
12. S.D. Kinrade and T.W. Swaddle, Inorg. Chem. 28, 1952 (1989).
13. D. Mueller, D. Hoebbel, and W. Gessner, Chem. Phys. Lett. 84 (1), 25 (1981).
14. J.W. Akitt, Prog. Nuc. Mag. Res. Spect. 21, 1 (1989).

IN-SITU PORE STRUCTURE ANALYSIS DURING AGING AND DRYING OF GELS

Douglas M. Smith*, Pamela J. Davis*, C. Jeffrey Brinker**
*UNM/NSF CENTER FOR MICRO-ENGINEERED CERAMICS, University of New Mexico, Albuquerque, NM, 87131, **Division 1846, Sandia National Laboratories, Albuquerque, NM, 87185

ABSTRACT

The use of NMR relaxation measurements for the in-situ study of pore structure evolution during gel aging and drying is illustrated. The change in the pore size distribution and surface area of both wet and dried gels is examined as a function of aging conditions including temporal aging, thermal aging, changing pH, and changing pore fluid. The effect of pore fluid pH on dissolution/reprecipitation in ordered packings of monodisperse silica spheres is also examined as a model system for particulate gels. As expected, the pore size distribution narrows with increasing time of treatment in high pH pore fluids. Interpretation of high pH results for the wet state is complicated by a microporous layer which forms on colloidal silica resulting in significantly larger wet surface area as compared to the final dried material. Narrowing of the pore size distribution, which is of interest for maximizing drying rates, is maximized in the least time by using either high pH or repeated ethanol washes for the base-catalyzed gel (B2) used.

INTRODUCTION

A major feature of sol-gel processing is the large degree of variation in pore structure (i.e., mean pore size, pore size distribution, surface area, porosity, etc.) that occurs both during processing and in the final product (coating, fiber, aerogel, or xerogel). Pore structure control at all processing stages is of great practical interest since pore structure plays an important role in fixing the highest drying rate that can be achieved without cracking (xerogels), sintering temperatures (dense glasses), and physical properties such as the refractive index or adsorption capacity. By varying process parameters such as temperature, pore solvent, pH, aging time, etc., large changes in the final structure may be realized. However, the relationship between these parameters and pore structure is unclear and may be only elucidated with in-situ characterization techniques.

Mat. Res. Soc. Symp. Proc. Vol. 180. ©1990 Materials Research Society

BACKGROUND-PORE STRUCTURE CHARACTERIZATION

The ability to monitor pore structure changes during aging and drying is complicated by the nature of sol-gel processing. In general, changes during processing have been inferred from the final dried gel since for traditional pore structure analysis (nitrogen adsorption/condensation and mercury porosimetry), the sample **must be dried before analysis**. However, chemistry and structure continue to evolve during aging and drying and the interpretation of how a parameter affects the final pore structure is not straightforward. The few studies of pore structure evolution in gels during processing use either scattering (SAXS, SANS), thermoporometry, NMR relaxation, or magnetic resonance imaging (MRI).

Scattering has primarily provided information on nucleation and growth mechanisms before the gel point [1,2] and/or the structure of the final xerogel or aerogel. The use of scattering for in-situ pore structure analysis suffers from limited length scales (1-20 nm, SAXS only), contrast problems, relation of results to pore size, multiple scattering, and errors resulting from desmearing. However, the approach is quick, allows extraction of all length scales at once, and accesses closed porosity.

Thermoporometry provides pore size information from comparison of melting and solidification thermograms (i.e., the freezing/melting temperature of pore fluid is a function of pore size) [3,4]. This approach is useful for determining pore size distribution with pores in the size range of 1.5 to 150 nm but suffers from limitations regarding its use for sol-gel processing. These include the fact that the pore fluid must be very pure (requires multiple washing which changes gel structure], is nonisothermal, and the volume changes associated with phase change could significantly affect the structure of the fragile gels. In addition, the nature of the thermoporometry experiment precludes the continuous study of changes in a single sample as it undergoes various aging and drying steps.

NMR spin-lattice relaxation measurements have proven to be a valuable tool for analyzing the pore structure of wet solids [5,6]. This technique is well suited for in-situ studies of gel structure as it is non-intrusive in the sense that the pore fluid is used as the probe, high purity fluids are not required, and the temperature is held constant. Pore size and surface area information are obtained from the fact that fluid near a surface will undergo spin-lattice (T1) and spin-spin relaxation (T2) at a faster rate than for the bulk fluid. From the two-fraction, fast exchange model, the measured T1 or T2 is related to the pore size by [7]:

$$\frac{1}{T_{1\text{-}2}} = \frac{1}{T_{1\text{-}2_{bulk}}} + \frac{\beta}{r_{pore}} \qquad (1)$$

From relaxation measurements of fluid in the pores and the bulk fluid, the pore size (which is actually the hydraulic radius or twice the pore volume to surface area ratio) maybe obtained if the surface interaction parameter, β, is known. For a porous solid, a distribution of relaxation times exists which must be extracted from the relaxation data. The principle advantage

of NMR relaxation measurements is the completely non-intrusive nature of the measurements, the short times required for analysis, and the ability to study sol-gel processing from the initial sol precipitation to the final dried gel.

The pore structure techniques described above employ the implicit assumption that the sample is homogeneous spatially. This may or may not be true for the initial gel and final dried gel and is almost certainly not true during processing. However, the ability to obtain the *spatial distribution of pore structure* would be of great utility for understanding the basic physics of processing as well as designing materials with tailored spatial distributions for applications such as optics and catalyst supports. Recently, Ewing and co-workers [8] have combined magnetic resonance imaging (MRI) and NMR relaxation to obtain the spatial distribution of porosity with spatial resolution of 60 μm and the spatially-averaged pore size distribution in a silica gel during drying. However, MRI is relatively slow which may limit its utility for sol-gel processing (i.e., many processing steps occur on shorter timescales than the one hour required for a single image). To overcome this problem, Majors, et al. [9] have demonstrated a scheme for radially symmetric samples which reduces imaging time to less than one minute. The exchange of D2O and H2O in a zirconia pellet was studied and radial proton concentration distributions (<1 minute per image) were extracted which compared well to diffusion theory. By using relaxation-weighted imaging, the actual spatial distribution of the pore size distribution could be obtained.

BACKGROUND-PROCESSING EFFECTS ON GEL PORE STRUCTURE

A number of treatments may be used to reduce drying time and tailor final pore structure. A common approach is to place the gel in a different solution before drying [10]. High pH solutions have been used to enhance dissolution/reprecipitation to promote neck formation between particles and thus strengthen the gel matrix. This will reduce shrinkage during drying and result in a larger final pore size. Alternatively, pore fluid may be exchanged with another solvent. Mizuno, Nagata and Manabe [11], interested in finding ways to reduce drying times needed to obtain monoliths, placed silica gels in various solutions including neutral water. The objective was to strengthen the matrix by replacing -OR with -OH and increase Si-O-Si bonds. These are only a few examples of structure modification and a more complete review is presented elsewhere [12].

In the studies described above, the effect of the various processing parameters on pore structure was assumed (i.e., no direct measurement of pore structure was attempted). Quinson, Dumas, and Serughetti [13] applied thermoporometry to obtain pore structure information for a single acid-catalyzed silica gel. Special care was taken to ensure that the

sample was repeatedly washed such that it only contained water and a narrow pore size distribution with radius of 2.5 nm was observed. Quinson and co-workers [15] employed thermoporometry to ascertain the effect of various pore fluids on the wet gel structure of a titania and a zirconia gel. Because thermoporometry was employed, samples were all analyzed with the same final pore fluid (decane). The pore volume and pore size were shown to increase with aging and solvent polarisability. Glaves and co-workers [15] have used NMR relaxation measurements to monitor pore structure evolution of two base-catalyzed silica gel samples aged in either ethanol or ethanol/KOH solutions. In addition to the variation of the wet gel structure with pore fluid, the changes in both surface area and pore size distribution during drying were obtained. As expected for the base-aged sample, the final pore volume was higher and the final surface area was lower than the sample aged in ethanol. However, the surface area and pore size distribution variations *during drying* suggest more complex physics and chemistry than is normally assumed.

EXPERIMENTAL

Silica gels were prepared via a two-step base-catalyzed procedure (designated B2) as described by Brinker et al. [16]. In the first step tetraethyl orthosilicate (TEOS), ethanol, water and HCl (molar ratios 1:3:1:0.0007) were heated under constant reflux for 1.5 hours. In the second step, 1 ml of 0.05 M NH4OH was added to 10 ml of the TEOS stock solution. The mixture was then allowed to gel (2 hours) in 5 mm NMR tubes and age in the mother liquor for 22 hours. In addition to gels, ordered packings of monodisperse spheres were prepared. 130 nm silica spheres were synthesized following Stober et al., [17] and ordering was conducted via centrifugation. Aging was done in KOH solutions for 24 hrs.

To study the effect of pore fluid on aging, samples were prepared and aged in mother liquor, ethanol, water, or consecutive ethanol-water baths. After the initial 22 hour aging period in mother liquor, gels were forced out of the NMR tubes and placed in the aging solvent. Aging was conducted at either ambient, 30 C, or 60 C. After aging, samples wore placed in NMR tubes and allowed to equilibrate at 30 C. NMR measurements on pore fluid were performed at 20 MHz on a Spin-lock CPS-2 pulse NMR using a 180^{o}-τ-90^{o} pulse sequence with 30 τ values varied non-uniformly from 100 μs to 9 s. The T1 distribution was determined with regularization [18]. To relate T1 to pore size, the "two-fraction fast-exchange" model [7] was used and the value of the surface-interaction parameter, β, was found via relaxation experiments on partially saturated samples [19]. Nitrogen sorption was used to obtain surface area [5-point BET analysis ($0.05<P/P_o<0.31$, N_2 area=0.162 nm^2)] and volume [1 point, $P/P_o=0.995$] of dried gels. Micrographs were obtained using a Hitachi S-800 SEM.

RESULTS AND DISCUSSION

The most common aging scheme is to allow the sample to remain in its mother liquor for an extended time after the gel point. During this time, chemical and structural changes continue which have been categorized as [10]: (1) hydrolysis or the reverse, reesterification, (2) polymerization, or depolymerization, (3) syneresis, and (4) coarsening (dissolution/reprecipitation). The effect of aging time on the wet pore size distribution (PSD) of B2 silica gel is illustrated in Figure 1. PSD's are presented as dV/dlogr plots so that the integrated area under the plot directly corresponds to the pore volume. Since these samples did not exhibit microporosity, it is apparent from Fig. 1 that the total pore volume is approximately constant during aging. This result is quite different from that reported for titania and zirconia gels [14] which indicated a large increase in pore volume with aging. With increased aging, one would expect a higher degree of condensation (i.e. an increase in Q4 silicon) and increased dissolution/reprecipitation which could lead to greater mechanical strength, and thus allow greater drying rates without cracking. However, even though the mean pore size is relatively constant, the narrower pore size distribution with increased aging time should also allow faster drying rates since stress during drying will be reduced [12].

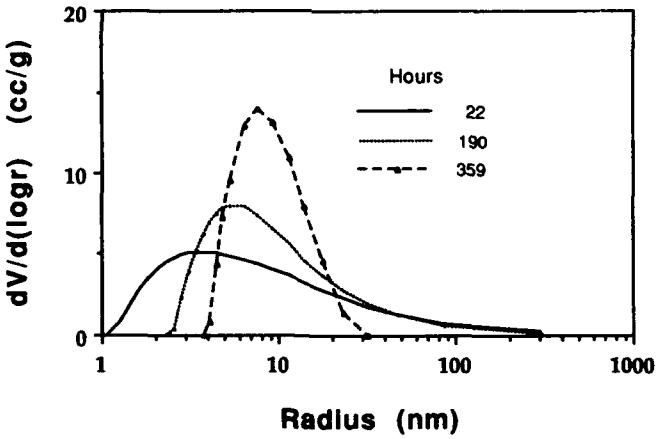


Figure 1 Effect of aging time in mother liquor at 30 C on the wet gel pore size distribution.

Since the time required to narrow the PSD is large, investigators often age gels at elevated temperature. This effect is illustrated in Figure 2 for gels aged at either 30 or 60 C. At the higher temperature, the mean pore size increases by a factor of two over that of the 30 C sample despite an **aging time which is almost two orders of magnitude shorter**.

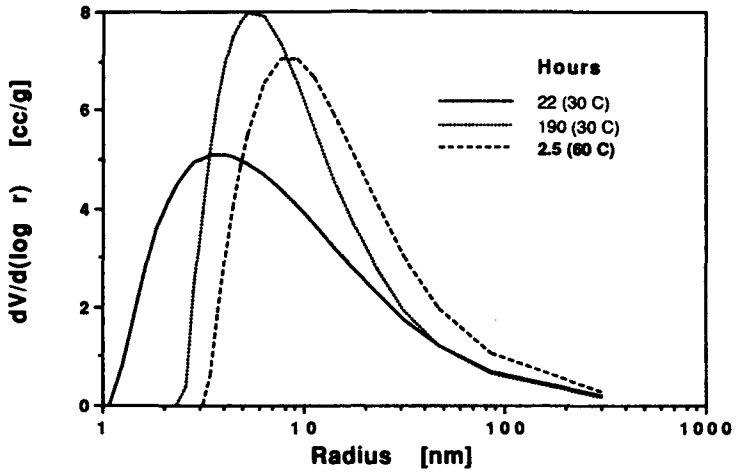


Figure 2 Effect of aging temperature on wet gel pore structure.

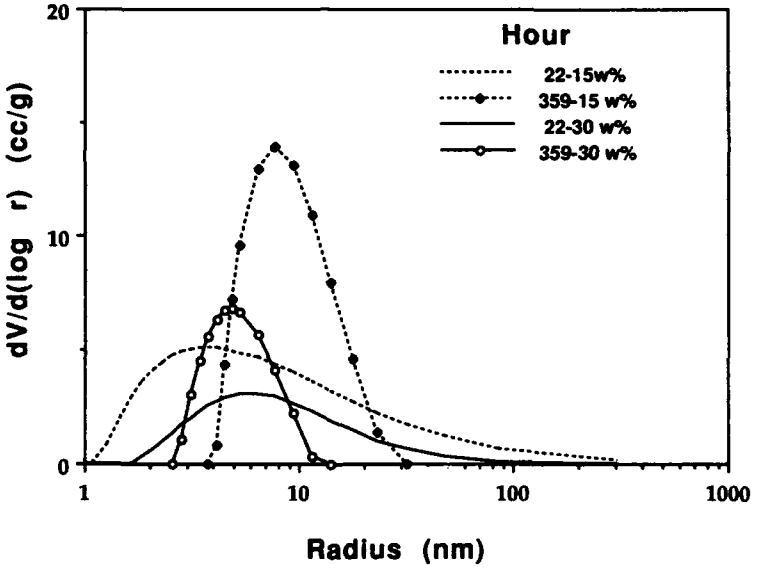


Figure 3 Effect of wet gel solids content on wet gel pore structure.

The effect of solids content on the wet gel PSD during temporal aging is illustrated in Figure 3. In general, the narrowing of the PSD with time is independent of solids content as both 15% and 30% exhibit similar broad distributions after 22 hours at 30 C which then narrow after extended

time. As expected, the area under the PSD (i.e., total pore volume) decreases with increasing solids content and the long time behavior appears to favor a smaller mean pore size with increasing solids content.

When a gel is repeatedly washed with ethanol, a dramatic narrowing of the pore size is observed. This narrowing is illustrated in Figure 4 and shows a much narrower PSD after 5 washings (120 hours total) than the gel simply aged in mother liquor for a comparable time (see Fig.1). The reasons for this result are unclear since one would expect decreased condensation and coarsening rates with ethanol as compared to mother liquor or water. This ethanol washing effect could be related to the increased concentration of Si-O-R groups at the pore surface.

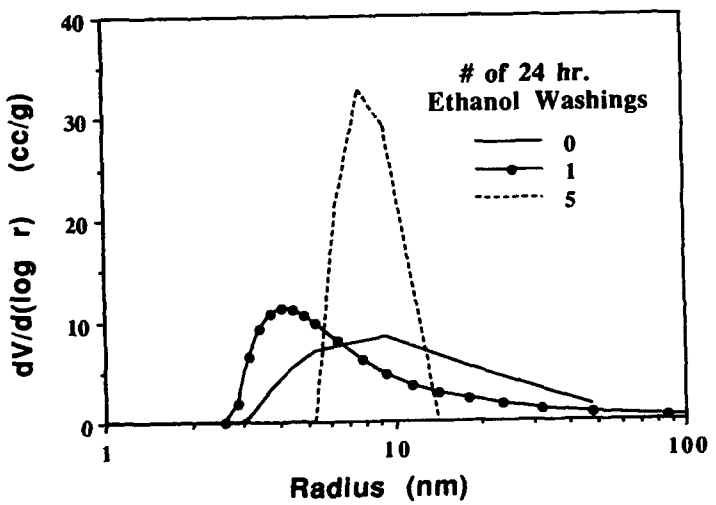


Figure 4 Effect of repeated ethanol washings on wet gel pore structure.

High pH solutions are often employed to promote dissolution-reprecipitation (Ostwald ripening) in particulate gels to increase pore size and matrix strength. To quantitatively illustrate this effect, ordered packings of monodisperse spheres were prepared since these packings have a known geometry and coordination number. The ordered nature and uniform particle size is apparent in Figure 5. The packings were infiltrated with KOH solutions of various strengths and the surface area was measured in solution after 24 hours as a function of pH (see Figure 6). With increasing pH, one would expect a *decrease* in surface area as both solubility and dissolution rate increase. However, a surface area *increase* is observed. This could be due to either microporosity in the toroidal regions between particles, if dissolution is occurring as large oligomers rather

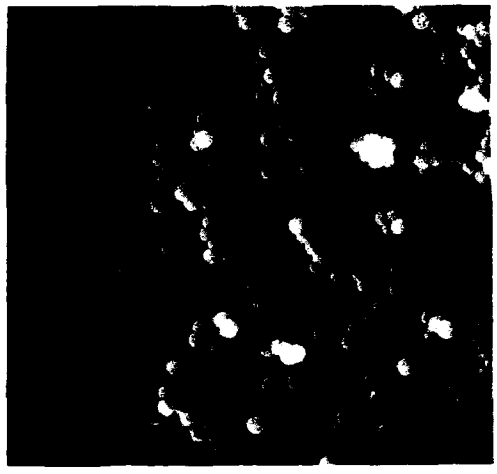


Figure 5 SEM micrograph of a sphere packing fracture surface before aging.

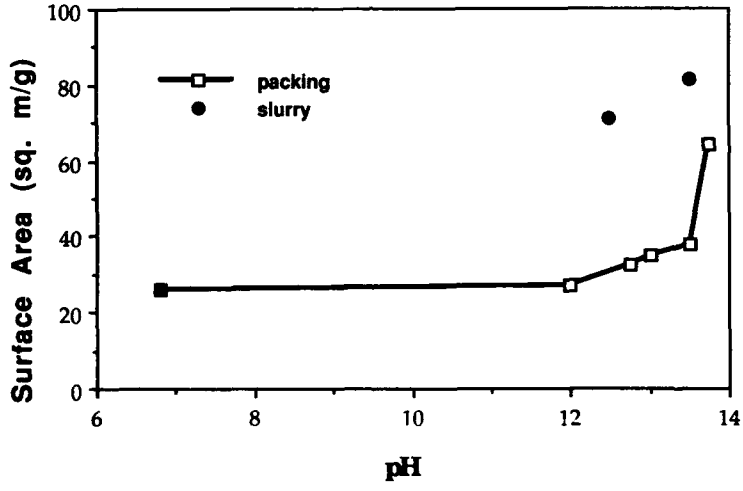


Figure 6 Effect of aging fluid pH on sphere packing and sphere slurry surface area.

than monomer, or as a result of a microporous gel layer occurring over the entire surface of the particles at high pH. Upon drying at 110 C under vacuum, the nitrogen surface area was found to be approximately 26 m2/g and independent of pH.

To ascertain which mechanism caused this surface area increase, a similar experiment was performed on a slurry of spheres in order to prevent precipitation in regions of negative curvature. At a given pH, an even larger surface area increase for the slurry is observed. To ensure

that this surface area increase was only due to the particles and not related to dissolved silica, the spheres were separated from the solution via centrifugation and the experiment repeated on the solution. Negligible surface area was noted and therefore, we attribute the increase in surface area to the formation of a microporous gel layer on the surface of silica spheres. The reason that the increase is less for the packing is the result of decreased surface available for the gel layer in the region of the particle necks. Further evidence for this microporous gel layer on colloidal silica at high pH has been obtained from SAXS and charge density measurements [20]. We have not observed this effect for Cab-O-Sil fumed silica or for Stober spheres heated at 750 C.

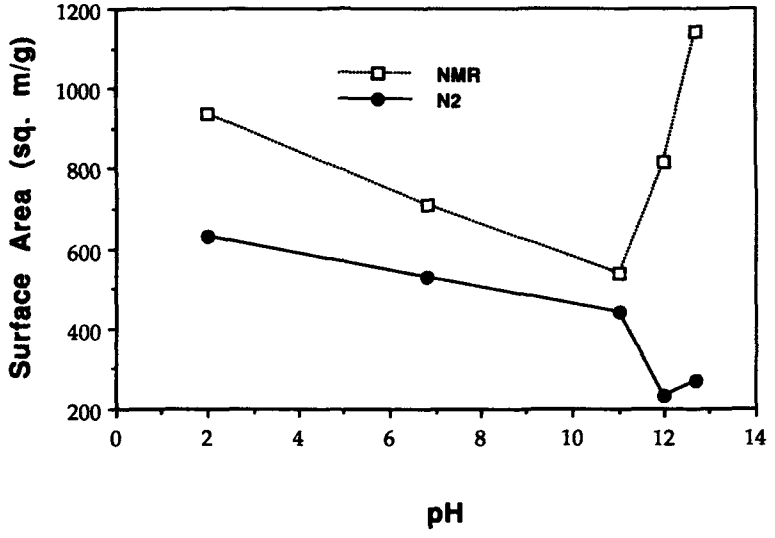


Figure 7 Effect of pH on the wet and dry surface area for B2 gels.

In assessing the effect of pore fluid pH on the surface area of wet B2 gels (after 24 hours of aging), a surface area increase is observed for pH 12 and greater (see Fig. 7). We attribute to the same mechanism as for the colloidal sphere packing described previously. The higher surface area at pH 2 as compared to neutral pH could be the result of the very low dissolution rate at this pH [21] which would serve to slow dissolution and repreciptation and thus lead to higher surface area. This result is supported somewhat by the nitrogen surface areas obtained after drying. At lower pH's, the dry surface areas parallel the wet values but at pH 12 and greater, the collapse of this microporous gel during the final stages of drying leads to a large difference between wet and dry values. The low surface areas and high pore volumes (not shown) of these gels are also consistent with increased dissolution/reprecipitation at high pH. A similar result was previously observed by Glaves and co-workers [15] for

B2 gels aged in ethanol/KOH solutions. The change in PSD after 24 hours with these different solutions is illustrated in Figure 8. Simply placing the gel in water serves to narrow the PSD considerably. Increasing the KOH concentration increases the degree of PSD narrowing and at a pH of 12.7, the PSD is considerably narrower than that obtained with either temporal aging for 359 hours, thermal aging, or ethanol washing. Despite the large differences in the wet gel PSD, the pore size distribution of the final dried gel (which was subsequently filled with water for NMR pore size analysis) was relatively independent of pore fluid (see Fig. 9). Between pH of 7 and 12.7, the mean pore size only varied from 2 to 2.5 nm.

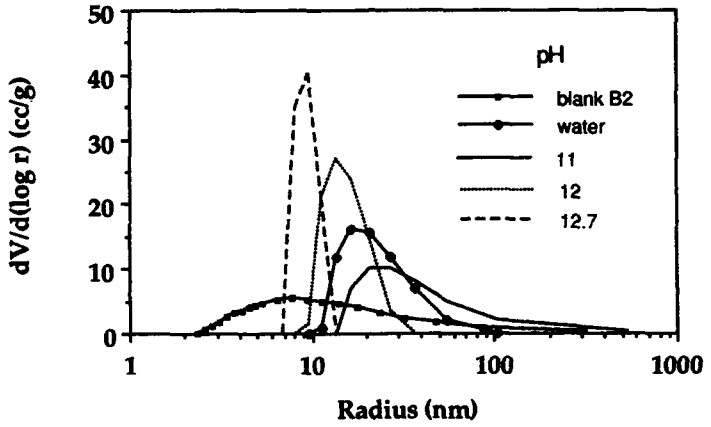


Figure 8 Effect of aging B2 gels in high pH pore fluids on wet gel pore structure.

While studying the effect of ethanol washing, we noticed that the wet surface area increased when placed in ethanol and decreased when it is placed in water. Figure 10 illustrates the variation of surface area (both wet and dry) as a function of the final fluid as a gel is processed through a series of baths. This result was unexpected and raises the question concerning whether "surface" is being created by the ethanol (i.e., breaking Si-O-Si bonds) or whether Si-O-R groups on the pore surface result in a larger apparent surface area (both wet and dry). This question is still under investigation although preliminary silicon NMR and Raman results indicate that some Si-O-Si bonds are broken (i.e., the Q3/Q4 ratio varies depending upon the final pore fluid).

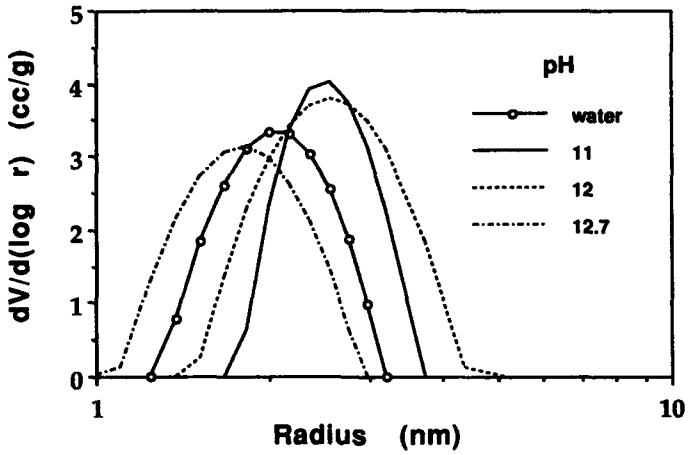


Figure 9 Effect of aging B2 gels in high pH pore fluids on xerogel pore structure (as measured with NMR).

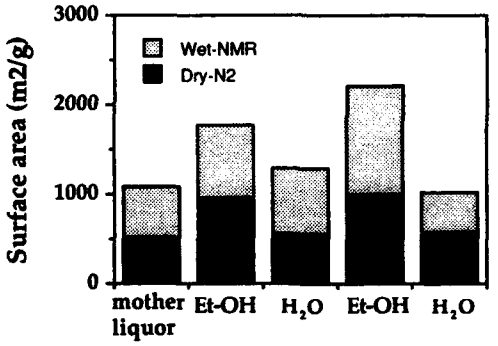


Figure 10 Variation of surface area (both wet and dry) for B2 gels as a function of the **last** fluid in which the gel was aged.

ACKNOWLEDGEMENTS

This work has been supported by Sandia National Laboratories (#05-5795). PJD was partially supported by a New Mexico Fellowship for Under-represented Groups in Science. The authors thank G. Johnston for N2 adsorption analysis, S. Thoma for sphere synthesis, and S. Hietala for SEM.

REFERENCES

1. Schaefer, D.W., and Keefer, K.D., BETTER CERAMICS THROUGH CHEMISTRY I, Eds. Brinker, Clark, Ulrich, Materials Research Society Pittsburgh, ULTRASTRUCTURE PROCESSING OF ADVANCED CERAMICS, Eds. Mackenzie and Ulrich, J. Wiley and Sons, New York, (1988)
2. Keefer, K.D., in BETTER CERAMICS THROUGH CHEMISTRY I, Eds. Brinker, Clark, Ulrich, Materials Research Society, Pittsburgh, 15, (1984)
3. Brun, M., Lallemand, A., Quinson, J., and Eyraud, C., Thermochim. Acta, 1977, 21, 59.
4. Eyraud, C., Quinson, J.F., and Brun, M., in CHARACTERIZATION OF POROUS SOLIDS, Eds. Unger, Rouquerol, Sing, Elsevier, Amsterdam, (1988).
5. Gallegos, D.P., Munn, K., Smith, D.M., and Stermer, D.L., J. Colloid Interface Sci., 1987, 119, 127.
6. Bhattacharja, S., D'Orazio, F., Tarczon, J.C., Halperin, W.P., and Gerhardt, R., J.Am.Ceram.Soc., 1989, 72, 2126.
7. Brownstein, K.R., and Tarr, C.E., J. Mag. Resonance, 1977, 26, 17.
8. Ewing, B., Davis, P.J., Majors, P.D., Drobney, G., Smith, D.M., and Earl, W.E., J. Am. Ceram. Soc., in press.
9. Majors, P., Smith, D.M., and Davis, P.J., AIChE Journal, submitted.
10. Scherer, G.W., J. Non-Cryst. Solids, 1988, 100, 77.
11. Mizuno, T., Nagata, H., and Manbe, S., J. Non-Cryst. Solids, 1988, 100,236.
12. Brinker, C.J., and Scherer, G.W., SOL-GEL SCIENCE, Academic Press, New York,1990.
13. Quinson, J.F., Dumas, J. Serughetti, J., J. Non-Cryst. Solids, 1986, 79, 379.
14. Quinson, J.F., Dumas, J., Chatelut, M., Serughetti, J., Guizard, C., Larbot, A., and Cot, L., J. Non-Cryst. Solids, 1989, 113, 14.
15. Glaves, C.L., Brinker, C.J., Smith, D.M., and Davis, P.J., Chem. Materials, 1989, 1, 34.
16. Brinker, C.J., Keefer, K.D., Schaefer, D.W., Ashley, C.S., J. Non-Cryst. Solids, 1982, 48, 47.
17. Stober,W., Fink, A., and E. Bohn, J.Colloid Interface Sci., 1968, 26, 62.
18. Gallegos, D.P., Smith, D.M., J. Colloid Interface Sci., 1988, 122, 143.
19. Davis, P.J., Gallegos, D.P., and Smith, D.M., Pow. Tech., 1987, 53, 39.
20. Axelous, M.A.V., Tchoubar, D., and Bottero, S.Y., Langmuir, 1989, 5, 1186.
21. Iler, R.K., THE CHEMISTRY OF SILICA, J. Wiley, New York, (1979).

RELATIONSHIP BETWEEN STRAINED SILICON-OXYGEN BONDS AND RADIATION INDUCED PARAMAGNETIC POINT DEFECTS IN SILICON DIOXIDE

W.L. Warren, P.M. Lenahan, C.J. Brinker* and C.S. Ashley*
The Pennsylvania State University, University Park, PA 16802
*Sandia National Laboratories, Albuquerque, NM 87185

ABSTRACT

We have investigated the radiation induced generation of paramagnetic point defects in high surface area sol-gel silicates containing various concentrations of the Raman active 608 cm^{-1} D_2 "defect" band attributed to cyclic trisiloxanes (3 membered rings). Our results indicate that strained silicon-oxygen bonds due to three membered rings are the dominant E′ (trivalent silicon center) and paramagnetic oxygen center precursors at high irradiation doses for silicates containing large concentrations of the D_2 species. These results directly demonstrate that atomic level stress does play a role in the radiation damage process of silicon dioxide.

INTRODUCTION

Silicon dioxide is one of the most important materials used in microelectronic and optical fiber technologies. It has long been recognized that SiO_2 can be damaged by ionizing radiation [1-4]. Ionizing radiation affects the insulating layers of metal oxide semiconductor field effect transistors (MOSFET's) [1,2] as well as the transmission properties of low loss optical fibers. Thus, a detailed understanding of the radiation induced defects (and precursors) in silicon dioxide is of considerable interest.

Electron spin resonance (ESR) is generally recognized as the most sensitive probe of atomic defect structure in amorphous silicon dioxide. Extensive ESR studies have been performed on quartz and bulk amorphous silicon dioxide subjected to various forms of irradiation (x-rays, gamma rays, and neutrons) [4-8]. These investigations have identified several intrinsic point defects; the most extensively investigated of which is the E′ center. The E′ center is an unpaired electron highly localized on an sp^3 hybridized orbital of a silicon backbonded to three oxygens [6,7]. One theoretical model identifies the E′ center as a hole trapped at the site of an asymmetrically relaxed oxygen vacancy [9,10]. The positive charge state of oxygen vacancy E′ centers in gamma irradiated thermally grown silicon dioxide films on silicon was experimentally established by Lenahan and coworkers [11,12]. ESR studies of irradiated fused silica glasses have also identified two intrinsic paramagnetic oxygen centers, namely the peroxy radical ($\equiv O\text{-}O\text{-}Si\equiv O_3$) and the non-bridging oxygen center ($\equiv O\text{-}Si\equiv O_3$) [4,8]

Mat. Res. Soc. Symp. Proc. Vol. 180. ©1990 Materials Research Society

In this study we report evidence for a new E′ and paramagnetic oxygen center precursor [13] - a structure involving strained Si-O bonds; to obtain this information we used Raman scattering and ESR experiments. It should be mentioned that for years people have proposed models involving atomic level stress in the radiation induced damage process in silicon dioxide [14-16]. The motivation for this work was to establish if atomic level stress is related to the generation of radiation induced point defects; our work provides strong evidence that this is the case, at least at high dose levels.

It should be emphasized, that our results are probably not specifically relevant to the MOS system, at least with regard to the E′ generation process in MOS thermal oxides [11,12]. However, we believe that our observations may be relevant to a wide range of fused silicas such as those used in optical fiber technologies.

Extensive Raman scattering experiments performed on silicon dioxide have provided information regarding bonding configurations in this material [17,18]. Prominent features in the Raman spectra of silicate gels are illustrated in Figure 1. The spectra consist of narrow bands at 490 and 608 cm^{-1} and broad features at 430, 800, 1065 and 1200 cm^{-1}. The broad features can be understood in terms of the vibrations of a continuous random network model [19,20]. The narrow bands at 490 and 608 cm-1 have not been explained by that model and have generally been attributed to defects labeled D_1 and D_2 respectively. (Normally the vibrational spectra of disordered solids consist of broad structureless bands due to the violation of selection rules as well as bond angle and force constant variations [20].).

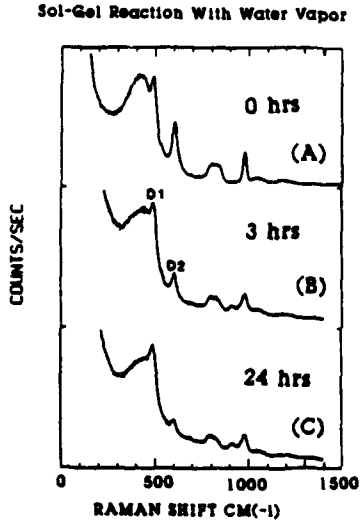


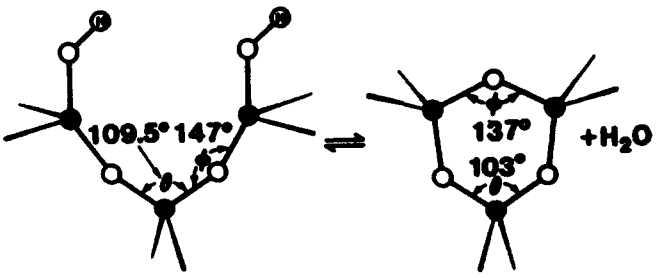
Figure 1 Raman spectra of sol-gel silicates annealed to 650°C then subsequently exposed to vapor for the various times (a) 0 hrs, (b) 3 hrs, and (c) 24 hrs. From Reference 24.

It is generally believed [21-27] (although not universally [28]) that the sharp D2 line results from oxygen ring breathing vibrations of highly regular, planar, strained, cyclotrisiloxanes (three membered rings) with Si-O-Si angles ϕ = 137°. Whereas, the <u>average</u> structure of amorphous SiO_2 is believed to consist mainly of puckered, unstrained, 5-8 membered rings with $\phi \cong 149°$ [29,30]. (An n membered ring contains n silicon tetrahedra connected by bridging oxygens.)

The Raman vibrational band of interest for this study was the 608 cm^{-1} D_2 'defect' band. We have monitored the radiation induced generation of paramagnetic point defects of bulk sol-gel silicates with varying relative intensities of the D_2 Raman band. We find a fairly large increase in E´ centers and paramagnetic oxygen centers for the gels with the largest D_2 intensities at high irradiation doses.

The evidence regarding the structural origin of the D_2 'defect' band found in conventional fused silica and high surface area silica gels is quite compelling. (1) The relative intensity of D_2 increases with glass fictive temperature [26] with an activation energy that agrees with molecular orbital calculations for the heat of formation of three membered structures [27,31] and with that found by differential scanning calorimetry measurements [24] in sol-gel glasses.

(2) Galeener et al. [23] calculated the force constants needed to vibrationally decouple these 'defect' bands from the continuous random network, thereby, explaining the narrow lines as well as the lack of silicon motion (i.e., the vibration involves nearly pure oxygen motion). (3) Brinker et al. [25] have performed ^{29}Si nuclear magnetic resonance and Raman scattering studies of high surface area silica gels demonstrating that the 608 cm^{-1} band is related to reduced Si-O-Si bond angles. The correlation of the ^{29}Si chemical shift and the Si-O-Si bond angle, ϕ, indicated that the structures responsible for D_2 have $\phi \cong 137°$ consistent with the formation of 3 membered rings according to [24,25]:



EXPERIMENTAL DETAILS

We use the same high surface area silica gels to establish the relationship between siloxane bond strain and radiolysis. The high surface area silica gels (surface area ≈ 850 m^2/g) were prepared using a two step acid-base hydrolysis procedure described in Ref. 24. After drying at 50 C the gels were heated to 650C in dry oxygen, cooled to room temperature, evacuated and sealed in glass test tubes under vacuum. (Gels annealed to 650C exhibit the largest D_2 concentrations [32].) Other sets of gels were collected after exposure of the gels to 100% relative humidity for either 3, 12 or 24 hrs. During the gamma irradiations and ESR measurements the gels were maintained under rigorously dry conditions. Since high surface area gels have large concentrations of strained rings, we believe that they are ideally suited to investigate the relationship between atomic level stress and radiation induced point defects.

The ESR measurements were made at room temperature and at 100K. (The paramagnetic oxygen center's lineshape tends to sharpen at lower temperatures; the E′ center easily saturates at low temperatures.) The Raman experiments were performed in flowing He using the 514.5 nm excitation line of an Ar^+ laser.

RESULTS

Exposure of the silicate gels to water vapor for increasing times results in a monotonic decrease of the Raman D_2 band as illustrated in Figure 1. This hydrolysis result has been explained by Brinker et al. [24] and is consistent with the work of Michalske and Bunker [33] dealing with strain enhanced reactivity of Si-O bonds. (We believe that exposure of the silicate gels to water vapor, at room temperature, is not destroying oxygen vacancies, rather it is simple hydrolyzing strained Si-O bonds according to the reverse of reaction 1.)

In figure 2 we illustrate ESR spectra of E′ centers in gamma irradiated (220 MRAD) silicate gels with different D_2 concentrations. The E′ center is identified by a zero crossing g value of 2.0004 and its double humped feature characteristic of axially symmetric point defects in an amorphous material. Figure 2 (a, b, and c) correspond to the samples shown in Figure 1 (a, b, and c) respectively. For example, the sample used in Fig. 2(a) has the largest D_2 concentration; the sample used in Fig. 2(c) has the smallest D_2 concentration. As Fig. 2 demonstrates, the irradiated gels with the largest D_2 concentration exhibit the largest concentration of E′ centers; the silicate gels with the smallest D_2 concentrations exhibit the smallest E′ concentration.

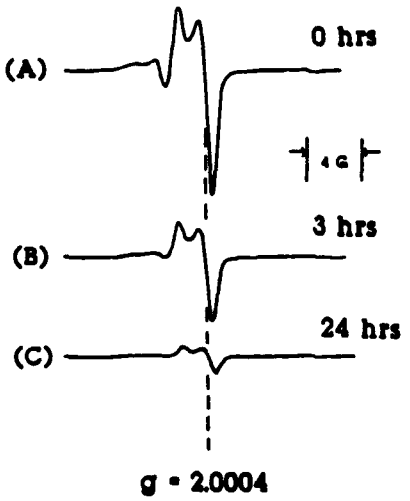


Figure 2 ESR spectra of E′ centers in irradiated silicate gels exposed to water vapor for the various times (a) 0 hrs, (b) 3 hrs, and (c) 24 hrs. All samples were irradiated to 220 MRAD.

Figure 3 illustrates the relative E′ concentration as a function of irradiation dose for silicate gels with two different D_2 concentrations. (The sample with the larger D_2 intensity was not exposed to water vapor; the silica gel with the smaller D_2 intensity was exposed to water vapor for 12 hrs.) Note that the relative E′ concentration is significantly greater (especially at higher doses) in the silicate gel with the largest D_2 concentration.

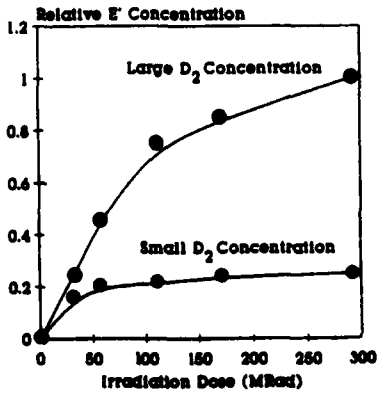


Figure 3 Relative E′ concentration vs. irradiation dose for silicate gels with different D_2 concentrations.

In Figure 4 we illustrate the relative concentration of paramagnetic oxygen centers vs. irradiation dose for the same samples illustrated in Fig. 3. As shown, the concentration of paramagnetic oxygen centers is also significantly greater in the silicate gels with the largest D_2 concentration.

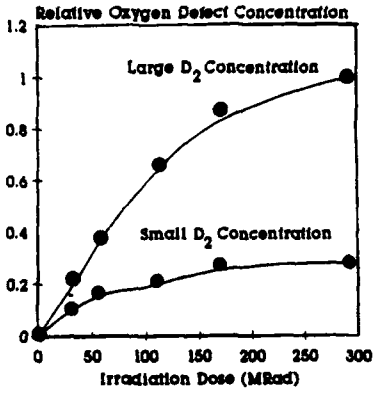


Figure 4 Relative paramagnetic oxygen center concentration vs. irradiation dose for silicate gels with different D_2 concentrations. The samples used are the same as those used in Figure 3.

DISCUSSION

Figures 1 through 4 show that at high irradiation doses, the concentration of radiation induced point defects is significantly greater when the relative concentration of the D2 species is greatest. Assuming that bond strain due to the small rings increases radiation sensitivity, we believe that this observation not only qualitatively agrees with and supports Galeener's [21-23] strained planar ring model for the D2 Raman band, but also provides clear evidence for a new fundamental precursor to both E′ and paramagnetic oxygen centers involving strained Si-0 bonds.

Our results strongly suggest that the dominant E′ generation mechanism at high dose levels is the rupture of strained Si-0 bonds. (Releasing the strain of the three membered ring.) Upon rupture of strained silicon-oxygen bonds we anticipate the generation of paramagnetic point defects. Our data supports this assumption. Therefore, we believe that large enhancement of both E′ centers and paramagnetic oxygen centers in silica gels with large D_2 concentrations is due to some type of strain enhanced radiolysis process.

Since we do not observe any broadening or distortion of the E′ spectrum due to dipole-dipole interactions (two unpaired spins in close proximity) the E′ centers and oxygen defect centers must be at least 10A apart. Therefore, it is unlikely that an E′ center and a paramagnetic oxygen center are nearest neighbors; the process mechanism is undoubtedly more complicated. (They may be created as such but other processes cause their ultimate separation.)

In summary, we have been able to demonstrate that strained silicon-oxygen bonds can be precursors to E′ centers and paramagnetic oxygen centers. This observation may be of considerable importance since it demonstrates that atomic level stress does play a role in the radiation damage process of silicon dioxide.

ACKNOWLEDGEMENTS

The authors would like to thank S.T. Reed for his technical assistance preparing the silica gels. We would also like to thank Joseph Bonner at the Pennsylvania State University's Nuclear Reactor for performing the gamma irradiations. This work was supported by the U.S. Department of Energy under contract number DE-AC04-76-DP00789.

REFERENCES

1) H.L. Hughes and R.R. Giroux, Electronics, 37, 58, (1964).
2) A complete discussion and list of references dealing with ionizing radiation effects on MOS devices can be found in, Ionizing Radiation Effects in MOS Devices and Circuits, eds. T-P. Ma and P.V. Dressendorfer, (Wiley N.Y., 1989).
3) E.W.J. Mitchell and E.G.S. Paige, Phil. Mag., 8, 1085 (1956).
4) D.L. Griscom and E.J. Friebele, Radiation Effects, 65, 63, (1982).
5) R.A. Weeks, J. Appl. Phys., 27, 1376 (1956).
6) R.H. Silsbee, J. Appl. Phys., 32, 1456 (1961).
7) D.L. Griscom, E.J. Friebele and G.H. Sigel, Solid State Commun., 15, 479 (1974).
8) E.J. Friebele, D.L. Griscom, M. Stapelbroek and R.A. Weeks, Phys. Rev. Lett., 42, 1346 (1979).
9) F.J. Feigl, W.B. Fowler and K.L. Yip, Solid State Commun., 14, 225 (1974).
10) K.L. Yip and W.B. Fowler, Phys. Rev. B, 11, 2327 (1975).
11) P.M. Lenahan and P.V. Dressendorfer, J. Appl. Phys., 55, 3495 (1984).
12) H.S. Witham and P.M. Lenahan, Appl. Phys. Lett., 51, 1007 (1987).
13) We are unable to specify if the paramagnetic oxygen centers are peroxy radicals or non-bridging oxygen centers since the g tensor elements of these two point defects are similar. ^{17}O isotope experiments are needed to prove the identity of our paramagnetic oxygen centers. Please see references 4 and 8 for the currently 'accepted' precursor models for these oxygen defect centers.

14) A.G. Revez, IEEE Trans. Nucl. Sci., NS-24, 2102, (1977).
15) F.J. Grunthaner and P.J. Grunthaner, Mat. Sci. Rep., 1, 69 (1986).
16) R.A.B. Devine and J. Arndt, Phys. Rev. B, 35, 9376 (1989).
17) G.E. Walrafen and J. Stone, Appl. Spectrosc., 29, 337, (1975).
18) R.H. Stolen and G.E. Walrafen, J. Chem. Phys., 64, 2623 (1976).
19) P.N. Sen and M.F. Thorpe, Phys. Rev. B, 15, 4030 (1978).
20) F.L. Galeener, Phys. Rev. B, 19, 4292 (1979).
21) F.L. Galeener, Sol. State Commun., 44, 1037 (1982).
22) F.L. Galeener, J. Non Cryst. Solids, 49, 53 (1982).
23) F.L. Galeener, R.A. Barrio, E. Martinez, and R.J. Elliot, Phys. Rev. Lett., 53, 2429 (1984).
24) C.J. Brinker, D.R. Tallant, E.P. Roth and C.S. Ashley, J. Non Cryst. Solids, 82, 117 (1986).
25) C.J. Brinker, R.J. Kirkpatrick, D.R. Tallant, B.C. Bunker and B. Montez, J. Non Cryst. Solids, 99, 418 (1988).
26) A.E. Geissberger and F.L. Galeener, Phys. Rev. B, 28, 3266 (1983).
27) M. O'Keeffe and G.V. Gibbs, J. Chem. Phys., 81, 876 (1984).
28) J.C. Phillips, J. Non Cryst. Solids, 63, 347 (1982).
29) R.J. Bell and P. Dean, Phil. Mag., 25, 1381 (1972).
30) A. Wright and J. Erwin Desa, Phys. Chem. Glass, 19, 140, (1978).
31) M.D. Newton and G.V. Gibbs, Physics and Chem. of Minerals, 6, 221 (1980).
32) V. Gottardi, M. Guglielmi, A. Bertoluzza, C. Fagano and M.A. Morelli, J. Non Cryst. Solids, 63, 71 (1984).
33) T.A. Michalske and B.C. Bunker, J. Appl. Phys., 56, 2686 (1984).

MOLECULAR ORBITAL MODELING OF WATER ADSORPTION ON A TETRASILOXANE RING

J. K. WEST AND S. WALLACE
Advanced Materials Research Center, University of Florida, One Progress Blvd. #14, Alachua, Fl 32615.

ABSTRACT

A water molecule hydrogen bonded to a surface SiOH group produces an IR vibrational transmission peak (ν_3) at 2.82 μm. Water was adsorbed into the pores of a metal alkoxide derived silica gel monolith, and the increase in the wavelength of the first vibrational overtone ($2\nu_3$) of this peak was measured as a function of the adsorbed water content W (g H_2O/g SiO_2). The peak shifted from 1.390 to 1.420 μm as W increased by 0.14 g/g. Intermediate Neglect of Differential Overlap (INDO) Molecular Orbital (MO) theory was used to model this process. The effect of a H_2O molecule, hydrogen bonded to a hydroxylated tetrasiloxane ring, on the structure of the ring and the water molecule was investigated. The bond length of the O-H group H-bonded to the water molecule increased, as expected from the increase in wavelength of the $2\nu_3$ IR peak.

INTRODUCTION

The adsorption of water onto the surface of a hydroxylated a-silica surface causes changes in the vibrational modes producing the IR transmission spectrum of this surface. The production [1] of monolithic geometric samples of microporous silica gel has made the direct experimental investigation of these changes easier. A typical silica gel monolith is made by the acid catalysis of silicon tetramethoxide. After drying at 180°C, a gel typically has a surface area of ≈0.45 cc/g, an average pore radius of ≈12Å and an average particle radius of ≈60Å. This means that these fractal materials are dominated by their interfacial properties. Therefore, for a silica gel sample in the beam of an IR spectrometer, the properties of the material are dominated by the surface.

An isolated surface silanol ($SiOH_a$) group produces an IR transmission peak, ν_1, at 2.675 μm. ν_1 is due to the O-H stretching vibration of isolated SiO-H_a groups [2]. A H_2O molecule H-bonded to $SiOH_a$ groups produces an IR peak (ν_3) at 2.82 μm. ν_3 is due to the O-H stretching vibration of $SiOH_a$ groups H-bonded to H_2O molecules [2]. In this investigation, the shift in the wavelength of the first vibrational overtone ($2\nu_3$ = 1.39 μm at W = 0.001 g/g) of ν_3 was measured as a function of the H_2O content W (g H_2O/g SiO_2).

The adsorption of H_2O into microporous silica gel monoliths has been shown experimentally to cause a small expansion of the gels [3-5]. It was proposed that the expansion was due to adsorption of H_2O molecules onto the hydroxylated surface of the silica gel [5]. West et al. [3] investigated this hypothesis using Intermediate Neglect of Differential Overlap (INDO) Molecular Orbital (MO) theory [6,7]. They examined the adsorption of a H_2O molecule on a ring of four hydroxylated silica tetrahedra, i.e. a hydroxylated tetrasiloxane ring. The H_2O molecule was adsorbed via the formation of H-bonds with two hydroxyl groups [1].

The exact ring size distribution in a-silica is unknown, but consists of rings ranging in size from 3 to ≥8 tetrahedra, with the median ring size containing 6 tetrahedra [8]. The trisiloxane ring forms in silica gels above 200°C, mainly on the surface, but is unstable in the presence of water [9]. During MO calculations the computational cost rapidly becomes prohibitive as the size of the cluster increases. Therefore, to model our experimental observations we chose the smallest structure which is stable in the presence of water and also found on the surface of pores in a-silica, i.e., a tetrasiloxane ring.

Mat. Res. Soc. Symp. Proc. Vol. 180. ©1990 Materials Research Society

Therefore, in this study, the same INDO MO tetrasiloxane ring was used to investigate the cause of the increase in the wavelength of the $2\nu_3$ IR peak. The influence of the adsorbed H_2O molecule, H-bonded to the hydroxylated tetrasiloxane ring, on the structure of the silanols and the H_2O molecule, was examined.

EXPERIMENTAL PROCEDURE

A metal alkoxide derived silica gel disc, sample number #114, was heat treated at 800°C for 4 hours. The gel disc had a thickness = 0.335 cm, bulk density = 1.55 g/cc, pore volume = 0.21 cc/g, surface area = 350 m^2/g and an average pore radius = 12 Å. A small amount of water was adsorbed into the micropores of the silica gel disc by condensation from the vapor phase. The disc was sealed in an airtight container and the water was allowed to equilibrate in the pores for 24 hours. The disc was then weighed and the transmission spectrum was measured using a Perkin-Elmer Lambda-9 UV-VIS-NIR Spectrophotometer. Another small amount of water was then adsorbed, allowed to equilibrate, weighed and the transmission spectrum measured again. This process was repeated until the pores were saturated with water.

RESULTS

Table I identifies the IR peaks and lists their wavelengths [2]. Figure 1 shows the IR transmission spectra of the silica gel disc #114 for various values of W. The peak at 1.365 μm, even though it is not exactly half the wavelength (2.675 μm) of the ν_1 peak, is the first vibrational overtone $2\nu_1$ [2]. $2\nu_1$ is due to isolated $SiOH_a$ groups and not due to H-bonded vicinal, or adjacent, $SiOH_a$ groups, because the gel has been heat treated to 800°C. Only one OH group per surface Si atom remains, and they are too far apart to form H-bonds. The $2\nu_1$ peak is also too sharp and symmetric to involve H-bonds, which would produce an asymmetric peak. The $2\nu_1$ peak can be seen to decrease in intensity as the $2\nu_3$ peak intensity increases concomitantly. The $2\nu_1$ peak disappears when the micropores are fully saturated, because all the $SiOH_a$ groups are H-bonded to H_2O molecules. The associated $2\nu_4$ peak (1.46 μm), due to the stretching vibration of O-H groups in H_2O molecules H-bonded to $SiOH_a$ groups, increases in intensity as the $2\nu_3$ peak increases. After the pores were full, #114 was heated at 180°C in vacuum to remove all the adsorbed H_2O and the IR spectrum was measured. It was very similar to the original spectrum at W = 0.00 g/g. Figure 2 shows the dependency of the $2\nu_1$, $2\nu_3$ and $2\nu_4$ peak wavelengths on W for #114. $2\nu_1$ and $2\nu_4$ are constant, while $2\nu_3$ increases as the H_2O content increases. The $2\nu_3$ peak initially appeared at 1.39 μm and shifted to 1.42 μm as W increased to 0.14 g/g. The same behavior was seen for other porous silica gel discs heat treated to different temperatures.

Table I. IR Transmission Peaks of H_2O Molecules H-bonded to Surface Silanols.

Wavelength (μm)	Identification	Peak Shape
1.365	$^{*}2\nu_1$	a very sharp symmetric peak
1.390	$^{**}2\nu_3$	a small peak (compared to ν_3)
1.460	$^{***}2\nu_4$	a small peak (compared to ν_4)

$^{*}\nu_1$: O-H stretching vibration of isolated surface $SiO-H_a$ groups.
$^{**}\nu_3$: O-H stretching vibration of surface $SiO-H_a$ groups H-bonded to H_2O.
$^{***}\nu_4$: O-H stretching vibration of H_2O molecules H-bonded to $SiOH_a$ groups.

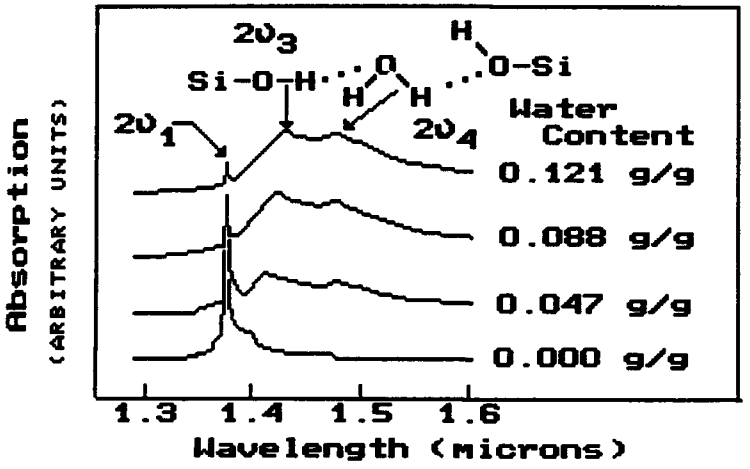


Figure 1. The near infrared (NIR) transmission spectra of the microporous silica gel disc #114 as a function of adsorbed water content W (g/g).

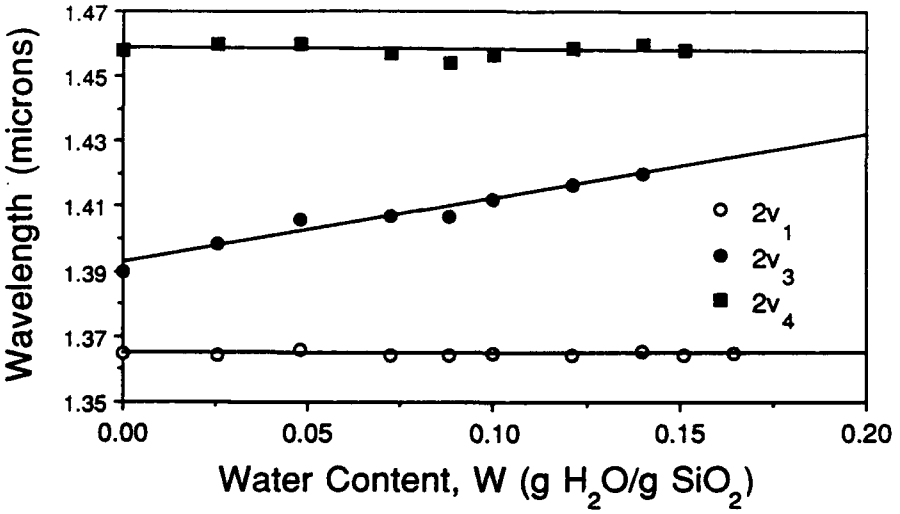


Figure 2. The dependency of the near infrared (NIR) peak positions on W (g/g).

Figures 3 and 4 show the schematics of the hydroxylated tetrasiloxane rings, with atom number designations, without and with an adsorbed H_2O molecule respectively. These structures were both optimized geometrically using an INDO MO program from the Quantum Theory Project (QTP) at the University of Florida [6-7]. In each case the three dimensional optimized geometry was used to calculate the interatomic distances for the entire cluster. Table II lists various average and specific bond lengths, calculated from these interatomic distances, with and without an adsorbed H_2O molecule.

Figure 3. Schematic of the tetrasiloxane ring with no H_2O molecule adsorbed.

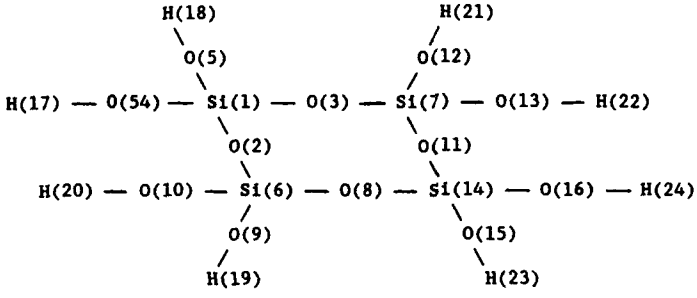


Figure 4. Schematic of the tetrasiloxane ring with a H_2O molecule adsorbed. (——) is a molecular bond. (..) is a hydrogen bond

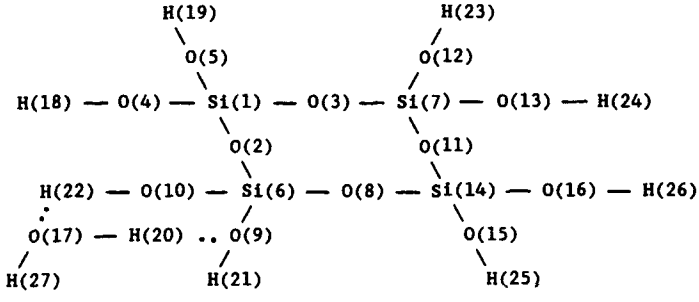


Table II. Comparison of Some Average and Specific Bond Lengths and Interatomic Distances in a Tetrasiloxane Ring With and Without a H-bonded H_2O Molecule. (-) is a Molecular Bond. (..) is a H-bond. (---) is an Interatomic Distance.

Bond Type	Average Bond Length (Å)		Bond Length Change	
	Without H_2O (Å)	With H_2O (Å)	(Å)	(%)
Si-O	1.700729 (σ_s=0.00462)	1.704992 (σ_s=0.00544)	0.004263	0.25
(in the $SiOH_n$ groups not H-bonded to the H_2O molecule)				
O-H	1.021267 (σ_s=0.00369)	1.024074 (σ_s=0.00329)	0.002807	0.27
(in the $SiOH_n$ groups not H-bonded to the H_2O molecule)				
Si---H	2.259144 (σ_s=0.03661)	2.246547 (σ_s=0.09158)	-0.012597	-0.56
(in all the $SiOH_n$ groups)				
Specific Bonds in the H_2O Molecule				
O(20)-H(17)	1.01913(i.e. free H_2O)	1.060329	0.041199	4.04
O(17)-H(27)	1.01913(i.e. free H_2O)	1.019337	0.000207	0.02
Specific Bonds in the =Si(6)O(10)-H(22)..(17)OH(20)H(27) Structure				
Si(6)-O(10)	1.700729	1.690545	-0.010184	0.60
O(10)-H(22)	1.021267	1.064406	0.043139	4.22
H(22)..O(17)	N/A	1.338446	-	-
Specific Bonds in the =Si(6)-[H(21)]O(9)..(20)HO(17)H(27) Structure				
Si(6)-O(9)	1.700729	1.737202	0.036473	2.14
O(9)-H(21)	1.021237	1.008782	-0.001246	-1.22
O(9)..H(20)	N/A	1.346744	-	-

The INDO MO stabilized structure of a free H_2O molecule gives an average O-H bond length of 1.01913 Å, with an H-O-H angle = 102.35°.

DISCUSSION

The optimized structure produced by the INDO MO program showed that the H_2O molecule was adsorbed by H-bonding to two SiOH groups with a common Si(6) atom, as shown in Fig. 4. The adsorption of the H_2O molecule did not cause any statistically significant change in the average length of the Si-O and O-H bonds in the SiOH groups not H-bonded to the H_2O molecule, i.e, the standard deviation values σ of these average bond lengths, listed in Table II, are larger than the calculated bond length changes.

As the $2\nu_3$ peak wavelength increases when W increases, while the $2\nu_1$ and $2\nu_4$ peaks stay constant, the bond strength of the O-H group H-bonded to the H_2O molecule and associated with the $2\nu_3$ vibration must decrease. Therefore the O-H bond length must increase, so the INDO MO model O(10)-H(22) bond length should increase. The H_2O molecule formed one H-bond between its O(17) atom and the H(22) atom of the Si(6)O(10)H(22) group, and one H-bond between its H(20) atom and the O(9) atom of the Si(6)O(9)H(21) group (Fig. 4). These H-bonds have very similar lengths, = 1.34±0.004 Å. The O(10)-H(22) and H(20)-O(17) groups associated with the H atoms forming these H-bonds also have similar bond lengths = 1.062±0.002 Å. The O(10)-H(22) stretching vibration, in the Si(6)O(10)H(22) group, causes the $2\nu_3$ vibration, while the H(20)-O(17) stretching vibration, in the H_2O molecule, causes the $2\nu_4$ vibration. The average O-H bond length (1.062 Å) is 0.041 Å (= 4.0 %) longer than the average non H-bonded O-H group. The INDO MO model therefore agrees with the interpretation of the experimental data, as the O(10)-H(22) bond length increases in length (Fig. 4), as predicted.

The O(9)-H(21) and O(17)-H(27) bonds are shorter and are not directly involved in the H-bonds, so they do not contribute to the IR peaks. All the bond length changes are due to charge redistribution caused by adsorption of the H_2O molecule. As the $2\nu_3$ wavelength increases as W increases, the length of the O(10)-H(22) bond should increase as the electron charge distribution is changed by adsorption of more H_2O molecules. As the $2\nu_4$ wavelength is constant as W increases, the length of the H-bonded O(17)-H(20) bond in the H_2O molecule should not be changed by the adsorption of more water molecules.

When the H-bonded groups are included, all the average bond lengths increase in length when a H_2O molecule is H-bonded to the silicate ring, but the Si---H distance decreases by 0.56%. This infers that, compared to the bare siloxane ring, the bond angles change to cause a distortion of the ring when a H_2O molecule is adsorbed. This affects both the IR spectra, as seen experimentally, and the thermal expansion behavior [3] due to adsorbed H_2O.

CONCLUSIONS

The adsorption of H_2O molecules onto the surface in the pores of a metal alkoxide derived silica gel monolith by H-bonding to surface $SiOH_n$ groups causes an increase in the wavelength of the associated IR peak, $2\nu_3$. This process can be modelled by INDO MO theory, showing the expected increase in bond length of the H-bonded O-H groups. The INDO MO model appears to reproduce the bulk properties of these silica gel monoliths. In typical MO theory the clusters do not in general predict bulk properties very well. One can therefore consider the possibility that the properties of these microporous gels are dominated by the surface chemistry and that the surface may be represented by this simple tetrasiloxane ring model.

ACKNOWLEDGEMENTS

The authors acknowledge support of AFOSR Contract #F49620-88-C-0073 and the SDI/AFOSR OGAMMS project and encouragement of D. R. Ulrich, L. Davis, and L. Burggraf. The INDO [7] program was made available by the Quantum Theory Project (QTP) at the University of Florida courtesy of Professors M. Zerner and R. Bartlett.

References

1. S.H. Wang, Ph.D Dissertation, University of Florida, 1988.

2. C.C. Perry and X. Li, "N.I.R. Studies of Monolithic Silica Gels," to be published in J. Chem. Soc. Faraday I Trans.

3. J.K. West, B.F. Zhu, Y.C. Cheng and L.L. Hench, "Quantum Chemistry of sol-Gel Silica Clusters," 5th International Workshop on Glasses and Glass Ceramics from Gels, Aug. 1989, Rio De Janeiro, Brazil.

4. L.L Hench and J.K. West, Chemical Reviews 90, 33-72 (1990).

5. B.F. Zhu, G.F. Wang and L.L. Hench, "Dilatometry of Gel-Silica," 4th International Conference on Ultrastructure Processing of Ceramics, Glasses and Composites, February 1989, Tucson, Arizona.

6. M.C. Zerner, G.H. Loew, R.F. Kirchner and U.T. Mueller-Westerhoff, J. Am. Chem. Soc. 102, 589 (1980).

7. M. Zerner et al., QTP, Univ. of Florida, Gainesville, Fl, Pgm No. 010183.

8. A.C. Wright and J.A. Erwin Desa, Phys. Chem. Glasses 19, 140 (1978).

9. C.J. Brinker, D.R. Tallant, B.P. Roth and C.S. Ashley, MRS Symp. Proceedings 61, 387 (1986).

PART V

Poster Session: Solution Chemistry, Processing Science, Electrical and Optical Properties, Thin Films and Fibers

CATALYTIC CONTROL OF SiO_2 SOL-GEL KINETICS - A MECHANISTIC STUDY OF BASES

JORGE SANCHEZ, MARY REESE, AND ALON McCORMICK
Department of Chemical Engineering and Materials Science, University of Minnesota, Minneapolis, MN 55455

ABSTRACT

The aim of this research was to determine the relative effects of three different base catalysts (NaOH, NH_4OH, and RbOH) on the rate of gelation of SiO_2 from reactive silicon ethoxide solutions in alcohol (the sol/gel method). The time to gelation was determined using a reaction protocol which assured that condensation was the rate controlling step. NMR spectroscopy was used to verify that the nature of the reacting polymers remained similar as the base catalyst was varied. It was determined that under these conditions the condensation reactions avoid diffusional limitations. Furthermore, the base catalyst serves to modulate both the activation energy and also the Arrhenius preexponential factor. This leads to the proposal of a new condensation mechanism.

INTRODUCTION

The sol/gel process constitutes the synthesis of an inorganic polymer gel network from a reactive solution of monomeric or sol moieties at or near room temperature. In this work we are interested in the reactions of silicon ethoxide in ethanol solution catalyzed by univalent hydroxides. It is important to better understand the chemistry and physics of this process in order to design materials systems with specified molecular structure and hence desired mechanical, optical, electronic, and chemical properties. Silica glasses and ceramics are currently used as catalysts, ion selective membranes, coatings, optical fibers, and lenses. The sol/gel preparation method is attractive in comparison to traditional methods because of its fast gelation times and its resultant low temperature sintering. Glasses with low thermal expansivity and highly porous powders are thus advantageously produced using the sol/gel method. [1 - 6]

The aim of this research was to determine the effects of various base catalysts on the reaction kinetics. Gel times were monitored for a variety of precursor solutions. Apparent activation energies are calculated using a simplified kinetic model incorporating well-justified mechanistic assumptions. The trends of gel times and activation energies were compared to rationalize the action of the catalyst.

THEORY

With the sol/gel technique, SiO_2 gel forms through hydrolysis and condensation of a silicon alkoxide: [1, 7 - 13]

Hydrolysis: $Si(OR)_4 + n\ H_2O = (RO)_{4-n}Si(OH)_n + n\ ROH$

Mat. Res. Soc. Symp. Proc. Vol. 180. ©1990 Materials Research Society

Condensation: $Si(OR')_4 + HOSi(OR')_3 \rightarrow (R'O)_3SiOSi(OR')_3 + R'OH$

(where R = proton or alkyl group; R' = proton, alkyl, or silicon; n=1,2,3, or 4).

Over the course of these reactions the solution increases in viscosity, finally setting into a solid gel at the gel time. Determining the gel time visually is often difficult since the gelation may not be a distinct, rapid process. This is particularly troublesome for base catalyzed systems. Some researchers have found it useful to monitor the viscosity, taking an arbitrary value to define the gel point. Alternatively, Brinker et al [1] have discussed a protocol by which one may observe a distinct gel point in base catalyzed systems; one must "prehydrolyze" the alkoxide using a very small concentration of acid before adding the base catalyst for condensation.

When adequate water is present, and if a prehydrolysis protocol is used (discussed below), we can assume that hydrolysis is rapid and comes to equilibrium. [14] If we assume that the condensation reaction is elementary, the rate of gelation is then given by

$$r_g = r_c = k_c C^n = k_{co} e^{-Ea/RT} C^n \qquad (1)$$

where r_g is the rate of gelation and r_c is the rate of condensation, which is nth order in the concentration of unreacted groups (C) with a rate coefficient k_c. E_a is the apparent activation energy; R, the gas constant; and T, the temperature. The order n must be greater than one since condensation is not unimolecular, so the rate expression can be integrated to give [15]

$$k_c t = \{1/(n-1)\} \{(1/[C_o - x])^{n-1} - (1/C_o)^{n-1}\} \qquad (2)$$

where t is the time of reaction, x is the extent of reaction, and C_o is the original concentration of condensible groups. Miller and Macosko [16] have shown that it reasonable to assume that gelation of polymers occurs at a specified extent of reaction which is primarily determined by the chemistry of the polymer itself. Therefore, we may assume that x is constant at the gel point as we vary the base catalyst. Hence, k_c is inversely proportional to the gel time and so we can determine the apparent activation energy by observing the gel time over a range of temperature. Furthermore, an Arrhenius plot can reveal whether diffusional limitations are present, since they will be manifested as curvature in the plot at high temperatures, leading to lower apparent activation energies.

NMR spectroscopy has been used to determine the extent of binding of alkali metal cations and to correlate this extent to the rate of silicate polymerization [17]. It has been proposed that the cation serves to provide stable intermediates in the polymerization reaction. The participation of this phenomenon in sol/gel polymerization can be detected if the activation energy fails to correlate with the condensation rate as the nature of the catalyst is varied.

EXPERIMENTAL

The alkoxide used was tetraethoxysilane (TEOS), used as supplied from Alfa. Absolute ethanol was used as the solvent to provide dilution of the alkoxide and mutual miscibility of it and the hydrolyzing water (distilled and deionized). The choice of ethanol minimizes the effect of ligand exchange reactions on the gelation rate. The catalysts used (in order of increasing cation size) were NaOH, NH_4OH, KOH, RbOH, and CsOH. TEOS, ethanol, water, and prehydrolyzing HCl were mixed in constantly stirred polypropylene vessel immersed in a controlled temperature bath to form a stable liquid solution according to the procedure of Brinker et al. [1] Then the base catalyst and further water were added to begin the gelation process. When gelation occurred, it was a visually and temporally distinct process, spanning a maximum of two minutes. ^{29}Si NMR spectra were acquired at 99.56 MHz using 100 rf pulses separated by a delay of 15 seconds.

RESULTS

Gel times of reacting alkoxide solutions are shown as a function of temperature in Figure 1. With a molar composition of 1 TEOS: 4 EtOH: 4 H_2O: 0.001 HCl: 0.001 MOH (where M=alkaline cation), the gel times increase in the order $Rb^+ < NH_4^+ < Na^+$. However, if the concentration of prehydrolyzing acid is decreased to 0.0005 HCl / 1 mol TEOS, the order is changed to $Rb^+ < Na^+ < NH_4^+$. In order to probe the molecular structure of the polymer with changing acid concentration, ^{29}Si NMR spectra were acquired. Figure 2 shows the spectra of NH_4OH catalyzed solutions after 21 hours of reaction. From these spectra it is evident that decreasing the HCl concentration strongly affects the structure of the polymers; the lower acid concentration results in an increase in the amount of singly hydrolyzed monomer and nonhydrolyzed endgroups, whereas it eliminates both doubly hydrolyzed middle groups and cyclic species. We interpret this to mean that decreasing the acid concentration induces the formation of more linear, less branched polymers. In order to study the effect of the alkaline catalysts, it is important to detect kinetic trends at a fixed acid concentration.

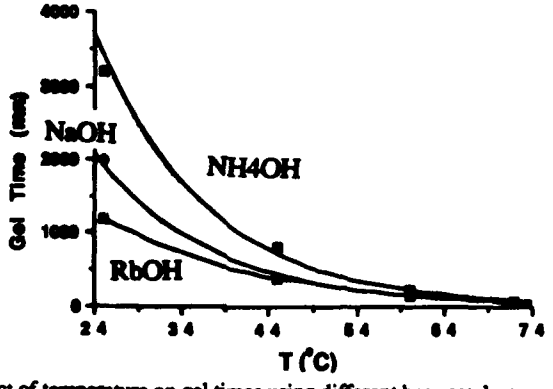


Figure 1. Effect of temperature on gel times using different base catalysts, using 0.001 HCl / TEOS for "prehydrolysis".

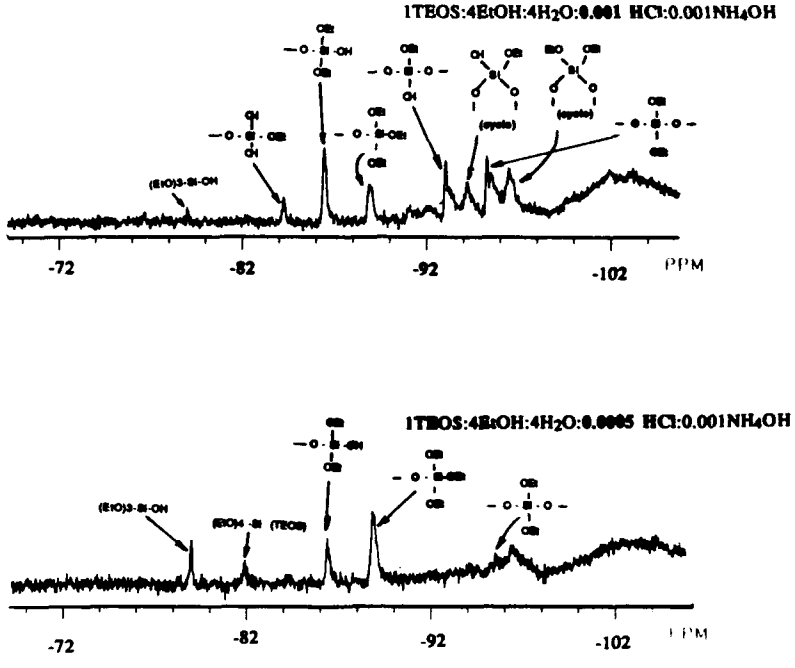


Figure 2. Effect of the prehydrolyzing conditions on the silicate polymer structure. ^{29}Si NMR spectra of solutions after 21 hours of reaction, the only difference being the concentration of HCl initially added.

Figure 3 shows a typical Arrhenius plot derived from the gel time data; Table 1 shows the activation energies thus determined. It should be noted that these apparent activation energies do not follow the trend expected from the gel time data.

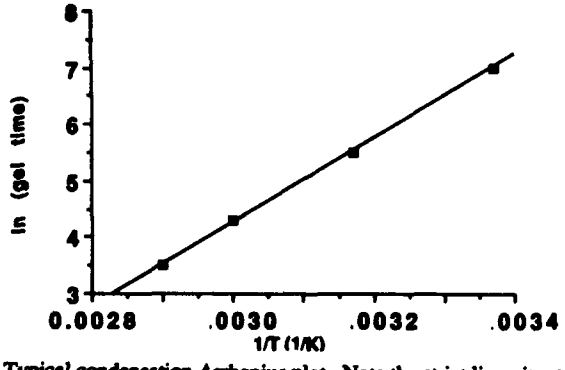


Figure 3. Typical condensation Arrhenius plot. Note the strict linearity, typical of all solutions studied. This solution is 1 TEOS : 4 EtOH : 0.001 HCl : 0.001 RbOH.

Table 1. Apparent activation energies for silica condensation

SYSTEM	BASE CATALYST	*Ea (kcal/mol)*
1 TEOS : 4 EtOH : 0.001 HCl : 0.001 base	NaOH	15.4
(High prehydrolyzing acid)	RbOH	14.9
	NH_4OH	12.8
1 TEOS : 4 EtOH : 0.0005 HCl : 0.001 base	NaOH	16.3
(Low prehydrolyzing acid)	NH_4OH	14.3
	KOH	13.3
	RbOH	12.8
	CsOH	12.5

DISCUSSION

The ^{29}Si NMR spectra indicate that is is necessary to focus on the reactions of similar polymers, hence at fixed HCl concentration. It is evident from the spectra that the "prehydrolysis" step actually initiates some condensation as well.

For a given acid contration (HCl / TEOS = 0.001) the apparent condensation rate coefficient increases at room temperature in the order $Na^+ < NH_4^+ < Rb^+$ (the reverse of the trend in gel time). Were the catalyst to act only to moderate the condensation activation energy, then the measured activation energy should decrease in the order $Na^+ > NH_4^+ > Rb^+$. However, the measured values in fact decrease in the order $NH_4^+ > Na^+ > Rb^+$. Similar discrepancies were noted for the reaction carried out with an acid content of 0.0005 HCl / 1 TEOS.

One explanation that has been proposed for unexpected trends in activation energy is the onset of diffusional limitations [18]. However, diffusional limitations should cause a bending of the Arrhenius curve to give an anomalously low activation energy, since the diffusion of silicates in solution requires only about 4 kcal/mol [19]. We observed no such manifestations.

We are forced to conclude that condensation requires an equilibrated intermediate as represented in the following reaction scheme:

$$1) \quad A^- + B^+ \overset{K_1}{=} B^+A^-$$

$$2) \quad B^+A^- + C \xrightarrow{k_2} B^+ + AC^-$$

the rate of reaction is given by

$$r = r_2 = k_2 [B^+A^-] [C] = k_2 K_1 [A^-] [B^+] [C]. \qquad (3)$$

The apparent activation energy and preexponential factor is then given by

$$E_{a,app} = E_{a2} - \Delta H_1 \quad (4)$$

$$k_{o,app} = k_{o,2}\ e\ (\Delta S_1/R). \quad (5)$$

From these expressions it is clear that the activation energy and preexponential factor are determined both by the elementary condensation reaction and by the thermodynamic of the preceeding equilibrium ion pairing reaction. There is NMR evidence that equilibrium alkali metal binding to silicate polymers provide stable intermediates in the condensation mechanism [17]. We attribute the discrepancy between gelation rates and activation energies to this phenomenon.

CONCLUSIONS

The rate of gelation of SiO_2 from TEOS was studied under conditions wherein the condensation reaction was rate limiting. Various catalysts serve to modulate the gelation rate, but this modulation can not be attributed to the activation energy alone. The data present strong evidence that the gelation kinetics are controlled by the provision of ion pair intermediates, which in turn are controlled by the alkali ion present.

REFERENCES

1 a. C. J. Brinker, K. D. Keefer, D. W. Schaefer and C.S. Ashley, J. Non-Cryst. Sol., **63**, 45, 1984.
1 b. C. J. Brinker, K. D. Keefer, D. W. Schaefer and C.S. Ashley, J. Non-Cryst. Sol., **48**, 47, 1982.
1 c. C. J. Brinker, K. J. Ward, K. D. Keefer, E. Holupka and P. J. Bray, ACS Polym. Prep., **28** (1), 428, 1986.
2. R. K. Iler, "The Chemistry of Silica," Wiley, New York, 1980.
3. K. D. Keefer, in "Better Ceramics Through Chemistry", MRS Symp. Proc Vol. 32, Elsevier, 1984, p. 15.
4. L. C. Klein, Ann. Rev. Mat. Sci., **15**, 227, 1985.
5. H. G. Sowman, Ceramic Bulletin, **67** (12), 1911, 1988.
6. D. R. Uhlmann and G.P. Rajendran, in "Ultrastructure Processing of Advanced Ceramics" (J. D. Mackenzie and D. R. Ulrich, eds.), Wiley, New York, 1987, p.241.
7. R. A. Assink and B. D. Kay, J. Non-Cryst. Sol., **99**, 359, 1988.
8. C.A. Balfe and S.L. Martinez, in "Better Ceramics Through Chemistry II", MRS Symp. Proc. Vol. 73, Mat. Res. Soc, 1986, p. 27.
9. J. D. Basil and C. -C. Lin, in "Ultrastructure Processing of Advanced Ceramics" (J. D. Mackenzie and D. R. Ulrich, eds.), Wiley, New York, 1987, p.783.
10. L. W. Kelts, N. J. Effinger and S. M. Melpoder, J. Non-Cryst. Sol., **83**, 353, 1986.
11. W. G. Klemperer, V. V. Mainz and D. M. Millar, in "Better Ceramics Through Chemistry II", MRS Symp. Proc. Vol. 73, Mat. Res. Soc, 1986, p. 15.
12 a. J. C. Pouxviel and J. P. Boilot, J. Non-Cryst. Sol., **94**, 374, 1987.
12 b. J. C. Pouxviel and J. P. Boilot, J. Non-Cryst. Sol., **89**, 345, 1987.
12 c. J. C. Pouxviel and J.P. Boilot, in "Ultrastructure Processing of Advanced Ceramics" (J. D. Mackenzie and D. R. Ulrich, eds.), Wiley, New York, 1987, , p.197.
13. C. W. Turner and K. J. Franklin, J. Non-Cryst. Sol., **91**, 402, 1987.
14. J. E. McGrath, in "Ultrastructure Processing of Advanced Ceramics" (J. D. Mackenzie and D. R. Ulrich, eds.), Wiley, New York, 1987, p.55.
15. P.W. Atkins, "Physical Chemistry", Oxford Press, Oxford, 1978.
16. D. R. Miller and C.W. Macosko, Macromolecules, **9**, 206, 1976.
17. A. V. McCormick and A. T. Bell, Catalysis Reviews, **31** (1), 97 (1989).
18. M. W. Colby and J. D. Mackenzie, J. Non-Cryst. Sol., **82**, 37, 1988.
19. R. M. Barrer, "Hydrothermal Chemistry of Zeolites," Butterworths, London, 1982.

ORGANIC CATALYSTS IN THE SILICA SOL-GEL SYSTEM

T.A. Gallo, B.L. Simms, . V.T. Brice
Akzo Chemicals Inc., ARLDF, Livingstone Avenue, Dobbs Ferry, NY 10522.

ABSTRACT

Ethyl silicate-derived silica gels were synthesized with organic acid and base hydrolysis catalysts. The nature of the organic catalyst was found to strongly affect dry gel structure and carbon content. No consistent relationship between dry gel structure and water content of the calcined gels was identified.

INTRODUCTION

Catalysts can strongly influence structure development in silica gels derived from metal alkoxides. Catalyst influence on gel structure has been demonstrated by Nogami and Moriya(1) and many others(2). Researchers have also studied the relationship between dry gel structure and calcination behavior(3). Few authors have characterized both dry gel structure and calcined gel properties from the perspective of catalyst effects. Organic catalysts are attractive for high purity applications because catalyst removal is complete at low temperatures(4).

EXPERIMENTAL PROCEDURE

TEOS, $Si(OCH_2CH_3)_4$ (Silbond Pure®, Akzo Chemicals Inc.), anhydrous ethanol, 18 megaohm water, and reagent grade catalysts were used as starting materials. Reagents were mixed at 35°C with the use of a shaker bath set at maximum speed. Acid catalysts were used for the Series I hydrolyses, while a combination of acid and base catalysts were used for the Series II and Series III hydrolyses. The mol ratio of TEOS: acid: water for the Series I and III gels was 1:0.5:6.25. The mol ratio of TEOS : acid : water for Series II gels was 1: 0.00045: 6.25. After 1hr. of reaction time with the acid catalyst, aqueous base was added to Series II and III hydrolyses bringing the final TEOS: water ratio to 1: 8.71. Series I-III samples are identified in Table 1.

Gel samples were air dried at 110°C, ground to -300/+106μ and dried under vacuum at 180°C. Surface characteristics were examined with a Micromeritics Digisorb 2600 using N_2 on samples outgased at 200°C. TGA and DSC experiments were performed in oxygen at 20°C per minute. Samples were then calcined in a tube furnace under dry oxygen (2.6 ppm water). Samples were fired rapidly to 1125°C, held for one hour and then heated over one

Mat. Res. Soc. Symp. Proc. Vol. 180. ©1990 Materials Research Society

hour to 1275°C and held for 2 hours. Water content of calcined samples was determined by IR spectroscopy on samples charged to a 3mm KBr cell. Reported water values were calculated assuming a molar absorptivity of 142(5) and are precise to ±5%.

TABLE 1. SAMPLE IDENTITY FOR SERIES I-III GELS

SAMPLE #	ACID	BASE	TEOS:ACID:BASE
I-A	formic	-	1:0.5:0
I-B	oxalic	-	1:0.5:0
I-C	acetic	-	1:0.5:0
I-D	nitric	-	1:0.5:0
II-A	nitric	NH_4OH	1:0.00045:0.00135
II-B	nitric	$(NH_4)_2CO_3$	1:0.00045:0.00135
II-C	nitric	$N(CH_2CH_3)_3$	1:0.00045:0.00135
II-D	nitric	$N(CH_2CH_3)_4OH$	1:0.00045:0.00135
II-E	nitric	$(NH_2)_2CO$	1:0.00045:0.00135
II-F	nitric	-	1:0.00045:0
III-A	formic	$N(CH_2CH_3)_4OH$	1:0.5:0.00135
III-B	formic	$N(CH_2CH_3)_4OH$	1:0.5:0.00437
III-C	formic	$N(CH_2CH_3)_4OH$	1:0.5:0.0219
III-D	formic	$N(CH_2CH_3)_4OH$	1:0.5:0.0437

RESULTS AND DISCUSSION

Data are summarized in Table 2. For the acid catalyzed gels, differences in [H+] did not account for differences in gel structure. Nitric acid catalyzed gels I:D and II:E,F had similar surface characteristics even though they were prepared with [H+] at 1M for I:D and 0.001M for II:E,F. The addition of urea caused sample II:E to have slightly smaller pores and significantly higher calcined water content than sample II:F even though pH was the same for both samples. The highest surface area gel, I:B, was prepared with oxalic acid at a calculated [H+] of 0.23M, while gels I:A from formic acid ([H+]calc =0.014M) and I:C from acetic acid ([H+]calc =0.0043M) exhibited low pore volumes and surface areas with severe hysteresis not seen for the other acid catalyzed gels. Based on these results it appears that the structure of an acid catalyzed gel is sensitive to catalyst attributes besides acid strength, perhaps differing hydrolysis mechanisms (6), hydrogen bonding, and/or steric effects(7).

Acid/base hydrolysis resulted in gels with coarser gel structures as compared to the fully microporous acid catalyzed gels. The Series II gels were essentially similar except for hysteresis. For the Series III gels, increasing base resulted in coarser gel structure with less bloating apparent after calcination. According to Iler(8), silica does not react appreciably to form silicate species below a pH of 10.8, and so is relatively insoluble in ammonium hydroxide. It was expected that using a stronger base such as triethyl amine would strongly affect the gel structure. As can be seen in Table II, no meaningful structural effects were discerned.

Table 2. Data for Series I-III Gels

		%C	TGA	water	Surface Area	Pore Dia	Pore Range	Pore Volume
			150-600°C, %	ppm	m^2/g	mode, Å	Å	cc/g
MICROPOROUS, NO HYSTERESIS								
	I-B	0.69	3.3	120	1050 (LANGMUIR)	18.8	<12.9-45.2	0.352
	I-D	0.84	3.4	159	690 (LANGMUIR)	14.8	<12.9-28.6	0.174
	II-E	3.35	7.6	213	601 (LANGMUIR)	15.8	<15.8-19.9	0.124
	II-F	3.42	7.5	115	640 (LANGMUIR)	19.9	<15.8-19.9	0.151
MICROPOROUS, HYSTERESIS								
	I-A	1.14	3.5	161	278 (LANGMUIR)	13.9	<12.8-17.0	0.013
	I-C	1.03	4.0	136	470 (LANGMUIR)	14.8	<12.8-17.5	0.054
	III-A$_o$	na.	na.	150	458 (LANGMUIR)	19.9	<15.8-125+	0.070
COMBINATION, NO HYSTERESIS								
	IIA	2.71	5.2	177	882 (LANGMUIR)	31.6	<16 - 50	0.427
	IID	3.02	4.6	159	599 (BET)	31.6	<15.8-50	0.404
	IIIB	na.	na.	207	738 (LANGMUIR)	25.1	<15.8-50++	0.206
	IIIC	na.	na.	206	602 (BET)	39.7	<15.8-50	0.406
COMBINATION, HYSTERESIS								
	IIB	2.56	4.2	154	859 (BET)	31.6	<12.6-63	0.573
	IIC	2.77	4.3	165	714 (BET)	31.6	<12.6-63	0.451
	IIID	na.	na.	169	703 (BET)	31.6	<15.8-199	0.496

TGA weight loss data and carbon contents of the dried gels follow the trend II:E,F > II:A-D > I:A,C >I:D,B. These data can be explained by more complete acid hydrolysis for gels prepared with more catalyst. Gels II:E,F and III:A tended to carbonize during calcination, which like high carbon content indicates insufficient hydrolysis. Ethoxy groups trapped in the gel skeleton are probably the source of carbon spots. DTA showed a peak for all samples at 275°C for combustion of ethoxy groups(2). The formic acid gel had an additional exotherm at 360°C. Formate groups bound to the silica skeleton may combust at this temperature.

Within experimental error (±5%), the water content of the calcined gels does not vary systematically with base strength, microporosity, or hysteresis. The organic catalysts or residues may be affecting water removal in a manner not obviously related to the structure of the dry gels, carbon content, or other factors discussed here. We are currently investigating the effect of organic catalysts on skeletal structure and the nature of residual organic species, which are factors known to influence water content of calcined silica gels.

CONCLUSIONS

Substituting organic amines for ammonia in the preparation of acid/base-catalyzed, TEOS-derived silica gels does not significantly alter dry gel structure. In contrast, substituting organic acids for conventional mineral acids in the preparation of acid-catalyzed, TEOS-derived silica gels can profoundly alter dry gel structure. The nature of this structural influence cannot be explained by acid strength alone and may be related to differing hydrolysis mechanisms, hydrogen bonding, and/or steric effects. Water content of the calcined gels does not vary systematically with base strength, microporosity, or hysteresis.

REFERENCES

1. M. Nogami and Y. Moriya, J. Non-Cryst. Sol., 37, 191 (1980).
2. L.C. Klein, Annu. Rev. Mater. Sci., 15, 227 (1985).
3. G.W.Scherer, C.J.Brinker, E.P.Roth, J. Non-Cryst. Sol., 72, 369(1985).
4. E. Termin, A.Lenz, and O.Bleh, U.S. Patent No.4 006 175 (February 1, 1977).
5. J.P.Williams,Y.Su, W.R.Strzegowski, B.L.Butler, H.L.Hoover, and V.O.Altemose., Am. Ceram. Soc. Bull.,55,524 (1976).
6. E.J.A.Pope and J.D.Mackenzie, J. Non-Cryst. Sol., 87, 185 (1986).
7. I.Artaki, T.W. Zerda and J.Jonas, J. Non-Cryst. Sol., 81, 381 (1986).
8. Ralph K. Iler,The Chemistry Of Silica, (John Wiley & Sons, Inc. 1979), p. 59.

THE INFLUENCE OF CATIONS ON GROWTH KINETICS OF SILICA AGGREGATES

THEO P.M. BEELEN, PETER W.J.G. WIJNEN, KEES P.J. RUMMENS AND RUTGER A. VAN SANTEN
Lab. Inorganic Chemistry and Catalysis, Eindhoven University of Technology, P.O.Box 513, 5600 MB EINDHOVEN, The Netherlands.

ABSTRACT

Silica gels are prepared by acidification (pH = 2 - 4) of water glass. SAXS measurements show that the gel consists of fractal aggregates (D = 2.2). Although the fractal dimension is not influenced by addition of cations, Al^{3+} and Mg^{2+} retard the growth of the fractal aggregates, while TMA^{+} has a promoting effect.

INTRODUCTION

Silica gels have been prepared by acidification of water glass, an aqueous solution of SiO_2 in NaOH. Lowering of the pH induces polymerization (condensation) reactions:

$$(HO)_3SiO^- + (HO)Si(OH)_3 == (HO)_3Si-O-Si(OH)_3 + OH^-$$

Consecutively, dimers are converted to trimers, tetramers, etc. The condensation reaction is catalysed by OH^-. Due to the tetrahedral O-Si-O angle and the lower pKa values of the OH-groups on dimers or polymers, ring closure reactions cause a predominance of rings and interconnected polymers, resulting ultimately in almost spherical silica particles [1].

After collision of these primary particles a bond between a -SiOH and a $-SiO^-$ group on the colliding particles may be formed, linking the particles together. In this way ramified aggregates are formed, forming ultimately a continuous network, the gel.

Due to the participation of SiO^- groups and OH^- ions in the polymerization and aggregation reactions, apart from the influence of the pH also electrolytes are expected to play an important part in the preparation of silica gel as is indicated by numerous experimentel results [1].

Recently much progress has been achieved by the application of ^{29}Si NMR, especially because this technique discriminates between the numerous oligomers of silica [2,3]. With this information we were able to show that for example the accelerating properties of potassium in the dissolution of silica in water glass could be attributed to an K^+ induced enhanced activity of OH^- on the Si-O-Si bond [4].

Also the formation of the fractal aggregates from the partially charged primary silica particles may be expected to be influenced by cations. Since ^{29}Si NMR does not give relevant information on a colloidal scale, SAXS has been chosen to observe the growth of the aggregates. Due to the fractal properties of the aggregates, the rate of growing and the size of the aggregates can be extracted very efficiently from the spectra [5].

Mat. Res. Soc. Symp. Proc. Vol. 180. ©1990 Materials Research Society

EXPERIMENTAL

Water glass was obtained by dissolution of Aerosil 380 (Degussa) in MOH (M = Li, Na, K, Rb, Cs or tetramethylammonia (TMA)) with Si/M = 3.0 mol/mol and [Si] = 1.5 mol/liter. Silica gel was prepared by addition of calculated quantities of water glass and a cation solution to a calculated quantity of 1.0 N HCl. If necessary, the pH was adjusted by titration of the reaction mixture with a concentrated solution of MOH.

SAXS spectra were measured using synchrotron radiation (λ = 0.154 nm) at Daresbury Laboratories (United Kingdom). With camera lengths of 4.5 and 0.65 m, Q-ranges of 0.07 - 0.3 and 0.2 - 2.5 nm^{-1} respectively could be measured. During preparation of the gel samples (liquid as well as gelatinous) could be measured in a cell with mylar windows and 1 mm pathway. The spectra were corrected for background and parasitic radiation.

In order to obtain from our spectra the fractal dimension D, the size of the primary particles r and the size of the aggregates ξ, the Porod region was fitted with the appropriate equation for the particle structure factor [6,7].

RESULTS

The most striking observation is the presence of a linear region with a slope of approximately -2.2 in the log(I) vs log(Q) plot in the SAXS spectrum of every reaction mixture at pH = 2 - 4. The Q range over which materials are fractal varies from 0.5 to 2 decades, depending on concentration and reaction time. According to Schaefer c.s.[8] and Vacher c.s.[9] and supported by computer simulations [10,11] a fractal dimension of 2.2 can be attributed to reaction limited cluster-cluster aggregation. This is in agreement with other experimental evidence [1]: a relatively slow reaction of the silica particles may be expected, due to the low concentration of both $-SiO^-$ groups on the surface of the particles and OH^- ions in the reaction mixture. Obviously the fractal dimension is not influenced by the addition or change of cations [12]; we may conclude that at pH = 2 -4 the fundamental mechanism of reaction limited cluster-cluster aggregation does not depend on the cation used in the water glass or on the addition of small amounts of cations to the reaction mixture.

However, as shown in figure 1, the size of the fractal aggregates varies with the addition of cations: highly charged ions (Al^{3+} or Mg^{2+}) retard the growth of the fractal aggregates. This relatively large effect (caused by only 1% Al^{3+} or Mg^{2+}) may be rationalized by assuming that the "tips" of the growing aggregates having the highest probability to locate a negative charge and are the most favourable growing sites. The more weakly bonded TMA^+ cations show the "classical" salt effect: shielding of the negative charge diminishes the repulsion of particles. This effect will be more pronounced for the small aggregates. At pH = 2 - 4 sodium in water glass may be replaced by lithium, potassium or cesium without causing an appreciable change in the growth of the fractal aggregates.

The size of the elementary particles that form the silica aggregates appears to be very small: only 0.3 - 0.4 nm, a near-molecular size. These orders of magnitude were also reported by Vacher c.s. [9] and Craievich c.s. [13] for neutrally reacted silica aerogels, prepared from tetramethoxysilane. Because the size of the elementary particles is calculated from data at Q

= 2.0 - 2.5 nm^{-1} (the upper limit at our experimental set-up), any (small) differences due to the addition or replacement of cations could not be demonstrated.

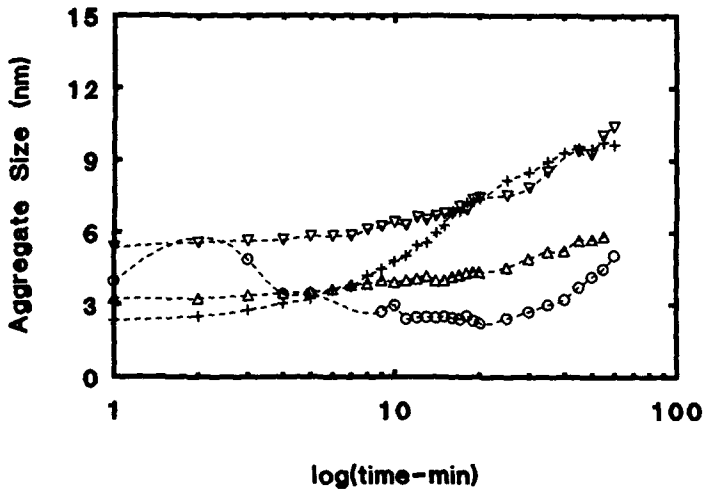


Figure 1: Influence of cations on the size of fractal aggregates; +: Na^+, Δ : Mg^{2+}, O: Al^{3+}, ∇: TMA^+.

Reaction mixtures with silica concentrations above approximately 1 weight % may give the transition from the colloidal solution to a gel in the timescale of the SAXS measurement. As reported earlier for TEOS-based silica gels [14,15] the SAXS spectra did not show any difference between the fractal dimension before or after the gelpoint. The size of the fractal aggregates showed increases continuously during gelation.

Due to the lower limit of Q = 0.07 nm^{-1} in the SAXS measurements, values of ξ greater than 15 nm could not be observed. Growing fractal aggregates, as well in colloidal solution (low silica concentration) as in gels, passed this value, so the ultimate aggregate size (if any exists) could not be measured. An indication of the final aggregate size was obtained by an exploratory USAXS (Ultra small angle X-ray scattering) measurement on a gel with a concentration of 2% silica. After 5 days ξ was found to be approximately 500 nm.

Gelation of the reaction mixture occurs approximately when, at sufficient high concentration of silica, the largest growing fractal aggregates are "touching" each other [15], forming a continuous network (figure 2). Analogous to the colloidal solution and due to the polydispersity of the fractal aggregates, also after the gelpoint the fractal aggregates keep growing by addition of small clusters or elementary particles, still present in the enclosed water.

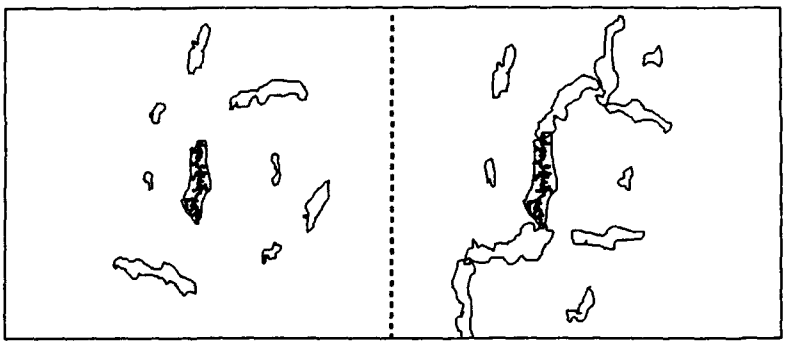


Figure 2: Vizualisation of gelation of fractal aggregates
Left: before gelpoint; right: after gelpoint

REFERENCES

1. R.K.Iler, The Chemistry of Silica (J.Wiley & Sons, New York, 1979).
2. A.V.McCormick, A.T.Bell and C.J.Radke, J.Phys.Chem. 93, 1733, (1989).
3. C.T.G.Knight, J.Chem.Soc. Dalton 1988, 1457-1460.
4. P.W.J.G.Wijnen, T.P.M.Beelen, J.W.de Haan, C.P.J.Rummens, L.J.M.van de Ven and R.A.van Santen, J.Non-Cryst.Solids 109, 85 (1989).
5. J.E.Martin and A.J.Hurd, J.Appl.Cryst. 20, 61 (1987).
6. J.Teixeira in On Growth and Form, edited by H.E.Stanley and N.Ostrowsky (Martinus Nijhoff, Dordrecht, 1986), p.145.
7. J.K.Kjems, T.Freltoft, D.Richter and S.K.Sinha, Physica 136 B, 285 (1986).
8. D.W.Schaefer, J.E.Martin, P.Wiltzius and D.S.Cannel, Phys.Rev.Letters 52, 2371 (1984).
9. R.Vacher, T.Woignier, J.Pelous and E.Courtens, Phys.Rev.B 37, 650^ (1988).
10. P.Meakin, Adv.Coll.Interf.Sc. 28, 249 (1988).
11. R.Jullien and R.Botet, Aggregation and Fractal Aggregates (World Scientific, Singapore, 1987).
12. T.P.M.Beelen, P.W.J.G.Wijnen, C.G.Vonk and R.A.van Santen, Cat.Letters 3, 209 (1989).
13. A.Craievich, D.I.dos Santos, M.Aegerter, T.Lours and J.Zarzycki, J.Non-Cryst.Solids 100, 424 (1988).
14. G.Dietler, C.Aubert, D.S.Cannell and P.Wiltzius, Phys.Rev.Letters 57, 3117 (1986).
15. B.Cabane, M.Dubois and R.Duplessix, J.Physique 48, 2131 (1987)

ACKNOWLEDGEMENTS

Financial support was given by the Dutch Department of Economic Affairs. SAXS measurements were performed at the Synchrotron Radiation Source, Daresbury, under terms of the SERC/NWO. Agreement. Special thanks to Dr.E.Towns-Andrews and Dr.W.Bras of the SRS.

SOLVENT SELECTION AND THE CONTROL OF SOL-GEL REACTIONS

K JONES, J M BOULTON AND H G EMBLEM,
Department of Chemistry, University of Manchester Institute of Science & Technology, UMIST, Manchester M60 1QD, United Kingdom.

ABSTRACT

The hydrolysis and gelation sequence occurring in the formation of a filament or a rigid coherent gel from an organic silicate requires a mutual solvent for the organic silicate and water if it is to proceed successfully. The solvent is usually a water-miscible alcohol. This alcohol can also be a reaction product, which makes the sequence very solvent dependent. The best control of both hydrolysis and gelation is obtained when the alcohol solvent and the organic silicate each contain the same alkoxy group. The gel resulting is also the best binder for refractory grain. Suitable systems are ethyl silicate and ethanol also isopropyl silicate and isopropanol. The formation of rigid coherent gels, or filaments which on firing convert to ceramic fibres, from hydrolysates of ethyl silicate and aluminium chlorhydrate species is also very solvent dependent. With glycol solvents, aluminium chlorhydrates do not form filaments nor ceramic fibres. With ethanol as solvent, aluminium chlorhydrate-polyol complexes readily form rigid coherent gels and filaments, hence ceramic fibres, because the polyol complex is formed by displacing coordinated water in the aluminium chlorhydrate. This reduces the amount of water available for reaction, which optimises filament and fibre formation.

INTRODUCTION

The hydrolysis and gelation sequence occurring in the formation of a filament or a rigid coherent gel from an organic silicate requires a mutual solvent for the organic silicate, water and any catalyst that might be desirable. The solvent is usually a water-miscible alcohol. However, because alcohols are frequently products of the resulting hydrolysis, the overall reactions can be very solvent dependent. The formation of hydrolysates from technical ethyl silicate and aluminium chlorhydrate species capable of forming rigid coherent gels and filaments which on firing convert to ceramic fibres is also very solvent dependent.

ETHYL SILICATE & TECHNICAL ETHYL SILICATE PREPARATION

The traditional procedure is to treat tetrachlorosilane with ethanol. Absolute ethanol gives tetraethoxysilane, also known as ethyl orthosilicate, having a silica equivalent of 28% w/w.

$$SiCl_4 + 4EtOH \dashrightarrow Si(OEt)_4 + 4HCl$$

Aqueous ethanol gives [1] a mixture of tetraethoxysilane and ethoxypolysiloxanes (ethyl polysilicates) formed by the condensation-polymerisation reactions resultant on water being present and catalysed by the by-product hydrogen chloride. Reaction conditions are chosen to give a product, ethyl silicate-40 (technical ethyl silicate), with a silica equivalent ca 40% w/w. A more recent procedure is the direct reaction of silicon and ethanol in the presence of metal alkoxides [2] to give tetraethoxysilane, which can be converted by controlled hydrolysis to ethyl silicate-40.

ALKYL SILICATE HYDROLYSIS PROCEDURES

A mutual solvent for water and an alkyl silicate, e.g. ethyl silicate, is required for hydrolysis procedures to work satisfactorily. Usually a catalyst (acid or base) is required. The solvent may be a water-miscible alcohol, glycol, ketone or glycol ether.

Mat. Res. Soc. Symp. Proc. Vol. 180. ©1990 Materials Research Society

Water-miscible alcohols are, as a rule preferred. The hydrolysis of an alkyl silicate yields an alcohol:

$$\geq Si(OR) + H_2O \dashrightarrow \geq Si(OH) + ROH$$

The alcohol by-product may be the same as the solvent alcohol, so the procedure is *therefore very solvent dependent.*

There are many procedures for the hydrolysis of ethyl silicate and other alkyl silicates. Methods have been devised [3] in which the required quantity of alkyl silicate, or other component is added in one, two or more portions. Time interval and/or temperature variations in such multi-stage processes are used to determine component additions, producing variations in gelation characteristics and gel properties. The best control of both hydrolysis and gelation is obtained when the alcohol solvent and the alkyl silicate each contain the same alkyl group. Examples of such systems are ethyl silicate and ethanol, also iso-propyl silicate and iso-propanol. Filaments can be obtained [4] from ethyl silicate hydrolysates prepared using organotin hydrolysis catalysts.

MANUFACTURE OF REFRACTORY SHAPES USING ETHYL SILICATE-40

A base-catalysed hydrolysis and gelation procedure [5, 6] is used to set a slurry of graded refractory grain and ethyl silicate-40. The 'green' moulding is air dried, then fired to obtain the refractory shape. The catalyst is one or more strongly basic amines, e.g. morpholine, piperidine, dicyclohexylamine. Aqueous ethanol is used to gel the amine/ethyl silicate-40 mixture. Gel time may be controlled by:

(i) varying the amount of amine,
(ii) varying the amount of water in the ethanol,
(iii) adding a solvent such as iso-propanol.

Excess iso-propanol gives brittle gels.

ALUMINIUM CHLORHYDRATE SPECIES

The aluminium chlorhydrates $Al_2(OH)_nCl_{6-n}$, where n is 1-5, are polar materials. The chlorhydrate preferred for sol-gel reactions with ethyl silicate is $Al_2(OH)_5Cl$ which is water soluble The aluminium chlorhydrates form complexes with polyols [7], the complex with 1,2-dihydroxypropane $Al_2(OH)_5Cl.CH_3CH(OH)CH_2OH.H_2O$, 'aluminium chlorhydrex' being typical. This is much less polar and is soluble in lower alcohols. Displacement of water by 1,2-dihydroxypropane reduces the amount of water available for reaction, which optimises [8] filament and fibre formation.

GELS FROM ETHYL SILICATE-40 AND ALUMINIUM CHLORHYDRATE SPECIES

The experimental procedures have been described previously [8, 9]. All alumina:silica ratios were in the mullite range. Table I shows the effect of ethanol solvent on gel formation with aluminium chlorhydrate. The effect of water is given in Table II and Table III shows the effect of reaction temperature and reaction time. All gels were coherent gels. Coherency does not necessarily equate with homogeneity and hence transparency. The results [10] show:

(i) refluxing time and volume of ethanol solvent are critical,
(ii) the amount of water is also critical, too much water giving opaque gels,
(iii) low reaction temperatures give opaque gels; for a rigid coherent transparent gel, the reaction temperature must not be less than 60°C,
(iv) the time required to form a gel decreases as the temperature is increased.

To obtain a rigid coherent gel from ethyl silicate-40 and aluminium chorhydrex using ethanol as solvent [8, 11], the amount of water must be as small as possible, especially if filament formation is also required. The reaction temperature should be maintained above 60°C and some of the solvent removed by distillation as the reaction proceeds.

Table I. Effects of ethanol solvent on gel formation with aluminium chorhydrate (16.4 g), technical ethyl silicate (10.0 g) and water (16.4 cm^3)

Ethanol vol (cm^3)	Time to reach reflux (min)	Reflux time (min)	Gel characteristics
25	22	6	slightly cloudy
35	16	13	slightly cloudy
45	34	16	slightly cloudy
55	18	26	clear, homogeneous
65	12	43	cloudy
85	25	67	cloudy
105	10	95	cloudy
125	15	140	cloudy

Table II. Effect of water on gel formation with aluminium chlorhydrate (16.4 g) and technical ethyl silicate (10.0 g) in ethanol (55 cm^3)

Water vol (cm^3)	Time to reach reflux (min)	Reflux time (min)	Gel characteristics
37.4	2	45	very cloudy
34.4	4	38	cloudy
31.4	5	33	very cloudy
28.4	10	23	cloudy
25.4	20	22	cloudy
22.4	2	26	cloudy
19.4	3	27	cloudy
13.4	4	26	almost transparent

Table III. Effect of temperature on gel formation with aluminium chlorhydrate (16.4 g), technical ethyl silicate-40 (10.0 g) and water (16.4 cm^3) in ethanol (55 cm^3)

Reaction temperature ^oC	Time required to form gel (min)	Gel characteristics
75	45	clear
70	56	clear
65	64	clear
60	75	clear
55	92	slightly cloudy
50	125	slightly cloudy

With ethanol as solvent, the rigid transparent coherent gel obtained from ethyl silicate-40 and either aluminium chlorhydrate or aluminium chlorhydrex crumbles into small grains if the ethanol is removed rapidly. Solvent and volatiles removal must therefore be slow. The use [12] of a low molecular weight diol (e.g. 1,2-dihydroxyethane, 1,2-dihydroxypropane) or N,N-dimethylformamide in the solvent system reduces the rate of solvent removal. The low vapour pressure of these bidentate ligands is thought to reduce the stress during drying. Table IV shows the effect of including 1,2-dihydroxypropane in the solvent system used in the preparation of rigid transparent coherent gels from ethyl silicate-40 and aluminium chlorhydrate. The effect of a mixed solvent comprising ethanol and 1,2-dihydroxypropane on gel formation from ethyl silicate-40 and aluminium chlorhydrex is shown in Table V and the effect of a solvent comprising ethanol and/or N,N-dimethylformamide is shown in Table VI. All gels were coherent, rigid transparent coherent gels being obtained from clear, homogeneous solutions.

Table IV. Effect of solvent (25% v/v 1,2-dihydroxypropane + 75% v/v ethanol) on gel formation with aluminium chlorhydrate (3.28 g), technical ethyl silicate (2.00 g) and water (3.28 cm^3)

Volume of solvent added (cm^3)	Gelation time (days)	Gel characteristics
5.0	9	cloudy
7.0	13	cloudy
9.0	11	slightly turbid
11.0	15	slightly turbid
13.0	18	slightly turbid
17.0	22	clear, coherent
21.0	30	clear, coherent

Table V. Effect of solvent (50% v/v N,N-dimethylformamide + 50% v/v ethanol) and water on gel formation with aluminium chlorhydrex (13.44 g) and technical ethyl silicate (5.00 g)

Volume of solvent added (cm^3)	Volume of water added (cm^3)	Time to reach reflux (min)	Reflux time (min)	Gel characteristics
27.0	1.5	6	93	clear, coherent
27.0	2.5	3	104	clear, coherent
27.0	3.5	7	97	clear, coherent
27.0	4.5	3	82	cloudy
27.0	5.0	9	67	cloudy
27.0	5.5	5	65	slightly turbid
27.0	6.5	4	72	cloudy
27.0	7.5	2	95	cloudy
17.0	2.5	7	36	clear, coherent
19.0	2.5	4	50	clear, coherent
21.0	2.5	8	69	clear, coherent
23.0	2.5	3	67	clear, coherent
25.0	2.5	3	84	clear, coherent
29.0	2.5	3	104	clear, coherent
31.0	2.5	3	133	slightly turbid

Table VI. Effect of solvent composition (ethanol/N,N-dimethylformamide, 27 cm^3) on gel formation with aluminium chlorhydrex (13.44 g), technical ethyl silicate (5.00 g) and water (2.5 cm^3)

Solvent composition ethanol (%v/v)	DMF (%v/v)	Time to reach reflux (min)	Reflux time (min)	Gel characteristics
0	100	7	17	clear, coherent
20	80	3	32	clear, coherent
40	60	3	64	clear, coherent
60	40	4	78	clear, coherent
80	20	4	74	slightly turbid
100	0	3	83	slightly turbid

FILAMENT AND CERAMIC FIBRE FORMATION FROM ALUMINIUM CHLORHYDREX

The preparation of ceramic fibre precursor solutions from aluminium chlorhydrex and alkoxysilanes has been described previously [8, 11, 12]. Uncomplexed aluminium chlorhydrates (sparingly soluble or insoluble in glycols) and alkoxysilanes do not readily form filaments. Aluminium chlorhydrex is formed by displacing coordinated water in the aluminium chlorhydrate. This reduces the amount of water available for reaction, which optimises filament and hence fibre formation. Using ethanol as solvent and keeping the water content to a minimum in the preparation of ceramic fibre precursor solutions from aluminium chlorhydrex and tetramethoxysilane, tetraethoxysilane or ethyl silicate-40, removal of solvent and volatiles led to viscosity of residual solution increases in the order:

$$\text{ethyl silicate-40} > Si(OMe)_4 > Si(OEt)_4.$$

This corresponds to the order of silica equivalence. The filaments formed from the solutions converted on firing into mullite ceramic fibres.

SUMMARY

(a) The best control of both hydrolysis and gelation of alkyl silicates is obtained when the alcohol solvent and the organic silicate each contain the same alkyl group. However, rapid removal of the alcohol during drying usually causes the gel to crumble.

(b) The use of mixtures of ethanol and either N,N-dimethylformamide or glycols such as 1,2-dihydroxyethane or 1,2-dihydroxypropane as solvent in the formation of gels from ethyl silicate-40 and aluminium chlorhydrate species reduces cracking of the gel during drying.

(c) For filament and hence ceramic fibre formation from aluminium chlorhydrex and alkyl silicates to be successful, the water content of the system must be minimal.

REFERENCES

1. H.G. Emblem and K. Jones, Trans. J. Brit. Ceram. Soc., 79 (4), lvi (1980).
2. H.G. Emblem, A.K. Das and K. Jones, U.S. Patent No. 4 211 717 (8 July 1980).
3. H.G. Emblem, Silicates Industriels, 44, 286 (1979).
4. K. Jones, H.G. Emblem and H.M. Hafez, J. Non-Cryst. Solids, 63, 201 (1984).
5. H.G. Emblem, Ceramurgia International, 1, 136 (1975).
6. K.D. Biddle, A.K. Das, K. Jones and H.G. Emblem, J. Appl. Chem. Biotechnol., 27, 565 (1977).
7. Revlon Inc., British Patent No. 1 009 959 (17 November 1965).
8. J.M. Boulton, K. Jones and H.G. Emblem, J. Mater. Sci., 24, 979 (1989).
9. J.M. Boulton, Ph.D Thesis, University of Manchester, 1987.
10. J.M. Boulton, H.G. Emblem and K. Jones, British Patent No. 2 173 179A (8 October 1986).
11. H.G. Emblem, K. Jones and J.M. Boulton, U.S. Patent No. 4 810 441 (7 March 1989).
12. H.G. Emblem, K. Jones and J.M. Boulton, British Patent No. 2 210 034A (1 June 1989).

INVESTIGATION OF THE SILICA NETWORK DURING THE SOL TO GEL TRANSITION AND FINAL XEROGEL PROPERTIES

PAUL R. SOSKEY, RANDALL E. NIKLES, GEORGE F. FATTMAN, ROBERT M. MININNI* AND DEBORAH A. GERENZA**
*EniMont America Inc., 2000 Cornwall Rd., Monmouth Jct., NJ 08852
**Rheometrics Inc., One Possumtown Rd., Piscataway, NJ 08854

ABSTRACT

Silica sols were produced with various catalysts (NaOH and HF). Dynamic small strain rheometry was used to probe the formation of the silica network from the sol state through the gelation point into the region of high modulus. These results were related to the dried xerogel properties of surface area and porosity.

INTRODUCTION

Various types of rheological measurements have been used to study the structure evolution of silica gel networks [1]. Many times large strain steady shearing flows are used to determine gel transitions, however, because the gel network is destroyed by the large strain, the gel point of the quiescent silica network actually occurs at an earlier time than measured. Others have used small strain, dynamic tests to follow gelation at a fixed frequency [2]. Winter and coworkers have shown that much information can be gained from the entire frequency domain as a function of the time of gelation in polymeric networks [3,4].

We will use these dynamic techniques to follow the gelation of silica gels from the initially mixed low viscosity fluid state, through the 3-D network growth (gelation), into the fully gelled (network syneresis) stage and relate these results to the porosity of the resultant dried xerogel.

EXPERIMENTAL

The tetramethoxysilane (TMOS) (Petrarch)/water silica sol system was studied using either hydrofluoric acid (HF) or sodium hydroxide (NaOH) (both from Fisher Scientific) as catalysts. The initial composition TMOS:H_2O was 1:16 with catalyst concentrations of 1.83×10^{-5}M (low) and 1.85×10^{-3}M (high) in the water for both catalysts. A fifth system using no catalyst was prepared as a control.

The initial reaction was carried out by vigorously stirring the components until a clear solution was obtained. The high NaOH catalyst sample did not form a clear sol prior to gelation and the sample was considered mixed when no phase separation was apparent. Mixing times for all samples ranged from 10-20 minutes and once mixed the samples were immediately analyzed.

Due to the wide range in dynamic storage modulus (G') from the initial sol to the latter stages of gelation and beyond, two instruments were used in this study. A low viscosity fluids rheometer (Rheometrics RFS II) was used to investigate the sol-to-gel transition and a higher viscosity rheometer (Rheometrics RMS 800) was used to investigate further network formation beyond the gel point.

Mat. Res. Soc. Symp. Proc. Vol. 180. ©1990 Materials Research Society

The RFS rheometer was fit with a couette fixture with dimensions: bob radius 16mm, bob length 33mm and cup radius 17mm. The sample was loaded into the fixture, the bob lowered and a layer of silicon oil (100 cp) was applied to the exposed sample area to reduce evaporation. The temperature was controlled by a circulating bath at 25°C.

Prior to gelation, a time sweep of the modulus was performed at a frequency (w) of 1 rad/s, strain of 0.9, with measurements every 20s. When G' reached 50mPa, the frequency dependence was measured through the gel point by varying the frequency from 30 to 0.6 rad/s (3 points per decade) (strain=0.2) with a 1s delay between sweeps. When G' reached 10Pa, the strain was reduced to 0.001 and an additional 50-100 sweeps were taken with a 1 or 5s time delay depending on reaction rate.

The RMS rheometer was fit with a 50mm diameter top plate and a 58mm rimmed bottom plate to contain the sample. The sol was poured into the bottom fixture and the top plate was lowered into the sol to a gap separation of 1.85mm. The lower plate was oscillated at 1 rad/s at 0.001 strain and the torque on the top plate was measured. When sufficient mechanical strength was achieved, the excess gel was trimmed to 50mm in diameter to ensure that the contribution to the measured torque was only due to the sample between the plates. A time sweep continued until the modulus peaked or the limitations of the sample fixture geometry were exceeded.

A portion of each gel was dried 24hr at 150°C, degassed 48hr under vacuum at 150°C and analyzed for surface area and porosity from the nitrogen adsorption/desorption isotherms obtained with a Micromeritics ASAP 2400 porosimeter.

RESULTS AND DISCUSSION

In these initial studies of silica gel network formation, several interesting rheological features were noted. During the initial stages, before the gel point, all of the systems show similar behavior except the NaOH High system. Whereas, the No Catalyst, HF High, HF Low, and NaOH Low systems show essentially a low modulus (that of water) right up until the gel point where a drastic increase occurs due to the 3-D network formation, the NaOH High system exhibits a gradual rise in G' before the gel point (see Figure 1). Other differences are seen in the frequency dependence before the gel point. The NaOH High system, as shown in Figure 2, has features very similar to polymeric systems having tetra-functionally crosslinked long flexible chains[3]. Near the gel point, G'=G" over the entire frequency domain and the slope on log-log coordinates is 0.5. After the gel point, G' is much higher than G" and becomes independent of frequency. A much different response is seen in the No Catalyst system, Figure 3. In the pre-gel state the sol behaves like a Newtonian liquid (G"/w is constant), but at low frequencies, G' is becoming independent of frequency, which indicates the presence of large structures. Whether these large structures are long chain branched structures or highly branched fractal clusters having many short segments has not be determined at this time. But the data clearly indicates that there are very large structures that are not forming a 3-D network along with smaller structures that are more viscous than water.

The gel times and the modulus at the gel point were determined for each system and the results appear in Table I. The gel times are reduced by adding high levels of either NaOH or

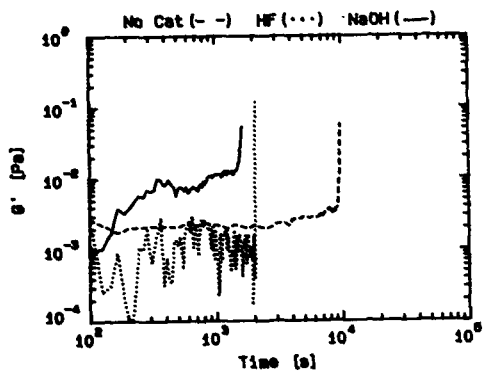


Figure 1. Modulus growth prior to gel point.

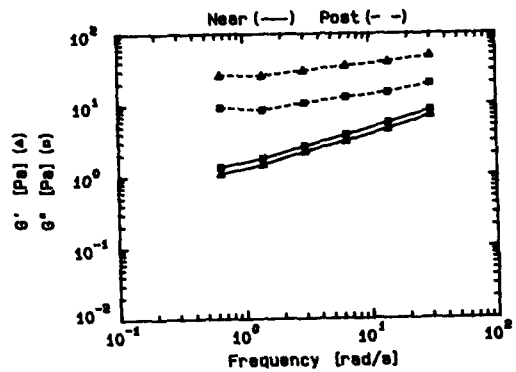


Figure 2. NaOH High Sol-Gel Transition.

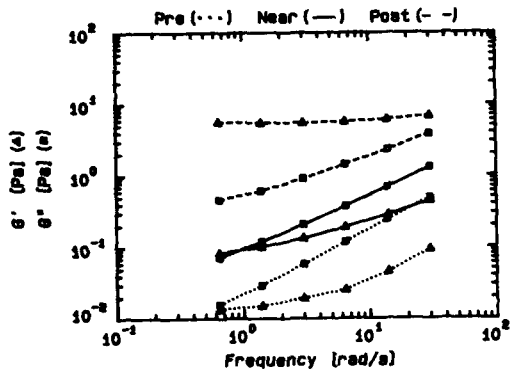


Figure 3. No Catalyst Sol-Gel Transition.

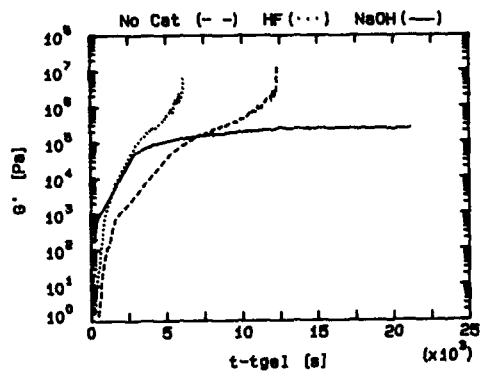


Figure 4. Modulus growth after gel point.

HF. Also the modulus level at the gel point is 300 times higher for the NaOH High than the other systems, again indicating that the structure is different from the others at the gel point.

TABLE I
Results of Rheology and Nitrogen Adsorption Measurements

SYSTEM	t_{gel} [s]	G'=G" @ gel [Pa]	ISOTHERM TYPE	SURFACE AREA [m^2/gm]	PORE VOLUME [cm^3/gm]	AVG. PORE DIAMETER [nm]
NaOH High	2,170	15.0	IV	676	0.479	2.8
NaOH Low	7,149	0.05	I	672	0.232	1.4
HF High	2,048	0.02	IV	786	0.397	2.0
HF Low	13,684	0.04	I	645	0.227	1.4
No Catalyst	10,525	0.09	I	684	0.238	1.4

The network syneresis is compared in Figure 4. Both the NaOH High and HF High systems proceed relatively quickly through the gel point, but the NaOH levels off to an equilibrium modulus of about 200 kPa and stays that way for a long time. The No Catalyst system has a slower syneresis immediately after the gel point but eventually forms a tighter network than the NaOH High system. This indicates that both the HF High and No Catalyst systems continue to react and form a tighter network after the gel point while the NaOH High forms a network with a lower crosslink density.

The nitrogen adsorption isotherms for the systems are shown in Figure 5. The isotherms for the NaOH Low, HF Low and No Catalyst systems show a type I isotherm behavior with a low total volume of absorbed nitrogen [5]. The isotherms for NaOH High and HF High show a type IV behavior with about double the total volume of adsorbed nitrogen.

The type I isotherm is indicative of a microporous material. In this study, for systems showing type I isotherms, the average pore diameter was less than 1.5nm with a pore volume of less than 0.238cm^3/g (Table I) of which 70% was micropore volume. The type IV isotherm is indicative of a mesoporous material. The NaOH High system had an average pore diameter of 2.8nm with pore volume of 0.479cm^3/g, of which only 9% was micropore volume. The HF High system was also type IV with average pore diameter 2.0nm and pore volume 0.397cm^3/g, of which 25% was micropore volume.

These results show a difference between the various systems. The HF Low, NaOH Low and No Catalyst systems were much less porous with porosity increasing from the HF Low to NaOH Low to the No Catalyst system. The NaOH High and HF High systems were about twice as porous with the NaOH High system yielding a 20% higher porosity than the HF High system.

CONCLUSIONS

The structure growth mechanisms are different in the NaOH High system than in the other silica systems of this study. The rheological results suggest that the NaOH High system sol grows structures evenly up to the 3-D gel point; whereas, the other systems have large and small structures throughout the gelation

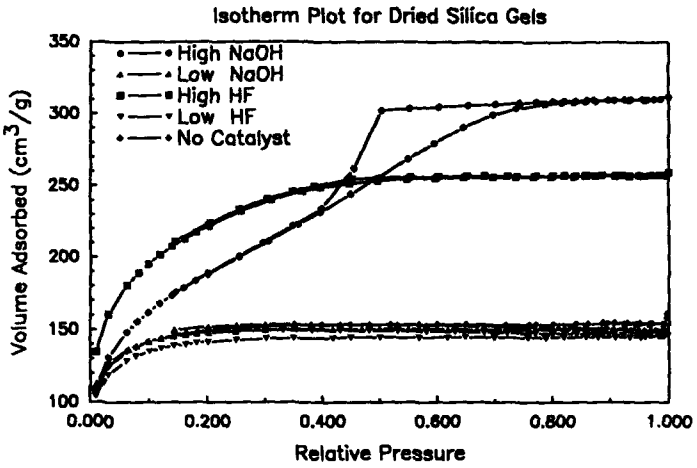


Figure 5. Adsorption Curves for Dried Xerogels.

and only interact near the gel point. Further syneresis of the NaOH High gel is a slow process with a lower crosslink density than the other systems which undergo syneresis faster and reach a much higher gel modulus. There appears to be a direct relationship between the gel modulus and the dried xerogel porosity. Rheological techniques such as these can be used in conjunction with light scattering and NMR techniques to further identify the growth mechanisms in silica sols.

ACKNOWLEDGMENTS

We wish to thank T. Che, H. Winter and M. Drzewinski for helpful technical discussions of Sol-Gel chemistry, polymer networks and characterization techniques. We appreciate the use of Rheometrics Inc. facilities for the low modulus measurements.

REFERENCES

1. M.D. Sacks and R.S. Sheu, J. Non-Cryst. Solids 92, 383 (1987).

2. S.A. Khan, E.M. Rabinovich, R.K.Prud'homme, M.J. Sammon, and N.J.Kopylov, in Better Ceramics Through Chemistry III, C.J. Brinker, D.E. Clark, D.R.Ulrich, Eds., (Mater. Res. Soc. Proc. 121, Pittsburgh, PA 1988) pp. 73-80.

3. H.H. Winter, Polym. Eng. Sci. 27 (22), 1698 (1987).

4. H.H. Winter, Progr. Colloid & Polymer Sci. 75, 104 (1987).

5. S.J. Gregg and K.S.W. Sing, Adsorption, Surface Area and Porosity, 2nd ed. (Academic Press, Inc., Orlando, FL, 1982),pp. 5, 111, & 195.

FORMATION OF SPINEL IRON OXIDE IN SOLUTION

Jean Pierre JOLIVET, Elisabeth TRONC, Philippe BELLEVILLE and Jacques LIVAGE
Chimie de la Matière Condensée, CNRS URA 302, Université P. et M. Curie,
4 Place Jussieu, 75252 Paris Cedex 05 France.

ABSTRACT

The alkalizing of aqueous mixtures $Fe^{III} + xFe^{II}$ has been investigated at pH ≈ 8 for $0 \leq x \leq 0.5$. Three composition zones have been observed. At $x<0.1$ goethite was the only stable product. At $0.1 \leq x \leq 0.25$ the early stage, characterized as mixed-valent protoferrihydrite, spontaneously transformed into nonstoichiometric magnetite. At $x>0.25$ the system, made of spinel particles, was homogeneous during all the evolution.

INTRODUCTION

Iron oxides and oxyhydroxides, crystalline and amorphous, are involved in many natural and industrial processes (corrosion, catalysis, magnetism...). Magnetite plays a special role because of its electronic and magnetic properties. The phase, largely nonstoichiometric runs from Fe_3O_4 to γ-Fe_2O_3. It can form under a great variety of conditions in aqueous medium. Formation mechanisms have generally been studied in connection with Fe^{II} oxidation or under stoichiometric conditions [1-3]. Formation in media poor in Fe^{II} has far less been investigated. Protoferrihydrite [4] (also named amorphous ferric hydroxide, ferric oxide gels) is a very poorly crystalline hydrated oxyhydroxide formed by fast hydrolysis of Fe^{III} ions. It is unstable in suspension. At low concentration, Fe^{II} ions induce transformation to goethite via dissolution reprecipitation processes [4,5]. The spinel phase forms at Fe^{II}/Fe^{III} ratios greater than 0.2 [5,6]. So far, to our knowledge, no detailed study of the process has been reported. Hence, we present an investigation of crystallization processes for Fe^{II}/Fe^{III} ratios varying in the range 0-0.5.

EXPERIMENTAL

Aqueous mixtures of $FeCl_3$ ($40cm^3$, 1M) and $FeCl_{2_3}$ (2M, 2M HCl) in various proportions were added to a NH_3 solution ($400cm^3$, 0.6M, pH≈11) under vigourous stirring at room temperature. Great care was taken to exclude oxygen at all the preparation stages. The solid was washed with degassed distilled water. Suspensions at pH near 8 were aged under argon pressure. Suspensions were also prepared by successive precipitation of Fe^{III} and Fe^{II} ions.

Suspension composition was determined by titrating iron potentiometrically. The chemical reactivity was characterized by reducing dissolution in acidic medium (2M HCl, 0.2M KI, 25°C). Electron micrographs and diffraction (ED) patterns were obtained using very dilute solutions evaporated onto a carbon-coated grid. X-ray diffraction (XRD) patterns were recorded using powders isolated by centrifugation and dried under reduced pressure. Mössbauer samples were made up of suspensions confined in a plastic cell and quickly frozen at 77K. The isomer shifts (IS) are given relative to metallic iron at room temperature. Other parameters are quadrupole splitting (QS), line width (W), hyperfine field (H).

RESULTS

Protoferrihydrite (PF) was characterized by quasi immediate reducing

Mat. Res. Soc. Symp. Proc. Vol. 180. ©1990 Materials Research Society

dissolution in acidic medium. The particles were of ca. 25-30Å. Diffraction patterns showed two (XRD: 2.6 and 1.5Å) or three (ED: 2.6, 2.1 and 1.5Å) diffuse bands. No evolution was observed after aging the suspension for one day. After one month, goethite was the only constituent. In the presence of Fe^{II}, three zones were observed depending on the ratio $x = Fe^{II}/Fe^{III}$. Both preparation routes, simultaneous or successive precipitation of Fe^{III} and Fe^{II} ions, led to similar results.

a) $0 \leq x \leq 0.1$

The initial system behaved like PF. After 1h aging, small spinel particles (*ca.* 30Å, ED rings at 3.0, 2.5, 2.1, 1.6, 1.5Å) and goethite particles coexisted. No change was observed after 1 day aging. After a month, only goethite was present.

b) $0.1 \leq x \leq 0.25$

Dissolution kinetics involved three successive stages, quasi immediate, rapid and slow. Each stage is characterized by only one type of particles (P_0, P_1 and P_2, respectively). The kinetic constant of each species and the proportion of iron involved were determined using a pseudo first order kinetic law.

Only P_0 was present in the early stage. P_1 and P_2 appeared within a few minutes of aging, they were practically the sole constituents after one day. Their proportions then remained constant even after several months. P_0 consisted in 25-30Å particles characterized as mixed-valent protoferrihydrite (see d). P_1 and P_2 were two distinct families of spinel particles.

Typical evolution of the system is given in Figure 1 for $x = 0.15$. At the equilibrium, P_1 particles were of *ca.* 40Å with composition $Fe^{II}/Fe^{III} = 0.07$. P_2 particles were prismatic crystallites of *ca.* 600Å with $Fe^{II}/Fe^{III} = 0.30$.

The P_2 particles decreased in size and proportion with increasing x. They were not observed at $x = 0.25$.

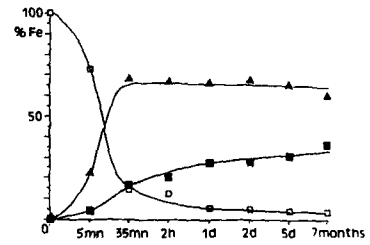


Figure 1: Time evolution of the system at Fe^{II}/Fe^{III}=0.15
(□) P_0, (▲) P_1, (■) P_2 particles

c) $x \geq 0.25$

The system was a single mode distribution of spinel particles during all the evolution. The initial mean size increased with x (x=0.30, $\bar{D}$=50Å σ=15Å; x=0.50, $\bar{D}$=65Å σ=18Å). The mean size increased during the first days of aging (x=0.50, 5 days, $\bar{D}$=105Å σ=24Å).

d) Mixed-valent protoferrihydrite.

Protoferrihydrite consists in a very poorly ordered arrangement of $Fe(O,OH,OH_2)_6$ octahedra. It is an amorphous magnet, of the speromagnetic type, with ordering temperature (T_0) near 100K [7, 8]. Below T_0, the spins in a particle are fixed relative to each other with random orientations and short range antiferromagnetic coupling due to superexchange interactions. The finite size of the particles gives rise to a net moment which fluctuates thermally, leading to superparamagnetic (SP) behaviour.

Identical ED patterns showed that the P_0 species (b) is structurally similar to protoferrihydrite. Mössbauer spectra show that it is also magnetically similar.

At 80K, the P_0 spectrum (Fig. 2) is a disymmetric quadrupole pattern made up of two components. The major one is due to the Fe^{III} ions, their surroundings appear somewhat more distributed than in PF. The minor component is due to the Fe^{II} ions, the parameters are typical of 6-fold coordination.

With decreasing temperature, a magnetic component grows at the expense of the quadrupole pattern, indicating SP behaviour. At 4K, apart from a residual component attributed to Fe^{III} species in small units [9], the spectrum is totally magnetically split. The blocking temperature (equal SP and magnetic fractions) is equal to 42K.

Discarding the presence of Fe^{II}, all of the results are typical data for PF particles [8-12].

At and above 110K, a fast electron exchange occurs between Fe^{II} and Fe^{III} ions, involving all the Fe^{II}. The Fe^{II} doublet is observed up to 100K. From 110K, a component with doubled relative area and isomer shift typical of the $Fe^{2.5+}$ state [13] appears. Because of the time window of Mössbauer spectroscopy, the electron hopping frequency ν verifies: $\nu \leq 10^7 s^{-1}$ at 100K and $\nu \geq 10^9 s^{-1}$ at 110K. Such a large variation, incompatible with small polaron theory, suggests that there is a discontinuity about 105K associated with the magnetic ordering transition. Electron hopping is a direct process, it requires ferromagnetic coupling of the Fe^{II} and Fe^{III} spins. Spin polarization accompanying the small polaron is indeed much easier in the paramagnetic state than in the speromagnetic one.

Mixed-valent protoferrihydrite is unstable with respect to dehydration. Freeze-drying or drying at room temperature under reduced pressure inevitably induced transformation into non stoichiometric magnetite, with no change in the particle size. This was clearly demonstrated by electron microscopy observations and drastic modifications in the Mössbauer spectra (Fig.2)

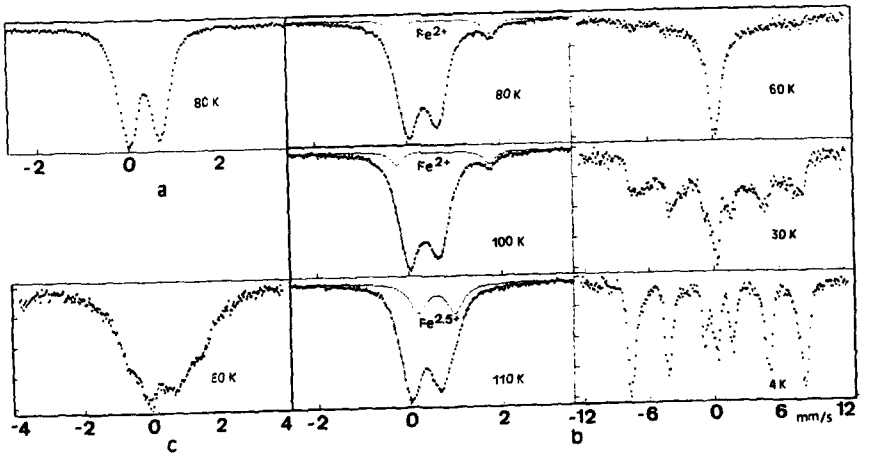


Figure 2: Mössbauer spectra of protoferrihydrite (PF) suspensions.
a: Pure PF. IS=0.44mm/s QS=0.70mm/s W=0.48mm/s.
b: Fe^{II}-PF (Fe^{II}/Fe^{III}=0.15) 4K: IS=0.46mm/s <H>=47.7T σ=6.9T
80K: Fe^{III} IS=0.45 QS=0.60 W=0.54mm/s - Fe^{II} IS=0.92 QS=1.99 W=0.32mm/s 10%
110K: Fe^{III} IS=0.40 QS=0.67 W=0.48mm/s - $Fe^{2.5+}$ IS=0.67 QS=0.80 W=0.43 23%
c: Freeze-dried Fe^{II}-PF.

DISCUSSION

The results show that all the Fe^{II} is taken up by protoferrihydrite and that the mixed-valent material is the precursor of the spinel phase. This phase is the only crystalline product formed at Fe^{II}/Fe^{III} ratios as low as 0.1.

The coexistence of two populations of spinel particles (P_1, P_2) with so distinct morphologies and compositions at intermediate x values proves that the transformation to spinel can proceed via two competing mechanisms:
1- dissolution of protoferrihydrite followed by nucleation and growth of the crystalline oxide
2- internal dehydration and rearrangement.

Mechanism 1 is responsible for the growth of the large P_2 particles. The reaction probably involves ferric ferrous hydroxo complexes that dissolve from the surface and reprecipitate as substoichiometric magnetite. Such complexes are also involved in the formation of spinel from γ-FeOOH in the presence of Fe^{II} [2]. The formation of goethite particles at $x<0.1$ proceeds in the same way [5].

Mechanism 2 predominates at $x \geq 0.25$. It leads to formation of small spinel particles. They are initially of *ca.* 25-30Å and grow by Ostwald ripening process.

Other divalent transition metal ions (M^{II}) also induce transformation into a spinel phase [14]. Though different experimental conditions make the comparison difficult, it seems that M^{II}/Fe^{III} ratios greater than 0.2 are required, and that the reaction proceeds via mechanism 1. This emphazises the special role of Fe^{II}.

We have shown that charge transfer occurs in Fe^{II}-protoferrihydrite. Electron mobility is a characteristic property of (nonstoichiometric) magnetite. It results from direct d-orbital overlapping giving rise to metal-metal bonding across edge-sharing octahedra [13]. Electron delocalization is likely the cooperative phenomenon that drives structural rearrangements in Fe^{II}-protoferrihydrite. We note that the limit $Fe^{II}/Fe^{III}=0.25$ at which mechanism 2 becomes the only pathway to the spinel, practically corresponds to the composition of the particles grown via mechanism 1. This might correspond to percolation threshold.

The transformation of protoferrihydrite into spinel by Fe^{II} adsorption shows that interfacial electron transfer can induce electron delocalization in the solid. Reversely, electron delocalization in spinel iron oxide leads to remarkable interfacial properties [15,16].

1. T. Misawa, K. Hashimoto and S. Shimodaira, Corros. Sci. 14, 131 (1974)
2. Y. Tamaura,K. Ito and T. Katsura, J. Chem. Soc. Dalton 1983, 189
3. R.M. Taylor and U. Schwertmann, Clay Miner. 10, 299 (1974)
4. F.V. Chukhrov, B.B. Zvyagin, L.P. Ermilova and A.I. Gorshkov, Proc. Int. Clay Conf. Madrid 1, 397 (1972)
5. R.M. Cornell and W. Schneider, Polyhedron 8, 149 (1989)
6. R. Massart and V. Cabuil, J. Chim. Phys. 84, 967 (1987)
7. E. Nunes Filho, E. Conforto and H.R. Rechenberg, J. Magn. Magn. Mater. 74, 125 (1988)
8. J.M.D. Coey and P.W. Readman, Earth Planet. Sci. Lett. 21, 45 (1973)
9. B. Rodmacq, J. Phys. Chem. Solids 45, 1119 (1984)
10. E. Murad, L.H. Bowen, G.J.Long and T.G.Quin, Clay Miner. 23, 161 (1988)
11. E. Murad and U. Schwertmann, Amer. Miner. 65, 1044 (1980)
12. C.W. Childs and J.H. Johnston, Aust. J. Soil. Res. 18, 245 (1980)
13. H. Eckert, in Mössbauer Spectroscopy Applied to Inorganic Chemistry, edited by G.J. Long (Plenum Press, 1987) vol.2, p.125
14. R.M. Cornell, Clay Miner. 23, 333 (1988)
15. J.P. Jolivet and E. Tronc, J. Colloid Interface Sci. 125, 688 (1988)
16. E. Tronc, J.P. Jolivet, P. Belleville and J. Livage, Hyperf. Int. 46, 637 (1989).

RELIABLE ELECTROKINETIC CHARACTERIZATION PROCEDURES FOR CERAMIC POWDERS

JIUN-FANG WANG, RICHARD E. RIMAN, AND DANIEL J. SHANEFIELD
Rutgers University, Department of Ceramics, P.O. Box 909, Piscataway, NJ 08855-0909

ABSTRACT

Microelectrophoresis is an important method for measuring surface properties of colloidal materials. In order to obtain reliable measurements, a good reference colloid must be chosen first, and both the behavior of the reference under a variety of measurement conditions and instrumental factors must be established. Polystyrene latex has proven to be a good reference material. Time-dependent, solids-loading, and electrolyte concentration effects are determined below in order to establish reproducible referencing conditions. Using these referencing conditions, surface properties of silicon nitride as a function of aging time and atmosphere are studied.

INTRODUCTION

Reproducible optimized processing is desired for preparation of defect-free ceramic materials. This can be accomplished by the use of electrostatically stabilized suspensions in forming processes such as slip casting. In order to avoid particle packing defects, it is desirable to process a suspension that is free of agglomerates. Agglomerate-free or stabilized suspensions can be obtained when the surface potential, ψ, is maximized (>25 mV). The surface potential can be inferred from calculation of the zeta potential, ζ, a measurement proportional to the electrophoretic mobility, μ. Thus, measurement of μ (defined as the drift velocity divided by the applied electric field) via commercially available microelectrophoresis instrumentation can be used to indicate the optimum conditions for suspension preparation [1]. However, for many ceramic materials, the isoelectric point (IEP), the pH at which μ is zero, is reported instead [2]. From this information, it is understood that, in a suspension free of surfactants or other adsorptive impurities, the surface charge is positive below and negative above the IEP.

A common problem encountered in consulting the ceramic colloids literature is the wide range of variability of IEP data for a given material [3]. This variation can be attributed to powder preparation techniques, sample history, suspension preparation methods, and/or equipment used to make the measurement. For silicon nitride powders, for instance, the IEP can range from 3 to 9 depending on the manufacturer and the atmospheric conditions under which it is stored [4]. In addition, microelectrophoresis can be performed with many types of instruments that vary mostly in the manner in which the drift velocity is measured. The relative contribution of this factor to variations in IEP data has not been assessed.

Many of the above problems could be solved if a universal reference colloid were selected for calibrating instruments prior to measurement of sample μ and a standard procedure were developed for sample preparation and μ measurement. A good reference colloid should exhibit (a) little sedimentation and agglomeration over the course of the microelectrophoresis experiment, (b) a surface potential as insensitive to pH as possible, (c) commercial availability in a highly pure and reproducible form, and (d) resistance to environmental factors that could change its properties upon storage. A reference colloid satisfying these conditions would provide for reproducible μ measurement and thus would be useful for standardizing the microelectrophoresis instrument. Polystyrene latex fulfills most of the criteria cited above (*except possibly* (d)). Furthermore, it has been used widely for electrophoretic studies for decades [5-7]. Features of polystyrene latex making it suitable for use as a reference colloid and procedures for obtaining accurate and precise μ measurements for the reference colloid and silicon nitride powder will be discussed.

EXPERIMENTAL

All chemicals other than those cited below were purchased from Aldrich Chemical Company, Inc. (Milwaukee, WI), were ACS reagent grade or better, and were used without

Mat. Res. Soc. Symp. Proc. Vol. 180. ©1990 Materials Research Society

further purification. Deionized water with a resistivity of 18 MΩ·cm filtered by a 0.22 μm membrane was obtained with a Milli-Q Water System (Millipore Corporation, Bedford, MA). Nitrogen with an oxygen content of less than 5 ppm was obtained from Matheson Gas Products (East Rutherford, NJ). Sulfate group-stabilized 0.5 μm polystyrene latex was purchased from Polysciences, Inc., Lot 81688 (Warrington, PA); Interfacial Dynamics Corporation (Portland, OR); and Sigma Chemical Company, Lot 98F0460 (St. Louis, MO). The former two were surfactant-free dispersions while the latter one contained 0.1-0.5 wt% surfactant. Silicon nitride powder (UBE SN-E10) was obtained from UBE Industries, Inc., Lot A810542 (New York, NY). Suspensions of polystyrene latex were prepared by diluting a concentrated commercial dispersion into a desired volume fraction with electrolyte solution. The suspension of silicon nitride powder was prepared by dispersing the powder in solution using an ultrasonic bath. Suspension pH was adjusted by addition of either HNO_3 or KOH solution, after which suspensions were stored in sealable Falcon polypropylene containers (American Scientific Products, Edison, NJ).

Prior to characterization, each suspension was divided into two groups for μ and pH measurements. A Brinkman 686 Titroprocessor with Metrohm (Switzerland) with Ag/AgCl double junction electrodes, calibrated using pH 4.00, 7.00 and 10.00 buffers, was used for pH measurements. A Malvern Zetasizer II with a Malvern System 4700c correlator at an electric field strength of 15 V/cm was used for microelectrophoresis. Since preconditioning the microelectrophoresis cell is important to obtaining reproducible measurements, a sample of the reference colloid was introduced into the cell and allowed to equilibrate for about 3 min before a second sample was introduced for actual measurement. μ and pH measurements were performed simultaneously at 25°C for each sample. At least seven measurements were made and subsequently averaged together to obtain each μ data point, except for time effect studies, which utilized a single measurement per data point.

RESULTS AND DISCUSSION

Of the three latexes described above, the Polysciences latex was selected as a reference because it displayed a high zeta potential (ζ~100 mV) and its mobility was the least sensitive to changes in pH for a given electrolyte concentration. For instance, when a 0.01 M KNO_3 electrolyte was employed over a pH range of 5.5 to 10.5 (Figure 1a), μ fell within the range of $(7.71\pm0.05)\times10^{-8}$ m^2/Vs. In contrast, for the latexes manufactured by Interfacial Dynamics and Sigma, μ varied over the ranges of (6.8 ± 0.09) and $(7.30\pm0.25)\times10^{-8}$ m^2/Vs, respectively, over the same pH range.

While initial measurements for identifying sample-oriented effects made this colloid appear optimum as a reference material, additional measurements were necessary to verify the operation of the microelectrophoresis equipment. The condition of the cell and the associated optics can be examined by using the reference colloid to check the stationary layer positions of the cell. This was accomplished by varying solution pH to vary the electro-osmotic velocity [8] of the suspending solution (Figure 1b). Using the intersection of two or more cell profiles yielded

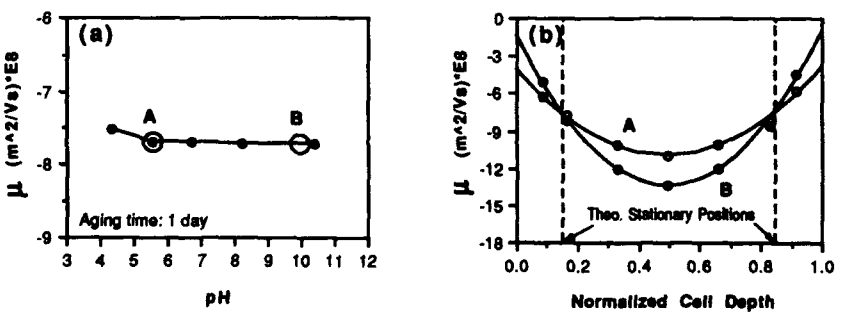


Figure 1. A 0.01 vol% polystyrene latex in 0.01 M KNO_3 solution: (a) mobility as a function of pH (b) cell mobility profiles as a function of pH

experimental stationary layer positions within 5 μm of the position determined from first principles. The symmetrical μ profiles also show that there are no dimensional asymmetries present. The steepness of the μ profile increases with pH; thus, when the stationary layer position is not properly located, μ is more subject to instrumental error.

Assuming the instrument is operating properly, obtaining reliable μ values for the reference colloid also depends on the sample preparation conditions. First, our studies revealed that a solids loading greater than 0.005 vol% was required before a constant μ could be obtained (Figure 2a). Using different instrumentation (Pen Kem 3000), this has also been found for calcite powders [9]. A decrease in the absolute value of μ has been attributed to hydrodynamic interactions [10] and colloidal phenomena such as double layer compression. In this experiment, however, the absolute value of μ was found to increase. This difference could have been caused by insufficient particle population in the sampling volume for laser Doppler velocimetry. Second, the mobility was found to vary with the time elapsed after introducing the sample into the microelectrophoresis cell, which also varied with the type and concentration of electrolyte (Figure 3). Therefore, all the measurements were performed immediately after injection into the conditioned sample cell (~2 s). This overall approach led to the collection of reproducible μ data. For instance, in a pH range of 5.5 to 10.5 and under the conditions summarized in Figure 1a, the average μ taken from μ plateaus measured 6 months apart differed by as little as 3.4×10^{-9} m^2/Vs.

After using the above reference colloid to check our instrument, μ studies on silicon nitride were conducted. In general, neither time dependency nor electrolyte effects were observed for this powder (Figure 3b). However, as with polystyrene latex, solids loading was found to strongly influence the μ (Figure 2b). Thus, in order to obtain reproducible μ measurements,

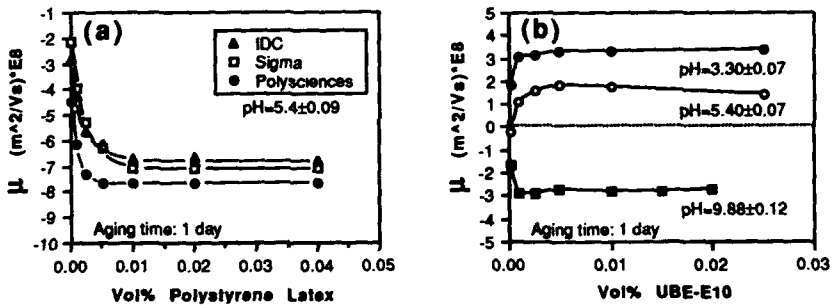


Figure 2. Electrophoretic mobility as a function of solids loading: (a) latex (b) Si_3N_4

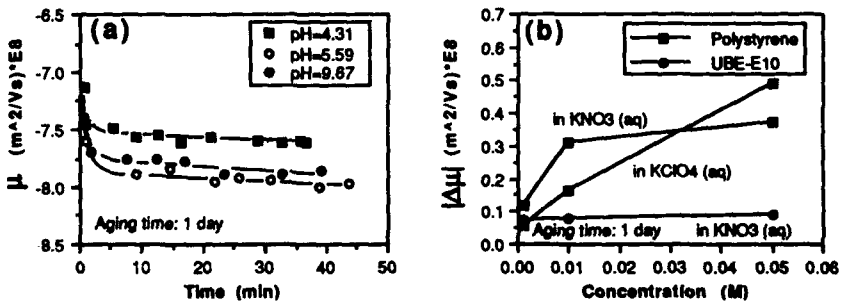


Figure 3. (a) mobility of 0.01 vol% polystyrene latex in 0.01 M KNO_3 solution as a function of time elaped after sample introduction (b) mobility shift of colloid within the first two minutes as a function of electrolyte concentration and type

slightly higher solids loadings (>0.01 vol%) are recommended for this powder. To examine μ as a function of aging time and environment, 0.01 vol% solids loading suspensions were either exposed to ambient air, stored under air in a sealed container, or stored under nitrogen in a sealed container for a period of 1 to 30 days. The IEP of 0.01 vol% UBE powder in 0.01 M KNO_3 solution shifted from 7.4 to 8.8 as it was aged 1 to 3 days (Figure 4). Aging in ambient air for 1 day increased μ greatly in the pH 7 to 8 range, while aging in the other two closed systems did not. At aging times greater than 3 days, the behaviors of different aging environments appear to converge. However, at these long aging times, at any pH value below the IEP, the magnitude of μ is greater than at shorter times regardless of the aging environment. The above results can be interpreted in terms of silicon nitride surface chemistry and its chemical interaction with water. This work will be presented in a future publication.

CONCLUSION

Based on criteria cited earlier, polystyrene latex has been identified as a good reference colloid for establishing the proper operation of a microelectrophoresis apparatus. However, the effects of solids loading, electrolyte concentration, and time on μ must be determined before reference μ values can be established for the colloid. Similar studies should be undertaken when examining any unknown material. When this is done, long-term time-dependent μ studies can be accomplished with minimal experimental error.

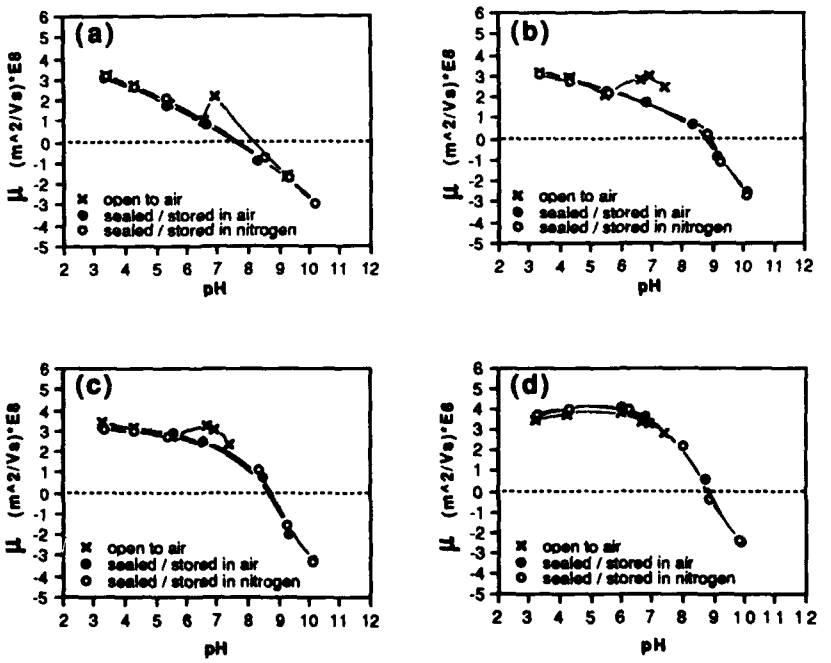


Figure 4. Electrophoretic mobility of silicon nitride powder (0.01 vol% in 0.01 M KNO_3) as a function of aging time and atmosphere: (a) 1 day (b) 3 days (c) 7 days (d) 30 days

ACKNOWLEDGMENTS

The authors would like to acknowledge the generous support of the U. S. Department of Energy, Assistant Secretary for Conservation and Renewable Energy, Office of Transportation Systems, as part of the Ceramic Technology for Advanced Heat Engines Project of the Advanced Materials Development Program, the Center for Ceramic Research at Rutgers University, and the New Jersey State Commission on Science and Technology.

Finally, the efforts of Ms. Kelly Griffin for the preparation of this manuscript are gratefully acknowledged.

REFERENCES

1. James S. Reed, Introduction to the Principles of Ceramic Processing, (John Wiley & Sons, Inc., New York, 1988), p.141.

2. G. A. Parks, Adv. Chem. Ser. 67, 121-160 (1967).

3. G. A. Parks, Chem. Rev. 65, 177-198 (1965).

4. L. Bergstrom and R. J. Pugh, J. Am. Ceram. Soc. 72 (1), 103-109 (1989); P. K.Whitman and D. L. Feke, ibid., 71 (12), 1086-1093 (1988).

5. R. H. Ottewill and J. N. Shaw, J. Electroanal. Chem. 37, 133-142 (1972).

6. W. D. Corry and G. V. F. Seaman, J. Colloid Interface Sci. 63 (1), 136-150 (1978); W. D. Corry, ibid., 63 (1), 151-160 (1978); H. Tamai, K. Niino, and T. Suzawa, ibid., 131 (1), 1-7 (1989).

7. B. J. Marlow, D. Fairhurst, and W. Schutt, Langmuir 4, 776-780 (1988).

8. Paul C. Hiemenz, Principles of Colloid and Surface Chemistry, 2nd ed. (Marcel Dekker Inc., New York, 1986), p.737.

9. B. Siffert and P. Fimbel, Colloids and Surfaces 11, 377-389 (1984).

10. J. L. Anderson, J. Colloid Interface Sci. 82 (1), 248-250 (1981).

FRACTAL CONCEPTS AND AGGREGATION OF IRON OXIDES

R. AMAL[1], J.A. RAPER[1], T.D. WAITE[2]
[1] University of New South Wales, School of Chemical Engineering, P.O. Box 1, NSW 2033, Australia.
[2] Australian Nuclear Science and Technology Organization (A.N.S.T.O.), Private Mail Bag 1, Menai, NSW, Australia.

ABSTRACT

The modelling of the aggregation kinetics of iron oxides has been succesful in predicting the increase in aggregate size as determined by dynamic light scattering measurements. The aggregates were found to exhibit fractal behaviour with fractal dimensions obtained from the scattering exponent in static light scattering studies dependent on the aggregation mechanism and ranging from 2.3 for rapid (diffusion limited) to 2.8 for slow (reaction limited) aggregation. Polydispersity and restructuring of aggregates were found not to affect the relationship between scattering exponent and aggregate fractal dimension. Excellent correspondence over a range of temperatures and ionic strengths has been obtained between results of sizing experiments using dynamic light scattering and sizes predicted using a modified Smoluchowski model incorporating fractal dimensions.

INTRODUCTION

The structure of solid materials has important implications in many natural and commercial processes. Both physical parameters, such as dimension, surface area and porosity, and chemical parameters, such as solubility and reactivity will be determined by structure. Well structured materials such as crystalline solids can readily be grouped according to their symmetries. However, this procedure is not possible for randomly formed materials such as aggregates which represent a large proportion of solid material of industrial interest. This lack of apparent symmetry has greatly impeded the progress in understanding random morphologies. However, in the last few years, considerable progress in the study of materials with random structures has been made as a result of the increasing use of fractal concepts [1]. Of particular interest here are the microscopic structures of oxides - materials that occur widely in nature and form the basis of many ceramic and catalyst preparations.

The aggregation kinetics of hematite particles has been studied using dynamic light scattering[2], and experimental results were compared with a model based on theoretical considerations accounting for diffusion, interparticle repulsive forces and the nature of packing within the aggregated material (and referred to below as the "modified Smoluchowski" model). Successful prediction of rapid (diffusion limited) aggregation kinetics was obtained assuming that the resultant aggregates behaved as fractals with a fractal dimension of 2.3. A somewhat higher fractal dimension appeared to be appropriate for aggregation under ionic conditions where a repulsion barrier exists (reaction limited aggregation)[3].

This paper discusses the results of experiments using static light scattering[3] to study the structure of colloidal hematite particles which are induced to aggregate at different rates by altering solution conditions (electrolyte concentration and temperature). The aggregates are considered to posses a fractal structure and the fractal dimension is measured at different electrolyte concentrations and over a range of temperatures.

THEORY

A fractal object is a rugose object whose rugosities show up at any length scale and is thus considered self-similar. In the general theory of fractals, the fractal dimension (d_f)[4,5] is defined as a number which quantitatively measures the more or less rugose aspect of the object, or

$$N_r \propto r^{-d_f} \qquad (1).$$

Mat. Res. Soc. Symp. Proc. Vol. 180. ©1990 Materials Research Society

The concept of fractal dimension is only properly defined when using an asymptotic limit to infinitely small lengths for aggregates the natural cut off is simply the radius of the primary particle, r_0.

Scattering experiments give access to the position correlations between particles in the aggregate and consequently appear to be a very useful tool to measure the fractal dimension[6]. In a scattering experiment, a beam of light of intensity, I_0, is directed on to a sample and the scattered intensity (photoncounts) is measured as a function of an angle θ to the incident direction. The incident and scattered beam are characterized by the momentum transfer $\vec{Q}$, with

$$Q = |\vec{Q}| = \frac{4\pi n \sin\left(\frac{\theta}{2}\right)}{\lambda_0} \quad (2),$$

where λ_0 is the wavelength in the vacuum, and n is refractive index of medium.

The intensity scattered (I_M) from a single fractal aggregate of mass M can be related to two factors[7,8,9] that describe the aggregate structure,

$$I_M \sim M^2 P(Q) S(Q) \quad (3),$$

where $P(Q)$ is the form factor, and $S(Q)$ the interparticle structure factor.

The form factor is related to the shape of the particle and the contrast which can be defined as the difference between the scattering properties of the particles and the equivalent quantity of the solvent.

The interparticle structure factor, S(Q), takes into account the interparticle correlations and describes the spatial arrangement of the particles. For a fractal object[10],

$$S(Q) \sim 1 + \frac{d_F \Gamma(d_F - 1) \sin((d_F - 1)\tan^{-1}(QR_g))}{(Qr_0)^{d_F}(1 + 1/Q^2R_g^2)^{\frac{d_F}{2} - \frac{1}{2}}} \quad (4)$$

where $\Gamma(x)$ is the gamma function of x.

At large Q ($Qr_0 \gg 1$), S(Q) is approximately equal to 1 and only the scattering due to individual particles is seen, i.e. $I(Q) \propto P(Q)$. At Q small compared to $1/r_0$, but large compared to 1/R ($\frac{1}{R} \ll Q \ll \frac{1}{r_0}$), P($Q$) is constant , hence I($Q$) depends only on its structure factor. Equation [4] can then be simplified to,

$$S(Q) \sim Q^{-d_F} \quad (5).$$

when R is much larger than r_0. The above equation is often used to analyse the scattered intensity by a fractal object, and it applies only in the range $\frac{1}{R} \ll Q \ll \frac{1}{r_0}$.

EXPERIMENTAL

Samples of approximately spherical hematite particles were prepared by the forced hydrolysis of a homogeneous iron salt solution under strictly controlled conditions[11,12]. In order to avoid multiple scattering, hematite samples were diluted to 1.95×10^{-4} M (approx. 2.25×10^{10} particles/ml).

A Malvern 4700 PCS system, utilizing a 15 mW, 633 nm He-Ne laser was used to measure the average size of the aggregating particles and scattered intensity (in terms of photoncounts) of the aggregates. Aggregation and scattering experiments were conducted at a zeta potential of 48 ± 2 mV (measured by Malvern Zeta Sizer IIC) at temperatures of 25°C, 35°C and 55°C, and salt (KCl) concentrations of 50, 60 and 80 mM. For each temperature and salt concentration, the variation in average size with time was determined by dynamic light scattering measurements

every 2-3 minutes for up to 1 hr. The intensity (photoncounts) of scattered light was measured at angles ranging from 15° to 90°, for 5 seconds at each angle. In order to comply with conditions governing the relation of scattering exponent to fractal dimension[3], the static light scattering experiments were carried out when the aggregates, containing a large number of primary particles, were typically about 1 micron in diameter.

RESULTS AND DISCUSSION

The plots of scattered intensity (photoncount) as a function of angle for 50, 60 and 80 mM KCl at different temperatures are shown in Figs 1a, b and c respectively with the slopes of the graphs representing the fractal dimension. These fractal dimensions vary with the aggregation mechanism prevailing which in turn depends on ionic strength and temperature.

At higher temperatures, the fractal dimensions of the aggregates in 50 and 60 mM KCl are significantly lower than at 25°C . As temperature increases, the repulsion barrier decreases and the sticking probability increases, resulting in much less penetration to the interior of the clusters with resultant formation of more tenuous aggregates. As expected in the absence of significant inter-particle (or inter-aggregate) repulsion, temperature has little effect on the fractal dimension of aggregates formed under diffusion limited conditions (80 mM KCl) with values of d_f at 25°C, 35°C and 55°C all in the vicinity of 2.3.

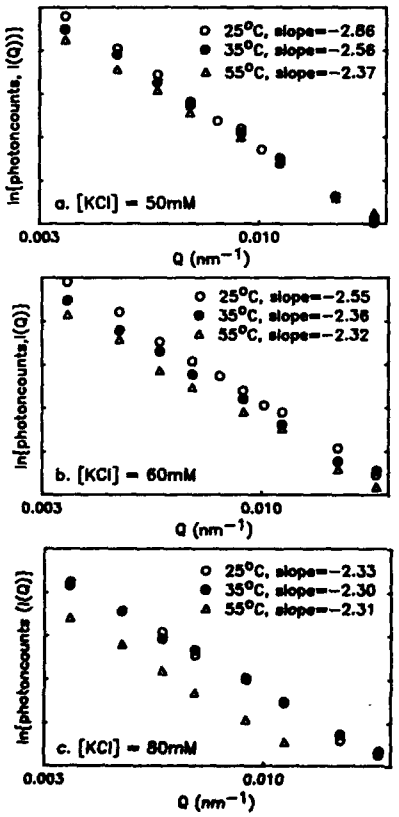


Fig. 1 Effect of temperature on scattering exponent for hematite aggregates formed in (a) 50mM, (b) 60mM, and (c) 80mM KCl.

The effect of temperature on the aggregation process has previously been modelled[13] with the theoretical predictions showing close agreement with experiment. The major influence of temperature on the aggregation process was on the repulsive energy of interaction and hence the stability ratio. At 50mM KCl, the repulsion barrier is still significant, so the aggregation rate increases markedly with temperature since it affects both the repulsive energy and the rate of particle diffusion. The change in aggregation rate attributable to the temperature dependence of diffusion was found to be minor. At 80mM KCl, attractive van der Waal forces dominate and the temperature affects diffusion only resulting in a relatively insignificant effect on aggregation rate.

At the slow rate of aggregation for which the probability of sticking is low, the aggregating clusters have the opportunity to explore a large number of possible mutual configurations, which leads to some interpenetration, and therefore denser aggregates. In contrast, in diffusion limited aggregation, the interior of the clusters is effectively screened from penetration since approaching particles readily adhere to other particles (high sticking probability) resulting in a more tenuous structure. The marked decrease in packing density on changing from aggregation under diffusion limited conditions to conditions under which a repulsion barrier is present is clearly seen in the transmission electron microscope prints in Fig.2



Fig. 2 Transmission Electron Microscope (TEM) plates of hematite aggregates formed at 25°C in (a) 50mM, and (b) 80mM KCl.

As discussed previously[2], the fractal dimension of 2.3 obtained here under diffusion limited aggregation conditions (no repulsion barrier) is only slightly less than the value expected from theoretical considerations for aggregates growing via particle-cluster diffusion limited aggregation (DLA)[14,15]. In particle-cluster DLA, clusters grow purely from monomers, which approach the cluster with a random walk trajectory. The random-walk nature of the approaching monomer favours growth on the extremities of the cluster, and thus, open, ramified geometries develop. Cluster-cluster diffusion limited aggregation (CA) is a variation of particle-cluster DLA where clusters combine with other clusters as well as with monomers. In CA, d_F is reduced substantially because two fractals are extremely unlikely to penetrate without contact. Widely spread, loosely packed structures are produced in cluster-cluster aggregation. Fractal dimensions on the order of 1.75 are to be expected where cluster-cluster aggregation is the dominant mechanism[16,17]. The fractal dimensions of greater than 2.3 obtained here are consistent with reaction limited particle-cluster aggregation. These values are generally considerably higher than results reported by other workers for aggregates of silica and gold for which cluster-cluster aggregation appears to be a more appropriate model[18,19,20]. This is undoubtedly due to the fact that the particle concentration is very low in this study.

Restructuring within the aggregate following initial coalescence has been observed for silica[21]. This would result in an increase in fractal dimension over time and does not appear to be significant in the case of the hematite aggregates considered here. No systematic change in scattering exponent with time was observed once the aggregates had reached approximately one micron diameter and before significant gravity settling occurred. This size represents the beginning of the range where the approximation $S(Q) \propto Q^{-d_F}$ is valid, i.e. when the cluster size is large compared to the primary particle size (at least an order of magnitude larger)[3].

The fact that scattering occurs from a broad distribution of particle sizes (i.e. a polydisperse system) could possibly mislead the determination of d_F from the scattering exponent. To compute the effect of polydispersity, the single particle intensity (I_M is approximately equal to $M^2S(Q)$, since P(Q) is constant for the range studied) must be averaged over the number distribution of particles N(M)[3,22], i.e.

$$I \sim \int M^2 N(M) S(Q) dM \qquad (6)$$

where M is the mass and S(Q) is the structure factor described earlier. The number distribution may range in form from a bell-shaped curve (Gaussian distribution), to a very broad power-law decay. If the distribution is narrow (as is the case for a bell-shaped curve), it will not change the asymptotic fractal behaviour $S(Q) \sim Q^{-d_f}$ but this may not be the case for power-law polydispersity, especially in a "gelation" regime which is characterised by the appearance of an "infinite" cluster at some finite time[5].

Theoretical number distributions for the cases studied here have been derived using the modified Smoluchowski model[3] for both diffusion limited and reaction limited aggregation are observed to be significantly less polydisperse than expected for power law behaviour. Thus, under all conditions considered here, the polydispersity in aggregate size is not great enough to modify the fractal dimension estimates obtained from static light scattering studies. This is no doubt attributable, to a large extent, to the low particle densities used in these studies.

Good correspondence between theory and experiment is obtained when these values of d_f are used to obtain aggregate size estimates using the modified Smoluchowski model, as can be seen from Fig.3. This result is particularly satisfying since the model predictions are obtained quite independently of the experimental data, i.e. no fitting parameters are required.

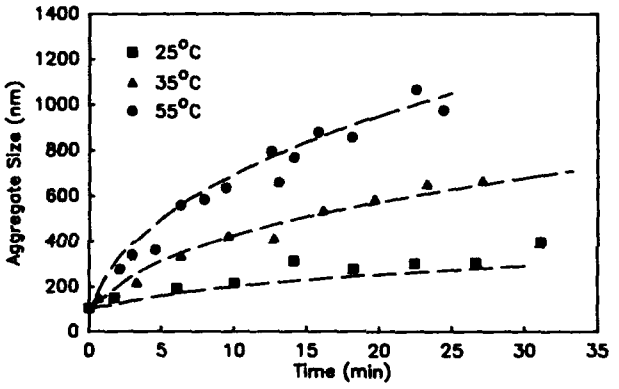


Fig. 3
Comparison of aggregation kinetics for hematite at 25°C, 35°C, and 55°C as determined by dynamic light scattering with kinetics predicted using the modified Smoluchowski model described in Ref.(2), incorporating d_f determined from static light scattering.

CONCLUSION

In this work, the fractal dimension of hematite aggregates has been measured using static light scattering techniques. Increasing salt concentration was found to increase the aggregation rate and the probability of adhesion yielding increasingly tenuous structures and thus lower fractal dimensions. For example, at 25°C scattering exponents of 2.86 ± 0.05, 2.55 ± 0.06 and 2.33 ± 0.06 were obtained for KCl concencrtrations of 50, 60 and 80 mM respectively once the scattering function (Q) was significantly greater than 1/R and R » r_0.

The effect of temperature on kinetics and structure of aggregating hematite particles follows the expected trend. Increasing the temperature increases the aggregation rate and decreases the packing density of the aggregates. The effect is more noticable at salt concentrations where both diffusion and repulsion, which will both be affected by temperature, are important contributors to the aggregation process (50mM for this system). Restructuring or polydispersity effects do not significantly affect these fractal dimension estimates.

Excellent correspondence over a range of temperatures and ionic strengths is obtained between aggregation kinetics as determined by dynamic light scattering and kinetics predicted using a modified Smoluchowski model incorporating fractal dimensions as determined by static light scattering.

ACKNOWLEDGEMENTS

The Australian Institute of Nuclear Science and Engineering (AINSE) is thanked for the financial support to one of the authors (R. Amal). In addition, the continuing assistance provided by the Australian Water Research Advisory Council (AWRAC) and the help of Mr. R. Blake in transmission electron microscopy (TEM) are gratefully acknowledged.

REFERENCES

1. B.B. Mandelbrot, The Fractal Geometry of Nature, (Freeman, New York, 1983).
2. R. Amal, J. Coury, J.A. Raper, W.P. Walsh and T.D.Waite, Colloids and Surfaces, in press.
3. R. Amal, J.A. Raper and T.D. Waite, J. Colloid and Interface Sci., in press.
4. R. Jullien and R. Botet, Aggregation and Fractal Aggregates, (World Scientific, Singapore, 1987).
5. J.E. Martin and A.J. Hurd, J. Appl. Cryst. 20, 61 (1987).
6. B.I. Berne and R. Pecora, Dynamic Light Scattering, (Wiley, New York, 1976).
7. J. Teixera, J. Appl. Cryst. 21, 781 (1988).
8. S.H. Chen and D. Bendedouch, in Enzyme Structure Method in Enzymology, edited by C.H.W. Hirs and S.N. Timasheff (Academic, New York, 1985).
9. J. Teixera, in On Growth and Form, edited by H.E. Stanley and N. Ostrowsky (Martinus Nijhoff, Dordrecht, 1986) pp. 145.
10. S.H. Chen and J. Teixera, Phys. Rev. Lett. 57, 2583 (1986).
11. E. Matijevic and P. Scheiner, J. Colloid and Interface Sci. 63, 509 (1978).
12. N.H.G. Penners and L.K. Koopal, Colloids and Surfaces 19, 337 (1986).
13. R. Amal, J.R. Coury, J.A. Raper and T.D. Waite, in The Institution of Chemical Engineers 5th International Symposium on Agglomeration, 25-27 September 1989, Brighton Centre, UK.
14. T.A. Witten and L.M.Sander, Phys. Rev. Lett. 47, 1400 (1981).
15. P. Meakin, Phys. Rev. A 27, 1495 (1983).
16. P. Meakin, Phys. Rev. Lett. 51, 1119 (1983).
17. M. Kolb, R. Botet and J. Jullien, Phys. Rev. Lett. 51, 1123 (1983).
18. D.W. Schaefer, J.E. Martin, P. Wiltzius and D.S. Cannel, Phys. Rev. Lett. 52, 2371 (1984).
19. D.A. Weitz, J.S. Huang, M.Y. Lin and J. Sung, Phys. Rev. Lett. 54, 1416 (1984).
20. J.P. Wilcoxon, J.E. Martin and D.W. Schaefer, Phys. Rev. A 39, 2675 (1988).
21. C. Aubert and D.S. Cannel, Phys. Rev. Lett. 56, 738 (1986).
22. J.E. Martin, J. Appl. Cryst. 19, 25 (1986).

S.A.N.S. STUDY OF FRACTAL ALUMINO-SILICATE AEROGELS

F.CHAPUT*, J.P.BOILOT *, A.DAUGER **, F.DEVREUX* AND A.DE GEYER***
*Laboratoire de Physique de la Matière Condensée, URA CNRS 1254, Ecole Polytechnique, 91128 Palaiseau Cédex (FRANCE)
**Ecole Nationale Supérieure de Céramique Industrielle, 87065 Limoges Cédex (FRANCE)
***Institut Laüe-Langevin, 156X. 38042 Grenoble Cédex (FRANCE)

ABSTRACT

Small angle scattering clearly shows that aluminosilicate aerogels, prepared from Si-Al double precursor, form mutually self-similar volume fractals at least in the range of densities 40-160kg/m^3. The structure, insensitive to the pH of the added water, consists of primary homogeneous rough units attached into volume fractal clusters (D=2.1).Heating at 800°C oxidizes residual organic groups and decreases the roughness of the unit particles. Densification above 900°C both implies increasing of the size of units and decreasing of the fractal domain.

INTRODUCTION

Aerogels are low-density porous materials made by supercritial drying of alcogels. The structure of silica aerogels is generally described in terms of fractal geometry from small-angle scattering data [1].Volume fractals are characterized by a fractal dimension D that can be between 1 (linear objects) and 3 (bubbles). Surface fractals are uniformly dense (D=3) but have rough surfaces with a surface fractal dimension D_S that can be vary between 2 and 3.By small angle neutron scattering (S.A.N.S), the angular dependence of the scattered intensity can be measured and, for fractal objects, the intensity profile has a power-law dependence when plotted versus the magnitude of the wave vector Q, $I=Q^{-P}$ where P is the Porod slope. The wave vector Q is related to the scattering angle Θ and consequently by scanning Θ, an object can be studied on different length scales (1-1000Å by S.A.N.S). Volume fractals yields scattering curves with slopes between -1 and -3 (P=-D). Smooth colloidal particles give slope of -4 and rough surface particles slopes between -3 and -4 corresponding to $P=-6+D_S$.

Most silica aerogels are produced by single-stage, base-catalyzed polymerization of TMOS or TEOS. The scattering curves, exhibit slopes of -4 and -2. The growth process first takes place by monomers adding to clusters (Eden growth) leading to uniformly dense and smooth structures. Above 20Å, a cluster-cluster regime gives a volume fractal structure (D=2) [2].

Under acidic conditions, there is a classic realization of RLCA (Reaction-limited cluster-cluster growth) in solution with a volume fractal dimension close to 2 [3]. However, in aerogels, a fractal dimension of 2.6 has been observed indicating collapse of the polymeric network [4].

Finally, mutual self similarity was found in a serie of neutrally reacted silica aerogels in the 100-350 kg/m^3 density range. The fractal dimension of 2.5 has been interpreted as the growth of infinite cluster of percolating network [5].

In this paper, we present some results on the structure (from SANS) and on the densification (from SAXS) of aluminosilicate aerogels prepared by supercritical drying of alcogels in the H_2O, HO^iPr, $(BuO)_2Al-O-Si(OEt)_3$ system [6]. SANS data clearly show that

aluminosilicate aerogels form mutually self-similar volume fractals at least in the investigated range of densities 40-160kg/m^3.

PRECURSOR

The crude formula of the aluminium-silicon ester is $(BuO)_2Al-O-Si(OEt)_3$. ^{27}Al NMR spectrum of the precursor (fig 1a) shows two resonances : a sharp peak ($\Delta\nu$=270Hz) at 0 ppm, characteristic of octahedral aluminium atoms in a symmetric site and a broad band ($\Delta\nu$=5000Hz) at 50 ppm indicating the presence of tetrahedral aluminium atoms. Assuming the smallest size for the molecular association,the solution can be seen as an equal distribution of tetramers and dimers [7].

The addition of water, involves a drastic and rapid change in the ^{27}Al NMR spectrum (fig.1b). The disappearance of the sharp band in the octahedral position is followed by the rising up of a new one at 49.4 ppm ($\Delta\nu$ =150Hz) which corresponds to 4-coordinated aluminium atoms in a very symmetric site. These changes observed in the NMR spectra correspond to important modifications around Al atoms resulting from the rapid hydrolysis of the Al-OR groups.

The ^{29}Si NMR spectrum of the precursor in the same conditions (fig.2) shows four groups of resonances. The spectrum seems to be the addition of an initial spectrum (A+C) and the same translated spectrum (+4.5 ppm) (B+D) with a different total intensity. The addition of 10 moles of water per mole of precursor provokes only the instantaneous disappearance of the second spectrum (B+D). The first group A is due to Q^1 silicon with one Si-O-Al type bonding. The four peaks correspond to the four possibilities to choose the 3 remaining bondings with OEt or OBu groups and the intensities of the peaks indicate that the probabilities are almost equal. The third group C can be attributed to Q^2 silicon with one Si-O-Al and one Si-O-Si type bonding on the basis that the chemical shift between set A and set C is the same as between Q^1 and Q^2 units in pure silica systems. The three peaks can also be explained by ester exchanges on the two remaining bondings.

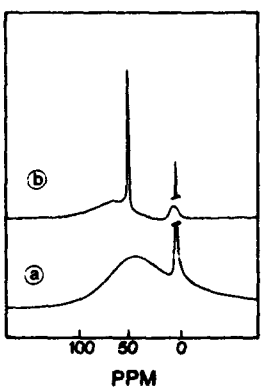


Figure 1: 104MHz-^{27}Al NMR spectra of the double alkoxide $(BuO)_2Al-O-Si(OEt)_3$ (ppm from $Al(H_2O)_6^{3+}$):a) in ^iPrOH b) after addition of water

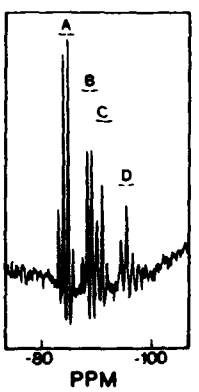


Figure 2: 80MHz-^{29}Si NMR spectrum of the pure double alkoxide $(BuO)_2Al-O-Si(OEt)_3$ (ppm from TMS).

The B and D resonance groups probably arise from silicon atoms equivalent to those of set A and C but connected to aluminium atoms in different ways, for instance through one oxygen atom participating to a Al-O-->Al bridge. These structures related to the molecular association would be destroyed by the addition of water and the rapid hydrolysis of the Al-OR groups. The gelation has been previously studied by SAXS [8]. In the first steps, due to the fact that the aluminium part of the precursor hydrolyzes more rapidly, a rapid formation of particles takes place by condensation between Al-OH groups, probably following the Eden growth mechanism. These particles are then agglomerated by a cluster aggregation process (D=1.9) chemically limited by the hydrolysis of the Si-OR groups. Therefore, the growth kinetics largely depends on the initial water concentration. However, in contrast with silica system, the gel time and the structure of polymers are not drastically change by pH variations of the added water [7]. Reactions are obviously catalyzed by protonic or hydroxyl species, but the amphoteric behavior of the sol (well known for aluminium hydroxides) implies a large addition of acid or base to modify the protonic activity of the alcoholic solution.

SELF SIMILARITY OF ALUMINO-SILICATE AEROGELS

Figure 3 shows Log-Log scattering curves for aluminosilicates aerogels heated at 400°C. The scattered intensities I(Q) are divided by the apparent density of the sample ($I'(Q) = I(Q)/\omega$), but curves are not shifted with respect to each other. The more interesting observation is obviously that the samples can not be distinguished in a large Q range. This result clearly demonstrates that aerogels have mutually self-similar fractal structure over the investigated range of densities.

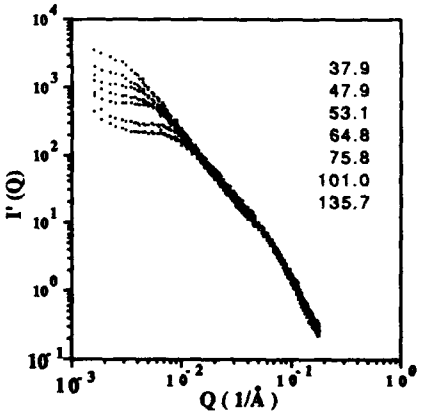
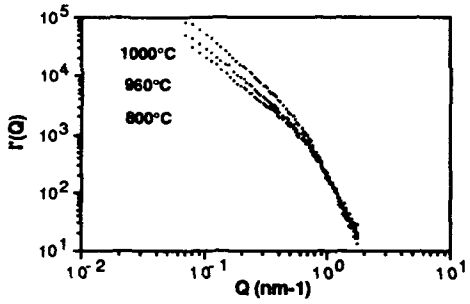


Figure 3: Scattering curves for different alumino-silicate aerogels revealing that samples are mutually self-similar. All the curves are labeled with ω in kg/m3. The order of the numbers correspond to the order of the data.

At high Q(> 8.10^{-2} $Å^{-1}$) a first power law regime is noted in the Porod range with a slope of -3.2. In the intermediate Q range, there is a second power law regime characteristic of the fractal structure with a slope of -2.10±0.05 [9].
Therefore, all the aerogels are characterized by a two-level structure consisting of primary rough units (size ~ 13Å) attached in volume-fractal clusters (D=2.1) This volume fractal dimension is consistent with the chemically limited cluster-cluster aggregation.
A third regime exists at small Q which is due to the finite correlation range of the fractals and which is consistent with uniform nonfractal long range structure. This domain broadens when the apparent density increases (from 38 to 136 kg/m^3), corresponding to a decrease of the fractal range (from 400 to 100Å).



By heating at 800°C, the roughness of elementary units decreases (the scattering curve approach slope of -4) [9]. The densification process takes place above 900°C with a slight decrease of the fractal range and a growth of the dense units (fig.4). The densification is stopped at about 1000°C by partial crystallization of mullite.

Figure 4: Scattering curve for aerogel sample heated at different temperatures. The order of the numbers correspond to the order of the data.

CONCLUSION

Due to the amphoteric character of the sol, the polymerization conditions in solution precursors do not drastically change the structure of the alumino-silicate aerogels. It can be represented by rough surface units that stick together into volume fractal cluster by RLCA mechanism. Mutual self-similarity is displayed in the 40-160kg/m^3 density range.

REFERENCES

1.D.W.Schaeffer and K.D.Keefer in Fractal in Physics, edited by L.Pietronero and E.Tosatti, (Elsevier Science Publishers B.V. 1986) p.39.

2.D.W. Schaefer, Revue de Physique Appliquée (Paris), 24, C4-121 (1989).

3.D.W.Schaeffer and K.D.Keefer in Better Ceramics Through ChemistryI,edited by C.J.Brinker, D.E.Clark and D.R. Ulrich, (Mater.Res.Soc.Proc.32, 1984) p.1.

4.D.W.Schaefer, C.J.Brinker, J.P.Wilkoxon, D.Q.Wu, J.C.Phillips and B.Chu in Better Ceramics Through Chemistry III,edited by C.J.Brinker, D.E.Clark and D.R. Ulrich, (Mater.Res.Soc.Proc.121, 1986) p.709.

5.R.Vacher, T.Woignier, J.Pelous and E.Courtens, Phys.Rev.B, 7,6500 (1988).

6. F.Chaput, A.Lecomte, A.Dauger and J.P.Boilot, Chemistry of Materials, 1,199 (1989).

7.J.C.Pouxviel and J.P.Boilot, J.of Materials Science 24,321 (1989).

8.J.C.Pouxviel, J.P. Boilot, A. Lecomte and A. Dauger, J.Physique (Paris) 48,921 (1987).

9.F.Chaput, J.P. Boilot, A. Dauger, F.Devreux and A.de Geyer, J. Non-Cryst. Solids, 116,133 (1990).

CHARACTERIZATION OF PARTIALLY CONDENSED SILICA FORMED FROM THE PARTIAL HYDROLYSIS OF TMOS

T.M. TILLOTSON AND L.W. HRUBESH, Department of Chemistry & Material Science, Lawrence Livermore National Laboratory, Livermore, CA 94550

ABSTRACT

A stable mixture of partially condensed polysilicates is formed from the sub-stoichiometric, acid catalysed hydrolysis of tetramethoxysilane [$Si(OCH_3)_4$] and the removal of the reaction- generated methanol by distillation. This mixture has been used as a precursor to make silica aerogels that show microstructural differences from base catalysed TMOS aerogels. In this paper, we report the analysis of this mixture for a determination of the type and distribution of the polysilicate species formed, and we include measurements of some physical properties of this fluid.

INTRODUCTION

Aerogels were first prepared in the early 1930's by Kistler in an effort to probe the nature of gels and gel struture[1]. Kistler's aerogels were time consuming to make and in the early 1960's a French graduate student working with Teichner used a silicon alkoxide instead of sodium silicate and the current "sol-gel" approach was born[2]. Silica aerogels are transparent solids with high surface areas, ultrafine cell/pore sizes, high melting points, low thermal conductivities, and unique acoustic properties. In recent years there has been a resurgence in aerogel research and where they were once just a scientific curiosity their unusual properties are beginning to find useful applications in the market place. One of the goals of aerogel makers is to control microstructure in an effort to tailor the aerogel properties. It is commonly believed that the molecular building blocks first formed in the initial hydrolysis of the alkoxide greatly influence the final microstructure. The evolution of these building blocks in acidic and basic mediums has been well studied[3,4,5,]. In this paper, we use NMR and GC/MS to describe a partially hydrolysed and condensed silica (C.S.) precursor.We also report on some of the physical properties of this fluid. This precursor has been successfully used to prepare uncracked, monolithic aerogel bricks with densities as low as .003 gms/cc[6]. Aerogels prepared with C.S. have compressive moduli 3-4 times higher than single step base catalysed aerogels[7].

EXPERIMENTAL

Preparation of C.S.

TMOS supplied by Petrach Systems, Inc. was used as the starting material. To obtain consistent and reproducible results, purification of the alkoxide is necessary. This is accomplished by fractional distillation using a 4' silvered, vacuum jacketed fractionating

Mat. Res. Soc. Symp. Proc. Vol. 180. ©1990 Materials Research Society

column filled with glass beads under a N_2 purge. The purified TMOS is mixed with a sub-stoichiometric amount of water (molar ratio: 1 TMOS:1.3 H_2O) and refluxed under acidic (10^{-5} moles) conditions for 16.0 hours. This amount of water is 65% of that required to form SiO_2 according to the net hydrolysis/condensation reaction:

$$Si(OCH_3)_4 + 2H_2O \rightleftharpoons SiO_2 + 4CH_3OH$$

Sufficient methanol is added to keep the mixture one phase.

All alcohol produced (+ added) by the reaction is distilled off and the remaining C.S.(oil) is collected. The product is diluted with a non-alcohol solvent to inhibit reverse equilibrium reactions back to the alkoxide, and stored for future use in the preparation of ultra-low density aerogels[6]. NMR results of C.S. stored in methanol will be discussed.

Characterization Methods

To elucidate the composition of the C.S., ^{29}Si NMR spectra were obtained at 59.62 MHz using a Bruker Model MSL 300 Fourier transform spectrometer. The experimental parameters were 5 μs observed pulse width, 1.10 sec. acquisition time, 4 sec. recycle delay and a 32k transform size. Gated decoupling was used to suppress the nuclear Overhauser effect. A "WALTZ-16" program was used to decouple protrons[8]. Chromium(III) acetylacetonate [$Cr(acac)_3$, 0.015M] was needed as a paramagnetic relaxing agent.

A Hewlett-Packard 5985 GC/MS was used to obtain the C.S. profile. A 30 meter, DB1 capillary column with a dimethylsiloxane coating was used in the gas chromatograph. The initial temperature was 70°C with a temperature ramp of 10°C/min.. The C.S. was initially diluted with methylene chloride prior to analysis. The mass spectral data was obtained at 70ev ionization and a source temperature of 200°C.

The measured physical properties of the C.S. included viscosity, density, and refractive index. The viscosity was determined emperically by the falling ball method. A sphere of known density and diameter is timed through a measured distance of the fluid-being sure to negate wall effects. The refractive index was measured on an Abbe Mark II Refractometer. The density was determined by weighing an accurately measured volume of the fluid.

RESULTS AND DISCUSSION

NMR Analysis

A typical ^{29}Si NMR spectrum with assignments is shown in Figure 1. Assignments were made from published literature [9,10]. The Q notation used to describe the silicic acid ester structures is that of Engelhardt et al.[11]. The superscript refers to the number of silica atoms bridged to the one under consideration. As can be seen from the spectrum, condensation has proceeded to the formation of linear chains and cyclic trimers and tetramers. Only trace amounts of fully linked (Q^4) species are present. Line broadening within a peak assignment relates to a distribution of molecular weight.

Figure 2 shows the re-esterification of C.S. in the presence of methanol. In the Q^2 region, the singular hydroxylated linear species decreases with an increase of fully esterified linear species. This process generates water which attacks another singular, linear hydroxylated species forming a double hydroxylated linear species. An increase in this particular peak results. The same tendency holds for the Q^1 reqion as well. It is interesting

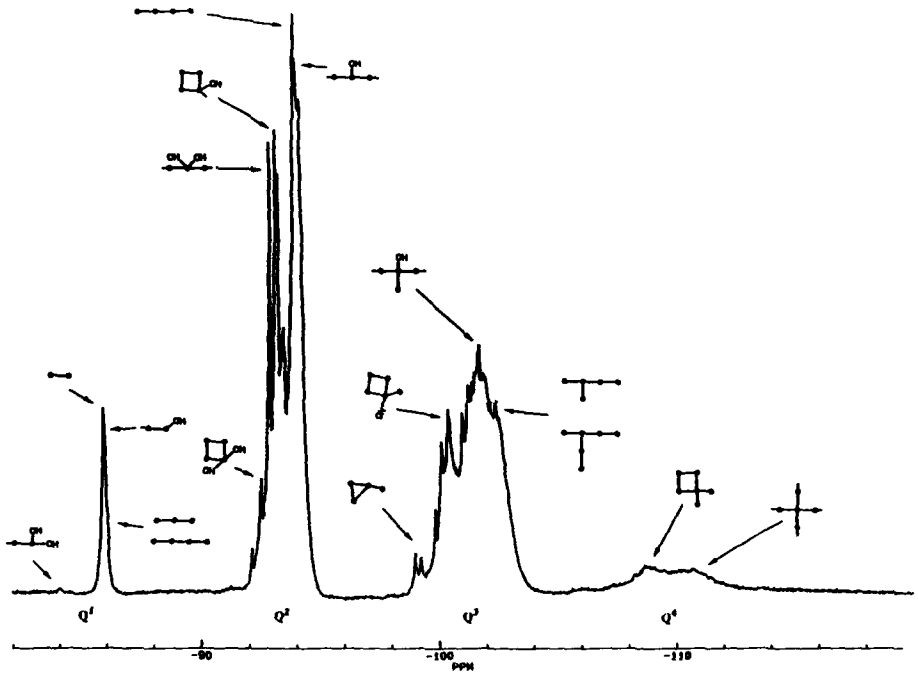


Figure 1. ^{29}Si NMR spectrum of C.S.

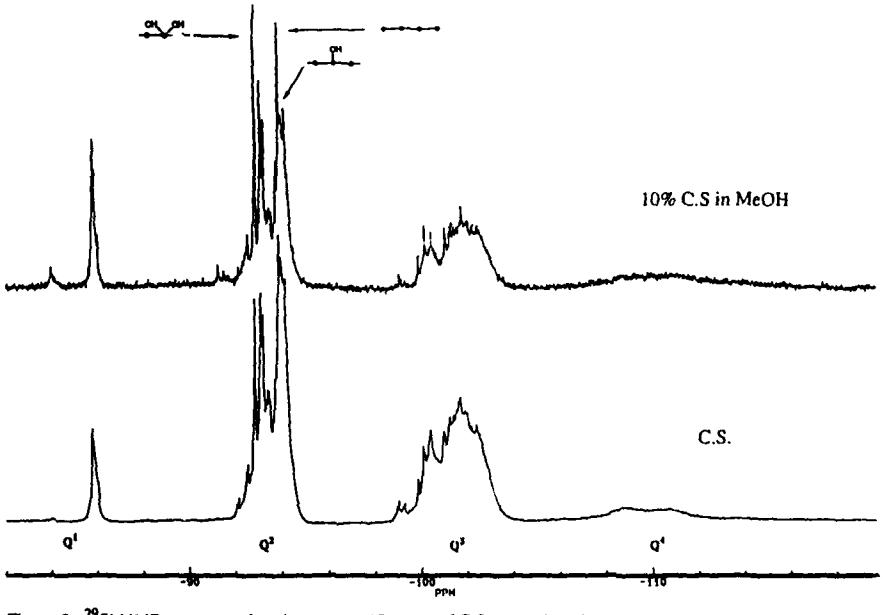


Figure 2. ^{29}Si NMR spectrum showing re-esterification of C.S. in methanol

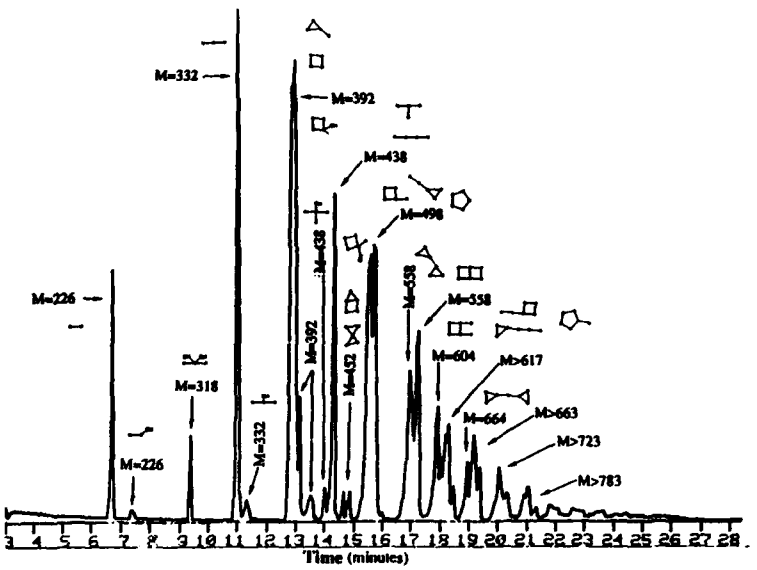


Figure 3. GC/MS profile of C.S.

to note that the cyclic hydroxylated species appear unchanged; perhaps this addition requires inversion. C.S. stored in acetonitrile showed no significant change.

GC/MS analysis

A typical GC/MS profile with mass numbers and assignments is shown in figure 3. The data suggests the formation of small linear chains and cyclic trimers and tetramers. This is in good agreement with the NMR results. Determination of the relative peak areas shows the cyclic tetramer and the cyclic trimer with one additional siloxane linkage to be the most abundant oligomeric species present. The addition of one siloxane linkage to these oligomers results in the next most abundant species. Further addition of siloxane linkages result in ring closure, giving a double trimer or double tetramer (ladder-like), and these are the third most predominate species present. Linear species greater than 4 siloxane links are not detected.

Physical Properties

The refractive index of the C.S. is 1.4063. The density is 1.328 gms/cc. The viscosity is 480 centipoise. This high viscosity suggests the average molecular weight to be in the 10^3 range. This appears to contradict the GC/MS data. It should be noted that due to the nature of mass spectroscopy, it is often times difficult to get good parent peak information. However, the GC/MS retention times of the major compounds correspond to standards with molecular weights between 200-400 amu.

SUMMARY

A method for preparing a partially hydrolysed and condensed silica precursor capable of producing ultralow-density aerogels has been given. The data suggests the formation of linear chains and cyclic trimers and tetramers. Future work will focus on the separation of these polysilicates.

ACKNOWLEDGMENTS

The authors would like to thank Jim Happe for the NMR spectra, Brian Andreson for the GC/MS profile, and Jon Poco for the viscosity data. Special thanks to Rick Pekala and Bob Sanner for help in the data interpretation.This work was performed under the auspices of the U.S. Department of Energy by the Lawrence Livermore National Laboratory under contract # W-7405-ENG-48.

REFERENCES

[1] S.S. Kistler, Nature,127,741 (1931).
[2] J. Fricke, Scientific American, 258(5), 92 (1988).
[3] W.G. Klemperer and S.D. Ramamurthi, in Better Ceramics through Chemistry,edited by C.J. Brinker, D.E. Clark, and D.R. Ulrich, Mater. Res. Soc. Proc. 121, 1 (1988).
[4] J.C. Pouxviel and J.P. Boilot, J. Non-Cryst. Solids, 89, 345 (1987).
[5] C.W. Turner and K.J. Franklin, J. Non-Cryst. Solids, 91, 402, (1987)
[6] L.W. Hrubesh, T.M. Tillotson, and J.F. Poco, this proceedings.
[7] J.D. LeMay, R.W. Pekala, and L.W. Hrubesh, Pacific Polym. Preprints, 1, 295 (1989).
[8] D. Neuhaus, J. Keeler and R. Freeman, J. Magnetic Resonance, 61 , 553 (1985).
[9] L.W. Kelts and N.J. Armstrong, J. Mater. Res., 4 (2), 423 (1989).
[10] H.C. Marsmann, E. Meyer, M. Vongehr, E. Weber, Makromol. Chem., 184, 1817 (1983).
[11] G. Engelhardt, H. Jancke, D. Hoebel and W. Wicker, Z. Chem., 14, 109 (1974).

CHARACTERIZATION OF ULTRALOW-DENSITY SILICA AEROGELS MADE FROM A CONDENSED SILICA PRECURSOR

LAWRENCE W. HRUBESH, THOMAS M. TILLOTSON, AND JOHN F. POCO
Chemistry and Material Science Department, Lawrence Livermore National Laboratory, Livermore, CA 94550

ABSTRACT

Silica aerogels having densities in the range of 0.003 to 0.05 g/cm^3, have been prepared from a condensed silica formulation involving a two-step hydrolysis/condensation process with tetramethoxysilane (TMOS). This work describes the preparation of these unique ultralow-density aerogels, and compares several of their properties with those of aerogels made by a single step, base catalysed process.

INTRODUCTION

The production of silica aerogels having less than 1% solids content using single step hydrolysis/condensation of silicon alkoxides is limited by the time necessary to gel an extremely dilute solution, and ultimately by the alcoholysis equilibrium reactions that reverse the hydrolysis/condensation process. One means to bypass this limitation is to use two steps; the first is to prepare a partially hydrolysed, partially condensed, polysilicate mixture from which all the alcohol is removed; the second is to add water to the polysilicate mixture in order to complete the hydrolysis, but this is done in the presence of a non-alcohol diluent. Thus, the minimal amount of alcohol that is present as a reaction product does not strongly influence the polycondensation that leads to gelation. Others have reported similar two-step methods in which the second step includes an alcohol diluent [1,2].

We have successfully used the above method to prepare gels that produced aerogels having as little as 0.13% solids content. The aerogels appear to have a microstructure that differs from the connected colloidal particle models that are reported for aerogels made from the single step, base catalysed TMOS process [3,4].

EXPERIMENTAL

Preparation

The method of preparation for the ultralow-density "alcogels" first involves the formation of a condensed silica oil (CS), as described previously [5]. The oil is prepared by reacting TMOS with a sub-stoichiometric amount of water in the presence of methanol, under acidic conditions (molar ratios: 1TMOS: 1.3H_2O: 2.4MeOH: 10^{-5}HCl). This mixture is refluxed for 16 hours before all the methanol is removed by distillation, leaving the condensed silica oil. The oil is then further reacted with sufficient water to complete the

Mat. Res. Soc. Symp. Proc. Vol. 180. ©1990 Materials Research Society

hydrolysis of the original amount of TMOS, with 100% excess, (ie. 1TMOS: 4.0H_2O). The reactions are done in a pyrex glass mold, in the presence of a non-alcohol diluent (eg. acetone or acetonitrile), under basic conditions (NH_4OH). The amount of diluent is chosen to give the target density, and the catalyst concentration (typically 10^{-4} molar) is selected to achieve a gel time of less than 72 hours.

The silica aerogel is obtained from the "alcogel" by the direct super-critical point extraction of the solvent liquid, by placing the glass mold in an autoclave. The temperature is ramped to 300°C at a rate of 20°C/hr, while holding the pressure that is generated by the solvent vapor, at approximately 136 bars. The vessel is then depressurized at a rate of 20 bar/hr and the aerogel is allowed to slowly cool while the vessel is purged with dry nitrogen gas. The final size of a typical sample is 2.5cm X 4.5cm X 15cm.

Analytical Methods

The primary analytical techniques that were used to characterize the structure of ultralow-density silica aerogels were transmission electron microscopy (TEM), small angle neutron scattering (SANS), and nuclear magnetic resonance (NMR) spectrometry. Other techniques that were used included BET nitrogen adsorption measurements for surface area, helium pycnometry for skeletal density, and UV-VIS spectrophotometry for transmissivity measurements.

A JOEL model 200CX scanning transmission electron microscope (STEM) was used to obtain micrographs of the aerogel materials. The aerogels were ground and wet with methanol, then atomized onto a formvar grid before beam exposure.

The neutron scattering data was obtained from the IPSN facility at Argonne National Laboratory. Thin slices (~2mm) of aerogels were prepared for neutron beam exposure.

The NMR data was obtained on a Bruker, Model 300MSL Spectrometer, operating at 59.62 MHz for the ^{29}Si nucleus. Two types of magic angle spinning (MAS) techniques were used. Normal Bloch decay spectra were obtained with high power proton decoupling (HPDMAS) at an 80 second recycle time. Cross polarizarization (CPMAS) spectra were obtained using a mixing time of 20 ms and a 10 second recycle time. The aerogel samples were mortared and packed into 7mm diameter zirconium oxide rotors and spun at a rate of 3.2 KHz.

RESULTS AND DISCUSSION

The TEM photomicrographs of the ultralow-density silica aerogel show long chainlike structure with many chain lengths as long as 20nm between apparent connections. The approximate width of the chains is 2nm and they are quite uniform. This is to be compared with the TEMs for base catalysed TMOS having about 4 times higher density, which show strings of beads. The beads have an average diameter of 12 nm and appear to be connected with minimal necking. The two structures are distinctively different; the first being polymer-cluster like and the latter is colloidal-bead like.

The SANS data for both the ultralow-density and base catalysed TMOS aerogels is

given in Fig.1. The limiting slope approaching -4 at large values of K indicates that smooth (non-fractal) surfaces exist for both types of aerogel in this size scale [6], ie. at dimensional scales of the order of 10Å. The ultralow-density aerogel also shows a second power-law regime at size scales > 10Å that indicates a volume fractal porosity nature [6]. This data is highly suggestive of a branched ladder polymer network that is much more expanded than a randomly branched polymer. Such a structure was reported for a similar two-step process as the one described here, with TEOS as the alkoxide precursor [1].

A comparison of the spectra from the two types of magic angle spinning NMR for the ^{29}Si nucleus, CPMAS and HPDMAS, gives information about the relative environments surrounding the silicon atoms. For example, CPMAS exhibits spectra obtained only from silicon atoms that are within a few bond lengths of a proton; whereas, HPDMAS derives spectra from all silicon atoms in the material. Such spectra are shown in Fig. 2 for the ultralow-density silica aerogel. The difference in peak ratios for the two spectra indicates that a large fraction (~50%) of all the silicon atoms are more than a few bond lengths distant from hydrogens. One can infer from this data that the aerogel consists of silica chains that are about 2.5 nm thick, in which about half of the silicon atoms are "core" atoms and the other half are near the surface of the chains where the hydrogens from the hydroxyl or methoxy termination groups are located. This is to be compared with the data from base catalysed TMOS where the peak ratios indicate a higher concentration of "core" silicon atoms (~70%). The base catalysed TMOS aerogels then would tend to consist of colloidal particles at least 5 nm in diameter. These data are then consistent with that obtained from the TEMs and SANS, which suggest a polymeric structure in the ultralow-density aerogel.

The BET surface area measurements for the ultra-low density silica aerogels are in the range of 550 to 650 m^2/g. These results are anomalously low as compared with both higher density, condensed silica derived aerogels and with base catalysed TMOS derived aerogels which give 850 to 950 m^2/g and 700 to 750 m^2/g, respectively. It is possible that the ultralow-density aerogels have micropores that are not interrogated by the nitrogen molecules, thus giving low values for surface area. In fact, results from helium pycnometry also suggest microporosity; the measured skeletal density for the ultralow-density aerogel was 1.81 g/cm^3, compared with 2.09 g/cm^3 for the base catalysed TMOS derived aerogels, both being lower than full density silica.

Lastly, the transmittance of the ultralow-density silica aerogel is considerably higher than the base catalysed TMOS derived aerogels for all wavelengths between 200 and 800 nm. This result is somewhat surprising because increased extinction at all uv-visible wavelengths is expected for scattering from the larger pores within the ultralow-density silica aerogel. This result suggests that this material has either smaller than expected pores or very uniform sized pores.

CONCLUSIONS

The data presented here suggests a microstructure for the ultralow-density silica aerogel that differs from the colloidal bead-like structure proposed for the base catalysed TMOS aerogels. The data is consistent with an interlinked polymer chain-like structure, with an average chain diameter of 2-3 nm and an average chain length >15 nm. The pores

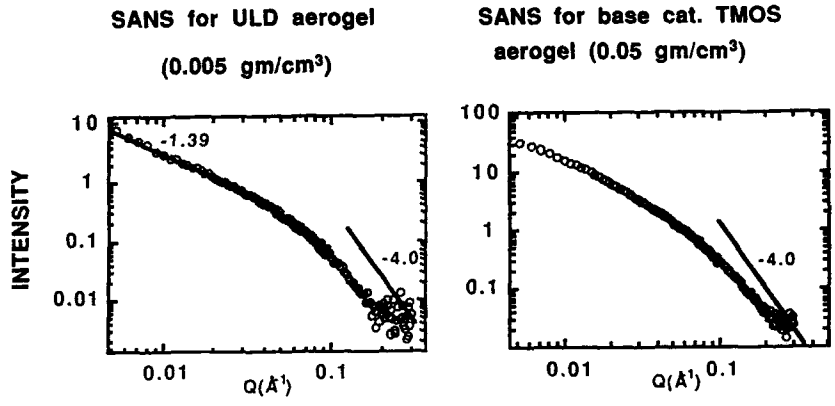


Figure 1. Small angle neutron scattering data for both ULD and base/TMOS aerogels. Porod slopes of approximately -4.0 for both types, suggest smooth (non-fractal) surfaces for size scales <~10Å. A highly fractal (polymerlike) is indicated by the -1.4 Porod slope for the ULD aerogel at size scales >10Å.

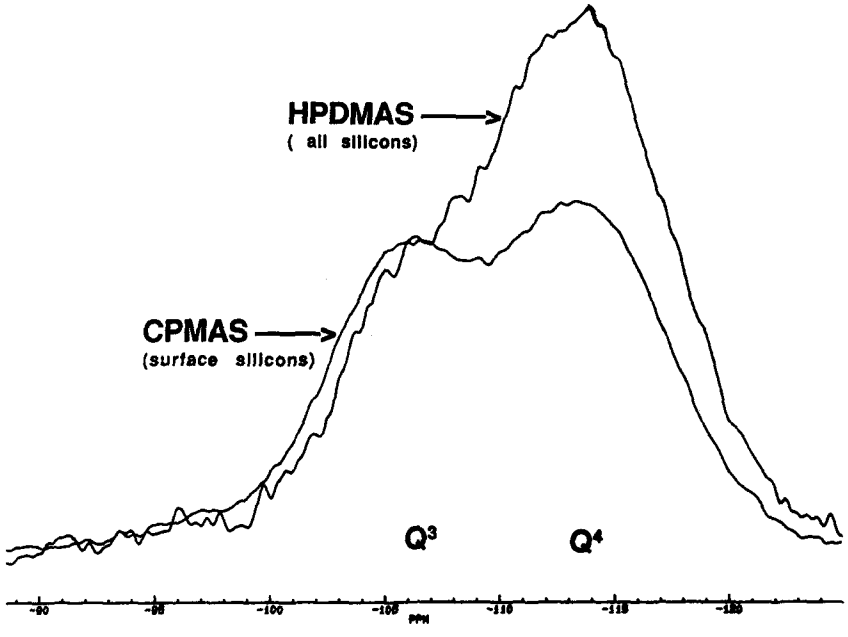


Figure 2. A comparison of CPMAS and HPDMAS ^{29}Si NMR scans for ULD aerogel shows that about 50% of the silicon atoms are "core" atoms, *ie.* more than a few bond distances from a proton. This data is used to determine an approximate average silica chain diameter of 20Å.

must not be larger than 50 nm, based on the high transmittance measured for this material.

The ultralow-density silica aerogels are highly transparent compared with higher density, single step produced aerogels. The transparency suggests very small particles and uniform pore size in these aerogels.

ACKNOWLEDGEMENTS

This work was performed under the auspices of the U.S. Department of Energy by Lawrence Livermore National Laboratory under Contract #W-7405-ENG-48. We thank D.W. Schaefer, Sandia National Laboratory Albuquerque, and J. A. Happe, Lawrence Livermore National Laboratory, for their assistance in interpreting the SANS and NMR data respectively.

REFERENCES

[1] D.W. Schaefer, J.P. Wilcoxen, K.D. Keefer, B.C. Bunker, R.K. Pearson, I.M. Thomas, and D.E. Miller, in Physics and Chemistry of Porous Media II, edited by J.R. Banavar, Joel Kolpik, and K.W. Winkler, (Am. Inst. Phys. Conf. Proc. 154, New York, 1987) p.63.

[2] C.J. Brinker, K.D. Keefer, D.W. Schaefer and C.S. Ashley, J. Non-Cryst. Solids 48, 47 (1982).

[3] S. Henning and L. Svensson, Phys. Scr. 23, 697 (1981).

[4] D.W. Schaefer and K.K. Keefer, Phys. Rev. Lett. 56, 2199 (1986).

[5] T.M. Tillotson and L.W. Hrubesh, in Better Ceramics Through Chemistry III, edited by C.J. Brinker, D.E. Clark, and D.R. Ulrich, (Mater. Res. Soc. Symp. Proc., 121, Reno, NV 1988), pp.685-689.

[6] D.W. Schaefer, Revue De Physique Appliquee, Colloque C4, Suppl. 4, April 1989.

MICROSTRUCTURAL DEPENDENCE OF AEROGEL MECHANICAL PROPERTIES

J.D. LEMAY, T.M. TILLOTSON, L.W. HRUBESH, AND R.W. PEKALA, Chemistry and Materials Science Department, Lawrence Livermore National Laboratory, Livermore, CA 94550

ABSTRACT

Aerogels are highly porous solids derived from the hypercritical drying of covalently crosslinked gels. SEM, TEM and scattering studies reveal that these materials have an open-cell morphology with a solid matrix composed of interconnected colloidal-like particles (30-200 A) Processing variables and synthetic conditions largely determine the microstructure and morphology. In this study, the structure-mechanical property relationships of silica, resorcinol-formaldehyde, and carbon aerogels are examined.

INTRODUCTION

At Lawrence Livermore National Laboratory we have been involved in the research and development of aerogels for a number of years. We particularly are interested in aerogels of low-density in the range of 0.030-0.300 g/cc. Our applications for these materials include high energy physics experiments like inertial confinement fusion (ICF). In addition to studying more common aerogels based on metal alkoxides (e.g., TMOS or tetramethoxysilane), we have developed new aerogels made of organic polymers and carbon [1-4]. We also have developed new technologies for making ultra-low density silica aerogels (0.005-0.020 g/cc) [5,6].

Low density aerogels are not robust materials, yet our applications require that we handle and machine precisely dimensioned parts from these delicate materials. Consequently we find it useful to evaluate their response to mechanical deformation. Like other workers [7-9] we also are interested in the general scientific characterization of these unique materials [4,10]. In this work we report on the compressive mechanical properties of silica, polymeric, and carbon aerogels.

EXPERIMENTAL

Synthesis

The precursors for the silica aerogels were "alcogels" prepared via the hydrolysis and polycondensation of tetramethoxysilane (TMOS) in aqueous methanol. Gels were prepared under acidic (HCl) and basic (NH_4OH) conditions using a TMOS:H_2O mole ratio of 1:4. The density of the alcogel was adjusted by the quantity of methanol diluent. We prepared a third type of aerogel by replacing the TMOS monomer with a syrup of partially hydrolyzed TMOS. To make the syrup we reacted TMOS with a sub-stoichiometric amount of water (molar ratio; 1TMOS:1.3H_2O) under acidic conditions, then isolated the product [4]. Alcogels were made from the resulting syrup under basic conditions [4,5].

The method of preparation for the polymeric aerogel is detailed elsewhere [1,2]. Briefly, it involved the polymerization of an aqueous solution of resorcinol and formaldehyde (mole ratio 1:2) in the presence of a basic catalyst (sodium carbonate). The density was adjusted through the concentration of the diluent (water).

The carbon aerogels were made by pyrolyzing the polymeric resorcinol-formaldehyde (RF) aerogels. The procedure is described elsewhere [3,4]. The RF polymer aerogel is readily pyrolyzed because it is a highly crosslinked, aromatic material. The carbon aerogel has a TEM morphology similar to its precursor, is amorphous as evidenced by x-ray diffraction, and has an empirical formula of $C_{99}N_1$ as determined by elemental analysis [4].

Mechanical Property Testing

The modulus (stiffness) and strength of the aerogels were measured in uniaxial compression at an initial strain rate of 0.1%/sec. The tests were performed under ambient conditions. The relative humidity was generally 50-70% during testing and no special precautions

Mat. Res. Soc. Symp. Proc. Vol. 180. ©1990 Materials Research Society

were taken to prevent moisture adsorption by the aerogels.

Two test specimen shapes were used: cubes about 1 cm on each side, were machined from production bricks, and 1-2 cm high cylinders were cut from 1 cm diameter molded pieces. Great care was taken to ensure that the end faces of the specimens were smooth and plane parallel. The cube specimens were shaped with a high speed circular saw on a modified end-mill. Specially designed vacuum chucks were used to hold the aerogel during shaping.

The compressive modulus was determined from the linear region of the load-displacement curve. The strength was determined as the stress at the 0.2% strain offset on the load-displacement curve. There is no fundamental reason for choosing this offset value, we simply have found it to be a convenient way to characterize and compare the strength of aerogels and other low density materials which exhibit diverse responses at higher compressive strains.

RESULTS AND DISCUSSION

As a consequence of their high porosity, foams and related materials exhibit elastic moduli many orders of magnitude smaller than their full density matrices. When measured as a function of density, the modulus and strength of foams often obey a simple scaling law. The aerogels investigated in this work also exhibit this behavior (Figs. 1-2).

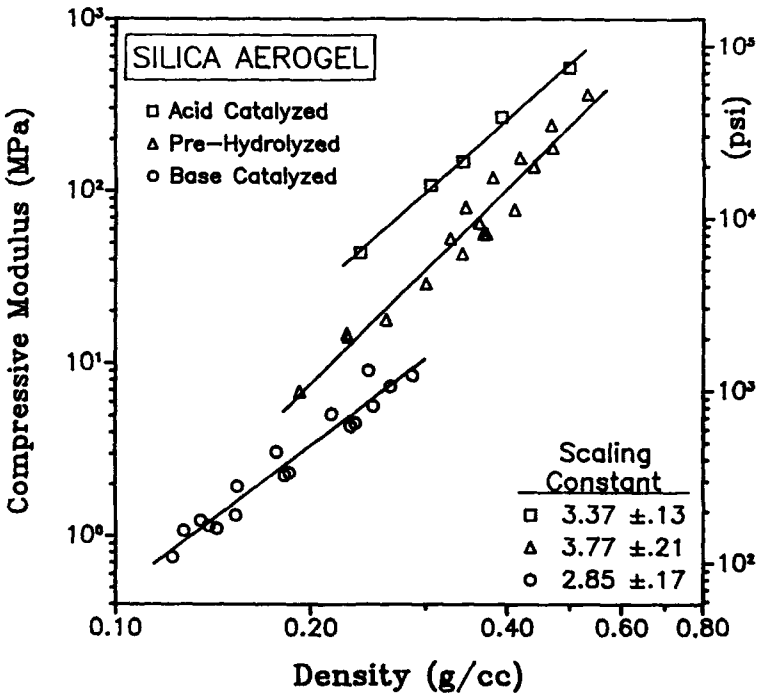


Figure 1. Silica aerogel compressive modulus as function of density.

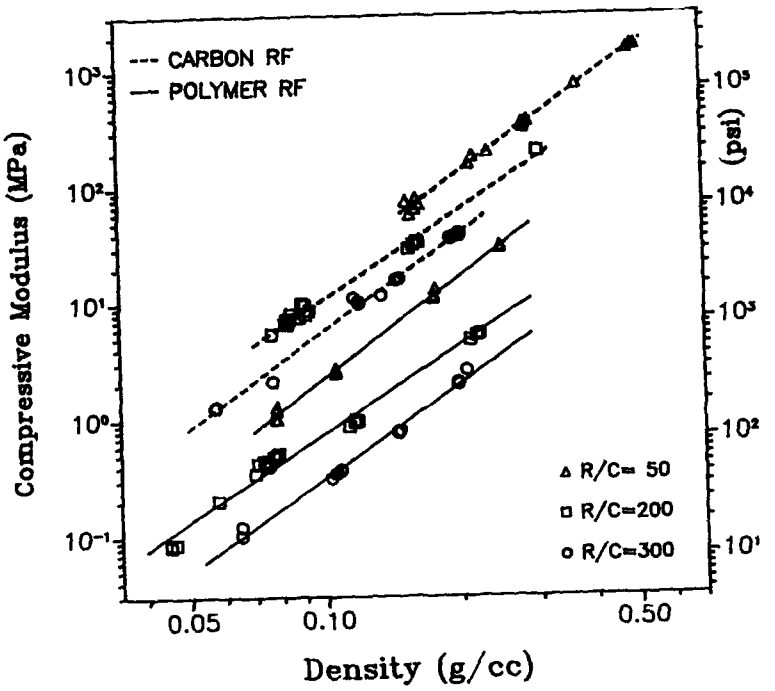


Figure 2. Polymer and carbon resorcinol-formaldehyde aerogel. Compresssive modulus as function of density. Scaling constants for polymer RF: R/C=50 (2.87±0.04), R/C=200 (2.48±0.08), R/C=300 (2.65±0.06). Scaling constants for carbon RF: R/C=50 (2.77±0.05), R/C=200 (2.53±0.06), R/C=300 (2.76±0.06).

Fig. 1 shows the compressive moduli of three types of LLNL produced silica aerogels as a function of density. At equivalent density the acid catalyzed aerogel is about 10X stiffer than the base. The pre-hydrolyzed aerogel falls between the two. Offset strength data is not shown, but exhibits a similar relationship. The strengths of the acid catalyzed aerogel span 1.4-9.0 MPa (0.24-0.39 g/cc), and the base 40-380 KPa (0.14-0.25 g/cc).

The data in Fig. 1 reveal distinct differences among the aerogel types. This coincides with differences in the morphologies of these materials as determined by TEM and scattering studies. Acid catalyzed aerogels reportedly have an entangled, chain-like (polymeric) morphology, while base catalyzed aerogels are composed of interconnected, smooth, spherical beads [11,12]. Scaling constants of 3.7±0.3 have been reported for acid and base catalyzed silica aerogels [7-9]. Our data for the acid catalyzed and pre-hydrolyzed aerogels are in agreement, but our base catalyzed aerogel exhibits a lower value of 2.85. We suspect that formulation differences (e.g., TMOS-to-catalyst ratio) may be responsible for the observed differences.

The modulus-density relationship of the polymeric RF aerogel is shown in Fig. 2. Compressive strengths are not shown, but exhibit similar behavior. For the R/C=300 RF aerogel the strengths span 6-140 KPa (0.065-0.21 g/cc), and for the R/C=50 aerogel they range from 40-800 KPa (0.08-0.25 g/cc).

TEM and scattering studies show an RF aerogel is composed of interconnected spherical particles whose sizes are controlled by the resorcinol-to-catalyst ratio [1,4,13]. At R/C=50 the particles have diameters of 30-50 A and are joined with large necks. At R/C=300 the particles have

diameters of 160-200 A and are lightly fused together. This morphology is consistent with the observed stiffness; at equivalent densities the R/C = 50 aerogel is about 7X stiffer than the R/C = 300 aerogel. The scaling constant for modulus-density relationship is 2.65 ± .20 and is unaffected by the catalyst level. It is lower than the 3.7 value reported for silica aerogels, but is similar to the scaling constant we obtained for our base-catalyzed silica aerogel. It may be significant that SAXS data reveals that RF aerogels are not mass or surface fractal materials like silica aerogels [13].

Compressive modulus data for the carbonized RF aerogels (CRF) are also shown in Fig. 2. The modulus-density relationships are similar to those of the precursors. The scaling constant remains about 2.65. The stiffness of the carbon foam is about 10X the precursor (same R/C and equivalent density). During pyrolysis the RF aerogels shrink while experiencing about a 50% weight loss. Accompanying the shrinkage are interesting changes in the particle size and apparent interparticle connectivity. There appears, however, to be no gross changes in the overall morphology as compared to the precursor [4]

SUMMARY

The mechanical properties of three different types of aerogels were investigated as a function of density. In all cases, the data were described by a simple scaling law. For silica aerogels, changes in the pH of the precursor gel result in gross changes in the final morphology. The mechanical response reflects this in widely variant scaling law relationships. The RF and carbon aerogels are distinctly different from the silica aerogels. The RF aerogels share a common chain-like, connected-bead structure. Changes in morphology caused by altering the catalyst level or pyrolysis (i.e., particle size and degree of interconnectivity) represent only subtle changes in the basic structure. The mechanical behavior reflects this in a consistent scaling law.

ACKNOWLEDGMENTS

This work was performed under the auspices of the U.S. Department of Energy by Lawrence Livermore National Laboratory under Contract #W-7405-ENG-48

REFERENCES

[1] R.W. Pekala, J. Mater. Sci., 24, 3221 (1989).
[2] R.W. Pekala and R.E. Stone F.M., Polym. Preprints, 29(1), 204 (1988).
[3] R.W. Pekala and F.M. Kong, Polym. Preprints, 30(1), 221 (1989).
[4] R.W. Pekala, C.T. Alviso and J.D. LeMay, submitted to J. Non-Cryst. Solids.
[5] T. Tillotson and L.W. Hrubesh, in Better Ceramics Through Chemistry III, edited by C.J. Brinker, D.E. Clark and D.R. Ulrich, (Mater. Res. Soc. Symp. Proc., 121, Reno, NV 1988), p. 685-689.
[6] L.W. Hrubesh, T.M. Tillotson and J. Poco, this issue.
[7] T. Woignier, J. Phalippou and R. Vacher, J. Mat. Res., 4(3), 688 (1989).
[8] T. Woignier, J. Phalippou, R. Sempere and J. Pelous, J. Phys. France, 49, 289, (1988).
[9] M.Gronauer, A. Kadur and J. Fricke in Aerogels, J. Fricke, ed., Springer-Verlag, Berlin, 1985, p167.
[10] J.D. LeMay, R.W. Pekala and L.W. Hrubesh, Pacific Polym. Preprints., 1, 295 (1989).
[11] C.J. Brinker and G.W. Scherer, J. Non-Cryst. Solids, 70, 301 (1985).
[12] D.W. Schaefer and K.D. Keefer, in Better Ceramics Through Chemistry, edited by C.J. Brinker, D.E. Clark and D.R. Ulrich (Mater. Res. Soc. Symp. Proc., 32, Albuquerque, NM 1984), pp. 1-14.
[13] D.W. Schaefer and R.W. Pekala, to be published

POSITRONIUM DECAY IN SILICA SOL-GELS

B. HOPKINS, C. A. QUARLES and T. W. ZERDA
Physics department, Texas Christian University, Fort Worth, TX 76129

ABSTRACT

Positronium lifetimes inside porous silica are measured and discussed in terms of surface interactions, oxygen and nitrogen induced quenching and pore sizes. Surface interactions are studied for silica gels having surfaces covered solely with hydroxyl or methoxy groups. A rapid decay of positronium inside the pores filled with gaseous or liquid oxygen is reported and explained in terms of quenching mechanisms. An increase in the measured lifetimes for pores filled with nitrogen is attributed to the change in the pore distribution function.

INTRODUCTION

Silica gels are networks of interconnected irregular silica particles with large numbers of voids or pores permeating the structure. The concentration of pores is on the order of 10^{18} pores/gram, with pore diameters ranging from about 10 to 1000 angstroms. The high concentration of pores accounts for the gels large surface area, in some cases in excess of 900 m^2/g. These properties make the gels excellent hosts for studying surface interactions.

Positronium is a short lived bound system composed of a positron and an electron. The positronium "atom" occurs in two ground states. Parapositronium (p-Ps) is the singlet state with total spin of zero. It has a self annihilation lifetime in vacuum of 0.125 ns and decays via 2 gamma emission. Orthopositronium (o-Ps) is the triplet state with total spin of one. Its free space lifetime is much longer, 140 ns, and decays via 3 gamma emission. The lifetime of parapositronium is comparable to the direct annihilation lifetime of positrons, making practical measurement difficult. O-Ps, however, survives long enough to interact with surrounding atomic and molecular electrons. This interaction leads to a shortening of its lifetime through various processes called quenching. Measurement of this shortened lifetime can thus yield information about the physical and chemical properties of the medium sampled by o-Ps.

Three types of quenching are possible. The positron of the positronium atom may directly annihilate via 2 gamma decay with a nearby atomic or molecular electron. This process is known as pickoff quenching. Alternately, the positron may encounter an unpaired electron which converts the orthopositronium atom to parapositronium (or vice versa). O-Ps converted to p-Ps then quickly decays via 2 gamma emission. This process is called conversion quenching. O-Ps may also reduce its lifetime by reacting chemically with its environment. This process is known as chemical quenching.

Positrons entering silica particles may form o-Ps and migrate into the pores, where they remain trapped and subsequently decay. These decays contribute to the long lived intensity component, I, characterized by an exponential decay

$$I = B \exp(-t/\tau) \qquad (1)$$

At low densities, $1/\tau$ increases with the concentration of the quenching substance, and to a first approximation, for thermalized positronium, the decay rates defined are proportional to the number of molecules per unit volume, N, and depend on the o-Ps speed as

$$1/\tau = 1/\tau_0 + N\sigma v \qquad (2)$$

where τ_0 is the lifetime in a degassed sample and σ is the cross section characteristic for the quenching process. Depending on the substance impregnating silica gels we may have different quenching processes.

Pick off quenching occurs when positronium collides with molecules which contain electrons with the appropriate spin orientation enabling fast decay. This process is always present, even in noble gases. The typical cross section for pick off quenching in gases is on the order of 10^{-21} cm^2; in nitrogen, it is 1.0×10^{-21} cm^2.[1] Conversion quenching is more effective than pick off quenching, its cross section in oxygen and NO has been estimated to be on the order of 10^{-19} cm^2.[1,2] Some molecules, such as nitrogen dioxide, ozone, or iodine, may reduce o-Ps lifetime

Mat. Res. Soc. Symp. Proc. Vol. 180. ©1990 Materials Research Society

through a chemical reaction in which a molecule-positronium complex is formed and subsequently decays. The cross section for this process is on the order of 10^{-16} cm^2.[2] When different quenching processes take place simultaneously, the measured decay rate is a sum of rates for different components. In order to separate these processes, we performed o-Ps decay measurements in gels of different pore sizes as a function of nitrogen or oxygen concentration when the gases had been adsorbed on the pore walls. Additional measurements were made of gels having modified surfaces to investigate chemical quenching of o-Ps by surface groups.

EXPERIMENTAL

Three types of silica gels were used in the experiments. Gels having well characterized pore diameters of 40 Å and 150 Å were purchased from Aldrich, another gel having an average pore diameter of 25 Å was prepared in our laboratory. The apparatus used consisted of a chamber to hold the silica gel sample and Na^{22} source, a pair of photomultiplier tubes with associated electronics for detecting the birth and decay of positrons, and a multichannel analyzer.

The first set of experiments measured o-Ps lifetime in the 40 Å and 150 Å gels for various concentrations of N_2 or O_2. The experiments were performed with the chamber of the apparatus kept in liquid nitrogen. Care was taken to ensure that the injected gas had adequate time to adsorb onto the gel.

The second set of experiments used the 25 Å gel to study o-Ps interactions with surface groups. O-Ps lifetimes were measured as a function of adsorbed nitrogen concentration for the untreated gel having its surface populated with OH groups. The measurements were then repeated after the OH groups had been replaced with OCH_3 groups.

RESULTS AND DISCUSSION

Previously [3] we studied the relationship between the observed lifetimes and pore diameters, and the correlation found is illustrated in Fig. 1. Slightly different dependencies were found for degassed samples and for samples filled with nitrogen or oxygen at normal pressure and room temperature. The lifetimes measured for degassed samples characterize the positronium quenching by the silica surface. The quenching process takes place only for positronium in thermal equilibrium, and because of that the lifetimes are temperature dependent and increase with lower temperatures [4,5]. From Fig. 1, it is seen that oxygen effectively reduces the lifetimes, while to the first approximation, the effect of nitrogen can be neglected. From the study of o-Ps lifetimes as a function of concentration of gaseous oxygen inside the pores at room temperature, we tested the validity of Eq. 2, compare Fig. 2. We found the cross sections for oxygen quenching to be about 1.5×10^{-19} cm^2, a value typical for the conversion mechanism.

We repeated this procedure at -192°C and in Fig. 3 we plot the observed lifetimes against the concentration of liquid oxygen or nitrogen adsorbed within the pores. Again, it is seen that oxygen decreases the lifetimes, and to our surprise, we found that Eq. 2 approximated nicely the

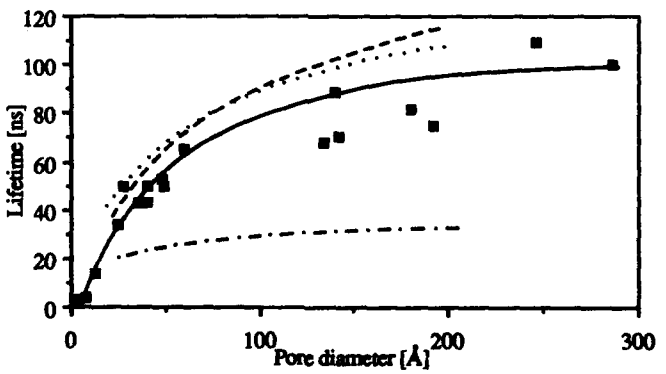


Fig. 1. O-Ps lifetimes versus pore size diameters, solid line in ambient atmosphere, broken line in vacuum, dotted line in nitrogen, dotted-dashed line in oxygen. For clarity reasons we show only the data obtained for the experiment in air.

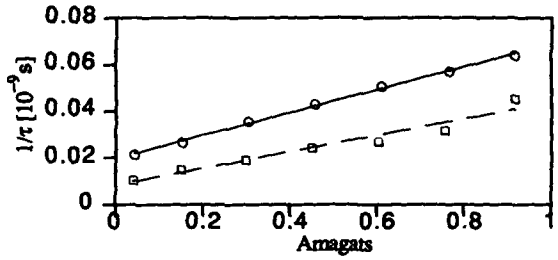


Fig. 2. Positronium lifetimes at 25°C in silica gels as a function of oxygen pressure. Circles 40 Å, squares 150 Å gels, lines denote the best fits to linear dependence on concentration, Eq. 2.

observed lifetimes, but only for concentrations less than those sufficient to form a single layer of molecules adsorbed on the silica surface. Also, the cross section was by two orders of magnitude smaller than that found at room temperature. The quenching cross sections, σ, found from least square fits of the experimental data to Eq. 2 were 2.2×10^{-21} and 4.6×10^{-21} cm^2, for the 40 Å and 150 Å gels, respectively. The discrepancy between the two results probably originated from the changes of average pore diameter of the 40 Å gel during the adsorption process. Adsorption of oxygen in the other sample, 150 Å in diameter, had little effect on the average pore size.

The addition of nitrogen to either sample causes the positronium lifetimes to initially increase, and the maximum is reached for the concentration slightly less than that necessary for a monolayer coverage. Two possible explanations can be offered. Pores within silica gels do not have uniform sizes, and nitrogen adsorbed may first fill small pores, shifting the average pore diameter toward larger values. Inside larger pores o-Ps is known to live longer and this effect may explain the observed increase of o-Ps lifetimes in silica with surfaces covered by nitrogen. An alternative explanation has been proposed by Chuang and Tao.[6] The attractive potential between nitrogen and positronium is weaker than that between o-Ps and silica. Adsorbed nitrogen prevents o-Ps from interacting with silica, and the observed lifetime increases. In order to test the latter hypothesis we conducted experiments with two identical samples but having different surface groups. Silica gels prepared via the sol-gel process have surfaces covered with hydroxyl groups, with the average number varying from 1 to 4.6 OH groups per nm^2, depending on the firing temperature. By boiling a sample in methanol one can replace hydroxyl groups with OCH_3 groups[7], which are less reactive, and this treatment should increase the measured lifetimes inside the pores. The effectiveness of replacement of the OH groups by the OCH_3 groups was studied using Raman spectroscopy. In Fig. 4 we show the spectra in the 3000 cm^{-1} region of the same sample before and after the treatment in methanol. It is seen that after the treatment the sample showed pronounced bands due to the C-H vibrations indicating that OCH_3 groups had been incorporated into the structure.

The replacement of hydroxyl groups with methoxy groups did not change the pore

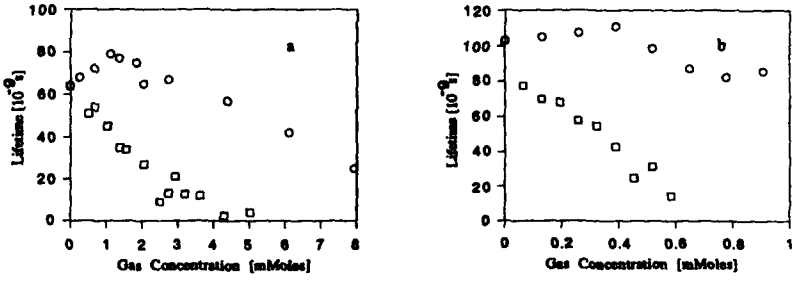


Fig. 3. Lifetime dependence on oxygen (squares) and nitrogen (circles) concentration in silica gels of pores 40 Å (a) and 150 Å (b) in diameter. Temperature -192° C.

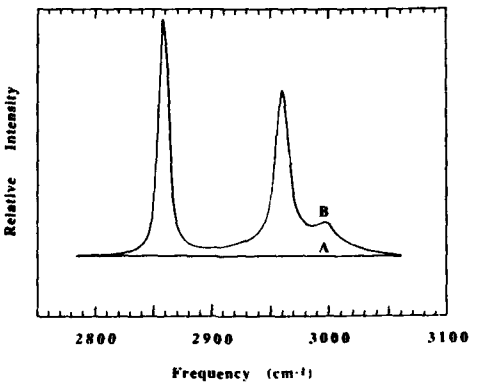


Fig. 4. Raman spectrum of silica gel before (a) and after (b) methanol treatment.

diameters. We ran BET tests before and after the treatment and we found the same results. When nitrogen was condensed inside methanol treated silica the lifetimes appeared to be concentration dependent with a similar trend to that shown in Fig. 3. This finding suggests that the initial increase in o-Ps lifetimes upon addition of nitrogen cannot be explained as the screening of interactive sites on the surface by a monolayer of nitrogen. We propose the other explanation suggesting that small pores are filled first, shifting the average pore size toward larger values. This effect may be used to evaluate pore size distribution and further work is in progress.

The initial increase in lifetimes has not been observed upon addition of oxygen because the pick off process is more effective in oxygen than it is in nitrogen. We estimated the cross section for the nitrogen pick off quenching from the decay of τ observed above the monolayer coverage. The decay can be characterized by the cross section $\sigma = 1.4 \times 10^{-21}$ cm^2 $\pm$ 0.5 x 10^{-21}cm^2, a value that correlates nicely with the data reported by McNutt and Summerour [8] for gaseous N_2, $\sigma = 1.0 \times 10^{-21}$ cm^2. Since the cross section for pick off quenching by oxygen is several times greater, it overshadows the changes in pore size distribution due to absorption of oxygen in small pores.

SUMMARY

1. Positronium decay can be used to measure pore sizes and pore size distribution.
2. At room temperature and ambient gases, the lifetimes are determined by the oxygen.
3. Oxygen in a gas phase causes o-Ps to decay through the conversion process, but oxygen adsorbed as a monolayer on the silica surface quenches o-Ps through a different process, characterized by a cross section of almost two orders of magnitude smaller, most likely through the pick off mechanism.
4. The initial increase of the lifetimes upon addition of nitrogen cannot be explained in terms of screening of OH groups, since the replacement of hydroxyl groups with OCH_3 groups leads to the same results.

LITERATURE

1 R. L. Klobuchar and P. J. Karol, J. Phys. Chem., 84, 489 (1980)
2 V. I. Goldanski, A. D. Mokrushin, A. O. Tatur, and V. P. Shantarovich, Appl. Phys., 5, 379 (1975)
3 T. W. Zerda, G. Hoang, B. Miller, C. A. Quarles, and G. Orcel, Better Ceramics Through Chemistry, III, Mat. Res. Soc. Symp. Proc. 121, 653 (1988)
4 I. T. Jakubov and A. G. Khraptak, Rep. Prog. Phys., 45, 687 (1982)
5 B. Hopkins and T. W. Zerda, Phys. Lett. A145, 141 (1990)
6 S. Y. Chuang and S. J. Tao, Can. J. Phys., 51, 820 (1973)
7 C. Morterra and M.J.D. Low, Ann. New York Aca. Sc., 220, 135 (1973)
8 J. D. McNutt and V. B. Summerour, Phys. Rev. B, 5, 2019 (1972)

This work was supported by AFOSR, grant 90-0165.

A COMPARISON OF TiO_2-SiO_2 AEROGELS AND XEROGELS

G. COGLIATI*, M. GUGLIELMI**, T.M. CHE*** AND T.J. CLARK***
*TEMAV, Laboratori di Medicina, Bologna, Italy.
** Universita di Padova, Dipartimento di Ingegneria Meccanica, Padova, Italy.
*** Enimont America Inc., Advanced Materials Department, Monmouth Junction, N.J. 08852

ABSTRACT

Titania-silica gels containing up to 30% titania have been obtained from silicon and titanium alkoxides and from silicon alkoxides and $TiCl_4$. These gels were then processed by normal drying and by hypercritical methods. The thermal evolution of these gel/glass systems, specifically with respect to crystallization behavior has been followed using x-ray diffraction and Raman spectroscopy. From these studies, it was found that not only the different chemistries, but also the different processing methods significantly affect the microstructure of these titania-silica systems.

INTRODUCTION

Silica-titania glasses have a very low thermal expansion (1,2) and high refractive indices (3,4). Unfortunately, they are difficult to fabricate by conventional techniques owing to their very high melting temperatures. As a result, many investigators (2,4-9) have employed sintering methods, such as sol-gel, which require much lower processing temperatures to prepare TiO_2-SiO_2 glasses.

A major problem in producing bulk glass by the sol-gel route is formation of cracks during the drying stage. In practice, ambient xerogel methods require considerable drying times, whereas with the use of hypercritical drying techniques, large aerogel monoliths can be obtained in a few hours with 100% certainty (10).

To date, few comparisons of multicomponent aerogels and xerogels have been made. In this paper, based on x-ray diffraction and Raman data , we compare various TiO_2-SiO_2 gels made using $TiCl_4$ or $Ti(OC_3H_7)_4$ with silicon tetramethoxide, and dried by the two different methods.

EXPERIMENTAL PROCEDURE

Preparation of gels

The procedure followed in this study for the preparation of xerogels and aerogels is summarized schematically in Figure 1. Colloidal solutions of hydrolyzed silicon and titanium alkoxides or silicon alkoxide and titanium tetrachloride gelled in several hours at room temperature. In all cases, gelation occurred more rapidly at higher Ti/Si ratios. The resulting transparent and homogeneous bulk gels were then dried by both normal and hypercritical methods. The xerogel and aerogel monoliths studied received heat treatments in which the samples, when heated to a given temperature and cooled, were either extracted for characterization or heated to the next higher heat treatment temperature. The heat treatments of 300, 700, and 900 °C were conducted in air for 24 hours soaking time, whereas the 1200 and 1500 °C heat treatments received 2 hour soak times in a helium atmosphere.

Mat. Res. Soc. Symp. Proc. Vol. 180. ©1990 Materials Research Society

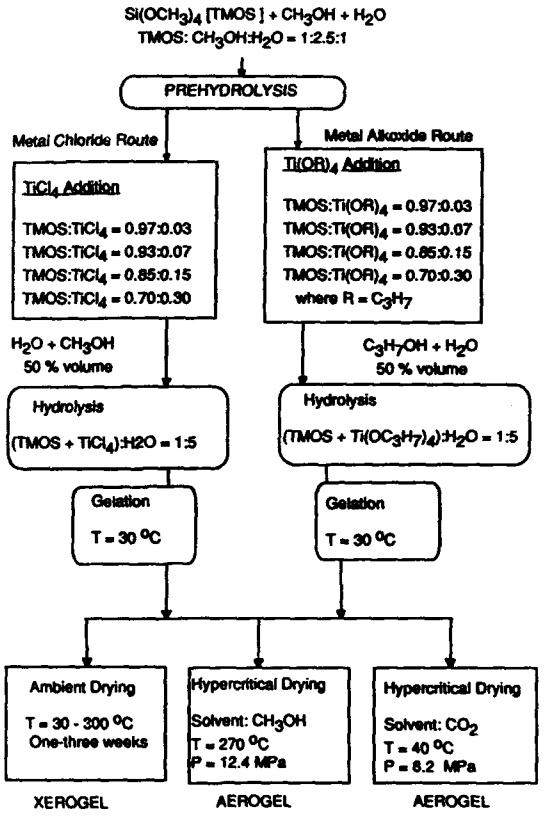


Figure 1. Preparation of titania-silica gels.

Gel characterization

Gels treated at the different temperatures have been characterized by x-ray diffraction, Raman spectroscopy, thermal analysis, scanning electron microscopy (SEM), surface area and density measurements. In this paper, only the XRD and Raman results are reported, deferring a more detailed discussion to a future publication.

X-ray powder diffraction and Raman spectroscopic methods were used to examine the phase composition of specimens. An automated diffractometer with Ni filtered Cu Ka radiation was used to generate patterns of 2 theta values from 5^{o} to 70^{o}. The Raman instrumentation has been described elsewhere (11,12). Raman spectra were collected at room temperature, at excitation wavelengths of 514.5 and 634.0 nm. Samples were cleaved to expose a fresh flat surface and irradiated at a spot by an incident beam 45^{o} to the sample face. The scattered light was collected and focused on entrance optics parallel to the sample face.

RESULTS AND DISCUSSION

Titanium tetrachloride can be readily substituted for titanium alkoxide and can be added to a prehydrolyzed silicon alkoxide, or first prehydrolysed and then added to the silicon alkoxide solution. Different multicomponent systems such as silica-germania glasses can also be made using silicon alkoxides and metal chlorides as starting materials (13).

X-ray diffraction results are summarized in Table I. Figure 2. shows x-ray diffraction patterns for a set of titania-silica samples containing 15 mol% TiO_2, which were obtained by the different chemical routes and drying procedures, and heated at 700 °C.

TABLE I. Summary of x-ray diffraction results for titania-silica aerogels and xerogels.

SAMPLE	TEMPERATURE (°C)				
	300	700	900	1200	1500
AI 3	**	***	***	***	-
AI 7	***	***	***	***	*
AI 15	***	***	***	***	*
AI 30	***	***	***	***	*(1)
BI 3	**	***	***	***	-
BI 7	***	***	***	***	*
BI 15	***	***	***	***	**(2)
BI 30	***	***	***	***	***(2)
AX 3	o	o	o	o	(2)
AX 7	o	o	o	o	o
AX 15	o	o	**	***	***
AX 30	o	*	**	***	***
BX 3	o	o	o	(2)	(2)
BX 7	o	o	o	o	*(2)
BX15	o	o	**	***	***
BX 30	o	*	**	***	***
BC 3	o	o	o	o	-
BC 7	o	o	o	o	-
BC 15	o	o	o	*	-
BC 30	o	o	*	**	*(1)(2)

KEY: o amorphous
Anatase content:
* low ** high *** very high
(1) presence of rutile
(2) presence of cristobalite

A: $Ti(OR)_4$ route
B: $TiCl_4$ route
I: Aerogel - dried in alcohol
C: Aerogel - dried in CO_2
X: Xerogel

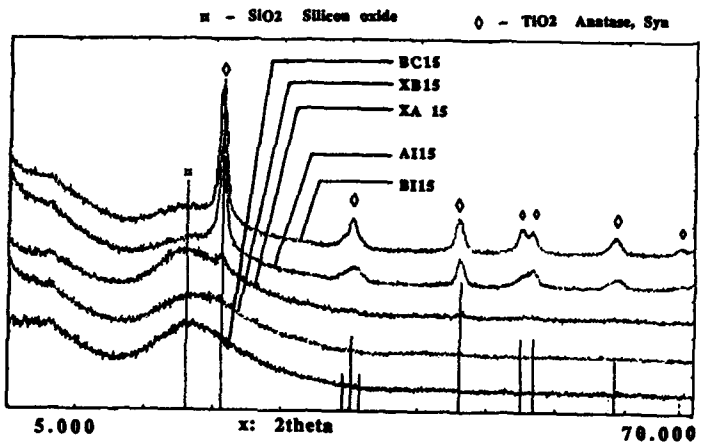


Figure 2. X-ray diffraction patterns of titania-silica aerogels and xerogels containing 15 mol% TiO_2 and heat treated to 700 °C.

From Table I, it is evident that all samples processed using aerogel techniques (AI and BI series) show anatase crystallization already at 300 °C, while xerogel processed samples (AX and BX series) were amorphous. Chemical processing differences in aerogel processed materials were identified by interpreting x-ray diffraction peak broadening effects (not shown). The microcrystalline nature observed from broadening showed that aerogels in which $Ti(OC_3H_7)_4$ was used had greater crystal size growth with increasing titania concentration than did aerogels processed using $TiCl_4$. The amorphous content of $TiCl_4$ systems remained constant up to 15mol% TiO_2, whereas that of $Ti(OC_3H_7)_4$ systems did not, as determined by the relative magnitudes of amorphous hump to peak heights in the x-ray patterns. Thus, it appears that if crystal growth is to be avoided in TiO_2-SiO_2 aerogels, the $TiCl_4$ system is the more desirable of the two synthetic approaches.

Based on peak broadening, the size of anatase crystals is estimated to be between 100 and 200 Å at 300 °C and about 500 and 600 Å at 1500 °C. At this temperature, aerogels show a decrease in the total content of crystalline phase, possibly due to partial dissolution in the silica matrix, as reported in Ref. 6.

Although hypercritical drying has been used successfully for the preparation of large silica gels and enables one to also obtain monolithic bodies in titania-silica systems, the aggressive environmental conditions of the autoclave (i.e., temperatures of 270 °C and pressures of 12.4 MPa), particularly in the presence of free water, can transform hydrous titania contained in the silica-titania gel to anatase. The formation of anatase during hypercritical drying is shown by the diffraction spectra of titania-silica aerogels with 3 to 30% titania.

If hypercritical drying is carried out at lower temperatures, by substituting liquid CO_2 for alcohol in the alcogel, the conversion of hydrous titania into anatase can be avoided. Aerogels (BC) dried under such conditions show greater stability than the analogous xerogels (BX). This type of processing allows the amorphous phase to persist in an otherwise crystallization-prone specimen up to 700°C, a unique finding in aerogel technology.

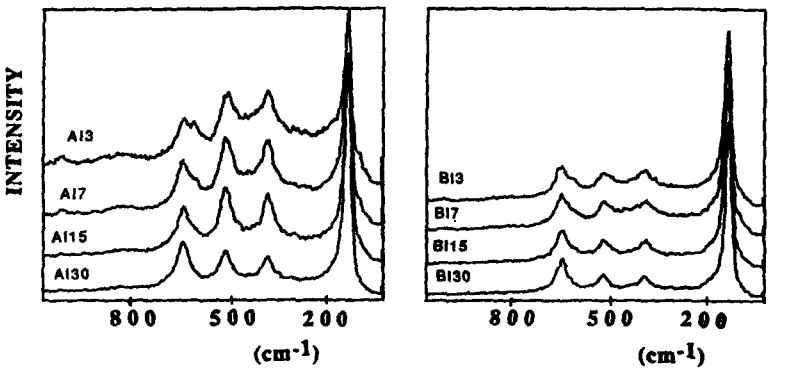


Figure 3. Raman spectra for aerogel series AI and BI heat treated to 700 °C.

Figure 3. shows the Raman spectra of aerogel series AI and BI which have been heat treated to 700 °C. The sharp 143 cm^{-1} and prominent 393, 515 and 638 cm^{-1} peaks are characteristic of crystalline TiO_2 anatase, whereas broad features at 435, 495 and 604 cm^{-1} are associated with silica emission bands (14,15,16). The spectral structure between 300 and 700 cm^{-1} wavenumbers varies significantly with changes in titania concentration. *For the 3 and 7 mol%* TiO_2 aerogels, Raman bands of silica apparently overlap with those of anatase. However, anatase features become more well-defined with increasing titania concentration, as observed for the 30mol% TiO_2 systems.

The richness of the low frequency modes is a clue that these peaks may give more detailed information about the fundamental interaction in these materials since they are important in understanding the weaker bonds of the structures.

At the excitation wavelength of 514.5 nm, fluorescence occurs in all titania-silica samples treated at 300 °C samples. By shifting to 634.0 nm, fluorescence is reduced and weak anatase bands were observed in both the AI and BI series.

CONCLUSIONS

1) Titanium tetrachloride is a useful precursor for the preparation of SiO_2-TiO_2 gels.

2) Anatase crystallization phenomena in TiO_2-SiO_2 gels induced by hypercritical drying using alcohol as a solvent can be avoided by substituting CO_2 for alcohol.

We wish to express our gratitude to P. Chiurlo and F. Pirini of Enichem for sample preparation and heat treatments. We also thank G. Del Piero of Enitricerche, R. Snyder and M. Bajak of Alfred University for X-ray characterization, and P.Dorain of Amherst College and M. Banash for Raman meaurements. Finally, we thank L. Costa, R. Mininni and S. Rohman for their support and valuable suggestions.

REFERENCES

(1) P.C. Schultz and H.T. Smyth in Amorphous Materials, edited by Douglas and Ellis (Wiley, New York, 1972) p. 453.
(2) K. Kamiya and S. Sakka, J. Non-Cryst. Solids 52, 357 (1982).
(3) C.J. Brinker and M.S. Harrington, Solar Energy Materials 5, 159 (1981).
(4) S.M. Melpolder, A.W. West, C.L. Barnes, and T.N. Blanton, "A study of phase transformations in TiO_2/SiO_2 sol-gel films as a function of compositions and heat treatment." (to be published in J. Mater. Sci.)
(5) K. Kamiya and S. Sakka, J. Mater. Sci., 15, 2937 (1980).
(6) B. E. Yoldas, J. Non-Cryst. Solids 38 & 39, 81 (1980); U.S. Patent 4,278,632 (July 14, 1981).
(7) C.J.R. Gonzalez-Oliver, P.F. James and H. Rawson, J. Non-Cryst. Solids 48, 129 (1982).
(8) Z. Deng, E. Breval and C. G. Pantano, J. Non-Cryst. Solids, 100, 364 (1988) .
(9) Y.C. Cheng and L.L. Hench, in Better Ceramics Through Chemistry III, edited by C.J. Brinker, D.E. Clark and D.R. Ulrich (Mater. Res. Soc. Proc. 121, Pittsburgh, PA 1988) pp. 596; in the Proceedings of the 4th Intn'l Conf. on Ultrastructure Processing of Ceramics, Glasses and Composites held Feb 1989 (to be published).
(10) J. Zarzycki in Ultrastructure Processing of Ceramic Glasses and Composites, edited by L.L. Hench and D.R. Ulrich (Wiley, New York, 1984) pp. 27-42.
(11) T.M. Che, J.J. Rafalko and P.B. Dorain, in Ultrastructure Processing of Advanced Ceramics, edited by J.D. Mackenzie and D.R. Ulrich (J. Wiley and Sons, Inc., New York, 1988), p. 827.
(12) P.B. Dorain, J.J. Rafalko, J.E. Feeney, C.E. Forbes, R.V. Carney and T.M. Che, in Better Ceramics Through Chemistry III, edited by C.J. Brinker, D.E. Clark and D.R. Ulrich (Mater. Res. Soc. Proc. 121, Pittsburgh, PA 1988) pp. 523-526.
(13) G. Cogliati and G. Bezzi, Italian Pat. 19403A/89 (Feb. 10, 1989).
(14) G. J. Exarhos and W. T. Pawlewicz, Applied Optics 23 (12), 1986 (1984).
(15) W.T. Pawlewicz, G.J. Exarhos, and W.E. Conaway, Applied Optics 22 (12), 1837 (1983).
(16) M.F. Best and R.A. Condrate, Sr., J. Mater. Sci. Letts. 4, 994 (1985).

THE EFFECTS OF HYDROLYSIS CONDITIONS, AND ACID AND BASE ADDITIONS, ON THE GEL-TO-CERAMIC CONVERSION IN SOL-GEL DERIVED $PbTiO_3$

ROBERT W. SCHWARTZ,* C. D. E. LAKEMAN, AND D. A. PAYNE
Department of Materials Science and Engineering, and
Materials Research Laboratory
University of Illinois at Urbana-Champaign,
105 S. Goodwin Ave., Urbana, IL 61801

ABSTRACT

Lead titanate was prepared by the sol-gel processing of metal alkoxide solutions. The effects of hydrolysis level (i.e., moles H_2O/mole $PbTiO_3$) and acid and base additions (HNO_3 or NH_4OH) on the properties of desiccated gels, and the gel-to-ceramic conversion, were studied. Microstructural, structural, and physical properties were characterized at three stages of the processing cycle: (i) the desiccated gel state; (ii) the amorphous state, following organic pyrolysis; and (iii) the crystalline state. Differences in the physical and structural properties for the desiccated gels, which were induced through manipulation of the hydrolysis conditions, persisted in the amorphous state after organic pyrolysis. Minor differences remained after crystallization. Variations in material properties, with low temperature processing (e.g., the gel-to-glass transformation), were considered from the standpoint of hydrolysis and additive effects on the gel network structure and consolidation behavior. Data are reported for the densification and crystallization behavior for the gels. Through proper control of hydrolysis conditions, relatively dense ceramics were obtained at temperatures as low as 700°C.

INTRODUCTION

In recent years, sol-gel processing has generated considerable interest. While most of this interest has focused on the processing of amorphous materials in the silica system, an increasing trend has been towards the fabrication of electronic components [1]. The processing route, includes: (i) hydrolysis of precursor solutions with controlled additions of water to form gels (or coatings); (ii) drying and heat treatment of the gels to form a "pure" amorphous material (e.g., pyrolysis of residual organic matter); and (iii) higher temperature heat-treatment for densification and crystallization. The transformations associated with the first two steps, i.e., the sol-to-gel and the gel-to-glass transformations, have been studied extensively for the silica system [2-4], and the effects of hydrolysis conditions, and acid or base additions, have been noted.

In a previous study, we demonstrated that through control of hydrolysis conditions, differences in the physical, structural, and microstructural properties of desiccated lead titanate ($PbTiO_3$) gels could be induced [5]. The focus of the present investigation is to characterize the transformation behavior (gel-to-glass and glass-to-ceramic) for the desiccated gels, and to determine if the property differences induced in the desiccated gels persist in the pure amorphous state and into the crystalline perovskite state. If the differences induced in the desiccated gels persist in the amorphous state, both the densification and crystallization behavior of the material could be affected [4,6,7].

Lead titanate was selected for investigation since the ABO_3 family of perovskite materials are widely used for their dielectric, ferroelectric, and electrooptic properties [8]. Numerous thin film applications based on PZT ($PbZrO_3$ - $PbTiO_3$) and PLZT (La modified PZT), most notably, radiation hard non-volatile memories [9] and optical storage devices [10], are under development. The preparation of PZT and PLZT monoliths by sol-gel processing is also of interest, since current processing methods require elevated temperatures [11].

---

* Present Address: Sandia National Laboratories, Albuquerque, NM 87185

Mat. Res. Soc. Symp. Proc. Vol. 180. ©1990 Materials Research Society

EXPERIMENTAL

A method developed by Budd et al. was followed for the synthesis of the Pb-Ti precursor solution [1]. Lead acetate tri-hydrate ($Pb(OOCCH_3)_2 \cdot 3H_2O$) was dehydrated by three successive distillations in HPLC grade 2-methoxyethanol ($CH_3OCH_2CH_2OH$). In a separate reaction vessel, titanium isopropoxide ($Ti(OCH(CH_3)_2)_4$) was refluxed for 30 minutes in 2-methoxyethanol, and the by-product of the reaction, isopropanol, was removed by distillation. This resulted in an alkoxide exchange between the original isopropoxy groups of the titanium precursor and the methoxyethoxy groups of the solvent, yielding titanium methoxyethoxide ($Ti(OCH_2CH_2OCH_3)_4$). The lead and titanium solutions were then reacted (130°C, 60 min.) and concentrated by vacuum distillation, to form a 1 molar Pb-Ti mixed metal alkoxide solution. The reactions were characterized by ^1H and ^{13}C NMR [12].

Gels were prepared by combining equal volumes of the 1 molar precursor solution with a solution of water, acid or base additive, and 2-methoxyethanol. Water additions (i.e., R, the molar ratio of water to mixed metal alkoxide) were varied from 2.0 to 4.0, in 0.5 molar steps. Both acidic (0.1 M HNO_3) and basic (0.1 M NH_4OH) hydrolysis conditions were studied. Gelation times ranged from 12 seconds to 22 hours.

After gelation, the gels were aged for 30 minutes, and dried at 140°C for 48 hours. Drying was essentially complete within the first 6 hours. Phase separation was observed for both acid and base gels. The approximate weight loss during drying was 80%, which was attributed to the evaporation of phase separated solvent.

After drying, the gels were lightly crushed in a mortar and pestle to form powders suitable for property characterization. The powders were also heat-treated under various conditions. Previous experiments had shown that for similar hydrolysis and drying conditions, the decomposition reactions were complete by 350°C, with crystallization occurring at temperatures above 400°C [6,7]. Therefore, amorphous $PbTiO_3$ was prepared by heating the gel-derived powders to 400°C at 10°C/min. and immediately quenching to room temperature. Skeletal densities for the amorphous materials were calculated from He gas pycnometry measurements, by assuming no inaccessible porosity. Heat treatment at 410°C, from 0.5 to 10 hours, was carried out to determine any variations in physical properties during the crystallization process. Surface area and pore size characteristics were determined by N_2 adsorption analysis (BET). Crystallinity of the gel-derived powders was determined by X-ray diffraction (Rigaku D Max; Cu K_α radiation; 45 kV, 20 mA).

Finally, the effects of water content, R, and acid and base additions, on microstructure development were investigated. Specimens were heated (10°C/min.) to 700°C for 60 minutes and later evaluated by scanning electron microscopy (SEM).

RESULTS AND DISCUSSION

In a previous study [5], we reported that the surface areas and pore volumes of desiccated $PbTiO_3$ gels increased with increasing R. We also determined that, for comparable water additions, base gels had higher surface areas and pore volumes than acid gels. The observed variations in physical properties were attributed to differences in the level of condensation resulting from hydrolysis. For example, as reported for the silica system [2], hydrolysis under basic conditions (and/or with large water additions) was believed to lead to more highly condensed (crosslinked) structures, which were less capable of consolidation during drying. Therefore, the corresponding desiccated gels were characterized by larger pore volumes and greater surface areas.

In the present study, we characterized variations in physical properties associated with the gel-to-glass transformation (i.e., the conversion of the desiccated gel to pure amorphous $PbTiO_3$ at 400°C). Results are given in Figure 1. For each of the hydrolysis conditions studied, surface area (Figure 1a) decreased with heat treatment to 400°C. However, differences in surface areas for the various amorphous materials (induced through manipulation of hydrolysis conditions) were still present after organic pyrolysis. Unlike the desiccated gels, however, the heat treated (pure amorphous $PbTiO_3$) gels prepared under acidic conditions were, in general, characterized by

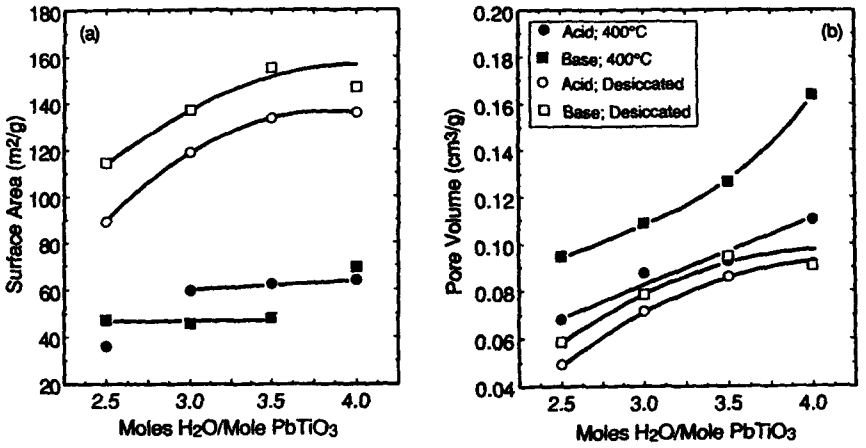


Figure 1. (a) Surface areas and (b) pore volumes, for desiccated $PbTiO_3$ gels and pure amorphous $PbTiO_3$.

greater surface areas than basic gels prepared with comparable water contents. Acid gels thus had a greater retention of their initial surface areas on heat treatment.

We also studied variations in pore volume with heat treatment, and the results are given in Figure 1b. As for desiccated gels, the amorphous $PbTiO_3$ gels prepared under basic conditions with large water additions, were characterized by the highest pore volumes. However, the pore volumes for the heat treated gels were substantially greater than the desiccated gels, i.e., pore volume increased with heat treatment to 400°C. The gels prepared under basic conditions also exhibited a greater increase in pore volume (with heat treatment) than the acid gels. The fact that the physical properties of the heat treated gels displayed different trends than the desiccated gels implies that the processes which occur during heat treatment, i.e.: (i) organic removal; (ii) continued condensation reactions (toward the equilibrium amorphous structure); and (iii) (macroscopic) consolidation of the gel; occur to different extents, depending on the initial hydrolysis conditions.

Other effects related to the hydrolysis conditions were also observed to persist in the heat treated (pure amorphous $PbTiO_3$) gels. Figure 2 gives results for structural free volume, which was calculated from the skeletal density of the amorphous material, and the theoretical crystal density, according to:

$$FV = 1 - (\rho_s/\rho_c) \qquad (1)$$

Gels prepared under hydrolysis conditions which gave higher levels of condensation (base addition, high R) were characterized by lower free volumes, as expected. Since the free volumes of the base gels were relatively independent of the amount of water used for hydrolysis, the amorphous materials prepared under basic conditions were evidently highly crosslinked, irrespective of R. If the results for these materials are considered from the standpoint of traditional glasses, the materials would be characterized as having few non-bridging oxygen species.

For gels prepared under acidic conditions, structural free volume decreased with increasing R. Thus, after heat treatment at 400°C, substantial structural differences existed in amorphous $PbTiO_3$ prepared under acidic conditions. Acid gels prepared with higher water contents were characterized by more highly condensed structures than those prepared with lower water contents. If the amorphous materials derived from acid, low water content gels are considered from the standpoint of traditional glasses, they would be characterized as having a greater number of non-bridging oxygens; i.e., the structures are less condensed than materials prepared under basic conditions, or under acidic conditions with high water contents. Structural differences

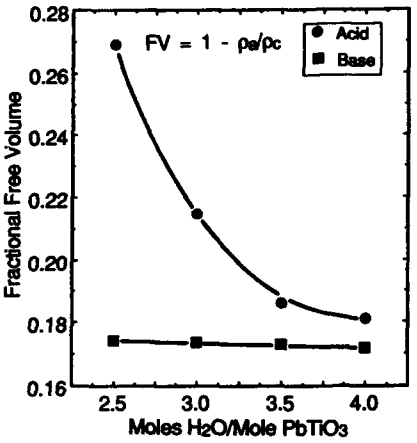


Figure 2. Free volume for amorphous $PbTiO_3$, prepared by heat treatment at 400°C.

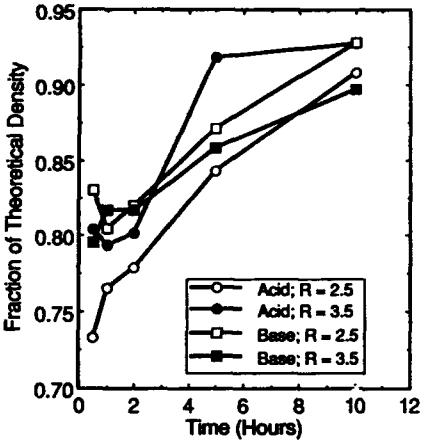


Figure 3. Effect of time at 410°C on skeletal density of sol-gel derived $PbTiO_3$.

of this nature are believed to be unstable, and with heat treatment near T_g should disappear. That is, the structures of the sol-gel glasses produced below the glass transition temperature relax toward the equilibrium melt structure with heat treatment near T_g [13].

Results for skeletal density variations, as a function of heat treatment time near T_c (the crystallization temperature) were in agreement with these predictions, and are shown in Figure 3. While the skeletal densities for the amorphous materials (heated to 400°C and quenched) were quite different, the effects diminished when heated at 410°C for extended times. For example, for a 10 hour heat treatment, i.e., after the onset of crystallization, all the skeletal densities reached ~90% of the theoretical crystal density (7.98 g/cm^3), irrespective of the hydrolysis conditions.

Another area of investigation was to determine whether gel densification was complete prior to the onset of crystallization. Therefore, the effects of prolonged heat treatment at temperatures near T_c on the physical properties of amorphous $PbTiO_3$ gels

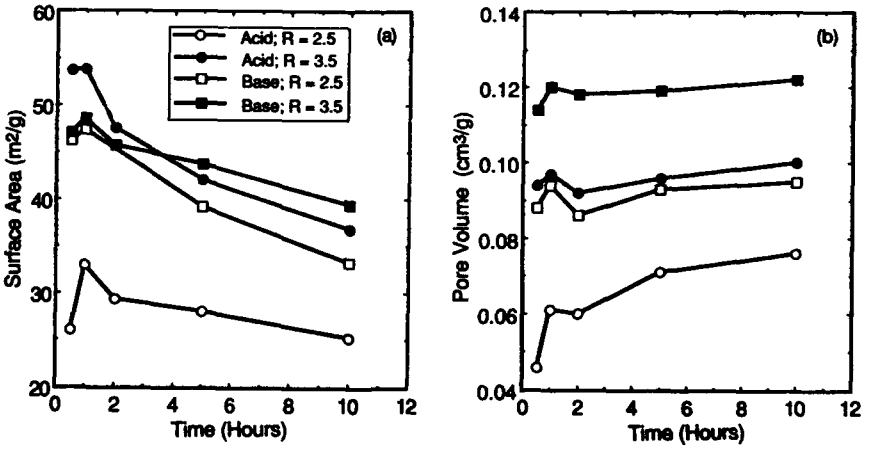


Figure 4. Variations in (a) surface area and (b) pore volume with time at 410°C.

were studied. Results are given in Figure 4 for the variations in surface areas and pore volumes with time at 410°C. While the materials were amorphous (to X-rays) for shorter heat treatment times, all materials heated for 10 hours were at least partially crystallized. As is evident in Figure 4, differences induced in the desiccated gels were still present after crystallization. While the surface areas (Figure 4a) of the materials decreased slightly with prolonged heat treatment at 410°C, the surface areas still varied from approximately 25 to 40 m^2/g, depending on the initial hydrolysis conditions. Pore volumes in the partially crystallized materials (Figure 4b) were also dependent on the hydrolysis conditions. In addition, all of the materials retained significant pore volumes after the onset of crystallization, irrespective of the hydrolysis conditions. Higher temperatures were necessary for complete densification (see below).

While considerable porosity was present in amorphous $PbTiO_3$ heated to 400°C and quenched (Figure 5a), gels heated to 450°C for 10 hours (Figure 5b) showed that not only crystallization, but also substantial densification, had occurred. Thus, within this narrow temperature range, both structural rearrangement on an atomistic scale (e.g., crystallization) and rearrangement on the microstructural scale (e.g., densification), take place. The implication of this result is that since both crystallization and densification occur at low temperatures, low temperature fabrication of ceramic monoliths should be feasible, through the use of appropriate processing conditions.

The effects of hydrolysis conditions on the development of ceramic microstructure in gels heated to 700°C for 60 minutes were characterized by SEM. Photomicrographs are given in Figure 6 for fracture surfaces of an acid, low water content gel (Figure 6a); and a base, high water content gel (Figure 6b). Even at this late stage in the processing cycle, minor effects attributed to the initial hydrolysis conditions were still present. For example, a ceramic derived from an acid, low water content gel had a larger grain size (~1.5 μm) and appeared less porous than a ceramic derived from

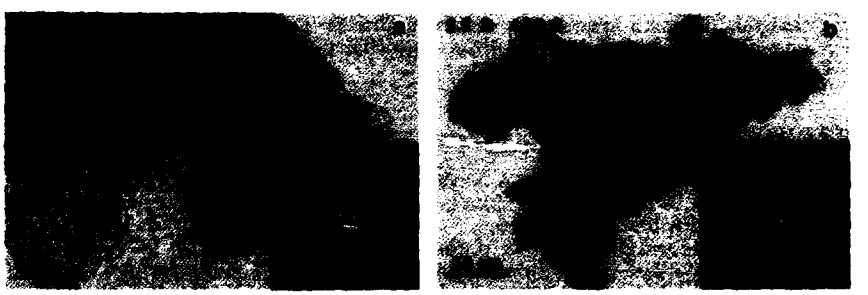


Figure 5. TEM photomicrographs of: (a) amorphous $PbTiO_3$ (400°C heat treatment; Hydrolysis Conditions: Base; R = 2.5); and (b) crystallized $PbTiO_3$ (450°C, 10 hour heat treatment; same hydrolysis conditions).

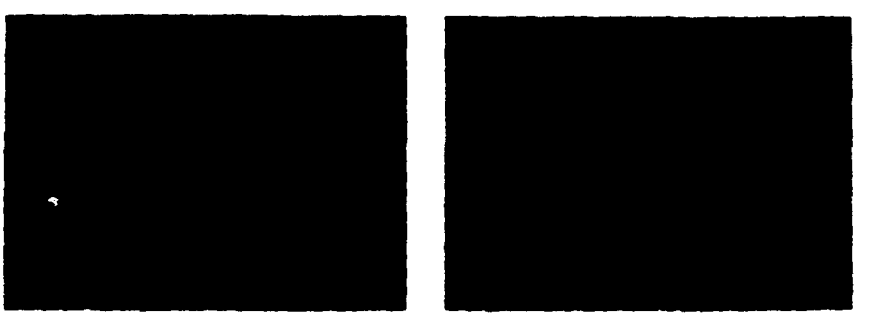


Figure 6. SEM fracturegraphs for $PbTiO_3$ microstructures: (a) acidic gel, R = 2.5; and (b) basic gel, R = 3.5. Heat treatment: 700°C, 60 min.

a base, high water content gel (grain size ~0.9 μm). Investigations of polished sections are underway to determine if there really is a true difference between the porosity contents for the two conditions. The dense uniform microstructure for the ceramic prepared under acid, low water additions, Figure 6a, indicates the temperatures required for fabrication of dense ceramics by sol-gel methods (i.e., 700°C) are considerably less than those required in the processing of co-precipitated PLZT powders (i.e., ~1100°C) [11].

CONCLUSIONS

Variations in surface area and porosity in desiccated $PbTiO_3$ gels, induced through control of the hydrolysis conditions, were studied as a function of heat treatment conditions, i.e., after the gel-to-glass and glass-to-ceramic transformations. Differences in the physical properties for the desiccated gels persisted in the pure amorphous state, following pyrolysis of residual organic matter. Differences induced in the skeletal structures for the amorphous materials were also noted, but were observed to decrease with time at temperatures near T_c. Heat treated (amorphous) gels were relatively porous, with crystallization starting prior to end-point densification. Studies in progress are concerned with obtaining dense amorphous $PbTiO_3$ (at lower temperatures) prior to crystallization.

ACKNOWLEDGEMENTS

We acknowledge the support of the U.S. Department of Energy under contract DMR DE-AC02-76ER01198. The use of facilities in the Center for Electron Microscopy, the Materials Research Laboratory, and the Center for Cement Composite Materials at the University of Illinois are gratefully acknowledged. We thank D. J. Eichorst and L. F. Francis for technical discussions.

REFERENCES

1. K. D. Budd, S. K. Dey, and D. A. Payne, in Better Ceramics Through Chemistry II, edited by C. J. Brinker, D. E. Clark, and D. R. Ulrich (Mater. Res. Soc. Proc. 73, Pittsburgh, PA 1986) pp. 711-716.
2. C. J. Brinker and G. W. Scherer, J. Non-Cryst. Sol., 70, 301 (1985).
3. C. J. Brinker and G. W. Scherer, in Ultrastructure Processing of Ceramics, Glasses and Composites, edited by L. L. Hench and D. R. Ulrich (John Wiley & Sons, Inc., New York, 1984), pp. 43-59.
4. C. J. Brinker et al., in Science of Ceramic Chemical Processing, edited by L. L. Hench and D. R. Ulrich (John Wiley & Sons, Inc., New York, 1986) pp. 37-51.
5. R. W. Schwartz, D. A. Payne, and A. J. Holland, Proc. Intl. Conf. Ceramic Powder Processing Science, Oct., 1988.
6. R. W. Schwartz and D. A. Payne, in Better Ceramics Through Chemistry III, edited by C. J. Brinker, D. E. Clark, and D. R. Ulrich (Mater. Res. Soc. Proc. 121, Pittsburgh, PA 1986) pp. 199-207.
7. R. W. Schwartz, PhD Thesis, University of Illinois, 1989.
8. B. Jaffe, W. R. Cook, and H. Jaffe, Piezoelectric Ceramics, (Academic Press, New York, 1971).
9. J. F. Scott and C. A. Araujo, Science, 246, 1400 (1989).
10. C. E. Land, M. A. Butler and S. J. Martin, IEEE IEDM Tech. Digest, 251 (1989).
11. G. H. Haertling in Ceramic Materials for Electronics, edited by R. C. Buchanan (Marcel Dekker, Inc., New York, 1986) pp. 139-225.
12. S. Ramamurthi and D. A. Payne, accepted for publication in J. Am. Ceram. Soc. (1990).
13. A. R. Cooper, in Better Ceramics Through Chemistry II, edited by C. J. Brinker, D. E. Clark, and D. R. Ulrich (Mater. Res. Soc. Proc. 73, Pittsburgh, PA 1986) pp. 421-430.

EFFECTS OF TRIOXANE ON SILICA GEL

XIAOMING LI and P.F. JOHNSON
New York State College of Ceramics at Alfred University, Alfred, NY 14802

ABSTRACT

Hydrolysis, condensation and thermal reactions of silica gels derived from TEOS with and without 1,3,5-trioxane ($C_3H_6O_3$) were studied. Effects of trioxane on viscosity and gelation time of solutions were determined. Specific surface, density, porosity and microhardness of gels were measured. The behavior of gels at elevated temperature was clarified using DTA, TGA, and dilatometry. The properties and structure of trioxane containing sol/gels may be explained by the role trioxane played in the sol-gel transition. The results of this investigation concerning sol-gel/gel-glass transitions, structure and properties of gels are presented.

INTRODUCTION

Trioxane ($C_3H_6O_3$) has been used as an additive to improve the optical and physical properties of porous silica glasses derived from alkoxide precursors through the sol-gel route [1]. The effects of trioxane on sol-gel reactions in the HF-catalyzed TEOS-C_2H_5OH-H_2O system have been studied by time-dependent Raman, FTIR and NMR spectroscopic techniques [2]. While previous studies concentrated on the effects of trioxane on hydrolysis kinetics of sols and on the structure and physical properties of gel derived glasses, the question of the extent to which trioxane can affect the thermal reaction, gel-glass transition and high temperature pyrolysis of gels has not been addressed. A knowledge of the thermal evolution of gels containing trioxane is very important for better understanding the effects of trioxane on sol-gel and gel-glass transition processes and for the selection of suitable thermal treatment schedules to remove gases and hydroxyl groups from the gels without breaking or bloating. The objectives of this work were to investigate reactions and transitions of silica gels containing trioxane at elevated temperatures and to clarify the role of trioxane in sol-gel and gel-glass transition.

EXPERIMENTAL

A standardized composition with the molar ratio of TEOS:H_2O:C_2H_5OH:additives = 1:4:4:0.1 was selected for all the solutions studied. The codes, additives and some sol-gel transition properties for different solutions are reported in Table I. The sols were prepared, typically, by mixing 42.1 ml of TEOS, 13.62 ml of water, 44.06 ml of ethanol and additives with vigorously stirring at room temperature until the solution was homogeneous. The resulting solutions were then poured in plastic containers with or without covers and allowed to gel at room temperature.

Table I. Codes, additives and gelation data for the test solutions*

Code	Additive	$pH(t_0)$	GT(O)	GT(C)	WL(T)	WL(G)	Gel Appearance
A	HCl	1.5	105	116	81.5	16.4	Transparent, cracks
B	NH_4OH	8.0	125	292	87.2	42.6	Transparent, cracks
T	Trioxane	5.45	136	420	59.3	50.0	Translucent, fewer crack
N	None	5.5	185	768	42.8	35.0	Translucent, more crack

* $pH(t_0)$, initial pH value; GT(O), gelation time (hrs.) in open system by viscometer measurement; GT(C), gelation time (hrs.) in closed system by fluidity observation; WL(G), weight loss (%) at gel time; WL(T), total weight loss (%) at room temperature.

The pH values of each solution were periodically measured with both a glass-electrode pH meter and Universal Indicator Paper (pH 0-14). The results obtained from both methods were quite consistent. Weight changes of different solutions sealed in 50 ml plastic beakers were measured at room temperature. A Brookfield viscometer with UL adapter was used to measure the viscosity of solutions which were opened to air. The solution used for measuring viscosity (about 20 ml for each measurement) was discarded after each determination. The time interval until the viscosity underwent substantial increase was considered to be the gelling time of sols in an open system. The gelling time for closed solution systems was determined by observing when the sol lost its fluidity, i.e. the meniscus of a sol in a container no longer remains horizontal when the container was tilted.

Surface area measurement of gels was carried out at liquid nitrogen temperature with a *Monosorb* direct reading surface area analyzer using the nitrogen adsorption method. The specific surface area was calculated using the BET method. Apparent density, bulk density, and porosity of dried gels were measured at room temperature by the Archimedes method with kerosene as the saturating liquid. Vickers hardness of dry gels was measured using a microhardness tester (Buehler Micromet II). The load was 20 g with a constant loading time of 10 seconds.

Computer interfaced thermal gravimetric analyzer (TGA) and differential thermal analyzer (DTA) were used to monitor behaviors of gels at elevated temperature. Both TGA and DTA were performed at a heating rate of 10 °C/min in flowing air. Linear shrinkage of dried gel with length of 4-5 mm were tested in a computer interfaced dilatometer with heating rate of 2 °C/min.

RESULTS AND DISCUSSION

The initial pH of all solutions is presented in Table I. Trioxane had little effect on solution pH; that is addition of trioxane did not change the pH value much with respect to the pH value of solution without any additives, as shown in Fig. 1. All solutions changed slightly to lower pH values except the pH value of the acid catalyzed sample (A) which increased slightly. The change in pH can be attributed to the dissolution of carbon dioxide in air into solution to form acidic carbonates. Fig. 2 shows that all sols have a similar viscosity response with time except that the transition points at which viscosity undergoes an abrupt increase are different for each sol. The difference in gelation time is also shown in Table I for the different solutions. Note that the data

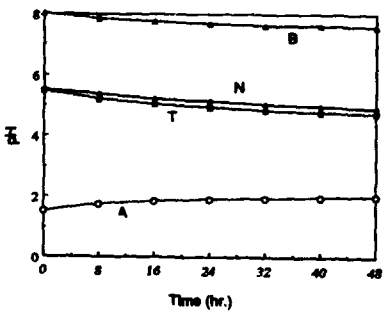


Figure 1, pH versus time for solutions for the first 48 hours after mix (see Table I for the sample codes).

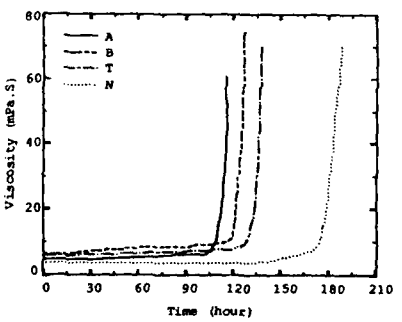


Figure 2, Viscosity vs time for solutions

for gelation time were obtained using two different methods. Figure 2 and Table I show that the viscosity and gelation times do not appear to correlate with the pH of solutions with different additives, despite the widely recognized fact that for the same catalyst, the pH of solution usually correlates with the time of gelation. The differences in observed gelation times using two different methods can be attributed to differences in samples and techniques. Solutions opened to air had higher viscosity and shorter gelation times than those which were closed, since the former has a higher evaporation rate and higher hydrolytic and condensation reaction rate due to additional catalysis on the sol-gel transition by carbonate and moisture from the air.

Table II. Surface tension, melting point and boiling point of various liquid solvents*

Solvent	ST	MP	BP
Ethanol	22.8	-114.4	78.4
Trioxane	32.9	62	114.4
DMF	35.8	—	153
Formamide	58.2	2.55	210
Water	72.8	0	100

* ST – surface tension (dyne/cm); MP – melting point (°C); BP – boiling point (°C)

Table III. Properties of dried xerogels with different additives

Code	BD	AD	PP	SSA	MH	Fire at 1250°C
A	1.441	1.878	34.5	177	68	break, foamed
B	0.727	2.056	66.95	178	36	break, foamed
T	0.977	2.029	55.59	260	66	keep shape
N	0.986	1.947	64.27	173	38	break, bloat

* BD – bulk density (g/cm^3); AD – apparent density (g/cm^3); PP – percent porosity (%); SSA – specific surface area (cm^2/g); MH – microhardness (kg/mm^2)

The structural characteristics and properties of gels obtained from TEOS using acidic or basic catalysts have been compared and discussed by many investigators [3-6]. The properties and thermal behavior of gel A (acid) and gel B (basic) in our study is in good agreement with observations in the literature. We focus our attention on the sample containing trioxane and use gel A and B as standard references. The solution containing the trioxane additive exhibited a longer gelation time than solutions A or B and shorter gelation time than the additive-free solution. This can be explained by the fact that the solution containing trioxane is expected to have a low evaporation rate because trioxane has relatively high melting point and boiling point, as shown in Table II. In addition, unlike most acidic or basic catalysts, adding trioxane to the sol system has little or no catalytic effect on the hydrolysis or condensation reaction rate [2]. Considering the above two points, one expects the solution containing trioxane to have longer gelation time than either the acid or base catalyzed solutions which may have higher hydrolysis and condensation rates than the trioxane containing solution. But on the other hand, trioxane is the anhydrous cyclic trimer of formaldehyde and is readily soluble in alcohols and dissolves in water into the monomeric state [7]. Trioxane in the solution may physically conjunct with the pre-gel silica polymer species. The involvement of trioxane into the sol or gel structure may increase the viscosity and rigidity and reduce the fluidity of silica sols. Recognizing that fluidity and rigidity determine the gelation time, the trioxane containing solution has a shorter gelation time than the solution without additives. Further evidence was provided by the microhardness measurement results shown in Table III. In general, Vickers hardness of silica gels correlate with the density of the gels; the higher the density, the higher the hardness and rigidity. But trioxane gel (T) is an exception. Its density is much lower than acid gel (A), but has almost the same hardness as the acid gel and higher hardness value than other gels which have density similar to gel T. It was reported that trioxane has been used as a binder and hardener for solidification and strengthening of protein materials [7] and water glass [8]. Despite having different reactions with water glass, protein materials and polymeric sols, trioxane may play, more or less, the role of a hardener in each case.

We must emphasise that besides enhancing the rigidity of the sol and gel, the incorporation of trioxane with monomer, dimer or other polymer species may cause

some steric hindrance effects on the bonding and connection within or between silicon containing particles in solution. This effect may also impede hydrolysis and/or condensation reactions of silica aggregates. The observation that trioxane lengthened the gelation time of HF-catalyzed silica alkoxide sol could be explained by this argument, i.e. trioxane in solutions may reduce the catalytic ability of HF since it may interrupt the incorporation and reaction possibilities of H^+ and F^- catalyst species with TEOS molecules or other reactive species.

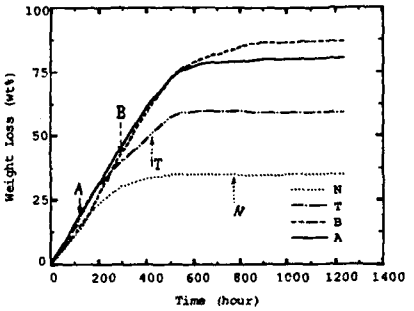


Figure 3, Weight loss at room T

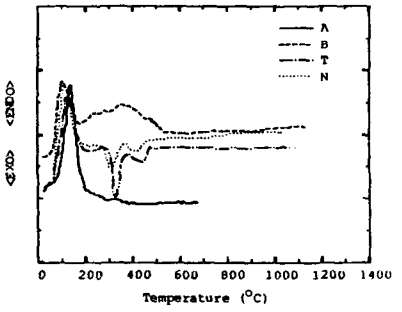


Figure 4, DTA of dried gels

Figure 3 presents the weight loss of solutions in paper covered containers at room temperature. It is notable that the no-additive sol and the trioxane sol exhibit much lower weight loss during the drying process than do the others. This is partly due to incomplete hydrolysis and condensation reactions in the sol which has no reaction catalysts (sample N). For the trioxane sample (T), in addition to incomplete reaction because trioxane does not catalyze (it may even impede) the hydrolysis and condensation reactions of alkoxide in solution, trioxane may also trap more water or other organic fractions in the gel due to its lower evaporation rate and due to the structural conjunction with other species. We expect the T and N gels to retain more water and/or organic residue than the A and B gels do. The TGA curves shown in fig. 5 prove that the trioxane sol (T) and the no-additive sol (N) have higher weight loss than other samples at elevated temperature. The arrows in the weight loss curves (fig. 3) correspond to the gelation time of each sample. The acid sol (A) gelled at quite low weight loss due to the high condensation rate caused by the acidic catalyst. The largest part of its weight loss occurred after gelation. In contrast, trioxane and no-additive samples lost most of their weight loss before gelation.

It is crucial to maintain the shape of monolithic gels during drying or heat treatment. The presence or absence of cracks observed in dry gels is shown in Table I. It is seen that dried gels with fewer cracks can be produced when the starting solutions contain the trioxane additive. It has been suggested that the effect of such additive as formamide (NH_2CHO) in decreasing drying stresses and crack formation may be attributed to its role in modifying the microstructure and texture of the gels by increasing pore size and improving pore size distribution [9]. In addition, additives, e.g. N,N-dimethylformamide (abridged to DMF), may also reduce capillary forces and cracks by reducing surface tension [10]. It is seen from Table II that the surface tension of trioxane is lower than that of water, formamide and DMF. TGA data in fig. 5, furthermore, prove that the trioxane sample has less free water, which has higher surface tension, but more hydroxyl, alkoxyl and other organic fractions, which has much lower surface ten-

sion. It is evident that when a low surface tension liquid remains in the pores on drying of the wet gels, the capillary force is small, resulting in the formation of crack-free dried gels. Considering the "binder" role of trioxane in the sol and gel structure, trioxane may also increase the rigidity and strength of gels. The effects of trioxane in suppressing cracking during the drying process seems to result from its low surface tension and its hardening role.

Table III lists some of the properties of the gels produced in this study. The trioxane sample had a substantially higher specific surface area than did the other samples. This suggests that the trioxane gel may have smaller, less crosslinked gel units, and a highly open and connected pore structure.

The TGA and DTA curves for the gels are illustrated in figures 4 and 5 respectively. All gels show an endothermic peak around 150 °C in the DTA curve which corresponds to the desorption of physical water. Although the different gels showed some similarities in DTA thermal behavior, gel T has more complicate thermal reactions than the others. The trioxane gel had a relatively small endothermic peak for free water desorption at 150 °C which suggests that less free water remained in its bulk. This was demonstrated to be the case using TGA. Both the no-additive and the trioxane gels showed two significant exothermic peaks between 250 °C and 500 °C corresponding to different thermal reactions. For the no-additive gel, this exotherm is attributed primarily to the combustion of alkoxy radicals. In the trioxane gels, combustion of trioxane additive may also contribute large exothermic effects, because trioxane is known as an efficient solid fuel with high heat energy.

TGA results provide complementary information concerning the composition, structure and thermal reaction of gels. It is notable that the TGA curves of the A, B and N gels have very similar shapes, but the TGA curve of trioxane gel shows different shape. Coincident with its small endothermic peak in DTA, trioxane gel has lower weight loss below 200 °C than the other gels which indicates that the trioxane gel contains less physically adsorbed water. In contrast, above 200 °C, T gel has significantly higher weight loss than the other gels. This indicates that the trioxane gel contains more organic residue, alkoxy and hydroxy radicals than the other gels. Supporting our earlier discussion, this difference suggests that trioxane undergoes less vaporization during the sol-gel transition and drying processes and can trap more organic fractions in the sol and gel. This may provide further evidence that trioxane may retard hydrolysis/condensation reactions and assist the formation of a highly esterified (terminal OR group) and less condensed gel. Further work is needed to get better understanding in these aspects.

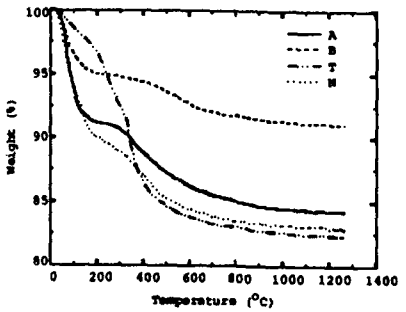


Figure 5, TGA of dried gels

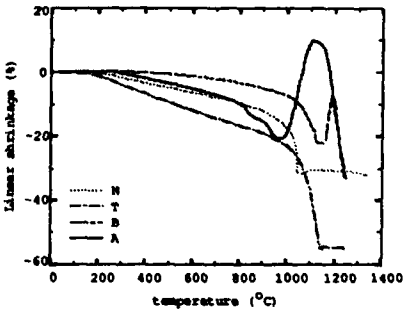


Figure 6, Linear shrinkage of dried gels

Shrinkage curves are shown in fig. 6 for gels with different catalyst additives. The shape and tendency of shrinkage curves of the acid and base samples are similar to that described by Brinker et. al. [6]. The trioxane gel shows a quite different shrinkage curve. The shrinkage of gels with the trioxane additive becomes apparent at 150 °C, while the other gels undergo an initial expansion, then begin to shrink only at higher temperature (about 250 °C). In particular, trioxane gel exhibits a higher shrinkage rate and larger total linear shrinkage over the entire temperature range than do the other gels. These differences can be explained by the effects of trioxane on gel structure. Voids in the trioxane gel may be created by decomposition and/or burn out of trioxane residues and alkoxy/hydroxy fractions at elevated temperature. The skeletal densification may take place sooner and faster during heating than for the other gels. Another major difference between the trioxane gel and other three samples is that the others show an expansion over the temperature range 1000-1200 °C, corresponding to a "bloating" effect (which was clearly visible after the treatment), while the trioxane gels do not exhibit such an effect and maintain their integrity during sintering, at least over the temperature range explored, as shown in fig. 6 and Table III.

CONCLUSIONS

In summary, trioxane has a strong influence on the sol-gel and gel-glass transition processes. The active role trioxane plays in determining the sol and gel structure may account for the unique properties of trioxane catalyzed gels. Trioxane may affect the composition of the sol and gel. Trioxane gels retain less free water, more alkoxy, hydroxy and organic fractions. Trioxane may modify sol and gel structure so that the gel possesses a higher surface area. More significantly, trioxane may improve the properties of the sol and gel. It can reduce volatility of organic fractions and reduce capillary forces and drying stresses in gels. It can increase the rigidity and strength of sol/gel and improve integrity of the gel during the drying and firing processes.

The authors gratefully acknowledge the partial support of Celanese Engineering Resins, Inc., Chatham, NJ.

REFERENCES

1. T.M. Che, R.V. Carney, G. Khanarian, R.A. Keosian, and M. Borso, J. Non-Cryst. Solids, 102 , 280-287 (1988).
2. P.B. Dorain, J.J. Rafalko, J.E. Feeney, C.E. Forbes, R.V. Carney and T.M. Che, Better Ceramics Through Chemistry III, eds., C.J. Brinker, D.E. Clark and D.R. Ulrich (MRS, Pittsburgh, PA. 1988) p.523-526.
3. E.J.A. Pope and J.D. Mackenzie, J. Non-Cryst. Solids, 87, 185-198 (1986).
4. S. Sakka and K. Kamiya, ibid., 48, 31 (1982).
5. R.K. Iler, Chemistry of Silica, (John Wiley, New York, 1979) p. 225.
6. C.J. Brinker, W.D. Drotning and G.W. Scherer, in Better Ceramics Through Chemistry, eds.,C.J. Brinker, D.E. Clark and D.R. Ulrich (Mater. Res. Soc. Proc. 32, North-Holland, New York, 1984) pp.25-32.
7. "Trioxane: Specialty Chemical", Celanese Engineering Resins, Inc., Chatham, NJ. p.1. (1987).
8. Y.Nakajima, H. Imamura and F. Nakamura, Japan Patent, Kokai No. 54-107,926 (24 August 1979).
9. L.L. Hench and G. Orcel, et. al., J. Non-Cryst. Solids, 82, 1 (1986); ibid, 79, 177 (1986); ibid, 104, 170 (1988); ibid, 105, 223 (1988);
10. T. Adachi and S. Sakka, J. Non-Cryst. Solids, 99, 118-128 (1988).

EFFECT OF DOPANTS ON THE CRYSTALLIZATION OF ZIRCON FROM ZIRCONIUM SILICATE GELS

J.D. BARRIE AND M.J. MESHISHNEK
Materials Sciences Laboratory, The Aerospace Corporation, Los Angeles, CA 90009-2957

ABSTRACT

Zirconium silicate gels containing small amounts of foreign cations were found to exhibit different crystallization behavior as compared to undoped gels. The reaction to form the zircon phase was enhanced by the presence of these dopants, with zinc oxide additions causing the largest decrease in crystallization temperature. The crystallization behavior of these gels is compared to that of zircon prepared from alternative processing techniques.

INTRODUCTION

The development of spacecraft thermal control coatings requires the production of pigments which resist color center formation in the natural space radiation (UV, electron, proton) environment. One compound which has been suggested as a possible candidate for this application is tetragonal $ZrSiO_4$ (zircon). Unfortunately, this material is difficult to prepare in high purity and fine particle size by traditional ceramic processing techniques [1,2]. The presence of transition metal impurities significantly reduces the suitability of materials for optical applications due to undesired absorption bands in the solar spectral region. Recent studies have shown that sol-gel processing offers distinct advantages towards the synthesis of high purity materials, often at substantially lower temperatures than is required for traditionally processed ceramics.

Zirconium silicate gels have received considerable attention of late as precursors for alkali resistant glasses and glass ceramics [3,4]. Studies have been performed to ascertain the devitrification behavior of glasses containing zirconia-silica ratios as high as 60-40 [4,5]. The crystallization behavior of zirconium silicate gels prepared with and without addition of crystalline zircon seeds has been explored to demonstrate the possibility of solid-state epitaxy effects [6]. This novel approach has demonstrated that the nucleation of the zircon phase is indeed a rate limiting step at temperatures below 1300°C in 50-50 zirconia-silica gels, and that the addition of seeds drastically lowers the temperature at which crystallization to form zircon proceeds at measurable rates.

This paper examines the applicability of sol-gel processing to the formation of zircon pigments for thermal control paints, and addresses the effects of small amounts of dopants (incorporated to alter the optical properties and radiation stability of the pigments [7]) on the formation of crystalline tetragonal $ZrSiO_4$.

EXPERIMENTAL PROCEDURES

Zirconium silicate gels were prepared using a base catalyzed reaction of alcoholic solutions of the precursors for each component of the gel. A solution containing tetraethoxysilane (TEOS), zirconium-n-propoxide [$Zr(OPr^n)_4$] and ethanol (1:1:8 mole ratio) was prepared under flowing nitrogen and stirred until homogeneous. No attempt was made to prehydrolyze any of the components. The resultant solution was stable and did not form a gel without intentional addition of water. To initiate gelation, the solution was transferred dropwise into a solution containing distilled water, 12N ammonium hydroxide, and ethanol (6:6:24 mole ratio, pH 14) at a rate of 3-4 cm^3/min under constant stirring. The strongly basic conditions resulted in essentially instantaneous hydrolysis of all the components of the precursor sol, forming a compositionally homogeneous amorphous gel.

For the doped gels, dopants were added to the initial solution in the form of alkoxides (di-s-butoxyaluminoxytriethoxysilane), nitrates (aluminum nitrate, yttrium nitrate), or chlorides (cerium chloride). When using the hydrated nitrates and chlorides, the dopant was first allowed to stir for several hours with TEOS and ethanol prior to addition of the $Zr(OPr^n)_4$ to prevent premature precipitation of zirconium hydrous oxides in the sol. Zinc oxide dopants were added directly to the

Mat. Res. Soc. Symp. Proc. Vol. 180. ©1990 Materials Research Society

ammonium hydroxide solution as powders prior to addition of the sol.

Following gelation, the resultant submicron powders were rinsed in distilled water, dried at 80-120°C for several days, and stored in sealed containers prior to firing. Conversion of the gels to oxide powders was done in platinum crucibles in an electric furnace. Heating and cooling rates were kept constant at 20°C/min. The crystallographic transformation of the powders was monitored by powder x-ray diffraction (filtered Cu Kα radiation). The amount of zircon formed was determined qualitatively using the ratio between the (200) peak of zircon and the (101) peak of anatase (added at a constant 0.20 weight fraction as an internal standard).

RESULTS

The structural evolution of zirconium silicate gels proceeds through initial precipitation of tetragonal zirconia from the amorphous hydrous oxide gels. This initial crystallization of tetragonal zirconia within a residual amorphous phase is essentially complete by 1150°C, and has been noted in the devitrification of zirconium silicate glasses derived by the sol-gel route [3]. The mechanism by which the metastable tetragonal zirconia phase forms has not been fully explained, although Clearfield [8] presents some evidence that the tetragonal structure is induced by the formation of tetrameric zirconyl species in the sol stage which then aggregate in an ordered fashion during hydrolytic polymerization. (In slowly hydrolyzed sols, the tetragonal zirconia structure is formed at low temperatures, while the initial amorphous structure of the observed gels arises from the rapidity of the base catalyzed gelation.)

Upon additional heating, the tetragonal zirconia/residual amorphous phase powders react further, resulting in formation of the zircon phase. The time and temperature required to complete this conversion was found to depend significantly upon the presence of dopant species in the gels, with undoped gels demonstrating the most sluggish reactivity. Fig. 1 shows the structural evolution of a zirconium silicate gel in which 5% of the silicon component has been replaced by aluminum. Unlike the case of the undoped gels, in which tetragonal zirconia remains the major constituent up to 1400°C for isochronal (4hr.) firings, the aluminum doped gel begins to transform to zircon at 1150°C (a), and the transformation is nearly complete at 1400°C (e). While isothermal firings indicate only partial conversion to zircon at 1300°C after 4hr, the reaction is nearly complete after 10hr.

This transformation behavior was found to differ significantly depending on the identity and amount of the dopant added to the gel. Using the 5% aluminum doped gel above as a baseline, it was found that 1% ZnO enhanced the formation of zircon, while lesser amounts of aluminum, or equivalent amounts of cerium or yttrium were less effective towards inducing zircon crystallization. Gels containing both zinc and aluminum dopants transformed to zircon more slowly than those containing zinc alone, with concomitant formation of zinc aluminate spinels. The growth of zircon in the singly doped gels as a function of firing temperature is shown in Fig. 2.

In most cases, the formation of zircon was accompanied by the appearance of cristobalite peaks in the x-ray diffraction patterns, although this was not the case in the yttrium doped gels. The undoped and aluminum doped gels typically contained small amounts of monoclinic zirconia after firing above 1100°C.

DISCUSSION

Many studies have been performed which investigate the formation of zirconium silicate (zircon) from a variety of crystalline and amorphous precursors. Studies using crystalline precursors [6,9,10] typically find that the formation of zircon is enhanced when either the zirconia source is monoclinic zirconia or the silica source is quartz. These observations can be explained by the Hedvall effect [11], i.e., that the additional energy imparted to the system by phase transitions occurring within the reactants (monoclinic to tetragonal zirconia, quartz to cristobalite) promotes the reaction to form zircon. The results obtained in our study supports these findings.

In undoped gels, the initial reactions lead to the formation of tetragonal zirconia and amorphous silica. The relatively low reactivity of these components, unaided by strongly driven phase transitions, leads to the observed sluggish transition of these gels to form zircon. Only after prolonged firings at elevated temperatures (e.g., 24 hours at 1300°C) is there any indication of $ZrSiO_4$ formation. This is in good agreement with earlier studies on the formation of zircon from an amorphous sol-gel route [12].

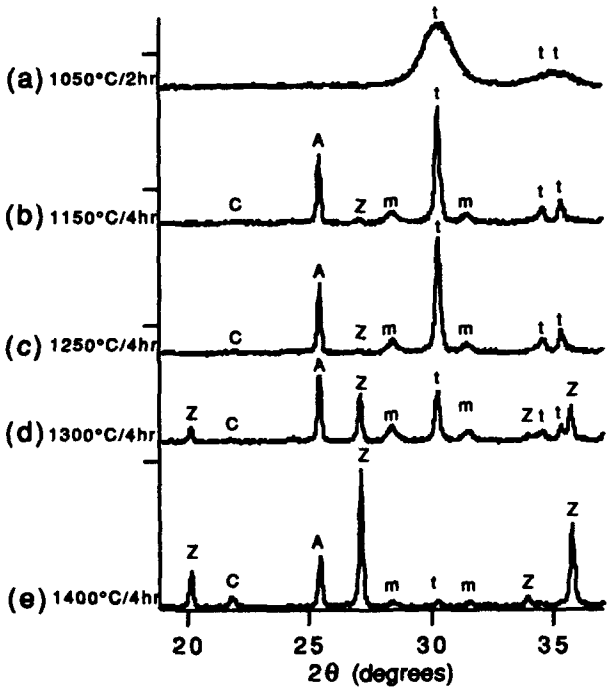


Figure 1. X-ray diffraction pattern of a zirconium silicate gel containing 5% aluminum upon firing for the conditions noted. Peak are labeled according to the convention: Z=zircon, C=cristobalite, A=anatase (internal standard), m=monoclinic zirconia, and t=tetragonal zirconia.

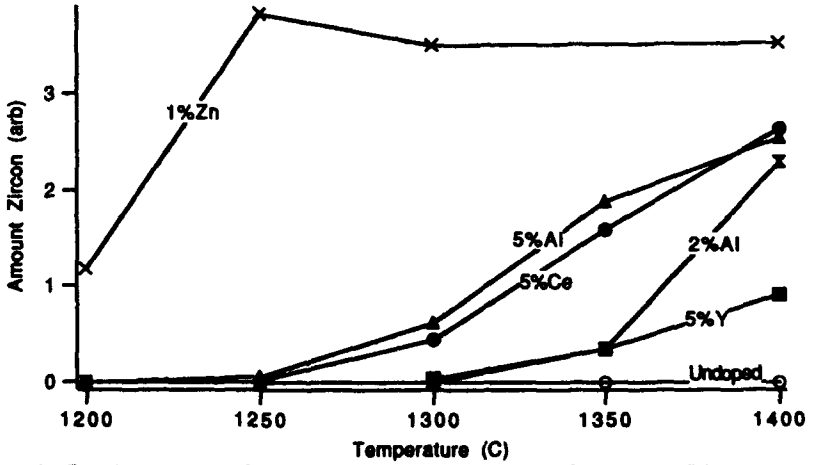


Figure 2. Relative amounts of zircon (as determined by x-ray diffraction) vs. firing temperature for isochronal anneals (4 hours) of zirconium silicate gels doped as noted.

However, in experiments using doped gels, the formation of zircon takes place at lower temperatures, and unlike the undoped gels, with accompanying formation of cristobalite. This suggests that the dopant, by some mechanism, enhances the reactivity of the amorphous silica phase, promoting interactions with itself (to form cristobalite) and with zirconia (to form zircon). Such a behavior with the addition of zinc oxide to ceramic systems is well known (the term mineralizer is frequently used). In the case of ZnO, the enhanced reactivity is thought to be of a solid state nature, rather than via the formation of a liquid phase. The weaker, but still significant, effects with the addition of aluminum, cerium, and yttrium also lead to the same conclusions. For while these dopants might be expected to stabilize the tetragonal zirconia phase, the reactivity of the system increases. In all instances the reaction to form zircon is faster in the presence of dopants than in the undoped gels. Thus the conclusion must be that the role of the dopant cations is as modifiers to the amorphous silicate network. The varying degrees of change in the reactivity are governed by a number of factors, including charge, electronegativity, and solubility of the dopants in the silica and zirconia phases.

The effects observed are in agreement with the work of Kadogawa and Yamate [13], who used other divalent cation mineralizers (incompatible with our studies) to lower the crystallization temperature of zirconium silicate gels, and Peplinkhouse [9], who observed a reduction in zircon crystallization temperature when mineralizers were added to mixtures of silica and zirconia.

CONCLUSIONS

The incorporation of divalent and trivalent cations into zirconium silicate gels strongly affects their crystallization behavior. In all cases the formation of tetragonal $ZrSiO_4$ is enhanced, with the ZnO containing gels having the lowest zircon crystallization temperatures. Each of the dopants seems to be acting as a classical mineralizer, with few complications such as the stabilization of intermediate phases. Thus the sol-gel route has been found to be an excellent technique for the synthesis of zircon with a controlled impurity content, i.e., where optical properties require the elimination of certain elements (such as iron or titanium) from the final powder, but where other dopants (either desired or innocuous) are tolerable. However, the results of this study raise the question as to whether the amorphous sol-gel route is the most appropriate for the formation of highly pure zircon. The increased reactivity of appropriately chosen crystalline precursors has been shown, and the purities obtained by the amorphous route are not unobtainable by these crystalline precursor processes.

ACKNOWLEDGEMENTS

The work was supported by the Aerospace Sponsored Research program. The authors appreciate the experimental assistance of K.A. Aitchison, P. Adams and J. Rodriguez. We thank A.B. Chase for many helpful discussions.

REFERENCES

1. C.E. Curtis and H.G. Sowman, J. Am. Ceram. Soc. 36, 190 (1953).
2. S.V. Ramani, et al., J. Am. Ceram. Soc. 52, 619 (1969).
3. Masayuki Nogami, J. Non-Cryst. Sol. 69, 415 (1985).
4. M. Nogami and M. Tomozawa, J. Am. Ceram. Soc. 69, 99 (1986).
5. Masayuki Nogami, J. Mat. Sci. 21, 3513 (1986).
6. Gabriel Vilmin, et al., J. Mat. Sci. 22, 3556 (1987).
7. A.B. Chase, et al., J. Appl. Phys. 38, 2469 (1967).
8. Abraham Clearfield, J. Mater. Res. 5, 161 (1990).
9. H.J. Peplinkhouse, J. Aus. Ceram. Soc. 15, 24 (1979).
10. K.V.G.K. Gokhale, et al., J. Mater. Sci. 4, 468 (1969).
11. J.A. Hedvall, "Reaktionsfachigkeit fester stoffe," (Verlag Johann Ambrosius Barth, Leipzig, 1938).
12. Richard F. Haaker and Rodney C. Ewing, J. Am. Ceram. Soc. 64, C-149 (1981).
13. Yukihiro Kadogawa and Tamotsu Yamate, Yogyo-Kyokai-Shi 93, 74 (1985).

EFFECT OF SnO_2 ON THE MECHANICAL PROPERTIES OF SiO_2/SnO_2 GEL-DERIVED COMPOSITES

R. DAL MASCHIO, S. DIRE', R. CAMPOSTRINI, G.D. SORARU AND G. CARTURAN
Dipartimento di Ingegneria dei Materiali, University of Trento, 38050 Mesiano, Trento, Italy.

ABSTRACT

The morphological evolution and SnO_2 crystallization of various gel-derived materials, composed of SiO_2-SnO_2 in the range from 34 to 5 wt % SnO_2, are studied in function of the thermal treatment in the interval 200-800 °C. SnO_2 phase separation occurring above 400 °C affects the density, the apparent porosity and mechanical properties like hardness and Young's modulus. At the lowest SnO_2 % a continuous density increase is observed on heating at variance with high tin dioxide contents for which the apparent density is almost constant. The results are discussed on the basis of SnO_2 crystallization, which occurs by two different mechanisms, evidenciated by X-ray analyses. The data will be compared with those of pure SiO_2.

INTRODUCTION

The synthesis of inorganic materials from solution by the sol-gel method allows complete phase homogeneity of precursors before chemical and thermal processes afford product formation. This homogeneous state is required for as long as possible during gel occurrence and subsequent heat treatments: thus,glass formation simply involves a continuous evolution of chemical and physical properties, whereas ceramics are born from sudden homogeneous nucleation. In the latter case, the absence of any crystalline phase detectable by X-ray analysis may not be a definite criterion for accepting the homogeneity of xerogels in the amorphous state, because of possible phase separation without crystallization. In the case of systems composed of different oxides and obtained from alkoxide precursors subjected to acid-catalyzed hydrolysis and condensation, phase separation without crystallization may be favoured by electronegativity differences among metal cations. The SiO_2/SnO_2 system a priori presents the most favourable features for observing separation of amorphous Sn(IV) oxides starting from $Si(OC_2H_5)_4$ and Sn(IV) species in strongly acidic alcohol solutions. The morphological evolution and SnO_2 crystallization of various gel-derived materials, SiO_2-SnO_2 in the compositional range from 34 to 5 wt % SnO_2, are studied in function of the thermal treatment in the interval 200-800 °C. SnO_2 phase separation and crystallization, occurring above 400°C, affects the density, the apparent porosity and mechanical properties like hardness and Young's modulus.

EXPERIMENTALS

Four compositions, corresponding to the molar ratios SiO_2/ SnO_2 1: 0.02, 1: 0.05, 1: 0.1 and 1: 0.2, were prepared by reacting $SnCl_4$ at 0 °C in an Ar flow with absolute ethanol. $Si(OC_2H_5)_4$ was added to the solutions at room temperature; the mixtures were refluxed for 2 h under vigorous stirring and subsequently hydrolized at room temperature. After about fifteen

Mat. Res. Soc. Symp. Proc. Vol. 180. ©1990 Materials Research Society

days the solutions, held in an open vessel, afforded solid gel pieces. These transparent,colourless monolithic gels were thermally treated in air at 200, 400, 600 and 800 °C with a heating rate of 2.5 °C/min. Apparent density measurements were performed by means of the Archimede's method in toluene. Hardness and Young's modulus were evaluated by Vickers and Knoop indentation method,respectively [1] .

RESULTS AND DISCUSSION

Simultaneous DTA + TG analyses performed with a heating rate of 10 K/min and alumina as reference sample, showed a thermal evolution substantially similar for all the compositions studied. In Figure 1 are reported the DTA and TG patterns of the sample with molar ratio 1: 0.2. It is possible to see a weight loss of about 48 % corresponding to a deep endothermic band centered at 150 °C, currently attributed to solvent evaporation and release of other by-products. Moreover an exothermic process occurs between 350 and 380 °C, tentatively assigned to primary SnO_2 separation.

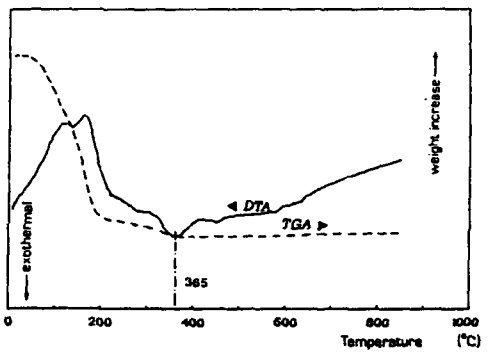


Figure 1 - DTA +TG of sample 1:02

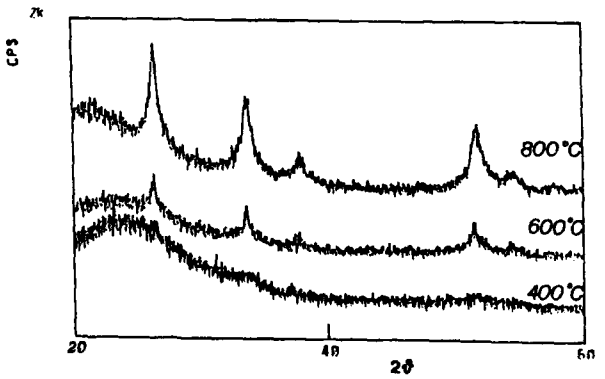


Figure 2- XRD of sample 1: 0.2 at different temperatures.

SnO_2 crystallization was ascertained by X-ray analysis, using Cu Kα radiation: relevant spectra for the same sample are reported in Figure 2 , where the phase evolution as function of temperature is shown. The determination of crystallite size for samples heated to 600 and 800 °C indicated a bimodal distribution of SnO_2 crystallites, falling in the interval up to 10 nm for about 80 % of the tin dioxide load, the residual fraction being observed at higher diameters. This microstructural situation was stable upon prolonged heatings for 5 days at 800 °C, suggesting that the bimodal distribution was not metastable, but rather the consequence of a two-step crystallization. Figure 3 shows the apparent density values as function of heating temperature for all the different compositions. For comparison the theoretic densities of samples constituted by silica glass (2.2 g/cm^3) and tin dioxide (6.95 g/cm^3) are also reported. These results suggest an increase of closed-pore volume, proportional to the SnO_2 content. In fact the composition 1: 0.02 at 200 °C displays an apparent density smaller than the corresponding value of silica (2.25 g/cm^3) [2], but approaches the theoretic density at 600 °C,being constant at 800 °C. On the contrary the composition with the highest SnO_2 load shows a density more or less constant as function of heating temperature, very far from the theoretic value .

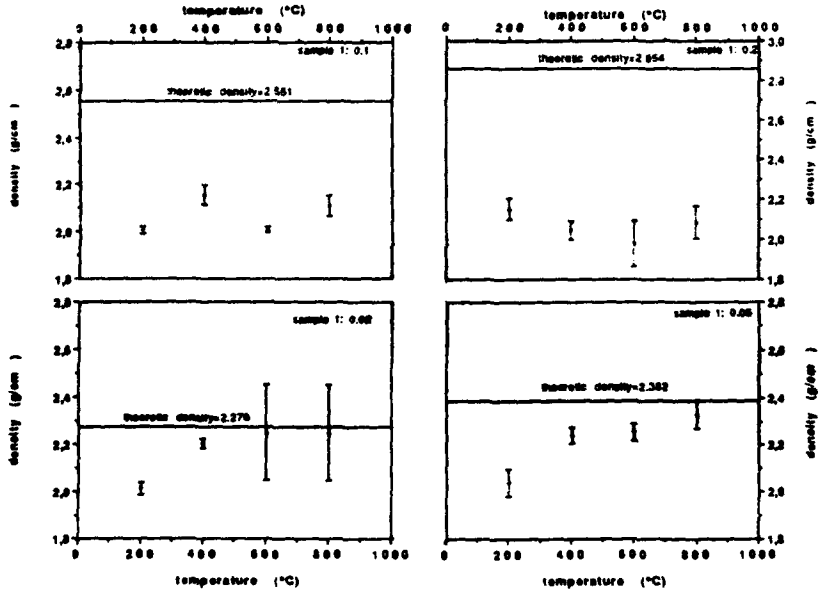


Figure 3 - Apparent densities of the different samples as fuction of temperature treatment

The Vickers hardness of these materials increases with temperature, as shown in Figure 4a. This trend is well evident in samples with the highest silica content, for which hardness values are comparable with those measured for silica gels [3]; as the tin dioxide content increases hardness is progressively lowered. Since the indentation hardness is determined by the area of specimen directly subjected to the applied load, hardness is directly affected by the total porosity. In case of our porous materials, the Young's modulus values reported in Figure 4b are similar for all samples untill 400 °C as observed for hardness trends; above 600 °C a general dependence of SnO_2 is observed, attributable to the formation of additional apparent porosity coarsened by a second crystallization of tin dioxide. The Knoop indentation method may be a reliable approach for measuring Young's modulus of xerogels: in fact for silica gel-derived materials Knoop results were found comparable with other methods [4,5].

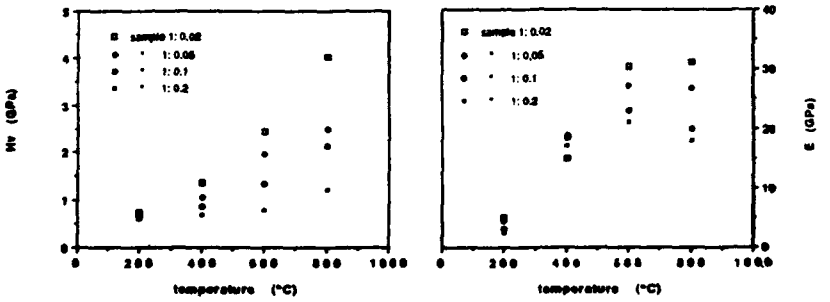


Figure 4 - a) Vickers hardness of the different samples as function of temperature treatment;
b) Young's modulus of the different samples as function of temperature treatment determined by the Knoop indentation method.

CONCLUSIONS

The addition of Sn(IV) to $Si(OC_2H_5)_4$ in strongly acidic alcoholic solutions modifies the SiO_2 gel properties. Moreover the crystallization of SnO_2, from 400 to 800 °C, probably occurs by two different mechanisms leading a noticeable closed porosity proportional to SnO_2 load. This phenomenon greatly influences mechanical properties like hardness and Young's modulus.

REFERENCES

[1] D.B.Marshall,T.Noma and A.G.Evans, J.Am.Ceram.Soc. **65**, C 175 (1982).
[2] N.Tohge,G.S.Moore and J.D.Mackenzie, J. Non-Cryst. Solids **63**, 95 (1984).
[3] M.Yamane,S.Aso,S.Okano and T.Sakaino, J. Mat. Sci. **14**, 607 (1979).
[4] T.Woignier,J.Phalippou and R.Vacher, Mat. Res. Soc. Symp. Proc. **121**, 697 (1988).
[5] G.D.Sorarù,M.Guglielmi and R.Dal Maschio, J. Non-Cryst. Solids **100**, 440 (1988).

CRYSTALLIZATION AND PHASE TRANSFORMATION OF ZrO_2-SiO_2 GELS

XIAOMING LI and P.F. JOHNSON
New York State College of Ceramics at Alfred University, Alfred, NY 14802

ABSTRACT

Pure SiO_2, ZrO_2 and SiO_2-ZrO_2 gels have been prepared by hydrolysis and gelation of tetraethylorthosilicate (TEOS) and zirconium acetate solution. The crystallization and phase transformation of SiO_2 and ZrO_2 in these gels have been followed up to 1450°C using differential thermal analysis (DTA), thermal gravimetric analysis (TGA) and X-ray diffraction analysis (XRD). The crystallization and phase transformation behavior of SiO_2 or ZrO_2 is quite different in different gel systems. It was found that in pure SiO_2 gel, the cristobalite phase was precipitated out at about 1000°C. In the pure ZrO_2 system, tetragonal (t-) phase zirconia was crystallized at about 430°C, t-ZrO_2 crystals grew three dimensionally and the activation energy for growth was calculated as about 365 $kJmol^{-1}$. But in the SiO_2-ZrO_2 system, the presence of ZrO_2 suppressed the crystallization of SiO_2, and SiO_2 increased the initial crystallization temperature and the stability of t-ZrO_2.

INTRODUCTION

Zirconia-containing silicate glasses have attracted much attention because of their excellent resistance to alkali corrosion and their low thermal expansion. Much work has been done on ZrO_2 based glass-ceramics due to the potential for transformation toughening. Attempts to toughen silicate glass by introducing ZrO_2 have been reported recently and these attempts show potential for improving fracture toughness [1-3]. Very few studies have been conducted on SiO_2-ZrO_2 binary glasses because these glasses are very difficult to prepare by conventional melting due to the very high melting temperature of the oxides. Recently, a low temperature synthesis method (the sol-gel process) has been proposed to prepare SiO_2-ZrO_2 glasses with zirconia contents up to 60 mol% [4,5]. However, the role and the influence of SiO_2 and ZrO_2 on the crystallization and the consequent phase transformation behavior in these gels are still unclear. The crystallization behavior of silica and zirconia in the binary system and subsystems derived through sol-gel processes need more study. In the present paper, the crystallization and phase transformation in pure SiO_2, pure ZrO_2 and SiO_2-ZrO_2 gels have been studied and compared.

EXPERIMENTAL

$Si(OC_2H_5)_4$ (TEOS) and zirconium acetate solution (22 wt.% ZrO_2), were used as precursor materials. The clear binary sol with the composition of 45 wt% ZrO_2 · 55 wt% SiO_2 was prepared using 2 steps. First, the TEOS, water, ethanol and HCl catalyst (in 1:1:4:0.1 mole ratio) were mixed by vigorously stirring at room temperature. The homogeneous solution was allowed to prehydrolyse for 1 hour at room temperature. Second, the zirconium acetate solution was added drop by drop into the prehydrolyzed silica alkoxide solution while continuously stirring. The resulting solution was then poured in a Teflon container and allowed to gel at room temperature. The pure SiO_2 and ZrO_2 gels were prepared as references, using the same precursors.

A differential thermal analyzer (DTA) (Model DTA 1700, Perkin-Elmer, Norwalk, CT) was used to observe the dehydration, condensation, decomposition, crystallization and phase transformation behavior of the gels. The heating rates were from 2.5°C to 20°C and α-alumina was used as the reference for the DTA. Thermal gravimetric

Mat. Res. Soc. Symp. Proc. Vol. 180. ©1990 Materials Research Society

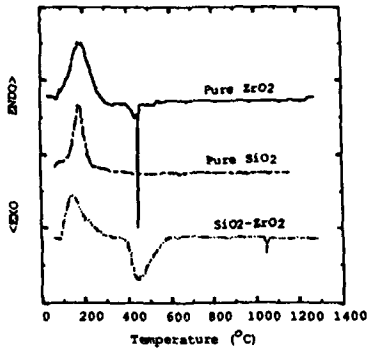


Fig. 1 DTA of gels (heating rate 10°C/min)

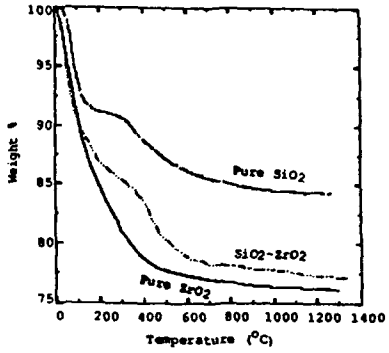


Fig. 2 TGA of gels (heating rate 10°C/min)

analyses (TGA) (Cahn TG716, Cahn Inst., Cerritos, CA) were performed using a heating rate of 10°C/min to get information complementary to DTA.

In order to avoid the transformation of tetragonal (t-) zirconia into monoclinic (m-) zirconia by the stresses imposed during x-ray diffraction sample preparation, the dried gel samples were crushed into powder prior to heat treatment. Firing of powders was performed in an electric furnace with flowing air. The samples were heated at a rate of 180°C/hr to the desired temperatures (400, 500, 800, 1000, 1200 or 1450°C) and held at that temperature for 2 hours. Finally, powders were cooled to room temperature by quenching in air.

Powder x-ray diffraction was performed using a x-ray diffractometer (Model 12000, Norelco, Phillips Electronic Instruments, Mount Vernon, NY) using Cu-Kα radiation with a single crystal graphite monochrometer. The XRD patterns were obtained for gels heat treated at different temperatures in order to determine the crystallinity and to identify the crystallized phases present at various temperatures.

RESULTS AND DISCUSSION

The DTA curves for the gels are illustrated in fig. 1 and the TGA results in fig. 2. All gels show an endothermic peak around 150°C in the DTA curve which corresponds to the weight loss in TGA caused by desorption of physically adsorbed water in that temperature range. It is notable that all TGA curves showed a significant weight loss around 400°C which is due primarily to the removal of chemically bonded water and the decomposition and pyrolysis of unhydrolyzed alkoxy radicals and organic fractions. The continuous weight loss above 450°C is presumably attributed to continued dehydroxylation of the gels. The DTA curves of both pure ZrO_2 gel and SiO_2-ZrO_2 gel showed a significant exothermic peak around 430°C. However, the peak for the pure zirconia gel was much narrow and sharper than that for the SiO_2-ZrO_2 gel. This may indicate that the exothermic effects of these two gels are caused by different reactions. The x-ray diffraction results (see figs. 3-5) show that the SiO_2-ZrO_2 gel (fig. 5) is still amorphous after heat treatment at 500°C, thus the exothermic reaction of SiO_2-ZrO_2 gel around 430°C is attributed to the decomposition and combustion of residue organic fractions. For pure zirconia gel on the other hand, the TGA curve (fig. 2) shows little weight loss around 430°C, and the x-ray diffraction results (fig. 3) indicate that the gel is amorphous after treatment at 400°C, but crystallised into the tetragonal phase of ZrO_2 after treatment at 500°C. Therefore, the sharp exothermic peak observed for the

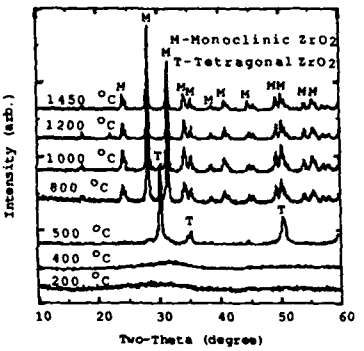


Fig. 3 XRD of pure ZrO2 gel

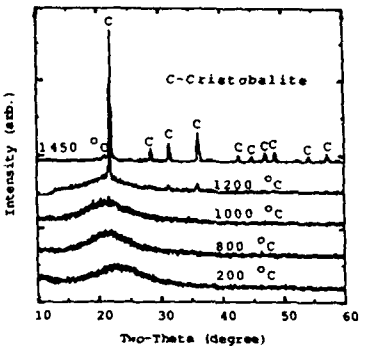


Fig. 4 XRD of pure SiO2 gel

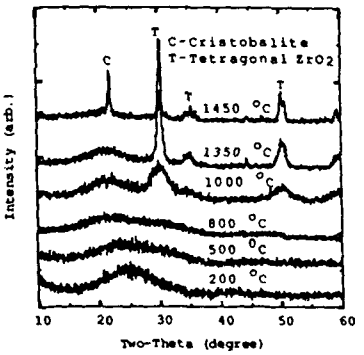


Fig. 5 XRD of SiO2-ZrO2 gel

pure zirconia gel at about 430°C is caused mainly by the crystallization of t-zirconia. In addition, the DTA curve for the SiO_2-ZrO_2 gel shows a small exothermic peak at about 1010°C. The corresponding TGA curve does not show any significant weight loss at that temperature. From the x-ray diffraction patterns shown in fig. 5, this peak could be attributed to the precipitation of tetragonal zirconia from the SiO_2-ZrO_2 binary gel. It is quite interesting that, for the pure SiO_2 gel, no significant exothermic peak was found on its DTA curve at temperatures from 300°C to 500°C. This may indicate that the pure SiO_2 gel had been more completely hydrolyzed (hence less pyrolysis and combustion of unhydrolyzed organic residues) than the pure ZrO_2 and the SiO_2-ZrO_2 binary gels. The weight loss of the pure SiO_2 gel around 400°C is primarily due to removal of chemically bonded water from the gel.

As shown by the x-ray diffraction patterns in figures 3,4 and 5, all starting powders were amorphous and there is no indication of crystalline phase in the gels below 400°C. The crystallization and phase transformation behavior of gels summarized from x-ray diffraction results is presented in Table I.

Crystallization/precipitation and phase transformation of tetragonal ZrO_2 in glass-ceramics are important for ZrO_2-toughened glass ceramics. It has been reported by several investigators that ZrO_2 may crystallise directly from the amorphous phase

Table I. Crystallization response of gels fired at different temperatures for 2 hours as shown by X-ray diffraction (A, Amorphous; C, Cristobalite; T, Tetragonal ZrO_2; M, Monoclinic ZrO_2).

Composition wt%	200°C	400°C	500°C	800°C	1000°C	1200°C	1450°C
Pure SiO_2	A	A	A	A	A	A+C	C
Pure ZrO_2	A	A	T+A	M+T	M+T	M	M
55 SiO_2·45 ZrO_2	A	A	A	A	A+T	T+A	T+C

into the tetragonal phase at low temperatures, even though the monoclinic phase is the thermodynamically stable phase at these temperatures. The tetrahedral zirconia phase, as already mentioned, begins to form in pure zirconia gel around 430°C. It is notable that the XRD pattern of SiO_2-ZrO_2 gel heated to 1000°C has a broadened peak at $2\theta \cong 30.2°$, indicating that the precipitation of very fine tetragonal zirconia crystals does not take place until temperatures above at least 800°C.

It is also interesting that the tetragonal phase of zirconia is more stable in the SiO_2-ZrO_2 system than in pure ZrO_2 gel. In pure ZrO_2 gels, most zirconia is transformed from the tetragonal phase to the monoclinic phase after treated at temperatures higher than 500°C. But in SiO_2-ZrO_2 gel, after heating upto 1350°C, the sample contained a well crystallized metastable tetragonal phase, without the monoclinic zirconia phase. The t-ZrO_2 phase was stabilized in the SiO_2 matrix even after heat treatment at 1450°C during which the amorphous silica matrix was crystallized into cristobalite. The transformation temperature of t- to m-ZrO_2 is strongly affected by the silica glass matrix.

Knowledge of the crystallization behavior of SiO_2 is also important in silicate glasses. In the pure SiO_2 gel, a cristobalite phase was crystallized from the amorphous phase at about 1200°C. This crystallization is undesirable because the phase transformation of cristobalite during heating causes a large volume change and may break the sample. On other hand, silica remains as amorphous phase in SiO_2-ZrO_2 gel even after heat treatment upto 1350°C. Zirconia has been used as nucleation agent in conventionally melted silicate glasses to induce and promote the crystallization of the glass. In this study, however, the presence of ZrO_2 suppressed crystallization of SiO_2.

Nogami *etal.* reported that in the SiO_2-ZrO_2 binary system, nuclei are formed in the gel; the t-ZrO_2 crystals grow three-dimensionally; the activation energy for crystal growth is about 680 kJ·mol^{-1} and seems to be independent of the ZrO_2 content [4]. But for pure ZrO_2 gel, the crystallization mechanism and kinetics still lack study. DTA can be used to study the crystallisation kinetics of glass-ceramics and the value of activation energy for the crystal growth can be evaluated using DTA data. The non-isothermal crystallization of glass is described by the equation [6]

$$\ln[-ln(1-x)] = -n\ln\beta - 1.052\frac{mE}{RT} + constant \qquad (1)$$

where x is the volume fraction crystallized at temperature T, β is the DTA heating rate and E is the activation energy for the crystal growth, R the gas constant. The constants n and m are numerical factors that depend upon the crystallization mechanism. The Avrami parameter, n, ranges between $n = 1$ for surface crystallisation and $n = 3$ for bulk crystallization. The value of m is equal to n when the nuclei are already formed in the glass before heating in DTA, or $m = n - 1$ when the nuclei are formed during DTA heating. The volume fraction of crystal precipitated at a temperature can be obtained by comparing the DTA peak area up to that temperature to the total peak area under the DTA curve. For the pure ZrO_2 gel, the volume fraction of crystal precipitated up to 425°C is plotted against the heating rate in Fig. 6. The relation between $ln[-ln(1-x)]$ and $ln\beta$ gives a straight line with a value of $n = 3.1$. The value of n may be taken as 3 because it should be an integer. The plot of $ln[-ln(1-x)]$

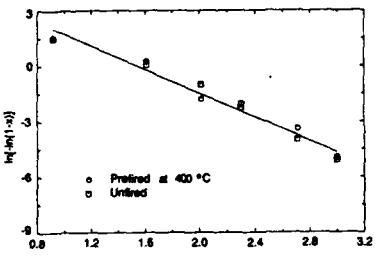


Fig. 6 Relation of crystal volume fraction with heating rate for ZrO2 gel

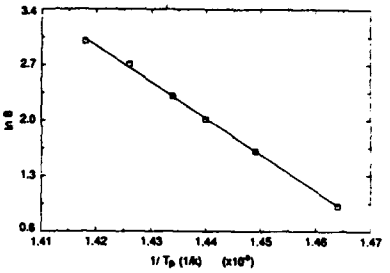


Fig. 7 Relation of heating rate with peak temperature for ZrO2 gel

against $ln\beta$ for the pure ZrO_2 gel which was preheated at 400°C for 1 hour for nucleation is also shown in Fig. 6. It is found that there is little change in the value of n, which indicates that the nuclei were already formed in the gel before DTA (i.e., before heat treatment) and the value of m is therefore 3. The experimental result, that both n and m are 3, suggests that in pure ZrO_2 gel as in SiO_2-ZrO_2 gel, bulk nucleation is dominant; the nuclei are sufficiently formed early in the gel stage before heat treatment and the crystals grow three-dimensionally.

Despite the similarity in crystallization mechanism for both pure ZrO_2 gel and SiO_2-ZrO_2 gel, the experimental results show that both SiO_2 and ZrO_2 have higher initial crystallization temperatures in SiO_2-ZrO_2 gels than in pure, their respective single component, gels and the tetragonal zirconia phase is more stable in SiO_2-ZrO_2 gel than in pure ZrO_2 gel. Whether the differences in crystallization and phase transformation behavior of SiO_2 and ZrO_2 in different gels can be related to the presence of anionic impurities or to the molecular structural configuration of ZrO_2 in glasses has not been addressed in this study. More work is required to clarify these details.

It is known that the degree of crystallization at the exothermic peak temperature reaches the same specific value, 0.7, regardless of the heating rate [6,7]. According to Eq. 1, the activation energy for crystal growth can be directly obtained from the slope of the straight line between $ln\beta$ and the reciprocal peak temperature, $1/T_p$. Figure 7 shows this relation. Using the slope of the straight line and the m value obtained above, the activation energy for growth was calculated to be 365 $kJ \cdot mol^{-1}$, which is much smaller than that for the SiO_2-ZrO_2 gel (680 $kJmol^{-1}$ in reference 4). More work is needed to determine why the t-ZrO_2 phase has lower initial crystallization temperature and crystal growth energy in pure ZrO_2 gel than in SiO_2-ZrO_2 gel. However, fig. 2 shows that the pure ZrO_2 gel exhibits higher weight loss than SiO_2-ZrO_2 gel, i.e., the ZrO_2 gel may have higher OH and organic fraction contents and lower viscosity than the SiO_2-ZrO_2 gel at temperatures below 400 °C. It is conceivable that this would result in a lower initial crystallization temperature and crystal growth activation energy in pure ZrO_2 gel than in SiO_2-ZrO_2 gel. It is also possible that t-ZrO_2 may kinetically grow faster in pure ZrO_2 gel than in SiO_2-ZrO_2 gel. It has been reported that t-ZrO_2 crystals larger than a critical size transform into m-ZrO_2 during cooling, and the critical size for the free particles of tetragonal sirconia is about 30 nm, while the critical particle size for constrained particles is much larger, e.g. 600 nm in an Al_2O_3 matrix [8]. From our STEM investigation results [9], the crystal size in pure ZrO_2 gel is about 30-50 nm after firing to 500°C and about 150-300 nm after firing to 1450°C. On the other hand, the size of ZrO_2 crystalline precipitate in SiO_2-ZrO_2 gel is smaller than 10

nm after firing to 1350°C. It is obvious in this study that tetragonal zirconia could be stabilized by the particle size effect. Small crystalline particle sizes favor stabilization of tetragonal zirconia and retain almost all of the ZrO_2 in the tetragonal phase. This fact may also be attributed to the greater interaction of SiO_2 and ZrO_2 in binary gels. It was possible to obtain a greater homogeneity and reactivity between the two oxides in the binary system, which prevents growth of the ZrO_2 crystals. The stability of the tetragonal phase of zirconium oxide largely depends upon the nature and amount of the second phase. The presence of SiO_2 mixed with ZrO_2 seems to decrease the formation of monoclinic zirconia. In addition, the growth of t-ZrO_2 is controlled by the Ostwald ripening coarsening process [4]. The diffusion and segregation of Si^{4+} or Zr^{4+} ions, which are expected to be the rate controlling steps in the crystallization and the phase transformation processes, are more favored in pure SiO_2 or pure ZrO_2 gels than in SiO_2-ZrO_2 binary gel.

SUMMARY

The crystallization and phase transformation behavior of ZrO_2 and SiO_2 in different systems derived by the sol-gel method have been investigated. It was found that:

1) In pure ZrO_2 gel, tetragonal zirconia precipitates at quite low temperature (around 430°C) and is easily transformed to the monoclinic phase. When heated to 1200°C, only the monoclinic phase is shown to be present by XRD.

2) In pure SiO_2 gel, the cristobalite phase precipitates at about 1200°C and the all gel is crystallized as cristobalite after heating to 1450°C.

3) In SiO_2-ZrO_2 gel, tetragonal zirconia precipitates at high temperature (above 800°C) and it is quite stable in the amorphous SiO_2 matrix. The precipitation (crystallization) temperature of cristobalite phase of SiO_2 is higher in SiO_2-ZrO_2 gel than in pure SiO_2 gel.

4) The activation energy for the crystallization of tetragonal ZrO_2 phase in pure ZrO_2 gel (365 $kJmol^{-1}$) is much lower than in SiO_2-ZrO_2 gel. The low temperature precipitation of metastable tetragonal zirconia crystal in pure ZrO_2 gel occurs due partly to the small activation energy of crystallization.

REFERENCES

1. Y. Ikuma, W. Komatsu and S. Yagashi, J. Mater. Sci. Lett., 4, 63-6, (1985).
2. M. McCoy, W.E. Lee and A.H. Heuer, J. Am. Ceram. Soc., 69, 292-6 (1986).
3. G.L. Letterman and M. Tomosawa, Am. Ceram. Soc. Bull., 65, 1370 (1986).
4. M. Nogami, *etal.*, J. Non-Cryst. Solids, 69, 415-423 (1985); ibid, 100, 298-302 (1988); J. Am. Ceram. Soc., 69, 99-102 (1986); J. Mater. Sci., 21, 3513-3516 (1986).
5. I.M.M. Salvado, C.J. Serna and J.M.F. Navarro, J. Non-Cryst. Solids, 100, 330-338 (1988).
6. K. Matusita *etal.*, Bull. Int. Chem. Res., Kyoto Univ., 59, 159 (1981); J. Mater. Sci., 19, 291 (1984).
7. T. Osawa, Polymer, 12, 150 (1971).
8. R.C. Garvie and M.F. Goss, J. Mater. Sci., 21, 1253 (1986).
9. Xaioming Li and P.F. Johnson, To be published.

PREPARATION OF THE POROUS SUPPORTS WITH SiO_2-ZrO_2-Na_2O COMPOSITION.

Y. TSURITA AND K. WADA
Research Center, Mitsubishi Kasei Corporation, 1000 Kamoshida-chou, Midori-ku, Yokohama City, 227 JAPAN

ABSTRACT

A new method for preparation of porous mixed oxide with SiO_2-ZrO_2-Na_2O composition was investigated by heating the sol-gel derived SiO_2 microsphere gel in the presence of $ZrOCl_2$ and NaCl. Surface of the products was composed of sponge-like structure, similar to the porous glasses manufactured by the phase separation method. Their pore volumes ranged from 1.0 to 1.5 cc/g(pore radius 100-1000Å) and their pore distributions were sharp, with peak tops of about 450-600Å in radius.

INTRODUCTION

Porous glasses containing ZrO_2 are of considerable technological interest due to their high resistant property to the alkaline solution. In recent years, two methods were reported to prepare these glasses. Eguchi et al. [1] have shown the preparation of SiO_2-ZrO_2 based porous glasses from SiO_2-ZrO_2-B_2O_3-CaO-Na_2O mother glasses by the phase-separation method. Nogami [2] prepared another SiO_2-ZrO_2 porous glass through the sol-gel route. The amount of ZrO_2 could be easily controlled with this method. However, it was difficult to obtain the porous glasses with pore size larger than 50Å in radius.

We have reported recently that a new method for preparation of SiO_2-ZrO_2-Na_2O porous glass through heating SiO_2-ZrO_2 gel in the presence of NaCl [3]. In this study, we will report the preparation of porous supports with SiO_2-ZrO_2-Na_2O composition by means of heating SiO_2 gel together with $ZrOCl_2$ and NaCl.

EXPERIMENTAL

Sample Preparation

Partial hydrolysis of tetraethoxysilane was performed by mixing 500g of tetraethoxysilane, 136.3g of ethanol, 43.2g of water, and 18.7g of 0.1N-HCl ethanolic solution and refluxing at 60°C for 30 minutes. This solution was heated at 120°C for 2 hours and 150°C for 1 hour under Ar atomosphere to remove volatile material. 44.5ml of the resultant solution, mixed with 7.5 ml of cyclohexane and 22.5ml of t-amylalcohol, was added dropwise into an aqueous solution, which was composed of 433.9g of water, 13.5g of ethanol and 3.4g of Tween 20(Polyethylenesorbitane monolaurate), under stirring at about 970rpm, to form an O/W emulsion. Then, 58.5ml of 17% ammoniac aquous solution was added during 40 minutes, and stirred for 5 hours and let stood over night. A white gel was formed immediately at addition of ammoniac solution. The supernant solution was removed by decantation, the gel was washed with ethanol, collected by filtration and dried at 120°C for 5 hours.

Zirconium oxychloride 0.40g together with 0.29g of sodium chloride, was dissolved in 5ml of water. This solution was added to the dried gel 1.0g described above and dried at 120°C for 5 hours. The impregnated gel was heated to 600°C at a rate of 2°C/min., and kept under stream of air for 3 hours and heated again at the designated temperature for 5 hours in the furnace. The calcined sample was washed twice with water and with hot water(90°C), then collected by filtration.

Mat. Res. Soc. Symp. Proc. Vol. 180. ©1990 Materials Research Society

Sample Characterization

The pore distribution and the pore volume of the products were measured by the mercury penetration porosimetry. The surface area was obtained by a multipoint nitrogen adsorption isotherm using the BET method. XRD measurements were made using Cu-Kα radiation and SEM observation were performed on gold-coated fracture surfaces. The chemical compositions were determined by X-ray fluorescence.

RESULTS

The SiO_2 gel, a starting material in this study, was obtained as nearly spherical particles of about 5 to 20 micron in diameter. The present method of preparing microsphere from alkoxide was originally reported by Unger [4]. The surface of microsphere gel was generally smooth with dense coated layer, but inside of it was porous. This gel was porous enough to adsorb almost all of the salt solution.

Table I shows pore characteristics of four samples prepared under different conditions. For sample (A) to (C), an amount of $ZrOCl_2$ and NaCl was adsorbed and heated at 700, 730 and 760°C, respectively, for 5 hours. Sample (D) was prepared by heat-treatment of SiO_2 gel without salt impregnation.

The surface area and the pore volume reduced gradually as heating temperature increased for sample (A) to (C). The pore size distribution curves, given in Figure 1, were also shifted to the direction of the larger pore radius. The pore size distribution curves of sample (A) to (C) were rather sharp with the peak tops of pore radius around 500Å and their pore volumes in the range of 100 to 1000Å were more than 1.0cc/g. Sample (D), on the other hand, had the larger surface area and pore volume, as compared to (A), with broad pore size distribution curves.

The SEM photographs of sample (B) and (C) are demonstrated in Figure 2 and 3, respectively. The sponge-like structure analogous to phase-separated porous glass was clearly observed in both figures. The size of the sponge-like glass skeleton was about 400Å for sample (B) and about 700Å for sample (C), which was in accordance with the order of pore size. On the contrary to sample (B) and (C), the sponge-like structure was not observed on the surface of sample (A) by SEM observation even at 30000 magnification. The coated layer of particles of sample (A) remained almost unchanged, and their morphology was almost those of the gel, similar to that of sample (D).

In Figure 4 is illustrated X-ray diffraction patterns of sample (A) to (C). Silica phase remained amorphous, although tetragonal ZrO_2 phase was identified. The intensities of ZrO_2 peaks were gradually reduced as heat treatment temperature increased. Chemical analysis of sample (A) to (C) were shown in Table II. Sample (A) to (C) contained appreciable amount of Na_2O as well as ZrO_2. In contrast, Cl contents were less than 0.2 wt%, although they were qualitatively determined by X-ray fluoresence. It was estimated that Cl incorporation into products were about 20 times less than that of Na.

Table I. Pore Characteristics of the SiO_2-ZrO_2-Na_2O Mixed Oxides.

Sample	Temp. (°C)	Surface Area(m^2/g)	Peak of Pore Radius(Å)	Pore Volume(cc/g) 100-1000Å	20-10000Å
A	700	77	400	1.88	2.41
B	730	48	453	1.45	2.09
C	760	23	604	1.01	1.13
D	700[1)]	255	149, 447	1.99	2.97

1) without salt impregnation

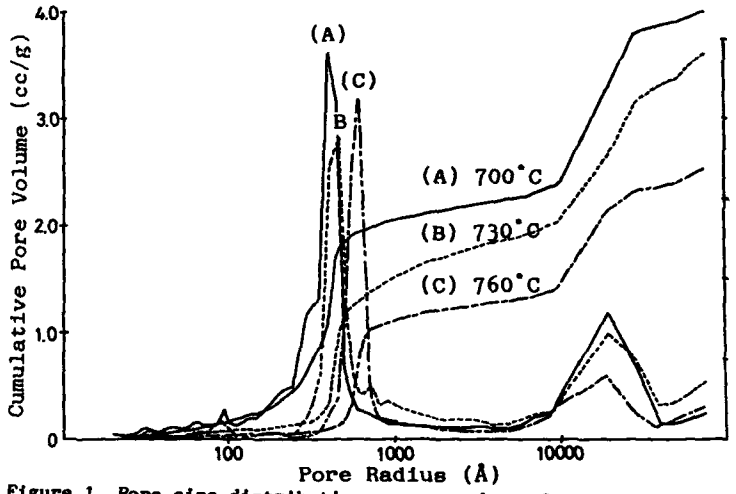


Figure 1. Pore size distribution curves and cumulative pore volume of the SiO_2-ZrO_2-Na_2O mixed oxides.

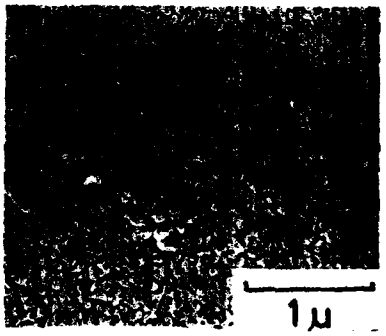


Figure 2. SEM micrograph of the sample (B).

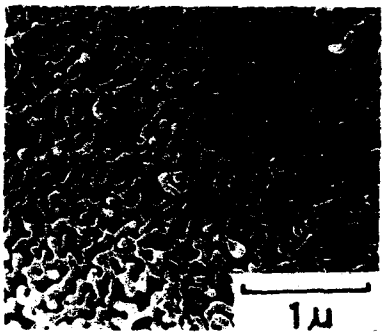


Figure 3. SEM micrograph of the sample (C).

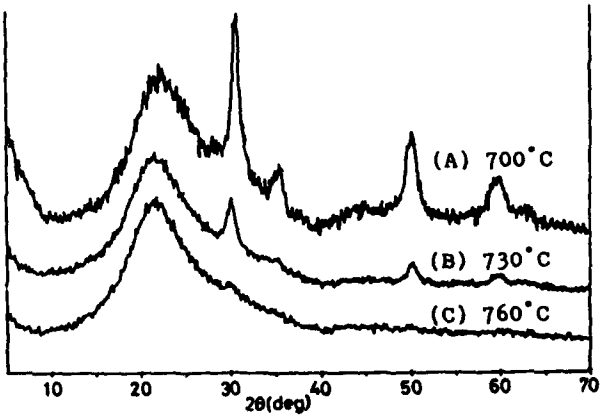


Figure 4.

X-ray diffraction patterns of the SiO_2-ZrO_2-Na_2O mixed oxides.

Table II. Oxides Compositions (wt%)

Sample	SiO_2	ZrO_2	Na_2O	Total
A	78.6	15.2	3.4	97.2
B	81.7	13.0	3.7	98.4
C	82.5	12.2	4.4	99.1

DISCUSSION

The results presented above illustrated that the porous supports with SiO_2-ZrO_2-Na_2O compositions were prepared by heating SiO_2 gel with $ZrOCl_2$ and NaCl. The pore characteristics and SEM observation suggested that shrinkage and sintering of the gel particles via liquid phase sintering were advanced as the heating temperature increased, the degree of them were in the order (D)<(A)<(B)<(C). The porous glass-like structure were clearly observed in the sample (B) and (C). The pore size equallization of these samples was attributed to formation of the glassy skeletons from the gel particles and to the rather uniform size of them.

It is well-known that salt impregnation of SiO_2 gel and the subsequent heat-treatment caused densification together with crystallization of SiO_2 gel to α-cristobalite [5]. The similar results were obtained when the same SiO_2 microsphere gel was heated with NaCl at 760°C for 5 hours [6]. In the presence of ZrO_2, crystallization of SiO_2 was supressed, and the incorporation of Na_2O into the compostion was identified. It was believed that the SiO_2-ZrO_2-Na_2O glasses were formed by the process described above, however a part of ZrO_2 was remained crystalline, which caused some heterogenity of ZrO_2 distribution.

The present procedure of making SiO_2-ZrO_2 based porous supports is quite simple compared with phase separation method, and especially suited for preparation of microsphere particles. In addition, pore volume of the products is larger than that of the conventional porous glasses, and their composition is unique owing to the presence of Na_2O.

CONCLUSION

The porous mixed oxide supports with SiO_2-ZrO_2-Na_2O composition were obtained when the sol-gel derived microspherical SiO_2 gel was heated together with $ZrOCl_2$ and NaCl at 730 and 760°C for 5 hours. They had the following properties:

1) The surface of the particles was glassy texture like that of the porous glasses derived from the phase separated glasses,
2) The pore size distributed mainly around 500Å in radius and the pore volume in the range of 100-1000Å was more than 1.0cc/g,
3) The approximate composition was SiO_2:ZrO_2:Na_2O=89:7:4 mol%. Silica phase remained amorphous, however there existed tetragonal ZrO_2 phase.

REFERENCES

1. K. Eguchi, H. Tanaka, T. Yazawa and T. Yamaguro, U.S.Patent No.4,778,777 (18 Oct. 1988).
2. M. Nogami, Yogyo-Kyokai-shi,93(4),195(1985).
3. Y. Tsurita, K. Kawai and K. Wada, The 30th Symposium on Glass, The Glass Division of the Ceramic Society of Japan(Kyoto, 1989), abstracts P.3.
4. K. Unger, J. Schick-Karb and K. Krebs, J. Chromatogr.,83, 5(1973).
5. K. Krebs and H. Heinz, D.E.Patent No. 2,042,910(1972).
6. Y. Tsurita and K. Wada, unpublished results.

STUDIES IN THE Ba-Ca-Al-O SYSTEM
CHEMICAL MODIFICATION OF ALUMINUM ALKOXIDE BY PROPIONIC ACID

V. HEBERT*, S. VILMINOT* and D. BRION**
* I.P.C.M.S., Groupe des Matériaux Inorganiques, EHICS, 1 rue Blaise Pascal, 67008 Strasbourg Cedex, France
** Thomson Tubes Electroniques, 2 rue Latécoère, Velizy-Villacoublay, France

ABSTRACT

Barium and calcium aluminate powders have been elaborated using chemical methods like coprecipitation, alkoxide polymerization and metalloorganic decomposition. These powders have been successfully used for impregnation of porous tungsten cathodes for use in electronic tubes. Spectroscopic studies on the modification of aluminum s-butoxide reveal that carboxylic acid substitutes OR groups forming preferentially bidentate chelating complexes.

INTRODUCTION

Dispenser cathodes for use in electronic tubes are currently elaborated by immersion in a melted oxide mixture of a porous tungsten element.

Tungsten powder, with a mean grain size around 4 um, is isostatically pressed into bars and subsequently sintered at 2200 °C under hydrogen atmosphere. In these conditions, the final porosity equals 18 %. The impregnated cathods are obtained by partial immersion in a melting of barium and calcium aluminate, the liquid entering the porosity by capillarity. The cathods are then chemically cleaned, to completely remove the surface aluminates, dried at 100°C and conserved in a nitrogen atmosphere in sealed pockets before use.

Different aluminates have been checked and typical compositions are referred as 4.1.1. (4BaO - 1CaO - 1 Al_2O_3) and 5.3.2. (5BaO - 3CaO - 2Al_2O_3). Barium is the emitting element, aluminum being introduced in order to limit Ba evaporation and calcium to lower the extraction energy.

The aluminates are currently prepared by solid state reaction from a mixture of $BaCO_3$, $CaCO_3$ and Al_2O_3 in stoichiometric proportions. One of the main problems encountered with the cathods elaborated from these powders is that the electronic emission stops before all the barium available inside the pores has been consumed. This observation leads to the possible existence of heterogeneities within the impregnant powder. Chemical routes, like oxalate coprecipitation, alkoxide polymerization and metalloorganic decomposition, have therefore been developed in order to improve the homogeneity, to obtain a more reactive powder and to lower the melting point. In a second part, we have considered the modification of aluminum alkoxide by propionic acid in order to get more insight into the elaboration process from metalloorganic decomposition.

POWDER ELABORATION

Three different routes have been used for the elaboration of barium and calcium aluminates : oxalate coprecipitation, alkoxide polymerisation and metalloorganic decomposition.

Oxalate coprecipitation

Whereas calcium oxalate is nearly insoluble in water, the barium compound is slightly soluble in acidic solutions. Addition of oxalic acid in an aluminum salt solution does not yield precipitation. It therefore appears necessary to adjust the pH value in order complete precipitation to be obtained.

Mat. Res. Soc. Symp. Proc. Vol. 180. ©1990 Materials Research Society

Another possibility is to use another solvent in which the corresponding oxalates are less soluble. Both processes have been developed. Aluminum, barium and calcium are introduced as nitrates, this anion being easily decomposed by further thermal treatment. The use of chlorides, that are much more soluble, has been avoided due to their possible retention in the powder

If precipitation is performed in aqueous solution, the pH value has to be adjusted to a value of 8.5 by means of ammonia, yielding a powder with a final composition very close to the expected one. For lower pH values, incomplete precipitation of barium is observed. For higher pH values, the final powder reveals a deficiency in both calcium and aluminum oxides. X-ray diffraction analysis on the precipitate shows the presence of $CaC_2O_4.H_2O$ and $BaC_2O_4.0.5H_2O$, aluminum hydroxide being not detected.

The other method concerns the use of a mixture of water and ethanol as a solvent. Whereas the nitrates are dissolved in water, oxalic acid is dissolved in ethanol, in order to achieve a 30/70 water to ethanol ratio. X-ray diffraction analysis reveals the presence of barium oxalate, calcium oxalate and $MAl_2(C_2O_4)_4.xH_2O$ double oxalates (M = Ba or Ca).

In both cases, the precipitates have been calcined at 1000°C before characterization.

Alkoxide polymerization

Whereas barium and aluminum alkoxides are soluble in their parent alcohol, this no more the case for calcium, whose alkoxides are insoluble solids. However, it has been shown [1] that heteroatomic alkoxides are often more soluble. This property has been used for the elaboration of a solution containing both Ca and Al .

Reaction of barium metal with ethanol yields barium ethoxide, $Ba(C_2H_5O)_2$, very easily. The same reaction with aluminum and calcium metals proceeds much more slowly and is activated under reflux by use of iodine as catalyst. According to the litterature [1], a mixed aluminum and calcium alkoxide is obtained with formulae, $Ca[Al(OEt)_4]_2$. The Al/Ca ratio corresponds to the 4.1.1 aluminate formulation. Both alcoholic solutions are mixed and gelation is performed by dropwise addition of water dissolved in ethanol under vigorous stirring yielding the formation of a translucent gel. After solvent elimination, the resulting powder appears to be amorphous by X-ray diffraction. Exposure to room atmosphere yields the formation of barium carbonate.

Metalloorganic precursor decomposition (M.O.D)

Such a route has been previously used in our laboratory [2, 3] in the elaboration of ceramic powders like titanates or YBaCuO. Aluminum s-butoxide, $Al(OC_4H_9)_3$ dissolved in the parent alcohol is added to a solution of barium and calcium propionates, giving rise to a clear solution. Thermal decomposition at 150°C yields the formation of a resin by polymerization. Further heating gives rise to the powder.

POWDER CHARACTERIZATION

The powders have been characterized by different methods such as T.G.A., D.T.A., X-ray diffraction, specific area measurements and microscopic observation. The main results are summarized in Table I.

TABLE I
Main characteristics of the 4.1.1. powders after 1000°C calcination

Process	Melting point (s)	X-ray diffraction	specific area m^2/g	S.E.M. observation
Oxalate	1469 - 1542	$Ba_3CaAl_4O_{12}$ + $BaCO_3$ + CaO	4	4 um
Alkoxide	1544	"	< 1	1 um
M.O.D.	1470 - 1556	"	12	6 um

The following observations can be drawn from these results :
- alkoxide polymerization is the only process that gives rise to a powder exhibiting a unique melting point,
- this same process yields powders with the smallest grain size,
- in all cases, the same phases appear to be present.

These powders have been used for impregnation of tungsten cathods and allow current densities of the order of 4 to 4.9 A/cm^2 to be obtained (4.1.1). The durability of the emission is actually under study.

MODIFICATION OF Al S-BUTOXIDE BY PROPIONIC ACID

The last part of this paper will focuse on the modification of aluminium s-butoxide by propionic acid, that takes place during the first steps of the MOD process. This study has been done by infra-red spectroscopy and ^{27}Al NMR. The evolution of the viscosity with increasing propionic acid amounts has also been followed.

Structure of s-$Al(OBu)_3$

The structure of aluminum alkoxides has been the object of numerous studies [4,5] which have shown that most alkoxides exist as dimers, trimers or tetramers. This association is related to the tendency of Al to maximize its coordination number. On the other hand, sterically bulky OR groups impede the conversion of tetra coordinated Al atoms to higher coordination. Aging also has a great influence since it has been shown that freshly distilled aluminum isopropoxide is proposed to be a trimer but rearranges to a tetramer after a few weeks at room temperature [6]. No definite answer concerning the structure of aluminum s-butoxide has been proposed and a mixture of oligomers has probably to be considered.

Viscosity evolution with propionic acid modification

This study has been carried out by using a concentric cylinder viscometer at room temperature. $Al(OBu)_3$ was dissolved in toluene at a concentration of 0.8 M. Increasing amounts of propionic acid were then introduced.

Up to Ac/Al = 1, Ac/Al being the molar ratio of propionic acid to aluminum alkoxide, the viscosity does not vary significantly. An important increase up to Ac/Al around 1.75 is then observed (Figure 1). Further acid addition promotes a strong decrease of the viscosity.

These results show that, in the domain 1 < Ac / Al < 1.8, the formation of cross linked species takes place resulting in an increase of the viscosity. Further acid addition promotes the rupture of intermolecular bonds yielding the viscosity decrease.

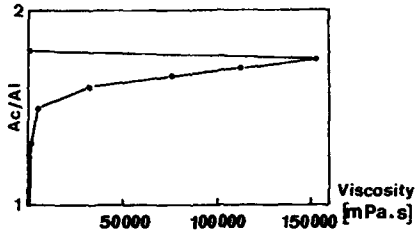


Figure 1 : Viscosity evolution with Ac/Al

Infra-red studies

The study has been performed on an FTIR Nicolet apparatus, the aluminum alkoxide being dissolved in CCl_4 (4wt %). Figure 2 gives some recorded spectra for different Ac/Al ratios. Propionic acid is expected to substitute OR groups giving rise to $Al(OR)_x(C_2H_5COO)_y$ species, as it has been already observed in the case of acetic acid [7]. Such species can be identified by I.R. spectroscopy with appearence of vibrations characteristic of the carboxylic group, whose positions depend on the mode of bonding : monodentate (M), bidentate bridging (B) or chelating (C). Except at low Ac/Al ratios (< 0.5), propionic groups mainly appear as bidendate chelating. A semi-quantitative evolution based on the band areas is represented on figure 3. It clearly appears that three kinds of carboxylic groups are present up to Ac/Al = 1. At Ac/Al = 1.8, a new band is detected around 1710 cm^{-1} whose position is characteristic of an excess of propionic acid. Its intensity increases with further acid addition, the other bands being unchanged.

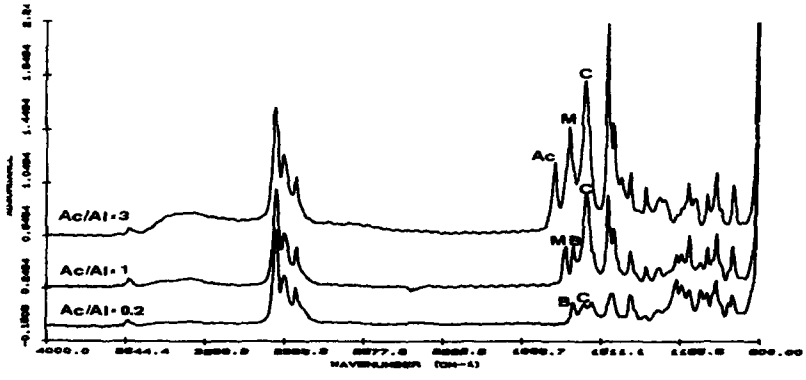


Figure 2 : Infra-red spectra after addition of propionic acid,
M = monodentate, B = bridging, C = chelating

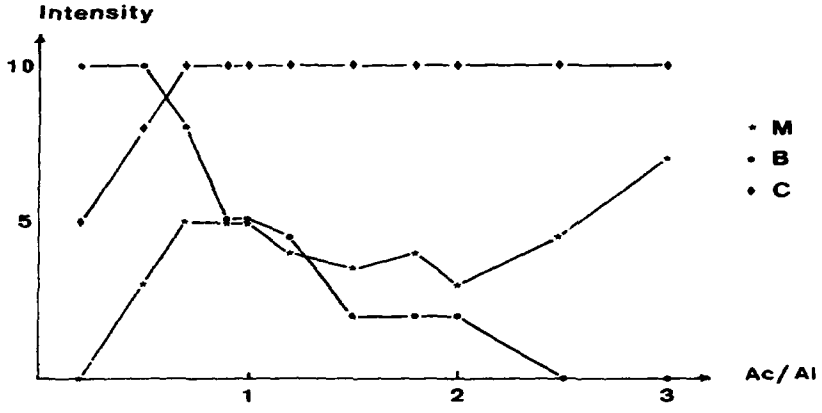


Figure 3 : Evolution of the infra-red absorption bands with Ac/Al

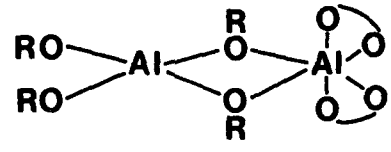
^{27}Al N.M.R. results

^{27}Al NMR spectroscopy is a promissing method of ascertaining the structures and presence of single oligomers in solution. A certain complication stems from the quadrupole moment of the ^{27}Al nucleus, which causes considerable dependence of the signal width on the gradient of dielectrical field around the Al nucleus. The quadruple broadening can be reduced partially by measuring spectra at 80°C.

Al(^{s}OBu)$_3$ has been dissolved in toluene and some spectra have been recorded after addition of increasing amounts of propionic acid.

Pure alkoxide reveals a broad line around 55 ppm that can be attributed to tetrahedrally coordinated aluminum. This result seems to indicate that Al(^{s}OBu)$_3$ is mainly present as a dimer.

For Ac/Al = 1, two signals with similar intensities are observed, one at 58 ppm, the other one at 9.7 ppm. It then appears that aluminum exhibits both tetrahedral and octahedral coordinations. Due to the relative intensities, a model with two chelating propionate groups on the same Al atom can be proposed.



Such a model has been evidenced in the X-ray structure of β-diketonate complexes [8]. However, other possibilities cannot be rejected, on the basis of infra-red results.

For Ac/Al > 1, the NMR spectra appear much more complicated with appearance of numerous new bands. Other measurements are in progress.

CONCLUSIONS

Chemical routes, like coprecipitation, alkoxide polymerization and metalloorganic decomposition, have been used for the elaboration of barium and calcium aluminates. Powder characterizations reveal that the alkoxide route allows fine powders with a unique melting point to be obtained. These powders have been successfully used for cathod impregnations, giving rise to emitting densities around 4 A/cm^2 (4.1.1 composition).
The modification of Al s-butoxide by propionic acid has been followed by infrared and ^{27}Al N.M.R. spectroscopies. These preliminary results seem to indicate that the carboxylic group is preferentially bonded to Al as a bidentate chelating ligand.

ACKNOWLEDGEMENT

We wish to thank the "Direction des Recherches, Etudes et Techniques" (DRET) for its financial support.

REFERENCES

1. R. von Scholder and H. Protzer, Z. Anorg. Allg. Chem. 340, 23 (1965).

2. E. El Hadigui, PhD. Thesis, Strasbourg University, (1988).

3. S. Vilminot, S. El Hadigui, A. Derory, M. Drillon, J.C. Bernier, J.P. Kappler, R. Kuentzler and Y. Dossmann, Mat. Res. Bull. 23, 521 (1988).

4. D.C. Bradley, R.C. Mehrotra and D.P. Gaur, in Metal Alkoxides (Academic Press, New York, 1978).

5. O. Kriz, B. Casensky, A. Lycka, S. Fusek and S. Hermanek, J. Magn. Res. 60, 375 (1984).

6. R.C. Mehrotra, J. Indian Chem. Soc. 30, 585 (1953).

7. K.C. Pande and R.C. Mehrotra, Z. Anorg. Allg. Chem. 236, 291 (1956).

8. J.H. Wengrovius, M.F. Garbauskas, E.A. Williams, R.C. Going, P.E. Donahue and J.F. Smith, J. Am. Chem. Soc. 108, 982 (1986).

SOL-GEL SYNTHESIS OF THIN FILMS FOR USE AS PLANAR WAVEGUIDES*

G.W. DALE, H.H. FOX, BRIAN J.J. ZELINSKI** and LAURA WELLER-BROPHY***
**Materials Science and Engineering Department, Arizona Materials Laboratory, University of Arizona, Tucson, Arizona 85721
***Optical Data Storage Center, Optical Sciences Center, University of Arizona, Tucson, Arizona 85721

SiO_2-TiO_2 sol-gel solutions and synthesis techniques have been developed to produce thin films of proper index, thickness and quality for use as planar waveguides. The composition of the synthesized films ranged from 50 to 68 mole % TiO_2 and produced layers with indices ranging from 1.7 to 1.8. Final film thicknesses ranged from 1000 to 3000 A and varied as a function of the coating chemistry and conditions. Also, changes in film shrinkage and index with heat treatment were determined and compared to literature data on similar films used as antireflective coatings. Finally, confirmation of the waveguiding qualities of these films was made through prism coupler measurements conducted by the University of Arizona Optical Sciences Center.

INTRODUCTION

Sol-gel technology has led to the development of gel forming solutions that are deposited on substrates, gelled, and then densified. These solutions, particularly those containing silica or titania precursors, have been used in a number of applications. Spin-on dielectric films of silica and titania have been developed to create an insulating layer of inorganic oxides on semiconductors such as GaAs and InP [1]. Antireflective coatings from SiO_2-TiO_2 have also been fabricated [2,3,4]. These methods involved tailoring the refractive index by varying the relative amounts of SiO_2 and TiO_2 in the resulting film.

Amorphous SiO_2 has an index of refraction of approximately 1.46, while TiO_2 has an index of refraction over 2.6. The thickness of the spun-on film depends on the spin speed, solution concentration, and solution chemistry. Thus, by tailoring the chemistry of the precursor solutions, films of desired index of refraction and thickness can be made.

Dielectric films may also be used as planar optical waveguides [5,6,7,8]. Unlike other approaches to waveguide synthesis, the sol-gel method permits the embossing of a master grating into the undensified waveguide for generation of integrated optic surface-relief gratings [5-8]. These gratings can be used as input and output couplers as well as Bragg reflectors. Roncone [9] et al. of the Optical Sciences Center at the University of Arizona have generated SiO_2-TiO_2 waveguides from commercial solutions with losses less than 1 dB/cm. They have also embossed surface features into the films of a depth and quality suitable for use in optical components.

In the present paper, the sol-gel approach is used to produce SiO_2-TiO_2 coatings for waveguide applications. The solutions, which are stabilized to hydrolysis using complexing agents [10,11], yield films of excellent homogeneity. The effect of composition on refractive index of films from the complexed solution is compared to literature data for all alkoxide solutions

*This paper was presented at the Fourth International Conference on Ultrastructure Processing of Ceramics, Glasses, and Composites, February 19-24, 1989, Tucson, AZ. In was inadvertently omitted from publication in the Proceedings of that Conference.

Mat. Res. Soc. Symp. Proc. Vol. 180. ©1990 Materials Research Society

[2,4]. The effect of processing conditions on shrinkage as well as refractive index is also discussed. The index and thickness results from prism coupler measurements of films which support waveguide modes are also reported.

EXPERIMENTAL

Solution Preparation:

Details of the solution synthesis will be presented in forthcoming papers. In general, tetraethoxyorthosilicate (TEOS), titanium butoxide, and a complexing agent were combined to form a 20 wt% solution in isopropanol (IPA). Solutions were prepared with compositions of 50:50, 42:58, and 33:67, moles SiO_2:TiO_2.

Sample Preparation:

The solutions were diluted in IPA to solids contents ranging from 3.3 wt% to 10 wt%. They were then spin coated onto single crystal silicon wafers at 4,000 rpm for 15 sec, covering the surface of the wafer with the solution prior to spinning. The samples were then heated in air. The effects of heat treatment were examined at temperatures ranging from room temperature to 600°C. The planar waveguide was produced from a 5wt% solution spin coated at 3,000 rpm for 45sec onto a soda-lime-silica microscope slide and fired at 400°C. All heat treatments consisted of plunging the samples into the hot furnace and withdrawing them after 15 minutes.

Sample Measurement:

The thickness and index of the samples were measured using a Gaertner L116-B ellipsometer employing a He-Ne laser (0.6328μm) at an incident angle of 70°. The substrate refractive index was taken as 3.85, with an extinction coefficient of -0.02. The measurements were made under computer control. The thickness of the samples were also measured using a profilometer (Dektak IIA). Agreement between the values obtained by both methods was good.

The solution used to generate the film which successfully coupled a mode was coated onto a silicon substrate, fired to 400°C for 15 min and examined by scanning electron microscopy using a JOEL JSM840A. The film was featureless, showing no apparent porosity or pinholes at 10,000X.

RESULTS

The effect of concentration on coating thickness and index was investigated using the 42:58 solution. The thickness was found to increase linearly with concentration. Refractive index was not found to vary with concentration within experimental error, the data varying by less than 3%.

The effect of heat treatment on shrinkage and refractive index was examined using the 58 mole% TiO_2 solution diluted to 5 wt% for coating. The shrinkage showed a steady decrease with temperature (see Fig 1), leveling off at about 350°C; however, at higher temperatures the film is still shrinking slightly. An interesting aspect of this curve is that it does not exhibit the two regimes of shrinkage typical of sol-gel films (see Fig 2). The low temperature shrinkage is usually attributed to condensation reactions activated by the moderate heating. The higher temperature shrinkage is due to viscous sintering of the oxide film. The heat treatment used in this investigation is probably not sufficient to yield fully dense films.

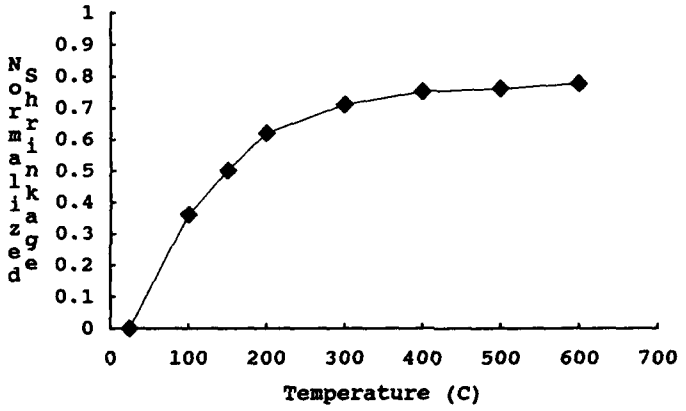


Fig 1: Per cent shrinkage versus temperature for 58 mole% TiO_2, 6.7wt% solution.

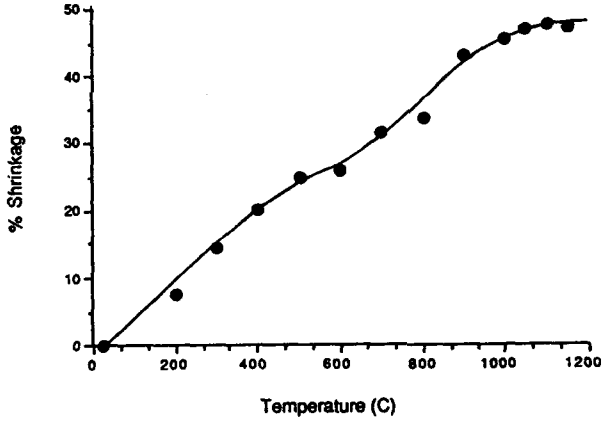


Fig 2: Typical shrinkage curve for sol-gel film.
Source: B.D. Fabes et al., J. Non-Crys. Solids 82 (1986) 349.

Details of the variation of index with heat treatment between the temperatures of 200 to 300°C were not obtainable. This was because ellipsometry measurements of films fired to these temperatures gave widely varying and inconsistent values of refractive index.

The index increased with temperature (see Fig 3), also leveling off at about 350°C. The increase in index would seem to be the result of the densification of the film with temperature.

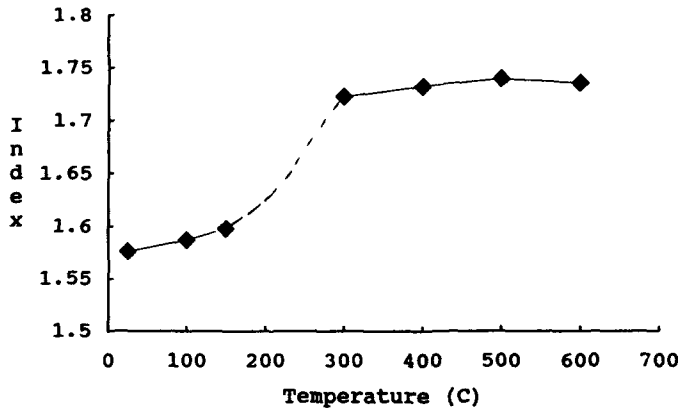


Fig 3: Refractive index versus temperature for 58 mole% TiO_2, 6.7 wt% solution. The dashed line indicates the temperature region over which widely varying and inconsistent values for refractive index were obtained.

The variation of refractive index with composition of the films was studied (see Fig 4). A best fit line was calculated by the least squares method for Brinker et al. [2], Yoldas [4], as well as for the current data. T-values were calculated for the three slopes to determine if the differences in slope were statistically significant. The values obtained were -0.038, 3.08, and 2.87 for Brinker et. al. vs. Yoldas, Brinker vs. current data, and Yoldas vs. current data, respectively at a confidence level of 0.95. Brinker and Yoldas used all alkoxide solutions while we added a complexing agent. The difference indicates that there is strong effect of precursors on the properties of the films.

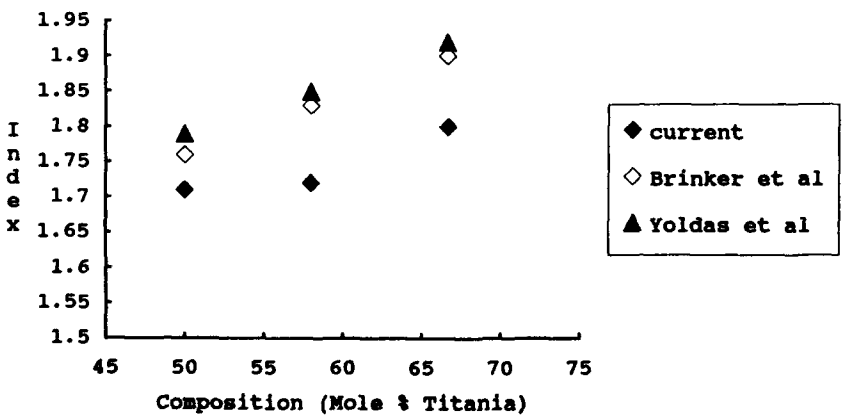


Fig 4: Refractive index versus composition for samples coated from a 10 wt% solution, fired at 400°C for 15 min. Data obtained is compared to data obtained by Brinker [2] and Yoldas [4].

Mode coupling was confirmed by prism coupler measurements of 50:50 SiO_2-TiO_2 films spun on soda-lime-silicate substrates at 3,000 rpm for 45 seconds. These measurements, made on two such films, provided values of film thickness and index of 2301 +/- 31 A and 1.7255 +/- 0.0023 respectively. The results compare favorably with ellipsometry measurements conducted on the same films spun on silicon substrates at 4,000 rpm for 15 seconds. The ellipsometry measurements indicated the thickness to be 1580 A and the index to be 1.732.

DISCUSSION

The temperature dependence of shrinkage and index (see Figs 2,4) are similar. At lower temperatures, less than 175°C, both properties show a strong dependence on temperature. The increased refractive index arises primarily from the increased density of the film. In the higher temperature region, greater than 300°C, both thickness and refractive index show a much weaker dependence on temperature. The difference in the temperature dependence of both properties can be explained by the liberation of solvent and further condensation reactions. Presumably, by 300°C the condensation of the SiO_2-TiO_2 network is virtually complete. Therefore, any changes in refractive index will be due only to decreases in the residual porosity, free volume, and decreasing hydroxyl content. At higher temperatures the only mechanism present for further shrinkage are viscous sintering and structural relaxation. Sintering at these temperatures is slow, requiring long times to densify the films completely. Presumably treatment above 600°C and longer than 15 min will continue to sinter the films; however in high TiO_2 content glasses it is possible that phase separation and crystallization of titania may occur before complete densification.

Between 175°C and 300°C the refractive index rises dramatically, indicating that there are more chemical reactions taking place. Samples prepared in this region, however, were not able to be measured successfully by ellipsometry. This is most likely due to rapid and uneven elimination of residual organic material leading to transient inhomogeneities in the film.

The dependence of refractive index on composition is significantly different from that previously reported [2,4]. The difference most likely is due to the effect of the complexing agent on the bonding of the alkoxide species. Gels made with the complexing agent form linear units that are weakly crosslinked. This produces a structure that is loose and more open in comparison to the others, thus yielding a lower refractive index. It is likely that the composition dependence of the refractive index (see Fig 5) is very different because the ultrastructure of the film depends on the relative amount of the complexing agent that is present during reaction.

CONCLUSIONS

A sol-gel approach to the synthesis of SiO_2-TiO_2 thin films for use as planar waveguides has been developed. The thickness and refractive index of the generated films stabilizes at temperatures of about 400-500°C. The final value and computational dependence of the refractive index differs slightly from those reported in the literature. It is likely that the use of different precursor materials lead to the observed variations. The use of these films as planar waveguides has been demonstrated by the observation of mode coupling in a 50 mole% SiO_2-TiO_2 film.

ACKNOWLEDGEMENTS

The financial support of the Optical Data Storage Center is gratefully acknowledged. We thank G. Teowee for experimental assistance. Special thanks to Ronald L. Roncone for the prism coupler measurements, Dr. B.D. Fabes for stimulating conversations, and Irene Browne for statistical analysis.

REFERENCES

1. R. Brusasco, et al., Mater. Res. Bull., 21 (1986) 301.

2. C.J. Brinker and M.S. Harrington, Solar Energy Materials, 5 (1981) 159.

3. R.B. Pettit et al., Solar Cells, 15 (1985) 267.

4. B.E. Yoldas, US Pat. #4,346,131 Aug 24, 1982.

5. K. Tiefenthaler et al., Proc. Soc. Photo-Opt. Instrum. Eng., 401 (1983) 165.

6. K. Heuberger and W. Lukosz, Appl. Optics, 25 (1986) 1499.

7. W. Lukosz and K. Tiefenthaler, Optics Letters, 8 (1983) 537.

8. N. Tohge et al., J. Non-Crys. Solids, 100 (1988) 501.

9. R.L. Roncone, L. Weller-Brophy, and B.J.J. Zelinski, "Sol-gel Synthesis of Planar Optical Waveguides and Integrated Components," Fourth International Conference on Ultrastructure Processing of Ceramics, Glasses, and Composites, February 19-24, 1989, Tucson, AZ.

10. C. Sanchez et al., J. Non-Crys. Solids, 100 (1988) 65.

11. H. Schmidt, J. Non-Crys. Solids, 100 (1988) 51.

PROCESSING OF SiO_2-TiO_2 THIN FILM WAVEGUIDES

L. Weisenbach*, T.L. Davis*, and B.J.J. Zelinski*
R.L. Roncone**, and L.A. Weller-Brophy**
*Arizona Materials Laboratories; **Optical Sciences Center;
University of Arizona, Tucson, AZ 85721

ABSTRACT

The shrinkage behavior and changes in refractive index of sol-gel derived SiO_2-TiO_2 thin films, with a composition of 50 mole %, were investigated. Two regions of shrinkage rate were observed, a rapid initial stage and a slower second stage. The refractive index of the film was found to be dependent upon the heat treatment. Samples prebaked to 100°C and processed at temperatures below 500°C were found to have lower indices than films processed without prebaking. Films heated to 700°C contained small crystallites of anatase uniformly distributed throughout the film.

INTRODUCTION

Thin films of SiO_2-TiO_2 have been studied previously as anti-reflectance coatings and planar waveguides. In 1979, Yoldas presented a method to synthesize uniform solutions of high titania content by compensating for the difference in hydrolysis rates of the components[1]. In 1981, Brinker et al.[2] investigated SiO_2-TiO_2 sol-gel films for use as anti-reflection layers. Lukosz et al. have used commercially processed solution to produce embossed gratings in thin SiO_2-TiO2 films with losses of < 1 db/cm in the waveguides.[3]

Recent work on this system in our laboratories has focused upon producing embossible, low-loss waveguide structures using solution chemistry techniques. A preliminary study by Dale et al.[4] investigated the effect of organic additive content and processing on the index and shrinkage of SiO_2-TiO_2 waveguides. Roncone et al.[5,6] studied the effect of processing on the embossibility of SiO_2-TiO_2 waveguides, for the purpose of producing passive optical devices, such as focusing grating couplers.

The purpose of this work is to investigate the densification behavior of SiO_2-TiO_2 thin films and characterize the change and reproducibility of refractive index and thickness with processing.

EXPERIMENTAL

An acid catalyzed solution of TEOS was prepared with a water:TEOS mole ratio of 2:1 and mixed for 30 minutes. Titanium tetrabutoxide was reacted with a complexing agent, 2,4-pentanedione (acetylacetone, acac), in a molar ratio of 1:2 and stirred for 20 minutes. The two solutions were mixed together in a molar ratio of 1:1 (SiO_2-TiO_2) and stirred for four days. This solution was diluted 1:1 by volume with distilled isopropanol prior to spinning.

Thin films were deposited onto a single crystal Si wafers by flooding the substrate with solution, and then spinning at 3000 rpm for 30 seconds using a Headway Spin Coater*. The coated substrate was then pre-baked for 1.5 minutes at 100°C prior to an isothermal heat treatment at higher temperatures. Thickness measurements were made on samples pre-heated to 100°C using a stylus

*Photo-Resist Spinner, model EC101, Headway Research, Inc., Garland, TX.

Mat. Res. Soc. Symp. Proc. Vol. 180. ©1990 Materials Research Society

profilometer[b], and multi-angle ellipsometry[c]. The pre-bake treatment was used because attempts to determine the just spun thickness of the films were not successful as the stylus scored the surface of the film and the ellipsometer gave erratic readings. Some samples were spun and then plunged into an isothermal furnace without pre-baking. Unless otherwise noted, the results presented refer to the pre-baked samples. The composition of the film samples was verified using RBS to be within 1 weight % of the target composition of 50 mole % TiO_2.

Shrinkage was determined using the expression $s = t_o - t/t_o$, where s= shrinkage, t = the film thickness after high temperature processing and t_o = the film thickness after the 100°C prebake. The thickness of the films after the 100°C prebake was 550 nm +/- 30 nm. The refractive index was measured using multi-angle ellipsometry. After firing at the processing temperature, the film thickness and index were remeasured.

RESULTS

Figure 1 is a plot of the relationship between shrinkage and time for the films processed at the indicated temperatures. Two regions of shrinkage rate are present. In the first few minutes at temperature, large amounts of shrinkage occur at high shrinkage rates. The rate and amount of shrinkage increase with temperature. In the second region, film shrinkage occurred at all temperatures at a much reduced rate. The films at all temperatures appear to approach a common endpoint shrinkage of 75%.

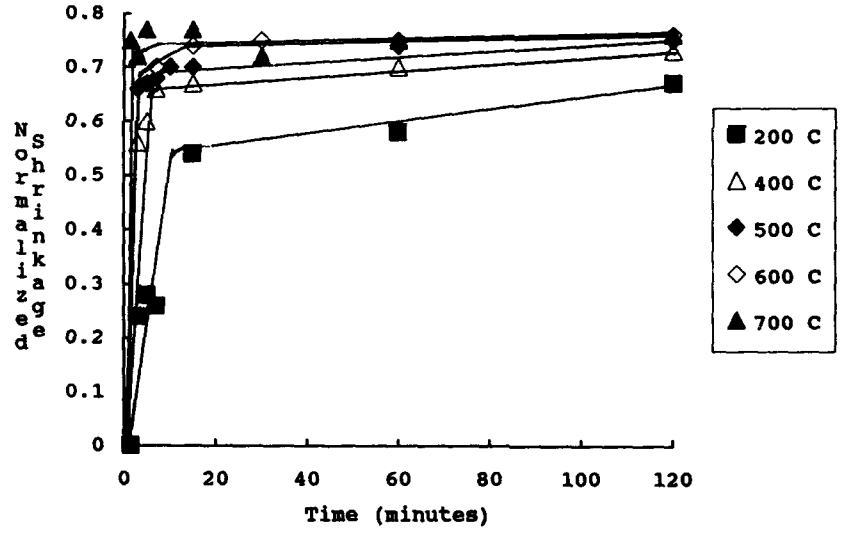


Figure 1: The normalized shrinkage of SiO_2-TiO_2 thin films is plotted as a function of the duration of isothermal heating at the indicated temperatures. The samples were prebaked for 1.5 minutes at 100°C.

---

[b]Dektak IIA Profilometer, Sloan Technology, Santa Barbara, Ca.

[c]Ellipsometer, model L116B, Gaertner Scientific, Inc., Chicago, Il.

Figure 2 is a plot of the normalized shrinkage of the films after 15 minutes of heat treatment. The shrinkage steadily decreases with temperature until about 400°C, when the curve flattens out, and appears to approach a final plateau of 75%. This shrinkage behavior is similar in form to that measured by Dale et al.[4] for films of 58 mole % TiO_2, synthesized using the same procedure.

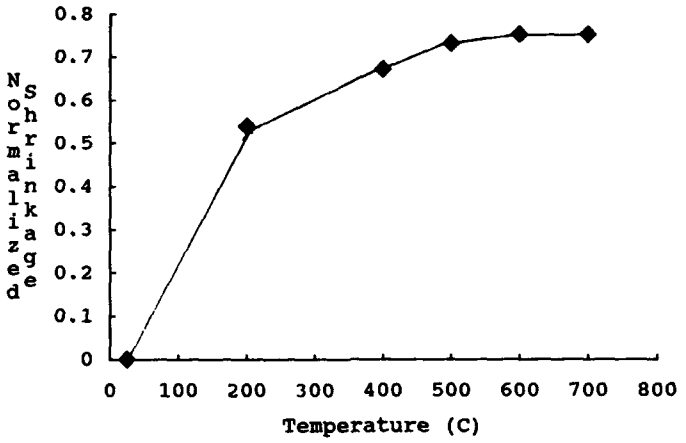


Figure 2: Normalized shrinkage plotted as a function of processing temperature for samples heated for 15 minutes.

The index change as a function of processing temperature at a constant time of 15 minutes is shown in figure 3. One set of samples in this study received a 1.5 minute pre-bake at 100°C, while the other set was plunged immediately into the hot furnace after spin coating. Between 200°C and 500°C, the index of the samples which were prebaked was lower than the samples which were spun and plunged immediately into the furnace. The largest divergence in index is seen at 400°C. Above 500°C, the differences between indices of the prebaked and non-prebaked samples become negligible. The DTA thermograph of a gel powder obtained when the coating solution was allow to evaporate to dryness exhibits a broad peak in the temperature range 200-500°C due to the decomposition of the organic complexing agent from the gel.

A plot of the normalized shrinkage versus refractive index is shown in figure 4a for samples heated for an hour at the indicated temperature. The figure shows the index increasing monatomically until 500°C, where the index levels off to a value of 1.74. Samples fired at 500°C and 600°C have almost identical values of index and thickness, indicating that an endpoint in development of film characteristics exists between these temperatures.

The increase in the index when the film is heated to 700°C, with no accompanying change in thickness, results from the presence of higher index anatase (TiO_2) crystallites within the film. Figure 4b is a high resolution micrograph of a sample heated to 800°C for 15 minutes showing small crystallites (<10nm in diameter) uniformly distributed throughout the film. Analysis of the optical diffractograms taken from these small crystallites revealed that they are anatase surrounded by an amorphous (presumably SiO_2-rich) matrix. The crystallization of anatase has been reported by other researchers as well.[7,8]

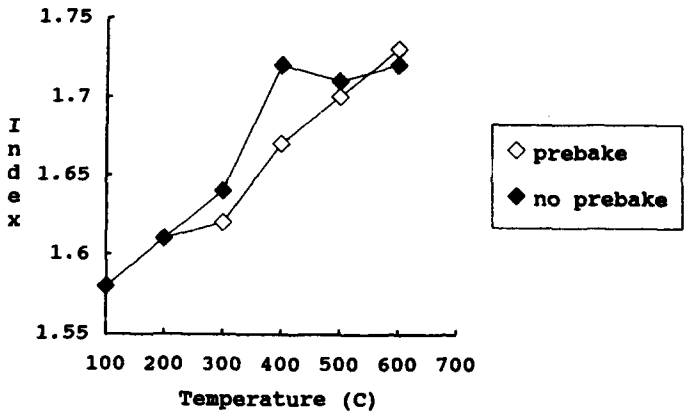


Figure 3: Refractive index plotted as a function of temperature for films fired for 15 minutes. The prebaked samples were heated for 1.5 minutes at 100°C prior to further isothermal processing.

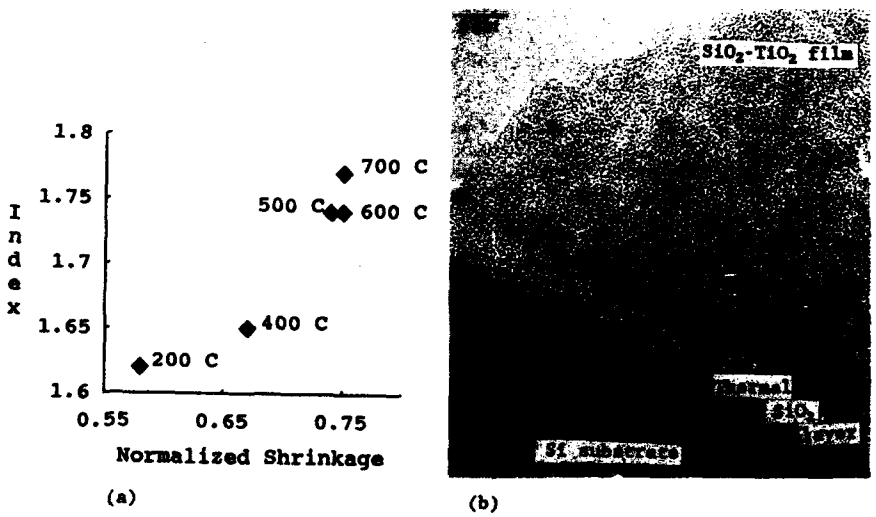


Figure 4: (a) Refractive index plotted as a function of normalized shrinkage for SiO_2-TiO_2 films fired for 1 hour at the indicated temperatures. (b) High resolution TEM micrograph of an SiO_2-TiO_2 thin film spun on a single crystal Si substrate and fired for 15 minutes at 800°C. Small crystallites of anatase are highlighted by the arrows.

DISCUSSION

The refractive index and thickness of the SiO_2-TiO_2 waveguides are strong functions of processing, with the duration and temperature of the heat treatment determining their values. In the temperature range where the organic chelating agent is decomposing, two regions of shrinkage rate are noted and the index is seen to be dependent upon the processing history of the film.

The role of the complexing agent in the solution is most likely to form linear units which are weakly crosslinked. The chelating molecule bonds to the Ti alkoxide specie and reduces the condensation rate by stearic hinderance. The presence of the organic complexing species in the film produces a flexible, relatively open skeletal structure. This structure contains a large amount of organic material consisting of unreacted hydoxyls and alkoxyls in addition to the chelating ligands.

Several shrinkage mechanisms may be operative in the films including, shrinkage via condensation reactions, structural relaxation, and viscous sintering. Condensation upon heating, resulting from the removal of complexing ligands, alkoxy and hydroxy groups, increases the skeletal density of the film. This process occurs quite rapidly at the temperatures of this study and leads to a rapid increase in skeletal density and film viscosity. This increase would naturally lead to the drastic reduction in the densification rate observed in the second region.

Another result of the higher viscosity may be the freezing in of excess free volume (formed by the removal of the large complexing groups via decomposition) in the skeletal structure of the film. This free volume would be removed only slowly at these viscosities by a structural relaxation mechanism. It is unlikely that viscous sintering plays any significant role in densification. However, this conclusion needs to be investigate further by determining if pores are present in the early stages of the process. TEM micrographs of a sample heated for 15 minutes at 400°C revealed no porosity present in the films[9].

The increase in refractive index with time and duration of heat treatment results from continued condensation. At short times and low temperatures, the more open film structure and the high carbon content resulting from the presence of the complexing agent results in a low value of refractive index. As the complexing agent decomposes and is removed from the structure, the skeletal density increases leading to an increase in refractive index.

The observation that the film index can be influenced by a prebake heat treatment suggests that the films contain some species which facilitate the condensation reactions. These species are most likely alcohols and acetylacetone. The prebake treatment to 100°C causes the volatilization of these species from the film. As a result, condensation reactions will be slower and the refractive indices will be lower in the prebaked samples than in films which were immediately immersed into a hot furnace. At temperatures above 500°C, the kinetics of the condensation reactions are apparently fast enough that the presence or absence of reaction enhancing agents is not important in determining the shrinkage or index development during a 15 minute hold.

CONCLUSIONS

The refractive index and film thickness of the SiO_2-TiO_2 waveguides were found to be strong functions of the thermal processing history. Under isothermal conditions, the shrinkage rate is initially very fast and then rapidly decreases to a much reduced rate. Between 200 and 500°C, index development is influenced by prebake heat treatments. Films which do not experience the prebake develop

higher indices during isothermal heat treatments. The presence of a prebake effect suggests that some volatile species are present in the film which facilitate the condensation reactions. An endpoint in processing is found in the temperature range 500-600°C. Also, heat treatments at 700°C cause small crystallites of anatase to crystallize uniformly throughout the film, leading to and increase in refractive index.

This work was supported by the Optical Data Storage Center at the Optical Sciences Center at the University of Arizona. The assistance of J. Leavitt and M. McCartney of the High Resolution Electron Microscopy Center at Arizona State University is gratefully acknowledged.

REFERENCES

1. B.E. Yoldas and T.W. O'Keeffe, Appl. Opt. 18(1979)3133.

2. C.J. Brinker and M.S. Harrington, Solar Energy Materials, 5(1981)159.

3. K. Tiefenthaler, V. Briguet, E. Buser, M. Horisberger and W. Lukosz, Proc. SPIE. 401(1983)165.

4. G.W. Dale, H.H. Fox, Brian J.J. Zelinski and Laura Weller-Brophy, these proceedings.

5. R.L. Roncone, L.A. Weller-Brophy, and B.J.J. Zelinski, presented at the Feb. 1989 Ultrastructure Conference in Tucson, AZ, to be published.

6. R.L. Roncone, L.A. Weller-Brophy, L. Weisenbach and B.J.J. Zelinski, submitted to the J. Non-Cryst. Solids for publication, July, 1990.

7. M.F. Best and R.A. Condrate, Sr., J. Mat. Sci. Lett., 4(1985)994.

8. S.M. Melpolder, private communication.

9. L. Weisenbach and B.J.J. Zelinski, to be published.

OPTICAL INTERFERENCE FILTERS BY SOL-GEL PROCESSING

J.L. KEDDIE AND E.P. GIANNELIS
Department of Materials Science and Engineering, Cornell University, Ithaca, NY 14853.

ABSTRACT

Optical interference filters have been synthesized by sol-gel. The selected filter is a multilayer of alternating TiO_2 and SiO_2 films. In transmission, the filter edge depends on the angle of incident light, which can be tailored through control of thickness and refractive index of the individual films. Theoretical modeling of the filter with film thicknesses obtained by Rutherford backscattering spectrometry is in good agreement with the experimental optical response.

INTRODUCTION

Optical filters that reflect or absorb light at selected wavelengths while transmitting in other regions are used to eliminate the halo effect on conventional cathode ray tubes (CRT) thereby increasing light output [1]. The presence of the halo inadvertently degrades the performance of the CRT display by decreasing the high spatial frequency contrast. This problem becomes exceedingly detrimental in high performance, high resolution displays, such as those used in defense systems.

Although antireflection (AR) coatings have been used for reducing the problem, they are inadequate when the incident light is at a high angle, such as with diffuse light sources like phosphors [1,2]. Using an interference filter, light emitted by the phosphor normal to the faceplate is transmitted, while light at an angle from the normal is reflected. Interference filters usually consist of a multilayered structure with layers alternating between high and low refractive index materials. One such filter, consisting of a TiO_2/SiO_2 multilayer, can increase the on-axis brightness of a CRT screen by a factor as high as 1.5 [3].

In the synthesis of a multilayer via sol-gel processing, several problems must be surmounted. One is the control of thickness and refractive index (optical thickness) of individual films that determine the optical characteristics of the filter. Two is the minimization of flaws and cracks. Three, and often overlooked, is the possibility of interdiffusion of the films, resulting in poorly defined interfaces and subsequently poor optical performance.

We report here the sol-gel synthesis of optical interference filters consisting of up to 16 alternating layers of SiO_2 and TiO_2. Rutherford backscattering spectrometry (RBS) is used to probe film interdiffusion and to determine the thickness of individual layers in the filter.

EXPERIMENTAL PROCEDURE

SiO_2 sols were prepared according to the literature except that the synthesis was conducted at room temperature [4]. TiO_2 sols with molar ratios $Ti:PrOH:H_2O:HCl$ of 1:11.4:1:1.8 were prepared by adding a solution of deionized H_2O in propyl alcohol to an acidified solution of titanium isopropoxide also in propyl alcohol [5]. Sols, diluted with the appropriate amount of alcohol, passed through 0.20 μm filters to eliminate any particulates before deposition. In some TiO_2 sols, half of the propanol was substituted by toluene. One inch diameter barium-strontium glass substrates were cleaned by successive immersion in trichlorotrifluoroethane, nitric acid, and a solution of methanol and acetone, each in an ultrasonic bath.

Films were deposited using a photoresist spinner.

Transmission spectra were obtained on a Varian Model 17D Spectrophotometer. RBS was performed with a collimated beam of $4He^{++}$ accelerated to a nominal energy of 3.0 MeV on a tandem accelerator. Current was near 15 nA for each run, and 15 μC of charge was collected. RBS data were analyzed with software developed at Cornell University [6]. Thickness and refractive index of single films were determined with a Rudolph Model 43603 ellipsometer at 632 nm.

RESULTS AND DISCUSSION

Successive coatings with alternating sols results in a TiO_2/SiO_2 multilayer with controllable thickness and refractive index. To produce a filter with specified optical performance, a series of experiments was conducted to determine the optimal conditions for depositing individual films with the required optical thickness. Cracks usually developed unless the films were consolidated at 450°C between each deposition of TiO_2/SiO_2 pairs. In addition, each film was heated at 150°C to avoid dissolution and intermixing during deposition of the next layer. Some flaws appeared to be due to bubble formation during spinning of the TiO_2 sol. To eliminate the problem, a systematic study substituted alternative solvents that could raise the surface tension of the sol. We found that substitution of toluene for a fraction of the alcohol resulted in flaw-free, optical quality multilayers with up to sixteen films.

Figure 1 shows normalized RBS data and a computer simulation for a sol-gel TiO_2/SiO_2 multilayer with 12 individual films (Filter A). Thicknesses of the films were calculated using density values obtained previously [7,8]. The average values were 99 and 70 nm for SiO_2 and TiO_2 respectively. We have observed that the first film spun on the bare substrate is always thicker than subsequent films from the same sol due to differences in surface energy between the bare substrate and subsequent films. In addition, films on the very top are slightly thicker, probably due to shorter annealing times. X-ray diffraction showed that the SiO_2 films were amorphous while the TiO_2 were in the anatase form.

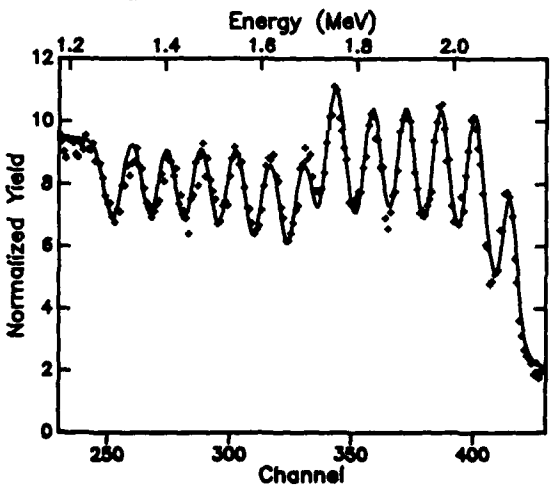


Figure 1. Experimental RBS data (+) and simulated spectrum (—) for Filter A

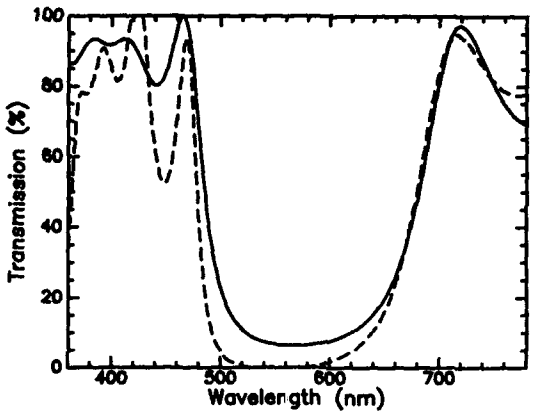


Figure 2. Optical transmission (— —) and simulated (—) spectra for Filter A

The optical spectrum of the multilayer is shown in Figure 2. A simulated transmission spectrum, generated by using the thickness values obtained from the RBS data and refractive indices of 1.42 and 2.08 for SiO_2 and TiO_2 respectively, is in excellent agreement with the experimental data.

Figure 3 shows the angular dependence of the transmission spectrum with respect to the incident light. Incident light at 470 nm is transmitted when normal to the substrate, while transmission drops to ~ 50% when the incident angle is 20° and becomes almost zero at 40°. The filter edge, defined as the wavelength corresponding to 50% transmission, shifts to lower values as the angle of the incident light increases from the normal to the substrate as shown in Figure 4. For comparison, the performance of a commercially available filter made by rf sputtering is also shown. The optical characteristics of the filter can be engineered by varying the optical thickness of individual films, as demonstrated by Filter B.

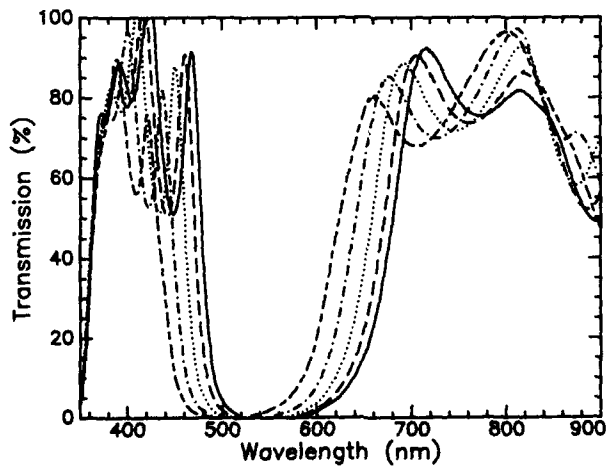


Figure 3. Optical Transmission for various angles of incidence; 0° (—); 20° (— —); 30° (···); 40° (—·—); 50° (— — —).

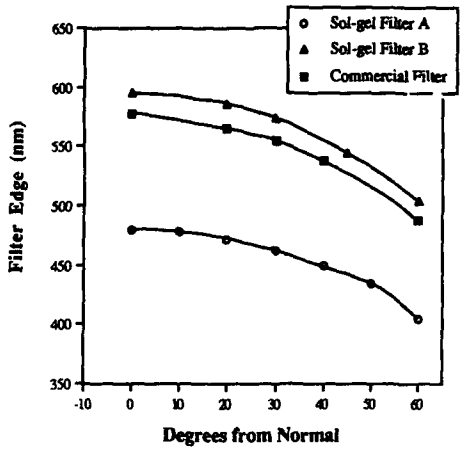


Figure 4. Filter edge vs. angle.

Since the optical performance of the filter is largely influenced by the sharpness of the interfaces, interdiffusion of layers was studied by RBS. The sharp edges in the RBS spectrum, (Figure 1), mitigate against extensive interdiffusion. To study further film interdiffusion, a bilayer consisting of one SiO_2 film on a thick TiO_2 film was analyzed by RBS before and after annealing at 450°C for two and ten hours. Again, no interdiffusion can be seen within the resolution of the RBS technique (~150 Å). Current experiments include marker displacement from the interface as well as x-ray reflectivity.

ACKNOWLEDGEMENTS

This work was sponsored, in part, by the Imaging and Sensing Technology Corporation and by the Cornell Ceramics Program whose funds are provided by IBM and Corning Inc. J.L.K. acknowledges the support of a DoEd Ceramics Fellowship. M. Uttormark wrote the computer program to simulate transmission spectra.

REFERENCES

1. J.P. Rancourt, SID Proceedings 25, 43 (1984).
2. O.S. Heavens, in Optical Properties of Thin Films, (Dover, New York 1967).
3. M. Green (private communication).
4. R.K. Brow and C.G. Pantano, in Better Ceramics Through Chemistry, edited by C.J. Brinker, D.E. Clark and D.R. Ulrich (Mat. Res. Symp. Proc. 32, Pittsburgh, PA 1984) pp. 361-367.
5. K.A. Berglund, C.L. Przybocki, and E.P. Giannelis, in Ultrastructure Processing of Advanced Ceramics, edited by J.D. Mackenzie and D.R. Ulrich, (John Wiley & Sons, New York, 1988) pp. 807-818.
6. L. Doolittle, Nucl. Instrum. & Meth., B9, 344 (1985).
7. J.L. Keddie and E.P. Giannelis, these proceedings.
8. J.L. Keddie and E.P. Giannelis, presented at the 1989 ACS Meeting, Indianapolis, IN, 1989 (submitted for publication).

Titania/Silica Sol-Gel Films: Comparison of Techniques for Thin Film Thickness Measurement

S. M. Melpolder, A. W. West, M. P. Cunningham and R. Sharma, Eastman Kodak Company, Rochester, New York, 14650-2019.

ABSTRACT

Two techniques for thin film measurement were compared: an optical method combining ellipsometry and reflectance spectroscopy, and cross-sectional transmission electron microscopy. These techniques were used to measure the absolute thicknesses of titania/silica sol-gel films in the size range 0.1 to 0.8 microns. The relative advantages and disadvantages of these methods will be described in this study.

INTRODUCTION

Many sol-gel thin film applications require homogeneous defect-free layers with tight tolerances for specific properties, i.e. refractive index, thickness, surface energetics, thermal expansion coefficient, etc. In particular the thin film thickness must be controlled within a few percent in most optical and microelectronic applications.[1-4] For example, the use of sol-gel thin films to produce multi-layer antireflective coatings [4,5] requires that the refractive index and thickness of individual layers be reproducible and of a predetermined value. Lukosz [6] initially reported on the use of sol-gel films of varying composition and refractive index to prepare low loss waveguides. In order to prepare these devices one must predetermine the film properties necessary to achieve the desired spectral response. As mentioned in the previous illustrations, both the refractive index and thickness of the sol-gel film are critical to its successful application. Through experimentation, one must determine if sol-gel processing can produce the required film reproducibility.

W. Beier [7] presented a technique for measuring film thickness by determining the substrate's weight gain after applying the sol-gel film. His accuracy for determining thickness was +/- 20 percent. Bel Hadj et. al. [8] used ellipsometry and interference spectra to determine the change in thickness and refractive index of titania and zirconia sol-gel films coated on soda-lime-silica substrates. Sakka et. al. [9] used refractive index data generated in this manner to estimate the residual porosity of the processed films. Various other authors have used the previously mentioned and additional methods for determining the thickness of sol-gel films coated onto silicon or glass substrates. [10-17]

EXPERIMENTAL

Synthesis and Sample Film Preparation

Tetraethyl silicate (TEOS) and tetraisopropyl titanate (TIPT) sol-gel solutions were prehydrolyzed separately. For the silica prepolymer a 1:10:2 molar ratio of TEOS, ethanol and water was used. In the case of the titania prepolymer TIPT, ethanol, hydrochloric acid (HCl) and water were reacted at 1:11:0.56:1 molar ratio. The TEOS and TIPT prehydrolyzed sol-gels were cooled to room temperature, their respective volumes measured and the molar concentration of each sol-gel calculated. The titania and silica sol-gels were mixed to prepare the desired titania/silica molar ratios of 40/60, 60/40 and 80/20.

Mat. Res. Soc. Symp. Proc. Vol. 180. ©1990 Materials Research Society

The desired sol-gel coating concentration was obtained by dilution with Punctilious ethanol and filtered through Gelman 0.2 micron CR filters attached to 30 ml luer-lock syringe. The sol-gels were coated onto <100> silicon wafers using a Headway spin-coater. Coating thickness has previously been shown to be inversely proportional to the square root of the spin-speed. [18] Spin-speed and sol-gel concentration studies were performed to determine the coating and solution conditions necessary to provide films of desired thickness for accurate ellipsometric analysis.

The coated films were thermally processed in a Fisher 495 Isotemp Ashing Furnace. The films were heated at 5°C to 150°C, held for 3 minutes and then heated at a rate of 3°C per minute to 175°C and held for 60 minutes. This initial heating was done immediately after coating to prevent film defects. The final heat treatment consisted of a 5°C per minute ramp to 450°C with a hold for 5 minutes and then a 3°C per minute ramp to 500°C and a hold for 60 minutes. The coatings were furnace cooled to room temperature with the door closed.

For multi-layer samples, the initial coating was processed to consolidation at 500°C as described above. The second coating and subsequent coatings were spin-coated onto the first or previous layer and then processed in the same manner. A maximum of 7 layers was deposited and evaluated.

PREPARATION OF SAMPLES FOR TRANSMISSION ELECTRON MICROSCOPY (TEM)

Cross-sections were prepared from all the samples for transmission electron microscopy examination. The samples were sliced into 1mm x 3mm rectangles and six of these pieces were glued together to form a block. The block was ground and polished from both sides to a final thickness of less than 50 microns, reinforced with copper aperture grids and ion-milled to perforation. Transmission electron micrographs were taken to show the individual layers in the multilayer samples. Measurements of layer thickness were determined from the negatives.

Optical Instrumentation

A Rudolf Auto EL II ellipsometer in a null-seeking configuration, equipped with a He/Ne laser light source, was used. Reduction of the del, psi data was accomplished with the McCrackin software package. [19] The reflectance spectra were taken on a Varian 2300 spectrophotometer equipped with an integrating sphere (single beam reflection optics). The model employed to calculate spectra was the Rouard [20] multilayer description
using the formalism described by Vasicek. [21]

RESULTS AND DISCUSSION

Optical measurements, theory and discussion

The measurement of thin film thicknesses and indices is frequently performed by ellipsometry, an optical method based on the classical theory of Drude. [22] The technique involves the measurement of the change in polarization of light reflected from a surface, a typical situation (single layer on a reflective support) represented schematically in Figure 1.

Drude's equations describing the above system have been extended to multilayers (Rouard's notation [20]) and absorbing films (Vasicek [21]). The above system can be very generally described as shown in the following equation:

$$\rho = \tan\Psi e^{i\Delta} = \frac{r_p}{r_s}$$

where

$$r_x = \frac{r_{12} + r_{23}e^{-i\Phi}}{1 + r_{12}r_{23}e^{-i\Phi}} \quad \text{and} \quad \Phi = \frac{4 \cdot \pi \cdot n \cdot d \cdot \cos(\phi_2)}{\lambda} \qquad (1)$$

Del and psi in the above equation are the ellipsometric quantities determined by the device and x = p or s corresponding to the Fresnel reflection coefficients for the appropriate interfaces (subscripts 12 indicating that between layers 1 and 2, etc.). Since r_p and r_s are (in the general case) complex, the ratio (ρ) is complex and normally solved by computer. In the usual case for which the index of the incident medium (air, most commonly) and the substrate are known, the equations contain three unknowns (the real and imaginary parts of the film index, and the geometric thickness). While del and psi are independent, the system cannot be fully determined unless one of the optical parameters (n, k or d) is known independently. For a nonabsorbing film (k = 0), therefore, a unique solution of n and d can be determined. It can be shown, however, that del, psi are periodically repeated with thickness (the instrument uses a polarizer/compensator/analyzer combination and any two azimuths of those components that are 180 degrees apart are optically indistinguishable). The film thickness (CYC) required to regenerate del/psi can be calculated from:

$$CYC = \frac{\lambda}{2} \frac{1}{[2(N2)^2 - \sin^2(\Phi)]^{\frac{1}{2}}} \qquad (2)$$

As a result films of thickness d are optically equivalent to films of thickness d' where:

$$d' = d + m * CYC \qquad m = 1,2,3..... \qquad (3)$$

In the absence of an independent method of determining the cycle number (m) of a thick film, the ellipsometric analysis is limited to film thicknesses less than one cycle. A number of metrics are available for the determination of m, however, and the reflectance spectrum has been found quite useful for the purpose. The process involves comparing the calculated reflectance spectrum for the equivalent optical thicknesses (corresponding to the m integers and the measured index) with the measured spectrum (dispersion of the film and substrate indices are commonly ignored). The process (essentially a fringe count method) is illustustrated in Figure 2. The measured spectrum (on the left) was obtained for a film on silicon which analyzed ellipsometrically as thickness = 205A, index = 2.168 and cycle = 1592 A. The three computed spectra on the right correspond to cycles m = 2, 3 and 4. Correlation of the measured spectrum with that corresponding to m = 3 shows the film of index 2.168 to be 4981 A thick.

Transmission Electron Microscopy

A representative transmission electron micrographs of the 7-layer sample is shown in Figure 3. All the layers in the multilayer samples could be distinguished in the electron image as the interfaces between the individual layers acted as scattering centers for the electrons, hence providing image contrast. Both the thicknesses of the individual layers and the total film thickness could be obtained from the micrographs. The measurements from TEM are listed in Table 1, together with the values obtained from the optical techniques.

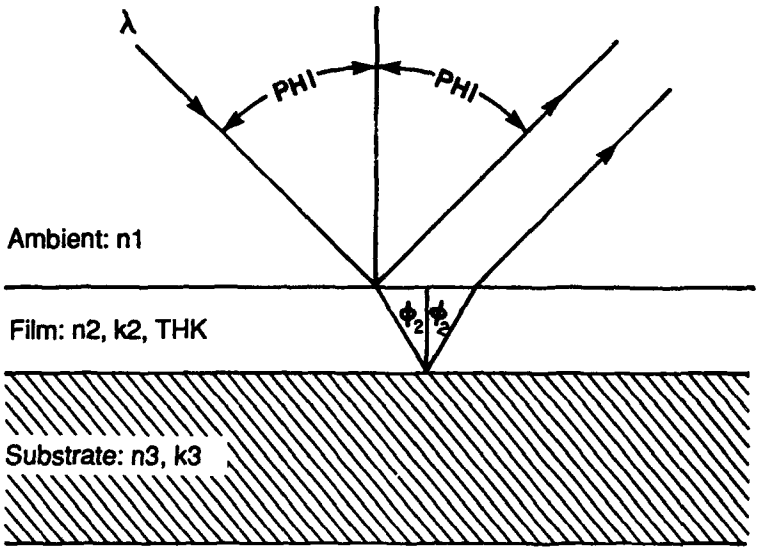


Figure 1. Ellipsometry set-up.

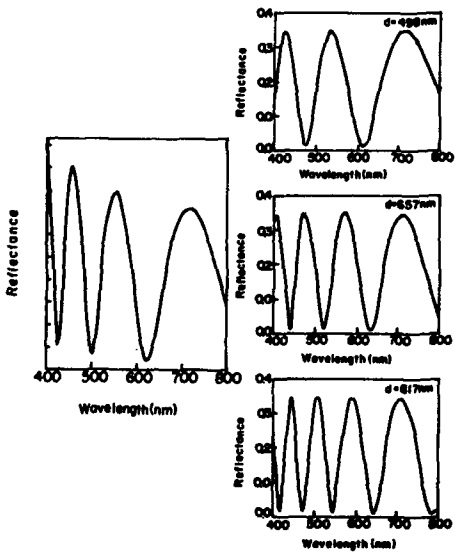


Figure 2. Comparison of theoretical and actual reflectance spectra.



Figure 5. TEM cross-section of crystalline 7- layer titania/silica film stack processed to 500°C

Table I. Absolute Thickness of Titania/Silica Layers

Number of Layers	Ellipsometry/Reflectivity (A)	Cross-Section TEM (A)
1	940 +/- 10	940 +/- 20
3	2670 +/- 10	2940 +/- 20
5	4360 +/- 10	4520 +/- 20
7	5880 +/- 10	6220 +/- 20

The layer thickness measurements from the TEM data were subject to two major sources of error. The first was the exact magnification of the micrographs. The magnification range of the TEM had been calibrated using standard samples, but could still be 5% in error. Secondly, it was not always possible to determine the exact position of the individual layers in the multi-layer samples owing to diffraction effects. This source of error was not so significant for the total layer thickness measurement as these interfaces tended to be better defined. A discrepancy will be observed between the sums of the individual layer thicknesses and the thickness measurements made over all layers.

For the multi-layer samples, small crystallites were observed to form during heat-treatment. The presence of these crystallites did not affect the optical measurements as their average size was less than 20nm.

CONCLUSIONS

A technique that uses both ellipsometry and reflectivity spectroscopy can be used to determine the absolute film thickness for both amorphous and crystalline layers accurately. For crystalline films, it was found that the crystallite size had to be less then 20nm or ellipsometry measurements were not valid. For films containing larger crystallites, cross-sectional TEM was the only available technique.

References

1. B.E. Yoldas and T.W. O'Keeffe, Appl. Opt. 18, 3133 (1979).
2. H. Dislich, Sol-Gel Thechnology for Thin Films, Fibers, Preforms, Electronics, and Specialty Shapes, Edited by L.C. Klein (1988) p. 50.
3. B.E. Yoldas, J. Non-Crystalline Solids 38,39, 81 (1980).
4. H. Schroeder, Phys. Thin Films 5, 87 (1969).
5. C.J.Brinker and M.S. Harrington, Solar Energy Materials 5, 159 (1981).
6. W. Lukosz and K. Tiefenthaler, Opt. Letters, 8 (10), 537 (1983).
7. W. Beier, A.A. Goktas and G. H. Frischat, Journal Non-crystalline Solids, 100, 531 (1988).
8. F. Belhadj, R. Sempere and J. Phallipou, Journal Non-crystalline Solids 82, 417 (1986).
9. S. Sakka, K. Kamiya and Y. Yoko in Inorganic and Organometallic polymers, Edited by M. Zeldin et. al. (ACS Symposium series 360 1987).
10. R.B. Pettit, C.S. Ashley, S.T. Reed and C.J.Brinker, Sol-Gel Technology for Thin Films, Figers, Preforms, Electronics and Specialty Shapes, Edited by L.C. Klein (1988) p. 80.
11. Y. Yamamoto, K. Kamiya and S. Sakka, Yogyo-Kyokai-Shi, 90 (6), 328 (1982).
12. J. Cheng and D. Wang, Journal Non-crystalline Solids, 100, 288 (1988).
13. B.E.Yoldas, Applied Optics, 21 (16), 2960 (1982).
14. M. Emili et. al. Journal Non-crystalline Solids 74, 129 (1985).
15. C.J.R. Gonzalez-Oliver, P.F. James and H. Rawson, Journal Non-crystalline Solids 48, 129 (1982).
16. M. Nogami and Y. Moriya, Yogyo-Kyokai-Shi 85, 59 (1977).
17. N.D.S. Mohallen and M.A. Aegerter, Journal Non-crystalline Solids 100, 526 (1988).
18. S.M. Melpolder and B.K. Coltrain in Better Ceramics Through Chemistry, edited by C.J. Brinker et. al. (Mater. Res. Soc. Proc. 121, Pittsburgh, PA 1988) pp. 811.
19. F. L. McCrackin, NBS Technical Note 479, "A Fortran Program for Analysis of Ellipsometer Measurements",1969.
20. P. Rouard, Annales de Physique, 7, 291 (1937).
21. A. Vasicek, Optics of Thin Films, Interscience Publishers, (1960).
    A. Vasicek, Optical study of a thin absorbing film on a metal surface, in Ellipsometry in the Measurement of Surfaces and Thin Films, Edited by E. Passaglia et al., NBS Miscellaneous Publication 256 (1963).
22. P. Drude, Ann. Physik. 272, 532 (1889).
    P. Drude, Ann. Physik. 272, 865 (1889).
    P. Drude, Ann. Physik. 275, 481 (1890).

HETEROMETALLIC ALKOXIDES AS PRECURSORS TO MULTICOMPONENT OXIDES

LILIANE G. HUBERT-PFALZGRAF, RENEE PAPIERNIK, MARIE-CECILE MASSIANI AND BERNARD SEPTE

Laboratoire de Chimie Moléculaire, Equipe de Recherche Associée au CNRS, Université de Nice-Sophia Antipolis, Parc Valrose, 06034 Nice, France

ABSTRACT

Lead(II) oxides are involved in various advanced materials. Their high volatility as compared to that of other elements makes chemical routes to such materials especially attractive. Various synthetic routes to lead(II) alkoxides have therefore been estimated. They display a strong tendency to undergo spontaneous condensation reactions, giving oxoalkoxides $Pb_4O(OR)_6$ (R = ^tBu, ^iPr, Et). Reaction between $Pb_4O(OEt)_6$ and $[Nb(OEt)_5]_2$ does not proceed by simple addition of the alkoxides, but the lead tetranuclear oxoalkoxide is transformed to a hexanuclear one, $Pb_6O_4(OEt)_4$, whose oxo ligands bear $Nb(OEt)_5$ moieties, the overall formula being $Pb_6O_4(OEt)_4[Nb(OEt)_5]_4$ 1. The stoichiometry between the two metals corresponds to that of the PNM ceramic, and ^{207}Pb NMR has been used as a tool to study the reactivity of 1 in the presence of various modifiers and magnesium ethoxide.

INTRODUCTION

Metal alkoxides $M(OR)_n$ are versatile molecular precursors of metal oxides [1]. Their attractive features include a high purity, a large solubility in a variety of solvents and their ability to lead to homogeneous media for multicomponent oxides such as NASICON, by forming heterometallic (double) metal alkoxides $MM'(OR)_{n+n'}$. This property has been considered as a way to "preform" the final material in solution [2].

Lead(II) oxides are involved in various advanced materials such as superconductors, dielectric ceramics or photoconductive systems [3]. The high volatility of the lead oxide, as compared to that of the other elements associated in the formulation of the multicomponent systems, results in a difficult control in the stoichiometry, and low temperature routes are thus especially attractive. Thus, an all-alkoxide route allowed the obtaining of the pure $PbNb_{2/3}Mg_{1/3}O_3$ (PNM) perovskite phase at 700°C [4]. This work gave evidence for the formation of a heterometallic Pb-Nb alkoxide, although its stoichiometry remained undetermined.

In this paper we describe the synthesis of $Pb_6O_4(OEt)_4[Nb(OEt)_5]_4$, whose stoichiometry corresponds to that of the two metals in the PNM material, and its unequivocal characterization by an array of techniques: infrared and nuclear magnetic resonance (^1H, ^{13}C and ^{207}Pb) spectroscopy and single X-Ray diffraction. In addition, the feasibility of monitoring the complex under different solution environments and studying hydrolysis reactions has been considered.

Mat. Res. Soc. Symp. Proc. Vol. 180. ©1990 Materials Research Society

EXPERIMENTAL

All reactions were conducted under inert atmosphere using Schlenk tube techniques. $[Nb(OEt)_5]_2$ and $KNb(OEt)_6$ were prepared according to the literature [5]. ^{207}Pb spectra have been recorded on solutions (Bruker AM-200 spectrometer) and the chemical shifts are reported with respect to $Pb(NO_3)_2$ as an external reference.

RESULTS AND DISCUSSION

Several synthetic routes can be considered for the formation of heterometallic alkoxides; the most common are the reaction between a metal chloride and a heterometallic alkoxide based on an alkali metal with formation of a salt and direct reaction between alkoxides (eq. 1):

$$MCl_n + nM'M''(OR)_{n'} \longrightarrow nM'Cl + M[M''(OR)_{n'}]_n \quad (1)$$

As lead(II) alkoxides are scarce, synthesis of a heterometallic alkoxide starting from lead chloride appeared attractive. However, the reaction between $PbCl_2$ and $KNb(OEt)_6$ in ethanol in reflux gives mainly unreacted potassium niobium ethoxide, and we therefore turned to reaction between alkoxides.

Various experimental procedures, starting from chloride $PbCl_2$, acetate $Pb(OAc)_2$, and silylamido $Pb[N(SiMe_3)_2]_2$ have been investigated for access to lead(II) alkoxides. Starting from the silylamido derivative offers the most selective synthetic route, since the only byproduct formed is a volatile amine and the reaction can be conducted at low temperature [6].

$$2Pb[N(SiMe_3)_2]_2 + 4ROH \xrightarrow{\text{hexane}} [Pb(OR)_2]_2 + 4HN(SiMe_3)_2 \quad R = {}^tBu \quad (2)$$

However, homoleptic alkoxides $Pb(OR)_2$ actually display a poor stability with respect to condensation reactions and formation of oxoalkoxides with loss of dialkyl ether, and this transformation could be followed in the case of the tertiobutoxide derivatives:

$$2[Pb(O^tBu)_2]_2 \longrightarrow Pb_4O(O^tBu)_6 + {}^tBu_2O \quad (3)$$

Such condensation reactions are favored by the decrease in the bulk of the alkoxo group, and isopropoxides or ethoxides are no longer stable as $Pb(OR)_2$ species, but only as $Pb_4O(OR)_6$ oxoalkoxides.

The formation of a Pb-Nb heterometallic species is evidenced by the fact that the poorly soluble $Pb_4O(OEt)_6$ undergoes complete dissolution in toluene or ethanol by addition of niobium ethoxide $Nb(OEt)_5$. Cooling down the alcoholic solution offered a crystalline product, whose infrared spectrum, different from that of the parent alkoxides (Figure 1) and high solubility even in hydrocarbon such as hexane suggest it to be a heterometallic alkoxide.

Unambiguous characterization was achieved by a single crystal X-ray diffraction structure determination [7]. These studies established the compound to correspond to $Pb_6O_4(OEt)_4[Nb(OEt)_5]_4$ 1, and Figure 2 represents the lead-niobium oxygen framework. It should be emphasized that the stoichiometry between the two metals Pb:Nb is 6:4, namely that which is required by the PNM ceramic, but also that the product obtained does not result from a simple addition reaction.

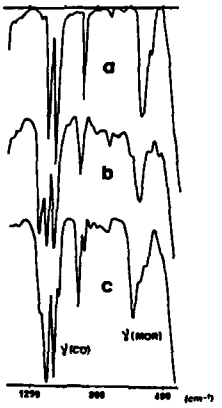


Figure 1 : Comparison of the infrared spectra of the homo- and heterometallic alkoxides
a: $Pb_4O(OEt)_4$; b: $Pb_6O_4(OEt)_4A_4$; c: $[Nb(OEt)_5]_2$ = A_2;

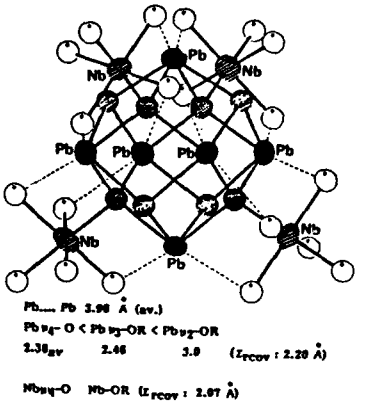


Figure 2: Metal-oxygen framework of 1

Indeed, the lead-oxygen core has been reorganized, with transformation of the tetranuclear oxoalkoxide to a hexanuclear one, as schematically shown in eq. 4:

$$3/2\ Pb_4O(OEt)_6 \longrightarrow Pb_6O_4(OEt)_4 + 5/2\ Et_2O \qquad (4)$$

The central lead-oxygen core $Pb_6O_4(OEt)_4$ resembles that of $Pb_6O_4(OiPr)_4$ which has been characterized by X-ray diffraction [8]. The overall heterometallic alkoxide can be viewed as a complex resulting from the association of Lewis acid, the monomeric niobium pentaethoxide fragment and the lead(II) oxoalkoxide $Pb_6O_4(OEt)_4$ via the triply bridging oxide ligand. Further stabilization is achieved by the doubly bridging ethoxide groups.

Knowledge of the structure of a heterometallic alkoxide related to a material offers the opportunity to gain additional information concerning its reactivity. Lead displays attractive NMR characteristics for a metal nucleus (I = 1/2, ∿10 times more sensitive than carbon) [9] and ^{207}Pb NMR has therefore been used as a tool to investigate the reactivity of 1 in solution. In fact, 1 displays a complex behavior in solution: different molecular species in dynamic equilibrium were obtained upon its redissolution even in a non polar medium such as toluene and the $^{207}Pb\{^1H\}$ spectra show several singlets (no Pb-Pb coupling was detected) at 2896, 2855 and 2826 ppm. The variation in their relative areas as a function of the molar ratio 1/Nb as well as of the dilution suggests that the heterometallic alkoxide undergoes dissociation reactions upon dissolution. Detection of free niobium pentaethoxide by infrared (rapid exchange is observed by ^1H and ^{13}C NMR) brings further evidence for dissociation and thus the formation of $Pb_6O_4(OR)_6[Nb(OEt)_5]_n$ ($n<4$) species.

The reactivity of 1 has been studied in the presence of various chemical modifiers such as acetic acid, 2-methoxyethanol and triethanolamine, which are often used during the sol-gel process to induce or slow down the hydrolysis-polycondensation reaction. These modifiers are all reactants having hydroxyl functionality, and thus may participate in substitution reactions

involving OR groups. Partial breakdown of the heterometallic species 1 is observed in the presence of acetic acid (formation of lead acetate, for instance) and 2-methoxyethanol, although new mixed metal Pb-Nb species are also formed. The potentially tridentate triethanolamine ligand seems more efficient in maintaining the heterometallic unit. Reactions of 1 with other alkoxides which may act as competing ligands were estimated with magnesium ethoxide, which is the derivative required on the way to the PNM ceramic. Infrared spectra gave evidence for the formation of a Nb-Mg mixed alkoxide, $Mg[Nb(OEt)_6]_2$ [10]. ^{207}Pb NMR suggests formation of Pb-Mg species (observed independently by allowing $Pb_4O(OEt)_6$ to react with $Mg(OEt)_2$) as well as terheterometallic Pb-Mg-Nb species. Further studies of the reaction of 1 are in progress.

It should be emphasized that despite its poor solublity, lead(II) acetate can be easily solubilized in the presence of niobium pentaethoxide in tetrahydrofurane; however, lead NMR established that no chemical transformation had occured; no heterometallic Nb-Pb was present, and the spectrum displayed only the resonance of unreacted $Pb(OAc)_2$ (2200 ppm).

CONCLUSION

A heterometallic lead(II)-niobium oxoalkoxide 1 in which the two metals present the stoichiometry required by the PNM ceramic has been obtained by reaction of $Pb_4O(OEt)_6$ with $Nb(OEt)_5$, and characterized by single crystal X-ray diffraction. Lead(II) NMR is useful for detection of alkoxide complex formation: the increase of the coordination number of the lead nucleus from 4 in the oxoalkoxide to 6 in the heterometallic complex corresponds to a drastic high field shift (more than 2000 ppm). ^{207}Pb NMR allows also monitoring of its evolution in the presence of different chemical modifiers such as acetic acid and triethanolamine as well as magnesium diethoxide, the alkoxide which is required for its conversion to the PNM material.

REFERENCES

1. L.G. Hubert-Pfalzgraf, New J. Chem. 11, 663 (1987).
2. H. Dislich, Angew. Chem. Int. Ed. Engl. 10, 363 (1971).
3. K. Okazaki, Ceramic Bull. 67, 1946 (1988).
4. F. Chaput, J.P. Boilot, M. Lejeune, R. Papiernik, L.G. Hubert-Pfalzgraf, J. Am. Ceram. Soc. 72, 1335 (1989).
5. D.C. Bradley, B.N. Chakravarti, W. Wardlaw, J. Chem. Soc. 1956, 2381. R.C. Mehrotra, M.M. Aggrawal, P.N. Kapoor, J. Chem. Soc.(A), 1968, 2673.
6. R. Papiernik, M.C. Massiani, L.G. Hubert-Pfalzgraf, Inorg. Chim. Acta 165, 1 (1989).
7. R. Papiernik, L.G. Hubert-Pfalzgraf, J.C. Daran, J. Chem. Soc., Chem. Commun., in the press.
8. A.I. Janovskii, N. Ya. Turova, E.P. Tu.. skaya, Yu. T. Struchkov, Koordinatsionnaya Khimiya, 8, 158 (1982) Engl. Trans..
9. J.J. Dechter "NMR of metal nucleides" Part I: Main group elements. Progress in Inorganic chemistry, ed J.S. Lippard; vol 29, 285 (1982); R.K. Harris, J.J. Kennedy. W. Mc Farlane, "NMR and the Periodic Table", ed. R.K. Harris, B.E. Mann, Academic Press, London 1978, p 366.
10. S. Govil, P.N. Kapoor, R.C. Mehrotra, J. Inorg. Nucl. Chem. 38, 172 (1976).

STABILIZATION, CHARACTERIZATION AND OPTICAL APPLICATIONS OF NIOBIUM AND TANTALUM OXIDE SOLS PREPARED VIA ALKOXIDE ROUTES

STEPHEN PARRAUD*, LILIANE G. HUBERT-PFALZGRAF* AND HERVE FLOCH**

*Laboratoire de Chimie Moléculaire, Associé au CNRS, Université de Nice-Sophia Antipolis, Parc Valrose, 06034 Nice, France

**Commissariat à l'Energie Atomique, Centre de Limeil-Valenton, 94195 Villeneuve St Georges Cedex, France

ABSTRACT

Hydrolysis of niobium and tantalum pentaethoxides in ethanol and in the presence of basic (ammonia, tetramethylammonium hydroxide, di and triethylamine) or acidic (nitric or hydrochloric acids) additives was investigated. Triethylamine gives monodispersed, small particles of amorphous M_2O_5,nH_2O (M = Nb, Ta). These colloidal suspensions were used to obtain thin films by spin-coating techniques. The coatings display a thickness of 100-300 nm and a refractive index around 1.7 . Laser damage tests at 1064 nm wavelength with a pulse length of 3 ns were carried out on the single layer systems. The threshold values (one-on-one) are in favor of the Ta_2O_5 coatings with an average of 14.5 ± 2.1 J/cm^2, by comparison with 8.3 ± 1.6 J/cm^2 for the Nb_2O_5 films.

INTRODUCTION

Two methods are commonly used to prepare coatings by the sol-gel process [1]. The first consists in an application of a precursor solution to a substrate with subsequent conversion of the precursor to an oxide on the surface; this usually requires water and heat. The second consists in an application of a colloidal suspension (sol) of a chemically converted oxide to a substrate with subsequent evaporation of the suspending medium at room temperature. The first method is in fact the most convenient one in view of the number of readily available suitable precursors, in contrast to the difficulty in preparing adequate colloidal oxide suspensions. However, it is now well established that this second method offers a route to films of much less internal stress, which can be easily stacked, and thus to antireflection coatings having a higher laser damage resistance than those conventionally deposited (PVD) [2].

This paper deals with our efforts directed towards the preparation of suitable colloidal suspensions of niobium and tantalum oxides. The availability of monodispersed M_2O_5 oxides should also facilitate their various other applications, for instance as high frequency oscillators, ceramic filters, composite fillers or catalysts [3].

Mat. Res. Soc. Symp. Proc. Vol. 180. ©1990 Materials Research Society

EXPERIMENTAL PROCEDURE

The alkoxides $[M(OEt)_5]_2$ M = Nb, Ta were synthesized according to the literature and purified by distillation [4].

Hydrolysis of $M(OEt)_5$ (M = Nb, Ta) in ethanol (0.2 M) was achieved by adding a similar volume of an ethanol solution of water (8- 40M) and triethylamine (0.018-0.05M. Vigorous stirring was maintained during the hydrolysis and a fluid, translucent, slightly blue, stable sol was obtained.

Particle sizes were estimated by sedimentation measurement ($\geq$ 100 nm) or by transmission electron microscopy. Single coatings were prepared by spinning aqueous ethanolic suspensions of M_2O_5 (containing $\sim$3% of oxide) on to 5-cm diameter fused silica substrates followed by an air-dry. All coatings were deposited at room temperature under stringently clean conditions. The coating suspensions were filtered through a 0.2 micron teflon filter before use. One layer at a spin speed of about 1300 rpm for Nb_2O_5 and two layers at 1150 rpm for Ta_2O_5, respectively, were required to give coatings with maximum reflectivity at 1064 nm wavelength.

RESULTS AND DISCUSSION

Metal alkoxides are appropriate metal-organic precursors for high purity oxides [5]. Suitable sols for spin-coating applications should have monodispersed particles, all about the same size in the size range of 10-30 nm , and with relatively high concentration of oxides ($\simeq$3%). The choice of niobium and tantalum was motivated by the high refractive index (2.1) as well as the transparency (up to 250 and 300 nm, respectively) of their dense oxides; furthermore, the oxides are chemically durable materials. Investigations concerning M_2O_5 coatings obtained by sol-gel techniques appear limited to tantalum [6].

Hydrolysis experiments were performed on niobium or tantalum pentaethoxides in ethanol. The liquid nature of these alkoxides is an attractive feature for obtaining high concentration oxide solutions, while ethanol is a wettable solvent, therefore, no addition of ionic superfactants was necessary for the coating applications. Obtention of colloidal suspension supposes the control of 2 types of reactions: the hydrolysis and the polycondensation process. A large number of parameters such as the hydrolysis ratio h ($[H_2O]/[M(OR)_5]$), the influence of the pH, the presence of acidic (HNO_3, HCl) or basic (ammonia, tetramethylammonium hydroxide, di and triethylamine) additives, the presence of modifiers (acetylacetone) have thus been investigated. The results are summarized in Table I . The best results were generally obtained with basic additives (although ammonia was observed to have a destabilization effect [7]) and especially with triethylamine which gives fluid translucent colloidal suspensions stable over several months (Figure 1). Acidic additives such as nitric or hydrochloric acids favor the formation of very small particles and of gels which display rheological properties convenient for coatings applications over a limited period of time (1 to 3 days in the case of tantalum). It must also be emphasized that despite

similar structures for the two alkoxides and similar electronegativity for niobium and tantalum, very large differences in the hydrolysis rates are observed. Niobium pentaethoxide is nearly 8 times more sensitive to hydrolysis than tantalum pentaethoxide.

Table I: Influence of the hydrolysis ratio and the additives of the media

	h	additive	additive/ $M(OR)_5$	media	particle size
Nb	2,5	-	-	precipitation	1μm
	5-12	NH_3	22-0,5	aggregates	10-500nm
	10-100	TMAH	0,2-0,5	blue to white gel	10-1000nm
	7-12	HNO_3	0,06-10	blue gel	10-200nm
		DEA or TEA		sol or gel	
Ta	20	-	-	precipitation	0.1μm
	10	TMAH	0,2	blue gel	5-10nm
	10	HNO_3	0,3	blue gel	5-10nm
	180-200	TEA	0,1-0,5	blue sol	5nm

TMAH = tetramethylammonium hydroxide: TEA = triethylamine; DEA = diethylamine

By contrast with the titanium alkoxides, hydrolysis under forced conditions (large excess of hot water) led to relatively large (0.5 to 1μm), nearly spherical, agglomerated particles which could not be redispersed with the variety of additives reported in Table I, including triethylamine.

Powder XRD patterns show that the oxides formed are always amorphous. Fig. 2 shows the transmission spectrum of a Nb_2O_5 coating with maximum reflection at 620 nm; the refractive index is 1.7 [8], the coating is therefore quite porous and also has a low abrasion resistance against an alcoholic drag-wipe.

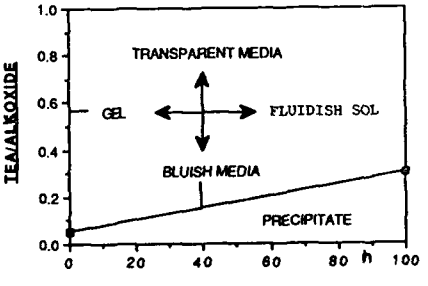


Fig.1. Diagram showing the aspect of the medium as a function of ratio (TEA)/alkoxide and the hydrolysis ratio h

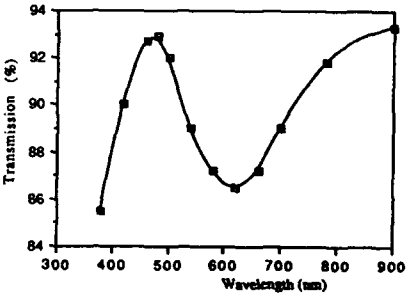


Fig.2. Transmission spectrum of a Nb_2O_5 monolayer coating

Laser damage threshold measurements conducted on the different HR coatings were carried out at 1064 nm with single shot pulses (1-on-1) of 3 ns. The results are summarized in Figure 3, and are clearly in favor of the Ta_2O_5 coatings with an average of 14.5 ± 2.1

J/cm^2 by comparison with 8.3 ± 1.6 J/cm^2 for Nb_2O_5. These thresholds compare well with the values obtained for other single layer systems such as Al_2O_3,nH_2O, SiO_2 or ThO_2 [9].

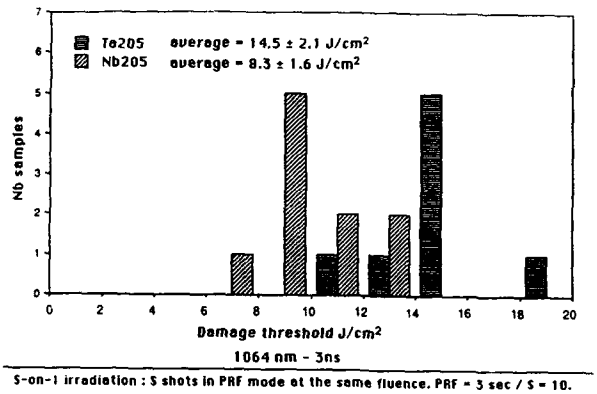


Fig. 3: Laser damage threshold (J/cm^2) measurements on niobium and tantalum oxide coatings.

Attempts to obtain multilayers were limited by peeling problems which occurred after four to five M_2O_5-SiO_2 pairs, probably as a result of stress in stacking (7-8 pairs are required to achieve a 99 % reflectivity).

CONCLUSIONS

Stable colloidal suspensions of amorphous niobium and tantalum oxides could be obtained by hydrolysis of the pentaethoxides in ethanol and in the presence of triethylamine. These sols were used for the obtaining of coatings on SiO_2 wafers via spin-coating techniques. Ta_2O_5 layers display interesting laser damage threshold values (14.5 ± 2.1 J/cm^2).

This work was performed under grant CEA-1879, and financial support is gratefully acknowledged.

REFERENCES

1. H. Schroeder, Physics of Thin Films 5, 87 (1969); J. Martinsen, R.A. Figot and M.W. Shafer, Mater. Res. Soc. Symp. Proc. 32, 145 (1984).
2. I.M. Thomas, Appl. Optics 26, 4688 (1987).
3. K. Tanabe and T. Ilzuka, "Catalytic Properties of Niobium Compounds", Technical Reports CBMM (Parts I,II, III) (03/83, 07/85, 08/85).
4. D.C. Bradley, B.N. Chakravarti and W. Wardlaw, J. Chem. Soc. 1956, 2381.
5. L.G. Hubert-Pfalzgraf, New J. Chem. 11, 663 (1987).
6. H.C. Ling, M.F. Yan and W.W. Rhodes, "Science of Chemical Processing", Ed. L.L. Hench, D.R. Ulrich; Wiley, New York, 198 , 285.
7. K. Nakanishi, Y. Takamiya and T. Shimohira, Yogyo Kyokai-Shi 94, 1024 (1986).
8. B.E. Yoldas, T.W. O'Keeffe, Appl. Optics 18, 3133 (1979).
9. H. Floch and J.J. Priotton, Proc. 21st Boulder Damage Symposium, Colorado, Nov. 1989.

MICROWAVE PROCESSING OF SOL-GEL DERIVED POTASSIUM NIOBATE

Z. Fathi, I. Ahmad and D.E. Clark, University of Florida

I ABSTRACT

Microwave energy has been used in a novel processing method. The relationship between processing, structure and properties of sol-gel-derived potassium niobate sol as well as thin films has been investigated. A comparison has been established between microwave and conventional heating for drying, calcining and crystallizing sol-gel-derived samples. Structural and phase changes were monitored by thermogravimetric analysis (TGA), differential thermal analysis (DTA) and x-ray diffraction (XRD).

II INTRODUCTION

Microwave energy is under evaluation as an alternative means of producing an array of ceramic products. The process consists of a conversion of microwave radiation into heat. The material itself is the source of heat which is generated by the dissipating microwave energy in the body. The origin of heating lies in the ability of the electric field to polarize charges in materials and the inability of these polarizations to follow extremely rapid reversals of the electric field. In addition to these polarization effects, there are direct conduction effects due to redistribution of charged particles under the influence of the externally applied electric field.

It has been reported that temperatures and times have been reduced in processing superconducting ceramics [1] using microwave energy. Potassium niobate has a higher electro-optic coefficient than lithium niobate. Therefore, lowering the processing temperatures and heating times of this material would be of extreme interest.

The main goal of this study was to investigate the variation of several processing parameters namely times, power levels and temperatures, on sol-gel-derived potassium niobate. One sol-gel system (the ethoxides) was selected for preparing the $KNbO_3$ sol and thin film samples. This system is suitable for microwave drying and sintering studies of potassium niobate.

III EXPERIMENTAL APPROACH

(a) MATERIALS

The sol-gel-derived samples were prepared by using niobium and potassium ethoxide precursors. Each precursor was diluted with ethanol and mixed to 1:1 molar ratio of potassium and niobium. This mixture was hydrolyzed with water at the ratio of H_2O/alkoxide = 1.75. Figure 1 is a process flow diagram of the sol-gel process used in this study.

The gel samples were obtained by separating the gels from the liquid phase by filtration. The sol-gel-derived thin films were prepared by spin-coating on

Mat. Res. Soc. Symp. Proc. Vol. 180. ©1990 Materials Research Society

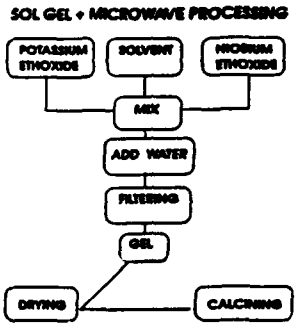


Figure 1. Schematic of the sol gel process.

fused-silica substrates. The substrates were spun at 2500 rpm for 20 sec.

(b) MICROWAVE SET UP

Drying and calcining were performed in the microwave set up shown in Figure 2. The sample was placed in an insulating material lined with a microwave susceptor. This is referred to as microwave hybrid heating because the microwave heats the susceptor which, in turn, heats the sample. The microwaves also interact with the sample. Altering the amount of susceptor material allows for for variation of the duty cycle of microwave power while still maintaining the same temperature. This provides a means of investigating the effects of the power level on crystallization of various phases. The temperature of the substrate is monitored by a shielded K-type thermocouple. It has been shown that hybrid heating results in much more uniform heating [2,3]. We have assumed that the substrate and the thin film are at the same temperature.

IV RESULTS AND DISCUSSIONS

(a) GEL

The gel derived from the filtration step described earlier has a different stoichiometry than the liquid phase due to the differences between the solubility of potassium and niobium [4].

In order to select the most appropriate process conditions, TGA and DTA analyses were performed in air up to 1000°C as shown in Figure 3. The DTA curve exhibits an endothermic peak at 100°C that corresponds to the removal of water and ethanol from the gel. Strong and broad exothermic peaks were detected at approximately 550°C. These peaks correspond to organic burnout and low temperature crystallization of the gel. Weak exothermic peaks, observed at higher temperatures, appear to be due to the perovskite crystallization and a phase transition. No detailed investigation has been done in this regard. The TGA shows a weight loss up to 200°C followed by another loss at around 550°C. A subsequent step was to draw a comparison between microwave hybrid heating and conventional heating in the area of drying and calcining .

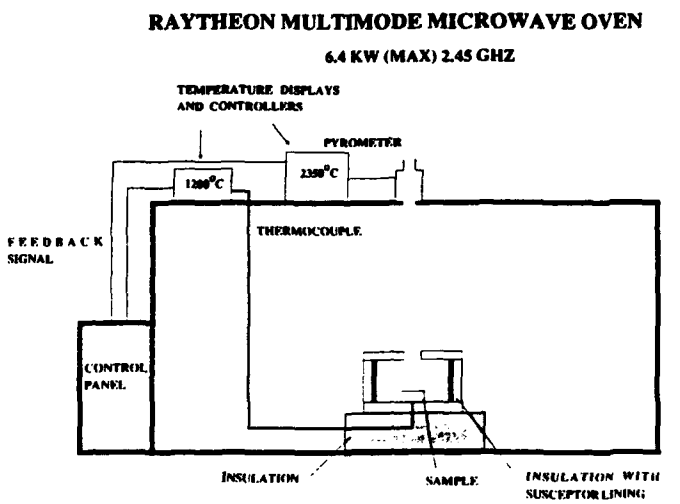


Figure 2. Microwave set up for drying and calcining.

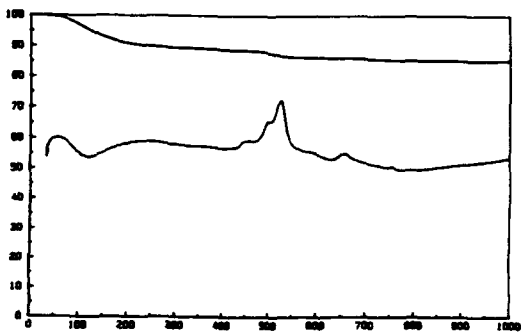


Figure 3. TGA, DTA give information about structural changes during heating.

Microwave heating shortened significantly the times for dehydration (drying) and organic burnout (calcining). Table 1 shows that dehydration and organic decomposition by microwave heating took 22.5 minutes at 100°C. Removal of organics by microwave took 85 minutes at 550°C. On the other hand, conventional processing required 24 hours at 80°C and 12.5 hours at 550°C for the completion of drying and calcining.Thus, microwave heating reduces time and saves energy.

CONVENTIONAL HEATING		
	Time	T°C
Drying	24 h	80
Calcining	12.5 h	550

MICROWAVE HEATING		
	Time	T°C
Drying	22.5 min	100
Calcining	85 min	550

Table 1.Comparison between the two processing procedures with regard to drying and calcining.

The XRD pattern (Figure 4) of gel samples heated at 550°C with 67% duty cycle (DC) and at 600°C with 80% DC under 800W incident power illustrate well-crystallized $KNbO_3$. The samples also exhibit a small fraction of $K_4Nb_6O_{17}$ [5]. The differences caused by gel filtration permit the formation of this phase.

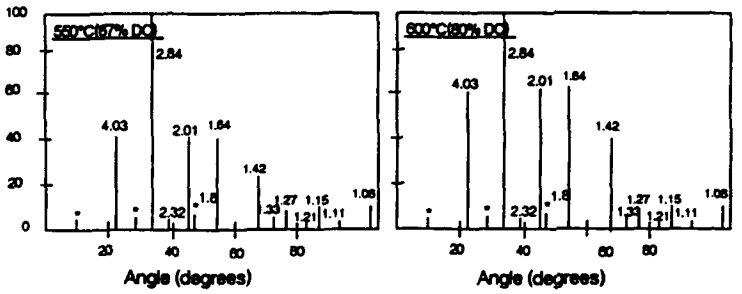


Figure 4. Illustration of full crystallization in the case of gel samples heat treated at 550°C and 600°C (* indicates the $K_4Nb_6O_{17}$ phase)

(b) FILMS

Three thin films were identically prepared and each subjected to a different heat treatment above the crystallization temperature. The molarity of the solution prior to spin-coating was 0.4 mol/l. Three layers were deposited on the fused silica substrates with the casting parameter discussed previously. The thickness of the films was approximately 2500Å. The duty cycle was a variable parameter that allowed the investigation of microwave energy interaction with the samples.

Sample (a) was conventionally heated from room temperature to 650°C. It was transfered to the microwave oven where it was held at 650°C for 60 min at 17% DC of an 800W incident power. Sample (b) was similarly taken to 650°C but kept at that temperature by hybrid heating at 70% DC of the same incident power. Sample (c) was subjected to a different initial heat treatment. It was taken to 650°C by microwave hybrid heating. The temperature was maintained in the microwave for

60 min at 70% power level.

Processing of coatings showed unexpected results. The examination of these samples by XRD showed poor crystallization and the pronounced peaks were not those of $KNbO_3$, as was the case of gel samples heat treated at 650°C. Instead, peaks of $K_4Nb_6O_{17}$-$3H_2O$ along with $K_4Nb_6O_{17}$ were observed.

In the case of thin films, the increase of surface area along with the interactions occurring between the sol and the substrate are believed to be the cause of the departure from the $KNbO_3$ phase. We believe that these substrate effects prohibit the $KNbO_3$ crystallization, but allow $K_4Nb_6O_{17}$ crystallization. Exposure of the films to moisture induces a subsequent transformation of $K_4Nb_6O_{17}$ to those of $K_4Nb_6O_{17}$-$3H_2O$.

Microwave heating enhanced the crystallization of the phase that was favored by thermodynamics. As shown in Figure 5a and 5b, the samples that were subjected to the same kind of heat treatment with different duty cycles exhibited more crystallization in the case of higher power levels. The examination of the XRD pattern of sample (c), microwave hybrid heated from the initial state at room temperature to the end of the heat treatment, shows even more crystallization than sample (b) which was subjected to the same duty cycle during calcining.

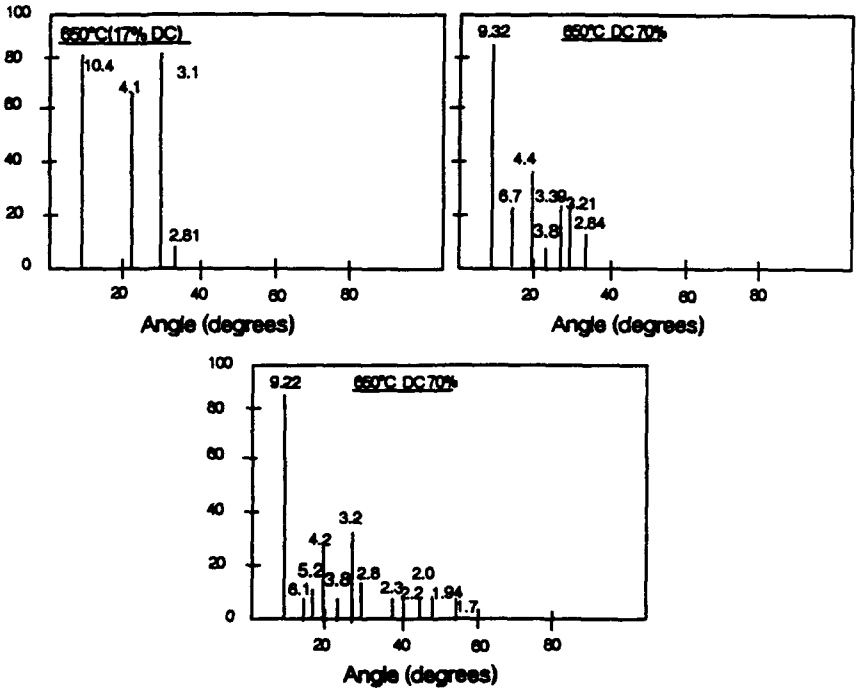


Figure 5a. 5b. 5c. The XRD patterns of thin films (a),(b) and (c) are shown.

V Summary

Microwave energy has been used for processing potassium niobate. Several processing parameters were investigated under this new approach. Microwave heating shortened significantly the times for dehydration and organic burnout in gel samples. The XRD pattern of the gel sample heated at 550°C exhibited well-crystallized $KNbO_3$ and a small amount of $k_4Nb_6O_{17}$. On the other hand, sol-gel derived thin films of potassium niobate showed different results. The present phases were $K_4Nb_6O_{17}$-$3H_2O$ and $K_4Nb_6O_{17}$. Microwave energy appears to enhance the crystallization of these phases.

Acknowledgement:

This project was funded by the Defense Advanced Research Projects Agency (DARPA).

Sol-gel-derived potassium niobate was provided by M.Sacks, Department of Materials Science and Engineering. University of Florida.

References:

1. I. Ahmad, G.T. Chandler and D.E. Clark, Processing of Superconducting Ceramics Using Microwave Energy, Presented at the Materials Research Society Symposium on Microwave Processing of Materials, Reno, Nevada, April 5-8, 1988. Published in the Proceeding;Microwave Processing of Materials, pp 239-246, vol.124. Edited by W.H. Sutton, M.H. Brooks and I.J. Chabinsky, Materials Research Society, Pittsburgh, PA, 1988.

2. A.S. De, I. Ahmad, E.D. Whitney and D.E. Clark, Effect of Green Microstructure on Microwave Processing of Alumina. Presented at the 14th Annual Conference on Composites and Advanced Ceramics, January 14-17, 1990, Cocoa Beach, Florida. To be published in the proceedings.

3. A.S. De, I. Ahmad, E.D. Whitney and D.E. Clark, Effect of Green Microstructure and Processing Variables on Microwave Sintering of Alumina. Presented at the Materials Research Society Spring Meeting, April 16-21, 1990, San Francisco, California. To be published in the proceedings.

4. M.M. Amini and M.D. Sacks, Sol-Gel Processing of Potassium Niobate. Presented at the Materials Research Society Spring Meeting, April 16-21, 1990, San Fransisco, California. To be published in the proceedings.

5. K. Nassau, J. Shieuer and J. Bernstein, *J. Sol. State. Sci.*, 116 [3] 348-55 (1969).

DIELECTRIC CHARACTERIZATION OF POLYCERAM FILMS

G. Teowee, J.M. Boulton, H.H. Fox, A. Koussa, T. Gudgel
and D.R. Uhlmann
Department of Materials Science and Engineering,
University of Arizona, Tucson, AZ 85721.

ABSTRACT

Polycerams are an emergent class of hybrid, multifunctional materials which combine the properties of organic and inorganic materials. Films have been prepared from silicon alkoxides and reactive, functionalized polymers such as triethoxysilyl modified polybutadiene (MPBD), (N-triethoxysilylpropyl)O-polyethylene oxide urethane (MPEOU) and trimethoxysilylpropyl substituted polyethyleneimine (MPEI). Characterization of dielectric constant and tan δ of the films has been carried out over a range of frequency from 500 Hz to 100 kHz; and the results are used to consider the potential of Polycerams as dielectric materials.

INTRODUCTION

Many desirable properties can be obtained by incorporating organic polymers in inorganic gels. In particular, the unique drying behavior of Polycerams allows the simple fabrication of monoliths and thick films without the cracking problems associated with conventional sol-gel derived alkoxide gels. A wide range of synthetic routes can be used to prepare these materials [1,2 e.g.]. One attractive method, which was chosen in this work, is to incorporate reactive functionalized polymers into the forming gel network. Previous examples of reactive polymers include silanol terminated polydimethylsiloxanes [3,4, e.g.] and triethoxysilyl terminated polytetramethylene oxide [5]. Schmidt has reported a dielectric constant of approximately 2-3 and a surface resistivity of $10^{16}\Omega$ for organically modified coatings [6,7]; however, no other electrical characterization of Polycerams has been published.

EXPERIMENTAL

Details of precursor materials can be found in an accompanying paper [8].

In initial experiments for MPBD [triethoxysilyl modified 1,2- polybutadiene] and MPEOU [(N-triethoxysilylpropyl) O-polyethylene oxide urethane] -modified silica, tetramethoxysilane (TMOS) was directly hydrolyzed with H_2O resulting in an exothermic reaction and the formation of a clear solution. The water was acidified to 0.15M HCl, and a molar ratio of 1 TMOS: 4 H_2O was used. The solution was stirred at room temperature for 10 min and the polymer was added in THF (1 g TMOS: 6 ml THF) to give a wgt ratio of 2 TMOS: 1 polymer. The resulting solution was stirred for 30 min prior to coating. This reaction scheme was unsuitable for MPEI [thriethoxysilylpropyl substituted polyethyleneimine], as the basic polymer solution (pH 9.4) resulted in rapid gelation. Therefore tetraethoxysilane (TEOS) was hydrolyzed with 0.15M HCl at a molar ratio of 1 TEOS: 2 H_2O in THF (1 g TEOS: 4.38 ml THF). The solution was refluxed for 15 mins and cooled; polymer was added and then directly used for coating.

Mat. Res. Soc. Symp. Proc. Vol. 180. ©1990 Materials Research Society

Coatings of each solution were applied to Pt-coated Si substrates at 2000 rpm for 20 secs. Films of neat polymer and silica were prepared by similar methods. The substrates were fabricated by sputtering Pt for 10 mins at 200 watt RF power under 20 m Torr Ar pressure onto oxidized Si wafers, resulting in films 1700Å thick. These were annealed for 30 mins at 700C. Coatings were dried at 50C for 24 hrs prior to electrical characterization. After drying, Pt dots with radius of about 0.70 mm were sputtered onto the coating using a shadow mask.

In the second set of experiments, the effects of the TMOS: PBD ratio on dielectric properties were determined. Coating solutions were prepared as above, except the solutions were refluxed for 30 mins prior to coating at various speeds for 20 secs Si wafers were also coated for FTIR analysis.

Capacitance and dissipation factor (tan δ) measurements were obtained in a shielded probe station under flowing dry N_2 gas using an HP 4192A impedance analyzer, controlled via GPIB from a personal computer. The signal amplitude was 0.005 V rms, while the frequency range was from 500 Hz to 100 kHz (the limit of the test fixture).

RESULTS AND DISCUSSION

In determining SiO_2 : polymer volume ratios, the following densities of the various components were taken: SiO_2, 2.05 g/cm^3; MPBD, 0.90 g/cm^3; MPEI, 0.91 g/cm^3 and MPEOU, 1.13 g/cm^3. The skeletal density of sol-gel derived SiO_2, prepared under acidic catalysis conditions, is taken from Ref 9. Results are tabulated in Tables 1 and 2.

TABLE 1

Polymer	TMOS: polymer wgt ratio	TEOS: polymer wgt ratio	SiO_2: polymer wgt ratio	Volume % polymer
MPBD	2:1	--	0.7895:1	74.3
MPEOU	2:1	--	0.7895:1	69.7
MPEI	--	2.737:1	0.7895:1	74.0

TABLE 2

TMOS:MPBD wgt ratio	SiO_2:MPBD wgt ratio	Volume % polyer
2:1	0.7895:1	74.3
2.67:1	1.0527:1	68.4
4:1	1.5790:1	59.1

FTIR was used to monitor drying of MPBD based Polyceram films on Si wafers. The coatings were heated at various temperatures using the schedule: room temperature, 24 hrs; heating temperature, 24 hrs; heating temperature, 24 hrs under vacuum (23.4 mm Hg). The results presented in Fig. 1 show that a 100C treatment in vacuum is necessary to dry the films.

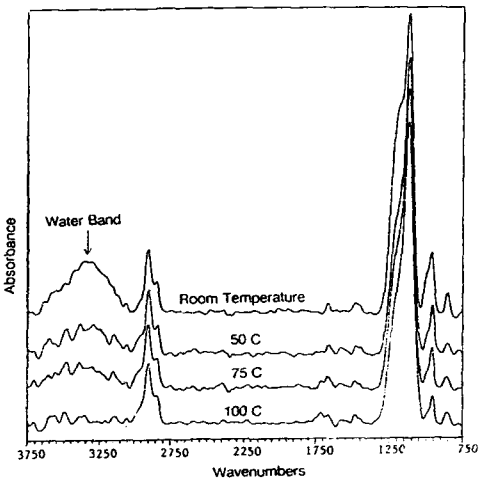


Figure 1. Infrared absorption for PBD based Polycerams dried under vacuum at room temperature, 50, 75, and 100C.

Data on dielectric constant and tan δ at 10 kHz and 0.005 V rms signal level for the different Polyceram films are presented in Table 3.

TABLE 3

Polyceram system	Dielectric constant	Tan δ
74.3 vol% MPBD	4.4	0.02
74.0 vol% MPEI	7.2	0.06
69.7 vol% MPEOU	7.8	0.16

Among the modified polymers, MPEOU is the most polar while MPBD is non-polar. Furthermore, MPEOU is conjugated, contributing an added polarizability arising from electron delocalization within the molecule. Hence it is to be expected, as reflected in Table 3, that the MPEOU film has the highest dielectric constant while the MPBD film has the lowest value.

Three compositions of MPBD films were investigated with different relative amounts of TMOS and MPBD. They all exhibit a similar dielectric constant (≈5.7) and tan δ (≈0.04), as can be seen in Table 4.

TABLE 4

Volume % PBD	E_r at 10 kHz, 0.005 V rms	Tan δ at 10 kHz, 0.005 V rms	Calculated E_r from end members
59.1	5.7	0.03	6.9
68.4	5.7	0.05	6.0
74.3	5.8	0.03	5.3

Note that the values of E_r shown in Table 4 (5.7) are notably higher than the value for the MPBD-based films presented in Table 3 (4.4). This difference very likely reflects the difference in film thickness and process conditions used to prepare the films. Such variations are deserving of further exploration, which is presently underway.

The dielectric properties of neat SiO_2 and MPBD films at 10 kHz and 0.005 V rms signal level which have been annealed at 100C under vacuum for 48 hrs are tabulated in Table 5.

Table 5

Film	Dielectric Constant
TMOS-derived SiO_2	13.0
TEOS-derived SiO_2	13.0
neat MPBD	2.7

Assuming for simplicity that the dielectric constant of the Polyceram reflects the volume fractions of the constituents and using the end-member values in Table 5, the calculated dielectric constants for the MPBD Polycerams shown in Table 4 were obtained.

There is a strong increase in tan δ at low frequencies for the Polyceram films (Fig. 2). Such behavior can be attributed to dc conduction since there is no strong dispersion in dielectric constant, which would be present in the case of relaxation [10]. To investigate the nature of the charge carriers within the film, capacitance vs. applied bias measurements were taken. If ionic impurities were present, then peaks or hysterisis would be expected. Fig. 3 shows a straight line, however; and hence the conduction is assumed to be electronic in nature.

The dielectric constants obtained for the MPBD-based Polyceram films lie between values for the end-members, MPBD and SiO_2, and are reasonably predicted by a simple volume fraction additive relation. In detail, the measured E_r's vary less with composition than predicted by the simple relation.

Figure 2. 2 TMOS: 1 MPBD Film at 0.005 V_{RMS}

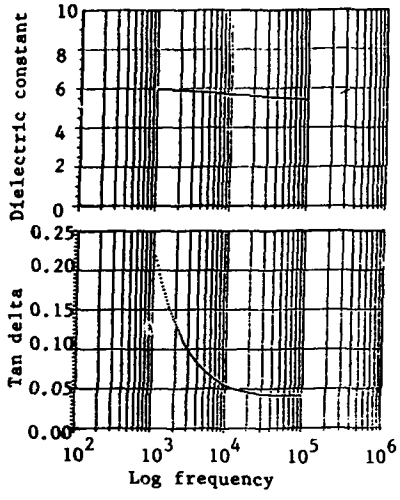
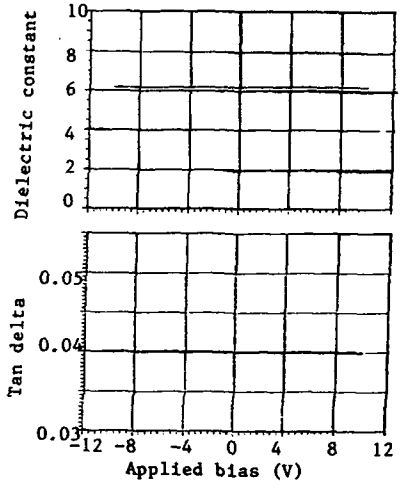


Figure 3. For 4 TMOS:1 MPBD Film at 1 KHZ, 0.005 V_{RMS}



More generally, the dielectric constants of about 13 obtained for TEOS- and TMOS-derived films which had been vacuum dried at 100C appear to limit the ability to cbtain Polyceram films with exceptionally low dielectric constants (assuming reasonable fractions of the inorganic constituent and TMOS/TEOS as precursors for that constituent). In this light, the low E_r values reported by Schmidt are all the more interesting.

Beyond this, it is clear from the present results that it is possible -- by control of chemistry and process conditions -- to vary the dielectric constants of Polyceram films over a wide range. Such films offer improved adhesion to inorganic surfaces and better abrasion resistance compared with polymer films (as observed here for MPBD-based films on platinized surfaces).

CONCLUSIONS

MPBD-based Polyceram films with polymer volume % content from 59.1 to 74.3 have been prepared; their dielectric constants and tan δ's are about 5.7 and 0.03 respectively. The E_r values are in the range predicted by the volume fractions from the E_r's of the end members. By varying the chemistry and process conditions, E_r can be varied over a considerable range. Finally, the relatively high value of E_r for vacuum-dried TMOS- or TEOS-derived films sets limits to the E_r's which can be obtained for Polyceramas using these precursors.

ACKNOWLEDGMENTS

Financial support for the present work was provided by the Air Force Office of Scientific Research. This support is gratefully acknowledged.

REFERENCES

1. H. Schmidt in Better Ceramics Through Chemistry, edited by C.J. Brinker, D.E. Clark and D.R. Ulrich (Mater. Res. Soc. Proc. 32, 1984) pp. 681-691.
2. H. Schmidt and B. Seiferling in Better Ceramics Through Chemistry II, edited by C.J. Brinker, D.E. Clark and D.R. Ulrich (Mater. Res. Soc. Proc. 73 1986) pp. 739-750.
3. C.S. Parkhurst, W.F. Doyle, L.A. Silverman, S. Singh, M.P. Anderson, D. McClurg, G.E. Wnek and D.R. Uhlmann, Ibid., pp. 769-773.
4. H.H. Huang, B. Orler and G.L. Wilkes, Macromolecules 20, 1322 (1987).
5. R.H. Glaser and G.L. Wilkes, Polymer Bull., 19, 51 (1988).
6. H. Schmidt, in Sol-Gel Science and Technology, edited by M.A. Aegerter, M. Jafelicci, Jr., D.F. Souza and E.D. Zanotto (World Scientific Publishing, Singapore, 1989), p. 432.
7. H. Schmidt, DVS-Berichte 110, 54 (1988).
8. J.M. Boulton, H.H. Fox, G.F.Neilson and D.R. Uhlman paper entitled "Synthesis and Structural Characteristics of Polycerams" presented at this proceedings.
9. C.J. Brinker, E.P. Roth, G.W. Scherer and D.R. Tallant, J. Non-Cryst. Solids 71, 171 (1985).
10. A.K. Jouscher, Dielectric Relaxation in Solids, Chelsea Dielectric Press, London (1983).

SOL-GEL THIN FILM ELECTRONIC PROPERTIES

W. L. Warren, P. M. Lenahan, C. J. Brinker*, G. R. Shaffer, C. S. Ashley*
and S. T. Reed*.
The Pennsylvania State University, University Park, PA 16802
*Sandia National Laboratories, Albuquerque, NM 87185

ABSTRACT

We have explored the effects of various processing parameters on the dielectric and electronic integrity of sol-gel derived silicate thin films and have identified several factors that strongly affect the thin film electronic properties. We find that sol-gel dielectrics can exhibit excellent dielectric integrity: viz., low interface trap densities and fairly good insulating properties approaching those of a thermally grown SiO_2 film on Si.

INTRODUCTION

Silicon dioxide thin films are extensively used in microelectronic devices as the gate and field oxides in metal-oxide-semiconductor-field-effect-transistors (MOSFET's), passivation layers, diffusion and oxidation barriers, and scratch resistant coatings. Currently, thermally grown silicon dioxide films on silicon (typical growth temperatures range from 800°C to 1100°C) are the best insulators and exhibit the lowest interface trap densities; they are the heart and soul of modern day microelectronic devices and are the standard by which other dielectrics are judged. In recent years; however, there has been a considerable amount of interest in the development of lower temperature/shorter time dielectric deposition schemes.[1-4] Some applications include III-V compound semiconductor MOSFET processing as well as primary dielectrics for thin film transistors.

In this study we have explored the electronic and physical properties of sol-gel-derived silicate thin films on silicon. We have investigated how various processing parameters affect the dielectric integrity of the silicate films on silicon and have identified several factors that affect the electronic properties of the silicate gel thin films. We find that (1) the water to silicon alkoxide ratio strongly affects both the film's electronic and physical properties; (2) the film's properties are relatively independent of the annealing ambient; and (3) a rather short (*5 min.*) anneal time at T>800°C is necessary to obtain sufficient insulating properties. Our results illustrate that sol-gel thin films on silicon can be of high quality; they exhibit low interface trap densities and fairly good insulating properties, indicating that sol-gel oxides may be potentially useful to the microelectronics community.

Mat. Res. Soc. Symp. Proc. Vol. 180. ©1990 Materials Research Society

EXPERIMENTAL DETAILS

The solutions used in this study were prepared using silicon alkoxides, $Si(OC_2H_5)_4$, as molecular precursors to SiO_2. In alcohol/water solutions the alkoxide is hydrolyzed and condensed to form Si-O-Si bonds as shown by the following net reaction.

$$n\ Si(OC_2H_5)_4 + 2n\ H_2O \rightarrow n\ SiO_2 + 4n\ (C_2H_5OH)$$

Many factors influence the structure of the inorganic polymers. The most important are the water to alkoxide ratio, pH, and aging conditions [5-9] of the initial solutions. Film porosity is largely determined by the polymer structure. For example, weakly branched species are fairly compliant and form denser oxides; however, highly crosslinked polymers resist the compressive forces of surface tension during drying, leading to larger pores that are only removed at higher temperatures by sintering.

The sol-gel solutions were prepared with varying water to silicon alkoxide ratios; the ratios investigated were 2.5, 5.0, 7.5, 10.0, 12.5, 15.0 and 20.0 to 1. Further details regarding solution preparation can be found in reference 5. The solutions were deposited on n-type (100) Si substrates with resistivities of 1-10 Ω-cm. Prior to film deposition the substrates were cleaned using a standard RCA procedure. The substrates were then immediately coated using either a dip coating apparatus or a commercial spinner. After deposition, the thin porous silicate layers were heat treated in air at 80°C to help burn off some of the residual organics and adsorbed water, followed by an anneal at higher temperatures in either an argon, air, or oxygen ambient. The annealing temperatures investigated were 500, 650, 725, 800, 900, and 1000°C. After the anneal Al was deposited on the films using an electron beam evaporator and a standard post-metallization anneal (5% H_2/95% N_2) at 400°C for 30 min. was performed.

Two factors that degrade MOSFET performance are interface traps at the silicon-oxide interface and large leakage currents through the dielectric. To evaluate the interface trap densities MOS high frequency (1MHz) and quasi-static CV measurements were performed. The mid-gap interface trap densities were calculated using the Terman [10] and combined High-Low [11] frequency methods.

The breakdown strengths (the electric field at which substantial leakage currents flow through the oxide) were evaluated using a corona discharge apparatus [12]. The corona ions charge the films surface. By measuring the potential across the film's surface using a Kelvin probe and and electrostatic voltmeter several minutes after charging, we evaluate an arbitrarily defined breakdown field corresponding to a current density of $\approx 10 \times 10^{-10}$ A/cm^2.

The etch rate experiments were performed using a buffered HF solution which etches a thermal oxide at $\approx$ 1 Å/sec. (More porous oxides exhibit faster etch rates, for example, air pressure chemical vapor deposited SiO_2 films etch 8 times faster than thermal oxides [13].)

Refractive index experiments were made using a Rudolf Auto-ELIV ellipsometer. Again higher refractive indicies are generally indicitive of a denser oxide [14]. For comparisons the refractive index of a thermal oxide was measured to be 1.461±0.002.

RESULTS

In Figure 1 we illustrate the breakdown strength and etch rate of a silicate thin film prepared using solutions with different water to silicon alkoxide ratios. The solution's water to silicon alkoxide ratio strongly affects the insulating properties (and density) of the thin films. Figure 2 further demonstrates the effect of the water to silicon alkoxide ratio (r) on the refractive index of the films. When r is between 10 to 15:1, the film's refractive index (and density) is about maximized. The refractive index measurements correlate extremely well with the breakdown strength and etch rates of Fig. 1. At very low (<5:1) or very high (>15:1) ratios the films properties are significantly degraded. The results, of the films prepared using solutions with lower water to silicon alkoxide ratios, came as a surprise. It is fairly well documented that bulk monolithic silicates prepared using solutions with low r values form more weakly branched polymers [9,15]; these species are quite compliant and during drying form denser oxides with small pores that collapse at lower temperatures via viscous sintering. Highly crosslinked polymers (formed at higher r values) are sufficiently stiff to resist the compressive forces of surface tension during drying; leading to larger pore sizes that sinter at higher temperatures.

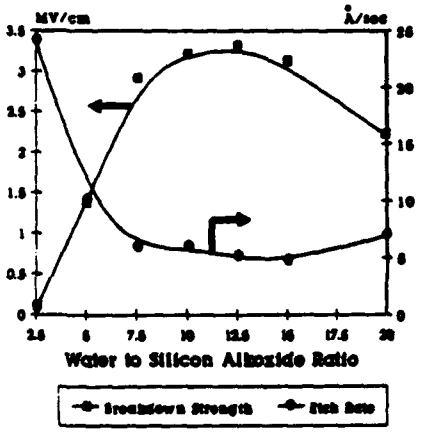


Figure 1. Breakdown strength and etch rate of sol-gel films on silicon prepared using solutions with different water to silicon alkoxide ratios. All films were annealed in argon for 5 min. at T = 800°C.

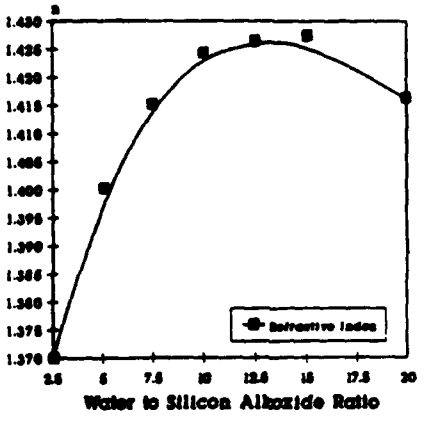


Figure 2 Refractive index of sol-gel films on silicon prepared using solutions with different water to silicon alkoxide ratios. All films were annealed in Argon for 5 min. at 800°C.

However, in this thin film study we find (1) that films prepared using solutions with low r values ($r \leq 7.5:1$) are more porous dielectrics (lower refractive indicies, lower breakdown strengths and faster etch rates), (2) films prepared with intermediate water ratio solutions (~10:1 to ~15:1) are the densest oxides and (3) films prepared using solutions with ratios $r \geq 15:1$ tend to again become porous. A possible explanation for our results may be provided by the work of Hurd et. al [16,17]; who observed the drying front of a dip coated film using imaging ellipsometry. Their results [17] on water alcohol mixtures demonstrate that during dip coating, water becomes concentrated near the drying line. Since all our solutions contain excess water ($r > 2$ according to eqn. 1), and since water has about a factor of three greater surface tension than alcohol, the capillary pressure exerted on the solid phase at the final stage of drying is larger for greater water to alkoxide ratios.

Our work strongly suggests that it is this additional "compacting" force in the films prepared using solutions with r values between 10 and 15 that leads to higher densities, smaller pores and lower sintering temperatures. However larger r values (> 15) apparently promote aging leading to much stiffer structures that resist collapse by the additional capillary pressure. This would explain the increase in porosity of the films prepared using the highest water ratios. These results strongly demonstrate that the polymer structure and deposition conditions affect the thin film properties and furthermore illustrate that one may employ different water to silicon alkoxide ratios to tailor the refractive index.

Figure 3 illustrates some of our CV measurements for a sol-gel thin film annealed at 800°C for 5 min in an argon ambient using a water to silicon alkoxide ratio of 12.5:1. Curves 3(a) and 3(b) are typical high frequency and and quasi-static CV curves for sol-gel films on silicon annealed at T≥725°C in any ambient as long as the water to alkoxide ratio is between 10:1 and 15:1. The mid-gap interface trap densities are always quite low (~8 x10^{10} cm^{-2} ev^{-1}); the films exhibit strong accumulation and inversion characteristics, and there is very little fixed 'net' charge in the dielectric. (All an indication of a fairly high

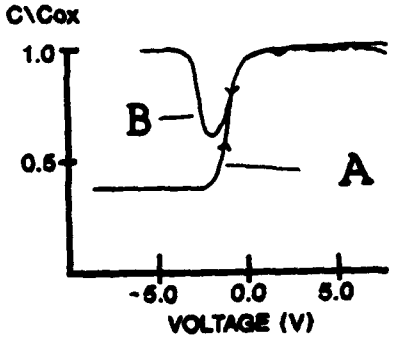


Figure 3 High frequency (A) and quasi-static (B) capacitance vs. voltage measurements for a silicate gel film annealed in argon for 5 min. at 800°C. The water ratio is 12.5:1.

quality dielectric.) Figure 4 illustrates that the mid-gap interface trap densities are quite low (~8 x10^{10} cm^{-2} ev^{-1}) for various anneal temperatures in an argon ambient. We believe that we are not growing a thermal oxide in the argon ambient. (For comparison we measure the mid-gap interface trap density of a high quality thermal oxide to be ~2 x10^{10} cm^{-2} eV^{-1}, the detection limit of our apparatus. Interface trap densities ≤ 10^{10} cm^{-2} eV^{-1} are typical for high quality thermally grown SiO_2 films on silicon after a forming gas or post-metallization anneal.)

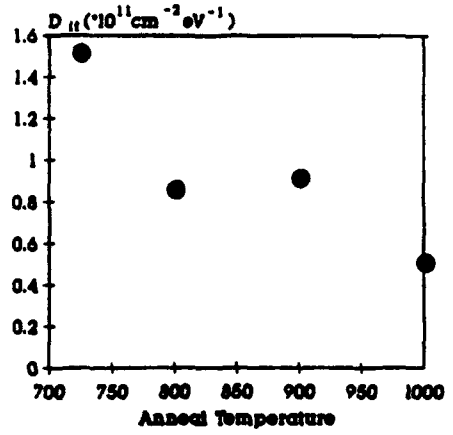


Figure 4 Mid-gap interface trap densities of the silicate gel thin films on silicon annealed at different temperatures. All anneals were performed in argon for 5 min. The films were prepared using solutions with a 12.5:1 water to silicon alkoxide ratio.

The breakdown strengths and etch rates of silicate gel thin films vs anneal time is illustrated in Figure 5. As demonstrated in Fig. 5 only a relatively short anneal time (5 min.) is needed to optimize the film's properties; longer anneal times did not generally improve the film's properties. This observation may be of considerable interest in applications involving substrates that can withstand high temperatures for only short times. A sol-gel derived thin film would be a viable candidate. (The films illustrated in Fig. 5 were all annealed in an argon ambient. The film thicknesses after annealing for 5, 15 or 30 min. were all identical (± 4Å). This is again consistent with the notion that we are not growing a thermal oxide. (It is conceivable that some of the adsorbed water in the films reacts at the silicon/silicon dioxide interface forming a very small thermal oxide, i.e., a few angstroms at most.)

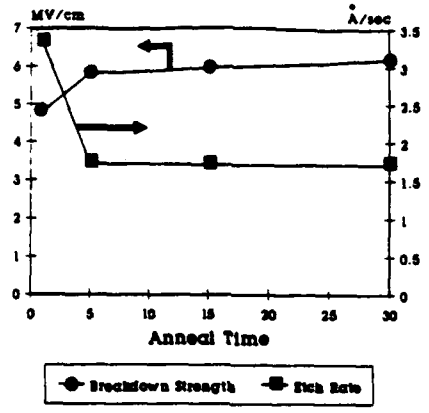


Figure 5 Breakdown strength and etch rates of sol-gel thin films on silicon annealed for different times in an argon ambient at 900°C. The solution's water to silicon alkoxide ratio was 12.5:1

In Figure 6 we shown the corona current density vs. electric field measurements for the silicate gel films annealed in argon at various temperatures. (The results are compared to a thermal oxide.) As shown, the films annealed at T≥800°C exhibit fairly good insulating properties. The sol-gel films annealed at 900°C and 1000°C for 5 min. are nearly identical to a thermal oxide.

Though all of the results discussed in this paper are for films annealed in an argon ambient, very similar results were also obtained for films annealed in an air or 0_2 ambient. The film's properties are relatively independent of the annealing ambient.

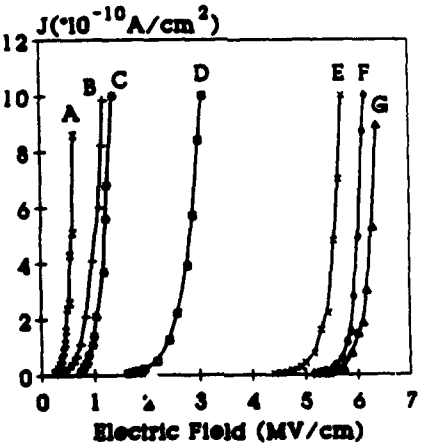


Figure 6 Current density vs. electric field measurements for sol-gel thin films annealed at A) 500°C, B) 650°C, C) 725°C, D) 800°C, E) 900°C and F) 1000°C for 5 min. in an argon ambient. Curve G) is for a thermal oxide.

OBSERVATIONS AND CONCLUSIONS

In summary we have been able to fabricate sol-gel silicate thin films on silicon of high quality. By varying some processing parameters we have been able to provide insight into fabricating silicate gel films of high dielectric integrity. We find (1) that the sol-gel properties are strongly affected by the water to silicon alkoxide ratio, (2) the films's properties are independent of annealing ambient and (3) that a relatively short anneal (5 min.) at $T \geq 800°C$ is needed to obtain sufficient densification and insulating properties.

REFERENCES

1) K. P. Pande and D. Gutierrez, Appl. Phys. Lett., 46, 416 (1985).
2) J. Batey and E. Tierney, J. Appl. Phys., 60, 3136 (1986).
3) P. G. LeComber and W. E. Spear, Seminconductors and Semimetals, D21, 89 (1984).
4) J. Lee, I-C Chen and C. Hu, IEEE Electron. Dev. Lett., 506 (1986).
5) C. J. Brinker, K. D. Keefer, D. W. Schafer, R. A. Assink, B. D. Kay and C. S. Ashley, J. Non Cryst. Solids, 63, 45 (1984).
6) K. D. Keefer in Better Ceramics Through Chemistry, Materials Research Society Sym. Proc., Vol. 32, eds. C. J. Brinker, D. E. Clark and D. R. Ulrich (North Holland, Amsterdam, 1984) p. 15.
7) C. J. Brinker, A. J. Hurd and K. J. Ward, Ultrastructure Processing of Advanced Ceramics, (Wiley, NY, 1988) p. 223.
8) D. W. Schafer, J. E. Martin, K. J. Ward and K. D. Keefer, in Physics of Finely Divided Matter, ed. by N. Boccara and M. Daoud (Springer-Verlag, Berlin, 1985) p. 13.
9) S. Sakka, K. Kamiya, K. Makita, and Y. Yamamoto, J. Non Cryst. Solids, 63, 223 (1984).
10) L. M. Terman, Solid State Electron, 5, 289 (1962).
11) E. H. Nicollian and J. R. Brews, MOS (Metal Oxide Semiconductor) Physics and Technology, (Wiley, NY, 1981) p. 800.
12) Z. A. Weinberg, W. C. Johnson and M. A. Lampert, J. Appl. Phys., 47, 248 (1976).
13) W. A. Pliskin and H. S. Lehman, J. Electrochem Soc., 112, 1013 (1965).
14) G. Lucovsky, M. J. Manitini, J. K. Srivastava and E. A. Irene, J. Vac. Sci. Tech., B5, 530 (1987).
15) C. J. Brinker, K. D. Keefer, D. W. Schafer and C. S. Ashley, J. Non Cryst. Solids, 48, 47 (1982).
16) A. J. Hurd and C. J. Brinker, Mat. Res. Soc. Sym. Proc., Vol. 121, p. 731 (1988).
17) C. J. Brinker, A. J. Hurd, D. R. Tallant and C. S. Ashley, submitted to Thin Solid Films.

SOL-GEL SYNTHESIS OF LEAD TITANATE FIBRES FOR USE IN THE FABRICATION OF PIEZOCERAMIC-POLYMER COMPOSITES

H. JANUSSON, C.E. MILLAR and S.J. MILNE
Division of Ceramics, School of Materials,
The University of Leeds, Leeds LS2 9JT, U.K.

ABSTRACT

Lead titanate fibres for use in piezoceramic-polymer composites have been prepared by extrusion of polymeric gels. The gels are formed from solutions of lead acetate, titanium isopropoxide and 2-methoxyethanol. The concentration of the solution, and amount of water and acid added, proved to have a strong influence on the suitability of the gel for extrusion purposes. The drying and firing conditions have been altered to obtain dense, fully crystalline $PbTiO_3$ fibres of 100 μm diameter.

INTRODUCTION

A range of piezoceramic-polymer composites have been designed for device applications such as sonar and medical diagnostics[1,2]. The polymer phase lowers density and permittivity and increases the elastic compliance of the composite relative to a single phase ceramic.

Composite systems based on unmodified $PbTiO_3$ are of interest because of their applications in hydrophones. The piezoelectric coefficients of unmodified $PbTiO_3$ lead to high hydrostatic voltage sensitivity, and the hydrostatic response can be further enhanced by fabricating highly anisotropic structures[1,3]. In this context piezoceramic-polymer composites comprising fibres of unmodified $PbTiO_3$ offer major benefits. By aligning the fibres anisotropic so-called 1-3 composites can be prepared. The numeric notation relates to the spatial arrangement or 'connectivity' of the ceramic and polymer phases[2]. This has a strong bearing on piezoelectric and mechanical properties. In the example quoted the fibres extend in 1-dimension and the polymer is continuous in 3-dimensions.

Reports in the literature indicate that fibrous unmodified $PbTiO_3$ can be prepared by hydrothermal reaction of appropriate inorganic salts. The diameters of the fibres produced are either in the range 1-10 μm[4] or 0.1-0.2 μm[5] depending on the conditions employed.

We have studied metallo-organic sol-gel routes based on lead acetate and titanium tetraisopropoxide to form gels which may be extruded into $PbTiO_3$ fibres. The conditions employed for gel and fibre production are now reported together with information on microstructures of composites prepared by combining the fibres with an epoxy resin.

EXPERIMENTAL

Gels were formed by the hydrolysis and condensation of refluxed solutions of $Pb(OOCCH_3)_2$, $Ti(OC_3H_7)_4$ and methoxyethanol solvent, $CH_3OCH_2CH_2OH$[6-8]. After refluxing, water and nitric acid were added to produce a 0.5 M solution of Pb/Ti with a water and acid concentration of 0.75 M and 0.002 M respectively. The gels were piston extruded through either ~650 μm or ~250 μm diameter orifices. The fibres were then dried and fired to convert to $PbTiO_3$. Hot stage microscopy was used to monitor crack formation during thermal conversion to the oxide. The decomposition

Mat. Res. Soc. Symp. Proc. Vol. 180. ©1990 Materials Research Society

process was examined with the aid of thermogravimetric (TGA) and differential thermal (DTA) analysis. X-ray diffraction was used to follow the crystallisation of the fibres as a function of temperature.

For composite manufacture, an epoxy resin was used as the matrix. The polymer was impregnated into a 'random' arrangement of fibres, and cured at 60°C. Microstructures of the resulting composites were examined using optical microscopy.

RESULTS

The extrusion conditions employed yielded either 150 μm diameter fibres of circular cross-section or ~100 μm diameter fibres of irregular profile. All thicknesses quoted refer to the diameter of fibres after firing at elevated temperatures; the lateral shrinkage during firing was ~25% of the diameter of the as-dried fibres.

Results are presented for three different drying methods:

i) drying at room temperature
ii) freeze-drying
iii) drying at ~125°C.

Extruded fibres, after drying in air, were invariably warped and cracked, Fig. 1. Freeze-drying also led to extensive cracking in each type of fibre. However by transferring extruded fibres directly to an oven at ~125°C cracking could be avoided in the 100 μm diameter fibres, Fig. 2a. Though cracking was reduced in the other, 150 μm diameter, fibres, a few isolated cracks were still observed, Fig. 2b. The integrity of the former sample was retained after firing at 500°C to convert the gel to the oxide. However the 150 μm diameter fibres exhibited further cracking during firing, the majority of which occurred between 200-250°C. This temperature range corresponds to the first combustion step identified in DTA/TGA experiments, Fig. 3. In the case of the 100 μm diameter samples, crack-free crystalline $PbTiO_3$ fibres were obtained after firing at > 500°C for 1 hour, Fig. 4.

The reduced tendency for cracking in the ribbed 100 μm diameter fibres, as compared to the 150 μm fibres, may be explained by the increased surface area/volume ratio of the former. This arises from their smaller overall diameter and their irregular 'ribbed' surface profile, Fig. 2a. Together these factors facilitate the elimination of volatile decomposition products, thereby reducing drying and shrinkage stresses, making possible

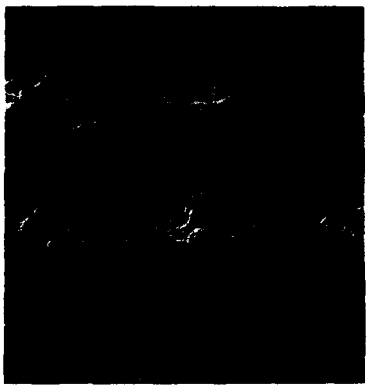


Figure 1
Scanning electron micrograph of an air dried fibre; bar represents 30 μm.



(a) (b)

Figure 2
Scanning electron micrographs of (a) 100 μm diameter ribbed $PbTiO_3$ fibres dried at 125°C (and fired at 700°C); (b) a 150 μm diameter $PbTiO_3$ fibre dried at 125°C (and fired at 700°C). Bar represents 30 μm.

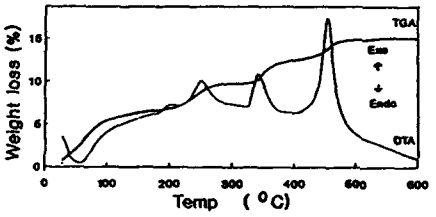


Figure 3
Differential thermal and thermogravimetric analysis of extruded fibres: heating rate 5°C/min.

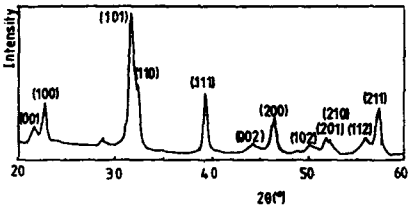


Figure 4
X-ray diffraction trace of $PbTiO_3$ fibres fired at 520°C. The unassigned peak at 28.8° 2θ disappeared on firing at higher temperatures.



Figure 5
Microstructure of a $PbTiO_3$ fibre-polymer composite. Bar represents 200 μm.

the synthesis of crack-free fibres of unmodified $PbTiO_3$.

The 100 μm fibres were subsequently used in the fabrication of polymer composites. The arrangement of the fibres within the polymer matrix is illustrated in Fig. 5.

It is intended to modify the forming process so as to align the fibres to produce anisotropic structures, and to maximise the volume fraction of the ceramic phase within the composite.

ACKNOWLEDGMENTS

H. Janusson wishes to thank Icelandic Alloys Ltd. for financial support. The authors wish to thank A.J. Moulson for useful discussions.

REFERENCES

1) R.E. Newnham, A. Safari, J. Giniewicz and B.H. Fox. Ferroelectrics 60, 15 (1984).
2) R.E. Newnham, D.P. Skinner and L.E. Cross. Mat. Res. Bull. 13, 525 (1978).
3) H. Banno. Ferroelectrics 50, 329 (1983).
4) T. Nishi, K. Igarashi, T. Shimizu, K. Koumoto and H. Yanagida. J. Mat. Sci. Letts. 8, 805 (1989).
5) M. Suzuki, S. Uedaira, H. Masuya and H. Tamura. In Ceramic Transactions Vol. 1, Ceramic Powder Science II, A, edited by G.L. Messing, E.R. Fuller and H. Hausner (Am. Cer. Soc., Westerville, 1988) pp. 163-171.
6) S. Gurkovich and J. Blum. In Ultrastructure Processing of Ceramics, Glasses and Composites, edited by L.L. Hench and D.R. Ulrich (Wiley, N.Y., 1984) pp. 152-160.
7) K.D. Budd, S.K. Dey and D.A. Payne. Br. Cer. Proc. 36, 107 (1985).
8) S.J. Milne (unpublished work).

MICROSTRUCTURAL EVOLUTION OF TiO_2 SOL-GEL THIN FILMS

J.L. KEDDIE and E.P. GIANNELIS
Department of Materials Science and Engineering, Cornell University, Ithaca, NY 14853.

ABSTRACT

Backscattering spectrometry has been used to determine the density of TiO_2 sol-gel films. The density of the as-deposited films relative to that of anatase varies slightly with respect to deposition conditions and is approximately 0.5. Annealing at temperatures as high as 750°C increases the relative density to 0.7 with concomitant decreases in the O:Ti ratio and H content but it does not result in complete densification. Film densities are consistently higher for films annealed under dynamic vacuum compared to those in air.

INTRODUCTION AND THEORY

Electronic and optical properties of thin films are strongly influenced by their microstructure, porosity and chemical composition [1]. Quantitative measurements of film composition and density, although a difficult task, are of the utmost importance in assessing the potential technological applications of sol-gel derived thin films [2].

In this paper we report the use of backscattering spectrometry to determine the density of as-deposited and annealed TiO_2 sol-gel films. The combination of backscattering and forward recoil spectrometry represents a powerful diagnostic technique capable of determining film stoichiometry, impurity levels and density. A detailed compositional analysis of the films will be communicated in a future paper.

In Rutherford Backscattering spectrometry (RBS) the energy of rebounding He^{2+} ions after impinging on a thin film is measured by an energy sensitive (silicon surface barrier) detector. The energy of the elastically backscattered ions is indicative of the mass of the target nuclei, resulting in elemental identification. Furthermore, He^{2+} backscattered by a nucleus significantly below the surface of the film will emerge with less energy than one scattered by the same nucleus at the surface [3].

The density (atoms/cm^3) for individual atoms is calculated by

$$N = Y \cdot \cos\beta \,/\, Q \cdot \Omega \cdot \sigma \cdot t \qquad (1)$$

where Y is the integrated peak count, β is the angle of the beam from the film normal, Q is the total number of incident particles Ω is the detector solid angle, and σ is the scattering cross section. The scattering cross section is given by

$$\sigma = (e^2 zZ/4E)^2 [\sin^{-4}(\theta/2) - 2(m/M)^2 + \ldots] \qquad (2)$$

where m, z and M, Z are the mass and atomic number for He ions and the target nuclei respectively, and θ is the scattering angle as defined in Figure 1. Chemical compositions can be calculated with an accuracy of 0.1%, while the uncertainty of areal densities is approximately 3% [4].

EXPERIMENTAL

A stock TiO_2 sol with molar ratios Ti:PrOH:H_2O:HCl equal to

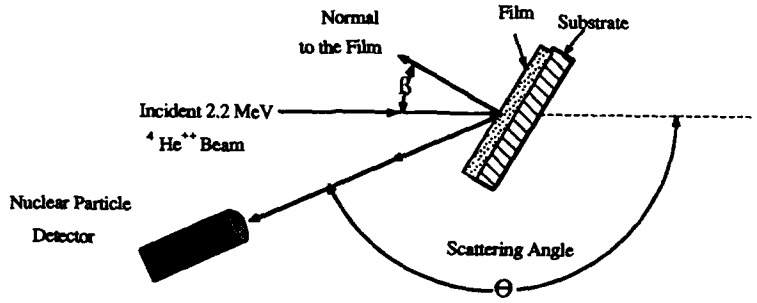


Figure 1. Experimental geometry for RBS.

1:11.4:1:1.8 was prepared by adding a solution of deionized H_2O in propyl alcohol to an acidified solution of titanium isopropoxide also in propyl alcohol. After 30 minutes the sol was diluted by adding the appropriate amount of alcohol and passed through a 0.2 μm filter to eliminate any particulates. TiO_2 films were deposited on (100) Si using a commercial photoresist spinner. Consolidation of the films was accomplished by heating in air or under vacuum at various temperatures for one hour.

Rutherford backscattering was performed with a collimated beam of $^4He^{2+}$ ions at an energy of 2.2 MeV and a current of approximately 20nA. The beam was accelerated by means of a tandem accelerator and focused onto a $4mm^2$ spot. $20\mu C$ of charge was collected for each spectrum. Data was analyzed with computer software developed at Cornell University [5]. Film thickness and refractive index were determined with a Rudolph Research Model Ellipsometer at 632 nm.

RESULTS AND DISCUSSION

Figure 2 shows the RBS spectra of an as-deposited TiO_2 film (2a) and after annealing at 750°C for one hour (2b). Note that chlorine is present in the film that has been only dried at room temperature. Chlorine was found to be eliminated entirely by annealing the film at 150°C. Carbon content was found to be low in the as-deposited films suggesting a minimal organic content. In contrast, films derived from Ti precursors containing strongly bonded and/or bulky ligands (acac or $C_5H_{11}O$) always exhibit significant amounts of carbon [6].

Table I shows the densities for various TiO_2 films, calculated by Eqn. 1. For a homologous series (i.e. films prepared from the same original sol but deposited at different spin speeds and/or annealed at different temperatures) the relative density, defined as the ratio of Ti atoms per nm^3 to 28.9, the number of Ti atoms per nm^3 for fully-dense anatase, is used as a measure for the degree of densification of the film. The number for anatase is obtained by assuming a bulk density of 3.84 g/cm^3.

For all films annealed at 350°C, the packing density varies between 19 and 24 Ti atoms per nm^3. The relative density of the films varies from 0.65 to 0.82. Films annealed in vacuum were consistently denser than those in air in agreement with values obtained for the refractive index. Although different spin speeds result in large film thickness variation, the density of the films seem to be largely unaffected. In addition, the density of the films varies slightly with sol concentration, with the concentrated sols producing denser films.

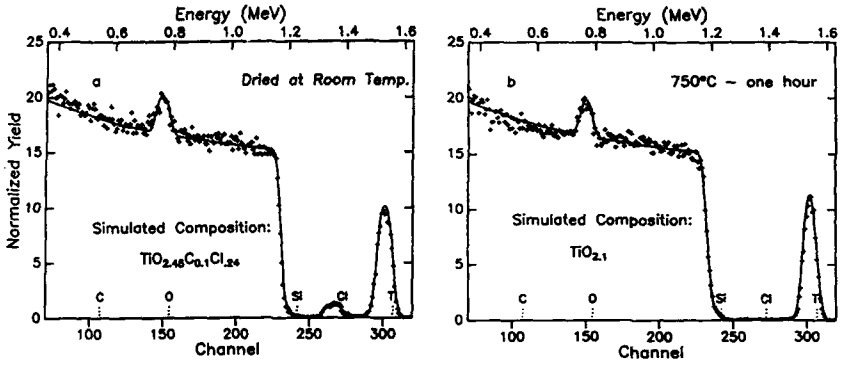


Figure 2. RBS spectra of as-deposited and annealed at 750°C TiO_2 films.

TABLE I
Density of TiO_2 Films

Dilution	Spin Speed (r.p.m.)	Atmosphere	Consolidation Temp.(°C)	Index	Ti Density (Atoms/nm^3)
3:1	6000	Air	350	2.026	18.7
3:1	6000	Vacuum	350	2.117	20.4
3:1	2000	Air	350	2.013	19.8
3:1	2000	Vacuum	350	2.147	20.3
1:1	3000	Air	350	2.121	21.1
1:1	3000	Vacuum	350	2.229	24.4
3:1	4000	---	---	1.883	13.9
3:1	4000	Air	150	1.971	17.7
1:1	4000	---	---	1.966	15.7
1:1	4000	Air	150	2.037	18.0

Figure 3 shows relative density as a function of annealing temperature for TiO_2 films spun at 2000 rpm and heat treated at the indicated temperature for one hour with a heating rate of 2°C/min. For comparison, the refractive index is also plotted as a function of annealing temperature. The as-deposited film exhibits a relative density of 0.4. The density of the film rapidly increases with increasing temperature but reaches a plateau around 350°C with a maximum relative density of 0.7 at 750°C. X-ray diffraction data indicate that partial crystallization to anatase has occurred at temperatures as low as 450°C. The O:Ti ratio decreases with increasing annealing temperature with a value of 2.1:1 at 750°C, approaching that for stoichiometric titanium oxide. The H content of the films (measured by Forward Recoil Spectrometry) also decreases with increasing temperature but remains in considerable amounts (H/Ti = 0.3) for films heated at 750°C, suggesting the presence of structural -OH or molecular H_2O.

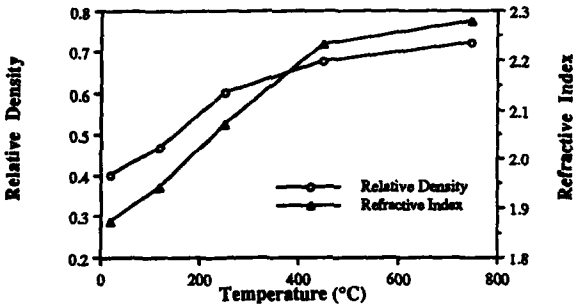


Figure 3. Relative density and refractive index vs. temperature.

The densification results are in marked difference to those obtained from SiO_2 sol-gel films. The relative density of as-prepared SiO_2 films starts at 0.75 and approaches 1.0 at temperatures as low as 450°C [7]. The observed high densities in silica films have been attributed to interpenetrating compliant precursors resulting in optimum packing [2].

In contrast, titania sols remain loosely packed and never reach the theoretical values for maximum density even at high annealing temperatures. Relatively high porosities have been observed for silica films with a high sticking coefficient, that tends to stiffen the film, resulting in a more open structure. Furthermore, increased fractal dimension for the precursor polymer species increases the number of intersections, resulting in mutually "opaque" species. Both effects would tend to form an open structure with relatively low densities [2]. The calculated packing densities are in agreement with the observed refractive indices of TiO_2 films that remain below 2.2. Small angle x-ray scattering data are needed to provide information on the fractal dimension of the TiO_2 polymer precursors.

Future experiments include detailed porosity measurements by analyzing the diffusion profiles of small probe molecules like I_2 by RBS. The technique allows for the calculation of diffusion coefficients for the probe and thus film porosities.

ACKNOWLEDGEMENTS

This work was sponsored in part by the Cornell Ceramics Program with funds provided by IBM and Corning Inc. and the Imaging and Sensing Technology Corporation. J.L.K acknowledges the support of a DoEd Ceramics Fellowship.

REFERENCES

1. D.R. Uhlmann and G.P. Rajendran, in Ultrastructure Processing of Advanced Ceramics, edited by J.D. Mackenzie and D.R. Ulrich (Wiley, New York, 1988) pp. 241-253.
2. C.J. Brinker, A.J. Hurd, K.J. Ward, ibid., pp 223-240.
3. W.-K. Chu, J.W. Mayer, M.-A. Nicolet, Backscattering Spectrometry, (Academic, New York, 1978).
4. J.A. Leavitt, L.C. McIntyre, M.D. Ashbaugh, B. Dezfouly, J.G. Oder, Applied Optics, 28, 2762 (1989).
5. L. Doolittle, Nucl. Instrum. & Methods, B9, 344 (1985).
6. J.L. Keddie and E.P. Giannelis, unpublished
7. J.L. Keddie and E.P. Giannelis, presented at the 1989 ACS Meeting, Indianapolis, IN, 1989 (to be submitted).

ELECTRON DIFFRACTION ANALYSIS OF THE STRUCTURE OF SiO_2 GEL-FILM

HISASHI OHSAKI*, MICHEL A. AEGERTER* AND TAKAKI SHICHIRI**
*Universidade de São Paulo, Instituto de Fisica e Quimica de São Carlos, São Carlos 13560, Brazil.
**Osaka City University, Department of Physics, Faculty of Science, Sumiyoshi-ku, Osaka 558, Japan.

ABSTRACT

The structure of self-supported SiO_2 gel-films prepared from acid and basic TEOS solutions is analysed by high energy transmission electron diffraction method. The reduced radial distribution function (RDF) curves show that all the films are already well dense despite the low drying temperature ($\lesssim$50° C) and short drying time ($\lesssim$30 s). The Si-O bond length of the gel-films prepared from highly acid and basic solutions is about 1.58 Å; it is smaller than that of bulk vitreous silica (1.61 Å) but similar to that of 80 Å thick evaporated a-SiO_2 film.

INTRODUCTION

Sol-gel process has a huge potential for producing functional materials using simple procedures. The gel materials are generally porous and a thermal treatment is necessary to transform them into dense glasses and/or ceramics. The microscopic and atomic structures of gel materials are therefore important parameters for the densification process.

In this study, the atomic network of thin SiO_2 gel-films is analysed for the first time by using electron diffraction method.

EXPERIMENTAL

The sols were prepared by mixing 15 ml TEOS and 28 ml ethanol. Sols labelled A-1, A-2 and I have been acidified by addition of aqueous HCl in order to get apparent pH (pH^*) of 0.6, 1.6 and 2.6 (isoelectric point of SiO_2), respectively, while the pH^* of sample B has been adjusted to 10.5 by adding aqueous NH_4OH. The ratio TEOS:H_2O:ethanol is kept almost constant for all the sols (1:5.8:7.1 in mole ratio). The sols were aged for 5 days without any evaporation.

The gel-films were prepared by the following procedures. A #100 mesh Cu grid with 0.24 mm diameter hole size was immersed into a sol and withdrawn vertically. Thin films of sol retained in the holes of the mesh grid were self-supported by the surface tension and they were then dried in warm air at 40 - 50° C for 10 - 30 s.

An electron diffraction apparatus was operated at an electron energy of 55.8 kev; the electron-beam size was about 70 μm and the beam current was of the order of 10^{-9} A. The range of the scattering angle corresponds to s_{min}=0.3 Å^{-1} and s_{max} =34 Å^{-1}, where $s=(4\pi/\lambda)\sin(\theta/2)$, θ is the angle between the incident and diffracted beam, and λ is the electron wavelength. The intensity of transmitted electron-beam was measured by a Faraday cage with an aparture of 0.1 mm in diameter; the Faraday cage captured the electron-beam with diverging angle until 0.016° (s=0.03 Å^{-1}). The transmittance for sample A-1, A-2, I and B were 9.4, 9.2, 18 and 5.4 % and the film thicknesses estimated from these values

Mat. Res. Soc. Symp. Proc. Vol. 180. ©1990 Materials Research Society

are about 500, 500, 400 and 600 Å, respectively.

The small values of transmittance indicate the occurence of multiple scattering so that the total diffracted intensity, Itot(s) can be written as

$$Itot(s) = Io \cdot N \{Jm(s) + Jel(s) + Jinel(s)\} + Imult(s) \qquad (1)$$

where Io is incident beam intensity, N is the number of SiO_2 unit compositions in the volume irradiated by the electron-beam, Jm(s), Jel(s) and Jinel(s) are interatomic interference, elastic atomic and inelastic atomic scatterings per unit composition, respectively, and Imult(s) is multiple scattering intensity. A division of Jm(s) by the Jel(s) gives the interference function M(s) and a sine-Fourier transformation of s·M(s) produces the differential RDF,

$$4\pi r\{D(r) - Do\} = \frac{2}{\pi} \int_0^{s_{max}} s \cdot M(s) \exp(-a^2 \cdot s^2) \sin(sr)\, ds \qquad (2)$$

where a is the artificial temperature factor used to reduce termination effects due to the finite measurement range and taken equal to 0.0506 Å in this study.

Jm(s) is determined from the experimentally obtained Itot(s) and the following considerations. Jel(s) and Jinel(s) are calculated by using the elastic and inelastic scattering factors for Si and O atoms [1]. Since Jm(0)=0 and assuming that Imult(0) is nearly zero, the extrapolation of Itot(s) for s=0 allows the determination of the tentative normalization constant $Io \cdot N = Itot(0)/\{Jel(0) + Jinel(0)\}$. Imult(s) was obtained by using the fact that Jm(s) is a smooth function oscillating around zero. The determined Imult(s) increases monotonically with s-value and consequently the determined Io·N is the best obtainable value.

RESULTS AND DISCUSSION

The differential RDF curves for the four samples are shown in Fig.1. The peaks on the curves inside r = 1 Å are apparently due to noise because no atomic pair with bond length less than 1 Å can exist. From the analogy of the atomic distances for vitreous silica and crystalline SiO_2, the peaks around 1.6 and 2.6 Å can be assigned to Si-O bonded pairs and O-Si-O atomic pairs, respectively. The slope of the internal part of the differential RDF reflects the bulk density of the sample; the straight dashed lines correspond to 4πrDo in eq.(2) calculated by using the density of vitreous silica (2.2 g/cm³). The slope is proportional to the experimentally obtained Jm(s), which is inversely proportional to the determined normalizing constant Io·N because the oscillating term Io·N·Jm(s) should be determined independently on the other terms in eq.(1). The determined normalizing constants are the maximum possible values because the values were obtained on the assumption of Imult(0)=0. Thus, the slope matched to the differential RDF curve should be equal to or smaller than the true slope. The reduced RDF, 4πrD(r), curves are shown in Fig.2. While the slopes have a large error (~20 %) due to the uncertainty on the drawing of the dashed line, the normal feature of the internal part of RDF's shows that the slopes do not differ too greatly from the true ones. This fact

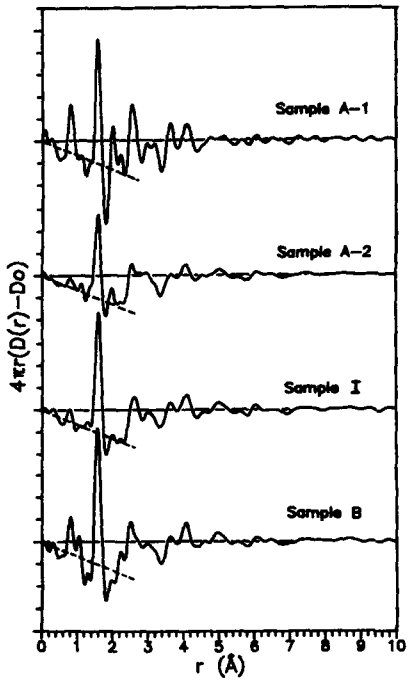


Fig.1 Differential RDF's for sample A-1, A-2, I and B.

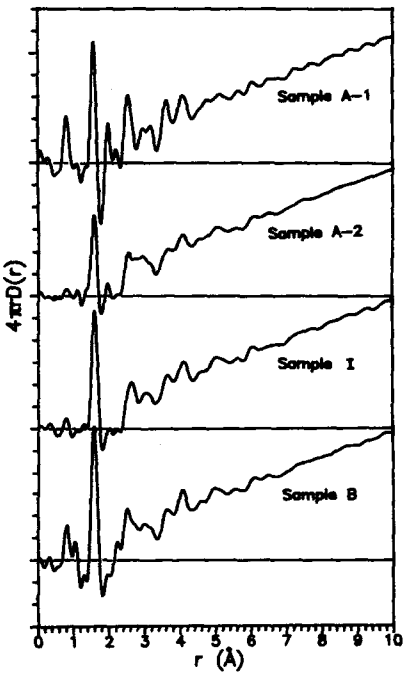


Fig.2 RDF's for sample A-1, A-2, I and B.

shows that the gel-films are well dense in spite of the low heating temperature (≲50° C) and the short heating time (≲30 s). It is well known that bulk SiO_2 gels are porous and have less density than that of vitreous silica. Then, the dense gel-films are supposed to be produced with easy displacement of atoms and molecules during the drying, which should be derived from the absence of substrate and/or their small thicknesses.

The Si-O bond lengths, O-O atomic distances of O-Si-O structure and O-Si-O angles calculated from these two distances are given in Table 1. Since the calculated O-Si-O angles are close to that of SiO_4-tetrahedron (110°), the gel-films are considered to be built up from SiO_4-tetrahedron units. The Si-O bond length of sample A-1, A-2 and B is 1.58 Å, and is smaller

Table 1. Si-O bond lengths, O-O atomic distances and calculated O-Si-O angles for sample A-1, A-2, I and B.

Sample	r_{Si-O}	r_{O-O}	∠O-Si-O
A-1	1.58 Å	2.55 Å	107.6°
A-2	1.58	2.55	107.6
I	1.60	2.63	110.5
B	1.58	2.52	105.8

Table 2. Si-O bond lengths, O-O atomic distances and calculated O-Si-O angles for evaporated a-SiO_2 films.

Thickness	r_{Si-O}	r_{O-O}	∠O-Si-O
4 Å	1.54 Å	2.48 Å	107.2°
10	1.54	2.51	109.8
20	1.57	2.56	109.6
40	1.57	2.58	110.3
80	1.58	2.58	109.3

than that of bulk vitreous silica (1.61 Å). Bond shortening has already been observed in the very thin films of evaporated amorphous SiO_2 (ev.a-SiO_2) [2]. The differential RDF curves for ev.a-SiO_2 films with 4, 20 and 80 Å thicknesses are shown in Fig.3. The peak heights of atomic pairs with large distances decrease remarkably with a decrease of film thickness. This result is explained by the fact that the number of atomic pairs with large atomic distance of thinner film is smaller than that of thicker film, and therefore indicates the consistency between the RDF curves. The Si-O bond lengths, O-Si-O atomic distances and calculated O-Si-O angles of ev.a-SiO_2 films are listed in Table 2. Since the O-Si-O angles are nearly equal to 110°, the ev.SiO_2 films are considered to be constructed from the SiO_4-tetrahedron units also. These results shows that the SiO_4-tetrahedrons shrink with the decrease of film thickness. Because of their short Si-O length (1.58 Å), sample A-1, A-2 and B are believed to be made up of loose bound grains. On the contrary, sample I which has 1.60 Å Si-O bond length has a well extended atomic network; the better quality of its atomic network may arise either from the paticular pH of the sol (isoelectric point of SiO_2) or the small film thickness (400 Å).

Since the extraneous scattering is not removed, it is difficult to assign the observed peaks around the Si-O-Si atomic peak (≈3.0 Å) or to decide them the noises. Thus, the exact nature of the tetrahedra arrangement in the films and the presence of other structural units still remain open questions.

CONCLUSION

The first results of electron diffraction analysis of self-supported SiO_2 films prepared by sol-gel method show that the films are already well dense. The films produced from highly acid and basic sols have a 1.58 Å Si-O bond length smaller than that of bulk vitreous silica (1.61 Å) but similar to that of 80 Å thick ev. a-SiO_2 film. The film produced from sol at pH*=2.6 (isoelectric point of SiO_2) has a 1.60 Å Si-O bond length and is believed to have a well extended atomic network. The variety of Si-O bond length of gel-films suggests the different degrees of atomic network, and make plausible the presence of possible ways to get high quality glass materials only by sol-gel process.

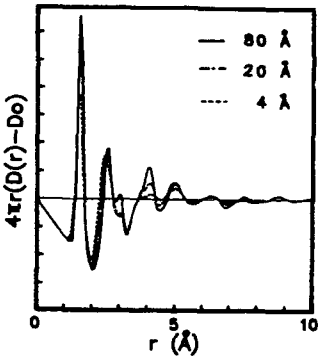


Fig.3 Differential RDF's for ev.a-SiO_2 films with 4, 20 and 80 Å thicknesses.

Work partly supported by CNPq and FAPESP (Brazil).

References

1. International Tables for X-ray Crystallography vol 4 (Kynoch Press, Birmingham, 1974), pp. 176 - 269.
2. K. Miura, M. Tada, H. Ohsaki, S. Kodera and T. Ino, J. Non-Cryst. Solids, 95&96, 1095 (1987).

PROPERTIES OF FILMS PREPARED FROM LOW SURFACE AREA/DENSITY ALUMINA-SILICA

S.L. Hietala, D.M. Smith, UNM/NSF CENTER FOR MICRO-ENGINEERED CERAMICS, University of New Mexico; V.M. Hietala, G.C. Frye, A.J. Hurd, and C.J. Brinker, Sandia National Laboratories, Albuquerque, NM

ABSTRACT

A sol-gel method was used to prepare bulk, closed pore, amorphous alumina-silica. Films prepared from this 47wt% Al_2O_3-SiO_2 composition were examined by SAW, ellipsometry and electrical measurements. The films were found to have a surface area of 1.1 cm^2/cm^2, a refractive index of 1.44 at 633 nm, and a relative permittivity of 6.2 at 200 KHz. These properties indicate potential applications as hermetic seals, barrier coatings, dielectric layers for capacitors and passivation coatings for electronic circuits.

INTRODUCTION

An amorphous alumina-silica material prepared via sol-gel routes was found to have an anomalously low surface area and density in a composition of approximately 47 wt% alumina [1]. From various techniques, it was determined that these properties were due to closed porosity in the material [2]. If closed porosity can be maintained in the films, they would be ideally suited for hermetic, thermal, and chemical barriers. The large amount of porosity also suggests it as a candidate for reasonably low relative permittivity ceramic coatings for electronic applications.

EXPERIMENTAL

The 47wt% alumina-silica sol was prepared using alkoxide precursors. Ethanol was added to TEOS in a round bottom flask. A solution of ethanol and HCl (molar ratios 1 EtOH: 1 conc. HCl: 0.8 TEOS) was added to the flask, then an appropriate amount of aluminum tri-sec butoxide (ASB) was added. This was allowed to react (with slight agitation) for several minutes, then diluted with ethanol, and refluxed at 353K overnight. The gel was formed by adding water (molar ratios 100 H_2O:Si) to the sol and allowing the gel to start forming. Films were prepared by spin coating at 2000 rpm.

Dynamic light scattering was performed on a series of gelling mixtures using a Wyatt spectrometer equipped with the autocorrelation option. The two components of each sample were filtered through a 0.2 μm filter into a clean, dust-free scintillation vial where they were gently mixed then place in the spectrometer. Temperature was controlled at 37.0 ± 0.5 °C. Focused HeNe light (633 nm) was scattered at a fixed angle of 92° and collected by a SelFoc optical fiber, which fed the scattered light to a Hamamatsu photomultiplier tube. The intensity autocorrelation function $\langle I(0)I(t)\rangle$ was obtained by feeding the photocurrent to a Langley-Ford 1096 digital autocorrelator via a preamplifier. The data were taken at 20 minute intervals continually from the time of mixing until the gel time, which was (crudely) determined by observing an aliquot.

To characterize porous films using surface acoustic wave (SAW) devices, the solution was cast onto a quartz substrate then placed in a brass test case with a stainless steel lid for gas inlet and outlet. The devices were cooled to liquid N_2 temperatures (77K, by immersion) and a gas mixture of He and N_2 was passed over the film. The frequency of the device was monitored as the N_2 concentration (p/p_0 where p is the N_2 partial pressure and p_0 is the N_2 saturation vapor pressure) in the gas stream is varied from zero up to about 0.95 and then back to zero by adjusting the relative flow rates of a N_2 stream and a He mix-down stream. The frequency shifts are used to determine the mass of N_2 adsorbed on the surfaces or condensed in the pores of the films as a function of the

Mat. Res. Soc. Symp. Proc. Vol. 180. ©1990 Materials Research Society

N_2 concentration (N_2 adsorption isotherm). If the SAW device is used as the feedback element of an oscillator circuit, relative changes in frequency (f) can be related to relative changes in wave velocity (v) which can then be related to changes in the film mass per area (m) by :

$$\frac{\Delta f}{f_o} = \frac{\Delta v}{v_o} = c_m f_o m \qquad (1)$$

where c_m is the mass sensitivity of the device (1.3×10^{-6} cm^2 s/g for quartz) and f_o and v_o are the unperturbed frequency and velocity . For the 97 MHz devices used in this study, a 10 Hz frequency change (typical noise level) is due to mass change of only 0.8 ng/cm^2. The N_2 adsorption isotherm was used to calculate the surface area of the film using the BET analysis and the pore size distribution by accounting for capillary condensation. Additional details on the experimental system and this characterization technique are given in reference [3].

The 47% sol-gel alumina-silica films, spin-coated on silicon, were analyzed by null ellipsometry. The home-built ellipsometer is in the "PCSA" configuration, i.e. polarizer, (quarter-wave) compensator, sample, analyzer. The compensator was set at 45° and the angle of incidence was 67.5°. An unfocused beam from a HeNe laser was first passed through a depolarizer then into the system optics. Two-zone measurements were made by finding nulls in the reflected intensity while varying the analyzer and polarizer angles. Two measurements were made at different spots in the central region. In each case the beam average over approximately 2 mm^2 of area and the two measured spots were at least 2 mm apart. Since reproducible results were obtained, defects and inhomogeneities apparently had no effect on the results.

The electrical properties of the Al_2O_3-SiO_2 films were characterized by the fabrication of simple parallel-plate capacitors from the film. A silicon wafer was used as a mechanical substrate onto which a 2000Å thick aluminum layer was e-beam evaporated to form the bottom electrode of the capacitors. The alumina-silica gel was then spin coated on this aluminum coated silicon wafer. The sample was heated to 325°C for 2 hours in an UHP Argon environment, which was found to greatly improve the films electrical properties. To form the individual test capacitors, a second aluminum evaporation (2000Å) with a shadow mask was used to form metal dots of approximately 300 μm diameter.

The capacitors were tested for electrical performance by using an HP4145A Semiconductor Parameter Analyzer and an HP4275A Multi-Frequency LCR Meter. The dielectric constant was determined from the measured capacitance by assuming an ideal parallel-plate model:

$$\varepsilon_r = \frac{t}{A\varepsilon_o} C, \qquad (2)$$

where ε_r is film's relative permittivity (dielectric constant), t is the measured film thickness, A is the metal contact area, ε_o is the free-space permittivity, and C is the measured capacitance. Fringing fields were safely neglected due to the thinness of the coating in relation to the test capacitors' diameters (over 3000 to 1). The test capacitors' areas were determined with an optical microscope. The films thickness was measured using ellipsometry and found to be relatively uniform over the sample and about 875 Å thick.

RESULTS AND DISCUSSION

In the light scattering experiment (Figure 1), the correlation functions were nonexponential decays that appeared to be the sum of two or more exponentials. The data were analyzed by fitting second-order cumulant to the early and late times in order to bracket the decays.

$$\ln\langle I(0)I(t)\rangle = \mu_o - \mu_1 t + (\mu_2/2)t^2 \qquad (3)$$

Thus the above formula was applied for $t \to 0$ and $t \to \infty$ separately. The first cumulant was related to a hydrodynamic radius R_h through the relation,

$$\mu_1 = 2 D q^2 = 2 \frac{kT}{6\pi\eta R_h} q^2 \qquad (4)$$

where D is the diffusivity, $q = \left(\frac{4\pi n}{\lambda}\right)\sin\left(\frac{\theta}{2}\right)$ is the scattering wavevector, n is the sample index of refraction, θ is the scattering angle, η is the viscosity, and T is the temperature.

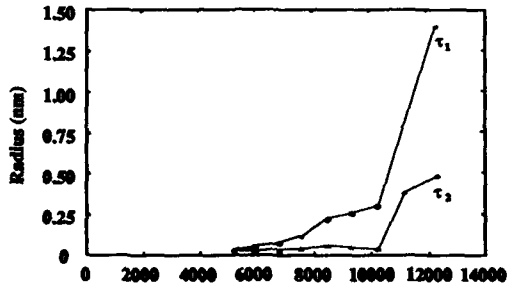


Figure 1. Light scattering results of 47% Al_2O_3-SiO_2 ASB (molar ratio $100H_2O$:Si).

The relatively smooth and featureless films were spun at $t/t_{gel} \approx 0.5$, which corresponds to ≈7200 seconds in Figure 1. ^{29}Si NMR by Pouxviel showed that even under slow hydrolysis conditions, the Si and Al reactions had proceeded sufficiently by this time [4]. Films made from solutions before $t/t_{gel} \approx 0.5$ were found to be quite thin, while films made at later times were found to have a varying degree of waviness, presumably due to the large variation in the features of the gel.

A SAW device was coated with the 47% alumina-silica to determine whether the low surface (and presumably the closed porosity) remain in the films. From Figure 2, it is show that the 47% alumina-silica film is found to have a surface area of 1 cm^2/cm^2, compared to a silica gel having a surface area of 46 cm^2/cm^2. These measurements would indicate that the low surface area, and thus the closed porosity remains in the film material.

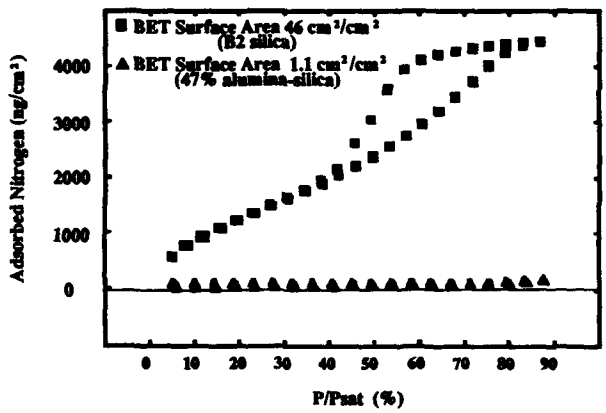


Figure 2. SAW measurements for 47% Al_2O_3-SiO_2 and silica films.

The refractive index (n), as measured by ellipsometry, was 1.44. Using a refractive index for the solid matrix as 1.55, the porosity is calculated to be 20%. In principle, the porosity and refractive index can be varied and still maintain closed porosity by proper selection of processing conditions.

Figure 3 shows a plot of density as a function of wt% Al_2O_3 for the bulk material. From the rule of additive densities the expected density of the 47% composition should be 2.65 g/cm^3, from the graph the density would be ≈2.52 g/cm^3. The measured density was 2.2 g/cm^3, which gives a porosity in the range of 15% to 20%. Theoretical porosity is similar to that obtained from ellipsometry (20%), whereas the measured (15%) is probably the result of the greater time available for morphological rearrangement during drying in the bulk as compared to films.

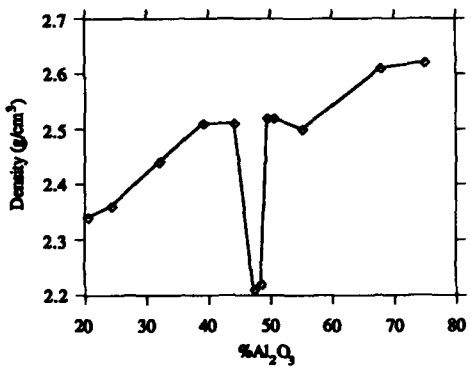
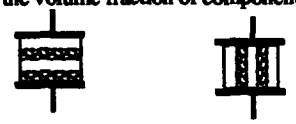


Figure 3. Density as a function of weight% alumina in 47% alumina-silica

Theoretical models for relative permittivity calculations (Figure 4) show two extremes which should bound the actual values obtained [5,6,7]. The series model (a) would bound the relative permittivity on the low side, and the parallel model (b) would bound the measurement on the high side. The general equation for the models is:

$$\varepsilon_r^n = \Sigma v_i \varepsilon_i^n \qquad (5)$$

where k is the relative permittivity of the composite material, k_i is the relative permittivity of the individual components and v_i is the volume fraction of components.



a. series model b. parallel model

Figure 4. Theoretical models for dielectric constant calculations.

An intermediate value between the series and the parallel models, is found by the "log" equation:

$$\log(\varepsilon_r) = \Sigma v_i \log(\varepsilon_i) \qquad (6)$$

These three equations are plotted versus porosity in Figure 5, assuming a homogeneous mixture of alumina-silica with relative permittivity of 5.7.

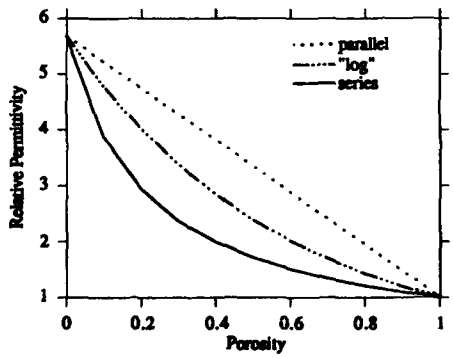


Figure 5. Theoretical dielectric constant as a function of porosity (equations 5,6).

For the range of porosity calculated from ellipsometry and density data, the relative permittivity is expected to be in the range of 2.6 to 5.0. For crystals and glasses:

$$\varepsilon_r = n^2 \qquad (7)$$

From the measured refractive index, if this were crystalline or glassy, we would expect a relative permittivity of 2.1.

The test capacitors were first tested with the Semiconductor Parameter Analyzer for leakage current. Virtually all of the capacitors tested (randomly over several cm^2) where seen to be leakage free at low test voltages. This gives a good indication of the pin-hole free nature of the film. The test capacitors' breakdown voltage was measured to be approximately 2 Volts. This corresponds to an electric field of approximately 230 KV/cm. The dielectric constant was measured to be virtually constant 6.2±0.2 over a frequency range of 10 KHz to 4 MHz. The measured quality factor (1/ loss-tangent) was found to be about 85 at 100 KHz.

CONCLUSIONS

The 47% alumina-silica films are relatively simple to process. Films of various thicknesses and homogeneity may be obtained in different stages of the process, dependent on the size of the polymers at various stages in gelation. The low surface area measured by SAW indicate that the closed porosity has been retained in the films. From the capacitance measurements, the spin-coated film was seen to be void of pin-holes and relatively uniform in thickness. The films relative permittivity was determined to be approximately 6.2±0.2 with a reasonable quality factor. This value was much greater than that predicted from ellipsometry measurements, possibly due to difficulty in measuring film thickness, the hydroxides space charge polarization, or high ionic compared to electronic contributions to the relative permittivity.

This film has potential use in two important electrical applications: dielectric for capacitors, passivation coating for microelectronic circuits. For these applications the film's primary benefit would be in the predicted low permeability which would provide excellent stability from possible environmental contaminants. For capacitors, the measurements presented give a direct indication of expected performance. The quality factor was observed to be dependent on the drying conditions. For a passivation coating, the film can be applied with low-temperature processing, which would allow for the passivation of temperature sensitive circuits (i.e. GaAs). With the film's predicted low permeability, a thin coat should be adequate for passivation. The dielectric constant is somewhat higher than desired, but a thin coating of the film should have little effect on a circuit's operation.

The possible future use of this film in these applications will depend on further studies of the electrical and mechanical properties of the film and studies of film quality versus drying conditions.

REFERENCES

[1]S.L. Hietala, D.M. Smith, J.L. Golden and C.J. Brinker, J. Amer. Cer. Soc. 72, 2354 (1989).

[2]S.L. Hietala, D.M. Smith, C.J. Brinker, A.J. Hurd, N. Dando and A.H. Carim, J. Amer. Cer. Soc. in press (1990).

[3]C.L. Glaves, G.C. Frye, D.M. Smith, C.J. Brinker, A. Datye, A.J. Ricco and S.J. Martin, Langmuir 5, 459 (1989).

[4]J.C. Pouxviel and J.P. Boilot in Ultrastructure Processing of Advanced Ceramics, edited by J.D. Mackenzie and D.R. Ulrich (1988) pp. 197-209.

[5]W.D. Kingery, H.K. Bowman and D.R. Uhlmann, Introduction to Ceramic, 2nd ed. (John Wiley & Sons, 1976) chapter 18.

[6]R.C. Weast, ed., CRC Handbook of Chemistry and Physics, 63rd ed. (CRC press, 1982-1983) p. B-143

[7]K. Wefers and G.N. Bell, Technical Paper #19, Alcoa Research Laboratories, 1972.

THIN ANISOTROPIC COATINGS BASED ON SOL-GEL TECHNOLOGY.

S. Randall Holmes-Farley and Lynn C. Yanyo
Lord Corporation, P. O. Box 8225, Cary, NC 27512-8225.

ABSTRACT

Using sol-gel technology, thin organic/ceramic (ceramer) coatings have been applied to metal surfaces in order to enhance such surface properties as adhesion promotion and corrosion prevention. Isotropic coatings have been found to be effective in certain applications such as corrosion prevention, but the formation of anisotropic coatings permits greater flexibility over the resulting properties. Isotropic coatings derived from tetraethoxysilane, for example, effectively inhibit corrosion while being only 100 to 1000 Å thick. These coatings do not, however, promote adhesion. Thin coatings made from traditional silane adhesion promoters alone are unable to prevent corrosion of metallic substrates.

Using monomers with appropriate reactivities permits the single-step synthesis of anisotropic coatings that can both promote adhesion and prevent corrosion. These types of anisotropic coatings allow the physical and chemical properties of a coating to be varied as a function of distance from the substrate and confer properties to the substrate that would not be possible from a single isotropic coating. The principle behind the construction of these anisotropic coatings is general enough that it can be used in many applications where microengineering of surface structures is important.

INTRODUCTION

Sol-gel coatings can be applied to substrates using two different methods. The first, and most widely used, involves making a coating material that is spread onto the substrate and subsequently cured. Typically these materials are made by the acid-catalyzed hydrolysis and partial condensation of metal alkoxides.[1-7] An alternative approach reported in this paper is the base-catalyzed growth of coatings directly on the substrate.

In this method metal alkoxides are mixed with solvent, water, and a basic catalyst in the presence of a substrate (such as aluminum). As the monomers condense, some of them react with the surface of the substrate. As condensation continues a coating is deposited onto, or more correctly reacted with, the substrate.

If the initial coating solution is formulated such that it contains several metal alkoxides of differing reactivity then the nature of the coating being deposited will be a function of time. The lowest layers of the coating will be derived from the most reactive monomers while the upper layers will be derived from the less reactive monomers. In this manner one can develop anisotropic coatings. The properties of these coatings can then be optimized so that each part of the coating provides optimum properties.

One might choose, for example, for the first layer to interact strongly with the substrate, an intermediate layer to provide some sort of barrier, and a final layer to provide compatibility with a subsequently applied top coat (e.g. paint or

Mat. Res. Soc. Symp. Proc. Vol. 180. ©1990 Materials Research Society

adhesive). Properties that can be altered as a function of depth into the coating include elastic modulus, free volume, density, index of refraction, chemical reactivity, barrier properties, electrical and thermal conductivity, and extent of cross linking.

RESULTS AND DISCUSSION

A typical isotropic coating made using this method of permitting monomers to react directly with a substrate can be made using the recipe below (Table 1).

Table 1. Typical isotropic coating recipe. Coating time 1- 24 h.

70 mL Ethanol	3 mL Concentrated Ammonium Hydroxide
27 mL Water	6 mL Tetraethoxysilane (TEOS)

This mixture is formulated in the presence of a metal substrate and results in an ultra-thin coating of SiO_2 on the surface. Aluminum, for example, will be coated with approximately 500 Å of SiO_2 in approximately 1 hour. Further exposure to the solution does not result in any additional thickness.

The thickness of this coating can be controlled by adjusting the amount of TEOS added to the recipe. Thicknesses can be obtained between 5 and 2000 Å (Figure 1).

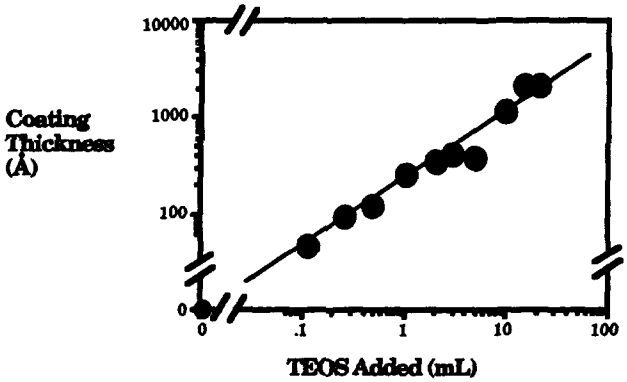


Figure 1. Thickness of SiO_2 coatings formed on aluminum as a function of the amount of TEOS added to recipe 1. Coating thicknesses were determined by ellipsometry and confirmed using ESCA sputter profiling, and gravimetric methods.

Repetitive applications of the coating results in additional layers of similar thickness (up to at least 10,000 Å) . By changing the monomer used in each coating one can develop layered coatings, albeit in a cumbersome process.

Applications of these isotropic coatings include corrosion protection, scratch and wear resistance, and adhesion promotion. Figure 2, for example, shows the time for a coated aluminum film to corrode in aqueous base while protected by various thicknesses of coating. Apparently these thin films are able to provide significant corrosion protection (slowing corrosion by several orders of magnitude) while being only 50 to 500 Å in thickness.

Anisotropic Coatings

While these isotropic coatings afford many useful properties, they require multiple coating applications if one wants to develop anisotropic coatings. Alternatively, one can make anisotropic coatings with a single application if

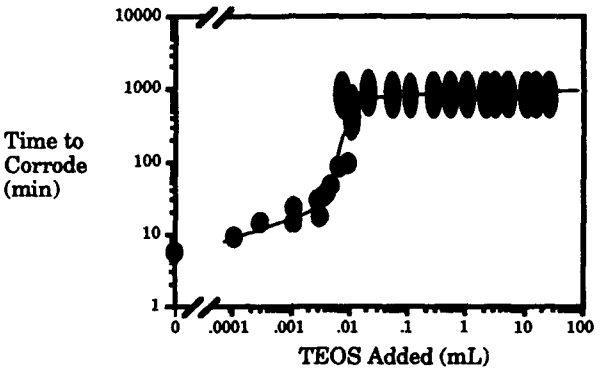


Figure 2. Time required to corrode an aluminum film in aqueous base (0.1 N NaOH) as a function of the coating applied. The aluminum sample was an evaporated film 2000 Å thick on a glass support. It was coated using the recipe in Table 1 with varying amounts of TEOS. Corrosion was monitored visually by loss of the reflectivity of the aluminum mirror.

multiple monomers of appropriate reactivity are chosen. Using known relationships between chemical structure and reactivity one can design mixtures of monomers where appropriate materials will end up in the desired location in an anisotropic coating. Using a single type of metal center, one can control reactivity in several ways. These include altering the type of functional group which will hydrolyze, the steric bulk of the hydrolyzing group, and the nature of other groups attached to the metal center.

In order to demonstrate the process, coatings were made from several test recipes that were then characterized in detail. These recipes were identical to that in Table 1 except that more than one silane was used at a time. Combination of TEOS (3 mL) and 3-aminopropyltriethoxysilane (3 mL), for example, provides an anisotropic coating because the aminosilane is significantly slower to react than the TEOS. Thus the inner, first deposited, regions of the coating are rich in SiO_2, while the outer, later deposited, regions are enriched in amino functionality. One way to assess the nature of such coatings is using ESCA combined with sputter profiling. Figure 3 shows that the outer region of the coating is indeed enriched in nitrogen, and that the lower regions contain much less.

These types of experiments can be repeated using the same aminosilane in combination with tetrabutoxysilane. This silane, however, reacts more slowly than the aminosilane, resulting in coatings where the inner region is enriched in aminosilane and the outer region contains only SiO_2. Similar experiments can also be performed with other functionalized silanes, such as 3-chloropropyltriethoxysilane. Combinations of three or more silanes have also led to appropriately layered structures. As an additional test of the anisotropic nature of these coatings, one can compare coatings made using this one-step process with coatings made by putting each silane down in a separate process. In general, the one-step coatings are found to be similar to those made in multiple coating steps.

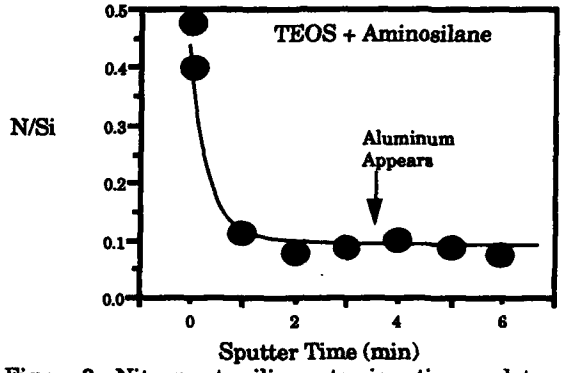


Figure 3. Nitrogen to silicon atomic ratios, as determined by ESCA, as a function of sputter time for anisotropic coatings made from TEOS and aminosilane. The sputter rate was ~80-100 Å/min.

Applications

There are, of course, a wide range of potential applications for such anisotropic coatings. Combination of corrosion protection and adhesion promotion, for example, demonstrates a case where single isotropic coatings cannot provide the same benefits as anisotropic or layered coatings. Adhesion promotion by aminosilanes is a widely practiced technology, and 3-aminopropyltriethoxysilane is an effective adhesion promoter for bonding aluminum substrates with a urethane adhesive (TEOS is not, Table 2).

Conversely, coatings derived from TEOS provide significant corrosion protection while those derived from aminosilane do not. In fact, it turns out that in mixed coatings of SiO_2 and aminosilanes, it is most important for the N/Si atomic ratio to be low (<0.05) for optimum corrosion protection and high (>0.1) for optimum adhesion promotion. If one makes coatings where the lower regions are primarily SiO_2 (forming a barrier) and the upper regions are primarily aminosilane (promoting adhesion) then one can get both properties optimized at once, a feat not possible with single isotropic coatings.

Table 2. Bond strengths of joints made from aluminum alloy coupons with various coatings using a two-part commercial urethane adhesive, Tyrite 7520. The joints were exposed to boiling water for 2 h prior to testing. The table also shows corrosion rates for evaporated aluminum samples with similar coatings in aqueous base.

Coating Ingredients	Bond Strength (kg/in^2)		Corrosion Rate
None	15		1 (by definition)
TEOS Only	0		0.002
Aminosilane Only	475		0.6
		Both Optimized	
TEOS + Aminosilane	620	<---------->	0.002
TBOS + Aminosilane	75		0.01
TEOS + Aminosilane + TBOS	30		0.003
TEOS, then Aminosilane	580		0.002
Aminosilane, then TEOS	0		0.3

CONCLUSIONS

Anisotropic coatings can be formed by taking advantage of the relative reactivity of monomers present in sol-gel reactions. These anisotropic coatings permit the properties of different regions of a coating to be independently optimized for different functions. These functions might include elastic modulus, adhesion promotion, barrier properties, coefficient of thermal expansion, and index of refraction to name a few. Anisotropic coatings can, for example, provide corrosion protection as effectively as SiO_2-only coatings and provide adhesion promotion as effectively as aminosilane-only coatings. While it is not discussed in this report there are instances where underbond corrosion must be prevented in order to attain maximum environmental resistance in bonding to metal (such as to steel in harsh environments). In these cases both adhesion promotion and corrosion prevention must be simultaneously optimized, as is obtained from anisotropic coatings. Thus, these single-step anisotropic coatings provide properties that cannot be obtained from isotropic coatings.

EXPERIMENTAL

The sol-gel coating solutions, unless otherwise specified, contained 100 mL of ethanol, 20 mL of water, 3 mL of concentrated ammonium hydroxide, and the silane monomers of choice (typically 6 mL). Samples were treated by immersion in the freshly prepared solution for 24 hours unless otherwise indicated and were then rinsed in ethanol, water, ethanol again, and allowed to air-dry. Samples for corrosion testing were heated to 100 °C for 1 hour prior to testing.

The substrates used for corrosion tests were thin films (1000-2000 Å) of aluminum (99.99%) that had been evaporated onto glass microscope slides. Corrosion testing was performed in 0.1 N NaOH by monitoring the presence of the mirror metal surface visually until it disappeared. Corrosion testing of metal coupons (aluminum 2024-T3 alloy) was performed by monitoring the rate of weight loss of samples exposed to either 0.1 N NaOH. Substrates for

adhesion tests were aluminum 2024-T3 alloy coupons. The coupons were bonded as 1" lap shears using Tyrite 7520 (Lord Corporation) two-part urethane adhesive. The samples were allowed to cure for four days at room temperature before testing. The joints were exposed to boiling water for 24 hours in an all-glass apparatus prior to testing.

ESCA sputtering was performed with 4 keV argon atoms. Atomic concentrations were determined from integrated peak areas. Binding energies were corrected for charging by arbitrarily assigning the adventitious carbon peak a binding energy of 284.6 eV. Ellipsometry was performed on a Rudolph Instruments Model 432A42B41 null point ellipsometer using 632.8 nm laser radiation. Thickness values were obtained by computer analysis with the assumption that the index of refraction of the coating was 1.4.

REFERENCES

1. Roy, R. , *Science* **238**, 1664 (1987).
2. Schmidt, H.; Scholze, H.; Kaiser, A., *J. Non-Crystalline Solids* **63**, 1 (1984).
3. Schmidt, H.; Scholze, H. *in* "Glass-- Current Issues" (A. F. Wright and J. Dupuy, Eds.), p. 263. Martinus Nijhoff, Boston, 1985.
4. Huang, H-H.; Wilkes, G. L., *Polymer Bulletin* **18**, 455 (1987). Huang, H-H.; Orler, B.; Wilkes, G.L., *Polymer Bulletin* **14**, 557 (1985). Huang, H-H.; Orler, B.; Wilkes, G.L., *Macromolecules* **20**, 1322 (1987).
5. Seiferling, B.; Schmidt, H., *Mat. Res. Soc. Symp. Proc.* **73**, 739 (1986).
6. Ravaine, D.; Seminel, A.; Charbouillot, Y.; Vincens, M., *J. Non-Crystalline Solids* **82**, 210 (1986).
7. Ulrich, D. R., *Chemtech* 242 (1988).

PARTICLE GROWTH AND DEVELOPMENT DURING THE IN-SITU PRECIPITATION OF SILICA IN A POLYMERIC MATRIX

PING XU, SHUHONG WANG, AND JAMES E. MARK
University of Cincinnati, Department of Chemistry and the Polymer Research Center, Cincinnati, OH 45221-0172.

ABSTRACT

The hydrolysis of tetraethoxysilane much used in the sol-gel approach to ceramics can be studied in a matrix isolation technique in which the silica thus formed precipitates within a polymeric material. This technique was applied here in the in-situ precipitation of silica particles in an elastomeric matrix of poly(dimethylsiloxane). Transmission electron microscopy and mechanical property measurements were carried out as a function of time over a period of 60 days. The equilibrium amount of silica precipitated was obtained relatively quickly, after approximately one day, but reorganization of the particles continued for several days thereafter. This "aging" process resulted in particles that are better defined and more uniform in size, but their ability to reinforce the elastomeric materials was only marginally increased. Scattering techniques are also being used to obtain additional information on this interesting process.

INTRODUCTION

Elastomers in the pure state generally lack useful properties simply because of their relatively low strength. To utilize them in practical applications, it is necessary to add fillers such as carbon black or finely powdered silicas to them in order to improve their mechanical properties. The mixing of typical particulate fillers into a polymer, however, is an energy-intensive process that can cause premature gelation, and it is frequently very difficult to control the structure of the resulting material, particularly the degree of particle dispersion or agglomeration [1-5]. For these reasons a number of studies were carried out to develop an efficient and practical technique for the generation or precipitation of a filler within a polymeric matrix.

It has now been demonstrated that networks of poly(dimethylsiloxane) (PDMS) $[-Si(CH_3)_2O-]_x$ may be swollen in tetraethoxysilane (TEOS) and the TEOS then hydrolyzed in situ [6-12]. Such a chemical reaction via the "sol-gel" process [13,14] can be used for precipitating the silica filler into previously cross-linked networks of PDMS. The reaction may be described by the equation

$$Si(OC_2H_5)_4 + 2H_2O \xrightarrow{\text{Catalyst}} SiO_2 + 4C_2H_5OH \qquad (1)$$

where water is obviously necesary for the in-situ hydrolysis. Filling PDMS networks using such a novel technique has been very successful in improving their mechanical properties [6-12].

A previous experiment [12] indicated that there might be an "aging" or "digestion" process in the in-situ precipitation of silica, such reorganization making the particles better defined, more uniform in size and less aggregated.

Mat. Res. Soc. Symp. Proc. Vol. 180. ©1990 Materials Research Society

The present investigation was carried out to provide additional information on this process, particularly by means of electron microscopy, and to compare the mechanical properties of the silica-filled PDMS at different stages by means of stress-strain measurements in elongation. It is hoped that a better understanding of the "aging" process can be obtained, in a way that transcends this particular elasticity application and provides information also of interest to the ceramics community. From this point of view, the in-situ precipitations can be thought of as a "matrix-isolation technique" [15] in which the polymer acts as a matrix for holding the ceramic-type particles while they are studied by microscopy or scattering measurements [16-18] to characterize their growth processes.

EXPERIMENTAL DETAILS

Preparation of networks

The polymer employed, hydroxyl-terminated PDMS having a number-average molecular weight of 2.1 x 10^4 g/mol, and TEOS were supplied by Petrarch Systems Company. The linear polymer chains were endlinked in the bulk (undiluted) state with a stoichiometrically equivalent amount of TEOS in a Teflon® mold at room temperature for three days, using 0.6 wt% stannous-2-ethyl-hexanoate (Sigma Chemical Co.) as a catalyst [19,20]. The resulting network sheet was extracted with toluene for three days, deswelled with methanol, and then dried to constant weight. The soluble fraction thus determined amounted to 9.58 wt %.

Precipitation of Silica

One strip cut from the network sheet was set aside as a reference sample (0 wt % filler). The other strips from the same network sheet were divided into two series. The first series, labelled A, was swelled with TEOS to the maximum extent attainable, which would yield large amounts of filler, thus facilitating the observation of the samples in transmission electron microscopy. Less TEOS was introduced into the second series, labelled B, to give the lower amounts of silica that are more suitable for stress-strain measurements in elongation. The swollen strips were then placed into an aqueous solution of diethylamine (2 wt %), and the hydrolysis of the TEOS was permitted to occur at room temperature for various periods of time, specifically a few hours up to 60 days. After the reaction, each strip was dried under vacuum and weighed, and thereby values of the weight percent filler incorporated were obtained.

Electron Microscopy

A piece of each filled strip was glued to a mounting pin using "5-Minute®" epoxy. Preparation of specimens from such strips was done on an ultramicrotome (FC 40 Reichert-Jung Co) at -130°C, with a controller initiating the delivery of a precise amount of liquid nitrogen. Specimen slices having a thickness on the order of 0.1 μm were obtained using a diamond knife, and were collected on copper grids. Specimens were examined in transmission with a Hitachi H-600 electron microscope operating at 75 KV.

Stress-strain Measurements

The stress-strain isotherms of uniaxial extension were obtained in the

usual manner [21,22]. The force and elongation measurements were made using a sequence of increasing values of the elongation or relative length of the sample $\alpha = L/L_0$, with frequent inclusions of values out of sequence to test for reversibility. The reduced nominal stress or modulus was calculated from the equation [23,24]

$$[f^*] = f^*/(\alpha - \alpha^{-2}) \qquad (2)$$

where $f^* = f/A^o$ is the nominal stress, f the equilibrium force, and A^o the area of the initial cross section in the reference state. All measurements were conducted at 25°C, and the elongation was generally increased to the rupture point of the sample.

RESULTS AND DISCUSSION

The rates of the precipitation reaction were characterized by plots of weight percent filler against time, as shown in Figure 1. The filled circles were

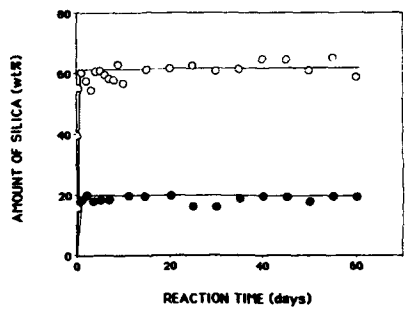


Figure 1. Weight percent filler precipitated shown as a function of time. The open circles represent the first set of samples (A) which were swelled with TEOS to the maximum extent attainable. The filled circles locate the second set of samples (B) which were swelled with TEOS to a lesser extent.

obtained from the first (A) series of swollen samples and the open circles from the second (B) series of swollen samples. The results show that the hydrolysis reaction is finished macroscopically after one day since amounts of filler precipitated are constant thereafter. However, the electron micrographs indicated that the microscopic "aging" process continued well after this point. Figures 2 and 3 illustrate typical electron micrographs obtained for samples A-1 and A-5; other micrographs are presented elsewhere [25]. Information on the "ages", amounts of filler, definition, and dispersion of all these A samples is summarized in Table I. Clearly, the particles in these five samples do not have a uniform size, and the diameter of some is as large as ~5,000 Å. These particles would be too large for effective reinforcement [1-5]. In fact, fully reinforcing fillers are generally taken to be those ranging below 500 Å in average particle diameter. Fillers coarser than this are considered only semireinforcing. Also, full reinforcement of a network by a filler can probably not be achieved unless the filler particles have been properly dispersed.



Figure 2. Transmission electron micrograph of sample A-1 at a magnification of 24,000 x. The length of the bar corresponds to 4,200 Å. For this and the following figures, sample details are given in Table I.



Figure 3. Micrograph of sample A-5 at 10,500 x. The length of the bar corresponds to 9,500 Å.

Table I. Amounts and characteristics of the precipitated silica

Sample[a]	Reaction time (hrs)	SiO_2 (wt %)	Diameter (Å)	Definition	Dispersion[b]
A-1	2.0	15.6	--	Poor	Fair
A-2	5.0	39.9	--	Poor	Fair
A-3	8.5	55.3	--	Poor	Fair
A-4	24.0	60.4	--	Poor	Fair
A-5	48.0	57.8	--	Poor	Fair
A-6	72.0	54.5	180-220	Good	Fair
A-7	96.0	60.7	~250	Good	Good
A-8	168.0	58.4	~250	Good	Good
A-9	240.0	56.8	~250	Good	Good

[a]Networks had been swollen with TEOS to the maximum extent attainable. [b]Lack of aggregation.

At approximately 72 hours, there seemed to be a critical stage at which reorganization was occurring, since the particles then had more uniform sizes, with diameters ranging from 180 to 220 Å. After 72 hours, the filler particles had a diameter of approximately 250 Å, were well defined and well dispersed (little aggregation). This is summarized in the last four rows of Table I, and the electron micrographs for two of these samples can be seen in Figures 4 and 5.

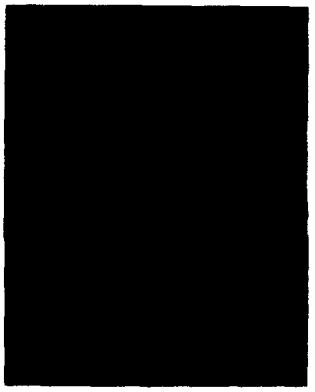


Figure 4. Micrograph of sample A-6 at 90,000 x. The length of the bar corresponds to 1,100 Å.



Figure 5. Micrograph of sample A-9 at 90,000 x. The length of the bar corresponds to 1,100 Å.

This result is very interesting. It indicates that there is an aging process in which digestion can make the particles better defined, more uniform in size, and less aggregated. The reorganization appears to occur around the third day (72 hours) of the hydrolysis reaction.

Obviously, the above process could also effect the reinforcing abilities of the precipitated particles. This reinforcing effect can be defined, in Wiegand's criterion, [26] as the increase in rupture energy, which may be measured by the area under the stress-strain curve obtained in an elongation test. The stress-strain isotherms for the second (B) series of the filled networks, including the corresponding reference network are shown in Figure 6. These isotherms are

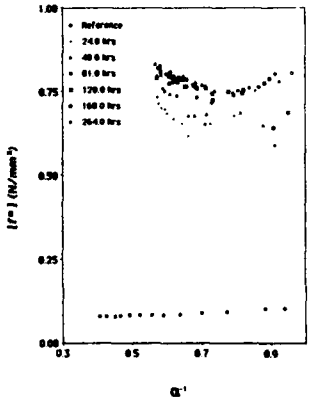


Figure 6. Reduced nominal stress shown as a function of reciprocal elongation for the second (B) series of silica-filled networks.

represented in the terms of Mooney-Rivlin plots [27,28] of the reduced nominal stress or modulus against reciprocal elongation. The upturns in modulus at high elongations clearly demonstrate the desired reinforcing effects. As expected, such reinforcement is absent in the reference network. The same

results plotted in a way that the area under each stress-strain curve corresponds to the rupture energy E_r are given elsewhere [25]. Values of the nominal stress at rupture, the elongation at rupture, and E_r are all given in Table II.

Table II. Ultimate properties of the silica-filled networks after various amounts of aging

Sample[a]	Reaction Time (hrs)	SiO_2 (wt %)	f_r^*,[b] (N mm^{-2})	α_r[c]	E_r[d] x 10^3 (J mm^{-3})
B-0	0.0	0.0	0.183	2.47	0.157
B-1	24.0	18.4	1.04	1.74	0.386
B-2	48.0	19.9	1.13	1.75	0.422
B-3	81.0	18.0	1.14	1.74	0.432
B-4	120.0	18.4	1.02	1.65	0.353
B-5	168.0	18.3	1.13	1.75	0.451
B-6	264.0	18.6	1.18	1.76	0.460

[a]Networks were swelled with TEOS to less than the maximum extent. B-0 is an unfilled network used as a reference material. [b]Nominal stress at rupture. [c]Elongation at rupture. [d]Energy required for rupture.

Values of the rupture energy are probably reliable to ± 10%. The values for samples B-1 through B-6, which have essentially constant wt % SiO_2, are seen to increase somewhat for the first 81 hrs, but to be essentially constant thereafter. Thus it seems that the aging process has only a marginal effect on improving such reinforcement.

Additional information on the growth and reorganization of in-situ precipitated particles is being obtained by carrying out neutron scattering measurements as a function of reaction time [18]. It will be very important to correlate these results with the micrographs and stress-strain isotherms described in this report.

The mechanism of this aging process could be very complicated. However, it is certainly expected that it will depend on the nature and concentration of the catalyst, the pH of the hydrolyzing solutions, and the temperature of the reaction. Similarly, there should be an aging process in the in-situ precipitation of other ceramic-type materials such as titania. Work on this issue is in progress.

ACKNOWLEDGEMENTS

The authors wish to thank Mr. Yan Huang of the Department of Pathology in the University of Cincinnati Medical Center for his generous assistance in the operation of the electron microscope. It is a pleasure to acknowledge the financial support provided by the National Science Foundation through Grant DMR 84-15082 (Polymers Program, Division of Materials Research).

REFERENCES

1. K. E. Polmanteer and C. W. Lentz, Rubber Chem. Technol., **48**, 795 (1975).
2. E. M. Dannenberg, Rubber Chem. Technol., **48**, 410 (1975).
3. M. P. Wagner, Rubber Chem. Technol., **49**, 703 (1976).
4. E. L. Warrick, O. R. Pierce, K. E. Polmanteer and J. C. Saam, Rubber Chem. Technol., **52**, 437 (1979).
5. J. R. Hamilton, "Silicone Technology", Interscience, New York, 1970.
6. J. E. Mark and B. Erman, "Rubberlike Elasticity. A Molecular Primer", Wiley, New York, 1988, pp. 145-153.
7. J. E. Mark and S.-J. Pan, Makromol. Chem. Rapid Comm., **3**, 681 (1982).
8. Y.-P. Ning, M.-Y. Tang, C.-Y. Jiang, J. E. Mark and W. C. Roth, J. Appl. Polym. Sci., **29**, 3209 (1984).
9. C.-Y. Jiang and J. E. Mark, Makromol. Chem., **185**, 758 (1984).
10. C.-Y. Jiang and J. E. Mark, Coll. Polym. Sci., **262**, 758 (1984).
11. Y.-P. Ning and J. E. Mark, Polym. Eng. Sci., **26**, 167 (1986).
12. J. E. Mark, Y.-P. Ning, M.-Y. Tang and W. C. Roth, Polymer, **26**, 2069 (1985).
13. Ultrastructure Processing of Advanced Ceramics, ed. by J. D. MacKenzie and D. R. Ulrich, Wiley, New York, 1988.
14. D. R. Ulrich, CHEMTECH, **18**, 242 (1988).
15. "Chemistry and Physics of Matrix-Isolated Systems", ed by L. Andrews and M. Moskovits, North-Holland Publishers, Amsterdam, 1989.
16. D. W. Schaefer, L. Jian, C.-C. Sun, D. McCarthy, C.-Y. Jiang, Y.-P. Ning, J. E. Mark, *and S. Spooner*, submitted to "Proceedings of Fourth International Conference on Ultrastructure Processing of Ceramics, Glasses, and Composites", ed. by D. R. Ulrich and D. R. Uhlman, Wiley, New York, 1990.
17. D. W. Schaefer, J. E. Mark, L. Jian, C.-C. Sun, D. McCarthy, C.-Y. Jiang, and Y.-P. Ning, in Polymer-Based Molecular Composites, ed. by D. W. Schaefer and J. E. Mark, Mat. Res. Soc., Pittsburgh, 1990.
18. D. W. Schaefer and J. E. Mark, unpublished results.
19. J. E. Mark and J. L. Sullivan, J. Chem. Phys., **11**, 1006 (1977).
20. M. A. Llorente, A. L. Andrady and J. E. Mark, J. Polym. Sci., Polym. Phys. Ed., **19**, 621 (1981).
21. J. E. Mark, J. Polym. Sci., Macromol. Rev., **11**, 135 (1976).
22. J. E. Mark, J. Chem. Educ., **58**, 898 (1981).
23. J. E. Mark, Adv. Polym. Sci., **44**, 1 (1982).
24. J. E. Mark and P. J. Flory, J. Appl. Phys., **37**, 4635 (1966).
25. Ping Xu, Ph.D. Thesis in Chemistry, University of Cincinnati, 1991
26. W. B. Wiegand, Can. Chem. J., **4**, 160 (1920).
27. L. R. G. Treloar, "The Physics of Rubber Elasticity", 3rd Ed., Clarendon Press, Oxford, 1975, pp. 96.
28. J. E. Mark, Rubber Chem. Technol., **48**, 495 (1975).

SOL-GEL DEPOSITION OF ELECTRONIC CERAMIC FILMS.

J.M. BELL*, B. BEN-NISSAN*, M. ANAST*, B.O. WEST**, L. SPICCIA**, J. CULLEN**, I. WATKINS*** and D. deVILLIERS**, G. JOHNSTON****

*University of Technology, Sydney, P.O. Box 123, Broadway, NSW, 2007 Australia
**Department of Chemistry, Monash University, Clayton, Victoria, 3168, Australia
***Department of Chemistry, Monash University; and Silicon Technologies Australia, 22 Sophia Street, Crows Nest, NSW, 2065, Australia
****Defence Science and Technology Organisation, P.O. Box 50, Ascot Vale, Victoria, 3032, Australia.

ABSTRACT

We describe a dip-coating method of depositing thin electronic ceramic coatings on various substrates from sol-gel solutions. The solutions we use are alkoxide-based, although the specific formulations depend on the system being deposited. We are working with two electronic ceramic systems: barium titanate on glass, and alumina, and yttrium barium copper oxide on alumina. We discuss methods used to reduce and remove processing defects such as crazing, cracking and pin-holing. We are also studying the effects of varying the processing conditions (dipping, hydrolysis and firing) on the electronic properties of the films. Initial results on $BaTiO_3$ indicate that it is better to deposit thin films (~0.1 - 0.2μm) and build up the coating thickness by repeated dipping.

INTRODUCTION

Deposition of electronic ceramic films, and in particular optical thin films from sol-gel solutions, has been successfully used for many systems [1], in particular cadmium stannate [2,3] and indium tin oxide [4,5]. We are using alkoxide based sol-gel solutions to deposit various other electronic ceramics in thin film form. Currently we are studying thin films of barium titanate ($BaTiO_3$) and the high T_c superconductors $YBa_2Cu_3O_7$ (referred to as 123).

There have already been many publications in this rapidly growing field on the deposition of the superconductors using sol-gel methods. Two current reviews covering this work into early 1988 [6,7] include the use of alkoxide based solutions. In several of the reports spin coating is used as the deposition technique, while numerous groups have reported superconductor preparation using aqueous solution techniques. We are using alkoxide based solutions and a dip-coating deposition method in our work as this has proved very successful for other systems [1].

The principal advantages of the sol-gel processing technique for thin films is the same as for bulk materials - a possible lowering of the sintering temperature required to form the ceramic with a desired crystal structure. This can be particularly beneficial in ceramic coatings as interactions with substrates can be a major problem, particularly with the high T_c superconductors [8]. Dip-coating also provides the possibility of large scale processing and good film homogeneity over large areas [1].

FILM PREPARATION

There are two main aspects to the film deposition technique we are using: preparation of appropriate solutions; and deposition of the film, including the conditions during dipping, hydrolysis of the film and firing conditions. These will be discussed briefly before we present initial results on $BaTiO_3$ films.

Mat. Res. Soc. Symp. Proc. Vol. 180. ©1990 Materials Research Society

Chemistry of Solutions

The barium titanate films have been deposited from solutions of barium isopropoxide and titanium n-butoxide dissolved in isopropanol. There are also some additives in the solutions. The hydrolysis reaction which occurs in the films is a multiple stage process, which may include the replacement of coordinated alkoxides by OH groups:

$$Ba(O^iPr)_2 + H_2O \rightarrow Ba(O^iPr)OH + {}^iPrOH$$

$$Ba(O^iPr)OH + H_2O \rightarrow Ba(OH)_2 + {}^iPrOH \quad (1)$$

A similar reaction occurs for the titanium n-butoxide component of the solution, and subsequent heat treatment of the film converts the intimately mixed hydroxides into $BaTiO_3$.

The solutions we have used for deposition of the 123 films contain yttrium isopropoxide/methoxyethoxide, barium ethoxide/isopropoxide and copper methoxide/ethoxide/ methoxyethoxyethoxide. Again hydrolysis is a multiple stage process leading to the evolution of alcohols, and subsequent annealing converts the resulting hydroxides into the 123.

Deposition and Firing Conditions

Deposition of the films takes place in a dry N_2 atmosphere, with the substrates being withdrawn vertically from the solution at a uniform rate. The films are dried for 10-15 minutes (to allow excess solvent to evaporate) and then hydrolysed for up to 24 hours in a low humidity atmosphere (up to 20%). The rate of hydrolysis is important, and a too rapid hydrolysis leads to crazing of the films. Each coating deposits a film of between 70 and 150nm, depending on the rate of withdrawal of the substrate from the solution (with faster withdrawal giving thicker films). Therefore several coats are often deposited to produce thicker films, and the films are hydrolysed and then fired to 600°C between coats.

Many of the $BaTiO_3$ films have been deposited on glass, and some on alumina. The 123 films have principally been deposited on alumina or on $BaTiO_3$ coated on alumina. The films on alumina have been fired at temperatures up to 850°C.

Surface preparation and surface condition play a major role in the quality of the final films. In the results reported here for films on glass, the slides have been heated to 600°C for 30 minutes and kept in a desiccator prior to deposition. The major problems we have encountered are the surface roughness of the alumina substrates, or dust on the substrates. To date this has prevented uniform and craze-free films being deposited on alumina, and we have observed that dust has nucleated cracking in several of the films deposited onto glass. Consequently measurements of electronic properties such as resistance often do not reflect intrinsic values for the films. This problem is currently being addressed.

RESULTS

Barium Titanate

X-ray diffraction results for the barium titanate films deposited on both glass and alumina indicate that cubic $BaTiO_3$ is being formed after heat treatment at 600°C (see fig. 1). The lattice parameter is a=3.99±0.02Å. This sintering temperature is significantly lower than the normal sintering temperature for bulk barium titanate of ~1380°C [9]. The films are quite uniform in appearance over the area of the film (25mm × 50mm), although the thickness deposited in each coat can be varied from 70 to 150nm . The coating thickness has been measured using a mechanical stylus-type profilometer and also using Rutherford Backscattering Spectrometry (RBS). A typical RBS spectrum for a $BaTiO_3$ film on glass is shown in figure 2. Using the Ba and Ti peaks, the film thickness is 130 nm (using a density of 6.0 gcm^{-3} - i.e. assuming $BaTiO_3$). This film has a single coat of $BaTiO_3$.

Scanning Auger microprobe analysis (SAM) and RBS have also been used to investigate

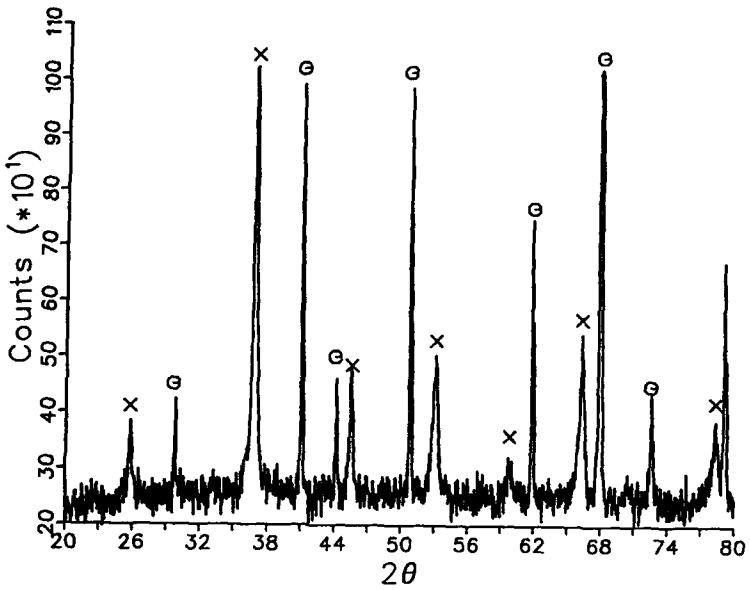


Figure 1. x-ray diffraction pattern obtained from a $BaTiO_3$ film (5 coats) deposited on alumina. Co K_α radiation (λ=1.7889Å) was used. × - $BaTiO_3$; Θ - alumina.

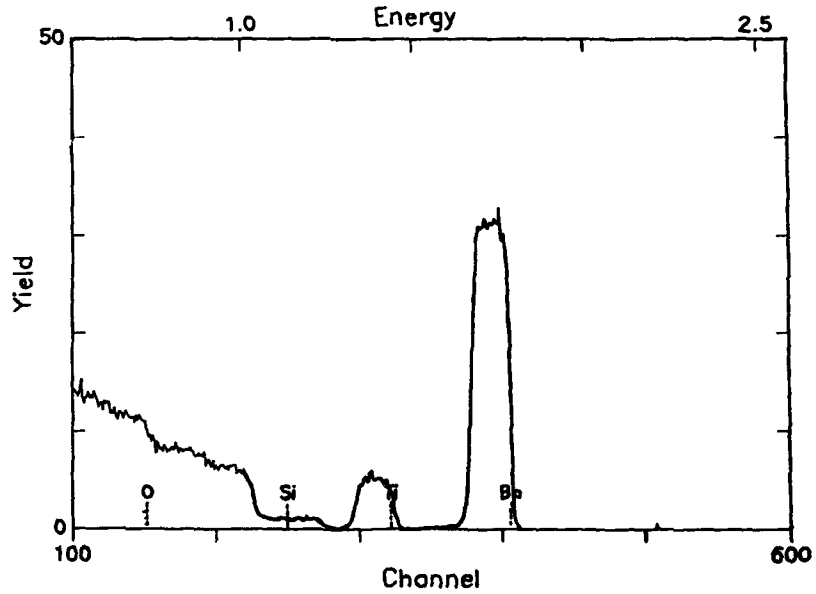


Figure 2. Rutherford Backscattering spectrum of a sol-gel deposited film of $BaTiO_3$ (single coat) on a glass substrate. The film was withdrawn solution at 31mms^{-1} dried for 5 minutes, hydrolysed for 1 minute in a 10% relative humidity atmosphere, and fired for 1 hour at 125°C and 1 hour at 600°C.

the composition of the films as well as to probe the substrate/film interface. Results for the barium titanate films on glass indicate very uniform concentration throughout the film, with a Ba/Ti ratio of 0.96. In some films there is a slight decrease in the barium content close to the $BaTiO_3$/glass interface. When used in conjunction, SAM and RBS are ideally suited to the characterisation of thin surface films [10]. Other analytical techniques will also be used, where appropriate, to examine these films.

Scanning electron micrographs of the surface of barium titanate films on glass and alumina show completely different microstructure. On glass the films are quite smooth, with only occasional defects, which are probably nucleated by dust. We have found that surface moisture on glass can cause severe crazing of the films. On unpolished alumina, however, the films are crazed and show evidence of severe cracking propagating through from layer to layer. This is probably due to the surface roughness of the alumina.

$YBa_2Cu_3O_7$

123 films deposited onto alumina and onto barium titanate coated alumina only show evidence of the 123 phase after heat treatment at temperatures above ~800°C. After annealing at 850°C for 1 hour we have found evidence of tetragonal 123 phase as well as some impurity phases, in particular CuO and Y_2BaCuO_5. Again films deposited directly onto unpolished alumina show severe cracking, and films deposited onto $BaTiO_3$ coated alumina also show evidence of cracking which appears to be propagating through from the substrate.

CONCLUSION

The dip-coating process and sol-gel solutions we are using have been able to produce the desired products ($BaTiO_3$ and 123) in thin film form. On suitable substrates we have been able to produce excellent quality films with uniform composition throughout the film (both through the film and across its surface), and with the desired structure. Problems with surface preparation can cause cracking in the films and we have not yet been able to demonstrate superconductivity in the 123 films.

ACKNOWLEDGEMENTS

The authors gratefully acknowledge financial support provided by the Australian Department of Industry and Commerce.

REFERENCES

[1] H. Dislich, Sol-Gel Technology for Thin Films, Fibres, Preforms, Electronics and Specialty Shapes, L.C. Klein (ed), Noyes Publications, New Jersey, 1988 (Chapter 4)
[2] H. Dislich, P. Hinz and G. Wolf, U.S. Patent No. 4,229,491 Dec. 13, 1977
[3] A.J. Koplick, International Patent Application No. PCT/AU87/00324, 1987
[4] N.J. Arfsten, R. Kaufman and H. Dislich, German Patent Application, 1983
[5] N.J. Arfsten, R. Kaufman, H. Dislich, Ultrastructural Processing of Ceramics, Glasses and Composites, (Wiley and Sons, 1984), Chapter 15
[6] H. Kozuka, T. Umeda, J. Jin, T. Monde and S. Sakka, Bull. Inst. Chem. Res., Kyoto University, 66 80 (1988)
[7] S. Sakka, MRS International Meeting on Advanced Materials 1989, 6 221 (1989)
[8] T. Asano, K. Tran, A.S. Byrne, M.M. Rahman, C.Y. Huang and J.D. Reardon, App. Phys. Lett. 54 1275 (1989)
[9] G. Tulloch, private communication.
[10] J.L. Cocking and G.R. Johnston,"Characterisation of Oxidised Surfaces", in Surface Analysis B. Sexton, R. Smart and J. O'Connor (eds), Springer Verlag, to be published

THE FORMATION OF THIN FILMS AND FIBERS OF TiC FROM A POLYMERIC TITANATE PRECURSOR

S-J. Ting, C-J. Chu, E. Limatta, J. D. Mackenzie* and T. Getman, M. F. Hawthorne**
* Department of Materials Science and Engineering and ** Department of Chemistry and Biochemistry, University of California at Los Angeles, Los Angeles, CA 90024

ABSTRACT

The synthesis and characterization of several polymeric titanates and their conversion to carbon deficient TiC is described. The physical properties of one of these titanates allows it to be drawn into fibers and applied to substrates as thin films. Pyrolysis of these fibers and films to carbon deficient TiC is described.

INTRODUCTION

The preparation of metallic carbides via metal-organic precursors is now well known [1-7]. However, while it is relatively easy to prepare ceramic carbide powders it is extremely difficult to fabricate fibers directly from the precursors. Titanium alkoxides are known to undergo trans-esterification [8] with carboxylic acid esters. This approach has been employed in the preparation of titanium alkoxides which could not be prepared via other routes [8]. The formation of polymeric titanium alkoxides via the transesterification of $Ti(O\text{-}i\text{-}C_3H_7)_4$ with bifunctional acetates and their subsequent pyrolysis to TiC_x (x<1) is described below. One prerequesite of such polymers is that they contain excess carbon which, during the pyrolysis process, will "burn-off" the oxygen in the system as carbon monoxide. This work represents part of our ongoing research which pertains to the preparation of thin films and fibers of amorphous carbides, amorphous oxycarbides and crystalline carbides from metal-organic precursors.

EXPERIMENTAL

Syntheses of Polymeric Titanium Alkoxides:

The typical procedure for conducting reaction H (see Table 1) involved the interaction of 2.27 g (7.99 mmol) of $Ti(O\text{-}i\text{-}C_3H_7)_4$ with 1.05 equivalents (1.87 g, 8.40 mmol) of α,α'-diacetate-o-xylene in toluene (200-250 mL). The $Ti(O\text{-}i\text{-}C_3H_7)_4$ was weighed in the dry box and quantitatively transfered, using toluene as solvent, to a 3-neck reaction flask which was stoppered via two stoppers and one stopcock. The α,α'-diacetate-o-xylene, previously dissolved in dry deoxygenated toluene, was then transfered onto the $Ti(O\text{-}i\text{-}C_3H_7)_4$ via a Cannula. An additional 200 mL of dry deoxygenated toluene was added to this solution. Under a flush of N_2 gas the stoppers were replaced by a Dean-Starke trap and condenser and by a reservoir bulb which was filled with (250 mL) of dry deoxygenated toluene. The reaction mixture was brought to reflux and the distillate which collected in the Dean-Starke trap was periodically drained off and its IR spectrum observed. This was continued until the IR absorption at ≈1740 cm^{-1} attributable to the carbonyl group of isopropyl acetate was no longer observed in the distillate. Periodically some toluene from the reservoir was added to the reaction to prevent it from distilling to dryness. The resulting solution was filtered and the toluene was removed under reduced pressure to yield 1.02 g (42% based upon $Ti(O\text{-}i\text{-}C_3H_7)_4$) of a tacky polymer.

^1H FT-NMR data: 7.55-6.79 ppm multiple resonances with a maximum at 7.11 ppm (D + E), 5.72-4.20 ppm multiple resonances with maxima at 5.24 ppm and 4.44 ppm (C + B), 2.25 ppm (F), 1.61-0.39 ppm with a maximum at 1.14 ppm (A). Integrated areas 20.9 : 25.1 : 1 : 61.5, respectively. Theoretical areas if x = 15 (Figure 1); 20 : 30 : 1 : 62. Using 15 as a good approximation of x, the MW_{ave} of product H was 4636. ^{13}C FT-NMR data: 142-139 ppm multiple resonances (G), 131-125 ppm multiple resonances (D + E), 79-70 ppm multiple resonances (C + B), 27-25 ppm multiple resonances (A), 21.3 ppm (F), no resonance assignable to carbon (H) was observed in the area of 170 ppm. The assignments refer to the corresponding carbon atoms labeled in Figure 1 or in the case of the ^1H FT-NMR the hydrogens bonded to them. IR data(cm^{-1}): C-H 2968 (m), 2865 (m), unassigned 1457(m), 1385 (m), 1328 (m), 1214 (m), 1060-950 (s, br) with

Reactions A - G were performed in a similar manner. The soluble products from reactions A - G were characterized spectroscopically by IR, ^1H FT-NMR and ^{13}C FT-NMR. Insoluble products were characterized spectroscopically by IR and solid-state ^{13}C FT-CPMAS-NMR.

Mat. Res. Soc. Symp. Proc. Vol. 180. ©1990 Materials Research Society

Thin Film and Fiber Formation:

All the low temperature (<600°C) sample-heating was carried out in the dry box under nitrogen in a home-built furnace. All the high temperature (>600°C) sample-heating was carried out under argon in a high temperature furnace (Thermal Technology Inc. Astro 1000A).

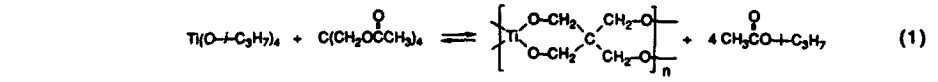
The structures of the thermalized samples at different temperatures were investigated using solid-state ^{13}C-CPMAS-NMR and/or IR spectroscopy. Samples pyrolyzed at temperatures higher than 1000°C were studied using XRD. Hand-drawn fibers were obtained from product H and cured at 80°C overnight in the dry box under a nitrogen atmosphere. The cured fibers were then pyrolyzed very slowly to 500°C under nitrogen. The resulting titanium oxycarbide fibers were then heated to 1500°C under argon for 4 hours.

Thin films were prepared by dipping a fused quartz or silicon substrate into a hexane solution of product H. The samples were then fired in an inert atmosphere from 500-1000°C for 1 hour. SEM, ellipsometer and Dektak were used to study the thickness and morphology of the films. DC conductivity was measured by the four probe method. UV-vis and IR spectroscopy were also used to characterize the optical properties of the films.

RESULTS AND DISCUSSION

Synthesis and Characterization of Polymeric Titanium Alkoxides:

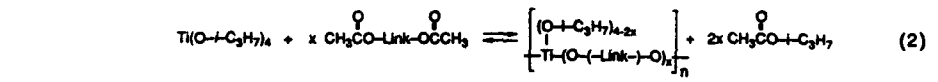
The reaction of $Ti(O\text{-}i\text{-}C_3H_7)_4$ with pentaerythritol tetraacetate (equation 1) led to the formation of a polymeric titanium alkoxide (product A).



(1)

The equilibrium of equation 1 was forced to the right by distilling away the isopropyl acetate as it was formed. However, as evidenced by IR and solid-state ^{13}C-CPMAS-NMR, the reaction could not be driven totally to completion. Presumably, this was due to the non-ideality of the polymer formed and its lack of sufficient flexibility to allow all the active sites to react with one another.

The encouraging results obtained upon pyrolysis of product A (see bleow) led us to investigate other acetates in the reaction with $Ti(O\text{-}i\text{-}C_3H_7)_4$, equation 2.



(2)

The results of these studies are presented below in Table I. The viscous tacky nature of product H allowed it to be drawn into fibers and applied on substrates as thin films.

The spectroscopic data for product H is given in the experimental section and a representation of its postulated structure is shown in Figure 1.

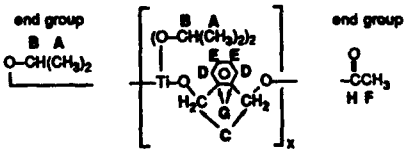


Figure 1: A representation of product H.

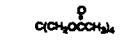
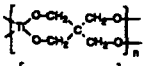
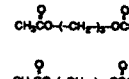
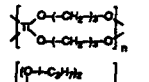
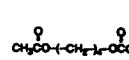
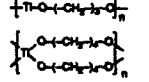
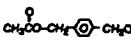
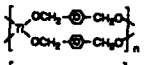
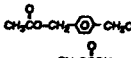
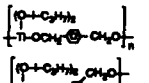
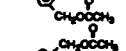
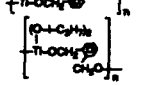
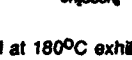
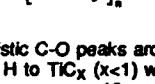
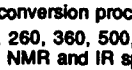
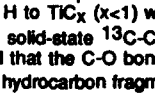
Formation of Thin Films and Fibers of Carbon Difficient TiC from Product H:

The gel which resulted from reaction A was pyrolyzed at 1050°C and shown to produce both Ti_2O_3 and TiC_x (x<1) while at 1500°C TiC_x (x<1) was formed as determined by XRD. This encouraging result led us to investigate other polymeric titanium alkoxides for use as precursors to thin films and fibers of TiC.

TGA analysis of product H revealed a 60% weight loss between 100 and 450°C and an additional 2-3% weight loss from 450-870°C. The weight loss above 870°C was not determined due

to the limitations of the TGA apparatus. The solid-state ^{13}C-CPMAS-NMR and IR spectra of

Table 1: Summary of Reactions of Acetate Esters with $Ti(O\text{-}i\text{-}C_3H_7)_4$

Reaction	Acetate	Ratio Acetate:$Ti(O\text{-}i\text{-}C_3H_7)_4$	Theoretical Stoichiometry of Product	Solubility	Temperature At Which TiC_x ($x<1$) Was Formed
A		1:1		Insoluble	1800°C
B		2:1		Insoluble	NA
C		1:1		soluble in toluene, benzene, and CH_2Cl_2	1800°C
D		2:1		soluble in toluene, benzene, and CH_2Cl_2	No TiC produced only Ti_2O_3
E		2:1		Insoluble	1200°C
F		1:1		Insoluble	1200°C
G		1:1		Insoluble	1200°C
H		1:1		soluble in toluene, benzene, and CH_2Cl_2	1200°C

a sample pyrolyzed at 180°C exhibited characteristic C-O peaks around 77 ppm and 1050 cm^{-1}, respectively. The conversion process of product H to TiC_x ($x<1$) was studied at various temperatures (180, 260, 360, 500, 700°C) using solid-state ^{13}C-CPMAS-NMR and IR spectroscopy. The NMR and IR spectra revealed that the C-O bonds in product H were broken by 260°C, producing titanium oxide and unsaturated hydrocarbon fragments. Chemical analyses of several samples of product H pyrolyzed at temperatures from 180 to 1500°C were obtained and are listed in Table II. These results indicate that the weight loss from 260 to 700°C is primarily due to the elimination of hydrogen and some carbon and oxygen. However, above 700°C carboreduction occurs, resulting in the production of a titanium oxycarbide. The IR spectrum of the 700°C sample indicates the reformation of C-O bonds. At 1500°C a crystalline phase TiC_x ($x<1$), which was characterized by XRD (Figure 2), is formed. The formation of a carbon deficient TiC at these pyrolysis temperatures is consistent with previous reports [9]. Even when amorphous carbon is mixed with the TiC_x ($x<1$) produced from the pyrolysis of product H and further pyrolyzed at 1500°C no additional carbon is incorporated in the TiC_x ($x<1$) as evidenced by XRD.

Table II: Elemental Analyses of Product H pyrolyzed at Various Temperatures

Temp.(°C)	Time (hr)	Wt. % Oxygen	Wt. % Carbon	Wt. % Hydrogen	Wt. % Titanium
180	1	23.41	56.53	4.46	15.60
360	1	24.42	42.17	1.83	31.58
700	1	24.85	42.85	<0.5	32.30
1200	4	13.36	33.42	<0.5	53.22
1500	4	3.04	41.72	<0.5	55.24

Fibers drawn from product H and pyrolyzed at various temperatures were investigated by SEM. The SEM pictures of these fibers pyrolyzed at 500 and 1500°C are shown in Figure 3. The fiber pyrolyzed at 500°C shows a smooth surface morphology, but the fiber pyrolyzed at 1500°C has a surface significantly composed of crystallites. Both fibers are porous due to extensive weight loss during pyrolysis and as a result are very brittle and difficult to handle.

Thin films, formed by dipping a substrate into a solution of product H followed by pyrolysis, varied in thickness from several angstroms to a few microns depending upon processing conditions. The SEM results do not reveal any visible cracks or pores in these films. These thin films show n-type conduction with room temperature DC conductivities of 0.7 and 800 $W^{-1}cm^{-1}$ for films pyrolyzed at

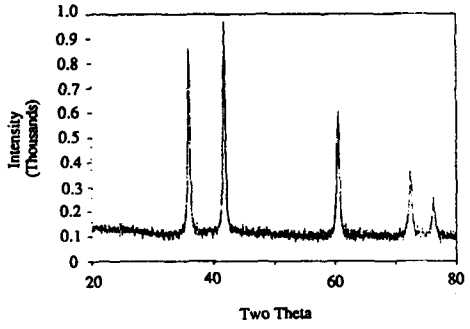


Figure 2: XRD Spectrum of TiC_x (x<1), pyrolysis temperature 1500°C.



(a) (b)

Figure 3: SEM photographs of fibers of product H pyrolyzed at (a) 500°C and (b) 1500°C.

800°C and 1000°C, respectively. As evidenced by the chemical analyses given in table II these films most likely consist of a titanium oxycarbide. These titanium oxycarbide films are amorphous to X-rays and their phase compositions are at the present time unknown. Even though these films contain excess carbon, it is unlikely that this carbon is responsible for the observed conductivity, since graphite is not an n-type conductor. The high conductivities of these titanium oxycarbide thin films suggest possibilities for future applications exist.

Acknowledgments: The support of this work by the National Science Foundation (Grant DMR-87-06379) is gratefully acknowledged.

REFERENCES

1. Yajima, S.; Hayashi, J.; Omori, M. Chem. Lett., 931 (1975).
2. Yajima, S.; Okamura, K.; Hayashi, J.; Omori, M. J. Am. Chem. Soc., *59*, 423 (1976).
3. Yajima, S.; Hasegawa, Y.; Okamura, K.; Matsuzawa, T. Nature, *273*, 525, (1978).
4. Wynne, K. J.; Rice, R. W. Ann. Rev. Mat. Sci., *14*, 297 (1984).
5. West R. W.; "Ultrastructure Processing of Ceramics, Glasses and Composites," Hench, L. L.; Ulrich, D. R.; (eds.), Wiley, NY, 19 (1984).
6. Yajima, S. Am. Ceram. Soc. Bull., *62*, 893 (1983).
7. Willis, R. R.; Markle, R. A.; Mukherjee, S. P. Am. Ceram. Soc. Bull., *62*, 904 (1983).
8. a) Bradley, D. C.; Mehrotra, R. C.; Gaur, D. P. "Metal Alkoxides," Academic Press, New York (1978). b) Bradley, D. C. Advan. Inorg. Chem. Radiochem., 15, 259 (1972).
9. Storm, E. K. "The Refractory Carbides," Margrave, J. L., Ed., Academic Press, NY, Chapter 1 (1967)

CERAMIC FIBER COATING BY A NON-AQUEOUS SOL-GEL PROCESS

F. C. MONTGOMERY, H. H. STRECKERT, R. O. HARRINGTON, J. L. KAAE, S. P. PAGUIO, AND D. R. WALL
General Atomics, San Diego, CA

ABSTRACT

Thin coatings of Al_2O_3, and Y_2O_3, have been prepared on desized Nicalon yarn. The layers were deposited by dip coating in homogeneous, alcohol solutions of partially hydrolyzed metal alkoxides. The coating thicknesses could be controlled by multiple dipping.

The uniformity of the coatings was affected by the alkoxide concentration. Solutions containing greater than 1 wt % equivalent oxide resulted in oxide bridging the void between the fibers.

Transmission Electron Microscopy (TEM) studies on alumina coatings formed by dip coating 300 mesh nickel grids, have shown that either eta or gamma alumina is formed after heating at temperatures as low as 700 °C. The rate of grain growth increases as the temperature increases. In addition, increased grain growth is observed for films produced from solutions with higher water:metal ratios.

The strength of coated fibers heat treated in air after coating has been determined. Alumina, and yttria coatings reduce the strength of the fiber after heating at temperatures above 900 °C. Scanning Auger analysis suggests that the coating is reacting with the fiber at these high temperatures.

INTRODUCTION

In the development of strong, tough ceramic fiber/ceramic matrix composites, the chemistry and properties of the fiber-matrix interface play an important role. Fiber coating can provide a means of controlling interfacial bond strength.

Thin oxide coatings can be produced by dipping a substrate into a homogeneous solution containing a precursor of the oxide. The precursor solution may be made from three basic types of solutions: hydrolyzable metal salts[1], colloidal sols[2], and polymerized organometallic species[3].

In order to utilize a metal alkoxide, reaction conditions must be found which produce a homogeneous solution. Several parameters affect the homogeneity of the solution as the metal alkoxide hydrolyzes and polymerizes. Some of the important parameters are (1) the hydrolysis and condensation temperature, (2) the concentration of metal alkoxide, (3) the pH of the solution and (4) the ratio of water to metal used during the hydrolysis. These factors can often alter the average molecular weight distribution of the resulting polymer and thus influence the microstructure of the final coating.

EXPERIMENTAL

Synthesis. Clear solutions of organo-aluminum were prepared by the controlled hydrolysis of dilute alcohol solutions of aluminum sec-butoxide (Alfa Inorganics). Initial experiments used sec-butanol and ethanol as the

Mat. Res. Soc. Symp. Proc. Vol. 180. ©1990 Materials Research Society

solvent, but it was found that the solutions were not stable and, after aging for several hours, formed a precipitate. Thus, the alkoxide was dissolved in 2-ethoxyethanol or 2-(2-ethoxyethoxy)ethanol (J. T. Baker) which had been dried by distilling from barium metal. The solutions were hydrolyzed at 55 °C by dropwise addition of distilled water (H_2O:Al= 0.25, 1.0, 2.0) dissolved in alcohol. The mixture was then heated for 1 to 15 hours at 55 °C to age the solution.

Yttrium isopropoxide was prepared by reaction of yttrium metal with dry isopropanol following the procedure of Mazdiyasni.[4]

Yttrium 2-ethoxyethoxide and yttrium 2-(2-ethoxyethoxy)ethoxide were prepared from yttrium isopropoxide by alcohol exchange at 125 °C. The isopropanol, as it was formed was swept from the vessel by flowing nitrogen. After reacting for 3 to 5 hours, the solution was cooled and filtered in a glove box to yield a clear pale yellow solution. The yields were not measured but the reaction was continued until isopropanol was no longer being evolved. The yttrium concentration was titrated with standard EDTA solution.

The coating solution was prepared from either alkoxide by the hydrolysis procedure described for the alumina precursor solution.

Coating. Nicalon fiber tows were dip coated using a microprocessor-controlled dip coater. Samples were dipped into the coating solution for 20 sec, and removed at 6 cm/min. The coating was dried at 350 °C prior to repeating the dipping cycle.

Calcining. Thermogravimetric studies on vacuum dried gels showed that the gels lost weight in air up to approximately 650 °C. Thus, after dip coating, portions of each coated tow were heated in air at 10 °C/min to 700, 900, 1100, or 1300 °C and held for 30 min. After the hold, the temperature was reduced at 20 °C/min to about 700 °C and then the furnace was turned off.

RESULTS AND DISCUSSION

The quality of the coatings was determined by scanning electron microscopy. Features which are considered detrimental to the coating are the following:

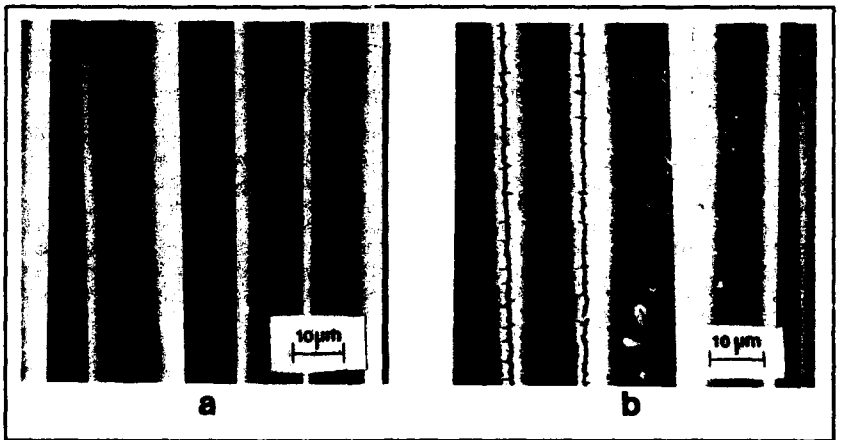


Figure 1. SEM photomicrographs showing yttria coatings on Nicalon: (a) 1 dip (b) 5 dips

(1) areas of coating bridging between fibers.

(2) tracking on the fibers (see fig. 1a), indicating the fibers had been stuck together.

(3) spallation of the coating.

(4) peel back of the coating.

SEM photomicrographs of typical yttria coatings on Nicalon fibers prepared from a 1 wt % oxide solution are given in figure 1. Bridging and peel back flaws are apparent on the sample dipped 5 times. The single dip coating, however, is uniform and adherent although some tracking is evident on one fiber.

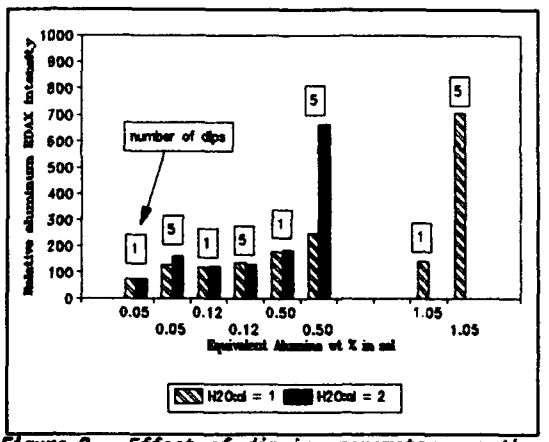


Figure 2. Effect of dipping parameters on the thickness of alumina coatings on Nicalon fibers.

In addition to SEM examination, the relative coating thicknesses were determined by EDAX analyses of the coating compositions. In this analysis, the silicon peak of the Nicalon substrate was used as an internal standard since the silicon signal decreased as the coating thickness increased. Figure 2 shows how process parameters affect this measure of the coating thickness. The thickness was fairly independent of the number of dips. The apparent large increase in coating thickness after 5 dips into a 0.51 wt % solution is due to severe bridging of the fibers. The amount of water used in the hydrolysis has little effect on the thickness of alumina coatings when the concentration of metal oxide is below 0.5 wt %. When the wt % metal oxide exceeds this concentration, 5 dips in a solution hydrolyzed with 2 moles water per mole of metal shows a significant increase in the thickness of the coating. SEM observations show that the coatings appear similar with minor

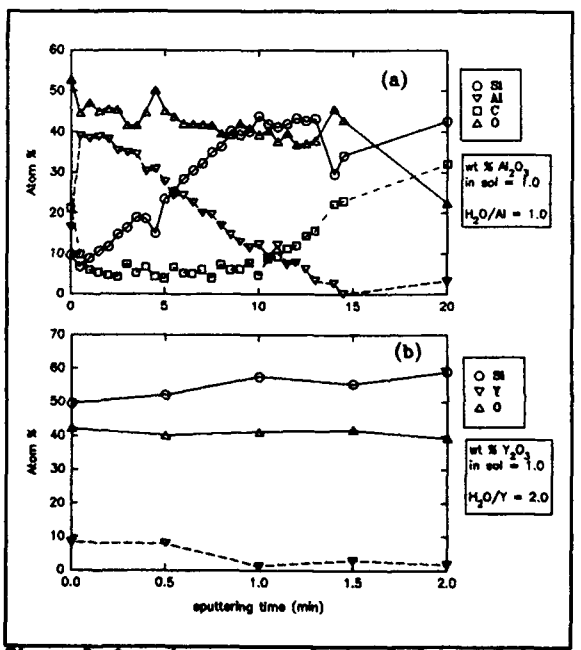


Figure 3. Scanning auger analysis of elemental depth profile for (a) Al_2O_3 and (b) Y_2O_3 on Nicalon fibers after heating to 1100 °C in air.

bridging between the fibers.

The structure of the solvent influences the coating, and the stability of the coating solution. The data in figure 1 were obtained using 2-ethoxyethanol as the solvent. With 1 mole of water per mole of metal, the

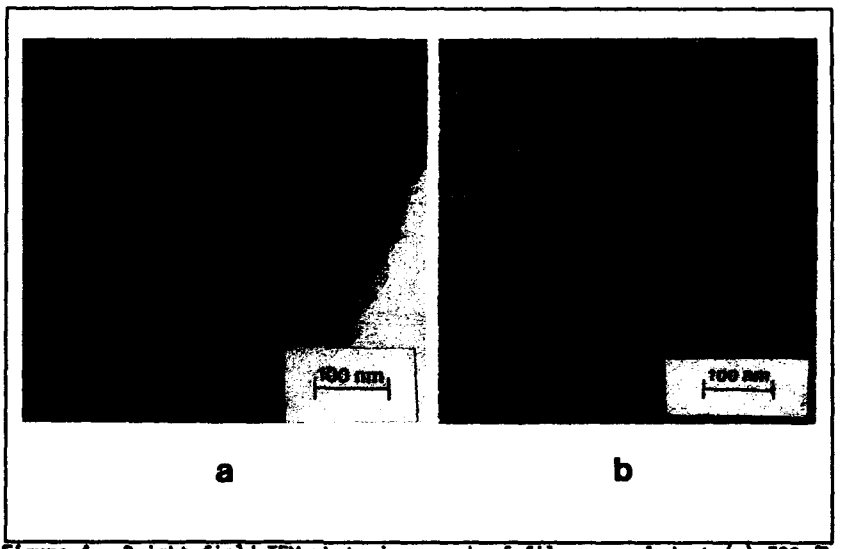


Figure 4. Bright-field TEM photomicrograph of films annealed at (a) 700 °C and (b) 800 °C.

solutions were stable for several months. However, when the molar ratio was increased the solutions would continue to thicken and would gel in a few days. With 2-(2-ethoxyethoxy)ethanol significant bridging was obtained at 1 wt % equivalent oxide. Furthermore, the solutions would gel within a few hours if the water:metal ratio was greater than one.

Figure 3 shows a scanning auger analysis of the elemental depth profile of alumina and yttria coatings on desized Nicalon after a 0.5 hr thermal anneal in air at 1100 °C. Depth profiling was accomplished by bombarding the sample with an argon ion beam. The elemental analysis is accurate to 1 percent. Relative to a silicon standard, one minute of ion bombarding is approximately 10 nm. However, the depth of penetration of the beam on the coated sample is *not* quantitatively known. The alumina coating contains an appreciable amount of silicon at the surface and the concentration of silicon increases steadily as the aluminum concentration decreases into the coating.

The yttria coating contains less metal than does the alumina coating. The alumina coating is about 40 atom % aluminum. The yttria coating is only about 10 atom % yttrium. Stoichiometric oxide coatings would be 40 atom % metal.

Transmission electron microscope specimens were prepared from nickel TEM grids that were Al_2O_3 coated from aluminum sec-butoxide hydrolyzed with 1 mole of water per mole of metal in 2 ethoxyethanol. A bright-field TEM micrograph of a hydrolyzed film annealed at 700 °C for 0.5 hr is shown in Figure 4a. Both the bright-field micrograph and the electron diffraction pattern suggest that the material is amorphous. There is no diffraction contrast typical of a crystalline material in the bright field image, and only diffuse scattering is present in the diffraction pattern.

A film annealed for 50 hr at 700 °C shows some crystallinity, with diffraction contrast from regions of about 100 Å in size. Interestingly, a similar film formed from a solution hydrolyzed with 0.25 mole H_2O per mole Al exhibited diffraction contrast from regions of less than 10 Å.

The bright field TEM micrograph and the electron diffraction pattern of a coating annealed at 800 °C, (fig 4b) also reveals evidence of crystallinity. Regions about 30 Å in size are present and the electron diffraction pattern is composed of spotty rings. The crystalline regions of a coating annealed at 900 °C are larger than those in the 800 °C annealed coating, measuring about 100 Å in size.

Table I. Planar spacings of various alumina phases and planar spacings of the coatings prepared in this study.

Sample	Eta	Gamma	800 C	900 C
Planar Spacings (Å)	4.60	4.53	4.45	4.56
	2.80	2.80	2.73	2.77
	2.40	2.39	2.35	2.39
	2.27	2.28	-	-
	1.97	1.98	1.96	1.97

The four largest atomic-plane spacings determined from the patterns of the 800 °C and 900 °C annealed films are compared with those of the eta and gamma phases of hydrated alumina in table I. The spacings are not close to the spacings of any of the other hydrated alumina phases. The 4.45 Å spacing for the film annealed at 800 °C is closest to that of gamma alumina. However, the 4.56 Å spacing in the 900 °C film is midway between eta and gamma alumina. Also, one diffraction ring, the ring for a 2.28 Å spacing, is missing from the diffraction patterns. The missing ring corresponds to diffraction from (222) planes [5], but a ring produced by diffraction from the parallel (111) planes with a 4.60 Å spacing is present. Thus, the absence of the ring is not due to crystalline preferred orientation in the films. In any case, the measured atomic plane spacings do not differentiate between the eta and gamma phases.

The tensile strength of the coated fibers has been measured. All of the coatings tested degrade the fiber strength during 0.5 hr anneals in air at temperatures greater than 700 C. Figure 5 compares the average failure load for individual fibers coated with alumina and yttria.

In Nicalon-aluminosilicate glass matrix composites,

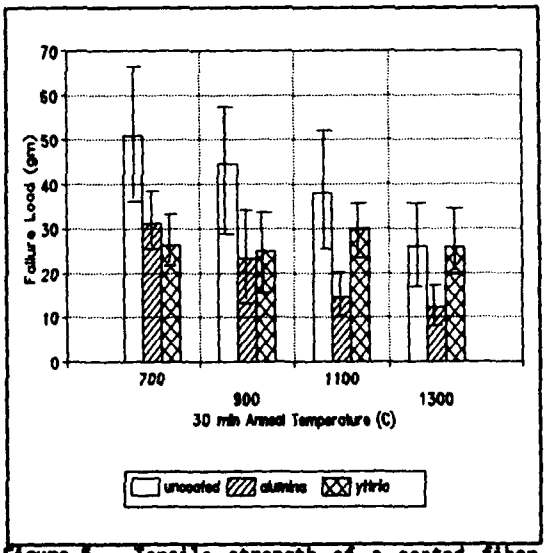


Figure 5. Tensile strength of a coated fiber after heating in air for 30 min at the indicated temperature.

reaction can occur between the glass matrix and the fiber when the composite is aged at 900 °C in air.[6] Presumably, our coatings are also reacting with the bulk fiber creating flaws from which cracks propagate during tensile loading.

CONCLUSIONS

Oxide coatings can be produced on Nicalon fiber using a dip coating technique in hydrolyzed yttrium and aluminum alkoxides. Coatings prepared from a solution containing more than 1 wt % oxide show flaws associated with bridging between the fibers of the tow. All coatings degrade the strength of the fiber presumably due to reaction with the fiber surface.

ACKNOWLEDGEMENTS

This research was supported by the Advanced Research Projects Agency of the Department of Defense and was monitored by the Air Force Office of Scientific Research under Contract No. F49620-89-C-0078. The United States Government is authorized to reproduce and distribute reprints for governmental purposes notwithstanding any copyright notation hereon.

REFERENCES

1. D. P. Partlow and B. E. Yoldas, Journal of Non-Crystalline Solids, 46, 153-161 (1981).

2. B. E. Yoldas, American Ceramic Society, Bulletin, 54, 289-290 (1975).

3. B. E. Yoldas, Journal of Non-Crystalline Solids, 63, 145-154 (1984).

4. K. S. Mazdiyasni, C. T. Lynch and J. S. Smith, Inorg. Chem., 5, 342 (1966).

5. Powder Diffraction File, edited by W. F. McClune (International Centre for Diffraction Data, Swarthmore, Pa).

6. J. J. Brennan in CERAMIC MICROSTRUCTURES '86, eds. Pask and Evans (Plenum Publishing Corp., 1988), pp.387-389.

IMPROVEMENT OF BUILDING MATERIALS PERFORMANCE BY SOL-GEL DERIVED COATINGS

WOLFRAM BEIER* AND IVAN ODLER**

* Schott Glaswerke, Hattenbergstraße 10, D-6500 Mainz, FRG
** Technical University Clausthal, Institute of Non-metallic Materials, Zehntnerstraße 2a, D-3392 Clausthal-Zellerfeld, FRG

ABSTRACT

Different multicomponent solutions have been developed by which building materials were coated. After drying and annealing, the coatings convert into silicate based glassy films. TEOS or fumed silica were used as silica carriers and by adding lead compounds also low melting compositions were prepared. In some cases it proved to be convenient to adjust the viscosity of the solutions by additions of suitable organic polymers. The heat treatment was done either in an electric furnace or by means of a special acetylene burner. The produced films can protect building materials against corrosion, may reduce the absorption and permeation of water or improve abrasion resistance.

INTRODUCTION

Several papers have been published on forming refractories from ceramic powders by the use of alkyl silicates as binders [1]. There have been published also data on the production of refractory materials entirely by sol-gel techniques [2]. On the other hand, not very much work has been done to improve building materials (or even whole constructions) by protective films applied by sol-gel processes. Therefore, a study was initiated, in which the possibilities of applying silicate based sol-gel glass films on building materials, such ceramic brick or concrete was explored. For that, we developed solutions which can be applied on the surface to be protected and may converted into sodium borosilicate glasses or to other (lead oxide containing) multicomponent glasses upon heating. The latter ones resemble certain commercial glazes. The necessary thermal energy was supplied by an electric furnace (laboratory studies) or by an acetylene burner (semi-technical conditions).

COATING OF CERAMIC BRICKS

The solutions to be used corresponded to the oxidic composition (in mol per cent) of $25Na_2O{\cdot}13B_2O_3{\cdot}62SiO_2$ (solution 1) and $15Na_2O{\cdot}35B_2O_3{\cdot}50SiO_2$ (solution 2). As starting materials $NaNO_3$, H_3BO_3 and tetraorthosilicate (TEOS) were employed. This set of relatively cheap compounds had already proved in [3] and [4].

Mat. Res. Soc. Symp. Proc. Vol. 180. ©1990 Materials Research Society

Samples from the interior of ceramic bricks were prepared by wet sawing. After storing them for 3 days at 25°C in a drying oven they were coated with the solutions. This was done three times within 2 min by the use of a fine brush. After the coatings had gelled the specimens were annealed at 700 or 1000°C in an electric furnace. Fig. 1 shows the surface of the uncoated brick while in Figs. 2 and 3 samples are displayed which were coated with solution 1 and annealed. It appears, that glassy films have formed at both 700°C and 1000°C. This way most of the small pores became sealed. The bigger pores, on the other hand, remained open as seen in Fig. 4, however, their interior surfaces became also coated. An even more dense coating could be obtained by the (B_2O_3-rich) composition 2, see Fig. 4.

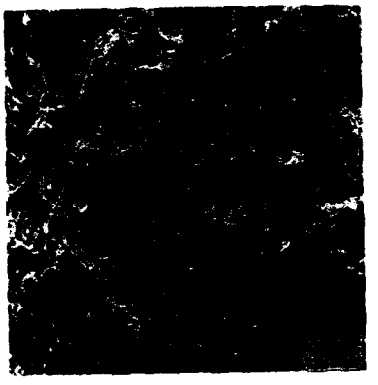


Fig. 1: SEM micrograph of the surface of an uncoated ceramic brick

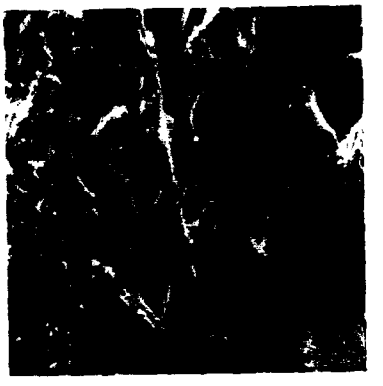


Fig. 2: Surface of a brick coated with solution 1, annealed at 700°C

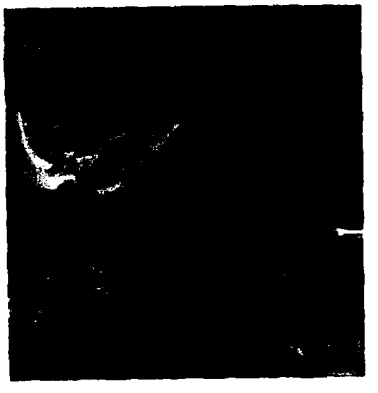


Fig. 3: Surface of a brick coated with solution 1, annealed at 1000°C



Fig. 4: Surface of a brick coated with solution 2, annealed at 700°C

Although the coatings applied so far are not perfect, they guarantee a significant protection of the surface. The resistance against water penetration was studied by applying a drop (1-2 ml) of water on the brick surface and measuring the time until it disappears, being soaken into the porous material. The following values were found:

without protective coating:	21 ± 4 sec
coating Nr. 1:	45 ± 3 sec
coating Nr. 2:	1633 ± 560 sec.

Corrosion studies revealed that the coatings were not attacked by storing the samples under water for up to 10 days but were moderately attacked by 1 n hydrochloric acid.

The burning of the whole sample in an oven may be used for ceramic bricks or similar burned materials that sustain high temperatures associated with the above glazing procedure. To apply a ceramic glaze on concrete or other materials that degraded at elevated temperatures, a technique has been developed in which the needed thermal energy was applied by a special burner developed for this purpose.

COATING OF CONCRETE PLATES

Concrete plates were coated by solutions whose compositions are listed in Table I.

Table I: Starting compounds, concentrations and oxidic composition of glazing solutions used for coating concrete

component	compound used	g of compound dissolved in 100 ml H_2O for solution			oxidic target composition in wt. % for glaze		
		3	4	5	3	4	5
Na_2O	$NaNO_3$		2,0			4	8
$Na_2O + B_2O_3$	$Na_2B_4O_7$			2.85			
CaO	$Ca(NO_3)_2 \cdot 4H_2O$			3.75			5
ZnO	$Zn(NO_3)_2 \cdot 4H_2O$	14.94	3.34		15	5	
PbO	$Pb(NO_3)_2$	22.24	11.64		55	43	
B_2O_3	H_3BO_3	3.63	1.62	6.0	7.5	5	35
Al_2O_3	$Al(NO_3)_3 \cdot 9H_2O$	1.00	8.05	2.62	0.5	6	2
SiO_2	a) Aerosil or b) TEOS	5.98 20.79	6.75	8.9 30.87	22	37	50

The solutions were prepared by dissolving all compounds with the exception of the SiO_2 carrier in water. Subsequently, the aerosil (amorphous SiO_2 with a mean particle diameter of 7 nm) was dipersed, leading to stable solutions of increased viscosity. There existed the possibility to increase the viscosity even further by adding 0.1 g of methylcellulose (MC) per 100 ml solution. If TEOS was employed as SiO_2 source, MC was added first (0.4 g per 100 ml). Then TEOS was added under vigorous stirring, resulting in a homogeneous fluid which was stable for between 30 min (solutions 3 and 4) and several hours (solution 5).

Most of the coating experiments were performed with solutions of type 3 (with aerosil plus MC or with TEOS plus MC) and of type 5 (with aerosil or with TEOS plus MC). These solutions were applied to the concrete surface using a fine brush. Solutions without MC did not form good coatings because they were soaked into the pores of the substrate too rapidly. Thus, the presence of MC was essential to obtain films of sufficient thickness. The adjustment of the right viscosity of the coating liquid was found to be critical. Generally, it proved to be better to apply several thin fluid films successively than only one thick film. By this method it was possible to over-come problems due to insufficient wetting, especially in the case of aerosil containing solutions.

After drying the applied coatings were converted into glassy films by the use of a acetylene-oxygene burner especially developed for this purpose. This way it was possible to heat up rapidly the coating to its melting temperature without damaging the underlaying concrete.

The coatings containing TEOS could be converted to glass easier (at lower temperatures) than those with aerosil. This oberservation is in line with results of investigations performed using a hot stage microscope. Flow points of 620 and 630°C (solution 3) and of 675 and 780°C (solution 5) were found for TEOS and aerosil containing gels, respectively.

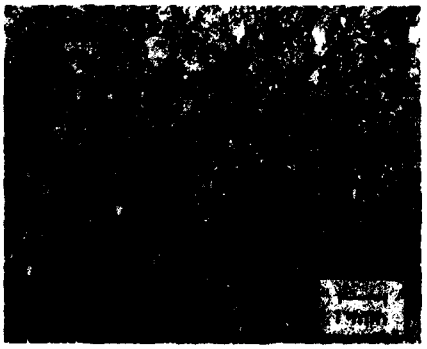


Fig. 5: Surface of a concrete plate prior of glaze applications



Fig. 6: Glaze form solution 3 (with aerosil), single coating

In Fig. 5 the surface of an uncoated concrete plate is shown, while coated samples are displayed in Figs. 6 and 7. It may be seen that the coarse structure of the substrates became covered by the glassy film. Nevertheless, the latter one was not formed perfectly. The thickness of it is not uniform and it contains some pores. Some of the experiments were made using two layers of glaze. Here a second layer was applied and burned a top of a first layer produced before. Such approach, however, did not produce an advantage, as compared to glazes produced in a single run. The most effective reduction of the water uptake (fivefold) was found in the case of a single layer of solution 1 with aerosil.



Fig. 7: Glaze from solution 3 (with aerosil), double coating

CONCLUSIONS

Techniques have been developed that enable to apply glassy films of variable composition on surfaces of ceramic bricks or concrete, using sol-gel methods. Even though such layers are not completely impermeable, they improve the chemical resistance and the physico-mechanical properties (abrasion resistance) of the materials considerably.

ACKNOWLEDGEMENTS

The authors thank Mrs. M. Bernds and Mrs. A. Rostek for experimental help.

REFERENCES

[1] K.D. Biddle, A.K. Das, K. Jones and H.G. Emblem.
J. Appl. Chem. Biotechnol. 27, 565 (1977)

[2] V. Gottardi, M. Guglielmi, A. Tiziani and G. Carturan.
J. Non-Cryst. Sol. 43, 105 (1981)

[3] S.P. Mukherjee. J. Non-Cryst. Sol. 63, 35 (1984)

[4] M.A. Villegas and J.M. Fernandez Navarro.
J. Non-Cryst. Sol. 100, 453 (1988)

GLASSES AND MULTI-COMPONENT SOL-GELS FOR USE AS HIGH-TEMPERATURE PROTECTIVE COATINGS

LAURI J. DeVORE* AND NORA R. OSBORNE**
*EG&G Mound Applied Technologies, P.O. Box 3000, Miamisburg, OH 45343
**University of Dayton Research Institute, 300 College Park, Dayton, OH 45469-0172

ABSTRACT

Two multi-component sol-gel compositions were developed and compared to several commercially available high-temperature glasses. All were then used and characterized as protective coatings for intermetallic titanium aluminide.

The sol-gels were studied as thin film coatings and the commercial glasses were studied as enameled coatings. Attention was given to (1) the effect of the application temperature on the original microstructure of the metal, and (2) the role of interfacial conditions between the glass and metal in cyclic and isothermal thermal cycles between ambient temperature and 760°C (1400°F).

TECHNICAL DISCUSSION

Several glass coatings were prepared using commercially available materials from Schott Glaswerke and Corning Glassworks. These glasses are readily available, inexpensive, and fully qualified and characterized by these companies. The glasses chosen were Schott's 8456 and 8450, alkaline-earth borosilicates; Corning's 7052, a borosilicate; and Corning code 1720, an aluminosilicate glass. The nominal composition of Corning code 1720 was used as a guide for the aluminosilicate sol-gel formulation, and a four component sol-gel developed by Sandia National Laboratories [2] as a nominal borosilicate sol. Both sol-gels were formulated and consolidated as described in reference [2].

Two process techniques were used to apply the glass compositions to the aluminide substrates. First, a simple air-brushing technique was used. The glass was powdered, suspended in amylacetate, and air-brushed onto all surfaces of the metal substrate.

The second method for application of the glass coat was dipping the sample substrate into a sol-gel. Dip coating then allows a continuous thin film ($< 0.05\mu m$) to be applied to a surface [3].

EXPERIMENTAL CONDITIONS

Ti_3Al coupons were supplied by Garrett Engine Division of Allied Signal and Rockwell International. These were cut into approximately 1 cm x 1 cm pieces, and each had a 1 inch platinum wire spot welded to a corner. This was done to facilitate the enameling, dipping, and oxidation test procedures.

Two different sample preparation approaches were tried for the coupons to be air-brushed. A number were etched using a dilute solution of HF and cleaned by four-step cleaning. Another group was polished to a 600 grit finish and four-step cleaned. After air-brushing the samples where hung in a box furnace heated to a temperature above the glass softening point to form a coherent coat. Table I shows the temperature and time parameters used to form an enamel for the commercial glasses chosen.

For the sol-gel samples the titanium aluminide pieces were polished with 600 grit silicon carbide polishing cloth and then four-step cleaned. The sol-gel coatings were applied using the dip-coating technique in a dry argon atmosphere. The substrates were withdrawn from the sol at a rate of 8 inches per minute. A total of four coats of the sol-gel were applied to each sample in this manner.

Mat. Res. Soc. Symp. Proc. Vol. 180. ©1990 Materials Research Society

OXIDATION TESTING

1) Cyclic Testing

Each sample was weighed to four decimal places using a Mettler analytical balance. The samples were then put into a box furnace at 760°C (1400°F) and left for a predetermined amount of time. The time for this test cycle can be found in Table II.

TABLE I

ENAMELING PARAMETERS FOR COMMERCIAL GLASSES FOR ALPHA TITANIUM ALUMINIDE

Sample Number *	Glass Code	Temperature °C	Temperature °F	Time	Comments
A 86	8456	870	1600	10	Isothermal test
A 61	8456	870	1600	10	Cyclic test
A 66	8450	840	1500	10	Cyclic test
A 66	8450	1120	1550	10	Isothermal test
B 41	7052	1120	2050	10	Cyclic test
B 47	7052	1115	2040	10	Isothermal test
R 01	7052	1115	2040	10	Cyclic test
R-05	7052	1115	2040	10	Isothermal test

*A,B = Garrett Ti_3Al, R = Rockwell Ti_3 Al

TABLE II

OXIDATION CYCLE TIMES

Cycle Number	Time (hr)	Total Time (hr)
1	2	2
2	4	6
3	2	8
4	8	16
5	8	24
6	24	48

2) Isothermal Cycle

For the isothermal cycle the samples where placed in the furnace at 760°C (1400°F) for 48 hours after which time they were removed, allowed to cool, and weighed.

RESULTS AND DISCUSSION

Prior to oxidation testing of each of the coating configurations, the samples were examined with a scanning electron microscope (SEM). The result of this examination shows that the underlying microstructure of the substrate was unaffected by the glass application of the 8450 and 8456 glass enamels (Figure 1a to 1c).

Also evident in these photomicrographs is the lack of intimate bonding between the air-brushed commercial glass compositions and the underlying metal.

The application of the 7052 at 1115°C (2040°F) for 10 minutes had a dramatic effect on the underlying aluminide microstructure (Figure 1d): increasing the beta grain size and destroying the lamellar structure of the alpha and beta phase structure within the grain, thereby changing the mechanical properties originally possessed by the substrate material.

In assessing the results of the cyclic oxidation tests it was assumed that any loss of weight indicated the loss of surface coating from the substrate (i.e., by spalling). This was the case for the Schott 8450 and 8456, and one of the Corning 7052 samples. Optical micrographs of the surfaces of these pieces indeed indicated that some of the surface coating is no longer present (Figures 2a to 2d).

The sol-gel coating was too thin to be seen in cross section even with the magnification available with the SEM. No microstructural changes were seen in the substrate surface.

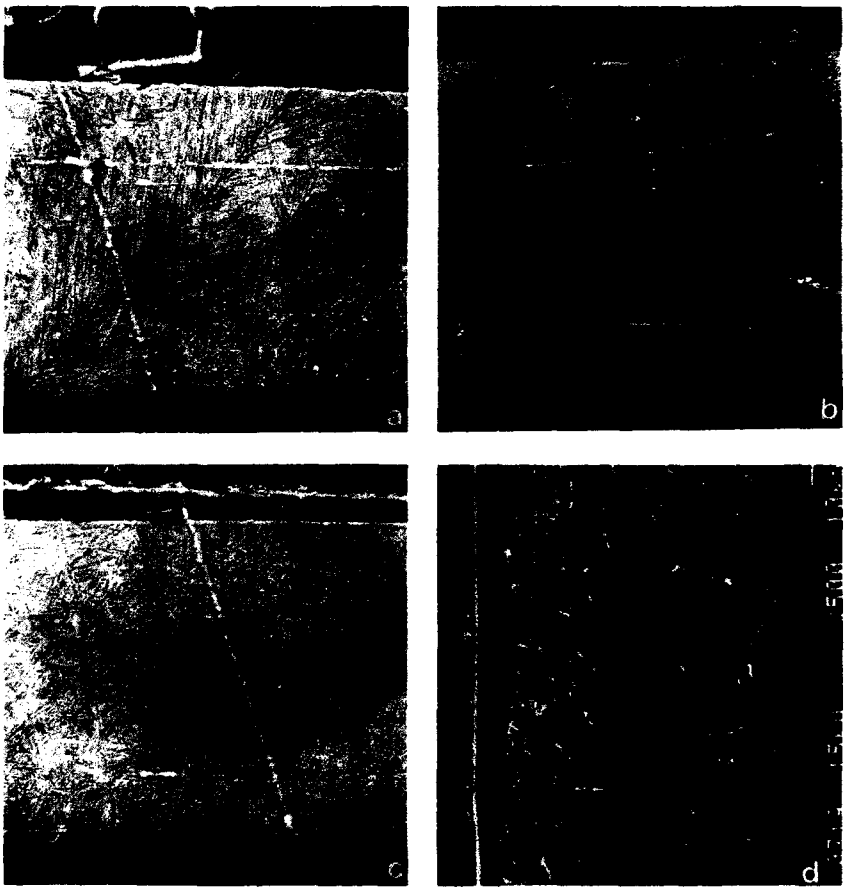


Figure 1. Glass coating on titanium aluminide surface prior to oxidation testing: (a) as received titanium aluminide coupon, (b) 8456 glass coating, (c) 8450 glass coating, and (d) 7052 glass coating. SEM micrographs with 500X magnification.

The results of the cyclic oxidation tests are to be found in Figure 3. Figure 4 illustrates microstructure of thermally cycled specimens.

While it appears that the Schott 8456 gained the little weight over the 48 hours of cyclic testing, optical examination revealed that the glass coating had spalled (Figure 4b) at the coupon edges and surfaces. Therefore the lower weight gain of this sample is spurious, as weight gained by the oxidizing surface was offset by the loss of the glass coating material due to spalling. Observation of the Schott 8450 (Figure 4c) revealed similar spalling and surface oxidation. This is most likely a result of the mismatch of thermal coefficients between the glasses and the metal.

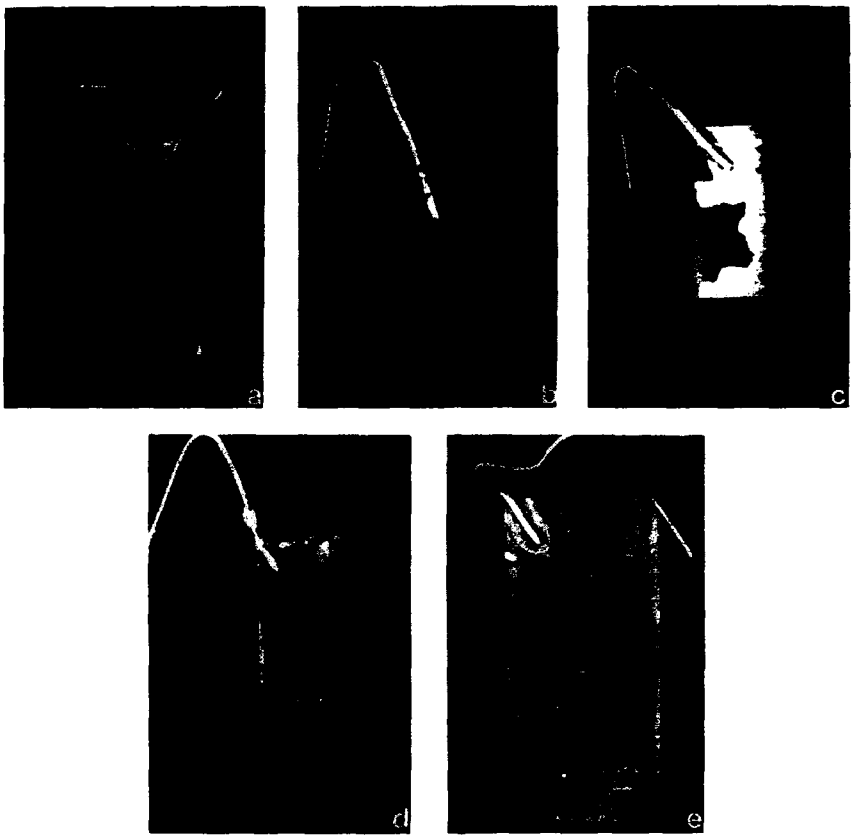


Figure 2. Optical micrographs of coupons after 48 hours of cyclic thermal testing:(a) bare titanium aluminide, (b) 8456 coated, (c) 8450 coated, (d) 7052 coated, and (e) aluminosilicate sol-gel coated. Original magnification 3X.

The Corning 7052 (Figure 4c) produced the least weight gain, and observation of the cycled samples showed bare edges but intact coating on the larger flat surfaces. Loss of weight was attributed primarily to loss of oxide scale from bare sample edges.

Figure 5 displays the weight loss per specimen for the isothermal cycle test. These results indicate that excellent protection was afforded the samples coated with the borosilicate enamel coatings. Unfortunately, the thermal mismatch between the glass and metal is too great for such coatings to be effective for cyclic use. Some component additions to these glasses, resulting in increased CTE, might be considered for improved glass to metal adherence.

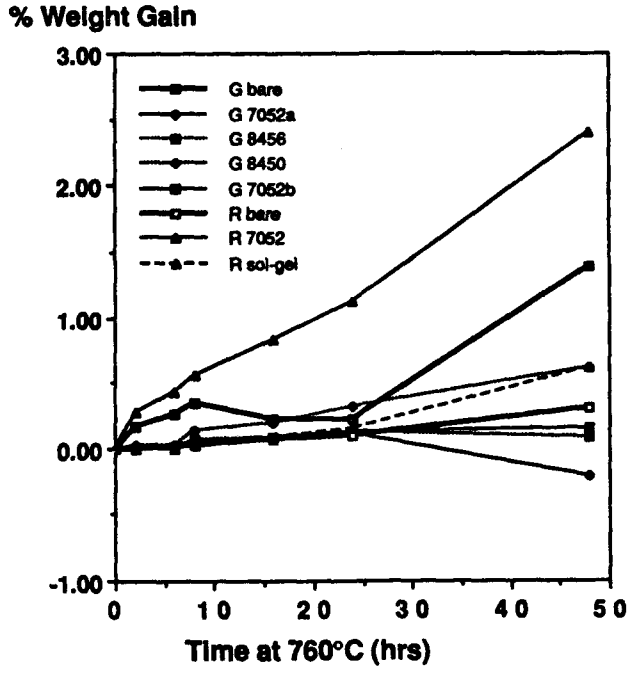


Figure 3. Results of the thermal cycle test from ambient to 760°C (1400°F). G = Garrett Ti_3Al, R = Rockwell Ti_3Al, Sol-gel is aluminosilicate.

CONCLUSIONS

- All the coatings studied provided some protection against oxidation damage at 760°C (1400°F) compared to the bare material exposed to similar conditions. Of all the glasses studied, the sol-gel thin film coatings appeared least effective.
- Corning code 7052 air-brushed on the polished substrate proved the most effective oxidation barrier during thermal cycling. The major weight gain of these samples could be attributed to the difficulty coating the sharp edges of the sample coupons.
- Enameling temperatures of 870°C (1600°F) and below for ten minutes had no effect on the microstructure of the substrate. Intimate bonds between the coating and the underlying metal surface were not formed.
- Enameling temperatures of 1100°C (2000°F) and above allow the glass to form intimate bonds between the glass and substrate surface but are at the material's beta transus temperature and therefore drastically alter the original metal microstructure.
- Both the aluminosilicate and the four-component sol-gel coatings proved less effective barriers against oxygen corrosion, either because of microporosity or microcracking of the thin film.

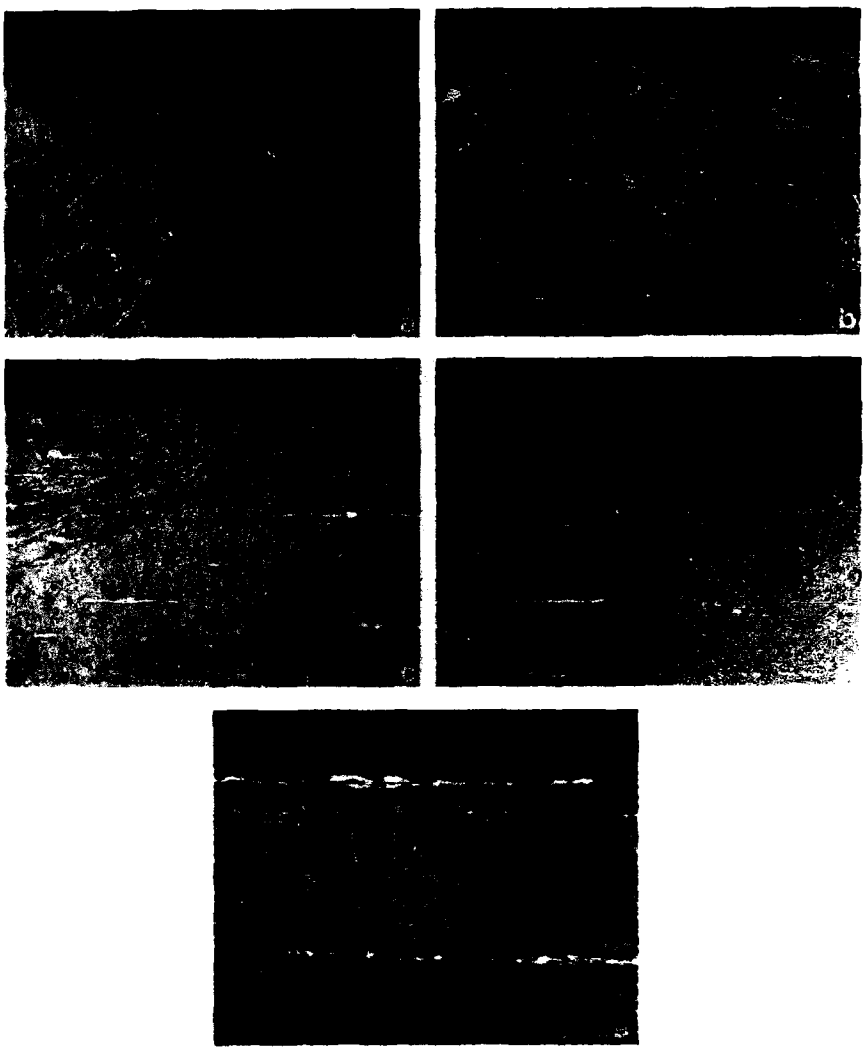


Figure 4. Optical micrographs of the glass/metal surface after 48 hours of thermal cycling: (a) bare titanium aluminide, (b) 8456 coated, (c) 8450 coated, (d) 7052 coated, and (e) aluminosilicate sol-gel coated. Original magnification 500X.

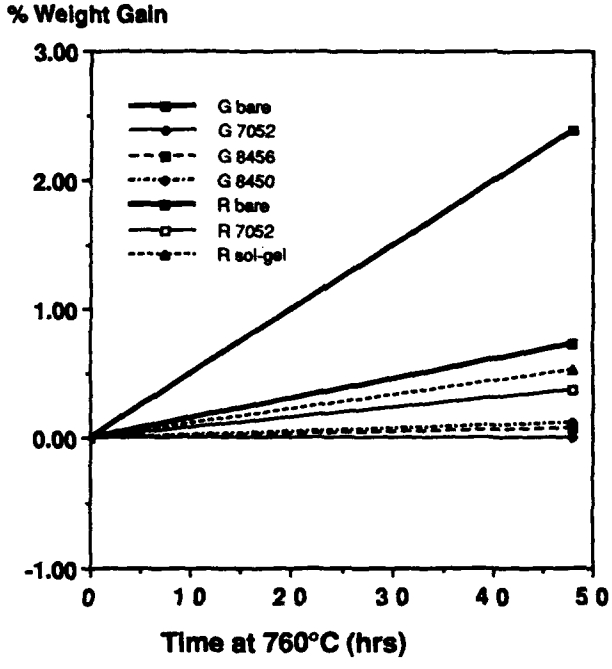


Figure 5. Results of the isothermal cycle test at 760°C (1400°F) for 48 hours. G = Garrett Ti_3Al, R = Rockwell Ti_3Al

ACKNOWLEDGEMENTS

We would like to thank Garrett Engine Division of Allied Signal, Phoenix, AZ, and Rockwell International, Downey, CA, for financial support and substrate material for this study.

REFERENCES

1. C. A. Barrett, Oxidation of Metals, Vol. 30, 1988.

2. Carol S. Ashley, Scott T. Reed, "Sol-Gel-Derived AR Coatings for Solar Receivers," Sandia National Laboratories, 1984.

3. Helmut Dislich, "Thin Films from the Sol-Gel Process," Sol-Gel Technology for Thin Films, Fibers, Preforms, Electronics and Specialty Shapes, Ed., Lisa C. Klein, Noyes Publications, 1988.

CHARACTERIZATION OF CERIA STABILIZED ZIRCONIA COATINGS ON METAL SUBSTRATES

ROSA DI MAGGIO*, PAOLO SCARDI* and ANDREA TOMASI°
*Department of Materials Engineering,University of Trento,Italy;
°Institute for Scientific and Thecnologic Research,Trento,Italy.

ABSTRACT

In this study ceria stabilized zirconia was used to obtain an uniform and adherent film on iron and 304 S.S.. Coatings were prepared by dipping in solutions of organometallic precursors of zirconium and cerium. Structure and morphology of samples were investigated using SEM and XRD techniques before and after thermal treatments. The oxidation behaviour in air of coated samples was followed through thermogravimetrical analysis in a range of temperature from 773 K to 1123 K. The preliminary results show, for the samples coated and pretreated in high vacuum at 923 K, a good decrease in oxidation rate.

INTRODUCTION

Until now material research has focused on the use of coating processes to provide materials with superior properties i.e. chemical durability, alkali resistance, heat resistance against oxidation. The sol-gel technique is suitable for producing oxide powders but also for forming thin oxide films on various substrates at low temperature with good homogeneity [1]. The dip-coating technique has been extensively studied as regards silica-based coatings and zirconia coating on glass [2,3]. In the recent years a few reports concerning sol-gel films on metal substrates were available in the literature[4,5]. The purpose of the present work is to show the role of the chemical and morphological parameters of the 18% mol CeO_2 stabilized-ZrO_2 films in improving the heat resistance of iron and 304 S.S. against oxidation.

EXPERIMENTAL PROCEDURE

All chemicals were commercially available analytical reagent-grade products. The solution for dip-coating was prepared adding the proper amount of zirconium tetra-n-butoxide (containing 50% of n-butyl alcohol) and cerium (III)-2-4-pentanedionate in the molar ratio of 82:18 to anhydrous ethyl alcohol to reach the total concentration of 0.3 mol/L. The solution obtained was stirred at room temperature until it clarified and was utilized immediately after. Substrates were pure iron and 304 S.S. sheets 20x10x2 mm^3. Before coating, samples were grinded on 1000 emery paper and then degreased ultrasonically in acetone. The coatings were produced by withdrawing the substrates from the solutions at a constant rate (0.5 cm/s) and dried at 353 K for one hour. Then the specimens were heat treated in vacuum at 653 K (10^{-3} or 10^{-5} torr).

The heat resistence of the coated sheets against oxidation was evaluated measuring the weight gain during 24h heat treatment in air at 753 K for iron and 1123 K for stainless steel specimens. The oxidation data were collected by a Mettler thermobalance TA1. Before and after heat treatment the surface

Mat. Res. Soc. Symp. Proc. Vol. 180. ©1990 Materials Research Society

coatings were observed using a Cambridge Scansion Electron Microscope whereas the structural characterization of the films and oxidation products on surface was performed by XRD and high-temperature XRD using a Rigaku diffractometer.

RESULTS AND DISCUSSION

The nature of the alkoxide derived coatings depends on the parameters of the dipping process and the precursor type and concentration in solution. Solvent type determines the solution stability and impacts the hydrolysis rates. Also, the use of either acid or base catalyst can produce a more or less open polymeric network. In this study, the choice of solution concentration produced a film with a thickness of 300 nm. The fast evaporation of solvent left pores in the film, making it visibly opaque.

A porous film cannot be protective for metal at high temperature. Figure 1 A shows the XRD spectra of a coated stainless steel treated at different temperature. The as dried coating was amorphous (a). The crystallization of the film begins at 923 K; in fact, the (111) peak of tetragonal stabilized zirconia appears in the spectrum recorded at this temperature (b), while at higher temperatures the metal oxidizes producing mainly iron and chromium oxides (d and e).

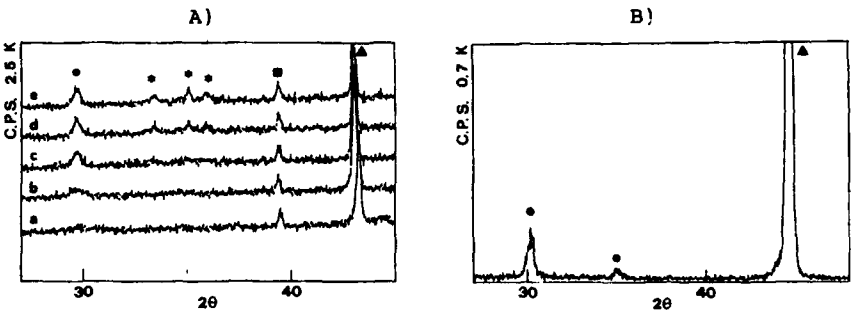


Fig.1 A) High temperature X-ray diffraction spectra of coated 304 S.S. (a) at 723 K; (b) at 923 K; (c) after 15 h at 1123 K; (d) after 17 h at 1123 K; (e) after 21 h at 1123 K. The dot refers to zirconia peak, the stars refer to iron and chromium oxides peaks, the triangle to austenite peak and the square to platinum peak (sample holder). B) X-ray diffraction spectrum of coated iron treated at 923 K in vacuum ($1 \cdot 10^{-3}$ torr) for 2 h. The dots refer to zirconia peaks and the triangle to iron peak.

Since the densification treatment of coated iron at high temperature led to an immediate oxidation of the metal, the treatments were conducted at 10^{-3} or 10^{-5} torr. The treatment temperature, 923 K, was selected to obtain also the crystallization of the film and to hinder outside diffusion of metallic elements and inside diffusion of oxygen. The treatment at 10^{-3} torr did not form a compact film without producing a noticeable quantity of iron oxide, whereas a lower pressure (10^{-5} torr) was suitable for the purpose. The same pretreatments were conducted also on the coated 304 S.S. specimens.

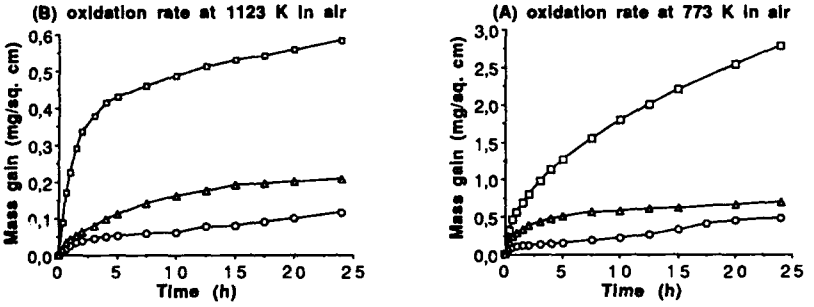


Fig.2 Oxidation curves for iron (A) and 304 S.S. (B);the circle symbols refer to coated and pretreated in high vacuum samples,the triangular symbols refer to coated samples and square ones to pure substrates.

The oxidation curves reported in fig.2 show the decrease of the oxidation rate for all coated samples, in particular for samples pretreated at 923 K and 10^{-5} torr. As shown in the micrographs of fig.3, the pretreatment did not change significantly the surface but tended to reduce voids and to crystallize the film, as confirmed by reduced oxidation rate, and XRD. The spheroidal clusters on the film were probably due to high concentration of dipping solution[5].

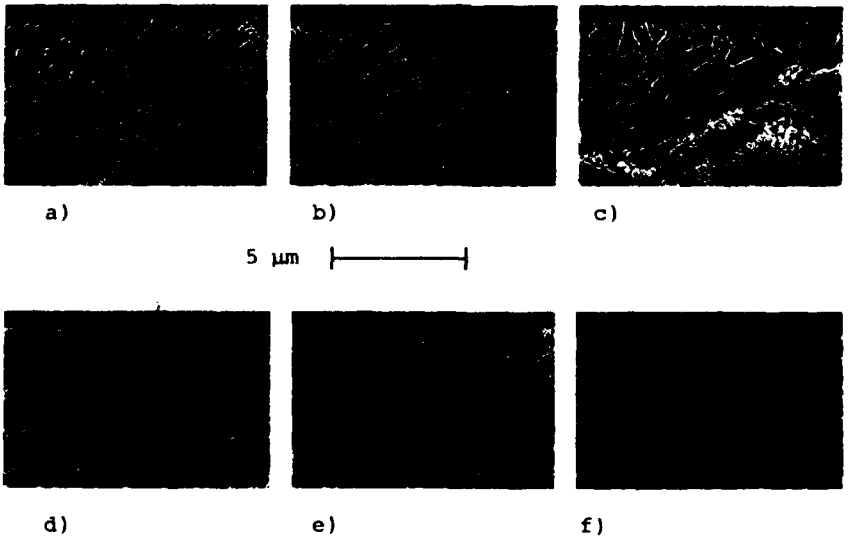


Fig.3 The morphology of the surface of the coated iron as dried (a), pretreated in vacuum (b) and after oxidation for 24 h in air (c). Picture (d), (e) and (f) show the coated 304 S.S. surface after same treatments.

Figure 1 B shows the diffraction pattern of pretreated sample in the angular range of (111) peak of zirconia. Peak

profile analysis gave 250Å crystallite size and $2 \cdot 10^{-3}$ microstrain. It was not possible to establish whether zirconia was cubic or tetragonal, since the poor crystallization and the thinness of the film produced very weak and broadened peaks. However, XRD analyses on well crystallized powder samples of the same composition showed the presence of a pure tetragonal phase[6]. At this stage the film, whose thickness was reduced to 200 nm, was macroscopically trasparent and continuous. The results of the oxidation resistance test are very encouraging; in fact, after 24h oxidation both samples did not show spalling phenomena and the oxide scales seem to be well adherent. SEM picture (Fig. 3c) shows the presence on the surface of Fe_2O_3 mixed with film residuals that are still adherent to iron substrates whereas Cr_2O_3 crystals are seen to emerge from the film on S.S. substrates (Fig. 3f).

CONCLUSION

In this preliminary work it was demonstrated the suitability of dip-coating technique to form adherent and protective films also on metal substrates. An improvement in resistence against oxidation of iron and 304 S.S. has been obtained especially for samples coated and pretreated in vacuum. In fact the densification and crystallization pretreatments in vacuum are necessary to retard the inside diffusion of oxygen and the outside diffusion of metallic elements.

REFERENCES

[1] "Sol-gel technology for thin films, fibers, preforms, electronic and specialty shapes".Edited by L.C.Klein,Noyes Publications, Parkridge, New Jersey, U.S.A.(1988).
[2] J.D.Mackenzie, Journal of Non-Crystalline Solids 100, 162-168 (1988)
[3] D.Kundu, P.K.Biswas and D. Ganguli, Thin Solid Films, 163, 273-27 (1988)8.
[4] "Coatings for high temperature applications". Chapter 6, pg. 169-192.Edited by E.Lang , Applied Science Publishers, London and New York, (1983).
[5] K.Izumi,M.Murakami,T.Deguchi,A.Morita,N.Tohge and T.Minami, J,Am. Ceram. Soc., 72 [8] 1465-68 (1989)
[6] L.Lutterotti & P.Scardi, J. Appl. Cryst. 23 (1990)

SOL-GEL PROCESSING OF $PbTiO_3$ FIBERS

S.I. Aoki, S. C. Choi*, D.A. Payne** and H.Yanagida
RCAST, The University of Tokyo, 4-6-1 Komaba, Meguro-ku, Tokyo, Japan 153
*Department of Materials Science and Engineering, Ajou University, Suwon, Korea
**Department of Materials Science and Engineering, University of Illinois at Urbana-Champaign, 105 South Goodwin Avenue, Urbana, IL 61801.

ABSTRACT

Lead titanate fibers were formed from lead acetate and titanium isopropoxide by sol-gel methods. Additions of acids and chelating agents were used to influence hydrolysis and condensation reactions. A variety of solvents were examined, and the effect of conditioning treatments at elevated temperatures were investigated. Data are reported for the rheological behavior of viscous sols, fiber drawing ability, pyrolysis and crystallization of gels and fibers. Features of the ceramic microstructure are reported. A pyroelectric effect was measured for $PbTiO_3$ fibers.

INTRODUCTION

Lead titanate is a ferroelectric material with the perovskite structure, and is a potential candidate for high temperature pyroelectric sensing applications due to its high Curie point (500°C) and spontaneous polarization (0.8 C/M^2). A fibrous form is the preferred geometry for the reduction of heat capacity and increased responsivity in small scale devices. Hence, the interest in the sol-gel processing of lead titanate fibers.

Recently, many kinds of oxide ceramics have been prepared from metal alkoxide solutions by sol-gel processing. In general, the method allows for reductions in firing temperatures and for the preparation of unusual forms, like continuous fibers. In previous work, SiO_2,[1] TiO_2,[2] and ZrO_2 [3] fibers were formed from corresponding metal alkoxide solutions. Little has been reported for the preparation of ferroelectric fibers. Fibers are usually drawn from viscous sols of high concentration, and with a preferred linear polymeric structure. It is important to control hydrolysis and condensation reactions, and to derive processing conditions for the accelerated volatilization of solvent. The latter can concentrate polymeric solutions without immediate gelation.

In this study, we report on the processing of lead titanate fibers derived from a lead acetate and titanium isopropoxide solution. Emphasis is placed on the processing conditions necessary for the drawing of continuous fibers.

EXPERIMENTAL PROCEDURE

Figure 1 illustrates the flow diagram for the process. A 1M stock solution of a Pb-Ti alkoxide complex was prepared from an equimolar anhydrous lead acetate and titanium isopropoxide solution according to a method originally reported by Budd et al.,[4] and with modification. Three anhydrous alcohols (methanol, 2-propanol and methoxyethanol) with different boiling points (65°C, 78°C, 125°C, respectively) were evaluated as suitable solvents. A 5ml alcoholic solution, which contained 0.01 mol of water, 0.005-0.02 mol acetic acid (AcOH) and 0-0.02 mol acetylacetone (acac), was added dropwise to 5ml of the stock solution, (i.e., 0.005 mol Pb-Ti alkoxide). Thus, the molar ratios of the Pb-Ti alkoxide stock solution (with respect to H_2O, AcOH and acac) were 1:2, 1:1-1:4; and 1:0-1:4, and the alkoxide concentration was 0.5mmol/g in the starting solution. The sols were placed in glass tubes (20mm ϕ x50mm) with perforated endcaps (six 2mm ϕ holes) and stored in temperature controlled baths at 15°C, 60°C and 90°C. Weight loss due to volatilization of solvents and additives was monitored and the corresponding

Mat. Res. Soc. Symp. Proc. Vol. 180. ©1990 Materials Research Society

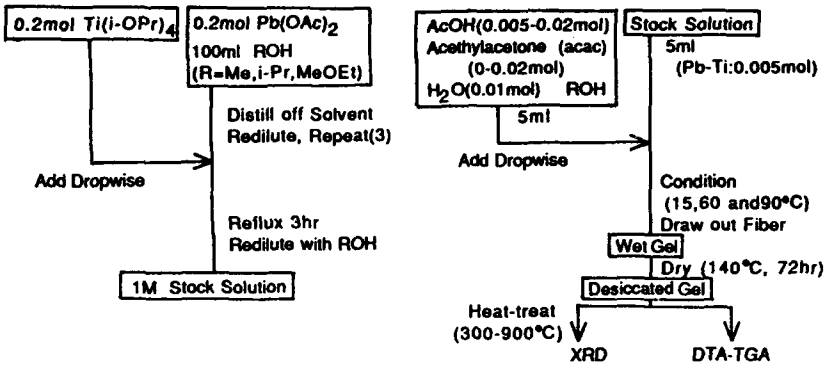


Figure 1. Flow Diagram for Sol-gel Processing

change in the Pb-Ti concentration was calculated up to gelation. The forming of fibers was evaluated by drawing on a glass rod. The viscosities of sols prior to gelation were determined on a rotating viscometer as a function of shear rate.

Gels were dried at 140°C for 72 hours, and DTA-TGA measurements were used to characterize pyrolysis behavior. Desiccated gels were heat-treated between 300°C-900°C for 1 hour, and XRD measurements were used to determine the crystallization characteristics of the heat-treated gels. The form and structure of drawn fibers, and heat treated ceramic microstructures, were evaluated by electron microscopy.

RESULTS AND DISCUSSION

Gelation behavior and fiber drawing ability

Figure 2 summarizes the gelation behavior and fiber drawing ability of sols conditioned at various temperatures in methanol or methoxyethanol solvent systems. The time-to-gelation (t_g) was defined as the time at which no visible flow occurred on inversion of the sample tube. Table 1 summarizes the concentrations for the systems at gelation. Concentration was determined from the weight change in the sol. Fiber drawing ability increased with acetic acid concentration and conditioning treatment temperature (e.g., 60 and 90°C). For example, fibers which could not be drawn at 15°C, could be successfully drawn at 60 and 90°C, with increasing AcOH additions in methoxyethanol. Gelation concentration was closely linked to fiber drawing ability. Sols that had a high concentration of Pb-Ti at gelation were better for fiber drawing. The t_g for fiber drawing systems was dependent on the thermal conditioning treatment and the boiling point of the alcohol used as the common solvent. It did not appear to be dependent on the gelation concentration. The results suggest the importance of solvent evaporation on fiber drawing ability. AcOH additives to the 2-propanol system caused precipitation, and no clear sols were obtained.

Figure 3 indicates the effect of acac additions on t_g and fiber drawing ability, for a system conditioned at 15 and 90°C. Gelation concentrations are summarized in Table 2. The T_g increased with additions of acac, especially at low temperature, and facilitated the drawing of fibers at 15°C. The results are consistent with the chelating ability of acac to delay hydrolysis and condensation reactions, and thus increase t_g for fiber drawing ability. Fibrous precipitates were noted before the gelation point, which disappeared on heating above 30°C.

Table I. Concentration of Pb-Ti at Gelation

solvent	methanol			methoxyethanol		
AcOH/	Conditioning Temperature (°C)					
Pb-Ti	15	60	90	15	60	90
1.0	0.62	1.16	1.52	0.54	1.75	1.38
2.0	0.76	1.53	1.86	0.62	1.95	1.95
4.0	0.99	1.67	1.89	0.69	1.75	2.08

concentration : mmol(Pb-Ti)/g-solution
underlined : fiber drawing sols

Table II. Effect of acac Addition on the Pb-Ti Concentration at Gelation

acac/	Conditioning Temperature (°C)	
Pb-Ti	15	90
0.0	0.76	1.86
0.5	1.82	2.06
1.0	1.97	1.95
2.0	1.89	1.89
4.0	1.80	1.82

concentration : mmol / g-solution
underlined : fiber drawing sols
solvent : methanol

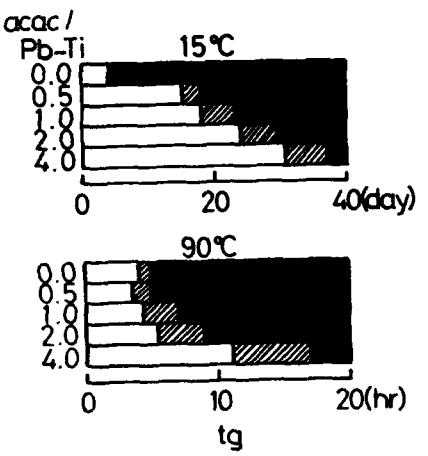


Figure 3. Effect of acac Additions on Time-to-Gelation and Fiber Drawing Ability
□: sol ▨: fiber drawing sols ■: gel
solvent: methanol, AcOH/Pb-Ti=2

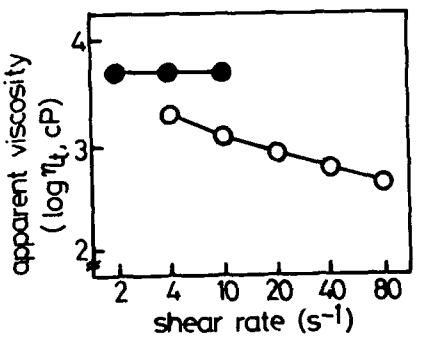


Figure 4. Shear Rate Dependence of Apparent Viscosity for Sols Prior to Gelation
●: fiber drawing sols (conditioned at 90°C)
○: no fiber drawing (conditioned at 15°C)
solvent: methanol, acac/AcOH/Pb-Ti=0/2/1

Pyroelectric measurements

Preliminary data are given in Figure 4 for pyrocurrent measurements made on lead titanate fibers heat-treated at 700°C. The measurements were for approximately 100 fibers, 2 cm long, connected in parallel with Ag paste, and supported on an alumina substrate. A picoammeter (HP 4140B) monitored the pyrocurrent, and a thermocouple determined the temperature. The pyrocurrent was greatest in the vicinity of the Curie point. The heating rate was 20°C/min. Pyrocurrent and fiber temperatures were monitored through use of a HP 9000 microcomputer. Work in progress is directed at lower heating rates, and with more thermally matched systems. Pyrocurrents were only detected in crystallized fibers heat-treated above 500°C. The magnitude of the pyrocurrent increased with heat-treatment temperature up to 800°C.

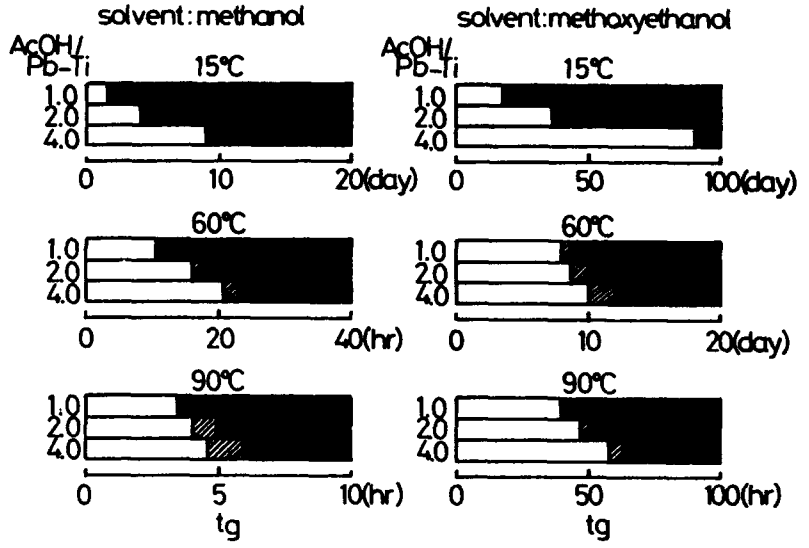


Figure 2. Time-to-Gelation and Fiber Drawing Ability for Pb-Ti Alkoxide Solutions
□: sol ▨: fiber drawing sols ■: gel

Rheology of sols

Figure 4 illustrates the shear rate dependence of apparent viscosity (η_{ti}) for sols prior to gelation. Fibers could be drawn from sols which had a constant viscosity (i.e., which were independent of shear rate). Sols which exhibited shear thinning were unsuitable for fiber drawing. Sakka and co-workers[5] investigated silicon alkoxide based systems and reported the viscosity of solutions of linear polymers was independent of shear rate; whereas shear thinning was a characteristic of high cross-linking. Results in this study are consistent with linear polymeric condensation under acid (AcOH) conditions, influenced by acac additions for the control of hydrolysis.

Pyrolysis and microstructure

Figure 5 gives XRD data for gels heat-treated at various temperatures. Crystallization started at 400°C, and the perovskite structure developed by 450°C. DTA and TGA data are given in Figure 6 for gels prepared with and without acac additions in methanol and conditioned at 90°C. Most of the weight loss was over by 300°C. Endotherms and exotherms at 260°C and 310°C were assigned to the volatilization and oxidation of residual organic groups. The exotherms at 450°C were assigned to crystallization and any residual organics. Gels containing acac had a larger exotherm around 450°C. This may have been associated with a larger free volume in the linear polymeric amorphous structure. Acac containing gels crystallized most readily, and it was possible to form polycrystalline lead titanate fibers at 500°C. Data in Figures 5 and 6 were for gels prepared past the fiber drawing point.

Figure 7 illustrates the form and structure of fibers heat-treated at 300°C and 500°C, before and after crystallization. Fibers were typically 50-70 μm in diameter and 20-30mm long. A smooth surface was obtained for dense amorphous fibers (300°C), and a fine microstructure developed on crystallization (500°C).

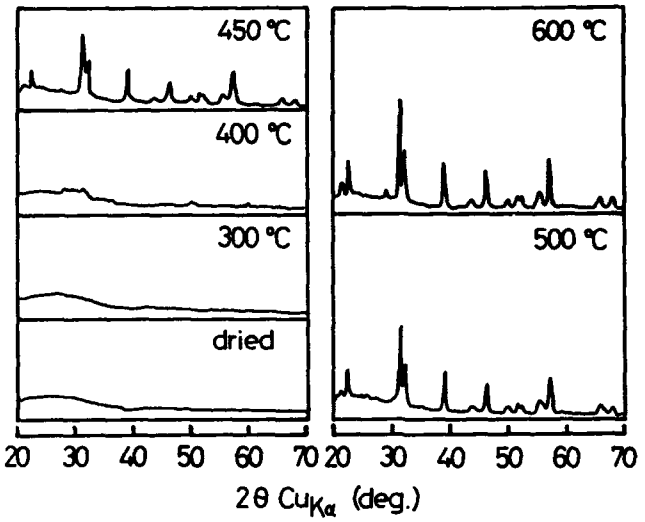


Figure 5. X-ray Diffraction Data for Heat-Treated Gels
solvent: methanol, acac/AcOH/Pb-Ti=0/2/1, conditioned at 90°C

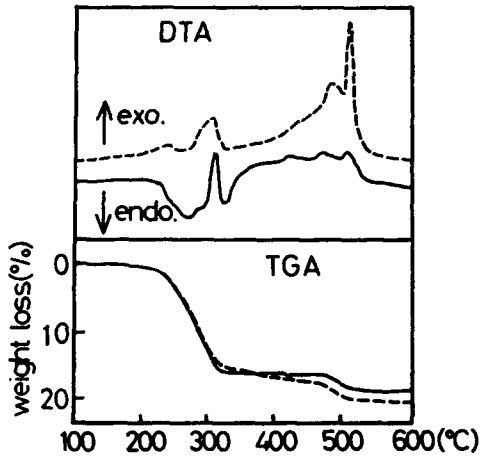


Figure 6. DTA-TGA Data for Desiccated Gels
——: acac/AcOH/Pb-Ti=0/2/1
– – – –: acac/AcOH/Pb-Ti=1/2/1
solvent: methanol, conditioned at 90°C

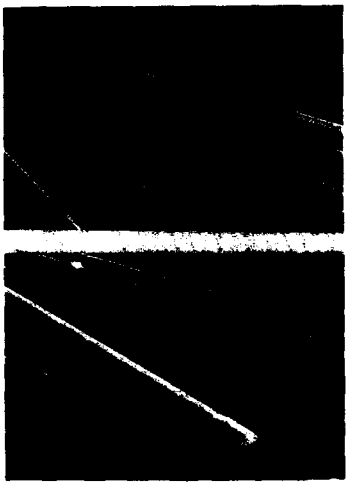


Figure 7. SEM Photomicrographs for Amorphous (300°C) and Crystallized Fibers (500°C)

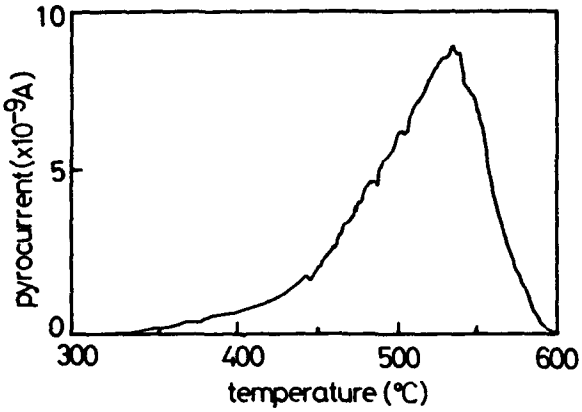


Figure 8. Pyrocurrent for Lead Titanate Fibers crystallized at 700°C heating rate : 20°C/min.

SUMMARY

Lead titanate fibers were successfully drawn from a Pb-Ti alkoxide solution which contained AcOH and which was conditioned at elevated temperatures. It was found that acac additions increased the time-to-gelation and facilitated fiber drawing ability. Sols which were used in fiber drawing had a constant viscosity i.e.,which were independent of shear rate. The results were consistent with linear polymeric structures. Lead titanate fibers crystallized into the perovskite structure at 500°C. Pyrocurrent measurements were determined, and increased with fiber heat treatment temperature.

REFERENCES

1. S. Sakka and K. Kamiya, in Emergent Process Methods for High Technology ceramics (Mater. Sci. Res. 17) edited by R.F. Davis, H. Palmour III and R.L. Porter (Plenum Press, New York, 1984) p. 88.
2. K. Kamiya, K. Tanimoto and T. Yoko, J. Mater. Sci. Lett. 5 , 402 (1986).
3. T. Yoko, K. Kamiya, K. Tanaka and H. Ito, '87 International Symp. & Exhib. in Science and Technology of Sintering, Tokyo, p. 542 (1987).
4. K.D. Budd, S.K. Dey and D.A. Payne, Brit. Ceram. Proc., 36, 107 (1985).
5. H. Kozuka, H. Kuroki and S. Sakka, J. Non-Cryst. Solids, 100, 226 (1988).

EVOLUTION OF SURFACE AREA DURING THE CONTROLLED GROWTH OF SILICA SPHERES

GREGORY H. BOGUSH,* C. J. BRINKER,* P. D. MAJORS** AND D. M. SMITH**
* Sandia National Laboratories, Albuquerque, NM 87185 USA
** UNM/NSF Center for Micro-Engineered Ceramics, University of New Mexico, Albuquerque, NM 87131 USA

ABSTRACT

Several mechanisms have been proposed for the growth of silica spheres by the controlled hydrolysis of silicon alkoxides, the limiting cases of which are the conventional and aggregative growth models. The evolution of surface area predicted from the two models is substantially different at early times into the reaction. In order to probe the change in surface area during growth, ^1H NMR measurements of the solvent were made during the growth process. It has been demonstrated that the spin-spin relaxation time (T_2) for an absorbed phase is less than that of the bulk solvent. Using this principal, the change in surface area can be followed in situ during the reaction. The experimental results were compared to the predictions of the conventional model and found not to be in agreement.

INTRODUCTION

According to the conventional model for the nucleation and growth of monodisperse particles, proposed by LaMer and Dinegar [1], a single burst of nucleation is followed by growth by monomer addition to the particle surface. Since all of the particles are formed at nearly the same time, they retain a narrow size distribution at the end of the reaction. More recently, evidence has been shown, for several systems, that aggregation during the growth process may be important [2,3]. The change in surface area predicted from these two models is quite different. For the conventional model, the change in surface area should be directly related to the change in particle size during growth, but if aggregation is occurring, a more complicated dependence might be expected.

Davis, et al., [4] have demonstrated that the rapid determination of surface area is possible with the use of ^1H NMR relaxation measurements. This method is based on the observation that the relaxation time for an absorbed phase is less than that of the bulk, therefore, the surface area can be related to the deviation of the measured relaxation time from the bulk relaxation time.

In this paper, the results of ^1H NMR spin-spin relaxation measurements made during the growth of silica particles from alkoxides are presented. These results are analyzed in an attempt to distinguish between the two growth mechanisms.

EXPERIMENTAL

To start the precipitation reaction, 2 ml of tetraethyl orthosilicate (TEOS) (Petrarch Systems, 99%), 2.3 ml of ammonium hydroxide (Fisher Scientific, Reagent Grade), 2 ml of deuterium oxide (Chemical Dynamics, 99.95 atom% D) and 40 ml of ethanol (Aaper Alcohol and Chemical, Absolute) were mixed together. An aliquot of the reaction mixture was then transferred to a 5 mm NMR tube.

Mat. Res. Soc. Symp. Proc. Vol. 180. ©1990 Materials Research Society

Temporally resolved ^1H NMR T_2 relaxation measurements were performed at a Larmor frequency of 250 MHz with a Bruker AC-250 NMR spectrometer. A Carr-Purcell Meiboom-Gill (CPMG) [5] echo train [90-(-t-180-t-)$_n$-acquire; τ=50 msec] was employed. Five measurements (each with different n values corresponding with experiment times of 0.2, 0.8, 1.4, 2.8 and 5.0 sec) were iteratively collected over several hours time. The data were spectrally resolved by Fourier transformation, and the methyl proton resonance T_2 values were determined from peak intensities. The temporal resolution is approximately 5 min.

RESULTS

The relaxation times obtained during the reaction are shown in Figure 1. Note that the data do not fall on a smooth curve, but there seems to be two distinct slopes. The surface area can be calculated from these data by using a two-phase fast exchange relationship

$$SA = C\ (1/T_2 - 1/T_{2b}) \qquad (1)$$

where SA is the surface area per unit volume, C is a constant dependent on material properties and experimental conditions and T_{2b} is the relaxation time of the bulk fluid. The parameter, C, can be determined from a sample of known surface area. T_{2b} can be obtained from an experiment with no TEOS present (for this experiment, T_{2b} was found to be 2.5 sec, which is very close to the T_2 data extrapolated to zero time).

The T_2 measurements were used in conjunction with the T_2 for the pure solvent (T_{2b}, SA=0) and Equation (1) to calculate the surface area at each point (Figure 2). The surface area increases to a plateau value at long times, at which point the scatter in the data increases. Again, as with the T_2 data, there are two distinct slopes to the surface area data.

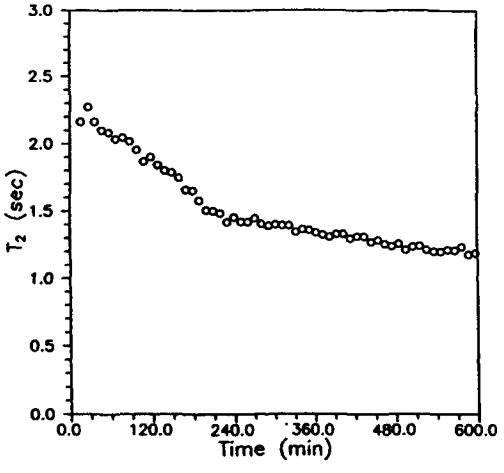


Figure 1 ^1H NMR Relaxation Time

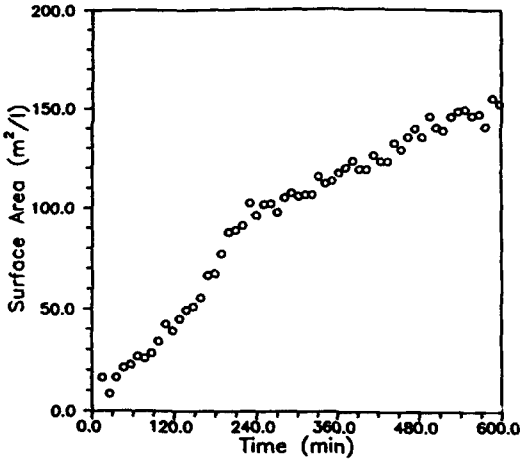


Figure 2 Change in Surface Area

DISCUSSION

By following the conventional model assumptions, the change in surface area during growth can be predicted. According to this model, all of the particles are nucleated in a single burst early in the reaction. The particles then grow by molecular addition to the particle surface. The surface area can be related to the average particle size by

$$SA = 4\pi r(t)^2 N \quad (2)$$

where N is the number density of growing particles and r(t) is the average particle size at time t. The average particle size has been shown to increase exponentially as [3,6]

$$r(t)^3 = r_\infty^3 [1-\exp(-kt)] \quad (3)$$

where r_∞ is the final average particle size, and k is a particle growth rate constant. Combining Equations (2) and (3), a relationship for the change in surface area as a function of time is obtained

$$SA = SA_\infty [1-\exp(-kt)]^{2/3} \quad (4)$$

where SA_∞ is the final surface area. If the particle growth can be described by the conventional model, a plot of $\log[1-(SA/SA_\infty)^{3/2}]$ versus time should fall on a straight line. Figure 3 shows this plot, in which it is clear that a straight line is not obtained.

The results presented here suggest that two different particle growth mechanisms may be involved at different times during the reaction. At early times, while the supersaturation is high, an aggregative mechanism may be dominant. However, at later times, when the supersaturation is low, a molecular addition mechanism may be dominant. The reason this crossover is not observed by other experimental techniques (such as particle size measurements by TEM) may be an increase in sensitivity of the NMR experiment.

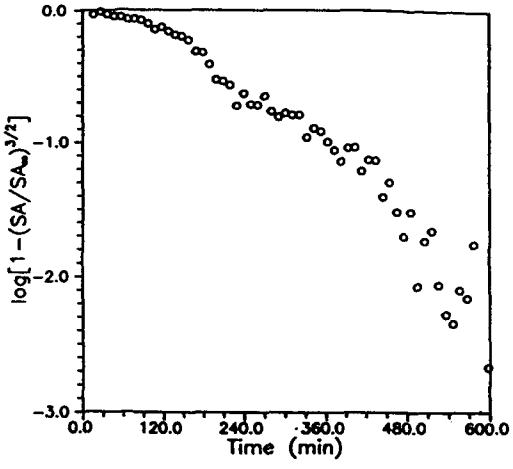


Figure 3 Fit to Conventional Model

CONCLUSIONS

The change in surface area during the growth of silica particles from alkoxides has been measured via ^1H NMR T_2 relaxation techniques. The data have been analyzed in terms of the conventional model for the nucleation and growth of monodisperse particles. The data do not agree with this model; instead, two growth regimes are apparent. These two regimes may be the result of an aggregative mechanism dominating growth at early times and monomer addition dominating at later times.

ACKNOWLEDGMENTS

This work was supported in part by the U. S. Department of Energy under contract #DE-AC-04-76DP00789 and the UNM/NSF Center for Micro-Engineered Ceramics at the University of New Mexico.

REFERENCES

1. V. K. LaMer and R. H. Dinegar, *J. Am. Chem. Soc.* 72, 4847 (1950).

2. P. J. Feeney, D. H. Napper and R. G. Gilbert, *Macromolecules* 17, 2520 (1984).

3. G. H. Bogush, G. L. Dickstein, K. C. Lee and C. F. Zukoski, in Better Ceramics Through Chemistry III, edited by C. J. Brinker, D. E. Clark and D. R. Ulrich, Materials Research Society, Pittsburgh, 1988.

4. P. J. Davis, D. P. Gallegos and D. M. Smith, *Powder Technology* 53, 39 (1987).

5. S. Meiboom and D. Gill, *Rev. Sci. Instrum.* 29, 668 (1958).

6. T. Matsoukas and E. Gulari, *J. Colloid Interface Sci.* 124, 252 (1988).

PART VI

Processing Science III: Drying, Densification and Crystallization

THE CRACKING OF SOL-GEL FILMS DURING DRYING

TERRY J. GARINO
Sandia National Laboratories, Electronic Ceramics Division 1842, Albuquerque, NM 87185

ABSTRACT

The cracking behavior of acidic silica sol-gel films during drying and low temperature heat treatment was studied. Films that cracked during drying exhibited a variety of unusual crack morphologies including sinusoidal cracks and parallel crack pairs. The effects of the water content of the sol and temperature on the critical thickness above which cracking of the films occurred were determined. The critical thickness decreased with increasing water content, most likely because the surface tension of the liquid in the pores of the gel increases with water content and because sols with low water concentrations did not gel until the solvent had evaporated. To determine why the critical thickness decreased with temperature, thermal analysis and shrinkage measurements of both constrained and unconstrained films were performed. Thermogravimetric analysis indicated that rapid weight loss occurred in the temperature region where the rapid decrease in critical thickness occurred. A small amount of shrinkage of the films also occurred in this region. Finally, shrinkage measurements of films debonded from the substrate indicated that shrinkage was very anisotropic with nearly all of the shrinkage occurring in the plane of the film and very little in the thickness direction.

INTRODUCTION

One limitation of the sol-gel process for forming films is that cracking of the films can occur during drying or heating. For a given sol, a critical film thickness exists above which cracking occurs. The critical thickness is generally <1μm. To produce thicker films, multiple coatings, with a thermal treatment between each coating, have been used. Besides being time consuming, the multiple coating process produces films that can be heterogeneous in structure since each layer has experienced a different thermal history.

The existence of a critical cracking thickness for films on substrates has been noted for a variety of materials [1,2] and has also been modeled [3-5]. For films that adhere well to the substrate, the critical thickness, h, is given by:

$$h = (K_{IC}/\sigma\Omega_c(\Sigma))^2 \qquad (1)$$

where K_{IC} is the critical stress intensity factor for the film, σ is the tensile stress in the film, and $\Omega_c(\Sigma)$ is a dimensionless quantity that is a function of the ratio of the Young's modulus of the film to that of the substrate, i.e. $\Sigma = E_f/E_s$. For sol-gel films, several processes occur during processing that generate tensile stresses in the film which can cause cracking.

Mat. Res. Soc. Symp. Proc. Vol. 180. ©1990 Materials Research Society

To form a film by the sol-gel process, a sol film is first formed on the substrate by spin or dip coating. Evaporation of the solvent in the sol takes place during and after coating, which brings the reactive species in the sol closer together promoting condensation reactions. Usually, the sol will gel before all the solvent has evaporated producing a gel film whose pores are filled with solvent. The removal of the solvent from the pores produces capillary stresses as the solvent meniscus enters the gel.

Several processes occur as the gel film is heated [6-8] which also produce stresses that may lead to cracking. Organic species remaining in the gel after drying are pyrolized. Condensation reactions occur which change the gel structure and can produce shrinkage. Structural relaxation and viscous sintering cause shrinkage at higher temperature. These processes generally occur concurrently at least in some temperature range as the gel is heated.

The goal of this work was to study the cracking behavior of silica sol-gel films prepared under acidic conditions. The effects of the hydrolysis ratio, R (the molar ratio of water to alkoxide in the sol), and temperature on the critical thickness for cracking were determined.

EXPERIMENTAL

Two stock sol solutions, one with ethanol as the solvent and the other with t-butanol, were prepared. The concentrations of components in the stock solutions were 2.15 M tetraethoxysilane, 2.15 M deionized water (R=1), and 1.6×10^{-3} M HCl. The TEOS was distilled under partial vacuum prior to use. The stock sols were heated for 27 hr at 55°C and then diluted 2 to 1 with solvent. Three sols were prepared from the ethanol stock sol by adding enough water to obtain R values of 2, 4, and 8 and then heating at 55°C for 16 more hours. The t-butanol stock sol (R=1) was used without any further modification.

The morphology of cracks formed during room temperature drying of films made from the R=4 and R=8 sols was examined using an optical microscope. These films were prepared by spreading a volume of the sol on a glass slide or a silicon wafer, so that the film thickness when dry would be above the critical cracking thickness. Crack growth in these films was observed and video taped using an optical microscope.

The critical cracking thickness of films prepared from the three ethanol based sols and the t-butanol sol was determined as a function of temperature between room temperature and 350°C. Films were cast on glass slides by spreading an appropriate volume of the sol on the slide such that cracking would occur. Films were heated on a hot plate sequentially for 20 min at each soak temperature and the thickness of the thickest uncracked region of a partly cracked film was measured using a profilometer.

Thermogravimetric analysis and differential thermal analysis were performed on films made from the R=4 and the R=1 sols that were removed from the substrate after heating to either 80°C (R=4) or 160°C (R=1). The analyses were done in flowing air (50 cc/min) with a heating rate of 5°C/min.

The surface area, pore size distribution and pore volume of films made from these same two sols were determined using nitrogen adsorption analysis. To perform this analysis, cracked films ~10 μm thick were removed from several large substrates (total area = ~100 cm^2) and heated to 160°C.

The shrinkage of constrained (attached to the substrate) and unconstrained (removed from the substrate) films prepared from the R=1 and the R=4 sols was also measured. The films used for constrained shrinkage measurements were spun cast at ~2000 rpm and heated to 160°C for 30 min prior to the first thickness measurement. The films were initially ~400 nm

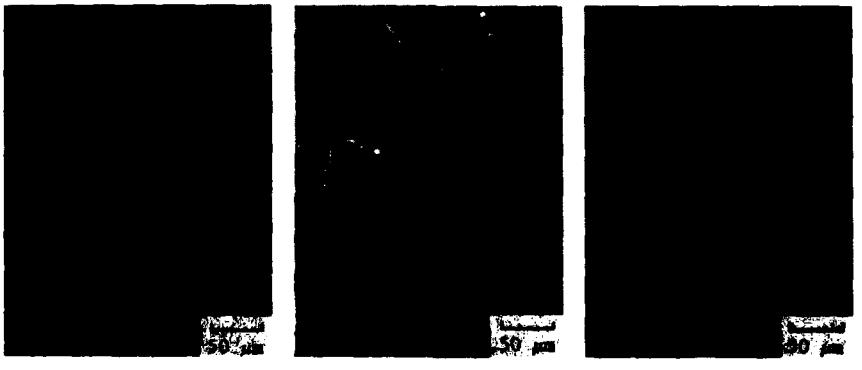
thick. Thickness of the constrained films were measured using the profilometer. A portion of the film was etched away with dilute HF or a KOH-isopropanol solution to create a step. Markers were scribed into each film so that exactly the same location was profiled each time. All films, both constrained and unconstrained, were measured after each 30 min soak in a sequential heating schedule where the films were placed directly in the hot furnace and removed and cooled immediately at the end of the soak.

Several small pieces of film were removed from cracked films made from each sol and photographed using an optical microscope. The same pieces were again photographed at the same magnification after each thermal treatment. The areal shrinkage of each piece was then determined from the micrographs. The thickness of the unconstrained pieces was measured using the profilometer. Care was taken so that only unwarped pieces were measured and that the same location on each piece was profiled after each thermal treatment.

RESULTS AND DISCUSSION

A variety of unusual crack patterns were observed in room temperature dried films prepared from R=4 and R=8 sols. Generally, a network of nearly straight cracks would form first and then curved cracks would nucleate from the straight cracks and grow into the uncracked regions. This result was in agreement with the model of Meakin [9,10,], although, as discussed below, some of the curved cracks had regular forms not predicted by the model. The rate at which cracks grew varied from microns to millimeters per second, indicating stable crack growth. As the film thickness increased beyond the critical thickness, the pieces formed displayed interference fringes indicating that the pieces were warped up from the substrate. For even thicker films, the pieces warped so severely that they became completely detached from the substrate.

Optical micrographs of some of these features are shown in Figure 1. Figure 1a shows cracks in a sinusoidal or sawtooth wave pattern. Sine wave buckles have been seen in films with compressive stress [1,11,12], but this is the first report of sine wave cracks. Another unusual feature present in some of the cracked films were pairs of parallel cracks. These varied in



a) b) c)

Figure 1. Crack morphologies produced by drying of sol-gel films: a) sinusoidal cracks; b) parallel crack pairs; and c) loop terminated crack pairs.

length from tens to hundreds of microns and were generally somewhat curved (see Figure 1b). The two cracks comprising the crack pair nucleated at the same time from a preexisting crack and grew at the same rate with a constant separation. Often, other curved cracks would nucleate from the parallel crack pair as it grew and would then grow into the surrounding uncracked areas. Usually, the crack pair would grow until it ran into another preexisting crack. However, sometimes each crack in the pair would curve to the outside and form a loop (see Figure 1c). These unusual crack morphologies must form due to a non-unifrom stress distribution, the causes of which are under investigation.

As mentioned above, the films from the R=4 and R=8 sols gelled after several minutes at room temperature. On the other hand, the films from the R=2 and R=1 sols became tacky liquids at room temperature which gelled when heated to ~140°C. The increase in gelation kinetics with increasing water content is consistent with the increase in condensation rate with extent of hydrolysis [13]. However, nitrogen adsorption analysis on films heated to 160°C indicated that the pore characteristics (pore size distribution, pore volume and surface area) did not vary significantly with R. This may be due to the fact that the pH of the sols was near the isoelectric point of silica where the condensation rate is low [13].

Figure 2 shows that the critical cracking thickness decreased strongly with both increasing water content in the sol and with increasing temperature. There are several possible reasons why the critical cracking thickness decreased with increasing sol water content, even though the pore characteristics of the films did not change. One explanation is that the composition of the liquid in the pores of the gels changes with R. This affects the capillary stress during drying since the stress is proportional to the liquid's surface tension. The higher R is, the richer the pore liquid will be in water, and thus the larger its surface tension will be. Also, for the low R sols, gelation did not occur until well above the boiling points of water and ethanol or t-butanol, so that a solvent phase was not present to produce capillary forces after gelation. This is similar to the results of Schlichting [14], who prepared 10 μm thick, crack-free films which had low water contents since they were hydrolized by exposure to air.

To determine the cause of the decrease in critical cracking thickness with temperature, thermal analysis and shrinkage measurements were performed. The thermogravimetric analysis results (Figure 3) indicated that the low R gel lost weight less gradually and at higher temperature, in the

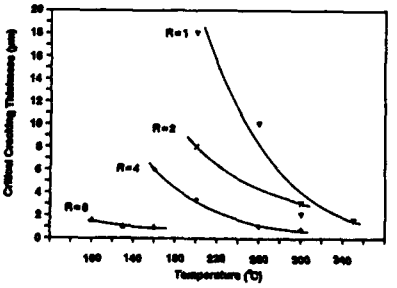


Figure 2

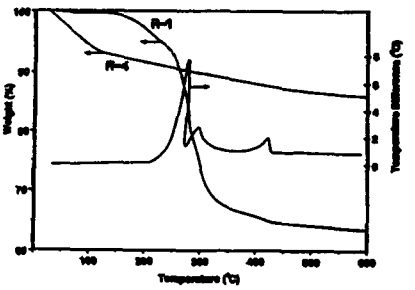


Figure 3

Figure 2. The effect of hydrolysis ratio, R, and temperature on the critical cracking thickness of silica sol-gel films.

Figure 3. Thermogravimetric and differential thermal analyses of the R=1 gel and thermogravimetric analysis of the R=4 film.

range where the critical thickness is sharply decreasing. The differential thermal analysis (Figure 3) indicated that the weight loss of this gel was associated with exothermic reactions. Therefore, the cracking could be due to the disruption of the structure that takes place when the rapid weight loss occurs. Alternately, capillary forces produced when a high boiling point liquid in the pores decomposes could cause cracking. This liquid could consist of siloxane oligimers not bound to the gel structure.

On the other hand, as Figure 4 shows, shrinkage is also occurring in the temperature range where the critical thickness decreases. The constraint of the substrate keeps the film from shrinking in the plane and therfore produces a tensile stress in the film [15]. This stress would be most likely to cause cracking when only a small amount of shrinkage has occurred since the magnitude of the free shrinkage rate, and thus the stress, is high and the structure is porous, and thus weak, at this point [15].

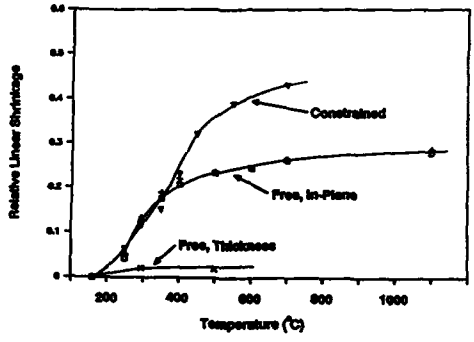


Figure 4. Relative linear shrinkage of unconstrained films prepared from R=4 (x, +) and R=1 ( ) sols both in the thickness direction and in the plane, and of a constrained film prepared from the R=1 sol (V).

As Figure 4 shows, films made from sols with different R values exhibited nearly identical shrinkage behavior as expected from the similar pore characteristics. Unconstrained films (removed from the substrate after drying) shrank in an extremely anisotropic manner, with almost all of the shrinkage occurring in the planar direction. This indicates that structural anisotropy must form in the gel films during constrained drying.

The shrinkage of the constrained film can be compared to that of the unconstrained film using the approach of Scherer [16]. The linear shrinkage rate in the i-direction during constrained sintering of a porous viscous material, ε_i, can be written as:

$$\varepsilon_i = \varepsilon_{i(free)} + (\sigma_i - N(\sigma_j + \sigma_k))/F \qquad (2)$$

where $\varepsilon_{i(free)}$ is the shrinkage rate in the i-direction when the constraint is not present, σ_{i-k} are the stresses in the i, j and k directions caused by the constraint, N is equilivent of the Poisson's ratio which approaches 0.5 as the porosity goes to zero, and F is the resistance to flow which approaches three times the viscosity as the porosity goes to zero. For a constrained film with z as the thickness direction, $\sigma_z=0$, $\varepsilon_x=\varepsilon_y=0$, $\varepsilon_{x(free)} = \varepsilon_{y(free)} = \varepsilon_{free}$ and, for the present case, as Figure 4 shows, $\varepsilon_{z(free)} \approx 0$. Using these substitutions in equation (2) and solving for ε_z gives:

$$\dot{\epsilon}_z = [2N/(1-N)]\ \dot{\epsilon}_{free} \qquad (3)$$

Since the value of N is approximately half of the relative density [17], equation 3 predicts that the linear shrinkage rate of the constrained film in the thickness direction should be less than that of the free film in the plane at low densities and greater than it at higher densities. This is consistent with the data in Figure 4.

CONCLUSIONS

Silica films prepared from acidic sols with low values of R do not crack at temperatures below 200°C unless they are thicker than 10 μm. However, their critical cracking thickness rapidly decreases between 250° and 350°C to about 1 μm, a value close to that of films made from high R sols. Film shrinkage and reactions causing weight loss occur in this temperature range. Finally, drying causes the structure of the films to be anisotropic in such a manner as to cause them to shrink primarily in the plane during heating, when free from the constraint of the substrate.

ACKNOWLEDGEMENTS

This work was sponsored by the Department of Energy, Contract DE-AC04.76-DP00789. The author is grateful to M. S. Harrington, D. Goodnow and C. S. Ashley for experimental assistance and to R. W. Schwartz for reviewing the manuscript.

REFERENCES

1. K.L. Chopra, Thin Film Phenomena, (McGraw-Hill Book Co., New York, 1969), pp. 311-313.
2. S.G. Shyu, T.J. Smith, S. Baskaran, and R.C. Buchanan in Better Ceramics Through Chemistry III, edited by C.J. Brinker, D.E. Clark and D.R. Ulrich (Mat. Res. Soc. Proc. 121, Pittsburgh, PA 1988) pp. 767-73.
3. M.S. Hu and A.G. Evans, Acta Metall. 37, 917 (1989).
4. M.S. Hu, M.D. Thouless and A.G. Evans, Acta Metall. 36, 1301 (1988).
5. G. Gille, Thin Solid Films 111, 201 (1984).
6. C.J. Brinker, G.W. Scherer and E.P. Roth, J. Non-Cryst. Sol. 72, 345 (1985).
7. P.F. James, J. Non-Cryst. Solids 100, 93 (1988).
8. F. Orgaz-Orgaz, J. Non-Cryst. Solids 100, 115 (1988).
9. P. Meakin, Thin Solid Films 151, 165 (1987).
10. A.T. Skjeltorp and P. Meakin, Nature 335, 424 (1988).
11. A. Alnaimi and S. Berg, in The Proc. of the Int. Vac. Congress, 8th, 1980, Vol. 1, Thin Films, ed. by F. Abeles and M. Croset, p. 336.
12. C. Weissmantel, C. Schurer, F. Frohlich, P. Grau, and H. Lehmann, Thin Solid Films 61, L5 (1979).
13. C.J. Brinker, J. Non-Cryst. Solids 100, 31 (1988).
14. J. Schlichting, J. Non-Cryst. Solids 63, 173 (1984)
15. G. W. Scherer and T. Garino, J. Am. Ceram. Soc. 68, 216 (1985).
16. G.W. Scherer, J. Non-Cryst. Solids 34, 239 (1979).
17. T.J. Garino and H.K. Bowen, J. Am. Ceram. Soc., 73, 251 (1990).

EFFECT OF INCLUSIONS ON SHRINKAGE

GEORGE W. SCHERER
E.I. DuPont de Nemours & Co., Central R & D Department, P.O. Box 80356, Wilmington, DE 19880-0356 USA

ABSTRACT

The effects of inclusions on densification are discussed, including their influence on the development of stresses during drying, and on the kinetics of sintering. Special attention is given to the problem of crystallization during sintering.

INTRODUCTION

Inclusions, such as particles or whiskers, are often introduced into gels to provide toughness to the sintered body. In other cases, inclusions appear spontaneously, as the glassy matrix crystallizes during aging or sintering. Whatever their origin, inclusions inhibit shrinkage of the body and thereby influence the development of stresses during drying and the rate of densification during sintering. In this paper, we examine these effects.

DRYING

Stresses arise during drying because of a gradient in the capillary tension in the liquid phase [1,2]. For a plate of thickness $2L$ drying from both faces, the drying stress is

$$\sigma_z = C_N H_G \left(\frac{\dot{V}_E}{L}\right)\left[\frac{\alpha \cosh(\alpha z / L)}{\sinh(\alpha)} - 1\right] \qquad (1)$$

where the constant $C_N \approx 1$, H_G is the viscosity of the solid network, $\dot{V}_E$ is the evaporation rate, z is the coordinate normal to the drying surface, and the parameter α is

$$\alpha = \sqrt{\frac{L^2 \eta_L}{D H_G}} \qquad (2)$$

where D is the permeability and η_L is the viscosity of the liquid in the pores. Inclusions stiffen the matrix, so they increase H_G; this reduces α and that leads to smaller drying stresses. That is, an increase in the macroscopic rigidity of the body tends to flatten the pressure gradient and reduce the macroscopic stresses. However, the *local* stresses might increase, because if the gel is trapped in the interstices of a relatively rigid network of particles, it cannot shrink, and the stresses may be even greater than in a film (which is constrained in only two directions).

When α is small, eq. (1) reduces to

$$\sigma_z \approx \frac{L \eta_L \dot{V}_E}{2D}\left(\frac{z^2}{L^2} - \frac{1}{3}\right) \qquad (3)$$

so the stress is inversely proportional to the permeability. In a composite, the permeability will be sensitive to the degree of wetting of the inclusions by the matrix. For instance, if hydrophobic whiskers were introduced into a hydrophilic gel, the gel would not adhere to the

whiskers, so open channels could form along the whiskers. Whiskers percolate readily (for example, whiskers with an aspect ratio of 10 to 1 have a percolation threshold, P_c, of only ~9 vol% [3]), so such channels could provide an easy path for fluid flow through the body, and this would substantially lower the drying stresses. However, those channels would probably open further during sintering and act as mechanical flaws in the resulting body.

Finally, inclusions toughen the matrix by interrupting crack growth, so the body could retain its macroscopic integrity, but be full of microcracks produced by local drying stresses. Such flaws could grow during sintering, and prevent complete densification.

SINTERING

Inclusions retard sintering, because the matrix around the perimeter of the inclusion is unable to contract freely. This is illustrated in Fig. 1 for the case of a particulate matrix. In effect, the inclusions create a hydrostatic tension in the matrix that reduces the sintering rate. For a viscous matrix, the linear contraction rate of the composite is given by [4]

$$\dot{\varepsilon}_c = \frac{(1-v)\dot{\varepsilon}_{fm}}{1+v\left(\frac{4G_c}{3K_m}\right)} \qquad (4)$$

where v is the volume fraction of inclusions, $\dot{\varepsilon}_{fm}$ is the linear contraction rate of the matrix alone (*i.e.*, the free strain rate), G_c is the shear viscosity of the composite, and K_m is the bulk viscosity of the matrix. This self-consistent solution is derived [4] by considering the situation of a cluster of matrix particles within the composite. That cluster constitutes a "core" that is surrounded by a "shell" (*viz.*, the composite) that contracts at a slower rate, so the core is subjected to hydrostatic tension; therefore it is the *bulk* viscosity of the matrix that appears in eq. (4). At the same time, the shell of composite undergoes shear deformation to accommodate the faster shrinkage rate of the core, so the *shear* viscosity of the composite appears in eq. (4). This model has been shown to work well in composites containing no more than ~12 vol% inclusions [5]. The most difficult aspect of applying the theory is knowing G_c. This is particularly problematic above the percolation threshold ($P_c \approx 16$ vol% for spherical particles in 3-D [6]), where G_c is expected to increase rapidly, and where simple models (such as the Hashin-Shtrikman bounds [7]) are expected to fail.

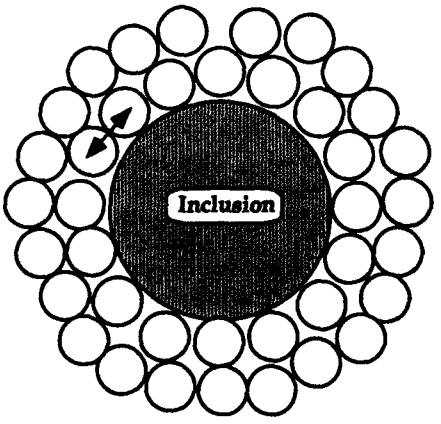


Fig. 1 Shrinkage of matrix particles (open circles) is severely inhibited around circumference of inclusion, but much less so in direction normal to surface of inclusion.

Recently, simulations (in 2 dimensions) using finite element analysis [8] have provided "data" for both $\dot{\varepsilon}_c$ and G_c, and have shown that eq. (4) (appropriately modified for 2-D) works quite well for $0 \le v \le 1$. The results are illustrated in Fig. 2 for two cases: inclusions that are wetted by the matrix (so that matrix particles sinter to the inclusions), and nonwetting inclusions. Clearly the latter inhibit densification even

more than the former. Even the wetting inclusions cause the sintering rate to approach zero near the percolation threshold, which is at $v \approx 0.5$ for the 2-D triangular lattice used in these calculations. The quality of the fit to the simulations suggests that the theory is adequate, and the difficulty in fitting the experimental data in ref. 5 was probably caused by uncertainty in the estimation of G_c.

The simulations show that the densification rate of an amorphous matrix is drastically reduced when the content of inclusions approaches the percolation threshold, where they can form a relatively rigid network. The threshold depends on the aspect ratio and degree of alignment of the inclusions; beyond P_c, the rigidity of the network that they form depends on how well they are wetted by the matrix. Good wetting allows the matrix particles to sinter to the inclusions, and permits a lubricating layer of glass to form between inclusion particles; in that case, the inclusion network could remain highly compliant until v is well beyond the threshold value. For example, in simulations of particles interacting by purely central forces (a fair model of lubricated inclusions), rigidity first appears at the usual percolation threshold (P_c), but the rigidity rises rapidly beyond a second "threshold" where many particles begin to collect into mechanically stable tetrahedral packing [9]. In the nonwetting case, the inclusions could sinter to each other and form a very rigid network immediately beyond P_c.

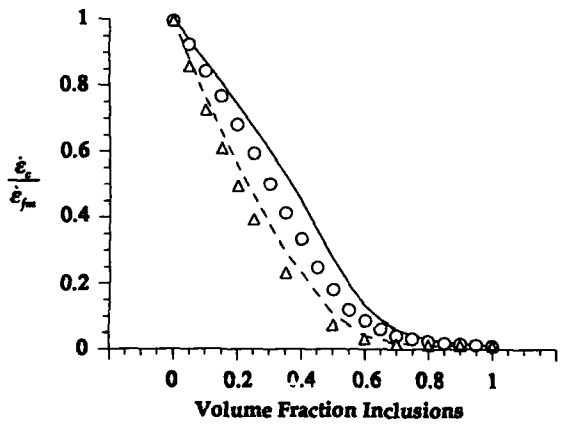


Fig. 2 Linear shrinkage rate of composite normalized by free strain rate of matrix, based on 2-D simulations by finite-element analysis (symbols) and 2-D version of eq. (4) (curves). The upper set (o, ——) is for inclusions that are wetted by the matrix, and the lower set (Δ, - - -) is for nonwetting inclusions. The percolation threshold in this case is $v \approx 0.5$.

CRYSTALLIZATION DURING SINTERING

Crystals that form during sintering are an important class of inclusions. Many types of gels (*e.g.*, some alkali silicates [10]) cannot be sintered to full density, because crystallization intervenes, and diffusive sintering is much slower than viscous sintering [11]. Mullite aerogels crystallize and can only be sintered to a relative density of $\rho \approx 0.5$, but the same material can be crushed and pressed into a pellet that sinters to clear glass [12], presumably because the denser material sinters faster and allows less time for crystal growth. Silica is so stable against crystallization that even aerogels can be sintered to clear glass [13,14], unless they are contaminated with alkali [15].

The competition between sintering and crystallization has been discussed by Uhlmann *et al.* [16-18] and Zarzycki [19] in terms of time-temperature-transformation (TTT) diagrams. By combining the theory of viscous sintering [20-22] with the Avrami analysis of the kinetics of

phase transformation [23], it is possible to predict the amount of crystallization that occurs by the time that sintering is complete. That approach is correct if the volume fraction of crystals is small, but otherwise it is necessary to take account of the effect of the crystals on the sintering rate. The simplest approach is to combine eq. (4) with the Avrami analysis, and that is what we will do shortly. However, first we pause to consider the limitations of that method.

The influence of the cyrstals on densification depends critically on *where* they are. If a layer of crystals formed first on the exterior of the body (because of heterogeneous nucleation), a rigid skin would result that could drastically retard sintering, even though a very small volume fraction of the glass had transformed. If the homogeneous nucleation rate (I_v) is high and the crystal growth rate (u) is small, there will be many tiny crystals within the glass, as shown schematically in Fig. 3. In that case it is probably reasonable to use the standard viscous sintering theory, but to correct the viscosity of the glass for the presence of crystallites by using a model appropriate for a slurry (*e.g.*, the Einstein equation for low concentrations or the Mooney equation for higher crystal contents [24]); then, as we shall see, the crystals have an important influence on the sintering kinetics. The most difficult case to analyze, illustrated in Fig. 4, is when both I_v and u are moderately large. Then the growth of many of the crystallites is terminated by pore surfaces, and it becomes difficult to predict the volume fraction transformed. The problem of growth within a finite region of glass has been solved by Weinberg *et al.* for growth within a thin sheet [25,26] or spherical particle [27], but the geometry is formidable even in those simple cases.

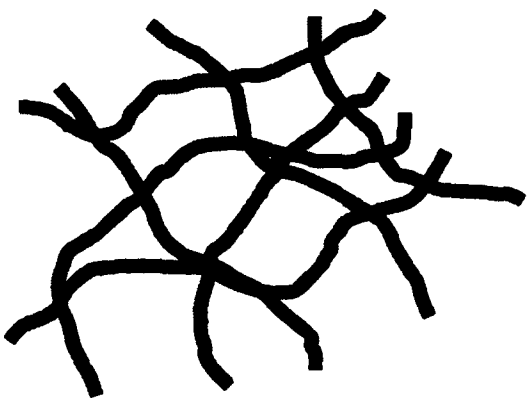


Fig. 3 Distribution of crystals (black dots) in gel network (grey chains) when the nucleation rate is large and the growth rate is small.

A simpler case, and the one we explore here, is when the nucleation rate is relatively low and the growth rate is high. Then, as shown in Fig. 5, the crystals readily grow to a size that is large compared to the scale of the microstructure of the gel, and it is easy to calculate the volume transformed.

Growth of inclusions

We are interested in calculating the volume occupied by a crystallite such as that indicated in Fig. 5,

$$v_c = \frac{4\pi}{3} r^3 \qquad (5)$$

That is, we do not care about the actual volume of crystalline material, $v_c\rho$, where ρ is the relative density of the network (*i.e.*, the volume fraction of solid phase). The factor that affects

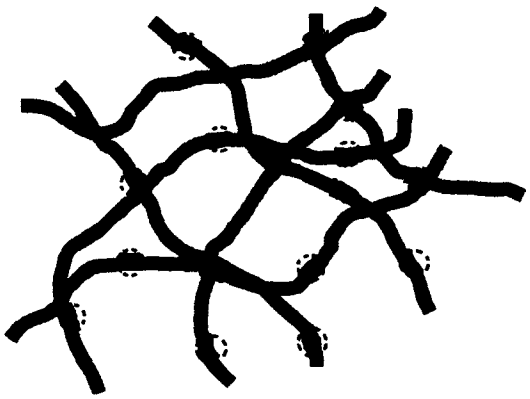


Fig. 4 When both the nucleation and growth rates are moderate, the growth of crystals (black circles) is interrupted by the pore surfaces.

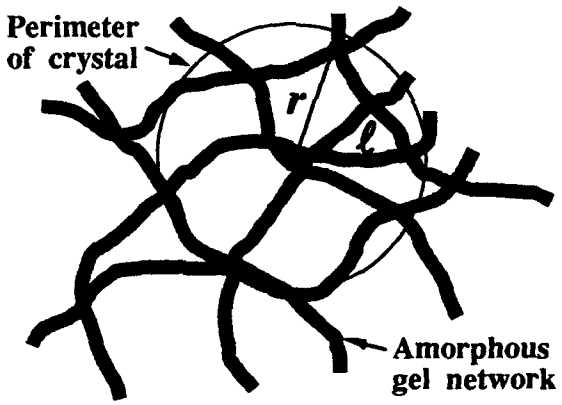


Fig. 5 When the nucleation rate is low and growth is fast, individual crystals are large compared to the scale of the gel structure. For a crystal to grow to a radius of r, it must trace a path of length ℓ.

the sintering rate is the volume fraction occupied by rigid crystalline inclusions, so we must calculate the number of inclusions of radius r. In a dense matrix, the size of a crystal is $r = u\,(t - t')$, where t' is the time at which it nucleated. In the present case, the crystal grows along a tortuous path of length $\ell = u\,(t - t')$, so the effective size of a crystal depends on the tortuosity (τ):

$$r(t,t') = \frac{\ell}{\tau} = \int_{t'}^{t} \frac{u}{\tau}\,dt'' \qquad (6)$$

Eq. (6) implies that a crystal arriving at a junction in the network grows at the same rate along every branch leading away; isotropic growth of this kind can probably be expected only for materials with a low entropy of fusion. If the matrix is fractal, as some aerogels are [28], then the radius scales with the path length according to

$$\ell \sim r^{d_{min}} \tag{7}$$

where d_{min} is the fractal dimension of the shortest path (or chemical distance) between two points in the network. If the network is a percolation cluster [29], $d_{min} = 1.34 \pm 0.01$, and if the network is grown by diffusion-limited cluster-cluster aggregation [30], $d_{min} = 1.25 \pm 0.05$. For a network that is fractal over a length scale $r \le \xi$, eq. (6) must be replaced by

$$r(t,t') = \begin{cases} \xi^{1-\tilde{\nu}} \left(\int_{t'}^{t} \frac{u}{\tilde{\nu}\tau} dt'' \right)^{\tilde{\nu}} & , r(t,t') \le \xi \\ \xi + \int_{t_\xi(t')}^{t} \frac{u}{\tau} dt'' & , r(t,t') \ge \xi \end{cases} \tag{8}$$

where $\tilde{\nu} \equiv 1 / d_{min}$ and

$$\xi = \int_{t'}^{t_\xi(t')} \frac{u}{\tilde{\nu}\tau} dt'' \tag{9}$$

Eq. (8) allows for scaling behavior as long as the crystal is smaller than the correlation length, ξ, and provides continuity in r and $dr/d\ell$ at $r = \xi$. Thus, the fractal structure can be taken into account, but it adds considerably to the complexity of the problem. In particular, the fractal dimension will increase and ξ will decrease as the network sinters, and there is presently no theoretical method for predicting those changes. Since d_{min} is not far from unity, we will ignore the fractal nature of the network in the following analysis. Qualitatively, the effect of a fractal structure is that the density is greater at shorter length scales, so the path is less tortuous and r increases more rapidly in a fractal than in a Euclidian network with the same macroscopic density (but, again, the effect is likely to be small).

For the situation depicted in Fig. 5, the most important change in the analysis of the transformation kinetics is that nucleation can only occur within the solid phase, which occupies a fraction ρ of the volume V of the sample. Thus the number of crystals nucleated between t' and $t' + dt'$ is

$$dn(t') = \rho(t')V(t')I_v(t')dt' = V_s I_v(t')dt' \tag{10}$$

where V_s is the volume of the solid phase, so $\rho = V_s / V$. The growth rate of each crystallite is $4\pi r(t,t')^2 dr / dt$, if growth is isotropic, so the rate of change of the total volume occupied by crystallites (V_c) is

$$\left. \frac{\dot{V}_c}{V_s} \right|_{iso} = \frac{4\pi u(t)}{\tau(t)} \int_0^t I_v(t') \left[\int_{t'}^{t} \frac{u(t'')}{\tau(t'')} dt'' \right]^2 dt'$$

$$= \frac{4\pi}{3} \frac{d}{dt} \int_0^t I_v(t') \left[\int_{t'}^{t} \frac{u(t'')}{\tau(t'')} dt'' \right]^3 dt' \tag{11a,b}$$

The superscript dot indicates a derivative with respect to time throughout this paper, and the

subscript *no* refers to the fact that we have neglected overlap of the growing crystals. If there is overlap, we can correct for it by recognizing that growth can only occur in the part of the network that is not already transformed, so

$$\frac{\dot{V}_c}{V_e} = \left(1 - \frac{\dot{V}_c}{V_e}\right)\left(\frac{\dot{V}_c}{V_e}\bigg|_{no}\right) \tag{12}$$

If ρ and τ are unity, then eqs. (11) and (12) can be integrated to obtain the classical result [23]

$$\frac{V_c}{V} = 1 - \exp\left[-\frac{4\pi}{3}\int_0^t I_v(t')\left[\int_{t'}^t u(t'')\,dt''\right]^3 dt'\right] \tag{13}$$

or, when I_v and u are constant,

$$\frac{V_c}{V} = 1 - \exp\left[-\frac{\pi}{3} I_v u^3 t^4\right] \approx \frac{\pi}{3} I_v u^3 t^4 \tag{14}$$

where the approximation applies when V_c/V is small. In our case, eqs. (11) and (12) lead to

$$v \equiv \frac{V_c}{V} = \rho\int_0^t \exp\left[-\int_{t'}^t \rho\left(\frac{\dot{V}_c(t'')}{V}\bigg|_{no}\right)dt''\right]\left(\frac{\dot{V}_c(t')}{V}\bigg|_{no}\right)dt' \tag{15}$$

Note that ρ represents the relative density of the uncrystallized portion of the matrix.

Constant temperature

If the sintering is performed isothermally, the free strain rate of the matrix can be written as

$$\dot{\varepsilon}_{fm} = -\frac{1}{2}\left(\frac{4\pi}{3}\right)^{1/3}\left(\frac{\gamma_{LV} n^{1/3}}{\eta}\right)\left(\frac{1}{\rho} - 1\right)^{2/3} \tag{16}$$

This is the Mackenzie-Shuttleworth expression [21], which is a good approximation to the behavior of a variety of materials [11] and is simple in form. In eq. (16), γ_{LV} is the surface tension, η is the viscosity of the glass, and n is the number of pores per unit volume of solid. Using eq. (16), and recognizing that $\dot{\rho}/\rho = -3\dot{\varepsilon}_c/(1-v)$, eq. (4) can be written as

$$\frac{d\rho}{d\theta} = \frac{3}{2}\left(\frac{4\pi}{3}\right)^{1/3}\frac{\rho^{1/3}(1-\rho)^{2/3}}{1 + v\left(\frac{4G_c}{3K_m}\right)} \tag{17}$$

where

$$\theta = \left(\frac{\gamma_{LV} n^{1/3}}{\eta}\right)t \tag{18}$$

To evaluate eq. (17) we must make some assumption about the rheology of the matrix, so we use a result suggested by numerical simulations [8] (which is stated here without justification,

but will be discussed at length in a future publication):

$$1+v\left(\frac{4G_c}{3K_m}\right)\approx\frac{(1+\nu_c)(1-v)}{1+\nu_c-3(1-\nu_c)v} \tag{19}$$

where Poisson's ratio for the composite (ν_c) is approximated by

$$\nu_c\approx\frac{v}{5}+\frac{1-v}{2}\sqrt{\frac{\rho}{3-2\rho}} \tag{20}$$

At a constant temperature, assuming homogeneous nucleation, I_v and u are constant; then, if we assume $\tau\approx 1$, eq. (15) reduces to

$$v=c\rho\int_0^\theta \exp\left[-c\int_{\theta'}^{\theta}\rho(\theta'')\theta''^3\,d\theta''\right]\theta'^3\,d\theta' \tag{21}$$

where

$$c=\left(\frac{4\pi}{3}I_v u^3\right)\Big/\left(\frac{\gamma_{LV}n^{1/3}}{\eta}\right)^4 \tag{22}$$

For a free matrix, the approximate time to complete sintering is $t_s\approx\eta/\gamma_{LV}n^{1/3}$ [11], so $c=\frac{4\pi}{3}I_v u^3 t_s^4$, and comparison with eq. (14) reveals that c is roughly the volume fraction of crystals that appears during the time required for sintering of the free matrix.

Fig. 6 shows what happens when c is small. The final crystallinity is ~15 vol%, but most of that growth occurs when the network is almost fully dense, so the residual porosity (trapped within crystallites) is < 1 vol%. When c is larger, crystallization begins while the density of the matrix is low, so substantial porosity is trapped within the crystallites. As shown in Fig. 7, the volume of crystals is then large enough to have a significant effect on the densification rate. When v approaches 50 vol%, densification of the matrix virtually stops, because the glass is held in the interstices of a rigid network of crystals. As a result, the matrix crystallizes completely, trapping residual porosity of ~10 vol%.

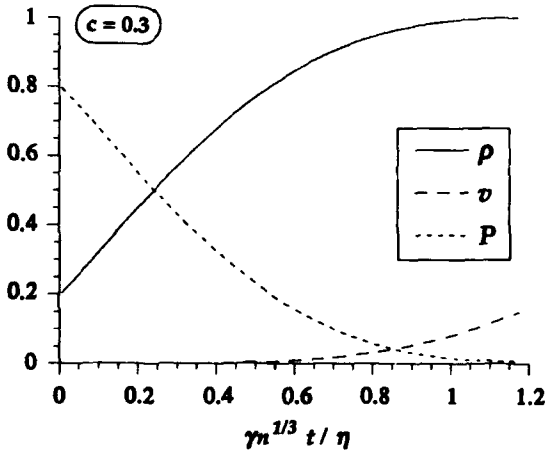


Fig. 6 Density of matrix (ρ), volume fraction of crystals (v), and porosity (P) versus reduced time θ when $c = 0.3$; initial relative density $\rho = 0.2$.

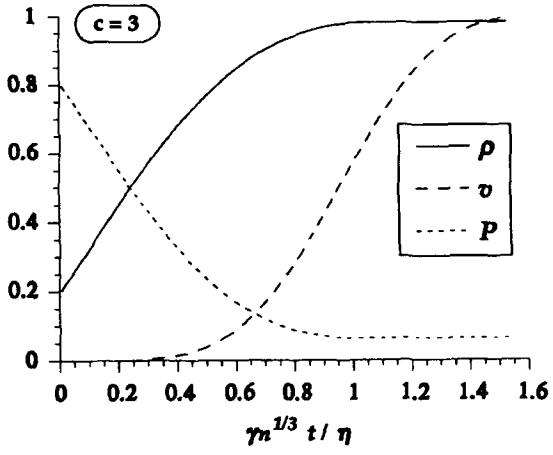


Fig. 7 Density of matrix (ρ), volume fraction of crystals (v), and porosity (P) versus reduced time θ when $c = 3$; initial relative density $\rho = 0.2$.

The variation of residual porosity with c is shown in Fig. 8. For a given material, it is much easier to sinter to full density if the initial density is high. If $c > 1$, the glass will crystallize completely, leaving residual porosity. If $\rho \geq 0.2$ and $c \leq 10$, the final porosity will be $\leq 15\%$, so it may still be possible to fully densify the crystalline body by treatment at higher temperature.

If the crystallites are small compared to the microstructure, as indicated in Fig. 3, then the volume fraction of the solid phase that is crystalline is given by eq. (14); to obtain the *transformed fraction of*

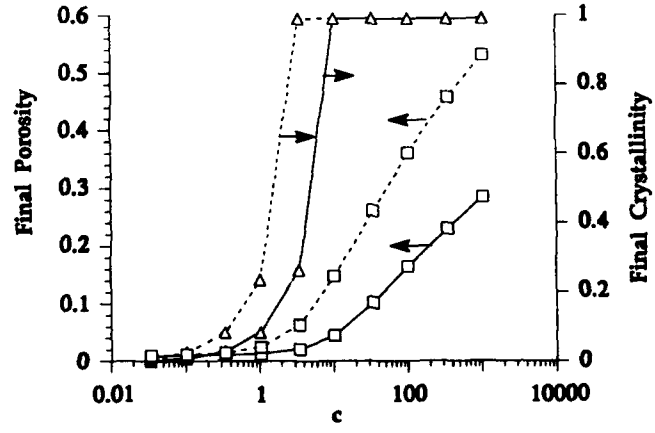


Fig. 8 Dependence of final porosity (□) and crystallinity (Δ) on c , defined in eq. (22), for initial relative densities of $\rho = 0.2$ (- - -) and 0.5 (——).

the body, we must correct for the porosity by dividing by ρ:

$$\frac{v}{\rho} = 1 - \exp\left[-\frac{c\theta^4}{4}\right] \tag{23}$$

The free strain rate is given by eq. (16), but the viscosity of the solid phase, η, is modified according to the Mooney equation (see ref. 24, p. 464-465):

$$\eta(effective) = \eta \exp\left[\frac{2.5v}{1-av}\right] \tag{24}$$

where the constant a is expected to have a value between 1 and 2; we use $a = 1.2$, which is in good agreement with numerical simulations [8]. Thus, using eqs. (16) and (24) the densification rate is

$$\frac{d\rho}{d\theta} = \frac{3}{2}\left(\frac{4\pi}{3}\right)^{1/3} \rho^{1/3}(1-\rho)^{2/3} \exp\left[-\frac{2.5v}{1-1.2v}\right] \tag{25}$$

Fig. 9 shows the predictions of eqs. (23) and (25) when $c = 3$. Comparison with Fig. 7 reveals that the body crystallizes completely in both cases, but slightly more porosity is retained when the crystals are distributed as in Fig. 3.

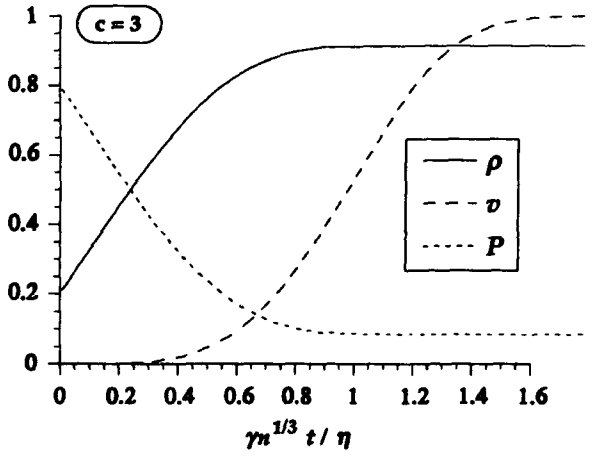


Fig. 9 Transformation kinetics for microstructure illustrated in Fig. 3: Density of matrix (ρ), crystalline volume fraction of solid phase (v), and porosity (P) versus reduced time θ when $c = 3$; initial relative density $\rho = 0.2$.

Transformation kinetics in gels

We have considered only the simplest possible case of sintering with crystallization. A

question of great importance is the influence of thermal history on the degree of transformation that occurs during densification. Zarzycki [19] has pointed out that u and I_v are inversely proportional to the viscosity, so the right-hand side of eq. (22) is independent of η. Therefore, factors (such as OH content) that affect η do not change the amount of crystallization that occurs during sintering. However, the driving forces for sintering and crystallization are different, so the rates of those processes are not identical. For example, changes in microstructure affect the sintering rate, but not the transformation rate. Consideration of the temperature dependence of u and I_v indicates that c is greatest at low temperatures (near 0.5-0.6 times the melting point), so slow heating through that range increases the degree of crystallization.

An important difficulty in predicting the degree of transformation is uncertainty about the values of the nucleation and growth rates. It has been observed by many workers [31] that the rates of nucleation and growth are greater in gel-derived materials than in conventionally prepared ceramics. However, much of that difference is believed to result from the enhanced atomic mobility provided by the high hydroxyl contents of the gels, and changes in mobility (as noted above) affect transformation and sintering equally, and are therefore not important in this connection. However, it has been plausibly argued [19] that gel-derived materials may have different nucleation barriers (because the OH affects the glass/crystal interfacial energy), and this means that data collected for conventional glasses may not be useful for predicting transformation rates in gels. There is also a difference in the susceptibility of gels and melts to contamination with heterogeneous nuclei: the former pick up dirt from glassware and unfiltered solvents, while the latter may incorporate particles from the raw powders, grinding media, or from attack of the crucible. A more exotic consideration is viscoelastic stress development [32], as crystals grow in a matrix of very high viscosity (gels typically sinter near the glass transition temperature [11]). Probably more important is the effect of the very high surface area of the gel on the driving force for crystallization. For example, as the crystal in Fig. 5 grows to volume V, it invests an energy equal to $(\gamma_{SV} - \gamma_{LV})\, VS_p/V_p$, where $\gamma_{SV} - \gamma_{LV}$ is the change in interfacial energy as the glass/vapor interface is replaced by a crystal/vapor interface, and S_p/V_p is the surface to volume ratio of the glassy phase. For typical gels, with specific surface areas of 500-1000 m^2/g, this strongly reduces the driving force for crystallization.

CONCLUSIONS

Although inclusions often impart beneficial properties to the final object, they are invariably troublesome in fabrication. Drying seems easier for composites, but that most likely comes at the cost of creating cracks or channels (around nonwetting inclusions) that will grow during sintering and deteriorate the properties of the product. Inclusions retard sintering of amorphous materials, but full densification can usually be achieved; the situation is quite different for crystalline matrices, where the presence of inclusions can preclude complete densification without applied pressure [11]. When large crystals grow in the matrix during densification, porosity will inevitably be trapped within the crystallites, and relatively extreme thermal treatments will be needed to eliminate it. We have shown that when a certain parameter [c in eq. (22)] is small, porosity can be eliminated. In the more realistic case of sintering during constant heating, it is difficult to predict the course of the transformation, because of the uncertain effects of the gel structure on the driving force for crystallization. In general, one can say that it is best to avoid slow heating through the low temperature range where the nucleation rate is great. Beyond this obvious advice, little can be said until more data are obtained regarding the thermodynamics of transformation of gel-derived materials.

REFERENCES

[1] C.J. Brinker and G.W. Scherer, Sol - Gel Science (Academic Press, NY, 1990) Ch. 7 and 8

[2] G.W. Scherer, J. Am. Ceram. Soc., 73 [1] 3-14 (1990)

[3] J. Boissonade, F. Barreau, and F. Carmona, J. Phys. A: Math. Gen., 16 , 2777-2787 (1983)

[4] G.W. Scherer, J. Am. Ceram. Soc., 70 [10] 719-725 (1987)

[5] M.N. Rahaman and L.C. De Jonghe, J. Am. Ceram. Soc., 70 [12] C-348-C-351 (1987)

[6] R. Zallen, The Physics of Amorphous Solids (Wiley, New York, 1983) Ch. 4

[7] Z. Hashin and S. Shtrikman, J. Mech. Phys. Solids, 11, 127-140 (1963)

[8] A. Jagota and G.W. Scherer, to be published

[9] See discussion in Ch. 5 of ref. 1, and references therein.

[10] M. Prassas and L.L. Hench, in Ultrastructure Processing of Ceramics, Glasses, and Composites, eds. L.L. Hench and D.R. Ulrich (Wiley, New York, 1984) p. 100-125

[11] See discussion in ref. 1, Ch. 11.

[12] M.N. Rahaman, L.C. DeJonghe, S.L. Shinde, and P.H. Tewari, J. Am. Ceram. Soc., 71 [7] C-338-C-341 (1988)

[13] J. Phalippou, T. Woignier, and J. Zarzycki, in Ultrastructure Processing of Ceramics, Glasses, and Composites, eds. L.L. Hench and D.R. Ulrich (Wiley, NY, 1984) pp. 70-87

[14] M. Prassas, J. Phalippou, and J. Zarzycki, in Science of Ceramic Chemical Processing , eds. L.L. Hench and D.R. Ulrich (Wiley, NY, 1986) pp. 156-167

[15] C. Zhu, J. Phalippou, and J. Zarzycki, J. Non-Cryst. Solids, 82, 321-328 (1986)

[16] D.R. Uhlmann, L. Klein, P.I.K. Onorato, and R.W. Hopper, in Proc. 6th Lunar Sci. Conf. (1975) p. 693-705

[17] D.R. Uhlmann and L.C. Klein in Proc. 7th Lunar Sci. Conf. (1976) pp.2529-2541

[18] D.R. Uhlmann, B.J. Zelinski, L. Silverman, S.B. Warner, B.D. Fabes, and W.F. Doyle, in Science of Ceramic Chemical Processing , eds. L.L. Hench and D.R. Ulrich (Wiley, NY, 1986) pp. 173-183

[19] J. Zarzycki, in Advances in Ceramics, Vol. 4 (Am. Ceram. Soc., Columbus, OH, 1982) pp. 204-216

[20] J. Frenkel, J. Phys. (Moscow) 9 [5] 385-391 (1945)

[21] J.K. Mackenzie and R. Shuttleworth, Proc. Phys. Soc. London, 62 [12-B] 833-852 (1949)

[22] G.W. Scherer, J. Am. Ceram. Soc. 60 [5-6] 236-239 (1977)

[23] J.W. Christian, The Theory of Transformations in Metals and Alloys, Part I, 2d ed. (Pergamon, New York, 1975) Chs. 1 and 12

[24] J. Happel and H. Brenner, Low Reynolds Number Hydrodynamics (Martinus Hijhoff, Boston, 1986) Ch. 9

[25] M.C. Weinberg, J. Non-Cryst. Solids, 72, 301-314 (1985)

[26] M.C. Weinberg and R. Kapral, J. Chem. Phys., 91 [11] 7146-7152 (1989)

[27] M.C. Weinberg, J. Non-Cryst. Solids, 76, 253-265 (1985)

[28] T. Woignier, J. Phalippou, and R. Vacher, J. Mater. Res., 4 [3] 688-692 (1989)

[29] H.J. Herrmann and H.E. Stanley, J. Phys. A: Math. Gen., 21, L829-L833 (1988)

[30] P. Meakin, I. Majid, S. Havlin, and H.E. Stanley, J. Phys. A: Math. Gen., 17, L975-L981 (1984)

[31] See discussion in ref. 1, Ch. 12

[32] R. Pascova, I. Gutzow, and J. Schmelzer, J. Mater. Sci., 25, 921-931 (1990)

HYBRID GELS DESIGNED FOR MULLITE NUCLEATION AND CRYSTALLIZATION CONTROL

JEFFREY C. HULING AND GARY L. MESSING
Department of Materials Science and Engineering, Pennsylvania State University, University Park, PA 16802

ABSTRACT

The controlled nucleation of phase transformations by seeding is an established technique for influencing transformation kinetics and sintered microstructures in ceramics. Previous studies have focused on seeding with ultrafine, solid particles having the requisite crystal characteristics for either homo- or heteroepitactic nucleation of the desired phase. Size separation of particulate seed crystals is not an efficient process and thus more recent efforts have concentrated on chemical approaches to nucleating solid phase transformations. Hybrid gels, in which two or more gels are combined to capitalize on the benefits of each, have been reported for the homoepitactic nucleation of mullite. In principle, the molecularly-mixed gel crystallizes to mullite at ~1000°C and, in turn, acts to nucleate the colloidal gel component's transformation to mullite at higher temperatures. However, the transformation sequence and kinetics are profoundly affected by the interfacial reaction between the two gels comprising the hybrid. This paper discusses how the physical distribution and chemistry of the gel components can be manipulated for the control of mullite nucleation, crystallization and microstructure development.

INTRODUCTION

Sol-gel processing provides several distinct routes [1] for synthesizing dense, pure mullite ($3Al_2O_3{\cdot}2SiO_2$). Colloidal or "diphasic" gels [2-7] consist of 10-100 nm particles of boehmite (γ-AlOOH) or γ-Al_2O_3 and colloidal silica. Upon heating, the independence of the individual phases is maintained to >1100°C, where viscous flow of the silica promotes densification prior to mullite crystallization [5-7]. More attention, however, has been focused on "molecularly-mixed", "polymeric", or "single phase" gels [3,8-13], which are produced by cohydrolysis or coprecipitation of aluminum and silicon salts and/or alkoxides. Processing of molecularly-mixed gels is intended to maximize the extent of direct alumina-silica bonding. In both cases, crystallization, densification and microstructure are indirectly controlled by changing precursors and processes to influence the scale of alumina-silica mixing. The term "control" is used loosely, however, since characterization of unfired gels is currently insufficient for relating alumina-silica mixing and gel structure to high-temperature behavior. More direct control over transformations has been achieved in α-alumina [14-16] and several sol-gel silicate systems [17,18] by addition of well characterized crystalline "seed" particles. The crystallites act as substrates for preferred epitactic nucleation. Sufficient concentrations of seeds effectively increase nucleation frequencies, allowing direct control over both transformation kinetics and microstructural development.

Despite the straightforward characterization of crystalline seed particles and the unambiguous experimental evidence of their role in nucleation catalysis [19], several difficulties limit their widespread use. The seeding phase must be both crystallographically effective as a substrate for epitactic nucleation and chemically nonreactive with the host system. To have an impact on a given transformation, seed particles must also induce nucleation frequencies surpassing the host system's intrinsic value, often by several orders of magnitude. To achieve this without filling the system with the crystalline seed phase, seed particle sizes must be <0.1 μm. Obtaining such particles often requires starting with large amounts of powder and performing comminution, dispersion and classification steps, with the attendant possibility of introducing chemical and/or phase impurities. An alternate route is to grow the seed crystals hydrothermally [17-19], but in practice this technique is limited with respect to the seed phases produced.

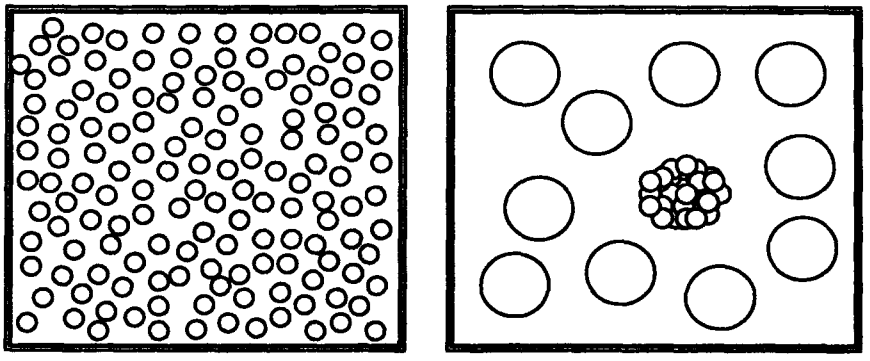
Mat. Res. Soc. Symp. Proc. Vol. 180. ©1990 Materials Research Society

Hybrid gels

The problems associated with obtaining ultrafine seed crystals in sufficient quantity and of sufficient purity can be avoided when an amorphous seeding gel can be dispersed in the original sol-gel system and crystallized *in situ* at a temperature lower than for the bulk gel. Nucleation control in mullite was the original objective of forming hybrid gels [20]. In general, hybrid gels can be defined as mixtures of differently processed gels which are formed to utilize advantageous characteristics of each. This approach is particularly suited to sol-gel mullite synthesis, as hybrid mullite gels utilize a molecularly-mixed component (crystallizing at low temperatures, but not easily densified as monoliths) to seed a colloidal component (densifying readily prior to higher-temperature crystallization). Obtaining the seed material involves a gel's chemical preparation, rather than the physical separation steps required when employing crystalline seeds from the outset. By manipulating sol-gel processing on several different levels (i.e., seed vs. matrix), the interactions between the interdispersed gels as each crystallizes can be affected to maximize the control possible over transformation kinetics and development of the sintered microstructure.

Just as processing methods combining alumina and silica dictate the behavior of molecularly-mixed and colloidal gels, the techniques for combining gel components determine a hybrid gel's characteristics. The concept of "scale of mixing" applies, since a gel component that is isolated as a result of poor mixing cannot fully impart its advantageous characteristics to a hybrid system. Maximum interdispersion of gels may also be unfavorable, since conversion of surface area to interfacial area and the breakdown of intrinsic gel structure can alter crystal nucleation and growth mechanisms. Factors to consider when processing hybrid gels therefore include the sizes, surface chemistries and morphologies (i.e., particulate vs. chainlike) of the gel components' units. The ratio of the gel components--a "compositional" variable that can be entirely independent of chemical stoichiometry--can also determine effective sizes and morphologies when one or both gels impinge to form a continuous network. Such definitive characterization of the hybrids is often prevented, however, by most gels' nanometer scale and amorphous nature.

It will be demonstrated that the interface between dissimilar gels has a profound effect on phase development, making design of the hybrid gel critical to the *in situ* formation of mullite seeds. Homogeneously-interdispersed *hybrid gels--influenced* most by the interface--are termed Type I. Those processed with coarser scales of gel mixing--and modified properties resulting from the reduced interface--are termed Type II. Schematic depictions of these gel structures are shown in Figure 1.



Type I Type II

Figure 1. Schematic representations of possible hybrid gel structure types containing differing extents of gel interface. Type II gels contain larger primary units or clusters of smaller units.

TYPE I HYBRID GELS

Type I gel synthesis

Preparation of the colloidal gel (73 wt% Al_2O_3, 27 wt% SiO_2) involves diluting a colloidal silica sol in deionized water and slowly (~ 1 g/min) adding boehmite (γ-AlOOH) powder while stirring vigorously. The final solids content is 20 wt% . After stirring for 1 day, concentrated nitric acid is added dropwise to lower the pH from ~8.5 to 3. This pH adjustment requires rapid passage through an intermediate pH regime of high viscosity caused by boehmite-silica heterocoagulation [21]. Gelation occurs in 1-2 hours. The wet gel is covered and kept for later use.

Preparation of the molecularly-mixed gel is modified from Okada et. al.'s procedure for their "SH" gel [11]. 100g aluminum nitrate nonahydrate ($Al(NO_3)_3{\cdot}9H_2O$) is dissolved in 100g absolute ethanol by stirring overnight at 55°C, followed by cooling to room temperature and addition of 17.4g tetraethoxysilane ($Si(OC_2H_5)_4$, TEOS). After stirring 2-3 hours at room temperature, the clear solution is heated and stirred at 55°C under reflux conditions until gelation (~4 days). Absolute ethanol is added (~70g) to allow the gel to be redispersed and stirring is continued at 65°C under reflux conditions for another ~8 days to ensure complete cohydrolysis. This yields an opaque dispersion of the molecularly-mixed gel in ethanol.

To promote compatibility of the molecularly- and colloidally-mixed systems the molecularly-mixed gel dispersion is converted to an aqueous medium. Ethanol is evaporated at 70°C and a total of 400-500g deionized water is added as needed to maintain the system's volume. The dispersion is loosely covered and boiled at 100°C, which results in a gradual (~5-6 hour) change from opacity to optical clarity. The dispersion is then cooled to room temperature and centrifuged at 2000 rpm for 25 min to remove any macroscopic gel heterogeneities. No significant settling of the gel occurs during centrifuging. The clear, aqueous dispersion is indefinitely stable without adjustment of pH.

Hybrid gels were prepared by combining the molecularly-mixed gel dispersion and the wet colloidal gel such that 25, 50, 75 and 90 wt% of the mullite totals would be derived from the molecularly-mixed component. These Type I gels were denoted $25M_I$, $50M_I$, etc. Mixing was achieved by mechanically rolling (150 rpm, 2 days) polyethylene bottles containing the two wet gels and several teflon-coated stirring bars. Deionized water was added to maintain low viscosity during mixing. Gels were dried at 90°C and crushed with a high purity alumina mortar and pestle.

Differential thermal analysis (DTA) was performed in flowing air on dehydroxylated (650°C) gel powders at a heating rate of 20°C/min to enhance crystallization exotherms. Phases crystallized were identified by x-ray diffraction (XRD) of samples following DTA heating to just above the relevant exotherms. Sintered gel microstructures (1300°C and 1550°C for 2 hours) were characterized by SEM and TEM of unsupported thin gel films [22]. TEM samples were ion milled ($\theta = 11°$, 3.5kV) for 1-2 hours and carbon coated.

~1000°C phase development

When nucleation control is achieved using crystalline seed particles, attention can generally be focused entirely on the transformation of the host or matrix system. In hybrid gels, however, understanding the initial *in situ* formation of the seed crystals is also necessary for interpreting these crystals' subsequent role in the overall transformation. Individually characterizing the gels comprising the hybrid is insufficient, as this approach neglects the gel interfaces and assumes that the seeding gel acts independently. Indeed, for hybrid mullite gels, the importance of proper "design" can be attributed directly to the key observation that the molecularly-mixed gel's inclusion in the hybrid results in a fundamental alteration in its phase development.

Hybrid gels in which the molecularly-mixed component predominates can be used to investigate *in situ* seed formation. DTA and XRD results for the individual molecularly-mixed gel (100M) and the $90M_I$ and $75M_I$ hybrid gels are shown in Figure 2. The intrinsic molecularly-

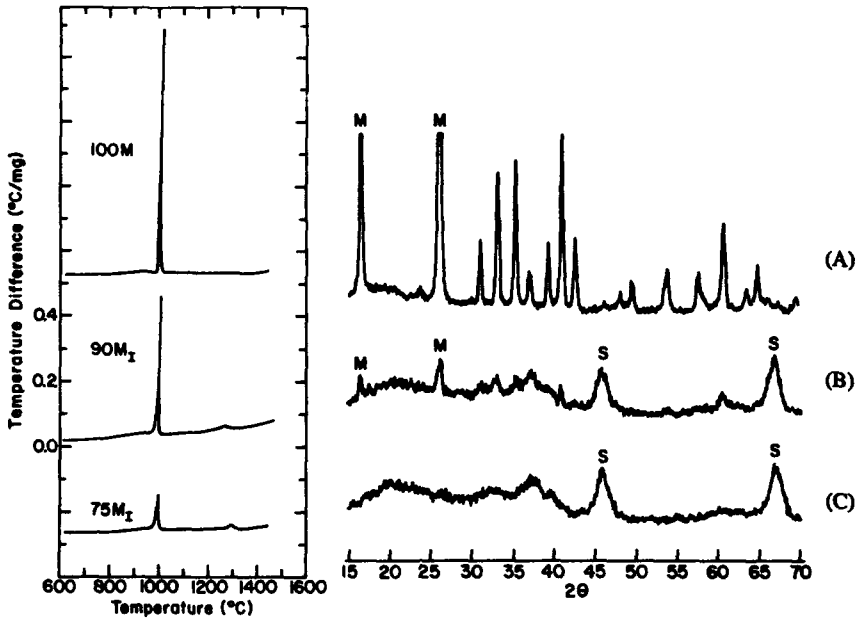


Figure 2. Differential thermal analysis and post-1000°C exotherm x-ray diffraction patterns of A) molecularly-mixed gel (100M), B) 90M$_I$ hybrid gel, and C) 75M$_I$ hybrid gel. (M = mullite, S = spinel)

mixed gel crystallizes directly to mullite during a sharp and intense exotherm at ~1000°C (Figure 2a). In contrast, the hybrid gel containing a colloidal component as low as 10 wt% (90M$_I$) crystallizes only a trace of mullite during its similarly sharp exotherm (Figure 2b). At greater concentrations of the colloidal gel, only a metastable cubic spinel (~$6Al_2O_3$·SiO_2 [11]) is detected following the hybrid gel's rapidly diminishing ~1000°C exotherm (Figure 2c).

Spinel formation during the ~1000°C exotherm is common in molecularly-mixed gels, but has been attributed solely to insufficiently intimate alumina-silica mixing (i.e., the kinetic favorability of maintaining processing-related alumina-silica segregation) [1,3,11-13]. Considering the amount of alumina and silica in the 90M$_I$ hybrid gel that is mixed on a scale known to permit direct mullite formation (Figure 2a), we would have expected 90% mullite at ~1000°C if, in fact, the scale of alumina-silica mixing was a sufficient parameter for predicting phase development. The apparent discrepancy is explained by recalling that phase transformations depend on kinetic as well as thermodynamic factors. The mere presence of a nucleus (i.e., seed particle) of a thermodynamically stable phase does not lead to transformation if kinetic limitations prevent growth. Similarly, given adequate kinetics, the growth of a metastable phase is not prohibited by thermodynamics if this phase is nucleated prior to a stable phase. In the present case the addition of the colloidal gel to the molecularly-mixed gel introduces nuclei for the metastable spinel phase. At ~1000°C, the colloidal gel consists of γ-alumina and amorphous silica, while the molecularly-mixed gel is initially x-ray amorphous. The spinel and γ-alumina are isostructural (i.e., both cubic) and have nearly identical lattice parameters (7.886Å vs. 7.906Å, respectively [23]), so the epitactic nucleation of spinel on γ-alumina is favorable. Kinetic limitations don't exist, as growth of the spinel at ~1000°C is well documented in the sol-gel mullite literature. The

molecularly-mixed gel is thus consumed by growth of the spinel and intrinsic mullite formation is precluded. The result, ironically, is that the molecularly-mixed "seeding gel" is itself seeded with the spinel phase by the system to which it is added.

Mullite crystallization - molecularly-mixed gel

The lack of direct ~1000°C mullite formation in the Type I hybrid gels does not invalidate the original premise of hybrid gel nucleation control, as the relevant requirement is only that mullite seeds form prior to the intrinsic crystallization of the colloidal gel component. Because diffusion limitations at ~1000°C determine the spinel-silica scale of mixing--or, alternately, scale of separation--this mixture is expected to be more readily recombined to form mullite than the discrete alumina and silica phases of the colloidal gel. In terms of phases present, the entire hybrid gel is now effectively colloidal ("diphasic") in nature, yet it contains localized regions of subcolloidal-scale alumina-silica mixing where mullite seed crystallization will be kinetically favored.

The formation of mullite seeds from the intermediate spinel-silica mixture can be isolated in hybrid-type gels consisting only of the molecularly-mixed gel and boehmite (γ-AlOOH). [This is equivalent to a hybrid gel whose processing intentionally omits colloidal silica.] The DTA traces of two such gels, the analogues of $25M_I$ and $50M_I$ hybrids denoted $25M_I'$ and $50M_I'$, are shown in Figure 3. As expected from the presence of boehmite-derived γ-alumina and the behavior shown in Figure 2, these gels' molecularly-mixed components form the spinel-silica mixture rather than mullite at ~1000°C. In the absence of colloidal silica, this mixture becomes the only source of mullite at higher temperatures. Exothermic reactions, confirmed by XRD as corresponding exclusively to mullite formation (no α-alumina), begin at ~1288°C and peak at ~1308°C in both gels (DTA heating rate = 20°C/min). This suggests the operation of a consistent mechanism for mullite seed crystallization from the spinel-silica mixture.

Mullite crystallization - overall

Following the *in situ* formation of mullite seeds, epitactic nucleation of mullite in the colloidal gel can occur. Despite the unique crystallization behavior of the two intrinsic gel components, Type I hybrid gels transform as if they are entirely homogeneous due to the similar "diphasic" nature of the colloidal gel and the spinel-silica mixture. Smooth and continuous sigmoidal transformation curves are obtained during isothermal heat treatments [24], as are single

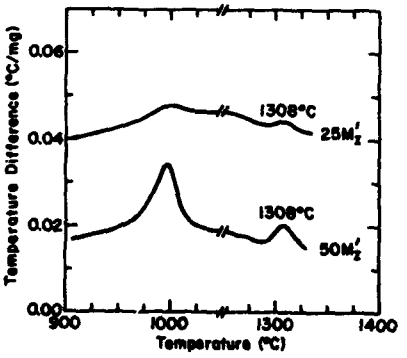


Figure 3. Differential thermal analysis (20°C/min) of $25M_I'$ and $50M_I'$ hybrid-type gels.

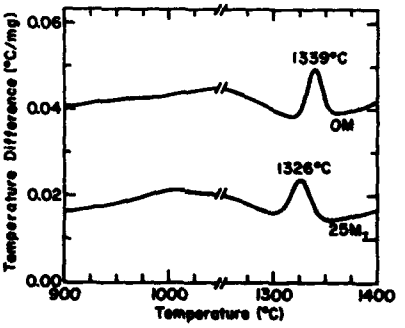


Figure 4. Differential thermal analysis (20°C/min) of colloidal gel (0M) and $25M_I$ hybrid gel.

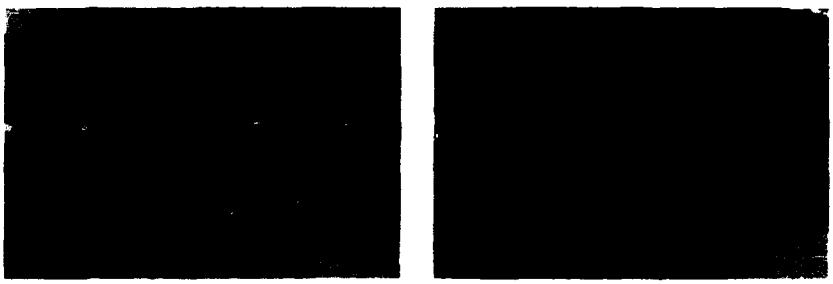


Figure 5. Microstructure of A) colloidal gel (0M) and B) 25M_I hybrid gel heated at 1550°C for 2 h.

DTA exotherms for mullite crystallization (Figure 4). In the absence of nucleation control, the colloidal gel (0M) displays a mullite crystallization exotherm having onset/peak temperatures of ~1320/~1339°C. When 25 wt% of a hybrid gel's mullite is derived from the molecularly-mixed gel (25M_I), these transformation temperatures are lowered to ~1300/~1326°C and the sintered grain size at 1550°C is reduced (Figure 5). These kinetic and microstructural changes are consistent with an increase in nucleation frequency. But the modest increase in grain number density and the failure of the colloidal gel to crystallize more rapidly following seed formation (DTA onset/peak at ~1288/~1308°C, Figure 3) both suggest a low yield of mullite seeds from the spinel-silica mixture.

In the conventional seeding work, it is possible to induce maximum apparent nucleation frequencies by adding several weight percent crystalline seed particles (d ~ 0.1 μm). While the seed/matrix interfacial area expected in the 25M_I hybrid gel is considerably greater than that present in conventionally seeded systems (considering the ultrafine scale and substantial concentration of the hybrid's molecularly-mixed component), the observed impact on the transformation is not proportionately enhanced. The reason for this discrepancy lies in the indirect nature of *in situ* mullite seed crystallization. By passing through the intermediate spinel phase rather than forming mullite seeds directly at ~1000°C, ultimate seeding effectiveness is diminished. Increasing the induced nucleation frequency by using gels >25M_I is not feasible, because the premise of hybrid mullite gels is to maintain a readily densifying colloidal gel matrix. Using higher concentrations of the molecularly-mixed gel is not necessary, however, since hybrid gel seeding effectiveness can approach that of conventional systems when the hybrid gel structure is properly designed to promote direct seed formation.

TYPE II HYBRID GELS

Hybrid gel design

The inefficient formation of mullite seeds in Type I hybrid gels can be traced to growth of the spinel in the same crystal orientation as an underlying γ-alumina "substrate"--a condition that necessarily indicates the loss of autonomy of those molecularly-mixed gel particles in which spinel crystallization occurs. The orientation relationship between the spinel and mullite crystal structures [23,25,26] subseqently promotes an effectively unified transformation from the spinel-silica mixture to mullite among the (oriented) spinel crystallites surrounding a given γ-alumina substrate. The number of particles per substrate can be substantial, as shown by the predominantly spinel crystallization of the 90M_I hybrid (Figure 2b). Consequently, mullite seed concentrations are obtained far below those expected based on the total number of molecularly mixed gel particles added. The molecularly-mixed gel's effective contribution toward seeding is thus severely limited by its particles' cooperative behavior during growth of the intermediate spinel. Controllably limiting the extent of this behavior can serve to increase the seeding gel's effectiveness.

The influence of γ-alumina as a substrate for spinel nucleation can be limited by increasing the size of the molecularly-mixed gel units dispersed in the colloidal gel. The optical clarity of the molecularly-mixed gel dispersion used for hybrid gel synthesis indicates an ultrafine particle size. The tremendous surface-to-volume ratio of such particles makes them especially sensitive to interfacial effects from their surroundings. But if these primary particles are grouped into larger clusters, the interfacial area per unit volume between the molecularly-mixed gel and γ-alumina is reduced. Because a larger fraction of the molecularly-mixed gel is then isolated from γ-alumina, intrinsic phase development is promoted. [Parallel reasoning explains the direct crystallization of detectable mullite in the $90M_I$ hybrid gel (Figure 2b).] This approach runs somewhat counter to that governing conventional seeding, in which effectiveness (based on weight percent added seeds) is increased by minimizing crystalline seed particle size and thereby increasing the interfacial area per unit volume with the host system. The difference, of course, is that the crystal structure of conventionally used seeds is unaffected by the system in which the seeds are placed. The net result of clustering will therefore reflect a balance between enhanced formation of mullite in the clusters and the decreased interfacial area between this mullite and the colloidal gel matrix to be seeded.

Type II gel synthesis

To allow direct comparison between the Type I and II hybrid gels, the molecularly-mixed gel used in this case is the same as that used previously. For Type II gels, however, the particles in this dispersion are grouped into larger clusters bound by hydrolyzed TEOS. The clear, aqueous gel dispersion is mixed with TEOS (and sufficient ethanol to obtain miscibility) to yield a mullite:excess silica ratio of 2:1. The mixture is stirred and heated at 55°C under reflux conditions and gels in ~1 day. From this point the procedure is nearly the same as described above (i.e., dilution with ethanol, redispersion by stirring, heating at 65°C, ethanol-to-water conversion) with the exception of boiling and centrifuging. Boiling does not yield a clear dispersion as it did previously, indicating a larger final particle/cluster size. To retain these clusters in suspension, centrifuging is limited to 5 min at 2000 rpm and is preceded by dilution of the dispersion to a solids content of ~4 wt% and its treatment in 150 ml batches with an ultrasonic horn for 90 sec. Type II hybrid gels containing 5 and 10 wt% of this clustered (molecularly-mixed gel + silica) mixture were prepared and characterized by DTA, SEM and TEM.

Note that because this modified seeding gel contains excess silica, the resulting Type II hybrid gels vary slightly in composition (0M = 73 wt% Al_2O_3, $5M_{II}$ = 71.8 wt% Al_2O_3, $10M_{II}$ = 70.6 wt% Al_2O_3). Such variation can be easily eliminated by small compensating adjustments in the colloidal gel's alumina content. In the present experiments, however, hybrids were prepared using a single batch of colloidal gel to ensure a strictly constant reference for unseeded crystallization behavior and microstructure development. In the temperature range of solid-state alumina-silica reactions (< ~1600°C), the kinetics and microstructure of mullite crystallization are affected far more by increased nucleation frequency than by small variations in bulk composition.

Mullite crystallization - overall

The DTA patterns shown in Figure 6 demonstrate the increased seeding effectiveness of the "clustered" Type II hybrids compared to the homogeneously-interdispersed Type I hybrids. Onset/peak temperatures of ~1285/~1317°C and ~1285/~1308°C are attained in the $5M_{II}$ and $10M_{II}$ hybrids, respectively, at equivalent molecularly-mixed gel contents of only 3.33 and 6.67 wt%. Note that the ~1308°C peak in the $10M_{II}$ hybrid directly coincides with that for the spinel + silica→mullite (seed formation) reaction (Figure 3). This is consistent with the formation of a high concentration of mullite seeds effectively and immediately nucleating further growth in the colloidal gel matrix. Although this shift in DTA peak temperature is still small compared to those possible when crystallization requires only a structural rearrangement (i.e., θ→α-alumina [14]), comparison between Type I and II hybrids shows that the necessary addition of the molecularly-mixed gel is reduced by nearly an order of magnitude when the hybrid gel structure is designed to account for the gel components' interfacial interactions. Determination of the optimum molecularly-mixed gel cluster size would lead to further improvement by balancing direct mullite formation and effective seeding concentration.

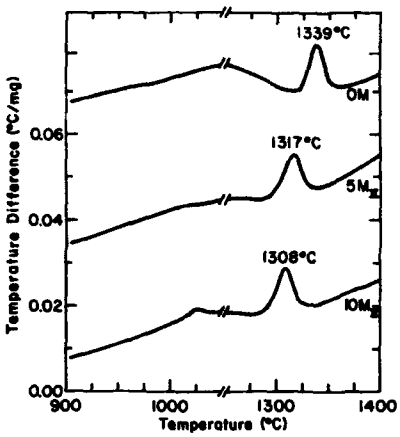


Figure 6. Differential thermal analysis (20°C/min) of colloidal gel (0M) and $5M_{II}$ and $10M_{II}$ hybrid gels.

Evidence of increased nucleation frequencies in the Type II hybrid gels is also seen in SEM micrographs following the gels' sintering at 1550°C (Figure 7). Greater increases in grain number density are now possible with smaller additions of the molecularly-mixed gel, as suggested by the DTA results. But perhaps more significant than the reduction in grain size is the accompanying improvement in microstructural homogeneity seen in TEM micrographs (Figures 8 and 9). At 1300°C the $10M_{II}$ gel's 0.1-0.2 μm grains allow most porosity to be on or close to the grain boundaries (Figure 8b). In contrast, growth of the corresponding colloidal gel grains from fewer mullite nuclei requires that reaction fronts envelop more gel volume--and porosity--necessarily isolating most pores much farther from the grain boundaries (Figure 8a). Because the diffusivity of vacancies through the crystalline mullite lattice is independent of microstructure, shorter times and/or lower sintering temperatures are sufficient for pore removal in the finer-grained gels. After 2 hours at 1550°C, the $5M_{II}$ and $10M_{II}$ gels are fully dense (Figure 9b, c), whereas pores characteristically remain entrapped (and become faceted [6,20]) in the colloidal gel (Figure 9a).

ANISOTROPIC GRAIN GROWTH IN HYBRID MULLITE GELS

The influence of controlled nucleation on microstructural development has generally been of interest only during the progression of a seeded transformation or during sintering of a seeded transformation product. There is, however, the potential for an additional role of seeding--

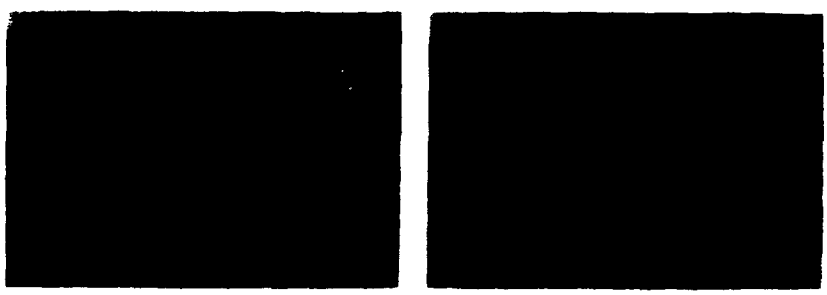


Figure 7. Microstructure of A) $5M_{II}$ and B) $10M_{II}$ hybrid gels heated at 1550°C for 2 h.

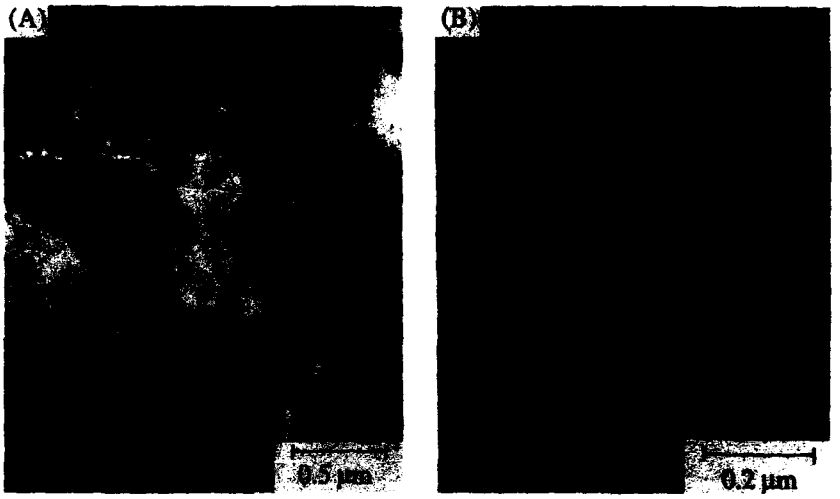


Figure 8. TEM micrographs of A) colloidal gel (0M) and B) 10M$_{II}$ hybrid gel heated at 1300°C for 2 h.

following full transformation or densification--when very fine-grained microstructures are produced. The large grain boundary energy per unit volume inherent in such microstructures makes them more susceptible to grain growth than the unseeded systems. Because unhindered growth of mullite favors the formation of anisotropic, needlelike grains, hybrid gel seeding and proper heat treatment permit tailoring of the microstructure beyond grain size reduction. Control of mullite's high-temperature anisotropic growth with seeding was the focus of recent work by Mroz and Laughner [27], who noted the improvement in toughness that such microstructures may allow by increasing the prevalence of crack deflection.

The development of equiaxed mullite microstructures in high purity sol-gel systems can be qualitatively attributed to kinetic limitations effectively nullifying mullite's thermodynamically preferred anisotropic growth. The "scarcity" of diffusing aluminum and silicon ions leads to their incorporation into the growing grains without diffusion to the most favorable sites. In contrast, more rapid material transport allows diffusing atoms more freedom to occupy thermodynamically favorable positions along the boundary, preferentially extending "chains" of octahedrally coordinated oxygen atoms parallel to mullite's c-axis. Anisotropic growth of mullite is thus observed in the presence of a liquid phase [28], either containing additives or intrinsically present at high temperatures (as predicted by the equilibrium Al_2O_3-SiO_2 phase diagram [29]). Heating mullite to 1650°C, where the liquid phase is present, therefore provides the means for anisotropic grain growth. Its development, however, depends on the driving force for grain growth. As this driving force increases with decreasing grain size, microstructural modification via anisotropic grain growth is expected at shorter times and lower temperatures in the hybrid gels than in the coarser, unseeded system. This is observed in the SEM micrographs of Figure 10, in which the equiaxed colloidal gel microstructure remains stable through 4 hours at 1650°C (Figure 10a, c), whereas the initially finer grains of the 10M$_{II}$ hybrid gel become uniformly elongated after only 1 hour (Figure 10b) and highly anisotropic after 4 hours (Figure 10d).

The observed modification in mullite grain morphology at 1650°C has been confirmed as being primarily a function of nucleation frequency and initial grain size, rather than composition and high-temperature phase equilibria. Colloidal gels slightly enriched in silica (i.e., 70 wt% Al_2O_3 to match the bulk composition of the 10M$_{II}$ hybrid) maintain stable equiaxed grains at 1650°C. Under the same conditions, fine-grained Type I hybrid gels and conventionally-seeded colloidal gels (both 73 wt% Al_2O_3) develop anisotropic-grained microstructures.

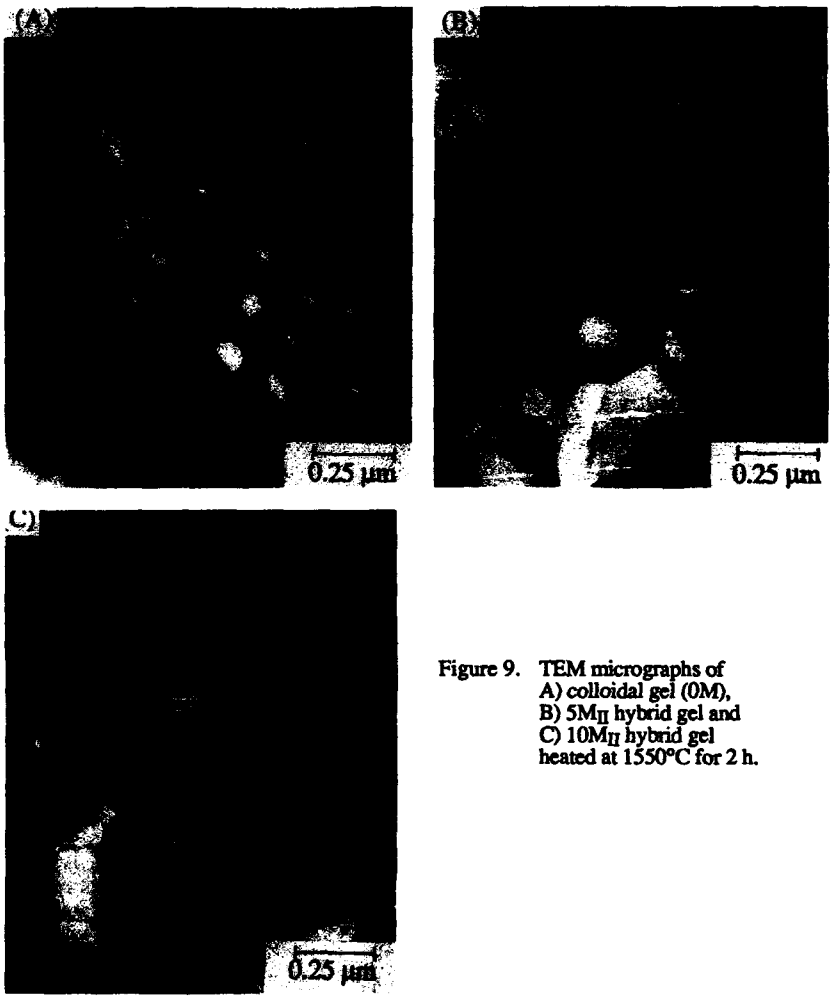


Figure 9. TEM micrographs of A) colloidal gel (0M), B) $5M_{II}$ hybrid gel and C) $10M_{II}$ hybrid gel heated at 1550°C for 2 h.

CONCLUSIONS

The hybrid gel approach utilizes chemical processing to control mullite nucleation and crystallization. Manipulation of alumina-silica mixing and distribution via combination of molecularly-mixed and colloidal gels promotes both *in situ* seed crystallization and low-temperature viscous densification. Although this technique avoids the addition of crystalline mullite seed particles to the gel, complications arise because the amorphous nature and nanometer scale of the gel components allow the hybrid gel interface to dominate phase development. Epitactic nucleation of the metastable spinel in the molecularly-mixed gel prevents direct ~1000°C mullite seed formation, necessitating hybrid gel design to limit the influence of the hybrid gel interface and increase seeding effectiveness. The fine-grained microstructures that are obtained enhance densification and allow for further microstructural tailoring.

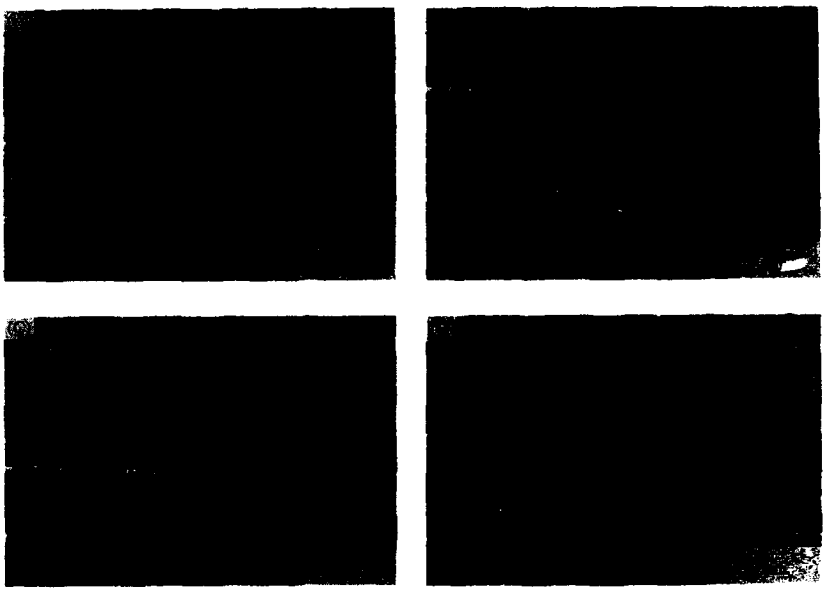


Figure 10. Microstructure of A) colloidal gel (0M), 1650°C, 1 h
B) 10M$_{II}$ hybrid gel, 1650°C, 1 h
C) colloidal gel (0M), 1650°C, 4 h
D) 10M$_{II}$ hybrid gel, 1650°C, 4 h.

ACKNOWLEDGEMENT

This work was performed at the Center for Advanced Materials of the Pennsylvania State University with funding from the Industrial Co-op Program.

REFERENCES

1. M.D. Sacks, H.W. Lee, and J.A. Pask, in Mullite and Mullite Matrix Composites (Ceramic Transactions, Vol. 6), edited by S. Somiya, R.F. Davis, and J.A. Pask (American Ceramic Society, Westerville, OH, 1990), p. 167.

2. B.B. Ghate, D.P.H. Hasselman, and R.M. Spriggs, Bull. Am. Ceram. Soc. 52 (9), 670 (1973).

3. D.W. Hoffman, R. Roy and S. Komarneni, J. Am. Ceram. Soc. 67 (7), 468 (1984).

4. M.G.M.U. Ismail, Z. Nakai, K. Minegishi and S. Somiya, Int. J. High Technol. Ceram. 2, 123 (1986).

5. N. Shinohara, D.M. Dabbs and I.A. Aksay, in Infrared and Optical Transmitting Materials (SPIE Vol. 683), edited by R.W. Schwartz (International Society for Optical Engineering, Bellingham, WA, 1986), p. 19.

6. W.C. Wei and J.W. Halloran, J. Am. Ceram. Soc. 71 (3), 166 (1988).

7. B. Sonuparlak, Adv. Ceram. Mater. 3 (3), 263 (1988).

8. K.S. Mazdiyasni and L.M. Brown, J. Am. Ceram. Soc. 55 (11), 548 (1972).

9. Y. Hirata, K. Sakeda, Y. Matsushita and K. Shimada, Yogyo-Kyokai-Shi 93 (9), 101 (1985).

10. L.A. Paulick, Y.F. Yu and T.I. Mah, in Ceramic Powder Science (Advances in Ceramics, Vol. 21), edited by G.L. Messing, K.S. Mazdiyasni, J.W. McCauley and R.A. Haber (American Ceramic Society, Westerville, OH, 1987), p. 121.

11. K. Okada and N. Otsuka, J. Am. Ceram. Soc. 69 (9), 652 (1986)

12. B.E. Yoldas and D.P. Partlow, J. Mater. Sci. 23, 1895 (1988).

13. A.K. Chakravorty and D.K. Ghosh, J. Am. Ceram. Soc. 71 (11), 978 (1988).

14. M. Kumagai and G.L. Messing, J. Am. Ceram. Soc. 68 (9), 500 (1985).

15. J.L. McArdle and G.L. Messing, Adv. Ceram. Mater. 3 (4), 387 (1988).

16. Y. Suwa, S. Komarneni and R. Roy, J. Mater. Sci. Lett. 5, 21 (1986).

17. G. Vilmin, S. Komarneni, and R. Roy, J. Mater. Res. 2 (4), 489 (1987).

18. G. Vilmin, S. Komarneni, and R. Roy, J. Mater. Sci. 22 (10), 3556 (1987).

19. J.L. McArdle, G.L. Messing, L.A. Tietz and C.B. Carter, J. Am. Ceram. Soc. 72 (5), 864 (1989).

20. J.C. Huling and G.L. Messing, J. Am. Ceram. Soc. 72 (9), 1725 (1989).

21. R.K Iler, J. Am. Ceram. Soc. 47 (4), 194 (1964).

22. J.C. Huling and G.L. Messing, J. Am. Ceram. Soc. 71 (4), C-222 (1988).

23. G.W. Brindley and M. Nakahira, J. Am. Ceram. Soc. 42 (7), 319 (1959).

24. J.C. Huling and G.L. Messing (unpublished work).

25. J.J. Comer, J. Am. Ceram. Soc. 44 (11), 561 (1961).

26. I.M. Low and R. McPherson, J. Mater. Sci. Lett. 7, 1196 (1988).

27. T. J. Mroz, Jr. and J. W. Laughner, J. Am. Ceram. Soc. 72 (3), 508 (1989).

28. W. Von Lohre and H. Urban, Ber. Dtsch. Keram. Ges. 37 (6), 249 (1960).

29. F.J. Klug, S Prochazka, and R.H. Doremus, J. Am. Ceram. Soc. 70 (10), 750 (1987).

MOLECULARLY MODIFIED ALKOXIDE PRECURSORS FOR SYNTHESIS OF DIELECTRIC CERAMICS.

PRADEEP P. PHULE AND FARIDA KHAIRULLA
Department of Materials Science and Engineering,
University of Pittsburgh, Pittsburgh, PA 15261, USA

ABSTRACT:

Chemical synthesis of titanate and zirconate based multicomponent electronic ceramics using molecularly modified alkoxide precursors is discussed. Controlled chemical polymerization of the modified alkoxides was conducted to prepare multicomponent gels which on calcination at moderate temperatures (700 -1000°C) formed high purity, ultrafine powders (e.g. $BaTiO_3$, $ZrTiO_4$, $LiTaO_3$). In the sol-precipitation technique modified precursors were used to prepare ultrafine (< 100 nm) and crystalline powders of such ceramics as $BaTiO_3$ and $BaZrO_3$ at low temperatures (< 100°C), under highly alkaline (pH > 13) conditions.

INTRODUCTION:

Following the pioneering works of Mazdiyasni et al. [1-2] , Flaschen [3], Claubaugh et al. [4] and Pechini [5], several other chemical processes for the synthesis of titanates and zirconates have been reported in the literature [6]. Alkoxide based chemical processing routes for synthesis of capacitor and microwave ceramics suffer from the extreme reactivity of the transition and alkaline earth metal alkoxides [7]. Furthermore, metal alkoxides exhibit a cation dependent differential reactivity i.e. different metal alkoxides (e.g. Ba and Ti) hydrolyze and polycondense at different rates. This can lead to chemical heterogeneities in the final ceramic product. Handling and storage of larger quantities and cost can also pose additional difficulties while using alkoxides as starting materials.

Problems associated with differential and extreme reactivity can be alleviated using such physical methods as lower temperatures, smaller concentrations or pre-hydrolysis of the slower reacting precursor. Central to the theme of this paper is the concept of chemical ways to gain intrinsic control of the transition metal alkoxide reactivity via purposeful modifications in their structure. As will be discussed shortly, such modifications lead to metallorganic precursors which are relatively resistant to hydrolysis. This genre of precursors, referred to as molecularly modified alkoxides, can be effectively used for fabrication of multicomponent ceramics in the form of powders, thin films or fibers [8]. The objective of this paper is to discuss the concept of molecular modification and applications of modified precursors for synthesis of ceramics.

Molecularly modified alkoxide precursors:

Reactions of certain metal alkoxides with such reagents as acetic acid, acetylacetone, esters and alcohols, leading to changes at a molecular level, have been known to chemists for well over twenty years [7,9]. Other modifying agents (e.g. diethanolamine) have also been reported [10]. Following are some examples of such modification reactions [7,9]:

Reactions with alcohols:

$$M(OR)_4 + 4\ HOR' \text{ -----> } M(OR')_4 + 4\ R\text{-}OH \text{ ----- (1)}$$

Reactions with Organic Esters:
$M(OPr)_4 + 4\ CH_3COOBu \text{ -----> } M(OBu)_4 + 4\ CH_3COOPr$ -- (2)

Reactions with organic acids:
$M(OR)_4 + CH_3COOH \text{ ----> } M(OR)_3(CH_3COO) + R\text{-}OH$ ---- (3)

Although such modification reactions have been documented in relatively older literature, it is only recently that modern analytical and spectroscopic techniques have been applied to follow such changes at a molecular level [11,12]. Livage and co-workers [12-14] have reported systematic studies on the chemistry of molecular modification reactions of titanium alkoxides.

Changes in the ionicity of the metal-oxygen bond and, in certain cases, the changes in coordination of the metal cations (e.g. 4 to 6 in case of Ti) are believed to be responsible for the occurrence of such modification reactions and have been discussed in the literature [14,15]. Modification reaction results in precursors with composite organofunctionalities bonded to the central cation. On exposure to water, the alkoxy groups hydrolyze rapidly while as the modifier groups can remain stable. This is believed to render the modified precursors moisture insensitive. For, zirconium n-propoxide modified using acetylacetone, in addition to the proposed modification reaction [16], formation of micellar structures, consisting of chelated molecules on the surface and unmodified molecules in the interior, has also been suggested as a potential mechanism for the decreased rates of gelation [11]. We are presently investigating applications of the modified precursors approach to prepare electronic ceramics (e.g. $BaTiO_3$, $BaZrO_3$, $ZrTiO_4$ and $LiTaO_3$). The objective of this paper is to present the experimental approach and discuss it in relation to the synthesis of such ceramics.

APPLICATIONS OF MODIFIED PRECURSORS FOR CERAMIC POWDER SYNTHESIS

Experimental procedure:

The transition metal alkoxide (e.g. Ti, Zr) is modified using acetic acid or acetylacetone. Deionized water in appropriate proportions can then be added to the modified precursor, without causing undesirable precipitation of transition metal hydrous oxide. The modified transition metal precursors can then be processed further to synthesize thin films, amorphous gels (low pH) and crystalline powders (high pH) at relatively low temperatures (Figure 1). It is inexpensive and convenient to introduce the alkali or alkaline earth components (e.g. Ba,Ca, Li) as carbonates (soluble in acetic acid) or acetates (soluble in water). Under acidic conditions the multicomponent sol can be allowed to gel. The kinetics of gelation can be controlled using the modifier / alkoxide molar ratio as well as the relative concentration of water. The gelation times usually increase considerably (from minutes to hours or days) on increasing the modifier concentration, as a result of the modification reactions discussed earlier. The dried gels can be calcined in air at intermediate (700-1000°C) temperatures to remove the organic fraction, thereby forming crystalline ceramic powders. We refer to this as the sol-gel process.

The multicomponent, stoichiometric sol can be subjected to highly alkaline (pH > 13) conditions to precipitate ultrafine powders at low temperatures (<100°C, upto 4h) which are suitably aged and vacuum oven dried (110-120°C, upto 24h) and washed to yield crystalline ceramic powders. We refer to this process as sol-precipitation.

Sol-Gel synthesis of alkaline earth titanates and zirconates:

Amorphous $BaTiO_3$ gels were prepared using titanium isopropoxide (modified using glacial acetic acid) and barium acetate [17,18]. Results of XRD and thermal analyses showed formation of small amounts of $BaCO_3$ and its subsequent reaction with amorphous titanium rich fractions as one of the mechanisms for formation of crystalline $BaTiO_3$ [19]. This mechanism has been confirmed by other researchers [20,21]. Hennings [21] has shown that, in this process, barium acetate remains within the pores of the titanium gel network. Crystallization of $BaTiO_3$ begins at temperatures as low as 550°C but higher temperatures (upto 800°C) are necessary for complete transformation to $BaTiO_3$, due to the formation of relatively stable barium carbonate. Tomandl et al. [22] used calcium and magnesium acetates to prepare uniformly doped $BaTi_xZr_{1-x}O_3$ powders by this process. Chaput and Boilot [23] have demonstrated the versatility of this approach by applying it to prepare multicomponent titanate-zirconate gels . Mohallem and Aegerter [24] have reported preparation of $BaTiO_3$ films on fused quartz substrates using similar precursors.

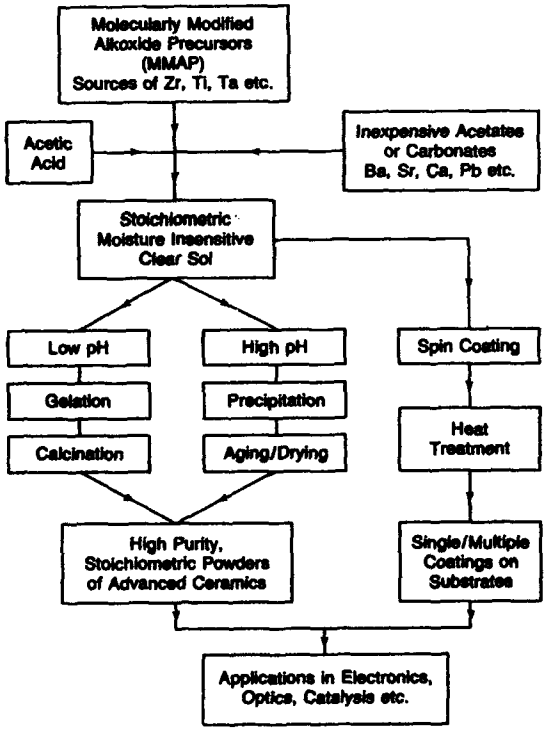


Figure 1. Processing of molecularly modified precursors

Sol-precipitation of alkaline earth Titanate zirconate powders:

As mentioned earlier, in this route mixed stoichiometric sol containing alkaline earth and transition metal precursors is added to a highly alkaline (pH >13) and intensely agitated solution of NaOH or KOH. Precipitation reactions are usually carried out in the temperature range 85-100°C [25]. Other researchers [20,21,23] have used similar precursors to precipitate $BaTiO_3$-$BaZrO_3$ powders. Wilson et al. [26] have developed a similar process for the synthesis of alkaline earth titanates in which the heat associated with chemical reactions was used to attain the necessary temperatures which is an advantage for potential commercial applications. Note that in contrast to the sol-gel route, crystalline and ultrafine powders are obtained at low (< 100°C) temperatures [25]. Similar observations were reported by Flaschen [3] and Kiss et al. [27] who used unmodified titanium alkoxide along with alkaline earth hydroxides. The mechanism proposed by Kiss et al. [27] and mentioned by other researchers [20,23] is an acid-base type reaction between a transition metal complex ($M(OH)_6^{-2}$) and the alkaline earth cation (e.g. Ba^{+2}):

$$M(OH)_6^{2-} + Ba^{+2} \longrightarrow BaMO_3 + 3\ H_2O \quad (M: Ti \text{ or } Zr) \quad \cdots (4)$$

We are presently investigating the kinetics and atomistic reaction pathways involved in synthesis of such ceramics. Barium zirconate is one of such ceramics synthesized in our laboratory using zirconium acetylacetonate and barium acetate as starting materials [28]. Figure 2 shows the morphology of $BaZrO_3$ powders consisting of 2-3 μm sized, apparently spherical particles which may consist of finer primary particles (Figure 3).

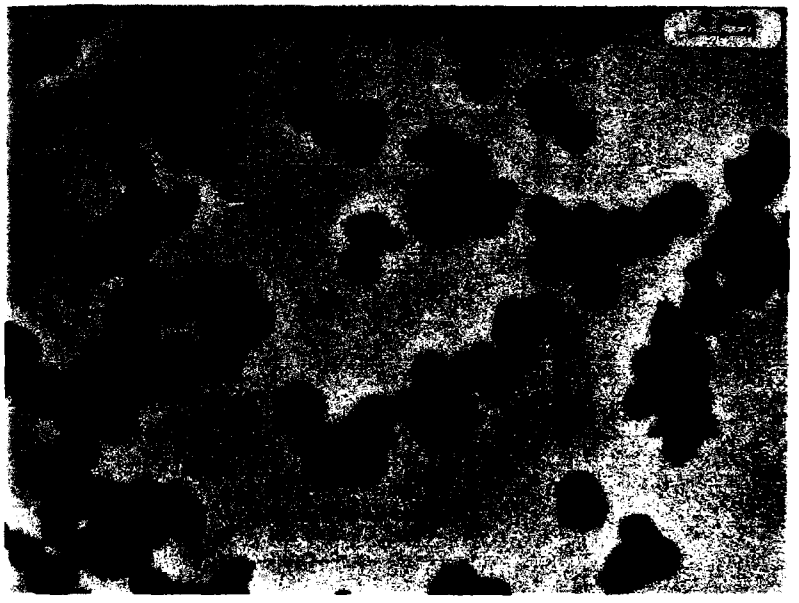


Figure 2. Transmission electron micrograph of $BaZrO_3$ powder prepared using sol-precipitation.

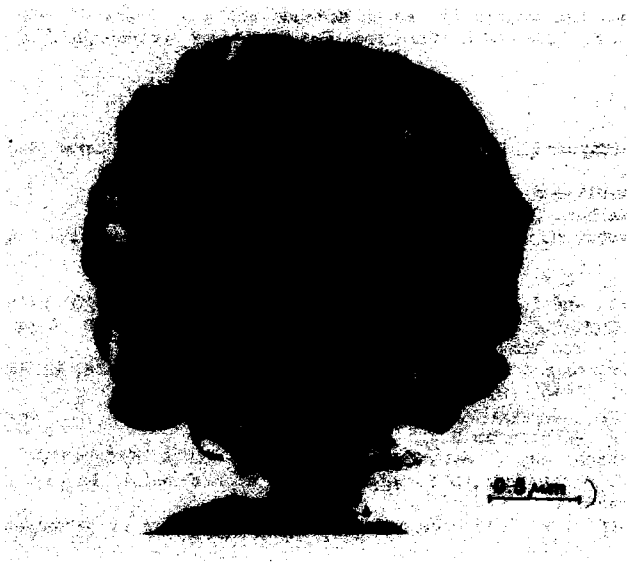


Figure 3. Transmission electron micrograph of a $BaZrO_3$ polycrystalline particle.

Preliminary results of our experiments on synthesis of $BaZrO_3$ tend to suggest that rapid precipitation of transition metal hydroxide, followed by subsequent incorporation of the alkaline earth component, may also be one of the reaction pathways for formation of crystalline ceramics at such low temperatures. Oven drying and aging of the precipitate formed at a given reaction temperature also appear to be important steps during the synthesis of ceramics using this route.

CONCLUSIONS:

Reactions of certain transition metal alkoxides with such reagents as acetic acid and acetylacetone generate moisture insensitive precursors which are useful as starting materials for synthesis of ceramics in the form of thin films or ultrafine powders. Under acidic conditions the modified precursors undergo controlled gelation (sol-gel process). Amorphous gels can be calcined to form ceramic powders. This process has been used to prepare high purity and stoichiometric powders of ceramics in the $BaTiO_3$-$BaZrO_3$ system. Under alkaline conditions (pH >13) the modified precursors can be used to precipitate crystalline and ultrafine (< 100 nm) powders at low temperatures ($<100^0C$) (sol-precipitation). The reaction pathways for the evolution of ceramics from metallorganic starting materials in the sol-gel and sol-precipitation routes are currently under investigation. Efforts are currently underway to synthesize $ZrTiO_4$, $LiTaO_3$ [29] and other electronic ceramic powders using these chemical processing routes.

ACKNOWLEDGEMENTS:

Partial financial assistance through a grant from the Alcoa Foundation is acknowledged. Assistance of George McManus and Bing Zhang of the Department of Materials Science and Engineering, University of Pittsburgh is appreciated.

REFERENCES:

1. K.S. Mazdiyasni, R.T. Dolloff and J.S. Smith, J.Am.Ceram.Soc. 52 [10] (1969).
2. K.S. Mazdiyasni and L. M. Brown, ibid, 55 (1972) 633.
3. S.S. Flaschen, J.Am.Chem.Soc. 77 (1955) 6194.
4. W.S. Claubaugh, E.M. Swiggard and R. Gilchrist, J. Res. Nat. Bur.Std. 56 (1956) 289.
5. M. Pechini, U.S. Patent 3, 370, 697, July 11, 1967.
6. P.P. Phule and S.H. Risbud, J. Materials Science 25 (1990) 1169.
7. Metal Alkoxides, D.C. Bradley, R.C. Mehrotra and D. P. Gaur, Academic Press, (1978) and the references therein.
8. W.C. LaCourse and S. Kim, in Sci. of Ceram.Chem.Proc. (Ed. L. Hench) Publ. Wiley Inter. (1986) 305.
9. The Organic Chemistry of Titanium, R. Feld and P. L. Cowe, (1965) Butterworths, Washington D.C.
10. Y. Takahashi and Y. Matsuoka, J.Mat.Sci.23 (1988) 2239-2266.
11. P.Papet, N. Le Bars, J.F. Baumard, A. Lemonte and A. Dauger, J.Mat.Sci. 24 (1989) 3850.
12. A. Leaustic, F. Babonneau and J. Livage, Chemistry of Materials 1 (1989) p. 240 and p. 247.
13. J. Livage, M. Henry, J.P. Joivet and C. Sanchez, Mat.Res.Soc. Bulletin, Vol.XV, No.1 (1990) 18.
14. J. Livage, M. Henry and C. Sanchez, Prog. Solid.State.Chem. 18 (1988) 259.
15. D.C. Bradley, in Metal-organic Compounds, (Advances in Chemistry), Publ. Am.Chem.Soc. 23 (1959) 10
16. J. C. Debsikdar, J. Non. Cryst. Solids. 86 (1986) 231.
17. P. P. Phule, J.E. Pemberton and S.H. Risbud, in " Symposium On Materials and Processes For Microelectronic Systems" (Editor K.M. Nair et al.) American Ceramic Society (1990) In Press.
18. P.P. Phule and S.H. Risbud, Advanced Ceramic Materials,3 [2] (1988) 183.
19. P. P. Phule and S.H. Risbud, in Better Ceramics Through Chemistry, Mat. Res. Soc. Symp. 121 (1988) 275.
20. F. Chaput and J.P. Boilot, in High Tech Ceramics (Editor P. Vincenzini) Elsevier, Amsterdam (1987) 1459.
21. D. Hennings, in Electroceramics (British Ceramic Proceedings No. 41) (Edited by A.J. Moulson, J. Binner and R. Morrell) (1989) 1.
22. G. Tomandl, H. Rosch and A. Stiegelschmitt in ref 17, p. 281
23. F. Chaput and J.P. Boilot, in Ref.19, p. 21.
24. N.D.S. Mohallem and M.A. Aegerter, in ref 17, p. 515.
25. P.P. Phule and S.H. Risbud, J.Mat.Sci. and Engg., B3 (1989) 241.
26. J.M. Wilson, D.L. Coller and S. Venkatramani, U.S. Patent, 4,670,243, June 2, 1987.
27. K. Kiss, J. Magder, M.S. Vukasovich and R.J. Lockhart, J.Am.Ceram.Soc. 49 [6] (1966) 291.
28. P.P. Phule and F. Khairulla, in Proc. Int. Conf. On Ceramic Powder Processing Science (Editor Gary L. Messing et al.) American Ceramic Society (1990) in press.
29. P.P. Phule, D.Dindinger and F. Khairulla, to be published.

EFFECT OF PRECURSORS ON LITHIUM INFILTRATED SILICA GELS STUDIED BY XPS

S.F. HO AND L. C. KLEIN
Rutgers-The State University of New Jersey, Ceramics Dept., P.O. Box 909, Piscataway, NJ 08855-0909.

ABSTRACT

Lithium silicate gels of composition 15 mole % lithia - 85 mole % silica were prepared by soaking highly porous silica gels in aqueous $LiNO_3$ or methanolic LiOH solutions. The fracture surfaces of these samples were studied by X-ray photoelectron spectroscopy (XPS). High resolution XPS core level spectra were collected such that both chemical shift and atomic concentration could be determined. While the average lithium content was slightly higher in $LiNO_3$ gels, only some of the lithium was associated with the silica network. In contrast, most of the lithium in LiOH gels was associated with the network.

INTRODUCTION

Lithium silicate gels have been prepared in two ways [1]. First, they have been prepared by hydrolyzing tetraethyl orthosilicate (TEOS) with aqueous solutions of lithium salts [2,3]. These are referred to as polymerized gels. Second, they have been prepared by soaking silica gels formed from colloidal sols in lithium salt solutions [4]. These are referred to as infiltrated gels. While the same bulk composition has been achieved with both methods, there are differences between polymerized and infiltrated gels because of the scale on which the two components are mixed [5]. The polymerized gels typically have porosity below 5 nm while the infiltrated gels have pore sizes about 250 nm [6].

The incorporation of lithium in both types of gels has been studied with MASNMR [5,7] and X-ray diffraction analysis [7]. The chemical uniformity has been determined through sectioning and atomic absorption spectroscopy [4,8]. Only in the case of the polymerized gels has XPS been used to follow the incorporation of lithium salts and the evolution of residues from the process [9].

In the previous study [9], polymerized gels were prepared with lithium nitrate using two concentrations of methanol [10]. Both thin films and fracture surfaces were analyzed. The most interesting result of this study was the interaction of methanol and nitrates, where the nitrates were able to oxidize the organics.

A similar study was carried out here on infiltrated gels prepared with both aqueous $LiNO_3$ and methanolic LiOH. The reason for using XPS is that while ^7Li NMR can detect the environment [5], XPS can provide semiquantitative analysis of the gel chemistry. Earlier studies using XPS in alkali silicate glasses [11-13] and, in one case, a sodium silicate gel [14] serve as good references.

EXPERIMENTAL PROCEDURES

Silica gels were prepared by mixing colloidal silica (Ludox-HS40,

Mat. Res. Soc. Symp. Proc. Vol. 180. ©1990 Materials Research Society

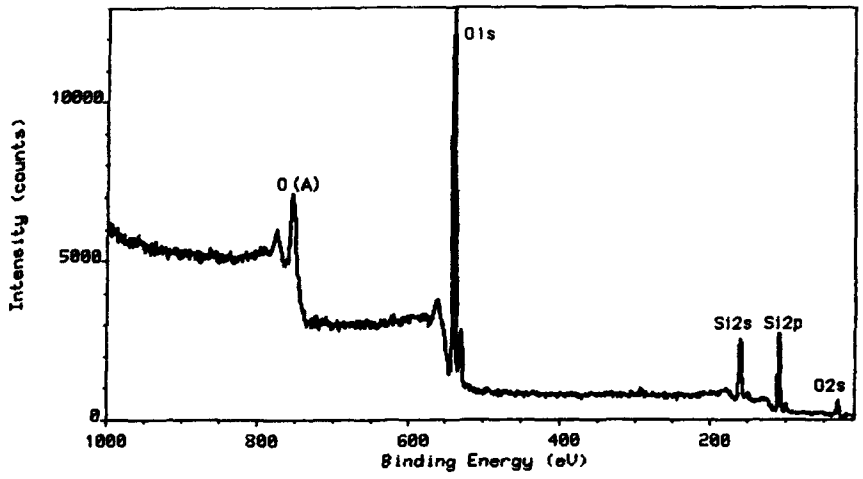


Figure 1 - XPS wide scan of colloidal silica gel before infiltration

Table I Binding Energies (BE) and Atomic Concentrations for $LiNO_3$ and LiOH Infiltrated Gels

	BE,eV	$LiNO_3$ Atomic Concentration %	LiOH Atomic Concentration %
Si 2p	103.2	19.8	23.5
C 1s	285.0	3.7	5.5
	286.8	2.8	2.8
	289.3	1.1	2.3
		7.6	10.6
Li 1s	56.0	12.5	9.2
O 1s	530.9	5.7	8.2
	532.7	45.0	43.7
	534.4	4.3	4.8
		55.0	56.7
N 1s	407.7	3.5	
	404.2	0.8	
	400.0	0.8	
		5.1	

du Pont, Wilmington, DE) with potassium silicate (Kasil-1, PQ Corp., Valley Forge, PA) in a 1:9 weight ratio and gelling with a water/formamide mixture [6]. Following ion exchange to remove Na and K, the highly porous samples were soaked in aqueous $LiNO_3$ or methanolic LiOH and washed finally in methanol [4]. The dried samples were monolithic disks 3.5 cm in diameter and 0.6 cm thick. The porosity of these gels was about 80%. Samples were outgassed at 100°C for one week. X-ray diffraction analysis did not detect crystallinity in these samples.

Fracture surfaces were taken from the edges of the disks. Two measurements were taken for each sample, and two samples were taken for each gel. The fracture surfaces were introduced into a Kratos XSAM 800 system (Kratos Analytical Instruments, Ramsey, NJ), equipped with XPS, AES, ISS and SIMS. Conditions were similar to those used previously to study potassium adsorption on conventional melted SiO_2 [15]. The excitation source used was Mg K alpha X-rays at 1253.6 eV and a base pressure of 10^{-8} Pa was maintained during analysis. The sampling area for XPS is about 2x2 mm^2. Wide scans were performed to check cleanliness and survey the surfaces. High resolution spectra were taken for O1s, C1s, N1s and Li1s regions. The core level spectra were referenced to the C1s lines at 285.0 eV. The binding energies and FWHM (full width at half maximum intensity) for N1s and O1s were checked using powdered lithium nitrate and the N1s peak at 407.7 eV was used for NO_3^-. The Si2p peak was situated at 103.2 eV for all samples, and this was checked by using pure silica gels and fused silica.

The samples were sputtered with 2 keV He^+ ions under 10^{-7} Pa. The beam current was about 2 micro A/cm^2. XPS measurements were conducted before and after 10 min ion sputtering to evaluate effects of ion sputtering on stoichiometry in gel surface layers.

RESULTS

Fig. 1 shows a typical wide scan of the XPS spectra which surveys all the elements present on the surface. The high resolution XPS core level spectra of C1s, O1s, and N1s are shown in Fig. 2. The peak positions have been corrected for static charging of the sample. Since the relative positions of the peaks are constant for a number of analyses, differential charging is not a problem. The binding energy values are referenced with C1s at 285 eV for hydrocarbon, Si2p at 103.2 eV for SiO_2 and N1s at 407.7 eV for NO_3^-. In general, the spectra show broad and asymmetric lines, indicating the overlap of several species. After satellite substraction, a best fit Gaussian computer program was used in order to obtain the relative intensity of each component in each region. The curves are fitted by varying only the intensity, while keeping the binding energy and FWHM values constant, until a close fit was obtained. The jagged lines represent the original, unsmoothed spectra. The solid lines represent the sum for each component, along with the fitted curves representing each oxidation state. The core level binding energies (BE) and atomic concentrations for the species in $LiNO_3$ and LiOH infiltrated gels are listed in Table I. The values of atomic concentration are determined from the relative peak areas of the curve-fitted spectra. The values of binding energy and atomic concentration are the averaging of four measurements for each gel. Additionally, some standards were checked. The O/Si ratio in an ion exchanged silica gel before infiltration was 2.1 which is close to the calculated value of 2.0. The N/Li ratio was 1.2 and the O/Li ratio was 2.9 for a powdered $LiNO_3$ sample.

Fig. 2a shows an example of the C1s XPS spectra. The shoulder at the higher BE side is particularly obvious, indicating a carbon-oxygen species.

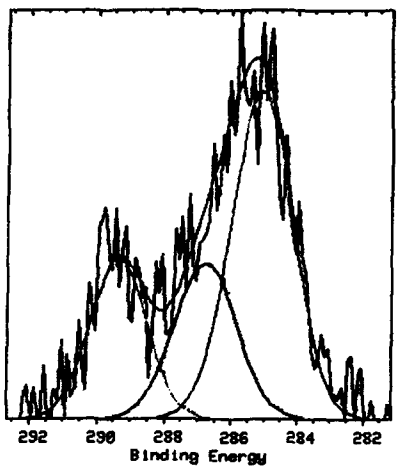


Figure 2a - C1s spectra for LiOH infiltrated gels

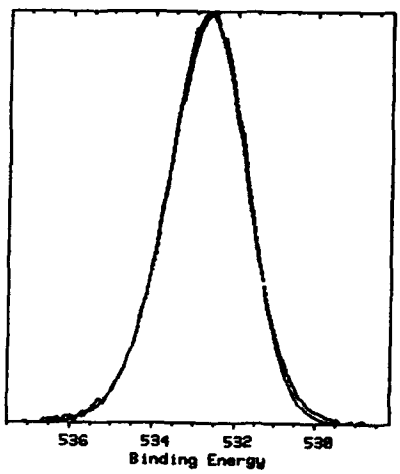


Figure 2b - O1s spectra for silica gel before infiltration

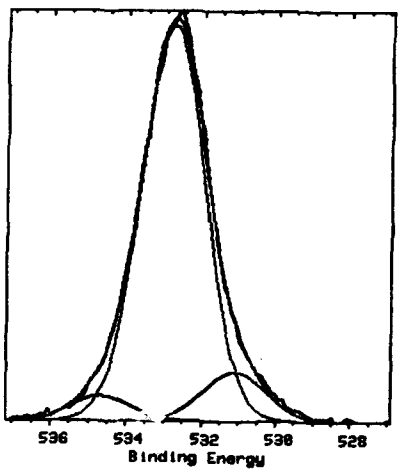


Figure 2c - O1s spectra for $LiNO_3$ infiltrated gels

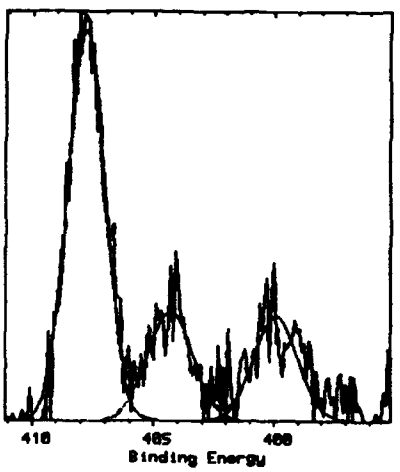


Figure 2d - N1s spectra for $LiNO_3$ infiltrated gels

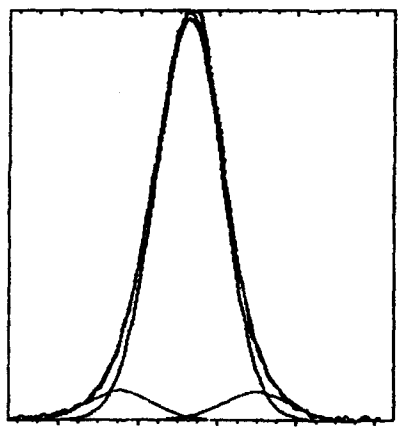


Figure 2e - O1s spectra for infiltrated gels after ion sputtering

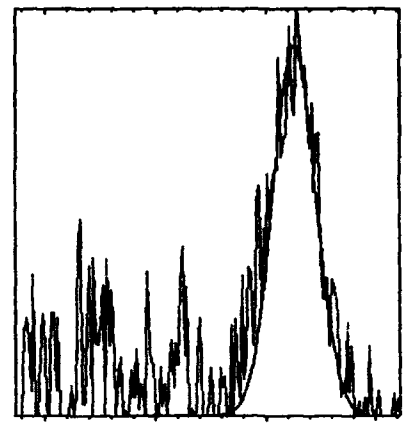


Figure 2f - N1s spectra for $LiNO_3$ infiltrated gels after ion sputtering

Table II Ratios of Species in $LiNO_3$ and LiOH Infiltrated Gels

Ratio	$LiNO_3$*	LiOH**
Li/Si	0.63	0.39
NBO/Si	0.29	0.35
NBO/BO	0.17 (0.16)	0.19 (0.19)
NBO/(BO + NBO)	0.15 (0.14)	0.16 (0.15)
Si/(BO + NBO)	0.51 (0.47)	0.46 (0.46)

* Based on bulk composition 13 mole % Li_2O - 87 mole % SiO_2
** Based on bulk composition 15 mole % Li_2O - 85 mole % SiO_2
Numbers in parentheses are the values calculated from the compositions based on NBO/Si ratios.

Table III Ratios of Species in $LiNO_3$ and LiOH Infiltrated Gels Before and After He^+ Ion Sputtering

	$LiNO_3$		LiOH	
Ratio	Before	After	Before	After
Li/Si	0.59	0.35	0.44	0.33
O/Si	2.66	2.29	2.47	2.34
C/Si	0.42	0.16	0.42	0.33
N/Si	0.24	0.06	----	

Curve-fitting gives rise to three components: hydrocarbon (285.1 eV), C–O (286.7 eV), and O–C = O (289.4 eV) (16,17). Such organics are probably residues from the methanol used for washing and soaking. Oxidized organics may result from esterification during the drying process, especially in the basic LiOH medium.

Examples of the XPS spectra of the O1s regions are shown in Fig. 2b for pure silica gels before infiltration and Fig. 2c of $LiNO_3$-infiltrated gels. The centers of the O1s regions are both situated at 532.7 eV. The O1s peak for pure SiO_2 shows a broad and symmetric line shape and best fit of the spectrum consists of one peak with FWHM = 2.5 eV. The best fit of the asymmetric O1s spectra of the infiltrated gels was obtained by using three peaks having approximately the same width (2.0 eV). The resulting differences in FWHM between pure SiO_2 and alkali silicate gels have also been reported in the literature [14]. Curve fitting was done in Fig. 2c by giving the maximum intensity for the center peak and then adding the second and third components. The shoulder at 530.8 eV is attributed to non-bridging oxygen (NBO) and the third component at 534.2 eV to carboxylate oxygen (O = C – O –), which corresponds to the C1s peak at 289.3 eV (O – C = O). The energy separation between BO and NBO is 1.9 eV, which is consistent with the reported values [12,14].

For the $LiNO_3$-infiltrated gels, N1s XPS spectra, as seen in Fig. 2d, show NO_3^- (407.7 eV) with minor amounts of NO_2^- (404.2 eV) and N^- (400.2 eV). The N1s peak at 400.2 eV is tentatively assigned to N^- based on the published value [18]. A small amount of N^- species was also detected on the powdered $LiNO_3$ sample, indicating that nitrates undergo some decomposition.

Considering the contribution of all oxygen-containing species, the actual BO concentrations are calculated according to:

$$I_{BO} = I_T - I_{NBO} - I_{C-O} - I_{O=C-O} - 3\,I_{NO_3}, \quad \text{where } I_T = \text{total oxygen.}$$

Table II lists the ratios of Li/Si, NBO/Si, NBO/BO, NBO/(NBO + BO) and Si/(NBO + BO). These values agree well with the calculated values given in parenthesis for the indicated oxide compositions.

After 1 hour of X-ray radiation, there was little difference in the XPS spectra, indicating little or no damage to gels, due to exposure to X-rays. However, ion sputtering had a more noticeable effect. This behavior is observed also in melted glasses [19]. In the gels, the XPS spectra of O1s (Figure 2e), C1s, and Li1s are similar before and after sputtering, but the N1s spectra in $LiNO_3$ infiltrated gels are not. As seen in Fig. 2f, the N1s peak appears at 398.7 eV, corresponding to N^{3-}. Although the presence of this species at 398.7 eV is not fully explained, the same species was reported previously [18]. It appears that chemical damages is introduced by using conventional ion sputtering techniques to clean surfaces on gels. Table III shows the concentrations of Li, C and O relative to Si before and after ion sputtering. The ratio of O/Si decreased by 14% and the ratio of Li/Si decreased by 41% for $LiNO_3$. The ratio of O/Si decreased by 5% and the ratio of Li/Si decreased by 25% for LiOH gels. In general, the degree of depletion by sputtering in the LiOH gels is less than that in $LiNO_3$.

DISCUSSION AND SUMMARY

According to the results of the XPS study, the main difference between

$LiNO_3$ and LiOH-infiltrated gels is that the Li/Si ratio is much higher than the NBO/Si ratio in the $LiNO_3$ gels while the ratios are about the same in the LiOH gels. This indicates that the lithium content is higher in the $LiNO_3$-infiltrated gels though less of the lithium is associated with the silica network than in the LiOH infiltrated gels. The Li not associated with the silica network is present as $LiNO_3$ and minor species such as $LiNO_2$. On the other hand, most of the lithium in LiOH-infiltrated gels is associated with the network. It appears that the Si network is attacked by the LiOH at low temperature creating NBO's. This behavior is in agreement with previous studies using ^{29}Si and ^{7}Li solid NMR and XRD [5,7].

Further evidence for this difference is the difference in behavior during ion sputtering. Generally, in alkali silicate glasses, there is a depletion of alkali ions at the surface because alkali ions diffuse inward as a result of the positive surface charge built up during low energy ion bombardment. Other factors such as preferential sputtering and thermal sputtering can not be excluded. Nevertheless, the large amount of Li loss, along with losses of N and O in $LiNO_3$-infiltrated gels, indicates that much of the Li is $LiNO_3$ and not Li associated with silica network. The ion bombardment of $LiNO_3$ results in the formation of alkali metal oxides with preferential loss of nitrogen [20]. In contrast, most of the Li in LiOH gels is associated with the silica network, which causes it to be more stable and resistant to ion sputtering.

ACKNOWLEDGEMENT

The financial support of the Fiber Optic Materials Research Program and NSF Materials Chemistry Program (DMR 88-08234) is gratefully acknowledged.

REFERENCES

1. L. C. Klein, Solid State Ionics 32/33 639 (1988).
2. H. de Lambilly and L. C. Klein, J. Non-Cryst. Solids 102 269 (1988).
3. S. Wallace and L. L. Hench, Cer. Eng. Sci. Proc., 5 568 (1984).
4. N. Le Bars and L. C. Klein, J. Non-Cryst. Solids (1990) to appear.
5. S. P. Szu, M. Greenblatt and L. C. Klein, J. Non-Cryst. Solids 122 (1990) to appear.
6. R. D. Shoup, in Ultrastructure Processing of Advanced Ceramics, Eds. J. D. Mackenzie and D. R. Ulrich (John Wiley & Sons, NY, 1984) p 347.
7. S. P. Szu, L. C. Klein and M. Greenblatt, J. Non-Cryst. Solids, (1990) to appear.
8. I. Schwartz, P. Anderson, H. de Lambilly and L. C. Klein, J. Non-Cryst. Solids 83 391 (1986).
9. S. F. Ho, L. C. Klein and R. Caracciolo, J. Non-Cryst. Solids 120 267 (1990).
10. H. de Lambilly and L. C. Klein, J. Non-Cryst. Solids 109 69 (1989).
11. D. S. Goldman, Phys. Chem. Glasses 22 128 (1986).
12. J. S. Jen and M. R. Kalinowski, J. Non-Cryst. Solids 38, 39 21 (1979).
13. R. Bruckner, H-U. Chun and H. Goretzki, Glastechn. Ber., 51 1 (1978).
14. H. Nasu, J. Heo and J. D. Mackenzie, J. Non-Cryst. Solids 99 140 (1988).
15. R. Caracciolo and S. H. Garofalini, J. Am. Ceram. Soc., 71 C346 (1988).
16. C. D. Wagner, W. M. Riggs, L. E. Davis and J. F. Moulder, Handbook of X-ray Photoelectron Spectroscopy, Perkin-Elmer Corp., Eden Prairie, MN, 1979.
17. D. T. Clark and H. R. Thomas, J. Polymer Science: Polymer Chemistry Edition 16 791 (1978).
18. R. G. Copperthwaite, S. Afr. J. Chem., 36 125 (1983).
19. R. K. Brow, J. Non-Cryst. Solids, 107 1 (1988).
20. S. Aduru, S. Contarini and J. W. Rabalais, J. Phys. Chem., 90 1683 (1986).

PHASE TRANSFORMATIONS IN ZrO_2-SiO_2 GELS

J. Campaniello, E. M. Rabinovich**, P. Berthet*, A. Revcolevschi* and Nonna A. Kopylov***
*Universite de Paris-Sud, Laboratoire de Chemie des Solides, 91405 Orsay cedex, France.
**AT&T Bell Laboratories, Murray Hill, NJ 07974, USA.

ABSTRACT

Transparent sols and gels in the ZrO_2-SiO_2 system containing 25, 50 and 75 mole % ZrO_2 were prepared using tetraethyl orthosilicate (TEOS) and Zr n-propoxide solution in the presence of acids. Heating the gels to 600°C yielded an amorphous product which at higher temperature crystallized with formation of tetragonal and monoclinic ZrO_2. Zircon crystallized slowly at 1600°C. The results are explained by metastable liquid-liquid phase separation in the studied system.

INTRODUCTION

High-zirconia ceramics can be of a potential use as high-temperature coatings and ceramic pigments. Sol-gel routes allow relatively low-temperature preparation of these kinds of materials, and that was the reason we wanted to study phase transformations in the wide range of gel-derived materials in the binary zirconia-silica system. Nogami and Tomozawa [1] studied crystallization in a gel glass of the $3ZrO_2 \cdot 2SiO_2$ composition and found that the tetragonal-monoclinic zirconia transformation leads to a higher fracture toughness of the material. Salvado and Navarro [2] prepared several binary compositions in the same system but their major concern was studying of gel bloating during firing. Monros et al. [3] prepared gels of the zircon $ZrSiO_4$ composition in which part of ZrO_2 replaced by V_2O_5. They showed that vanadium has a decisive effect on the formation of zircon at as low as 800°C, while in the vanadium-free composition, zircon formation was not observed below 1300°C. The purpose of the present study was to examine phase transformations in materials prepared by sol-gel methods in a wider range of the binary ZrO_2-SiO_2 system.

EXPERIMENTAL PROCEDURES

Three compositions containing 25, 50 and 75 mole % ZrO_2 were prepared from tetraethyl orthosilicate (TEOS) and Zr n-propoxide (70% solution in n-propanol). TEOS dissolved in ethanol (1:2 molar ratio) was partially hydrolyzed with 1N HCl (1:1 molar ratio of H_2O:TEOS) and kept at 60°C for 1 hour. This solution was slowly added to the Zr n-propoxide solution while stirring, and the resulting sol was kept at 60°C for 4 days. To achieve complete hydrolysis, 10N HNO_3 was slowly dropped into the sol up to a final H_2O: TEOS ratio equal to 11:1. By aging the sol for several days at 60°C a transparent yellow gel expelling solvent was obtained. Following this procedure gels Zr50A (50 mole % ZrO_2) and Zr25A (25 mole % ZrO_2) were formed. Another way of achieving a complete hydrolysis was to slowly drop the intermediate sol into an excess of 1N HNO_3 (H_2O:TEOS = 270:1). In this case, gelation was obtained by evaporation (gel Zr50B, 50 mole % ZrO_2). Gels Zr25C, Zr50C and Zr75C (25, 50 and 75 mole % ZrO_2 respectively) were similarly prepared but by substituting concentrated HCl for HNO_3 at 5 moles water per 1 mole TEOS total; these sols gelled without expelling solution. All these methods are called "direct methods".

Another method of gels preparation was "redissolution method". Gels Zr50D (50 mole % ZrO_2) and Zr25D (25 mole % ZrO_2) were prepared by drying the mixtures of partially hydrolyzed TEOS and Zr n-propoxide (with the weight loss of about 60%) and by dissolving the formed yellow solids in 1N HNO_3. The new sols, contained about 3.5 wt. % solids, were evaporated on the bath at 60°C up to 25% concentration and then gelled without evaporation.

Mat. Res. Soc. Symp. Proc. Vol. 180. ©1990 Materials Research Society

To obtain monolithic pieces of the gels, they were slowly dried at room temperature, and yellow transparent solids were formed. For phase transformation studies, the specimens were dried at 150°C and then fired at different temperatures for 2 hr (except Zr25C, Zr50C and Zr75C) in an electrical tube furnace at a heating rate of 100°C/hr. The phase compositions were studied using XRD, CuKa. Pore size distributions were determined with an AutoPore 9200 mercury porosimeter (of Micromeretics), and the surface areas were measured by the BET method. Chemical analyses of dry gels were done by the EDX method. DTA curves were obtained using DuPont 9900 Thermal Analyser.

RESULTS AND DISCUSSION

All the gels, although quite similar in their appearance, are different in their pore structure and surface areas, depending on the preparation method. As seen from Table 1, values for the surface area are rather unusual and hardly believable, although they were relatively fairly reproduced when specimens, dried at 250°C, were tested. All the gels prepared with large amounts of concentrated acids showed low surface areas, especially gel Zr50D prepared by the redissolution method. Its surface area value is obviously wrong because this gel, like the others, could not be dried easily to a monolithic piece as would be expected from a material having such a low surface area; besides, this gel had pores as small as 57 nm which cannot correspond to this low value of the area. As known, water molecules form hydrogen bonds with the OH end groups [4], and they can be retained at rather high temperatures. Probably, the acid molecules form strong chemical bonds and create a surface state which cannot allow nitrogen adsorption during the BET surface area measurements, thus disturbing them.

Phases formed in the studied gels during heat treatments are summarized in Table 2; formation of phases in gels Zr50A and Zr50C is shown in Figs. 1 and 2. The most important observation is the difficulty of the formation of zircon $ZrSiO_4$ in these materials. Majority of the gels are amorphous up to at least 600°C, and then crystallization of ZrO_2 starts with formation of tetragonal phase which transforms to monoclinic at higher temperatures. In some cases formation of cubic zirconia was observed (Fig. 3). However, the corresponding X-ray lines were broad, which makes difficult a distinction between the cubic and tetragonal forms of ZrO_2 [5]. The crystallization of silica as cristobalite is only observed for samples with 25 and 50 mole % ZrO_2 fired at 1600°C. Zircon was formed in various amounts after firing at 1600°C, depending on the initial composition and preparation method. In gels Zr25C, Zr50C and Zr75C it was not seen even after 4 hours at 1500°C. The highest amount of zircon was obtained in sample Zr50D prepared by the "redissolution method". However, EDX analysis gave for this sample a Zr:Si composition equal to 58:42 to be compared with Zr:Si = 52:48 for sample Zr50A. Gels with only 25% ZrO_2 seem to crystallize more slowly, especially redissolved gel Zr25D, the only one which appears amorphous even after firing at 800°C. Crystallization of the studied gels proceeds rather slowly: the DTA curves (Fig. 4) do not record crystallization at the heating rate of 10°C/min indicating only the loss of water and organics at low temperatures.

It is interesting to compare this result with another high-temperature system studied by Rabinovich et al. [6]. A gel of the yttrium orthosilicate composition Y_2SiO_5 doped with Tb was prepared and appeared amorphous up to 800°C. After that the orthosilicate started to form without appearance of any of the individual oxides. The authors considered this result as a strong, albeit indirect, indication that formation of a network of the amorphous orthosilicate was already achieved during gelation.

If the same would be the case for the zirconia-silica system, formation of the uniform Zr-O-Si network, especially in the 50:50% compositions, would mean that zircon should appear as the first crystal phase because it is definitely stable below 1676°C (Fig. 5A) [7]. On the other hand, if the pure ZrO_2 is formed inside the gels, it probably would not survive in the

Table 1

Apparent BET Surface Areas and Positions of Maxima on Pore Size Distribution Curves for Dried ZrO_2-SiO_2 Gels

Gel No.	Amount of ZrO_2, mole %	Method of Preparation	BET Surface Area, m^2/g	Maximum of Pore diameters, nm
Zr50A	50	Direct, HNO_3	109	27 to <3
Zr50B	50	Direct, large excess of H_2O/HNO_3	3.8	250 and 21
Zr50C	50	Direct, HCl	5.5	
Zr50D	50	Redissolution	0.1	57
Zr25A	25	Direct, HNO_3	247	

amorphous state up to 600-800°C: Mazdiyasni et al. [8], Komarneni, Roy et al. [9] and Kundi et al. [10] showed that pure zirconia gel crystallizes at as low as 250-300°C, and formation of all three modifications was observed.

An explanation of the difference between the two systems can be found by considering their phase diagrams (Fig. 5). The liquid-liquid phase separation area in the Y_2O_3-SiO_2 diagram (Fig. 5B) is far from the orthosilicate composition, which melts without decomposition. On the other hand, the relatively flat liquidus curve in the ZrO_2-SiO_2 system is interrupted only by a narrow region of the stable phase separation in the middle of the diagram (Fig. 5A) and not by a maximum corresponding to any stoichiometric compound; zircon decomposes before melting. If this region of phase separation widens in the metastable sub-liquidus area [11], it can include the zircon composition. In fact, Salvado and Navarro [2] showed phase separation in the zirconia-silica system by electron microscopy.

Table 2

Crystal Phases in Fired Gel Samples

Temp., °C	Zr50A	Zr50D	Zr50B	Zr25A	Zr25D
600	A	A	A	A	A
800	T(B)	T(B)	T(B)	T(B)	A
1000	T+M	T	T	T(B)	T(B)
1200	T+M	M+T	T+M	T+M	T+M
1600	Z+M+T	Z+M+T	T+Cr+M+Z	Cr+T+M+Z	M+Z+Cr
	Zr25C	Zr50C	Zr75C		
600	A	C	C		
1000	T(B)	T	C or T		
1350	T(B)	M+T	C or T		
1500/0 hr	T	M+T	M		
1500/2 hr	T+X+M	M	M		
1500/4 hr	T+X+M	M	M		

Phases: ZrO_2: C-cubic, T-tetragonal, M-monoclinic; Z-zircon $ZrSiO_4$; Cr-cristobalite; X-unknown phase. "B" means broad lines at the beginning of crystallization.
The major phase appears first in the table.

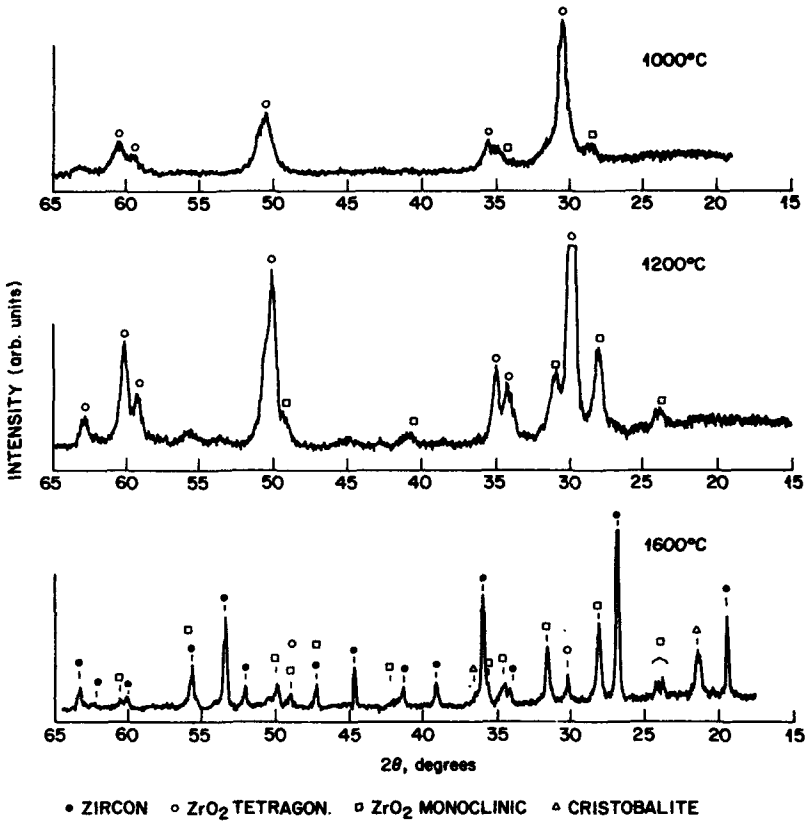


Fig. 1. XRD graphs for gel Zr50A fired at 1000°, 1200° and 1600°C.

Theoretically, the lower the temperature, the wider the region of liquid-liquid phase separation in the same system. In the practical silicate systems, reduction in temperature and increase in viscosity do not allow the development of the separation at very low temperatures, but this is quite different when a structure is formed in a sol in the process of gelation when the initial viscosity is very low. In this case it is thermodynamically reasonable to expect phase separation practically throughout the entire ZrO_2-SiO_2 system, and formation of the zircon structure in the sol-gel would not occur. Instead some kind of interwoven diphasic gel should be formed, one high-silica, and the other - high-zirconia. In this case crystallization of ZrO_2 is not surprising, and formation of zircon should wait until the material is fired at high temperature for a long time. This result coincides with findings of other authors [1,3]. Formation of the tetragonal (or cubic) ZrO_2 as the first phase instead of low-temperature monoclinic phase (stable up to 1200°C) means that the gels have structures more similar to high-temperature melts.

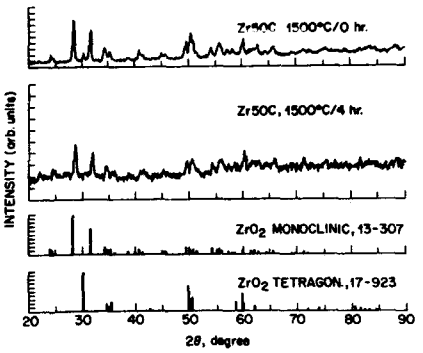


Fig. 2. XRD graphs for gel Zr50C fired at 1500°C for different times. The numbers on the standard patterns for ZrO_2 correspond to the card numbers in ref. [5].

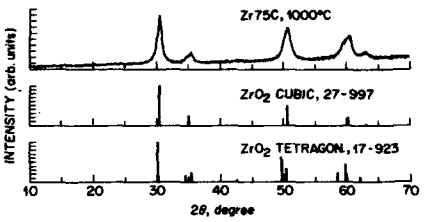


Fig. 3. An XRD graph for gels Zr75C fired at 1000°C.

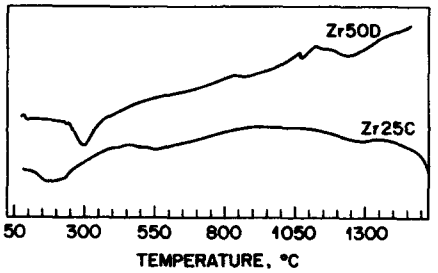


Fig. 4. DTA curves for gels Zr50D and Zr25C.

CONCLUSIONS

Gels in the zirconia-silica system can be formed by cooperative hydrolysis of silicon and zirconium alkoxides in a strongly acid media. All gels are transparent and yellow.

Firing of the gels up to at least 600°C yields an amorphous products while at higher temperatures various forms of ZrO_2 appear. Only at high temperatures (around 1600°C) formation of zircon is observed. This is explained by occurrence of metastable liquid-liquid phase separation in the ZrO_2-SiO_2 system which prevents formation of the homogeneous Zr-O-Si network which could crystallize directly to zircon.

ACKNOWLEDGEMENTS

The authors are indebted to A. J. Bruce for making DTA and to C. R. Kurkjian for helpful discussions.

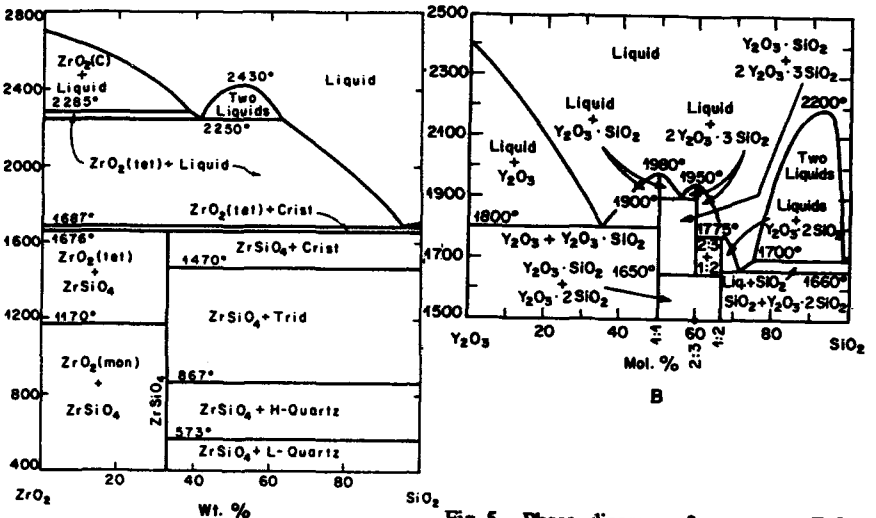


Fig. 5. Phase diagrams for systems ZrO_2-SiO_2 (A) and Y_2O_3-SiO_2 (B) [7].

REFERENCES

1. M. Nogami and M. Tomozawa, J. Amer. Ceram. Soc. *69* (2), 99-102 (1986).
2. I. M. M. Salvado and J. M. F. Navarro, J. Mater. Sci. Lett. *9*, 173-176 (1990).
3. G. Monros, J. Carda, P. Escribano, and J. Alarcon, ibid. *9*, 184-186 (1990).
4. D. L. Wood, E. M. Rabinovich, D. W. Johnson, Jr., J. B. MacChesney, and E. M. Vogel, J. Amer. Ceram. Soc. *66* (10), 693-699 (1983).
5. Powder Diffraction File, Inorganic Phases (JCPOS, Swarthmore, 1984).
6. E. M. Rabinovich, J. Shmulovich, V. J. Fratello, and N. J. Kopylov, Ceram. Bull. *66* (10), 1505-1509 (1987).
7. E. M. Levin, C. R. Robbins and H. F. McMurdie, Phase Diagrams for Ceramists, 1969 Supplement (Amer. Ceram. Soc., Columbus, 1969), Figs. 2388 (p. 107) and 2400 (p. 110).
8. K. S. Mazdiyasni, C. T. Lynch, and J. S. Smith, J. Amer. Ceram. Soc. *49* (5), 286-287 (1966).
9. S. Komarneni, R. Roy, E. Breval, M. Ollinen, and Y. Suwa, Adv. Ceram. Mater. *1* (1), 87-92 (1986).
10. P. Kundi, D. Pal and S. Sen, J. Mat. Sci. *23*, 1539 (1988).
11. R. Roy, J. Amer. Ceram. Soc. *43* (12), 670-671 (1960).

CRYSTALLIZATION OF IN-SITU SiC-MULLITE COMPOSITES FROM MULTICOMPONENT ALUMINA-SILICA GELS

S. Jagota, A. Parvizi-Majidi
Center for Composite Materials and the Department of Mechanical Engineering, University of Delaware, Newark, Delaware 19716.

ABSTRACT

Silica and alumina gels were mixed to make a hybrid of a mullite precursor gel and a silicon carbide precursor gel. The crystallization of these above 1400 °C, to form in-situ composites of silicon carbide whiskers in a matrix of mullite, cristobalite and a glassy phase, was studied for different processing conditions.

INTRODUCTION

The sol-gel route to the synthesis of crystalline ceramics offers a means of control over the final microstructure by suitable manipulation of the precursor structure during the chemical processing step. This can be an attractive way to synthesize ceramic-ceramic composites where the starting precursor materials are chosen and mixed so that, on crystallizing at high temperature, a reinforcing whisker phase and a glass-ceramic matrix form in-situ.

In the alumia-silica gel system, it has been seen that the precursors chosen, and the conditions under which they are mixed and gelled influence the phases formed, the temperature of crystallization and the final morphology attained by the crystals [1-8].

Yoldas and coworkers [1-3] have studied the ultrastructure of alumina-silica gels and its correlation to the high temperature crystallization processes. The precursors used were alkoxides of aluminum and silicon. Two types of gels were identified: (i) polymeric, with an intimate bonding of Al and Si, and (ii) colloidal, with coarser mixing. For the right stochiometry of alumina and silica, mullite forms directly from the amorphous polymeric gel at 980°C; wheras in the colloidal gels a spinel phase forms first and mullite forms between 1300-1400 °C. Pouxviel and Boilot [4] studied the chemical and kinetic features of the reactions between various precursors in this system. Wei and Halloran [5] have looked at the phase transformations in colloidal aluminosilicate gels. Okada and Otsuka[6] have characterized the formation of an intermediate spinel phase in the crystallization of mullite from diphasic alumina silica gels made from silicon alkoxide and aluminum nitrate under different hydrolysis conditions. Chakravorty and Ghosh[7] studied the formation of the spinel phase in and aluminum nitrate derived alumina system with varying amounts of colloidal silica. Messing and Huling[8] used the lower mullite crystallization temperature in polymeric gels compared to colloidal gels to seed colloidal gels with polymeric gels. By this technique, they synthesized in-situ seeded hybrid gels with a lower crystallization temperature and a finer mullite grain size than in unseeded colloidal gels.

Mat. Res. Soc. Symp. Proc. Vol. 180. ©1990 Materials Research Society

In this study, we draw upon this background to synthesize a multi-component gel, which, on crystallization, will form an in-situ composite of silicon carbide whiskers in a mullite matrix. Figure 1 is a schematic of the process. A silicon carbide precursor gel is mixed with a colloidal mullite precursor gel and crystallized to form mullite grains and SiC whiskers along with a glassy phase whose occurence depends on the relative amount of alumina versus silica in the precursor. The SiC precursor gel was made by doping a silica sol with carbon and a nickel nitrate catalyst. These materials, on heat treatment between 1300-1700°C, have been shown by Yamamoto[9] to form SiC whiskers. The mullite precursor gel was a colloidal gel of type used by Yoldas[3].

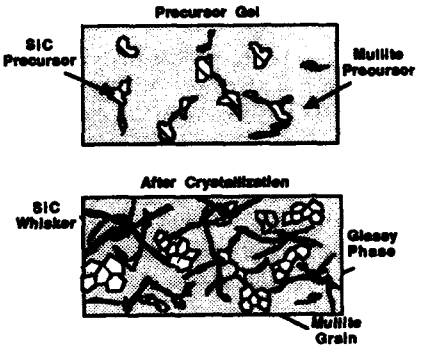


Fig. 1: Schematic of the Crystallization Process

EXPERIMENTAL

The mullite precursor gel was made by hydrolyzing Al-sec-butoxide and adding to it tetra-ethyl-ortho-silicate to form a colloidal mullite precursor gel [1-3]. The silicon carbide precursor sol was a silica sol made by hydrolysis of TEOS under acidic conditions[10]. A low water content gel with linear polymers was made. The linear polymer recipe was used to enhance whisker growth of SiC. This sol was doped with 325 mesh carbon particles and 7wt% nickel nitrate with respect to the weight of silica. The carbon content in the gel was varied from 25wt% to 100wt% with respect to the weight of silica. This silicon carbide precursor sol was added to the mullite precursor before the latter gelled, the mixture homogenized by stirring, and allowed to gel. It gels in a relatively short time of 2-3 minutes, trapping the SiC precursor sol (with the carbon particles) homogeneously throughout. This hybrid gel was dried at 60°C and crystallized above 1400°C in a reducing atmosphere of nitrogen + 1% hydrogen gas. TEM specimens of the gels were made by dipping tungsten grids in the wet gel to form a thin film on the grids. These were crystallized above 1400°C and could be viewed directly in the TEM. Table I lists the different conditions used.

Table I: Experimental Conditions Used

Specimen	Overall Al_2O_3 vs SiO_2	Mullite Pre. vs. SiC Pre.	C-content in SiC Precursor	Crystallization Temperature
1. MuSiC-1	18 wt% Al_2O_3 82 wt% SiO_2	47wt%Mullite 53wt% SiC	25% of SiO_2 by wt. in SiC Precursor	1400°C
2. MuSiC-2	18 wt% Al_2O_3 82 wt% SiO_2	47wt%Mullite 53 wt% SiC	25% of SiO_2 by wt. in SiC Precursor	1500°C
3. MuSiC-3	24 wt% Al_2O_3 76 wt% SiO_2	73 wt%Mullite 27 wt% SiC	100% of SiO_2 by wt. in SiC Precursor	1500°C

RESULTS AND DISCUSSION

Figure 2a shows a TEM micrograph of a specimen with 73% mullite precursor and 27 % SiC precursor with a carbon content of 25% by weight of silica in the SiC precursor, crystallized at 1400 °C (MuSiC-1 in Table I). Mullite grains are seen growing throughout the film in an amorphous, silica-rich matrix. Very fine SiC whiskers, 5-10 nm in width, can be seen growing between the grains in the glassy phase. The X-Ray diffraction pattern of this sample, shown in Figure 2b shows the presence of mullite and cristobalite. No silicon carbide was detected nor were any larger silicon carbide whiskers seen, indicating that, at 1400 °C, the reaction to form silicon carbide whiskers was very slow and the very fine and few whiskers formed only in the thin film samples.



Figure 2a: TEM micrograph of a thin film sample of MuSiC-1.

On increasing the crystallization temperature of the same precursor to 1500 °C (specimen MuSiC-2 in Table I), growth of silicon carbide whiskers was seen to be enhanced as seen in Fig. 3a. The X-ray diffraction pattern shows the presence of β-silicon carbide with the appearance of the characteristic peak near $2\theta = 36^{o}$ as can be

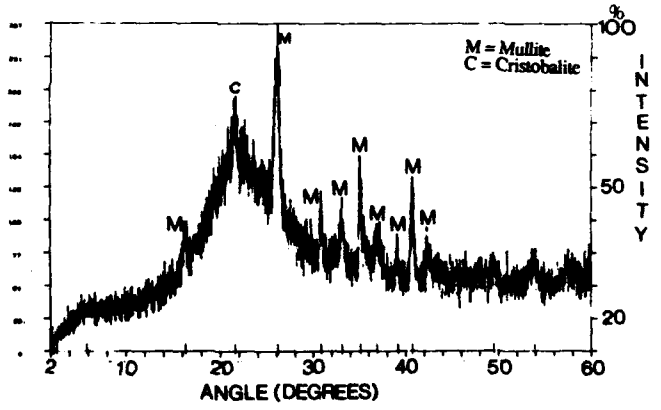


Figure 2b: Powder X-Ray diffraction pattern of MuSiC-1.

seen in Fig. 3b. The microstructure now consists of longer (10-20μm) whiskers growing out from whisker clusters as shown in Fig 3a. The clusters, which are the starting points for the whisker growth, are often found in "craters" 10-20μm in diameter. Since the whiskers are thought to grow from the interface between the carbon particles and the siliceous material in this reaction [9], and the size of the clusters correlates well with the carbon particle size, it is likely that the "craters" represent the sites where the carbon particles were present. These whisker growth sites are surrounded by the glassy phase and fine (0.5-1.0μm) grains. It is likely that the whisker clusters will be surrounded by the glassy phase since the whiskers grow in the high silica regions of the hybrid gel. This also correlates well with the observations on MuSiC-1 where the fine whiskers are seen growing into the amorphous region.

It is clear that the whisker length and distribution would depend on the extent of SiC precursor gel within the hybrid gel and the size and distribution of the carbon particles within the SiC precursor gel.

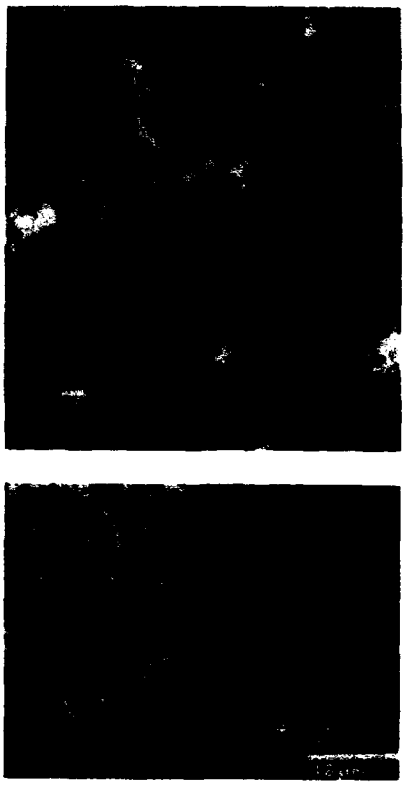


Figure 3a: SEM micrographs of MuSiC-2 (Fracture surface).

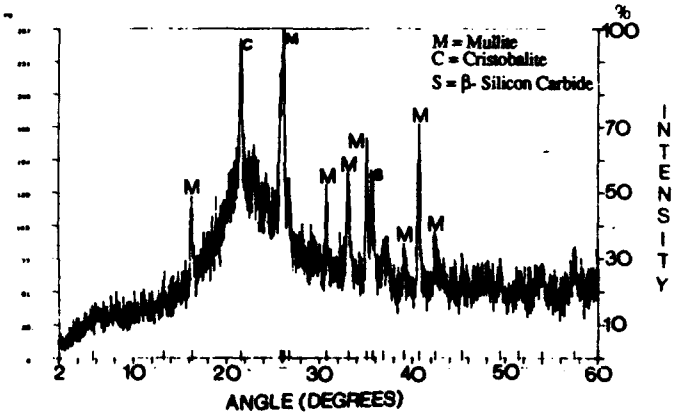


Figure 3b: X-Ray pattern of MuSiC-2.

Thus, reducing the size and number of the carbon particles and reducing the size of each SiC precursor gel pocket should lead to longer and fewer whiskers with finer "craters" which can be healed by sintering of the glassy phase.

This is borne out by observations on the third set of samples (MuSiC-3 in Table I) which had four times as much carbon in the SiC precursor gel as the first two and was crystallized at 1500 °C. Here, the glassy phase did not form - the sample crumbled easily into a powder. Large areas of interconnected whisker network "mats" were seen as shown in Fig. 4a. As expected, the whiskers are shorter in this sample (3-5μm in length) as the distance between carbon particles on which they nucleate is smaller. The X-ray pattern from this sample (Fig. 4b) shows the presence of β-SiC along with mullite and cristobalite. The β-SiC peaks have grown in intensity compared to MuSiC-2. This indicates that increasing the carbon content of the SiC precursor leads to growth of SiC whiskers at the expense of the glassy phase which was seen to be present in MuSiC-1 and MuSiC-2 but not in MuSiC-3.



Figure 4a: SEM micrographs of MuSiC-3

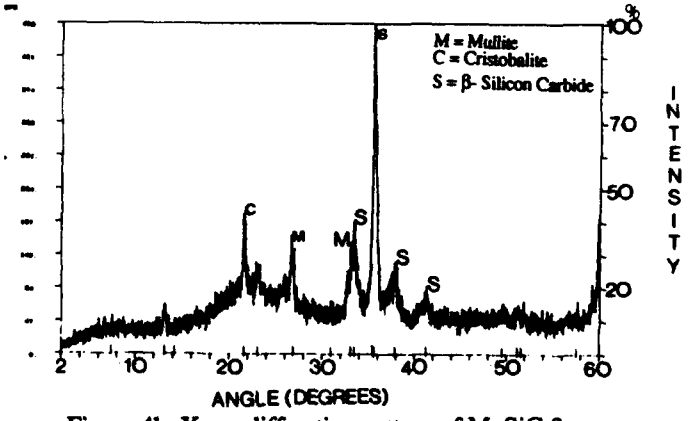


Figure 4b: X-ray diffraction pattern of MuSiC-3.

SUMMARY

(i) High silica, multicomponent gels of alumina-silica form mullite, cristobalite, and a glassy phase rich in silica on heat treatment above 1400°C.

(ii) Two seperately hydrolyzed sols (a "mullite precursor" and a "silicon carbide precursor") are mixed, gelled and crystallized. An in-situ composite of silicon carbide whiskers in a matrix of mullite, cristobalite and a glassy phase rich in silica is formed.

(iii) Since the whiskers are surrounded by a silica rich glassy phase, and grow out from localized clusters, it is clear that a physical separation between the two precursor gels was achieved within the scale observed.

(iv) At 1400°C, the silicon carbide whiskers formed are very fine (2-10nm in diameter), and can only be seen using the TEM.

(v) At 1500°C, "pockets" of whiskers are seen surrounded by a matrix of mullite and the glassy phase.

(vi) On increasing the carbon content with respect to the silica, the siliceous material preferentially transforms to silicon carbide whiskers and the glassy phase is absent. The resulting ceramic is an intertwined whisker network with loose mullite pieces.

ACKNOWLEDGEMENTS

Support for this work from the Air Force Office of Scientific Research under contract number AFOSR-87-0383 is gratefully acknowledged. Dr. M.A. Saltzberg of E.I. Du Pont de Nemours & Co. is thanked for his help with the X-Ray measurements. D. Liu of Univ. of Delaware is thanked for his help with microscopy.

REFERENCES

1. Yoldas B.E., Ceram. Bull., **59,** (4), p. 479, 1980
2. Yoldas B.E., Pask J.A., Zang X.W., Tomsia A.P., J. Am.Ceram. Soc., **70,** (10), p. 704, 1987
3. Yoldas B.E., Partlow D.J., J. of Mater.Sci., **23,** p. 1895, 1988
4. Pouxviel J.C. and Boilot J.P., p.197 in "Ultrastructure Processing of Advanced Ceramics" , J.D. Mackenzie and D.R. Ulrich (Eds.), John Wiley &Sons,1988.
5. Wei-Cheng W., Halloran J.W., J. Am. Ceram. Soc., **71,** (3), p. 166, 1988
6. Okada K., Otsuka N., J. Am. Ceram. Soc., **69,** (9), p. 652, 1986
7. Chakravorty A.K., Ghosh D.K., J. Am. Ceram. Soc., **70,** (3), p. C46, 1987
8. Huling J.C., Messing G.L., J. Am. Ceram. Soc., **72,** (9), p. 1725, 1989
9. Yamamoto A., US Patent # 4,500,504, Feb.1985
10. Klein L.C., Ann. Rev. Mater. Sci., **15,** p.227, 1985

PART VII

Thin Films and Fibers

RHEOLOGY FOR BETTER SOL-GEL FIBER AND FILM FORMATION

C. W. MACOSKO, M. L. MECARTNEY, AND L. E. SCRIVEN
Department of Chemical Engineering & Materials Science, University of Minnesota, Minneapolis, MN 55455

ABSTRACT

Flow behavior of a liquid or suspension depends on how stress varies with strain rate, strain-rate rotation, and strain history, as well as the progress of evaporation, extent of reaction, and degree of aggregation in sol-gel systems. Rheological methods suitable for measuring flow behavior are summarized. Examples of measurements and microstructural observations by transmission electron microscopy made during gelation of four sol-gel systems are presented. The relation of rheological response to microstructure is discussed.

INTRODUCTION

During manufacturing of coated films continuously in a steady-state process like die coating or slot coating, the liquid being coated is first *extended* in one direction inside the die as the incoming flow is spread out into a layer proceeding to the exit slit. Then it is *extended* in a second direction in the deposition zone as the exiting flow is accelerated to the speed of the substrate being coated. Meanwhile it is narrowed in a third direction. The liquid is also *sheared* inside the die and in the deposition zone, because liquid does not slip at the die surfaces or the substrate surface. In drawing fibers, the liquid being processed is *extended* in one direction while being narrowed in the other two; it is *sheared* inside the passages and orifice of the die but very little within the fiber. The liquid's drawability, or spinnability, depends on its response to extension. Coating or spinning is followed by solidification by drying and reaction, which induce shrinkage, the converse of extension, and generally shear as well.

Rheology

The ways that liquids and not-yet-rigid solids respond to extensional, or compressional, and shearing stresses, or strains, are the subject of rheology [1,2]. Rheology pertains not only to steady-state formation of films and fibers, but also to batch processing like spin coating and dip coating, which may be dominated by transient effects.

The way that a liquid responds to shear and extension is a matter of its microstructure. When compact molecules of nanometer scale constitute a liquid, local rearrangement by thermal motions is ultrafast (e.g. nanoseconds and quicker) and so is relaxation into local thermodynamic equilibrium structure. Then viscosity, the ratio of resulting stress to the responsible shear rate or extension rate, depends only on temperature, pressure and composition, and not on deformation rate. The liquid is Newtonian.

In contrast, when colloidal particles of sub-micron or micron scale densely populate a liquid suspension, Brownian movement is sluggish, thermodynamic equilibrium may be practically unattainable, and relaxation into local mechanical equilibrium structures is little faster than flow itself (e.g. time scales of fractions of a second and up) [3]. Then viscosity depends directly on deformation rate and is typically shear-thinning (viscosity falls with rising shear rate) and often extension-thickening (viscosity rises with rising extension rate). Tenuous mechanical assemblies erected by colloidal forces between particles usually play a big role, because they can stand up, with only minor creep, to low stresses up to some level (yield stress) and during flow break up by degrees into dynamic populations of smaller and smaller assemblages as the applied stress mounts.

In yet another contrast, when long, thermally writhing, entangled, and ultimately breakable polymer molecules constitute a melt liquid, or densely populate a solution with more compact solvent molecules, there is a whole range of size scales of arrangement at thermodynamic equilibrium. The shortest of these can be approached rapidly by thermal motion, the longest not,

Mat. Res. Soc. Symp. Proc. Vol. 180. ©1990 Materials Research Society

so that there is a spectrum of relaxation times into local equilibrium structures (e.g. milliseconds to minutes and longer) [4]. The viscosities of polymeric solutions and melts depend not only on deformation rate, but also on the history of deformation if the responsible flow is not as slow as the slowest mode of internal relaxation. Contributing to this are the more or less tenuous entanglement nets when the chain-like molecules are long, especially if they are branched or bridged: during flow these nets may break up by degrees as the applied stress is raised; in extreme cases individual molecules too may break. In steady shearing, viscosity often drops for a while, a behavior called thixotropy; in steady extension (which is hard to prolong), viscosity may rise for a bit, which is called rheopexy. Moreover, owing to the writhings and entanglements of the chain-like molecules, concentrated solutions and melts are elastic like rubber to a degree, particularly when applied stress changes rapidly; that is, the material possesses elastic moduli, the ratios of resulting stress to the responsible shear or tensile deformation. In general, polymeric solutions and melts are *viscoelastic*, their viscosities and elasticities depending on molecular size, stiffness, branching and bridging (crosslinking), on the distributions of these properties, and on the history of deformation or strain. Because of the thermally-driven relaxation modes, the important history at any instant is the rates of the most recent deformations: viscoelastic liquids are said to have fading memories.

The distinction between shearing and extending flow bears emphasizing. Long, flexible and writhing molecules in a melt or good solvent shape up as random coils at equilibrium. In shearing flow every neighborhood of the liquid rotates (such a flow is said to have vorticity), but the rate-of-strain field is everywhere fixed and the same. The principal direction of extension is 45° from the velocity direction; of compression, 135°. Consequently, when the strain rate is enough to deform the molecular coils, they tend to align in the principal direction of extension but only temporarily, between 180° tumbles that carry them through a compressional orientation. Thus they do not suffer a persistent extensional strain. In extending flow they do, for no neighborhood rotates at all with respect to the principal direction of extension, which coincides with the velocity direction, and that of compression, which is at 90°. If the flow is strong and long enough, the extensional strain can draw coils out straight and even break the extended molecules. It is the strain-rate rotation and thus the persistence of strain that distinguishes extending from shearing flow.

In dip coating, shear rates and extension rates are low, from around 1 to 100 s^{-1}. In spin coating, shear rates may peak early in spin-off at 10^5 s^{-1}, extension rates at 10^3 s^{-1}, but all fall quickly thereafter. In slot and roll coating, shear rates are often around 10^4 s^{-1}, extension rates 10^3 to 10^4 s^{-1}. In fiber drawing, extension rates can reach 10^3 s^{-1} and more, according to the draw speed and diameter reduction; beyond the orifice from which the fiber is drawn there is little shearing. Thus the flows used to form films and fibers mix shear and extensional deformation in various proportions and cover a wide range of rates [5]. The response of the liquid to any mix, and means of analyzing and predicting that response, are the stuff of rheology.

Sol-to-gel rheology

Sol-to-gel processing is a great challenge because a system starts as a solution of various compact molecules, or as an unconcentrated suspension of submicron colloidal particles in such a solution. Then it transforms through reaction or aggregation or both, usually accompanied by evaporation. The system becomes a denser and denser population of lengthening, branching, entangling, bridging polymer molecules or similarly growing, ramifying, interfering, aggregating colloidal particles. As it does so it loses its simple Newtonian rheology, acquires deformation-dependent viscosity and then elasticity, likewise deformation-dependent. Ultimately the assemblages responsible for this viscoelastic behavior develop a strong enough network of elastic linkages on large enough scales to qualify the transformed system as a gel. That is an elastic solid that creeps negligibly in time intervals of first interest. Longer time scales matter, though, and the challenge to rheology continues after a gel state is reached. Subsequent chemical reaction, colloidal consolidation, and drying induce strains, stresses, internal relaxation, external creep, and sometimes breakage of the solid material [6].

The goal is to understand how flow behavior and structure development relate to the way the *state of stress* throughout film or fiber formation responds to *deformation* (*strain rate, strain-rate rotation,* and *strain history*), and is influenced by the *extent of reaction* and *degree of aggregation,* and by the *progress of evaporation* in sol-gel systems.

In the next section we review the major rheological methods available and discuss which might be best for sol-gel studies. Then we present some new rheological and microstrucural measurements taken during the gelation process on four different sol gel systems, including what may be the first extensional data.

RHEOLOGICAL MEASUREMENTS

Both stress and deformation need to be measured over a range of stress levels, deformation magnitude and rate. Normally in complex flow geometries, such as die coating and fiber drawing, deformation is determined by careful measurement of tracer displacements and velocities in a transparent fluid. The spatial variation of stress components can be measured by optical techniques. While such studies are quite important they are difficult, time-consuming and require special liquids.

The strategy of the rheologist is to pick a very simple flow geometry such that the kinematics can be determined from boundary displacements or flow rates and the stresses evaluated from boundary forces or pressures. Such simple flow geometries in which both stress and deformation can be determined for an unknown material are called *rheometers*. In addition to stress and deformation a rheometer must be able to control the state of the sample, i.e. its temperature, composition, residence time. This is particularly important for sol-gel systems which react or aggregate with time at a rate that varies with temperature and may depend strongly on evaporation of volatiles. Settling can also be a factor.

There are two basic rheometers: simple shear and extension. The shear geometries are much more common and there is a wide choice of commercial instruments. Extension is much more difficult to achieve in a rheometer, especially for low viscosity liquids.

Shear response

Figure 1 shows the four most common shear rheometers. The first three, concentric cylinders, cone and plate, and parallel plates, can all be obtained by simply changing fixures on one well-constructed rotational instrument. The capillary rheometer requires a separate pressure driven apparatus. Both the capillary and the parallel plates generate non-homogeneous deformations. This means, as explained below, that they cannot accurately measure strain dependent material functions (standard types of response).

For sol-gel work the concentric cylinders rheometer is our first choice. With a narrow gap the flow is homogeneous and the complete range of shear material functions can be measured. The concentric cylinders arrangement is well suited for loading and unloading low viscosity liquids. The ratio of surface to volume is low enough that evaporation can be easily prevented. The planes in which the liquid is sheared lie perpendicular to gravity, which reduces the effects of settling. Good temperature control is possible with a recirculating liquid bath.

Figure 2 indicates the ranges of viscosity and shear rate that can be measured with the rheometers available in our laboratory; these are typical of state-of-the-art commercial instruments. The concentric cylinders rheometer, in both the rate-controlled and the stress-controlled versions, is the most sensitive for low viscosity measurements. With the parallel plates rheometer it is easy to set a very narrow gap and reach higher shear rates. The capillary rheometer is also useful for high shear rates, and because it has no free surfaces it is the best choice for evaporation control. Moreover, it can serve as a first simulation of process flows in pipes, ducts, and passages. The cone-and-plate rheometer is used when normal stresses in viscoelastic liquids are to be measured.

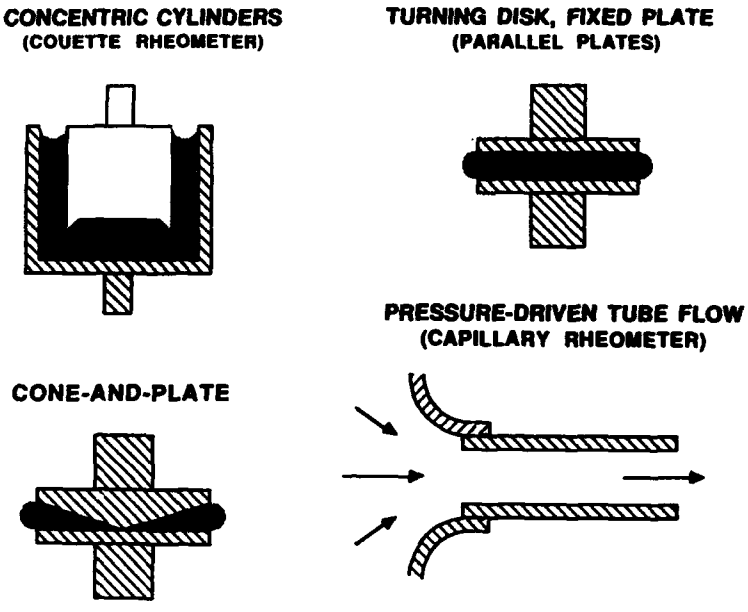


Fig. 1 The four most common shear rheometer geometries.

Once a rheometer has been chosen there is still the question of just what to measure. The rheological material functions can be broken down into three strain regimes: small strain, large strain, and steady straining. If the strain (or, equivalently, the rate of strain times time) is small, the stresses vary linearly with strain. They are independent of the type of strain; shear and extension give the same result. A viscosity can be defined which depends only on time or, equivalently, frequency. The regime in which this can be done is called linear viscoelastic and is illustrated by the central curve in Fig. 3 [cf. 4].

The linear viscoelastic regime is particularly useful for following certain kinds of microstructural change in a material with time. For example, by continuously oscillating a sol-gel sample at small strain and measuring the in-phase and out-of-phase stress, the gelation process can be followed from low viscosity liquid to rubbery gel. In this there is some similarity to spectroscopic techniques like infrared. The small amplitude wiggles at various frequencies are means of probing the average size and even the size distribution of polymer segments between entanglements or of distinct aggregations of colloidal particles [3,4].

Figure 3 also shows the other two regimes. Above some critical shear strain (displacement per unit distance), unity for polymers but as low as one one-hundredth for suspensions, the transient viscosity depends on both time and strain or strain rate. Finally at large strains, above seven for polymers, the viscosity becomes independent of time and depends only on rate of strain. This steady straining regime is perhaps most familiar since it is the basis of the normal definition of viscosity, already mentioned in the Introduction.

Figure 3 also indicates that at large strains there can be significant differences between the viscosities defined from shearing and extensional deformation.

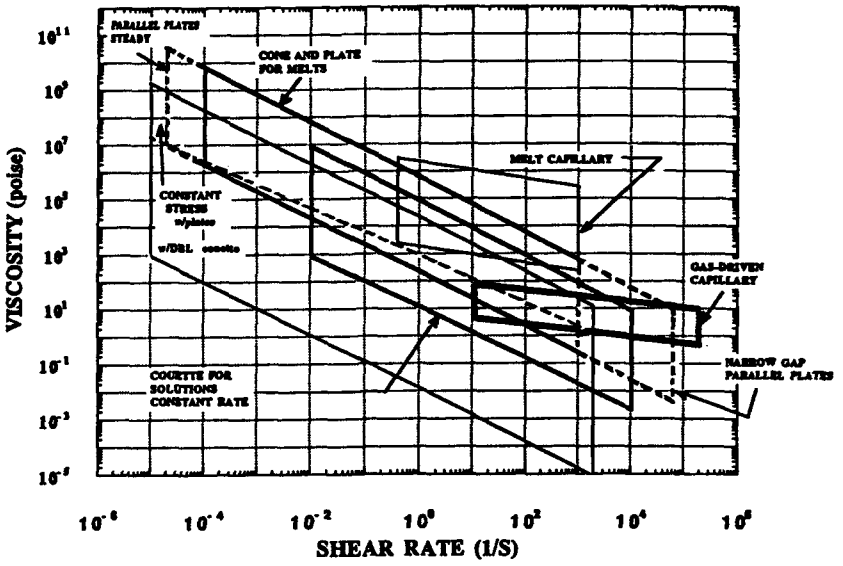


Fig. 2 Viscosity and shear rate ranges of state-of-the-art shear rheometers.

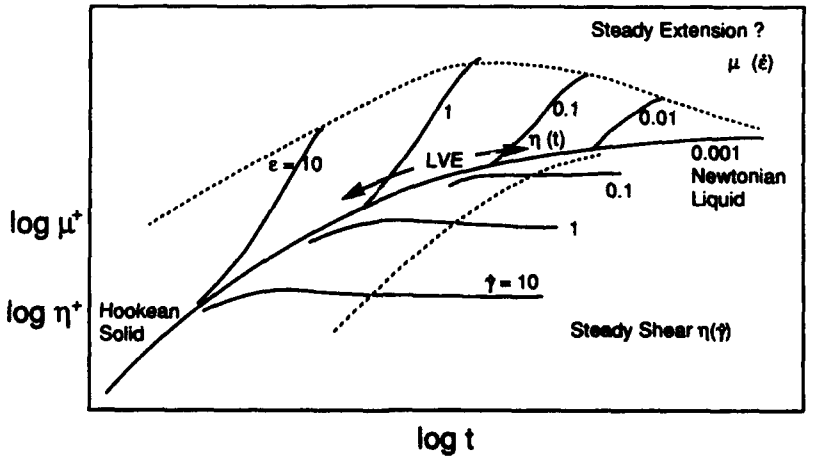


Fig. 3 Transient shear and extensional viscosities of a polyethylene melt vs. time at various shear rates. The heavy central curve is the linear viscoelastic behavior. The area between the dashed lines is the large strain regime; outside them is the regime of steady rate of straining [adapted from Laun, 1978].

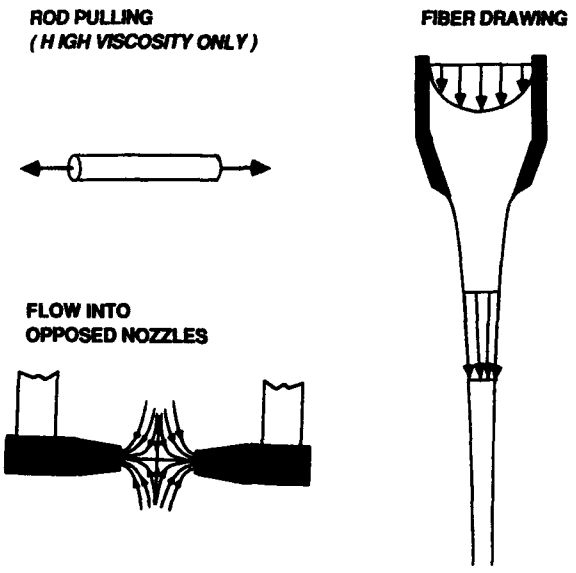


Fig. 4 Three leading geometries for measuring extensional response.

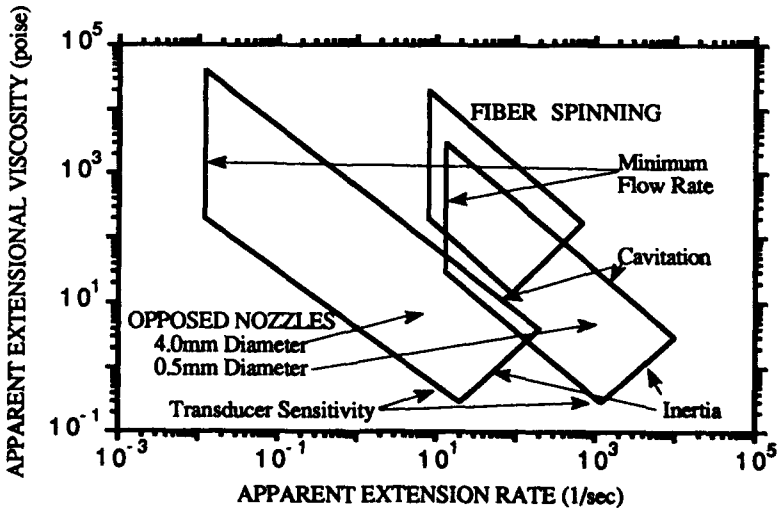


Fig. 5 Ranges of apparent extensional viscosity and extension rate of fiber drawing ('spinning') and opposed nozzles ('jets') devices.

Extensional response

As stated above, extensional rheometry of liquids is difficult. With high viscosity samples it is possible to use tests designed for solids. The most common, see Fig. 4, is to form a rod of a frozen sample, grab its ends, melt it and pull. This technique was used to get the polyethylene melt data shown in Fig. 3. But even with such a high viscosity sample it is not possible to reach the steady straining region, which is at extensional strain beyond seven or so.

With lower viscosity samples it is impossible to "grab and pull." Many ingenious alternatives have been tried, mostly without great success. The most common technique is fiber drawing (Fig. 4). This flow is close to the spinning process used to make polymeric and ceramic fibers. To turn this flow into a rheometer, the drawing force and fiber diameter profile must be measured. If there are volatile constituents, great effort must be made to avoid evaporation. The range of attainable deformation rates is limited. Moreover, the extensional viscosity interpreted from force, draw profile and flow rate measurements is only *apparent*. Under the best circumstances the fiber draws down in such a way that the extension rate is uniform along it and the total strain is about two. This falls somewhere in the lower area of the large strain regime illustrated in Fig. 3. Usually the extension rate is not uniform along the fiber, and the apparent viscosity really depends on strain and rate of strain. Further complications are the liquid's memory of its flow in the delivery tube and swelling as it emerges, its inertia, and the forces of gravity, air drag, and surface tension. All conspire to cause strain rate to vary along the fiber, so that the apparent viscosity is an unknown average of neighboring curves in Fig. 3 [7].

A recently advanced alternative for extensional measurements on lower viscosity samples is the opposed nozzles geometry (Fig. 4) [8,9]. With this geometry there is much less problem with evaporation and it is much easier to use. However, the flow is not homogeneous: like the capillary rheometer it has a range of strain and a mix of shear and extension [10]. So the opposed nozzles device measures an *apparent* extensional viscosity, an average over a range of extensional strains with some contribution from shear stresses. Figure 5 indicates that the range of the opposed nozzles is much wider than that of fiber drawing. We used an opposed nozzles device for the extensional measurements reported below.

Although currently there is no true extensional rheometer for lower-viscosity liquids, we expect that the opposed nozzles device can detect any strong extensional thickening when it occurs, as in experiments reported below. That truly steady extensional straining cannot be achieved seems not a severe limitation, because the extensional strains in fiber and film formation processes are unlikely to exceed those attainable in existing laboratory devices.

Rheological measurements, material functions, and particularly the advantages and limitations of various rheometers are covered by Barnes et al. [11] and Macosko [2].

Rheological measurements can be used to characterize starting liquid and the course of a particular process, so that processability and product properties can be correlated and predicted from such measurements. At the other extreme of application, the results of appropriately extensive measurements can be used to deduce a rheological equation of state, or constitutive relation. With an accurate constitutive relation, flow behavior and microstructure development could in principle be predicted for a range of process designs and conditions, so that the best could be chosen. An application that falls between has already been mentioned: probing the microstructure of the polymeric liquid or particulate suspension in order to understand it well enough to estimate the effects of changed circumstances. In this sort of application, other probes can be valuable too, as the next section testifies.

RHEOLOGICAL BEHAVIOR AND STRUCTURAL DEVELOPMENT DURING GELATION

Structural development during the transformation from sol to gel can be captured by cryogenic transmission electron microscopy (cryo-TEM) [12-14]. In this technique, thin films of the liquid are very rapidly quenched and then directly imaged on a cold-stage in the TEM. Correlating the images with rheological measurements of the liquid in the same state as just before quenching sheds light on the relation of rheology to microstructure. What follow are among the first attempts at pairing the two approaches we know of.

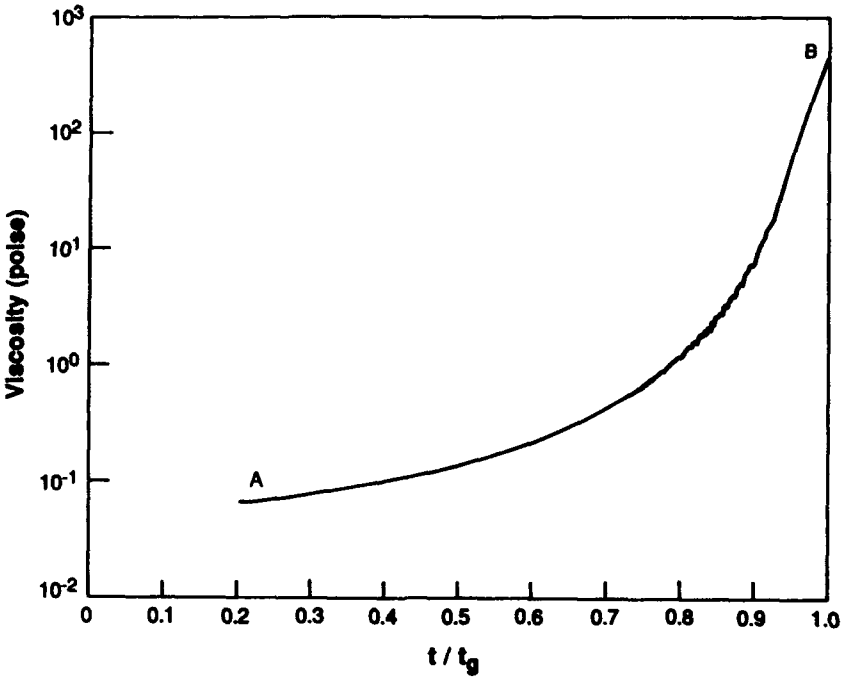


Fig. 6 Shear viscosity of gelling colloidal silica (Ludox) at 24°C. Gel time (t_g) of 1315 sec.

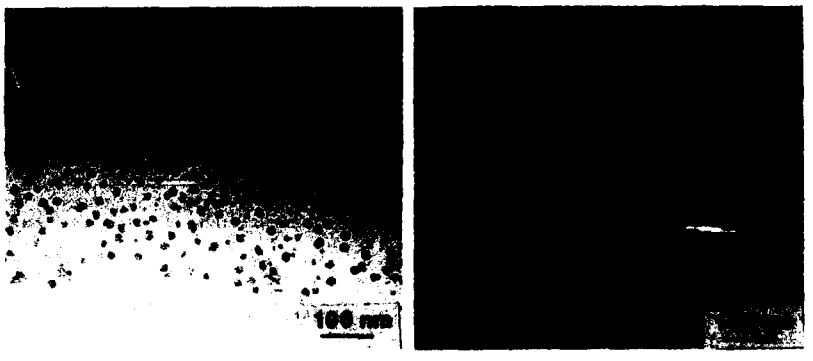


Fig. 7 Colloidal silica, 5 wt% in water. (a) Sol. (b) Gel after addition of NaCl.

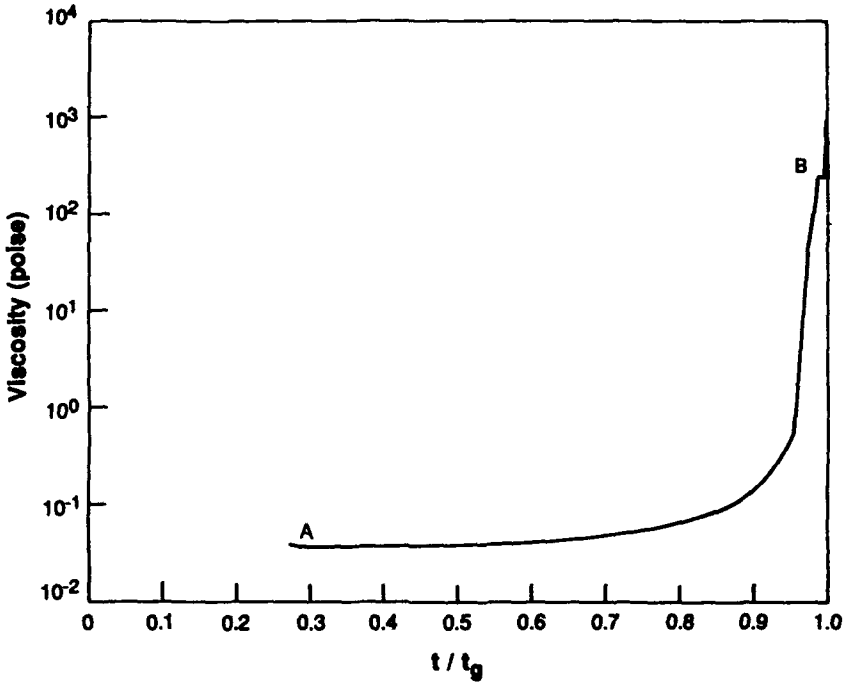


Fig. 8 Shear viscosity of gelling base catalyzed TEOS at 30°C. Gel time (t_g) of 1018 sec.

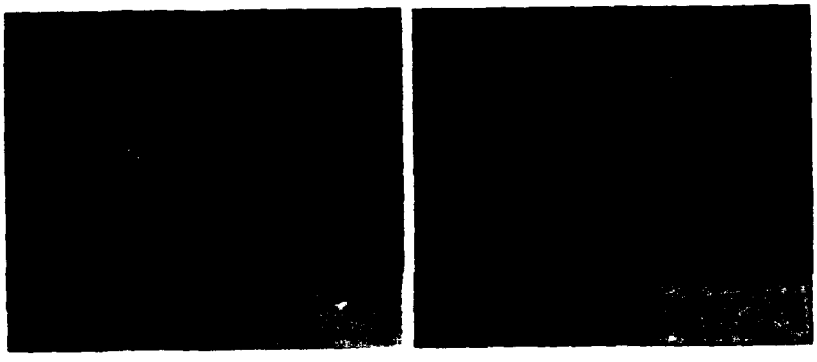


Fig. 9 Base catalyzed TEOS, 0.14M in n-propanol. (a) Sol. (b) Gel after addition of NH_4OH.

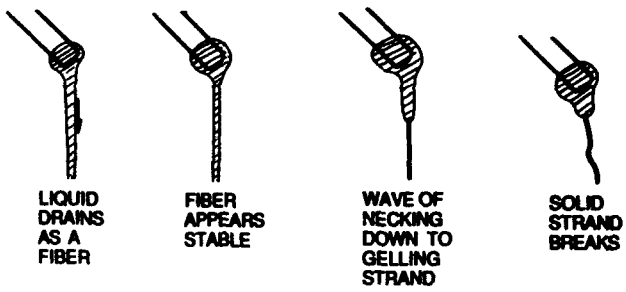


Fig. 10 Fiber formation by acid catalyzed TEOS, concentrated by evaporation.

The sol-to-gel transition in colloidal silica is illustrated in Fig. 6. The measured viscosity of the system rises over four orders of magnitude as the system gels. The measurements were made at a succession of constant values of applied shear stress in a concentric cylinders rheometer. Varying the shear stress from 10 to 100 dynes/cm^2 did not affect the gelation time, and so it was assumed that shearing at shear stresses below 100 dynes/cm^2 did not interfere significantly with the gelation process. The corresponding cryo-TEM pictures in Fig. 7 document the transition from dispersed colloidal particles in the sol, to a particle network in the gel (which has the elastic properties of a solid). In the intermediate stages, polydisperse colloidal aggregates were observed to form, and this floc formation was judged responsible for the continuous increase in viscosity.

The gelation of base catalyzed tetraethoxysilane solution (TEOS) also displayed over four orders of magnitude increase in the measured viscosity during gelation; however, the viscosity rose sharply only near the end of the gel time, as Fig. 8 shows. Changing the applied shear stress did alter the gelation time of this system, it was discovered. The cryo-TEM pictures indicate that small, 40Å silica-rich clusters form which then link up to make the gel network (Fig. 9). The induction-like time span during which the viscosity is not changing significantly is thus the time required to form the clusters. Their subsequent aggregation and linking up into a network evidently is responsible for the sharp rise in viscosity. Interestingly, even shear rates less than 1 s^{-1} were found both to inhibit cluster aggregation and to slow gelation.

Acid-catalyzed TEOS required extremely long times (days to weeks) to gel when the solution was prepared and kept in closed containers to prevent evaporation. Cryo-TEM studies never detected the formation of discrete particles: only a uniform contrast was observed in pictures of states all the way from the sol to the gel (similar to Fig. 9 (a)). Acid-catalyzed TEOS samples were evaluated for fiber forming ability by dipping a rod into each and withdrawing it. Fibers could not be formed from solutions that had gelled in a *closed* container; stable fibers could be pulled only after the TEOS solution had been concentrated by evaporation, as previously reported by Sakka et al. [15,16]. Not only did the evaporation-concentrated material yield a stable fiber whenever a rod was withdrawn from liquid. The fiber also showed a spontaneous wave of necking down, the result being a gelling strand, as diagrammed in Fig. 10. This observation indicates that rheological change accompanies evaporative concentration of the liquid. Altered extensional viscosity was suspected.

An opposed nozzles device was employed to measure apparent extensional viscosities of solutions kept sealed and others left open to the air. In both cases the extensional viscosity was substantially greater than the value expected from the previously measured shear viscosity at the same elapsed fraction of the gel time, as recorded in Figs. 11 and 12. However, the viscosity increases of the open, evaporating solutions appeared to be far quicker (by five-fold) and more

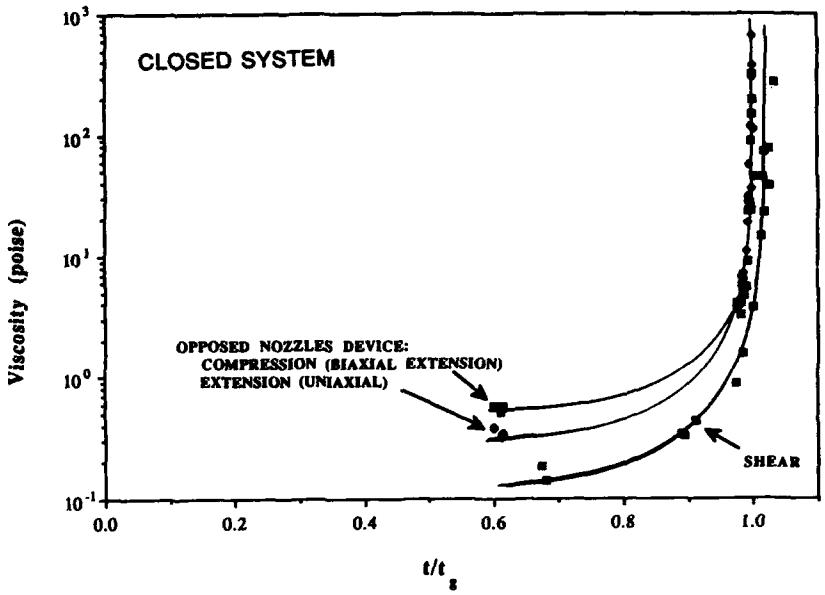


Fig. 11 Extensional and shear viscosities of gelling acid catalyzed TEOS at 25°C. Gel time (t_g) of five days.

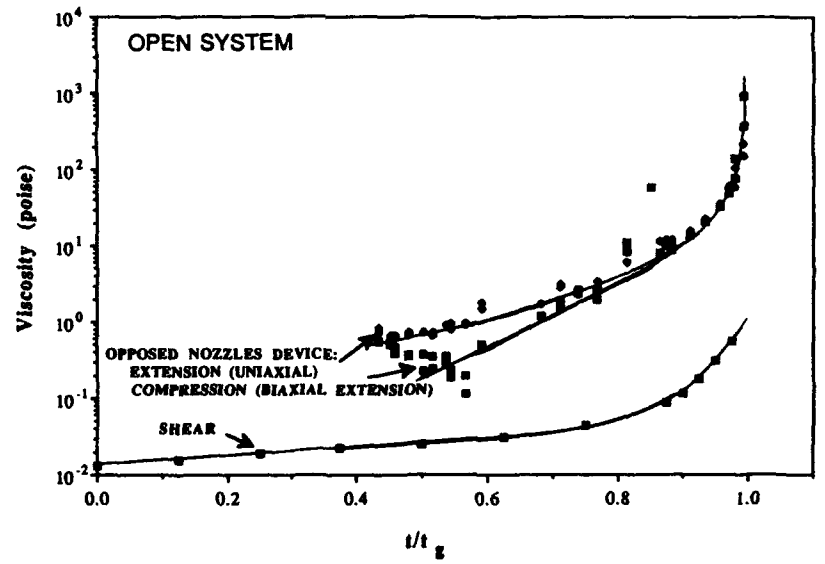


Fig. 12 Extensional and shear viscosities of evaporating and gelling acid catalyzed TEOS at 25°C. Gel time (t_g) less than 24 hours. Shear data from Ref. [15].

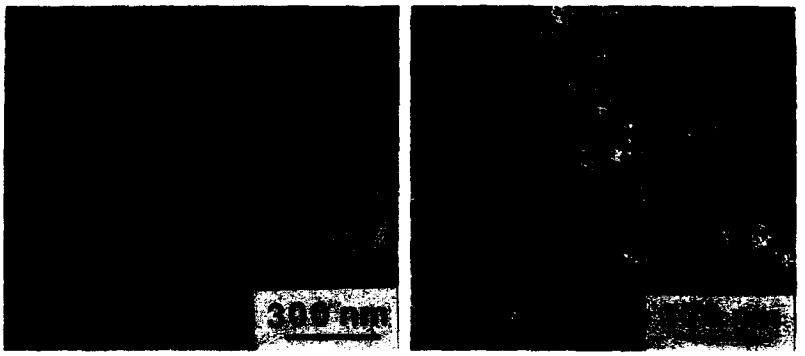


Fig. 13 Vanadium pentoxide prepared by ion exchange from 0.5M sodium metavanadate in water. (a) Unsheared. (b) Sheared.

uniform (less abrupt in the late stage) than the increases of the solutions kept sealed. We speculate that by concentrating the sols by evaporation, the viscosity can be raised to a given value with less extensive crosslinking polymerization of the TEOS, leaving the polymer molecules more readily aligned by extensional flow and thereby improving drawability.

The sol-to-gel transition in the divanadic acid/vanadium pentoxide (V_2O_5) system is interesting because ribbon-like colloidal fibrils form rather than isometric particles or polymeric structures: see Fig. 13(a). Experiments with this system are described in another article [17]. Judged by the micrographs, the fibrils are extremely flexible (180° turns are visible) and intertwined. Upon shearing at a quite low applied shear rate in a concentric cylinders rheometer, the viscosity of the partially gelled sol falls, i.e. it is thixotropic. But then the response reverses and the viscosity climbs, i.e. it is rheopectic — until the response reverses again. Similar behavior was noted by Juliusburger and Pirquet [18]. A possible explanation is that shearing for a time breaks and disentangles the fibrils so that viscosity falls, but then the fragments begin aligning and aggregating so that viscosity rises. Cryo-TEM pictures of the sheared material do show evidence of fragmentation and increased aggregation; Fig. 13(b) is an example.

These four instances suggest the value of correlating cryo-TEM images and other probes of structural development with rheological measurements. Of course, to understand the way that the gelling liquids respond to stress and strain in film formation and fiber drawing requires much more extensive measurement and imaging. Probing by scattering methods can be useful too. Theory needs to be developed in order to interpret well the results, and convert them into a rheological equation of state for quantitative purposes.

STRUCTURE IN RHEOLOGY

Structure involved in rheological response is not necessarily the structure revealed by electron microscopy or scattering methods. Viscosity and elasticity arise in stress transmission through the system. What matters to stress transmission is the dynamics of three-dimensional networks of forces between the parts, whether the parts are colloidal particles, polymer molecules or assemblages of these. The forces are likely to be continuously distributed in stiffness and range. There are just as likely to be peaks in the distributions, by virtue of the separations of the parts, or their orientations, or their internal organizations. Then the network of forces is subject to progressive breakdown and reordering during flow, according to the strain that is generated and the persistence with which that strain operates on the various scales of the network.

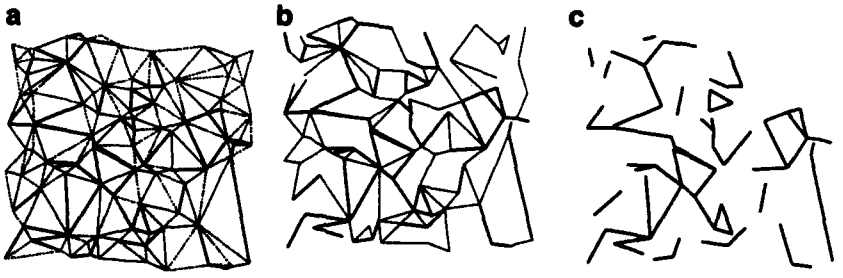


Fig. 14 Rheological response arises in evolving networks of forces (see text).

The role of forces distributed in stiffness and range can be illustrated by supposing there are three peaks: weak, medium, and strong forces. As diagrammed in Fig. 14(a), all together they form a network of bonding forces that transmits stress, whether in shear or extension. If a rheological test *breaks* the weak ones, or otherwise fails to sample them, the network it would sense, shown in Fig. 14(b), is still connected. Force networks do evolve with straining, with reaction or aggregation, and with concentration, as by evaporation. For example, straining of a gelling material may break many of the weakest links in the growing networks of parts, the parts themselves meanwhile evolving. If a rheological test breaks all of the force linkages up to the strongest, or otherwise fails to sample them, what it would sense, shown in Fig. 14(c), is *not* connected and so cannot transmit stress. It is the dynamics of three-dimensional networks of forces that dictate rheology.

What would be a marvel for understanding how rheological response depends on structure, would be anything akin to a stereo microscope for *forces*, a means of visualizing *dynamics*. The dynamics may go well beyond the impressions conveyed by ordinary images.

ACKNOWLEDGEMENTS

T. Nagase contributed to shear rheometry, R. C. Navarrete and R. A. Cairncross to extensional rheometry and fiber-forming studies, and J. K. Bailey made cryo-TEM studies. Support was provided by the NSF Center for Interfacial Engineering at the University of Minnesota and AFOSR contract 49620-89-C-0050.

REFERENCES

1. R. B. Bird, R. C. Armstrong, and O. Hassager, Dynamics of Polymeric Liquids, 2nd ed., Wiley, New York, 1987.
2. C. W. Macosko, Rheological Measurements, VCH Publishers, New York, to appear.
3. W. B. Russel, D. A. Saville, and W. R. Schowalter, Colloidal Dispersions, Cambridge University Press, New York, 1989.
4. W. D. Ferry, Viscoelastic Properties of Polymers, 3rd ed., Wiley, New York, 1980.
5. P. R. Schunk and L. E. Scriven, J. Rheol. 34, in press (1990).
6. C. J. Brinker and G. W. Scherer, Sol-Gel Science, Academic Press, San Diego, 1990.
7. R. B. Secor, P. R. Schunk, T. B. Hunter, T. F. Stitt, C. W. Macosko, and L. E. Scriven, J. Rheol. 33, 1329 (1989).
8. G. G. Fuller, C. A. Cathey, B. Hubbard, and B. B. Zebrowski, J. Rheol. 31, 235 (1987).
9. K. J. Mikkelsen, C. W. Macosko, and G. G. Fuller, Proc. Xth Int. Congr. Rheol. Sydney 2, 125 (1988).
10. P. R. Schunk, J. M. de Santos, and L. E. Scriven, J. Rheol. 34, 387 (1990).
11. H. Barnes, J. F. Hutton, and K. Walters, Rheological Behavior, Elsevier, London, 1989.
12. J. K. Bailey, J. R. Bellare, and M. L. Mecartney, in Specimen Preparation for Transmission Electron Microscopy of Materials, eds. J. C. Bravman, R. M. Anderson, and M. L. McDonald (Mater. Res. Soc. Proc. 115, Pittsburgh, 1988) 69.
13. J. Bellare, J. K. Bailey, and M. L. Mecartney, in Ultrastructure Processing of Advanced Ceramics, eds. J. D. Mackenzie and D. R. Ulrich, Wiley, New York (1988) 835.
14. J. K. Bailey, T. Nagase, S. M. Broberg, and M. L. Mecartney, J. Noncryst. Solids 109, 198 (1988).
15. S. Sakka and K. Kamiya, J. Noncryst. Solids 48, 31 (1982).
16. S. Sakka and H. Kozuka, J. Noncryst. Solids 100, 142 (1988).
17. J. K. Bailey, T. Nagase, G. A. Pozarnsky and M. L. Mecartney, these proceedings.
18. F. Juliusburger and A. Pirquet, Trans. Farad. Soc. 32, 445 (1936).

THE PROCESS OF GEL FIBER FORMATION

N.TANEDA, T.KAWAGUCHI, D.ARAI, AND K.MATSUZAKI
Asahi Glass Company Ltd., Advanced Glass R&D Center, Hazawa-cho, Kanagawa-ku, Yokohama-shi, 221 Japan

ABSTRACT

The gel fiber formation was studied for the spinnable silica sols prepared from a mixture of TEOS, H_2O, EtOH and HNO_3 (1 : 2 : 2 : 0.01, in mole ratio). The effect of polysiloxane molecular size in the spinning sol on spinnability indicated that the tough skeleton of gel, which is preferable for fabrication of high-strength fiber without breakage, was formed by the selective connection of large size polymers (about 10^6 in M.W.) during the spinning. It was also found that the smaller size polymers in gel fiber continued to react with water in the atmosphere after the spinning, and attached to the skeleton to strengthen the fiber.

INTRODUCTION

It is well known that the sol from TEOS solution prepared under the condition that H_2O/TEOS ratio is less than 2 with acid catalysis is spinnable. Several authors have studied the spinnability as functions of starting compositions, rheological behavior of the sol, and polymer structure [1-6]. However,the details have not been reported so far.

In this article we studied the effect of molecular size of polysiloxane in the sol on spinnability by Size Exclusion Chromatography (SEC)[7], stretch factor, and the strength of gel fiber.

EXPERIMENTAL

Tetraethylorthosilicate (TEOS) was used as a starting material. The mixture of TEOS, EtOH, H_2O, and HNO_3 in the mole ratio of 1: 2 : 2 : 0.01 was stirred vigorously at room temperature, and then the solution was kept at about 79° C under EtOH reflux. The gelation point was determined when EtOH did not reflux. The gelation time(t_g) was about 70hrs.

The spinning sols were prepared by cooling down the solutions after certain refluxing. Since in the previous work[8] the sols with viscosity at 25° C above 50 poise were found to be suitable for the dry-spinning, in this study the viscosity was adjusted to be 50 to 80 poise by extracting some extent of the solvent from each solution. The lower the average molecular weight of sol, the more its solvent should be extracted to adjust the viscosity. The sols were turned into gel fiber by the dry-spinning method as reported in reference[9].

The molecular weight (M.W.) of spinning sols and gel fibers were analyzed by SEC with a differential refractometer (Waters Associates Model R401). THF was made to flow through 4 columns (ULTRASTYRAGEL 500A, 10^3A, 10^4A, 10^5A, made by Waters Associates) at the rate of 1.0 ml/min. Samples were diluted to 1wt% in the solid content in tetrahydrafuron (THF) and filtered

Mat. Res. Soc. Symp. Proc. Vol. 180. ©1990 Materials Research Society

by disk filter of 0.7μm in pore size before the measurement. Molecular weight(M.W.) was represented by polystyrene standard.

The tensile strength of gel fiber mono-filament of 25mm in length was measured with a strain rate of 0.5mm/min. by an Instron model 1122.

RESULTS AND DISCUSSION

Polymerization of the sols

Figure 1 shows the growth of Si-O-Si bonds with time for the sols obtained in this study. Since under an acidic condition H_3O^+ is attracted to Si having more (negatively charged) OR groups[9], at an early stage of t/t_g=0.10 (Fig. 1a), both monomer and dimer are disappeared. With the reaction time the molecular distribution shifts to higher molecular size and becomes broader. Finally at t/t_g=0.97 siloxane polymers of 10^6 in M.W. are formed, though those of 10^3 in M.W. still remain. Figure 2 shows the variation of Mn(number-average molecular weight) and Mw (weight-average molecular weight) as a function of reduced time (t/t_g). Mw/Mn ratio increases from about 2 (t/t_g=0.10) to about 40 (t/t_g=0.97).

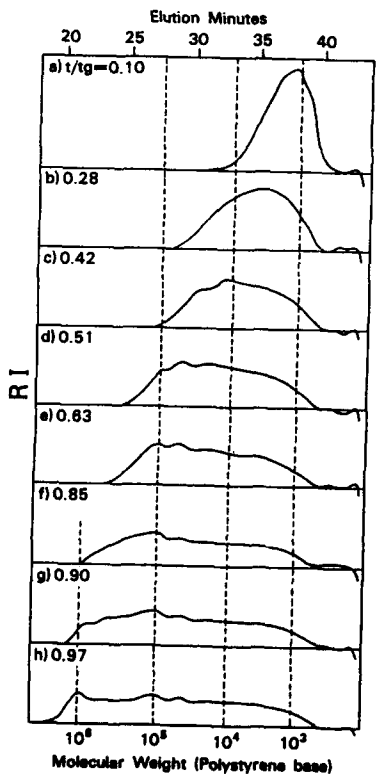


Fig. 1 (left) Molecular size distribution curves of solution (TEOS:H_2O:EtOH:HNO_3=1:2:2:0.01) by SEC as a function of t/t_g.

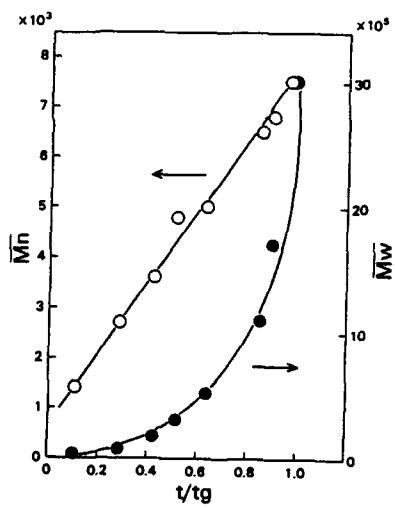


Fig. 2 (above) Changes of Mn and Mw of the solution with t/t_g.

Dry spinning

The spinning results are summarized in Table 1 and Fig. 3. The stretch factor represents the spinnability of sol. The sol prepared at t/t_g=0.35 had the smallest stretch factor and the corresponding gel fiber tend to break easily just after being extruded from nozzles. The state of the gel fiber was "Wet" and the strength was very low. Namely, the sol of t/t_g=0.35 was not suitable for spinning. On the other hand the sol of t/t_g=0.97 had excellent spinnability; high stretch factor and continuous spinning without breakage. The gel fiber was "Dry" and the tensile strength was high enough to be handled.

It can be said from the numerous experiments on spinning that the size of polymers of the spinning sol are important factor for the spinnability. Since the viscosity can be altered by the solid content, we presumed that high molecular weight of sol is a dominant factor for excellent spinnability.

Gelation during the dry-spinning

Figure 4 shows the differences between gelation under EtOH reflux and that by a dry-spinning. In the former, the gelation is not accompanied by EtOH evaporation; weight, volume, and solid content of gel are invariable through the sol-gel transition. On the contrary, the gelation by a dry-spinning is accompanied by a large amount of EtOH evaporation and volume shrinkage; weight of the gel fiber reduces to 65% of the sol and volume becomes about 40%. Since the spinning time is much shorter than the time for the sol to gel transition under EtOH reflux, it is predicted that there are some differences in the

Table 1. Spinnability of the sols of different average molecular weight

Sol			
t/tg	0.35	0.51	0.97
Average Molecular Weight ($\overline{Mn}$)	3100	4800	7500
Solid Content (wt%) *1	58	52	46
Viscosity at 25°C (poise)	76	50	70
Gel Fiber			
Stretch Factor *2	9.8	18.9	39.1
State	Wet	Dry	Dry

*1 The weight of the solid remained after heating the sol at 900°C for 2h divided by the weight of the sol.

*2 Cross section area of a nozzle divided by that of the gel fiber.

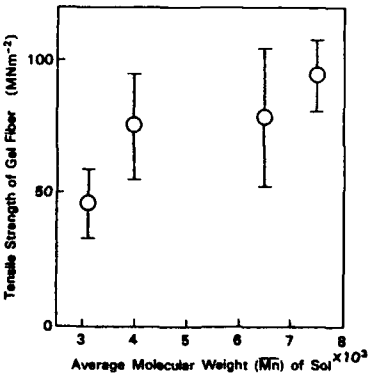


Fig. 3 Tensile strength of gel fibers v.s. Mn of the sols. The fibers were kept at 25°C, 50%RH for 5 days before the measurement. A width of strength means 1σ.

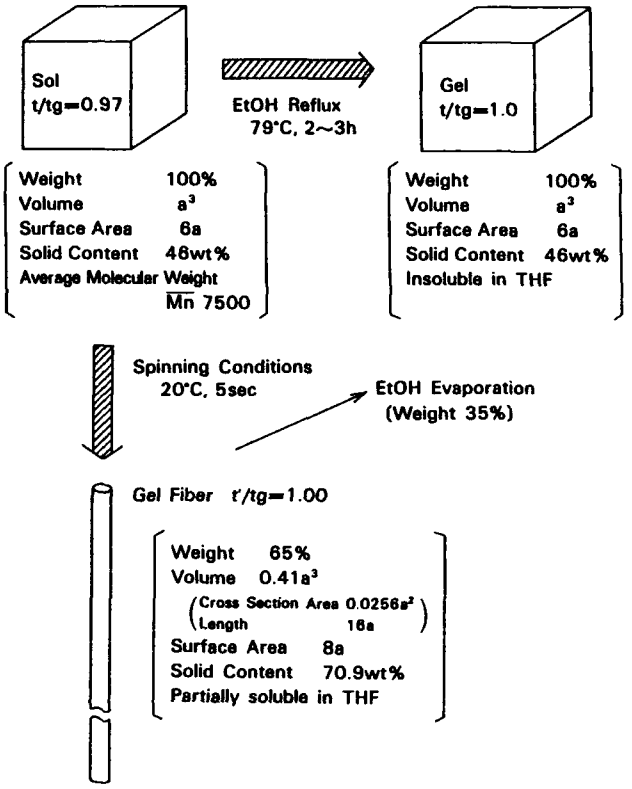
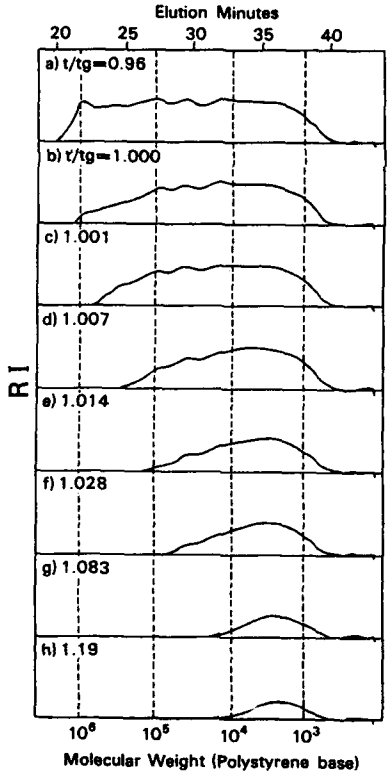


Fig. 4 Differences between gelation under EtOH reflux and by dry-spinning

micro-structures. Then the solubility of the gels in organic solvents such as THF and EtOH was studied.

The gel formed without EtOH evaporation was insoluble in THF; almost all siloxane polymers form the gel skeleton network and EtOH is trapped inside it (Fig. 7b). In contrast, the gel fiber by spinning partially dissolved in THF, which suggests that the structure of gel fiber was fragile. And then the molecular sizes of dissolved siloxane polymers were detected by SEC as shown in Fig. 5.

It is noticed that a part of polysiloxane around 10^6 in M.W. was lacking in the curve at $t'/t_g=1.000$ (Fig. 5b) compared with the curve at $t/t_g=0.96$ (Fig.5a). This suggests that the polymers around 10^6 in M.W. were cross linked to each other, formed the skeleton (spanning cluster[10])of gel fiber during the spinning, and became insoluble in THF. In other words polymers lower than 10^5 in M.W. weren't cross linked in the short-time-spinning. As mentioned before, the gel fiber obtained from the sol at $t/t_g=0.96$, which contains "large" polysiloxane, is dry and strong (Fig. 3). Such strong and tough skeleton of gel fiber was formed by the "large" polymers. On the other hand, the gel fiber



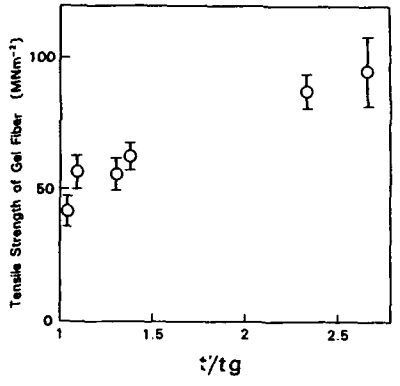


Fig. 6 (above) The change in tensile strength of gel fiber with reduced time t'/t_g.

Fig. 5 (left) Molecular size distribution curves of polymers dissolved from gel fiber.

formed from the sol at t/t_g=0.35, which is composed of only smaller polymers (lower than 10^5 in M.W.), is wet and weak, because the sol has no polymers that can form the tough skeleton.

Figure 5 c)-h) show the molecular size distribution curves of gel fiber that was held in the atmosphere of 25°C and 50% RH. With the aging time the larger size polymers become insoluble in THF. Consequently, the polymers of smaller size continued to connect to the skeleton of the fiber and the mechanical strength of gel fiber became high (Fig. 6). Figure 6 also suggests that the degree of condensation of gel fiber increased even beyond t'/t_g=1.2, after which no signal was detected on SEC curves for the dissolved polymer in THF.

Based on the above results, schematic drawings of the gel and gel fiber formations are shown in Fig. 7. The curved line represents a siloxane polymer. Open circles show newly formed connective point through the gelation. Since the dry-spinning is accompanied by a large amount of EtOH evaporation from the sol, siloxane polymers "gather" together in the gel fiber, but only large polymers (10^6 in M.W.) cross link to form the skeleton with the small size polymers remaining in the spanning cluster.

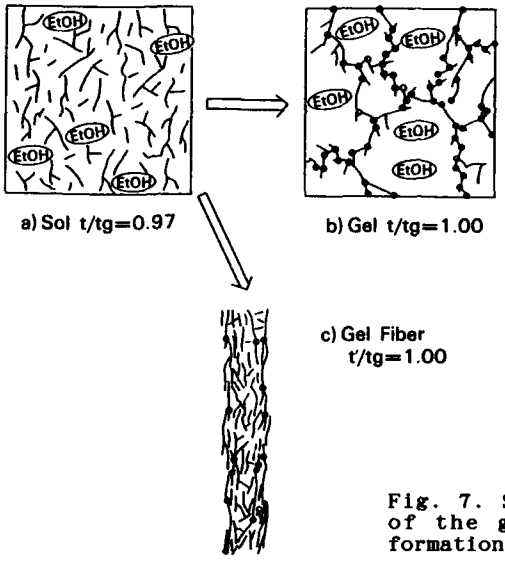


Fig. 7. Schematic drawings of the gel and gel fiber formation.

CONCLUSIONS

The effect of molecular size of polysiloxane on spinnability and gel fiber formation has been studied. The following results are obtained;

1. The most preferable sol for the spinning is composed of the polymers in the wide range of 10^3 to 10^6 in M.W.
2. The "large" polymers of 10^6 in M.W. are preferable for achieving excellent spinnability and strong gel fiber, since the "large" polymers form tough skeleton of the fiber on the spinning.
3. The polymers of smaller than 10^5 in M.W. react with H_2O in the atmosphere and continue to attach to the skeleton of gel fiber. The reactions start from the larger polymers and result in strengthening the fiber.

REFERENCES

1. S.Sakka and K.Kamiya, J.Non-Cryst.solids, 42, 403 (1980)
2. S.Sakka and H.Kozuka, ibid., 100, 142 (1988)
3. K.Kamiya, Y.Iwamoto, T.Yoko and S Sakka, ibid., 100,195(1988)
4. H.Kozuka, H.Kuroki and S.Sakka, ibid., 100, 226 (1988)
5. M.Sacks and R.Sheu, ibid., 92, 383 (1987)
6. C.J.Brinker and R.A.Assink, ibid., 111, 48 (1989)
7. B.E.Yoldus, ibid., 82, 11 (1986)
8. K.Matsuzaki, D.Arai, N.Taneda, T.Mukaiyama and M.Ikemura, ibid., 112, 437 (1989)
9. K.K.Keefer in Better Ceramics Through Chemistry, edited by C.J.Brinker, D.E.Clark and D.R.Ulrich, (Mater. Res. Soc. Proc. 32.) p15-24
10. G.W.Scherer, Yogyo-Kyokai-Shi, 95(1), 21 (1987)

SOL-GEL FILM FORMATION BY DIP COATING

ALAN J. HURD and C. JEFFREY BRINKER
Sandia National Laboratories, Albuquerque, NM 87185-5800

ABSTRACT

The physical aspects of sol-gel film formation are discussed, including the steady state film profile during dip coating, evaporation, and capillary phenomena. It is argued that, since the evaporation rate increases singularly near a sharp boundary (analogous to an electric field singularity near a sharp conductor), the film profile near the drying line falls off precipitously, following the inverse form of the evaporation singularity. Finally, the large tensile pressures in the solvent during the final stage of drying of a porous film are discussed from the point of view of controlling the degree of capillary collapse.

INTRODUCTION

Manufactured coatings are fundamental to our Information Age Society. From Wall Street to the local library, much of the world's production of new wealth and wisdom is necessarily archived on magnetic, optical, or photographic coatings. Expanding markets can be expected for coatings on optics, integrated circuits, microsensors (including bioactive layers), and separation membranes. To track the demand of these and other future applications, the materials and processing of coatings deserve exploration.

Sol-gel films, belonging to the broad class of coatings applied via a liquid carrier, have enjoyed recent attention. Although they have been studied since WWII [1], their use has not been widespread in spite of potential advantages, not the least of which is simplicity. Whereas deposition from the gas phase requires expensive vacuum equipment, sol-gel coatings can usually be applied with a minimum of investment while often surpassing the conventional coating in quality.

Deposition by dip coating proceeds through overlapping stages: When a substrate is withdrawn slowly from a sol, containing polymeric or colloidal species in suspension, a film of liquid becomes entrained on the surface. The film thins through gravitational draining, capillary-driven flows, and, most importantly, evaporation, culminating in a well defined drying line beyond which lies a nearly dry film. When the recession speed of the drying line (relative to the substrate) matches the withdrawal rate, steady state conditions (relative to the reservoir) prevail.

In the meantime, the particles in the entrained liquid, which are often reactive and tend to gel, experience a rapidly concentrating environment. Whereas the dilute sol in the reservoir might gel in months, the entrained sol has only seconds to react, albeit in less dilute states. The sol may pass through a transient gel-like state before the drying line passes; during the final stage of evaporation, large capillary stresses can develop in the network, causing it to collapse partially. The remnant porosity is evidence for the fleeting "gel" state, and varying its structure through chemical and physical means serves to tune the film characteristics. Thus sol-gel thin films can differ greatly in structure from bulk xerogels or aerogels [2] if desired.

Indeed, it is this structural diversity that makes sol-gel films interesting from an application standpoint, not to mention the advantages of low temperature processing at ambient pressure. Our goal is to understand how the structure arises during film formation.

Mat. Res. Soc. Symp. Proc. Vol. 180. ©1990 Materials Research Society

THE DRAG OUT PROBLEM

Through ellipsometric imaging [6], the thickness profile of entrained solvent during dip coating has been measured. In order to simplify the analysis, we consider a pure solvent without the complicating aspects of suspended solids. In the experiments, a 1 cm-wide strip of optically polished silicon was drawn from a solvent reservoir at a speed $u_o \approx 1$ mm/s. The region of entrained liquid film was illuminated at an incident angle of 67.5° with monochromatic light through a polarizer-compensator-sample-analyzer arrangement [6], and the polarizers were adjusted so that fringes could be seen at every quarter wavelength of optical thickness. Representative profile data are shown in Fig. 1a for ethanol.

The hydrodynamic factors in dip coating were first calculated correctly by Landau and Levich [4] and recently generalized by Wilson [5]. These authors did not consider the case of evaporation. A first attempt at such a theory was made by Hurd and Brinker [6], who assumed that the evaporation rate was constant along the entrained liquid film and ignored surface tension. The predicted thickness profile was a linear wedge, connecting to the reservoir with a ~100 Å radius of curvature. The profile data in Fig. 1a clearly indicate that the evaporation rate is not constant, but accelerates near the drying line, as manifest by the more rapid thinning there. In the following development, the local evaporation rate is shown to be controlled by the vapor diffusion away from the film; near the drying line the evaporation rate increases in singular fashion and this singularity is manifested in the thickness profile.

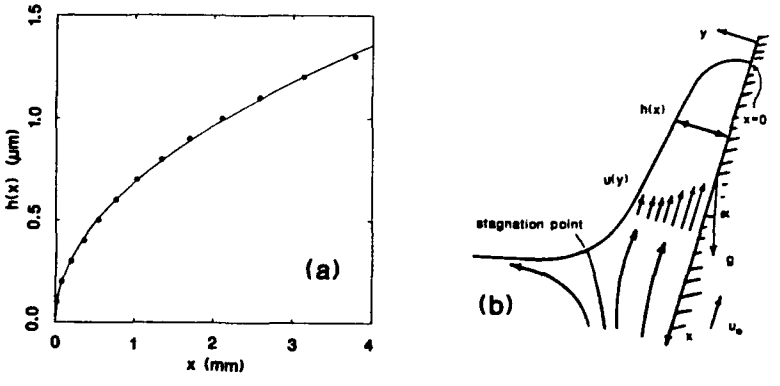


Figure 1. (a) Thickness profile for ethanol (note the expanded thickness scale). The fit represents $h(x) \sim x^{\eta}$ with $\eta = 1/2$. (b) Geometry.

In view of the thinness of the film compared to its width and breadth and small slope of the entrained layer (Fig. 1a), a lubrication approximation applies, in which the liquid velocity $\vec{u}$ is parallel to the substrate and only gradients normal to the substrate are important, i.e. $\vec{u} \cdot \nabla \vec{u} = 0$. In the region of the reservoir meniscus, the liquid cannot be considered thin, but there the flows are negligible. Thus we expect the profile of a static gravitational meniscus to apply at the bottom (where evaporation effects are not important). Here we set up the full problem for later reference, embellishing Wilson, although we discuss only the thin film in the region for which we have optical profiles--not too close to either the drying line or the meniscus.

The substrate is pulled from the reservoir with speed u_o at an angle α from the vertical. (This geometry removes infinite derivatives in the development. It is permissible, of course, to take the limit $\alpha \to 0$ in the end.) Let x measure distance along the substrate from the drying line toward the reservoir, and let y be normal to the film (Fig. 1b). The Navier-Stokes equations in the lubrication approximation are

$$0 = -\frac{\partial p}{\partial x} + \eta \frac{d^2u}{dy^2} + \rho g \cos\alpha \quad , \tag{1}$$

$$0 = -\frac{\partial p}{\partial y} - \rho g \sin\alpha + \frac{d\Pi(y)}{dy} \quad , \tag{2}$$

where η is the viscosity, ρ is the liquid density, $\Pi(y)$ is the disjoining pressure, u is the flow in the x direction, and p is the total pressure. The boundary conditions are

$$u = -u_0 \qquad \text{on } y = 0 \quad , \tag{3}$$

$$\frac{du}{dy} = 0 \; ; \; p = -\gamma\kappa \qquad \text{on } y = h(x) \quad , \tag{4}$$

where γ is the surface tension coefficient, κ is the curvature and h(x) is the profile of the liquid. The curvature is given by the formula

$$\kappa = \frac{d^2h/dx^2}{\left(1 + (dh/dx)^2 \right)^{3/2}} \quad , \tag{5}$$

and by integrating Eq. (2) with its boundary condition Eq. (4) the pressure can be found. Next, the velocity can be found by integrating Eq. (1),

$$u = -u_0\left[1 + f(x)h(x)y - \frac{1}{2} f(x)y^2 \right] \quad , \tag{6}$$

where $f(x)=(\rho g/\eta u_o)(\sin\alpha\, h_x-\cos\alpha)-(\gamma/\eta u_o)\kappa_x-(1/\eta u_o)(d\Pi(h)/dh)h_x$. An equation for the steady state h(x) can be found by equating the mass flux $J(x)=\int_0^h \rho u \, dy$ to the evaporative loss between x and the drying line,

$$J(x) = -\int_0^x E(x)\, dx \quad . \tag{7}$$

The quantity E(x) is the evaporation rate (g cm^{-2} sec^{-1}) at point x.

Let $d=(\eta u_o/\rho g)^{1/2} \approx 10$ μm, $D=(\gamma/\rho g)^{1/2} \approx 1$ mm (the gravitational capillary length), $Ca=\eta u_o/\gamma \approx 10^{-5}$ (the capillary number), and $\delta=(Ca)^{1/6}$. Following Wilson, we scale h by δd and x by $d^{1/3}D^{2/3}$ yielding

$$\phi^3 \frac{d}{d\xi} \frac{\phi_{\xi\xi}}{(1+\delta^4\phi_\xi^2)^{3/2}} = 3[\phi - j(\xi)] - \pi_\xi \phi^3 \phi_\xi - \delta^2 \cos\alpha\, \phi^3 + \delta^4 \sin\alpha\, \phi^3 \phi_\xi \, . \tag{8}$$

Here $\phi=h/(\delta d)$, $\xi=x/(\delta L)$, $j(\xi)=(\delta d\rho u_o)^{-1}\int^x E(x)dx$, and $\pi(\xi)=\Pi(h)/(\delta L\gamma)$. The disjoining pressure Π can include van der Waals, osmotic, and double layer forces. We limit ourselves to regimes in which Π is neglible, e.g. pure nonaqueous solvents of thickness greater than 500 Å.

Now we focus on the thin entrained film within, say, several microns of the drying line (where the profile slope ϕ_ξ is still small). Equation (8) shows that near the dr z line for small ϕ

$$\phi \to j(\xi) \qquad (\xi \to 0) \quad . \tag{9}$$

The local evaporation rate E(x) must be equal to the diffusive flux of vapor, $-D_v(\partial c/\partial y)_{y=h}$, from the liquid surface. D_v is the vapor diffusivity and c is the vapor concentration. The vapor concentration follows the steady state diffusion equation,

$$\nabla^2 c = 0 \quad ; \quad c = c_o \text{ on the liquid surface} \quad , \tag{10}$$

$$c_y = 0 \quad \text{on the dry substrate } x < 0 \ , \tag{11}$$

where the first boundary condition, borrowed from Maxwell's study of evaporating drops [7], applies when the mean free path of the vapor molecules (~10^3 Å) is small compared to the extent of the liquid surface. The second boundary condition ensures there's no evaporative source above the drying line; it can be trivially satisfied by symmetry after reflecting the problem near the drying line about the plane y=0.

Equation (10) is equivalent to that for the electrostatic potential around a conductive object, with the electric field at the surface being analogous to the evaporation rate E(x) and the flux $j(\xi)$ analogous to the charge accumulation between 0 and ξ. Near any sharp boundaries, the electric field (evaporation rate) diverges but the charge (vaporized mass) must remain integrable. This divergence in evaporation accounts for the blunt profile noted in Fig. 1 as shown below.

Since the profile h(x) is not known a priori, Eq. (10) is a free boundary problem. However, since the entrained film is very thin compared to its breadth and length, the vapor sees it as infinitely thin; hence, its detailed shape doesn't matter. The solution for the potential and field near the edge of a thin sheet is [8]

$$c \approx c_o - a_1 r^{1/2} \sin(\theta/2) \quad , \tag{12}$$

$$E = -D_v \frac{\partial c}{\partial y}\Big|_{y=0} \approx D_v a_1 x^{-1/2} \quad , \tag{13}$$

where (r,θ) are cylindrical coordinates $r\sin\theta = y$ and $r\cos\theta = x$. The constant a_1 must be determined from boundary conditions. Using Eq. (9), the film profile is

$$h(x) \to \frac{D_v a_1}{\rho u_o} x^{1/2} \quad . \tag{14}$$

Fitting the data of Fig. 1 to the form $h=cx^\nu$ yields $\nu=0.50\pm0.01$, in agreement with Eq. (14), with $c^2\approx1$ Å. Taking $D_v\approx0.1$ cm^2/s and a saturation vapor pressure of about 40 torr (ethanol), we find $a_1\approx10^{-4}$ g cm$^{-7/2}$; the concentration drops by 10% at a distance of 1 cm from the film's surface.

Equation (14) holds over the experimentally observable range 50 μm < x < 1 cm, and it can be shown that the curvature is small in this range. Nearer the drying line, however, the capillary pressure cannot be ignored. Equation (8) can be improved by rescaling in view of Eq. (14). Let $\xi=\delta^{10}X$, $\phi=\delta^{10}\Phi$, and $j=\delta^{10}\Psi$, then ignoring higher powers in δ we obtain

$$\Phi^3 \Phi_{XXX} = 3(\Phi - \Psi) \quad , \tag{15}$$

which should be good when capillary pressure is important. Inevitably, the van der Waals forces will be dominant, since $\pi(\xi)\to\xi^{-n}$ (n=3 or 4), at which point static wetting should pertain [9].

An interesting feature of this phenomenon is the fact that the strength of the singularity is geometry dependent: The effect of changing the substrate from a plane to a line (cylinder with small radius) changes the profile in a characteristic way through the singularity strength (exponent) in Eq. (13). For coating a circular cylinder of decreasing radius, the strength passes from 1/2 for a large radius (because the film is locally a sheet) to 1 as the radius vanishes. This property has been demonstrated experimentally (to be reported elsewhere). Thus, we would expect a singularity of strength 1 for spinning or coating sol-gel fibers.

SOL STRUCTURE AND CAPILLARY COLLAPSE

In the prototypical sol-gel process, silicates dissolved in alcohol are provided with varying amounts of water at a given pH to promote hydrolysis and subsequent condensation reactions. The polymers generated range from small, weakly branched, compliant oligomers to compact colloidal spheres depending on pH.

We can guess at the course of events during drying by following Scherer's analysis [10] for xerogels. After emerging from the drying line, the newly deposited film is still covered with liquid. As the liquid evaporates and the gas-liquid interface begins to invade the pore space, menisci develop with a mean radius of curvature r that is initially infinite (flat) but rapidly decreasing. Assuming quasistatic conditions and good wetting (so that $\cos(\theta_{wet})$ is of order 1), there must be a pressure drop across the interface given by the Young-Laplace equation [11]

$$\Delta p = -\frac{2\gamma}{r} \quad , \tag{16}$$

where γ is the surface energy. The network will compress under the capillary pressure, eventually compacting beyond the elastic limit. In the last stages, the menisci have radii comparable to the pore size in the compacted network.

Now it is clear how the sol structure plays a role, since for non-interpenetrating clusters the size of the pores in the initial network will be comparable to the precursor size. Small precursors will normally have small pores with large capillary pressures, and vice versa for large particles. These trends have been observed [12] in the refractive index of films formed from silicate sols aged for as long as three weeks during which the precursor particles grew large enough to make the sol turbid. The refractive index, which is sensitive to the porosity, decreased from over 1.40 to below 1.20.

For a 1 μm pore half-filled with water, Eq. (16) implies a pressure difference of about 1 atm. Since the meniscus is curved away from the liquid, the pressure in the liquid is lower than that of the gas phase, and, for pores of 1 μm and smaller, the liquid pressure goes negative. One might expect the water simply to boil, limiting the pressure drop to about 1 atm. However, it appears that liquids in sufficiently small pores are able to overexpand, a condition analogous to superheating, because nucleation of vapor bubbles is suppressed by the small pore volume [13]. That is to say, the pore volume available to the bubble is smaller than a critical nucleus. An estimate of the absolute limit of this overexpansion is given by the negative portion of the van der Waals loop, which represents metastable states with large chemical potential and is shown in Fig. 2 as the section from A to B. The maximum tensile pressure at B is of order 1000 atm, beyond which some part of the liquid spontaneously vaporizes.

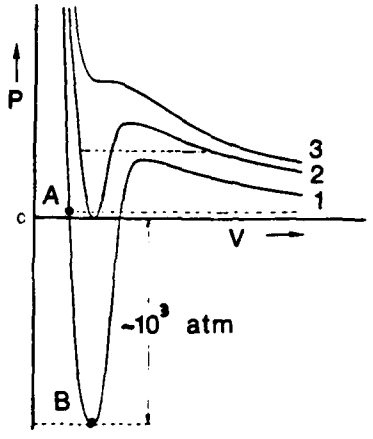


Figure 2. Van der Waals phase diagram for water. By the equal-area construction, point A represents equilibrium liquid. Overexpanded liquid in capillaries lies on the metastable branch AB. Higher temperatures are represented by lines 2 and 3. (From Ref. 13)

DISCUSSION

The determination of the entrained film profile provides a great deal of information about the environment experienced by a sol particle as it is carried from the reservoir to the drying line. By conservation of nonvolatile mass, the concentration of solids $\chi(x)$ must satisfy $\chi(x)h(x)$=constant for all positions above the "stagnation point"--the point on the liquid surface below which the liquid returns to the reservoir--which is normally in the gravitational meniscus region. Hence, for planar geometry we expect $\chi \sim x^{-1/2}$, i.e. the concentration diverges as the evaporation rate. The mean particle separation is quite precipitous, $\Delta r \sim \chi^{-1/3} \sim x^{1/6}$; half of the decrease in Δr occurs within the last 2% of the entrained film. The situation is not so clear for the rate of reaction, which can be characterized by the inverse of the time Δt for diffusing to the nearest particle. If the viscosity η diverges as some power of the volume fraction χ^s, we have $\Delta t \sim \eta \Delta r^2 \sim x^{1/3-s/2}$; diffusion-limited reactions would be expected to accelerate if $s<2/3$.

With the possibility of pore liquid overexpansion, it is easy to see why capillary forces can be overwhelming during the capillary collapse stage of film formation. It is interesting that during this stage the pores are filled with the chemical equivalent (from a chemical potential standpoint) of superheated liquid [14], which may help to patch together any undone reactions (although transport is severely limited after deposition).

It should be possible to diminish the maximum tensile pressure by simply heating the liquid, as the upper curves in Fig. 2 illustrate. Thus, if the pore tensions are limited only by maximum overexpansion, heating during film formation would cause less capillary collapse.

There is an apparent difficulty with the argument regarding suppression of nucleation in small pores: the vapor phase is already present at the interface and shouldn't have to nucleate but simply to propagate--a dilemma not addressed in the literature. An alternative view, in which there would be less overexpansion, is that the the system adjusts its contact angle to keep the meniscus from curving beyond some value. The cost in free energy due to this accommodation at the contact line would be

mitigated by less expansion work on the liquid. A similar idea, in which the region near the contact line is distorted by evaporative flow, has recently been developed by P. C. Wayner [15].

It is important to note that, even if the menisci are flat (contact angle=90°) and the Laplace pressure drop is zero, strong forces and torques are exerted on the walls of the pore by the surface tension with the possibility of collapse. (A torque could arise, for example, when flat menisci on either side of a thin wall are at different levels.) Detection of capillary pressures is an outstanding realm for experiments.

ACKNOWLEDGMENTS

The authors have benefited by helpful discussions with L. E. Scriven, P. R. Schunk and G. W. Scherer. This work was supported by Sandia National Laboratories under Department of Energy Contract DE-AC04-76-DP00789.

REFERENCES

1. H. Schroder, in Physics of Thin Films: Advances in Research and Development, edited by G. Haas and R. E. Thun, 5, 87 (1969).

2. C. J. Brinker, A. J. Hurd, G. C. Frye, K. J. Ward, and C. S. Ashley, in the Proceedings of the Fourth International Conference on Ultrastructure Processing of Ceramics, Glasses and Composites, J. Non-Crystalline Solids, (in press, 1990).

3. A. J. Hurd and C. J. Brinker, J. Phys. France 49, 1017 (1988).

4. L. Landau and B. Levich, Acta Physicochim. (URSS) 17, 42 (1942).

5. S. D. R. Wilson, J. Engg. Math. 16, 209 (1982).

6. A. J. Hurd and C. J. Brinker, in Better Ceramics Through Chemistry III, edited by C. J. Brinker, D. E. Clark, and D. R. Ulrich (Materials Research Society, Pittsburgh) 121, 731 (1988).

7. N. A. Fuchs, Evaporation and Droplet Growth in Gaseous Media, (Pergamon, London, 1959) chapter 1.

8. J. D. Jackson, Classical Electrodynamics, (Wiley, NY, 1975) section 2.11.

9. J. G. Truong and P. C. Wayner, Jr., J. Chem. Phys. 87, 4180 (1987).

10. G. W. Scherer, J. Non-Cryst. Solids 107, 135 (1989).

11. L. Landau and I. Lifshitz, Fluid Mechanics, (Pergamon, Oxford, 1959) chapter 7.

12. C. J. Brinker, A. J. Hurd, and K. J. Ward, in Ultrastructure Processing of Advanced Ceramics, edited by J. D. Mackenzie and D. R. Ulrich (Wiley, NY, 1988) p. 233.

13. C.G.V. Burgess and D. H. Everett, J. Colloid and Interface Sci. 33, 611 (1970).

14. L. E. Scriven, private communication (November, 1989).

15. P. C. Wayner, private communication (June, 1990); see also J. Schonberg and P. Wayner, AIAA Proceedings 90-1787.

SOL-GEL COATINGS ON ACOUSTIC WAVE DEVICES: THIN FILM CHARACTERIZATION AND CHEMICAL SENSOR DEVELOPMENT

GREGORY C. FRYE, C. JEFFREY BRINKER, ANTONIO J. RICCO, STEPHEN J. MARTIN, JANICE HILLIARD, AND DANIEL H. DOUGHTY
Sandia National Laboratories, Albuquerque, NM 87185

ABSTRACT

We have investigated the use of porous oxide coatings, formed using sol-gel chemistry routes, as the discriminating elements of acoustic wave (AW) chemical sensors. These coatings provide several unique advantages: durability, high adsorption capacity based on large surface areas, and chemical selectivity based on both controlled pore size and acid/base, ion exchange or chelation chemistry. The porosity of these coatings is determined by performing nitrogen adsorption isotherms using the AW device response to mass changes to monitor the uptake of nitrogen at 77 K. These studies demonstrate how sol-gel chemistry and film deposition can be combined to tailor the microstructure of thin oxide coatings. The chemical sensitivity and selectivity obtained with this class of coatings will be demonstrated using several examples: hydrous titanate ion exchange coatings, zeolite/silicate microcomposite coatings, and surface-modified silicate films.

INTRODUCTION

Sol-gel processing involves the hydrolysis and condensation of metal organic or inorganic precursors to form inorganic polymers in solution [1]. By varying the reaction conditions (e.g., reaction protocol, concentration of catalyst, water or metal precursor), the structure of these polymers can be varied from weakly branched chains to highly ramified structures (i.e., resembling a tumbleweed) to dense colloidal particles [2]. Prior to gelation, films can be prepared from these solutions by either spin- or dip-coating. The final film structure is dictated by the film forming procedure and the polymer structure: dense films are formed from weakly branched polymers, while high surface area porous films are formed from highly ramified polymers or dense colloidal particles [3]. The pore size distribution in the porous films can be tailored by varying the size and shape of the precursor polymers as well as by varying the coating procedure or thermal treatment [4]. In this paper, the application of these controlled microstructure oxide coatings for chemical sensor coatings will be discussed.

Coatings that provide both chemical selectivity and increased sensitivity are critical for the development of effective chemical sensors [5,6]. Chemical selectivity is achieved by selective sorption of a single species or a class of species while increased sensitivity is obtained by high sorption capacities. Some examples of the types of sensor coatings that have been previously employed are organic polymers [5,7], phthalocyanines [5] and biological agents [8]. For sensors based on AW devices, gas phase sensors utilizing surface acoustic wave (SAW) devices [5,7] and liquid phase sensors utilizing either acoustic plate mode (APM) devices [9] or Lamb wave devices [8] have been developed.

Compared to these coatings, controlled porous oxide coatings can provide several unique advantages as the discriminating elements of chemical sensors: (1) resistance to thermal or chemical degradation, (2) high surface area and pore volume resulting in large sorption capacities and increased sensitivity, (3) controlled microstructure (i.e., pore size distribution) providing chemical discrimination based on molecular size, (4) capability to easily modify the chemical nature of the surfaces to provide discrimination based on chemical interactions, and

Mat. Res. Soc. Symp. Proc. Vol. 180. ©1990 Materials Research Society

(5) minimal changes in film properties (e.g., viscoelastic properties) during sorption resulting in simplified analysis of sensor response. Specific examples to be discussed are: (1) the use of SAW devices coated with zeolite microcrystals embedded in a dense sol-gel matrix to provide size dependent chemical selectivity, (2) the use of APM devices coated with hydrous oxides with large ion exchange capacities for sensing ionic species in solution, and (3) the addition of chemically reactive surface groups to porous oxide films using silane coupling agents.

Acoustic Wave Devices

Acoustic wave devices consist of input and output interdigital transducers formed on a piezoelectric substrate such as quartz or lithium niobate. When an alternating voltage is applied to the input transducer, it generates an alternating mechanical strain field (due to the piezoelectric nature of the substrate). This launches an acoustic wave which travels along the surface (e.g., a surface acoustic wave: SAW) or through the bulk of the substrate (e.g., an acoustic plate mode: APM). This wave interacts with thin films or adsorbed species on the device surface before being converted back into an electrical signal by the output transducer. This interaction results in an alteration of the velocity of the wave.

Changes in wave velocity can easily be monitored by operating the device as the feedback element of an oscillator circuit using an RF amplifier. In this configuration, changes in frequency (f) can be directly related to changes in wave velocity (v). In situations where the velocity shift (Δv) is dominated by changes in the mass density of the film, these frequency changes (Δf) can be directly related to changes in mass density Δm (mass/area) using:

$$\frac{\Delta f}{f_o} = \frac{\Delta v}{v_o} = - c_m \Delta m , \qquad (1)$$

where v_o and f_o represent the unperturbed velocity and frequency, respectively. The parameter c_m is a mass sensitivity constant which depends on the piezoelectric substrate, the acoustic wave being used, and the device frequency. To illustrate the extraordinary sensitivity of these devices, the 97 MHz SAW devices used in this study have a typical short term frequency stability in operation of about 10 Hz, giving a mass resolution of 0.8 ng/cm^2 of film (c_m = 125 cm^2/g for this device).

Surface acoustic waves resemble a wave on water, exhibiting displacement in the direction of propagation as well as normal to the substrate. If a liquid is placed in contact with a SAW device, the normal component of displacement results in the generation of compressional waves in the liquid. These compressional waves carry the acoustic power away from the substrate making the operation of the SAW device difficult. However, acoustic plate modes having displacement in the plane of the substrate and perpendicular to the direction of propagation can also be excited [9]. When a liquid is placed in contact with an APM device, only viscous coupling of the wave occurs. This results in a relatively small amount of wave attenuation, making these devices effective as liquid phase sensors. In addition, these waves travel through the bulk of the crystal with equal amplitude at both surfaces. This allows the liquid to be contacted to the unelectroded side of the crystal, protecting the transducers from the liquid. APM devices can also act as extremely sensitive microbalances. For the 158 MHz APM device used in this study, the mass sensitivity is within a factor of three of the SAW device (c_m = 43 cm^2/g, determined by monitoring frequency during the vacuum evaporation of metal onto the substrate). Additional details on both SAW [5] and APM [9] devices are given elsewhere.

RESULTS AND DISCUSSION

Characterization of Film Porosity

In developing oxide coatings for chemical sensors, the microstructural properties of potential films must be characterized. The frequency response of a coated SAW device is used to monitor the uptake of nitrogen (at 77 K) as a function of the partial pressure (p) of nitrogen in the gas phase over the device. This type of measurement, called a nitrogen adsorption isotherm, can be used to determine [10]: (1) sample surface area using the BET analysis, (2) total pore volume based on the maximum uptake at partial pressures close to the saturation vapor pressure (p_o) at the temperature of the run, and (3) pore size distributions based on an analysis considering capillary condensation into the pores.

The experimental system used for these measurements is shown in Fig. 1. To remove adsorbed species from the surfaces of the film prior to a run, the test case and a coil on the gas inlet side are placed in an oven and heated to 160 °C for two hours under dry nitrogen. A pure helium stream is then passed over the device while the test case and coil are immersed in a dewar flask of liquid nitrogen to maintain the device and gas stream at 77 K. During a run, computer-operated mass flow controllers are used to vary the relative flow rates of a nitrogen carrier stream and a nonadsorbing helium mix-down stream. In this way, normalized nitrogen partial pressure (p/p_o) is varied from zero to about 0.95 and back to zero. Nitrogen adsorption isotherms obtained in this manner for two films are shown in Fig. 2. The sol-gel system used contains SiO_2, B_2O_3, Al_2O_3 and BaO in ratios (by weight) of 71:18:7:4 (details of the sol-gel preparation are presented elsewhere [11]). Films were formed on the SAW device surface by dip-coating followed by a 400 °C anneal for 5 minutes.

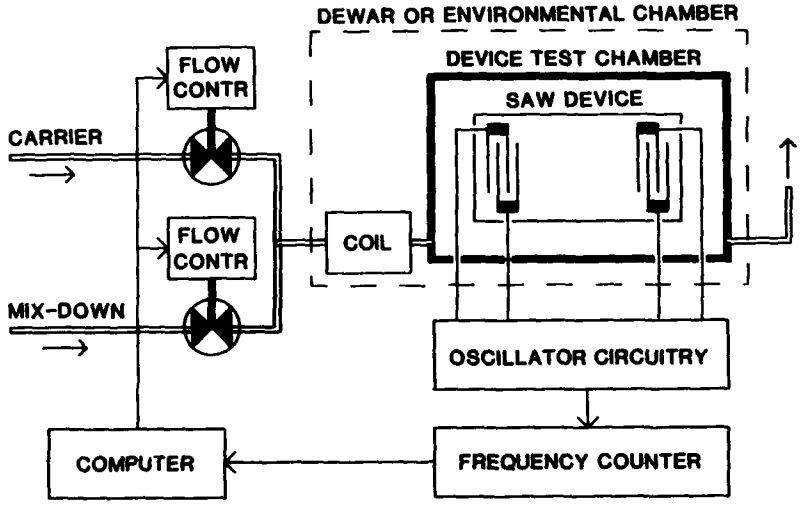


Fig. 1: Schematic of experimental system used to monitor nitrogen adsorption on the surfaces of porous thin films formed on SAW devices. The device is maintained at 77 K by immersion in a dewar flask filled with liquid N_2. The N_2 partial pressure is controlled by varying the relative flow rates of N_2 and He streams while the mass of adsorbed N_2 is determined by monitoring changes in the SAW frequency.

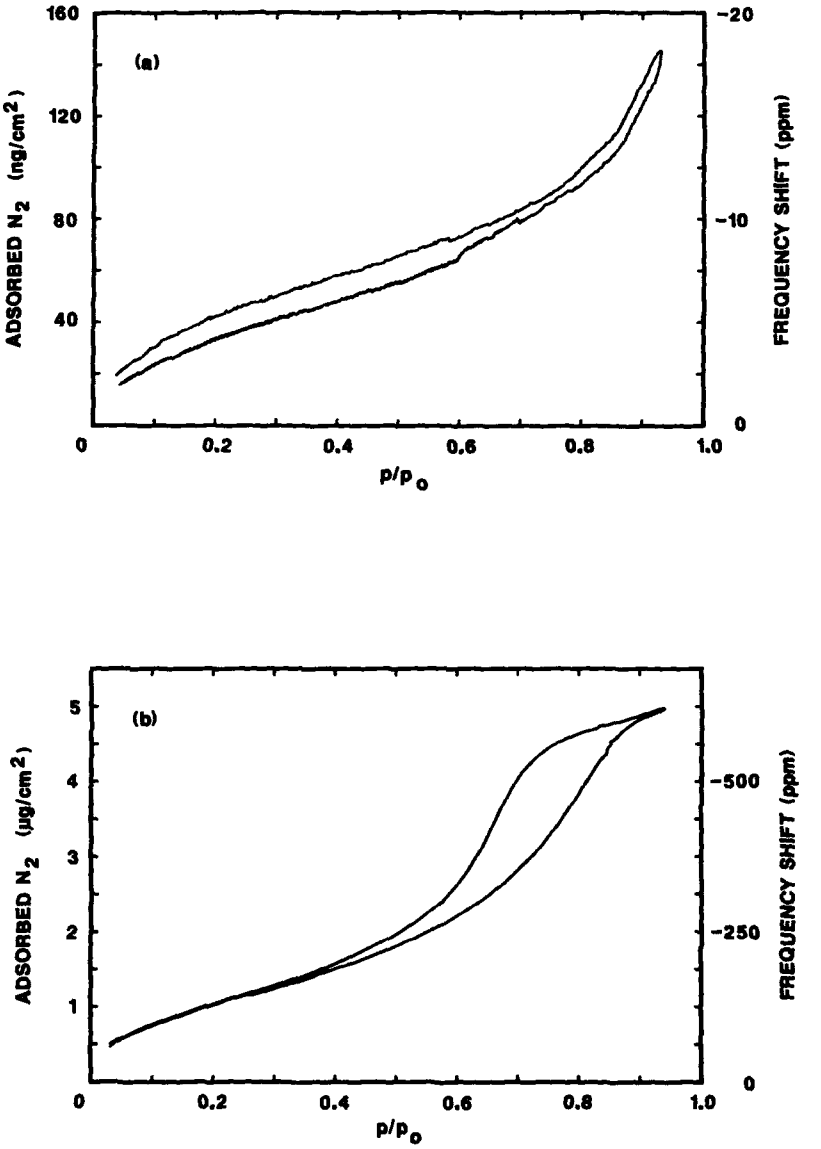


Fig. 2: Nitrogen adsorption isotherms using coated SAW devices for films formed from (a) unaged and (b) aged sol-gel solutions. A BET surface area of 1.3 $cm^2/(cm^2$ of film) for the film formed from the unaged sol indicates this film is nonporous while a value of 33 cm^2/cm^2 obtained for the film formed from the aged sol indicates it is highly porous.

The first film (Fig. 2a) was formed by dip-coating using the unaged sol which contains very small polymeric precursors (hydrodynamic radius ~3 nm). The total amount of adsorption is small and the shape of the isotherm is Type II, typical of nonporous samples [10]. The BET surface area is 1.3 $cm^2/(cm^2$ of film), very close to the value of 1.0 cm^2/cm^2 expected for a flat, nonporous film (the slightly higher value may be indicative of surface roughness). These results agree with ellipsometric (Rudolph AutoEL IV) analysis which gives a film thickness of 120 nm and a refractive index of 1.46, very close to the value expected for a dense film of this composition.

The second film (Fig. 2b) was formed by dip-coating after aging the same sol for three weeks at 50 °C and pH 3. This aging results in larger (hydrodynamic radius ~25 nm), highly ramified polymeric species which, due to their inability to interpenetrate, create porosity in the film [3]. This porosity is verified by ellipsometry which gives a refractive index of 1.18. A volume percent porosity of 56% was calculated from this value using the Lorentz-Lorenz relationship and a skeletal refractive index of 1.45. A percent porosity of 52%, in good agreement with this result, was calculated from the nitrogen adsorption isotherm by determining the volume of nitrogen adsorbed (per unit area) at high partial pressures (p/p_o = 0.94) and comparing to the film thickness (148 nm). The isotherm shape is Type IV, typical of porous samples with pore diameters in the range of 3 to 50 nm. The BET surface area is 33 cm^2/cm^2, indicating a significant amount of porosity for this thin film (this corresponds to a surface area of ~250 m^2/g of film). Using multiple coats to obtain a film thickness on the order of 1 μm, surface area enhancements of 200 or more could be obtained with this system.

The pore size distribution obtained from the desorption branch of the isotherm for the porous film (Fig. 2a) is shown in Fig. 3. A unimodal distribution with a median pore diameter of 6.2 nm is obtained. Even though these pores are too large to exclude many species on the basis of size, smaller pore sizes are obtained with this system using shorter aging times [4,11]. This allows the pore size to be varied over a significant range by simply varying the aging time prior to film formation. Additional details on the characterization of this system as well as on the use of different reaction protocols (e.g., acid vs. base catalysis) are presented elsewhere [4,11,12].

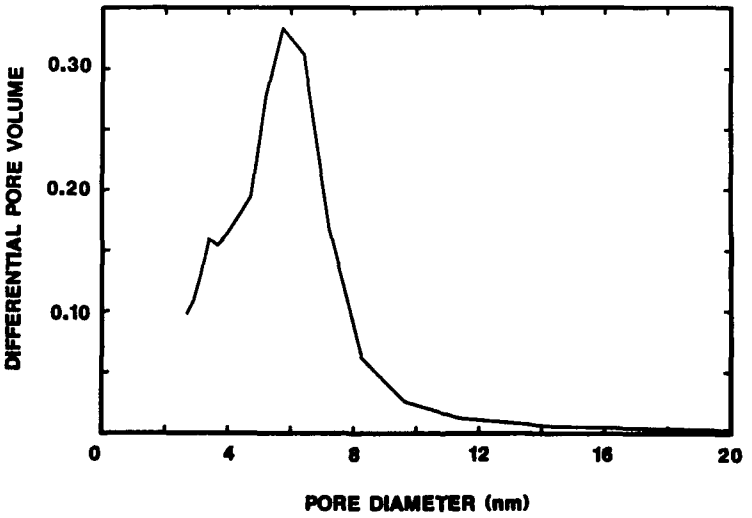


Fig. 3: Pore size distribution obtained from the desorption branch of the nitrogen adsorption isotherm for film formed from the aged sol (see Fig. 2b). Median pore diameter is 6.2 nm.

To investigate the effect of film-forming procedure on film microstructure, two SAW devices were dip-coated from the same particulate sol followed by a 400 °C anneal for 10 minutes. The sol, prepared according to the Stöber process [13], resulted in colloidal silicate particles having a diameter of 55 nm. The only difference between the two coatings was the dip-coating rate: 5 versus 18 inch/min. The results of the SAW nitrogen adsorption studies are listed in Table I. Theoretical values for the surface area and percent porosity are also listed. These values were calculated based on the refractive index and film thickness (obtained using ellipsometry) and the known particle size. The faster dip coating rate entrains a thicker layer of the sol which results in a significantly thicker film (130 and 260 nm for 5 and 18 inch/min, respectively). This thicker coating results in a higher surface area. The BET surface areas obtained from the SAW nitrogen adsorption isotherms are in good agreement with the calculated values, helping to verify the absolute accuracy of this technique.

The faster coating rate also appears to result in a denser particle packing. This is reflected in lower values for percent porosity for the 18 inch/min sample (calculated as described above except a skeletal refractive index of 1.4, calculated for 90% density in the matrix and a refractive index of 1.45 for a fully dense material of this composition, was used). The refractive index values were 1.228 and 1.262 for the 5 and 18 inch/min samples, respectively. The experimental SAW values and the calculated values are again in good agreement for both films tested. The denser packing at the faster rate is also seen in smaller values for the median pore diameter (calculated from the desorption branch). Results of this type of film characterization study are critical in determining how to tailor surface area and pore size to fit a given sensing application based on controlling sol-gel chemistry, reaction protocols and film-forming technique.

Table I: Comparison of experimental (SAW nitrogen adsorption) and calculated values for the properties of films formed at two dip-coating rates from solutions of 55 nm diameter silicate particles formed by the Stöber process [13].

Dip Coating Rate (inch/min)	Percent Porosity		Surface Area (cm^2/cm^2 of film)		Median Pore Diameter (nm)
	Nitrogen Adsorption ($p/p_o = 0.96$)	Calculated (Refractive Index)	Nitrogen BET	Calculated	
5	36%	40%	8.7	8.6	18.1
18	27%	32%	16.4	19.9	15.0

Zeolite/Silicate Microcomposite Coatings

The most dramatic demonstration of chemical selectivity based on size exclusion will be obtained with a film with a single characteristic pore size. Sol-gel chemical routes can provide a narrow range of pore sizes; however, the random nature of this process always results in a distribution in pore sizes (see Fig. 3). One model inorganic porous system with unimodal pore sizes is the zeolites (molecular sieves). The most common zeolites are aluminosilicates which, due to their cagelike crystalline structures, have a single pore size that dictates accessibility to molecular adsorbate species. For example, the ZSM-5 zeolite has an opening with dimensions of 0.55 by 0.60 nm.

Zeolites can be synthesized using hydrothermal techniques. By rapid quenching at the early stages of the reaction, small (< 1 μm crystallite size) ZSM-5 crystals are formed [14].

To create an AW device coating that utilizes the unimodal pore size of zeolites, these small crystals are embedded in a dense thin-film sol-gel matrix [15]. This matrix forces adsorption to occur exclusively within the zeolite channel system. SEM analysis shows that the zeolites protrude from the sol-gel matrix. Quantitative titration of intrazeolite acid sites with organic bases such as pyridine indicate that the zeolite channels remain accessible [16].

The selectivity of a SAW device coated with this ZSM-5 zeolite/silicate microcomposite film has been previously demonstrated using molecular probes with kinetic diameters ranging from 0.38 to 0.62 nm [16]. At relatively low vapor concentrations (0.1% of saturation for each species), large negative frequency shifts were observed for methanol and isopropanol, which have kinetic diameters (0.38 and 0.47 nm, respectively) less than the zeolite pore size. These frequency shifts indicate significant amounts of adsorption in the pores of the zeolite crystals: 540 and 840 ng/cm^2 for methanol and isopropanol, respectively. A small (approx. 1% of the signal observed with methanol and isopropanol) positive frequency shift was observed upon exposure to the larger iso-octane (kinetic diameter = 0.62 nm). The cause of this small response is unknown since a mass loading increase alone always results in a decrease in SAW frequency. These results serve as proof-of-principal that dramatic discrimination based on size exclusion effects can be obtained using controlled microstructure coatings.

Hydrous Oxide Ion Exchange Coatings

It is well known that hydrous oxides, such as sodium titanates or niobates, act as ion exchange materials with large ion exchange capacities. This capability can be used to advantage in nuclear waste applications [17] or in the preparation of catalysts which, due to the highly dispersed nature of the ion exchanged metal atoms, show high activity even at low metal loading [18]. By preparing coatings from these materials on acoustic plate mode (APM) devices, these large ion exchange capacities should result in large sensor responses during the exchange of ions from solution. Chemical selectivity can be varied by the choice of cations used (e.g., niobates form strongly acidic supports, titanates form amphoteric supports, and lanthanides form basic supports) and by controlling pore sizes.

To investigate the utility of these coatings, a sodium titanate system with a sodium:titanium ratio of 1:2 was chosen [17,18]. The standard preparation technique for this material results in a solution which thickens too quickly to be usable in forming homogeneous coatings. However, by diluting to 25% by volume in hexane, reasonably homogeneous coatings are formed by spin-coating at 4000 rpm. Film thickness per coat is 300 nm. Initial experiments investigated the APM response during the uptake of aqueous Ni^{2+} at pH 6. In contrast to results obtained using bulk titanates [18], the APM response indicates the ion exchange is far from complete in films and is only partially reversible (significant amounts of exchanged Ni^{2+} appear to remain in the film after treatment with pH 3.0 HNO_3 and 1.0 M $NaNO_3$ solutions).

To verify the APM results, similar coatings were formed on silicon and analyzed using a Tracor 5000 energy dispersive X-ray fluorescence (XRF) spectrometer. Based on the amount of titanium in the film, Ni^{2+} exchange is incomplete (only 6% after 10 min in a 0.05 M $Ni(NO_3)_2$ solution at pH 5.8). This incomplete exchange is verified by the observation that only 35% of the Na^+ initially present in the film was removed. The partial irreversibility of the Ni^{2+} exchange is consistent with the lack of an experimentally significant change in the Ni/Ti ratio after a pH 3.0 HNO_3 rinse, a subsequent 1.0 M $NaNO_3$ rinse and, finally, a 0.1 M EDTA (ethylenediaminetetraacetic acid) rinse at pH 6.5.

In contrast, XRF analysis of a second film for the ion exchange of Ag^+ indicates that exchange from a 0.05 M solution at pH 8 is effectively complete (97% of theoretical with only 3% of the initial Na^+ remaining in the film). In addition, the Ag^+ can be effectively removed

from the film: only 23% remained after a pH 3.0 HNO_3 rinse, 15% after a subsequent 1.0 M $NaNO_3$ rinse and 9% after a final 0.1 M EDTA rinse. Based on these results, Ag^+ exchange experiments were performed on a second coated APM device. Peristaltic pumps were used to pump solutions to and from a cell holding the liquid in contact with the unelectroded side of the coated APM device.

The results, shown in Fig. 4, are in good qualitative agreement with the XRF data. When a pH 8.0 solution of NaOH is replaced with a 0.05 M $AgNO_3$ solution at the same pH, a frequency decrease of about 190 ppm is observed after an initial frequency increase. Assuming the frequency response is due to changes in the mass loading of the film, this shift corresponds to a change in the film mass density of 4.4 $\mu g/cm^2$. This value is significantly lower than the value of 40 $\mu g/cm^2$ calculated for complete exchange of Ag^+ for Na^+ for a film thickness of 600 nm (two coats were used), a sodium titanate skeletal density of 2.4 g/cm^3, 40% porosity and a mass per ion exchange site of 177 g/mole (assumes site has form $HTi_2O_5^-$). This difference may indicate that many of the ion exchange sites are inaccessible. Work is ongoing with this system to determine the cause of this reduced response and to determine if the film-forming process can be altered to prepare coated APM devices which exhibit the dramatically larger expected response (full exchange of Ag^+ should give a frequency decrease of about 1800 ppm). The initial upward spike appears to be due to the loss of liquid flow which occurs during the change of solutions and was observed every time the solutions were changed. It should be possible to remove this spurious signal using a solvent delivery system that can change solutions without loss of flow.

When the pH 8.0 $AgNO_3$ solution is replaced with a NaOH solution at the same pH, a 60 ppm frequency increase is observed, indicating that about 30% of the Ag^+ is removed from the film. When a pH 3.0 HNO_3 solution is used, an additional frequency increase of over 110 ppm is observed. The total frequency increase in these two steps indicates that 90%

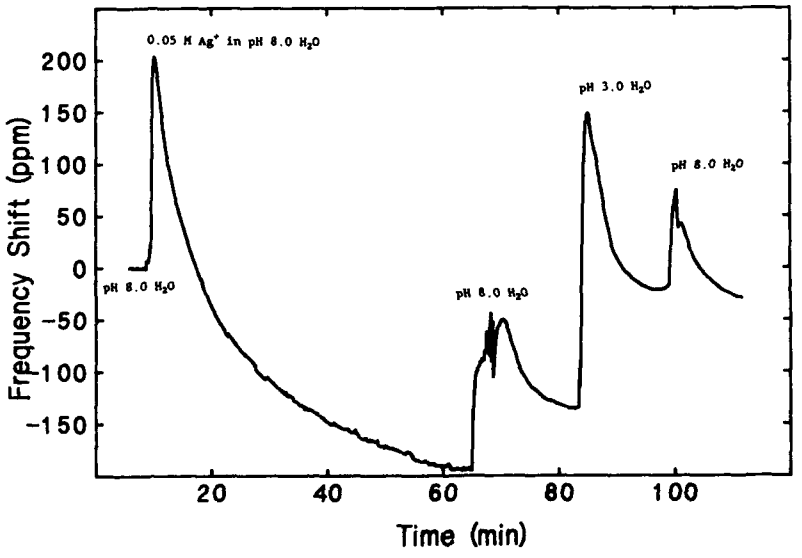


Fig. 4: Frequency response of sodium titanate-coated APM device during ion exchange of Ag^+. A mass increase of 4.4 $\mu g/cm^2$ is detected for this exchange. Reversibility is indicated by the frequency returning to near its original value after a pH 3.0 rinse.

of the exchanged Ag^+ has been removed, verifying the reversibility of this exchange process (this value may be a slight overestimate since the ion exchange sites will contain H^+ at this pH rather than Na^+ after the Ag^+ is removed). Except for the upward spike, a relatively small frequency shift is observed when the pH 3.0 HNO_3 solution is replaced with the pH 8.0 NaOH, indicating that the frequency increase seen with the pH 3.0 solution is due to mass loss during Ag^+ removal rather than some other effect related to the pH change. These results demonstrate that the large ion exchange capacities of hydrous oxide materials can be used to provide large sensor responses. Future work with these coatings will focus on: (1) optimizing the film-forming process to maximize sensor response and reproducibility, (2) determining the selectivity of the ion exchange process to ionic species of interest, and (3) investigating the variability in ion exchange properties obtainable with various hydrous oxides.

Surface Modification Using Silane Coupling Agents

Another technique being investigated to take advantage of the high surface area and controlled pore structure of sol-gel coatings is the derivatization of the coating surfaces with ligands that selectively bind chemical species of interest. The derivatizing agents used in this study are silane coupling agents (e.g., $XSi(OR)_3$ where R is an alkyl group and X is a ligand). The specific agent used, designated TMS-DETA, has a diethylenetriamine (DETA) ligand separated from the Si by a propyl chain: $(CH_3O)_3Si(CH_2)_3NH(CH_2)_2NH(CH_2)_2NH_2$. Two techniques for performing this derivatization have been investigated.

The first technique involves the addition of the TMS-DETA to the sol-gel solution during preparation to form particles coated with DETA. Derivatized films could then be formed by dip- or spin-coating from this solution. This procedure was used to alter a sol-gel process to make particles with diameters of approximately 25 nm (based on the Stöber process [13]). The results are summarized in Table II. The TMS-DETA has a significant effect on the stability of the sol-gel solution: as the TMS-DETA concentration is increased, the system changes from a stable sol to a flocculated sol to a gel. The uptake of Cu^{2+} after treatment with 1.0 M $Cu(NO_3)_2$, determined by dissolution of the sample and analysis by atomic absorption spectroscopy, appears to be stoichiometric with the amount of DETA used in the sol-gel preparation (i.e., one Cu^{2+} per DETA molecule). This indicates the ligands are accessible for binding from solution. In addition, a deep blue color is observed in the samples at higher DETA concentrations, typical of copper amine complexes. It was observed that this color lightened upon removal of water (sample is stored in a dry environment) and deepened upon exposure to water vapor. This is probably due to removal of water molecules which are acting to fill the fourth coordination site of the copper. If the dry sample is exposed to ammonia, the color deepens rapidly and remains dark even if placed in a dry environment, indicating that the ammonia molecule is more strongly attached due to its better ability to complex the copper. This sensitivity to ammonia could be used to prepare a dosimetric ammonia sensor from these coatings.

The second technique involves the preparation of a porous coating from a standard particulate sol followed by treatment of the surfaces of the sample with the TMS-DETA (from a dilute solution in ethanol). This technique allows the desired pore structure (allowing for the decrease in the pore dimensions due to the attached surface layer) to first be formed using already characterized sol-gel protocols. For this study, particulate silicate films were deposited by spin-coating a solution containing 29 nm diameter Stöber particles. XRF analysis indicated that the uptake of Cu^{2+} in the as-deposited film was less than 0.1 $\mu g/cm^2$ of film after a 5 minute treatment in 1 M $Cu(NO_3)_2$ followed by rinsing with deionized water. However, after the diethylenetriamine ligands were silane-coupled to the surfaces, the Cu^{2+} uptake from a similar treatment increased to 3.0 $\mu g/cm^2$. Based on the film thickness (800 nm) and the particle diameter, this amount of Cu^{2+} can be used to calculate the surface area

Table II: Gel behavior and uptake of Cu^{2+} for a sol-gel system prepared using the Stöber process altered by the addition of TMS-DETA.

Mole Percent		Gel		Color After
DETA/Si	Cu^{2+}/Si	Behavior	Appearance	Cu^{2+}
0.0	0.4	stable	granules	pale green
0.3	0.5	flocs	flakes	lt. blue
1.0	1.0	gels	chunks	deep blue
5.0	5.7	gels	chunks	v. deep blue

per DETA molecule (assuming the Cu^{2+} is bound stoichiometrically and that the film is 60% dense). The value calculated is 0.35 nm^2 per molecule, which represents about one DETA for every 2.7 Si at the surface. Since the silane coupling agent is trifunctional and can form up to three siloxane linkages, this value is in good agreement with a full coating of the DETA ligands on the surfaces of the film. This type of film is currently under test with APM devices. Since a wide variety of ligands with silane coupling groups are commercially available, this generic technique should be able to provide high surface area coatings with tailored chemical selectivities.

CONCLUSIONS

Sol-gel chemistry can be used to prepare thin oxide sensor coatings that provide both high sensitivity, due to high surface areas, and chemical selectivity, due to both steric and chemical factors. Coating microstructure can be evaluated by monitoring nitrogen adsorption/desorption at 77 K using SAW devices as sensitive microbalances. Gas and liquid phase AW sensor coatings based on zeolite/sol-gel, hydrous oxide ion exchange and surface-derivatized sol-gel coatings have been demonstrated.

The authors gratefully acknowledge helpful discussions and technical assistance of C. S. Ashley, S. L. Martinez, B. J. Lammie and K. L. Higgins (XRF) of Sandia National Laboratories and T. Bein and K. Brown (zeolite synthesis) of the University of New Mexico. This work was partially supported by the Advanced Industrial Materials Program of the U. S. Department of Energy and was performed at Sandia National Laboratories, supported by the U.S. Department of Energy under contract number DE-AC04-76DP00789.

REFERENCES

1. C. J. Brinker and G. W. Scherer, Sol-Gel Science: The Physics and Chemistry of Sol-Gel Processing (Academic, San Diego, 1990).
2. C. J. Brinker, J. Non-Cryst. Solids, 100, 31 (1988).
3. C. J. Brinker, A. J. Hurd and K. J. Ward in Ultrastructure Processing of Advanced Ceramics, edited by J. D. Mackenzie and D. R. Ulrich (Wiley, New York, 1988), p. 223.
4. C. J. Brinker, G. C. Frye, A. J. Hurd, K. J. Ward and C. S. Ashley, in Proc. IVth Int. Conf. on Ultrastructure Processing of Glasses, Ceramics and Composites, edited by D. R. Uhlmann and D. R. Ulrich (Wiley, New York, 1990), in press.
5. M. S. Nieuwenhuizen and A. Venema, Sensors and Materials, 1, 261 (1989).

6. H. Wohltjen, Anal. Chem., 56, 87A (1984).
7. S. L. Rose-Pehrsson, J. W. Grate, D. S. Ballantine, Jr. and P. C. Jurs, Anal. Chem., 60, 2801 (1988).
8. B. J. Costello, B. A. Martin and R. M. White, in Proc. 1989 IEEE Ultrasonics Symp. (IEEE, New York, 1989), pp. 977-981.
9. S. J. Martin, A. J. Ricco, T. M. Niemczyk and G. C. Frye, Sensors and Actuators, 20, 253 (1989).
10. S. J. Gregg and K. S. W. Sing, Adsorption, Surface Area and Porosity, 2nd ed. (Academic, New York, 1982).
11. G. C. Frye, S. J. Martin, A. J. Ricco and C. J. Brinker, in Chemical Sensors and Microinstrumentation, edited by R. W. Murray, R. E. Dessy, W. R. Heineman, J. Janata and W. R. Seitz (ACS, Washington, 1989), Ch. 14.
12. C. L. Glaves, G. C. Frye, D. M. Smith, C. J. Brinker, A. Datye, A. J. Ricco and S. J. Martin, Langmuir, 5, 459 (1989).
13. W. Stöber, A. Fink and E. Bohn, J. Coll. Int. Sci., 26, 62 (1968).
14. T. Bein, K. Brown, C. J. Brinker, Studies in Surface Science and Catalysis, 49, 887 (1989).
15. G. C. Frye, A. J. Ricco, S. J. Martin and C. J. Brinker, in Better Ceramics Through Chemistry III, edited by C. J. Brinker, D. E. Clark and D. R. Ulrich (Mater. Res. Soc. Proc., 121, Pittsburgh, PA 1988), pp. 349-354.
16. T. Bein, K. Brown, G. C. Frye and C. J. Brinker, J. Amer. Chem. Soc., 111, 7640 (1989).
17. R. G. Dosch, T. J. Headley and P. Hlave, J. Amer. Cer. Soc., 67, 354 (1984).
18. B. C. Bunker, C. H. F. Peden, S. L. Martinez, E. J. Braunschweig and A. K. Datye, in Characterization and Catalyst Development: An Interactive Approach, edited by S. A. Bradley, M. J. Gattuso and R. J. Bertolacini (Amer. Chem. Soc., Washington, 1989), Ch. 8.

OXOMETALATE-GLASS COMPOSITES AND THIN FILMS

Karin Moller*, Thomas Bein* and C. Jeffrey Brinker**
*Department of Chemistry and Center for Micro-Engineered Ceramics, University of New Mexico, Albuquerque, NM 87131
**Sandia National Laboratories, P. O. Box 5800, Albuquerque, NM 87185

ABSTRACT

New glass-composites with ion exchange properties have been developed. Ammonium 12-molybdophosphate (AMP) $(NH_4)_3PMo_{12}O_{40}$, and ammonium 12-tungstophosphate (AWP) $(NH_4)_3PW_{12}O_{40}$, known for their ion exchange capabilities, are included either in preformed aerogels with defined pore size, or are added to sol-gel mixtures during the process of gel formation. Characterization is carried out by FTIR, Raman and EXAFS spectroscopy. Ion exchange capacities for the oxometalate precursors are determined for silver and rubidium and are compared to those of the glass composites. Glass composites show high ion exchange capacity, but some portion of the metalate complexes leaches from the glass during the procedure. This is in contrast to thin composite films, which have almost no porosity and do not show loss of metalate. EXAFS spectroscopy demostrates that the oxometalate microstructure is maintained in glass composites and that rubidium ions after ion exchange in glasses occupy similar cation positions as in the precursor compounds.

INTRODUCTION

The combination of different functional properties in glass-based composites offers great potential for the design of tailored materials. Examples include sol-gel derived glass-organic composites, glass-included laser dyes, catalysts, and nonlinear optical materials.

In view of the increasing demand for stable, ion-selective sensors we have initiated a program aimed at the design of tailored thin films with selective ion exchange capabilities. In combination with highly sensitive acoustic devices, it is envisioned that inexpensive, rugged ion sensors for process and environmental monitoring can be designed. The concept is based upon the encapsulation of oxometalate clusters in porous, sol-gel derived glasses. The resulting materials combine selective ion exchange sites with tailored porosity, such that ultimately large fractions of unwanted species (e.g., organics, biological matter) are screened from the ion exchange sites. The following benefits are expected from this approach: The design of *ion exchange composites* allows independent adjustment of both ion selectivity through the choice of different oxometalates, and porosity through the choice of sol-gel chemistry. Furthermore, the resulting inorganic films are temperature stable up to at least 300°C and not subject to fouling.

Heteropoly oxometalates such as anions with the Keggin structure are known since the last century, but their crystal structure was first solved by Keggin in 1934. Figure 1 depicts the Keggin anion structure and a defect structure with one MO_6 octahedron missing. These materials find numerous applications in catalysis, analytical chemistry and biochemical or medical areas. Their ability to exchange their counter cation for alkali ions was first recognized by Smit[1] and has since been used in column chromatography and in paper chromatography. Keggin ions have been used to exchange alkali cations as well as radioactive pollutants. General reviews are available.[2,3,4,5]

Mat. Res. Soc. Symp. Proc. Vol. 180. ©1990 Materials Research Society

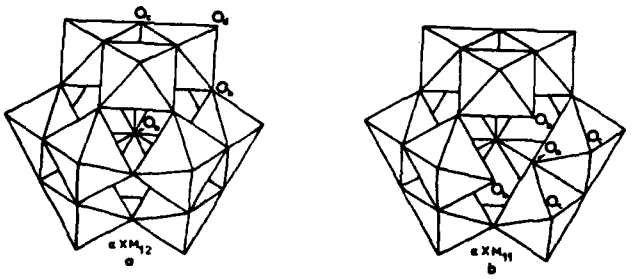


Figure 1: Idealized Keggin structure XM_{12} (a) and defect Keggin structure XM_{11} (b). The central XO_4 tetrahedron is not shown. O_a = oxygen shared by 3 MO_6 and the central XO_4 tetrahedron, O_b and O_c = oxygen shared by corner and edge linked MO_6, O_d = terminal unshared oxygen

This communication reports on the design of 12-molybdophosphate and 12-tungstophosphate ions encapsulated in silicate glass bodies in bulk form. FTIR, FT-Raman, EXAFS, and ion exchange data demonstrate the feasibility of creating intact intra-glass oxometalate ions that are accessible for ion exchange through the pore system of the matrix.

EXPERIMENTAL:

1. Sample Preparation

a) Ammonium 12-molybdophosphate (AMP) $(NH_4)_3PMo_{12}O_{40}$. Highest yield (82 - 95% after work-up) is obtained by stepwise combining stoichiometric amounts of Na_2MoO_4, H_3PO_4, and NH_4NO_3 (in 0.1 M HNO_3) under acid conditions. 1 molar aqueous solutions were added in a volume ratio 12:1:3 after acidifying the sodium molybdate solution with 13 M HNO_3 to pH 1.6. The slightly yellow color of the molybdate turned to strong yellow immediately after addition of phosphoric acid. Precipitation of the ammonium salt occured promptly.

b) Ammonium 12-phosphotungstate (AWP) $(NH_4)_3PW_{12}O_{40}$. Sodium tungstate is insoluble in acid solutions and forms a thick white precipitate when acidified with HNO_3. Thus, 10 ml WO_4^{2-} and 0.9 ml 1 M NaOH and 0.9 ml of 1 M H_3PO_4 are combined, followed by addition of 2.5 ml NH_4NO_3 at pH 7 and acidification to pH 1.5. AWP precipitates as a white solid (yield 92%). The corresponding white silver salt is prepared by adding $AgNO_3$ before acidification (Yield 50%).

c) Assembly of AMP within pores of aerogels. To a slurry of 1g TEOS-derived B2-Aerogel (pore size 10-500 Å) in 10 ml H_2O, 4 ml of 1 M Na_2MoO_4 and 2 ml of 13 M HNO_3 are added. The slurry is stirred for 10 minutes before adding 0.33 ml of 1 M H_3PO_4, and finally, 1 ml of 1 M NH_4NO_3. A green color resulting from reduction of the AMP was reversed to yellow upon adding 2 ml 30% H_2O_2. After filtration the yellow solid was dried at 85°C.

d) Preparation of glasses containing oxometalates

HMP-Glass. 3 g of crystalline 12-molybdophosphoric acid ($H_3PMo_{12}O_{40}$; HMP) and 7.3 ml EtOH and 1 ml 0.1 M HNO_3 and 7.3 ml TEOS and 2 ml 0.05 M NaOH are combined in this sequence (molar ratio of HMP:SiO_2 = 1:20). The suspension was sonicated for 3 minutes and left at room temperature. After two days a greenish gel had formed.

AMP-Glass. Synthetic AMP + TEOS + EtOH in a molar ratio of AMP:SiO_2 = 1:20: Stoichiometric amounts of 1 M Na_2MoO_4 (40 ml) and 1 M H_3PO_4 (3.33 ml) solutions (at pH = 1.5, 6 ml 13 M HNO_3) were combined. Water was evaporated at 75 C to about half the volume (25 ml) until a yellow cloudiness indicated the starting point for precipitation. 14.6 ml TEOS were added to the warm, clear solution under strong stirring, and immediately stoichiometric amounts of NH_4NO_3 in ethanol were added (1.1 g in 1 ml 0.1 M HNO_3 plus 14.6 ml EtOH). A cloudy yellow color appeared. Stirring was continued under slow cooling of the slurry. A thick paste was formed after 2 hours. After 1 day ethanol was partially removed by heating in a water bath. A hard, yellow glass formed.

2. Characterization

Metal contents of glasses were determined by atomic absorption. The samples were analyzed as-synthesized and after each subsequent treatment by FT-IR in the form of KBr pellets. For FT-Raman experiments, a Spectrum SL301 Nd:YAG laser (1064 nm, ca. 1.0 W) was focused on a 1-mm capillary containing the powdered sample. Light collection was done with a modified Mattson Polaris interferometer, detection with an InGaAs detector (EPITAXX). EXAFS measurements were peformed at the X-11A beamline at NSLS (Brookhaven National Laboratories) with an electron energy of 2.5 GeV and ring currents between 90 and 180 mA. Data were collected with a Si(400) crystal pair monochromator at the Mo K-edge (20,000 eV) and at the W L_{III}-edge (10,207 eV) at ca. 100 K. Rubidium-exchanged samples were also examined at the Rb K edge (15,200 eV). Data analysis was performed following standard procedures.[6]

3. Ion exchange

Ion exchange was performed on bulk oxometalates as well as on glass composites by adding stoichiometric or excess amounts of $AgNO_3$ or $RbNO_3$ in acid solutions (e.g., 500 mg AWP and 50 ml of 0.01 M $RbNO_3$ in 0.1 M HNO_3). Samples were stirred for ca. two hours in exchange solutions, filtered and further analyzed. Back-exchange capabilities were examined on bulk oxometalates by adding varying amounts of NH_4NO_3 in acid solution.

RESULTS AND DISCUSSION

Bulk oxometalates

Characteristic modes of the M-O and P-O vibrations appear between 200 and 1100 cm^{-1} in the IR and Raman spectra. The main IR vibrations at 1064, 964, 875, 795 and 595 cm^{-1} of the molybdate ions, or, 1081, 990/982, 890, 805 and 535 cm^{-1} of the tungstate ions are assigned as the asymmetric P-O, M-O_d (O_d = terminal oxygens), and M-O-M vibrations according to Rocchiccioli-Deltcheff.[7] Raman spectra show mainly the symmetric M-O_d band around 1000 cm^{-1} and a convolution of the symmetric P-O and asymmetric M-O_d band around 990 cm^{-1}.

Inclusion of Keggin ions in preformed aerogel

The preparation of oxometalates in preformed glasses resulted in a loading of ca. 8 wt% Mo in B2-aerogel and a yellow color indicated formation of AMP. The IR spectrum is shown in Figure 2. The silica support blocks out a region between 1350 and ca. 1000 cm^{-1} and obscures an even wider range in the IR. However, the main bands of the Keggin ions (1064, 970, 875, 795 cm^{-1}) are still visible as superimposed peaks when compared with the precursor included in the Figure.

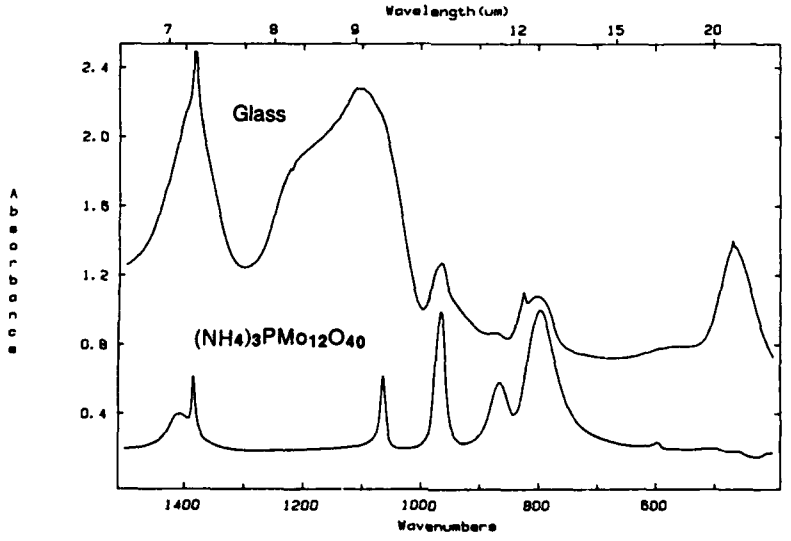


Figure 2: FTIR spectrum of the preformed aerogel with included $(NH_4)_3PMoO_{40}$ in comparison to the precursor

When a part of this sample was washed with a small amount of water at room temperature, the color changed from yellow to white and no Keggin ions were detectable in the solid. Heat treatment in air up to 200 C was thought to favour condensation reactions between the aerogel and the Keggin ions. A similar washing procedure as above still reduced the molybdenum content, but left ca. 50% attached to the solid. After a subsequent ion-exchange experiment with silver nitrate, all remaining molybdenum ions were found in the wash solution.

Inclusion of Keggin ions during gellation

To avoid or reduce the loss of molybdenum from supported samples upon washing, a different strategy for encapsulation of Keggin ions was developed: Oxometalate complexes were synthesized in the presence of sol-gel precursors for the silicate matrix. It was anticipated that bottleneck pores develope which restrict mobility of the Keggin ions but render access for smaller cations. Several different glasses were prepared varying in the sol-gel route and/or the Keggin ion present. A representative IR spectrum is shown in Figure 3 (AMP in TEOS + EtOH). The high loading of ca. 38 wt% of Mo allows for ready detection of the Keggin vibrations which confirm that the Keggin structure is maintained in the glass. The thermal stability of this glass was tested by heating up to 400 ^{0} C in oxgen. Raman spectra of a representative experiment are shown in Figure 4. It is clearly visible that decomposition occurs between 200 and 400 ^{0} C. Aging temperatures were therefore restricted to 200 ^{0} C.

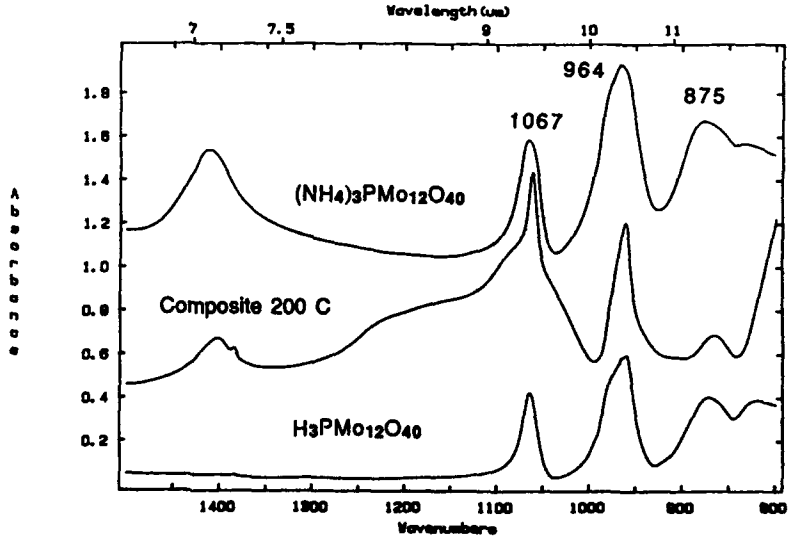


Figure 3: FTIR spectra of "in-situ" formed composite TEOS + EtOH + $(NH_4)_3PMoO_{40}$ in comparison to the precursor $(NH_4)_3PMoO_{40}$ and H_3PMoO_{40}

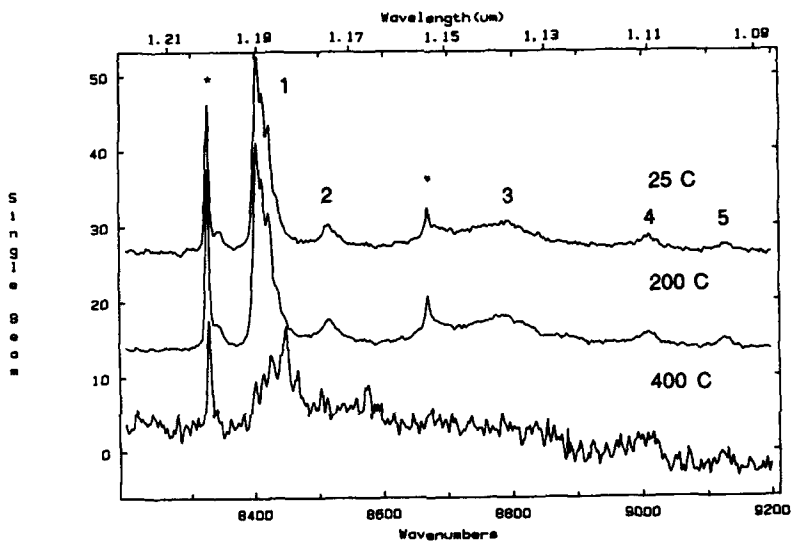


Figure 4: *FT-Raman spectra of the thermal degradation of "In-situ" formed composite TEOS + EtOH + $(NH_4)_3PMoO_{40}$. Wavenumbers are given (the laser line is at 9388 cm^{-1}). Stokes shifts are as follows (subscripts see Figure 1[9]):*

(1) 989 cm^{-1}: Mo-O_d symmetric stretch
(2) 879 cm^{-1}: Mo-O_b-Mo asymmetric stretch
(3) 600 cm^{-1}: Mo-O_c-Mo symmetric stretch
(4) 381 cm^{-1}: Mo-O-Mo bending
(5) 250 cm^{-1}: Mo-O_a-Mo symmetric stretch
* : NO_3^-

Ion exchange

The bulk oxometalates were ion exchanged with rubidium and silver by offering stoichiometric amounts of the cations at room temperature. AMP, AWP and the respective silver salt exchange under these conditions 50% of their cations for rubudium, while AMP and AWP exchanged only 12-15 % of their ammonium ions for silver. However, a 100% exchange is achieved upon offering excess of silver nitrate.

When silver salts of the molybdenum and tungsten Keggin ions were exposed to ammonium ions, back-exchange to the ammonium form occured for AgMP up to 92% and for AgWP up to 54% in a 3 M NH_4NO_3 solution.

The glass composites exchanged larger fractions of their protons or ammonium cations, e.g., 12 - 76% for Ag and 42 - 92% for Rb. However, some leaching of the oxometalates was observed for all different porous glasses. Composites made with TEOS showed a loss of 30 - 58% Mo or W, while glasses made from A2 solutions (TEOS + EtOH refluxed at 60 C for several hours) showed a loss from 16 - 35 %. The preformed aerogel lost up to 98% after two successive exchange cycles. The loss of Keggin ions is effectively suppressed in thin films of similar compositions which were found to be non-porous. Multicomponent glasses which retain porosity even in thin films are presently studied.

EXAFS analysis

EXAFS measurements were performed on the bulk oxometalates as well as on glass composites before and after ion exchange. EXAFS allows to determine the local structure around the X-ray absorbing atom of choice and can provide detailed information about bond distances, coordination numbers and types of atoms in the nearest neighbor shells. Figure 5 shows Fourier transformed molybdenum EXAFS data of the precursors AMP and HMP, overlayed with the respective composites formed with these Keggin ions. A large peak indicating the oxygen environment of the molybdenum atoms is visible between 0.5 and 2 Å (Bond distances appear at ca. 0.5 Å to lower bond distances due to phase shift effects). The mean bond distances obtained from X-ray diffraction are 1.70 Å for the terminal oxygens, 1.92 Å for oxygens bridging the molybdenum octahedra, and 2.43 Å for the oxygen linked to the central phosphorus atom. The second and third shells arise from Mo-Mo bonds at 3.42 Å from edge-shared octahedra and at 3.70 Å from corner-shared octahedra. It can clearly be seen that precursor and glass composites have the same local structure. A quantitaitve analysis of these data is in progress.

When a HMP/TEOS composite is analyzed after rubidium exchange, the Mo-edge EXAFS data do not show any sign of degradation (see Figure 6; the imaginary parts of the Fourier transformations are shown in addition to the magnitudes. The former give valuable information about the nature of neighbors or overlap of peaks). The rubidium edge data show a large contribution around 2.5 Å (uncorrected for phase shift) which indicates a Rb-O interaction, while the peak around 3.9 Å arises from the Rb-Mo bond. This spectrum is identical to that taken from the bulk rubidium phospho molybdate and indicates that the rubidium ions occupy identical cation positions in both compounds. When fitted with adequate reference compounds a bond distance of ca. 4.4 Å can be expected. To our knowledge the only complete determination for cation positions in Keggin ions is done with combined neutron- and X-ray diffraction by Brown et al.[8] Their distance of hydrated protons to molybdenum atoms agrees closely with the above observations.

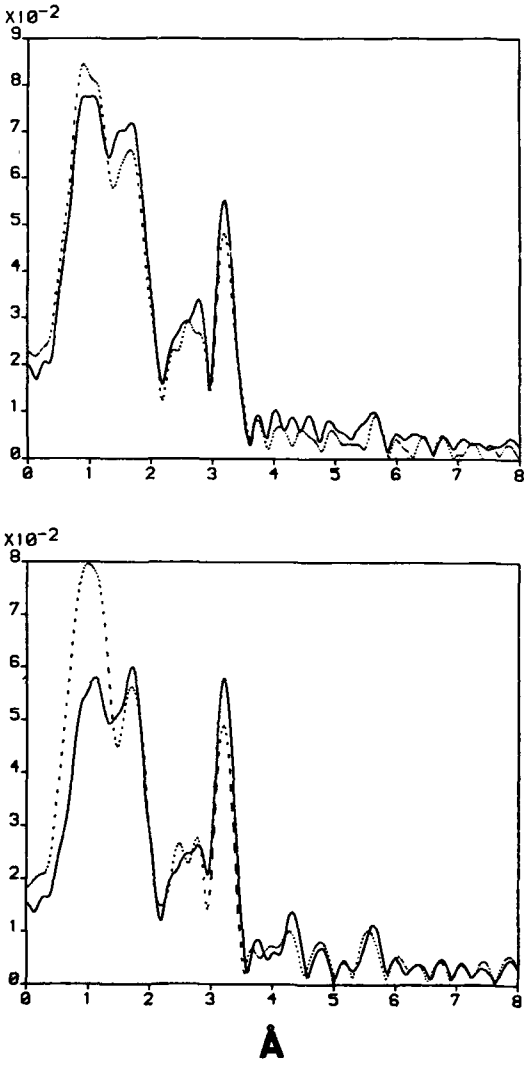


Figure 5: Molybdenum EXAFS data: top: Fourier transformation of the precursor $(NH_4)_3PMo_{12}O_{40}$ data (solid line) as compared to the aerogel composite broken ine). Bottom: Fourier transformation of the precursor $H_3PMo_{12}O_{40}$ data (solid line) as compared to the TEOS composite (broken line)

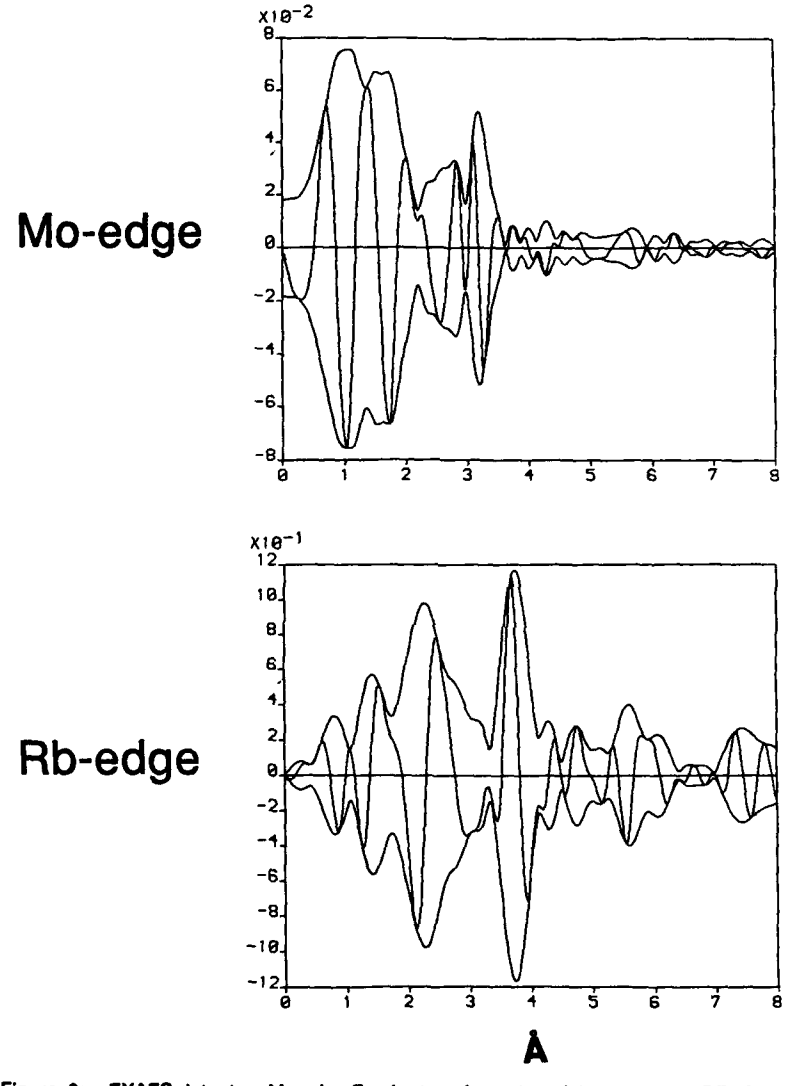


Figure 6: EXAFS data: top: Mo-edge Fourier transformation of the composite TEOS + $H_3PMo_{12}O_{40}$ after Rb ion exchange. Bottom: Rb-edge: corresponding Fourier transformation of the above composite

This study shows that Keggin ions can be occluded in glassy substrates with no side products, by either assembling the components in the pores of pre-formed glass, or by in-situ formation in precursor gels. In porous glasses, ion exchange similar to bulk reactions is observed, and cations are shown to be coordinated to the metalate framework. These glass composite offer a potential for the design of thin films with ion exchange capability.

ACKNOWLEDGMENT

Financial support is gratefully acknowledged from Sandia National Laboratories (K. M., T. B.). A portion of the work was performed at Sandia National Laboratories and supported by the U.S. Departmenty of Energy under contract number DE-AC-04-76DP00789. The operational funds for NSLS beamline X-11A are supported by DOE grant DE-AS-05-80ER10742.

1 Smit, J. v. R. *Nature* **1958**, *181*, 1530

2 Weakley, T. J. R. in "Structure and Bonding", Vol. 18, Ed. Dunitz, J. D. Springer Verlag, Berlin 1974

3 Tsigdinos, G. A. in "Topics in Current Chemistry", Ed. Dewar, M. J. S. et al., Springer Verlag, Berlin 1978

4 Pope, M. T. "Heteropoly and Isopoly Oxometalates", Springer Verlag, Berlin 1983

5 Misono, M. *Catal. Rev. - Sci. Eng.* **1987**, *29*, 269

6 Lee, P. A.; Citrin, P. H.; Eisenberger, P.; Kincaid, B. M., Rev. of Modern Physics, 53 (1981) 769-806

7 Rocchiccioli-Deltcheff, C.; Thouvenot, R.; Franck, R. *Spectrochim. Acta* **1976**, *32A*, 587

8 Brown, G.M.; Noe-Spirlet, M.-R.; Busing, W. R.; Levy, H. A. *Acta Cryst.* **1977** *B33*, 1038

INHOMOGENEITIES IN SOL-GEL COATINGS

B. D. Fabes, D. L. Klein, and L. J. Raymond
University of Arizona, Department of Materials Science and Engineering, Tucson, Arizona 85721

ABSTRACT

The structure of sol-gel derived silica coatings was investigated using nanoindentation, chemical etching, and cross-sectional TEM. For coatings heated at 100 °C, the surfaces were harder, etched slower, and appeared less porous than the interior of the coatings. For samples fired at higher temperatures (400-800 °C), the surfaces remained harder and etched slower than the interior, even though the porosity appeared to be evenly distributed throughout the thickness of the coating. It is proposed that this difference is due to inhomogeneities on two scales in the coatings: bulk porosity and skeletal strain.

I. BACKGROUND

It is often assumed that the structure of a sol-gel coating is the same near the surface as throughout the bulk of the coating. However, we recently found that the hardness of tetraethoxysilane (TEOS) derived silica coatings is significantly higher at the surface than within the bulk of the coating [1]. The goal of this study was to further characterize the structure of sol-gel coatings as a function of depth, and to gain insight into what causes the surface to be different from the interior. Three characterization techniques - nanoindentation, chemical etching, and cross sectional TEM - were used to probe the structure of sol-gel coatings as a function of depth. These techniques are sensitive to different features of the coating structure, and therefore allowe the scale of the inhomogeneities to be probed.

A description of the coating preparation process is given in the following Section. The details of the characterization techniques, a description of the features to which they are sensitive, and the results for the TEOS coatings are presented in Section III. These results are discussed in Section IV.

II. COATING PREPARATION

TEOS derived silica coatings were prepared by hydrolyzing 1 mole of TEOS with 2 moles of water, diluted in 4 moles of ethanol. HCl was used to bring the solution pH to 2: the solutions were then allowed to react for at least two weeks before coating.

Coatings were made by withdrawing silicon or sapphire substrates from the TEOS solution at a controlled rate. All substrates were cleaned in an ultrasonic bath using a warm detergent solution and rinsed in deionized water prior to coating. For the nanoindentation experiments, sapphire substrates were used so that there would be a large difference between the hardness of the coating and that of the substrate. Using a computer to continually vary the coating speed, a linear gradient was produced in the thickness of the coatings on sapphire so that a range of thicknesses could be tested on each sample. For etch rate and TEM studies, silicon wafers were withdrawn from the TEOS solution at a constant rate, resulting in a constant coating thickness.

Mat. Res. Soc. Symp. Proc. Vol. 180. ©1990 Materials Research Society

To measure the thickness using a mechanical profilometer, all samples were heated at 100 °C in air for 15 minutes, after which a step was made in the coating either by scraping off a small area with a razor blade or using photoresist and etching back the coating, as described in Section III. Next, the samples were fired in air at 400, 500, 600, 800, or 1000 °C, by placing the coated substrates directly into a hot furnace for 30 minutes.

III. CHARACTERIZATION TECHNIQUES AND RESULTS

A. Nanoindentation

Recent advances in instrumentation have enabled the mechanical properties of exceptionally small volumes of materials to be probed in a routine fashion [2]. One of the most natural uses of this kind of instrumentation is the characterization of thin coatings and films. We used a Nanoindenter (manufactured by Nano Instruments, Knoxville, TN) to measure the hardness of the TEOS coatings on sapphire. The Nanoindenter has a load resolution of less than 0.3 μN and a displacement resolution of 0.2 nm. The hardness is determined by measuring the load (applied by an electromagnetic loading coil) vs. displacement (measured via a capacitance displacement gauge) as a diamond stylus penetrates into the coatings. In the present experiments, the diamond penetrated into the coatings at a controlled rate of 1 nm/s for the top 30 nm of each coating, and then at 2 nm/s until the maximum load was achieved. The details of determining the hardness from the load/displacement curve, which involves correcting for irregularities in the shape of the diamond and determining the elastic modulus using a small AC current superimposed on top of the DC drive current, are given elsewhere [3,4].

The hardness of the TEOS coatings as a function of indenter depth is shown in Figure 1. For each firing temperature, four different thicknesses were probed on the wedge-shaped coatings. Each data point represents the average of eight indents at each coating thickness. For the coatings fired at 100 °C, there appears to be a surface "crust," roughly 30 nm thick, in which the hardness is higher than the interior of the coating. Beyond 30 nm, the hardness is relatively insensitive to indenter depth. In this region the properties of the coating are being probed, with little influence from the substrate. As the indenter continues to penetrate into the coating, the substrate is eventually reached, resulting in a rapid increase in hardness. The depth at which this occurs corresponds closely with the thickness of the coating.

Firing at 400 °C increases the overall hardness of the coating, and decreases the depth over which the hardness is independent of the substrate. This latter effect is due to the penetration of the plastic strain field into the substrate, as discussed in Reference 5. The top 30 nm, however, is still significantly harder than the interior of the coating. For the coating fired at 800 °C, the overall hardness increases, and the top 30 nm is still significantly harder than the interior. Finally, after firing at 1000 °C, the hardness reaches that of bulk fused silica (14 GPa), and a surface crust is still apparent.

Of particular interest is the surface crust, which indicates that the structure of the surface of the TEOS coatings is different from that of the interior. The hardness measurements are sensitive to both porosity and strain in the skeletal structure of the silica coatings [6]. An increase in either porosity or skeletal strain would devrease the hardness. Hence, these data indicate that at all temperatures the surface is either less porous or has a less strained structure than the interior.

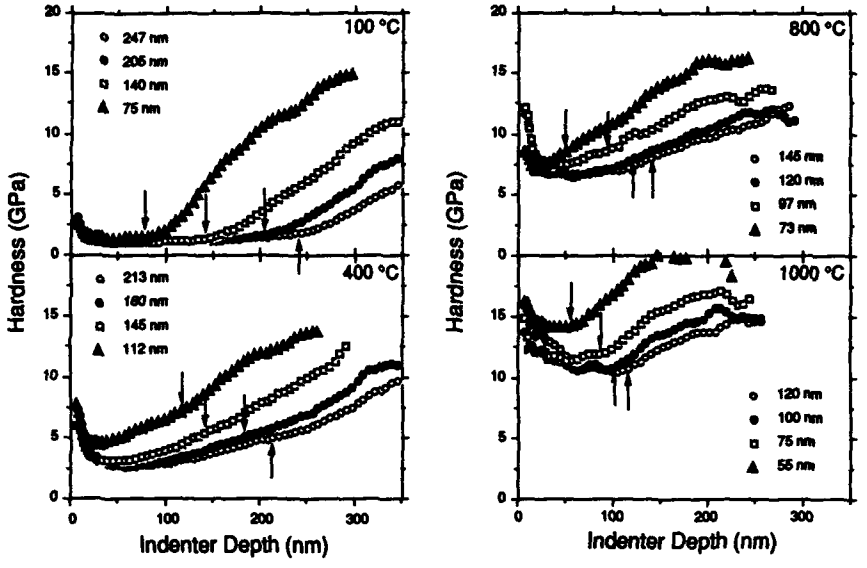


Figure 1: Hardness of TEOS coatings on sapphire substrates. Different symbols refer to different coating thicknesses. Arrows indicate coating/substrate interfaces.

B. Etch Rate Studies

The resistance of the TEOS coatings to attack by HF is also sensitive to porosity and strain: bulk porosity and strain in the skeletal structure both increase the etch rate [7]. To examine the dependence of etch rate on depth, steps were formed on the coatings on silicon substrates by masking half of the coating with positive photoresist and removing the unmasked coating with a buffered HF solution ($1HF:6NH_4F$). Next, the photoresist was removed with ethanol, exposing a sharp step over which thickness measurements were made. The HF solution was then diluted in water (1:250 etchant:H_2O for coatings fired at 100 °C; 1:40 for coatings fired at 500 °C; and full strength for coatings fired at 1000 °C) so that the etch rate of each of the coatings was approximately 5 Å/s at the surface.

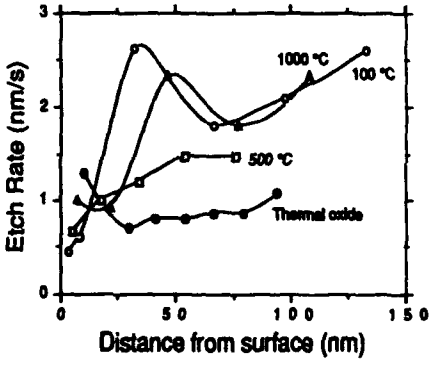


Figure 2: Etch rate of TEOS coatings in buffered HF solutions

Next, the coatings were etched for intervals of 15 s, after which the thickness was measured across the step using a mechanical profilometer. The etching and thickness measurements were then repeated until the coatings were removed. Care was taken to make sure that the same part of the step was measured after each etching step, and at least five thickness measurements were made for each data point.

To make sure that any differences in etch rate were due to the coatings, and not to the etching process, a thermally grown silica film was prepared by heating a silicon wafer for 12 hours at 900 °C in air. The etch rate of this film was then measured using the same technique as for the TEOS coatings.

The result are shown in Figure 2. The etch rates are quite varied within in the bulk of the coatings. However, the etch rates for all of the TEOS samples increased over the first 30-50 nm, indicating that the surfaces of the TEOS coatings have lower porosity, or are less strained, than the interiors.

C. TEM

Cross-sectional TEM images were obtained for coatings fired at 100 and 600°C on silicon. The details of the sample preparation are given in Reference 12. The results are shown in Figures 3 a and b. The porosity, which is evident as 2-5 nm spheres in the micrographs, appears to diminish near the surface of the sample fired to 100 °C. When fired to 600 °C, on the other hand, the porosity appears to be distributed evenly.

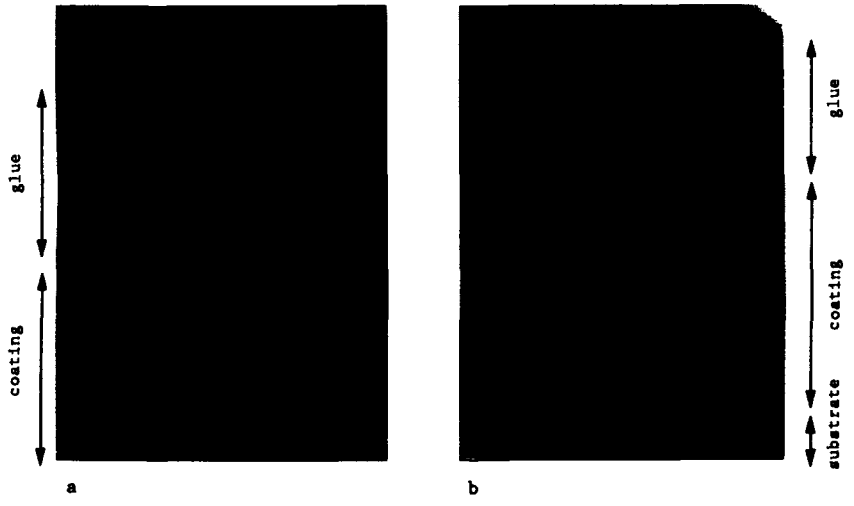


Figure 3: Cross sectional TEM micrographs of TEOS coatings on Si (a) fired at 100 °C, and (b) fired at 600 °C.

IV. DISCUSSION

The nanoindentation and etch rate studies show that TEOS coatings are harder, and more etch resistant near the surface than within the bulk of the coatings for all firing temperatures. The TEM micrographs, on the other hand, indicate that the distribution of porosity in the film depends on the firing temperature. Since the hardness and etch rate are sensitive to both porosity and skeletal strain, while the TEM is sensitive only to porosity, these results suggest that inhomogeneities in TEOS coatings arise on two scales - in the bulk porosity and in the skeletal strain.

For the coatings fired to intermediate temperatures, the difference between the density near the surface and that at the interior of the coating is not large enough (Figure 3b) to account for the large drop in hardness (up to a factor of 3) near the surface. This supports the conclusion that inhomogeneities exist on at least two scales.

Whether these inhomogeneities are characteristic of all sol-gel coatings, of TEOS coatings, or of the particular processing steps used here is unclear. It is not difficult to propose a number of mechanisms which, individually or in combination, could cause the structure of sol-gel coatings to vary with depth. For example, even though the coatings are generally confined from contracting parallel to the substrate, this confinement is certainly more severe near the substrate than at the surface of the coating. It is possible that the coatings can contract, to some extent, parallel to the substrate near the surface. This would lead to a denser, less strained surface.

It is also possible that the rate of evaporation of the solvent during the coating process is much higher at the surface than in the interior of the coating. This can cause the surface to shrink more than the interior, and lead to a higher density at the surface than in the interior of the coating [13].

Finally, hydrolysis of strained bonds, which causes a relaxation in of the strain, is probably easier at the surface than within the coating. The relaxation of strained siloxane linkages is known to form more robust structures, with decreased etch rates [7]. Hydration also blocks water from traveling to the interior of the film [7], which would cause the surface to be noticeable harder, more resistant to etching, and less strained than the interior. This effect is likely to be especially important at temperatures greater than about 350 °C, where highly strained three-membered siloxane rings are formed by condensation reactions [14]. Inside the porous coating the siloxane network might become highly strained, while the availability of water from the atmosphere prevents the formation of strained structures near the surface of the coating.

Finally, it is interesting that the nanoindentation and etch rate results indicate that there is residual strain in the structure of sol-gel coatings, even after heating to 1000 °C, where shrinkage has stopped and the coatings are nominally dense and pore-free. This result is consistent with IR measurements on thermally grown silica [11], and strength measurements on sol-gel strengthened fused silica glass [15], which both suggest that significant residual stress, not associated with differences in coefficients of thermal expansion, may exist in silica coatings even after high firing temperatures.

V. SUMMARY

Based on the variation of hardness and etch rate with depth, and on TEM micrographs, we have proposed that inhomogeneities can arise in sol-gel coatings on two scales - in the distribution of porosity and skeletal strain throughout the thickness of TEOS coatings. The cause of these inhomogeneities is currently unknown, but may involve differences in the confinement of the coating near the substrate vs. near the surface, higher evaporation rates at the surface, or increased hydration at the surface. Finally, the nanoindentation and etch rate data suggest that a residual stress exists in these coatings, even after firing to 1000 °C.

ACKNOWLEDGEMENTS

This research was sponsored in part the Facility for High Resolution Electron Microscopy, in the Center for Solid State Science at Arizona State University, established with support from the National Science Foundation (Grant No. DMR-86-11609); by NSF Grant No. DMR-8903386; and by a University of Arizona Undergraduate Fellowship Grant. The authors would also like to acknowledge the experimental assistance of Tian-Ho Lim and Cecilia Flamme, and the many helpful suggestions of Dr. Warren Oliver.

REFERENCES

1. B.D. Fabes and W.C. Oliver, to be published in *J. Non-Cryst. Sol.* . (1990).
2. W.C. Oliver, *MRS Bulletin* , 11, (5) 15-19 (1986).
3. J.B.Pethica and W.C. Oliver, pp. 13-23 in Thin Films: Stresses and Mechanical Properties , edited by C. Bravman, W. Nix, D. Barnett, and D. Smith *Mater. Res. Soc. Proc* . 130, Pittsburgh, PA. (1989).
4. M.F. Doerner, and W.D. Nix, *J. Mater. Res* . 1, 601-609 (1986).
5. B.D. Fabes and W.C. Oliver, to be published in Proceedings of Symposium K of the Spring Meeting of the Materials Research Society, San Francisco, Ca, 1990.
6. K.D. Cornett, B.D. Fabes, and W.C. Oliver, to be published in Proceedings of Symposium K of the Spring Meeting of the Materials Research Society, San Francisco, Ca, 1990.
7. W.A. Pliskin, *J. Vac. Sci. Tech* .., 14 (5) 1064-1081 (1977).
8. A. Paneva and I. Ohlidal, *Thin Solid Films*, 145, 23-27 (1986).
9. T. Easwarakjanthan, C. Michel, and S. Ravelet, *Surface Science* , 197, 339-345 (1988).
10. G.H. Bu-abbud, N.M. Basura, and J.A. Woodlam, *Thin Solid Films* , 138, 27-41 (1986).
11. J.T. Fitch, C.H. Bjorkman, J.J. Summakeris, and G. Lucovsky, pp. 289-294 in Thin Films: Stresses and Mechanical Properties , edited by C. Bravman, W. Nix, D. Barnett, and D. Smith, *Mater. Res. Soc. Proc* . 130, Pittsburgh, PA. (1989).
12. L. Weisenbach, D.L. Klein, B.J.J. Zelinski, and B.D. Fabes, these Proceedings.
13. G.W. Scherer, *J. Non-Cryst. Sol.*, 89, 217-238 (1987).
14. C.J. Brinker, D.R. Tallant, E.P. Roth, and C.S. Ashley, *J. Non-Cryst. Sol* . 82 117-126 (1986).
15. B.D. Fabes and D.R. Uhlmann, *J. Amer. Ceram. Soc* .., 73 (4) 978-988 (1990).

DENSIFICATION AND CRYSTALLIZATION OF THIN TRANSITION METAL OXIDE COATINGS FROM METAL ALKOXIDES

H. HIRASHIMA, R. MURATAKE, T. YAMASHITA, and T. CHIBA
Department of Applied Chemistry, Faculty of Science and Technology, Keio University, 3-14-1, Hiyoshi, Kohoku-ku, Yokohama 223 Japan

ABSTRACT

Monolithic gels of V_2O_5, Ta_2O_5, and Nb_2O_5 have been prepared from $VO(C_2H_5O)_3$, $Ta(C_2H_5O)_5$, and $Nb(C_2H_5O)_5$ through hydrolysis in ethanol Solutions. The conditions for gel formation have been determined. Thin coatings of these gels, less than 100 nm in thickness, have been prepared by dip coating. Changes in the thickness, d, and refractive indices, n, have been measured by ellipsometry during drying. In the first stage of drying, d decreases and n increases rapidly. Densification of the coatings takes place due to evaporation of solvent. In the following stage, increase in d and decrease in n have been observed for thin V_2O_5 gel coatings, about 30 nm or less in thickness. These results suggest that coarsening of pores and/or increase in surface roughness take place due to release of the capillary pressure during drying. Both d and n have increased with increasing number of dipping. After heat treating, decrease in d and increase in n have been observed.

INTRODUCTION

Thin coatings of transition metal oxides have interesing physical properties, such as electronic and optical properties. They can be applied for *microelectronics, micro-optics, protective* coating applications, *etc.*. Thin oxide coatings of good homogeneity can be prepared through the sol-gel technology [1]. The sol-gel process is considered to be suitable for preparation of thin coatings. In this work, thin coatings of V_2O_5, Ta_2O_5, and Nb_2O_5 have been prepared from metal alkoxides through hydrolysis and dip coating. Densification and crystallization of these coatings during drying and heat treating have been investigated.

Hydrous V_2O_5 gel is known to be highly conductive and anisotropic [2]. Ta_2O_5 and Nb_2O_5 have high dielectric constant. Preparation of these oxide gels from metal alkoxides have been reported [3-6].

EXPERIMENTAL PROCEDURE

Metal alkoxides, $VO(C_2H_5O)_3$, $Ta(C_2H_5O)_5$, and $Nb(C_2H_5O)_5$, were dissolved into anhydrous ethanol, and hydrolyzed at room temperature with and without catalysts. HCl or other inorganic acids have been used as catalyst. The conditions for gel formation, concentrations of H_2O and metal alkoxides, and pH have been determined. pH of alcoholic solutions has been measured by glass electrode pH meter using an electrode with a variable sleeve. Crystallization behaviours of the gels have been investigated by TGA-DTA and X-ray diffraction. Gel coatings have been prepared by dip coating. The sols or ultrasonically peptized gels have been used as dipping solutions. Soda-lime-silicate or silica glass plates, whose surface roughness was about 6 nm, have been used as substrates. The withdrawal rate has been 5 to 20 cm/min. Dipping has been repeated after drying at room temperature or after heat treating. The gels and the surface of the gel coatings have been observed by SEM and TEM. The thickness, d, and refractive indices, n, of the gel coatings have been measured with an automatic ellipsometer (Shimadzu, AEP-100) during drying and after heat treating.

Mat. Res. Soc. Symp. Proc. Vol. 180. ©1990 Materials Research Society

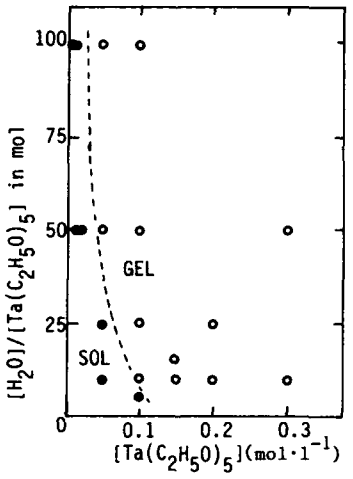


Fig.1 Gel formation from $Ta(C_2H_5O)_5$ at room temperature. [HCl]=0.1 N.

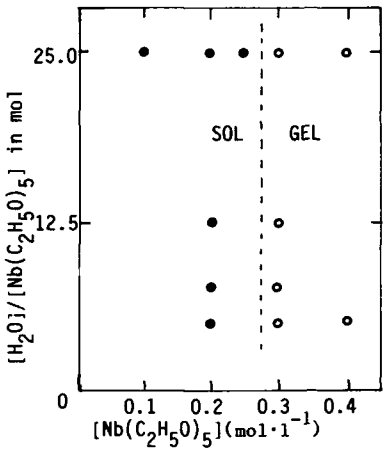


Fig.2 Gel formation from $Nb(C_2H_5O)_5$ at room temperature. [HCl]=0.1 N.

RESULTS AND DISCUSSION

Gel Formation

Monolithic gels of hydrous V_2O_5 have been obtained with and without acidic catalysts, when pH $\lesssim$ 2.2 [7]. The gelation time is a few seconds. The color of the solution changes from red-orange to green during gelation and aging due to reduction of V^{5+} to V^{4+}. The fraction of reduced V ion is about 0.2 or more [7]. Monolithic gels of Ta_2O_5 and Nb_2O_5 have been obtained with acidic catalysts, when pH $\lesssim$ 3 (Fig. 1, 2). The gelation time, several minutes to about 100 h, becomes shorter when the concentration of H_2O or metal alkoxides is increased.

Hydrous V_2O_5 gels are fiber-like, as shown in Fig. 3, and about 10 nm or less in thickness. On the other hand, Ta_2O_5 and Nb_2O_5 gels are granular and 200 to 300 nm in diameter (Fig. 4).

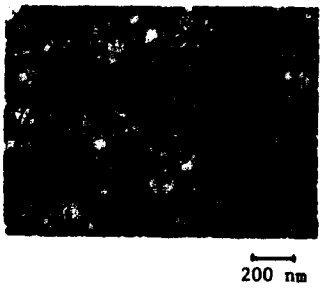


Fig.3 TEM photograph of V_2O_5 gels from $VO(C_2H_5O)_3$, dried at room temperature.

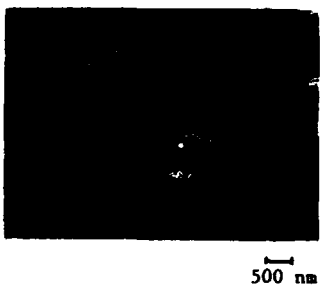


Fig.4 SEM photograph of Ta_2O_5 gels from $Ta(C_2H_5O)_5$, dried at room temperature.

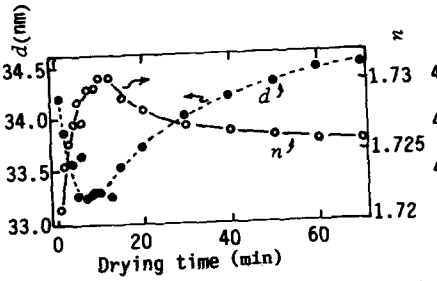


Fig.5 Changes in d and n of V_2O_5 gel coating, dip-coated 3 times, during drying at room temperature.

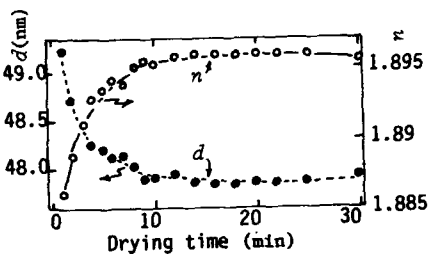


Fig.6 Changes in d and n of V_2O_5 gel coating, dip-coated 10 times, during drying at room temperature.

Drying of V_2O_5 gel coatings

The hydrous V_2O_5 gels are known to have a layer-like structure [2]. It was reported that the fibrous polymer was oriented in thin V_2O_5 coaings [8]. It was also suggested that the V_2O_5 gels had a 3-dimensionally ordered structure [7]. An example of the changes in d and n of V_2O_5 coatings is shown in Fig. 5. In the first stage of drying, d decreases and n increases rapidly. Densification of the gel coating takes place due to evaporation of solvent. In the following stage, d increases and n decreases. These results indicate that the coatings become less dense. These results may be attributed to coarsening of pores in the coating and/or increase in surface roughness. Both effects are considered to be due to release of capillary pressure during drying [9]. The increase in d and the decrease in n during drying have been hardly observed after 10 repetitions of the dip-coating process (Fig. 6). After each dipping, the gel coating was dried at room temperature for 30 min. Both d and n of the coatings, dip-coated more than 10 times, changed little after drying for 30 min. Effects of dipping numbers on d and n are shown in Fig. 7. Both d and n are increased by repeating dipping, and come to saturated values. It seems that rearrangement of the fiber-like polymers of hydrous V_2O_5 takes place during the repeated dip-coating process, and the coatings are densified.

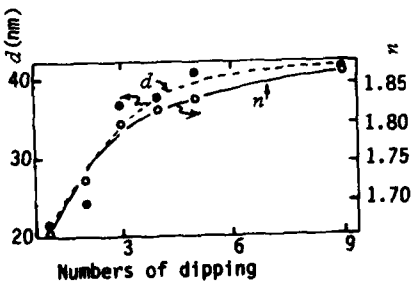


Fig.7 Effect of dipping number on d and n of V_2O_5 gel coatings, dried at room temperature.

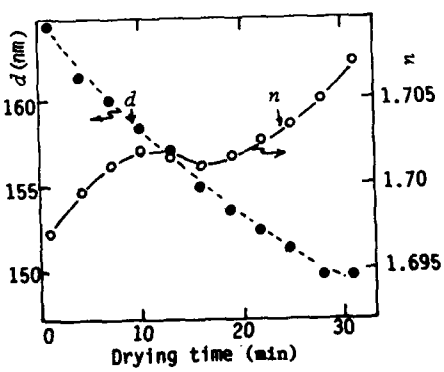


Fig.8 Changes in d and n of Nb_2O_5 gel coatings, dip-coated 3 times, during drying at room temperature.

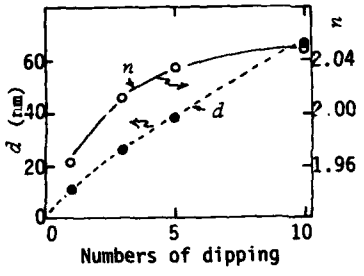


Fig.9 Effect of dipping number on d and n of Nb_2O_5 gel coatings, heat treated at 500°C for 30 min.

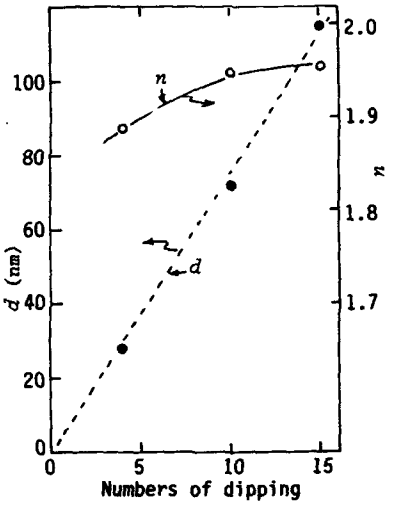


Fig.10 Effect of dipping number on d and n of Ta_2O_5 gel coatings, heat treated at 500°C for 30 min.

Drying of Ta_2O_5 and Nb_2O_5 gel coatings

An example of the changes in d and n of these gel coatings during drying is shown in Fig. 8. In the first stage of drying, d decreases and n increases. In the following stage, decrease in n is less significant than in the case of V_2O_5 gel coatings, and increase in d is scarcely observed. The difference between the drying behaviours of V_2O_5 gel coatings and Ta_2O_5 or Nb_2O_5 gel coatings is considered to be attributed to the difference of the capillary pressure in the wet gel coatings, because the diameter of the granular gels of Ta_2O_5 and Nb_2O_5 is much larger than the thickness of the fiber-like gels of V_2O_5.

Both d and n of Ta_2O_5 and Nb_2O_5 gel coatings have increased with increasing number of dipping (Fig. 9). n increases after the first few dippings and comes to a saturated value. However, saturation of d is not significant in comparison with the case of V_2O_5 gel coatings. When the coatings of Ta_2O_5 and Nb_2O_5 gels were heat treated at 300 to 500°C for 5 min after each dipping process, d increased proportionary to the number of dipping (Fig. 10).

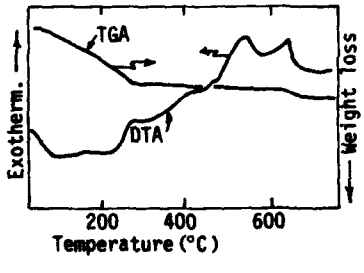


Fig.11 TGA-DTA curves for Ta_2O_5 gel, hydrolyzed at 25°C with 0.1N HCl.

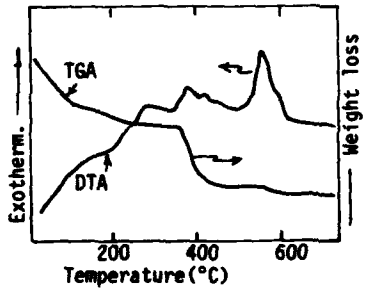


Fig.12 TGA-DTA curves for Nb_2O_5 gel, hydrolyzed at 25°C with 0.1N HCl.

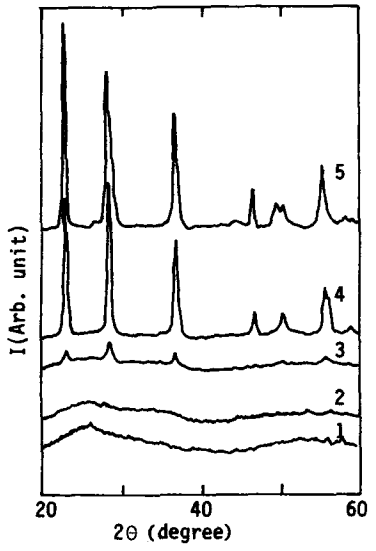


Fig.13 X-ray diffraction patterns of Ta_2O_5 gels, (1) dried at room temperature, heat treated for 2h at (2) 350°C, (3) 480°C, (4) 560°C, and (5) 750°C. (CuKα radiation)

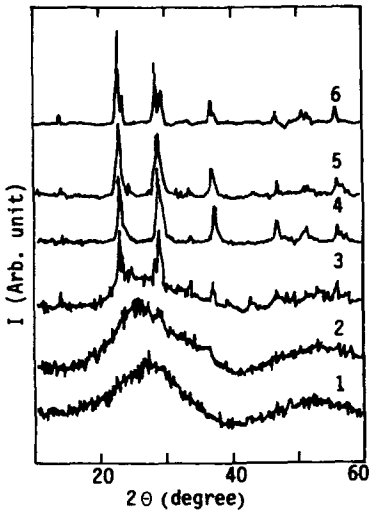


Fig.14 X-ray diffraction patterns of Nb_2O_5 gels, (1) dried at room temperature, heat treated for 2h at (2) 280°C, (3) 350°C, (4) 500°C. (5) 570°C, and (6) 750°C. (CuKα radiation)

Crystallization of Ta_2O_5 and Nb_2O_5 gel coatings

Crystallization temperatures of Ta_2O_5 and Nb_2O_5 gels have been determined by DTA (Fig. 11, 12). After the heat treatment at various tempertures, X-ray diffraction of the gels has been measured. Diffraction peaks of Ta_2O_5 have been observed after heat treating at 480°C for 2 h (Fig. 13). n of the Ta_2O_5 gel coatings increases remarkably up to about 500°C (Fig. 15). d of the coatings also changes in this temperature range. Similar results of

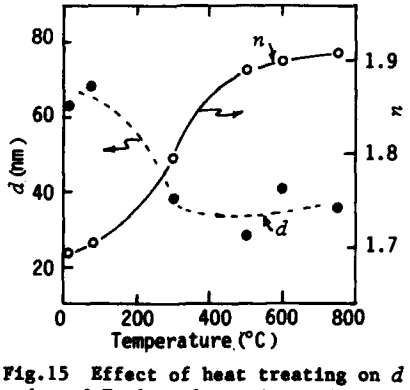


Fig.15 Effect of heat treating on d and n of Ta_2O_5 gel coatings, dip-coated 4 times.

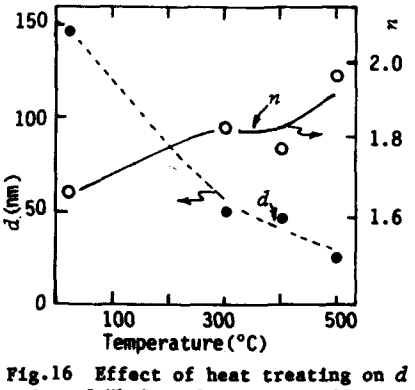


Fig.16 Effect of heat treating on d and n of Nb_2O_5 gel coatings, dip-coated 3 times.

shrinkage of Ta_2O_5 gels have been reported [5]. Both d and n changes little after heat treating at temperatures higher than about 500°C. n of the crystallized Ta_2O_5 coatings is near to that of sputtered Ta_2O_5 coatings [10].

Diffraction peaks of Nb_2O_5 have been observed after heat treating of Nb_2O_5 gel coatings at 350°C for 1 h (Fig. 14). n of the Nb_2O_5 gel coatings decreases after heat treating at 400°C (Fig. 16). This result suggests that the surface roughness and/or porosity of the gel coatings are increased by crystallization. After the heat treatment at 500°C, however, d decreased and n increased. These results may be attributed to the further crystallization and rearrangement of the particles by heat treating.

Both Ta_2O_5 and Nb_2O_5 coatings are transparent.

CONCLUSIONS

Gel coatings of hydrous V_2O_5, Ta_2O_5, and Nb_2O_5, about 10 to 100 nm in thickness have been prepared from metal alkoxides through hydrolysis and dip coating. Changes in and of the coatings have been measured by ellipsometry during drying and heat treating. The densification behaviours during drying are affected by morphology and size of gel particles. V_2O_5 gel coatings, consisted of thin fibrous polymers, become less dense during drying due to release of capillary pressure. However, such phenomena are hardly observed for granular gel coatings of Ta_2O_5 and Nb_2O_5.

Effects of crystallization on and of the gel coatings have been also discussed.

REFERENCES

1. D.R. Uhlmann and G.P. Rajendran, in Ultrastructure Processing of Advanced Ceramics, edited by J.D. Mackenzie and D.R. Ulrich (J. Wiley and Sons, New York, 1988) pp. 241-253.
2. J. Livage, in Better Ceramics Through Chemistry, edited by C.J. Brinker, D.E. Clark, and D.R. Ulrich (Mater. Res. Soc. Proc. 32, Pittsburgh, PA 1984) pp. 125-134.
3. H. Hirashima, T. Koyama, and T. Yoshida, Yogyo-Kyokai-Shi, 93, 554(1985).
4. C. Sanchez, M. Navabi, and F. Taulelle, in Better Ceramics Through Chemistry III, edited by C.J. Brinker, D.E. Clark, and D.R. Ulrich (Mater. Res. Soc. Proc. 121, Pittsburgh, PA, 1988) pp. 93-104.
5. L.A. Silverman, G. Teowee, and D.R. Uhlmann, in Better Ceramics Through Chemistry II, edited by C.J. Brinker, D.E. Clark, and D.R. Ulrich (Mater. Res. Soc. Proc. 73, Pittsburgh, PA, 1986) pp. 725-730.
6. C. Alquier, M.T. Vandenborre, and M. Henry, J. Non-Cryst. Solids, 79, 383 (1986).
7. H. Hirashima, K. Tsukimi, and R. Muratake, Seramikkusu-Ronbun-Shi, 97, 235 (1989) [J. Ceram. Soc. Jpn. Inter. Ed., 97, 232 (1989)].
8. H. Hirashima and S. Kamimura, in Better Ceramics Through Chemistry III, edited by C.J. Brinker, D.E. Clark, and D.R. Ulrich (Mater. Res. Soc. Proc. 121, Pittsburgh, PA, 1988) pp. 779-784.
9. G.W. Scherer, J. Non.Cryst. Solids, 100, 77 (1988).
10. H.K. Pulker, Coatings on Glass, (Elsevier Scientific Publishers, Amsterdam, 1984) p. 371.

PART VIII

Ceramic Processing of Natural Systems

BIOMIMETIC CERAMICS

PAUL CALVERT
Arizona Materials Labs. 4715 E. Fort Lowell Rd, Tucson AZ 85718

ABSTRACT

This paper discusses the possible advantages to be gained from a bio-mimetic approach to ceramics and reviews the work now in progress that will lead us to be able to mimic biological structures with synthetic materials.

BIOLOGICAL CERAMICS

There are many biological materials that can be thought of as ceramics, including tooth and shell. In general these materials are usually composites with low volume fractions of polymer present that modify the properties without detracting from the hardness ceramic. Examples that we might wish to emulate in synthetic ceramics include:

(a) mammalian tooth, with a high volume fraction of hydroxyapatite rods bound together by protein to form an outer wear-resistant layer over tougher dentine [1];

(b) nacreous shell where aragonite plates are stacked in a bricks-in-wall type of structure with a thin layer of chitin and protein acting as mortar [2];

and (c) sea-urchin spine, a porous single crystal of calcium carbonate, covered with a protective polymer layer and toughened by protein entrained actually within the crystals [3].

More general arguments about why we might wish to mimic other aspects of biological materials have been given elsewhere [4]. As illustrated in table 1, we can

Table 1

Strength of Biological Ceramic Composites

	Mineral %	Strength MPa	Toughness J m^{-2}
Enamel	92	76	200
Whale bulla	66	33	200
Dentine	48	250	550
Bone	41	270	1700
Antler	31	179	6200
Nacre	96	170	350-1240
Alumina	100	100-1000	50

From Vincent [13]

Mat. Res. Soc. Symp. Proc. Vol. 180. ©1990 Materials Research Society

see bone-like materials as offering a range of very tough composite structures with properties varying from those of a ceramic to those of a reinforced rubber. The materials can be assembled into structures with internal composition gradients allowing complex structures to be formed without any joints between materials with different properties.

GOALS FOR BIOMIMETIC CERAMICS

With the examples outlined above in mind, it is possible to put together a list of the benefits that might be expected from the development of bio-mimetic ceramics.

The most obvious benefit is that it should be possible to produce materials with the high hardness and chemical resistance of ceramics by room temperature formation methods. Such a material could have applications as coatings and linings and, by analogy with tooth, in various cutting applications where a ceramic edge is backed by an integrated composite body.

The major limitation is that the maximum operating temperature will be limited by the polymeric component. If we are willing to assume that some softening of a minor polymer component will not greatly detract from the performance of a polymer-bound ceramic, like tooth, we can expect a temperature ceiling of somewhere in the range of 300-400°C. There are polymers that can withstand higher temperatures without decomposition, like polyphenylene, but they tend to be brittle and so would be poor binders. Even with this temperature limitation, the material would compare favorably with partially stabilized zirconias.

With the inclusion of a polymeric binder, surrounding grains, with a volume fraction of about 5%, we can expect to add substantial toughness to the ceramic. This is suggested by the studies of Aksay and Sarikaya showing the polymer phase in Abalone [5] shell being stretched out in fibrils across a growing crack. From the example of sea urchin spine [6], we can also expect to be able to incorporate toughening polymers within a ceramic single crystal, and to be able to control the growth morphology of this crystal to conform to an arbitrary pre-defined shape.

Matrix control of ceramic particle formation should allow us to form anisotropic particles from materials that are normally equiaxed or spherical. This could occur through the preferential adsorption of growth poisons to developing crystal surfaces, as seems to occur during the growth of aragonite in either prism or platelet form. In addition, a matrix is not necessarily an isotropic environment. Particle formation in a highly oriented polymer medium with large differences in modulus and surface energy in different directions can be expected to lead to changes in the particle growth morphology. We have studied methods for growing oriented organic particles in polymer matrices, as have some others [7,8].

If we had access to highly anisotropic ceramic powders, we could use these to reinforce conventional ceramics as has been done with silicon carbide whiskers. We could also, in principle, make ceramics completely from anisotropic particles and toughened by the pull-out of rods or plates at a crack surface. The problem in this case is to achieve der ٩ packing of the fibers. This problem has been resolved in a rat's tooth (ref. 1, p.1. .) but is achieved by the packing occurring as the rods are actually formed. We may be able to similarly grow green bodies containing a high enough fraction of rods to be sinterable.

The effectiveness in biomineralization of control over the deposition site, suggests that we could produce complex structures by growing ceramic deposits at specific sites on a surface. Such deposits might be localized on a silicon surface to

provide part of a sensor structure, for instance.

BIOPARTICLES

One direct application of biological methods in ceramics could be to use organisms as a source of particles. The range of minerals synthesized by organisms is large [1] and this range can probably be greatly extended if abnormal levels of metals are included in the growth medium. Thus it has recently been shown that yeast can produce particles of cadmium sulfide if it is grown in a calcium-rich medium [9]. Presumably this is a detoxification reaction.

The magnetotactic bacteria form small single crystal particles of magnetite, each one surrounded by a membrane which controls inter-particle interactions [10]. In principle such particles could be harvested and used as a dispersant-treated powder for magnetic media. However, the costs involved in forming powders by fermentation in a dilute suspension and subsequent separation from the bacterium, may be prohibitive.

Possibly there are some markets where the small size and reproducibility of this route makes the process viable. There may also be sense in adopting a "biomimetic" approach to precipitating powders, in that we should endeavor to form the powder with a dispersing coating in place around each particle and never remove this until the final sintering step, hence avoiding the formation of hard agglomerates. Ring [11] has in essence studied such a process of dispersion during growth of titania particles from alkoxide.

ONGOING WORK

A number of groups are studying shells and teeth from the point of view of explaining the source of the toughness and strength in these materials. The background has been well discussed in the books of Wainwright et al. [12] and Vincent [13]. Heuer and Laria [14] and Aksay and Sarikaya [5] are studying mollusc shell with a view to elucidating the fracture mechanism and defining the fracture behavior. This has also been studied by Jackson, Vincent and Turner [15].

In this meeting Aksay has discussed the preparation of ceramic composites using principles taken from these shell structures.

Mann and Heywood [16] have been studying the formation of calcium carbonate at lipid monolayers in order to discover the mechanisms of control operating in shell formation. Addadi and Weiner have been investigating the effect of various acidic macromolecules in this system. Nancollas and co-workers are carrying out similar studies of the influence of additives on hydroxyapatite formation [17].

Rieke and Tarasevich are investigating methods of modifying surfaces to promote local precipitation and attachment of inorganic particles such as iron oxides and sulfides [18].

Our work has focussed on establishing methods of forming metal and oxide particles in polymer films, including iron oxides, iron and titanates [19]. Now we are setting up a light scattering system to continuously monitor particle growth in polymer films and so learn more about the mechanisms of precipitation in a matrix.

This work on the formation of second phase particles in polymer is clearly related to that on ceramers and polycerams which is discussed later in this meeting.

Once we have decided that interesting structures can be produced by the combination of polymer and ceramics, there are a multitude of methods of actually carrying out this combination.

The work by Zelinsky, Uhlmann and co-workers, and by Schmidt is discussed elsewhere at this symposium. Nominally single-phase silica-polymer blends are formed by various strategies of sequential or concurrent polymerization and gelation. Wilkes and co-workers have produced single phase blends of alumina and polyether by a similar route [20].

Mark has precipitated iron oxides into butyl rubber [21], and titania into silicone rubber [22]. In the first case the volume fraction of filler was low, up to 2%, but in the latter case it reached 44 vol% based on dense titania. The titania was introduced by swelling silicone rubber in liquid titanium alkoxide and then transferring the swollen rubber to water containing an acidic or basic catalyst.

K.A.Mauritz [23] has produced composites of titania in polybutylmethacrylate up to about 11 vol% titania . Films were cast from solution and hydrolysed in moist air. Satisfactory films were obtained with titanium tetraethoxide and tetrabutoxide but not with the tetraisopropoxide or zirconium tetrabutoxide. this presumably reflects different degrees of liquid-liquid miscibility. This group has also produced composites of silica precipitated into Nafion fluorocarbon membranes [24].

So far there have been developed methods to produce polymer-modified glasses (ceramers and polycerams) with polymer fractions varying from very low up to 50% or more. These materials are commonly transparent but may be phase separated on a micro scale. We also have methods for the formation of micron or sub-micron particles of amorphous oxides in polymers. We have found that many of these oxides can readily be crystallized in the polymer at low temperatures by a hydrothermal treatment. These particles can be formed at volume fractions up to about 50%. We have also shown that such composites can be sintered to dense ceramic [25]. We do not yet have a route to very high volume fractions of ceramic or glass particles surrounded by a thin layer of polymer (<10vol%). We also do not have a route to a continuous phase glass or ceramic system toughened by small inclusions of polymer such as is suggested by the sea urchin spine. Even at a single composition there are clearly several distinct composite morphologies that can be formed.

Here too there may be a lesson from biology in that most of the human body is constructed from one structural polymer, collagen, one film-former, keratin, one mineral, hydroxyapatite, one rubber, elastin, and a group of closely related ionic polysaccharides. Skin, bone, tendon and cartilage are built from varying arrangements of these components. Hence we can expect ceramic/polymer blends to give us a wide range of microstructures, morphologies and properties.

FUTURE DEVELOPMENTS

Current work can be expected to take us to the point of being able to make biomimetic thin ceramic films. Questions that remain untackled at this point include approaches to making bulk material, methods for producing non-oxide or sulfide ceramic particles, and the use of high temperature polymers as matrices to provide better thermal resistance in polymer ceramic composites.

References

1. H.A.Lowenstam and S.Weiner, "On biomineralization" Oxford University Press 1989

2. J.D.Currey, in "The Mechanical Properties of biological materials" Symp. Soc. Exptl. Biol. 34, eds. J.F.V.Vincent and J.D.Currey, 1980, Cambridge Univ. Press.

3. K.M.Towe, "Echinoderm calcite", Science 157, 1048, (1967)

4. P.Calvert, "Bio-mimetic processing of ceramics and composites", Proc. 4th Ultrastructure Conference, Tucson, Az, 1989. In press.

5. M.Saraikaya, K.Gunnison, M.Yasrebi and I.A.Aksay, "Mechanical property-microstructure relationships in Abalone shell" Materials Res. Soc. Symp. 174, 109 (1990)

6. A.Berman, L.Addadi and S.Weiner, "Sea urchin polymers interact with growing calcite", Nature 331 546 (1988)

   L.Addadi, A. Berman, J.Moradian-Oldak and S.Weiner, "Molecular recognition between protein and crystal: relevance to biomineralization" Presented at Materials Res. Soc. Symp., Boston, 1989

7. M.A.Moskvina, A.V.Volkov, T.Ye.Grokhovskaya, A.L.Volynskii and N.F.Bakeyev, "A study of the state of low molecular weight organic acids in oriented polymer matrices" Polymer Sci. USSR 26 2648 (1984)

8. A.V.Volkov, M.A.Moskvina, A.L.Volynskii and N.F.Bakeyev, "Thermodynamic characteristics of melting and crystallization of low molar mass compounds in micropores of oriented polymer matrices" Polymer Sci. USSR 29 1814 (1987)

9. C.T.Dameron, R.N.Reese, R.K.Mehra, A.R.Kortan, P.J.Carroll, M.L.Steigerwald, L.E.Brus and D.R.Winge, "Biosynthesis of cadmium sulphide quantum semiconductor crystallites" Nature 338 596 (1989)

10. S.Mann, R.B.Frankel and R.Blakemore, "Structure, morphology and crystal growth of bacterial magnetite", Nature 310 405 (1984)

11. J.H.Jean and T.A.Ring "Nucleation and growth of monosized TiO_2 powders from alcohol solution", Langmuir 2 251 (1986)

12. S.A.Wainwright, W.D.Biggs, J.D.Currey and J.M.Gosline, "Mechanical Design in Organisms" Princeton University Press, 1986.

13. J.F.V.Vincent "Structural biomaterials", Macmillan, 1982.

14. V.J.Laria and A.H.Heuer, " The microindentation behavior of several mollusk shells" Materials Res. Soc. Symp. 174, 125 (1990).

15. A.P.Jackson, J.F.V.Vincent and R.M.Turner, "The mechanical design of nacre" Proc. Royal Soc. B234, 415 (1988); A.P.Jackson and J.F.V.Vincent, "A physical model of nacre", Composites Sci. and Tech. 36 255 (1989).

16. S.Mann, B.R.Heywood, S.Rajam and J.D.Birchall, "Controlled crystallization of $CaCO_3$ under stearic acid monolayers" Nature 334 692 (1988)

17. M.Johnsson, C.Richardson, E.J.Bergey, F.A.Scannapieco, M.J.Levine and G.H.Nancollas "The influence of salivary proteins on the growth, aggregation and surface properties of hydroxyapatite particles" Materials Res. Soc. Symp. 174, 81 (1990).

18. P.C.Rieke, S.B.Bentjen, B.J.Tarasevich, T.S.Autrey and D.A.Nelson, "Synthetic surfaces as models for biomineralization" Materials Res. Soc. Symp. 174, 69 (1990)

19. C.A.Sobon, H.K.Bowen, A.Broad and P.D.Calvert, "Precipitation of magnetic oxides in polymers" J.Materials Sci. Lett. 6, 901 (1987)

P.Calvert and S.Mann, "Review: Synthetic and biological composites formed by in-situ precipitation" J.Materials Sci 23, 3801 (1989)

P.D.Calvert, A.Broad and G.Cloke, "Magnetic particles in polymer films by in-situ precipitation" Polymer Preprints 29(2), 246 (1988)

20. B.Wang, H.Huang, A.B.Brennan and G.L.Wilkes, "Synthesis and characterization of new alumina-containing organic/inorganic hybrid materials" Polymer Prep. 30(2) 146 (1989)

21. S.Liu and J.E.Mark "Precipitation of iron oxide filler particles into an elastomer" Polymer Bull. 18 33 (1987)

22. S.-B. Wang and J.E.Mark "In-situ precipitation of reinforcing titania fillers", Polymer Bull. 17 271 (1987)

23. K.A.Mauritz and C.K.Jones, "Novel poly(n-butylmethacrylate)/ titanium oxide alloys produced by the sol-gel process for titanium alkoxides", J.Appl. Polymer Sci. (1989)

24. K.A.Mauritz, R.F.Storey and C.K.Jones, "Nafion-based microcomposites: silicon oxide-filled membranes" ACS Symposia (1989)

25. P.D.Calvert and R.A.Broad, "A 'bio-mimetic' route to barium titanate sheets", Materials Res. Soc. Symp. 174, 61 (1990).

BIOMIMETIC PROCESSING OF CERAMICS AND CERAMIC-METAL COMPOSITES

M. YASREBI, G. H. KIM, K. E. GUNNISON, D. L. MILIUS, M. SARIKAYA, and I. A. AKSAY

Department of Materials Science and Engineering; and
Advanced Materials Technology Center, Washington Technology Centers,
University of Washington, Seattle, Washington 98195 USA

ABSTRACT

Biomimetic design and processing of laminated B_4C-Al cermets, based on knowledge gained from the microstructure-property characterization of abalone shells, is described. In the nacre section of the shell, the microstructure is highly organized as $CaCO_3$ (aragonite) crystals, with a thickness of 0.25 μm, separated by a layer of organic matter 300-500 Å thick. This organization forms a miniature "brick and mortar" microstructure. The resultant strength and fracture toughness of the nacre, i.e., 180 MPa and 7 MPa-$m^{1/2}$, are many orders of magnitude higher than those of monolithic $CaCO_3$. The processing of laminated B_4C-Al cermets, based on the microstructure of the nacre, was performed by a combination of tape casting of the ceramic and infiltration of the metal. The resultant cermets displayed a 40% increase in both fracture toughness and strength over monolithic B_4C-Al cermets.

INTRODUCTION

The use of composite materials has become popular and frequently necessary to meet the requirements of technology. The employment of composites is well appreciated from the fact that unique arrangements of constituent materials not only satisfy specific requirements but also exhibit properties superior to the sum of each component.

Laminated composites which have planar geometry are one example and can be found both in nature and early civilizations. Examples are seashells, glued woods, and metallic armor. Even though exotic techniques and materials are introduced in the processing of laminated composites for modern applications, the flexibility of offering specific anisotropic properties, such as a specific strength, toughness, and stiffness, makes laminated composites attractive and provides an edge over single-phase materials.

The discovery that modern laminates formed from composites with a nanoscale architecture have enhanced properties has drawn much attention. It has led to the reexamination of the structure-property relationship in composites with different scales of size. Eutectic composites, frequently known as *in situ* composites, exhibit a well-aligned fibrous or platelet-reinforcing phase by directional solidification or by phase transformation, the classical example being the pearlite structure. A wide range of materials belongs to this group such as metal-metal,[1] metal-ceramic,[2] intermetallic-intermetallic,[1] metal-intermetallic,[3] and ceramic-ceramic[4-6] systems. In all cases, the size dependency of properties was observed and is known as the Hall-Petch relationship, $\sigma = \sigma_o + kd^{-1/2}$, for ductile phases and the Orowan relationship, $\sigma_f = YK_{IC}d^{-1/2}$, for brittle phases. Although directional solidification is a thermodynamically-driven process, precise control of the interfacial characteristics and composition of the composites was possible even when the size was reduced to a few microns. Similar microstructures can be obtained at the nanometer range through the use of physical or chemical deposition techniques which are not limited by thermodynamic parameters. The subsequent enhancement

Mat. Res. Soc. Symp. Proc. Vol. 180. ©1990 Materials Research Society

of properties results in unique behavior which is not only size dependent[7,8] but also dependent on the nature of the interface,[9,10] a phenomenon known as the supermodulus effect.[11]

A laminated architecture is especially useful in naturally-occurring composites such as seashells where it maximizes strength and toughness, sometimes exceeding the properties of the constituent materials by more than 20 times.[12,13] It should be noted that the biologically-produced laminates are formed *in situ* as are eutectic-like composites and have the same nanometer scale as superlattices. The classical work of Cook and Gordon[14] on the importance of interfacial bond strength in determining toughness can be seen in the enhancement of toughness in laminates as well. Refined models[15,16] are found in brittle matrix composites with all necessary microstructural dependencies. Our interpretation of the enhanced strength of biological laminates requires that a ductile-phase reinforcement be present so that the strength of the composite exceeds that of the strength of the component phases. This behavior has been observed in ceramic-metal composites which have been processed under the presence of strong wetting conditions where a liquid phase has formed between the molten metal and the ceramic phase such as in sintered WC-Co[17-19] and liquid metal-infiltrated B_4C-Al composites.[20-23]

It is therefore apparent that further enhancement of strength and toughness is possible by employing a laminated microstructure with a smaller size scale while keeping the ductile-phase reinforcement, as in B_4C-Al cermets. It will be shown in this study that the properties of laminated B_4C-Al composites indeed exhibit a size dependency in producing desirable enhancements but do so without sacrificing density of the composite. In the following section, therefore, we give a summary of the possible strengthening and toughening mechanisms in the nacre section of the abalone shell and draw certain design guidelines for ductile-brittle laminate materials. This will be followed by a section on the preliminary studies of B_4C-Al laminated structures which already exhibit superior mechanical properties over other existing cermet structures.



Figure 1. SEM images showing the two possible toughening mechanisms that significantly contribute to the toughening of the nacre section of the abalone shell: (a) sections, (b) ligament formation.

POSSIBLE TOUGHENING MECHANISMS IN LAMINATED MICROSTRUCTURES IN SEASHELL: EXAMPLE, NACRE

Structural components in biological systems such as load-carrying skeletons, grinding components such as teeth, and impact resistant "coats" like seashells, all have highly organized microstructures composed of an organic matrix and an inorganic major phase. In processing these structural components, the organism has full control so that the composite is tailor-made to fulfill certain functions in the body. In all these cases, because of the highly organized microstructures, biological composites have unique properties not yet achieved in synthetic materials. Therefore, it is imperative to examine biological composites to understand the relationship between microstructure and properties. Here we summarize mechanical property-microstructure relations in the nacre of abalone shell, draw some guidelines for laminated materials design, and subsequently apply these to the design and processing of laminated B_4C-Al cermets.

In general, seashells have various microstructures, each designed and processed to have optimum mechanical properties, such as adequate toughness, strength, hardness, or wear-resistance depending on the living environment of the animal. Nacre is a common structure found in many seashells and it primarily provides "toughness" to the shell. In the case of red abalone (*Haliotis refuscens*), the shell in the transverse direction (through thickness) consists of an outer prismatic layer and an inner nacre layer.[12,13] Two forms of $CaCO_3$, calcite and aragonite, constitute the inorganic component of the composite in the prismatic and nacreous layers, respectively.[12] The microstructure and mechanical properties of the nacreous layer are described here only when relevant to the present work.

The nacreous layer is composed of 95% $CaCO_3$ by volume and is organized in a "brick and mortar" configuration with the remaining organic matrix (proteins, macromolecules, and chitin). The $CaCO_3$ layers are individually composed of hexagonal shaped crystallites with a thickness of 0.25 μm. The organic layer between the $CaCO_3$ layers has a total thickness of about 20-50 nm and is composed of several layers of different organic components, the detailed structure of which is still not well understood.[13]

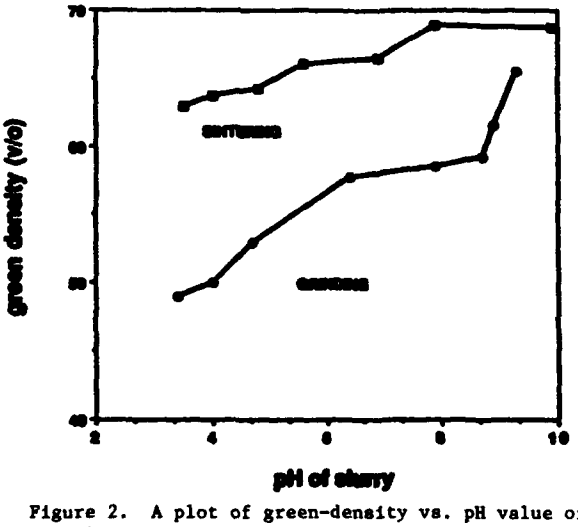


Figure 2. A plot of green-density vs. pH value of the slurry.

The mechanical properties in terms of fracture toughness (a straight notched three-point bend) and fracture strength (four-point bend) have been evaluated in the transverse direction. Typical values of σ_f and K_{IC} are 180 MPa and 7.0 MPa-$m^{1/2}$, respectively. These high values for mechanical properties may be explained based on the behavior of crack propagation during failure. The study of crack propagation features reveals a high degree of tortuosity not seen in monolithic ceramics such as brittle Al_2O_3 or ZrO_2. Certain toughening mechanisms such as microcrack formation, crack branching and blunting, and plate "pull-out" all operate in the nacre. However, the more than 20-fold increase in fracture toughness of the shell, which consists of 95% $CaCO_3$ and 5% organic matrix, compared to monolithic $CaCO_3$, cannot be explained by any of these mechanisms. However, two other mechanisms not usually seen in synthetic composites probably are the causes of the extensive toughness and strength increase. Both sliding of $CaCO_3$ layers on each other and organic "ligament" formation between layers occur when the resolved applied stresses are parallel and perpendicular to the layers, respectively (Figures 1(a) and (b)). The sliding mechanism in the nacre is reminiscent of plastic deformation by the movement of dislocation on slip planes in metals. Therefore, the propagating crack can only advance under constrained crack opening conditions, and only after considerable energy absorption, which results in a toughness increase. Both of these toughening mechanisms require that the organic phase be highly plastic and that the interface between the $CaCO_3$ and the organic phase be "strong."[13] In the above qualitative analysis neither the crystallographic configuration of the individual $CaCO_3$ plates nor the organization of the macromolecules (which are in the liquid crystalline form) is considered.

DESIGN GUIDELINES ON LAMINATED MATERIALS

The unusual combination of mechanical properties in the nacre as compared to synthetic ceramics and composites comes from (i) the intrinsic properties of the component phases (inorganic-brittle and organic-soft), (ii) the unique and highly ordered microstructure, and (iii) the size of the layers. Therefore, a number of design guidelines can be drawn from the study of the seashells. Based on the study of nacre, synthetic composites should possess:

(i) a laminate thickness of the hard-brittle component of less than 1 μm and a soft component of less than 1000 Å;

(ii) a highly plastic soft phase;

(iii) strong interfaces between the soft and the hard phases;

(iv) the ability of the soft phase to bind to the hard phase (strong interfacial bonding) and provide either plasticity to the whole composite (for sliding) or form ligaments to constrain crack opening, depending upon the resolved applied stresses

In practical processing, these guidelines may be difficult to apply. However, they are useful in the sense that they serve as ultimate conditions to be achieved for submicron laminate design. In the present study with B_4C-Al, mimicking lamination even with laminate thicknesses larger than 10 μm resulted in both fracture toughness and fracture strength improvements of more than 40%, as discussed in the next section.

PROCESSING OF LAMINATED B_4C-Al COMPOSITES

Materials

Two types of B_4C powders (supplied by the ESK Company) were used as starting powders. The main difference between the two powders that is of interest for this work was their packing behavior as a function of pH, as shown in Figure 2. ESK 1500 B_4C shows a lower packing green density compared to ESK sintering powder at all pH values.[24] The pH was adjusted with reagent grade HCl or NH_4OH. Rhoplex HA-8, a polyacrylic-based emulsion from Rhom and Haas, was used as a binder. DF-160L foamaster from Henkle was used as a defoamer agent. Finally, aluminum alloy 1100 was used as the source of the metal phase.



Figure 3. Laminated B_4C-Al composites processed by the first method. Arrows show Al-rich regions.

Fabrication of the Laminated Structure

The laminated composites were formed by three basic methods: (i) Partially sintered B_4C tapes were sandwiched with Al sheets and then heated to induce infiltration. (ii) Green B_4C tapes were stacked, partially sintered, and then metal infiltrated. (iii) Green B_4C tapes of different porosity were laminated (stacked and pressed), partially sintered, and then metal infiltrated.

In the first method, after B_4C tapes were cast, each tape was individually sintered to the desired density between polished graphite discs in order to prevent curling. Sintered tapes were then stacked with Al sheets and the whole stack was then heated to induce infiltration. The resulting structure was a B_4C-Al composite with Al interlayers (Figure 3). In the second method, B_4C tapes were stacked and the entire stack was then sintered. The resulting sintered body was composed of individual tapes of known density which were tightly sintered together but had almost a continuous thin gap between the tapes. The body was then infiltrated with aluminum. The resulting structure was a B_4C-Al composite with a thin ($\sim 5\,\mu m$) Al interlayer (Figure 4). This method was used when B_4C tapes were thinner than 90 μm. At these thicknesses, tapes could not be sintered by the first method without introducing defects into them. In the third method, tapes of B_4C with different green densities were stacked and laminated under pressure and temperature. The laminated body was then sintered and subsequently infiltrated with Al. The resulting structure is a B_4C-Al composite with graded morphology (Figure 5).



Figure 4. Laminated B_4C-Al composites processed by the second method. Arrows show Al-rich regions.



Figure 5. Laminated B_4C-Al composites processed by the third method. Arrows show Al-rich regions.

RESULTS: MICROSTRUCTURES VERSUS MECHANICAL PROPERTIES IN B_4C-Al MICROLAMINATES

The fracture strengths of the B_4C-Al composites were evaluated with four-point bend specimens, having a size of approximately 3 mm × 3 mm × 55 mm with a 1 μm surface finish. The test conditions were as follows: minor span size 12.7 mm, major span size 38.1 mm, and crosshead speed 0.05 mm/min. Fracture toughness was measured using approximately the same size bars with a single straight notch. The notch was cut by a diamond wheel saw with a 250-micrometer width. The tip of the notch was damaged by using 1/4 micrometer diamond paste and a razor blade. The ratio of the notch size to the sample height was 0.33. A three-point bend fixture and a crosshead speed of 0.05 mm/min were used.

Mechanical property testing of laminated B_4C-Al cermets showed an increase in fracture strength and toughness over the same Al-content materials processed with a monolithic morphology. Both the laminated structures with continuous Al layers (methods i and ii) or with graded structures (method iii) showed significant increases in fracture strength over monolithic material (Figure 6). However, the fracture toughness of the structures with continuous Al layers was found to be lower than the monolithic material. Further, as the Al content increased, the value of fracture toughness decreased. This is due to regions in the microstructure where Al is depleted, as shown in the scanning electron microscope (SEM) image (Figure 7). This depleted Al region is partially due to the precipitation of AlB_2 in the Al layers as well as processing defects caused by the infiltration of thin, sintered boron carbide tapes. In a fully dense composite without interfacial reaction products, the Al layers act as effective barrier against crack propagation (Figure 8).

The Al content of laminated samples in Figure 7 was altered by changing the ratio between the Al-rich and B_4C-rich layers in the microstructure. In Figure 9, the fracture strength and fracture toughness values are plotted versus the thickness ratios for laminated samples of Figure 6. It was revealed that a ratio of 6 to 1 of high boron carbide content tape to low boron carbide tape (and hence the Al-rich region in the post infiltration microstructure) with a 33.5 vol. % Al content (Figure 6) results in the highest fracture strength (945 MPa). Samples with a continuous Al layer do not show a maximum in fracture strength and the trend on fracture toughness is the opposite compared to graded samples.

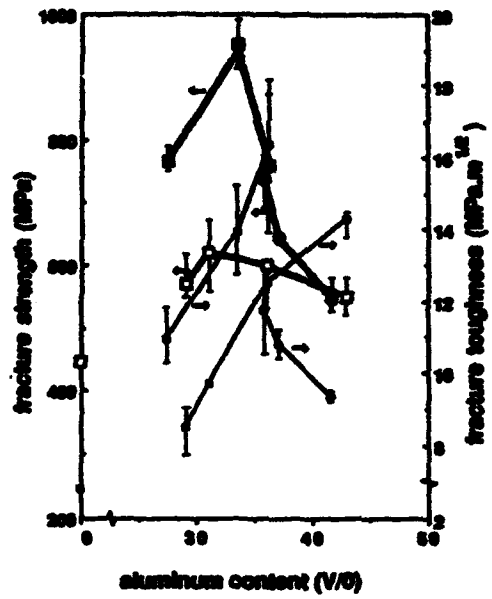


Figure 6. Fracture strength and fracture toughness of B_4C-Al composites. (□) monolith, (●) laminate with continuous Al layers, (■) laminate with graded layers.



Figure 7. An example of depleted Al region.



Figure 8. Blunting of a crack at the Al-rich region (SEM image).

After the proper ratio of high B_4C content to low B_4C content (or Al-rich laminae) was determined to be 6 to 1, simultaneous changes in the size of both laminae were made while maintaining the ratio.

The effect of changing the thickness of the laminae on both fracture strength and fracture toughness is shown in Figure 10. As expected from the Hall-Petch relation, the coarsening of the microstructure by increasing the tape thicknesses degraded the mechanical properties, with values approaching those for monolithic samples. Finer 6 to 1 ratio graded laminate structures have not been processed at this time due to the difficulty in casting and handling tapes thinner than 15 μm.

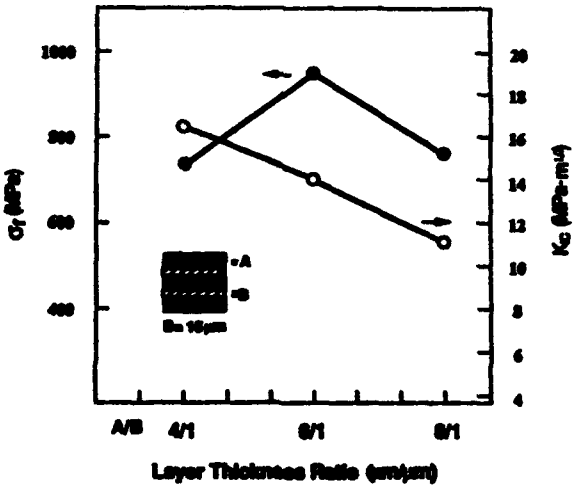


Figure 9. Fracture strength and fracture toughness plotted against B_4C thickness ratios.

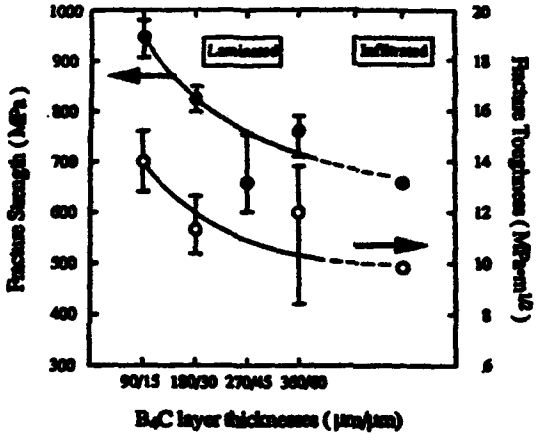


Figure 10. Fracture strength and fracture toughness vs. B_4C thickness plots.

SUMMARY AND CONCLUDING REMARKS

It was illustrated in this work that by processing materials based on the microstructures in biological systems, it is possible to significantly improve their properties. In biological systems, such as in the nacre section of the abalone shell, the microstructure is highly controlled, down to the nanometer scale. In the nacre shell structure, the component phases, $CaCO_3$ (aragonite) and organic matrix (a composite of chitin and macromolecules) form laminates 0.25 μm and 0.05 μm thick, respectively, stacked together to form an overall thickness up to a centimeter. Because of this unique microarchitecture, and also due to the properties of interfaces and the organic layer, unusual toughening and strengthening mechanisms operate, resulting in unexpectedly high mechanical strength and toughness values.

The processed B_4C-Al laminated cermets, based on the design principles outlined in the nacre, also show improvement in mechanical properties, both in fracture toughness and strength. These laminates were processed by tape casting of the B_4C layers which were then infiltrated with molten Al. The resulting microstructure produces layers of B_4C and Al, which are both continuous (unlike in the nacre) and have minimal reaction products at metal-ceramic contacts but still ensures a highly strong interface (like in the nacre).

Neither the fracture toughness nor the fracture strength of the nacre can be predicted based on the known relationships between the fracture toughness and critical flaw size (as in the Griffith relation), nor between the strength and the grain (or laminate) size (as in the Hall-Petch relationship). It should be noted that seashells have many different shapes with different microstructures, but all are based on the same basic components, i.e., $CaCO_3$ and the organic component.[12] Their microstructures have widely varying properties. The organic component can have its own unique "microstructure" in each of these cases. These issues have not been addressed in this paper. Only the gross microstructural features of the nacre have been mimicked in B_4C-Al laminates. In addition, in the case of B_4C-Al cermets, the size of the laminated layer is far from what might be required to achieve the unusual increases in mechanical properties as seen in the nacre. These issues, therefore, call for further detailed

studies in the biomimicking area in order to process highly ordered and tailored microstructures to achieve specific, non-isotropic properties in materials.

ACKNOWLEDGMENTS

This work was supported by the Air Force Office of Scientific Research (AFOSR) and was monitored under Grant Nos. AFOSR-87-0114 and AFOSR-89-0496.

REFERENCES

1. F. D. Lemkey, in ***Industrial Materials Science and Engineering***, edited by L. E. Murr (Marcel Dekker, New York, 1984), p. 441.

2. J. D. Holder and G. W. Clark, in ***Advanced Fibers and Composites for Elevated Temperatures***, edited by I. Ahmad and B. R. Noton (American Institute of Mining, Metallurgical, and Petroleum Engineers, Inc., New York, 1980), p. 225.

3. A. S. Yue, in ***Quantitative Relation Between Properties and Microstructure***, edited by D. G. Brandon and A. Rosen (Israel University Press, Jerusalem, 1969), p. 209.

4. W. J. Minford, F. L. Kennard, R. C. Bradt, and V. S. Stubican, in ***Ceramic Microstructures '76: With Emphasis on Energy-Related Applications***, edited by R. M. Fulrath and J. A. Pask (Westview Press, Boulder, Colorado, 1977), p. 456.

5. V. S. Stubican, R. C. Bradt, F. L. Kennard, W. J. Minford, and C. C. Sorrel, in ***Tailoring Multiphase and Composite Ceramics***, edited by R. E. Tressler, G. L. Messing, C. G. Pantano, and R. E. Newnham (Plenum Press, New York, 1986), p. 103.

6. J. D. Hong, K. E. Spear, and V. S. Stubican, *Mat. Res. Bull.*, **14**, 775 (1979).

7. A. F. Jankowski and T. Tsakalakos, in ***Layered Structures and Epitaxy, MRS Symp. Proc., Vol. 56***, edited by J. M. Gibson, G. C. Osbourn, and R. M. Tromp (Materials Research Society, Pittsburgh, Pennsylvania, 1986), p. 407.

8. D. Baral, J. B. Ketterson, and J. E. Hilliard, *J. Appl. Phys.*, **57** (4) 1076 (1985).

9. D. Wolf and J. F. Lutsko, *Phys. Rev. Lett.*, **60** (12) 1170 (1988).

10. R. C. Cammarata, in ***Multilayers: Synthesis, Properties, and Non-Electronic Applications***, edited by T. W. Barbee, Jr., F. Spaepen, and L. Greer (Materials Research Society, Pittsburgh, Pennsylvania, 1988), p. 315.

11. R. C. Cammarata, *Scripta Metallurgica*, **20**, 479 (1986).

12. J. D. Currey, *Journal of Materials Education*, **9** (1,2) 120 (1987).

13. M. Sarikaya, K. E. Gunnison, M. Yasrebi, and I. A. Aksay, to appear in ***Materials Synthesis Utilizing Biological Processes, MRS Symp. Proc., Vol. 174***, edited by P. Ricke, P. Calvert, and M. Alper (Materials Research Society, Pittsburgh, Pennsylvania, 1990), p. 109.

14. J. Cook and J. E. Gordon, *Proc. Roy. Soc.*, **A282**, 508 (1964).

15. L. S. Sigl, P. A. Mataga, B. J. Dalgleish, R. M. McMeeking, and A. G. Evans, *Acta Metall.*, **36**, (4) 945 (1988).

16. A. G. Evans and D. V. Marshall, *Acta Metall.*, **37** (10) 2567 (1989).

17. V. D. Kristic and M. Komac, *Phil. Mag.*, **A51** (2) 191 (1985).

18. G. Kreimer, ***Strength of Hard Alloys*** (Consultants Bureau, New York, 1968), p. 6.

19. H. F. Fischmeister, in ***Science of Hard Materials***, edited by R. Viswanadham, D. Rowcliff, and J. Gurland (Plenum Press, New York, 1983), p. 1.

20. A. J. Pyzik, I. A. Aksay, and M. Sarikaya, in ***Ceramic Microstructures '86: Role of Interfaces***, edited by J. A. Pask and A. G. Evans (Plenum Press, New York, 1987), p. 45.

21. D. C. Halverson, A. J. Pyzik, and I. A. Aksay, *Cer. Eng. Sci. Proc.*, **6**, 736 (1985).

22. D. C. Halverson, A. J. Pyzik, I. A. Aksay, and W. E. Snowden, *J. Am. Ceram. Soc.*, **72** (5) 775 (1989).

23. A. J. Pyzik and I. A. Aksay, in preparation.

24. M. Yasrebi, D. L. Milius, G. H. Kim, and I. A. Aksay, University of Washington, unpublished result (1990).

SYNTHESIS OF NANOCERAMIC PARTICLES BY INTRAVESICULAR PRECIPITATION

SUHAS BHANDARKAR,* ISKANDAR YAACOB AND ARIJIT BOSE
Department of Chemical Engineering, University of Rhode Island, Kingston, RI 02881
*AT&T Bell Laboratories, 600 Mountain Avenue, Murray Hill, NJ 07974

ABSTRACT

Nanometer sized magnetic particles have been fabricated by aqueous phase coprecipitation inside single compartment vesicles. These vesicles were generated by sonicating egg yolk phosphatidylcholine molecules in an appropriate ionic solution containing the reactant cations. Using cobalt and ferric nitrate as the starting solution, the reaction product was the desired cobalt ferrite; direct formation of the oxide is potentially a very important step. For the barium and ferric nitrate systems, the reaction product could not be identified easily. However, we have not been able to produce barium ferrite directly. In an attempt to compare the effect of drastic changes in the microenvironment, we have also completed aqueous phase precipitation in multilamellar vesicles. For the aluminum nitrate system, precipitation takes place only in the outermost "annular" space. Multiple particles are formed, and the resultant diffraction pattern shows a close match with an aluminum hydroxide chloride complex. This differs significantly from the product in single compartment vesicles, where β-Al_2O_3 was formed, and in free precipitation which resulted in $Al(OH)_3$.

INTRODUCTION

Phospholipid vesicles form an organically constrained nanometer sized aqueous core that can serve as unique reactors for the synthesis of nanometer sized ceramic particles. The organic membrane is permeable to anions but does not permit transport of cations. Utilizing this key property, reaction can be confined to the intravesicular space only, producing both single component and composite nanoparticles [1-3]. Precipitation within vesicles also offers other important pathways for the mediation of final particle size and phases. These include polar head group mediated organization of the reactant cations that lead to unexpected phases [3], fine control of the intravesicular supersaturation as well as concentration with a concomitant control on the final particle size, phase and morphology. In fact, precipitation within these highly constrained domains gives product that is significantly different in crystallinity, morphology, size and phase from the same reaction in free solution. In this paper, we explore aqueous phase reactions in both single compartment and multilamellar vesicles (MLV). The aqueous regions in MLV form a microenvironment for precipitation that is quite different even from the encapsulated regions in single compartment vesicles because of the extreme proximity of the polar head groups in neighboring bilayers. These head groups can act as parallel templates predisposing the organization of the reactant cations, and restricting the range of phases that are possible in the final product.

Because of their practical utility, the experiments reported here for the single compartment vesicles are from attempts to produce nanometer sized magnetic particles--more specifically, barium and cobalt ferrite ($BaFe_{12}O_{19}$ and $CoFe_2O_4$ respectively), by coprecipitation. These particles have a host of commercial applications, including longitudinal and perpendicular recording, ferrofluids and magnetic inks. They can also be sintered together to produce larger permanent magnets. Cobalt ferrite can be produced by coprecipitation of cobalt and ferric ions at relatively low temperatures (≈60°C), and

Mat. Res. Soc. Symp. Proc. Vol. 180. ©1990 Materials Research Society

therefore held the potential of forming intravesicular magnetic particles *in situ*. For the multilamellar vesicles, we have worked with precipitation of $AlCl_3$, primarily for comparison with the reaction product in single compartment vesicles.

EXPERIMENTAL STRATEGY

Precipitation in Single Compartment Vesicles

All chemicals--$Ba(NO_3)_2$, $Fe(NO_3)_3.9H_2O$, $Co(NO_3)_2$ and HaOH--were obtained reagent grade from Sigma Chemicals. Reverse osmosis single distilled water was passed through a 4-stage Millipore Milli-Q system, and all solutions were made using this water. The cation ratio in the solution was kept equal to that in the desired ferrite phase. The total cation concentration in the Ba-Fe and Co-Fe systems was 0.1 M and 0.15 M respectively. The details of the precipitation technique are given in Bhandarkar and Bose [3], and are only briefly summarized here, and shown schematically for the Co-Fe system in Fig. 1. Egg yolk phosphatidylcholine (pc) molecules are added to the appropriate ionic solution to form a 1% w/w pc solution. This mixture is then sonicated until single compartment vesicles are formed. This solution is then passed through a sodium form ion exchange column, so that all the extravesicular cations are replaced by sodium ions. Sodium hydroxide is then added to the extravesicular phase. Because the vesicle wall is permeable to cations, the hydroxyl ions permeate into the intravesicular space and react with the available cations to form a product.

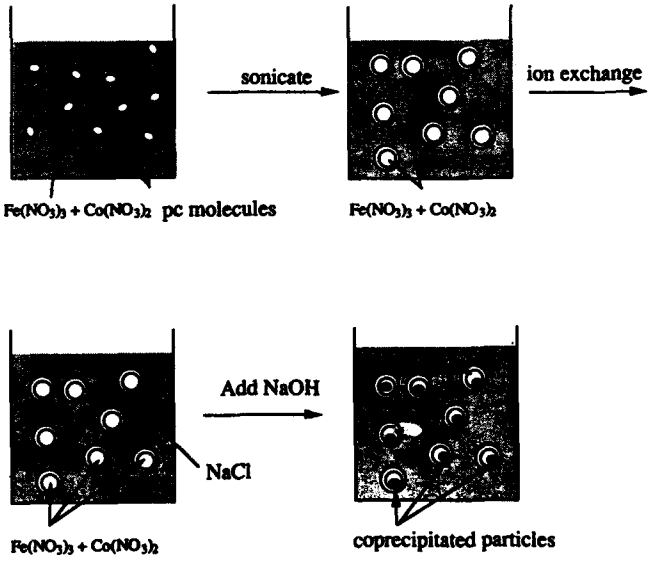


Figure 1. Schematic illustration of the process used for intravesicular coprecipitation of cobalt ferrite.

Precipitation in Multilamellar Vesicles

MLV were formed in a 1 M reagent grade $AlCl_3$ solution by sonicating only briefly (approximately 5 min). The remaining steps are identical to those reported above for single compartment vesicles.

All experiments have been conducted at room temperature. The products in both cases were examined by transmission electron microscopy. Electron diffraction was completed to identify the product phases.

RESULTS AND DISCUSSION

Figure 2 is an electron micrograph of the intravesicular product for the Co-Fe system, clearly showing nearly spherical particles of average size 15 nm. The corresponding wide area electron diffraction pattern is indexed in Table I. The product has all the intense peaks of $CoFe_2O_4$, which is the desirable ferrite phase. However, some additional peaks are also apparent, indicating the presence of an additional phase(s). We are currently in the process of making magnetic susceptibility measurements of suspensions of these particles to further identify the magnetic properties of this material. It is important to note that magnetic cobalt ferrite can be formed by free precipitation only at temperatures about 60°C--at room temperature the reaction product is invariably a mixture of cobalt and ferric hydroxide, which, of course, is not magnetic. The direct formation of the oxide in intravesicular coprecipitation is potentially extremely important and has been observed in other systems [1,2].

Table I

Lattice Spacings

Intravesicular Product (electron diffraction)	$CoFe_2O_4$ (X-ray Card #)
-	4.86
4.3	-
-	2.97
2.55	2.53
-	2.08
-	1.70
1.60	1.60
1.47	1.48
1.30	-

The product for the Ba-Fe system is shown in Fig. 3. No close match could be obtained for the resulting electron diffraction pattern, almost certainly excluding the possibility that barium ferrite had been formed. Further investigation is needed to determine if other ratios of Ba to Fe ions will result in the desired oxide phase.

Figure 4 is a transmission electron micrograph of the product formed by reaction of $AlCl_3$ with hydroxyl ions in multilamellar vesicles. It is apparent that product appears only in the outermost aqueous region--all reactant anions are apparently consumed there. Also evident is the formation of several particles at various points in the aqueous region. Electron diffraction revealed that the product was polycrystalline AlOOHCl. This is entirely different from the reaction product inside single compartment vesicles, where β-Al_2O_3 had been formed [2].

CONCLUSIONS

Intravesicular precipitation and coprecipitation is a novel method for producing nanometer sized ceramic particles. We have been able to produce cobalt ferrite, a material of great interest because of its magnetic properties. For the particular conditions studied in the barium-iron system, the product is not barium ferrite. Current research is focused on the development of appropriate conditions for the direct production of the useful magnetic phase.

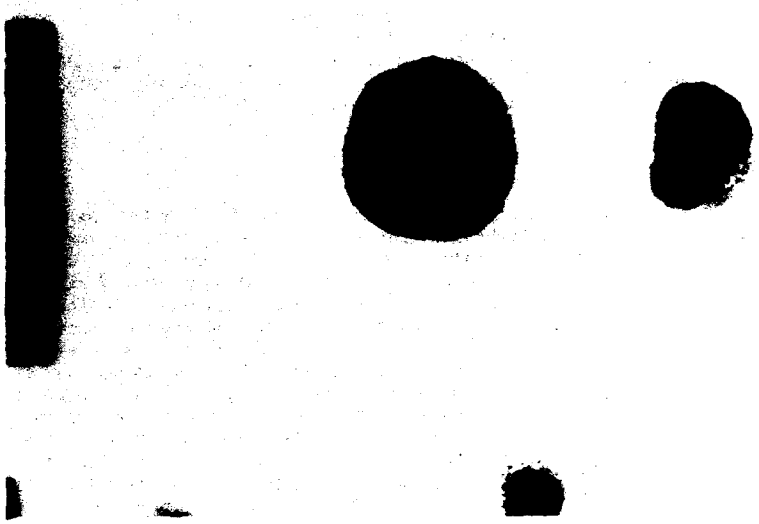


Figure 2. Electron micrograph of product formed from the coprecipitation of cobalt and ferric nitrate in single compartment vesicles.



Figure 3. Electron micrograph of product formed from the coprecipitation of barium and ferrice nitrate in single compartment vesicles.

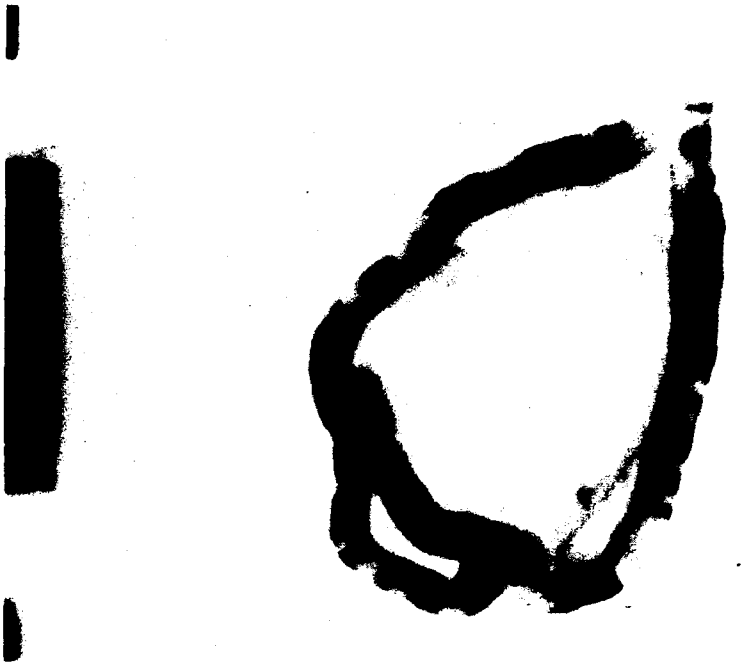


Figure 4. Electron micrograph of product formed from the precipitation of particles in multilamellar vesicles.

Precipitation for aluminum chloride solution in multilamellar vesicles takes place only in the outermost aqueous region. The product is a polycrystalline aluminum hydroxide/chloride complex, quite different from the β-Al_2O_3 produced in single compartment vesicles.

ACKNOWLEDGEMENTS

This work was supported in part by the National Science Foundation (CBT 8803047). We thank G. Jolly for extensive help in the use of the electron microscope.

REFERENCES

1. Mann S., Hannington, J. P., J. Colloid Int. Sci. 122, 326 (1988).
2. Bhandarkar, S., Bose, A., J. Colloid Int. Sci. 135, 531 (1990).
3. Bhandarkar, S., Bose, A., J. Colloid Int. Sci. 139, xxx (1990).

PART IX

Structure/Properties I: Electrical

WET CHEMICAL DERIVED FILMS FOR ELECTRICAL APPLICATIONS

D.R. Uhlmann, G. Teowee, J.M. Boulton and B.J.J. Zelinski
Department of Materials Science & Engineering,
University of Arizona,
Tucson, Arizona 85721

ABSTRACT

Wet chemical methods have been used with success to synthesize films for a variety of electrical applications. After first reviewing the important microstructural features of films, the present paper focuses attention on ferroelectric (FE) films. The present state of and critical issues facing wet chemically derived FE films are considered. The needs for more extensive microstructural characterization and for more systematic exploration of electrical behavior are emphasized.

I. INTRODUCTION

Wet chemical or sol-gel deposition of films is a rapidly advancing technology. Coatings can be formed from solution by a number of methods, including spin, dip, spray and roller coating; a wide range of compositions can be synthesized, including multicomponent materials; and doping can readily be effected.

The application of sol-gel methods to forming films is natural in that maximal advantage of the wet chemical approach can be taken, while cracking can be avoided - at least for coatings of up to 0.5 μm in thickness. Thicker coatings can be prepared by using several coat-and-fire steps or organic modification. Further, the inherently high raw material cost of wet chemical processing is relatively unimportant in the case of coatings.

The use of coatings in electrical applications is an area of considerable importance. Such coatings include: ferroelectric (FE) thin films, spin-on glasses, tantalum oxide, silicon oxynitride, high temperature superconductors, fast ion conductors, electrochromic films and transparent conductive coatings.

For reasons of space, the present paper will focus attention exclusively on FE films. The characteristics of such films prepared by wet chemical methods will be compared with those of films prepared using vapor deposition methods; and critical issues which must be addressed for the implementation of wet chemical FE films are considered.

It seems clear, however, that most thin film efforts - including FE thin films - are property driven. Definition of a desired combination of properties leads to specification of a composition; and variations in properties are effected by changes in chemistry and processing. In such developments, relatively little attention is directed to microstructure - despite the key role played by microstructure in the development of materials science and engineering as a discipline. For this reason, it seems appropriate to consider the important

Mat. Res. Soc. Symp. Proc. Vol. 180. ©1990 Materials Research Society

microstructural features of films, whether deposited by wet chemical methods or by physical deposition (as sputtering). The importance of microstructure in thin film technology has been emphasized in a recent review [1]; and this importance seems destined to grow during the coming decade.

II. MICROSTRUCTURE OF FILMS

The important microstructural characteristics of films include: (a) grain size; (b) porosity; (c) chemistry; (d) phase assembly; (e) orientation; and (f) substrate-film interactions. Also of importance are multilayer films. Each of these will now be discussed.

1. Grain Size: A characteristic feature size is observed, even in amorphous films. In wet chemical derived films, this represents local fluctuations in density and composition; while in physically deposited films, it is often related to columnar artifacts of the deposition process. After heat treatment, the grain size of the crystallized film is often comparable to the film thickness; but with appropriate treatment of at least some compositions, grain sizes much larger than the film thickness can be obtained.

In both wet-chemical and physically-deposited films, the grain size is important: The curvature of the solid-vapor interface provides the driving force for densification; and many properties of films (often for poorly-understood reasons) depend upon the grain size. In many films, particularly those deposited from the vapor phase, there exists a gradient in grain size though the thickness of the film, which can have a significant influence on structural evolution and property development. In cases where large grain sizes are required for obtaining desired properties, the potential low temperature processing advantage of wet chemical methods can be rendered ineffective when subsequent high temperature treatments are required to achieve the desired grain size.

2. Porosity: Porosity represents an almost-ubiquitous feature of as-deposited films of all types. The porosity can be discrete or interconnected, but is most often interconnected - for vapor deposited as well as for chemically-derived films. The volume fraction of pores is large, being typically about 50% for wet-chemical films and 30% for sputtered films as examples.

Because of the high volume fraction of small pores in typical films, the atmosphere can have a considerable effect on the evolution of microstructure (and hence properties). As an example, changes in atmosphere can lower the solid-vapor interfacial energy (and hence decrease the driving force for densification), but can raise the dihedral angle in polycrystalline arrays (and hence provide a driving force for densification where none existed before). Besides such effects on densification, porosity in thin films can play a significant role in the development of pinholes (the bete noire of thin films).

3. Chemistry: Most ceramics of technological interest are multi-component. Issues therefore arise with respect to cation ratios, cation-to-anion ratios, and retained organic species, hydroxyls, and gases in the deposition chamber (depending on the method of depositing the films). The capability of depositing multicomponent films represents a notable potential advantage of wet chemical methods; but this advantage has been poorly exploited to date.

Because of the large specific surface areas of most films, the chemical interaction of the film with the vapor phase is a matter of considerable importance. Such interaction during deposition affects strongly the structure of the as-deposited films for physically-deposited as well as chemically-deposited films. After deposition and throughout the period when high, fine porosity prevails, issues such as the instability of most oxides with respect to hydrolysis are significant; and interaction with the vapor can have a considerable effect upon densification and crystallization behavior, and even upon end use performance.

4. Phase Assemblage: Both physical and wet-chemical methods frequently produce as-deposited films which are amorphous or are comprised of metastable crystalline phases. Upon heat treatment, the amorphous films convert to stable crystalline phases, often via metastable crystalline phases. In few if any cases has the potential been realized for developing tailored metastable phase assemblages; and this represents an opportunity for future development.

5. Orientation: Orientation in films can be produced by the deposition process itself (e.g., the columnar features in sputtered films), or by unidirectional shrinkage and densification/ crystallization in post-deposition processing. The substrate can have both structural and chemical effects on orientational anisotropy (see below); and even amorphous substrates can have orientation-inducing effects.

6. Substrate-Film Interaction: Substrate-film interactions can be structural, chemical or mechanical in character. Structural (epitaxial) effects of substrates represent an area of outstanding opportunity for the coming decade. Such effects are expected when there is a strong crystallographic relationship between the substrate and film phases; but these relationships are often not apparent à priori (depending on the planes involved); the substrate surface can differ appreciably in chemistry (and hence in structure) from the bulk; and prediction of epitaxial effects is in general a far-from-exact science. Further complication is provided by the role of defects in the surface of the substrate (ranging from dislocations to scratches).

Chemical influences of the substrate include wetting, adhesion (where wet chemical methods can provide a notable advantage), surface segregation of impurities and adsorption of vapor species, and interdiffusion and reaction on heat treatment to form interphases between the film and the substrate.

Mechanical influences include tensile stresses produced by densification and crystallization of the film (or by its transformation to a phase of higher density), tensile or compressive stresses produced by the deposition process itself (as in some vapor deposited films), and tensile or compressive stresses associated with differential thermal contraction of film and substrate. Wet chemical methods can offer advantages in connection with the last effect.

III. FERROELECTRIC (FE) THIN FILMS

Notable examples of FE films include $BaTiO_3$, $SrTiO_3$, $KNbO_3$, $PbTiO_3$, and $Pb(Zr,Ti)O_3$. These are widely used, often doped to obtain desired properties, in a variety of applications and devices. Among these are pyroelectric detectors, thermistors, capacitors, displays and piezoelectric transducers. Conventional techniques used to deposit these films include evaporation and sputtering as well as use of powder slurries. With such methods, control of stoichiometry is difficult to achieve; and the high substrate temperatures required to establish satisfactory FE properties, combined with the extended times required for deposition, restrict the choice of substrates and can impair the underlying device profiles.

1. Lead Titanates: The lead titanate family includes lead titanate ($PbTiO_3$), lead zirconate titanate (PZT) and lead lanthanum zirconate titanate (PLZT). In combination with various dopants, they constitute the most versatile class of perovskite ferroelectrics, and are extensively employed for their ferroelectric, piezoelectric, electrooptic and pyroelectric properties. Their applications range from capacitor materials and optical modulators to electrooptic shutters. Sol-gel derived PZT films have also been exploited for IC neural networks [2].

Table I provides representative values of the properties which have been obtained by sputtering and wet-chemical methods for PZT and PLZT films. It is evident that bulk ceramics and thin films are characterized by different dielectric properties, and that the properties of thin films themselves cover a wide range. This is not surprising in light of the myriad of factors - chemical, processing and structural - which can influence properties.

The lead-poor pyrochlore phase is often detected in as-deposited sputtered $PbTiO_3$, PZT and PLZT films at intermediate substrate temperatures [4,5,7,19-22]. Post-deposition annealing at higher temperatures is used to transform this phase into the perovskite structure and also serves to optimize the FE properties. Lack of reproducibility and non-stoichiometry of the films pose serious problems, especially during multitarget sputtering or multisource evaporation. At elevated substrate temperatures, the volatility of lead is a matter of concern. Incorporating excess lead or lead oxide in the targets has been employed; but this approach remains quite system- and set-up-specific. In many cases, the chemical, microstructural and even the single-phase characteristics of the films are suspect, since

Table I
Ferroelectric Properties of Various Lead Titanate Thin Films

Method	Dielectric Constant E_r	Dissipation Factor tan δ	Permanent Polarization Pr(μC/cm2)	Coercive Field Ec(kV/cm)	Composition (Zr/Ti) (La/Zr/Ti)	Ref
Rf mag sputtering	400		40	150	45/55	3
Rf mag sputtering	300-500	0.02-0.2	12.5	90	65/35	4
Rf mag sputtering	350			35	90/10	5
DC mag sputtering	194	0.1-0.3	12	40	52/48	(1μm)6
DC mag sputtering	820	0.1-0.3	70		52/48	(3μm)6
Rf diode sputtering	751		20.4	23-3	52/48	7
Sol-Gel Methods on Various Substrates						
Pt			36	40	53/47	8
ITO	260	0.1-0.7	6.6	26.7		9
Pt	1000	0.02	5	8	8/65/35	10
Si(100)	130	0.17			7/65/35	11
Au	225	0.004			7/65/35	11
Si			2.2	7.5	50/50	12
Pt	1200	0.01-0.02			50/50	13
Pt	1000	0.01-0.02			44/56	13
Pt (Amorphous PZT)	35-50	0.005-0.001				13
Pt	500	0.026	10	37	53/47+2 at % Nb	14
Pt	300	0.05	21.8	81.6		15
Stainless Steel	400	0.4			50/50	16
Pt	500	0.06	12	40	50/50	17
Bulk Ceramics	425		33	6.5	50/50	12
Bulk Ceramics	750	0.004	45	17	53/47	18

PbO X-ray diffraction peaks have been detected in otherwise amorphous as-deposited films [6,23].

Besides pyrochlore formation at substrate temepratures below 550C, a lead-deficient $PbTi_3O_7$ phase can be formed at higher temperatures [24,25]. There is also ample evidence of epitaxy in the literature, as illustrated by PLZT on sapphire [22,26], (111) PZT films on (111) platinum [27], and C-axis oriented $PbTiO_3$ films on MgO [24,25,28].

Wet chemical synthesis of lead titanate films usually uses a mixture of Pb salts such as acetates [29] with Zr/Ti alkoxides, in some case reacting them in methoxyethanol [30] to form complex alkoxides.* Recent reports suggest an all-alkoxide route [31], based on forming Pb alkoxides via reaction of anhydrous Pb acetates with Na alkoxides. The presence of Na, even in concentrations as low as 100 ppm, may prove deleterious to performance, however, especially if the films are used in combination with MOS device circuitry. Films obtained using metallorganic decomposition (MOD) with ethylhexanoate or neodecanoate precursors [17, e.g.] tend to crack due to the low solids content and the corresponding large film shrinkage during subsequent pyrolysis.

The pH of the precursor solution plays a poorly understood role in affecting the final properties of sol-gel derived films. Beyond this, it appears that results obtained on SiO_2 cannot be extrapolated freely to other systems, notably those based on Pb-Zr-Ti precursors. Specifically, amorphous acid-catalyzed $PbTiO_3$ films are denser and have higher dielectric constants after low temperature heat treatment than those which are base catalyzed; but crystalline acid-catalyzed films have slightly lower dielectric constants and dielectric strengths [32]. Based on our data and those of others, there exists an optimum degree of hydrolysis of the solutions, which depends on the composition, concentration, starting materials and post-deposition processing. The presence of adequate amounts of water lowers and shrinks the temperature window where the pyrochlore phase is found. Extensive hydrolysis produces amorphous, porous films which do not densify even at high temperatures [29]. The detailed character of the structure before curing thus strongly affects the ultimate film properties.

The choice of precursor does not greatly affect the crystallization behavior; but some difference in DTA peaks can be detected due to dissimilar chemical environments [30]. In MOD- processed films, there exists not only a high tendency towards cracking, but also some carbonate formation resulting from the high organic content. Some organics are still present even at 400C [17], which can induce voids if they are burned off at temperatures above those required for densification of the film.

From Table I, values of the dielectric constant and dielectric loss of sol-gel derived films range from 35 to 1800

*Methoxyethanol is teratogenic, and can cause neurological and hematological damage even at the ppm level.

and 0.001 to 0.7 respectively. There exists a glaring lack of a standard form in reporting ferroelectric film properties. Such properties are functions of film thickness, grain size (Fig. 1), applied d.c. bias (Fig. 2), amplitude (Fig. 3) and frequency (Fig. 4) of the probe signal, as well as the measurement geometry and specifics. The measured dissipation factor, tan δ, is actually the composite tan δ of the device (usually a capacitor structure) under test and consists of the intrinsic material tan δ plus a contribution from the series contact resistance, ωRC. The present authors have noted an increase in tan δ at high frequencies and near the bridge resonance frequency. Further, the series or parallel equivalent circuit mode used during measurement should be duly noted, particularly in lossy systems.

The level of the signal amplitude influences the dielectric content and loss as demonstrated in Fig. 3 for a PZT film synthesized in our laboratory. At higher amplitudes, polarization reversals occur and lead to anomalous increases in dielectric constant and loss due to the nonlinear contribution from the hysteresis loop. Even in the case of a non-FE film, the signal level influences the impedance, notably when a barrier is present [33, e.g.]. The barrier impedance dominates at low signal levels, and the bulk impedance at higher signal levels.

The choice of electrodes is important, particularly if the FE film is doped with off-valent dopants leading to semiconducting properties. The contacts formed may be rectifying or ohmic, thus affecting the electrical characteristics. While a metal-FE-Si structure is simple (notwithstanding interfacial reaction layers), the resulting electrical characteristics (e.g., hysteresis loop) are asymmetric. The voltage drop across the Si depletion region makes difficult the task of determining accurately the coercive field. Under suitable conditions, Si can also inject carriers into the film.

With all these considerations in mind, Table I and any other comparison of FE film properties should be taken with care. With these reservations, the higher loss for crystalline films (compared with amorphous films) is due to a contribution from the nonlinear (hysteresis loop) nature of the films. Although the values of properties indicated in the Table are subject to various chemical and physical considerations, the most decisive factor is the choice of substrate. The highest E_r is found for films deposited on either bulk Pt or Pt films. The selection of substrate is crucial with respect to substrate-film interdiffusion and reaction [5,34, e.g.]. Methods of circumventing or mitigating harmful interactions with ceramic substrates (e.g., rapid thermal annealing or intermediate passivation layers such as SnO_2) seem deserving of greatly expanded attention.

Si is recognized to inhibit crystallization of PZT films unless the film is thick enough (~1μm) [11] or based on either an intermediate layer of Pt or $PbTiO_3$ [35]. There are cases, however, where a highly insulating oxide, e.g., SiO_2, is desired

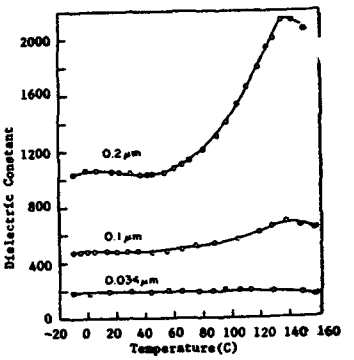


Fig.1 Variation of dielectric constant of $BaTiO_3$ films of varying grain sizes with temperature[48].

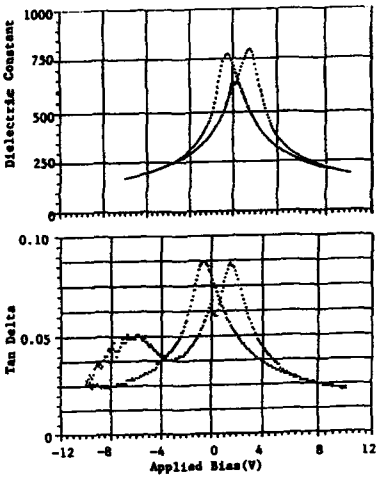


Fig.2 Effect of applied bias on sol-gel 53/47 PZT film (2300A,550C-30mins).

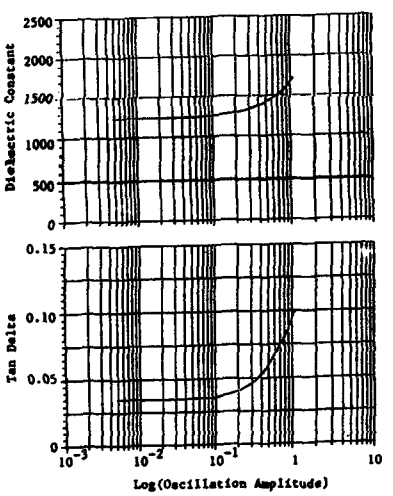


Fig.3 Effect of signal amplitude on sol-gel 53/47 PZT film (2100A,650C-30mins).

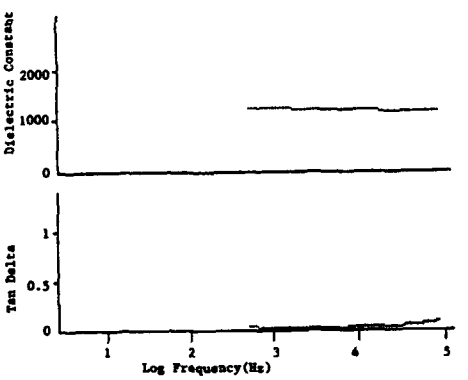


Fig.4 Effect of frequency on sol-gel 53/47 PZT film (4700A,700C-30mins).

as a barrier toward charge injection into the films, thereby reducing the conductivity contribution to the dielectric loss.

Lead titanate films showing a high degree of preferred orientation on single crystal MgO have been demonstrated [36]. Goosey et. al. [37], however, did not observe any such epitaxial effect on either MgO or on highly oriented Pt films. Both sets of investigators used similar precursors and chemistry; but the former group [36] noted that lower degrees of hydrolysis lead to a looser network which promotes favorable epitaxial rearrangements.

As in the case of sputtered films, the paraelectric pyrochlore phase is observed in many sol-gel derived films. Only at temperatures higher than 525C for PZT [17] or 600C for PLZT [18] is the monophase perovskite structure obtained. For $PbTiO_3$, perovskite films have been obtained between 500C and 570C. At lower and higher temperatures, pyrochlore and $PbTi_3O_7$ are, respectively, found [36]. In contrast, no other secondary phase was reported for a $PbTiO_3$ film fired at 700C [37]. Once again, the amount of hydrolysis plays a significant role in phase development. In both sputtered and sol-gel derived PZT films, the presence of refractory ZrO_2 helps to avoid the formation of the Pb-poor $PbTi_3O_7$ phase.

2. <u>$BaTiO_3$ and $SrTiO_3$:</u> $BaTiO_3$ has been the most intensively studied FE material. $SrTiO_3$ is commonly used in conjunction with $BaTiO_3$ to downshift the Curie temperature, and when doped with cations such as W, Y or Nb, to produce materials with exceptionally high E_r in boundary layer capacitors.

A comparison of the properties of $BaTiO_3$ films prepared using various techniques, including sol-gel methods, is presented in Table II. A wide variation is seen in the values of E_r, dielectric loss, remanent polarization and coercive field - demonstrating again the importance of experimental details on final film properties.

Si substrates yield relatively low values of E_r(<300), caused by the formation of interfacial layers such as SiO_2 or $Ba_2TiSi_2O_8$ [39]; while Pt represents a better substrate, either in film or bulk form, as with $PbTiO_3$ films. Relatively little dielectric characterization has been carried out on sol-gel derived $BaTiO_3$ films. Most sputtered films require annealing at temperatures in the range of 1000C, in either air or oxygen, to promote crystallinity and obtain better FE properties.

One notable feature in the synthesis of $BaTiO_3$ is the absence of any intermediate phase prior to formation of the perovskite structure. This stands in contrast to the amorphous-pyrochlore-perovskite evolution observed for $PbTiO_3$-based compositions. While sputtered films are highly oriented [40-42, e.g.], the present authors are unaware of sol-gel $BaTiO_3$ films with pronounced preferred orientation. Table II shows that the dielectric constants of films approach or even exceed those of bulk samples; but the polarization remains substantially below bulk values. Note that films with E_r values below 1400 (the bulk value) exhibit polarizations closest to those of bulk samples. Internal stresses within the grains, presumably causing the high

TABLE II
Properties of $BaTiO_3$ Films

Method/Substrate	Dielectric Constant E_r	Dissipation Factor Tan δ	Remanent Polarization P_r ($\mu C/cm^2$)	Coercive Field E_c(kV/cm)	Ref.
RF Sputtering/Si	300				42
RF Sputtering/Si	10-110		1		
RF Sputtering/Si	120	0.15			39
RF Sputtering/Pt			6	27	40
RF Sputtering/Pt	1680	0.03	0.8	3	41
RF Sputtering/Pt	16-1900	0.005-0.065	0.32	3	42
RF Sputtering/Si	10-40		1.28		43
DC Sputtering/Pt	1700	0.018	0.2		44
Evaporated/Pt	1050-1350		3-4		45
Polycrystalline Bulk Ceramics	1400		8-10		67
Monodomain Single Crystal			26		67
Sol-gel/Si Crystalline, 600C, 4 hrs.	53		0.339	0.080	46
Sol-gel/Pt Crystalline, 1200C max. temp.	200-1000	0.03-0.1	3.1		47

E_r (>1400), are also responsible for the clamping effect on polarization.

The simplest method used to make precursor solutions for $BaTiO_3$ or $SrTiO_3$ involves mixing the two alkoxides [49-52]. With such solutions, one alkoxide species - $Ba(OR)_2$ - tends to hydrolyze and condense more rapidly than the other, leading to the development of island-like heterogeneities during polymerization.

This problem can be mitigated by several approaches. These include using different alkoxide species with balanced reactivities; using double alkoxides; lowering the reaction temperature; substituting the Ba alkoxide with metal salts such as Ba naphthenate [53], Ba chelates [54] or Ba hydroxide [55]; and preparing a polymeric resin via glycols and/or oxalates. Yet another possibility involves the use of complexing agents or chelates such as 2,4-pentanedione [56] or glycerin [57]. Such chelates act to stabilize the alkoxide species in the precursor solution by partial substitution of the reactive alkoxy groups.

Ta, Nb and Sr-doped $BaTiO_3$ films have been prepared, where the dopants were introduced as alkoxides in solution [50]. This ease of introducing dopants provides the ability to tailor specific properties such as Curie temperature, dielectric constant, dielectric loss, and temperature coefficient of permittivity, as well as to obtain positive thermal coefficients of resistance.

Sol-gel derived $BaTiO_3$ and $SrTiO_3$ films crystallize at about *600C and 650C [58], respectively*, although some researchers report crystallization temperatures as low as 500C [55]. The as-deposited amorphous $BaTiO_3$ films typically have higher dielectric strengths than those of crystallized films [55] (see Table III). One explanation for this behavior, involving breakdown along the grain boundaries, is supported by the fact that polycrystalline $BaTiO_3$ has a lower breakdown field than single crystalline material. Table III also shows that amorphous sol-gel derived $BaTiO_3$ films exhibit higher dielectric strengths than sputtered ones, likely due to their high homogeneity and low incidence of defects, and perhaps the lack of a columnar structure in the sol-gel derived films.

Table III: Breakdown Fields of $BaTiO_3$ Films

Form	Breakdown Field 10^4V/cm	Ref.
Sputtered Film (amorphous)	1.8	42
Sputtered Film (Crystalline)	0.47-0.87	42
Bulk Ceramic	0.14	42
Single Crystal	0.40	42
Sol-Gel Film (amorphous)	8-9	54

While wet chemical methods are extensively used in the synthesis of $BaTiO_3$ and $SrTiO_3$ powders, their use in the direct preparation of films remains to be widely exploited.

3. Ferroelectric Memory: FE memory is not a new phenomenon. The characteristic polarization-electric field hysteresis loop long ago suggested the possibility of binary data storage; and a metal-FE-semiconductor transistor was proposed as early as 1974 [59]. FE memory offers the advantages of non-volatility, low power consumption, potentially high data packing density and enhanced radiation hardness compared with semiconductor memory. Previous FE memory devices have suffered from the lack of a time-invariant coercive field - i.e., materials whose polarization can switch at any applied voltage after long times.

Materials considered for FE memory include KNO_3 [60], PVDF [61], Bi titanate [62], $BaTiO_3$ [63] and PZT [64]. PZT is considered the most promising candidate, since its properties can be tailored by doping (e.g., with La to obtain PLZT) and control of microstructure. Other materials suffer from drawbacks such as hygroscopicity, high leakage currents, cracking, low thermal stability or high coercive fields.

The two major techniques used to deposit PZT films have been sol-gel methods and sputtering. Sputtered films generally have columnar microstructures and large grains, and are formed at slow deposition rates. In contrast, sol-gel processing yields fine-grained films which contribute to the depinning of domain walls to alleviate fatigue [65]. High purity materials are used, promoting close control of stoichiometry and reproducibility of the film properties. The relative ease of introducing dopants facilitates materials engineering and the systematic exploration of solid solutions. Doping of PZT films has been successfully demonstrated in the case of PLZT [30] and Nb-doped PZT [14].

It is well-known that dopants which cause A-position vacancies in the ABO_3 perovskite cell exhibit high E_r, low aging rates, decreased coercive fields and relatively square hysterisis loops. Even without dopants, FE films on Pt or passivated Si have been obtained with high E_r (1000-1250), low dielectric loss (<0.06) and a high resistance towards fatigue.

There exists a lack of detailed studies of FE film-electrode interactions in spite of voluminous scattered reports of ohmic contacts to bulk semiconducting FE titanates. Electrode diffusion into the FE layer increases in severity in the sequence In, Ag, Al, Sn-Au and Pb [66]. Liquid electrolytes [67, e.g.] may inhibit the carrier injection which is responsible for space change phenomena, but may add a corrosion problem.

The major problems which threaten the eventual viability of FE memory devices remain aging and fatigue. Aging, usually manifest as a logarithmic decrease of E_r with time, has variously been attributed to domain relaxation as the domain structure evolves upon cooling from the Curie point to a thermodynamically more stable state, or to a buildup of space charge within the grain boundaries, domain walls, defects or interfaces which

gives rise to an internal bias opposing the remanent polarization. Sol-gel derived films, with their smaller grain sizes, should age faster if the space change mechanism is predominant; but to date there has been no detailed study of the dependence of aging rate on grain size in either chemically derived or sputtered films.

Fatigue, a dynamic degradation associated with cycling of the polarization, has variously been imputed to dendrite formation, electrode diffusion, or microcracking. The dendrites are conductive Ti^{+3} filaments, caused by the reduction of Ti^{+4} ions under high local field conditions. These may span across the device, shorting it out. In addition to distortions of the hysterisis loop, shifts in E_r, spontaneous polarization and coercive field have been observed.

While chemically derived PZT films with attractive combinations of properties have been demonstrated, their optimization entails further work, especially with respect to aging and fatigue. The potential importance of sol-gel processing for preparing FE memory devices is illustrated by the number of organizations (including our laboratory) pursuing its development.

IV. CONCLUSIONS

Wet chemical methods offer promise for forming thin films of a range of materials for electrical applications. Potential advantages of such methods include low processing temperatures, avoidance of columnar structures, formation of tailored metastable phase assemblages, and the potential ease of forming chemically homogeneous multicomponent films and films with selected dopants.

To date, wet-chemical methods have been successful in obtaining FE films with properties approaching bulk ceramic values. The principal advantages of these methods compared with sputtering is improved control of stoichiometry and ease of doping, as well as the lack of a dependence on vacuum equipment. The potential utility of low processing temperatures for wet-chemically derived films remains to be properly established by detailed studies of pyrolysis, densification behavior, crystallization pathways, coarsening behavior and dielectric properties as functions of chemistry and processing conditions (including post densification heat treatments). Among these, the nucleation and crystallization of the pyrochlore and perovskite phases, as well as the pyrochlore-to-perovskite transformation and the control of grain size distribution deserve particular attention.

Considerable focus has been placed on relations among chemistry, processing conditions and properties. Even here, there exists a general lack of systematic investigations and of studies directed to elucidating mechanisms and understanding phenomena. Without such foundations, it will be difficult for wet chemical methods to compete with established physical deposition methods.

There also exists a notable lack of microstructural characterization of wet chemically deposited films. This represents an area of opportunity for materials scientists; and establishment of the relations of chemistry and processing to microstructure, and of microstructure to properties, will almost certainly be fruitful. Such studies should be directed to systems and applications where the effort can be justified. With such efforts, one can be optimistic about achieving a greater fraction of the considerable potential of wet chemical processing.

ACKNOWLEDGMENTS:

Financial support of the present work was provided by the Air Force Office of Scientific Research. This support is gratefully acknowledged.

REFERENCES

1. D.P. Birnie III and D.R. Uhlmann, paper presented at the 1st International Ceramic Science & Technology Congress, Anaheim, CA, 1989.

2. L.T. Clark, R.O. Grondin and S.K. Dey, Proc. of the 1st IEE Int'l. Conf. Artificial Neural Networks, London, 1989 (in press).

3. R. Takayama and Y. Tomita, J. Appl. Phys. 65, 1666 (1989).

4. A. Croteau, S. Matsubara, Y. Miyasaka and N. Shohata, Jpn. J. Appl. Phys. 26 (Suppl. 2), 18 (1987).

5. M. Adachi, T. Matsuzaki, T. Yamada, T. Shiosaki and A. Kawabata, Jpn. J. Appl. Phys. 26, 550 (1987).

6. K. Sreenivas and M. Sayer, J. Appl. Phys. 64, 1484 (1988).

7. A. Okada, J. Appl. Phys. 48, 2905 (1977).

8. S.K. Dey, K.D. Budd and D.A. Payne, IEEE Trans. on Ultra, Ferro and Freq. Control 35, 80 (1988).

9. B. Yi, Z. Wu and M. Sayer, J. Appl. Phys. 64, 2717 (1988).

10. D.A. Payne, paper presented at Ultrastructure Meeting, Tucson, 1989.

11. V.K. Seth and W.A. Schulze, Proc. First Symp. Integ. Ferroelectrics, Colorado Springs, 1989, pp. 175-184.

12. C.J. Chen, E.T. Wu, Y.M. Xu, K.C. Chen and J.D. Mackenzie, Ibid., pp. 185-188.

13. S.K. Dey and R. Zuleeg, Ibid., pp. 189-194.

14. B.A. Tuttle, T.J. Garino, D.M. Doughty, S.L. Martinez and J.L. Yio, paper presented at Amer. Cer. Soc. Annual Meeting, Indianapolis, IN, 1989.

15. C.C. Hsueh and M.L. McCartney, Ibid.

16. R.A. Lipeles, N.A. Ives and M.S. Leung, in Science of Ceramic Chemical Processing (edited by L.L. Hench and D.R. Ulrich, Wiley, 1986) pp. 320-326.

17. R.A. Lipeles and D.J. Coleman in Ultrastructure Processing of Advanced Ceramics (edited by J.D. Mackenzie and D.R. Ulrich) pp. 919-924 (1988).

18. G.M. Haertling, Am. Ceram. Soc. Bull. 43, 875 (1964).

19. T. Shiosaki, M. Adachi, S. Mochizuki and A. Kawabata, Ferroelectrics 63, 227 (1985).

20. R.N. Castellano and L.G. Feinstein, J. Appl. Phys. 50, 4406 (1979).

21. M. Ishida, M. Matsunami and T. Tanaka, J. Appl. Phys. 48, 951 (1977).

22. H. Adachi, T. Mitsuyu, O. Yamazaki and K. Wasa, J. Appl. Phys. 60, 736 (1986).

23. K. Sreenivas, M. Sayer and P. Garrett, Thin Solid Films 172, 251 (1989).

24. K. Fijima, S. Kawashima and I. Veda, Jpn. J. Appl. Phys. 24 (Suppl. 2), 482 (1985).

25. K. Fijima, Y. Tomita, R. Takayama and I. Veda, J. Appl. Phys. 60, 361 (1986).

26. H. Adachi, T. Kawaguchi, M. Kitabatake and K. Wasa, Jpn. J. Appl. Phys. 22 (Suppl. 2), 11 (1983).

27. H. Volz, K. Koger and H. Schmitt, Ferroelectrics 5[illegible] (1983).

28. M. Okada, S. Takai, M. Amemiya and K. Tominaga, Jpn. J. Appl. Phys. 28, 1030 (1989).

29. R.A. Lipeles, D.T. Coleman and M.S. Leung, in Better Ceramics Through Chemistry, II, edited by C.J. Brinker, D.E. Clark and D.R. Uhlmann (MRS Sym. Proc. 73, 1986) p. 665.

30. K.D. Budd, K. Dey and D.A. Payne, Br. Ceram. Proc. 36, 107 (1986).

31. T. Nanao and T. Eguchi, Jpn. Kokai Tokkyo Koho, JP 61/97159 A2 15 May 1986.

32. K.D. Budd, S.K. Dey and D.A. Payne, Ref. 29, p. 711.

33. A.K. Jonscher in Dielectric Relaxation in Solids, Chelsea Dielectric Press, London, 1983.

34. M. Kojima, M. Okuyama, T. Nakagawa and Y. Hamakawa, Jpn. J. Appl. Phys. 22 (Suppl. 2), 14 (1983).

35. S.L. Swartz, paper presented at the 1st Intl. Ceramic Science & Tech. Congress, Anaheim, 1989.

36. C. Chen, D.F. Ryder and W.A. Spurgeon, J. Am. Ceram. Soc. 72, 1495 (1989).

37. M.T. Goosey, A. Patel, I.M. Watson, R.W. Whatmore and F.W. Ainger, Brit. Cer. Proc. 41, 49 (1989).

38. R.W. Vest and J. Xu, Ferroelectrics 93, 21 (1989).

39. C. Hu, Ph.D. Dissertation, Univ. New Mexico, 1979.

40. C.A.T. Salama and E. Siciunas, J. Vac. Sci. Tech. 9, p. 91.

41. M. Schafer, M. Schmitt, K.M. Ehses and G. Kleer, Ferroelectrics 22, 775 (1978).

42. T. Nagatomo and O. Omoto, Jpn. J. Appl. Phys. 26 (Suppl. 2), 11 (1987).

43. K. Sreenivas and Abhai Mansingh, Proc. of 6th IEEE Intl. Conf. on Appl. Ferro., 1986, p. 602.

44. J.K. Park and W.W. Granneman, Ferroelectrics 10, 217 (1976).

45. Y. Shintani and O. Tada, J. Appl. Phys. 41, 2376 (1970).

46. Y. Iijima, Jpn. J. Appl. Phys. 24 (Suppl. 2) 401 (1985).

47. E. Sanchez, paper presented at 1st Intl. Ceramic Sci. & Tech. Congress, Anaheim (1989).

48. J.J. Xu, A.S. Shaikh and R.W. Vest, IEEE Trans. UFFC 36, 307 (1989).

49. L.A. Suchoff, U.S. Pat. 3002861, Oct. 3, 1961.

50. J.J. Mitchell, U.S. Pat. 3066048, Nov. 27, 1962.

51. S. Sakka, Kagaku Sochi 27, 98 (1985).

52. B.A. Paulson, Rept. IS-T-1336 (NTIS) (1987).

53. J. Fukushima, K. Kodaira and T. Matsushita, Amer. Ceram. Soc. Bull. 55, 1065 (1976).

54. A.R. Pebler and R.G. Charles, U.S. Pat. 4485094, Nov. 27, 1984.

55. R.G. Dosch in Better Ceramics Through Chemistry I, edited by C.J. Brinker (MRS Symp. Proc. 32, 1984) p. 157.

56. N.D.S. Mohallem and M.A. Aegerter in Better Ceramics Through Chemistry, III, edited by C.J. Brinker, C. Clark and D. Ulrich (MRS Symp. Proc. 121, 1988) p. 515.

57. K. Sakashita, Jpn. Kokai Tokkyo Koho JP 63/2850, 7 January, 1988.

58. T. Yoko, K. Kamiya and S. Sakka, Res. Rep. Fac. Eng. Mie Univ. 49 (1987).

59. S. Wu, IEEE Trans. Electron Devices ED21, 499 (1974).

60. A. Kulkarni, G. Rohrer, S. Narayan and L. McMillan, Thin Solid Films 164, 339 (1988).

61. N. Yamauchi, Jpn. J. Appl. Phys. 25(4), 590 (1986).

62. T.E. Luke, IEEE Trans. Electron Devices ED16, 576 (1969).

63. A. Mansingh, K. Sreenivas and T. Sudersena Rao, Proc 6th Intl. Meeting on Ferroelectrics, PA, 1986.

64. J.F. Scott, L. Kammerdiner, M. Parris, S. Traynor, V. Ottenbacher, A. Shawabkeh and W.F. Oliver, J. App. Phys. 64(2), 787 (1988).

65. J.F. Scott and C.A. Paz de Araujo, Science 246, 1400 (1989).

66. D.B. Fraser and J.R. Maldonado, J. Appl. Phys. 41(5), 2172 (1970).

67. T.L. Rose, E.M. Kelliner, A.N. Scoville and S.E. Stone, J. Appl. Phys. 55(10), 3706 (1984).

68. I.M. Pratt, Proc. IEEE 59, 1440 (1971).

CRYSTALLIZATION KINETICS OF METALLO-ORGANICS DERIVED PZT THIN FILM

K.C. Chen* and J. D. Mackenzie
University of California, Los Angeles, Dept. of Materials Science and Engineering, Los Angeles, CA 90024

ABSTRACT

PZT films on fused silica substrates were prepared by a multiple dipping-firing process from a stable solution of titanium isopropoxide, zirconium n-propoxide and lead 2-ethylhexanoate. The crystallization kinetics of the amorphous PZT films was studied by quantitative X-ray analysis. The crystallization of the amorphous film to perovskite phase involved a transitional pyrochlore structure phase. The entire crystallization was described by a consecutive phase transformation process in which nucleation dominated.

INTRODUCTION

Crystallization of amorphous phases has been an interesting subject of both scientific and practical importance. During the past decade, there have been notable advances in understanding the nucleation and growth of crystals from glass-forming systems. Knowledge of crystallization has led to the ability to control the microstructure and the properties of glass-ceramics. Recently, the crystallization of amorphous systems which do not contain any glass formers have been studied. These systems include metallic glasses, splat-quenched materials, sol-gel and metallo-organics derived amorphous phases [1-7]. In the sol-gel and metallo-organic processing, low temperature processed materials were obtained and then converted to ceramics by calcination at high temperatures. During crystallization of sol-gel derived ceramics, metastable or transitional phases are often observed prior to the formation of the final stable phases [2,4]. Therefore, the crystallization process is usually not a single step transformation process. In this paper, the crystallization kinetics of lead zirconate titanate film which involved a transitional phase will be described.

EXPERIMENTAL PROCEDURE

Zirconium n-propoxide liquid+ was first introduced into an oven-dried 250 ml flask. A pre-determined amount of titanium isopropoxide+ was added so that the final Zr/Ti ratio was 52/48. The solution was stirred for 2 to 4 hours before the required amount of lead 2-ethylhexanoate+ was added. The resulting solution, having a final composition of $Pb(Zr_{0.52}Ti_{0.48})O_3$, was then stirred for 18 hours. The homogeneous solution was stored in a glass flask for later film preparation. After pyrolysis, the solution contained 28 weight percent of oxide. Isopropanol was used to dilute the solution into individual solutions with oxide contents of 7, 14, 17.5 weight percent.

Fused silica substrates (1"x1" and 2"x2") were dipped into the solution and withdrawn at a constant speed of .75 cm/min. The dipped films were dried at 100°C for 20 minutes and then fired at 400°C for 20 minutes after each dip. This dipping-firing cycle was repeated until film thickness was 2 μm. All substrates were processed under the same conditions to ensure the same thickness.

X-ray diffraction was performed with a Norelco X-ray diffractometer. The intensities of the (111) peak of the perovskite phase and the (400) peak of the pyrochlore phase were measured using a scanning rate of 0.2°/min. The integral intensities were determined by measuring the areas under the diffraction peaks with a planiometer. Using these peaks, the crystal sizes were calculated from the Scherrer formula using the corrected half width. Commercial tungsten and lead titanate powder (>1 μm grain size) were used as standards to correct the inherent instrumental peak broadening. Thin films calcined at 550°C for 80 hours were used to determine the intensity for complete crystallization.

* Current address: General Atomics, PO Box 85608, San Diego, CA 92138-5608
+Alfa Products

Mat. Res. Soc. Symp. Proc. Vol. 180. ©1990 Materials Research Society

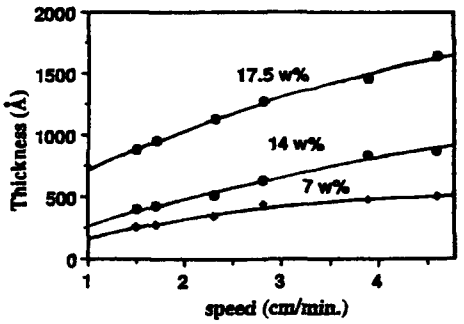


Figure 1. Thickness of the single-dipped films as a function of the solution concentration and up-drawing speed.

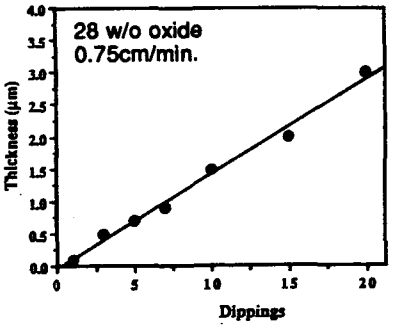


Figure 2. Thickness of the film versus the number of dipping cycles.

RESULTS AND DISCUSSIONS

Film preparation

For single-dipped films, the thickness increased with the up-drawing speed and the concentration of the solution (Fig. 1). The thickness (t) versus up-drawing speed (v) followed a $t = v^n$ relationship with n values that ranged from 0.54 to 0.74. The average value was 0.64, which was within the range of values of 0.5 to 0.667 described by Schröeder [7]. A multiple dipping and firing process was used to increase the film thickness. The thickness increased linearly with an increasing number of dips (Fig. 2). A thickness of approximately 2 μm was obtained after dipping 15 times into 28 w/o oxide solution using a drawing rate of 0.75 cm/min.. Film thicknesses larger than 2 μm usually led to cracking. Therefore, 2 μm crack-free films were used in this crystallization study.

Crystallization study

1) Phase study

The PZT films calcined at 400°C were found to be amorphous using selective area electron diffraction technique. TEM verified there was no phase separation. X-ray diffraction showed a pyrochlore structure phase crystallized from the amorphous film and coexisted with the perovskite structure phase between 400°-600°C (Fig. 3). The lattice parameters of the pyrochlore (formula $A_2B_2O_6$) are shown in Table 1. The time required for complete transformation of the pyrochlore phase to perovskite was strongly temperature dependent. Study of the time-temperature-transformation (T-T-T) relation indicated these two phases coexisted between 400°-600°C (Fig. 4). The time in which the two phases co-existed decreased as the temperature increased. It took more than 32 hours for complete transformation at 400°C but the transformation took less than 30 minutes at 600°C. The nose of this T-T-T curve was estimated to be less than 1 minute at 600°-650°C.

2) Crystal size analyses

X-ray diffraction peaks of the pyrochlore were very broad at all temperatures and times. The diffraction peaks of the perovskite also had broadening but were not as distinct as those of the pyrochlore. The size of the pyrochlore crystal, determined by the broadening, remained fairly

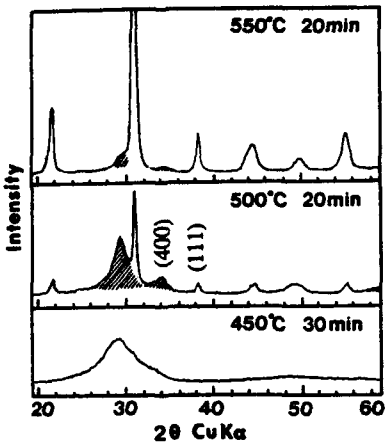


Figure 3 X-ray diffractions of PZT films showing the transitional pyrochlore structure phase (shadowed).

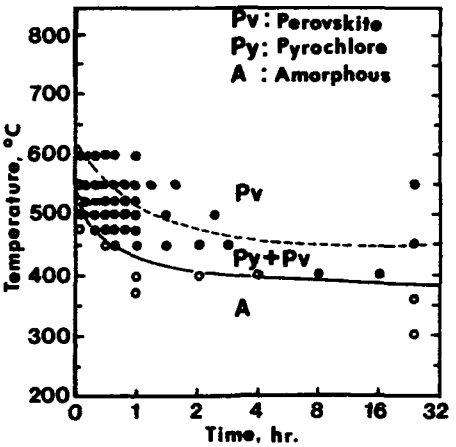


Figure 4. Time-Temperature-Transformation plot of PZT films on SiO_2.

constant at 40-60 Å between 400°-600°C. The perovskite also had a fairly constant size, approximately 200-300 Å at 450°-550°C (Table 2). Transmission electron micrographs confirmed these calculated results. The constant crystal sizes indicated that nucleation rather than grain growth was the major process in both the crystallization of the pyrochlore from the amorphous phase and the transformation of the pyrochlore to the perovskite.

Crystallization kinetics study

Quantitative X-ray analysis was used to follow the crystallization kinetics. Figure 5 shows the *absolute* volume fraction of the transformed perovskite as determined by the integral intensity of (111) diffraction peaks. The amount increased with increasing temperature. The crystallization of the perovskite was very slow at 450-550°C. After 90 minutes at 500°C, the PZT film contained only 60 volume percent of the perovskite phase. The films completely transformed into perovskite at 600°C after 2 hours. There was a characteristic S-shape curve at the beginning of the 500°C and 525°C isothermal transformation curves. These characteristic curves were also observed by Yoshikawa and Tsuzuki [1].

The *absolute* volume fraction of pyrochlore in the films could not be determined because 100% pyrochlore was never obtained. The *relative* amounts were determined by measuring the integrated intensities of (400) peaks at 34° (2θ). The amount present was strongly dependent on temperature (Fig. 6). The time-temperature dependence generally followed a bell-shape curve between 450-600°C. The time to reach the highest intensity decreased as temperature was increased. The largest amount of the pyrochlore was observed at 550°C.

The crystallization from the amorphous phase to the final perovskite phase had to be described by two kinetic processes. The T-T-T diagram showed that the formation of the pyrochlore required an induction time and existed prior to perovskite formation. The two phases coexisted between 450-500°C. Constant crystal sizes of the pyrochlore and the perovskite indicated nucleation dominated the entire crystallization process. The nucleation dominated phase transformation and the variation of the amount of each phase as a function of temperature and time suggested that the process was a consecutive reaction. The transformation kinetics were described as:

$$A \xrightarrow{K_1} Py \xrightarrow{K_2} Pv \qquad (1)$$

Table 1. Lattice parameter of the pyrochlore structure phase crystallized from amorphous PZT film

2θ	(hkl)	d_{hkl}	$h^2+k^2+l^2$	a
29.40	222	3.0379	12	10.524
34.05	400	2.6329	16	10.532
49.02	440	1.8567	32	10.503
58.25	622	1.5826	40	10.498

a_o = 10.476 Å

(a vs. $(1/2)[(\cos^2\theta/\sin\theta)+(\cos^2\theta/\theta)]$)

Table 2. Crystal sizes of the perovskite phase determined by X-ray diffraction broadening of (111) peak.

Temp. (°C)	Crystal Size (Å) Time (min.)		
	20	40	60
450	-	-	328
500	250	255	270
550	227	267	267

in which A, P_y and P_v represent amorphous, pyrochlore and perovskite phases, respectively. Both K1 and K2 are first order reactions. The first order reactions implied that the reactions were homogeneous, *viz.* the probability of the crystallization of the pyrochlore phase from the amorphous phase was the same throughout the amorphous phase and grain growth rate was small. According to the first order reaction, the fraction of the amorphous phase, X_A, after time t was:

$$X_A = \exp(-K_1 t) \quad (2)$$

$$\ln(1-X_A) = -K_1 t \quad (3)$$

Since the phase transformation of pyrochlore to perovskite also occurred homogeneously, the following reaction applies: [9]

$$dX_{Py}/dt = K_2 X_{Pv} \quad (4)$$

where X_{Py} is the volume fraction of the pyrochlore. The rate of the pyrochlore accumulation, dX_{Py}/dt, in the film was equal to the difference between the rate of formation from amorphous phase, $-dX_A/dt$, and the rate of transformation into perovskite, dX_{Pv}/dt :

$$dX_{Py}/dt = -dX_A/dt - dX_{Pv}/dt \quad (5)$$

By integration, the volume fraction of the transition pyrochlore, X_{Py}, and the volume fraction of the perovskite, X_{Pv}, at time t were determined by:

$$X_{Py} = (K_1/(K_2-K_1))[\exp(-K_1 t)-\exp(-K_2 t)]$$
$$= m\,[\exp(-K_1 t)-\exp(-K_2 t)] \quad (6)$$

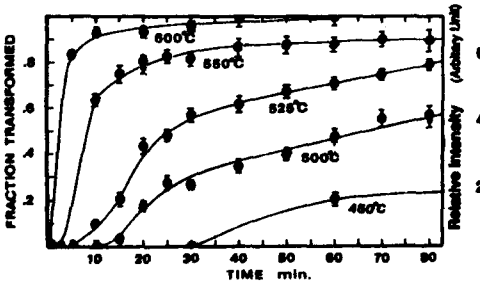


Figure 5. Isothermal transformation curves of perovskite phase using (111) peaks

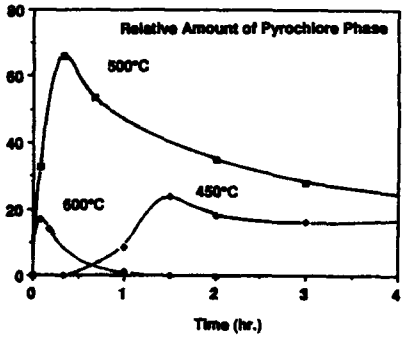


Figure 6. Relative intensities of pyrochlore determined by (400) peaks

Table 3. K_2 values (in sec^{-1}) calculated for different K_1/K_2 (=R) ratios.

Temp. (°C)	t_{max} (min.)	K_2 (sec^{-1}) R=1.50	R=2.00	R=5.00	R=10.00	R=50.00
450	90	1.50×10^{-4}	1.30×10^{-4}	7.40×10^{-5}	4.70×10^{-5}	1.50×10^{-5}
500	20	6.80×10^{-4}	5.80×10^{-4}	3.30×10^{-4}	2.10×10^{-4}	6.70×10^{-5}
600	5	2.70×10^{-3}	2.30×10^{-3}	1.30×10^{-3}	8.50×10^{-4}	2.70×10^{-4}

Table 4. Best fit of K_1 and K_2 values with diffraction results.

Temp. (°C)	K_1/K_2	K_1 (sec^{-1})	K_2 (sec^{-1})
450	1.25	2.07×10^{-4}	1.65×10^{-4}
500	10.00	2.10×10^{-3}	2.10×10^{-4}
600	1.0001	3.3335×10^{-3}	3.3332×10^{-3}

$$\text{and} \quad X_{Pv} = 1 - X_A - X_{Py} = (1+m)[1-\exp(-K_1 t)] - m\,[1-\exp(-K_2 t)] \qquad (7)$$

where m equaled to $(K_1/(K_2-K_1))$. The amounts of pyrochlore and perovskite present were complex functions of time.

An analytical numeric approach was used to determine the volume fraction of the amorphous PZT and the absolute amount of the pyrochlore at any time since X-ray diffraction could not be used. The time to reach the maximum amount of the pyrochlore, t_{max}, at any temperature was deduced by differentiating equation (6):

$$t_{max} = \frac{\ln(K_1/K_2)}{K_1-K_2} \qquad (8)$$

The observed t_{max} values, 90 minutes, 20 minutes and 5 minutes (450°, 500° and 600°C respectively) were substituted into equation (8) and K_1 and K_2 values were calculated by assuming different K_1/K_2 ratios (=R) (Table 3). The calculated K_1 and K_2 values were substituted back into equations (6) and (7) to obtain the $X_{Py}(t)$ and $X_{Pv}(t)$ transformation curves for these temperatures. The calculated curves for a series of K_1 and K_2 values are shown in Figure 7 (a)-(f). The characteristic bell-shaped transformation curve of the pyrochlore phase was clearly seen at 600°C. The transition pyrochlore phase could be observed even if the value of K_1/K_2 was equal to 1.00001. These calculated $X_{Pv}(t)$ curves were compared with the observed $X_{Pv}(t)$ values from X-ray diffraction. Other values were calculated for $X_{Py}(t)/X_{Py}(t_{max})$ for $t \geq t_{max}$ and compared with the observed ratios. The K_1 and K_2 values that best agreed with the results from X-ray diffraction are shown in Table 4. The accuracy of this approach was limited by the determination of t_{max} and the intensity fluctuation of the XRD curves.

By assuming the Arrhenius relation of K_1 and K_2 as a function of temperature, the activation energies were calculated to be 22 KJ/mole and 26 KJ/mole for K_1 and K_2, respectively.

CONCLUSION

PZT films on fused silica substrates were prepared by a multiple dipping-firing process using a stable metallo-organic solution. The crystallization of the amorphous film to perovskite phase involved a transitional pyrochlore structure phase. The entire crystallization was described by a consecutive phase transformation process in which nucleation dominated.

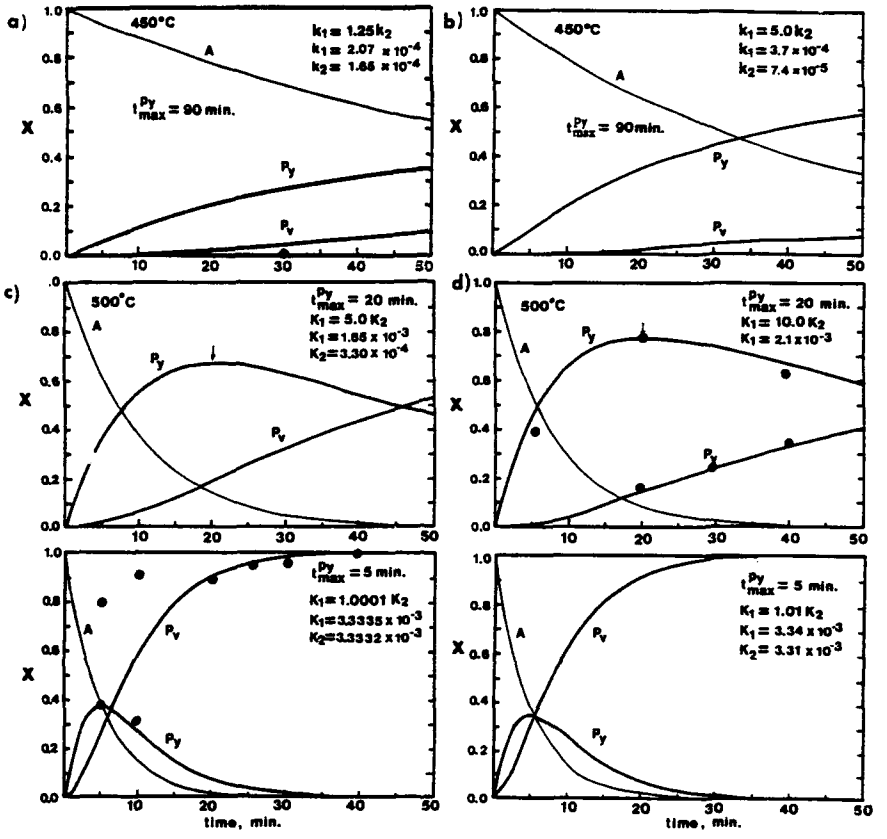


Figure 7. The calculated transformation curves of the amorphous phase A, pyrochlore phase P_y and perovskite phase P_v based on the shown t_{max} and K_1/K_2 values for (a)-(b) 450°C; (c)-(d) 500°C; and (e)-(f) 600°C. (• are observed values)

ACKNOWLEDGEMENTS Research was supported by Air Force Office of Scientific Research, Directorate of Chemical and Atmospheric Science.

REFERENCES

1. Y. Yoshikawa and K. Tsuzuki, J. Amer. Ceram. Soc. 73, 31 (1990).
2. O. Yamaguchi et al, J. Amer. Ceram. Soc. 72, 1065 (1989); J. Amer. Ceram. Soc. 69, C-256 (1986); J. Amer. Ceram. Soc. 69, C-20 (1986); J. Amer. Ceram. Soc. 67, C-150 (1986); J. Amer. Ceram. Soc. 68, C-173 (1985).
3. A. S. Shaikh and G. M. Vest, J. Amer. Ceram. Soc. 69, 682 (1986).
4 S. R. Grucovich and J. B. Blum, Ferroelectric 62, 189 (1985).
5. J. Fukushima, K. Kodaira and T. Matsushita, J. Mater. Sci. 19, 595 (1984).
6. R. A. Lipelles and D. J. Coleman in Ultrastructure Processing of Advanced Ceramics, Eds. by J. D. Mackenzie and D. R. Ulrich, John Wiley and Sons, N. Y. (1988) 919.
7. H. Schroeder, in Physics of Thin Films Vol. 5, G. Hass and R. E. Hass Eds. Academic Press, N. Y. (1969) pp. 87-141.
8. A.C.D. Chaklader and A. L. Roberts, J. Amer. Ceram. Soc. 44, 35 (1961).

EVOLUTION OF MOLECULAR STRUCTURE IN ALKOXIDE-DERIVED LITHIUM NIOBATE

DENNIS J. EICHORST AND D. A. PAYNE
Department of Materials Science and Engineering, and the Beckman Institute for Advanced Science and Technology, University of Illinois at Urbana-Champaign, Urbana, IL.

ABSTRACT

Structural rearrangements during the sol-gel processing of lithium niobate were investigated by FTIR and Raman spectroscopic methods. The reaction of lithium ethoxide with niobium ethoxide resulted in the formation of a bimetallic alkoxide, $LiNb(OEt)_6$, which could be crystallized from solution. Single crystals were comprised of helical polymeric units consisting of niobium octahedra linked by lithium in tetrahedral (distorted) coordination. Successive crystallizations from solution allowed for the enhanced purification of the alkoxide precursor. Hydrolysis of the bimetallic alkoxide resulted in the formation of an amorphous network structure, which contained niobium-oxygen octahedral units modified by lithium. Heat-treatment facilitated structural rearrangements for the niobium environment, which allowed for the formation of the lithium niobate crystal structure. Further heat-treatment above 700 °C resulted in structural changes associated with lithium oxide volatility.

INTRODUCTION

Sol-gel processing of lithium niobate has recently received attention for the preparation of stoichiometric material at reduced temperatures.[1-4] Typically, an ethanol-based alkoxide system, in which a bimetallic complex, $LiNb(OEt)_6$, is formed, is used for the preparation of lithium niobate. Hydrolysis and condensation of the alkoxide results in formation of oligomeric structures in solution, and the formation of a "gel" on extended oligomerization. Condensed structures obtained in the early stages of processing have an influence on the subsequent crystallization behavior on heat-treatment. Therefore, so as to obtain a better understanding of the sol-gel process, the evolution of structure was investigated from the precursor alkoxide stage, through gelation, and crystallization. In this paper we report on the formation and crystal structure of the bimetallic alkoxide, $LiNb(OEt)_6$, which can be considered as a "molecular building block" for the fabrication of lithium niobate ceramics.

Previous studies of amorphous niobates, which were prepared by sputtering or roller quenching methods, indicated an amorphous niobium oxide network which was relatively unaffected by alkali ions.[5,6] The presence of polycondensed niobate species, consisting primarily of edge-shared niobium octahedra, were also reported for solution processing methods. Bradley reported on the formation of $Nb_8O_{10}(OEt)_{20}$ during controlled hydrolysis of niobium ethoxide solutions.[7] The hexaniobate ion, $Nb_6O_{19}^{8-}$, was also proposed for alkaline niobate solutions.[8,9] Dissociation of the complex alkoxide, $LiNb(OEt)_6$, upon hydrolysis, could possibly occur to give either (i) polycondensed niobate species or (ii) a niobium oxide network with a random distribution of lithium ions. This could result in a reduction of the stoichiometry and homogeneity control, potentially offered by the complex alkoxide precursor. So as to evaluate this possibility, amorphous lithium niobate was compared with amorphous niobium oxide in the present study. Furthermore, structural rearrangements on heat-treatment were characterized by spectroscopic methods, to determine a possible crystallization route.

Mat. Res. Soc. Symp. Proc. Vol. 180 ©1990 Materials Research Society

EXPERIMENTAL PROCEDURE

All reactions, prior to hydrolysis, were carried out in dry nitrogen. Ethanol (anhydrous grade) was dried over magnesium metal. Lithium ethoxide was prepared by addition of lithium metal to dry ethanol. Niobium ethoxide was prepared by the reaction of niobium chloride and ethanol in benzene, and subsequently purified according to a method of Bradley.[10] The clear solution obtained was characterized by ^{13}C NMR spectroscopy.

Precursor "$LiNbO_3$" alkoxide solutions were prepared by refluxing a mixture of lithium and niobium ethoxides in excess ethanol, for 24 hrs, as previously reported.[11] Concentration, by distillation, gave a 0.8 M stock solution. Lithium niobate gels were obtained by the addition of 2.5 eq of water (diluted in ethanol) to give a 0.5 M solution which formed a "gel" upon ageing. Niobium oxide gels were prepared by hydrolysis of 0.5 M niobium ethoxide solutions. The gels were dried at 140 °C for 24 hrs and subsequently heat-treated in air (1hr) at temperatures ranging between 300 and 800 °C, forming either amorphous or crystalline lithium niobate (or niobium oxide) powders. The amorphous structure, and the amorphous-crystalline transformation, were characterized by FTIR and Raman spectroscopy.

Crystallites were obtained by further concentration of the stock solutions prior to hydrolysis. Crystallites obtained by this method were unsuitable for x-ray structure analysis. Therefore, the crystallites were redissolved in refluxing ethanol, and concentrated to give a supersaturated solution. Slow cooling of the solution resulted in the growth of single crystals, 2-5mm in dimensions, which were suitable for x-ray structure determinations.[12] Crystals were purified by successive crystallization from ethanol, and subsequently dissolved (in ethanol) to give a pure solution.

RESULTS AND DISCUSSION

The dimeric nature of niobium ethoxide, with edge-shared niobium octahedra, was confirmed by ^{13}C NMR spectroscopy (Fig. 1). The spectrum contained a pair of quartets (~20 ppm) corresponding to the methyl carbons of bridging and terminal ethoxy ligands. A pair of triplets at ~68.5 ppm corresponded to the methylene carbons of the ethoxy groups. Integration of the peak areas gave a 1:4 ratio, consistent with the bridging and terminal alkoxy ligands present in the dimeric structure.[11] Studies of a structurally similar niobium methoxide have shown rapid exchange of bridging and terminal alkoxy groups by an intermolecular exchange process.[13] The reaction of lithium ethoxide with niobium ethoxide was shown to occur rapidly on the NMR time scale.[11] A reaction may occur during the terminal–bridging ligand exchange, giving the bimetallic alkoxide $LiNb(OEt)_6$.

The single crystal x-ray structure for the alkoxide complex (Fig. 2) consisted of infinite helical polymers comprised of niobium-oxygen octahedra linked by lithium in a tetrahedral (distorted) environment.[12] Each niobium coordination sphere contained a cis-pair of terminal ethoxy ligands. Hydrolysis could preferentially occur for terminal ethoxy groups present for similar units in solution, resulting in the formation of a gel network. The gel network could contain (i) niobium-oxygen octahedra linked by lithium (from the precursor structure), and (ii) either corner-shared, or edge-shared niobium-oxygen octahedra, which resulted from condensation reactions between additional helical units.

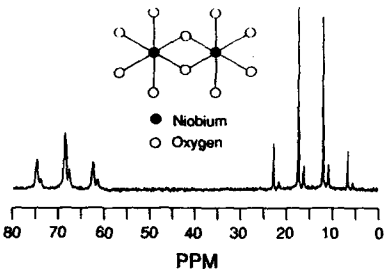


Fig. 1. ^{13}C spectrum for niobium ethoxide, indicating the dimeric structure for the alkoxide.

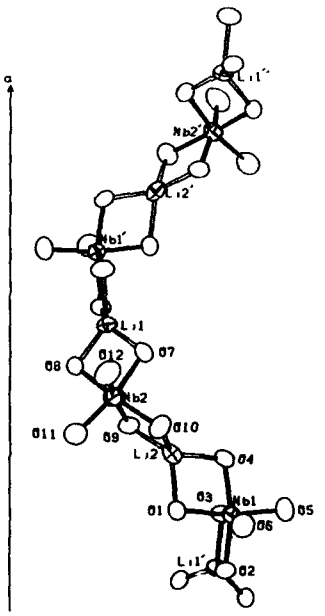


Fig. 2. Single crystal structure for the bimetallic alkoxide, $LiNb(OEt)_6$.

Chemical microanalysis of lithium niobate prepared by the process had a Li/Nb stoichiometry of 1:1. The crystal structure obtained indicates a 1:1 Li:Nb ratio; stoichiometrically correct for lithium niobate, suggesting an additional method for stoichiometry control. Material prepared from a niobium excess (nominal 15%) solution had a Nb:Li ratio of 1.18:1. Successive crystallization and filtration of the alkoxide crystals resulted in material with a 1.01:1 Nb:Li ratio, indicating the successive crystallization method is a viable technique for purification and stoichiometry control in the alkoxide processing of lithium niobate.

Infrared spectra of amorphous lithium niobate and niobium oxide (heat-treated at 300 °C) are given in Figure 3. Infrared bands at ~970 and from 1400 – 1700 cm^{-1} are within the frequency ranges observed for niobium-oxygen octahedra in niobate materials. Differences observed in the spectra indicate modifications to the amorphous niobium oxide network by lithium, contrary to results obtained by physical deposition techniques.[5,6] The results suggest the structural features (i.e., niobium-oxygen octahedra linked by lithium) of the mixed-metal alkoxide are maintained during gelation. A probable gelation mecha..ism, therefore, is hydrolysis (and condensation) of terminal alkoxy ligands of the helical polymers, which result in a gel network of niobium-oxygen octahedra linked by lithium.

Crystallization was observed to occur at 450 °C by the appearance of Raman bands as indicated in Figure 4. The results are consistent with previous thermal analysis, and x-ray diffraction studies, of sol-gel derived lithium niobate.[1] The Raman bands below 700 cm^{-1} were consistent with single-crystal values reported by Barker and Loudon.[14] However, the band at 850 cm^{-1} was displaced from the expected value (870 cm^{-1}) suggesting considerable distortion for the material heat-treated at 450 °C.

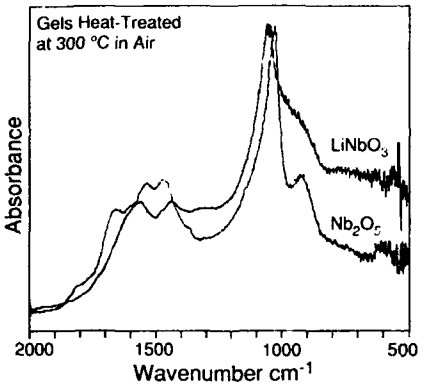


Fig. 3. Infrared spectra for amorphous niobium oxide and lithium niobate.

Heat-treatment to 600 °C resulted in a band shift to the expected value of 870 cm^{-1} (Fig. 5). Further heat-treatment resulted in additional structural changes as observed by a decrease in the relative intensity of the 870 cm^{-1} band. The band was attributed to the ν_1 stretching mode of the niobium-oxygen octahedra, and has been shown to be sensitive to local order.[15] Heat-treatment at 800 °C resulted in the formation of a doublet (~250, 260 cm^{-1}) which was previously reported for the congruent (but non-stoichiometric) composition (48.6% Li_2O) for lithium niobate.[16] This doublet might indicate lithium oxide volatility for heat-treatment at high temperatures.

Figure 6 illustrates diffuse reflectance infrared spectra for heat-treated lithium niobate powders. Heat-treatment between 400 and 500 °C resulted in the formation of a new band at 1740 cm^{-1}, which was characteristic of crystalline lithium niobate. Further heat-treatment also resulted in structural changes observed in the IR spectra. The band at 1635 cm^{-1} decreased in intensity similar to the 870 cm^{-1} Raman band. Spectra obtained at 800 °C were similar to a congruent single crystal sample, again indicating volatility of lithium oxide in the temperature range 700-800 °C.

CONCLUSIONS

Lithium and niobium ethoxides reacted to form a bimetallic alkoxide, $LiNb(OEt)_6$. The double alkoxide consisted of niobium-oxygen octahedra, which were linked by lithium in a distorted tetrahedral environment. The niobium coordination sphere contained a cis-pair of terminal alkoxy ligands. Gel formation was proposed to occur through hydrolysis and subsequent condensation of terminal ethoxy ligands. The resulting amorphous structures were found to consist of niobium-oxygen octahedral networks, modified by the presence of lithium. Heat-treatment of the amorphous material resulted in crystallization at ~450 °C. This was indicated by the appearance of a new IR band and several Raman bands. Structural changes were

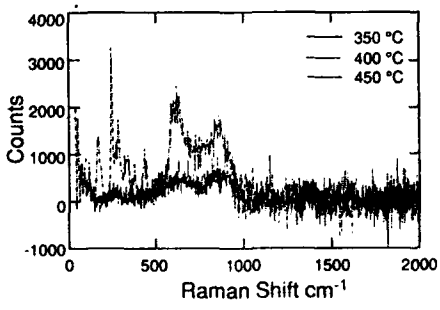


Fig. 4. Raman spectra for heat-treated gels.

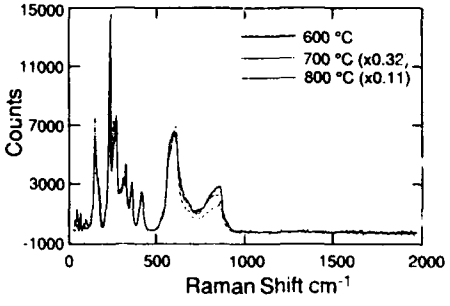


Fig. 5. Raman spectra for crystalline lithium niobate.

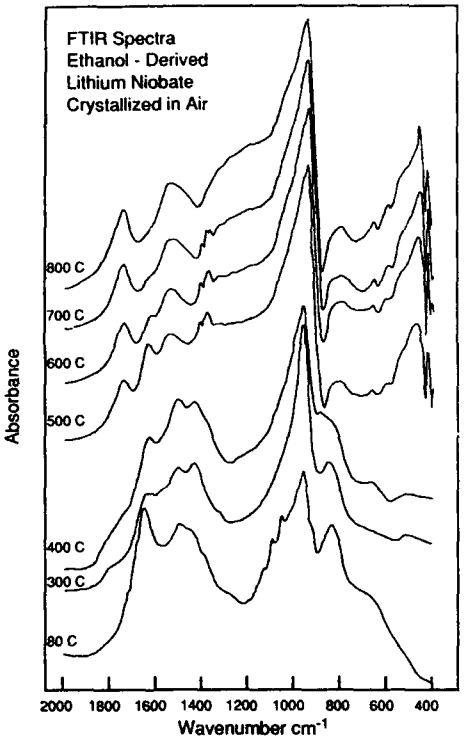


Fig. 6. Infrared spectra for heat-treated lithium niobate.

observed to occur at elevated temperatures (>700 °C) and were attributed to lithium oxide volatility. The results indicate the influence of the precursor alkoxide structure on the formation of an amorphous oxide network and subsequent crystallization behavior. Furthermore, the sensitivity of spectroscopic techniques to the study of amorphous-crystalline transformations, and subtle structural changes on volatilization, was demonstrated.

ACKNOWLEDGEMENTS

We acknowledge the support of an IBM Fellowship on Materials and Processing Sciences, and the U.S. Department of Energy under contract DE-ACO2-76ER01198. The authors also thank Dr. K. E. Howard and Dr. S. R. Wilson for single crystal studies. The use of facilities in the School of Chemical Sciences at the University of Illinois is acknowledged. Collaboration with Dr. B. A. Tuttle and Dr. D. Tallant on Raman spectroscopy at Sandia National Laboratories is also acknowledged.

REFERENCES

1. D.J. Eichorst and D.A. Payne in Better Ceramics Through Chemistry III, edited by C.J. Brinker, D.E. Clark and D.R. Ulrich (Mater. Res. Soc. Proc. 121, Pittsburgh, PA 1988) pp. 773-778.
2. M.I. Yanovskaya, et al., J. Mat. Sci. 23, 395 (1988).
3. S.I. Hirano and K. Kato, Adv. Ceram. Mat. 3, 503 (1988).
4. D.F. Partlow and J. Greggi, J. Mater. Res. 2, 595 (1987).
5. K. Nassau, C.A. Wang and M. Grasso, J. Am. Cer. Soc. 62, 503 (1979).
6. M. Kitabatake, T. Mitsuyu and K. Wasa, J. Appl. Phys. 56, 1780 (1984).
7. D.C. Bradley, M.B. Hursthouse, and P.F. Rodesiler, Chem. Comm. 1968, 1112.
8. I. Lindqvist, Arkiv För Kemi, 5, 247 (1952).
9. B.A. Tuttle (private communication).
10. D.C. Bradley, B.N. Chakravarti, and W. Wardlaw,. J. Chem. Soc., 1956, 2381.

11. D.J. Eichorst, K.E. Howard and D.A. Payne in Ultrastructure Processing of Ceramics, Glasses and Composites, edited by D.R. Uhlmann, M.C. Weinberg, S. H. Risbud and D.R. Ulrich (John Wiley & Sons, New York, NY in press, 1990).
12. D.J. Eichorst, K.E. Howard, D.A. Payne and S.R. Wilson, Inorg. Chem. 29, 1458 (1990).
13. J.G. Reiss and L.G. Hubert-Pfalzgraf, Chimia 30, 481 (1976).
14. A.S. Barker, Jr., and R. Loudon, Physical Review 158, 433 (1967).
15. A.A. McConnel, J.S. Anderson and C.N.R. Rao, Spectrochimica Acta 32A, 1067 (1976).
16. Y. Okamoto, P. Wang and J.F. Scott, Physical Review B 32, 6787 (1985).

PREPARATION OF SINGLE-PHASE $KNbO_3$ USING BIMETALLIC ALKOXIDES

MOSTAFA M. AMINI AND MICHAEL D. SACKS
Ceramics Division, Department of Materials Science and Engineering, University of Florida, Gainesville, FL 32611

ABSTRACT

Single-phase $KNbO_3$ was prepared using bimetallic alkoxides. Potassium-niobium ethoxide, $KNb(OC_2H_5)_6$, and potassium-niobium propoxide, $KNb(OC_3H_7)_6$, were synthesized and subsequently hydrolyzed using several water concentrations. Potassium-deficient particles were rapidly precipitated when higher water concentrations were used and this resulted in the formation of a multiphase material after calcination. In contrast, single-phase $KNbO_3$ powders could be prepared by two methods: (1) hydrolysis of $KNb(OC_3H_7)_6$/propanol solutions using 1 mole water (per mole of propoxide) added as a water/propanol solution and (2) hydrolysis of $KNb(OC_2H_5)_6$/ethanol solutions using 1 mole of water (per mole of ethoxide) added as a water/methanol solution. The latter method was also used to form thin films of $KNbO_3$.

INTRODUCTION

Due to its high electro-optic and nonlinear optical coefficients and good photorefractive properties, potassium niobate ($KNbO_3$) is of great interest for a variety of applications, including optical waveguides, frequency doublers, holographic storage systems, etc. [1-3] The conventional process for preparing potassium niobate involves mixing potassium carbonate and niobium oxide powders and subsequently reacting the mixture at high temperatures. [4-6] However, due to the relatively coarse scale of mixing of the reactants, it is difficult to obtain a chemically homogeneous, single-phase product. In addition, the high temperatures required for the chemical reaction also result in difficulties in maintaining the desired stoichiometry due to preferential volatilization of K_2O. Furthermore, the conventional process is not applicable for the formation of thin films. In recent years, processing of ferroelectric thin films by sol-gel methods has been actively investigated. [7-12] The capability of achieving homogenous mixing of components on an extremely fine scale (e.g., molecular- or nanometer-level) offers the possibility of carrying out reactions at temperatures low enough to be compatible with semiconductor device technology. Only a few investigations of sol-gel processing of potassium niobate have been reported. Wu et al. [13] used potassium and niobium ethoxide precursors to synthesize potassium niobate, but were unable to form single-phase $KNbO_3$ as precipitates were reported to be deficient in potassium. Swartz et al. [14] used potassium and niobium methoxyethoxides to prepare potassium niobate. Bulk samples were reportedly single phase, but thin films had unidentified second phase(s) according to XRD results. Tuttle and co-workers [15] used potassium hydroxide and niobium ethoxide to prepare single-phase $KNbO_3$ powders and thin films. They also observed differences in phase development during heat treatment for bulk gels vs. thin films. A potassium deficient phase, $K_4Nb_6O_{17}$, and a "low temperature," non-perovskite $KNbO_3$ phase were observed in some thin film samples.

The present investigation was undertaken to identify processing conditions for low-temperature synthesis of single-phase $KNbO_3$ powders and thin films using bimetallic alkoxides as the precursor materials. In this paper, we report on the synthesis and characterization of the alkoxides and the resulting oxides produced after the processing steps of hydrolysis/condensation, drying, and calcination.

EXPERIMENTAL

All reactions and manipulations were carried out under dry nitrogen using standard Schlenk techniques. [16] Niobium ethoxide, $Nb(OC_2H_5)_5$, was prepared using the procedure of Bradley et al. [17] in which of niobium chloride, $NbCl_5$, (Alfa Products, Danvers, MA; Aldrich Chemical Co., Milwaukee, WI.) is reacted with ethanol. Potassium ethoxide, KOC_2H_5, was synthesized by reacting potassium (Fisher Scientific, Pittsburgh, PA) and ethanol. The

Mat. Res. Soc. Symp. Proc. Vol. 180. ©1990 Materials Research Society

bimetallic, or "double," ethoxide was prepared by mixing the potassium and niobium ethoxides and refluxing for 24 hours. Potassium propoxide, niobium propoxide, and potassium-niobium propoxide were prepared using similar procedures except that n-propanol was used as a reactant instead of ethanol.

Alkoxides were hydrolyzed using several water concentrations (0.75 - 6.0 moles of water per mole of alkoxide). $KNb(OC_2H_5)_6$/ethanol solutions were hydrolyzed by adding either water/ethanol or water/methanol solutions, while $KNb(OC_3H_7)_6$/propanol solutions were hydrolyzed using water/propanol solutions. Reactions were allowed to continue for approximately one day after the water addition. Solvents were removed either by evaporation (to form gels) or by filtration (when particle precipitation occurred), followed by drying in air (~60-80°C) for approximately one day. "Stable" sols were used to form thin films by spin coating. After drying, powders and films were calcined in air for 5 hours at temperatures in the range 150-850°C.

Ethoxides were characterized by nuclear magnetic spectroscopy, NMR, (Varian, Sunnyvale, CA) and mass spectroscopy (Model MS-30, AEI Scientific Apparatus, Ltd., Manchester, England). Proton NMR spectra were obtained for niobium ethoxide dissolved in deuterated toluene ($C_6D_5CD_3$), potassium ethoxide dissolved in a deuterated dimethyl sulfoxide ($(CD_3)_2SOCD_3$), and niobium-potassium ethoxide dissolved in deuterated benzene (C_6D_6). Niobium 93 NMR spectra were collected for ethoxides dissolved in ethanol. Spectra were referenced to $NbCl_6^-$ in CH_3CN. Mass spectroscopy on potassium-niobium ethoxide was carried out using an accelerating voltage of 70 eV. Elemental analyses (Galbraith Laboratories, Knoxville, TN) for carbon and hydrogen were carried out on the potassium-niobium ethoxide.

Phases in calcined samples were determined using X-ray diffraction, XRD, (Model APD 3720, Philips Electronic Instruments Co., Mt. Vernon, NY). Elemental analyses (Galbraith Laboratories) for niobium and potassium were carried out on selected samples.

RESULTS AND DISCUSSION

Characterization of Ethoxides

Proton NMR data for the potassium, niobium, and potassium-niobium ethoxides are shown in Table 1. Potassium ethoxide showed a CH_2 quartet (δ = 3.45-3.53 ppm) and a CH_3 triplet (δ = 0.90-0.96 ppm). Niobium ethoxide showed two triplets (δ = 1.25-1.30 and 1.37-1.42 ppm) and two quartets (δ = 4.35-4.40 and 4.48-4.55 ppm). Two triplets and quartets are observed because of the dimeric nature of niobium ethoxide [18], i.e., there are CH_2 and CH_3 protons associated with both bridging and terminal alkoxy groups in the dimeric molecule. The bimetallic potassium-niobium ethoxide shows a triplet (δ = 1.36-1.40) and a quartet (δ = 4.44-4.51). The absence of CH_2 protons at δ = 3.45-3.53 indicates coordination of potassium ethoxide to niobium ethoxide, providing clear evidence for the formation of the "double" alkoxide.

Table 1. Proton NMR Data

Compound	Solvent	CH_2(q)*	CH_3(t)*
$K(OC_2H_5)$	$(CD_3)_2SO$	3.45-3.53	0.90-0.96
$Nb(OC_2H_5)_5$	$C_6D_5CD_3$	4.35-4.40, 4.48-4.55	1.25-1.30, 1.37-1.42
$KNb(OC_2H_5)_6$	C_6D_6	4.44-4.51	1.36-1.40

* q = quartet, t = triplet

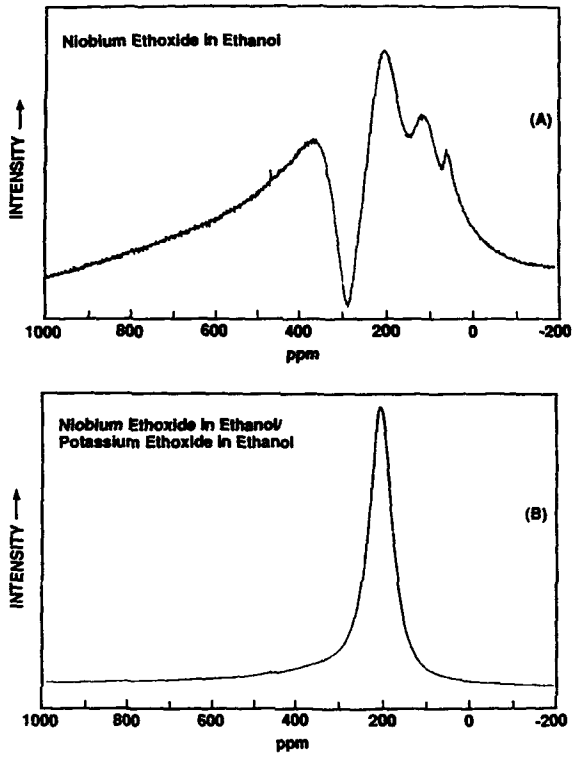


FIG. 1. (A) ^{93}Nb NMR spectrum for niobium ethoxide/ethanol solution and (B) ^{93}Nb NMR spectrum obtained ~5 min after a potassium ethoxide/ethanol solution was mixed with a niobium ethoxide/ethanol solution.

The formation of the bimetallic ethoxide was also indicated by ^{93}Nb NMR results. Fig. 1A shows the spectrum for niobium ethoxide in ethanol. Multiple peaks in the spectrum probably arise due the presence of monomers and dimers of niobium ethoxide in the ethanol solution. Fig. 1B shows the spectrum obtained ~5 minutes after a potassium ethoxide/ethanol solution was added to the niobium ethoxide/ethanol solution. The disappearance of the extra peaks in Fig. 1A is consistent with the formation of potassium-niobium hexa-ethoxide, $KNb(OC_2H_5)_6$.

Mass spectroscopy also provided evidence for the formation of the bimetallic ethoxide, as $KNb(OC_2H_5)_5^+$ fragments were observed. Chemical analysis of the potassium-niobium ethoxide showed 35.3 wt% carbon and 7.2 wt% hydrogen. These values are in good agreement with the calculated values of 35.82 wt% carbon and 7.51 wt% hydrogen for $KNb(OC_2H_5)_6$.

Effects of Processing Conditions on Phase Development and Chemical Composition

The molar ratio of water/alkoxide had a significant effect on the hydrolysis/condensation reaction kinetics and on the physical and chemical characteristics of the product. In one series of experiments, a 0.25 molar solution of potassium-niobium ethoxide in ethanol was mixed with

varying amounts of water (0.75 - 6.0 moles water/mole of ethoxide) which was added as a 2.5 molar solution in ethanol. Solutions containing more than ~2.5 moles water/mole ethoxide became opaque immediately and rapid sedimentation of precipitated particles was evident within a few minutes. The precipitated particles obtained in this manner were collected by filtration, dried at ~80°C, calcined at various temperatures, and analyzed by X-ray diffraction. XRD showed that samples prepared with 5 moles of water per mole of ethoxide were amorphous both after drying and calcination at 475°C. Calcination at 600°C resulted in weak crystallization (Fig. 2), but most of the peaks were not associated with $KNbO_3$. The major crystalline phase(s) appeared to be a mixture of "potassium-deficient" compounds, i.e., $K_2Nb_3O_8$, $K_4Nb_6O_{17}$, and $K_4Nb_6O_{17} \cdot 3H_2O$ [19], although identification of the phases was uncertain. Extensive crystallization of $KNbO_3$ occurred as the calcination temperature was increased, but it is evident from Fig. 2 that the potassium-deficient phase(s) still remained. The deficiency in potassium (i.e., relative to $KNbO_3$) is not due to preferential volatilization of K_2O during heat treatment, but instead develops during the precipitation process. This was proven by carrying out chemical analyses of powders heat treated at 150 and 750°C. In the former sample, the analysis showed 50.3 wt% Nb and 16.3 wt% K, corresponding to an Nb/K mole ratio of 1.30. Upon calcination to 750°C, the Nb and K concentrations increase (to 58.3 and 19.5 wt%, respectively), but the mole ratio (1.26) remains unchanged (within experimental error). (The increases in the weight percentages of Nb and K upon calcination to 750°C reflect

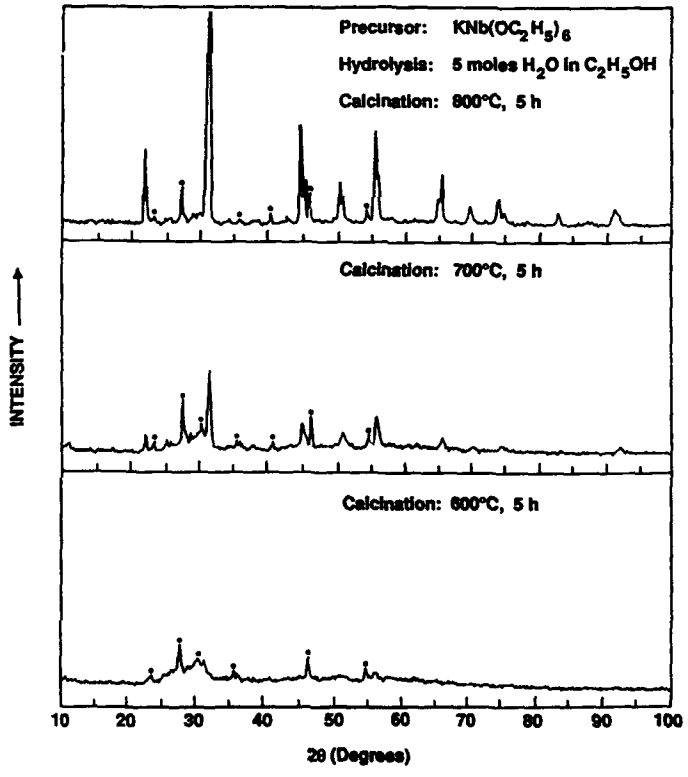


FIG. 2. XRD patterns for samples prepared with 5 moles water per mole of potassium-niobium ethoxide which were calcined at the indicated temperatures. Asterisks indicate that peaks are associated with potassium-deficient phase(s). Other peaks are for $KNbO_3$.

the elimination of residual solvent, hydroxyl groups, and carbonaceous material from the precipitates. Thermal gravimetric analysis shows that ~14% weight loss occurs upon heat treatment to 750°C [20].) The high Nb/K mole ratio of the precipitates (i.e., relative to the 1:1 mole ratio in the bimetallic alkoxide) indicates that excess potassium remains in solution during the hydrolysis/condensation process. This was confirmed by analyzing the filtrate collected from a precipitated suspension in which the alkoxide was hydrolyzed with 6 moles of water/mole of ethoxide. The residual potassium concentration in solution was 0.11 wt%, while the niobium concentration was <0.0002 wt%. Despite the successful synthesis of potassium-niobium ethoxide, it is evident that molecular-scale mixing is disrupted during subsequent processing.

Precipitation of particles occurred much more slowly as the amount of water added during hydrolysis of the potassium-niobium ethoxide was decreased. However, even with low concentrations of water, it was not possible to produce single-phase $KNbO_3$ when hydrolysis was carried out using water/ethanol solutions. For example, Fig. 3 shows XRD results for a sample prepared with only 1 mole water/mole ethoxide which was calcined at 700°C. In addition to $KNbO_3$, the potassium-deficient $K_4Nb_6O_{17}$ and $K_4Nb_6O_{17} \cdot 3H_2O$ phases [21] are also present. It is noted, however, that the $KNbO_3$ peaks are more intense (relative to the potassium-deficient phases) compared to the samples hydrolyzed with 5 moles water/mole ethoxide and calcined at the same temperature (Fig. 2). Thus, further efforts were directed developing processing conditions in which hydrolysis rates were reduced.

One approach for decreasing the hydrolysis rate involved using the potassium-niobium propoxide precursor. It has been reported that increasing the size of the alkoxy group decreases the rate of hydrolysis in some alkoxides (e.g., silicon alkoxides). [22] This is generally attributed to steric effects. In the present study, it was observed that sols prepared with the bimetallic propoxide would remain clear (i.e., no visual evidence of precipitation) for several days or longer if the concentration of water was less than ~2 moles water/mole propoxide. Evaporation of solvent from a solution prepared with 1 mole water/mole propoxide

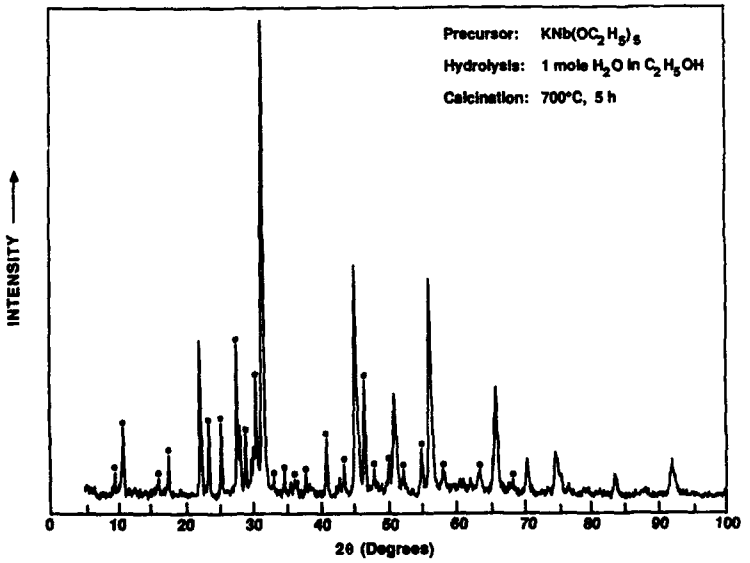


FIG. 3. XRD pattern for sample prepared with 1 mole of water per mole of potassium-niobium ethoxide and calcined at 700°C. Asterisks indicate that peaks are associated with potassium-deficient phase(s). Other peaks are for $KNbO_3$.

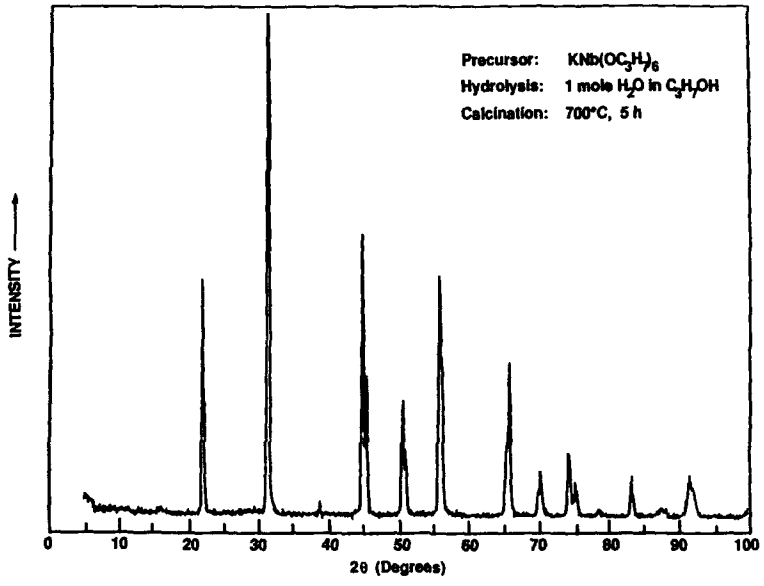


FIG. 4. XRD pattern for sample prepared with 1 mole of water per mole of potassium-niobium propoxide and calcined at 700°C. Single-phase $KNbO_3$ is formed.

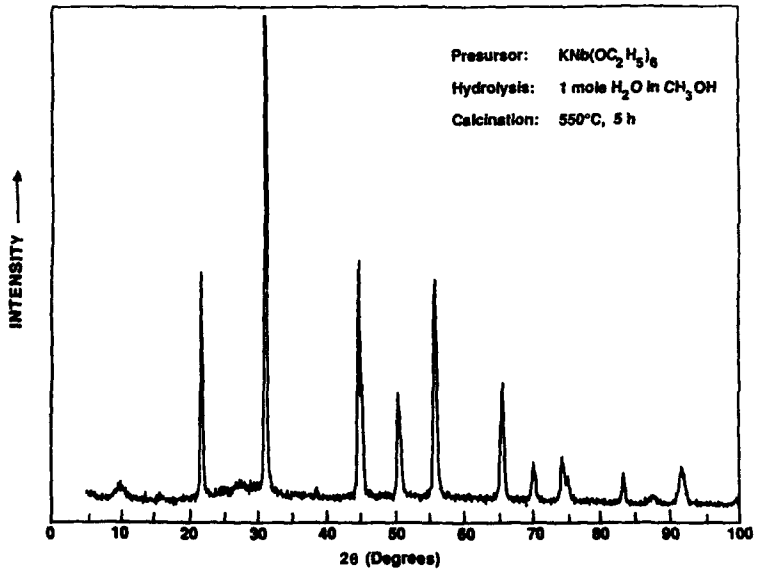


FIG. 5. XRD pattern for sample prepared with 1 mole of water per mole of potassium-niobium ethoxide and calcined at 550°C. Sample was hydrolyzed using water/methanol solutions. Single-phase $KNbO_3$ is formed.

resulted in the development of a clear gel. After drying and calcining at 700°C, single-phase $KNbO_3$ was produced, i.e., no traces of potassium-deficient phases were detected by XRD (Fig. 4). The pattern also shows obvious peak splitting at $2\theta \approx 45$, 51, and 74° which is indicative of the formation of the orthorhombic phase of $KNbO_3$. [23] (The orthorhombic polymorph is the equilibrium phase at room temperature. [24] However, the cubic phase [25] was obtained when low calcination temperatures were used. Also, higher temperatures were required to observe peak splitting when samples were prepared under rapid hydrolysis conditions. For example, in Figs. 2 and 3, negligible peak splitting is observed in samples calcined at 700°C.)

Another approach used to prepare single-phase $KNbO_3$ involved carrying out hydrolysis of the bimetallic ethoxide using water/methanol solutions, i.e., instead of water/ethanol solutions. Sols prepared with 1 mole water/mole of ethoxide would remain clear for many weeks if exposure to the atmosphere (i.e., water vapor) was avoided. As in the case of propoxide solutions hydrolyzed with 1 mole of water, evaporation of solvent resulted in the formation of a clear gel. XRD showed that samples were extensively crystallized (primarily to the cubic phase) after calcination at only 550°C (Fig. 5). More extensive peak splitting was

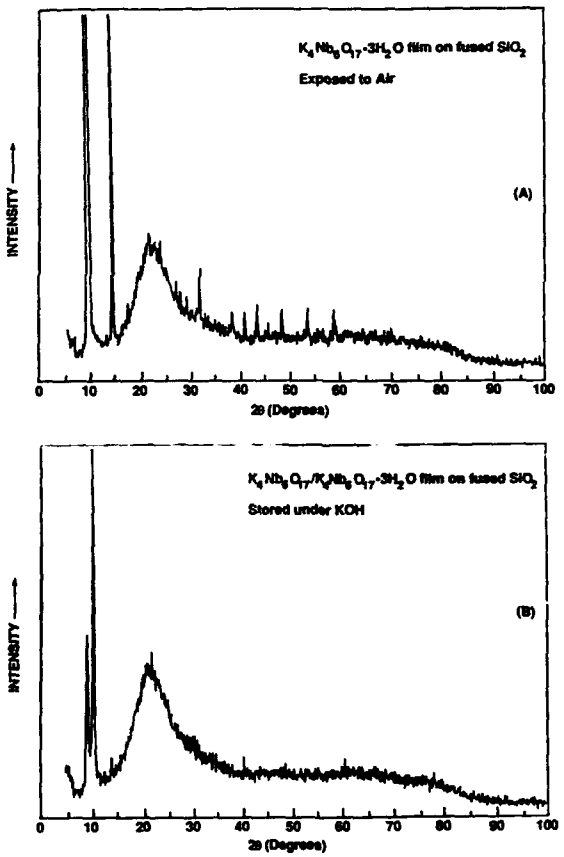


FIG. 6. XRD patterns for thin films deposited on fused silica and calcined at 700°C. (A) Film exposed to air forms the potassium-deficient hydrate phase, $K_4Nb_6O_{17}\cdot 3H_2O$. (B) Film stored under KOH has less hydrate phase and more $K_4Nb_6O_{17}$. $KNbO_3$ is not observed in either film.

observed after calcination at higher calcination temperatures. Chemical analyses showed that a sample calcined at 150°C had 47.1 wt% Nb and 18.7 wt% K (Nb/K mole ratio of 1.06), while a sample calcined at 750°C sample had 52.9 wt% Nb and 22.7 wt% K (Nb/K mole ratio of 0.98). The mole ratios agree well with the 1:1 ratio expected for $KNbO_3$. Furthermore, the Nb and K weight percentages for the 750°C calcined sample are very close to the calculated values for $KNbO_3$ of 51.61 wt% Nb and 21.71 wt% K. The mechanism responsible for the reduced hydrolysis/condensation rate during processing with water/methanol solutions is not understood at the present time. However, recent proton NMR results [26] have shown that the addition of methanol to niobium ethoxide results in an exchange of the ethoxide group for the methoxide group. Thus, carrying out hydrolysis in water/methanol solutions may result in the formation of a bimetallic potassium-niobium methoxide. In turn, this alkoxide may be less susceptible to dissociation (i.e., compared to the bimetallic ethoxide) during hydrolysis.

The clear sols prepared with 1 mole of water (in methanol) per mole of ethoxide were used to form thin films by spin coating. However, as observed by other workers, [10,14,15] phase development in thin films was highly dependent upon the nature of the substrate. For example, it was not possible to form $KNbO_3$ when fused silica was used as the substrate. Figure 6 shows typical XRD patterns obtained for samples calcined at 700°C. In the Fig. 6A, the sharp peaks are associated with the potassium-deficient hydrate phase, $K_4Nb_6O_{17} \cdot 3H_2O$. (The broad peak centered at $2\theta \approx 22°$ is due to the fused silica substrate.) The film in Fig. 6A was left exposed to the atmosphere after calcination. In contrast, Fig. 6B shows the XRD pattern for a film stored under KOH after calcination. In this case, the hydrate peaks were significantly reduced, but the major phase present was still the potassium-deficient $K_4Nb_6O_{17}$ phase.

Thin films of $KNbO_3$ could be prepared by using KBr substrates. Figure 7 shows the XRD pattern for a sample prepared after calcination at 700°C. The peaks labeled "S" are due to the KBr substrate, while the peaks labeled "K" are due to $KNbO_3$. The latter peaks match extremely well with those observed in Figs. 4 and 5 for single-phase $KNbO_3$, although peak splitting indicative of the orthorhombic phase was not observed in this sample.

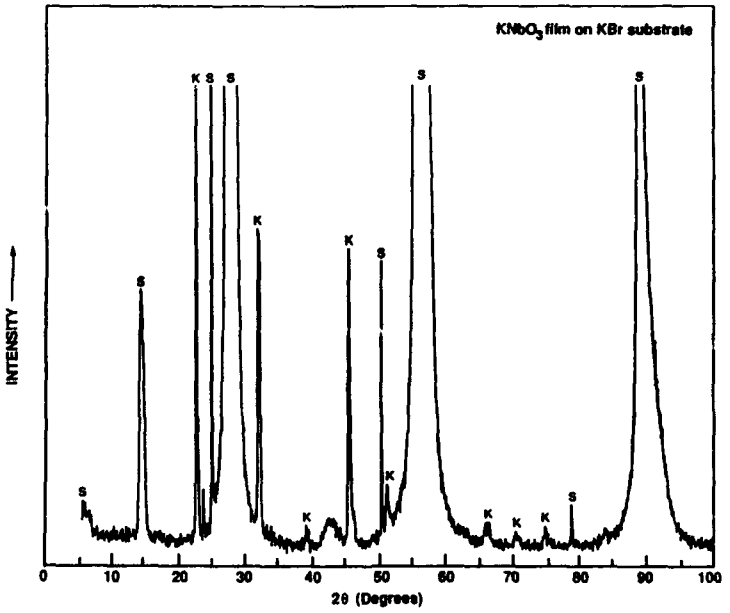


FIG. 7. XRD pattern for $KNbO_3$ thin film formed on KBr substrate.

ACKNOWLEDGMENT

The authors gratefully acknowledge support from the National Science Foundation, Division of Materials Research, Ceramics and Electronic Materials Program (DMR-8451916) and the Defense Advanced Research Projects Agency (MDA972-88-J-1006).

REFERENCES

1. P. Gunter, Phys. Rep., 93 (4) 199-299 (1982).
2. M.K. Chun, L. Goldberg, and J.F. Weller, Appl. Phys. Lett., 53 (13) 1170-1171 (1988).
3. B.A. Tuttle, Mater. Res. Soc. Bull., 12 (7) 40-45 (1987).
4. A. Reisman and F. Holtzberg, J. Am. Chem. Soc., 77 (8) 2115-2119 (1955).
5. U. Fluckiger, H. Arend, and H.R. Oswald, Bull. Am. Ceram. Soc., 56 (6) 575, 577 (1977).
6. W. Xing, H. Looser, H. Wuest, and H. Arend, J. Crystal Growth, 78 431-437 (1986).
7. R. Lipeles, D. Coleman, and M. Leung, in Better Ceramic Through Chemistry II, edited by C.J. Brinker, D.E. Clark, and D.R. Ulrich (Mater. Res. Soc. Proc. 73, Pittsburgh, PA 1986) pp. 665-670.
8. G. Yi, Z. Wu, and M. Sayer, J. Appl. Phys., 64 (5) 2717-2724 (1988).
9. D.P. Partlow and J. Greggi, J. Mater. Res., 2 (5) 595-605 (1987).
10. S.-I. Hirano and K. Kato, Adv. Ceram. Mater., 3 (5) 503-506 (1988).
11. D. J. Eichorst and D.A. Payne, in Better Ceramic Through Chemistry III, edited by C.J. Brinker, D.E. Clark, and D.R. Ulrich (Mater. Res. Soc. Proc. 121, Pittsburgh, PA 1988) pp. 773-778.
12. M.I. Yanovskaya, E.P. Turevskaya, A.P. Leonov, S.A. Ivanov, N.V. Kolganova, S.Yu. Stefanovich, N.Ya. Turova, and Yu.N. Venevtsev, J. Mater. Sci., 23 (2) 395-399 (1988).
13. E.T. Wu, A.X. Kuang, and J.D. MacKenzie, Proc. of the Sixth IEEE International Symposium on Applications of Ferroelectrics, 388-390 (1986).
14. S.L. Swartz, P.J. Melling, and C.S. Grant, in Optical Materials: Processing and Science, edited by D.B. Poker and C. Ortiz (Mater. Res. Soc. Proc. 152, Pittsburgh, PA, 1989) pp. 227-232.
15. B.A. Tuttle, B.C. Bunker, D. L. Lamppa, R.G. Tissot, and J.L. Yio, to be published in the proceedings of Ceramic Thick and Thin Films, 91st Annual Meeting of the American Ceramic Society, Indianapolis, IN, 1989.
16. D.F. Shriver and M.A. Drezdzon, The Manipulation of Air-Sensitive Compounds, 2nd ed. (Wiley-Interscience, New York, 1986).
17. D.C. Bradley, B.N. Chakravarti, and W. Wardlaw, J. Chem. Soc., 2381-2384 (1956).
18. D.C. Bradley and C.E. Holloway, J. Chem. Soc. (A), 219-223 (1968).
19. Powder Diffraction File, Card Nos. 14-287, 21-1295, and 21-1297, Joint Committee on Powder Diffraction Standards, Swarthmore, PA.
20. M.M. Amini and M.D. Sacks, submitted to J. Am. Ceram. Soc.
21. K. Nassau, J.W. Shiever, and J.L. Bernstein, J. Electrochem. Soc.: Solid State Science, 116 (3) 348-353 (1969).
22. M. Guglielmi and G. Carturan, J. Non-Cryst. Solids, 100 16-30 (1988).
23. Powder Diffraction File, Card Nos. 9-156 and 32-822, Joint Committee on Powder Diffraction Standards, Swarthmore, PA.
24. E. Wood, Acta Cryst., 4 353-362 (1951).
25. Powder Diffraction File, Card No. 8-212, Joint Committee on Powder Diffraction Standards, Swarthmore, PA.
26. S.K. Showalter and M.M. Amini, unpublished work.

INTERCALATION CHEMISTRY: A NOVEL APPROACH TO MATERIALS DESIGN

E.P. GIANNELIS, V. MEHROTRA AND M.W. RUSSELL
Department of Materials Science and Engineering, Cornell University, Ithaca, NY 14853.

ABSTRACT

Intercalation of layered solids is used as a means to manipulate a variety of molecular and polymeric species into well-ordered multilayer films with an architecture controllable at the molecular level. Dielectric, conductivity and optical measurements demonstrate the potential of developing new families of materials with new functionalities by exploiting the synergistic effect of guest/host interactions.

INTRODUCTION

Molecular level electronic and optical devices in which individual molecules would function as a self-contained device are being discussed as an alternative approach to current solid state devices [1,2]. Molecular devices become particularly attractive when one considers the relentless increase in circuit densities that is forcing the semiconductor industry to continuously reduce the size of circuit elements. It is expected that within the next thirty years the size of electronic components will be on the order of a few nanometers or the size of individual molecules.

Current IC fabrication technology involves microstructure pattern fabrication and sculpturing on three-dimensional blocks of silicon. Alternatively, in molecular devices, components will be arranged into complex, well-defined molecular assemblies by virtue of atomic or molecular forces in much the same way that functional components are assembled in living organisms.

The ability to engineer and assemble components into controllable, well-defined supermolecular arrays is the most critical obstacle in creating functional molecular devices. It is the thesis of this paper that intercalation of layered solids offers the means to manipulate the structure of supermolecular assemblies at the molecular level. Thus, anisotropic materials with two-dimensional microstructures, nanometer architecture and controlled interfaces can be assembled providing new molecular tools to Materials Engineering. Though interest in intercalation has grown steadily over the years, most of the work has focused on the effect of intercalation on the physical properties of the host [3].

This paper reviews our efforts to develop new intelligent materials from intercalated solids with unique responses to electrical, optical and chemical stimuli. The desired properties/functions are introduced by fine-tuning specific guest-host interactions resulting in molecular ensembles with potential applications as sensors, transducers, and memory devices.

We begin by reviewing some of the essential features of intercalation of layered solids. Then a discussion on the structural characteristics and intercalation properties of layered silicates and layered double hydroxides is presented.

Mat. Res. Soc. Symp. Proc. Vol. 180. ©1990 Materials Research Society

GENERAL FEATURES OF INTERCALATION OF LAYERED SOLIDS

Layered solids can ingest foreign species into the galleries between the layers to form intercalated materials [3]. For example, intercalation compounds like graphite and transition metal chalcogenides have been studied quite extensively over the past several decades. In this paper we will introduce a "new" class of host solids, namely, the complex layered oxides (*CLOs*), that have largely been ignored by the materials and the solid state community.

CLOs, like the more traditional layered solids, exhibit a rich intercalation chemistry with unique properties. In order to put the intercalation properties of *CLOs* into perspective, we will review Solin's classification of layered solid hosts. According to Solin, layered hosts can be classified into three general categories corresponding to the degree of transverse layer rigidity [4].

Graphite and BN with atomically thin sheets belong to Class I. As a result the layers are "floppy" allowing for transverse distortions of the layers. Class II contains materials like TaS_2 and FeOCl with layers often composed of three strongly bonded atomic planes that leads to a "stiffer" layer structure. Layered silicates with as many as seven atomic planes in individual layers belong to Class III and exhibit a high degree of layer rigidity with respect to transverse layer distortions. The layer rigidity has a profound effect on the physical phenomena and properties of intercalated solids exhibit which might enhance or limit their potential applications.

STRUCTURES OF COMPLEX LAYERED OXIDES

Since the majority of our work has concentrated on layered silicates and layered double hydroxides (LDHs) we limit our discussion to these two layered solids.

The structure of 2:1 layered silicates consists of two tetrahedral sheets fused to an edge-shared octahedral sheet (Figure 1) [5,6]. The type and population of the cations in the octahedral sheet distinguishes between various layered silicates. For instance, when all octahedral sites are occupied by magnesium, the known filler talc is obtained. Alternatively, in pyrophyllite only two-thirds of the octahedral sites are filled with aluminum. The stacking of the tetrahedral and the octahedral sheets results in a commensurate arrangement eliminating the strain that is often developed in incommensurate structures. For example, in crysotile and related asbestos minerals, the strain induced by structural mismatch causes the layers to curl and adopt a fiber-like morphology. In crystals of talc and pyrophyllite the layers are held together by weak dipolar and van der Waals forces creating interlayers or galleries between the layers. The sum of a single layer (~10 Å) plus the interlayer represents the repeat unit of the multilayer and is calculated from the 001 harmonics obtained from x-ray diffraction patterns.

In contrast to talc and pyrophyllite where the layers are electrically neutral, micas (muscovite and phlogopite) exhibit a net charge of negative two per unit cell due to the isomorphous substitution of silicon by aluminum

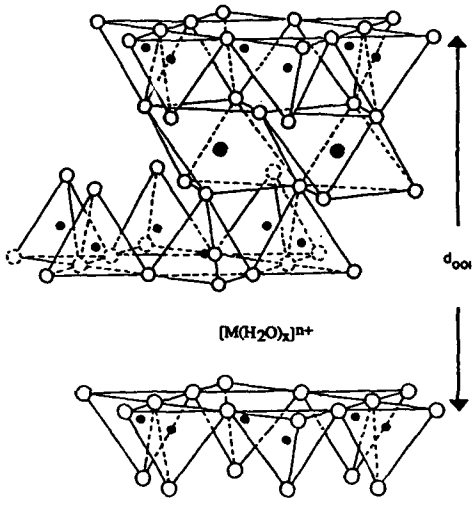


Figure 1. Idealized structure for 2:1 layered silicates.

in the tetrahedral sheet. To balance the layer charge deficiency, potassium ions are located in the interlayer region at regular positions. In fact, the gallery potassium ions are located at the center of the hexagonal arrays created by the oxygen atoms of the tetrahedral sheet resulting in a superlattice.

The talc-pyrophyllite group and the micas represent the end members of a hierarchy defined by the degree of layer charge neutrality. Mica-type silicates (MTSs), otherwise known as swelling silicates, with layer charge densities in the range, $0 < x < 2$, define a separate family of host lattices with unique physical and chemical properties not found in the end members. Similarly to micas, gallery ions are incorporated in the structure of swelling silicates to balance the charge deficiency in the layers. When the charge deficiency originates from the octahedral sheet (i.e. Mg^{2+} substituting for Al^{3+}) the negative charge is distributed over all oxygens of the framework resulting in a turbostratic arrangement. In other words, layer ordering occurs in the c direction but the layers tend to be randomly stacked with respect to the a and b axes of individual layers. In contrast, the layer charge created in tetrahedral sheets tends to be more localized yielding a greater three-dimensional order.

In contrast to MTSs, LDHs have the reverse polarity with respect to layer and gallery ion charge. They consist of positively charged, brucite-like ($Mg(OH)_2$-like), layers resulting from the displacement of divalent cations in the octahedral layer by trivalent cations separated by hydrated gallery anions [7]. If one considers the possible combinations of divalent/trivalent cations a very large range of solids with idealized formulas of the type $[M^{II}_{1-x}M^{III}_{x}(OH)_2][A^{n-}]_{x/n} \cdot yH_2O$ can be synthesized.

In the above chemical formula the divalent and trivalent cations occupy octahedral positions in the hydroxide layers and A^{n-} is the gallery anion.

A brief statement should be made about the origin and availability of both MTSs and LDHs and their ability to form films. Although both classes can be found in nature in both polycrystalline and single crystal forms, we have mainly concentrated on synthetic materials that allow us to better control their morphology, chemical composition and surface properties. In addition, CLOs can readily form thin films and coatings on various substrates by spinning or casting techniques.

INTERCALATION PROPERTIES OF CLOs

The most striking property of MTSs is their ability to ingest (intercalate) a variety of guest species in their galleries due to the much weaker interlayer forces compared the intralayer forces that bind the atomic planes together [5]. The hydrated gallery cations in MTSs can be readily exchanged with almost any cation by simple ion exchange reactions, distinguishing them from the end members of the group (talc and micas).

In contrast to graphite which is amphoteric, MTSs will accept only positively charged or neutral molecules without any charge exchange mechanism. Since no charge exchange is taking place, intercalation of MTSs is less disruptive and very facile. A diverse class of cations (mono- and polynuclear, organic, inorganic, organometallic and biological) can be introduced in the galleries.

MTSs are also known for their ability to intercalate a large number of polar neutral molecules in their galleries with certain degree of orientation and alignment. The enhancement of orientation and alignment upon intercalation can be exploited to produce, for example, materials with large optical non-linearities. The guest species can enter in stages, i.e. one monolayer at a time and, in some instances, as many as twenty monolayers can be accommodated. For example, intercalation of water under controlled conditions produces a monolayer of water in the galleries for partial pressures of water between 0.1 and 0.6, while for pressures between 0.6 and 0.9, a bilayer is formed.

Similarly, LDHs can accommodate a large number of anions and polar neutral molecules in their galleries but size/charge requirements for the guest species are more stringent than with the MTSs. The size/charge requirement imposes severe limitations to the range of guest species that can be intercalated in LDHs [8].

DIELECTRIC PROPERTIES OF CLOs

An integral part of our effort is to develop new generations of environmentally stable materials for optoelectronic packaging applications. Our strategy includes intercalation of low permittivity polymers between the layers of a robust layered oxide [25]. As a result, we have embarked on a detailed study of the dielectric properties of pristine layered solids and the effect of polymer intercalation on their dielectric properties [9].

The dielectric response of a heterogeneous solid contains contributions

from permanent and induced dipoles and the motions of ions and electrons. Furthermore, the dielectric properties of heterogeneous materials cannot always be described by the sum of those of the individual components [10]. The motion of charge carriers is a cooperative phenomenon and might be hindered by the structure of the material. This is particularly true when one component adopts a network structure which is not realizable in the bulk. The consequence of the restricted motion is that an extremely large dielectric permittivity results especially at low frequencies.

The outstanding experimental phenomena of CLOs that any theory needs to explain are [11]: (a) their extremely high susceptibilities when water molecules are intercalated in the galleries (orders of magnitude greater than that for water) and (b) the frequency dependence of the real and imaginary part.

The real and imaginary part of the dielectric susceptibility versus frequency are plotted in Figure 2a for an air- dried sample of LDH. For comparison the dielectric response of Li-fluorohectorite is shown in 2b. The seemingly different behavior of the two classes of layered solids is understood in terms of infrared divergence theories and models invoking fractal time processes and fractal structure.

The intercalated water molecules and/or gallery ions in both solids can form hydrogen-bonded islands (clusters) with partially ordered structures. These H-bonded systems can be described by percolation structures in which their connectivity is described by the probability of hydrogen bonding [12].

In the absence of an externally applied field the material will be neutral and, most likely, unpolarized. An externally applied field will uniformly polarize the system by a succession of proton transfers (hops) within the hydrogen bonded cluster array either within the same cluster (intracluster polarization) or between different clusters (intercluster polarization) creating $-OH^-$ and OH_3^+ at each end of the path. Relaxation is achieved either by charge recombination within the same cluster or between different clusters or some other routes that do not necessarily involve charge transport. The latter mechanism can involve, for example, molecular rotation following hydrogen-bond breaking and subsequent re-creation [10].

The frequency-dependent response of systems, where charge recombination is the only relaxation mechanism, shows a continuous crossover from intracluster group oscillations at high frequencies to the longer-range intercluster charge transport at lower frequencies. In contrast, systems that possess other routes of dipolar relaxation in addition to charge recombination will exhibit a separate loss peak in their frequency-dependent response. Since some of the water molecules in MTSs have protons inside the ditrigonal cavity of the silicate surface, the regularity of hydrogen bonding among the gallery water molecules is broken in places [13]. These defects permit a variety of reorientational motions that are not possible in LDHs, resulting in a loss peak in the dielectric response of MTSs. The difference in the structure of intercalated water becomes apparent when one considers the hydroxylated galleries of LDHs.

Alternatively, the dielectric response of LDHs is modeled using a random walk of charge carriers (H^+) on a percolation cluster [14]. The

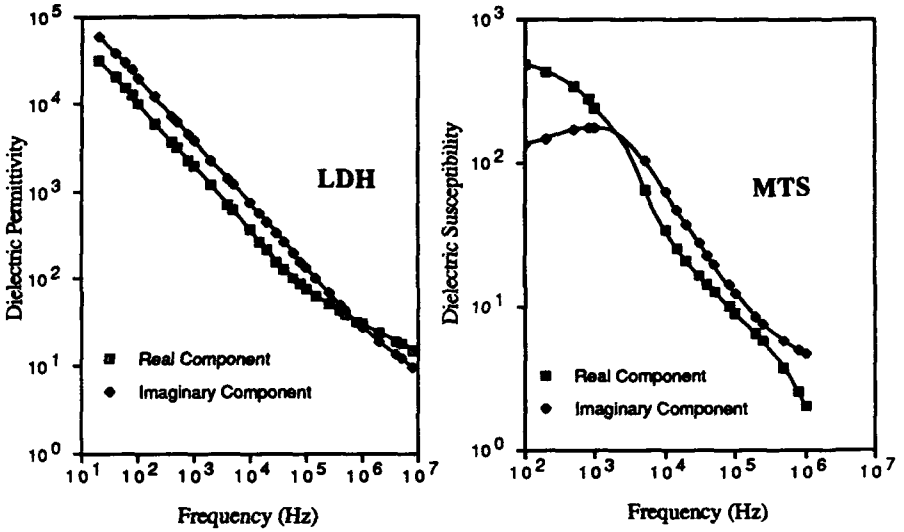


Figure 2. Dielectric susceptibility vs. frequency for LDH and MTS.

response of the material at low frequencies is understood in terms of a fractal time process. The latter is the result of a waiting time distribution between successive hops. On the other hand, the high frequency behavior is due to a fractal time process operating on fractal structure, much like the percolation structures formed by H-bonded water molecules.

SUPERMOLECULAR ASSEMBLIES

The utilization of layered solids to control the structure of the guest species in a molecular assembly is demonstrated by the intercalation of Cu coordinated porphyrin molecules in the galleries of two different MTSs with varying charge density. The orientation of the gallery species is dictated by the basal surface area per exchange site that, in turn, depends on the layer charge density of the host [15].

X-ray diffraction patterns of fluorohectorite (high layer charge density) and hectorite (low charge density) intercalated solids show crystallographically well-ordered structures with 001 harmonics corresponding to a primary repeat unit (d-spacing) of 20.1 and 14.0 Å for fluorohectorite and hectorite respectively. The difference of 4.4 Å from the corresponding 9.6 for the silicate framework for hectorite is in accord with the expected size of the porphyrin ring plane parallel to the silicate layers (Figure 3). In contrast, the observed 10.5 Å difference for fluorohectorite is consistent with an inclined arrangement of the porphyrin ring plane with respect to the silicate layers. An inclined arrangement will be favored when the size of the guest molecules exceeds the area available per exchange site.

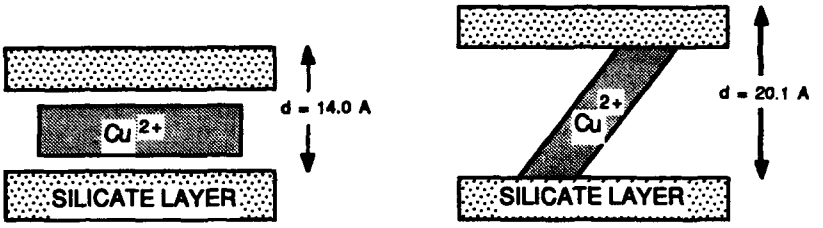


Figure 3. Schematic illustration of porphyrin intercalated in MTSs

The different orientation of the porphyrin guest layer in the two intercalates was verified by anisotropic electron spin resonance spectroscopy. In hectorite, the perpendicular or parallel component is observed, when the magnetic field is oriented parallel or perpendicular to the layers respectively. In contrast, the esr spectrum of fluorohectorite intercalates is orientation independent. The orientation independent spectrum suggests a preferred orientation of the porphyrin molecules with the molecular ring oriented near 45° degrees with respect to the host layers in agreement with x-ray diffraction data.

The ability to control the orientation and alignment of guest species can be used to manipulate the properties of the supermolecular ensemble. For example, the photophysical properties of transition metal complexes can be mediated by fine-tuning the guest-host interactions [16]. Current studies include evaluation of these well-organized molecular assemblies as tunable non-linear optical and photoresponsive (hole burning) materials.

CONDUCTING-INSULATING MULTILAYERS

A large effort of our research is focused on the development of well-defined, two-dimensional molecular assemblies of electroactive polymers. Such architecture can lead to materials with highly anisotropic dielectric, conducting and optical properties. In our approach, intercalative polymerization of a suitable monomer in the galleries of the host is used as a means to process insulating-conducting composites into thin films with a multilayer structure and molecular dimensions.

Electrically conducting polyaniline films can be formed by a simple intercalative polymerization of aniline in Cu-exchanged fluorohectorite [17]. The aniline monomer reacts with Cu^{2+} to form an intermediate ($PhNH_2 \cdot^+$) that initiates the polymerization to polyaniline. The reaction can be represented by the following equation, where the horizontal lines identify the layered structure.

$$Cu^{2+} + nC_6H_5NH_2 \longrightarrow Cu^{2+}(PANI)$$

X-ray diffraction patterns of oriented films exhibit a highly ordered two-dimensional structure. Several (001) harmonics are observed corresponding to a primary repeat unit (d spacing) of 14.9 Å. The 5.3 Å guest layer is in agreement with intercalation of single chains of polyaniline.

Spectroscopic studies (UV-visible, IR and Raman) have established the presence of the insulating form of polyaniline for the as prepared sample. After exposure to HCl vapors the 2.4 eV band gradually disappears while a new band centered at 1.6 eV and extending into the near IR appears characteristic of the conducting form of polyaniline (Figure 4) [18].

The room temperature in-plane conductivity of HCl exposed samples is 0.05 $Ohm^{-1}cm^{-1}$ an increase by five orders of magnitude with respect to Cu-exchanged host. Variable temperature in-plane conductivity measurements show that as the sample is heated from room temperature the conductivity increases with increasing temperature as expected for semiconducting behavior or different variable range hopping processes. The conductivity increases reversibly from room temperature to about 60 °C, above which the conductivity starts to decrease slowly. Preliminary conductivity measurements perpendicular to the silicate layers affirm the highly anisotropic nature of the material.

The electroactive polymer/layered solid hybrids represent a new class of two-dimensional conductors [17,19]. They consist of single conducting polymer chains alternating with the host layers with a well-defined multilayered structure. Since the polymerization reaction takes place

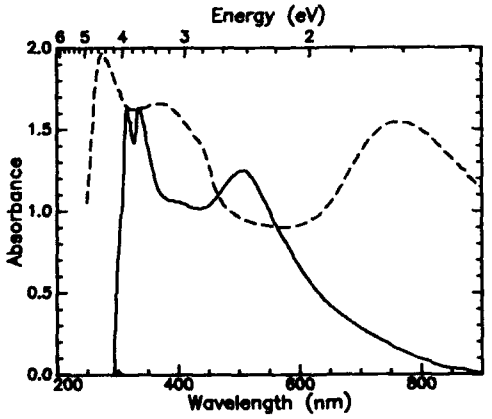


Figure 4. Electronic absorption spectra of: (a) as-prepared PANI intercalated MTS (solid line); (b) after exposure to HCl vapors (broken line)

between the confining walls of the host matrix, the polymer might be forced to attain conformations unrealizable in the bulk which, in turn, might influence its transport properties.

BIOMIMETIC SENSORS

In this section, a brief description will be presented of our efforts to develop new generations of artificial biosensors that imitate the gustatory and olfactory cells in living organisms. The receptor element of the artificial membranes is based on synthetic amphiphiles incorporated in the galleries of CLOs while transduction is based on capacitance and surface acoustic wave measurements (Figure 5).

In designing new sensory devices, biological systems can serve as prototypes for the development of new types of chemical sensors. They are well known for their ability of molecular recognition, signal transduction and chemical regulation. The faculties of sensing and transduction coupled with memory and logic functions define the highest degree of intelligent characteristic of organized beings.

Specific receptor proteins are usually involved in molecular recognition of various chemical substances. However, recognition of certain chemicals can be accomplished without the presence of specific protein receptors reducing the level of complexity inherent to biological systems [20].

The immobilization of synthetic amphiphiles in a polymer matrix and their unique sensing capabilities have been recently reported [21]. However, organic solvents and high ionic activity solutions can damage the artificial membrane. In our approach some of these limitations can be circumvented by using a robust layered template to assemble the membrane.

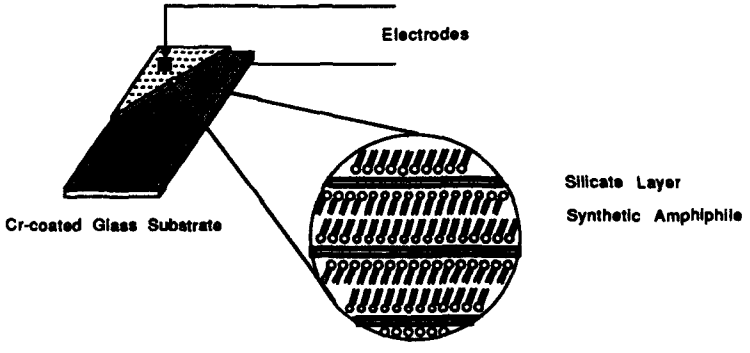


Figure 5. Schematic of an artificial sensor.

Artificial membranes have been synthesized by intercalating dialkyl ammonium cations and succinate anions in CLOs. The materials can be easily casted or deposited onto a substrate providing an artificial skin of several microns thick. The layered host not only provides the means to assemble the multibilayer but also imparts strength to the film so that it can withstand harsh physicochemical or physiological environments.

X-ray diffraction shows that the artificial skins possess self-assembling properties resulting in well-organized bilayers of the amphiphile alternating with the host layers. Furthermore, the materials undergo a phase transition or "melting" at characteristic temperatures that changes the fluidity of the artificial membrane [22]. The bilayer forming and liquid crystalline transition temperature are common characteristics of biological membrane systems [21]. We are currently evaluating the sensing capabilities of the artificial membranes in the presence of various poisons and odorants. These artificial membranes are likely to exhibit a size and shape selectivity due to diffusional barriers imposed by the layered template.

MOLECULARLY ENGINEERED NANOSTRUCTURES

The design of materials with nanometer dimensions is the subject of intense current research [23,24]. Solid materials with particles between 0.5 and 10 nm exhibit novel electrical, optical, magnetic and chemical properties due to their extremely small dimensions.

Synthetic strategies for nanophase materials typically involve the following steps: cluster formation, cluster isolation, and cluster assembly. A critical obstacle in assembling and maintaining a nanophase structure is the tendency of the molecular clusters to aggregate in order to reduce the high energy associated with their high surface to volume ratio. One successful approach to molecular cluster stabilization is their inclusion in a 3D template that physically prevents cluster aggregation [23].

Alternatively, intercalation of molecular clusters in the galleries of CLOs has also produced thermally stable materials with regular void structure available for adsorption and catalytic reactions [6,8]. Although their uses in areas like separations and catalysis is already well established, we were the first to exploit their regular void structure as a means to develop new materials with low dielectric constant for electronic packaging applications [25]. The low dielectric constant (Figure 6) is achieved by introducing a regular void structure. The well-ordered interconnected structure can be controlled by the proper choice of molecular props and solid host lattice.

However, the novelty of this process lies with the ability to assemble and maintain a nanophase structure composed of "molecular" oxides. These nanometer size oxides, consisting mainly of surface atoms, represent a new class of materials with yet to be learned properties.

CONCLUSIONS

Intercalation of layered solids can be used to manipulate a variety of molecular and polymeric guest species into well ordered multilayer films

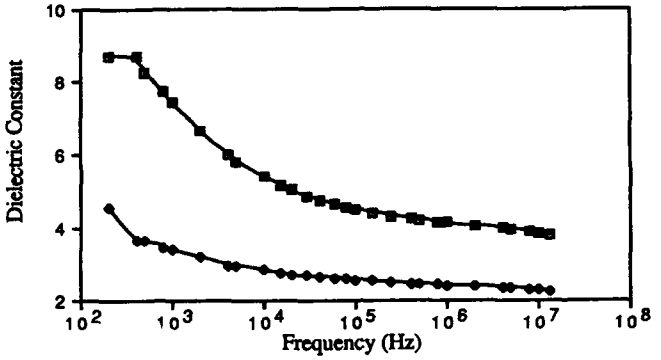


Figure 6. Relative dielectric permittivity of LDH intercalated with: (a) $[SiV_3W_9O_{40}]^{7-}$ (open squares); (b) $[PV_{14}O_{42}]^{9-}$ (filled squares).

with an architecture controllable at the molecular level. Due to the self-assembled nature of the host matrix, it is possible to construct two-dimensional materials with highly anisotropic dielectric, electronic and optical properties. Various new functions can be introduced by manipulating the guest-host interactions leading to molecular level devices.

ACKNOWLEDGMENTS

This work was sponsored by the National Science Foundation (DMR-8818558) through the Materials Science Center at Cornell. M.W. Russell acknowledges the support of an IBM Fellowship administered through the Cornell Ceramics Program.

REFERENCES

1. Molecular Electronic Devices II, edited by F.L. Carter (Marcel Dekker, New York, 1984).

2. M.J. Bowden, in Electronic and Photonic Applications of Polymers, edited by M.J. Bowden and S.R. Turner (ACS, Washington DC, 1988) pp. 1-73.

3. Intercalation Chemistry, edited by M.S. Whittingham and A.J. Jacobson (Academic Press, New York, 1982).

4. S.A. Solin, in Intercalation in Layered Solids, edited by M.S. Dresselhaus (Plenum Press, New York, 1986) pp. 145-154.

5. T.J. Pinnavaia, Science, 220, 365 (1983).

6. T.J. Pinnavaia, in Chemical Physics of Intercalation, edited by A.P. Legrand and S. Flandrois (Plenum Press, New York, 1987) pp. 233-252.

7. W.T. Reichle, CHEMTECH, 58 (1986).

8. T. Kwon and T.J. Pinnavaia, Chem. Mat., 1, 381 (1989).

9. V. Mehrotra and E.P. Giannelis, unpublished data.

10. L.A. Dissado and R.M. Hill, J. Chem. Soc., Faraday Trans., 80, 291 (1984).

11. H. Bidadi, P.A. Schroeder and T.J. Pinnavaia, J. Phys. Chem. Solids, 49, 1435 (1988).

12. R. Blumberg, H.E. Stanley, A. Geiger, P. Mausbach, J. Chem. Phys., 80, 5230 (1984).

13. G. Sposito and R. Prost, Chemical Reviews, 82, 554 (1982).

14. G.A. Niklasson, J. Appl. Phys., 62, R1 (1987).

15. E.P. Giannelis, unpublished data.

16. M.D. Newsham, E.P. Giannelis, T.J. Pinnavaia, D.G. Nocera, J. Am. Chem. Soc., 110, 3880 (1988).

17. V. Mehrotra and E.P. Giannelis, in Polymer Based Molecular Composites, edited by D.W Shaefer and J.E. Mark (Mater. Res. Soc. Proc. 171, Pittsburgh, PA 1990).

18. J.C. Chiang and A.G. MacDiarmid, Synth. Met., 13, 193 (1986).

19. M.G. Kanatzidis, C.-G. Wu, H.O. Marcy and C.R. Kannewurf, J. Am. Chem. Soc., 111, 4139 (1989).

20. Biochemistry of Taste and Olfaction, edited by R.H. Cagan and M.R. Kore (Academic Press, New York, 1981).

21. Y. Okahata, H. Ebato, K. Taguchi, J. Chem. Soc., Chem. Comm., 1363 (1987).; Y. Okahata and G. Enna, ibid., 1365 (1987).

22 M.W. Russell and E.P. Giannelis, unpublished data.

23. G.A. Ozin, A. Kuperman and A. Stein, Angew. Chem. Int. Ed. Engl., 28, 359 (1989).

24. P. Enzel and T. Bein, J. Phys. Chem., 93, 6270 (1989)

25. V. Mehrotra, T. Kwon and E.P. Giannelis, in Advanced Electronic Packaging Materials, edited by J. Partridge, C-Y. Li, C.J. Chen, A. Barfknecht (Mater. Res. Soc. Proc. 167, Pittsburgh, PA 1990).

PREPARATION OF COPPER AND COPPER-BARIUM-YTTRIUM SOLS FROM METAL 2-(2-ETHOXYETHOXY)ETHOXIDES AND CONVERSION OF COPPER-BARIUM-YTTRIUM ALKOXIDE PRECURSORS TO $Ba_2YCu_3O_{7-\delta}$.

Mary Rose Scozzafava, Wendell E. Rhine, and Michael J. Cima
Ceramics Processing Research Laboratory, Massachusetts Institute of Technology,
Cambridge, MA 02139

ABSTRACT

The hydrolysis of copper 2-(2-ethoxyethoxy)ethoxide solutions and barium-yttrium-copper 2-(2-ethoxyethoxy)ethoxide solutions were investigated. Copper sols with particle sizes of 3-10 nm have been prepared from THF solutions. Sols from barium-yttrium-copper alkoxides were also prepared in THF with particle sizes of 4-10 nm as determined by transmission electron microscopy (TEM) and 50-80 nm as determined by photon correlation. Compositional analysis showed that the sols had a similar composition to the parent solution. Choice of atmosphere and solvent system played an important role in the progress of the hydrolysis reaction. Powders obtained from barium-yttrium-copper solutions can be converted to $Ba_2YCu_3O_{7-\delta}$.

INTRODUCTION

Sol-gel synthesis has been studied intensively as a fabrication method for superconducting films and powders [1-7]. The process involves dissolution of barium, yttrium, and copper alkoxides in a common solvent followed by addition of water which initiates hydrolysis and condensation reactions which can produce either a sol or gel. The resulting solutions can then be spin- or dip-coated onto substrates or dried to obtain powders which, upon heat treatment, yield high T_c superconducting oxides. The insolubility of Cu(II) alkoxides, however, has limited the success of this route.

Recent improvements in preparing soluble copper alkoxides involved the use of polydentate ligands in which the second heteroatom can help satisfy the coordination sphere of copper and increase its solubility [3-7]. The preparation of bis(2-(2-ethoxyethoxy)ethoxide)-copper(II), $Cu(OCH_2CH_2OCH_2CH_2OCH_2CH_3)_2$, is part of an ongoing effort to develop soluble copper alkoxide precursors to apply sol-gel technology to the preparation of superconducting oxide films and powders [3]. Preliminary investigations showed that copper 2-(2-ethoxyethoxy)ethoxide [2-(2-ethoxyethoxy)ethoxide = 2,2-EEE)] is a good candidate for use in sol-gel procedures [3]. $Cu(2,2\text{-EEE})_2$ is highly soluble in both THF and toluene.

Further motivation for the study of soluble copper alkoxides is that copper sols could be used as a route to extremely fine copper particles. Metal precipitates are used in glass coatings to change their optical properties. Typically, the particles are introduced by fuming salts of the metal onto the glass surface. Copper sols instead could be spin-coated with a silica sol and then fired under a reducing atmosphere to give monodispersed copper metal [8].

In this paper, we report on the hydrolysis behavior of $Cu(2,2\text{-EEE})_2$ and of mixtures of copper, barium, and yttrium 2-(2-ethoxyethoxy)ethoxides. Conditions for formation of stable sols of both copper and barium-yttrium-copper are described. Powders prepared from these precursors can be converted to $Ba_2YCu_3O_{7-\delta}$ (BYCO).

Mat. Res. Soc. Symp. Proc. Vol. 180. ©1990 Materials Research Society

EXPERIMENTAL PROCEDURE

All reactions were conducted under an inert atmosphere using dried solvents. 2-(2-Ethoxyethoxy)ethanol was distilled from K_2CO_3 and dried over molecular sieves prior to use. $Cu(2,2\text{-}EEE)_2$ was prepared by an alkoxide exchange reaction in toluene between $Cu(OMe)_2$ and 2-(2-ethoxyethoxy)ethanol (Aldrich Chemical, Milwaukee, WI) [9]. The resulting blue solution was filtered to remove an orange solid (possibly a Cu(I) decomposition product), and the copper concentration of the blue solution was determined by iodimetric titration or inductively coupled plasma (ICP) analysis. $Cu(2,2\text{-}EEE)_2$ was isolated as a solid by evaporation of toluene under reduced pressure, followed by heating to 80°C under vacuum to remove unreacted 2-(2-ethoxyethoxy)ethanol. Elemental analysis established that the solid was contaminated by 2.49 wt% LiCl. $Ba(2,2\text{-}EEE)_2$ was prepared from the reaction of barium metal with 2-(2-ethoxyethoxy)ethanol. The resulting amber solution was filtered to remove unreacted barium, and the barium concentration was determined by gravimetric analysis or ICP analysis. $Y(2,2\text{-}EEE)_3$ was prepared by an exchange reaction in toluene between yttrium isopropoxide (Alfa Chemicals, Ward Hill, MA) and 2-(2-ethoxyethoxy)ethanol. The resulting colorless solution was filtered, and the yttrium content was determined by complexometric titration or ICP analysis. Both barium and yttrium solutions were used as prepared.

Hydrolysis was carried out under inert atmospheres to avoid moisture and CO_2 contamination. $Cu(2,2\text{-}EEE)_2$ in toluene and/or THF was hydrolyzed by addition of a THF aliquot containing varying amounts of DI H_2O. Toluene solutions of $Ba(2,2\text{-}EEE)_2$ and $Y(2,2\text{-}EEE)_3$ were hydrolyzed by passing moist argon or air over standing solutions. Copper-barium-yttrium alkoxides in toluene and/or THF were hydrolyzed by the addition of a THF aliquot containing DI H_2O or by passing moist argon or air over a standing solution. Hydrolysis resulted in homogeneous solutions, sols, or precipitates. Sols were characterized by photon correlation (Coulter Photon Analyzer N4) and TEM (Jeol [200]CX). Solids were characterized by scanning electron microscopy (SEM), diffuse reflectance infrared Fourier transform spectroscopy (DRIFTS), thermal gravimetric analysis (TGA), and elemental analysis (E+M Microanalytical Laboratories, Corona, NY).

RESULTS AND DISCUSSION

Hydrolysis of Copper Alkoxide Solutions

A $Cu(2,2\text{-}EEE)_2$ solution was prepared at 0.030 M in 2:1 toluene:THF and was hydrolyzed. No precipitation or gelation was observed when 0.2 equivalents H_2O were added. Addition of 0.5 equivalents H_2O resulted in the formation of gels which densified to approximately one-seventh of their original volume through synersis within 24 h. Above 0.5 equivalents H_2O, the hydrolysis products rapidly precipitated from solution. Precipitates were dried under vacuum at 80°C.

Table I presents hydrolysis and TGA data for selected reactions. TGA data for precipitates indicated that reaction of copper 2-(2-ethoxyethoxy)ethoxide with water was not

Table I. Hydrolysis of 0.030 M $Cu(2,2\text{-}EEE)_2$ in 2:1 Toluene: THF as a Function of H_2O.

Eq H_2O Added	Hydrolysis Product	% Weight Loss (by TGA)
0.2	soluble	--
0.5	gel	--
0.75	gelled ppt	--
1.0	gelled ppt	40.4
2.0	gelled ppt	25.1
4.0	gelled ppt	32.2
20.0	gelled ppt	13.0

Table II. Hydrolysis of 0.026 M $Cu(2,2\text{-}EEE)_2$ in THF as a Function of H_2O.

Eq H_2O Added	Hydrolysis Product	Particle Size	
		By Photon Correlation	By TEM
0.3	soluble		
1.0	sol	2.6 ± 3 nm	
1.5	sol	3.3 ± 2 nm	3-10 nm
2.0	gelled ppt		
4.0	gelled ppt		

quantitative. Weight loss decreased with increasing water addition up to 20 equivalents H_2O, indicating the extent of hydrolysis was not complete but rather increased steadily with increasing water. In addition, IR spectra of precipitates showed a significant amount of alkoxide remained, although the intensity of the bands associated with the alkoxide (ν 1450-1050 cm^{-1}) decreased with increasing water addition. The intensity of the 1597 cm^{-1} band (δ_s HOH) increased with increasing water addition in these IR spectra despite heating to 80°C under vacuum, and the water was presumed to be coordinated to copper.

Hydrolysis of $Cu(2,2\text{-}EEE)_2$ proceeded differently in the more polar solvent THF. A 0.026 M solution of $Cu(2,2\text{-}EEE)_2$ in THF was hydrolyzed as above. Addition of 0.3 equivalents H_2O to the solution resulted in a soluble copper hydrolysis product which did not scatter light, while addition of two or more equivalents H_2O resulted in precipitation of the hydrolysis product. With 1.0 and 1.5 equivalents added H_2O, the copper solutions scattered light, indicating that these solutions were sols containing particles of 2.6 ± 3 and 3.3 ± 2 nm, respectively. Slight modifications of the experimental conditions changed the particle size of the sol. For example, a 20:1 THF:toluene solution of 0.034 M $Cu(2,2\text{-}EEE)_2$ hydrolyzed with 1.25 equivalents H_2O afforded a sol with a particle size of 54 ± 8 nm. Table II summarizes the hydrolysis behavior of a THF solution of $Cu(2,2\text{-}EEE)_2$.

TEM photomicrographs of the copper sol confirmed the results from photon correlation. Electron diffraction indicated the particles were crystalline and ranged in size from 3 to 10 nm (Fig. 1). A small region was observed where the particles were not of uniform size and crystallinity. Figure 2 shows an area (>20 nm) whose diffraction pattern indicated that this small region had a high degree of order. Powders isolated by flocculating the sol with toluene and centrifuging the resulting gel under an inert atmosphere, however, were amorphous by

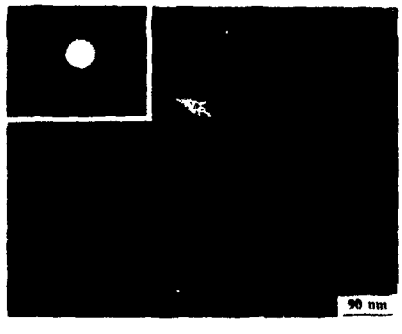


Fig. 1. TEM photomicrograph of particles (3-10 nm) from the copper sol in THF prepared by addition of 1.0 equivalent H_2O.

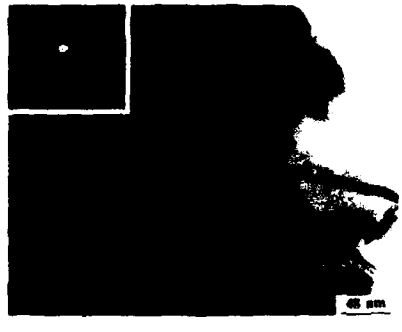


Fig. 2. TEM photomicrograph of a crystalline region of the copper sol in THF prepared by addition of 1.0 equivalent H_2O.

X-ray powder diffraction (XRD). Atmosphere played an important role in determining the composition of the copper sols. Copper gels which were prepared and dried in air had IR spectra containing bands typical for copper basic carbonates (1510 and 1444 cm^{-1}), while IR spectra of the sol prepared under inert atmospheres did not. These observations suggest that the crystallinity observed for the copper sols by TEM was due to the formation of copper basic carbonates while exposed to air on the TEM grid.

Hydrolysis of Barium-Yttrium-Copper Alkoxide and Formation of BYCO

The individual barium, yttrium, and copper 2-(2-ethoxyethoxy)ethoxide solutions in toluene hydrolyzed very differently. $Cu(2,2\text{-EEE})_2$ (0.04 M) gelled readily when moist argon (45% RH) was passed over the solution. Yttrium 2-(2-ethoxyethoxy)ethoxide and barium 2-(2-ethoxyethoxy)ethoxide hydrolyzed very slowly under the same experimental conditions. The supernatant above a gelled yttrium sample ($[Y]_{initial}$ = 0.05 M) still contained 5-6% of the starting yttrium after five days. A 0.2 M barium solution did not gel at all after five days, but instead formed a precipitate. Thirteen percent of the starting barium was still in solution. The different behaviors of the three metals in the presence of water reflect the different reactivities of copper, barium, and yttrium alkoxides.

Hydrolysis of a barium-yttrium-copper 2-(2-ethoxyethoxy)ethoxide solution, a precursor to superconducting BYC oxides, proceeded with no obvious segregation despite variations in the hydrolytic behavior of the individual metal alkoxides. Complete precipitation of all three metals occurred when 1.0 equivalent H_2O was added directly to a precursor solution ([Cu]=0.051 M, [Ba]=0.034 M, [Y]=0.018 M) in toluene. ICP analysis confirmed the absence of any detectable metal ions in the supernatant. The IR spectrum and TGA data showed that the powder did not consist of the corresponding oxides or hydroxides but still contained alkoxide groups. The difference in behavior of a mixed-metal solution as compared to the single metal solutions suggests molecular interaction is occurring in the multimetal system.

A precursor solution in toluene ([Cu]=0.051 M, [Ba]=0.034 M, [Y]=0.017 M) was gelled by passing moist argon (45% RH) over the solution for 24 h. Analysis of the supernatant liquid above the densified gel showed that it contained 1.7%, 1.7%, and 1.9% of the starting barium, yttrium, and copper, respectively. Although gelation was not complete, the same relative amounts of barium, yttrium, and copper remained behind in solution, thus preserving the original metal stoichiometry. Indeed, when the gel was dried and fired to 900°C, BYCO was identified as the primary phase by XRD (see below).

Precursor solutions in THF ([Cu]=0.06 M, [Ba]=0.04 M, [Y]=0.02 M) were hydrolyzed by the direct addition of up to 2 equivalents H_2O (Table III). Addition of 2.0 equivalents H_2O to the precursor solution afforded an immediate precipitate, yet the supernatant still had a significant metals content. A sol was obtained by the addition of 1.0 equivalent H_2O to the

Table III. Hydrolysis of Precursor Solution in THF as a Function of H_2O.[a]

Eq H_2O Added	Hydrolysis Product	Particle Size	
		By Photon Correlation	By TEM
0.5	soluble		
1.0	sol	55 ± 35 nm	4-10 nm
1.5	gelled ppt		
2.0	gelled ppt		

[a][Cu]=0.06 M, [Ba]=0.04 M, [Y]=0.02 M



Fig. 3. TEM photomicrograph of particles (4-10 nm) from a barium-yttrium-copper sol prepared by addition of 1.0 equivalent H_2O.

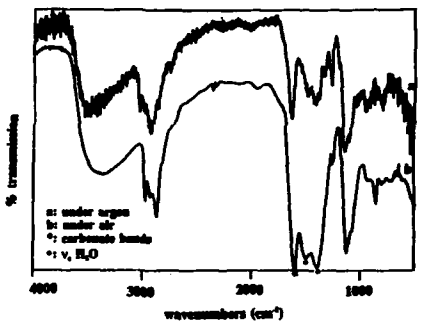


Fig. 4. (a) IR spectrum of a moist argon-hydrolyzed barium-yttrium-copper dried gel; (b) IR spectrum of an air-hydrolyzed barium-yttrium-copper dried gel. • indicates bands for coordinated H_2O and * indicates bands typical for metal carbonates.

precursor solution. The particle size as determined by photon correlation ranged from 20 to 95 nm. When sols were allowed to stand overnight before sampling, particles typically had values of 65-85 nm. These results differed significantly from the particle sizes as determined by TEM. Figure 3 shows a TEM photomicrograph of particles from a sol prepared by addition of 1.0 equivalent H_2O to the solution. Particle sizes ranged from 4 to 10 nm and were amorphous. A barium-yttrium-copper gel was obtained in 64% yield when the sol was flocculated as described above for the copper sol. ICP analysis of the supernatant liquid established that barium, yttrium, and copper were still present in a 2.00 : 1.02 : 2.94 ratio, respectively. The supernatant liquid still contained particles 48 ± 13 nm in size as determined by photon correlation. Concentration of the sol after flocculation can account for $35 \pm 4\%$ of the original metals content, assuming that the ratio of scattering intensity to concentration remains constant for the sol. This suggests that no soluble metal alkoxide remains in solution. Optimization of the flocculation process would undoubtedly improve the yield of barium-yttrium-copper powder.

When hydrolysis was carried out with moist air rather than moist argon, the reaction proceeded differently. Reaction occurred much more slowly, gelling over a week instead of a day. The IR spectrum of the air-hydrolyzed gel contained strong bands at 1400 and 1510 cm^{-1} which are typical of copper and barium carbonates (Fig. 4b) [10]. The moist argon-hydrolyzed gel did not have any bands attributable to carbonates in its IR spectrum (Fig. 4a). The morphologies of the dried gels were also quite different. Hydrolysis by moist argon afforded a powder consisting of small particles, while hydrolysis by moist air gave dense solids with no discernable substructure.

BYCO powders were prepared from powders precipitated from toluene solution. Precipitation was complete by ICP analysis when 1.0 equivalent H_2O (of total metals) was added to a 1.0 N total metals precursor solution. The resulting powder was barium-deficient. Upon firing to 900°C under O_2, BYCO was observed as the primary product by XRD (Fig. 5). CuO and BaY_2CuO_5 (121) were observed as minor impurities.

BYCO was prepared from gels which were obtained by passing moist argon over precursor solutions in THF. In this case, precipitation was not complete. BYCO was observed as the major phase by XRD, although significant amounts of CuO, $Y_2Cu_2O_5$, 121, and other

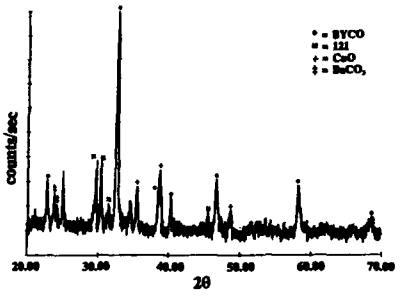


Fig. 5. XRD pattern obtained from barium-yttrium-copper precursor powders precipitated by addition of 1.0 equivalent H_2O in toluene. Powders were heated to 900°C under O_2.

unidentified phases were also observed.

CONCLUSIONS

Stable copper sols were prepared from $Cu(2,2\text{-}EEE)_2$ in THF. Copper, barium, and yttrium 2-(2-ethoxyethoxy)ethoxides were dissolved in THF to obtain a homogeneous solution and were hydrolyzed to form a sol. Evidence suggests that a soluble trimetallic precursor hydrolyzed to form a sol a with similar composition as the solution. Rupich et al. [11] reported the synthesis of a soluble molecular precursor with the composition $Ba_2YCu_3O_3(MeOEt)_7$ from a soluble oxide polymer $(CuO)_n$ and barium and yttrium 2-methoxyethoxides. The similarity of the two alkoxides makes the formation of soluble mixed-metal precursors in our system reasonable.

Barium-yttrium-copper 2-(2-ethoxyethoxy)ethoxide solutions can be used to form films or hydrolyzed to obtain BYCO powders.

REFERENCES

1. S. Hirano, T. Hayashi, R.H. Baney, M. Miura, and H. Tomonaga, Chem. Lett. 1988, 665-668.
2. H.S. Horowitz, S.J. McLain, A.W. Sleight, J.D. Druliner, P.L. Gai, M.J. VanKavelaar, J.L. Wagner, B.D. Biggs, and S.J. Poon, Science 243, 66-69 (1989).
3. M.R. Scozzafava, W.E. Rhine, and M.J. Cima in High Temperature Superconductors: Fundamental Properties and Novel Materials Processing, edited by J. Narayan, C.W. Chu, L.F. Schneemeyer, and D.K. Christen (Mater. Res. Soc. Proc. 169, Pittsburgh, PA 1990), in press.
4. S.A. Kramer, G. Kordas, J. McMillan, G.C. Hilton, and D.J. Van Harligan, Appl. Phys. Lett. 53 (2), 156-158 (1989).
5. W.G. Fahrenholz, D.M. Millar, and D.A. Payne, in Ceramic Superconductors II, edited by M.F. Yan (American Ceramic Society, Inc., Westerville, OH, 1988) pp. 141-147.
6. K. Nonaka, T. Kaneko, K. Hasegawa, Y. Kishio, K. Takahashi, K. Kobayashi, Y. Kitazawa, and K. Fueli, Jap. J. Appl. Phys. 27 (5), L867-L869 (1988).
7. M.R. Scozzafava, W.E. Rhine, and M.J. Cima, in Superconductivity and Ceramic Superconductors, edited by K.M. Nair (American Ceramic Society, Inc., Westerville, OH, 1990), in press.
8. A. Durán and J.M. Fernández Navarro, Glastechn. Ber. 56K, I614 (1983).
9. J.V. Singh, B.P. Baranwal, and R.C. Mehrotra, Z. Anorg. Allg. Chem. 477, 235-240 (1981).
10. K. Nakamota, Infrared Spectra of Inorganic and Coordination Compounds (Wiley-Interscience, New York, 1970), pp 169-171.
11. M.W. Rupich, B. Lagos, and J.P. Hachey, Appl. Phys. Lett. 55 (23), 2446-2449 (1989).

ION-IMPLANTATION EFFECTS ON SPIN-ON-GLASS (SOL-GEL) SiO_2 FILMS

Y. SHACHAM-DIAMAND*, N. MORIYA** and R. KALISH**
*214 Phillips Hall, Cornell University, Ithaca, NY 14853
**Solid State Institute, Technion – I.I.T., Haifa 32000, Israel

ABSTRACT

Silicon and phosphorus ions were implanted into Spin-On-Glass (Sol-Gel) SiO_2 films and were found to modify the material properties. Two SOG types, polysiloxane and silicate, were ion-implanted with doses in the $5 \times 10^{14} - 1.65 \times 10^{16}$ cm^{-2} range and energies of 40keV - 190keV. The implanted SOG on silicon samples were characterized by ellipsometry, infra-red spectroscopy, etching and capacitance measurement of aluminum/SOG/silicon devices. The results indicate that the polysiloxane type SOG shrinks due to the implant and its effective refractive index increases. The ion-implant of the polysiloxane SOG also changed its structure and composition as seen by the variations of the infra-red transmission spectrum, etching characteristics, and dielectric constant. Silicate SOG exhibits less shrinkage due to the implant but its other characteristics show dependence on the dose similar to that of the polysiloxane SOG.

INTRODUCTION

Spin-On-Glass (SOG), or Sol-Gel, layers have become part of the Very-Large-Scale-Integration (VLSI) technology for Integrated-Circuits (IC) production. The final properties of the fully annealed SOG are comparable to those of Chemical-Vapour-Deposited (CVD) SiO_2, which is widely used in VLSI technology [1]. The CVD oxide is commonly used as a part of the dielectric insulation between the first metal level and the substrate or between metal levels on the chip. As the chip dimensions shrink, the vertical topography dimensions become the same size as the lateral dimensions. CVD oxide may fail to reliably cover steep steps and narrow trenches in such topographies. In this case, SOG offers better step-coverage due to the self-planarizing properties of its liquid state. The fluid SOG coats even harsh topographies and results in a more moderate topography which can be used as a base for the subsequent steps (e.g. CVD oxide, sputtered metal). SOG is typically combined with CVD oxide in multi-layer metal-interconnect structures realized in VLSI technology. For example, in a layered CVD oxide/SOG/CVD oxide structure one takes advantage of the planarizing properties of SOG with the qualified integrity of the CVD oxide.

Spin-on-glass is often called sol-gel, a term which aptly describes the two states of the material. Initially, it is a silicon compound dissolved in organic solvents. The liquid is spin-cast on the silicon wafer at a typical spin-speed of 3000-7000 RPM for 20-30 seconds. After a thermal stabilization step at relatively low temperatures (90°C–120°C) the film is processed at a sequence of increasing temperatures in the 180°C–450°C temperature range. At elevated temperatures, the material polymerizes and forms a silicon-oxygen backbone chain with an organic group attached to it. Two types of SOG materials are discussed here [2]: polysiloxane and silicate. The polysiloxane SOG contains carbon when annealed at temperatures

Mat. Res. Soc. Symp. Proc. Vol. 180. ©1990 Materials Research Society

below 800–850°C and is converted to carbon free SiO_2 at higher temperatures. It can be as thick as 4000Å without cracking and its uniformity over a 6 inch wafer can be better then 1%. The other SOG studied, the silicate type, contains much less carbon even after a 260°C anneal. However, thicker films of this type tend to crack. Therefore, its thickness is limited to the 1000-1500Å range. The silicate SOG discussed here contains 2% phosphorus to increase the material's immunity to cracking.

There are several processes occurring during the SOG film formation: polymerization, solvent evaporation, and out-diffusion of by-products. The result is a change in the chemical and structural characteristics of the material. These processes depend on the material properties and on the annealing conditions: temperature cycle, ambient and substrate. In this research, the maximum allowed anneal temperature is 450°C since the SOG is used to planarize structures with aluminum metallization. Ion implantation is found to affect the material properties in such a manner that it can be classified as an annealing technique. Upon impact, the impinging ions transfer their energy to the material atoms through a series of collisions. The result is a compositional and structural change due to the reordering of the material molecules. Solvent atoms which are still attracted to the SOG matrix also can be knocked away. The ion-implanted material differs from the original and the properties which are important for the material processing and its integration within a VLSI process are summarized here.

EXPERIMENTAL

The spin-on-glass materials under study were:

1. Allied 110 & 111 – polysiloxane type materials supplied by Diffusion Technology Allied Signal Ltd
2. Tokyo Ohka OCD-2P and Allied 112P – silicate type SOG.

The SOG was dispensed on single-crystal n-type, 100 silicon wafers and immediately baked on a hot plate at 80–120°C. The samples were then annealed at 180°C, 260°C and 450°C. The samples were implanted with phosphorus and silicon atoms with energy in the 40–190keV range and dose up to 1.65×10^{16} cm^{-2}. After the ion-implantation, the optical density and the thickness of the layers were characterized by a Rudolph Research and a Gaertner L-117 ellipsometers. Both systems use HeNe Lasers operated at 6328Å and computerized data transfer and analysis. The SOG thickness was also measured by the Tencor Alpha-Step profilometer using special patterns of SOG lines on silicon substrate.

Similar samples were prepared on high-resistivity ($> 5 \times 10^3 \Omega \cdot cm$) silicon wafers polished on both sides. The coated wafers were characterized by a Mattson Fourier transform infra-red (FTIR) spectrometer using a similar uncoated silicon wafer as a reference. The samples were tilted about 20° off the beam path to eliminate the interference effect due to internal multiple reflections inside the wafer.

Following optical characterization, aluminum dots were evaporated through a shadow mask, forming MOS capacitors with an area of about 2×10^{-3} cm^2. The capacitors were annealed at various temperatures, up to 450°C, in a N_2/H_2 (10%) ambient. The capacitance versus voltage characteristics were measured using an HP-4275 LCR meter and the data was transferred to an HP-9000/236 workstation for storage and analysis.

Implanted samples were used to study etching in a Buffered HF solution mixed 1:20 in water. The etching temperature was in the 18°C–21°C range. Similar

samples were etched in an argon plasma in a Physical Electronics model 590A using 1.5keV Ar^+ ion sputter etch. Simultaneous monitoring of the peak-to-peak height of the corresponding KLL Auger transition of Si, O, C and P was used to monitor the etching end point.

RESULTS

Ellipsometry: After the ion implantation, the appearance of that SOG film illuminated by white light changed from a blue colour, which is typical for ~1200Å thick SOG on silicon, to lighter blue, or transparent. This result indicates that the SOG film optical density or its extinction coefficient is changed by the implant. The raw ellipsometric data of Allied 110 SOG films implanted with silicon, phosphorus or both are summarized in Table 1.

Table 1: Ellipsometric characterization of ion-implanted Allied 110 SOG.

ion	dose (cm^{-2})	energy	Δ	ψ	n	d(Å)
none	–	–	89.11°	41.90°	1.362	1142
Si	10^{15}	70 keV	74.30°	39.20°	1.526	905
P	10^{15}	70 keV	74.49°	39.32°	1.525	912
Si + P	10^{15} each	70 keV	71.60°	36.50°	1.586	820

The rest of the results described here are limited to the phosphorus implantation. Ellipsometric data of the Allied 110 SOG implanted with 60keV phosphorus ions (Fig. 1) exhibit a continuous change of Δ as a function of the implanted dose. The data were analyzed assuming a single non-absorbing homogeneous film on the silicon substrate. The effective thickness and the effective refractive index were

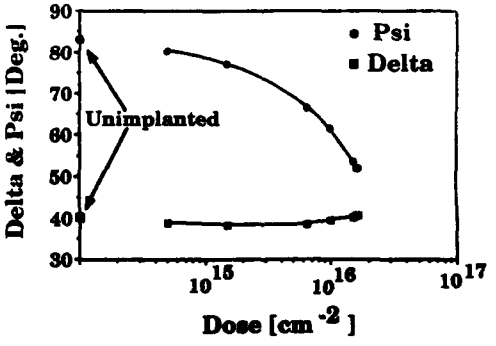


Fig.1: Ellipsometry results for the 60 KeV phosphorus implanted Allied 110 SOG.

calculated as a function of the dose. The implanted layer thickness, as measured by the Alpha-Step, agrees to within 10% with the thickness derived from the ellipsometer measurements. The effective thickness decreases with increasing dose, while the refractive index increases monotonously.

The results for the silicate type SOG show that the film thickness initially decreased with a low implant dose but increased with the dose in the 10^{15} - 1.65×10^{16} cm^{-2} range. The effective refractive index of the silicate decreases initially with the dose but in the 10^{16} cm^{-2} range it increases. 190keV phosphorus implanted polysiloxane and silicate SOG also change their colour and optical density. However, the effective values were almost independent of the dose in the $5 \times 10^{14} - 1.5 \times 10^{15}$ cm^{-2} range.

Infrared spectroscopy: The change in the IR spectrum due to the implant (Fig. 2) was more pronounced for the polysiloxane than for the silicate. The as-is polysiloxane absorption peak due to the Si-O bond stretching is at ~1030 cm^{-1} and it shifts to ~1010 cm^{-1} after 10^{15} cm^{-2}, 60keV phosphorus implant. The peak becomes wider and more symmetric after the implant. Another change due to the implant is the decrease of the absorption band due to $CH_3 - Si$ bond stretching at ~1200 cm^{-1} [2]. The water related absorption bands near 3500 cm^{-1} are slightly lower after the implant.

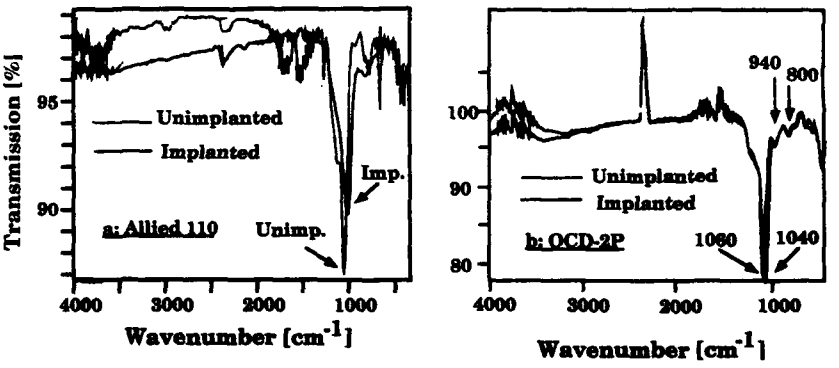


Fig. 2: Infra-red transmission spectra of a) polysiloxane (Allied 110) and b) silicate (OCD-2P) SOG.

The Si-O bond absorption peak at ~1060 cm^{-1} of the as-is silicate (Fig. 2b) is also shifted by about 20 cm^{-1} to ~1040 cm^{-1} after the implant. However, the overall shape of the Si-O absorption peak is only slightly changed. The small absorption band near ~1200 cm^{-1} remains almost unchanged after the implant while the Si-OH absorption peak near ~940 cm^{-1} is lowered.

Etching study: Typical etch rate in 1:20 BHF at 21°C is more than 2500 Å/min. for the polysiloxane and ~ 4000 Å/min. for the silicate. After the implant (60 keV,

phosphorus, 10^{15} cm^{-2}), the etch rate of the silicate SOG drops to $\sim$ 1200 Å/min. The ion implantation also reduces the polysiloxane etch rate in BHF. However, the etch is not linear with time; there is no measureable etching for the first 45 seconds. At about 1 minute, a very thin layer was detached and the SOG thickness started to decrease nonlinearly with etch time at an average etch rate of $\sim$ 200 Å/min.

The polysiloxane sputtering etch rate in argon plasma was 82Å/min and after a 10^{15} cm^{-2} 60 keV phosphorus implant it decreased to 68Å/min. The silicate sputtering rate was 49Å/min, under identical conditions and it increased slightly to 54Å/min after the 10^{15} cm^{-2}, 60 keV phosphorus implant.

Capacitance measurement: Aluminum/SOG/silicon devices with unimplanted SOG give conventional CV curves with a flat band voltage of about −0.7 Volts and a small hysteresis which depends on the maximum sweep voltage. The ion-implanted device capacitance was independent of the sweep voltage and it was about 30% lower than the oxide capacitance of the unimplanted MOS devices.

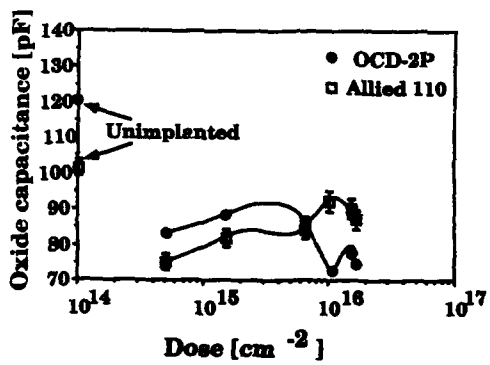


Fig. 3: The oxide capacitance (100KHz) as a function of the dose of 40KeV phosphorous ions implanted into SOG.

The maximum capacitance could be converted to a dielectric constant assuming that the SOG layer thickness is similar to the effective thickness as derived by the ellipsometric technique. The oxide dielectric constant has a slight dependence on the dose and it is about 30% lower than that of the unimplanted SOG layers.

DISCUSSION

The first issue to be discussed is interpretation of the ellipsometry results. The data is analyzed assuming a single transparent uniform layer on a silicon substrate. In the case of the 60KeV phosphorus implant, the ion range may be smaller than the layer thickness and part of the layer may be unchanged. In this case, the SOG film consists of a modified layer on top of an unmodified layer and should be analyzed as a two-layer structure. However, comparing the ellipsometry

results to the height measurement of SOG steps showed only a 10% difference. A different situation may occur at higher energy; we can assume a uniform SOG layer. For high dose, it is possible that the dose reaches the substrate and forms an amorphous silicon layer. In that case, analyzing the data assuming a uniform SOG layer on a thin amorphous layer on top of the single-crystal silicon may yield more accurate results.

The second issue is the interpretation of the infra-red transmission spectra. The results indicate that the ion implantation does change the material specific absorption peaks and therefore we may assume that there are structural and compositional variations. In the polysiloxane, there is a change in the Si-O bond absorption peak which indicates a different distribution of those bonds. There is also less $Si\text{-}CH_3$ related absorption which indicates the annealing effect of the implant.

The compositional and structural changes of the ion-implanted SOG results in a reduction in the etch rate in BHF. This fact can also be explained by assuming that after the implant the material is denser and less porous. Also there is a decrease in the dielectric constant which suggests a different molecular arrangement. The last two results are important for the integration of such SOG films into an integrated circuit technology.

CONCLUSION

The ion implantation is shown to change the material properties of both SOG types studied. The change in the film characteristics can be monitored by ellipsometry, assuming a single transparent layer on silicon. However, a multi-layer model is required for more accurate results. Changes in the molecular bonding absorption due to the implant are observed by infra-red spectroscopy. These changes are similar to those observed after elevated temperature annealing. Therefore, the ion-implantation technique of SOG formation is suggested as a low temperature annealing process. The ion-implant also affects the material stress which is of great concern for the overall integrated circuit reliability. The etch rate in BHF of the implanted SOG can be lowered to a value such that it would be compatible with CVD oxide for a multilayered structure. The ion-implanted SOG capacitors have lower capacitance than unimplanted devices. This is important for applications where the multi-level interconnect delay time is of concern. In summary, ion implantion into SOG results in a material with interesting properties that should be investigated.

ACKNOWLEDGMENT

This research was partly sponsored by National Semiconductor Inc. The authors wish to thank A. Peer, the Technion - I.I.T , I. Rotstein, and E. Teerosh, National Semiconductor Inc., and Liang-Yuh Chen and J. Keddie, Cornell University, for their technical support. In addition, the authors wish to thank Prof. N. MacDonald, Cornell University, for his support and S. Kugelmass and Miss C. Kuhl for their help in preparing the manuscript.

REFERENCE LIST

[1] F. Dupuis, W.G. Oldham, and Y. Shacham-Diamand, VLSI Symposium, 52 (1985).

[2] P. Pai, A. Chettey, R. Roat, N. Cox and C. Ting, J. of Electrochemical Society, 11, 2830 (1989).

[3] Y. Shacham-Diamand and I. Nachumovski, J. of Electrochemical Society, 137, 190 (1990).

CHEMICAL SYNTHESIS OF ALUMINUM NITRIDE POWDERS

PHILLIP R. COFFMAN*, WILLIAM T. PETUSKEY*, AND SANDWIP K. DEY**
*DEPARTMENT OF CHEMISTRY
**DEPARTMENT OF CHEMICAL, BIO, AND MATERIALS ENGINEERING
ARIZONA STATE UNIVERSITY, TEMPE, AZ 85287

ABSTRACT

An organoaluminum precursor was synthesized by a low temperature reaction and characterized by NMR, FTIR and mass spectrometry. This compound was pyrolyzed under several experimental conditions to obtain aluminum nitride powders. The pyrolyzed products were subsequently characterized by XRD and SEM. The mechanisms of precursor development and subsequent pyrolysis are discussed.

INTRODUCTION

Aluminum nitride, AlN, is a ceramic being developed for use in the electronics industry as a substrate material for VLSI packaging [1]. The current method of substrate production involves dispersing AlN powders in a slurry, tape casting into green sheets, electroding, stacking and co-firing. The powders used in this process are usually synthesized by the direct nitridation of aluminum or the carbothermal reduction of alumina. There are several detriments to these powders; they contain residual reactants (alumina, carbon, or aluminum) and they have large and irregular particle sizes, making them difficult to densify.

The synthesis of AlN powders by chemical methods offers the distinct advantage of being able to control the morphology and size distribution of the powder. Several groups have made aluminum nitride powders by the pyrolysis of organometallic precursors [2-4].

The precursor chosen for pyrolysis in this study was dimethylaminoalane, $AlH_2N(CH_3)_2$. It was first synthesized by Wiberg and May [5] in 1955 and then by Ruff and Hawthorne in 1960 [6]. It is formed in high yields (63-89%) from the reaction of lithium aluminum hydride, $LiAlH_4$, and dimethylamine hydrochloride, $[NH_2(CH_3)_2]Cl$.

$$LiAlH_4 + [NH_2(CH_3)_2]Cl \longrightarrow AlH_2N(CH_3)_2 + 2H_2 + LiCl$$

Dimethylaminoalane was reported by Wiberg to have a melting point of 89 - 90°C, to decompose at around 130°C, and to sublime under vacuum at 40 - 60°C. There is a discrepancy between Wiberg and Ruff as to what is the degree of association in solution. In diethylether, Wiberg stated that it was 2.16, and in benzene 2.36. Ruff reported that the degree of association is 2.99 in benzene. A mass spectral study was done of this compound and it was found to be trimeric in the gas phase [7].

There are a number of reasons why dimethylaminoalane was selected as the precursor to aluminum nitride. First, aluminum-nitrogen bonds are formed quite readily at a low temperature. The ease of formation of amine adducts to aluminum is Al-H > Al-C > Al-X where X is a halogen. Dimethylaminoalane is quite volatile and thus can be easily purified by sublimation. The theoretical ceramic yield of aluminum nitride from dimethylamionoalane is 56.1%. In solution, the trimeric form already has formed the six-membered ring that is found in the wurtzite structure of aluminum nitride (Fig. 1). Consequently, polymerization at low temperatures followed by pyrolysis could be a facile, alternative low temperature route to dense, monolithic AlN, thus completely bypassing the powder processing step.

This paper discusses a route to the synthesis of aluminum nitride powders via the pyrolysis of dimethylaminoalane.

Mat. Res. Soc. Symp. Proc. Vol. 180. ©1990 Materials Research Society

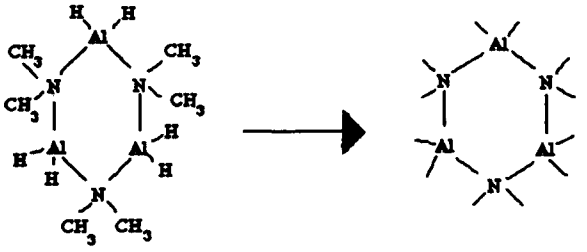


Fig. 1: The Conversion of Dimethylaminoalane to Aluminum Nitride

EXPERIMENTAL

Organoaluminum compounds are quite water and oxygen sensitive. In all procedures, standard Schlenk techniques were used for maintaining an inert atmosphere of purified nitrogen from a gettering system that provides gas with less than 1 ppm each of O_2 and H_2O. A glove box was utilized for solids transfers and filtering.

Diethylether was the chosen solvent since $LiAlH_4$ is very soluble in it; also it is less likely to leave decomposition residues than other solvents due to its high volatility. This solvent was purified by distilation under N_2 with the highly efficient water and oxygen scavenger sodium-benzophenone.

Lithium aluminum hydride solutions were prepared by dissolving purified $LiAlH_4$ into the H_2O and O_2-free diethylether. This solution was filtered over a bed of celite (a diatomaceous earth) in a fritted glass funnel. Then they were standardized before use by measuring the evolved hydrogen from the hydrolysis reaction with reagent grade butanol. A specially designed inert atmosphere manometer was used for this task.

In the glove box, 300 ml of 0.5207 M $LiAlH_4$ was measured in a graduated cylinder. Dimethylamine hydrochloride was weighed to 12.7208 g and transferred to a Schlenk tube. This left $LiAlH_4$ slightly in excess. The solid was added to the reaction flask, maintained at -10°C by a diethyleneglycol slush bath, over the course of 1.0 hr. This was left for 0.5 hr. until no H_2 gas was evolved and warmed to room temperature over a period of 2.0 hr. The LiCl was filtered the same manner as the $LiAlH_4$. Ether was evaporated from the solution to yield a wet white powder. This was transferred to a sublimation vessel and was sublimed for 2.0 hr in an oil bath maintained at 60°C. A vacuum of 3×10^{-4} torr was used and a cold finger of dry ice/acetone (-70°C) condensed the vapor. The yield of sublimed product was 6.0196 g (76.8%). The product was characterized by NMR by dissolving into dueterated benzene (Fig. 2). An infrared spectrum was taken and mass spectrum was performed on the sample.

From this point, the thermal processing of the precursor went two routes. In the first route, monomeric dimethylaminoalane was pyrolyzed at 470°C. The heating rate was 6.5°C/min, and a flow of N_2 at 10 cc/min was used.

In the second route, dimethylaminoalane was polymerized in order to observe the effect of an extended Al-N bond network on the resulting powder. This was accomplished by dissolving 2.6776 g of the monomer in approximately 400 ml of xylenes which were dried over molecular sieves before use. This solution was then refluxed under nitrogen for 2.5 hr. at 136°C. A grey powder was formed and filtered in a medium fritted funnel; the yield was 0.4950 g. The powder was left to dry in the glove box overnight and then was heated under a 10 cc/min flow of nitrogen to 1200°C at a rate of 6.5°C/min., held for 2.0 hr and cooled to room temperature.

RESULTS AND DISCUSSION

The NMR spectrum of dimethylaminoalane is given below (Fig. 2). Singlets of the methyl protons are seen at 2.80 and 2.21 ppm and the singlets due to the hydride protons are observed at 1.22 and 0.87 ppm. The quartet centered at 3.25 and the triplet at 1.10 ppm indicate the presence of an ethyl group, which is undoubtably due to diethylether. Since the product underwent sublimation, it is doubtful that the ether is a result of the product not being dry; most likely, an ether adduct is formed. The formation of such an adduct is not mentioned in the literature, but oxygen containing groups often replace nitrogen in nitrogen- bridged oligomers [8].

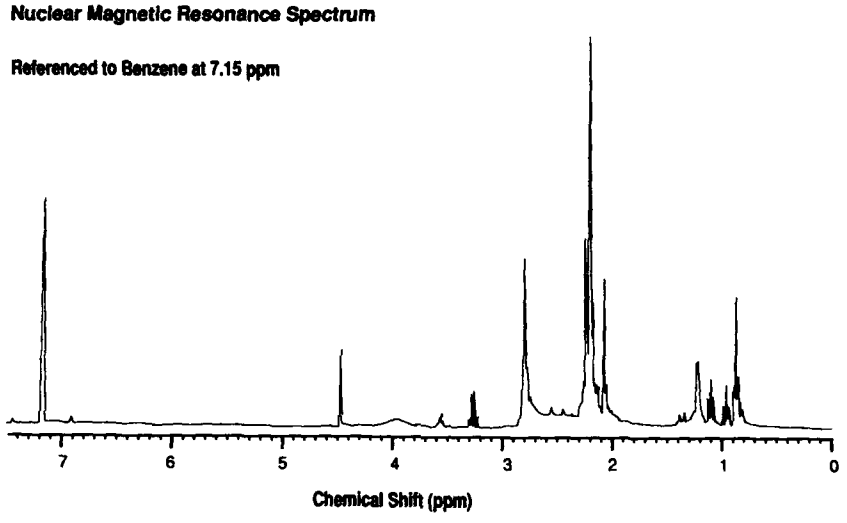


Fig. 2: ^1H NMR Spectrum of Dimethylaminoalane

The mass spectrum of the sample was in agreement with Yee and Ehrlich with the exception of some small peaks above mass 219 possibly due to residual lithium and chlorine. Also, the intensity of mass 145 doubled possibly due to the ether adduct ion $H_6C_2NAlH{\cdot}C_4H_{10}O^+$.

In the thermal processing of monomeric dimethylaminoalane, a white smoke formed at low temperature (ca. 100°C) and adhered to the sides of the quartz reaction tube. At higher temperatures a black powder formed and was analyzed by X-ray powder diffraction to be metallic aluminum.

In the polymeric processing route, 0.2030 g of a dark grey powder was formed after pyrolysis from an initial weight of 0.2688 g of the polymer, which was a 75.5% yield. This was analyzed to be AlN by powder X-ray diffraction (Fig. 4).

The infrared spectrum of dimethylaminoalane, in accord with its structure, shows five distinct regions (Fig. 3 A). The C-H stretch at 2960 cm^{-1} is due to the methyl groups. The Al-H stretch at 1860 cm^{-1} is indicative of a N-bridged alane. At 1510 cm^{-1} and at 1380 cm^{-1} is observed C-H bending and the C-N stretch respectively. The Al-N stretch is seen as a broad band from 1200-500 cm^{-1}. The spectrum of the polymerized precursor (Fig. 3 B) shows that a N-H stretch appears, probably due to a cross-linked N-H bond in the polymer. The Al-H band disappears and the C-H bands diminish, which indicates that hydrogen is the first specie evolved in the condensation. The C-N band is present,

indicating that carbon is still included in the polymer, and the Al-N region broadens. In the spectrum of AlN (Fig. 3 C), the C-N band is still visible, which indicates carbon is present. The N-H band increases and a small band at 1600 cm^{-1} due to N-H or O-H appears [10]. These data indicate that water has reacted with the AlN surface.

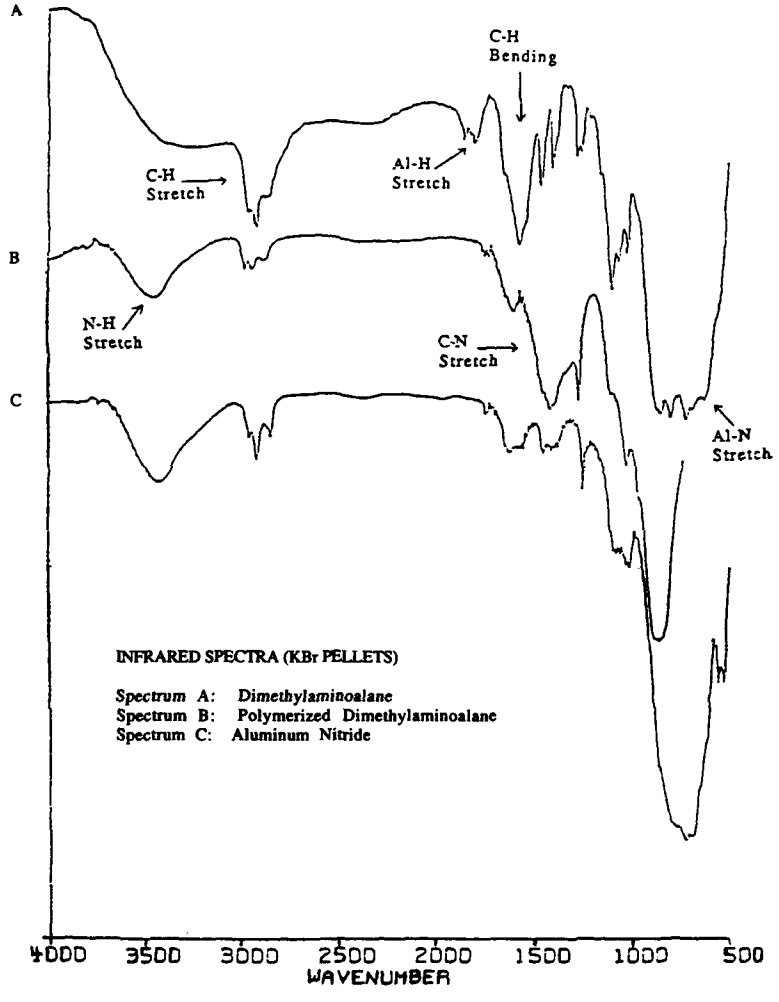


Fig. 3: Infrared Spectra of Dimethylaminoalane Monomer, Polymer, and Aluminum Nitride

The X-ray powder diffraction pattern (Fig. 4) shows that the oxygen stabilized cubic phase of AlN is a major impurity phase. This spinel has an unknown oxygen content up to a maximum of 34% for aluminum oxynitride, Al_3O_3N. The appreciable oxygen content is most probably due to the ether adduct and also due to the formation of water in the quartz reaction tube since sialon deposits were formed on the wall of the tube. No Al_4C_3 or Al_2OC (isostructural with AlN) phases are observed.

X-Ray Powder Diffraction

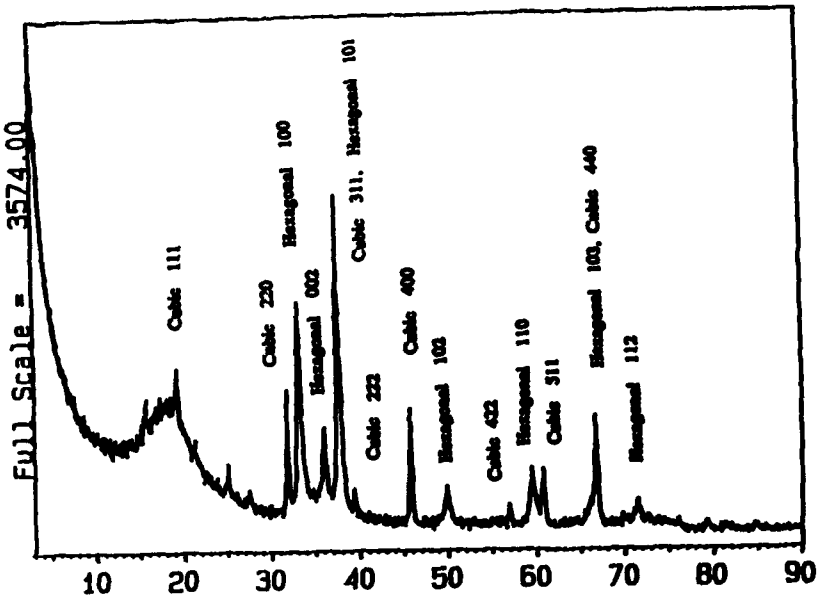


Fig. 4: X-ray Powder Diffraction Pattern (10 scans)

A scanning electron microscope was used to study the morphology and particle size of the powder. The below micrograph (fig. 5) shows a very porous structure with grain sizes of 0.2 microns and less.



Fig 5: Scanning Electron Micrograph of a Crushed Agglomerate

CONCLUSIONS

Dimethylaminoalane was synthesized and characterized by NMR, FTIR and mass spectrometry. Pyrolysis of the monomer yielded metallic aluminum, while the polymerized precursor yielded aluminum nitride. Carbon and oxygen impurites were detected by FTIR and X-ray diffraction, respectively.

ACKNOWLEDGEMENTS

The X-ray data were obtained on equipment purchased under NSF grant number DMR-8406823. NMR spectra were obtained on a Varian Gemini 300 purchased with funds from the NSF chemical instrumentation grant number CHE-8813109. Electron microscopy and IR spectroscopy were performed with instruments provided by the Center for Solid State Electronics Research.

REFERENCES

1. R. R. Tummala, Am. Ceram. Soc. Bull. 67 [4], 752 (1988).

2. L. Maya, Advanced Ceramic Materials 1, 150 (1986).

3. A. Ochi, W.E. Rhine, and H.K. Bowen in Better Ceramics Through Chemistry III, edited by C.J. Brinker, D.E. Clark, and D.R. Ulrich (Mater. Res. Soc. Proc. 121, Pittsburgh, PA 1988) pp. 663-666.

4. L.V. Interrante, L.E. Carpenter II, C. Whitmarsh, and W. Lee in Better Ceramics Through Chemistry II, edited by C.J. Brinker, D.E. Clark, and D.R. Ulrich (Mater. Res. Soc. Proc. 73, Pittsburgh, PA 1986) pp. 99-114.

5. E. Wiberg and A. May, Z. Naturforsch 10B, 229 (1955).

6. J.K. Ruff and M.F. Hawthorne, J. Amer. Chem. Soc. 82, 2141 (1960).

7. D.Y. Yee and R. Ehrlich, J. Inorg. Nucl. Chem. 27, 2681 (1965).

9. Wiberg, p.235.

10. L.H. Little, Infrared Spectra of Adsorbed Species, (Academic Press Inc., New York, 1966), pp. 228-273.

PART X

Structure/Properties II: Optical

GRIN ROD OF LARGE DIAMETER AND LARGE DELTA-N

MASAYUKI YAMANE, ATSUO YASUMORI, MITSUNOBU IWASAKI AND KAZUTAKA HAYASHI
Tokyo Institute of Technology, Dept. of Inorganic Materials, 2-12-1, Ookayama, Meguro-ku, Tokyo 152, JAPAN

ABSTRACT

A gradient-index glass rod of about 13 mm in diameter and 20 mm in length with the refractive index difference of about 0.05 between center and perimeter has been prepared by the sol-gel process from a precursor solution consisted of tetramethoxysilane, tetraethoxysilane, boron ethoxide and aqueous solution of lead acetate. A bubble free wet gel of about 35 mm in diameter and 50 mm in length was obtained by adding acetic acid to the precursor solution as a buffering agent. The liquid in the micropores of the wet gel was totally replaced with acetone. Then the compositional gradient of lead was formed in radial direction of the gel by soaking in an ethanolic solution of potassium acetate. A transparent r-GRIN rod of about 10 mm in diameter was obtained by the sintering of the gel at 580°C.

INTRODUCTION

A gradient index (GRIN) glass rod having a continuous variation in refractive index, particularly those having a large diameter with large delta-n , is one of the materials which are advantageously produced by the sol-gel process over conventional methods [1]. The preparation of r-GRIN rods of about 7 mm in diameter with delta-n of about 0.04 was possible by the sol-gel process using an aqueous metal salt solution as a source for index-modifying cations [2]. The method which was developed by the authors is potentially applicable to the production of a material having a diameter larger than 10 mm with delta-n of 0.05 or more, although the technique has not yet been established. The problems to be solved in this method in order to produce a GRIN material of this size are inclusion of bubbles during casting of a sol, migration of index-modifying cations during drying, deformation of a gel in the initial stage of drying due to its own weight, and the onset of fracture during drying.

This paper reports the study on the elimination of these problems in order to establish the procedure for the production of r-GRIN rod having a diameter larger than 10 mm with delta-n of 0.05, which is hardly attainable by the conventional process of GRIN preparation such as ion-exchange, molecular stuffing, and so on [3].

The main techniques introduced in the modification were; (1) the introduction of acetic acid in the precursor sol as a buffer to control gelling time for the elimination of bubble inclusion, (2) total replacement of water in a gel with acetone prior to the formation of concentrational gradient of lead, in order to minimize the distortion of the formed concentrational profile due to the migration of lead ions and to eliminate the deformation of the gel upon drying, (3) the employment of ethanolic solution of potassium acetate as a source for

Mat. Res. Soc. Symp. Proc. Vol. 180. ©1990 Materials Research Society

potassium ion, and (4) the total replacement of acetone for ethanol after the formation of concentrational profile of lead.

EXPERIMENT

Gel preparation

The experiment was carried out on the precursor sol corresponding to a glass of the composition $26PbO-7B_2O_3-67SiO_2$ (mol%) using tetramethoxysilane (TMOS), tetraethoxysilane (TEOS), triethoxyboron ($B(OET)_3$), and aqueous lead acetate solution (aq- PbAc) as starting materials. Aqueous lead nitrate solution which was employed in the previous work [1-2] to control gelling time was not used due to high solubility to ordinary solvents.

A mixture of 30 ml of TMOS , 30 ml of TEOS and 12.4 ml of $B(OET)_3$ was hydrolyzed with 25 ml of aqueous HCl solution of pH=2. The mixture was then added to 107.6 ml of 1.25 mol/l aq-PbAc at the existence of 5-20 ml of acetic acid and stirred for 2.5 min. The eventual solution , a sol, was casted in a polypropylene vial of about 35 mm inside diameter up to the depth of about 50 mm. Gelling time and its relation with bubble formation was observed on the sol at room temperature with a cover of aluminum foil.

Pretreatment of a wet gel

A wet gel formed in a polypropylene vial was subjected to pretreatments prior to the formation of concentrational gradient, in order to enhance gel strength and to replace acetone for water in the micropores.

The enhancement of gel strength which was necessary to keep the gel monolithic throughout the process and to avoid the deformation during drying, was made by aging at both 30°C for 1-7 days and 60°C for 1-3 days. The desirable conditions of aging was discussed on the basis of the measurements on volume shrinkage of the gel and the separation of lead ions by syneresis.

The conditions for the complete replacement of acetone for water in the micropores which was necessary to hinder the migration of lead ions and the deformation of a gel during drying was investigated from the point whether coarse crystals of lead acetate was formed on gel surface or not when the aged gel was soaked at 30 C for 2 days in a bath of isopropanol-acetone system of various compositions, i. e., i-PrOH/AcOH = 80/20, 50/50, 20/80, 0/100 . The volume of the solution in the bath was kept at 50 ml, approximately the same as the volume of a gel.

Formation of concentration gradient of lead

After the total replacement of acetone for the liquid in the micropores ,a wet gel containing fine crystals of lead acetate on micropore wall was soaked in 0.61 mol/l ethanolic solution of potassium acetate at room temperature for 2-48 h.

During this treatment, the concentration gradient of lead ions was formed in the radial direction by the gradual dissolution of the precipitated fine lead acetate crystals and subsequent diffusion of lead ions through micropores. The gel was then transferred to a bath of isopropanol-acetone system for the complete removal of the intermingled ethanol and reprecipitation of the dissolved lead acetate crystals during treatment.

Drying and sintering

The gel thus treated was placed on a teflon sheet in a glass container and covered with an aluminum foil. The drying was made by slowly evaporating acetone through a pin-hole formed on the aluminum foil. At the end of drying, the gel was about 20 mm in diameter and 30 mm in length and free from crack.

The dried gel was placed in a fused quartz reaction tube which was, in turn, placed holizontally in an electric furnace, and subjected to the heat treatment for densification. The heat treatment consisted of a 5°C/h ramp in temperature from room temperature up to 580°C with 24 h isothermal treatments at 200°C, 360°C, 460°C, 510°C, and a 48 h isothermal treatment at 580°C . Oxygen gas was fed into the reaction tube at a rate of about 60 ml/min up to a temperature slightly above 460°C , at which point helium was substituted for oxygen for the remainder of the heating cycle. At the and of the 580°C treatment, the temperature was reduced to room temperature at a rate of 60°C/h.

Chemical analysis of solution separated from a gel during aging

The amount of lead and boron ions excluded from a gel by syneresis during aging was measured by emission spectroscopy with inductive coupling plasma (ICP) method. After the predetermined time of aging, whole the solution separated by syneresis was collected by pouring it in a glass container and diluted to the level of 10 ppm in the weight of B and Pb, followed by subjecting to the measurement.

Measurement of lead concentration and refractive index profile of glass

The measurement of the distribution of lead concentration in the gel-derived glasses was made by energy-dispersive spectroscopy for X-ray quanta (EDS). Discs of lead silicate glasses of about 1 mm thickness were cut out of the central part of the cylindrical sample glasses. The glass disc polished plane parallel was coated with carbon and subjected to the measurement by EDS under acceleration voltage of 20 kV through the slit at an angle of 30°.

The profile of refractive index of the gel derived glasses were determined by measuring the reflectivity at various points on the surface of the same sample glasses used for EDS measurement.

RESULTS AND DISCUSSION

Effect of acetic acid on the gelling time and volume shrinkage

The gelling time of a sol increased with the increasing amount of acetic acid as it is shown in Fig. 1. All the samples containing more than 1 mol of acetic acid per mol of lead acetate, i. e., 8.5 ml AcOH per precursor solution, whose gelling time was longer than 15 min , turned to bubble free cylindrical gels of 35 mm in diameter and 50 mm in length. But those containing less amount of acetic acid included many bubbles due to too short gelling time.

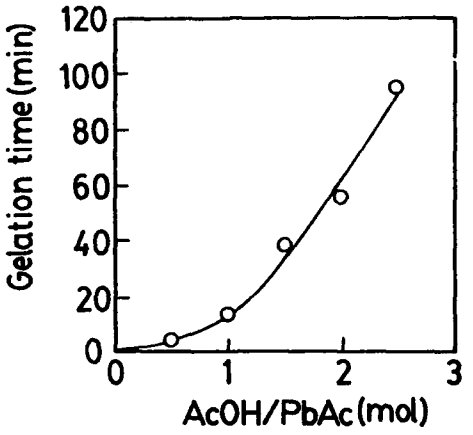


Fig. 1. Buffering effect of acetic acid on gelling time.

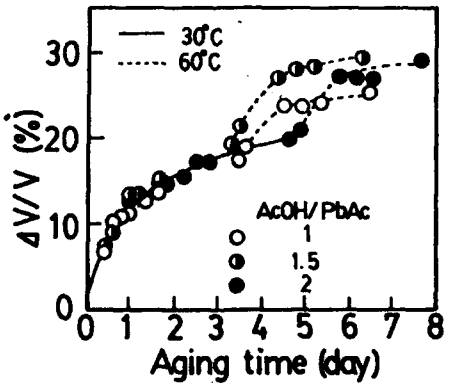


Fig. 2. Volume shrinkage of a gel during aging.

As acetic acid is necessary only as buffering agent, it is better to remain with the introduction of minimum amount to get bubble free gels. Then , in order to assure of the homogeneous mixing and to allow further scaling up to larger gels, the introduction of about 2 mol of acetic acid per mole of lead acetate, i. e., 15 ml per precursor solution, which gives the gelling time of about 1 h is considered to be appropriate.

The change in the volume of these gels by syneresis during aging at 30°C and subsequent holding at 60°C is shown in Fig. 2. It is known that the change is the same for all the samples without regard to the amount of introduced acetic acid. The rate of shrinkage at 30°C decreased gradually with time and became very low after 3-5 days, at which points the temperature was raised to 60°C for further aging.

The gels subjected to the aging at both 30°C and 60°C were strong enough to remain monolithic throughout the handling in the subsequent treatment, but those aged at 30°C alone were not strong enough.

Loss of lead ions during treatments

The lead ions excluded from a gel by syneresis was proportional to the volume shrinkage of the gel without regard to the amount of introduced acetic acid. This relationship, which manifests the non-incorporation of lead ions in skeletal structure, is shown in Fig. 3. It should be noted from Figs. 2 and 3 that about 30% of the introduced lead ions is lost if all the separated liquid is poured-off after aging at 60°C.

The circles in Fig. 4 depict the results for the soaking of gels in the solutions of isopropanol-acetone system after the aging at 60°C. That is, the gels subjected to the soaking in the solution containing acetone more than 40 %, which are represented by the closed circles in the figure, resulted in the formation of coarse crystal of lead acetate on gel surface and disintegrated in several pieces. The loss of lead ions from such gels is represented by the vertical axis of the figure. On the other hand, gels soaked in the solution containing isopropanol more than 40 %, which are represented by open circles did not result in the formation of coarse crystals and remained monolithic, although additional loss of about 30 % of lead ions was inevitable.

The formation of coarse crystals in the solution of high acetone content, which was remarkable for the gel containing large amount of acetic acid, is attributed to the low solubility of lead acetate to acetone, i. e., 1.2×10^{-4} mol/l at 30°C compared with 5.4×10^{-3} mol/l for iso-propanol. That is, when a gel is immersed in the solution of isopropanol-acetone system, the interdiffusion between the solution and the liquid filling micropores of the gel takes place in the vicinity of gel surface. As the liquid comes out of the gel contains large number of lead ions and acetate ions, the solution of high acetone content is easily supersaturated, leading to the nucleation of lead acetate crystals at gel surface. And the nucleated crystals further grow to coarse ones by the supply of lead and acetate ions from the liquid in the micropores.

On the other hand, if the acetone content is not very high, the solution is not supersaturated so easily. Once the interdiffusion between the solution and the liquid in the pores takes place without causing nucleation at gel surface, the solution

can continuously penetrate in the gel by gradually increasing its concentration with time. And after a prolonged time, most of the liquid in the micropores of the gel is replaced with the solution of isopropanol-acetone system, leading to the precipitation of fine lead acetate crystals on the micropore wall.

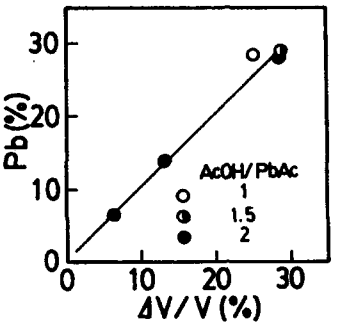


Fig. 3. Reration between loss of introduced lead ions and volume shrinkage.

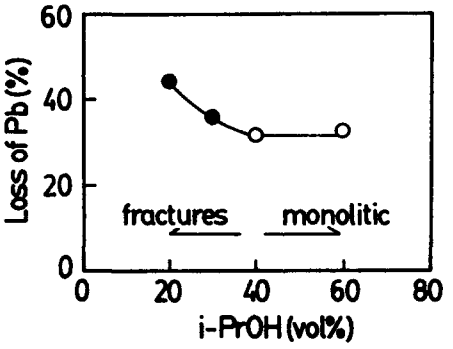


Fig. 4. Loss of lead ions by soaking in the solution of isopropanol-acetone system.

Since the crystallization tendency is enhanced by the existence of large number of acetate ions, it is better to extract acetic acid from the aged gel first, and then replace acetone from the solution which comes in the gel during treatment, in order to avoid the formation of coarse crystals at gel surface.

The treatment of a gel for the extraction of acetic acid without decreasing lead content will be made by soaking the gel in a solution of isopropanol-water system saturated with lead acetate. The replacement of acetone for the solution of isopropanol-water system which comes in the gel by this treatment should be made in several steps starting with the soaking in a solution of isopropanol-acetone system of low acetone content.

The flow chart of the treatment determined on the basis of the above discussion is shown in Fig. 5. That is, a gel formed from the precursor sol containing 2 mol of acetic acid per mol of lead acetate was aged at 30°C for 5 days and then transferred in 50 ml bath of isopropanol-water system (iso-PrOH/H_2O = 80/20 in vol) saturated with lead acetate to be soaked at 60°C for 2 days for the purpose of further aging and the extraction of acetic acid without reducing lead content. The gel, then, is soaked successively in baths of isopropanol-acetone system of the compositions iso-PrOH/AcOH = 80/20, 50/50 , 0/100 (in vol) at 30°C for 2 days, respectively, in order to replace acetone totally for the liquid in the micropores.

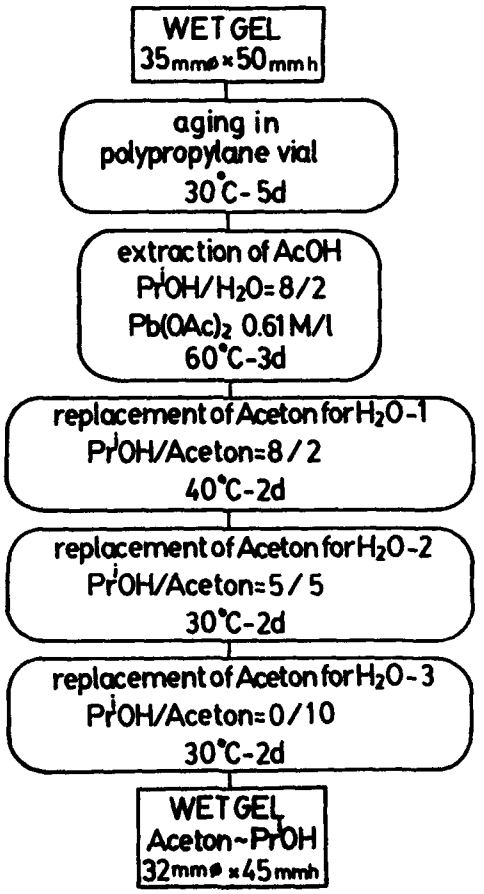


Fig. 5. Flow chart of treatment for the complete replacement of acetone for water.

The latter steps for the total replacement of acetone for the liquid in micropores were also introduced for the maintenance of the profile of lead concentration formed by the following soaking of the gel in ethanolic solution of potassium acetate.

Profiles of lead concentration and refractive index

Glasses obtained by immersing gels in ethanolic solution of potassium acetate for various length of time after the treatment according to the flow in fig. 5, subsequent replacement of acetone for ethanol, and drying and sintering according to the prescribed heating cycle were about 13 mm in diameter and 20 mm in length. They were clear, transparent and free from bubbles. The profiles of lead concentration in radial direction in these glass rods are shown in Fig. 6.

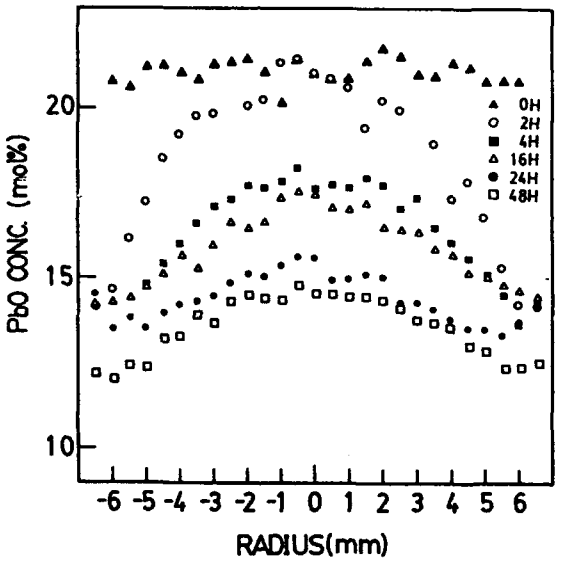


Fig. 6. Profile of lead concentration in the radial direction of gel-derived glass rods.

It is known from the figure that the concentration of lead decrease to the level of 20 mol% in PbO by the pretreatments of a gel prior to the formation of concentration gradient. The parabolic concentration profile of lead was formed by the soaking for 4 h with the concentration difference of about 5 mol% between center and perimeter, which decreased with time went on.

The difference in the refractive index between the center and perimeter of the glass obtained by the soaking for 4 h was about 0.05 as it is known from Fig. 7. The delta-n of 0.05 is the largest among those reported for the r-GRIN glass rods of the diameter larger than 10 mm. By the elaboration on the optimum conditions of the soaking for the formation of concentration gradient of lead, further improvement of delta-n will be possible.

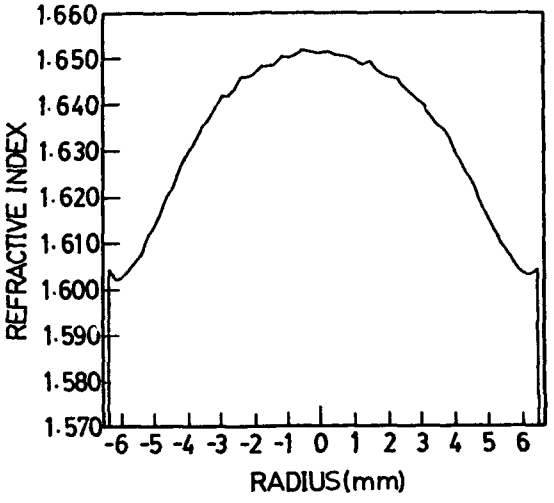


Fig. 7. Profile of refractive index of GRIN rod obtained by soaking in aq-KOAc for 4 h.

REFERENCES

1. M. Yamane, J. B. Caldwell and D. T. Moore, J. Non-Cryst. Solids, 85, 244 (1986)

2. M. Yamane, H. Kawazoe, A. Yasumori and T. Takahashi, J. Non-Cryst. Solids, 100, 506 (1989)

3. M. Yamane, to be published in the proceedings to the 4th International Symposium on Ultrastructure Processing.

STUDIES ON THE REPRODUCIBLE PRODUCTION OF GRIN (GRADIENT INDEX) GLASS RODS BY A SOL-GEL PROCESS

J. Brian Caldwell, Tessie M. Che, Richard W. Cruse, Robert M. Mininni, Randall E. Nikles, Victor N. Warden and Mark A. Banash, Enimont America Inc., 2000 Cornwall Road, Monmouth Junction, NJ 08852

ABSTRACT

Optical quality radial gradient-index (GRIN) glass can be made by first leaching a TiO_2-Al_2O_3-SiO_2 gel in aqueous sulfuric acid solution, then drying and firing the gel. In this paper, we present details of a study on the reproducible production of GRIN glasses by this sol-gel process. Physical and optical data on the intermediate gels and resulting gradient-index glass will be discussed.

INTRODUCTION

A sol-gel technique has been used recently to make radial gradient index glass rods of good quality with the TiO_2-Al_2O_3-SiO_2 system [1]. The technique involves acid-leaching a multicomponent silicate gel to create a radial composition gradient of TiO_2 within the gel. This gel is then fixed, dried and sintered to make gradient-index glass. The product is highly refractory, has a very low coefficient of thermal expansion and possesses optical properties suitable for use in imaging arrays and fiber optics. In this paper, we address the problem of refractive index profile reproducibility.

EXPERIMENTAL PROCEDURE

A TiO_2-Al_2O_3-SiO_2 gel was synthesized using an established procedure [1] for preparing multicomponent silicate gels from metal alkoxides. Tetramethoxysilane (Huls Petrarch Systems), methanol, N,N-dimethylformamide (Fisher), titanium isopropoxide and aluminum di(sec-butoxide)acetoacetic ester chelate (Alfa Products) were used without further purification. With vigorous stirring, 118.5 ml (0.796 moles) of tetramethoxysilane (TMOS) were added to a solution containing 191.3 ml (4.723 moles) of methanol and 191.3 ml (2.47 moles) of N,N-dimethylformamide in a 1000 ml round-bottom flask. After 20 minutes, 14.4 ml of 0.1M HCl were added to the reaction mixture. After 30 minutes, a mixture consisting of 13.6 ml (0.046 moles) titanium isopropoxide ($Ti(OC_3H_7)_3$) and 28.52 g (0.094 moles) of aluminum di(sec-butoxide) acetoacetic ester chelate was added, and the hydrolysis and polycondensation reactions were allowed to proceed for one hour. Finally 53.7 ml (2.98 moles) of water

Mat. Res. Soc. Symp. Proc. Vol. 180. ©1990 Materials Research Society

were added to complete the reaction. Gelation occurred within several hours at room temperature.

REPRODUCIBILITY STUDY

Two separate batches of solution were prepared, each having a volume of 611.4 ml. Twenty (20) cylindrical gel rods, each 15 x 96 mm long, were made from each batch by casting the material in polypropylene centrifuge tubes. All gel rods were treated during the leaching and fixing steps in the following manner. After a gelation period of approximately 2 to 3 hours, the samples were allowed to age for 24 hours at 25°C and then at 60°C for 24 hours. The gels were allowed to cool to 25°C over a 24 hour period and then were transferred to 25 x 120 mm Pyrex tubes filled with 50 ml 3.0 *M* aqueous H_2SO_4. After leaching with gentle agitation for 24 hours, the acid leaching media was decanted off. The gels were then "fixed" (i.e., the leaching was arrested) by the addition of 50 ml methanol to each test tube and the systems were then gently agitated for three (3) days. This fixing step was repeated twice with fresh methanol and with a reduced agitation period of two (2) days. The gels were then dried at 60°C for 24 hours. Next the gels were calcined in a box furnace where the temperature was gradually raised from 25°C to 180°C at 0.3°C/minute, from 180°C to 400°C at 0.7 °C/minute and finally from 400°C to 550°C at 1°C/minute. After 24 hours the samples were allowed to cool back to 25°C before final sintering. This was carried out by placing the samples on a platinum gauze substrate inside a quartz tube in a tube furnace. The samples were heated in air to 1100°C at 60 °C/minute from 25°C, then to 1400°C at 40°C/minute and finally to 1500°C at 20°C/minute. Once 1500°C was reached the furnace was shut off. By this point the samples had densified into transparent GRIN rods. The exact furnace temperature distribution was not known, but since all glasses were fully sintered and the components in the glasses are not mobile this was not considered important.

OPTICAL CHARACTERIZATION

Refractive index profiles were measured by Mach-Zehnder interferometry using a HeNe laser (wavelength = 632.8 nm). The samples were prepared by cutting a thin (≈2

mm) wafer perpendicular to the cylindrical axis of each GRIN rod. The wafer was then ground and polished on both sides using conventional techniques to a surface accuracy of better than 1/4 wavelength. Figure (1) shows a typical interferogram. Each line, or fringe, in the interferogram represents a region of constant refractive index.

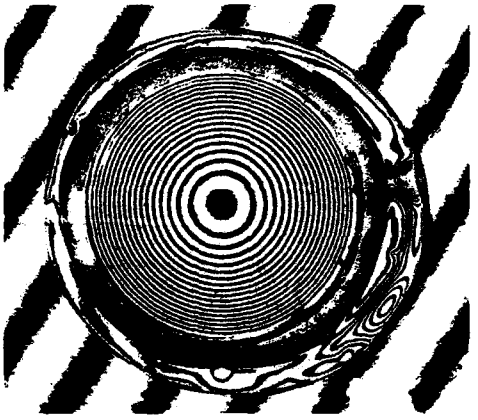
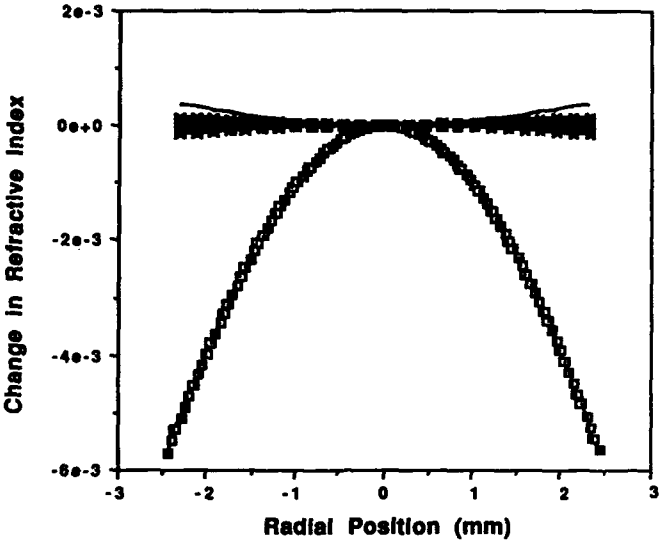


Figure 1 - Typical Lens Interferogram

The change in index between two adjacent fringes is given by $\Delta n = \lambda/t$, where Δn is the index change, λ is the wavelength, and t is the thickness of the sample. Index profiles were determined by first manually measuring the position of each fringe along a line passing through the center of the interferogram. This raw data is subject to error due to wedge in the sample and/or a misplaced origin, so it was processed by fitting to an even order polynomial with an added linear term, changing the origin until the RMS error of the polynomial fit was minimized (see figure 2).

Sample wedge was then assumed to be represented by the linear term in the fit, and was subtracted from the data. Profile difference plots were determined by averaging the data computed from the fitted polynomial, and then subtracting this average profile from each individual profile, which were also computed from their fitted polynomial. We determined by repeatedly measuring a single sample that the maximum index change measurement error is about 0.00001, or 0.2% of the total index change of the samples in this study.



2).

Figure 2 - Refractive index change versus radial position. The large parabolic curve shows the refractive index profile of a typical sample in this study. The 28 tightly bunched curves at the top of the figure show the index profile difference between each sample and the average of all 28 samples

RESULTS AND DISCUSSION

Figure 3 shows the index profile deviations between five different samples cut from the middle 1/3 of a single rod. The largest total deviation is about 2.3% of the total index change, as indicated on the figure. This error is probably due to irregularities in the gel mold and/or diffusion from the ends of the rod during leaching.

Figures 4 and 5 show profile deviations between 13 samples from batch A, and between 15 samples from batch B, respectively. The maximum deviation in batch A is about 5.5%, and in batch B about 9.1%. Since each sample in both batches was leached, fixed, and dried in a separate container, it is likely that these deviations are due to localized variations in leaching time, leaching bath volume to gel volume ratio, gel diameter, etc.

Figure 6 shows the deviations of the average of the 13 profiles from batch A and the average of the 15 samples from batch B from the average index profile of all 28 samples. These deviations are similar in magnitude to the measurement error.

It is evident from the above figures that batch to batch index profile variations are much less significant than variations within a batch or even variations within a single rod. It must be emphasized however that even though the two different batches studied here

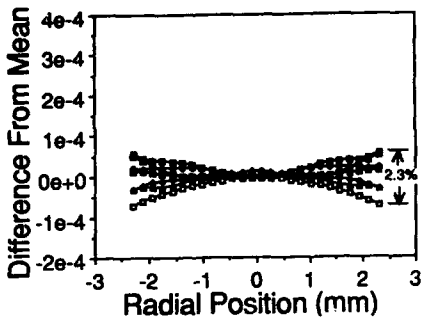


Figure 3 - Index profile differences between seven different samples cut from the middle 1/3 of a single rod in batch A. The largest total deviation shown is 2.3% of the total index change of the average profile.

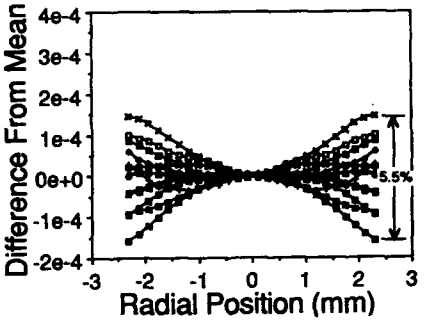


Figure 4 - Index profile differences between the 13 samples in batch A. The largest total deviation shown is 5.5% of the total index change of the average profile.

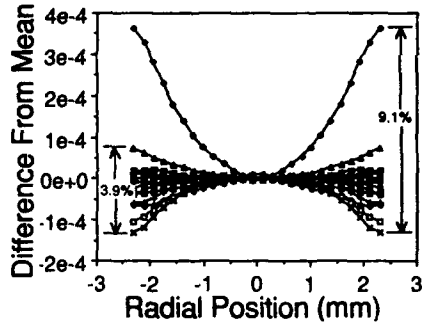


Figure 5 - Index profile differences between the 15 samples in batch B. The largest total deviation shown is 9.1% of the total index change of the average profile.

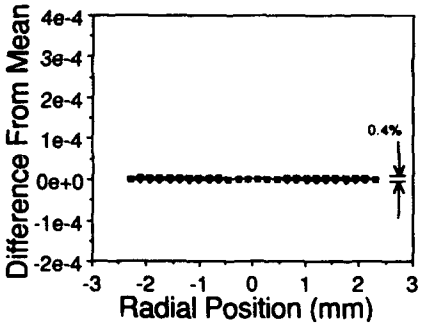


Figure 6 - Deviation of the average batch A profile and the average batch B profile from the average of all 28 profiles from both batches.

were prepared separately by two different researchers, they were made at the same time using the same starting chemicals. A more thorough study would have to account for variations in starting materials, ambient temperature and humidity during gel preparation, gel aging time and temperature, etc.

The tolerances published by Nippon Sheet Glass (NSG) [2] on the index profile variation of their Selfoc GRIN rods, which are made by ion exchange, are equivalent to a total deviation of 6% within a single batch and 10% between batches. Since none of the samples in this study exceeded this deviation, we are optimistic about the prospect for commercializing the sol-gel method for producing gradient-index glass.

REFERENCES

1) J. B. Caldwell and D. T. Moore, "Sol-Gel Method for Making Gradient-Index Glass, U.S. Patent 4,797,376, January 10, 1989.

2) Literature published by Nippon Sheet Glass America, Inc. , 28 Worlds Fair Drive, Somerset, NJ 08873

LIGHT HARVESTING MOLECULAR ASSEMBLIES IN THE DESIGN OF HIGHLY LUMINESCENT SOL-GEL DERIVED GLASSES

Joel I. Dulebohn,* Béatrice Van Vlierberge,* Kris A. Berglund,* Ronald B. Lessard,§ Jeong-a Yu,§ and Daniel G. Nocera§
*Department of Chemical and Agricultural Engineering, §Department of Chemistry, and the Center for Fundamental Materials Research, Michigan State University, East Lansing, MI 48824

ABSTRACT

Sol-gel derived molecular composites exhibiting intense luminescence, induced from efficient energy transduction processes, have been prepared. The composites are comprised of an $Eu^{3+}\subset$2.2.1 cryptate complex or native Eu^{3+} ion embedded in sol-gel derived titania glass films. The titania glasses contain interconnected porous networks that permit the diffusion of exogenous substrates, such as the salts of benzoic and 4-*tert*-butylbenzoic acids, through the film. Interaction of the substrate with the embedded lanthanide complex is indicated by enhanced luminescence from the lanthanide ion. The carboxylic acid salts whose electronic excited states are produced upon capture of incident photons, undergo facile transfer of their electronic energy to the lanthanide ion. By monitoring europium ion luminescence, the diffusion constants of the benzoate and 4-*tert*-butylbenzoate salts have been measured. Although the diffusion of the 4-*tert*-butylbenzoate is slower than that of benzoate, the overall higher sensitivity of the former is consistent with hydrophobic guest-host interactions. These new molecular composites relying on the immobilization of an absorption-energy-transfer-emission molecular assembly in porous, optically transparent ceramic glasses may be useful in the design of practical sensing devices.

INTRODUCTION

The design of many optical sensors is predicated on the development of suitable matrix supports containing chromophores or lumophores whose chemical or physical properties are modified in the presence of exogenous substrate molecules. The successful realization of optically integrated sensors necessarily requires the production of matrices that allow a target molecule to contact the sensing molecule while retaining their optical transparency. One approach is to use a porous matrix wherein the pores are small relative to the wavelength of light used. Fabrication of the matrix at low temperature is advantageous because thermal degradation pathways of chromophores and/or lumophores is circumvented. The ability to process porous glasses at or near room temperature, which embed a variety of molecules with specially tailored optical and chemical properties, provides for the design of novel molecular composites for chemical and optical sensors. The high porosities of sol-gel derived glasses [1,2], which have often been considered a drawback [3], permit molecules to be brought in contact with embedded sensing molecular assembly by diffusion of exogenous substrate through the glass. In fact the glass can actually be thought of as a membrane composed of interconnected pores. The opportunity to prepare films of small thickness by the sol-gel approach [4] should in principle permit the response time of the sensing process to be greatly reduced.

Our general strategy for the development of new molecular composites for sensing applications is centered around the incorporation of inorganic lumophores into a sol-gel derived glass. We have demonstrated that oxide glasses can accommodate inorganic clusters [5], porphyrins [6], and lanthanide cryptate

Mat. Res. Soc. Symp. Proc. Vol. 180. ©1990 Materials Research Society

compounds [7] with retention of their excited state properties. Of particular interest to the design of sensors are films containing lanthanide cryptates. The approach in the current work is derived from a scheme in which the luminescence of the lanthanide cryptate is activated by the presence of a molecule to be sensed. Because lanthanides in general exhibit low absorption cross-sections, luminescence from the lanthanide under direct illumination is weak [8]. Notwithstanding, luminescence from the lanthanide can be greatly enhanced by introduction of a light harvesting center (LHC) which efficiently collects photons, and subsequently transfers its energy to the Ln^{3+} ion to produce intense Ln^{3+} luminescence [9-12]. This absorption-energy-transfer-emission (AETE) process may take place by either intermolecular or intramolecular steps. However, the intermolecular AETE is often much less efficient than a corresponding intramolecular process owing to the exponential distance dependence of energy transfer [13,14]. In the intermolecular process, the Ln^{3+} ion and LHC must come in close proximity to one another before energy transfer can occur.

As previously shown, the deleterious effects of O–H oscillators on the excited state properties of Ln^{3+} ions [15-16] can be minimized by encapsulating the ions in molecular cages of a cryptand ligand [12,17-19]. The two nitrogens and five oxygens comprising the three straps of the cryptand ligand occupy seven of the nine coordination sites of the Ln^{3+} ion. The presence of the two remaining coordination sites of the Ln^{3+} cryptand complexes provides the opportunity to supplement an otherwise inherently inefficient intermolecular AETE by efficient intramolecular AETE. The emission intensity from the lanthanide center can be greatly enhanced by employing a functionalized LHC that can bind the caged Ln^{3+} ion. We have been able to increase the emission efficiency of Tb^{3+} and $Eu^{3+}\subset$2.2.1 complexes by upwards of three orders of magnitude upon coordination of β-diketonates and carboxylic acids owing to the much stronger absorption cross-section of the light-harvesting center as compared to the native $Ln^{3+}\subset$2.2.1 complexes [20]. The AETE process has provided us with a strategy for designing optical sensors because the dramatic increase of lanthanide ion luminescence upon coordination of exogenous substrate to the Ln^{3+} ion permits the LHC to be detected by simply monitoring emission intensity from the lanthanide center.

Successful operation of AETE-based sensing in sol-gel films requires the successful execution of several concerted processes. Firstly, the target molecule (in this case also the LHC) must diffuse through the porous network of the film to find an accessible lanthanide cryptate. Secondly, the film must not interfere with the AETE between the cryptate and the LHC. Finally, the film must possess optical properties which permit facile observation of AETE. We now report the preparation of titania films containing native Eu^{3+} or $Eu^{3+}\subset$2.2.1 ions that demonstrate AETE when exposed to solutions containing the salts of benzoic and 4-*tert*-butylbenzoic acids.

EXPERIMENTAL

Synthesis

The light harvesting benzoate and 4-*tert*-butylbenzoate compounds and compounds used for the preparation of sol-gels were obtained from Aldrich Chemical Co. and used without further purification. Encapsulation of Eu^{3+} by the cryptand 4,7,13,16,21-pentaoxoa-1,10-diazobicyclo-[8.8.5]-tricosane (⊂2.2.1) was accomplished by following previously described methods [7]. The product $[Eu\subset 2.2.1]Cl_3$ was characterized by electronic absorption and emission spectroscopy.

Preparation of Films

A neat solution of titanium isopropoxide contained in a screw-top vial was charged with lauric acid. To this solution valeric acid was added. The resulting yellow solution was mixed with an aqueous solution of $[Eu\subset 2.2.1]Cl_3$ or $EuCl_3 \cdot 6H_2O$. Thin films of the lanthanide-based lumophore were made by spin casting the appropriate solution on a quartz slide (50 x 10 mm). The lanthanide-based films were coated with a lanthanide-free titania film. The coatings were prepared by a similar procedure except water was substituted for the lanthanide ion solution. Film thicknesses, measured on a DEKTAK IIA profilometer, were 6000 ± 1000 Å.

Methods

The luminescence of thin films was monitored on an emission spectrometer constructed at Michigan State and described elsewhere [21]. The 313-nm excitation wavelength used for steady-state emission experiments was selected by excitation and emission monochromators with slit widths of 3 and 5 mm, respectively. The entrance slit of the emission spectrometer was equipped with a Schott OG-570 cut-off filter. Emission spectra were corrected for the instrument response function by methods described elsewhere [21].

Diffusion of the LHC's into the titania films was monitored by detecting the luminescence of the europium ion at 616 nm. Diffusion measurements were made by placing the uncoated side of the quartz slide against the face of a 1 cm quartz cuvette. The excitation beam illuminated the thin film by passing through the uncoated surface of the quartz slide, which was placed at a 60° incident angle to the excitation beam. All experiments followed the same procedure. The emission intensity of the dry film was recorded at 616 nm. A NaOH solution of pH = 9.1 was placed in the cuvette until a steady-state emission response was achieved after which the solution was replaced with a NaOH solution containing the carboxylate LHC (pH = 9.1). After a steady-state response was reached the cell was charged with a pH = 9.1 aqueous NaOH solution. The diffusion response of the LHC's was measured on films exposed to solutions 0.050 to 0.00050 M in 4-*tert*-butylbenzoate, and 0.072 to 0.0048 M in benzoate.

The kinetic diameters of the LHC's were determined from the equivalent of a sphere of diameter d_i, which was evaluated from $d_i = (d_1 d_2 d_3)^{1/3}$ where d_i defines the x, y, and z molecular dimensions. The diameters d_i were computationally measured from molecules in energy minimized conformations that were ascertained by using the MM2 Allinger force field [22] as implemented by PC Model (Serena Software).

RESULTS AND DISCUSSION

Equilibrium Experiments

The emission spectra of an $Eu^{3+}\subset 2.2.1$ containing titania film as prepared after equilibration with a pH = 9.1 NaOH solution, and subsequent exposure to sodium 4-*tert*-butylbenzoate solution, are shown in Figure 1a. Similarly, Figure 1b displays the emission spectra of a film containing the chloride salt of Eu^{3+} without encapsulation by the $\subset 2.2.1$ cryptand. In each case the AETE process is demonstrated by the significant increase in emission upon introduction of the LHC sodium 4-*tert*-butylbenzoate. This is particularly noteworthy because the excitation was at 313 nm, which is coincident with the low energy tail of the

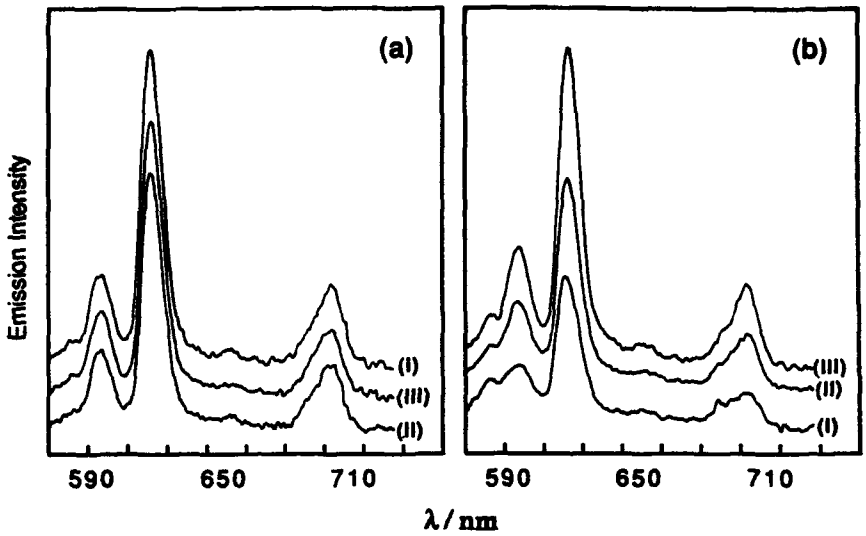


Figure 1. Steady-state emission spectra (λ_{exc} = 313 nm) of a titania film embedded with (a) $EuCl_3 \cdot 6H_2O$ and (b) [Eu⊂2.2.1]Cl_3. Spectra (I), (II) and (III) are those of the film in air, in NaOH solution of pH = 9.1, and in NaOH solution containing 4-*tert*-butylbenzoate at a concentration of 0.0048 M, respectively.

sodium 4-*tert*-butylbenzoate absorption. It was not possible to excite at the absorption maximum of the 4-*tert*-butylbenzoate ion (λ_{exc} = 266 nm) owing to strong absorption of the titania film in this spectral region [23].

Comparison of Figures 1a and 1b reveals that the emission intensity of the Eu^{3+}⊂2.2.1 film increases upon equilibration with NaOH solution whereas that of the Eu^{3+} film decreases. For the latter, nine coordination sites are available in principle for OH^- coordination. Because coordinated OH^- provides an efficient deactivation pathway of electronically excited lanthanide ions [15,16], it is not surprising that diminished luminescence intensities are observed upon contacting the Eu^{3+} impregnated titania film with aqueous solutions of pH = 9.1. Conversely, seven of the coordination sites of the lanthanide metal center are occupied by the cryptand in the Eu^{3+}⊂2.2.1 complex. Accordingly, only two OH^- ions at most can coordinate to the europium ion. That the luminescence intensity from the Eu^{3+}⊂2.2.1 complex increases upon contacting the film with basic solutions indicates the removal of high energy oscillators such as OH^- or H_2O from the coordination sphere of the lanthanide ion. The pK values of hydrous titania (Ti—OH) are in the range of 3-4 [24], indicating that such sites may be deprotonated in aqueous solutions of pH = 9.1. Our results imply that there may be direct interaction between these deprotonated Ti—O^- sites of the film and Eu^{3+}⊂2.2.1 with the possibility of direct coordination to the europium ion. Owing to these minor modulations in emission intensity of Eu^{3+} and Eu^{3+}⊂2.2.1 titania films upon contact with basic solutions, luminescence from films exposed to LHC carboxylates were referenced to the film, which had been previously exposed to aqueous solutions at pH = 9.1.

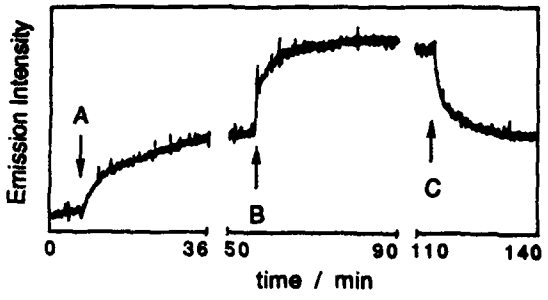


Figure 2. Emission intensity at 616 nm (λ_{exc} = 313 nm) of a titania film embedded with $Eu^{3+}\subset$2.2.1. Time 0 defines intensity of film in air; at A the film contacts a NaOH solution of pH = 9.1; at B the film contacts a NaOH solution containing benzoate at a concentration of 0.048 M; and at C the film is reintroduced to the NaOH solution containing no benzoate.

Dynamic Experiments

Real time experiments were conducted wherein the emission intensity at λ = 616 nm was recorded upon contacting Eu^{3+} and $Eu^{3+}\subset$2.2.1 embedded titania films to solutions of different constitutions. Figure 2 shows the approach of the luminescence to its steady-state intensity upon exposure of a $Eu^{3+}\subset$2.2.1 titania film to a native NaOH solution with subsequent introduction to a solution containing benzoate LHC. Similar results were obtained for the 4-*tert*-butylbenzoate LHC. It is important to note that the $Eu^{3+}\subset$2.2.1 embedded film (~ 3000 Å) was overlaid by one (~ 3000 Å) that contained no metal complex. Thus the pronounced increase of the emission intensity resulting from exposure to LHC solutions (a feature also observed for Eu^{3+} films) does *not* arise from a surface effect but necessarily requires the LHC to diffuse through the pores of the titania glass.

The intensity versus time data coupled with measurements of the film thickness by profilometry permitted the calculation of diffusion coefficients by the method of McKay [25]. The calculated diffusion coefficient for sodium 4-*tert*-butylbenzoate was lower than that for sodium benzoate for both europium ion films (see Table I). The kinetic diameter of 4-*tert*-butylbenzoate is larger than that of benzoate (k_D = 7.7 Å and 6.1 Å, respectively). Yet the former gave steady-state luminescence responses similar if not greater than that observed for the smaller benzoate LHC. These results suggest that the differences in diffusion may not be attributed exclusively to pore size effects, but specific guest-host interactions of the film with the LHC's are also likely to play a prominent role in the diffusivity of these species. Regardless of the diffusion mechanism, the data indicate selective transport in the titania films.

Table I. Diffusivities of LHC Carboxylates in Titania Films Containing Europium Complexes

Complex	Diffusion Coefficient (cm^2/s) of Benzoate	Diffusion Coefficient (cm^2/s) of 4-*tert*-Butylbenzoate
$[Eu\subset 2.2.1]Cl_3$	$5.0 (\pm 2.1) \times 10^{-12}$	$2.1 (\pm 0.6) \times 10^{-12}$
$EuCl_3 \cdot 6H_2O$	$8.6 (\pm 4.2) \times 10^{-12}$	$1.3 (\pm 1.0) \times 10^{-12}$

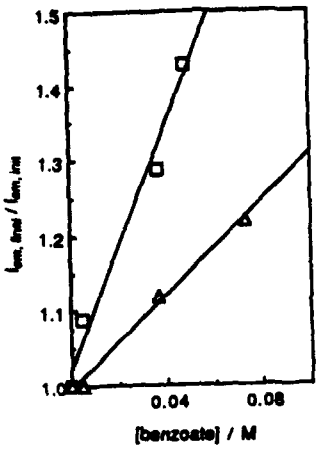


Figure 3. Ratio of emission intensity at 616 nm after equilibration with benzoate solution to that after equilibration with pH = 9.1 NaOH solution for titania films embedded with [Eu$C_{2.2.1}$]-Cl_3 (□) or $EuCl_3 \cdot 6H_2O$ (△) as a function of benzoate concentration.

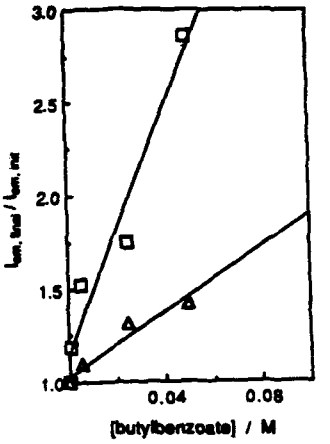


Figure 4. Ratio of emission intensity at 616 nm after equilibration with 4-*tert*-butylbenzoate solution to that after equilibration with pH = 9.1 NaOH solution for titania films embedded with [Eu$C_{2.2.1}$]Cl_3 (□) or $EuCl_3 \cdot 6H_2O$ (△) as a function of 4-*tert*-butylbenzoate concentration.

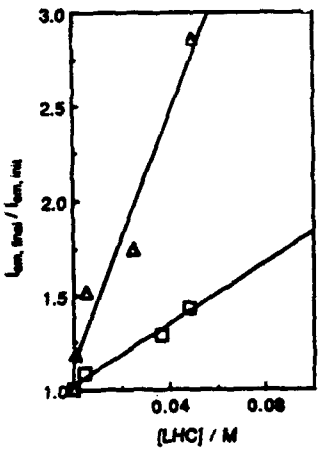


Figure 5. Ratio of emission intensity at 616 nm after equilibration with a LHC solution (benzoate (□), 4-*tert*-butylbenzoate (△)) to that after equilibration with NaOH solution (pH = 9.1) for titania films embedded with [Eu$C_{2.2.1}$]-Cl_3 as a function of LHC solution concentration.

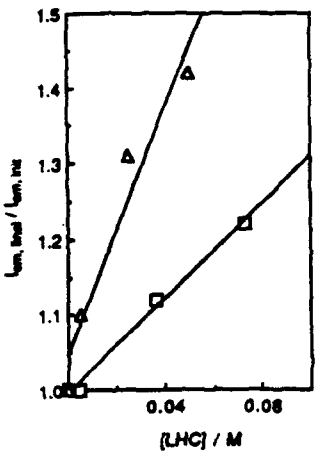


Figure 6. Ratio of emission intensity at 616 nm after equilibration with a LHC solution (benzoate (□), 4-*tert*-butylbenzoate ((△)) to that after equilibration with NaOH solution (pH = 9.1) for titania films embedded with $EuCl_3 \cdot 6H_2O$ as a function of LHC solution concentration.

Detection Sensitivity

The ratio of maximum emission intensity after LHC exposure to emission intensity after sodium hydroxide treatment as a function of LHC concentration in solution is depicted in Figures 3-6. The slope of the line reflects the sensitivity of the film to the LHC with a steeper slope corresponding to higher sensitivities. Over the concentration ranges studied, the response was linear indicating that the sensing film had not become "saturated". This is quite remarkable since the equivalents of the carboxylate (10^{-6} moles) in solution was 10^4 greater as compared to the equivalents of $Eu^{3+}/Eu^{3+}\subset 2.2.1$ (10^{-10} moles) in the film.

The cryptate form of Eu^{3+} demonstrates higher selectivity for both the benzoate and 4-*tert*-butylbenzoate anions than the simple Eu^{3+} ion as shown by the steeper slope of the former in Figures 3 and 4. Both films demonstrate more selectivity toward the 4-*tert*-butylbenzoate over the benzoate. This further substantiates the assertion of the presence of additional interactions between the 4-*tert*-butylbenzoate anion and the titania film as compared to that of the benzoate ion.

Conclusion

The porosity of sol-gel processed glasses and films can be considered an attribute for sensing applications. We have demonstrated that selective sensing films can be produced by coupling an AETE process with transport through a sol-gel film. This approach is general and may be extended to the study of transport through sol-gel based membrane films.

ACKNOWLEDGEMENT

Financial support from the Center of Fundamental Materials Research at Michigan State University, the Ford Motor Company, and the Department of Energy (PRDA DE-RA22-88PC88903) are gratefully acknowledged. D.G.N. is a NSF Presidential Young Investigator and an Alfred P. Sloan Fellow.

REFERENCES

1. S. P. Mukherjee, *J. Non-Cryst. Solids*, **42**, 477 (1980).
2. L. L. Hench, in *Science of Ceramic Chemical Processing*, (Wiley-Interscience, New York, 1986), p. 52.
3. E. J. A. Pope and J. D. MacKenzie, *MRS Bulletin*, March 17/May 15, 1987, p. 29.
4. C. D. Gagliardi and K. A. Berglund, *Mat. Res. Soc. Symp. Proc.*, **155**, 127 (1989).
5. M. D. Newsham, M. K. Cerreta, K. A. Berglund and D. G. Nocera, *Mat. Res. Soc. Symp. Proc.*, **121**, 627 (1988).
6. R. B. Lessard, M. M. Wallace, W. A. Oertling, C. K. Chang, K. A. Berglund and D. G. Nocera, *Mat. Res. Soc. Symp. Proc.*, **155**, 109 (1989).
7. R. B. Lessard, K. A. Berglund and D. G. Nocera, *Mat. Res. Soc. Proc.*, **155**, 119 (1989).
8. S. P. Sinha, in *Systematics and the Properties of the Lanthanides*, NATO ASI Series No. 109, edited by S. P. Sinha (D. Reidel, Dordrecht, 1983) p. 451.
9. E. R. Bernbaum, *Gmelin Handbook of Inorganic Chemistry*, 8th ed., vol. 39, D5, edited by T. Moeller (Springer, Berlin, Heidelberg, 1982) p. 1.
10. W. DeW. Horrocks, Jr., in *Progress in Inorganic Chemistry*, vol. 31, edited by S. J. Lippard (John Wiley & Sons, New York, 1984) p. 1.

11. F. S. Richardson, *Chem. Rev.*, **82**, 541 (1982).
12. G. Blasse, G. J. Dirksen, N. Sabbatini, S. Perathoner, J. M. Lehn and B. Alpha, *J. Phys. Chem.*, **92**, 2419 (1988).
13. H. Shou, J. Ye and Q. Yu, *J. Luminescence*, **42**, 29 (1988).
14. H. Shou, Q. Yu and J. Ye, *J. Luminescence*, **40/41**, 682 (1988).
15. W. DeW. Horrocks, Jr. and D. R. Sudnick, *Acc. Chem. Res.*, **14**, 384 (1981).
16. Y. Haas and G. Stein, *J. Phys. Chem.*, **75**, 3677 (1971).
17. B. Alpha, V. Balzani, J-M. Lehn, S. Perathoner and N. Sabbatini, *Angew. Chem. Int. Ed. Engl.*, **26**, 1266 (1987).
18. G. Stein and E. Würzberg, *J. Chem. Phys.*, **62**, 208 (1975).
19. N. Sabbatini, S. Dellonte, M. Ciano, A. Bonazzi and V. Balzani, *Chem. Phys. Lett.*, **107**, 212 (1984).
20. S. P. Sinha, in *Complexes of the Rare Earths* (Pergamon Press, Oxford, 1966) p. 145, p. 148.
21. R. D. Mussell and D. G. Nocera, *J. Am. Chem. Soc.*, **110**, 2764 (1988).
22. N. L. Allinger, *J. Am. Chem. Soc.*, **99**, 8127 (1977).
23. M. J. Payne and K. A. Berglund, *Mat. Res. Soc. Symp. Proc.*, **73**, 627 (1986).
24. M. Abe, in *Inorganic Ion Exchange Materials*, edited by A. Clearfield (CRC Press, Boca Raton, Florida, 1982) p. 185.
25. A. T. McKay, *Proc. Phys. Soc.*, **42**, 547 (1930).

SOL-GEL PROCESSED INORGANIC AND ORGANICALLY MODIFIED COMPOSITES FOR NONLINEAR OPTICS AND PHOTONICS

PARAS N. PRASAD*
*Photonics Research Laboratory, Department of Chemistry, State University of New York at Buffalo, Buffalo, N.Y. 14214

ABSTRACT

The newly emerging field of Nonlinear Optics and Photonics offers tremendous opportunities for material scientists. In this paper, chemical processing using the sol-gel method is described for the preparation of new composite materials of both a silica glass and a V_2O_5 gel with a π conjugated polymer poly-p-phenylene vinylene up to 50% by weight. The composite films show highly improved optical quality with large third-order nonlinear optical coefficients, the latter from the conjugated polymer. Optical waveguiding through the film has been achieved. Nonlinear optical studies using femtosecond degenerate four wave mixing and power dependent waveguide coupling have been successfully performed. Also, to investigate the use of such films for optical recording, a two-dimensional grating structure has successfully been produced.

INTRODUCTION

Photonics has been labelled by many as the technology for the 21st century. It is a multidisciplinary field which has captured the imaginations of scientists and engineers worldwide. In my view, this field offers tremendous opportunities for materials scientists. Chemical processing can provide new ceramic composite materials with multifunctionalities needed for photonics applications. In this article I hope to highlight this point.

Photonics describes the technology in which a photon is used to transmit, process and store information with an obvious gain in speed, bandwidth and density of information processing. The technology, therefore, deals with high density optical data storage, optical processing of information and image analysis. In addition, there is a need for devices to provide sensor protection against laser threat.

Some of the needed operational functions are frequency conversion, light modulation and optical switching. For these functions one needs nonlinear optics which describes processes occurring under the influence of a laser pulse. The resulting polarization in the medium can be written in the form of a power series expansion in the electric field strength as [1]

$$\vec{P} = \chi^{(1)}\cdot\vec{E} + \chi^{(2)}:\vec{E}\vec{E} + \chi^{(3)}\vdots\vec{E}\vec{E}\vec{E} + \quad (1)$$

The term $\chi^{(1)}$, the linear susceptibility, describes the linear optical effect such as absorption, refraction, etc. under ordinary light intensities and is related to the refractive index of the medium as

$$1 + 4\pi\chi^{(1)} = n^2 \quad (2)$$

The terms $\chi^{(2)}$ and $\chi^{(3)}$ called second and third order nonlinear susceptibilities, respectively, quantify the second and third order nonlinear optical processes. For all optical processing of information, the important nonlinear process is third order, the manifestations of which are third-harmonic generation and intensity dependence of refractive index. It is the latter which provides the method of light control by light and can be

Mat. Res. Soc. Symp. Proc. Vol. 180. ©1990 Materials Research Society

used to produce nonlinear optical output-input relations for optical information processing (Figure 1). Conjugated polymers with extensive

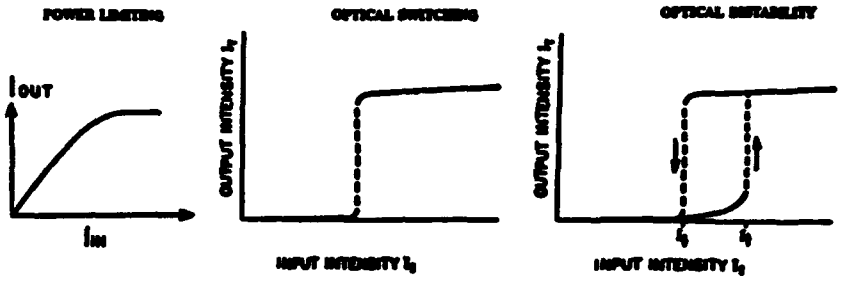


Figure 1: Nonlinear Optical input-output relations

π-electron delocalization have emerged as an important class of third-order nonlinear optical materials because the π-electrons make a large contribution to optical nonlinearity. In addition to having a large nonlinear coefficient $\chi^{(3)}$ needed so that a nonlinear component can be switched with low energy pulses, the materials must also have mechanical strength, environmental stability, high optical damage threshold and low optical losses. Organic polymeric materials are, in general, optically lossy. Inorganic glasses, particularly silica, are excellent photonic media; high quality fibers and films with extremely low optical losses can be prepared. However, the nonlinear optical coefficients of these glasses are extremely low. There is a need, therefore, to optimize both the nonlinear coefficient $\chi^{(3)}$ and the optical losses. An obvious approach will be to make a composite of a conjugated polymer and an inorganic glass. The preparation of such composites run into two difficulties (i) High temperature processing of glass cannot be used as most polymers decompose by 300-350° C. (ii) Because of the incompatibility of the organic polymeric and inorganic glass structures, phase separation often occurs at higher compositions.

We have recently developed such composites using the sol-gel chemical processing method [4]. In our opinion, this approach opens up an important avenue to produce novel composite structures for applications in both photonics and electronics. In this paper, the merits of the sol-gel processing technique for photonics are briefly discussed. Then, the characterization of these composites, their nonlinear optical studies and optical wave guide experiments are presented.

MERITS OF THE SOL-GEL PROCESSED COMPOSITES

Sol-gel processing of composite structures offers the following advantages for photonics:

a) tremendous flexibility to introduce multifunctionality desired for device applications. This flexibility enables: (i) preparation of numerous composite structures incorporating various inorganic and organic species because of the sol-gel low temperature chemical processing, (ii) use of infiltration to incorporate molecular species into the pores and layers, (iii) conducting chemistry in the pores and layers before densification,

(iv) making novel unusual molecular composites of the sol-gel glass and a third-order nonlinear optical polymer.

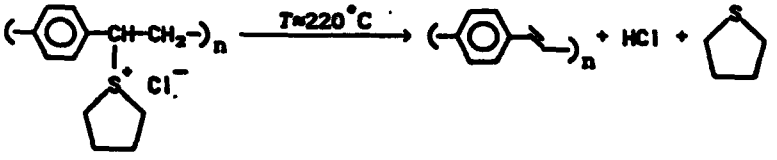
b) opportunity to make various guided-wave structures such as planar waveguides, channel waveguides and fibers.

c) electric field poling, during gelation, for dipole alignment needed for second order effect, as poling is more effective due to increased molecular mobility of the structure.

d) opportunities to prepare composites with unusual electronic and optical properties by using heterostructures consisting of mixed valence inorganic semi-conductors and p-type organic semiconductors.

THE NEW COMPOSITE GLASS-POLYMER MATERIALS

Using the sol-gel processing technique we have prepared several inorganic oxide: conjugated polymer composites in which the two components are homogeneously mixed. Up to 50% by weight polymer could be incorporated without phase separation. The conjugated nonlinear optical polymer is poly-p-phenylene vinylene (abbreviated as PPV, shown below). In our approach we start with a water soluble sulfonium salt polymer precursor of PPV which when cast in the film form and heated above 230° C undergoes the following elimination reaction to produce the conjugated polymeric structure of PPV [5].



Precursor polymer **PPV**

To prepare the new composites, the PPV polymer precusor is homogeneously mixed with the sol-gel precursor in a common solvent. The film is cast and during the heat treatment the polymer precursor converts into the final conjugated polymer. The result is an optically transparent film of wave guiding quality (i.e., very low optical losses). The formation of this compatible blend is due to a synergistic effect occurring during the chemical transformation of each component. We do not know at this stage if they are molecularly mixed. However, the excellent optical quality clearly indicates that if phase-separated regions exist, they are much smaller than the wavelength of light.

We have prepared composites of the PPV polymer with the sol-gel processed silica glass and V_2O_5 gel. In both cases optical quality films were obtained. The U.V. visible absorption spectra of both silica:PPV and V_2O_5 gel:PPV composites indicate quantitative conversion of the PPV precursor to the conjugated PPV structure.

At this stage, only the silica:PPV composite has been characterized in more detail. Both DSC and TGA thermal analysis have been performed on this composite material. The results indicate that the conversion of the PPV precursor to the final conjugated PPV structure is indeed facilitated in the

composite structure. The conversion temperature shifts from 230° C, found for the pure PPV precursor, to 140° C in the composite structure [4].

A number of linear and nonlinear optical studies have been performed on the composite films. A film of about one micron thickness was used to conduct optical waveguide studies. At 1.06μm, propagation distances of up to 2 cm through the film were readily achieved. An estimation of the waveguide loss is about ~4dB/cm. We believe that by optimizing the processing variables, this loss can be greatly reduced. The waveguide prism coupling experiment also yielded information on the refractive indices of the TE and TM modes at 1.06μm. These two modes of propagation differ in the polarization of the wave. In the TE mode, the electric field vector of the propagating waveguide mode lies in the plane of the film, while for the TM mode it is outside the plane of the film [6]. The refractive indices are 1.72 and 1.60 for the TE and TM modes at 1.06μm indicating a birefringence even in the as-cast film. The higher refractive index for the TE mode may be the result of a preferential alignment of the polymer chains in the plane of the film. In the optical waveguiding arrangement with the prism coupler we have also obtained the Raman spectra of the film; the vibrational bands due to the PPV polymer correlate nicely with those obtained for the pure PPV material.

Nonlinear optical studies have been carried out in both the bulk configuration and the waveguide geometry. A convenient method to measure the third-order nonlinear optical coefficient, $\chi^{(3)}$, and its time-response is degenerate four wave mixing (DFWM) which has been described in detail elsewhere [7]. The method can best be understood by using a grating picture. Two coherent beams of same frequency interact in a medium such as the silica: PPV film and set up an intensity modulation pattern due to interference. Since for a third order material the refractive index is dependent on the intensity, a refractive index modulation (grating) results. A third beam, the probe beam, of the same frequency is diffracted from this grating to produce the signal, the intensity of which is proportional to the square of $\chi^{(3)}$. The decay of the signal intensity as a function of the time delay of the probe beam with respect to the interfering beams gives direct information on the response time of the third-order optical nonlinearity. We have conducted this study using 400 femtosecond pulses from a Nd:Yag laser pulse compressed amplified system at 602 nm. The $\chi^{(3)}$ value obtained is ~3 x 10^{-10} esu for a ~50:50 composite; this value is fairly high [8]. The response time is limited by the pulse width of the laser. We have also conducted the DFWM studies using 50 femtosecond pulses from an amplified colliding-pulse mode-locked laser system [9]. The nonlinearity in the composite responds on this time scale, and the response is again limited by the pulse width. We therefore observe ultrafast nonlinear response in femtoseconds for this composite material.

In the waveguide arrangement, we have investigated the third-order optical nonlinearity by investigating the power dependent coupling angle at 1.06μm using a grating coupler arrangement [6]. The film of the silica:PPV composite is deposited on a quartz substrate on which input and output grating couplers have been fabricated using the ion milling technique. The input wave couples through the grating at a specific angle which is determined by the refractive index of the film. As the intensity of the beam is increased, the refractive index of the film changes leading to a change of the coupling angle. We have successfully observed this intensity dependent coupling angle behavior [10]. This phenomenon is also of interest from device application point of view as it can be used for optical switching and optical power limiter operations.

From device application perspective, we have also investigated the films of the silica:PPV composite for the fabrication of two-dimensional gratings [11]. Crossing of two femtosecond pulses at 602 nm was used for this fabrication. For a two dimensional grating, the film is rotated by 90°

and the crossing angle is changed. The result is optical recording of a two dimensional grating of two different periods. Our preliminary investigation indicates that the grating is not formed by laser ablation but is a result of intensity dependent two-photon absorption which induces chemical changes in the polymer precursor and/or produces laser densification of the composite. Figure 2 shows the diffraction pattern of a He-Ne laser beam

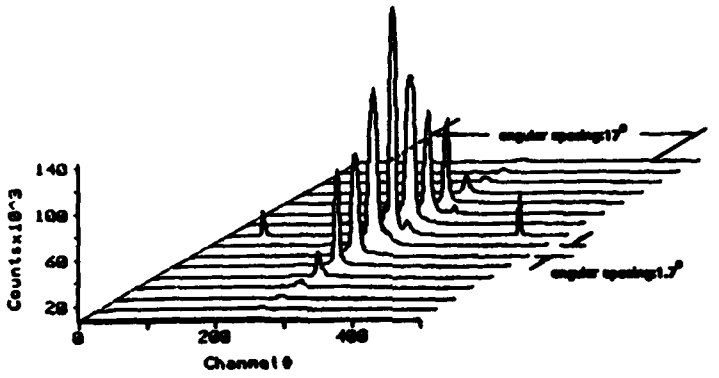


Figure 2: Diffraction pattern from a two-dimensional grating fabricated in the silica:PPV film

from the grating. It clearly exhibits the two different grating spacing in the two transverse directions. Such composite films, therefore, can also be useful for optical recording.

ACKNOWLEDGEMENT

This research was supported by the Office of Innovative Science and Technology - Defense Initiative Organization and the Air Force Office of Scientific Research, the directorate of Chemical and Atmospheric Sciences through contract numbers F4962087C0097 and F4962090C0021.

REFERENCES

1. Y. R. Shen, "The Principles of Nonlinear Optics", Wiley & Sons (New York, 1984).

2. "Nonlinear Optical and Electroactive Polymers", Eds. P. N. Prasad and D. R. Ulrich, Plenum Press (New York, 1988).

3. P. N. Prasad and D. J. Williams, "Introduction to Nonlinear Optical Effects in Molecules and Polymers", Wiley & Sons (New York, in Press).

4. C. J. Wung, Y. Pang, P. N. Prasad and F. E. Karasz, Polymer (in Press).

5. D. R. Gagnon, J. D. Capistran, F. E. Karasz, R. W. Lenz and S. Antoun, Polymer 28, 567 (1987).

6. G. I. Stegeman, Thin Solid Films 152, 231 (1987).

7. M. Samoc and P. N. Prasad, J. Chem. Phys. 91, 6643 (1989).

8. C. J. Wung and P. N. Prasad, unpublished result.

9. Y. Pang and P. N. Prasad, unpublished result.

10. R. Burzynski, D. N. Rao and P. N. Prasad, unpublished result.

11. G. S. He, G. Xu, C. J. Wung, and P. N. Prasad, unpublished result.

INCORPORATION OF POLYANILINE INTO A SILICA GEL VIA THE SOL-GEL TECHNIQUE

F. NISHIDA*, B. DUNN*, E.T. KNOBBE*, P.D. FUQUA*,
R.B. KANER†, and B.R. MATTES†
*Department of Materials Science and Engineering, University of California, Los Angeles.
†Department of Chemistry and Biochemistry, University of California, Los Angeles.

ABSTRACT

The sol-gel process has been used to incorporate a conjugated polymer, polyaniline, in silica gel. The emeraldine base form of the polymer is partially solubility in aprotic polar solvents which are compatible with the sol. The effect of sol environment on the emeraldine base form of polyaniline was investigated. The soluble emeraldine base form is maintained at pH ≥ 2.4 enabling good optical quality gels to be synthesized. The type of alkoxysilane and the water ratio used in preparing the sol influence the solubility of the emeraldine base.

INTRODUCTION

The use of the sol-gel process to incorporate optically active organic molecules is well established. A number of optical properties have been demonstrated including luminescence, photochromism, laser action and optical gain [1-3]. From these studies it is evident that the gel serves as a chemically and thermally stable host material with good optical properties. In the work to date, the sizes of the incorporated guest molecules have been in the range of the gel pore diameter (or smaller). The molecules are likely to be encapsulated by the gel matrix and there is evidence that the optical properties are influenced by interaction with the matrix [4]. The present investigation extends this work on the synthesis of organic-doped gels by considering the incorporation of a polymeric species which is substantially larger than the pore diameter. In particular, polyaniline-doped gels have been synthesized to take advantage of the nonlinear optical properties of conjugated polymers.

Conjugated polymers are promising candidates for nonlinear optical materials due to their extended network of delocalized pi-electrons. Recent work on conjugated polymers such as polydiacetylene [5] and polythiophene [6] have demonstrated large third order nonlinear susceptibilities, $\chi^{(3)}$. These conjugated polymers, however, generally exhibit poor processing characteristics. They are environmentally unstable and somewhat intractable. As a result, attempts to fabricate optical devices using conjugated polymers have been impeded.

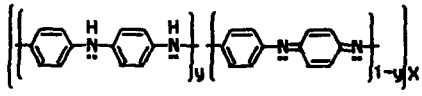
The conducting polymer, polyaniline, is an exception to this behavior as it is both environmentally stable and processible. The emeraldine base form of polyaniline exhibits partial solubility in aprotic polar solvents such as dimethyl formamide (DMF) and N-methyl pyrrolidinone (NMP). We have used this characteristic to synthesize silica gel monoliths containing 2-ethyl polyaniline [7]. Degenerate four-wave mixing measurements of these materials indicate that $\chi^{(3)}$ for the doped gel was approximately 30% of the value obtained for CS_2 at 1.06 μm (i.e., ≈ 5×10^{-13} esu).

In the present study, details of the synthesis of polyaniline-doped silica gels are reported. An important consideration in this work is the use of a solvent for polyaniline that is compatible with the gel. The effects of different synthesis variables including water concentration, pH, and alkoxysilane composition on the solubility of the emeraldine base form of polyaniline and gel formation are discussed.

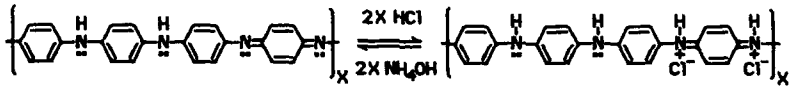
Mat. Res. Soc. Symp. Proc. Vol. 180. ©1990 Materials Research Society

BACKGROUND--POLYANILINE

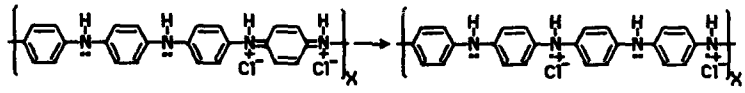
Polyaniline has recently generated considerable interest due to its relatively high electrical conductivity and inherent stability with regard to oxygen and moisture. Polyaniline can exist in five different oxidation states depending on the conditions employed for synthesis. Emeraldine base, ideally, is a form of polyaniline which is exactly half oxidized with y = 0.5 in the following formula:



Of polyaniline's five oxidation states, emeraldine exhibits the widest range of electrical conductivity spanning from the insulating regime ($\sigma \leq 10^{-10}\ \Omega^{-1}cm^{-1}$) to the metallic regime ($\sigma \approx 5\ \Omega^{-1}cm^{-1}$) following treatment with protonic acid [8,9]. The conductivity can be varied continuously by controlling the degree of acid doping. While other conjugated polymers undergo changes in oxidation state following doping with an oxidant or reductant, emeraldine is unique since conductivity is produced by treatment with acid. There is no formal change in the oxidation state of the polymer. The chemical reversibility of this acid/base reaction is described as follows:



Magnetic, optical, and transport experiments suggest that emeraldine salt is a metallic conductor with a finite density of states at the Fermi energy level [9]. The electrical conduction in emeraldine salt is believed to occur by a polaron conduction mechanism [9,10]. The acid doping of emeraldine base to emeraldine salt results in formation of bipolarons as illustrated above. Subsequently, an intramolecular redox reaction is believed to occur which results in the creation of separated polarons:



The increased charge delocalization in the electrically conductive state is particularly interesting for nonlinear optics.

The change in electronic structure induced by protonation of emeraldine base alters the absorption property of the polyaniline [10,11]. The characteristic absorption peaks of emeraldine base are at 3.5 eV (354 nm) and 2.0 eV (620 nm) and solutions appears deep blue in color. The 620 nm absorption is thought to be related to formation of an exciton. The formation of emeraldine salt is accompanied by a disappearance of the peak at 620 nm due to the rearrangement of the quinoid ring system to the benzenoid system of the polaron structure. The appearance of two new peaks at 3 eV (420 nm) and 1.5 eV (830 nm) are also associated with polaron formation. This results in a green color for the emeraldine salt, which rapidly precipitates from most solutions. Consequently, conversion from emeraldine base to emeraldine salt in sol can be probed by monitoring these absorption peaks.

The most significant feature of polyaniline from sol-gel chemistry considerations is its solubility in organic solvents. The solubility affords an opportunity to incorporate this conducting polymer (albeit in its insulating form) in a sol-gel matrix. The solubility of the emeraldine base can be improved further by either of two methods. The first is to incorporate long, flexible substituents onto the polymer backbone. Alkylation of polyaniline improves solubility and even gives some solubility in alcohols. The solubility of the unsubstituted emeraldine base may also be increased by successive treatments with acid and base followed by exposure to tetrahydrofuran (THF). Treatment with THF appears to swell the polymer and increase its surface area, resulting in a larger fraction of soluble amorphous polyaniline.

EXPERIMENTAL PROCEDURES

An emeraldine salt form of polyaniline was chemically synthesized by the acid catalyzed oxidative polymerization of aniline [8]. The solubility of the polyaniline was increased by repetitive treatments with 0.1M NH_4OH, THF, and 1.0M HCl in that order [12]. A final NH_4OH treatment converted emeraldine salt to emeraldine base before storage.

Approximately 0.15 g of polyaniline (PANi) were ground to a fine powder in an agate mortar and pestle, followed by swelling with THF. After the THF evaporated, the powder was added in small portions to 7 ml of NMP in a glass mortar while stirring and grinding the mixture. The solution was then vacuum filtered through a 0.7 mm glass fiber filter (Whatman GF/F) of known weight. Three additional milliliters of NMP were used to wash the mortar, pestle, and filter (total of 10 ml NMP). The filter was vacuum dried at 95° C to evaporate NMP, then weighed to determine the weight of polyaniline dissolved. The concentration of polyaniline was approximately 3.7 ± 0.2 mg/cc.

The solubility of polyaniline was investigated in various compositions of silica sol. Sols were prepared by the sonogel method [13] using tetramethoxysilane (TMOS: Aldrich Chemical 98%) and/or tetraethoxysilane (TEOS: Fisher reagent grade), 0.04N HCl, and distilled water. Mixed TMOS-TEOS sols were prepared by initially hydrolyzing a small portion of TMOS, and subsequently adding the remaining constituents slowly.

The solubility of emeraldine base was studied in a series of samples which independently considered variations in both the precursor to water ratio and the TMOS-TEOS ratio. The effect of water content was investigated in TMOS and TMOS-TEOS sols (1:1 mole ratio) at 1:1, 1:2.5, 1:4, and 1:10 mole ratio of alkoxysilane to water. For these samples, a constant 4 v/o of 0.04N HCl was used (this gave pH= 2.4 ± 0.2 when mixed with 7 parts sol and 3 parts NMP). The sols prepared for determining the effect of different precursors (TMOS *vs* TEOS) contained 25, 50, 75, and 100 m/o TMOS and used the same 1:2.5 mole ratio of precursor:water and 4 v/o of 0.04N HCl. Finally, the effect of pH was investigated by preparing sols with 1:2.5 mole ratio of water at 2, 4, 8, 12, and 16 v/o of 0.04N HCl. In all cases sols were mixed first with NMP, then with the polyaniline solution in 7:1:2 volume ratio of sol:NMP:PAN solution. The final mixtures were filtered through 0.7 mm filter paper and cast into polystyrene cuvettes to form thin monoliths. By employing standard cuvettes, optical absorption measurements were used to monitor the concentration of the polyaniline in the sol.

RESULTS AND DISCUSSIONS

The concentration and, therefore, the solubility, of emeraldine base in TMOS and TMOS-TEOS (1:1) sols was monitored by measuring the magnitude of the characteristic absorption at 630 nm. Figure 1 indicates that the solubility increases sharply as the water ratio reaches 2.5, and then remains relatively constant. This behavior is somewhat surprising since polyaniline is insoluble in water and yet the lowest optical density (OD) is observed in the sol containing the lowest water content. The results suggest that the emeraldine base has a greater affinity for hydroxyl groups than alkyl groups since a high concentration of the hydrolyzed product occurs at the greater water content.

The effect of precursors and the TMOS/TEOS ratio on the solubility of the emeraldine base is not yet clearly established. As suggested in Fig. 1 (at the lowest water content) there is a trend towards increasing optical density at greater TMOS contents. This behavior is probably associated with the higher hydrolysis rate for TMOS and the faster formation of the favorable hydroxyl-silane environment for the emeraldine base.

The acid content of the sol has a decided effect on the synthesis and formation of polyaniline-doped gels. The pH was varied in a series of samples from pH 1.7 to pH 2.8 by increasing the volume percent of 0.04N HCl in in the sol-NMP mixture. The data for the sols fall into three regimes (Figure 2). At pH ≥ 2.4, polyaniline exists primarily in the emeraldine base form and gels of good optical quality are readily prepared. The principal absorption peak at 630 nm is dominant, although it is interesting to note that there is a small shoulder at 420 nm which suggests a small amount of emeraldine salt present in the sol. At pH ≤ 1.8 another regime is

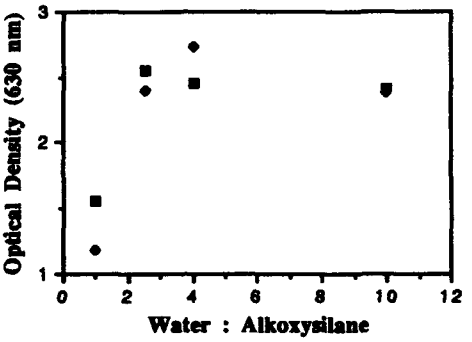


Figure 1. Absorption (optical density) of emeraldine base in TMOS (o) and TMOS-TEOS sol (+) as a function of water: alkoxysilane ratio.

observed. In this case the characteristic peaks of emeraldine salt at 420 nm and 800 nm are clearly visible, while the peak at 630 nm has completely disappeared. This indicates that the emeraldine base is no longer present in the sol. In these low pH materials, the polymer precipitates gradually with time and gelation is severely hindered if not altogether suppressed. The third regime, 1.8 < pH < 2.4, is intermediate and there is evidence for both emeraldine salt and base; there are peaks at 630 nm, 420 nm and a shoulder at 800 nm. In this pH range, gels form slowly. Several days are required and precipitation occurs during gelation. The resulting gels are of poor optical quality.

The chemical changes which occur during the sol-to-gel transition for pH 2.4 are indicated in the optical absorption spectra of Figure 3. The NMP solution of the emeraldine base serves as a reference spectrum. The NMP solution is actually rather basic (pH ≈ 12) and only the strong absorption band of the emeraldine base form of PAN is observed. In the PAN-doped silica sol, the same peak dominates although the emeraldine salt is evident by the slight shoulder at 420 nm and by the reduced transmission above 750 nm. The latter effect would arise from the presence of the 800 nm peak of the emeraldine salt form. The aged gel (Fig. 3) exhibits a greater concentration of the emeraldine salt. The shoulder at 420 nm is more pronounced and the transmission in the infrared is reduced further.

The various pH dependent results observed in PAN-doped sols can be explained by considering charging effects on gel surfaces. Colloidal silica has an isoelectic point at pH 2.2, [14] and for the current study involving silicon oxide based structures, only relatively small deviations from this value would be expected. At low pH (e.g., pH 1.8) the net charge of the silica network is expected to be positive due to the presence of $Si\text{-}OH_2^+$ groups on the surface of the gel particles. In contrast, at pH above the 2.2 range (e.g., pH 2.4), the presence of $Si\text{-}O^-$ anionic groups is expected to produce a negative charge.

The existence of these surface charges leads to interactions between PAN and the gel matrix and influences the form of polyaniline present in sols and gels. The range of pH values used for gel synthesis are close to the isoelectric point and enable trends to be determined. At pH < 1.8, the positive charges on the particles sufficiently influence the PAN such that only the emeraldine salt form of the polymer is observed. As pH increases above 1.8, the emeraldine salt content is decreased while the emeraldine base form increases in concentration.. Above pH 2.4, the salt content becomes vanishingly small as the negative surface charges dominate. Aging of the gel causes a different effect. At pH 2.4, the aging process apparently leads to an increase of the

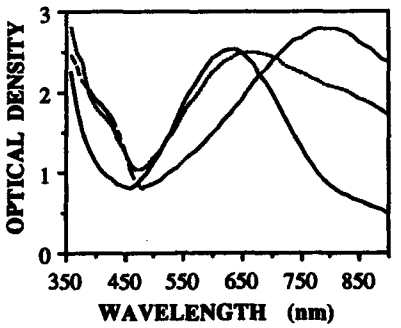


Figure 2. Absorption spectra of polyaniline in sol at pH = 1.8 (dashed), 2.0 (dotted), and 2.4 (solid). Water ratio in sol is 2.5.

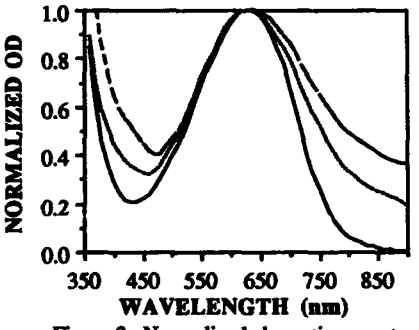


Figure 3. Normalized absorption spectra of emeraldine base in NMP (solid), sol of pH=2.4 (dotted), and aged gel (dashed).

positive surface charges as indicated by the absorption spectrum in Fig. 3. As prior work has shown, aging of the gel forces the guest species to be in greater contact with the gel surface and thus diminishes screening effects of the solvent.[4] In general, the pH dependence shown for PAN-doped gels is consistent with that observed for dye-doped gels. In the latter systems, surface charges stabilized different luminescent species in the gel depending upon pH [4].

CONCLUSIONS

The solubility of the emeraldine base form of polyaniline enables one to use the sol-gel method to prepare silica gels doped with this conjugated polymer. An important aspect of the synthesis is the requirement that the solvent for the polymer be compatible with the gel. In the present study the aprotic solvent, NMP, was employed and gel synthesis was investigated as a function of water ratio, different alkoxysilanes, and the amount of acid present in the sol. It was found that the solubility of emeraldine base was higher in sols containing more hydrolyzed species, and in sols prepared from smaller alkoxysilanes. The pH of the starting sol has a profound effect on gel formation. The role of the pH is to effectively charge the surface of the gel particles and to alter the local chemical environment of the guest species. Good optical quality gels were formed when the emeraldine base form was stabilized, while the presence of emeraldine salt at pH < 2.0 led to precipitation and hindered gelation.

ACKNOWLEDGEMENTS

This research has been supported by the National Science Foundation (DMR 87-06010, ENG 88-11629 and CHE 86-57822) and by the Lockheed Missiles and Space Company, Palo Alto, CA.

REFERENCES

1. D. Avnir, D. Levy, and R. Reisfeld, J. Phys. Chem., 88, 5956 (1984).
2. D.Levy and D. Avnir, J. Phys. Chem. 92, 4734 (1988).
3. E.T. Knobbe, B. Dunn, P.D. Fuqua, and F. Nishida, Applied Optics, in press.
4. J.C. Pouxviel, S. Parvaneh, E.T. Knobbe and B. Dunn, Solid State Ionics 32/33, 646 (1989).
5. G.M. Carter, M.K. Thakur, Y.J. Chen, and J.V. Hryniewicz, Appl. Phys. Lett., 47, 457 (1985).
6. R. Dorsinville, Opt. Lett., 14, 1321 (1989).
7. E.T. Knobbe, B. Dunn, P.D. Fuqua, F. Nishida, R.B. Kaner, and B.M. Pierce, Proc. Am. Ceram. Soc., October, 1989, in press.
8. W.-S. Huang, B.D. Humphrey, and A.G. MacDiarmid, J. Chem. Soc., Faraday Trans. I, 82, 2385 (1986).
9. A.J. Epstein, J.M.Ginder, F.Zuo, H.-S. Woo, D.B. Tanner, A.F. Richter, M. Angelopoulos, W.-S. Huang, and A.G. MacDiarmid, Synth. Met., 21, 63 (1987).
10. M.G. Roe, J.M. Ginder, P.E. Wigen, A.J. Epstein, M. Angelopoulos, and A.G. MacDiarmid, Phys. Rev. Lett., 60, 2789 (1988).
11. J.M. Ginder, A.J. Epstein, and A.G. MacDiarmid, Synth. Met., 29, E395 (1989).
12. B.R. Mattes, E.T. Knobbe, P.D. Fuqua, F. Nishida, B.M. Pierce, B. Dunn, and R.B. Kaner, in New Materials for Nonlinear Optics, edited by G. Stucky, S. Marder, and J. Sohn, (American Chemical Society, Washington D.C.), in press.
13. L. Esquivias and J. Zarzycki, in Proceedings of the Third International Conference on Ultrastructure Processing, edited by J.D. Mackenzie and D.R. Ulrich, (John Wiley & Sons Inc., New York, 1988), p. 255.
14. R.K. Iller, The Chemistry of Silica, (John Wiley & Sons, New York, 1979).

OPTICAL SWITCHES BASED ON VANADIUM DIOXIDE FILMS GROWN BY THE SOL-GEL PROCESS

Richard S. Potember and Kenneth R. Speck
The Johns Hopkins University Applied Physics Laboratory
Laurel, Maryland 20723, USA

ABSTRACT

Vanadium dioxide thin films have been grown from vanadium tetrakis (t-butoxide) by the sol-gel process. A new method for the synthesis of the vanadium precursor was also developed. Films were deposited by dipcoating glass slides from an isopropanol solution, followed by post-deposition annealing of the films at 600°C under nitrogen. The properties of these films, to a high degree, were a function of crystalline boundaries and crystalline grain size. These gel-derived VO_2 films undergo a reversible semiconductor-to-metal phase transition near 72°C, exhibiting characteristic resistive and spectral switching comparable with near stoichiometric VO_2 films prepared on non-crystalline substrates by other techniques. Films were doped with hexavalent transition metal oxides to demonstrate lowering of the transition of the transition temperature.

INTRODUCTION

Vanadium dioxide is known to undergo a reversible thermally-induced semiconductor-to-metal phase transition at 68°C [1,2]. Associated with this transition, the material exhibits large changes in its optical, electrical, and magnetic characteristics with respect to temperature [3,4]. This anomalous behavior has prompted considerable interest in the fabrication of vanadium dioxide thin films for scientific investigation and for use in various technological applications [5,6]. Recently, VO_2 has been studied for use as an energy-conserving coating for windows and walls. Other applications include electro- and photo-chromic devices, thermal sensors and transparent electrical conductors.

There have also been numerous studies involving the incorporation of various transition metal ions into the VO_2 lattice. It was observed that the transition temperature may be raised or lowered, depending on the valence of the dopant ion.

Mat. Res. Soc. Symp. Proc. Vol. 180. ©1990 Materials Research Society

Tungsten, molybdenum, and tantalum ions are known to decrease T_t with increasing concentration, with tungsten having the largest effect per atomic percent added [6-9]. In each case, the resistance ratio before and after the transformation decreases quickly for low dopant levels. However, large changes in the infrared transmission are observed even when the resistance ratio is small [7].

Processing of these VO_2 films is shown schematically in Figure 1. Thin films of VO_2 were deposited by dipcoating glass slides from an isopropanol solution. Dopant ions were placed into the crystal structure of the vanadium dioxide by combining isopropanolic solutions of the vanadium tetrakis (t-butoxide) with those of tungsten or molybdenum (VI) oxytetrachloride (Alfa). Tungsten and molybdenum were chosen as dopants because of the very large effects they have on the transition temperature [7-9]. The overall reaction leading to VO_2 formation is

$$nV(OR)_4 + 2nH_2O \longrightarrow (VO_2)_n + 4n\text{t-buOH} \qquad (1)$$

where M = MoO, WO. The molar ratio of metal ions in the film is assumed to be the same as the molar ratio of metal ions in solution from which the films were grown [7]. Slides were often coated more than one time to build up the desired thickness. To convert the films into the VO_2 phase, they were annealed under nitrogen to achieve complete dehydration, residual solvent removal, and crystallization.

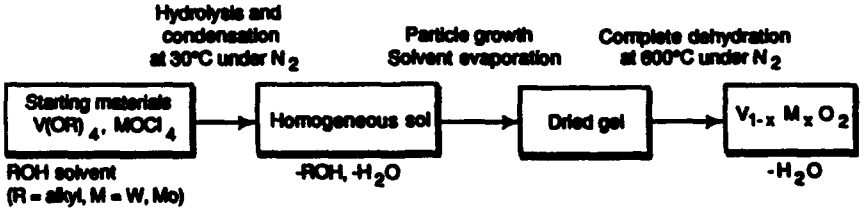


Figure 1: Preparation of $V_{1-x}M_xO_2$ thin films by the sol-gel method.

A pressure versus temperature equilibrium diagram for the V-O system is plotted in Figure 2 [10]. Vanadium dioxide is easily

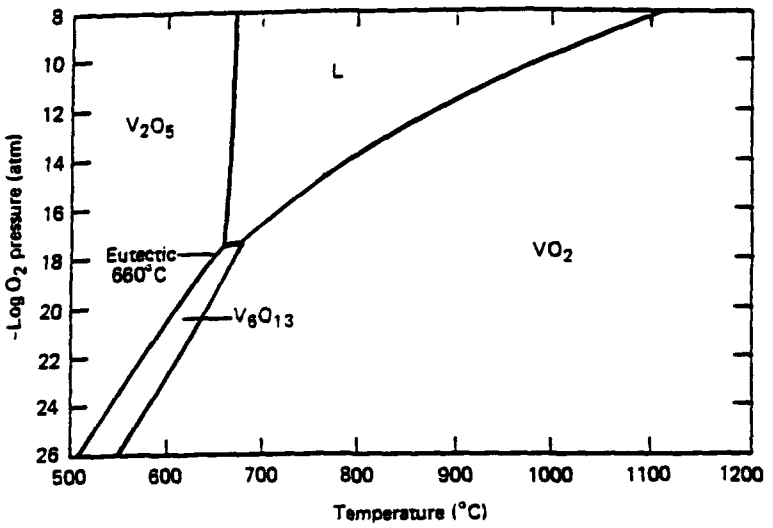


Figure 2: Pressure versus temperature phase diagram, Ref. [10].

oxidized by heating near 600°C in air. Conversely, it is known that V_2O_5 loses oxygen on heating in high vacuum at 600°C [11]. It is clear from this figure that isobaric heating at 10^{-19} torr near 600°C transforms $V_2O_5 \rightarrow V_6O_{13} \rightarrow VO_2$. Isothermal decompression at 600°C and lower oxygen partial pressures causes the same transformation. Note that V_2O_5 melts at 660°C.

The partial pressure of oxygen required for the reduction of V_2O_5 to VO_2 is not as low as indicated in Figure 2. A eutectic point exists in the vanadium-oxygen system at 600°C. At 600°C, the equilibrium oxygen pressure for VO_2 is 10^{-20} torr. Lowering the oxygen pressure, isothermally, is necessary to reduce VO_2. The partial pressure required to do this is orders of magnitude higher than can be achieved in the best vacuum systems available. Therefore, at 600°C and 1 mtorr, V_2O_5 is reduced while VO_2 is not [10]. This type of reduction can also be achieved in a nitrogen atmosphere.

The electrical and optical properties of the gel-derived VO_2 films were measured when heated through the transition temperature. The experimental setup was the same as previously described [14,15]. The arrangement allowed for the concurrent measurement of the electrical resistance and optical transmission at 2400 nm of the film as a function of temperature.

RESULTS

The near-IR transmittance at 2400 nm of 1000 Å thick film on glass is plotted in Figure 3A. There was an abrupt decrease in transmission near 65°C, beginning slightly before the change in resistance occurs as expected. Large spectral switching occurred when the resistive switching was between two to three orders of magnitude. The usual hysteresis effect caused the transmission to increase 10 degrees lower on cooling. The cooling portion of the curve shows an anomalous hysteresis due to a (210) texturing of the film [12].

The switched and unswitched transmittance spectra shown in Figure 3B is typical for these gel-derived vanadium dioxide films. The observed transmission changes between 400 to 2500 nm are consistent with that reported for VO_2 [13]. Above T_t, the transmission is low at wavelengths longer than 1000 nm. The film thickness was measured to be 1000 Å for Figure 3B.

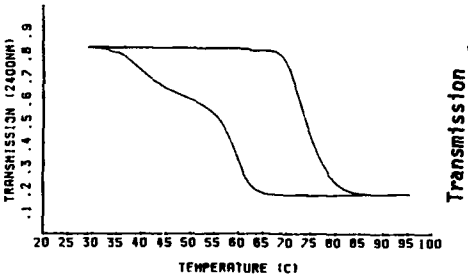


Figure 3A: Temperature dependence of optical transmission at 2400 nm for a vanadium dioxide film 1000 Å thick on glass.

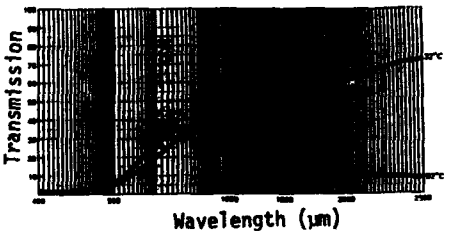


Figure 3B: Spectral transmission of a 1000 Å thick VO_2 film above and below the transition temperature on glass.

The optical transmission of a 250Å thick $V_{0.98}Mo_{0.02}O_2$ film at 2400 nm is shown in Figure 4(a). It was assumed that the concentration of the dopant in the film was the same as that in solution. The transition temperature, taken as the inflection point of the heating curve, is near 56°C. Resistance changes were minimal, and therefore not included here.

The results obtained for a 500 Å thick $V_{0.99}W_{0.01}O_2$ film are shown in Figure 4(b). The phase transition occurred over a larger range of temperatures, but the transition temperature (T_t = 35°C) was significantly lower than the undoped or molydenum doped films. Although the dopant ions greatly influenced the transition temperature of vanadium dioxide, they had little effect on the observed spectral transmission [3,7]. The results were similar to other work involving doping vanadium dioxide.

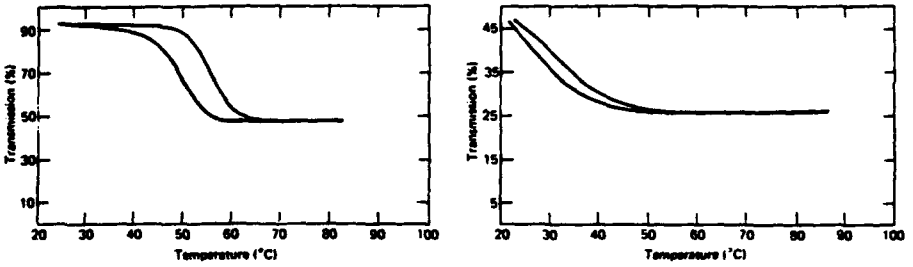


Figure 4: (a) Temperature dependence of the transmission at 2400 nm for 250 Å thick $V_{0.98}Mo_{0.02}O_2$ film and for (b) 500 Å thick $V_{0.99}W_{0.01}O_2$ film.

CONCLUSION

Doped and undoped vanadium dioxide thin films were deposited on glass slides by dipcoating from an isopropanol solution of vanadium tetrakis (t-butoxide). A new method was discovered for the synthesis of the vanadium precursor.

The sol-gel process provides a versatile way of making doped vanadium dioxide devices. This technique permits mixing of the constituents at the molecular level, which leads to a more homogeneous product. It has been demonstrated that the addition of tungsten and molybdenum depresses the switching temperature with increasing concentration.

Potential advantages of this new approach for producing vanadium dioxide thin films via the sol-gel process are numerous. The process does not require an expensive vacuum system to grow films, and the instrumentation that is required is rather simple. Large surface area may be coated with a homogeneous thickness, and

gel process affords the possibility of coating substrates which have a variety of sizes, shapes, and thicknesses. In many areas, the sol-gel method is an attractive alternative to the vapor deposition of vanadium dioxide.

ACKNOWLEDGMENT

This work was supported by the U.S. Navy under Contract No. N00039-87-C-5301.

REFERENCES

1. F. J. Morin, Phys. Rev. Lett., 3 (1959) 34.
2. D. Adler, Rev. Mod. Phys., 40 (1968) 714.
3. H. W. Verleur, A. S. Barker, Jr., and C. N. Berlund, Phys. Rev. Lett., 172 (1968) 788.
4. C. N. Berglund and H. J. Guggenheim, Phys. Rev., 185 (1969) 1022.
5. F. A. Chudnovskii, Sov. Phys. Tech. Phys., 20 (1976) 999.
6. G. V. Jorgenson and J. C. Lee, Solar Energy Materials, 14 (1986) 205.
7. C. B. Greenberg, Thin Solid Films, 110 (1983) 73.
8. J. B. MacChesney and H. J. Guggenheim, J. Phys. Chem. Solids, 30 (1969) 225.
9. J. B. Goodenough, J. Solid State Chem., 3 (1971) 490.
10. G. A. Nyberg, Ph.D. Thesis, Cornell Univ., (1985).
11. J. B. MacChesney, J. F. Potter, and H. J. Guggenheim, J. Am. Ceram. Soc., 51 (1968) 176.
12. W. Haidinger and D. Gross, Thin Solid Films, 12 (1972) 433.
13. C. H. Griffiths and H. K. Eastwood, J. Appl. Phys. 45 (1974) 2201.
14. T. E. Phillips, R. A. Murphy, and T. O. Poehler, Mat. Res. Bull., 22 (1987) 1113.
15. K. R. Speck, H. S-W. Hu, M. E. Sherwin, and R. S. Potember, Thin Solid Films, 165 (1988) 317-322.

VANADIUM PENTOXIDE GELS: STRUCTURAL DEVELOPMENT AND RHEOLOGICAL PROPERTIES

J.K. BAILEY, T. NAGASE, G.A. POZARNSKY, and M.L. MECARTNEY
Department of Chemical Engineering and Materials Science, University of Minnesota, Minneapolis, Minnesota 55455

ABSTRACT

Cryogenic transmission electron Microscopy (cryo-TEM) and rheological characterization were conducted in order to understand structural development of vanadium pentoxide gels during processing. Sols were prepared by ion exchange from sodium metavanadate solutions. Cryo-TEM revealed that fine threads about 1.5nm wide initially form and grow into ribbons approximately 25nm wide and at least 1000nm long. The threads appear to self assemble into the ribbons. During this structural development, the dynamic viscosity increased. Upon steady shearing of the sols, the system exhibited thixotropy, i.e. the viscosity decreased with time under constant shear stress and subsequently rheopexy, the viscosity increased with time. Comparison of the structure before and after shearing indicated that during the rheological experiments aggregation of small particles or fragments was occurring.

INTRODUCTION

Vanadium pentoxide gels have several useful applications such as anti-static coatings and switching devices. The production of these materials by a sol-gel route is suitable for novel processing applications such as extrusion and thin film coatings. This study investigates the development of microstructure in vanadium pentoxide gels produced from ion exchange of sodium metavanadate solutions through cryogenic transmission electron microscopy and rheological characterization.

Some of the earliest work on characterizing the structure of vanadium pentoxide sols was performed by Heller, Watson, and Wojetowicz [1]. The resulting gel structure, examined by viewing dried gels in the TEM was composed of V_2O_5 ribbons 6.5 nm wide by over 500nm long [2]. Recently Livage and coworkers [3,4] have performed extensive studies on the structure and electrical properties of vanadium pentoxide gels produced by ion exchange of sodium metavanadate solutions and have determined by X-ray and electron diffraction that dried gels (xerogels) form layered sheets comprised of V_2O_5 ribbons. While there have been studies which characterize the structure of the xerogels, there has been relatively little work on characterizing how the structure forms and how the processing affects the structure. We report

Mat. Res. Soc. Symp. Proc. Vol. 180. ©1990 Materials Research Society

here preliminary results on direct observation by cryo-TEM of the developing structure in the liquid state and the changes that the material undergoes during prolonged shearing.

EXPERIMENTAL

The vanadium pentoxide sols were made by first preparing a solution of sodium metavanadate 0.35M - 0.5M in deionized water. The solution was run through an ion-exchange column containing Dowex 50W-X2 resin which had been thoroughly washed with HCl and subsequently rinsed with deionized water [6]. The vanadium concentrations studied varied from 0.35 to 0.5M Vanadium. The effluent sols contained 3-100mM residual Na in this column determined by atomic emission spectroscopy.

The cryo-TEM was performed by placing a drop of the sol at the desired point in the reaction on a holey carbon grid and blotting the grid to produce a thin liquid film spanning the grid holes. The sample was rapidly frozen by plunging into liquid ethane which vitrified the liquid trapping the sol structure in place. This technique is described fully in reference [5].

Rheological characterization was performed on a Rheometrics Fluids Rheometer. The Couette rheometer fixtures consisted of a titanium bob and a hardened aluminum cup. Both dynamic and steady shear tests were performed. The shear rate varied from a 0.03 to a $0.3s^{-1}$

RESULTS

The prepared solution is a deep yellow solution of vanadic acid. As it gels, it darkens to an orange-yellow and subsequently red precipitates form which are visible to the unaided eye. These precipitates continue to form and settle until the entire container is filled with the precipitates. At this point, the precipitates form the dominant phase in the material and the sol again becomes apparently homogeneous to the unaided eye, but a deep blood red color. The red sol is initially liquid but over time it gels into an elastic solid gel. The time that the solution requires to gel is strongly dependent on both the vanadium concentration and the residual sodium concentration, and ranged from 1 to 14 days for the concentrations used in this work.

The development of the fibrous microstructures can be seen in Figures 1a-c which are cryo-TEM micrographs for sols at various points along the way to gelation. Because the cryo-TEM solutions were taken from various solutions which took slightly differing times to gel, the times are scaled to a reference time, which is the time at which the solution became the homogeneous blood red sol, i.e. when the precipitation of the red precipitates had been completed. Figure 1a shows the structures present in the sol at a time t/t_r of 0.2, shortly after the solution had just started to form red precipitates The structures seen are fine wispy threads of V_2O_5. These threads are separate from each other and are unaggregated. Figure 1b shows the microstructure of the sol at $t/t_r \approx 1.0$ when the sol is almost finished the precipitation. The micrographs shows thicker strands, which we have called fibers, are approximately 25 nm wide

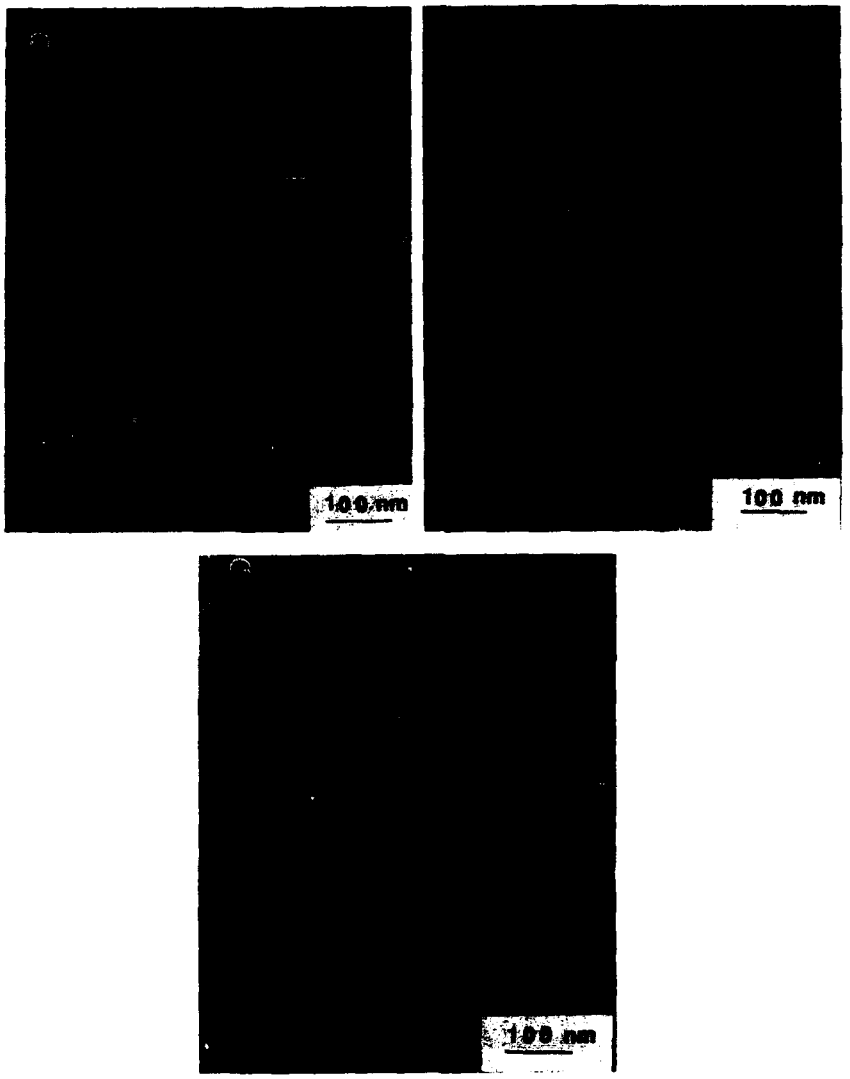


Figure 1: Stages in the formation of a 0.5M Vanadium pentoxide gel observed by cryo-TEM.
(a) fast-frozen sol at t/tr = 0.2
(b) fast frozen sol at t/tr = 1.0
(c) fast frozen sol at t/tr = 2.0

and over 1000 nm long. They are now of significant length and overlap with one another in the solution. Notice that some of the fibers split along their length and appear to be comprised of several smaller fibers aligned together Figure 1c shows the microstructure of the sol at $t/t_r \approx 2.0$ when the sol has turned into a homogenous red sol. The viscosity of the sol at this stage in the reaction was too high to successfully blot on the grid, so the solution was diluted approximately 10:1 by volume with deionized water. The microstructure appears similar to that shown in Figure 1b, however in this figure the fraying is less evident; however, longitudinal striations along the fiber length are visible.

Rheological characterization was conducted on the sol after it had become homogeneous and red. A steady shear test was conducted on the material at a strain rate of $0.3s^{-1}$ and the results are shown in Figure 2. Initially, the material is thixotropic, i.e. the viscosity decreases as a function of time. The viscosity then reaches a lower bound after which it begins to rise again, or become rheopexic. The material was examined using cryo-TEM in both the sheared and unsheared state. Figure 3a shows the V_2O_5 sol before shearing, corresponding to point a on Figure 2. Figure 3b shows the V_2O_5 sol after shearing, corresponding to point b on Figure 2. The V_2O_5 solutions were diluted approximately 100:1 before the cryo-TEM samples were prepared. The unsheared solution was a thick solution at approximately $t/t_r \approx 2$, while the sheared sample had the appearance of a brown muddy solid. In some samples, up to 1.5 wt% Al contimination from the rheometer fixtures was found.

DISCUSSION

The fibrous nature of the vanadium pentoxide sols has previously been determined; however, the growth process that leads to the formation of these fibers has not been investigated in detail. Figures 1a through 1c give a preliminary indication of this process. Initially small threads form which are on the order of 2nm wide by 100nm long. These threads grow lengthwise, but subsequent self assembly of these threads into ribbons is indicated by Figure 1b showing that the ribbons are comprised of individual threads which in places have become frayed to show the constituent threads. It appears from the micrographs that the threads self assemble edge to edge, probably due to the surface charges on the edges.

Figures 3a and 3b show the structure of a sol (at $t/t_r \approx 2$) before and after shearing. The unsheared material is comprised of the fibers similar to Figure 1c. In the sheared material one can see agglomerates of smaller particles which have formed in the mats of the V_2O_5 fibers. The small particles may be fragments of the larger ribbons or aluminum vanadate particles formed from acidic vanadium oxy-hydroxides reacting with the aluminum contaminants.

Unbroken fibers may undergo shear alignment (detangling) as the material is sheared. This shear alignment may give rise to the viscosity decrease with time. The fiber fragments or particles that form appear to be unstable to aggregation. When they aggregate, they trap

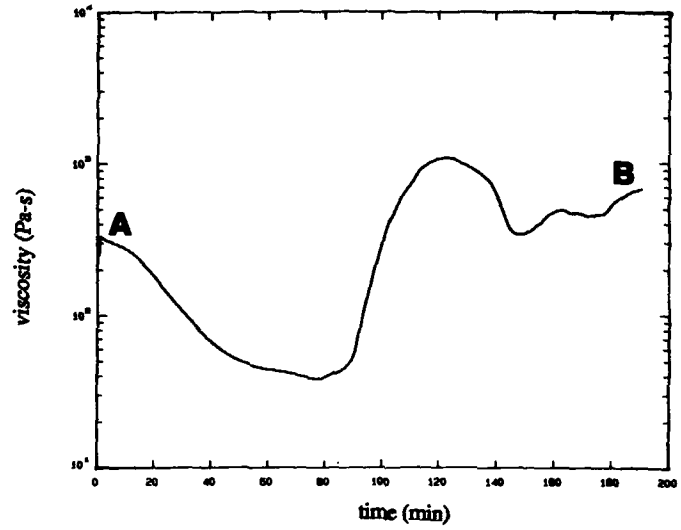


Figure 2: Viscosity vs. time for a 0.5M vanadium pentoxide gel at a constant shear rate of 0.03s



Figure 3: Unsheared and sheared vanadium pentoxide gel structures observed by cryo-TEM.
(a) unsheared - corresponds to point A in Figure 2.
(b) sheared - corresponds to point B in Figure 2.

unbroken fibers in the aggregate and a network structure begins to build. The junctions in the network are large aggregates.of the smaller particles.

CONCLUSIONS

We have directly observed the structural development of vanadium pentoxide gels in the liquid state using cryo-TEM. The V_2O_5 gels first form small threads which grow into fibers. Some evidence of edge to edge self assembly of these threads is seen in the structure of frayed ribbons. The final ribbons appear to be comprised of many of these threads.

Upon steady shearing, the V_2O_5 sols first showed rheopexic behavior and subsequently became thixotropic. The cryo-TEM results indicate that during shearing, aggregation of small particles occurrs. It is postulated that the time thinning behavior is due to shear alignment, and the time thickening behavior is due to aggregation of the small particles which create entanglement points for the remaining unbroken ribbons.

ACKNOWLEDGMENTS

This work was supported by Air Force Office of Scientific Research contract number 49620-89-C-0050. The Center for Interfacial Engineering, a National Science Foundation Engineering Research Center, is acknowledged for support of GAP and access to the CM30 TEM. Professors H.T. Davis and L.E. Scriven are thanked for the use of the controlled environment vitrification system. J. Livage and C. Sanchez of the University of Pierre and Marie Curie in Paris are acknowledged for stimulating our research in this area and for continuing discussions.

REFERENCES

1. Watson, J.H.L., Heller, W., and Wojetowicz, W.J., Science 109, 274 (1949).
2. Wojetowicz, W.J., Ph.D. thesis, Wayne State University, 1953.
3. J. Legendre and J. Livage, J. Colloid and Interface Sci. 94, 75 (1983).
4. J. Legendre, P. Aldeberet, N. Baffier, and J. Livage, J. Colloid and Interface Sci. 94, 84 (1983).
5. J.K. Bailey, J.R. Bellare, and M.L. Mecartney in Specimen Preparation for Transmission Electron Microscopy of Materials, edited by J.C. Bravman, R.M. Anderson, and M.L. McDonald (Mater. Res. Soc. Proc. 115, Pittsburgh, 1988) p. 69.
6. N. Gharbi, C. Sanchez, J. Livage, J. Lemerle, L. Nejem, and J. Lefebvre, Inorg. Chem. 21, 2758 (1982).

PART XI

Poster Session: Novel Processing, Superconductors

PREPARATION OF PHENYLSILOXANE FILMS VIA SOLUTION DEPOSITION TECHNIQUES

E.W. Burkhardt*, R.R. Burford**, and J.H. Deatcher*

*Akzo Chemicals Inc., Livingstone Ave., Dobbs Ferry, NY 10522
**Chisholm Institute of Technology, Department of Chemistry, East Caulfield, Victoria, Australia, 3145

ABSTRACT

Thin films (1-10μ thick) can be spin coated on a variety of substrates from formulations containing polyphenylsiloxanes and alkylsilicates. These films may be cured either thermally or photochemically, yielding films with good adherence to the substrate. The combination of photolysis and thermolysis results in changes in the film hardness characteristics. The use of a mask during photocuring results in films which may be developed in either a positive or negative fashion. The preparation of various formulations along with film curing processes will be discussed.

INTRODUCTION

Silsesquioxanes ($R\text{-}SiO_{1.5}$) are interesting materials in that they possess both organic and inorganic properties. These materials have been the object of investigation for use in areas such as interlayer dielectrics [1-3], modifiers for glassy materials [4,5], and protective coatings for low earth orbit environments [6-8]. The solubility of silsesquioxane oligomers is dependent in part upon the nature of the organic group present, the size of the polymer chain, and also the degree of crosslinking (free hydroxyl content). We have found polyphenylsilsesquioxane (Wacker brand SY-430) to be a useful component in formulations for the spin deposition of siloxane films. Our goal was to develop systems which would exhibit film characteristics such as good adhesion to a variety of substrates, planarity, increased thickness without cracking, flexibility, and variable curing methods.

EXPERIMENTAL

Description of reagents and systems prepared

The systems consist of mixtures of SY-430 with a variety of alkylsilicates. SY-430 [9] is a phenylsilsesquioxane oligomer with an average molecular weight of 1700, containing ~5 wt% free hydroxyl groups and a softening point of 50°C. SY-430 is known to react with a number of functional organic groups through its free -OH groups and is thermally stable up to temperatures of 450°C. Alkylsilicates used include tetraethylorthosilicate (TEOS), triethoxyvinylsilane (TEVS), and triethoxyphenylsilane (TEPS). A nomenclature system has been developed in order to quickly identify the systems as to their composition. In some cases, SY-430 is dissolved in an organic solvent such as toluene or 1-methoxy-2-propanol, followed by addition of

Mat. Res. Soc. Symp. Proc. Vol. 180. ©1990 Materials Research Society

tetraethylorthosilicate (TEOS). This system is given the designation "α". The weight ratio of SY-430 to TEOS can vary from 10:1 to 3:1, with a 6:1 ratio giving the best results. The weight ratios of solvent to SY-430 and TEOS can vary depending on the film thickness desired. A minimum solvent:SY-430:TEOS ratio for good films is about 10:6:1, generally a ratio of 15:6:1 is used.

Systems can also be prepared without organic solvent by dissolving SY-430 directly into an alkylsilicate. These systems are designated by a number followed by either a "β", "Γ", or "δ". The number represents the weight ratio of SY-430 to alkylsilicate and β, Γ, δ represent TEOS, TEVS, TEPS respectively. For example, 1.25 β represents a system in which the weight ratio of SY-430 to TEOS is 1.25:1. Photolysis of these systems have been carried out in 1" diameter quartz tubes using a water cooled Ace Hanovia mercury vapor lamp (type L, 450 watt).

Spin deposition and curing methods

Spin coating of substrates was carried out using a Headway Research photoresist spinner (EC 101 D). Films are prepared by flooding a substrate with the solution followed by spinning for a period of 60 seconds, at a speed of 2000 rpm. The film can then be cured either thermally or photochemically. Thermal curing is generally accomplished by passing the coated substrate through an Intex belt furnace (350°C, 20 minutes). Photocuring is accomplished by exposure to UV light (254 nm) from a medium pressure Hg lamp for up to 1.5 hours followed by heat treatment at 100°C for one hour. Using these conditions, films can be spin deposited on substrates such as Si, glass, Al_2O_3, and Kapton. Thicknesses of from 1 to 10 μ as measured by profilometry (Dektak model 3030) or ellipsometry (Gaertner model L116A) on Si wafers are attainable. Film thickness was found to vary no more than 1.7%.

By using a photomask, the film may be developed in either a positive or negative fashion. Treatment with solvent removes the masked portion (negative image), while treatment with buffered HF removes the exposed portion (positive image). Cured films adhere well to all substrates tested. Films applied to rigid substrates pass the standard cross hatch Scotch tape test (ASTM-D3359). A combination of photolysis followed by thermolysis results in films that are harder and thicker than films cured in the reverse order.

RESULTS AND DISCUSSION

Effect of photolysis on siloxane systems

Systems containing only SY-430 and alkylsilicate are viscous solutions, with viscosity increasing as the weight ratio of SY-430 to alkylsilicate increases. For example, the viscosity of a 1.0 β system is 43 cp., while the viscosity of a 1.5 β system is 199 cp. The Γ and δ systems show similar viscosity characteristics.

Upon photolysis, the viscosity of the solutions, and resulting film thicknesses increase (Figure 1). Continued photolysis results in systems which yield cracked films.

GC analysis of a photolyzed 1.25 β system indicated that

free ethanol is generated, while TEOS is consumed. This process continued after photolysis had ceased (Table I), as evidenced when solutions were analyzed 15 hours later. Heating these solutions alone does not result in significant amounts of ethanol production. Species such as ethyl silicate dimers and trimers were not detected. Ethanol is the byproduct of the condensation between the ethoxy groups on TEOS and silanol moieties with formation of Si-O-Si bonds. The observed increase in the amount of free ethanol in these systems after photolysis, and the increased film thickness obtained from these systems suggest that condensation between the free -OH groups of SY-430 and the -OEt ligands in the alkylsilicates is occurring.

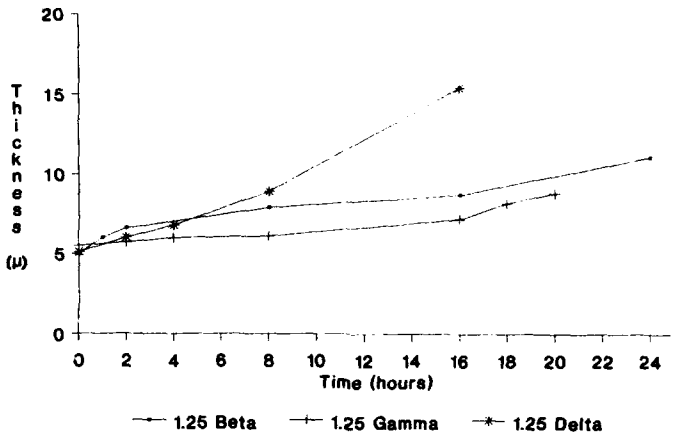


Figure 1: Thickness of cured films as a function of photolysis time.

Table I: Ethanol and TEOS Levels Photolyzed 1.25 ß Systems

Photolysis Time	Wt% Free EtOH	Wt.% TEOS
as prepared	0.12	44.5
2 hrs.	1.13	41.7
2 hrs. (15 hr. delay)	3.20	34.8
4 hrs.	2.10	39.6
4 hrs. (15 hr. delay)	4.10	32.4

While solid state ^{29}Si NMR analysis of resins obtained from the photolysis of SY-430 with TEOS did not reveal the presence of any "D" type Si species (Si bound to two C atoms), a weak resonance at -102 ppm corresponding to a Q^4 (Si with four Si-O-Si linkages) was observed (Figure 2). The formation of a Q^4 Si would suggest that multiple condensation reactions can occur between TEOS and SY-430. The participation of the phenyl groups of SY-430 in photochemically induced coupling reactions is not

believed to occur. GC-MS of 1.5 ß, Γ, and δ systems do not indicate the presence of any benzene or biphenyl. Likewise, ^{13}C NMR analysis of photolyzed ß systems do not indicate the presence of biphenyl moieties or any perturbation of the phenyl rings.

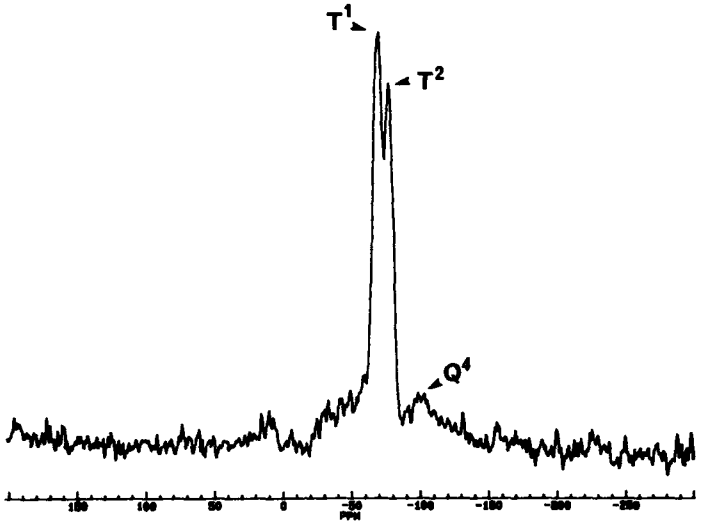


Figure 2: Solid state ^{29}Si NMR spectrum of photolyzed resin. Integrated relative intensities of the $T^1:T^2:Q^4$ are 1.0:0.73:0.17.

Effect of photolysis and thermolysis on film curing

The hardness of α system siloxane films was tested using a Nano Instruments mechanical properties microprobe (nano indenter). The effect of various curing methods on the hardness characteristics was examined. A series of 3 μ thick films were prepared and cured either by photolysis only, photolysis followed by thermolysis, thermolysis followed by photolysis, or thermolysis only. Thermolysis temperatures of 270°, 330°, and 400°C were employed. Films were photolyzed in all cases for 1 hour, while thermolysis was carried out for 16 hours. Absolute hardness was measured at a depth of 1μ and hardness relative to an uncured film at a depth of 0.25 μ were determined. The relative hardness values were obtained by dividing the hardness of the cured film by the hardness of the uncured film. The results obtained are shown below (Table II).

Table II: Hardness Measurements of Cured Films

Curing conditions	Hardness (1μ, GPa)	Relative Hardness (0.25μ)
uncured	0.12	---
1 hr. UV no heat	0.10	0.88
no UV , 16 hr. 270°C	0.20	1.0
1 hr. UV bht, 16 hr. 270°C	0.30	1.6
1 hr. UV aht, 16 hr. 270°C	0.28	1.9
no UV , 16 hr. 330°C	0.18	1.0
1 hr. UV bht, 16 hr. 330°C	0.28	1.3
1 hr. UV aht, 16 hr. 330°C	0.24	1.4
no UV , 16 hr. 400°C	0.21	1.4
1 hr. UV bht, 16 hr. 400°C	9.20	112.5
1 hr. UV aht, 16 hr. 400°C	0.32	1.8

bht = before heat treatment aht = after heat treatment

Solids obtained from α systems which were photolyzed followed by thermal drying and from thermal drying without prior photolysis were examined by TGA. At 400°C the photolyzed material retained 94.5% of its original weight, while the non-photolyzed material retained only 87.7%. Between 400°C and 800°C the weight loss is the result of removal of the phenyl rings. At 800°C the residual weight of the photolyzed material is 75.9%, while the non-photolyzed material had a 66.8% residual. The differences in the weights during elevated heat treatment is most probably the result of TEOS incorporation during photolysis which is then converted into SiO_2 at elevated temperature.

The curing procedure also has an effect on the final film thickness. Using an α system with an 11:6:1 ratio, thicker films are obtained when cured by photolysis followed by thermolysis as compared to treatment in the reverse order (Table III).

Table III: Effect of Cure Process on Film Thickness

Cure Order	Thickness (μ)	% Loss
uncured	3.6	--
UV, no heat	3.5	3
UV, 270°C	3.4	6
270°C, UV	2.0	44
UV, 330°C	2.8	22
330°C, UV	1.4	61

The dominant factors controlling the thickness of an uncured film during spin deposition are the viscosity of the solution and the spinning speed. The shrinkage of sol-gel derived films is generally due to the removal of volatile species along with network consolidation during film curing. The hardness of a film will be determined, in part, by the rigidity of the film matrix. With organosiloxane systems, an increase in the SiO_2 content would result in a more rigid matrix. With a boiling point of 168°C, any free TEOS present in a thin film would be volatilized during thermal curing steps. The increased thickness for films obtained from photo/thermal curing is most likely the result of retention of TEOS moieties via photo-induced condensation reactions with SY-430. This conclusion is also supported by the hardness and TGA studies. With TEOS incorporated into the network, the overall inorganic (SiO_2) content of the film is

increased when temperatures are high enough to result in the removal of the -OEt ligands (400°C), resulting in harder films and greater weight retention.

CONCLUSIONS

The preparation of new systems for the spin deposition of siloxane films has been investigated. The mixture of a variety of alkylsilicates with polyphenylsilsesquioxane results in materials which exhibit interesting photocuring properties. Photolysis of these systems prior to or after spin deposition results in increased film thickness. The incorporation of alkylsilicate into the polyphenylsilsesquioxane network during photolysis is believed to be responsible for the observed film characteristics.

ACKNOWLEDGMENT

R. Burford acknowledges the financial support of Akzo Chemicals Inc. during his sabbatical leave at Akzo Research Laboratory Dobbs Ferry.

REFERENCES

1. W.E. Estes and W.E. Marsh, U.S. Patent No. 4 663 414 (5 May 1987).
2. G.E. Whitwell and J.H. Deatcher, U.S. Patent No. 4 758 620 (19 July 1988).
3. W.E. Estes, J.H. Deatcher, G.E. Whitwell, U.S. Patent No. 4 801 507 (31 January 1989).
4. H. Schmidt in Better Ceramics Through Chemistry, edited by C.J. Brinker, D.E. Clark, and D.R. Ulrich (Mater. Res. Soc. Proc. 32, Albuquerque, NM 1984) pp. 327-335.
5. H. Schmidt and B. Seiferling in Better Ceramics Through Chemistry II, edited by C.J. Brinker, D.E. Clark, and D.R. Ulrich (Mater. Res. Soc. Proc. 73, Palo Alto, CA 1986) pp. 739-750; C.S. Parkhurst, W.F. Doyle, L.A. Silverman, S. Singh, M.P. Andersen, D. McClurg, G.E. Wnek and D.R. Uhlmann, ibid., pp.769-773.
6. H.D. Burns, A.F. Whitaker and R.C. Linton, Surface and Coatings Tech. 39/40, 627 (1989).
7. N.H. Hundley and W.J. Patterson, NASA Technical Paper 2476[N8526990/NSP].
8. C.A. Arnold, D. Chen, Y.P. Chen, J.D. Graybeal, R.H. Bott, T. Yoon, B.E. McGrath, and J.E. McGrath, Proc. of ACS Div. of Polym. Matls. Sci. Eng. 59, 934 (1988).
9. Wacker-Chemie GmbH, product bulletin 3729, October 1988.

SYNTHESIS AND STRUCTURAL CHARACTERISTICS OF POLYCERAMS

J.M. Boulton, H.H. Fox, G.F. Neilson and D.R. Uhlmann,
Department of Materials Science and Engineering,
University of Arizona, Tucson, AZ 85721.

ABSTRACT

Sol-gel techniques are readily applicable to the preparation of Polycerams. These hybrid materials uniquely combine organic and inorganic functionalities at the molecular level. Polycerams have here been prepared from tetraethoxysilane and modified, functionalized polybutadiene, polyethylene oxide urethane and polyethyleneimine. The structures and physical characteristics of the materials are herein reported.

INTRODUCTION

Conceptually there are many ways to create organically modified ceramics (Polycerams). Various precursors can be used to tailor both the type and degree of organic modification. For example, organo-alkoxy silanes can be used effectively to prepare organically modified silicates [e.g. 1,2]. An alternative approach is the entrapment of monomers in a porous gel followed by subsequent polymerization; as an example, PMMA has been incorporated into silica gels [e.g. 3]. One attractive approach is the use of reactive, functional polymers which can co-condense with hydrolyzed alkoxides resulting in the formation of three-dimensional structures. Reactive polymers incorporated into silica-based Polycerams include polydimethylsiloxane, either silanol [4,5] or triethoxysilyl [6] terminated; triethoxysilyl terminated polytetramethylene oxide [7] and trimethoxysilyl functionalized polyimides and polyarylene ether ketones [8]. Inorganic networks are not restricted to silica: e.g., polytetramethylene oxide has been incorporated into networks prepared from chelated Al alkoxides [9]. In this work, novel silica-based Polycerams have been prepared from functionalized organic polymers, namely triethoxysilyl modified 1,2-polybutadiene (MPBD), (N-triethoxysilylpropyl) o-polyethylene oxide urethane (MPEOU) and trimethoxysilylpropyl substituted polyethyleneimine (MPEI).

EXPERIMENTAL

Tetraethoxysilane (TEOS) and modified polymers were obtained from Petrarch (Bristol, PA). The MPBD was received as a 50 wgt. pct. toluene solution; the MPEI was 50 wgt. pct. in iso-propanol (IPA); and the MPEOU was neat. All other reagents were reagent grade. The first step in preparing MPBD and MPEOU Polycerams was the same: TEOS and H_2O (acidified with 0.19 M p-toluene sulfonic acid) were reacted by refluxing at a 2:1 H_2O: TEOS molar ratio for 15 min. in tetrahydrofuran (THF) with 1g TEOS: 3 ml THF. The MPEI reactions were similar except IPA was the solvent (MPEI is insoluble in THF). Next the modified polymer was added. With MPBD and MPEOU, the reaction mixture was refluxed for 30 min., whereas with MPEI the solution was cooled to room temperature. This was due to the short gelation times of MPEI solutions. The reaction mixtures were poured into polypropylene beakers and loosely covered with foil. The MPBD

Mat. Res. Soc. Symp. Proc. Vol. 180. ©1990 Materials Research Society

and MPEOU solutions all gelled within 36 hours, while those of MPEI gelled within an hour. Polycerams were formed from all three modified polymers, with weight ratios of reactants, TEOS: polymer of 1: 0.25, 0.5, 1 and 2.

RESULTS AND DISCUSSION

Monolithic materials, in the range 2.5 to 20g, were obtained from all the compositions explored. All the samples were highly transparent. Those of MPBD were pale yellow, while those of MPEI and MPEOU were clear (e.g., Fig. 1). A variety of techniques were employed to investigate the structural characteristics of the materials. These included SEM, BET, density measurements, FTIR and SAXS. SEM examination of the fracture surfaces of the Polycerams indicated that the samples appeared similar, even at a magnification of 10,000X. The fracture surfaces were smooth and pore-free within the resolution of the microscope. Little contrast was observed, suggesting little or no variation in composition within a resolution of ~ 0.1μm.

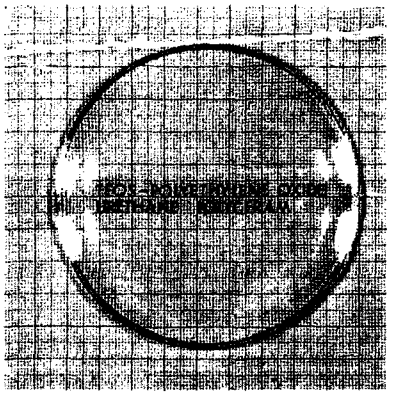


Fig. 1. A transparent TEOS-MPEOU Polyceram (1 division = 1 cm)

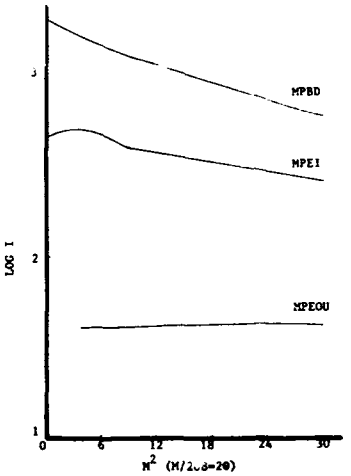


Fig. 2. SAXS profiles of Polycerams

The pore-free character of the Polycerams was confirmed by BET measurements, in which no specific surface areas could be detected. This characteristic of organically modified materials is quite remarkable, and has been observed by other workers [e.g., 10].

Room temperature densification was assessed by density measurements using displacement methods. Theoretical densities were calculated from the density values of the individual components of the gels: MPBD, 0.90 g/cm^3; MPEI, 0.91 g/cm^3; and MPEOU, 1.13 g/cm^3. The density of the silica component was taken to be 2.05 g/cm^3, a value reported for the skeletal density of SiO_2 gels prepared under acidic conditions [11]. The Polycerams had theoretical densities of 80 to 100%. Higher theoretical densities were obtained with increasing polymer volume

fractions. The MPEI and MPEOU gels had higher theoretical densities compared to materials of similar polymer contents containing MPBD. Organic modification therefore results in very different densification behavior compared to inorganic gels where high temperature treatment is necessary to achieve anything like full density. The organics allow the network to relax at low temperature, resulting in a dense, pore-free body.

FTIR analysis of the MPEOU Polycerams showed shifts in the vibrational frequencies of the organic species upon incorporation into the silicate network. Specifically, the carbonyl stretching frequency shifted to a lower wavenumber in the gel (1730 to 1700 cm^{-1}), indicating a weaker bond, most likely due to hydrogen bonding between the carbonyl and other hydroxyl groups. No major shifts were observed for the MPBD and MPEOU Polycerams.

Homogeneity of the Polycerams was investigated by SAXS. Clear, free-standing films were cast from solution with the composition 1g TEOS: 0.5 g polymer. This composition corresponds to 79.8%, 79.6% and 75.9% volume fractions of polymer for the MPBD, MPEI and MPEOU systems respectively. A high degree of homogeneity was anticipated (at least for sizable spatial scales), since even bulk samples were transparent and large differences exist between the refractive indices of the organic and inorganic phases.

The SAXS intensities, corrected for background and absorption, are shown in the form of Guinier plots in Fig. 2. As shown there, the scattering was in the order MPBD>MPEI>>MPEOU. The scattering from the MPBD and MPEI Polycerams was notable higher than that from homogeneous silicate glasses; while that from the MPEOU Polyceram was comparable to but somewhat larger than that from silicates. The slopes of the curves in Fig. 2 are proportional to R^2, where R is the radius of the inhomogeneity (assumed to be spherical in shape).

For MPBD, the data indicate a range of particle diameters from 66-44Å; while for the MPEI Polyceram, data indicate a diameter of 34Å. The maximum in intensity at low angles in this system very likely reflects a correlation distance resulting from nanophase separation. The absence of such a maximum in the MPBD data may simply reflect the dispersivity in sizes of the inhomogeneities.

The horizontal intensity vs. M^2 plot for the MPEOU Polyceram may reflect the asymptotic scattering from simple compositional fluctuations (similar to that seen in homogeneous melted glasses but higher because of the higher compressibility of the Polycerams compared with inorganic glasses. The overall scattering from the MPEOU Polyceram is consistent with a material having a high degree of chemical homogeneity.

The structures of Polycerams are expected to depend on a number of factors relating to the precursors and synthesis conditions. Several are pertinent to the reactive modified polymer. Molecular weight is of considerable importance, and influences directly the level of homogeneity that can be obtained.

The type and number of reactive functional groups are also expected to have important effects on the final structural characteristics. Alkoxysilyl modification provides almost - ideal functional groups for incorporation into alkoxide-derived gels due to the similarity in reaction rates which they provide. Silyl functions on the polymer would also increase the mutual

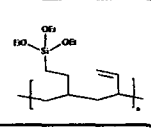
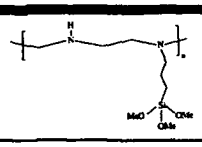
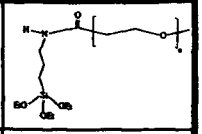
solubility of the polymer and the alkoxide, thereby promoting homogeneity. The number of reactive groups would affect the number of tie-points of the polymer into the inorganic network, thus affecting its relaxation behavior.

Polarity is a key concern, since inorganic oxide networks are polar while most organic polymers show a range of polarities depending on the type of functionality. Note in this regard that MPEOU is the most polar, and MPBD the least polar, of the organics used in the present study. Similar polarities and mutual solubility seem required for forming chemically homogeneous Polycerams. The pH of the polymer in solution can also dramatically affect the network structure, as demonstrated for alkoxide-derived silica gels prepared under acidic and basic conditions [12].

The properties of the modified polymers used in this study are compared and contrasted in Table I. The properties of the modified polymers are consistent with the results obtained in this work. Shorter gelation times were obtained with MPEI due to its basic nature and the presence of trimethoxysilyl compared with triethoxysilyl groups. The effective pH's of the solutions before gelation were 9.2 for the MPEI, 3.2 for the MPBD and 3.6 for the MPEOU. Homogeneity was dependent both on the molecular weight and polarity of the polymer. The highest homogeneity was obtained with MPEOU due to its low molecular weight and high polarity. The higher molecular weight and lower polarity polymers, MPEI and MPBD, formed Polycerams exhibiting microphase separation on a nanoscale.

These considerations illustrate the capability of wet chemical processing for tailoring the structures of organic-modified inorganics on a scale of nanometers. By control of chemistry and processing, Polycerams can be formed as novel hybrid materials with considerable potential for providing new combinations of functionality.

Table I. *Properties of Modified Polymers*

	MPBD	MPEI	MPEOU
Structure			
Approximate M.W.	3500-4000	1500-2000	300-400
Chain Length (no. of monomers)	~74	~32	~4
Modification	triethoxysilyl	trimethoxysilyl	triethoxylsilyl
Degree of Modification	One silane for every 20 monomers	One silane for every 20 monomers	One silane for every 4 monomers
Polarity	Non-polar (insoluble alcohol)	Relatively polar (soluble in alcohol)	Relatively polar (soluble in alcohol)
Apparent pH	7.2	9.4	7.6

CONCLUSIONS

New hybrid materials have been prepared by the incorporation of polybutadiene, polyethylene oxide urethane and polyethyleneimine into silica gels. Large-sized transparent monoliths could readily be obtained for all three systems. The structures of the Polycerams were consistent with the characteristics of the polymers and ranged from chemically homogeneous to microphase separated materials.

ACKNOWLEDGMENTS

Financial support of Cardinal IG and the Air Force Office of Scientific Research is gratefully acknowledged.

REFERENCES

1. H. Schmidt in Sol Gel Science and Technology, edited by M.A. Aegerter, M. Jafelicci Jr., D. F. Souza and E.D. Zanotto (World Scientific Publishing, Singapore, 1989), p. 432.
2. H. Schmidt, H. Scholze and G. Tunker, J. Non-Cryst. Solids 80, 557 (1986).
3. E.J.A. Pope, M. Asami and J.D. Mackenzie, J. Mater. Res. 4, 1018 (1989).
4. C.S. Parkhurst, W.F. Doyle, L.A. Silverman, S. Singh, M.P. Anderson, D.McClurg, G.E. Wnek and D.R. Uhlmann in Better Ceramics Through Chemistry II, edited by C.J. Brinker, D.E. Clark and D.R. Ulrich (Mater. Res. Soc. Proc. 73, 1986) pp. 769-773.
5. H.H. Huang, B. Orler and G.L. Wilkes, Macromol. 20, 1322 (1987).
6. J.E. Mark and C.C. Sun, Polym. Bull. 18, 259 (1987).
7. H.H. Huang and G.L. Wilkes, Polym. Preprints 28, 244, (1987).
8. M. Spinu, C. Arnold and J.E. McGrath, Polym. Preprints 30, 125 (1989)
9. B. Wang, H. Huang and G.K. Wilkes, Polym. Preprints 30, 146 (1989).
10. H. Schmidt, J. Non-Cryst. Solids 112, 419 (1989).
11. C.J. Brinker, E.P. Roth, G.W. Scherer and D.R. Tallant, J. Non-Cryst. Solids 71, 171 (1985).
12. C.J. Brinker and G.W. Scherer, J. Non-Cryst. Solids 70, 301 (1985).

POLYMERIZATIONS OF ALKENYLSILANES USING EARLY TRANSITION METAL CATALYSTS

JOHN MASNOVI*, XIN Y. BU*, PAULA CONROY*, A. HARRY ANDRIST*, FRANCES I. HURWITZ† AND DOUG MILLER#
* Cleveland State University, Cleveland, OH 44115
† NASA Lewis Research Center, Cleveland, OH 44135
# Cedarville College, Cedarville, OH 45314

ABSTRACT

Oxidative coupling of primary alkylsilanes catalyzed by Group IVB metallocene complexes leads predominantly to linear polysilanes, as first reported by Harrod. We have investigated the polymerization of ethylsilane and vinylsilane using dimethyltitanocene in order to determine the suitability of such polymers as precursors to Si-C based ceramics for application as coatings or composite matrices. A photochemical procedure for initiation of polymerization is described. Ethylsilane forms polysilanes (which contain a -Si-Si-Si-Si- backbone) by a step growth mechanism. Vinylsilane shows some Si-Si formation; however, polymerization by several different routes, including formation of polycarbosilanes (which contain a -Si-C-Si-C- backbone) by hydrosilation reactions and crosslinking *via* metathesis, predominate. The carbosilane polymer has high char yield (60-75%) and appears advantageous for conversion into silicon carbide, as determined by X-ray diffraction.

INTRODUCTION

Polymerization of primary alkylsilanes ($R\text{-}SiH_3$) by dimethyltitanocene (cp_2TiMe_2) and related catalysts was discovered by Harrod several years ago [1]. Linear polysilanes with n ~ 10 (Eq. 1) were reported to form by a process which occurs in two stages. In the first stage, step-growth polymerization proceeds *via* a radical process. Following an induction period, a second stage, characterized by formation of bimetallic Ti(III) species, proceeds to form the linear polymer without indication of short chain oligomers [2].

$$n\ R\text{-}SiH_3 \xrightarrow{cp_2TiMe_2} H\text{-}\underset{H}{\overset{R}{Si}}\text{-}\left[\text{-}\underset{H}{\overset{R}{Si}}\text{-}\right]_{n-2}\text{-}\underset{H}{\overset{R}{Si}}\text{-}H + (n-1)\ H_2 \qquad (1)$$

Our goal in this study was to determine the suitability of polysilanes produced in this manner for use as precursors to silicon carbide coatings

Mat. Res. Soc. Symp. Proc. Vol. 180. ©1990 Materials Research Society

and composite matrices [3]. An immediate problem associated with characterization of the polymers concerns the variable nature of the induction period preceding the second stage of the polymerization. Different polymers apparently result during each of the two stages [2]. The properties of bulk polymer would be expected to depend upon the extent of polymerization which occurs during each stage. Therefore, a means of initiating the second stage of polymerization was sought initially in order to provide more uniform and reproducible polymerization.

Furthermore, crosslinks generally confer enhanced structural integrity to polymers. Features which promote crosslinking would be expected to benefit char yield, by reducing loss of small silane fragments on pyrolysis, and thus enhance the conversion of polymer into silicon carbide [3]. Alkenyl functional groups may form crosslinks by several pathways [4]. Consequently, the polymerization of vinylsilane (CH_2=CH-SiH_3) was examined. The polymerization of ethylsilane (CH_3-CH_2-SiH_3), a saturated alkylsilane, also was selected for comparison in this study.

RESULTS AND DISCUSSION

Initiation

Dimethyltitanocene, prepared from reaction of dichlorotitanocene and methyllithium, forms yellow crystals in hexane at -77°C [5]. Warming the pure solid above 0°C can result in sudden and dramatic decomposition. The material is more stable in hexane solution, and cp_2TiMe_2 is conveniently stored (in the dark at -30°C for at least one month) and dispensed in this form.

Addition of cp_2TiMe_2 to ethylsilane or vinylsilane in hexane or THF solvent results in polymerization following an induction period. The onset of polymerization is characterized by a dramatic change in color from yellow to brown, and then to dark green or blue. Karrod has found that the species responsible for the dark color correspond to Ti(III) complexes related to the active catalyst [2]. The length of the interval preceding the color change depends upon, among other things, the catalyst, temperature, and exposure to light. Thus, higher concentrations of catalyst, as well as use of catalyst of lower purity, or heating to 40-50°C, all serve to accelerate the onset of polymerization.

Each of these methods has attendant disadvantages. Catalyst is difficult to separate from polymer, and, at high concentration, remaining catalyst contaminates the polymer. Impure catalyst may behave inconsistently and will incorporate impurities into the polymer. The polymerization of alkylsilanes is exothermic and liberates hydrogen gas, so that heating to initiate reaction can be hazardous, particularly when the

polymerizations are run on a large scale.

Photochemical initiation proved to suffer none of these limitations. Heating is not required; initiation may be effected safely in an ice-water bath. Relatively low (mM) concentrations of catalyst may be employed. Typically, a thick-walled Pyrex Schlenk flask with Teflon stopcock containing silane monomer, catalyst and airless solvent is freeze-thaw evacuated and placed 5-10 cm from a 450 W medium pressure Hanovia mercury lamp housed in a water-cooled quartz immersion well. Brief (10-60 min.) irradiation using catalytic amounts of cp_2TiMe_2 causes an initial change in color from yellow to brown, and eventually to dark green or blue over a longer period. No polymerization is evident before these color changes occur. The progress of polymerization was found to be identical regardless of whether initiation was accomplished photochemically or thermally. Prolonged irradiation after the onset of polymerization and color change affected neither the rate nor the course of polymerization. Furthermore, irradiation of the silanes alone resulted in no reaction [6]. These results indicate that the role of light is solely to activate the catalyst, presumably involving labilizing a Ti-C bond. Apparently the same active catalyst (represented as "cp_2Ti" [2]) is produced regardless of the method of initiation, and the same polymer forms (see below).

The photochemical method for initiation also was found to be applicable when dimethylzirconocene (cp_2ZrMe_2) was used as catalyst. Zirconocene catalysts are effective in polymerizations of alkylsilanes [2,7]. We have found that cp_2ZrMe_2 reacts stoichiometrically with vinylsilane and is not an efficient catalyst for polymerization, however.

Polyethylsilane

Use of the milder conditions attending photochemical initiation facilitates mechanistic studies. Polymerization of ethylsilane (0.6 M ethylsilane and 0.014 M cp_2TiMe_2 in THF with 20 min. irradiation) was examined. After 7 d., spectroscopic analysis (GC/MS and ^1H, ^{13}C and ^{29}Si NMR) revealed a distribution of short oligomers with n = 1-7, predominantly of the type indicated in Eq. 1 (R = CH_2CH_3), as expected for a step-growth polymerization. After longer times (30 d.), or with higher concentration of catalyst (0.06 M), the distribution of oligomers shifts toward higher molecular weight (predominantly n = 5-12) as identified by GC/MS. Sensitivity for detection of the higher polymers ($n \geq 10$) is reduced due to lower volatility and the presence of a large number of stereoisomers. The liberation of gaseous hydrogen was evident from pressurization of the reaction vessel concurrent with polymerization.

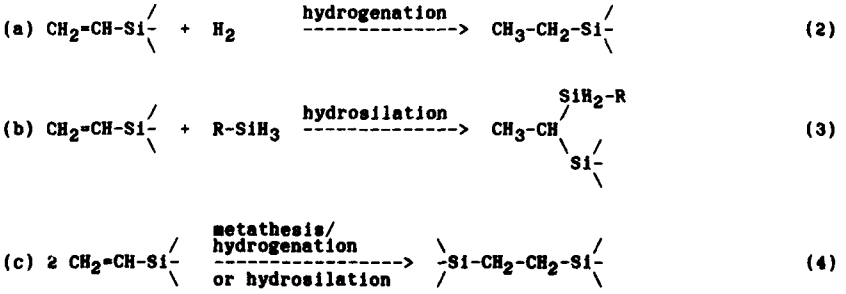
One apparent discrepancy between these results and reports by Harrod [1,2] concerns the step-growth nature of the polymerization. Differences

in catalyst concentration may be responsible. The active catalyst may depend upon concentration; for example, dimeric metal complexes may be involved at high concentration. Alternatively, high concentrations of catalyst and elevated temperature may lead rapidly to formation of polymer of higher molecular weight, and the lower molecular weight oligomers may be overlooked. Experiments to further address these possibilities are in progress. In any event, the polymers are mostly linear, possessing a backbone of -Si-Si- bonds and pendant alkyl substituents.

Polyvinylsilane

Polymerization of vinylsilane under identical conditions proceeded efficiently. The reaction vessel was not pressurized during the polymerization, indicating that significant liberation of hydrogen gas was not occurring. Analysis by GC/MS suggested that vinylsilane also polymerizes by a step-growth mechanism, and the molecular weight distribution of polyvinylsilane resembles that of polyethylsilane with a similar history. The molecular structue of polymer derived from vinylsilane, however, differed significantly from that of polyethylsilane.

Most revealing were differences in the spectroscopic properties (NMR and IR) of the two polymers. The polymer of vinylsilane exhibited a higher proportion of protons attached to Si (Si-H) compared to C (C-H). The ratio Si-H / C-H is 1.0 in vinylsilane (compared to 0.42 in the polymer) and 0.60 in ethylsilane (compared to 0.17 in polyethylsilane). Vinyl groups are observed spectroscopically (NMR and IR) in the polymer at very early times (or at longer times using lower concentration of catalyst), but the centers of unsaturation are consumed rapidly as polymerization progresses. The mature polymer contains only saturated hydrocarbon groups. These groups are of three basic types, (a) CH_3-CH_2-Si, (b) $CH_3-CH(Si)_2$ and (c) $Si-CH_2-CH_2-Si$, with the latter two predominating. Such substituents apparently arise from the reactions indicated in Eqs. 2, 3 and 4. Hydrogenation (Eq.



2) is a relatively minor pathway, presumably because little, if any, gaseous H_2 is produced by dehydrogenative coupling (Eq. 1). Olefin metathesis (Eq. 4) is evident by GC/MS analysis. Hydrosilation (Eq. 3) appears to be facile, and this reaction affords a polycarbosilane (-Si-C-Si-C- backbone). Details of the spectroscopic assignments will be reported elsewhere [8].

Thermogravimetric analysis indicates that the polycarbosilane derived from vinylsilane is pyrolyzed more efficiently than is polyethylsilane (-Si-Si-Si-Si- backbone) [9]. Thus, the char yield of vinylsilane polymer was found to be 60% compared to a char yield of 10% for polyethylsilane formed under the same conditions (see above). Longer reaction times (or higher concentrations of catalyst) give more viscous materials and higher char yields for both polymers. Analysis by X-ray diffraction of materials pyrolyzed to 1200°C in argon demonstrates a greater tendency for SiC formation from the vinyl polymer than from polyethylsilane. Application to the preparation of ceramic coatings and matrices currently is under investigation.

Acknowledgement

The authors would like to thank Dr. A. Wolff for preliminary experiments, T. Hionidou and A. L. Rivera for technical assistance, and the NASA Lewis Research Center for support of this work under cooperative agreement NCC 3-63.

References

[1] E. Samuel and J. F. Harrod, J. Am. Chem. Soc. 106, 1859 (1984).

[2] J. F. Harrod in Inorganic and Organometallic Polymers, edited by M. Zeldin, K. J. Wynne, and H. R. Allcock (ACS Symposium Series, 1988), Vol. 360, p. 89, and references therein.

[3] D. J. Carlsson, J. D. Cooney, S. Gauthier, and L. J. Worsfold, J. Am. Ceram. Soc. 73, 237 (1990).

[4] C. L. Schilling, Jr., Brit. Polym. J. 18, 355 (1986); C. L. Schilling, Jr., J. P. Wesson, and T. C. Williams, Ceram. Bull. 62, 912 (1983); J. Polym. Sci.: Polymer Symposium 70, 121 (1983).

[5] H. G. Alt, F. P. Di Sanzo, M. D. Rausch, and P. C. Uden, J. Organomet. Chem. 107, 257 (1976); G. J. Erskine, J. Hartgerink, E. L.

Weinberg, and J. D. McCowan, ibid., 170, 51 (1979).

[6] Silanes do react under far-uv irradiation. See: J. C. Dalton, Org. Photochem. 7, 149 (1985); R. West, L. D. David, P. I. Djuorvich, H. Yu, and R. Sinclair, Am. Ceram. Soc. Bull. 62, 899 (1983).

[7] W. H. Campbell and T. K. Hilty, Organometallics 8, 2615 (1989).

[8] J. Masnovi, X. Y. Bu, P. Conroy, and K. Beyene, unpublished results.

[9] S. Yajima, J. Hayashi, M. Omori, and K. Okamura, Nature 261, 683 (1976); S. Yajima, J. Hayashi, and M. Omori, Chem. Lett. 1975, 931.

HIGH RESOLUTION TEM OF ORGANIC AEROGELS AND INORGANIC AEROGELS

GEORGE C. RUBEN AND *RICHARD W. PEKALA
Department of Biological Sciences, Dartmouth College, Hanover, NH 03755
*Chemistry & Materials Science Department, Lawrence Livermore National Laboratory, Livermore, CA 94550

ABSTRACT

A base catalyzed silica aerogel and three base catalyzed resorcinol-formaldehyde (RF) aerogels were imaged with a new vertical platinum-carbon (Pt-C) replication technique. In deep gels single molecular chains can be visualized with transmission electron microscopy (TEM) with 9-10 Å thick Pt-C replicas backed with 110-130 Å of carbon [2]. The three RF aerogels produced with [Resorcinol]/[Catalyst] ratios (R/C) of 50, 200, and 300 had densities of 0.103, 0.063, and 0.065 gm/cc and had surface areas of 905, 580, and 390 m^2/gm, respectively. The gel connectors and junctions in RF 300 and RF 200 were composed of 210±30 Å and 140±10 Å beads which were joined by polymeric chains covering an area less than half the bead's diameter and within a bead diameter's distance. The gel connectors and junctions in RF 50 were frequently composed of beads of about 120±10 Å joined over an area larger than half the bead's diameter. Similar to the silica aerogel (0.065 gm/cc, 113±10 Å beads), the beads were frequently connected over several bead diameter's distance from each other.

INTRODUCTION

The ultrastructure of resorcinol-formaldehyde (RF) and silica aerogels largely depends upon the catalyst conditions used in their respective sol-gel polymerizations. Silica gels are usually produced from the hydrolysis and condensation of tetramethylorthosilicate (TMOS) or tetraethylorthosilicate (TEOS) in the presence of an acid or base catalyst. Under acidic conditions, linear or slightly branched siloxane chains are formed which entangle and then crosslink to form a gel. Under alkaline conditions, highly branched "clusters" are formed. These "clusters" eventually crosslink through their surface silanol groups (Si-OH) to produce a gel. Each of the above reaction pathways has been mapped onto a simple physical growth model. Under acid catalyzed conditions, reaction limited cluster-cluster growth is favored and leads to aerogels that are mass fractals. In contrast, monomer-cluster growth is promoted under alkaline conditions, leading to aerogels of compact interconnected particles.

Organic aerogels formed from the polycondensation of resorcinol with formaldehyde can only be produced under base catalyzed conditions. The [Resorcinol]/[Catalyst] ratio (R/C) is the major factor that controls the size of RF "clusters" generated in solution. These "clusters" contain surface hydroxymethyl groups (-CH_2OH) that condense to form a gel. [Resorcinol]/[Catalyst] ratios of 50-300 provide an acceptable range in which transparent gels can be produced.

The particle size, surface areas, cell size, density, and mechanical properties of the resultant RF aerogels depend upon the R/C ratio [1]. Organic aerogels are generally composed of interconnected spherical particles (30-200 Å diameter) that are derived from the "clusters" generated in solution. At R/C=300, predominantly large particles are lightly fused together giving a "string of pearls" appearance and a low surface area (~400 m^2/g). At R/C=50, predominantly small particles are tightly fused together giving a fibrous appearance and a high surface area (~900 m^2/g). As expected, the mechanical properties of these aerogels are quite different. At equivalent densities, RF 50 aerogels prepared at R/C=50 are ~7X stiffer in compression than RF 300 aerogels prepared at R/C=300.

Although bulk material properties (e.g., modulus) are a function of aerogel ultrastructure, previous efforts directed at imaging aerogels at the molecular level have not been successful until now. In this study, three RF aerogels (R/C=50; 200; 300) and a base catalyzed silica aerogel similar to RF aerogel, R/C=50, were fractured and surface replicated with 9-10 Å of platinum-carbon (Pt-C). High resolution transmission electron microscopy (HRTEM) was used to examine the surface replicas in stereo with a tilt series at 10^4-10^5 magnification though no stereo-images appear in this report. Individual polymer chains and crosslinking junctions were visualized in all the aerogels although only representative images will be presented in this article.

Mat. Res. Soc. Symp. Proc. Vol. 180. ©1990 Materials Research Society

EXPERIMENTAL

Gel preparation has been previously described [1]. Briefly , resorcinol and formaldehyde were mixed in deionized and distilled water at a mole ratio of 1:2. Sodium carbonate was then added as the base catalyst. The RF solution was poured into 23 x 85 mm glass vials which were tightly sealed and placed into an oven to cure at 85-95°C. Depending upon the percent solids and catalyst level, gel times varied from several hours to days. Typically, the RF gels were cured for seven days and then removed from their glass containers and placed in a 0.1% trifluoroacetic acid solution at 45°C. The acid treatment increased the modulus of the gels through additional crosslinking provided by the condensation of hydroxymethyl groups to form ether bridges.

In preparation for supercritical drying, the gels were exchanged into an organic solvent which was compatible with liquified carbon dioxide, such as acetone, methanol, or isopropanol. The solvent filled gels were placed into a jacketed pressure vessel (Polaron Equipment Ltd., Wateford, England) which was then filled with carbon dioxide. After the carbon dioxide was completely exchanged for the solvent in the pores of the gels, the vessel was heated 15°C above the critical temperature (T_c=31°C). The samples were maintained at 46°C for a minimum of four hours, and then the pressure was slowly released through an exit valve. At atmospheric pressure, the samples were removed and held in front of a light source to ensure that the aerogels were transparent.

The RF aerogels were prepared for HRTEM by first fracturing them with a razor knife while submerged in a liquid nitrogen bath. In a few cases the aerogels fractured spontaneously in liquid nitrogen without mechanical application of the knife. Unlike the RF aerogels which are a dark wine color, the silica aerogel was transparent and very difficult to see. Because liquid nitrogen could shatter the silica aerogel and it was invisible in liquid nitrogen, the nitrogen bath was avoided and the silica aerogel was fractured with tweezers at room temperture. Aerogel pieces were then loaded onto the stage of the Balzer's 300, evacuated to $5x10^{-8}$ torr.and cooled to -185°C. The specimens were platinum-carbon (Pt-C) replicated at an almost vertical angle (80°) and backed with a rotary deposited carbon film at a 100° angle. The silica and RF aerogel samples were replicated as follows:

Name	Density (gm/cc)	Pt-C film thickness	Carbon film thickness
silica	0.06	9.3Å	121Å
RF 50	0.103	9.3Å	123Å
RF 200	0.063	10.0Å	121Å
RF 300	0.065	9.3Å	121Å

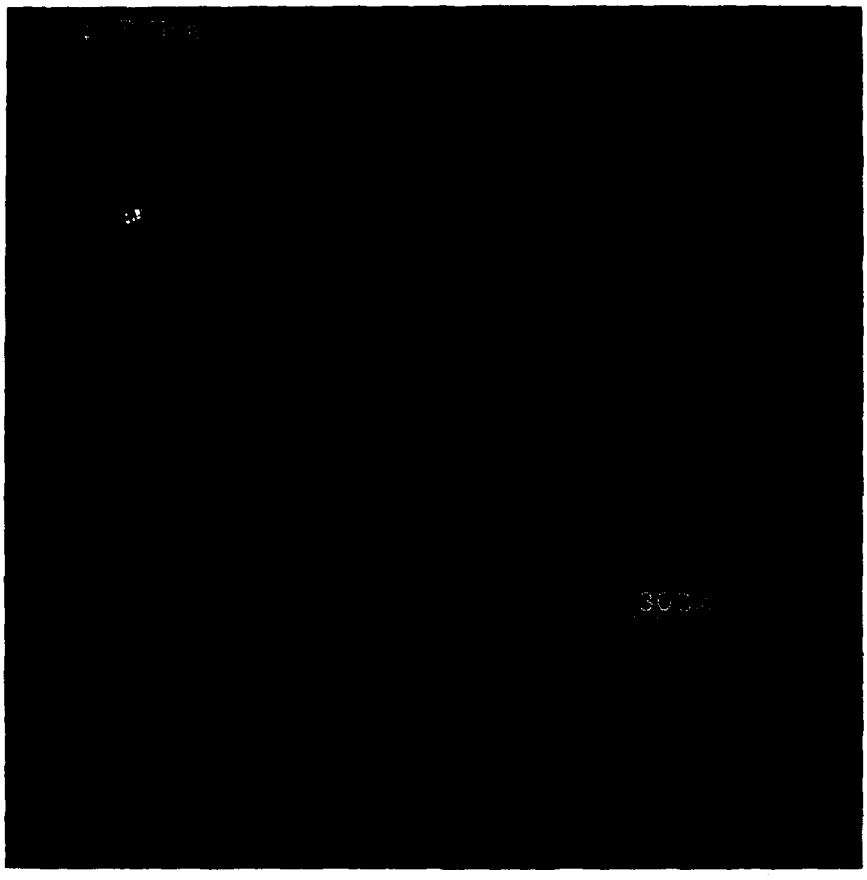
The silica replica was removed with dilute hydofluoric acid and the RF replicas were removed from the RF aerogel with full strength chlorox bleach. The replicas were floated (washed) on distilled water and then picked up on 300 or 400 mesh copper grids. The replicas were imaged in the JEM 100CX TEM with a 2625Å depth of field and with a 6.6Å resolution [2]. Kodak 4489 film was used and image reversals and prints were made as previously described [2].

From previous work a 9.3Å thick Pt-C film increases the average polysiloxane chain of ~4.1Å [3,4] by roughly 5.6Å to a Pt-C coated average chain thickness of 9.7Å [2]. It is assumed that the average unbranched RF chain thickness is between 3-7Å and its width is increased by a 9.3 or a 10Å thick Pt-C film by 5.6 or 6Å. A Pt-C coated RF chain should average between 9-13Å which is the chain size found in all the Pt-C replicated RF aerogels.

RESULTS

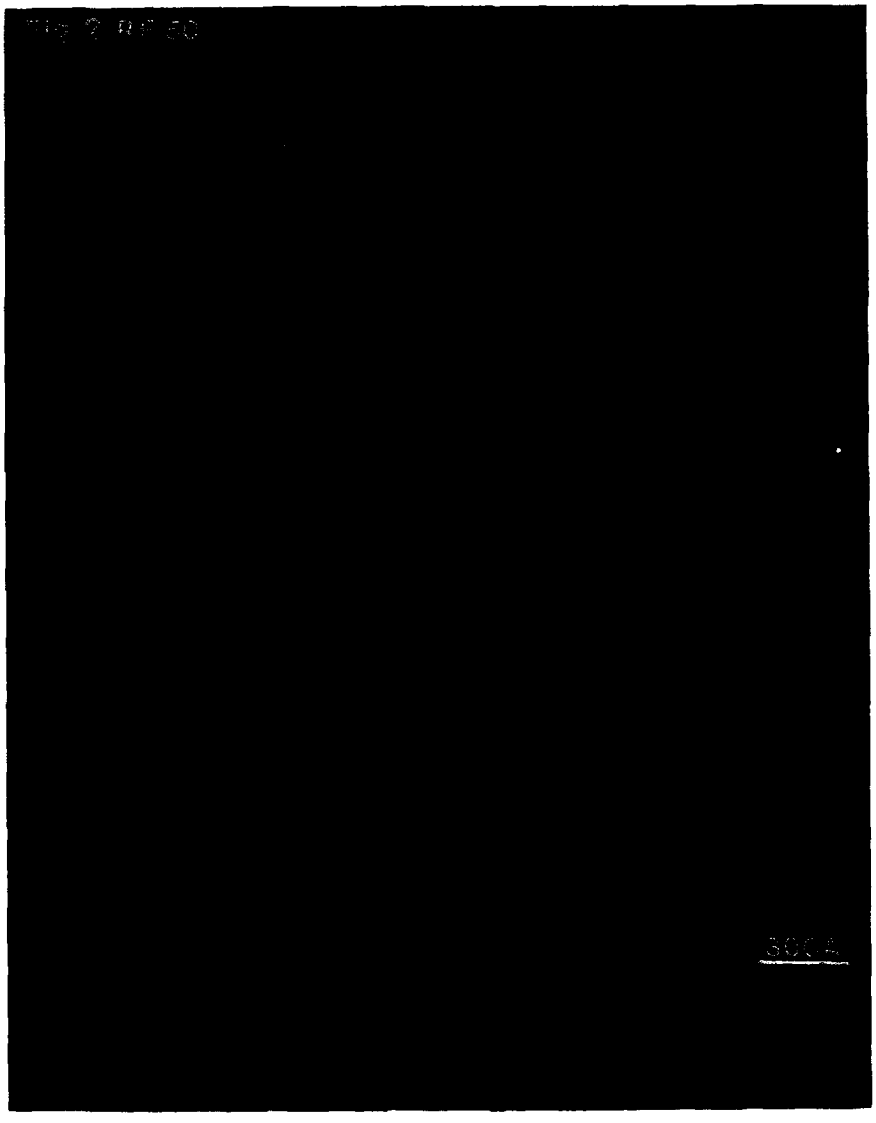
Silica Aerogel

The aerogel filaments or connectors contain many small beads. The bead diameters measured in stereo-images range from 86-132Å . The average bead diameter was approximately 113±10Å assuming a spherical bead shape . Frequently the connectors had a beads on a string morphology. It was not uncommon to find adjacent beads separated by 1-5 bead diameters and connected with 2-4 Pt-C coated polymeric filaments which each had a ~10Å width. A representative image of the silica aerogel is shown in Fig. 1. Unlike the RF aerogels (Figs. 2-4) which are of good contrast, this silica aerogel replica still contains unremoved silica which is probably responsible for its lower contrast. While low contrast does not affect image resolution, it makes the beads and polymeric filaments harder to see.



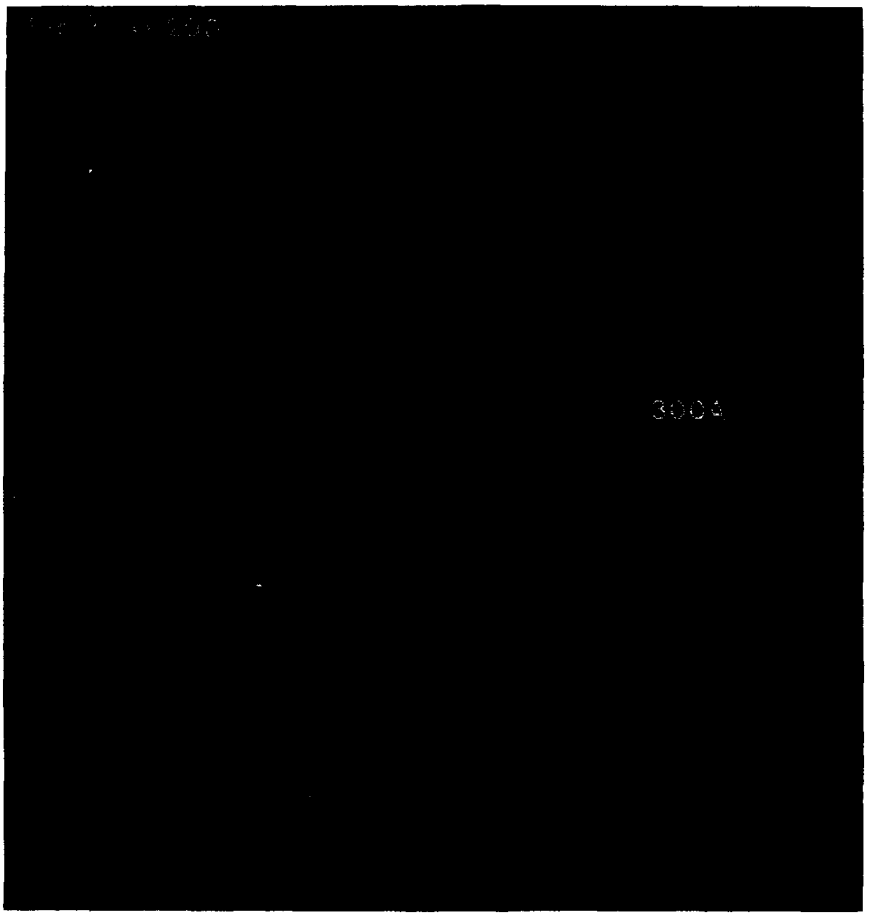
RF 50 Aerogel

This aerogel (Fig. 2) is more like the silica aerogel (Fig. 1) than either RF 200 (Fig. 3) or RF 300 (Fig. 4). The beads are not always evident in this aerogel. Nonetheless, the bead sizes measured when viewing this aerogel in stereo range from 93-166Å, and average about 120±10Å. In the areas where beads are difficult to find, it appears that either polymeric chain growth without intervening beads or molecular chain growth connecting the beads has made them indistinguishable. In consequence these aerogel connectors often look like grouped polymeric chains or segmented worms. The aerogel connectors in RF 200, RF 300 and the silica aerogel frequently look more like beads on a string, which suggests that the connections between beads are generally not thicker than a bead radius whereas in RF 50, the bead connections generally appear to be larger than the bead radius. The aerogel connectors in RF 50 often appear thicker than those in the silica aerogel and the connectors appear to occur with equivalent frequency per area in both gels. There also appear to be junctions of up to five connectors in RF 50 whereas in the silica aerogel we have seen no more than three connectors forming a junction. The very high surface area in this aerogel is probably an indication that the polymeric chain growth connecting the beads is of lower density than the individual beads. Since the bead size increases respectively, from RF 50, RF 200, to RF 300, and since the amount of polymeric lower density chain growth mass connecting the beads decreases in this series, the "lower density polymeric chain bead connections-higher density bead" hypothesis is consistent with the trend of decreasing surface area measured by the BET method.



RF 200 Aerogel

This aerogel (Fig. 3) when viewed in stereo demonstrates that the connectors have a string of beads appearance. The beads range from 130-150Å in diameter (140±10Å average) within a connector with fine chains connecting them together. The polymeric connections between beads average 40-60Å in width, generally less than the average bead radius of 70Å, and this polymeric material can sometimes extends 3-4 bead diameters to the next bead. The connector diameters are dominated by the bead diameters and have an average diameter of 130±30Å. The beaded connectors in this aerogel are rarely straight. In RF 50 the connectors tend to be thinner and less nonlinear.

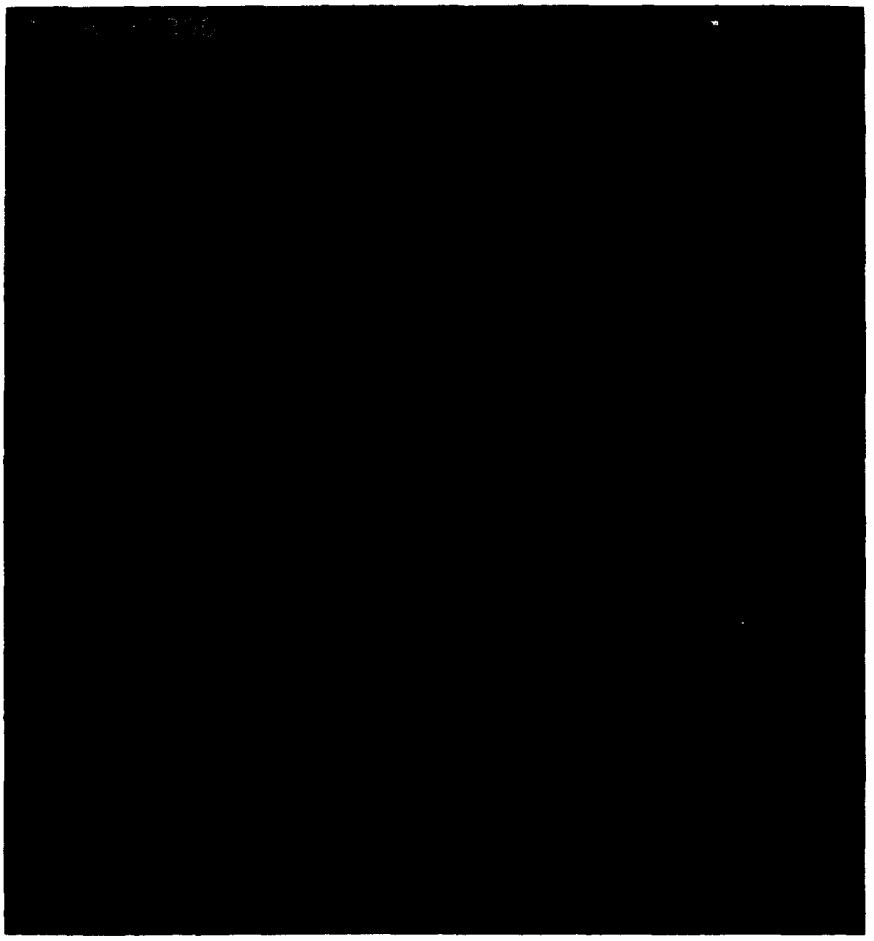


RF 300 Aerogel

This aerogel (Fig. 4) is more obviously particulate than either RF 50 (Fig. 2) or RF 200 (Fig. 3). There appears to be a maximum of 10-12 beads before a connector joins a junction. The connectors look like beads on a string which are sometimes only joined by a few chains. The polydisperse bead sizes, measured perpendicular to the connectors, range from 160-300Å and average 210±30Å. Strings with the same maximum number of 10-12 beads have also been seen in RF 200. The appearance of the connectors in RF 200 is different from RF 300. In RF 200 the beads appear to be fused together with a lumpy appearance and with good polymeric chain connections. In RF 300 the beads in each chain are more prominent and the connection diameter between beads is a smaller fraction of the bead diameter than in RF 200.

CONCLUSIONS

We have shown that vertically Pt-C replicated silica and RF aerogels can be visualized with HRTEM. The images have been correlated with density, surface area and compressive modulus measurements. The images and measurements help explain the properties of the aerogels.



ACKNOWLEDGMENT

I wish to thank LLNL for supporting this work, Blanca Haendler who was instrumental in arranging this collaboration, and Dartmouth's Rippel Electron Microscope facility for the use of its equipment.

REFERENCES

1. R.W. Pekala, J. Mater. Sci. 24 (9), 3221 (1989).

2. G.C. Ruben , J. Elect. Microsc. Tech., 13, 335 (1989).

3. G.C. Ruben and M.W. Shafer in Better Ceramics Through Chemistry II, edited by C.J.Brinker, D.E.Clark, and D.R.Ulrich (Mater. Res. Soc. Proc. 73, Pittsburgh, PA 1986) pp.207-212 .

4. M.W. Shafer, D.D. Awschalom, J. Warnock and G.C. Ruben, J. Appl. Phys., 61, 5438 (1987).

A NEW SYNTHETIC ROUTE TO ORGANIC AEROGELS

R.W. PEKALA AND C.T. ALVISO, Department of Chemistry & Materials Science, Lawrence Livermore National Laboratory, Livermore, CA 94550

ABSTRACT

The aqueous, sol-gel polymerization of melamine with formaldehyde, followed by supercritical extraction, leads to the formation of a new type of organic aerogel. Synthetic conditions (e.g. reaction time, pH) affect the density, transparency, and microstructure of the resultant aerogels. Unlike previous organic aerogels based upon resorcinol-formaldehyde, the melamine-formaldehyde aerogels are both colorless and transparent. Low densities (0.1-0.8 g/cc), high surface areas (~1000 m^2/g), and optical clarity are only a few of the promising characteristics of this new material.

INTRODUCTION

Aerogels are a special class of low density, open-cell foams. These materials have continuous porosity, ultrafine cell/pore sizes (< 500 Å), and a solid matrix composed of interconnected colloidal-like particles or polymeric chains with characteristic diameters of 100 Å. This microstructure is responsible for the unusual acoustic, mechanical, optical, and thermal properties of these materials [1,2].

The hydrolysis and condensation of metal alkoxides (e.g. tetramethoxy silane) is the most common synthetic route for the formation of *inorganic aerogels* [3-5]. Our research has focused on sol-gel polymerizations that lead to *organic aerogels*. The reaction pathway, microstructure, and properties of these new materials are analagous to their inorganic counterparts. Furthermore, our organic aerogels are distinctly different from the 'aerogels' that Kistler prepared from nitrocellulose, cellulose, agar, and egg albumin [6].

Previous work has shown that organic aerogels can be formed from the base catalyzed, aqueous polymerization of resorcinol (1,3 dihydroxy benzene) with formaldehyde [7-10]. Although resorcinol-formaldehyde (RF) aerogels exhibit minimal light scattering, these materials are dark red in color and have a large absorption coefficient within the visible spectrum. The color centers in RF aerogels result from oxidation products (e.g. quinones) formed during the sol-gel polymerization. Their presence has limited the use of these materials in certain optical applications where an aerogel is required to be both colorless and transparent.

In order to circumvent this problem, we are forming colorless gels from the aqueous polycondensation of melamine (2,4,6 triamino s-triazine) with formaldehyde. Synthetic conditions (e.g. pH, reaction time) affect both the transparency and microstructure of the resultant melamine-formaldehyde (MF) aerogels. This paper describes in detail the synthesis and characterization of these new organic aerogels.

Mat. Res. Soc. Symp. Proc. Vol. 180. ©1990 Materials Research Society

EXPERIMENTAL

The polycondensation of 3-6 moles of formaldehyde (37.6 %; methanol stabilized; J.T. Baker) with 1 mole of melamine (99+ %; Aldrich Chemical) was carried out in deionized and distilled water using 10-100 millimoles of sodium hydroxide as a base catalyst. The above slurry was heated for 10-15 mins. at 70 °C to form a clear solution. This solution was allowed to cool to 45 °C, at which time, concentrated hydrochloric acid (36.5%) was added. If the solution was heated too long at 70 °C or the pH was not properly adjusted, a white precipitate was formed and a gel could not be obtained. To form transparent gels, the pH of the MF solution was required to be 1.5-1.8 when measured at 23 °C. Outside of this range, translucent or opaque gels were formed.

The pH adjusted, melamine-formaldehyde solution was poured into 23 x 85 mm glass vials, sealed, and cured under various conditions. Solutions containing ≥ 20 % reactants gelled in less than 24 hours at room temperature, while solutions containing 7 % reactants gelled in approximately 4 weeks at a cure temperature of 85-95 °C. As the reaction progressed, all formulations acquired a light blue haze.

In preparation for supercritical drying, the crosslinked gels were removed from their glass vials and placed in an ammonium hydroxide solution to neutralize the HCl within the pores. The gels were then exposed to a 50:50 mixture of acetone:water, followed by a 75:25 mixture, and finally 100% acetone. Multiple exchanges with fresh acetone were used to remove residual water from the gels.

The acetone-filled, MF gels were dried in a jacketed pressure vessel (Polaron Equipment Ltd., Watford, England) using carbon dioxide as the supercritical fluid (T_c= 31 °C; P_c= 1100 psi). Details of this procedure have been described elsewhere [7,8]. MF aerogels removed from the pressure vessel were transparent, indicative of the ultrafine cell size (< 500 Å) of these porous solids. All samples were stored in desiccators to inhibit moisture adsorption and prevent cracking.

RESULTS AND DISCUSSION

Melamine is a hexafunctional monomer capable of reaction at each of the amine hydrogens. Under alkaline conditions, formaldehyde adds to the above positions to form hydroxymethyl (-CH_2OH) groups. In the second part of the polymerization, the solution is acidified to promote condensation of these intermediates, leading to gel formation. The principal crosslinking reactions include the formation of (1) diamino methylene (-$NHCH_2NH$-) and (2) diamino methylene ether (-$NHCH_2OCH_2NH$-) bridges [11,12]. Figure 1 outlines the MF reaction and depicts the formation of a crosslinked polymer network.

At present, the role of solution pH (acidification) and its effects upon gel clarity are not totally understood. All melamine-formaldehyde solutions develop a blue haze as they cure. This phenomenon is associated with Rayleigh scattering from MF "clusters" generated in solution. These "clusters" contain surface functional groups (e.g. -CH_2OH) that eventually crosslink to form a gel. We believe that the aggregation and crosslinking processes are strongly pH dependent. Thus, only a small pH window exists for the preparation of transparent gels.

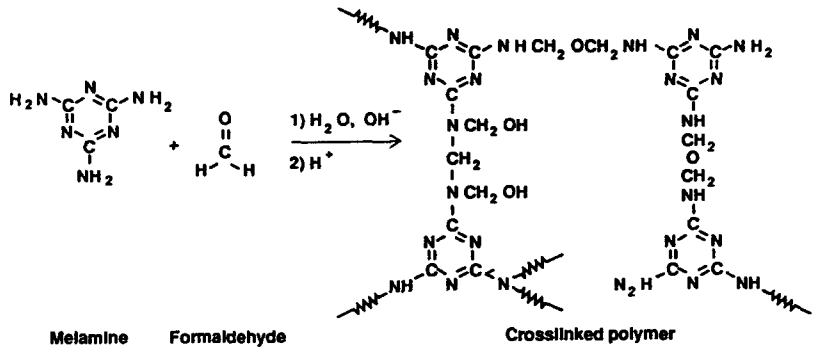


Figure 1. A schematic diagram of the reaction of melamine with formaldehyde.



Figure 2. A 17 mm thick, transparent MF aerogel with density equals 0.3 g/cc.

Melamine-formaldehyde aerogels have been synthesized with densities ranging from 0.1-0.75 g/cc. Figure 2 shows an MF aerogel after supercritical drying. The aerogel is both colorless and transparent. The latter property indicates that the cell/pore size and characteristic particle size (referred to as "cluster" size in solution) are less than 1/20th the wavelength of visible light. The optical clarity of melamine-formaldehyde aerogels is equivalent to that of many silica aerogels.



Figure 3. Scanning electron micrograph of a melamine-formaldehyde aerogel.

The fracture surface of an MF aerogel is shown in Figure 3. SEM reveals that the aerogel is composed of interconnected particles with diameters < 500 Å. At this magnification, it is difficult to tell if the particles are composed of even smaller subunits. BET nitrogen adsorption measurements give a surface area of 970 m^2/g. Further evaluation of the aerogel microstructure is under investigation using transmission electron microscopy and small angle x-ray scattering.

SUMMARY

Organic aerogels that are both colorless and transparent have been prepared from the aqueous, sol-gel polymerization of melamine with formaldehyde. These aerogels have low densities, high surface areas, continuous porosity, and ultrafine cell/pore sizes (< 500 Å). Their organic composition provides these materials with many potential advantages over conventional inorganic aerogels (e.g. insulating properties).

ACKNOWLEDGMENTS

This work was performed under the auspices of the U.S. Department of Energy by the Lawrence Livermore National Laboratory under contract # W-7405-ENG-48.

REFERENCES

[1] J. Fricke, Sci. Am., 258(5), 92 (1988).
[2] J. Fricke, in Sol-Gel Science and Technology, M.A. Aegerter, M. Jafelicci, D.F. Souza, and E.D. Zanotto, eds., New Jersey: World Scientific Publishing, 482 (1989).
[3] S.J. Teichner, G.A. Nicolaon, M.A. Vicarini, and G.E.E. Gardes, Adv. Coll. Interf. Sci., 5, 245 (1976).
[4] C.J. Brinker, K.D. Keefer, D.W. Schaefer, and C.S. Ashley, J. Non-Cryst. Solids, 48, 47 (1982).
[5] C.J. Brinker, K.D. Keefer, D.W. Schaefer, R.A. Assink, B.D. Kay and C.S. Ashley, J. Non-Cryst. Solids, 63, 45 (1984).
[6] S.S. Kistler, Nature, 127, 741 (1931).
[7] R.W. Pekala and F.M. Kong, J. de Physique, Colloque Suppl., 50(4), C4-33 (1989).
[8] R.W. Pekala, J. Mat. Sci., 24, 3221 (1989).
[9] R.W. Pekala and F.M. Kong, Polym. Prpts., 30(1), 221 (1989).
[10] R.W. Pekala and R.E. Stone, Polym. Prpts., 29(1), 204 (1988).
[11] W.J. Blank, J. Coatings Tech., 51(656), 61 (1979).
[12] I.H. Updegraff, "Amino Resins," in Encyclopedia of Polymer Science and Engineering, 2nd ed., Vol. 1, New York: John Wiley & Sons, 752-789 (1985).

CRYSTALLIZATION OF PYROLYZED POLYSILAZANES

Roger L. K. Matsumoto, Hercules Incorporated, Research Center, Wilmington, DE 19894

ABSTRACT

Polysilazanes are inorganic polymers which convert to a ceramic material when pyrolyzed. Initial pyrolysis results in a solid, amorphous material. Further heating transforms the amorphous structure to a crystalline material. In addition to the Si-N linkages in the polymer backbone, polysilazanes generally contain appreciable amounts of carbon in side groups. Consequently, pyrolysis can result in mixed Si_3N_4 - SiC crystalline materials. It will be shown that either Si_3N_4 or SiC could be selectively crystallized depending upon processing conditions.

INTRODUCTION

Polysilazane compounds are defined by Si-N linkages in the polymer backbone. Although polysilazanes containing no Si-C bonds have been shown to pyrolyze to silicon nitride exclusively (1), most polysilazanes of practical interest have organic groups attached to silicon. Figure 1 shows a generalized polysilazane structure. These polysilazanes may produce mixed Si_3N_4 - SiC ceramics upon pyrolysis (2-4).

EXPERIMENTAL PROCEDURE

Polysilazanes of the composition $(Si_{1.0}N_{1.0}C_{1.4}H_{5.4})_x$ were pyrolyzed under either nitrogen or argon. Materials were pyrolyzed from 1200°C to 1600°C in 100°C intervals under nitrogen and at 1200°C and 1600°C under argon. The polysilazanes were filled with an alpha silicon nitride powder (UBE SN-E10) to 20 weight percent (w/o) and were pyrolyzed under nitrogen to 1200°C and 1600°C. They were also filled with alpha silicon carbide powder (Starck A-10) to 50 w/o and pyrolyzed under argon to 1200°C and 1600°C. A polysilazane filled with 50 w/o beta silicon carbide whiskers (American Matrix) was pyrolyzed under argon to 1600°C. In all cases the heating rate used was 10°C/min and the time at maximum temperature was 2 hours. All pyrolysis

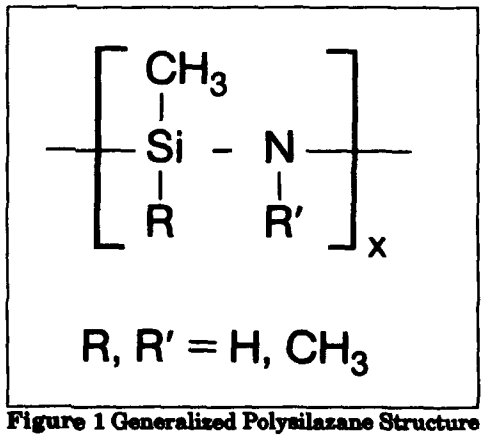


Figure 1 Generalized Polysilazane Structure

Mat. Res. Soc. Symp. Proc. Vol. 180. ©1990 Materials Research Society

products were examined by X-ray diffraction (XRD).

RESULTS

The evolution of crystallinity in the pyrolyzed unfilled polysilazane fired under nitrogen is shown by XRD patterns in Figure 2. Up to 1400°C, the pyrolysis product remains amorphous. By 1500°C, it has crystallized to both the alpha and beta forms of silicon nitride. The relative intensities of the alpha and beta polymorphs do not change upon further heating to 1600°C.

The XRD patterns of the pyrolysis products of unfilled polysilazanes under argon are shown in Figure 3. At 1200°C, the material is completely amorphous. It has completely crystallized by 1600°C, however this time mostly beta silicon carbide (3C polytype) has formed.

Filling the polysilazane with alpha silicon nitride powder results in differences in the pyrolysis product (Figure 4) compared to the product of the unfilled polysilazane. At 1200°C, the filled sample shows alpha silicon nitride peaks over the amorphous background of the pyrolyzed polysilazane. By 1600°C, the crystallinity is well pronounced, but unlike the unfilled material which contained substantial beta phase, the filled material consists largely of the alpha phase.

Using alpha silicon carbide powder in polysilazane and pyrolyzing in argon, a high degree of crystallinity to the alpha phase is reached by 1200°C as shown in Figure 5. Crystallization is complete by 1600°C with no change in the relative intensities of the various alpha silicon carbide polymorphs.

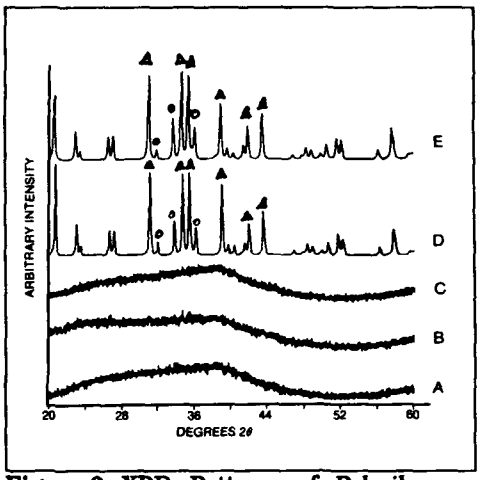


Figure 2 XRD Patterns of Polysilazanes Pyrolyzed to; (A) 1200°C; (B) 1300°C; (C) 1400°C; (D) 1500°C; and (E) 1600°C Under Nitrogen.
(a) Denotes Alpha Silicon Nitride Peaks, (o) Denotes Beta Silicon Nitride Peaks.

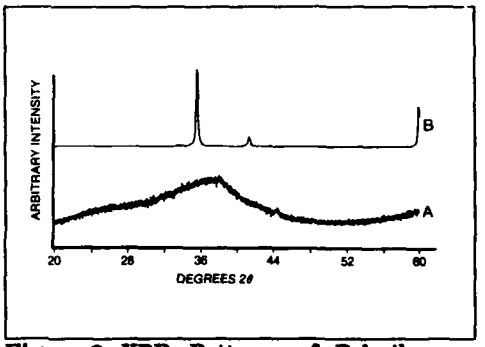


Figure 3 XRD Patterns of Polysilazanes Pyrolyzed to (A) 1200°C and (B) 1600°C Under Argon.

The pyrolysis of the beta silicon carbide-containing polysilazane results in complete crystallization to beta silicon carbide as shown in Figure 6.

DISCUSSION

Pyrolysis of unfilled polysilazanes in the two atmospheres to 1200°C resulted in black, amorphous bodies. These amorphous bodies crystallized into different structures depending upon the atmosphere when pyrolyzed to the higher temperature of 1600°C. The evolution of crystallization shown in Figure 2 demonstrates that this happens over a relatively narrow temperature range.

Filling the polysilazanes prior to pyrolysis results in crystallization at lower temperatures. This would be expected since the fillers act as seeds so that the crystallization can proceed epitaxially. The epitaxial nature of this growth is demonstrated by comparing Figures 2 and 4 for the case of silicon nitride. The addition of a 95% alpha phase powder results in the suppression of the beta phase formation during crystallization. The effect is also seen with silicon carbide. The phase that crystallizes from unfilled polysilazane when pyrolyzed in argon is beta silicon carbide (Figure 3), but when alpha silicon carbide powder is added to the polysilazane, only alpha silicon carbide results after crystallization (Figure 5). In contrast, when beta silicon carbide whiskers are added, the crystallization produces only beta silicon carbide (Figure 6).

CONCLUSION

Despite the fact that most polysilazanes have both Si-N and Si-C bonds, the crystallized

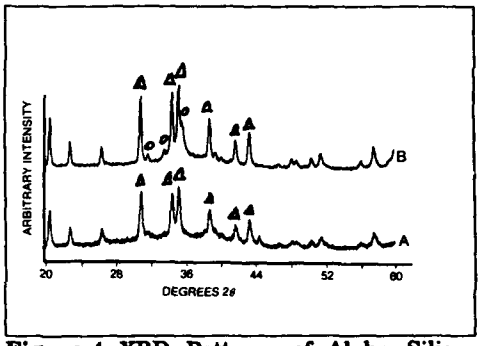


Figure 4 XRD Patterns of Alpha Silicon Nitride-Filled Polysilazanes Pyrolyzed to (A) 1200°C and (B) 1600°C Under Nitrogen. (▲) Denotes Alpha Silicon Nitride Peaks, (o) Denotes Beta Silicon Nitride Peaks.

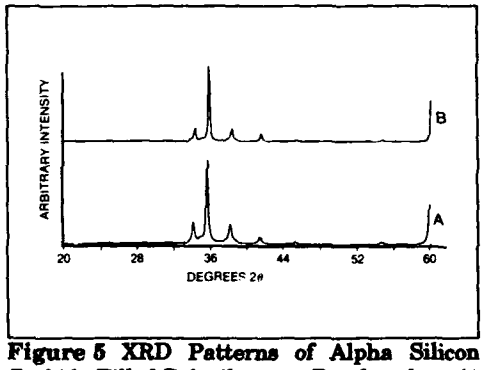


Figure 5 XRD Patterns of Alpha Silicon Carbide-Filled Polysilazanes Pyrolyzed to (A) 1200°C and (B) 1600°C Under Argon.

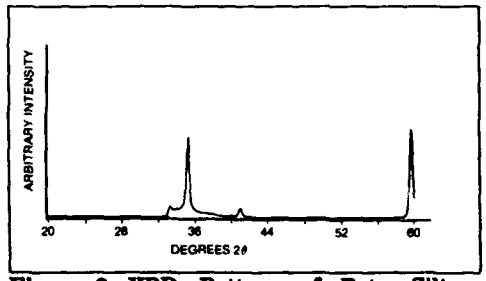


Figure 6 XRD Pattern of Beta Silicon Carbide-Filled Polysilazane Pyrolyzed to 1600°C Under Argon.

pyrolysis product contains only one ceramic material by XRD. Thus, crystallization after pyrolysis in nitrogen results in silicon nitride, while in argon the result is silicon carbide. This shows that the other possible phase is a minor component of the product. Providing seeds in the form of crystalline powders reduces the temperature at which the crystallization of the pyrolyzed polysilazane occurs. The growth of the crystalline material from the amorphous pyrolysis product is shown to be epitaxial. The crystal structure of the product depends upon the structure of the seeds.

REFERENCES

1. D. Seyferth, G. H. Wiseman, C. Prud'homme, J. Amer. Ceram. Soc. 66 (1) C13-C14 (1983).

2. R. R. Wills, R. A. Markle, S. P. Mukherjee, Ceram. Bull. 62 (8) 904-915 (1983).

3. B. E. Walker, Jr., R. W. Rice, P. F. Becher, B. A. Bender, W. S. Coblenz, Ceram. Bull. 62 (8) 916-923 (1983).

4. D. Seyferth, G. W. Wiseman, Science of Ceramic Chemical Processing (J. Wiley, New York, 1986) p. 354.

PRE-RESONANCE RAMAN CHARACTERIZATION OF METAL-ORGANIC FILMS FROM TITANIUM ALKOXIDE CARBOXYLATE COMPLEXES

CHARLES D. GAGLIARDI, DILUM DUNUWILA, AND KRIS A. BERGLUND
Michigan State University, Department of Chemical Engineering and Center for Fundamental Materials Research, East Lansing, MI 48824.

ABSTRACT

Metal-organic films were produced at ambient temperatures and pressures by the controlled hydrolysis of carboxylic acid and titanium isopropoxide mixtures. Pre-resonance Raman spectroscopy was used to study the effect of the organic acid chain length upon the nature of the resulting film. Propionic, butyric, valeric, hexanoic, and octanoic acids were studied, resulting in a proposed correlation between film quality and certain spectroscopic features of the alkoxide carboxylates. The choice of the carboxylic acid and the presence of an appropriate amount of water were shown to be critical in the development of a good film.

INTRODUCTION

Coating materials produced from the controlled hydrolysis of titanium alkoxide carboxylates offer additional versatility and performance over standard sol-gel films. Two patents exist for the manufacturing of acyl-group-containing polymeric titanium compounds from titanium alkoxide and carboxylic acid precursors [1]. In the first of these patents [2], the alkoxide and carboxylic acid mixture is heated under reflux, followed by the removal of alcohol and alkyl ester by distillation. Under these conditions the only water present is that produced by the generation of the alkyl ester, and the resulting polymer is dependent upon the molar ratio (R_a) of alkoxide to acid [1,2]. Thus, $[\text{-O-Ti(OR)(OCOR')-}]_n$, $[\text{-O-Ti(OR)(OCOR')-O-Ti(OCOR')}_2\text{-}]_n$, and $[\text{-O-Ti(OCOR')}_2\text{-}]_n$ represent the polymeric structures resulting from R_a values of 2.0, 2.5, and 3.0, respectively. In the second patent [3], the alkoxide is first reacted with the carboxylic acid, and is then hydrolyzed with additional water. The byproducts of the reaction are removed by distillation as in the first patent, and the polymeric product is reported to have the structure $[\text{-O-Ti(OH) (OCOR')-}]_n$. The materials produced by these methods have found wide application as highly refractive coatings for glass and other substrates, and water-resistant, protective films.

The materials currently under investigation do not require refluxing at elevated temperatures or the removal of reaction byproducts by distillation; the procedure is thus more direct and cost effective. The resulting films are likewise optically transparent and water resistant. In the two patents previously referenced, longer chain length carboxylic acids are preferred. In the current work, relatively short chain length acids are the objects of study.

MATERIALS AND INSTRUMENTATION

The titanium isopropoxide and the carboxylic acids (propionic, butyric, valeric, hexanoic, and octanoic) were obtained from the Aldrich Chemical Company and used without further purification. The microscope slides, which were used as substrates for the films, were standard, pre-cleaned slides manufactured by VWR Scientific Inc.. All water was de-ionized, with a resistance of 18 Mohm.

Raman spectra were collected with a Spex 1877 triple spectrometer equipped with a diode array detector using the 363.8 nm line from an argon laser. Samples were held in quartz cuvettes fitted with Teflon caps.

Mat. Res. Soc. Symp. Proc. Vol. 180. ©1990 Materials Research Society

EXPERIMENTAL PROCEDURE

The liquid carboxylic acid (propionic, butyric, valeric, hexanoic, or octanoic) and the titanium isopropoxide were first combined in a glass scintillation vial and thoroughly mixed with a vortex mixing device. The samples were made with the molar ratios described in Table I such that each sample had a total volume between 3 and 5 ml. For those samples requiring water, the water was added next and the sample was again thoroughly mixed. Films were then spin-cast on glass substrates by wetting the top surface of the glass and then spinning it about an axis perpendicular to the wetted surface. The glass slides were always centered about the axis of rotation, and they were allowed to spin for at least 5 minutes for sufficient drying.

Lauric acid and titanium isopropoxide mixtures were also studied to determine the effect of adding small amounts of lauric acid to the coating solutions previously described. In this study, varying amounts of lauric acid were added to the alkoxide, and Raman spectra were taken of the resulting solution.

TABLE I. Composition of coating solutions and description of resulting films[a].

Acid	R_a[b]	R_w[c]	Film Description
Propionic	2.5	0.0	extensive cracking, flaking
Propionic	10.0	0.0	extensive cracking, flaking
Butyric	2.5	0.0	extensive cracking, flaking
Butyric	10.0	0.0	moderate cracking, flaking on edges
Valeric	2.5	0.0	extensive cracking, flaking
Valeric	10.0	0.0	moderate cracking, flaking on edges
Hexanoic	2.5	0.0	extensive cracking, flaking
Hexanoic	10.0	0.0	slight cracking, slight shrinkage at edges, soft
Octanoic	2.5	0.0	slight cracking, moderate shrinkage at edges, soft
Octanoic	10.0	0.0	never hardens, evaporates over time
Propionic	2.5	1.4	extensive cracking, flaking
Propionic	10.0	1.4	moderate cracking, slight flaking on edges
Butyric	2.5	1.4	extensive cracking, flaking
Butyric	10.0	1.4	no cracking, good uniformity and adhesion
Valeric	2.5	1.4	extensive cracking
Valeric	10.0	1.4	no cracking, very good uniformity and adhesion
Hexanoic	2.5	1.4	no cracking, extensive shrinkage at edges, soft
Hexanoic	10.0	1.4	never hardens, evaporates over time
Octanoic	2.5	1.4	slight cracking, moderate shrinkage at edges, soft
Octanoic	10.0	1.4	never hardens, evaporates over time

[a]The described characteristics appear much more quickly for the solutions without water. [b]R_a is the molar ratio of carboxylic acid to alkoxide. [c]R_w is the molar ratio of water to alkoxide.

RESULTS AND DISCUSSION

The pre-resonance Raman spectra presented in Fig. 1 show the results of adding small quantities of lauric acid to TiPT. The vibrational band assignments for TiPT have been discussed in several previous papers [4,5,6]. However, due to coupling between C-O and C-C vibrational modes, the band assignments have been difficult to make [6]. The strongest TiPT peaks occur at 1026 cm^{-1} and 1182 cm^{-1}. The peak at 1026 cm^{-1} has been associated with the (C-O)Ti stretching vibration [4]. The infrared assignment for this stretch was given as 1005 cm^{-1} [6]. The band at 1182 cm^{-1} has been taken as predominantly a skeletal stretch similar to the IR peak reported at

1170 cm^{-1} [5]. It is likely that both the 1026 cm^{-1} and 1182 cm^{-1} bands represent coupled vibrational modes; therefore, they should not be expected to agree exactly with literature values for the pure vibrational modes. Discrepancies between the IR and Raman peaks can also be expected due to the different selection rules. The peaks of intermediate intensity at 565 cm^{-1} and 612 cm^{-1} may be taken as the symmetric and antisymmetric stretch of Ti-O, respectively [4,6]. The weak peaks at 1129 cm^{-1} and 852 cm^{-1} agree closely with the IR reported values of 1131 cm^{-1} and 851 cm^{-1} for a coupled C-O stretch and skeletal vibration, and a pure skeletal stretch, respectively. The band at 1182 cm^{-1} diminishes with increasing amounts of acid, and the isopropanol peak at 819 cm^{-1} begins to appear as the iPr-O-groups on the titanium are displaced by carboxylate ligands. The symmetric Ti-O stretch at 565 cm^{-1} also decreases, leaving the other Ti-O stretch at 612 cm^{-1} undiminished. The relative peak intensities of the 565 cm^{-1} and 612 cm^{-1} vibrations appear to change more with the addition of lauric acid than with shorter chain-length acids. This could account for the stabilizing effect of adding small amounts of lauric acid to the other coating mixtures.

Coating solutions and descriptions of the resulting films are presented in Table I. The best film without water resulted from hexanoic acid, R_a = 10.0. With water, the best film resulted from valeric acid, also with R_a = 10.0. The film solutions containing no added water produced less stable films, in general, than those from solutions with added water. However, a particular acid at a given R_a may produce a better film without water than with water as exemplified by hexanoic acid at R_a = 10.0. In general, it might also be said that higher R_a values produce better films than lower R_a values, yet octanoic acid produces better films at the lower R_a , with or without water.

The Raman spectra of 'water free' coating solutions, shown in Figures 2 and 3, look very similar; it appears that all of these carboxylic acids interact with the TiPT in a similar way. The lower R_a

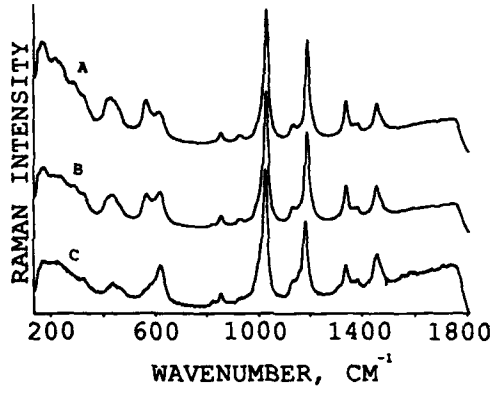


Figure 1. Raman spectra showing the effects of increasing concentrations of lauric acid on titanium isopropoxide (TiPT). (A) Pure TiPT, R_a = 0, (B) TiPT + lauric acid, R_a = 0.12, (C) TiPT + lauric acid, R_a = 0.62. (R_a = the molar ratio of acid to alkoxide.)

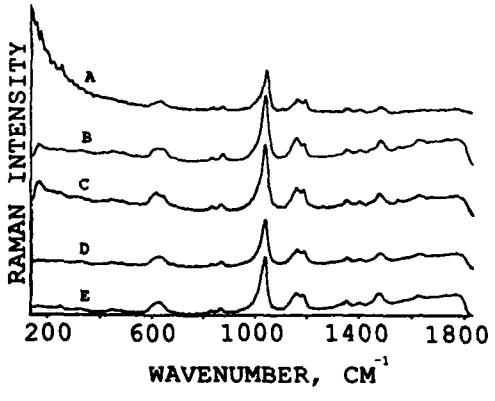


Figure 2. Raman spectra of coating solutions having a low acid molar ratio (R_a = 2.5) and no water. (R_w = 0.0.). Acids used: (A) propionic, (B) butyric, (C) valeric, (D) hexanoic, and (E) octanoic. (R_a = the molar ratio of acid to alkoxide and R_w = the molar ratio of water to alkoxide.)

solutions are distinguished from the higher R_a solutions by different relative peak intensities for the band at 1182 cm^{-1} . This band is generally less dominant at the higher R_a values. However, there are no features which strongly distinguish between the different carboxylic acids, which shows the great similarity of their reactions with the TiPT .

In Fig. 4, the higher R_w (molar ratio of water to alkoxide) solutions are clearly distinguished from those of the other solutions. In the 'water-free' mixtures there is a fairly symmetrical, broad band near 600 cm^{-1} which contains both the 565 cm^{-1} and 612 cm^{-1} Ti-O stretching vibrations. After the addition of water, this broad band becomes highly unsymmetrical as the 612 cm^{-1} vibration dominates the 565 cm^{-1} vibration. This result shows the dramatic impact that water has on the alkoxide carboxylates and demonstrates part of the role of water in creating a stable film. The band near 600 cm^{-1} appears increasingly unsymmetrical as the chain length decreases, except for the mixture containing propionic acid, which had the least asymmetry. The band appearing near 430 cm^{-1} is also interesting. It appears that the integrated intensity of this band is greatest for butyric and valeric acid mixtures. Thus, the bands near 430 cm^{-1} and 600 cm^{-1} may both be correlated with film quality. The development of these bands may also indicate the degree of polymerization. Another band of interest is the *isopropanol* band at 819 cm^{-1}. This band appears slightly larger in the butyric and valeric acid coating solutions, indicating that the alkoxide carboxylate complexes formed from these acids may have a greater tendency to release isopropanol, perhaps through greater polymerization. It is also possible that the iPr-O- groups on these complexes are more easily removed by hydrolysis. Thus, it appears that the complexes formed from different carboxylic acids differ in certain aspects of their reaction with water, and these spectroscopically observable differences may by correlated with film quality.

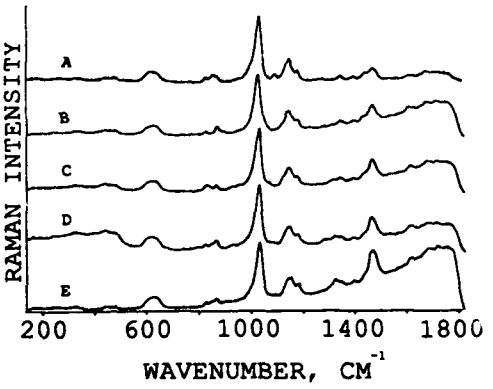


Figure 3. Raman spectra of coating solutions having a high acid molar ratio (R_a = 10.0) and no water. (R_w = 0.0.). Acids used: (A) propionic, (B) butyric, (C) valeric, (D) hexanoic, and (E) octanoic. (R_a = the molar ratio of acid to alkoxide and R_w =the molar ratio of water to alkoxide.)

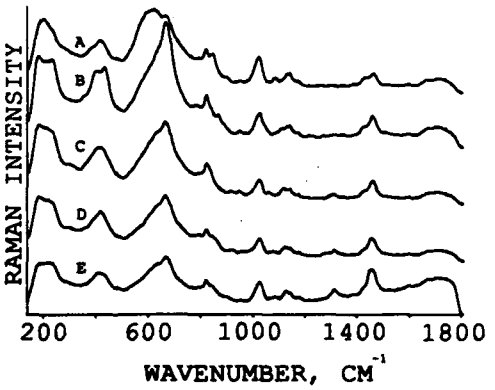


Figure 4. Raman spectra of coating solutions having a high acid molar ratio (R_a = 10.0) and added water (R_w = 1.4). Acids used: (A) propionic, (B) butyric, (C) valeric, (D) hexanoic, and (E) octanoic. (R_a = the molar ratio of acid to alkoxide and R_w = the molar ratio of water to alkoxide.)

CONCLUSIONS

Pre-resonance enhanced Raman spectroscopy is very useful in studying the differences in the alkoxide carboxylates since it emphasizes the chemistry of the complex over the differences in the vibrational bands of the individual acids. Although the reactions between the acids and the TiPT are very similar, greater differences among the complexes appear after the addition of water. The film-making quality of the solution may be correlated with the asymmetry of the broad band near 600 cm^{-1} and with the integrated intensity of the band near 430 cm^{-1}. The results demonstrate the critical choice of the carboxylic acid and the role of water in achieving good film quality.

ACKNOWLEDGMENTS

The support for this work by the Composite Materials and Structures Center (CMSC) and the Center for Fundamental Materials Research (CFMR) at Michigan State University is gratefully acknowledged. All Raman spectra were taken at the Michigan State University LASER Laboratory.

REFERENCES

1. R. Feld, P. L. Cowe, The Organic Chemistry of Titanium (Butterworth and Co., Washington, 1965) pp. 84-85.
2 C. M. Langkammerer, U.S. Patent No. 2 621 193 (p December 1952).
3 J. H. Haslam, U.S. Patent No. 2 621 195 (9 December 1952).
4 K. A. Berglund, D. R. Tallant, R. G. Dosch, in Science of Ceramic Chemical Processing, edited by L. L. Hench, D. R. Ulrich (John Wiley and Sons, New York, 1986) pp. 94-99.
5 V. A. Zeitler, C. A. Brown, J. Phys. Chem. 61, 1174 (1957).
6 D. C. Bradley, R. C. Mehrotra, D. P. Gaur, Metal Alkoxides (Acad. Press, New York, 1978) pp. 117, 119-121.
7 R. C. Mehrotra, and R. Bohra, Metal Carboxylates (Acad. Press, New York, 1983) pp. 233-240.
8 J. Livage in Better Ceramics Through Chemistry II, edited by C. J. Brinker, D. E. Clark, D. R. Ulrich (Mater. Res. Soc. Proc. 73, Pittsburgh, PA 1986) pp. 717-724.
9 C. D. Gagliardi, K. A. Berglund, in Processing Science of Advanced Ceramics, edited by I. A. Aksay, G. L. McVay, D. R. Ulrich (Mater. Res. Soc. Proc. 155, Pittsburgh, PA, 1986) pp.127-135.

STABILITY OF BORON NITRIDE COATINGS ON CERAMIC SUBSTRATES

ABHAYA K. DATYE*, XIAOMEI QUI*, THEODORE T. BOREK*, ROBERT T. PAINE* AND LAWRENCE F. ALLARD#
*Center for Microengineered Ceramics, University of New Mexico, Albuquerque, NM 87131.
#High Temperature Materials Laboratory, Oak Ridge National Laboratory, Oak Ridge, TN 37831.

ABSTRACT

When BN is synthesized via polymeric precursors and applied to ceramic substrates, tough adherent coatings of hexagonal-BN (h-BN) are obtained after annealing at 1200°C in N_2. The study of these coatings is facilitated by using nonporous oxide powders containing single crystal particles of submicron size (e.g. cubes of MgO) as model ceramic substrates. These oxide powders permit high resolution TEM examination of the BN coatings with no further sample preparation. In this study, samples of BN/MgO cubes containing 50 wt% BN were heated in air at elevated temperatures for 16 hours to study the oxidation resistance of BN coatings. The BN coating was found to be stable at 600°C, but the 700°C-treated sample showed evidence for partial amorphization of the coating and reaction with MgO. A significant fraction of the MgO in the 800°C-treated sample had transformed to $Mg_2B_2O_5$. The reaction of MgO with the BN coating under oxidizing ambients leads to loss of the cubic morphology in the precursor powder.

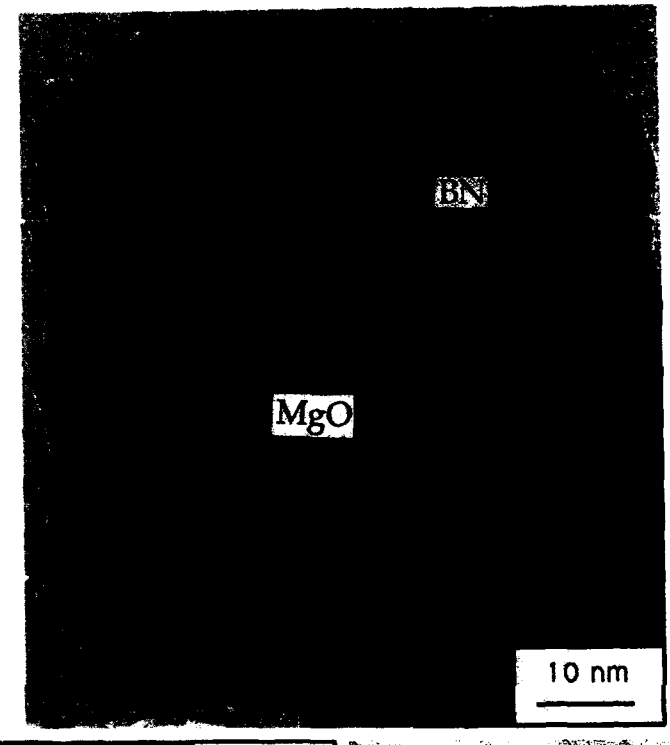
INTRODUCTION

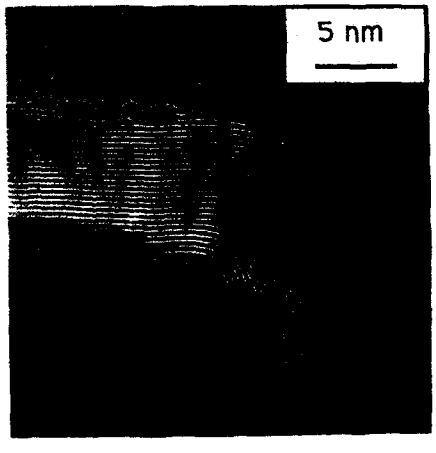
Ceramic coatings represent an important means to modify interfaces in composite materials. Boron nitride coatings can be used to prevent reaction at the fiber-matrix interface and to improve fiber pullout, which is important for attaining high toughness in these composites. Fiber coatings can also protect the fibers from mechanical damage and chemicaliy isolate the fiber from the matrix during processing. Little is known about the high temperature oxidation resistance of ceramics such as BN. The oxidation of bulk BN powders [1] and aerogels [2] at elevated temperatures has been reported in the literature. However, thin films of BN on ceramic substrates may behave differently and should be investigated before these coatings can be incorporated in composite materials. This study is part of a larger program aimed at examining the applicability of BN coatings to oxide and nonoxide ceramic substrates. Since the coatings of interest are only applied as thin films, it is necessary to use transmission electron microscopy (TEM) to observe changes caused by oxidation. Cross-section TEM of thin coatings is fraught with the difficulties in preparing thin sections and associated artifacts due to sample preparation. Hence, we have used nonporous oxide powders as model ceramic substrates to facilitate study of these materials [3-5]. The sample was similar to that reported earlier [4-5] and was prepared by physically mixing equal weights of MgO smoke cubes and a preceramic BN polymer, and heating under N_2 at 1200 °C for 12 hours. The TEM samples were prepared by simply dipping a holey carbon TEM grid into the powder and dusting off the excess. Details of the BN polymer synthesis have been reported elsewhere [6].

RESULTS

Figure 1 shows a micrograph of the BN/MgO sample after heat treatment in N_2 at 1200 °C. A thick film of crystalline h-BN is seen on the surface of the MgO crystals. Similar films were seen also on the model Al_2O_3 and TiO_2 substrates with the film thickness decreasing with increasing surface area of the precursor powder. In all instances, the (002) lattice fringes in the BN are locally parallel to the oxide surface. While the BN coating completely envelops the MgO particles, the BN lattice fringes can be only be seen at the edges of the MgO particles (Fig. 1). This is because the BN is turbostratic and the BN sheets are disordered with respect to each other. Hence,

Mat. Res. Soc. Symp. Proc. Vol. 180. ©1990 Materials Research Society





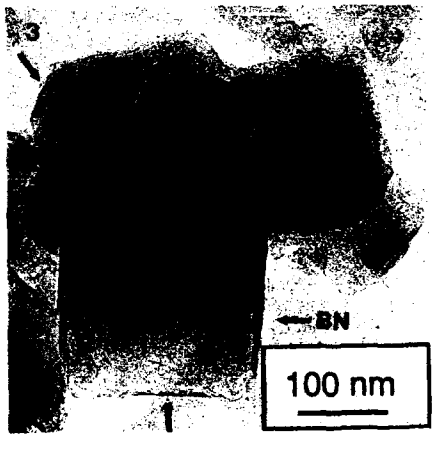


Figure 1. Low magnification TEM image of BN/MgO sample
Figure 2. Higher magnification view of BN/MgO showing the crossed MgO (200) lattice fringes (2.1 Å) and the BN (002) 3.45 Å lattice fringes. The (002) planes in BN are always locally parallel to the oxide surface.
Figure 3. BN/MgO heated in air at 600°C for 16 hours.

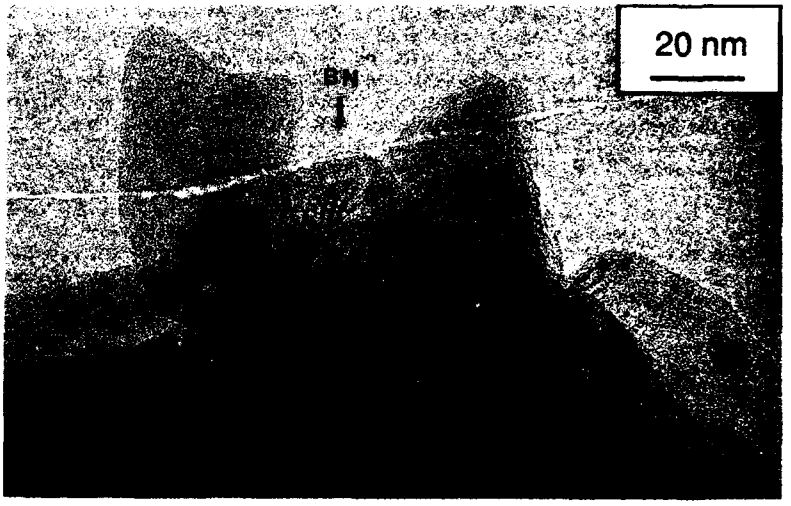


Figure 4. BN/MgO heated in air at 700 °C for 16 hours. Portions of the BN coating appear amorphous. The altered shape of the surface of the particle indicates transformation from the cubic morphology of the precursor powder due to reaction of MgO with the BN coating.

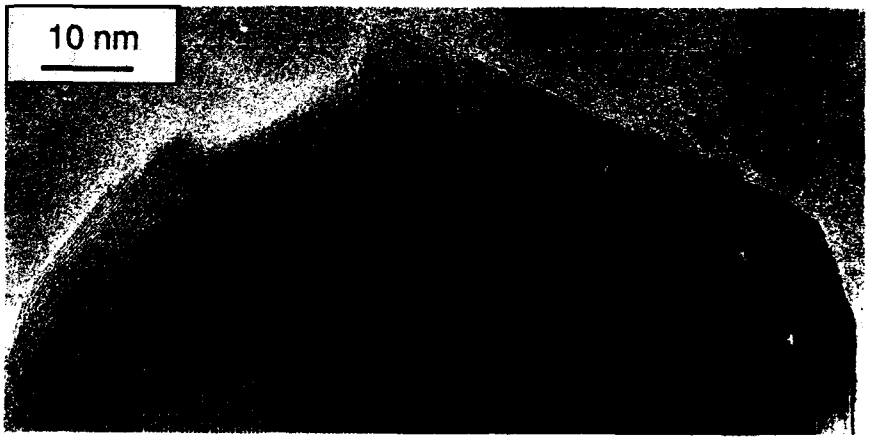


Figure 5. BN/MgO heated in air at 800°C for 21 hours. While much of the BN coating is still intact on this particular grain, the substrate lattice fringes indicate that it is no longer MgO but has transformed to $Mg_2B_2O_5$.

the BN imaged along the [001] direction does not interfere with the MgO lattice image (Fig. 2). The (002) interplanar spacing in the BN coating is approx. 3.45 Å which is larger than the 3.3 Å spacing in crystalline h-BN. The larger interplanar spacing is consistent with its turbostratic nature. In the BN-coated sample, the MgO retains its cubic morphology but develops well-defined (110) and (111) microfacets. The BN appears to be quite mobile at the treatment temperature of 1200 °C since it tends to spread on the MgO leading to almost complete coverage of the MgO surface.

The sample of BN/MgO was heated in air for 16 hours at 500°C, 600°C, 700°C and 800°C. No change in the BN coating was detected in the sample heated up to 600°C. Figure 3 shows a low magnification view of the 600°C-treated sample where the MgO powder can be seen to have retained its cubic morphology and the thin BN coating is still intact. The sample treated at 700°C, however, showed several elongated crystals that looked distinctly different from the cubes in the precursor powder. In addition, portions of the BN coating appeared amorphous and did not exhibit the characteristic (002) lattice fringes of h-BN (Fig. 4). Most of the BN coating had disappeared in the 800°C-treated sample. Only few of the grains showed the BN coating originally present on the MgO surface. Figure 5 shows one such grain where part of the surface is still covered by crystalline BN, however the elongated shape of this crystal clearly indicates that the substrate is no longer MgO. Indeed, the larger lattice spacings seen in this crystal correspond to $Mg_2B_2O_5$. Other grains in the 800°C-treated sample exhibit an amorphous coating similar to that seen in figure 5. Thermogravimetric analysis shows negligible weight gain (due to oxidation) in the 800°C-heated sample confirming that oxidation of the thin BN films is nearly complete in 16 hours at 800°C.

CONCLUSIONS

The work presented here shows that BN coatings on oxide substrates such as MgO are stable to treatment in air at temperatures up to 600 °C. At higher temperatures, the BN presumably transforms to B_2O_3 which reacts with MgO to form $Mg_2B_2O_5$. At 800 °C, a substantial fraction of the MgO has transformed to $Mg_2B_2O_5$ and only small patches of the BN coating are left behind. It is remarkable that the patches of BN left behind in the 800°C-heated sample adhere to the substrate despite the pronounced changes in the shape of the underlying substrate particles. This indicates that the h-BN must be held quite strongly to the substrate and is not easily dislodged, the sheet-like structure allowing it conform to the contours of the substrate.

ACKNOWLEDGEMENTS

This work has been supported by the UNM/NSF Center for Microengineered Ceramics which is funded by NSF (CDR-8803152), Sandia and Los Alamos National Laboratories, the New Mexico Research and Development Institute and the ceramics industry. A portion of the TEM work on this project was performed at the Microbeam Analysis Facility within the Department of Geology at the University of New Mexico. The high resolution TEM studies were conducted at the High Temperature Materials Laboratory, ORNL, supported by the U.S. DOE, Office of Transportation Systems, under contract DE-AC05-84OR21400 with Martin Marietta Energy Systems Inc..

REFERENCES

1. N.G. Coles, D. R. Glasson and S. A. A. Jawaweera, J. Appl. Chem., 19, 178 (1969).
2. T. T. Borek, D. A. Lindquist, G. P. Johnston, S. L. Heitala, D. M. Smith and R. T. Paine, submitted to the J. Am. Ceram. Soc.
3. A. K. Datye and N. J. Long, Ultramicroscopy, 25, 203 (1988).
4. R. T. Paine, C. K. Narula, R. Schaeffer and A. K. Datye, Chem. Mater., 1, 486 (1989).
5. A. K. Datye, R. T. Paine, C. K. Narula and L. F. Allard in Interfaces between Polymers, Metals and Ceramics, edited by B. J. DeKoven, A. J. Gellman and R. Rosenberg (Mater. Res. Soc. Proc. 153, Pittsburgh, PA 1989) pp. 97-102.
6. R. T. Paine and C. K. Narula, Chem. Rev., 90, 73 (1990).

XPS Characterization of Mixed Carbides Obtained from Polymer Precursors

GAETANO GRANOZZI[§], ANTONELLA GLISENTI[§] AND GIAN D. SORARU[§§]

[§]Dipartimento di Chimica Inorganica, University of Padova, Via Loredan 4, 35131 Padova (Italy)

[§§]Dipartimento di Ingegneria dei Materiali, University of Trento, 38050 Mesiano, Trento (Italy)

Abstract

Polymer precursors for Si-C, Si-Ti-C-O and Si-Al-C-O systems have been obtained from polycarbosilane and the corresponding metal alkoxides. X-ray Photoelectron Spectroscopy (XPS) has been used to follow the structural evolution of these preceramic compounds during the pyrolysis process.

Introduction

In recent years many efforts have been devoted to obtain high-tech non-oxide ceramics from polymer precursors [1]. This process is particularly attractive for its potential use in fabricating difficult to shape forms, like fibers, or coatings of highly refractory ceramics such as SiC, Si_3N_4, BN, AlN, TiC and B_4C. According to this route, the starting metal-organic polymer is converted into the final ceramic material by a pyrolysis process in an inert atmosphere. The first product that appears after the decomposition of the organic components is usually an amorphous solid that transforms into a microcrystalline material by further rising the firing temperature [2]. A detailed characterization of the ceramic structures at various stages of the firing process should bring important information to better understand the relationship between the precursor polymers and the final ceramic product. In this field, the most studied system is silicon carbide obtained from polycarbosilane (PC) following the process developed by Yajima [3]. It has already been shown that the same polymer can be modified by reacting with Ti, Al and Zr alkoxides to form precursors for Si-Ti-C-O [4], Si-Al-C-O [5] and Si-Zr-C-O [6] ceramics. In this paper the pyrolysis processes of PC and modified polycarbosilanes containing Ti (PTC), and Al (PAC) have been followed by X-ray Photoelectron Spectroscopy (XPS). It will be shown that, XPS analysis can bring useful and complementary information for the structural characterization of the ceramic products.

Experimental section

Ti-modified PC has been obtained reacting a commercially available polycarbosilane (Dow Corning X9-6348) with titanium n-butoxide in xylene following a published procedure [4]. PAC samples were prepared following the same route using Al sec-butoxide. Chemical analysis gave an atomic ratio

Mat. Res. Soc. Symp. Proc. Vol. 180. ©1990 Materials Research Society

(M/Si) of 0.15, and 0.24 for Ti, and Al, respectively. Thermogravimetric analysis (TGA) has shown that for all the systems the decomposition of organic components is almost complete around 800°C. According to these results the precursor polymers have been fired in Ar flow at 10°C/min at various temperatures from 840°C up to 1500°C.
In order to minimize surface contamination, the fired samples were ground into fine powders and pressed to form thin pellets just before XPS measurements. VG ESCALAB MKII spectrometer operating at 10^{-9} mbar with Al-Kα radiation (hν=1486.6 eV) was used to record XPS spectra. To evaluate the presence of charging effects, XPS spectra were also recorded for dilute samples obtained by embedding small quantities of the powders into indium foils. Only small differences were generally found between the two sampling methods and the reported B.E. values were corrected accordingly.

Results and discussion

Si-C system. Selected Si(2p) and C(1s) spectra of PC and its pyrolysis products are reported in Figure 1. The B.E. of Si(2p) in the precursor polymer (101.3 eV) is typical of silicon atoms in silanes [7]. The corresponding C(1s) spectrum of PC shows a peak at 284.6 eV assigned to the organic groups, mainly CH_3 and CH_2, bonded to the silicon atoms of the polymer chains.
At 840°C the Si(2p) peak shifts to 100.7 eV and in the C(1s) spectrum a shoulder appears at 283 eV. These values are typical of SiC ceramics and show that the silicon carbide network is formed at this stage of the firing process. In a previous work it has been shown that an amorphous homogeneous silicon carbide phase with excess of carbon (C/Si=1.6) is formed at 840°C [8]. The local environment of Si atoms in this disordered phase seems to be very close to that of crystalline SiC materials; actually, the Si(2p) spectrum does not show any relevant difference in the sample fired at 1500°C, where a microcrystalline SiC based ceramic is formed [7].
A quite different behavior is evident from the analysis of the C(1s) region: at 840°C a very broad peak which spans both the B.E. regions typical of SiC (283 eV) and graphite (284.4 eV) is present.

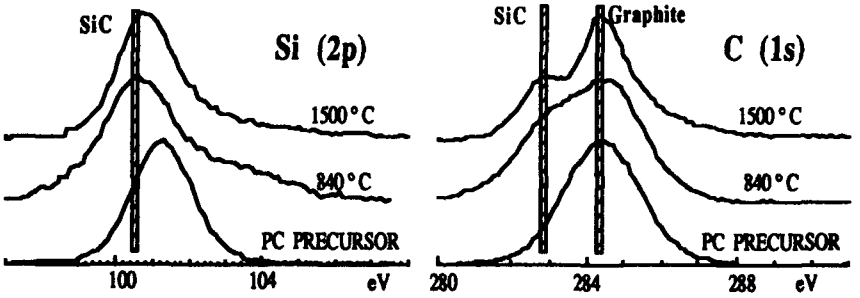


Figure 1. Evolution with the firing temperature of the XPS Si(2p) and C(1s) peaks for PC.

Therefore, the local environment around the carbon atoms seems to be more complex than the corresponding silicon one: while Si atoms are present only in SiC_4 sites, C atoms form analogous CSi_4 units together with $CSi_{4-x}C_x$ ($1<x<3$) units. Graphite-like sites, where no Si atom is surrounding the C atoms are also present in the amorphous phase. Our XPS data are consistent as well with some residual C-H bonds, as revealed by chemical analysis [6]. In the C(1s) XPS spectra of the sample fired at 1500°C some high temperature induced reordering process on the carbon sites is evident: two components corresponding to SiC and graphite phases are now highly predominant and we suggest that the intermediate $CSi_{4-x}C_x$ units are negligible in the final ceramic product.

Si-Ti-C-O system [9]. Selected Ti(2p) and Si(2p) spectra of PTC at various stage of the pyrolysis process are reported in Figure 2. Ti(2p) spectrum of PTC precursor shows a spin doublet $2p_{1/2}$-$2p_{3/2}$ (at 465.2 and 459.5 eV, respectively) typical of Ti-O bonds. At 840°C a new component appears at 455.4 eV, to be assigned to the $Ti(2p_{3/2})$ peak of TiC. This suggests that Ti-C bonds start to be formed at this stage of the pyrolysis. By raising the firing temperature the Ti-O component decreases and the Ti-C one increases. At 1500°C Ti-O bonds almost disappear and the formation of the TiC phase is completed.

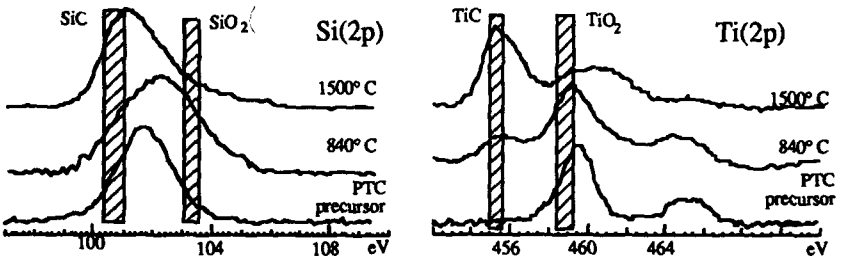


Figure 2. Evolution with the firing temperature of the XPS Si(2p) and Ti(2p) peaks for PTC.

With respect to PC, the Si(2p) peak of PTC (101.7 eV) shows a small shift toward higher B.E. values, in agreement with the formation of new SiC_3O sites in the polymer chain [10].
At 840°C the peak broadens and its maximum shifts at 102 eV. A detailed analysis of the band envelope has shown that this peak has to be fitted with three components: the SiC (ca.101 eV), SiO_2 (ca.103 eV) and an intermediate one (ca. 102 eV) that could be assigned to $SiC_{4-x}O_x$ ($1<x<4$) units, where Si atoms form both Si-O and Si-C bonds. When the temperature is increased up to 1500°C a microcrystalline SiC/TiC ceramic is formed and the Si(2p) XPS pattern shows, as expected, the predominant contribution of the SiC phase.

Si-Al-C-O system. Si(2p) peak of PAC precursor does not show significative difference of B.E. (101.4 eV) and linewidth compared to PC: the reaction with Al alkoxide does not form new Si sites in the polymer chain, in

agreement with ^{29}Si MAS-NMR studies [5]. Going on with the pyrolysis, the B.E. value of Si(2p) peak progressively shifts toward the value of SiC ceramics. Similarly, the evolution with the firing temperature of the C(1s) spectra does not show any relevant peculiarity with respect to that found for PC.
On the contrary, quite informative is the analysis of the evolution of Al(2p) reported in Figure 3.

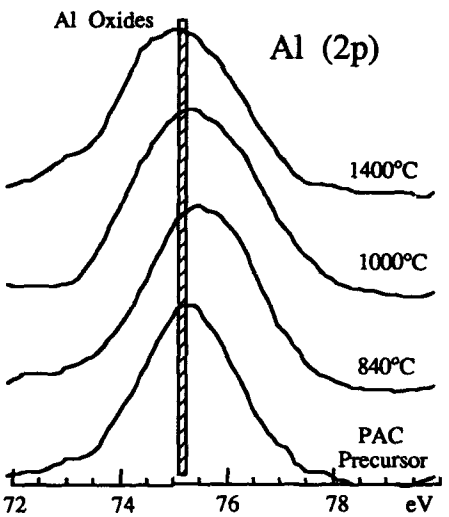


Figure 3. Evolution with the firing temperature of XPS Al(2p) peak of PAC

It is quite clear that the pyrolysis of PAC up to 1400°C does not destroy the existing Al-O bonds. This evidence is in tune with ^{27}Al MAS-NMR data which reveal that only a limited amount of Al-O bonds have been transformed into Al-C bonds at this temperature [5]. Actually, preliminary x-ray diffraction data suggest that in the final ceramic the Al containing phase is composed by a solid solution of Al_2OC in SiC 2H [6].

References

[1] G. Pouskouleli, *Ceram. Internat.* **15**, 213 (1989).
[2] B. A. Bender, R. W. Rice and J. R. Spann, *J. Am. Ceram. Soc.* **70**, C58 (1987).
[3] S. Yajima, J. Hayashi and M. Omori, *Chem. Lett.* 931 (1975).
[4] S. Yajima, T. Iwai, T. Yamamura, K. Okamura and Y. Hasegawa,, *J. Mat. Sci.* **16**, 1349 (1981).
[5] F. Babonneau, G. D. Soraru and J. D. Mackenzie, submitted for publication.
[6] G. D. Soraru, F. Babonneau and J. D. Mackenzie, see this volume.
[7] C. D. Wagner, W. M. Riggs, L. E. Davis; J. F. Moulder and G. E. Muilenberg, Handbook of X-ray Photoelectron Spectroscopy, Physical Electronics Division, Perkin-Elmer Corp., Eden Prairie, MN, 1979.
[8] G. D. Soraru, F. Babonneau and J. D. Mackenzie, *J. Mat. Sci.*, to be published.
[9] G. D. Soraru, A. Glisenti, G. Granozzi, F. Babonneau and J. D. Mackenzie, submitted for publication.
[10] F. Babonneau, G. D. Soraru and J. D. Mackenzie, *J. Mat. Sci.*, to be published.

MIXED CARBIDES VIA POLYMER ROUTE

GIAN D. SORARU[1], FLORENCE BABONNEAU[2] AND JOHN D. MACKENZIE[3]
[1]Dipartimento di Ingegneria dei Materiali, University of Trento, 38050 Mesiano, Trento, Italy.
[2]Chimie de la Matière Condensée, Université Paris 6, 4 place Jussieu, 75005 Paris, France.
[3]Department of Materials Science and Engineering, Boelter Hall 6531, University of California, Los Angeles, CA 90024, USA.

ABSTRACT

Several polymetallocarbosilanes, pre-ceramics precursors for Si-M-C-O systems, have been prepared from polycarbosilane and metallic alkoxides, $M(OR)_n$ with M = Ti, Zr and Al. Polymers have essentially been characterized by Magic Angle Spinning Nuclear Magnetic Resonance (MAS-NMR). The pyrolysis process has been followed for each system with X-Ray Diffraction (XRD) and MAS-NMR. The role of the metallic element M on the transformation process of these systems will be discussed.

INTRODUCTION

Among the new methods for processing non-oxide ceramics with improved properties, pyrolysis of metal-organic polymers is taking an increasing important role, especially for the production of fibers [1]. One of the most attractive and challenging features of this process is the possibilities to control the microstructure and the properties of the final ceramic material by chemically modifying the polymer composition and/or its structure. Reacting a polycarbosilane precursor for SiC fibers with a titanium alkoxide, a new polymer is obtained that gives, after pyrolysis, ceramic materials in the Si-Ti-C-O system [2]. Commercially available TYRANNO fibers produced from this polytitanocarbosilane, display superior tensile strength compared with SiC NICALON fibers [3].

Similar procedures can give the opportunity to modify the polycarbosilane with different elements just by changing the nature of the metal alkoxide. Using this strategy, a large variety of new metal-organic polymers, precursors for Si-M-C-O systems, can be prepared. This paper will present results concerning Si-Ti (PTC), Si-Zr (PZC) and Si-Al (PAC) systems.

EXPERIMENTAL SECTION

The polymers PTC, PZC and PAC have been prepared from polycarbosilane and metal alkoxides ($Ti(OBu^n)_4$, $Zr(OBu^n)_4BuOH$ and $Al(OBu^s)_3$) according to a procedure already published[2]. Chemical analysis (M/Si) gives the following results for PTC (0.15), PZC (0.12) and PAC (0.24).The MAS-NMR spectra have been recorded on Bruker MSL 300 and 400 spectrometers and the XRD patterns on a Philips equipment using a CuKα radiation.

EXPERIMENTAL RESULTS AND DISCUSSION

Characterization of modified polycarbosilanes

The problem in this characterization was to understand how the metallic element was

Mat. Res. Soc. Symp. Proc. Vol. 180. ©1990 Materials Research Society

incorporated into the new PC based polymer. Previous works[2] suggested the formation of Si-O-M bridges between the PC chains and the alkoxide part.

The ^{29}Si CPMAS-NMR spectrum of pure PC (Figure 1a) shows two peaks at -0.8 ppm and - 17.6 ppm assigned respectively to SiC_4 units in which Si atoms are bonded with four C atoms and SiC_3H units in which Si atoms are bonded with three C atoms and one H atom [4]. In the spectra of Ti and Zr modified polycarbosilanes (PTC and PZC), the intensity of the peak around -18 ppm decreases and a new absorption appears around 10 ppm, assigned to SiC_3O units [5]. Therefore the reaction between PC and Ti or Zr alkoxides seems to occur via the consumption of Si-H bonds of the polycarbosilane and the formation of new Si-O bonds.

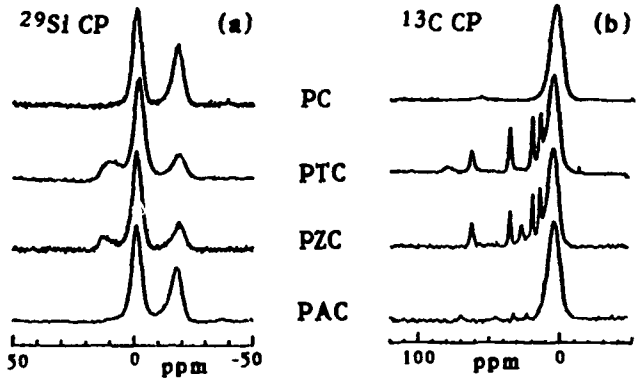


Figure 1: ^{29}Si (a) and ^{13}C (b) CP MAS-NMR spectra of PC, PTC, PZC and PAC precursors.

^{13}C CPMAS-NMR spectra of PTC and PZC samples (Figure 1b) display one broad band centred around 5 ppm due to C atoms of the PC chains and several common peaks at 14.6, 19.8, 35.7 and 62.3 ppm that can be assigned to the C atoms of the butoxy groups. The peak at 62.3 ppm due to the CH_2 groups bound with the O atom, i.e. M-O-$\underline{C}H_2$, is quite sensitive to the nature of M. A comparison between the chemical shift values for $Ti(OBu^n)_4$ (74.4 ppm), $Zr(OBu^n)_4$ (67.4 ppm), $Si(OBu^n)_4$ (63.0 ppm) and n-butanol (61.4 ppm), show that the residual alkoxy groups are mainly bound with a Si atom of the PC chain: the cleavage of M-OBu bonds and the formation of Si-OBu seems to occur during the preparation of these samples. The small peak at 78.9 ppm in the PTC spectrum could indicate however, that few OBu groups are still bound to Ti atoms.

This study seems to show that the formation of Si-O bonds in PTC and PZC is related to the presence of non hydrolyzed Ti and Zr alkoxides which afford Si-OR bonds in the modified PC. The results on the Si-Al system agree with this assumption: no Si-O bonds appear in the ^{29}Si NMR spectrum of PAC where extensive hydrolysis of the butoxy groups occurred during the preparation as shown by the ^{13}C NMR data. It seems that in these PC modified polymers, no chemical bonds exist between the PC chains and the M containing part.

Characterization of the pyrolysis process

XRD study: Pyrolyzed PC is known to crystallize in SiC 3C at around 1000°C [4]. The three modified PC samples exhibit quite different crystallization processes (Figure 2). The PTC system does not show any pattern due to TiO_2. It starts to crystallize around 1200°C in a SiC 3C / TiC mixture. The PZC system first shows the crystallization of ZrO_2 at 700°C. Then by increasing the temperature up to 1200°C, the SiC 3C and ZrC phases starts to appear leading a mixture of these two well-crystallized phases at 1500°C. At this temperature, the SiC 3C phase appears to be better crystallized in PTC and PZC samples than in pure PC sample. As for the PAC system, the first crystalline phase to appear is SiC 3C around 1200°C. But in this case, an other polytype of SiC seems to be formed at 1500°C, corresponding to SiC 2H. No other phase seems to be present, but SiC 2H is known to form a solid solution with Al_2OC. Such a solid solution can be present in this material.

The nature of M seems to play a key role in the transformation process of these pre-ceramics polymers. In order to get a better understanding of this phenomenon, the evolution of the local environment of Si atoms during the pyrolysis has been followed by ^{29}Si MAS-NMR in the various systems.

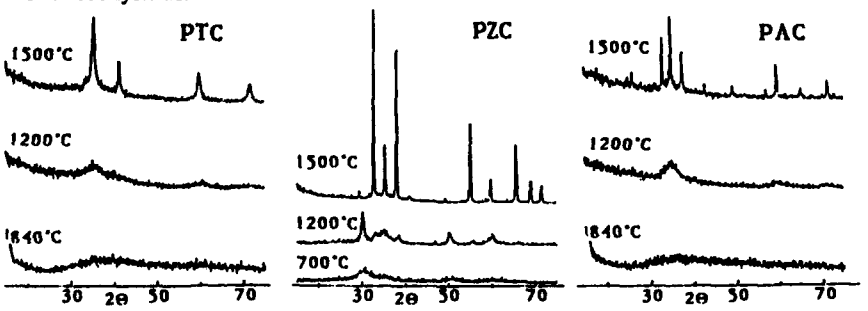


Figure 2 : XRD patterns of PTC, PZC and PAC fired at various temperatures.

^{29}Si MAS-NMR study: Pyrolyzed PC samples are known to give a peak characteristic of SiC_4 units that is continuously shifting during the pyrolysis from 0 to -16 ppm . The spectrum at high temperature (T≥1500°C) reveals three components at -16, -20 and -24 ppm whose assignments have been discussed in a previous paper [6]. The evolution of the linewidth of this peak reveals a disordering of the system up to 840°C, and then an ordering leading to the crystallization of the SiC phase. A detailed NMR study on the PTC system has already been published and has shown the formation of $SiC_{4-x}O_x$ up to 1000°C and then a consumption of the Si-O bonds (Figure 3) certainly by reaction with the excess carbon[5]. In this case a Ti K-edge X-ray Absorption Near Edge Spectroscopy (XANES) and Extended X-ray Absorption Fine Structure (EXAFS) study, as well as X-ray Photoelectron Spectroscopy) XPS experiments, show the presence of Ti-C bonds at 840°C. The behaviour of the PZC system is different : the evolution of the local environment of Si atoms is similar to the one in the PC system, with no formation of Si-O bonds. The NMR spectra of both PTC and PZC samples at 1500°C display a very similar features which are almost identical to those found for PC. Up to 1200°C, the

evolution for the PAC system is similar to that of PC, but at 1500°C, a broad peak centered on -20 ppm is present . The broadness of this peak is due to a distribution of Si sites in the sample. The range of chemical shift values corresponds more to α polytypes. This spectrum agrees with the assumption that a solid solution between SiC 2H and Al_2OC exists in this sample.

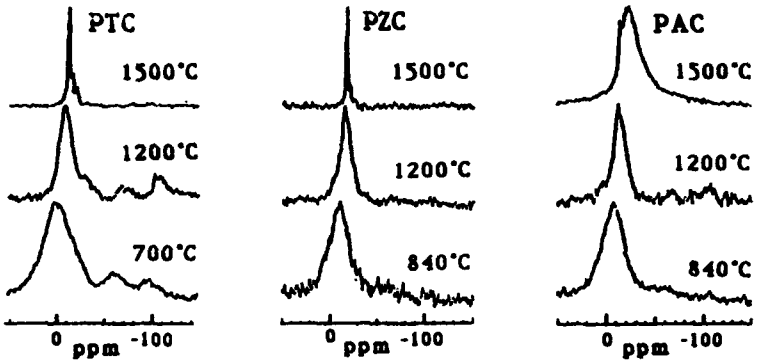


Figure 3 : ^{29}Si MAS-NMR spectra of PTC, PZC and PAC samples fired at various temperatures

CONCLUSION

The reaction between polycarbosilane precursor for SiC and a metallic alkoxide, $M(OR)_n$, with M=Ti, Zr or Al can lead to new polymers which are precursors for Si-M-C-O systems. The characterization study performed on these polymers, using mainly MAS-NMR, does not seem to show any chemical bonding such as Si-O-M bridges between the PC chains and the M-containing part. The alkoxy groups seem to hydrolyzed during the preparation, partially for the PTC and PZC systems and almost totally for the PAC system. The formation of some oxide based particles can thus be assumed inside the PC chains matrix. This study also shows that the nature of M has a great influence on the transformation process of these polymers during their pyrolysis: in the case of PTC, the Ti-C bonds are formed in the amorphous state around 800°C, by reaction of Ti-O bonds with the Si-C bonds present in the pyrolyzed PC chains, while for PZC, Zr-C bonds are formed above 1200°C by a carbothermal reduction of crystalline ZrO_2 particles with the carbon rich silicon carbide matrix. The PAC system illustrates the influence of M on the kind of SiC polytype formed at high temperature.

ACKNOWLEDGEMENTS

The authors would like to thank NSF (87 06379) and NATO for financial support of this work.

REFERENCES

[1] K. J. Wynne and R. W. Rice, Ann. Rev. Mater. Sci. **14**, 297 (1984).
[2] S. Yajima, T. Iwai, T. Yamamura, K. Okamura and Y. Hasegawa, J. Mat. Sci. **16**, 1349 (1981).
[3] Y-C. Song, Y. Hasegawa, S-J. Yang and M. Sato, J. Mat. Sci. **23**, 1911 (1988).
[4] Y. Hasegawa and K. Okamura, J. Mat. Sci. **18**, 3633 (1983).
[5] F. Babonneau, G. D. Soraru and J. D. Mackenzie, J. Mat. Sci. **25**, 000 (1990).
[6] G. D. Soraru, F. Babonneau and J. D. Mackenzie, J. Mat. Sci. **25**, 000 (1990).

LASER Ddensification MODELING

TAIPAU CHIA*, L. L. HENCH*, CHAOBIN QIN** AND C. K. HSIEH**
*Advanced Materials Research Center, University of Florida, One Progress Blvd., #14, Alachua, FL 32615.
**Department of Mechanical Engineering, University of Florida, Gainesville, FL 32611.

ABSTRACT

A three-dimensional transient model for heat conduction in silica glass is developed. The model simulates a three-dimensional temperature distribution in a silica glass irradiated by a moving CO_2 laser. Both the reflectivity of the glass surface and the strong attenuation of the laser energy in the glass medium are accounted for by a detailed radiation analysis. The energy absorbed by the glass is determined to be confined in a 10 μm thickness; the laser irradiation is thus treated as a boundary condition. The heat diffusion equation is solved by an alternating-direction-implicit method.

INTRODUCTION

Many models have been developed for predicting the temperature distribution inside materials treated with laser heating [1-3]. In this paper the temperature rise is analyzed. The results are useful to determine the effect of applying a CO_2 laser on a porous gel silica glass monolith. Previous papers report the processing and properties of the alkoxide derived gel silica investigated in this paper [4-6].

The laser energy is assumed to be absorbed and totally transformed into heat. Based on high absorption coefficient [7] of the glass, the laser energy is determined to be absorbed primarily within a very thin layer (~10 μm) into glass surface. The Gaussian distribution of this energy is integrated within the absorption layer, and the absorbed energy is treated as a boundary condition in the analysis.

The model developed in this paper simulates the three dimensional heat transfer in the silica glass irradiated by a moving CO_2 laser. Relative temperature distributions at various laser power settings and travelling velocities are evaluated numerically. Parametric studies for the effects of the heat transfer coefficient on the glass surface and the thermophysical properties of the glass medium are also investigated. It is well known that the properties of gel silica glasses are strongly related to their processing temperature. The results presented in this paper can thus be used to evaluate the property changes due to the temperature rise in the gel silica glass.

FORMULATION OF THE PHYSICAL MODEL

The physical system under investigation is shown in Figure 1. A focused CO_2 laser beam is travelling in the x direction. The thickness of the glass substrate is in the z direction, and because of the motion of the beam, the temperature distribution in glass is symmetrical with respect to the x-z plane; only one half of the medium is thus needed for analysis.

Mat. Res. Soc. Symp. Proc. Vol. 180. ©1990 Materials Research Society

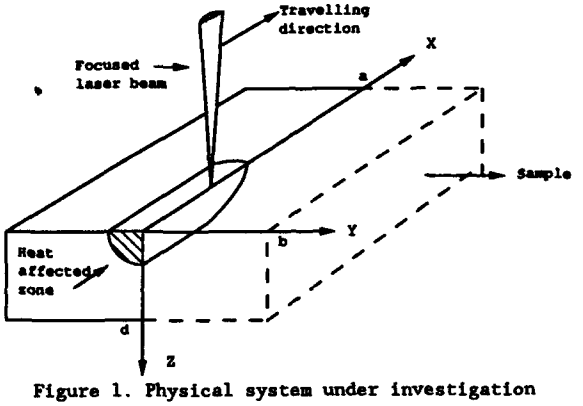


Figure 1. Physical system under investigation

Table I. Calculational Variables and Values

	Nomenclature	Values
a	Sample length	0.4 cm
b	Sample width	0.2 cm
c	Specific heat [12]	10.5 J/g°C
d	Sample thickness	0.3 cm
D	Heat diffusivity	6.5×10^{-4} $(=k/\rho c)\cdot cm^2/sec$
h	Heat transfer coefficient	7.1×10^{-3} $w/cm^2{}^\circ C$
I_o	Laser intensity	3.3×10^4 w/cm^2
k	Thermal conductivity [13]	1.5×10^{-2} $w/cm^\circ C$
q	Heat flux	
Q	Absorbed laser power density	10^7 $(=q/\Delta z)$ w/cm^3
Q	Absorbed laser power	
R	Reflectivity	0.17
t	Time	
Δt	Time step	
T	Temperature	
T_∞	Room temperature	24°C
v	Travelling velocity	0.04 cm/sec
w	Half width of laser beam	0.01 cm
ΔZ	Depth	
α	Absorption coefficient	6.5×10^{-1} μm^{-1}
ρ	Density	2.2 g/cm^3

The thermal conductivity of the glass is small; the heat affected zone is highly localized and represented by the shaded lines in the figure. The irradiated energy is transformed into heat and diffused into the glass medium by conduction, while the surface of the glass dissipates heat by convection and radiation to the surroundings [8].

The thermal effect of the laser irradiation can be evaluated by a detailed radiation analysis. Accounting for both the reflectivity of the glass surface and the absorption of the glass medium, the heat generated by the laser beam can be derived as

$$Q = \int_0^\infty I_o(1-R) \exp(-2r^2/w^2) [1-\exp(-\alpha\Delta z)] 2\pi r dr \qquad (1)$$

Here all notations have been defined in Table I. For the CO_2 laser (10.6

μm) used in this work, the generated heat is determined to be confined to a glass thickness of 10 μm, at which depth the laser energy is attenuated to 0.15% of its surface value. This depth is small enough to permit the laser heating to be treated as a boundary condition. On the back side (z=d), an adiabatic condition is imposed because of the small thermal conductivity of glass. The problem can then be formulated mathematically as follows: [9]

Governing Equation:

$$\rho c \partial T/\partial t = \nabla \cdot (k \nabla T),\ T(x,y,z,t),\ \begin{matrix} 0<x<a \\ -b<y<b \\ 0<z<d \end{matrix},\ t>0 \qquad (2)$$

Initial Condition:

$$T(x,y,z,0) = T_\infty \qquad (3)$$

Boundary Conditions:

$$k\partial T(0,y,z,t)/\partial x = h[T(0,y,z,t)-T_\infty] \qquad (4)$$

$$T(a,y,z,t) = T_\infty \qquad (5)$$

$$T(x,\pm b,z,t) = T_\infty \qquad (6)$$

$$q(vt,y,0,t)+k[\partial T(vt,y,0,t)/\partial z]-h[T(vt,y,0,t)-T_\infty] = 0 \qquad (7)$$

$$\partial T(x,y,d,t)/\partial z = 0 \qquad (8)$$

The problem as given can only be solved exactly for a special case in which the laser beam has travelled a long distance to the extent a quasi-steady state is reached. At that time the glass temperature is invariant with time in a coordinate system that is travelling along with the beam. For the general case of small time or sample size in a fixed coordinate system, the temperature is time dependent, and the problem must be solved numerically. [10]

For the present work, a finite-difference, alternating-direction-implicit (ADI) method is used to solve the problem. [11] The intense heat from the laser beam requires the use of a very thin surface layer together with small time steps in order to assure a convergent solution. The criterion for stable solution is found to be $D\Delta t/(\Delta z)^2<0.5$, which governs the selection of time steps and spatial increments in the numerical solution. An IBM Converted Monitor System (CMS) was used for the computation.

RESULTS AND DISCUSSION

Values of the parameters used in the computation are summarized in Table I. Of those listed in the table, the values of D, h, Q, and v are also changed in order to examine their effects on the temperature changes. For graphical presentation of results, composite diagrams (see Figures 2 through 5) are constructed so that the temperature profiles in both x and $|y|$ directions can be viewed simultaneously. All temperatures are plotted for the distributions at the surface (z=0), and they are normalized by using the peak values evaluated at the beam center; in all instances those evaluated with the tabulated parameters are used for control. It is noted that in each of these plots, the laser beam has moved to x equal to 0.32 cm, and the temperature profiles in the y direction are those of T evaluated at this x position.

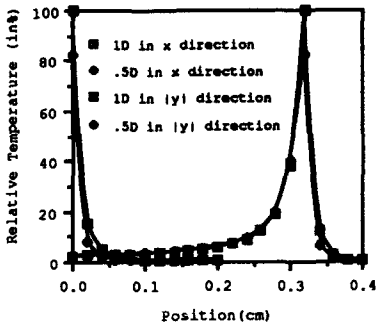


Figure 2. Relative temperature profiles with different heat diffusivities

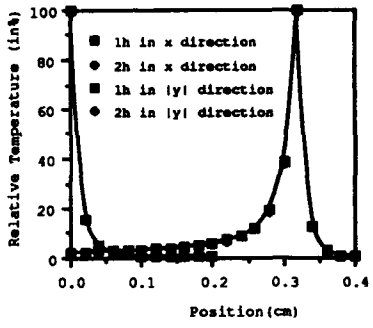


Figure 3. Relative temperature profiles with different heat transfer coefficients

As shown in Figure 2, a reduction of the thermal diffusivity by one half has a small effect of lowering the peak temperatures. For the temperature distributions in the x direction, the temperature gradients at the leading sides (x>0.32 cm) are always greater than those at the trailing sides (x<0.32 cm), a typical phenomenon for the problem investigated. In fact, the trailing side temperatures are practically unchanged with the diffusivity changes. Physically, the temperature decreases at small thermal diffusivities can be attributed to the large heat capacitance, which permits more heat to be stored in the glass medium.

Doubling the heat transfer coefficient (h) has a negligible effect in changing the surface temperatures; see Figure 3. The h value quoted in the table accounts for both free convection and radiation. Notice that, while the peak surface temperature at the beam center is high, the area over which this temperature is found is small. As a result, the heat transfer coefficient has negligible effect on the surface temperatures.

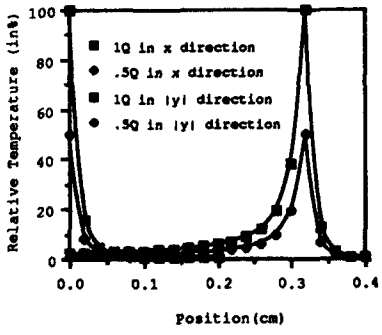


Figure 4. Relative temperature profiles under different power settings

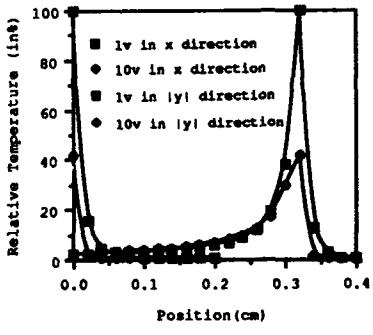


Figure 5. Relative temperature Profiles with different travelling velocities

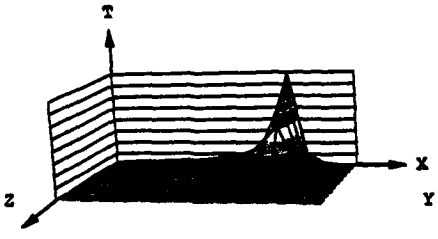


Figure 6. Three-dimensional temperature distribution on X-Z plane

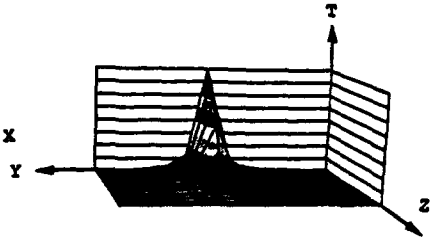


Figure 7. Three-dimensional temperature distribution on Y-Z plane

We expect that a reduction of laser power and an increase of the laser velocity would lower the peak temperatures found on the surfaces; see Figures 4 and 5. The major difference between Figures 4 and 5, however, is in the trailing sides. A reduction of the power is shown to have a dominant effect in lowering the trailing side temperatures.

The temperature attenuation in the z direction are shown in Figures 6 and 7. In these figures, the values of the parameters are listed in Table I. Those peak temperatures at z=0 correspond to peak curves presented earlier in the composite plots in Figures 2 through 5.

To complete this study, a numerical experiment was performed to test the convergence of the numerical solution. The time steps were successively reduced by half and the peak temperatures are compared for convergence. As shown in Figure 8, the temperatures converged to within 0.4% for time steps changing from 0.002 to 0.001 second. The results presented in this paper were obtained by using a time step of 0.002 second, a compromise between accuracy and economy.

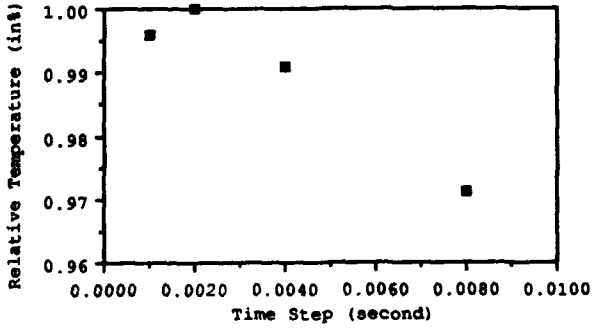


Figure 8. Convergence of the solution

CONCLUSIONS

Parametric effects on the calculated temperature distribution in the silica glass are investigated. The results show that the laser irradiated area is highly localized. The results presented in this paper are useful to correlate the laser treatment with the property changes in the irradiated area of the gel silica glass.

ACKNOWLEDGEMENTS

The authors are grateful for the financial support of the Air Force Office of Scientific Research under contract #F49620-88-C-0073, and the encouragement of Dr. Donald R. Ulrich.

REFERENCES

1. M. Rappaz, B. Carrupt, M. Zimmermann and W. Kurz, Helvetica Physica Acta 60, 924-936 (1987).

2. C. Y. Chang, Y. K. Fang, B. S. Wu, and R. M. Chen, Mat. Res. Soc. Symp. Proc. 23, 497 (1984).

3. I. D. Calder and R. Sue, J. Appl. Phys. 53 (11), 7545 (1982).

4. L. L. Hench, S. H. Wang, and J. L. Nogues, SPIE 878, 76 (1988).

5. L. L. Hench, in Science of Ceramic Chemical Processing, edited by L. L. Hench and D. R. Ulrich (Wiley-Interscience, 1986), pp. 52-64.

6. S. C. Park and L. L. Hench, in Science of Ceramic Chemical Processing, edited by L. L. Hench and D. R. Ulrich (Wiley-Interscience, 1986), pp. 168-172.

7. C. K. Hsieh and K. C. Su, The Journal of Solar Energy Science and Technology 22, 37 (1979).

8. J. H. Batteh, J. Appl. Phys. 53 (11), 7537 (1982).

9. M. N. Ozisik, in Heat Conduction,Wiley-Interscience, 1980, p. 6

10. D. Rosenthal, Trans. Am. Soc. Mech. Engrs. 68, 849 (1946)

11. M. N. Ozisik, in Heat Conduction,Wiley-Interscience, 1980, pp. 493-495

12. Y. S. Touloukian and E. H. Buyco, in Thermophysical Properties of Matter, The TPRC Data Series, Vol. 2, 1970, p. 202.

13. Y. S. Touloukian, R. W. Powell, C. Y. Ho, and P. G. Klemm Thermophysical Properties of Matter, The TPRC Data Series, Vol. 2, 1970, p. 922.

THE USE OF SOLUBLE METAL-POLYSELENIDE COMPLEXES AS PRECURSORS TO BINARY AND TERNARY SOLID METAL SELENIDES

S. Dhingra and M. G. Kanatzidis*

Department of Chemistry and Center for Fundamental Materials Research, Michigan State University, East Lansing MI 48824 USA

ABSTRACT

The use of several soluble metal polychalcogenides to prepare solid state materials is presented. Thermal gravimetric analysis (TGA) data, under inert atmosphere, of the molecular compounds $(Ph_4P)_2[Cd(Se_4)_2]$, $(Ph_4P)_4[Cu_2Se_{14}]$, $(Ph_4P)_2[Cu_4Se_{12}]$, $(Ph_4P)_4[In_2Se_{21}]$ and $(Et_4N)_3[M_3Se_{15}]$, (M=In, Tl), show that the corresponding binary solid state compounds are formed as single phases at temperatures as low as 530 °C. We have grown films of CdSe, $Cu_{2-x}Se$, β-In_2Se_3, TlSe and $CuInSe_2$ using these complexes as precursors. The films were prepared by pyrolysis of green precursor films, cast from DMF solutions. $CuInSe_2$ was prepared by co-thermolysis of Cu/Se_x and In/Se_x complexes. The chemical, X-ray, spectroscopic and electron microscopic characterization of these molecular precursor-derived films as well as their charge transport characterization is reported.

INTRODUCTION

Compared to the extensive investigations into the chemistry of molecular precursor materials for the synthesis of metal oxide ceramics and semiconductors, little work has been carried out in the area of chalcogenide solid state materials, particularly involving the heavier chalcogens. Of the molecular chalcogenides, sulfides are the most studied. The work on sulfides has concentrated on volatile species primarily for metal-organic chemical vapor deposition (MOCVD) work (e.g synthesis of ZnS and CdS).[1] The volatility of molecular metal-chalcogenides decreases rapidly from S to Te. The task of producing stable volatile M/Q (Q=Se,Te) compounds for MOCVD is extremely difficult. On the contrary it considerably easier to synthesize pure non-volatile complexes of metal-chalcogenides, and thus it would be highly desirable if methods were developed to fabricate chalcogenide films of comparable quality to those obtained by MOCVD. The molecular chalcogenide chemistry we have been developing in our laboratory, places us in an advantageous position to explore the possibilities for the synthesis and film fabrication of solid state binary or ternary sulfides, selenides and tellurides from the corresponding molecular complexes. Solid state chalcogenides enjoy such practical applications as IR detection and imaging[2], electroluminescent devices[2,3], optoelectronics[4], solar cells[5] and high energy density rechargeable batteries.[6] Todate, most of these materials are made at temperatures greater than 700 °C. Here we report our preliminary results on the use of soluble metal/polyselenides as precursors to prepare films of important solid state binary and ternary selenides.

EXPERIMENTAL SECTION

The precursor polyselenide complexes were prepared as described previously.[7,8] The X-ray powder diffraction patterns of all materials were recorded with a Phillips XRG-3000 computer controlled powder diffractometer. Ni filtered, Cu radiation was used. Thermal gravimetric analyses were performed on a Cahn TG System 121 under flowing nitrogen. A typical heating rate of 5 °C/min was used. Infrared spectra were recorded as KBr and CsI pellets on a Nicolet 740 FT-IR spectrometer. Scanning electron (SEM) and transmission electron

Mat. Res. Soc. Symp. Proc. Vol. 180. ©1990 Materials Research Society

(TEM) microscopy was done using a JEOL 35CF and JEOL 100CX respectively. Green precursor films were cast from concentrated dimethylformamide solutions onto hot (~150-160 °C) substrates of pyrex glass, quartz, stainless steel, carbon and copper. The various substrates were studied in order to evaluate their influence on film quality and homogeneity. The coated substrates were then placed inside a tube furnace which was heated at 550 °C and were pyrolyzed under flowing nitrogen. The resulting films were examined with X-ray diffraction, SEM and TEM microscopy and IR spectroscopy.

RESULTS AND DISCUSSION

The structures of polyselenide complexes $(Ph_4P)_2[Cd(Se_4)_2]$[7], $(Ph_4P)_2[Cu_4Se_{12}]$[8a], $(Ph_4P)_4[Cu_2Se_{14}]$[8b], $(Ph_4P)_4[In_2Se_{21}]$[8c,d] and $(Et_4N)_3[M_3Se_{15}]$[8d] (M=In, Tl), are shown in figure 1. Thermal gravimetric analysis (TGA) data, under inert atmosphere, of these compounds show that the corresponding binary solid state compounds are formed as single phases at temperatures as low as 530 °C. The TGA diagrams, figure 2 of the compounds show that the onset temperature for weight-loss correlates with the stability of the organic counterion i.e $Ph_4P^+ > Et_4N^+$. This implies that the rate determining step for the decomposition is the nucleophilic attack of a coordinated Se_x^{2-} ligand in the anion on the alkyl (or aryl) group of a cation to form an alkylated Se species.

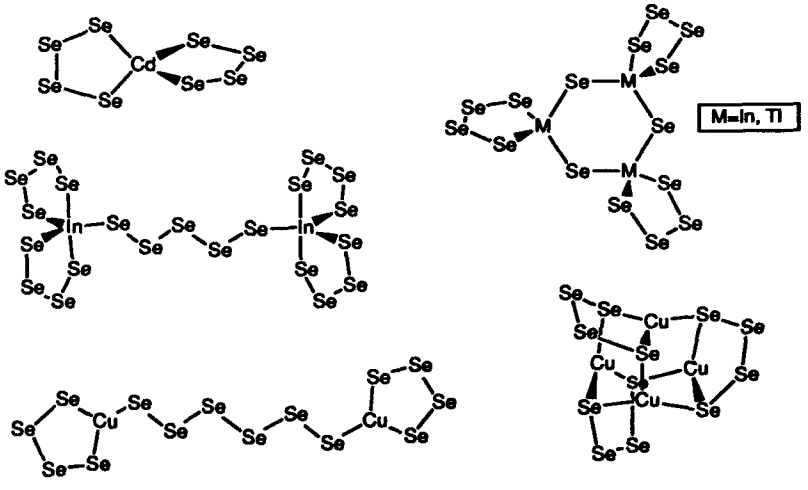


Figure 1. The schematic structures of the polyselenide precursor complexes

We have grown solid films of CdSe, $Cu_{2-x}Se$, β-In_2Se_3, TlSe and $CuInSe_2$ using these complexes as precursors. The films were prepared by pyrolysis of green precursor films, cast from DMF solutions. $CuInSe_2$ was prepared by co-thermolysis of Cu/Se_x and In/Se_x complexes in the proper stoichiometry. In a typical experiment $(Et_4N)_3[In_3Se_{15}]$ and $(Ph_4P)_2[Cu_4Se_{12}]$ or $(Ph_4P)_4[Cu_2Se_{14}]$ were dissolved in DMF in a 4:3 and 2:3 molar ratio respectively. These proportions result in a Cu:In ratio of 1:1. Better β–In_2Se_3 films were obtained from the $(Ph_4P)_4[In_2Se_{21}]$ complex.

The decomposition reaction for CdSe and $CuInSe_2$ are shown in eq. 1 and eq. 2.

$$(Ph_4P)_2[Cd(Se_4)_2] \longrightarrow CdSe + Ph_2Se + Ph_3P + Ph_3PSe \quad \text{eq. 1}$$

$$1/3(Et_4N)_3[In_3Se_{15}] + 1/4(Ph_4P)_2[Cu_4Se_{12}] \longrightarrow CuInSe_2 + Et_2Se + Ph_2Se + Ph_3P + Et_3N + Ph_3PSe \quad \text{eq. 2}$$

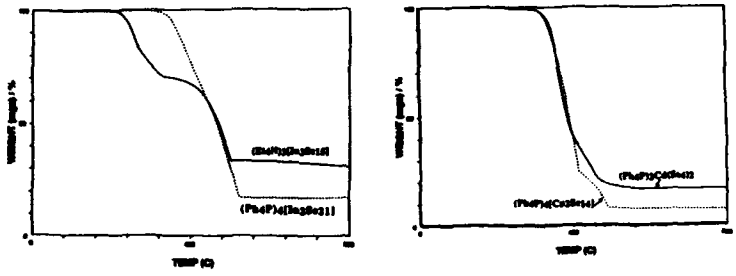


Figure 2. TGA data for the precursor polyselenide complexes

All precursor complexes gave the corresponding crystalline binary phases (i.e. CdSe, $Cu_{2-x}Se$, β–In_2Se_3, TlSe) in pure form as evidenced by X-ray diffraction.[9] Typical X-ray diffraction patterns are shown in figure 3. Examination of these films by selected area electron diffraction (SAD) with a TEM also confirmed the identity of the phases. An example SAD pattern for β–In_2Se_3 and $CuInSe_2$ is shown in figure 4. The IR spectra of the films showed no residual hydrocarbon peaks (from the organic counterions).

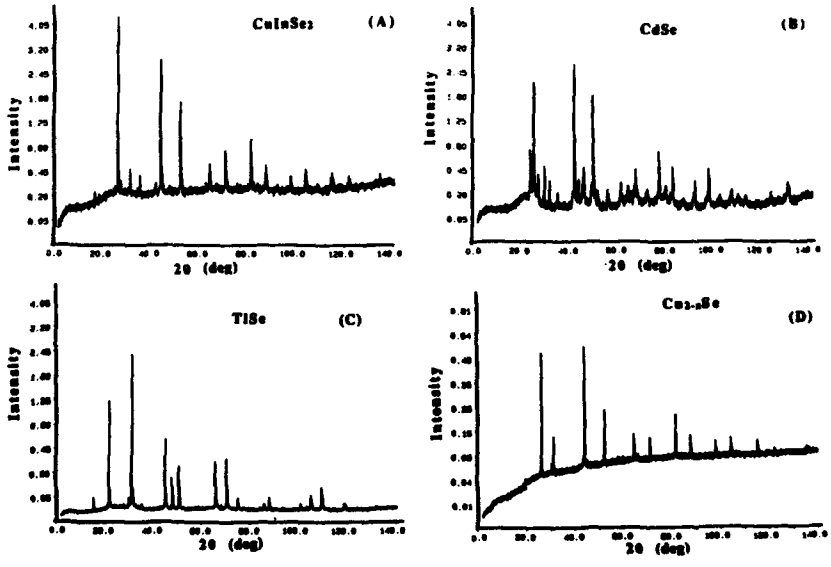


Figure 3. X-ray diffraction patterns of films of (A) $CuInSe_2$, (B) CdSe, (C) TlSe and (D) $Cu_{2-x}Se$

At this stage only relatively thick films (~25-35 μm) were made in order to evaluate the film forming ability of the precursors. Thin films should be fabricable with the use of a special spin-coater equipped with a substrate heater. Significant preferential orientation was not observed in

the films of CdSe, β–In_2Se_3 and $CuInSe_2$. However, films of TlSe showed considerable preferential orientation regardless of substrate. In TlSe the *h00* and *hh0* class of reflections are greatly enhanced while *h0l* reflections are diminished. This indicates that the c-axis of the tetragonal unit cell[9] of the TlSe crystallites is parallel to the substrate. This may be due to partial melting of TlSe during film formation at 530 °C. The quality of the $CuInSe_2$ films depended on the substrate. In general, the best quality films in terms of smoothness and contiguity were obtained on carbon and pyrex substrates. The quality of the precursor green films (smoothness and thickness homogeneity) was reflected in the quality of the final chalcogenide film. Often films showed cracks or pinholes arising from the relatively large shrinkage associated with the pyrolysis of the precursor complexes. It should be noted for example that $(Ph_4P)_2[Cd(Se_4)_2]$ will lose 86.5% of its mass to yield the final CdSe product. For $CuInSe_2$ the weight-loss is 70%. In order to improve the quality of the final films complexes with higher M/Se ratio are needed which will not require such a drastic weight-loss thus reducing the extent of shrinkage.

The morphology of $CuInSe_2$ films on various substrates was examined by SEM. Figure 5 shows several micrographs of films of this material on several substrates. The films have a granular microcrystalline nature with an average crystallite grain size of ~1 μm. The conductivity of $CuInSe_2$ produced from the co-thermolysis reaction of eq. 2 is ~10^{-4} $\Omega^{-1}cm^{-1}$. Thermoelectric power (TP) measurements show that the $CuInSe_2$ films are p-type degenerate semiconductors. This is consistent with heavy doping with nitrogen and/or phosphorous.[10]

In the case of CdSe films, we detected (by X-ray diffraction) both hexagonal (major) and cubic (minor) polytypes. Since there is significant overlap of the low angle diffraction peaks of the hexagonal and cubic forms, the presence of cubic CdSe is suspected from the high angle data. The conductivity of the CdSe films is of the order of 10^{-7} $\Omega^{-1}cm^{-1}$. The very low conductivity did not allow for reliable TP measurements to be made. Corresponding data for $Cu_{2-x}Se$, TlSe and β–In_2Se_3 are not available at this time. SEM photographs of CdSe, TlSe, β–In_2Se_3 and $Cu_{2-x}Se$ are shown in figure 6. Further details and complete characterization of all the films will given elsewhere.

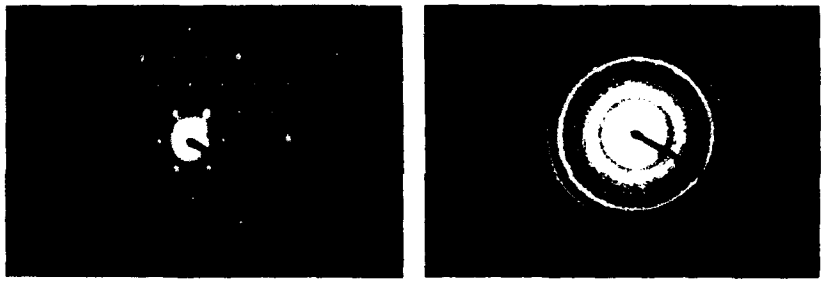


Figure 4. SAD patterns obtained for β–In_2Se_3 (left) and $CuInSe_2$ (right).

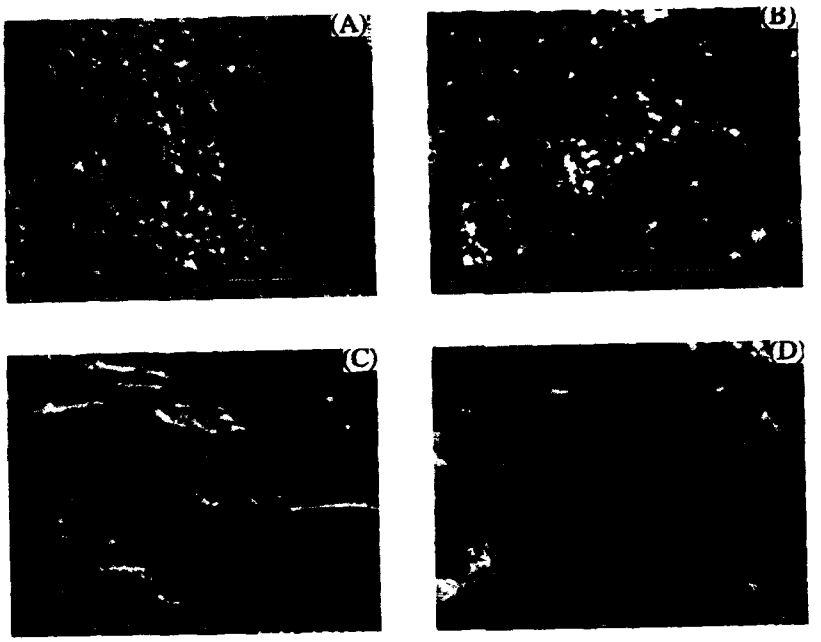


Figure 5. SEM photographs of $CuInSe_2$ films on (A) quartz, (B) pyrex, (C) stainless steel and (D) carbon substrates.

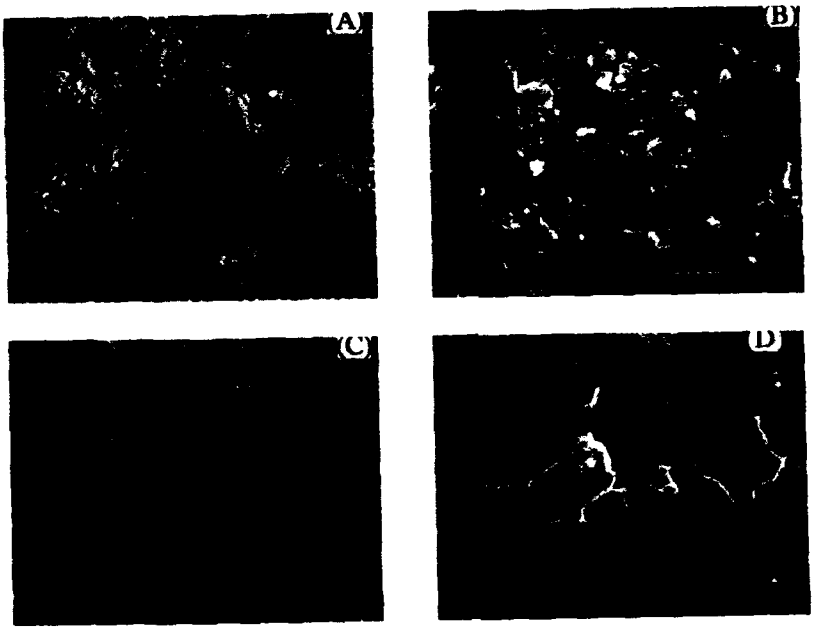


Figure 6. SEM photographs of films of (A) CdSe on carbon, (B) TlSe on quartz, (C) β-In_2Se_3 on quartz and (D) $Cu_{2-x}Se$ on carbon.

CONCLUSIONS

Single phase binary and ternary chalcogenide films of CdSe, $Cu_{2-x}Se$, β-In_2Se_3, TlSe and $CuInSe_2$ have been prepared at 530 °C using molecular precursor polyselenide complexes. For $Cu_{2-x}Se$, β-In_2Se_3, TlSe and $CuInSe_2$ this is the first time these materials have been made by molecular precursor methods. Prepared by this method, $CuInSe_2$ is p-type. One of the limitations of the molecular precursor method is the large weight-loss associated with pyrolysis which can result in cracked and discontinuous films. Although this could be avoided by preparing good green precursor films, molecular precursors with high M/Se ratio are desired to help solve this problem.

Acknowledgement Financial support from the Center for Fundamental Materials Research (CFMR) Michigan State University and the National Science Foundation for a Presidential Young Investigator Award, CHE-8958451 is gratefully acknowledged. We thank Professor C. R. Kannewurf and Don C. DeGroot (Northwestern University) for TP and conductivity measurements on the $CuInSe_2$ samples.

REFERENCES

1) Fan, G.; Williams, J. O. *J. Chem. Soc. Faraday Trans.* **1987**, 83, 323-338

2) (a) Smith, R.A. in "Semiconductors" pp. 438, Cambridge University Press, 1978. (b) Bartlett, B.E. et al. *Infrared Phys.* **1969**, 9, 35.

3) Kun, Z. K. *Solid State Technology* **1988**, 31, 77-79.

4) Ballman, A.A.; Byer, R.L.; Eimerl, D.; Feigelson, R.S.; Feldman, B.J.; Goldberg, L.S.; Menyuk, N.; Tang, C.L. *Applied Optics* **1987**, 26, 224-227.

5) (a) Mickelsen, R.A.; Chen, W.S. in "Ternary and Multinary Compounds," Proceedings of the 7th Conference, Deb, S.K. and Zunger, A. Eds., Materials Research Society, 1987, pp. 39-47. (b) Steward, J.M.; Chen, W.S.; Devaney, W.E.; Mickelsen, R.A. Deb, S.K. and Zunger, A. Eds., Materials Research Society, 1987, pp. 59-64.

6) (a) Whittingham, M.S. *Science* **1976**, 192, 1125. (b) Whittingham, M.S. *J. Solid State Chem.* **1979**, 29, 303-310.

7) (a) Kanatzidis, M. G. Abstracts of 196th *ACS National Meeting*, Los Angeles **1988**, INORG 469. (b) Kim, K.-W., Dhingra, S.; Kanatzidis, M. G. unpublished

8) (a) Cusick, J.; Scudder, M. L.; Craig, D. C.; Dance, I. G. *Polyhedron* **1989**, 8, 1139-1141 (b) Kanatzidis, M. G.; Huang S.-P.; Dhingra, S. unpublished (c) Kanatzidis, M. G.; Dhingra, S. *Inorg. Chem.* **1989**, 28, 2024-2026 (d) Dhingra, S.; Kanatzidis, M. G. submitted for publication

9) (a) β-In_2Se_3: Popovic, S.; Tonejc, A.; Grzeta-Plenkovic, B.; Celustka, B.; Trojko, R. *J. Appl. Crystallogr.* **1979**, 12, 416-420 (b) TlSe: Ketelaar, J. A. A.; t'Hart, W. H.; Moercl, M.; Polder, D. *Z. Kristallogr.* **1939**, 101, 396-405

10) SEM-EDS analysis of the $CuInSe_2$ films indicated the presence of traces of P (<0.07 % per weight)

CHEMICALLY DERIVED YTTRIA-STABILIZED ZIRCONIA FOR PLASMA-SPRAYING

FAWZY G. SHERIF* AND H. HERMAN**
*Akzo Chemicals Inc., Research Department, Dobbs Ferry, NY 10522
**State University of New York at Stony Brook, Department of Materials Science and Engineering, Stony Brook, NY 11794

ABSTRACT

Yttria-stabilized zirconia powders were prepared by three chemical routes utilizing emulsion hydrolysis techniques. Metal alkoxides, acetates and mixtures of alkoxides and acetates were used as starting materials. Under controlled hydrolysis conditions, particles with different morphology and size were obtained. Spherical or granular particles in the range of 20-60u in diameter were formed. The grain size varied from 0.1-0.2u. The powders were applied successfully as plasma spray coatings. The chemical uniformity was demonstrated by the presence of 100% non-transformable tetragonal zirconia in the powder and in the coating.

INTRODUCTION

Although extensive studies were carried out on the chemical synthesis of ceramic oxide powders[1], only moderate efforts have been directed towards preparing chemically uniform oxide powders for plasma spray coating[2]. A number of chemical methods developed in the past decade were utilized to achieve high purity and phase uniformity. Phase uniformity is essential for durable coatings in thermal barrier applications. One example is the yttria partially stabilized zirconia.

The goal of this work is to demonstrate that chemically produced yttria-stabilized zirconia powder, under proper synthesis condition, mainly contains the non-transformable tetragonal zirconia crystalline phase needed for the plasma spray coating applications. Most commercial plasma-spraying powders are usually made by blending the individual oxides, melting, thermal spraying or rapid solidification. These processes often result in molecularly non-uniform compositions, with variable mixtures of cubic, tetragonal and monoclinic zirconia.

EXPERIMENTAL

Three chemical processes were carried out. Each process depended upon the raw materials used:

Mat. Res. Soc. Symp. Proc. Vol. 180. ©1990 Materials Research Society

From Yttrium Acetate and Zirconium n-Butoxide-A

Commercial yttrium acetate tetrahydrate was dehydrated at 110°C/4hrs. Anhydrous yttrium acetate (69.6g) was mixed with 1215g of zirconium n-butoxide butanol complex in a five-liter flask under nitrogen. The mixture was refluxed at 130°C until the yttrium salt went into solution. A liquid (250g) was then distilled at 114°C from the solution. The residue was cooled down to room temperature, 2200g of toluene was added, and the resulting solution was stirred vigorously. Water (213cc) was then added and the stirring of the resulting emulsion was continued until gelation occurred. The gel was filtered and dried in air at 125°C for four hours, then milled gently until all powder passed through a 140-mesh screen. The powder was calcined at 200°C, 400°C, 800°C, and 1100°C, each for two hours. The weight of powder was 356.8g. The powder was classified by sieving through a 500-mesh screen using an Alpine air jet sieve. The yield was 260g.

From Yttrium and Zirconium Alkoxides-B

A solution of yttrium isopropoxide in toluene, 21.3 wt.%, was refluxed with a solution of zirconium n-propoxide in propanol, 73.6 wt.% under nitrogen. The free propanol was then distilled off at 93°C. The mixture was diluted with n-heptane to give final concentrations of [Y]=0.07M and [Zr]=0.69M. 12 moles of water were added in a few seconds and the two phases were stirred vigorously until a gel formed. The gel was aged 4 hrs., filtered, air dried, and oven dried at 125°C/4 hrs. The powder was gently milled and sieved through a 140-mesh screen (100u). It was then calcined and classified as above.

From Yttrium Acetate and Zirconium Acetate-C

An aqueous solution containing 2.13 moles of zirconyl acetate and 0.37 moles of yttrium acetate was emulsified with three times its volume of n-heptane using Span 80 as an emulsifier. Ammonia was then introduced into the emulsion. The precipitate was filtered, water washed, dried, calcined and classified as above.

POWDER EVALUATION OF PLASMA SPRAY COATING

The powders from the above three chemical routes were evaluated for plasma spray coating and compared to a commercial 8% wt. Y_2O_3 zirconia powder[3]. The properties of the powders are given in Table I. The plasma spray parameters used were similar to a typical Metco 3MB gun operation.

DISCUSSION

Ester Elimination - Precedure A

Butyl acetate elimination[4] was accomplished by distilling off the vapors from the reaction mixture at 130°C-200°C. The reaction can be represented by equation (1):

$$Y(OCOCH_3)_3 + Zr(OC_4H_9)_4 \longrightarrow CH_3COOC_4H_9 + C_4H_8 + (CH_3COO)_2Y\text{-}O[Zr\text{-}(OC_4H_9)_2]OH$$

The commercial zirconium n-butoxide butanol complex was used. In addition to the one mole ester collected per one mole yttrium acetate, the free butanol corresponding to the complex was also distilled off. Both butanol and butyl acetate formed a distillable azeotrope. The composition of the azeotrope was quantitatively identified by GC analysis. The elimination of the ester and the free butanol suggested the condensation of Y with Zr in one compound. Further identification of this compound will be discussed in a separate paper.

The DTA of the hydrated powder, Figure 1, shows the initial endotherm at about 125°C due to water and toluene evaporation. The exotherm at 380.7°C is due to combustion of acetates. The very sharp peak at 470°C indicates the crystallization of amorphous zirconia. The effect of increasing calcination temperature from 600°C to 1600°C on powder properties was investigated. At the low temperature of 600°C, the nontransformable tetragonal ZrO_2 was detected by X-ray diffraction. The microstructure at 800°C and 1600°C is shown in Figure 2.

Condensation of Double Alkoxides - Procedure B

This condensation reaction is known[5], e.g. for aluminum and zirconium[6]. Controlled hydrolysis in non-aqueous solvents gave a hydrated powder with residual alkoxides which could be detected by thermal analysis. The DTA shown in Fig 1 describes two combustion exotherms at 276°C & 351°C. In addition, the very sharp peak at 470°C for ZrO_2 crystallization was similar to the hydrated product obtained from the acetate and alkoxide. The microstructure is similar to that shown in Figure 2.

TABLE I
Properties of Powder

Procedure Raw Material	A All Alkoxide	B Acetate/Alkoxide	C All Salts	Commercial Metco 204NS
Morphology	Granular	Granular	Spherical	Spherical
Bulk Density,g/cc	1.99	2.08	2.6	2.5
Flow, cc/sec.	1.8	1.7	1.1	1.0
Median Particle Size,u	55	50	53	41
% <24u	2.4	3	4	20
Crystal Structure	100% T'[1)]	100% T'[1)]	100% T'[1)]	67%T', 33%M[1)]

[1)] T', Non Transformable Tetragonal ZrO_2 phase; M, Monoclinic

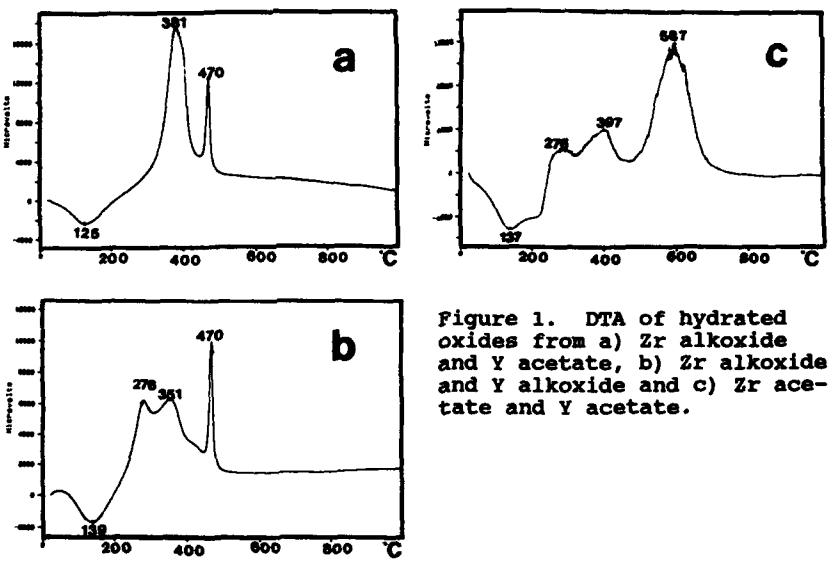


Figure 1. DTA of hydrated oxides from a) Zr alkoxide and Y acetate, b) Zr alkoxide and Y alkoxide and c) Zr acetate and Y acetate.

Emulsion Coprecipitation - Procedure C

In this system, yttrium acetate and zirconyl acetate dissolved in water were emulsified with heptane using Span 80 according to the procedure described by Akinc[7]. The emulsion was treated with ammonia gas and the basic acetate-hydroxide formed as spheres. The size of the spheres was decreased with reducing agitation and increasing emulsifier concentration. Thermal analysis of the powder formed by this route showed the acetate decomposition at 276°C and 397°C. In addition, a broad zirconia peak at 550°-650°C is obtained as shown in Figure 1. Crystallization of ZrO_2 must have occurred in this range, which is much higher than that using zirconium alkoxide hydrolysis in nonaqueous systems.

Plasma Spray Coatings

The most significant differences between chemically prepared powders and the commercial product were phase uniformity and particle size. The chemically prepared coatings contained 100% nontransformable tetragonal zirconia, T'. The commercial coating contained 97% T' and 3% monoclinic. This monoclinic may enhance macrocracking as it appears to exceed the smaller micro amounts responsible for transformation toughness.

Particle morphology did not appear to affect deposition efficiency (DE). However, particle size did. For example, powder C with median particle size of 53u gave 69% DE, while the commercial powder size of 41u gave 53%. Furthermore, powder C contains only 4% <24u fines while the commercial powder contains 20% as shown in Table I.

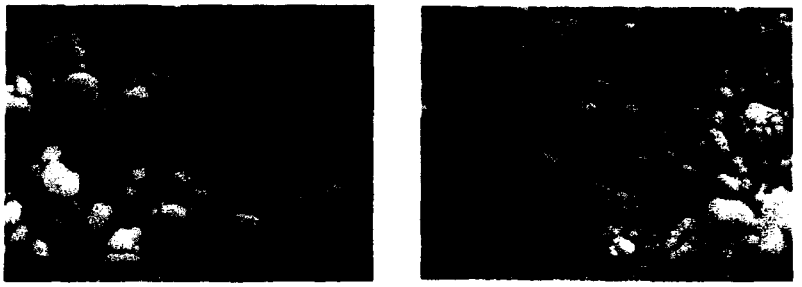


Figure 2. Microstructure of YSZ powders calcined at A, 800°C and B, 1600°C

CONCLUSION

Yttrium and zirconium alkoxides, acetates and alkoxide-acetate mixtures were hydrolyzed in water/oil emulsions under controlled conditions to produce three 8% yttria-stabilized zirconia powders. The powders performed satisfactorily as plasma spray coatings. The powders and the coatings contained 100% nontransformable tetragonal zirconia, a property not found in a commercial physically prepared powder containing the same concentration of yttria.

ACKNOWLEDGEMENTS

The authors wish to acknowledge the contribution of V.Brice and F.Cambria of Akzo Chemicals Inc. and G.Bancke of SUNY, Stony Brook in obtaining the analytical and powder evaluation data.

REFERENCES

1. K.S.Mazdiyasni, Ceramics International 8, 42(1982); Better Ceramics Through Chemistry, edited by C.J.Brinker, D.E.Clark and D.R.Ulrich (Mater.Res.Soc.Proc. 32, Albuquerque, New Mexico 1984) pp. 175-186; B.Fegley, Jr. and E.A.Barringer, ibid, pp. 187-197.
2. G.Gowda, J.Mater.Sci.Lett., 5, 1029(1986).
3. F.N.Longo, N.F.Bader,III, and M.R.Dorfman, US Patent No. 4,450,184 (22May1984).
4. M.Osgan, J.J.Pasero and Ph.Teyssie, J.Polymer Sci.,B,88, 319(1970).
5. D.C.Bradley, R.C.Mehrotra and D.P.Gaur, Metal Alkoxides, (Academic Press, New York, 1978), p.306.
6. R.C.Mehrotra and A.Mehrotra, Inorg.Chim.Acta Revs.5,127 (1971).
7. M.Akinc and K.Richardson, Better Ceramics Through Chemistry, edited by C.J.Brinker, D.E.Clark and D.R.Ulrich (Mater.Res.Soc.Proc. 73, Palo Alto, Ca. 1986) pp.99-109.

EMULSION PRECIPITATION AND CHARACTERIZATION OF ZIRCONIA

Lieh-Jiun Shyu* and Frank M. Cambria*
* Akzo Chemicals Inc., Livingstone Ave., Dobbs Ferry, NY 10522

ABSTRACT

Zirconia and yttria-stabilized zirconia (YSZ) powders were prepared from water/oil emulsions followed by high temperature calcination. The morphology and particle size were correlated with several variables such as composition of emulsions, concentration of starting materials and surfactants, stirring rate, hydrolysis rate and calcination temperature. The powders were characterized according to crystalline phase, particle size distribution, and flow rate. Emulsion precipitation typically yielded spherical zirconia particles which were either solid or hollow. Particle size could be controlled from submicron to a few hundred microns depending primarily on the composition of the emulsion and stirring rate during hydrolysis. SEM/EDX results showed that yttria was uniformly distributed throughout the zirconia particles. The crystalline phase of the powders after calcination at 800°C was entirely non-transformable tetragonal. The flow rate increased with increasing particle size and with increasing sphericity.

INTRODUCTION

Zirconia powder is useful in many advanced structural and electrical ceramics applications. Because of its low thermal conductivity and relatively high thermal expansion coefficient, it has been considered a good thermal barrier coating in heat engines [1,2]. The powder is typically coated on the engine parts by plasma spray techniques. This technology requires that the powder has good flow and large particle size. The performance of the thermal barrier coating is dramatically influenced by the initial powder size distribution and chemical homogeneity [3].

It is known that zirconia can be stabilized by alloying it with CaO, MgO or Y_2O_3 [4]. In this paper, we have studied yttria stabilized zirconia powders which were prepared by emulsion hydrolysis.

The emulsion hydrolysis technique has been used to prepare ceramic powders with spherical morphology [5,6,7]. This technique allows precipitating powders with a controlled particle size distribution and shape. The emulsion droplets serve as microreactors during hydrolysis. However, most of the research in this area has focused on the preparation of fine particles. Our intention in this work was to prepare powders with a particle size range of about 30 to 80 microns suitable for plasma spray coating applications.

EXPERIMENTAL

Yttria-stabilized zirconia powder was prepared from zirconium compounds, such as zirconium oxyacetate or zirconium oxychloride premixed with yttrium acetate or nitrate in a water-in-oil (w/o) emulsion. The organic phase was heptane, hexane, toluene, or mineral oil. The emulsifier used was either cationic or non-

Mat. Res. Soc. Symp. Proc. Vol. 180. ©1990 Materials Research Society

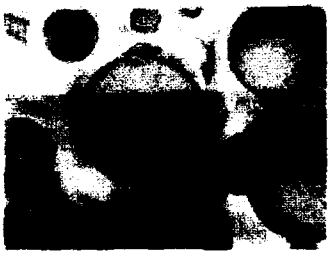
ionic surfactant, such as alkyl quaternary ammonium chloride or sorbitan monooleate. The emulsion was agitated in a round bottom flask with a mechanical stirrer and precipitation took place when a base compound, such as alkyl amine, ammonia or ammonium hydroxide was introduced. The precipitates were centrifuged, washed with water and heptane, dried at 110°C, and then calcined in accordance with following heating cycle:

Temp. (°C)	Time (hrs)	Temp. (°C)	Time (hrs)
25-200	2	800	2
200	2	800-1100	2
200-400	2	1100	5
400	2	1100-25	5
400-800	2		

The precipitated and calcined powders were analyzed for chemical compositions, crystalline phase, particle size distribution and morphology. The zirconium and yttrium were analyzed by proton induced X-ray emission. The crystalline phase was determined by X-ray diffraction (XRD). The particle size was analyzed using laser diffraction. The morphology was studied by optical microscopy and scanning electron microscopy.

RESULTS AND DISCUSSION

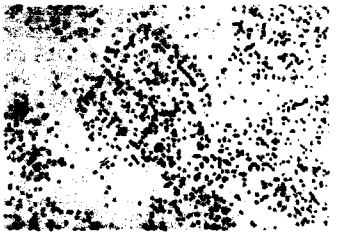
In this work, the yttria level incorporated in YSZ was typically 8% by weight. SEM/EDX mapping of yttrium and zirconium reveals that yttria is uniformly distributed in the YSZ particles (Fig. 1).



(a)



(b)



(c)

Fig.1 - SEM/EDX mapping of YSZ, (a) particles examined, (b) Zr mapping, (c) Y mapping.

The XRD scans show that pure zirconia powders precipitated in the w/o emulsion are amorphous; after calcination at 1100°C the material is monoclinic. YSZ, precipitated under the same conditions and calcined at 800°C, is non-transformable tetragonal, t' [8] (Fig. 2). Apparently, yttria-doped zirconia powder converts at a much lower temperature from the monoclinic to the tetragonal phase than pure ZrO_2 powder.

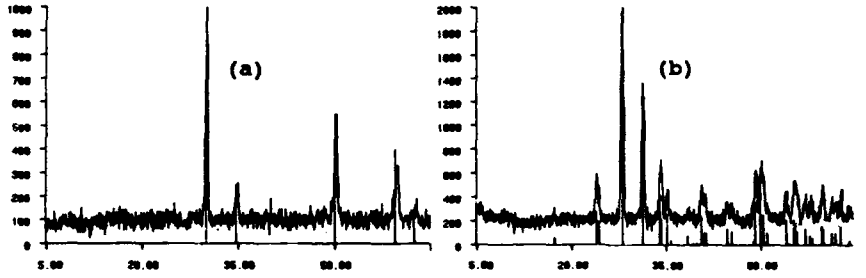


Fig. 2 - XRD patterns (a) YSZ tetragonal, (b) ZrO_2 monoclinic

YSZ particles prepared from w/o emulsions with a suitable surfactant are spherical. The irregularly-shaped YSZ particles are formed in the absence of surfactant (Fig. 3).

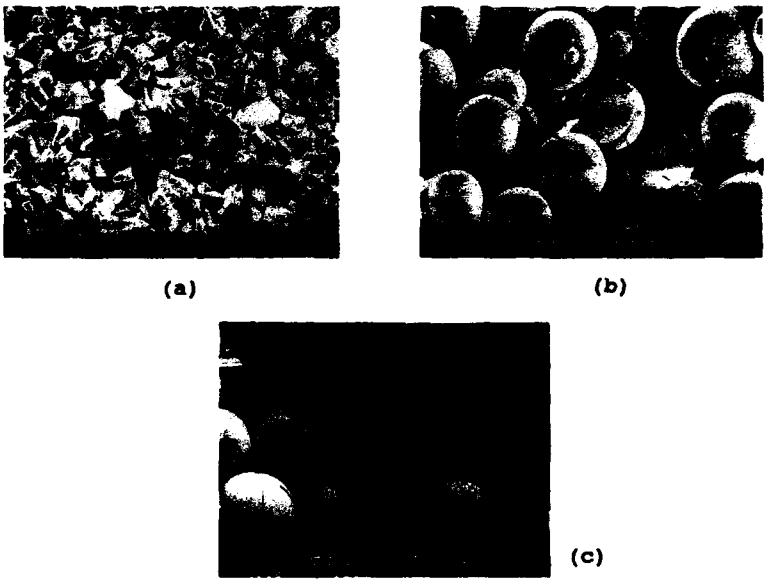


Fig. 3 - YSZ precipitated from w/o emulsions. (a) No surfactant was used, (b) with surfactant SMO - slow hydrolysis (pH increased from 3 to 8 in 2 hrs), (c) with surfactant SMO - fast hydrolysis (pH increased from 1 to 9 in 30 min). SMO - sorbitan monooleate

The particle size of YSZ depends on stirring rate during hydrolysis and the composition of the emulsions. When ultrasonic vibration was applied during hydrolysis, submicron particles formed. In general, the slower the stirring, the larger the particles formed. The more surfactant used, the smaller the particles tend to be. However, the size of the precipitate is governed by the size of the water droplets in the emulsions (Table I).

Table I. The effect of emulsion compositions and stirring Rates on the particle size of the precipitates

heptane/water vol. ratio	surfactant (vol. %)	stirring (rpm)	mean size (microns)
9.0	0.1	320	90
3.0	1	320	68
3.0	1	450	53
1.0	2	320	55
1.0	2	450	30
3.0	8	320	31

Starting materials: $ZrO(Ac)_2$: 2.31 M, $Y(Ac)_3$: 0.22 M, surfactant: sorbitan monooleate, shape of particles: spherical

Fast hydrolysis yielded hollow spheres of YSZ, while slow addition of base resulted in solid spheres. The hollow spheres are very fragile and tend to break (Fig. 3). Chemical analysis indicates that the precipitate is $Zr(OH)_x(CH_3COO)_{3-x}$ where x varies from 0.3 to 3 when $ZrO(CH_3COO)_2$ was used as a starting material. Calcination at 800°C or above is sufficient to remove the acetate group and form the t' phase. Calcination also reduced the particle size by about 20%. The starting materials and solvent chosen did not seem to significantly affect the particle size and morphology. In order to obtain spherical particles, a relatively stable emulsion has to be formed during hydrolysis. The following surfactants were found suitable: quarternary ammonium chloride and sorbitan fatty acid esters, such as sorbitan monooleate or monolaurate. The flow rates are higher for the spherical powders than those of irregularly shaped materials. It was also observed that the larger the particles, the better the powder flow (Table II).

Table II. The relationship of particle size and morphology with flow rate of YSZ powders

Mean Size (microns)	Particle Shape	Flow Rate (cc/sec)
31	spherical	1.3
44	spherical	1.6
72	spherical	2.1
84	irregular	1.6
63	irregular	0.9

CONCLUSIONS

Yttria-stabilized zirconia with a controlled particle size and spherical morphology can be prepared by emulsion precipitation technique. This powder calcined at 800°C only exhibits the non-transformable tetragonal phase. Due to chemical homogeneity, desirable particle size range and good flow features, this powder is suitable for plasma spray coatings applications.

REFERENCES

1. R. J. Bratton and S. K. Lau, Adv. Ceram., Edited by A. H. Heuer and L. W. Hobbs, 3, 226-240. 1981.

2. W. H. Rhodes and S. Natansohn, Ceram. Bull., 68 (10), 1804-1812, 1989.

3. Keller, R. J., Research and Development for Improved Thermal Barrier Coatings, Report No. AFWAL-TR-4008, April 1984.

4. E. C. Subbarao, Adv. Ceram., Edited by A. H. Heuer and L. W. Hobbs, 3, 1-24, 1981.

5. M. Akinc and K. Richardson, Mat. Res. Soc. Symp. Proc., 73, 99-109, 1986.

6. P. Reynen, H. Bastius and M. Fiedler, Ceramic Powders, Elsevier Scientific Publishing Co., Amsterdam, p. 405, 1983.

7. A. R. Hardy, G. Gowda, T. J. McMahon, R. E. Riman, W. E. Rhine, and H. K. Bowen, Preparation of oxide powders, John Wiley & Sons, Inc. New York, NY 1987.

8. K. Muraleedharan and J. Subrahmanyam, J. Am. Ceram. Soc., 71 (5), C226-C227, 1988.

TRANSPIRATION COOLED POROUS TYPE VI SILICA ROCKET WINDOWS

ALBERT G FOSMOE II AND LARRY L. HENCH
Advanced Materials Research Center, University of Florida, One Progress Blvd., #14, Alachua, Fl 32615

ABSTRACT

A novel use of sol-gel derived porous Type VI silica for high performance rocket guidance system windows is evaluated. The samples produced for this study were optically transparent hydrofluoric and/or nitric acid catalyzed tetramethylorthosilicate (TMOS) xerogel monoliths with average pore radii of 1.2, 5.0, and 8.0nm. Maximum He transpiration velocities of up to 3 cm/sec, 3 times the velocity needed for transpiration cooling, are measured for a 5.0 nm sample at 3.2 MPa. Transpiration velocities of 0.6 cm/sec result in cooling effects as large as 44°C from 160°C.

INTRODUCTION

The sol-gel method provides many unique possibilities in the design of modern optical materials not available by the traditional melt methods[1-3]. Of interest here is the ultraporous structure of Type VI silica, an intermediate product of Type V fully dense gel-silica[3]. Recent advances at the Advanced Materials Research Center (AMRC) in the development of sol-gel technology has made possible the reliable production of Type VI ultra-pure silica monoliths with a wide controllable range of porosity and pore morphology[4-6].

This porosity may potentially be used and modified advantageously for rocket window applications. Specifically, the transpiration of gases through the interconnecting permeable structure should provide a significant cooling effect, thus increasing the working performance of hypersonic (mach > 5) rocket guidance system windows. The properties needed in the severe operating conditions of optically transmitting rocket windows include: structural strength, high temperature stability, thermal shock resistance, and broad band optical transmission over wide temperature ranges.

Previous work in this area by the authors concentrated on the first steps in proving the concepts[1]. These steps included the demonstration of UV transmission at elevated temperatures and determination that transpiration flow is possible through optically transparent monoliths. UV transmission was qualitatively shown to exist at temperatures >1000°C. Transpiration data was also presented, however, velocities were incorrectly reported low by a factor of ten. It is the intent of this work to evaluate samples with average pore radius in the low mesopore range, approximately 5 nm, in an attempt to increase transpiration velocities to well above the approximately 1 cm/sec needed for transpiration cooling[7]. Cooling effects resulting from He transpiration will also be explored.

Mat. Res. Soc. Symp. Proc. Vol. 180. ©1990 Materials Research Society

The shock wave preceding a rocket under high mach conditions involves an intense thermal boundary next to the exterior surface of the rocket[8]. If this exterior surface is an optical transmission window with a temperature dependant bandpass, the increased temperature resulting from radiant and conductive heat from this boundary layer to the window will dramatically affect its optical throughput. Radiant transfer can be decreased with a reflective surface. A reflective surface will not however, reduce the large amount of heat transfered by conduction. A very effective method for lowering the conduction involves transpiration cooling. This is the flow of fluids, in this case a gas, through a porous exterior surface which effectively reduces the boundary layer temperature gradient with respect to distance from the surface. This lowers the conduction transfer rate. Transpiration velocities as low as 1 cm/sec lead to a significant cooling effect. Higher transpiration velocities bring more significant results[7].

EXPERIMENTAL PROCEDURE

The sol-gel monoliths used in this study were produced by the hydrolysis and polycondensation of the alkoxide precursor TMOS followed by aging, drying and stabilization (thermal treatment) at ambient pressures. Discs were sectioned from dried(180°C) rods before additional thermal treatment. After stabilization, samples were polished to a 18 μm surface and a thickness of 2.00 mm.

Transpiration measurements as well as the cooling tests were obtained using the set-up in Fig. 1. All samples were outgassed by heating in vacuum before flow and cooling measurements. Flows were determined at a range of operating pressures for each sample using a soap bubble flow meter with graduations of 1, 10, 100 ml and 99.99% purity He. This generated a calibration curve for each sample of flow versus pressure. This calibration curve was used in the cooling measurements to determine the flow rate, given the operating pressure throughout the run.

The cooling effect was also measured using the same apparatus(Fig. 1). A Campbell Scientific CR10 datalogger was used to monitor the five K-type thermocouples and the pressure transducer. Thermocouple 1, inside the system, measured the temperature of the internal face of the window. Thermocouple 2, made of fast response 0.01 inch diameter wires, measured the temperature at the external face of the window. Thermocouple 3 measured the ambient temperature of the surroundings to get a base temperature. Thermocouple 4 measured the temperature of the heat source and thermocouple 5 measured the temperature of the sample mount for safety concerns.

The heat source was an Omegalux CIR series high watt density heating cartridge capable of heating to 500°C. The test runs for cooling were started at set elevated flow velocities with heat impinging upon the surface. The system was allowed to equilibrate to a steady state equilibrium under these conditions. At this point the flow was reduced to zero and held until a second steady state equilibrium was reached at which point the flow was increased back to the initial rate. The temperature changes of all the thermocouples and simultaneous pressure of the system were recorded.

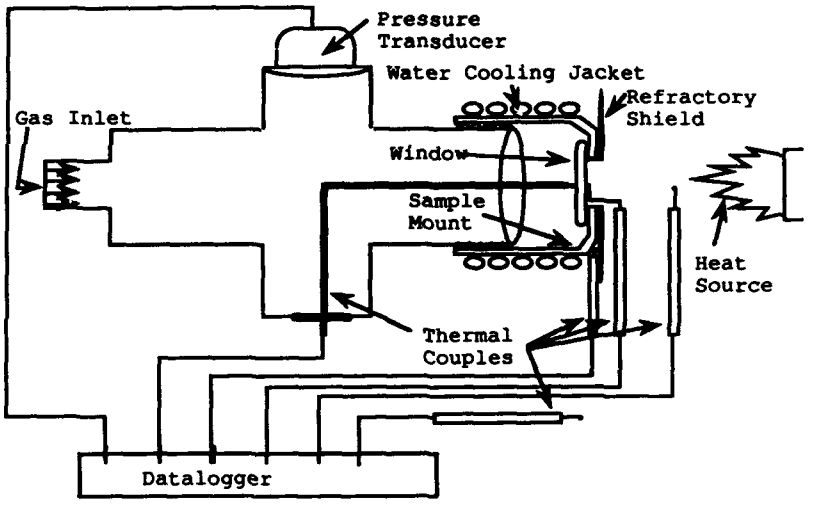


Figure 1. Test apparatus for transpiration and cooling tests.

The pore morphology, i.e., average pore radius, multipoint BET surface area, and volume fraction porosity were determined using isothermal nitrogen adsorption-desorption isotherms obtained on a Quantachrome Autosorb-6.

RESULTS

Fig. 2 shows transpiration flow velocities verses differential pressure through samples of 1.2, 5.0 and 8.0 nm average pore size.Each sample has been stabilized to 180 °C. The maximum flow rate observed during this study was 2.9 cm/sec at 3.2 MPa (~460 psi) for a 500°C stabilized 5.0 nm average pore radius sample.

Figs. 3 and 4 demonstrate a cooling effect due to the transpiration of helium through a sample, 180°C heat treated, with an average pore radius of 5.0nm. Fig. 3 shows that an initial increase in flow to a steady state of 0.38 cm/sec results in a drop in the temperature to 46°C at the heated face of the window at which point it stabilizes. When the flow rate is decreased from 0.38 to 0.0 cm/sec over a period of 2 minutes, the temperature increases by 25°C from 46°C to 71°C. Fig. 4 shows that a flow rate of 0.52 cm/sec maintains the temperature at the face of the window in an approximate steady state equilibrium value of 116°C. When the flow rate is reduced to 0.0 cm/sec in a period of 100 seconds, the temperature at the face of the window increases to 147°C and finally reaches a high of 160°C. This 44°C increase is shown to be completely reversible to the initial value of 116°C when the transpiration is resumed.

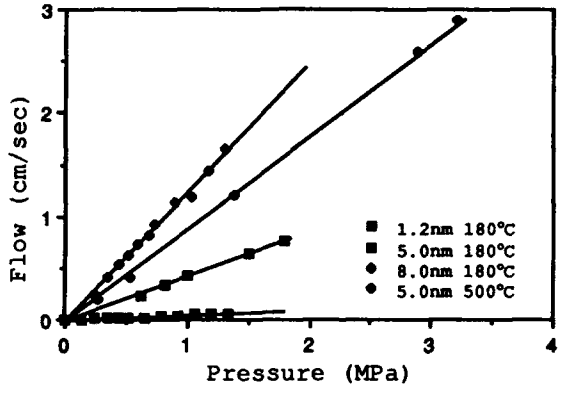


Figure 2. Transpiration flow verses pressure for three different average pore radius samples stabilized to 180°C.

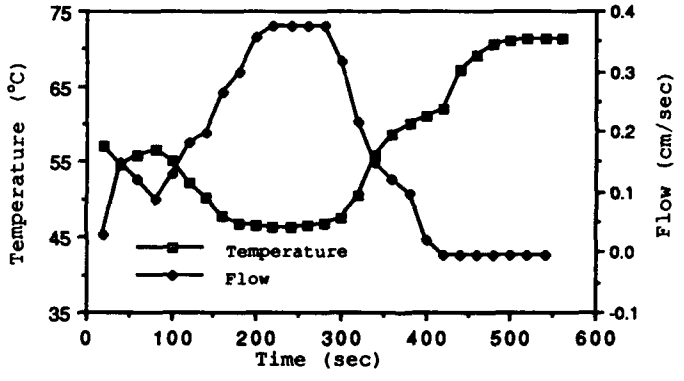


Figure 3. Change in temperature verses transpiration flow and time.

DISCUSSION

It is apparent from the observed transpiration flows that the permeability of the porous glasses to He flow is quite high. As permeability is a limited descriptive value, it is necessary to determine the type of mean value it represents. Porous media can be divided into two distinct categories, consolidated and unconsolidated[9]. Unconsolidated media is composed of discrete particles. Porosity in this media is dependant upon particle size and type of packing. A consolidated media is one which the solid structure forms a continual and generally permanent network. Processes of making consolidated media include sintering,

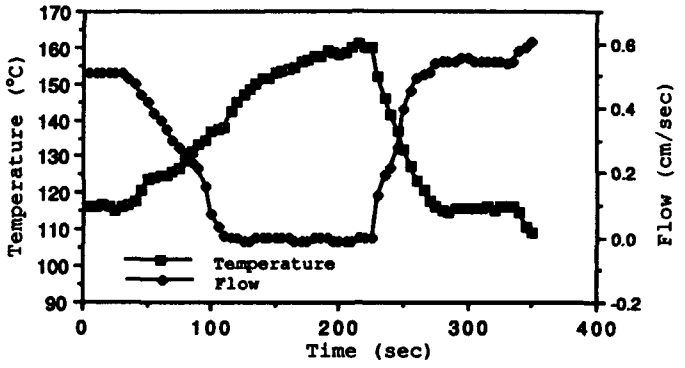


Figure 4. Change in temperature verses transpiration flow and time.

deposition from solution, polymeric growth and selective dissolution. Type VI silica is a consolidated porous media. It has been shown to possess virtually total interconnectivity[4].

The Reynolds numbers calculated for the He flow velocities encountered in this study are on the order of 1 X 10^{-7} at low pressures to 1 X 10^{-3} at higher pressures[10]. These values indicate that the flow is laminar in nature[11]. In addition, since the flow speed of the gas is low throughout the system compared to the speed of sound in the gas, the flow can be treated as incompressible flow [11]. If the length scale of the transpiration gas flow is large compared to the mean free molecular path, the gas can be treated as a continuum[11]. If the mean free path of the molecules is larger than the pore radius, then Knudsen flow becomes a factor[12]. The pore size distribution will become an important factor in any attempt at a complete analysis of flow. Thus it appears for the most part there is an incompressible laminar flow through a highly porous consolidated medium of a gas which can be treated as a continuum.

These conclusions are supported by examining the flow data. For this type of flow it is expected that the flow rate will increase proportional to the pressure gradient across the sample. Figure 2 shows that this is the case for the velocities reported here and in fact is true for all values measured to date. Scheidegger points out that for turbulent flow, the pressure relates to throughput by a quadratic function[12]. Our results appear to rule out turbulent flow in these samples.

CONCLUSIONS

We have presented evidence of transpiration through porous Type VI sol-gel silica optical windows at rates higher than those necessary for transpiration cooling in the proposed application environment. In addition, there is evidence of convection cooling

due to gas transpiration through the window. Therefore, the passage of gas through the window does have a cooling effect. However, the experimental set-up does not permit achieving the conditions necessary to prove that the flows and convective cooling observed are sufficient for transpiration cooling as generally defined. Additional studies are in progress to determine the effects on the thermal boundary under conditions closer to practical applications.

ACKNOWLEDGMENTS

The authors gratefully acknowledge the Air Force Office of Scientific Research for the financial support under contract #F49620-88-C-0073 and are grateful for the continued encourgement of D. R. Ulrich.

REFERENCES

1. L. L. Hench, A. G. Fosmoe II, presented at the 1989 MRS Fall meeting, Boston, MA, 1989.

2. L. L. Hench, S. H. Wang, and J. L. Nogues, in Multifunctional Materials, edited by Robert L. Gunshor, (SPIE: Bellingham, Washington, 1988) Vol. 878, p 76.

3. L. L. Hench and J. K. West, in Chem. Rev. 90, 33-70 (1990).

4. W. Vasconcelos, Ph.D. Thesis, University of Florida, 1989.

5. E. Elias, Masters Thesis, University of Florida, 1989.

6. D. Parsell (private communication).

7. U. Kurzweg (private communication).

8. J. D. Anderson, in Introduction To Flight, 3rd ed. (McGraw-Hill Book Company, New York, 1989) p. 125.

9. P. C. Carman in Flow of gases Through Porous Media, (Academic Press INC., London, 1956) p. 7.

10. A. G. Fosmoe and L. L. Hench (to be submitted J. Materials Science.)

11. D. J. Tritton in Physical Fluid Dynamics, 2nd ed. (Oxford University Press, New York, 1988) p. 67.

12. A. E. Scheidegger in The Physics of Flow Through Porous Media, 3rd ed. (University of Toronto Press, Toronto, 1974) pp. 38-39.

PLASMA SYNTHESIS OF FINE CERAMIC POWDERS BY A NOVEL COUNTER-FLOW LIQUID INJECTION METHOD.

P. Kong, T.W. Or, L. Stachowicz and E. Pfender. Center for Plasma-Aided Manufacturing, Dept. of Mech. Eng., University of Minnesota, Minneapolis, MN 55455, USA.

ABSTRACT

Ceramic powders of carbides, oxides, solid solutions of oxides, magnetic and non-magnetic spinels, superconductors and composites have been successfully synthesized in a thermal plasma jet reactor using a novel counter-flow liquid injection plasma synthesis (CF LIPS) method developed to overcome the problems associated with solid injection and to realize the benefits of gas phase reactions and counter-flow injection. Standard material characterization techniques have been used for powder analysis.

INTRODUCTION

Liquid Injection Plasma Synthesis (LIPS) has been developed for achieving the benefits of gas phase reactions and avoiding the problems associated with powder injection. Although gaseous precursors are preferable they are severely limited for metals. LIPS offers a number of significant advantages over solid injection plasma synthesis: (1) The availability of liquid precursors for ceramics is extensive; (2) The reaction is essentially gas phase, fast and complete; (3) The time required for complete evaporation of liquid droplets is substantially shorter than for solids; (4) Complete control of the molar concetrations of liquid reactants results in products with precise chemical compositions.

There are two types of LIPS, the parallel-flow [1,2] and counter-flow injection [3,4,5,6]. A new approach, the counter-flow LIPS, provides additional advantages over the parallel-flow LIPS method: (1) The heat transfer between the plasma and the liquid droplets is substantially higher due to the higher relative velocities between droplets and the plasma; (2) The residence time for the liquid droplets in plasma is much longer (>100ms). This ensures complete evaporation of the liquid precursors, i.e. a gas phase reaction; (3) Large recirculation zones are observed in the reactor which is important for particle size control; (4) Long high temperature ridges (>>2500K) exist in the reactor.

EXPERIMENTAL PROCEDURE

The experimental setup for the counter-flow LIPS reactor is shown schematically in Fig.1. The reactor consists of a high power, swirl stabilized DC plasma torch operated with Ar at atmospheric pressure. The typical power input for pure Ar plasma ranges from 9 to 30

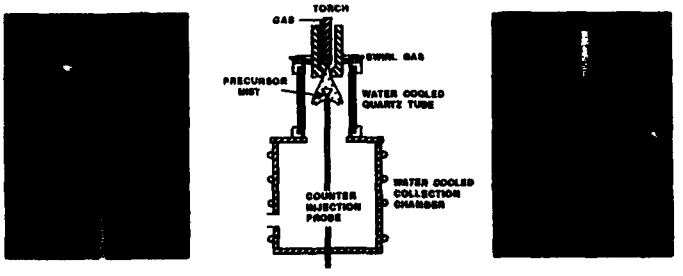


Fig. 1 DC counter-flow LIPS reactor and its operation.

Mat. Res. Soc. Symp. Proc. Vol. 190. ©1990 Materials Research Society

kW and increases to higher values if diatomic gases are added to the main flow. Precursors together with atomizing gases are injected against the plasma flow for vaporization. A well defined stagnation region is formed at the confluence of the two flows as shown in Fig. 1. At the outflow of the confluence fine particles nucleate from the supersaturated vapor. Precursor preparation makes use of soluble metal nitrates for oxides and liquid phase metal-organics such as alkoxides for carbides. The atomizing gas is either O_2 or compressed air for oxides and Ar for carbides. The excess amount of carbon is controlled by using Ar/CO_2 as atomizing gases.

RESULTS AND DISCUSSION

Table I is a summary of the powders made by the present method. Material characterizations include X-ray diffraction, electron microscopy, EDX, thermogravimetric analysis for carbides, particle size analysis by centrifugal sedimentation and BET, T_c measurements for superconductors and vibrating sample magnetometer (VSM) for magnetics. Some of the results are shown in Figs. 2 to 4.

Table 1. SUMMARY OF DC COUNTER-FLOW LIPS.

CARBIDES	B_4C ,SiC and ZrC
OXIDES	Al_2O_3, MgO, NiO, CoO, ZrO_2, Y_2O_3, and CeO_2
SOLID SOLUTIONS	Y_2O_3 & CeO_2:Y_2O_3 stabilized ZrO_2
	Co, Mg, Ni, and Zn aluminates
SPINELS	Co, Mg, Ni, Cu, and Zn ferrites
	Co, Mg, Ni, and Cu chromites
SUPERCONDUCTORS	$YBa_2Cu_3O_{7-x}$, Bi-Sr-Ca-Cu-O_X (2212 and 2223 phases)
COMPOSITES	$[ZrC]_x$:$[ZrO_2]_y$

The X-ray line profiles (Fig. 2) indicate that the particle size is comparable for different product group of powders. The particle morphology as well as particle size analysis

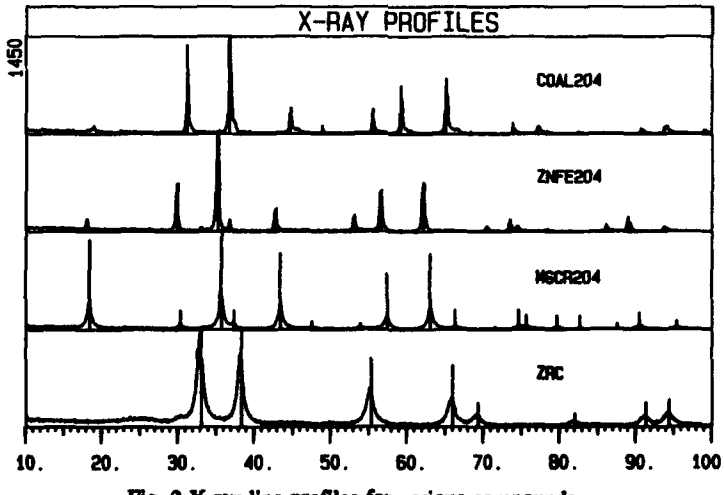


Fig. 2 X-ray line profiles for various compounds.

confirm the above. SEM analysis (Fig. 3) reveals that the majority of the particles are spherical and have a narrow size distribution ranging from 0.5 to 1.5 μm. The roundness and smoothness of the surfaces for some of these particles suggest a liquid phase growth process. Besides spherically smooth particles, some condensed particles have also been observed indicating that the newly formed particles act as nucleation centers for the incoming vapor.

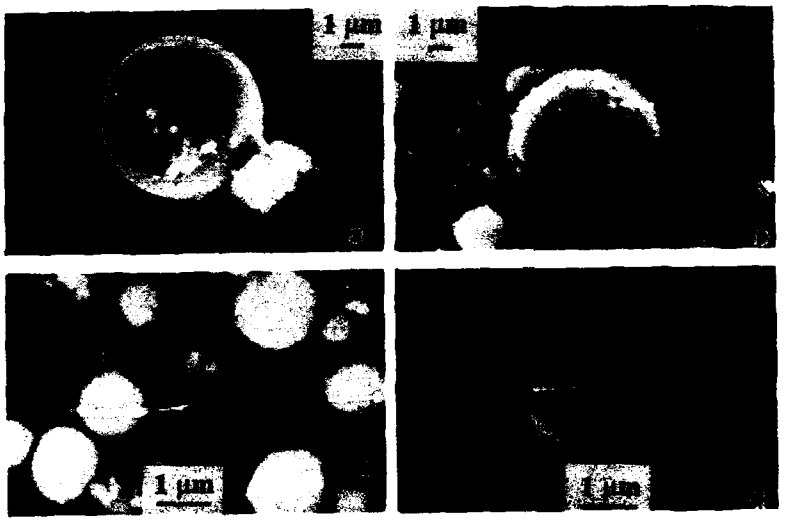


FIg. 3 SEM micrographs for (a) ZrC, (b) 9 Y_2O_3:ZrO_2, (c) $CoAl_2O_4$ and (d) $NiAl_2O_4$.

T_c measurements (Fig. 4) for Bi-Sr-Ca-Cu-O_x superconductors indicate multiple phase formation. Both types of the superconductors has substantial lower room temperature electrical resistivity than the reference standard materials and both reach zero resistance at a slightly higher temperature than the standards. The research on this group of materials is still in progress.

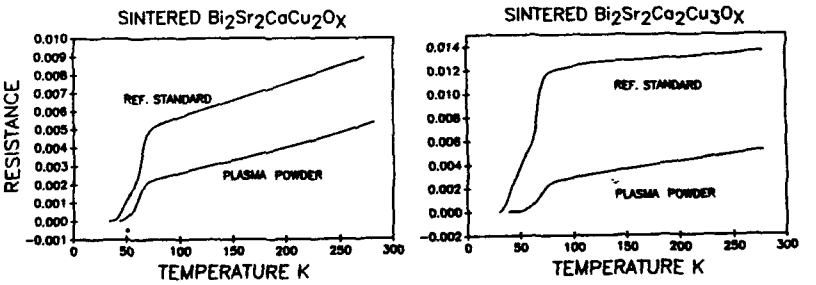


Fig. 4 T_c measurements for the Bi-Sr-Ca-Cu-O_x superconductors.

The magnetic properties measurements performed show that some spinels behave like paramagnetic materials, others as a soft or hard ferromagnetics. The saturation magnetization

as a function of the applied magnetic field is shown in Fig. 5.

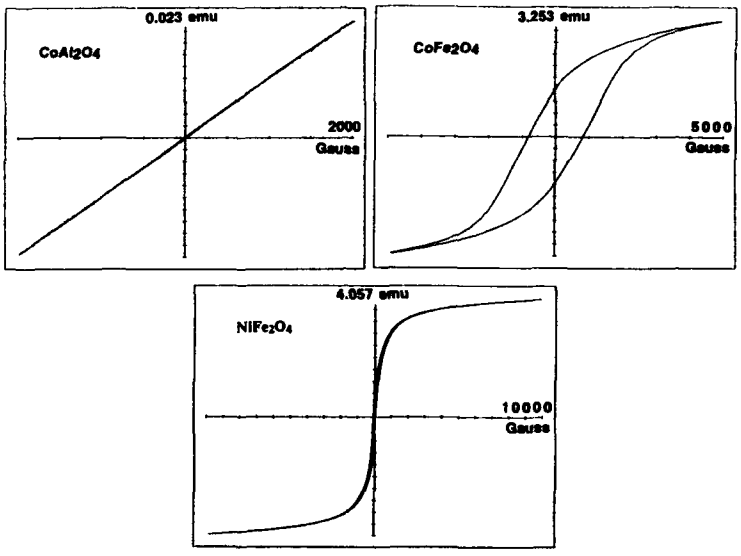


Fig. 5 Magnetic measurements for the spinels.

SUMMARY

Counter-flow LIPS is a new promising process for powder synthesis. This process holds substantial advantages over both the parallel flow LIPS and the solid injection plasma synthesis. Synthesis of carbides, oxides, magnetic and non-magnetic spinels, superconductors, solid solutions and composites has been demonstrated. The powders synthesized by this method will be used in future plasma sintering studies.

ACKNOWLEDGEMENTS

This work has been supported by DOE/FG02-85ER-13433.

REFERENCES

1. Y. Lau, P. C. Kong and E. Pfender, *Proc., ISPC8, Vol. 1, p. 101 (1987), Tokyo, Japan.*
2. Y. Lau, P. C. Kong and E. Pfender, *Ceramic Transactions, Vol. 1, Part A, p. 298 (1988).*
3. P. C. Kong and E. Pfender, *Proc. of the 2nd Int. Conf. on Cerm. Powder Processing Sci., Oct. 12-14, 1988, Berchtesgaden, FRG (in press).*
4. P. C. Kong and E. Pfender, *Proc. of Int. Sym. on Combustion and Plasma Synthesis of High Temp. Materials, San Francisco, Oct. 26-28, 1988 (in press).*
5. P. C. Kong, *Invited Lecture, 9th Int. Sym. on Plasma Chemistry, Pugnochiuso, ITALY, p. XI, Sept 1989, and J. of Pure & Applied Chem. 1990 (in press).*
6. S. H. Paik, Xi Chen, P. Kong and E. Pfender, Submitted to *J. Plasma Chem. and Plasma Processing, (1990).*

MORPHOLOGY CONTROL IN PRECURSOR CERAMIC POWDER PRODUCTION BY THE ELECTRICAL DISPERSION REACTOR

Michael T. Harris, Timothy C. Scott, Osman A. Basaran
and Charles H. Byers
Chemical Technology Division, Oak Ridge National Laboratory, Oak Ridge, Tennessee

ABSTRACT

The Electrical Dispersion Reactor (EDR) allows the continuous production of composite oxide ceramic precursor materials. Silica particles in the form of highly porous shells are produced by the hydrolysis of tetraethylorthosilicate as the continuous phase and water-ammonia as the disperse phase, reflecting the diffusion of the silicon moiety into the dispersed phase. Alternately, denser silica particles result when aqueous solutions of sodium metasilicate are dispersed in a continuous phase containing acetic acid in 2-ethyl-1-hexanol. Additionally, spherical particles in the size range 0.1 to 2 microns are produced from the dispersion of aqueous solutions containing cupric chloride or a mixture of cupric chloride, yttrium nitrate, and barium nitrate (3:1:2 molar ratio) into a continuous organic phase containing ammonia.

INTRODUCTION

The dispersion of liquid drops by an intense electric field has been investigated for many years (1,2). In recent years, this technique has been used to develop electrically driven solvent extraction devices which produce controlled emulsions consisting of micron-size drops in a continuum (3). Likewise, the electrostatic atomization of liquid droplets into air to form micron-size ceramic powders has also been investigated (4). It is the purpose of this study to investigate the formation ceramic precursor particles in a liquid-liquid system where the drops are highly conducting aqueous solutions and the continuous phase is a non-conducting organic solvent (e.g. 2-ethyl-1-hexanol). The device in which this occurs is called the Electrical Dispersion Reactor (EDR). This device was investigated for synthesizing micron size porous shells and dense spherical particles of single component and mixed hydrous oxide particles in organic solvents. Particles synthesized in organic solvents tend to form soft agglomerates which are easily redispersed by ultrasonication.

EXPERIMENTAL

Figure 1 shows a schematic of the EDR. The basic concept of the EDR involves the creation of a microreactor in the form of micron-size droplet within a liquid continuous phase. A drop containing an aqueous solution is introduced between electrodes on which is imposed an intense, pulsing, dc electric field (6 to 10 kV/cm and pulsing frequencies between 1 to 3 kHz). Under properly selected conditions the drops are shattered, creating an emulsion consisting of micron-size droplets in a close size range. This is used as the

Mat. Res. Soc. Symp. Proc. Vol. 180. ©1990 Materials Research Society

basis for a reactor, with some of the reactants present in the continuous phase and some in the drops.

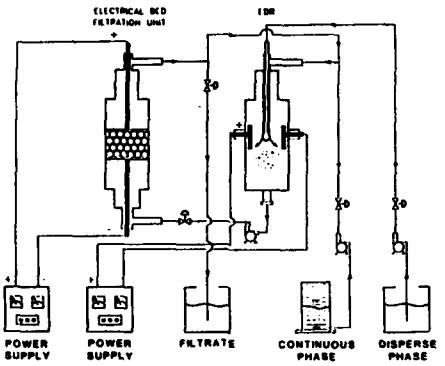


Figure 1. Configuration of the Electrical Dispersion Reactor, which incorporates an electrostatic filter on the continuous phase recycle stream.

Two modes of operation have been tested. In the first mode, the continuous phase was an alkoxide (tetraethylorthosilicate, TEOS) and the drops contained 0.7 M NH_4OH . The second mode involved placing the precipitation agent (*acetic acid for sodium metasilicate*, or ammonia or oxalic acid for metal salts) in the continuous organic phase (2-ethyl-1-hexanol) and the metal, in the form of a metal salt (*sodium metasilicate*, cupric chloride, yttrium nitrate, barium nitrate, or aluminum nitrate) in the aqueous drop.

After the particles had formed, the particles were removed by centrifugation and washed several times with ethanol. The particles were then dried for 24 hours. The particles were imaged before and after the washing and drying steps by either scanning or transmission electron microscopy.

RESULTS AND DISCUSSION

Figure 2 shows the particles produced from the dispersion of aqueous drops consisting of 0.7 M NH_4OH into the TEOS continuous phase. These particles are the result of the collapse of porous spherical shells. Initially, TEOS reacts with the surface of aqueous-ammonia drops to form silica. Since TEOS is immiscible with water, the diffusion of the TEOS into the interior of the particle is inhibited and a silica shell is formed. When the particles are dried without washing or are washed with ethanol, the water is removed from the interior of the drop and it collapses. These particles are similar to powder aerogels with respect to their high porosity. Particle diameters were a few tenths of a micron.

Denser particles are formed when the metal is put into the aqueous phase, as is shown in Figures 3 and 4. Silica particles are formed from the reaction of aqueous sodium metasilicate in *drops* with acetic acid in a 2-ethyl-1-hexanol *continuous phase* (Figure 3). In Figure 4, cupric chloride, yttrium nitrate, and barium nitrate salts contained in aqueous drops react with hydroxide ions, which are formed when ammonia diffuses from

the continuous phase (2-ethyl-1-hexanol:ethanol) into the droplets. Since all reactants are very soluble in the aqueous phase, diffusion is fast and precipitation occurs throughout the microdroplets. In most cases, the precipitated hydrous metal oxides remain in the aqueous phase since they are insoluble in the continuous organic phase. This is very attractive for the synthesis of mixed metal oxide particles because there is homogeneity on the micron to submicron level.

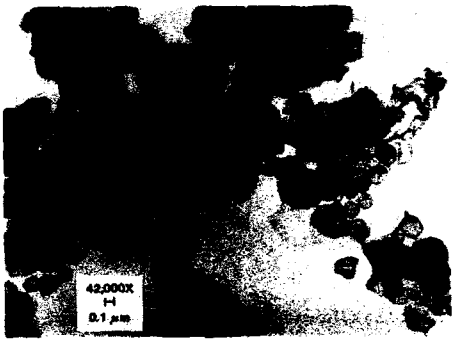


Figure 2. Silica particle produced in the EDR [0.7 M NH_4OH (dispersed phase) and TEOS (continuous phase)].

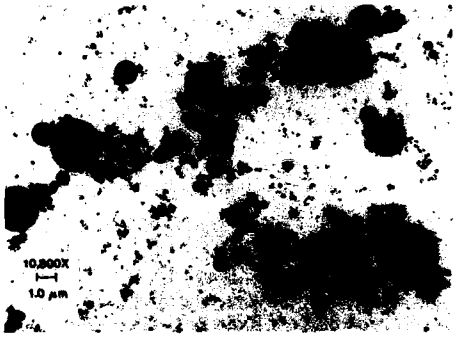


Figure 3. Silica particle produced in the EDR [sodium metasilicate in water (dispersed phase) and acetic acid in 2-ethyl-1-hexanol (continuous phase)].

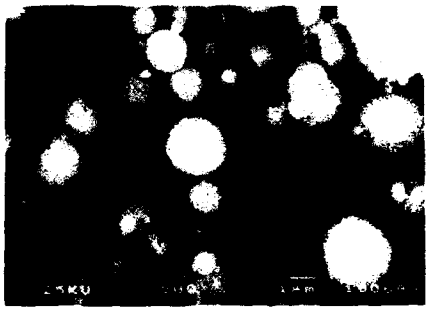


Figure 4. Particles produced in the EDR containing hydrous oxides of Y-Ba-Cu (approx. 1:2:3 molar ratios).

CONCLUSIONS

These tests have shown that the synthesis of submicron- to micron-size hydrous metal oxide ceramic precursor particles can be formed by imposing intense, pulsing, dc electric fields on a conducting liquid drop suspended in a nonconducting liquid. The characteristics of the particles can be changed by strategically locating the reactants in the proper phase. Future experimental work will involve larger-scale synthesis of powders in the EDR and comparing the sinterability, composition, and the ability of these powders to produce improved ceramics to precursors produced by other methods. Moreover, theoretical work is underway to shed light on the mechanisms of drop/particle formation from orifices in electric fields by finite/boundary element analysis (cf. [5]).

ACKNOWLEDGMENTS

The authors would like to thank Ronald R. Brunson for his assistance. This research was sponsored by the Office of Basic Energy Sciences, U. S. Department of Energy under contract DE-AC05-84OR21400 with Martin Marietta Energy Systems, Inc.

REFERENCES

[1] R. L. Neubauer and B. Vonnegut, J. Colloid Interface Sci. 8, 851 (1953).
[2] V. G. Drozin, J. Colloid Interface Sci. 10, 158 (1955).
[3] T. C. Scott, Separation and Purification Methods 18, 65-109 (1989).
[4] E. B. Slamovich and F. F. Lange, Mater. Res. Soc. Proc. 121, 257 (1988).
[5] O. A. Basaran and L. E. Scriven, Phys. Fluids A 1, 799 (1989).

DC Plasma Synthesis of Aluminum Nitride Ceramic Powders

Z. P. Lu and E. Pfender

Department of Mechanical Engineering
University of Minnesota
Minneapolis, Minnesota 55455, U. S. A.

A novel Triple DC Torch Plasma Reactor (TTPR) has been developed for the plasma synthesis of fine ceramic powders. The reactor consists of three identical plasma torches. The plasma jets from these torches form a converging plasma volume into which the starting powder is fed. Thermodynamic equilibrium calculations have been performed for predicting the behavior of an aluminum-nitrogen system. Aluminum nitride has been synthesized by using the TTPR operating in the non-transferred mode. Product characterizations indicate that single hexagonal phase AlN ceramic powder has been obtained.

INTRODUCTION

AlN ceramics have a relatively high thermal, but very low electrical conductivity [1], and they have approximately the same thermal expansion coefficient as silicon [2]. Because of these properties this material is attracting increasing attention in the electronic packaging industry [3]. This man-made ceramic material has been synthesized by carbothermal reduction of alumina. Thermal plasma synthesis of AlN has been studied over the past decades because the unique features of thermal plasmas, such as high energy content and controlled atmosphere, are useful for producing a high purity product. A brief review of the history of thermal plasma synthesis of AlN has been given in a previous paper [4].

In the present work, AlN has been synthesized in a novel Triple Torch Plasma Reactor. The characterizations of the product agree with the predictions from the equilibrium thermodynamic considerations. Single hexagonal phase AlN is confirmed by X-ray powder diffraction and TEM micrographs. Both TEM and centrifugal sedimentation reveal that the powder produced has a submicron median size (number-wise).

EQUILIBRIUM MODELING OF THE SYNTHESIS

A computer program, SOLGASMIX-PV [5], was used for calculating the chemical equilibria of a nitrogen-aluminum system with various aluminum to nitrogen ratios. The results show that for the system with an aluminum to nitrogen mole ratio smaller than 0.5, the reaction $2\ Al + N_2 \rightarrow 2\ AlN$ is complete. One of the computational results is shown in Fig. 1. The results also show that AlN is the only solid phase product below 2700 K, i.e. complete conversion is possible. Because there is no liquid phase of AlN, gas phase AlN begins to sublimate at a temperature of 2700 K and a proper quenching temperature around 2500 K is suggested.

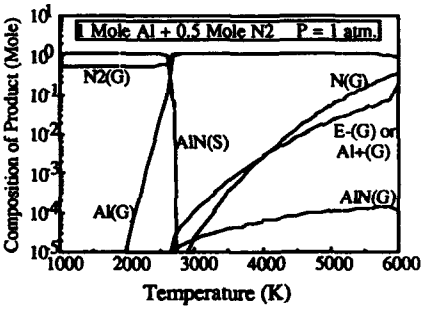


Fig. 1: Equilibrium Composition of an Al-N System

EXPERIMENTAL SETUP AND RESULTS

Due to the short residence time in the plasma region, full evaporation of the solid particles, which is essential for vapor phase reactions requires small particle sizes (micron size). However, feeding of such small powder of raw material represents a severe problem due to the high viscosity of thermal plasmas. To improve penetration of particulates into a thermal plasma, the TTPR [4] has been developed for the synthesis of fine ceramic powders.

The heart of the system consists of three identical DC plasma torches each of which can operate at a power level of 3 - 30 kW. These three torches are connected to a linkage which provides tilting as well as longitudinal motion. The linkage system is mounted on a water cooled flange which sits on top of a vacuum chamber (Fig. 2). The torches penetrate into the chamber through three flexible welded metal bellows, which offer the necessary flexibility for changing the orientation of the torches, ensuring at the same time vacuum tightness of the chamber. The operating conditions were as follows: for each torch, current I = 300 A, voltage V = 60 V, argon flow rate = 6 liters/min, nitrogen flow rate = 7 liters/min. The carrier gas and sheath gas for the powder feeding were nitrogen with flow rates of 3.5 and 5 liters/min, respectively. The reactor vessel was evacuated to 10^{-2} torr and back filled with argon before starting the plasma torches. The reaction was performed at atmospheric pressure. The powder feed rate was far below the stoichiometric value to ensure a nitrogen-rich environment for the completion of the reaction.

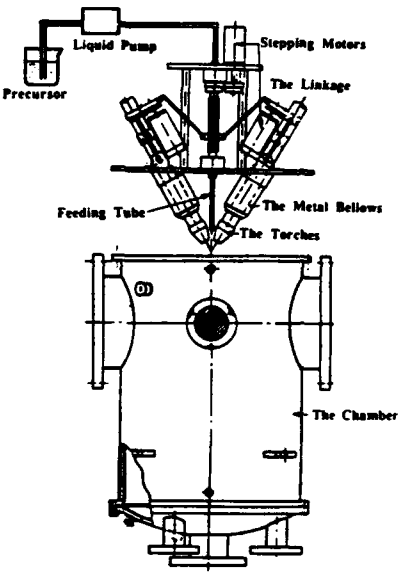


Fig 2: The Linkage and the Reactor Vessel

AlN ceramic powder has been produced using the TTPR system operating in the non-transferred mode. The plasma jets were coalescing forming a temperature valley in the center (Fig. 3). The aluminum powder was fed through a water cooled feeding tube into this region. The powder used is ALCOA aluminum powder with a median size of 1 to 2 μm. Nitrogen was used as the carrier and sheath gas for introducing the powder into the plasma.

The product was collected from a quartz tube downstream of the plasma jets. The powder was white and very fluffy. X-ray diffraction was used to identify the phases in the final product. The result is shown in Fig. 4 and this result was compared with standard X-ray diffraction data. Figure 4-a corresponds to the sample collected from the quartz tube which is located 15 cm downstream from the converging point of the plasma jets. Except for the hexagonal phase with peaks at 33.2°, 36.0°, 37.9°, etc, the X-ray results also show the existence of the cubic AlN which has peaks at 45.8° and 66.9°. The characteristic aluminum peak (at 38.5°) is very low compared to the AlN peaks indicating that only very little aluminum remains unreacted in the final product. Figure 4-b corresponds to the sample collected from the quartz tube which is located 5 cm downstream from the converging point of the plasma jets. It can be seen that the ultrafine particles are greatly reduced as indicated by the low base line intensity of the diffraction pattern. The cubic phase of AlN is basically eliminated due to the lower quenching rate caused by the relocation of the quartz tube. The close distance between the quartz tube and the plasma region keeps the quartz tube red hot.

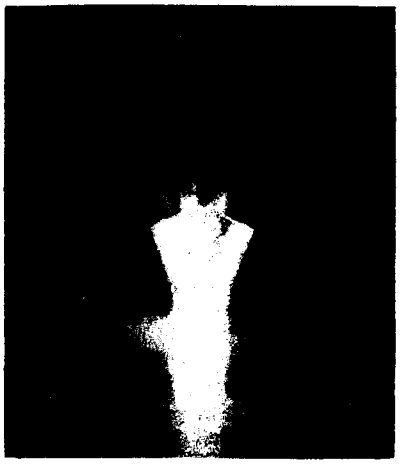


Fig. 3: Three Coalescing Plasma Jets

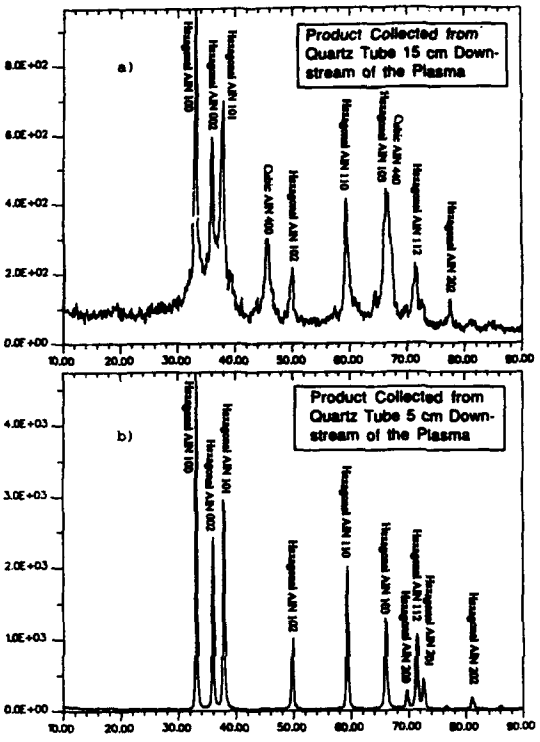
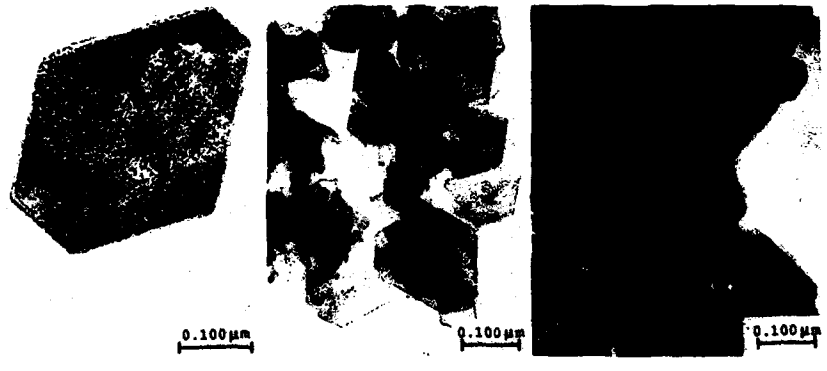


Fig. 4: X-Ray Diffraction Profiles of Products

The unreacted aluminum content is also eliminated in this case.

Figure 5 shows the TEM micrographs of the product. Figure 5-a shows a single hexagonal shaped particle. The size of this particle is about 370 nm. Figure 5-b shows an assembly of such hexagonal platelets while Fig. 5-c reveals some of the sintered hexagonal platelets. This is probably due to continuous exposure of particles deposited on the quartz tube to high temperature for a relatively long period of time. Figure 6 shows the powder size distribution obtained by centrifugal sedimentation. It shows both distributions by size as well as by mass. The number-wise median is *about 0.3 μm while the* mass-wise median is about 2μm. This result matches the visual observation from TEM.



(a) (b) (c)

(a) A Single Particle;
(b) An Assembly of Particles;
(c) Partially Sintered Particles;

Fig. 5: TEM Micrographs of AlN Powder

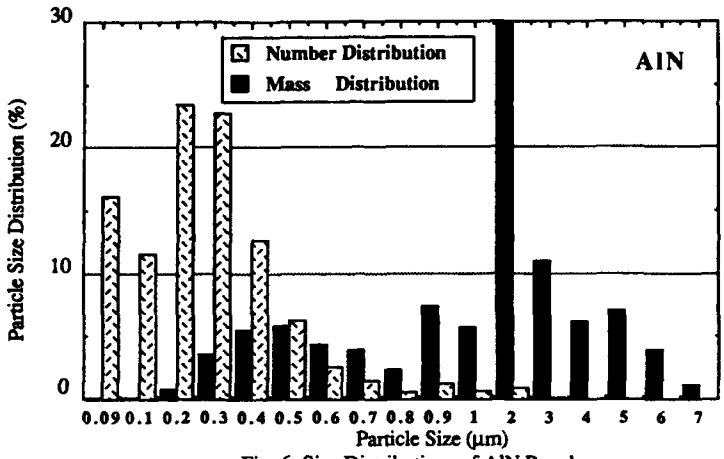


Fig. 6: Size Distributions of AlN Powder

CONCLUSIONS

Plasma synthesis of AlN with the TTPR has been demonstrated. Both X-ray diffraction and TEM show that the hexagonal phase AlN was obtained. A nitrogen-rich atmosphere is crucial for the completion of the reaction. The positioning of the collection surface has a large effect on the phase composition of the final product. Hotter surfaces reduce the formation of the cubic phase of AlN due to the reduced quenching rate. The TEM and centrifugal sedimentation reveal that the powder produced has a submicron median size (number-wise).

ACKNOWLEDGMENT

This work has been supported by DOE under grant DOE / FG 02-85 ER-13433 and by Aluval (Pechiney), France. The computer time has been granted by the ACS of the University of Minnesota.

REFERENCES

[1] G. A. Slack, "Nonmetallic Crystals with High Thermal Conductivity", *J. Phys. Chem. Solids* **34**, 321 (1973).

[2] W. Werdecker and F. Aldinger, "Aluminum Nitride--An Alternative Ceramic Substrate for High Power Applications in Microcircuits", *IEEE Trans.* **CHMT-7**, 399 (1984).

[3] D. Fister and H. C. Starck, "AlN and BN Powders for Advanced Applications", *Ceram. Eng. Sci. Process.* **6**, 1305 (1985).

[4] Z. P. Lu and E. Pfender, "Synthesis of AlN Powder in a Triple Torch Plasma System", in *9th Int. Symp. on Plasma Chem.*, Edited by R. d'Agostino, Pugnochiuso, Italy, Sept.4-8, 675 (1989).

[5] T. M. Besmann, "SOLGASMIX-PV, a Computer Program to Calculate Equilibrium Relationships in Complex Chemical Systems", Oak Ridge National Laboratory, Oak Ridge, **Report ORNL/TM-5775** April (1977).

EFFECT OF NITROUS OXIDE GAS ON CVD DIAMOND FILM DEPOSITION

H. KOINUMA, M. YOSHIMOTO, Y. TAKAGI, A. B. SAWAOKA, T. HASHIMOTO*, T. NAGAI**, and T. SHIRAISHI**
Research Laboratory of Engineering Materials, Tokyo Institute of Technology, 4259 Nagatsuta, Midori-ku, Yokohama, 227 Japan
* Department of Industrial Chemistry, Faculty of Engineering, Tokyo University, 7-3-1 Hongo, Bunkyo-ku, Tokyo, 113 Japan
** Department of Communications, Faculty of Engineering, Tokai University, 1117 Kitakaname, Hiratsuka, Kanagawa, 259-12 Japan

ABSTRACT

The addition of nitrous oxide (N_2O) gas in the hot-filament chemical vapor deposition of carbon film from mixtures of methane and hydrogen was found to increase remarkably the content of diamond structure in the film. Increased particle size and crystal orientation parallel to the (111) direction were also obtained by the N_2O addition. Mass spectrometry revealed that the vapor phase reaction was scarcely affected by the N_2O addition.

INTRODUCTION

Diamond film preparation from the gas phase has been achieved by various chemical vapor depositions using rf plasma[1], microwave plasma[2], dc arc[3] and hot filament[4]. Among them, hot-filament CVD is a simple and low cost process and can be a practically useful method if the formation of a diamond phase could be accelerated and purified by a catalytic effect of additives. Kawato and Kondo reported that the addition of oxygen to a mixture of methane and hydrogen was effective for increasing the diamond phase fraction in the film, although significant amount of amorphous phase still remained[5]. In this study, the effect of nitrous oxide gas (N_2O) addition was examined in the hot-filament CVD of carbon films from mixtures of methane and hydrogen. The oxygen radical which could be easily generated by the decomposition of N_2O was presumed to be more effective than molecular oxygen for the production of diamond phase. N_2O has the N-O bond dissociation energy (197.6kJ/mol) lower than the O-O bond dissociation energy (490.4kJ/mol) of molecular oxygen. An attempt was made to investigate the gas phase reaction by mass spectroscopy.

EXPERIMENTAL

Figure 1 shows the schematic diagram of hot-filament CVD

Mat. Res. Soc. Symp. Proc. Vol. 180. ©1990 Materials Research Society

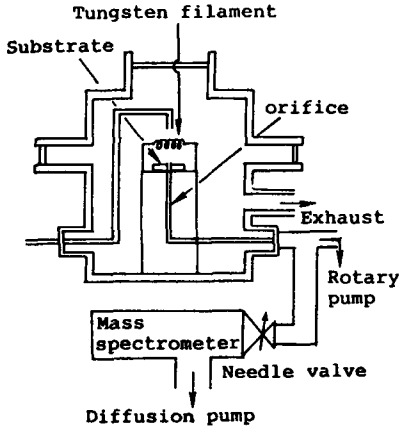


Figure 1 Schematic diagram of hot-filament CVD apparatus.

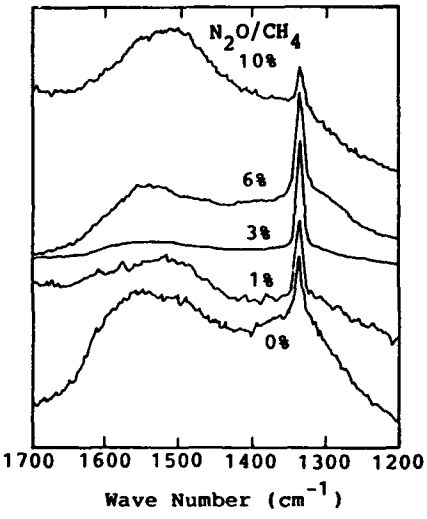


Figure 2 Raman spectra of the films prepared at various N_2O/CH_4 ratios.

apparatus used in this study. Typically, a mixture of 1.5sccm of methane and 50sccm of hydrogen was introduced to the chamber. The molar ration of N_2O to CH_4 was varied from 0 to 10%. The temperature of tungsten filament was kept at 2300°C, as measured by a two-color band-type pyrometer (Chino Works, Ltd., IR-AQ model). The substrate, Si(111), was placed 2mm below the filament and heated at 750°C. The reaction was carried out at 100 Torr for 4 hours. The gas phase species between the substrate and filament can be introduced into a quadrupole mass spectrometer (SKK Vacuum Engineering Co., Ltd., model SELECTOR 100) through a 0.1mm diameter orifice. The amounts of diamond and amorphous carbon in the films prepared were evaluated by Raman spectroscopy, using a JASCO-NR1 100 model. The crystal structure, morphology, and composition of the films were analyzed by x-ray diffraction (XRD: MAC Science MXP^3), scanning electron micrography (SEM: JEOL JSM-100), and x-ray photoelectron spectroscopy (XPS: JEOL JPS-80), respectively.

RESULTS

Figure 2 shows the Raman spectra of films prepared at various N_2O/CH_4 ratios. The peak at 1333cm^{-1} is assigned to diamond and the broad peak around 1500cm^{-1} to amorphous carbon. At the 3% addition of N_2O, the maximum intensity of the diamond peak and the minimum intensity of the amorphous peak were observed. Figure 3 shows SEM images of the films prepared in the absence

(a), and in the presence of 3% N_2O (b) and 6% N_2O(c). Ball-like grains with diameters near 40μm were observed in the film prepared without N_2O addition, whereas diamond-like crystals with an 80μm diameter were clearly observed when 3% N_2O was added. a further increase of N_2O concentration to 6% decreased the diameter of the particle to about 50μm. When the CH_4/H_2 ratio was increased to 6%, graphite was preferentially obtained even in the presence of N_2O. XRD analysis verified that the intensity of the diamond (111) peak was remarkably increased by the 3% N_2O addition. The contamination of nitrogen in the films was not observed by XPS measurement.

DISCUSSION

In order to evaluate the relative concentration of diamond to amorphous carbon semi-quantitatively, the area ratio of Raman peak of diamond to that of amorphous carbon was measured. Figure 4(a) shows the dependence of both the peak area ratio and

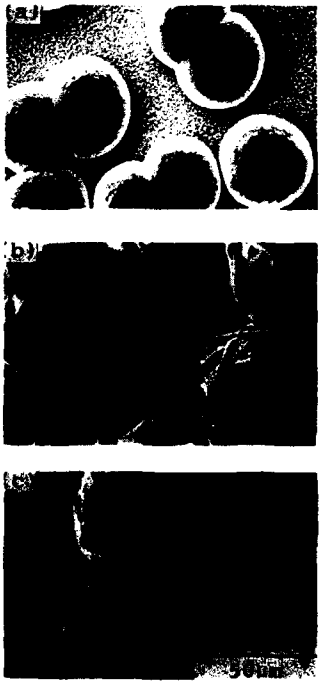


Figure 3 SEM images of the films prepared with N_2O/CH_4 ratios of (a) 0%, (b) 3%, and (c) 6%.

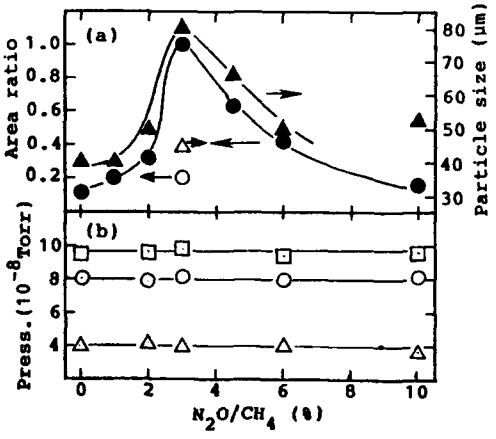


Figure 4 (a) Dependence of the area ratio of the Raman peak for diamond to that for amorphous carbon (●) and the particle size (▲) on N_2O/CH_4 ratio. The results of O_2 addition are also shown by open circle (area ratio) and open triangle (particle size).
(b) Dependence of partial pressure of species detected by quadrupole mass spectroscopy on N_2O/CH_4 ratio. Mass numbers are 2(○), 15(△), and 16(□).

the particle size, estimated from SEM image, on the N_2O/CH_4 ratio in feed. Increasing the N_2O/CH_4 ratio up to 3% increased both the diamond concentration and the particle size of the deposition. However, further addition of N_2O decreased the diamond concentration and particle size. As is also shown in Fig.4(a), 3% O_2 addition was less effective for increasing diamond content than N_2O addition. To explain this, a modification of gas phase reaction or an activation of surface reaction such as etching of amorphous carbon can be considered. Quadrupole mass spectrometry was conducted to check the former possibility. Figure 4(b) shows the partial pressures of mass number 2(H_2), 15(CH_3: cracking pattern of CH_4), and 16(CH_4). The amounts of these species were almost unchanged in the reaction systems of various N_2O/CH_4 ratios, indicating no visible change in the vapor phase. It is more probable that N_2O and/or its decomposed species activate a surface reaction reducing the amorphous carbon content.

Thus, N_2O additions were found effective for increasing diamond phase in the films prepared from a mixture of CH_4 and H_2 by hot-filament CVD method.

ACKNOWLEDGMENT

The authors are grateful to Dr. S. Okazaki (Tokyo Institute of Technology) for Raman spectroscopy measurement. This study was supported in part from Fundamental Research on Physics, Chemistry, and Life Science Under Microgravity Condition.

References

1. S. Matsumoto, M. Hino, and T. Kobayashi, Appl. Phys. Lett. 51, 737 (1987).
2. Y. Mitsuda, T. Yoshida, and K. Akashi, Rev. Sci. Instr. 60, 249 (1989).
3. Y. Akatsuka and Y. Hirose, Jpn. J. Appl. Phys. 27, L1600 (1988).
4. Y. Hirose and Y. Terasawa, Jpn. J. Appl. Phys. 25, L519 (1986).
5. T. Kawato and K. Kondo, Jpn. J. Appl. Phys. 26, 1429 (1987).

SUPERCONDUCTING FIBERS FROM ANHYDROUS METAL CARBOXYLATES

RICHARD M. LAINE,* KAY A. YOUNGDAHL, RICHARD A. KENNISH, MARTIN L. HOPPE, ZHI-FAN ZHANG and D. JEAN RAY, Contribution from the Polymeric Materials Laboratory of the Washington Technology Center and the Dept of Materials Science and Engineering, University of Washington, Seattle, WA 98195

ABSTRACT:

A variety of anhydrous Y, Ba and Cu carboxylates were synthesized and screened for utility as spinnable precursors to 123 superconducting fibers. Simple extrusion studies demonstrate that THF solutions of mixtures of Y, Ba and Cu isobutyrates with some Ba 2-ethyl- hexanoate can be used to form 70 μm dia. precursor fibers. Following a curing at 150°C for 24-48 h, pyrolysis of these fibers in air to 900°C, with controlled heating rates, gives dense, flexible ceramic fibers 15-20 μm in dia. These fibers have the appropriate orthorhombic phase. Flux exclusion measurements indicate the fibers are superconducting; but ΔT_c is not optimal.

INTRODUCTION

The rush to develop practical applications for the new, high T_c superconducting ceramic oxides has led to tremendous advances in thin film processing with respect to reproducibility, phase purity and high J_c.[1,2] By comparison, bulk materials lag far behind. There are many reasons for this, but the need to develop high J_c bulk materials is the primary obstacle.[3]

In principle, the development of superconducting fibers or wires should offer a transition between thin films and bulk because the dimensions required to obtain flexibility and mechanical strength in ceramic fibers are within an order of magnitude of the dimensions of the thin films. Unfortunately, there are no generally accepted or straightforward methods for the fabrication of thin, oxide ceramic fibers of any type. Consequently, progress in this realm is relatively slow by comparison with the processing technologies being developed for thin film applications.[4-9]

One major objective of our research program is to develop standard processing methodology for the design, synthesis and processing of organometallic preceramic polymers into oxide and non-oxide ceramic fibers. In this paper, we present an overview of our recent efforts to develop anhydrous metal carboxylate precursors to the $YBa_2Cu_3O_{7-x}$, 123 superconducting oxide ceramic. More detailed studies will be presented in a series of papers published elsewhere.[10-12]

RESULTS AND DISCUSSION

We have examined the utility of metal carboxylates as precursors to 123 fibers because they

Mat. Res. Soc. Symp. Proc. Vol. 180. ©1990 Materials Research Society

offer several advantages over sol-gel processing approaches. In particular, their rheological properties are controlled by electrostatic and mechanical crosslinking interactions rather than hydrolytically induced crosslinking. These same crosslinking mechanisms permit effective atomic mixing of the metal components in the precursors polymers. In contrast, atomic mixing in sol-gel processing, especially of multicomponent oxides, is often difficult to obtain because the hydrolysis rates of the various alkoxide speces frequently differ by orders of magnitude.[13-15] Furthermore, close control of drying does not play a role in carboxylate processing of ceramics.

Metal carboxylates offer additional advantages including: (1) ease of synthesis, (2) stability to O_2 and H_2O, (3) structural diversity for manipulating precursor rheology and, (4) the possibility of forming multimetallic clusters, e.g. $CuSr_2(HCO_2)_6{\cdot}8H_2O$ and $CuSr(HCO_2)_4$.[16,17]

Mixed-metal carboxylates are potentially valuable for synthesizing 123 preceramics wherein a portion of the multimetallic oxide superstructure of the superconductor product is preformed. These precursors should greatly facilitate conversion to the final ceramic product. Indeed, Sauer et al have recently reported a related complex that may offer just such utility.[18]

Finally, a number of research groups have already demonstrated that the metal carboxylate "soaps" can be used very successfully to make thin films. Unfortunately, the simplest soap system, the all octanoate or 2-ethylhexanoate system does not provide access to intact ceramic fibers; although, it permits drawing of thin self-supporting precursor fibers. The primary problem appears to be the excessive volume changes that occur during pyrolytic conversion. It is these changes that lead to complete destruction of the precursor fiber during pyrolysis.

Consequently, we have sought to prepare metal carboxylate precursors that offer the excellent spinnability of the 2-ethylhexanoate system but with higher density and higher ceramic yields. Higher densities and ceramic yields will reduce volume changes and thereby reduce the stresses that are incurred during the densification processes. The end result should be intact ceramic fibers.[19-20]

Synthesis

The first step in the process was to develop clean synthetic routes to anhydrous carboxylates of all of the metals involved in the 123 system. Although, all of the carboxylates are stable to water, the anhydrous requirement stems from the desire to avoid "melting". The hydrates, when heated to the point of dehydration, generate sufficient quantities of free H_2O which partially dissolves some of the carboxylates.[21] This dissolution gives the appearence of "melting" and causes segregation.[22]

The following routes are extremely effective for the one-pot synthesis of metal carboxylates:

$$Ba + 2RCO_2H \xrightarrow{\text{trace EtOH/20°C/THF}} H_2 + Ba(O_2CR)_2 \qquad (1)$$

$$Y + 3RCO_2H \xrightarrow{\text{trace } HgCl_2\text{/THF reflux}} 1.5H_2 + Y(O_2CR)_3 \qquad (2)$$

$$CuO + 2RCO_2H + (RCO)_2O \xrightarrow{\text{xylene/reflux}} RCO_2H + Cu(O_2CR)_2 \quad (3)$$

$$Cu(O_2CR)_2 + Cu\ Foil \xrightarrow{CH_3CN/reflux} RCO_2H + 2Cu(O_2CR) \quad (4)$$

Preparation directly from high purity metal permits the synthesis of pure carboxylates and offers the opportunity to prepare very pure 123.

Physicochemical Characterization of Carboxylates

Although, we have prepared upwards of 30 different complexes,[10,11] we will focus here on the metal isobutyrates as these complexes offer nearly optimal properties for processing precursor fibers and then superconductor fibers. Purity of the complexes was established by chemical analysis and confirmed by thermogravimetric analysis (TGA, Table 1).

We have assessed a variety of carboxylate mixtures as to ceramic yield, solubility and "spinnability" and find that the following 1:1:1:3 stoichiometric mixtures provide the best properties:

$Y(O_2CCHMe_2)_3$: $Ba(O_2CCHMe_2)_2$: $Ba[O_2CCH(Et)(CH_2)_3CH_3]_2$: $3Cu(O_2CCHMe_2)_2$

$Y(O_2CCHMe_2)_3$: $Ba(O_2CCHMe_2)_2$: $Ba[O_2CCH(Et)(CH_2)_3CH_3]_2$:$3Cu(O_2CCHMe_2)$

Compound	Ceramic Yield Wt. % (Theory)	Decomp Product[a] % Metal (Theory)	Product
$Ba(O_2CCHMe_2)_2$	61.4 (63.4)	70.6 (69.6)	$BaCO_3$
$Ba[O_2CCH(Et)(CH_2)_3CH_3]_2$	45.9 (46.6)	70.4 (69.6)	$BaCO_3$
$Y(O_2CCHMe_2)_3$	32.2 (32.2)	78.8 (78.7)	Y_2O_3
$Cu(O_2CCHMe_2)_2$	29.5 (33.5)	78.5 (79.9)	CuO

Table 1. TGA results for Selected Metal Carboxylates. Heating rates used were 5°C/min in air to 900°C. a. Determined by chemical analysis.

We actually extrude rather than spin mixtures of these complexes dissolved in THF. Typically, 5 g of a stoichiometrically correct mixture of the various monomers will dissolve in 4 ml of THF if a few drops of isobutyric acid are added. Fibers for this study were extruded using the high pressure extruder shown schematically in Figure 1. Extrusion rate is controlled by

controlling the gas pressure at the top of the extruder (normally 200-300 psig).

The extruded fiber leaves 140 μm diameter spinneret and undergoes self-drawing such that at 0.5 m below the spinneret hole, a 70 μm dia. fiber can be "collected" across a square dowel framework with a spacing of approximately 10 cm. Thicker or thinner fibers can be collected by carefully choosing the distance from the spinneret.

The extruded fiber is allowed to "dry" for several hours to days at room temperature prior (see Figure 2) and then "cured" at 150°C. The curing process crosslinks the fibers prior to pyrolysis.

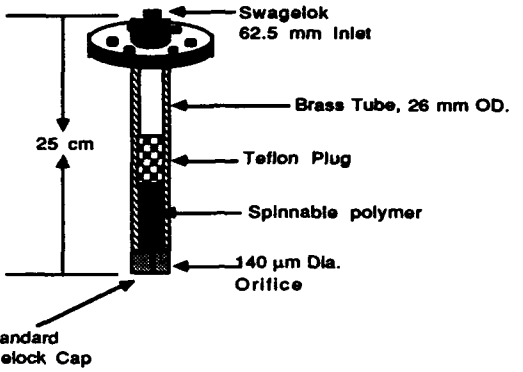


Figure 1. High Pressure Extruder Made From Swagelock Fittings.

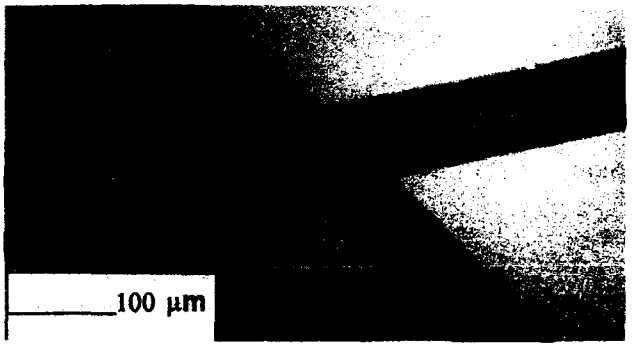


Figure 2. 123 Metal Carboxylate Precursor Fibers. 70 μm dia. fibers, extruded from a $Y(O_2CCHMe_2)_3$: $Ba(O_2CCHMe_2)_2$: $Ba[O_2CCH(Et)(CH_2)_3Me]_2$: $3Cu(O_2CCHMe_2)_2$ THF solution.

Pyrolysis Studies

Coincident with the spinning studies, studies were conducted to establish the decomposition patterns of the individual components of the two spinnable systems as a function of temperature and reaction atmosphere. The decomposition ranges for the various compounds are shown in Table 2. The Cu (II) system TGA is shown in Figure 3.

Compound	O_2 (°C)	Air (°C)	N_2 (°C)
$Y(O_2CCHMe_2)_3$	230-270	230-290	300-420
$Y[O_2CCH(Et)(CH_2)_3CH_3]_3$	170-230	230-300	350-480
$Ba(O_2CCHMe_2)_2$	260-315	250-340	250-510
$Ba[O_2CCH(Et)(CH_2)_3CH_3]_2$	240-270	250-335	300-480
$Cu(O_2CCHMe_2)_2$	190-240	220-250	245-270

Table 2. Decomposition Range for Selected Metal Carboxylates. Heating rates were 5°C/min to final temperature of 900°C. $Cu(O_2CCHMe_2)_2$ decomposes to Cu° and the Ba carboxylates decompose to $BaCO_3$ even in N_2.

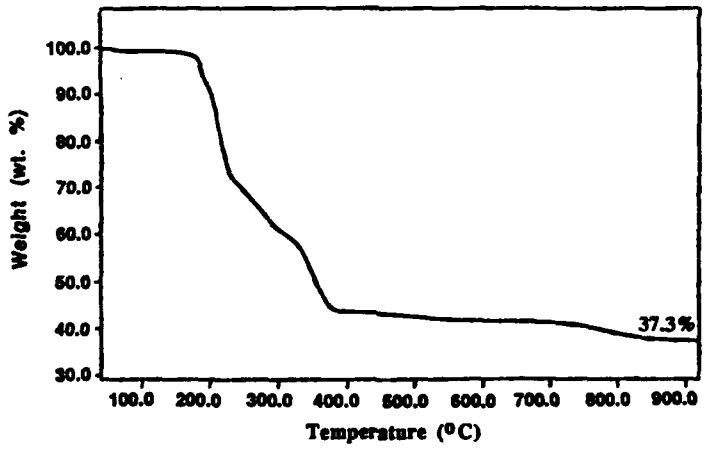


Figure 3. TGA of Cu (II) Spinning Mixture in Air. Heating rate 5°C/min to 950°C.

The TGAs of Ba isobutyrate and 2-ethylhexanoate are similar. Both convert in air, to $BaCO_3$ at 230-350°C, but never convert to the oxide even at 900°C, as expected. The yttrium isobutyrate TGA is clean, it decomposes in air over the range of 240-290°C. However, in O_2, yttrium isobutyrate literally burns as was confirmed by DTA studies.[11]

The Cu isobutyrates behave quite differently. The Cu (II) derivative decomposes at 180-230°C and the Cu (I) derivative decomposes at ≈130-190°C. In each case, initial weight loss is followed by a sizable weight gain. This behavior is indicative of initial reduction to copper metal followed by reoxidation to CuO or Cu_2O. The formation of Cu metal is consistent with the XRD results for pyrolysis of the Cu (II) system in N_2. In the latter case, no oxygen is available and copper metal is observed at as low as 300°C. In contrast, the XRD of a sample heated in air (Figure 4) shows no sign of copper crystallites nor is there evidence for extraneous phases.

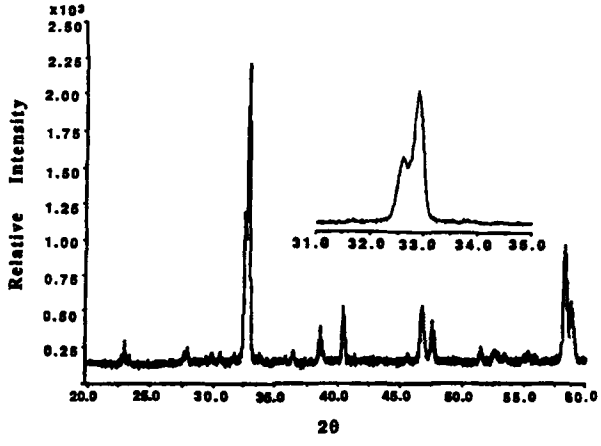


Figure 4. XRD of Cu (II) Spinning Mixture Heated to 950°C in Air at 1°C/min.

The Figure 4 XRD displays a standard splitting at 32.5° 2θ indicative of an orthorhombic phase. As discussed elsewhere,[10,11] this is insufficient proof of superconducting properties. We rely on flux exclusion and conductivity measurements for proof of superconductivity.

Pyrolysis of Fibers. Following extrusion and cure, the fibers can be heated slowly (0.2-0.5°C/min) to 500°C to remove the major portion of the organics. The 500°C fibers appear dense and do not exhibit any microstructure. Final heating to 900°C provides a relatively dense fiber ≈ 15-20 μm in diameter with grain sizes <1 μm (Figure 5). If heating is too rapid or too high (930°C), then one obtains fibers that exhibit large voids, melting or excessive grain growth. Thus, precise control of pyrolysis conditions is necessary to ensure high quality fibers.

The fibers obtained in this fashion exhibit superconductivity with onset at 90K and zero resistance at approximately 77K.[23,24] Fibers of 10 μm diameter can be produced with lengths of

up to 5 cm. These fibers can be bent 90°. Reproducibility remains a very significant problem as it is difficult to control the heating rates at the appropriate times and temperatures.

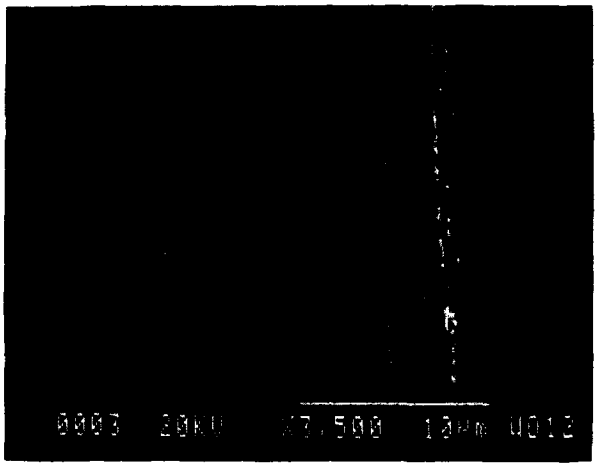


Figure 5. SEM Image of Precursor Fiber Heated to 900°C. Heating rate 0.5°C/min to 500°C and 1°C/min to 900°C.

ACKNOWLEDGEMENTS

We would like to thank the Defense Advanced Research Projects Agency (DARPA Order No. 6499) for support of this work through AFOSR contract No. F49620-88-C-0143. We would also like to thank Professor I. A. Aksay, Mr. W. Carty, Dr. G. Stangle and Dr. J. Javadpour for helpful discussions during the early stages of this work. We would also like to thank Dr. T. Yin and Mr. S. McElhaney for helpful discussions on synthetic strategies.

REFERENCES

1. Physical Properties of High Temperature Superconductors I, D.M. Ginsberg, Editor, (World Scientific Publishers, Teaneck, N.J. 1989).
2. Y. L. Chen, J. V. Mantese, A. H. Hamdi, and A. L. Micheli, J. Mat. Res. 4, 1065 (1989).
3. a. J. V. Mantese, A. L. Micheli, A. H. Hamdi, and R. W. Vest, MRS Bulletin, 14, 48 (1989). b. R. W. Vest and J. Xu, IEEE Trans. UFFC 35, 711 (1988). c. J. J. Xu, A. S. Shaik, and R. W. Vest, Thin Solid Films 161, 273 (1988). d. J. J. Xu, A. S. Shaik, and R. W. Vest, IEEE Trans. UFFC 36, 307 (1989).
4. S. Horikiri, K. Tsuji, Y. Abe, A. Fukui and E. Ichiki, U. S. Pat 4,101,615 July, 1978.

5. M. Klee, G. M. Stollman, S. Stotz and J. W. C. de Vries, Sol. St. Comm. 67, 613 (1988).
6. A. Gupta, R. Jagannathan, E. I. Cooper, E. A. Giess, J. I. Landman, and B. W. Hussey, Appl. Phys. Lett. 52, 2077 (1988).
7. T. Kumagai, H. Yokota, K. Kawaguchi, W. Kondo, S. Mizuta, Chem. Lett., 1987, 1645.
8. M. E. Gross, M. Hong, S. H. Liou, P. K. Gallagher, J. Kwo, Appl. Phys. Lett. 52, 160 (1988).
9. H. Nasu, S. Makida, T. Kato, Y. Ibara, T. Imura, Y. Osaka, Chem. Lett. 1987, 2403.
10. First paper in this series: W. M. Carty, G. C. Stangle, R. M. Laine and K. A. Youngdahl, SAMPE 1988 Spring Meeting (Seattle) SAMPE Quart., Oct., (1988) p 3.
11. R.M. Laine, K. A. Youndahl, R.A. Kennish, M.L. Hoppe, Z.F. Zhang, and D. J. Ray, submitted for publication.
12. D. J. Ray, Z.F. Zhang, and R.M. Laine, Inter/Micro-90, Chicago IL, Aug 20-23, 1990 submitted for publication.
13. See for example: a. J. Livage, M. Henry, C. Sanchez, Prog. Sol. State Chem. (1989) p 1. b. Sol-Gel Technology for Thin Films, Fibers, Preforms, Electronics, and Specialty Shapes, L. Klein Ed. (Noyes Publ. Park Ridge, N. J., 1988). c. Better Ceramics Through Chemistry III, Mat. Res. Soc. Symp. Proc., C. J. Brinker, D. E. Clark, D. R. Ulrich Eds. (Mat. Res. Soc. Proc. 121, Pittsburg, PA 1988). d. Science of Ceramic Chemical Proc., ed. L. L. Hench and D. R. Ulrich (Wiley-Intersci., New York 1986). e. Internat. Conf. on Ultrastructure Proc. of Ceramics, Glasses and Composites, ed. L. L. Hench and D. R. Ulrich eds (Wiley-Intersci., New York 1984).
14. a. H. Dislich, J. Non-Cryst. Solids, 57, 371 (1983). b. M. W. Colby, A. Osaka and J. D. Mackenzie, J. Non-Cryst. Solids, 99, 129 (1988).
15. L. C. Klein, Ann. Rev. Mater. Sci., 15, 227 (1985).
16. R. F. Baggio, P. K. de Perazzo and G. Polla, Acta Cryst. C41, 194 (1985).
17. R. F. Baggio, M. A. R. de Benyacar, P. K. de Perazzo and G. Polla, J. Solid State Chemistry, 56, 298 (1985).
18. N. N. Sauer, E. Garcia, K. V. Salazar, R. R. Ryan, and J. A. Martin, J. Am. Chem. Soc., 112, 1424 (1990).
19. T. Umeda, H. Kozuka, and S. Sakka, Adv. Cera. Mat. 3, 520 (1988).
20. S. Hirano, T. Hayashi, R. H. Baney, M. Miura, H. Tomonaga, Chem. Lett. 4, 665 (1988).
21. G. Micera, P. Piu, L. S. Erre, F. Cariati, Thermochim. Acta, 84, 175 (1985).
22. J. C. W. Chien, B. M. Gong, J. M. Gadsen, R. B. Hallock, Phys. Rev. B, 38, 8535 (1988).
23. J. D.Mackenzie et al, Mat. Res. Soc. Proc. Mat. Res. Soc. Meeting, April 1988, Reno, NV.
24. R. M. Laine, K. A. Youngdahl, W. M. Carty, G. C. Stangle, C. Han, R. A. Kennish, S. McElhaney, T. K. Yin, S. Sarikaya, and I. A. Aksay, Proc. A.Cer.S. Meeting, May 1988, Cincinnati, OH.

FABRICATION OF SUPERCONDUCTING Bi-Sr-Ca-Cu-O OXIDE FILMS USING THE METAL ALKOXIDE METHOD

SHINGO KATAYAMA AND MASAHIRO SEKINE
Colloid Research Institute, 350-1 Ogura, Yahata-higashi-ku, Kitakyushu 805, Japan

ABSTRACT

Superconducting films in the Bi-Sr-Ca-Cu-O system were fabricated using metal alkoxides. To make a mixed alkoxide solution into a dip-coating solution, insoluble Cu alkoxide was modified with 2-dimethylaminoethanol and insoluble Bi alkoxide was dissolved in the presence of Ca and/or Sr alkoxides. The structures of these alkoxide derivatives were studied by FT-IR, ^{1}H-NMR, and EXAFS. The film with Tc(zero) =115K was fabricated using the alkoxide solution with a nominal composition of Bi:Sr:Ca:Cu=2:2:3:4.

INTRODUCTION

Bi-Sr-Ca-Cu-O films have been fabricated using the metal alkoxide method[1,2], because of advantages for obtaining shaped materials such as bulks, films, and fibers, as well as pure and homogeneous products. For applying this method for fabricating Bi-Sr-Ca-Cu-O films, a homogeneous solution of alkoxides is first prepared as the starting solution. However, it is difficult to prepare this solution due to the insolubility of Cu and Bi alkoxides in common organic solvents. In the case of Cu alkoxides, there are some reports that Cu alkoxide is chemically modified so that it can be dissolved in organic solvents[3-5], but little is known of the structure of modified alkoxides and the effects of modifiers. In the case of Bi alkoxides, the preparation of an alkoxide solution in the Bi-Sr-Ca-Cu-O system has been reported[1,2], but without any discussion on the solubility increase of Bi alkoxides.

In this paper, a solution of Bi, Sr, Ca, and Cu alkoxides was prepared and the mechanism of solubility increase of Cu and Bi alkoxides is discussed. Furthermore, Bi-Sr-Ca-Cu-O films fabricated using alkoxide solutions with various compositions, and their superconductivities were characterized.

EXPERIMENTAL

1 mol of $Cu(OCH_3)_2$ was modified using 2 mol of 2-dimethylaminoethanol to dissolve in ethanol. The structure of the modified Cu alkoxide was investigated using ^{1}H-NMR and EXAFS. $Bi(O\text{-}iC_3H_7)_3$ was dissolved into an ethanol solution of $Ca(OC_2H_5)_2$ or $Sr(OC_2H_5)_2$. The clear homogeneous alkoxide solution obtained at a (Ca or Sr)/Bi molar ratio of 0.5 was isolated by evaporating the solvent under reduced pressure to give a solid product. These alkoxide derivatives were analyzed by FT-IR.

Fig.1 shows the process for the fabrication of Bi-Sr-Ca-Cu-O films. The fired films were examined using XRD and SEM. The resistivity of the films was measured by the conventional four-probe method.

Mat. Res. Soc. Symp. Proc. Vol. 180. ©1990 Materials Research Society

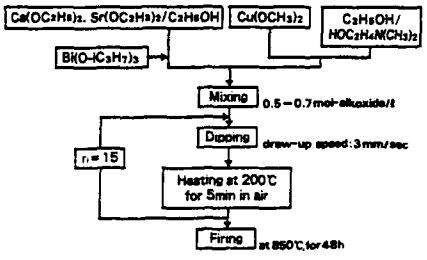


Fig.1 Process for the fabrication of Bi-Sr-Ca-Cu-O films.

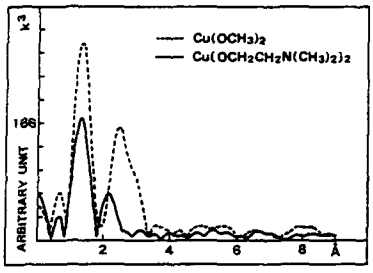


Fig.2 Fourier transform of EXAFS spectra of $Cu(OCH_3)_2$ and modified Cu alkoxide. The phase shift was not considered.

RESULTS AND DISCUSSION

Preparation of homogeneous alkoxide solution

$Cu(OCH_3)_2$ is insoluble in common organic solvents, but the addition of 2-dimethylaminoethanol to an organic solvent made it soluble. The results of ^{1}H-NMR spectra of the modified Cu alkoxide revealed the formation of $Cu[OCH_2CH_2N(CH_3)_2]_2$ by an OR-substitution reaction of $Cu(OCH3)2$ with 2-dimethylaminoethanol. Fig.2 shows the Fourier transform of the EXAFS spectrum of $Cu(OCH_3)_2$ and that of the modified Cu alkoxide. $Cu(OCH_3)_2$ had two distinct peaks, one located at the same position as that of CuO and corresponding to the nearest oxygen atoms of Cu neighbors, and another corresponding to the nearest copper atoms of Cu neighbors because of the highly polymeric structure of $Cu(OCH_3)_2$[6]. In the modified Cu alkoxide, however, only a single peak appeared at the same position as the first peak for $Cu(OCH_3)_2$. These results mean that the modified Cu alkoxide exists in a monomeric form as a result of the OR-substitution and can dissolve in a solvent.

Bi alkoxides are also insoluble in organic solvents and usual chemical modifiers such as β-diketones, β-keto esters, and alkanolamines are ineffective for increasing its solubility. Addition of 1g of $Bi(O\text{-}iC_3H_7)_3$ to 50ml of an ethanol solution of $Ca(OC_2H_5)_2$ or $Sr(OC_2H_5)_2$ gave a clear solution at a (Ca or Sr)/Bi molar ratio of 0.5 or above, although a suspension was obtained less than a (Ca or Sr)/Bi molar ratio of 0.5. A possible explanation for this is as follows: double alkoxides are generally much less associated in organic solvents than the component alkoxides, and thus show a fair amount of solubility in a solvent[7]. Also, the association of $Bi(O\text{-}iC_3H_7)_3$ may be destroyed by the formation of a double alkoxide($MBi_2(OR)_8$ M=Ca or Sr). The FT-IR spectra of the Bi-Ca alkoxide derivative had an absorption band at 621cm^{-1} which was not found in the spectra of $Bi(O\text{-}iC_3H_7)_3$, $Bi(OC_2H_5)_3$, and $Ca(OC_2H_5)_2$. Also in the case of the Bi-Sr alkoxide derivative, a new band was observed at 559cm^{-1}. It is assumed that these new bands are due to the formation of a double alkoxide of Bi with Ca or Sr.

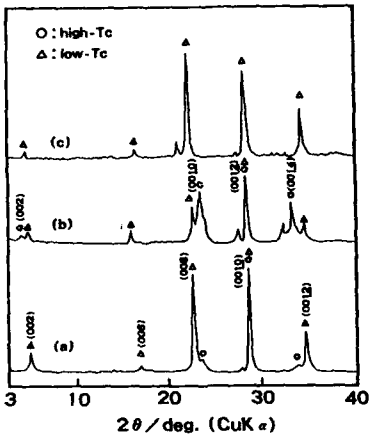


Fig.3 XRD of Bi-Sr-Ca-Cu-O films. (a):2223, (b):2234, (c):2245.

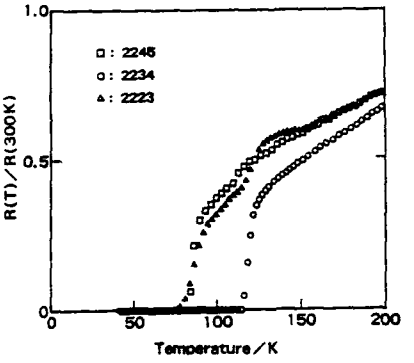


Fig.4 Temperature dependence of electrical resistivity for Bi-Sr-Ca-Cu-O films.

Characterization of Bi-Sr-Ca-Cu-O films

Fig.3 shows XRD of Bi-Sr-Ca-Cu-O films and their temperature dependence of resistivity is shown in Fig.4.

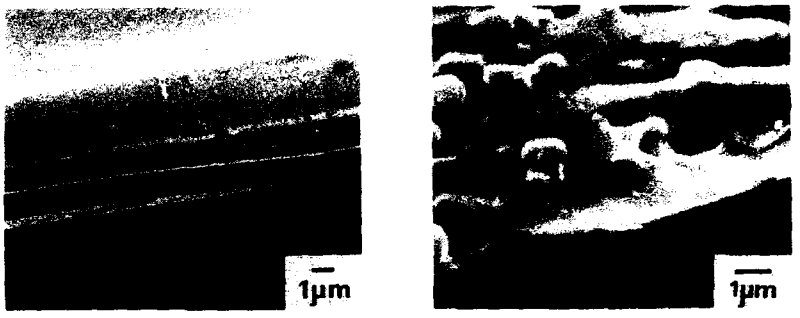
The 2223 film, same composition as the high-Tc phase, had mainly the low-Tc phase, but a small amount of the high-Tc phase was also observed. The temperature dependence of resistivity of this film showed two drops, first a little drop near 120K corresponding to the high-Tc phase and a second drop with Tc(zero)=80K corresponding to the low-Tc phase.

To increase amount of the high-Tc phase, an addition of excess Ca and Cu[8] was investigated in this process. Although the high-Tc phase was not observed in the 2245 film, the 2234 film mainly had the high-Tc phase with a strongly preferred orientation to the c-axis perpendicular to the substrate. Also, in this process, an addition of excess Ca and Cu was effective to increase amount of the high-Tc phase. Although XRD of the 2234 film exhibited the high-Tc and low-Tc phases, this film had one drop transition in resistivity with the Tc(onset)=122K and Tc(zero)=115K corresponding to the high-Tc phase. The single-step transition is related to a continuous high-Tc phase superconducting path.

SEM photographs of 2234 films before firing(a) and after firing(b) are shown in Fig.5. The film before firing had flat surface with a film thickness of about 1 μm. The crystals of the fired film show a two-dimensional plate-like orientation with a film thickness of about 0.5 μm.

CONCLUSIONS

(1) Insoluble $Cu(OCH_3)_2$ was modified using 2-dimethylamino-ethanol to be dissolved. The modified Cu alkoxide was formed by the OR-substitution reaction of the alkoxide with 2-dimethyl-



(a) (b)

Fig.5 SEM micrographs of Bi-Sr-Ca-Cu-O(2234) films before firing(a) and after firing(b).

aminoethanol and possessing a monomeric form dissolved in ethanol.
(2) $Bi(O\text{-}iC_3H_7)_3$ was completely dissolved in the presence of $Ca(OC_2H_5)_2$ or $Sr(OC_2H_5)_2$ and the formation of a double alkoxide of Bi with Ca or Sr was suggested.
(3) The Bi-Sr-Ca-Cu-O film on MgO(100) with Tc(zero)=115K was fabricated using an alkoxide solution with a nominal composition of 2:2:3:4.

ACKNOWLEDGMENTS

The authors are grateful to the Japan Key Technology Center for the financial support. Thanks must also be given to Dr. Y. Udagawa and Dr. K. Tohji at Institute for Molecular Science for their helpful comments in conducting the EXAFS experiments. The assistance of Miss A. Kamimura is greatly acknowledged.

REFERENCES

1. S. Hirano, T. Hayashi, and H. Tomonaga, Jpn. J. Appl. Phys. 29(1), L40(1990).
2. T. Kobayashi, K. Nomura, F. Uchikawa, T. Masumi, and Y. Uehara, Jpn. J. Appl. Phys. 27(10), L1880(1988).
3. T. Nonaka, K. Kaneko, T. Hasegawa, K. Kishio, Y. Takahashi, K. Kobayashi, K. Kitazawa, and K. Fueki, Jpn. J. Appl. Phys. 27(5), L867(1988).
4. T. Monde, H. Kozuka, and S. Sakka, Chem. Lett. 1988, 287 (1988).
5. H. Zheng, M. W. Colby, and J. D. Machenzie, Better Ceramics Through Chemistry III, edited by D. E. Clark and D. R. Ulrich (Mater. Res. Soc., Pittsburgh, PA, 1988), p.537.
6. C. H. Brubaker, Jr. and M. Wicholas, J. Inorg. Nucl. Chem. 27, 59(1965).
7. D. C. Bradly, R. C. Mehrotra, and D. P. Caur, Metal Alkoxides (Academic Press, London, 1978). p.308-334.
8. A.Sumiyama, T. Yoshitomi, H. Endo, J. Tsuchiya, N. Kijima, M. Mizuno, and Y. Oguri, Jpn. J. Appl. Phys. 27(4), L542 (1988).

POLYFUNCTIONAL CARBOXYLIC ACIDS AS COPRECIPITATING AGENTS FOR BARIUM, YTTRIUM, AND COPPER

Robert B. Hallock, P.O. Rexer, M.S. Jolly, W.E. Rhine, and M.J. Cima
Ceramics Processing Research Laboratory, Massachusetts Institute of Technology,
Cambridge, MA 02139

ABSTRACT

The suitability of several polyfunctional carboxylic acids as coprecipitating agents for Ba, Y, and Cu was investigated. Essentially complete precipitation from alcoholic solutions was achieved for all three metals when tartaric acid was employed as the precipitating agent. The amorphous precipitate formed under these conditions was composed of uniform particles about 50 nm in diameter, and was converted readily to high purity $Ba_2YCu_3O_{7-x}$.

INTRODUCTION

The formation of $Ba_2YCu_3O_{7-x}$ from coprecipitated oxalate salts has been claimed to offer several advantages over solid state reaction between the oxides, including improved homogeneity, lower temperature synthesis, better superconducting properties, and sintering to nearly theoretical density [1-4]. The main disadvantage encountered in oxalate coprecipitation is the incomplete precipitation of one or more of the metals, resulting in loss of control over the stoichiometry of the precipitate [1-4]. We have investigated the use of several polyfunctional carboxylic acids as precipitating agents for Ba, Y, and Cu. The extent of precipitation of all three metals was monitored by inductively coupled plasma emission spectroscopy (ICP) analyses of the filtrates from the coprecipitation reactions. None of the acids investigated gave complete precipitation of all three metals from aqueous solution. However, in a mixed solvent system (ethanol/water), the use of tartaric acid allowed the isolation of a highly reactive amorphous precursor to $Ba_2YCu_3O_{7-x}$.

EXPERIMENTAL PROCEDURE

Solubility Studies

The carboxylic acids were dissolved in a minimum amount of water and added to aliquots of a stock aqueous solution of Ba, Y, and Cu acetates (0.1175 M Ba, 0.0578 M Y, 0.1762 M Cu) such that the mole ratio of reagents was 2Ba : 1Y : 3Cu : 7acid. The resulting precipitates were isolated by filtration and their morphologies examined by scanning electron microscopy (SEM). The filtrates were diluted 1:100 and analyzed for Ba, Y, and Cu by ICP (Laboratory for Special Analysis, Randolph, MA). In several cases, crystals formed from the filtrate over a period of days or weeks. These crystalline products were isolated and characterized.

Mat. Res. Soc. Symp. Proc. Vol. 180. ©1990 Materials Research Society

Tartaric Acid Coprecipitation from Ethanol/Water Mixtures

Barium acetate (7.67 mmol), yttrium acetate (3.83 mmol), and copper acetate (11.50 mmol) were dissolved at room temperature in a mixture of 400 mL ethanol and 200 mL water. The acetate solution was added over a period of about 30 s to a solution of the tartaric acid in 600 mL ethanol. A blue gelatinous precipitate formed upon mixing. The precipitate was isolated by filtration and dried overnight at 45°C.

Formation of $Ba_2YCu_3O_{7-x}$ from Coprecipitated Tartrate Precursors

The coprecipitated powders were fired in $BaZrO_3$ crucibles. For reduced pressure firing, the tube furnace was continuously evacuated with a mechanical pump while the total pressure was adjusted by bleeding oxygen into the system. All samples were cooled under 1 atm O_2. The resulting $Ba_2YCu_3O_{7-x}$ was characterized by X-ray diffraction and carbon analyses (E+R Microanalytical Laboratory, Corona, NY). A variety of firing schedules were investigated.

RESULTS AND DISCUSSION

The solubilities in water of the Ba, Y, and Cu derivatives of several carboxylic acids, as determined by ICP, are listed in Table I. No attempt was made to adjust pH, and in all cases the pH of the filtrate was 4.0-5.0. The tartaric acid derivatives had the lowest solubilities of the acids which were investigated as well as the most promising morphologies; therefore, further work on this system was pursued. In addition to the precipitates which formed initially, crystals slowly formed in the filtrates from the tartaric and adipic acid reactions. The former was identified as the known compound Cu(tartrate)·$3H_2O$ [5] on the basis of thermal gravimetric analysis (TGA). The crystalline product isolated from the adipic acid filtrate was shown to be a previously unreported mixed metal compound of the formulation $BaCu(adipate)_4$ on the basis of TGA and analytical data [calculated (found) %: Ba, 17.57 (17.56); Cu, 8.13 (8.17); C, 36.89 (36.85); H, 4.13 (4.36)]. It is not possible to distinguish between the two possible formulations, $BaCu[OOC(CH_2)_4COOH]_4$ and $BaCu[OOC(CH_2)_4COO]_2 \cdot 2[HOOC(CH_2)_4COOH]$, on the basis of the available data. Although the crystals appeared to be single tetrahedrons (Fig. 1), Laue photographs of

Table I. Concentration (mol/L) of Metals Remaining in Aqueous Filtrates from Coprecipitation Reactions.

Acid	Ba	Y	Cu
Succinic $HOOC(CH_2)_2COOH$	7.2 E-2	2.8 E-3	1.6 E-2
Adipic $HOOC(CH_2)_4COOH$	.27	2.1 E-3	4.7 E-3
Tartaric HOOC-CH(OH)CH(OH)-COOH	2.6 E-4	5.0 E-4	2.4 E-4
Polyacrylic $[-CH(COOH)CH_2-]_n$	5.6 E-2	3.9 E-2	6.2 E-3

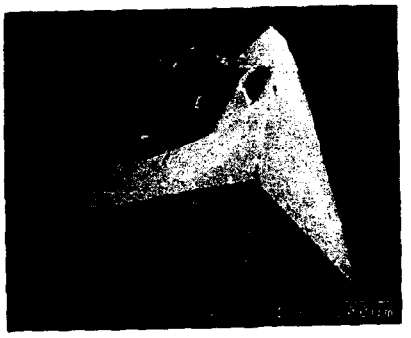


Fig. 1. Crystals of $BaCu(adipate)_4$.



Fig. 2. Amorphous Ba, Y, Cu tartrate precipitate from ethanol/water mixture.

apparently single tetrahedrons show multiplet crystal patterns. The formation of a Ba-Cu compound has also been observed in our laboratory as a product of oxalate coprecipitation, and we have recently reported the synthesis and crystal structure of the related compound $BaCu(C_2O_4)_2 \cdot 6H_2O$ [6]. Maleic acid caused only the slow crystallization of $Cu(maleate) \cdot H_2O$ and was not investigated further.

Coprecipitation with Tartaric Acid in Ethanol/Water Mixtures

Although coprecipitation with tartaric acid was the most promising of the precipitating agents initially investigated, the solubilities of the three metals in aqueous solutions were still significant ($2\text{-}5 \times 10^{-4}$ M). In order to achieve complete precipitation of all three metals, the addition of ethanol was investigated as a method for reducing solubility. Some water was necessary to dissolve the acetates since it was not possible to dissolve them in pure ethanol. A similar approach has been applied successfully to oxalate coprecipitation [4]. Initially, the reaction was run at elevated temperature (~80°C) under saturated conditions. Tartaric acid dissolved in a minimum of alcohol was added to a saturated solution of the acetates in 4:1 ethanol:water (final solution 5:1 ethanol:water). ICP analysis of the filtrate showed that complete precipitation had occurred with only trace amounts of Ba (1 ppm), Y (<1 ppm), and Cu (5 ppm) remaining in solution. The precipitate was not uniform; rather, two different morphologies were observed by SEM. Once it had been established by ICP that the tartrates had essentially no solubility in 5:1 ethanol:water, the reaction was run under more dilute conditions. The precipitate which formed under these conditions was composed of agglomerated spherical particles about 0.05 μm in diameter and was very uniform in appearance (Fig. 2). X-ray powder diffraction shows that the precipitate is amorphous.

Formation of $Ba_2YCu_3O_{7-x}$ from Coprecipitated Tartrates

The precipitates from both experiments described above were fired under various conditions in order to determine the lowest temperature required for complete conversion to high purity $Ba_2YCu_3O_{7-x}$. A summary of the firing schedules and purity of the resulting $Ba_2YCu_3O_{7-x}$ is given in Table II. As residual $BaCO_3$ may remain undetected by X-ray

Table II. Firing Schedules and Conversion of Tartrates to $Ba_2YCu_3O_{7-x}$.

Sample	P_{O2} (torr)	Temp (°C)/Time	%C (found)	% Conversion	Phase(s)
2RH57	760	850/16 h	0.496	84.4	T'
2RH57	760	add. 900/1 h	0.019	99.4	O
3RH4	2.5	850/1 h	0.054	98.3	O
3RH6	2.5	800/2 h	0.044	98.6	O
3RH8	1.5	775/10 h	0.193	93.9	O
3RH10	0.4	700/5 h	0.562	82.4	O, $BaCuO_2$
3RH17	~.03	700/14.5 h			O, ?

The same batch of tartrates was used throughout. % conversion = 100 - (mol CO_2 remaining in sample/mol Ba in sample). T' = tetragonal phase; O = orthorhombic phase.

powder diffraction, the $Ba_2YCu_3O_{7-x}$ formed in this work was characterized by carbon analysis in addition to X-ray powder diffraction. Firing of the precipitate obtained from dilute solution for 16 h at 850°C resulted in the isolation of a tetragonal phase (T') as observed by other workers [7]. The carbon content of this phase was quite high (0.496 wt%), which if present as carbonate ion would correspond to a stoichiometry of $Ba_2YCu_3(CO_3)_{.31}O_x$. Additional firing of this material for 1 h at 900°C resulted in the formation of the superconducting orthorhombic phase $Ba_2YCu_3O_{7-x}$ with low carbon content (0.019 wt%).

Data obtained by firing the same batch of coprecipitated tartrates (from dilute solution) at reduced pressures are given in Table II. The pressure of oxygen was maintained within the stability limits of $Ba_2YCu_3O_{7-x}$ as defined by Bormann and Nölting [8]. It is interesting that firing under reduced pressure (with subsequent cooling in 1 atm oxygen) yielded the orthorhombic phase, even at temperatures as low as 700°C (Fig. 3). This is in marked contrast to firings at atmospheric oxygen pressure where the T' phase formed at temperatures below 900°C.

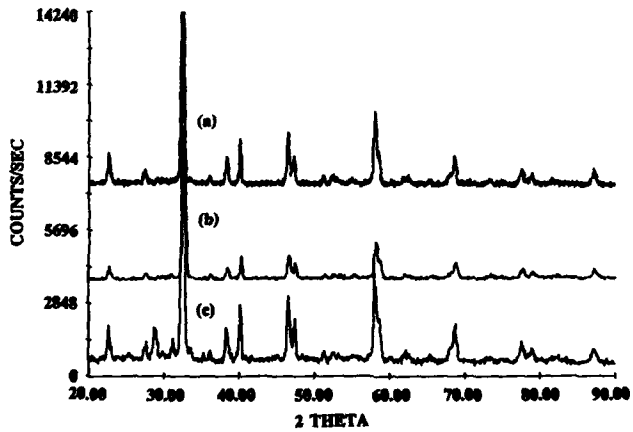


Fig. 3. X-ray diffraction pattern of $Ba_2YCu_3O_{7-x}$ obtained from tartrate precursor and fired under the following conditions: (a) 16 h 850°C, 1 h 900°C, 760 torr O_2; (b) 1 h 800°C, 760 torr O_2; and (c) 14 h 700°C, ~.03 torr air.

CONCLUSIONS

Essentially quantitative coprecipitation of Ba, Y, and Cu has been achieved using tartaric acid in a mixed ethanol/water solvent. The resulting amorphous precipitate has a uniform morphology composed of agglomerated spherical particles about 0.05 μm in diameter. This precursor is converted readily to orthorhombic $Ba_2YCu_3O_{7-x}$ by 900°C at atmospheric pressure, and at temperatures as low as 700°C under reduced pressure; however, the morphology of the tartrate precursor is not preserved upon conversion to $Ba_2YCu_3O_{7-x}$. The low (0.019 wt% C) carbon content of the $Ba_2YCu_3O_{7-x}$ obtained via this coprecipitation route is in marked contrast to the solid state synthesis of $Ba_2YCu_3O_{7-x}$. In our laboratory, the solid state process ($BaCO_3 + Y_2O_3 + CuO$), typically leads to $Ba_2YCu_3O_{7-x}$ with 0.3-0.6 wt% C and requires initial milling followed by three firings of 20 h each at 950°C with intermediate grinding.

ACKNOWLEDGMENTS

The authors would like to acknowledge the contributions of Bill Davis and Simon Bott for attempting crystallographic studies of $BaCu(adipate)_4$ and the experimental assistance of Jonathan Lee through the UROP program at MIT. This work has been generously supported by DARPA under contract #MDA972-88-K-0006.

REFERENCES

1. P. Peshev, G. Gyurov, I. Khristova, K. Petrov, D. Kovacheva, Y. Dimitriev, N. Nencheva, and E. Vlakhov, Mat. Res. Bull. 23, 1765 (1988).
2. S. Vilminot, S. El Hadigui, A. Derory, M. Drillon, J.C. Bernier, J. Kappler, R. Kuentzler, and Y. Dossmann, Mat. Res. Bull. 23, 531 (1988).
3. X.Z. Wang, M. Henry, J. Livage, I. Rosenman, Solid State Comm. 64, 881 (1987).
4. T. Yamamoto, T. Furusawa, S. Hideaki, K. Park, T. Hasegawa, K. Kishio, K. Kitazawa, and K. Fueki, Supercond. Sci. Technol. 1, 153 (1988).
5. W.F. Linke, Solubilities of Inorganic and Metal Organic Compounds (D. Van Nostrand, New York, 1958), p. 915.
6. R.B. Hallock, W.E. Rhine, M.J. Cima, S.J. Bott, and J.L. Atwood in Superconductivity and Ceramic Superconductors, edited by K.M. Nair (American Ceramic Society, Westerville, OH, 1990), in press.
7. See for example X.G. Wang, M. Henry, J. Livage, and I. Rosenman, Solid State Comm. 64 (6), 881 (1987).
8. R. Bormann and J. Nölting, J. Appl. Phys. Lett. 54 (21), 2148 (1989).

SYNTHESIS OF SUPERCONDUCTING THIN FILMS BY ORGANOMETALLIC DECOMPOSITION

CHRISTOPHE BARBE AND TERRY A. RING
Powder Technology Laboratory, Swiss Federal Institute of Technology, CH-1015 Lausanne, Switzerland

1) INTRODUCTION

The discovery of high critical temperature superconducting oxides [1,2] has stimulated intensive research activities aimed not only at understanding the physical mechanisms of superconductivity, but also developing techniques to produce these ceramics in useful forms. A promising application for superconductors is in electronic components industry which has given rise to an interest in the various ways of producing thin films of superconducting materials.

Physical depositions techniques have been successful in producing films with the desired physical characteristics (i.e, high Tc and Jc), but these processes are expensive and do not allow any versatility in the substrate geometry. Chemical deposition techniques such as the spray, dip, and spin coating of a solution onto a substrate, are attractive because they avoid these problems. This is why we have focused our attention on the deposition of solutions by these techniques to produce the superconducting thin films of $YBa_2Cu_3O_{7-x}$, also known as the 1:2:3 phase.

Out of the many chemical routes for producing superconducting thin films [3-8], the process that we have found to show the most promise is the dipping-pyrolysis procedure for a carboxilate solution of yttrium, barium and copper in chloroform. The solution chemistry, drying, pyrolysis, and high temperature treatment of the film will be discussed in detail.

2) EXPERIMENTAL PROCEDURE

Various organic salts [9-14], differing by the carbon chain length, have been used to prepare solutions for a dip (or spin) and pyrolysis process. The following precursors were used in our experiments: 1) copper 2-ethyl hexanoate, 2) barium 2-ethyl hexanoate, and 3) either yttrium naphtenate or yttrium 2-ethyl hexanoate. These three compounds are mixed in the desired 1:2:3 stoichiometric ratio in chloroform to make homogeneous viscous solution. In reality this 1:2:3 stoichiometric ratio was not achieved exactly. The elemental analysis of the precursors showed an inaccurate assay (as provide by the supplier) which had lead us to a 1:2:3.1 in the (Y+Ba+Cu) 2-Ethyl hexanoates solutions.

The solutions were then slowly deposited on an appropriate substrate by dipcoating. Because of the low surface tension of those solutions, any number of ceramic substrates can be used. The rheological properties of these solutions were studied in order to control film thickness during the dipcoating procedure.

Thermal analysis of the different solutions was used to define the parameter of the heat treatment specifically. The results of this analysis suggested the steps for the heat treatment. The final films were then analyzed by X-ray diffraction, EDX, SEM and four point resistivity measurements. The results are presented below.

Mat. Res. Soc. Symp. Proc. Vol. 169. ©1990 Materials Research Society

3) RESULTS AND DISCUSSION

3.1 Solutions Chemistry

The solution obtained by the mixing of copper 2-ethyl hexanoate, barium 2-ethyl hexanoate and yttrium naphtenate in chloroform has a transparent green color. By photon correlation spectroscopy and chemical analysis, we have discovered particles of yttrium naphtenate in the solution with an average diameter of 0.11μm. The presence of these particles is important because they produce inhomogeneities in the film during the thermal decomposition. This was avoided by using yttrium 2-ethyl hexanoate which is completely soluble in chloroform.

3.2 Solutions rheology

Figure 1 shows how the viscosity of the solution is related to the concentration of the precursors in chloroform. At working concentration and shear rates (<50 s^{-1}), these solutions exhibit Newtonian behavior. At high concentrations these solutions became rheologically plastic. This means that for a constant dipping speed, the solution viscosity will determine the film thickness. Solution viscosities ranging between 0.2 and 1 Pa s give thicknesses between 20-30 μm, on a dry film basis. If the film is too thin, "islands" of material will be formed and another deposition is needed to fill the gaps between the islands. On the other hand, if the film is too thick, solvent or organic matter will be trapped and the film will crack during the heat treatment.

3.3 Thermal analysis results

Thermogravimetric Analysis (TGA) of the film dried at room temperature shows a weight loss below 150°C and Differential Scanning Calorimetry (DSC) shows an endothermic peak at the same temperature which indicates solvent being evaporated. Therefore, some chloroform remains inside the film after room temperature drying and its effect can be disastrous for the film during the heat treatment. Because the top layer of film dries faster than the interior, a crust of dried material is formed which traps the solvent inside the film. When the temperature is increased, the chloroform vapor expands and pushes this gas-tight crust upwards and we obtain a weak and open structure resembling a "soufflé". To bypass this problem, we dry the samples slowly (12 h from 25°C to 150°C) to allow the diffusion of solvent out of the film without breaking the film.

Thermogravimetric analysis (TGA), in an oxygen atmosphere, was also used to study the decomposition of organometallic molecules into metal oxides. A comparison between the decomposition curve of the 1:2:3 solution and the curve for each of the precursors (Figure 2) can be used to assign a chemical reaction to each step. The first weight loss step at 270°C after the solvent loss is due to the pyrolysis of the Cu 2-ethyl hexanoate into CuO. The second (350°C) and third steps (400°C) are the weight losses corresponding to the transformation of Ba 2-ethyl hexanoate into $BaCO_3$ and Y naphtenate into Y_2O_3, respectively. The last step (800°C to 900°C) correspond to the transformation of $BaCO_3$ into BaO. If the pyrolysis is done under a nitrogen atmosphere, then decarbonation occurs at lower temperature (700°C to 800°C). This removal of $BaCO_3$ is important since it has a drastic effect on the physical characteristics (Tc and Jc) of the final material.

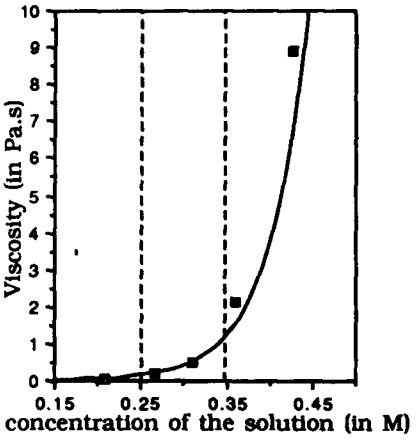


Figure 1: viscosity of the solution vs concentration of metals

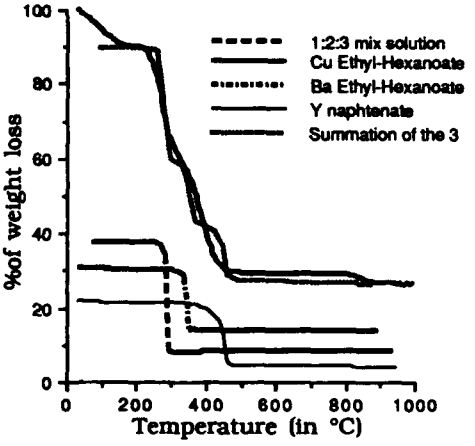


Figure 2: Thermal decomposition of the solutions

3.4 Analysis of fired films

From thermal analysis data, the following heat treatment was established:

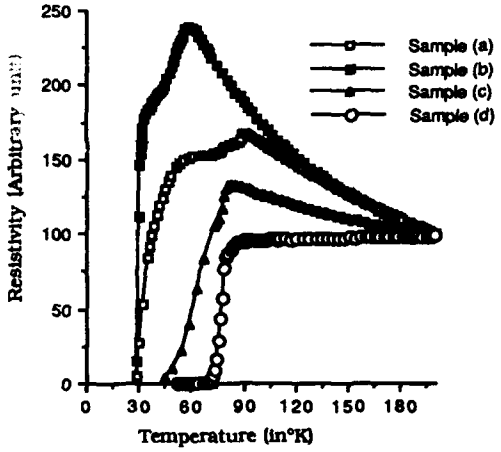
- drying at room temperature about 1 h
- drying from 50°C-150°C in oven 12 h (air)
- pyrolysis from 30°C to 910°C at 5°/min in pure oxygen
- firing at 800-910°C for 1-12h in oxygen
- cooling to room temperature (cooling rate of the furnace=10 h) in oxygen

Films have been synthesized on either Al_2O_3 or MgO substrates. The contribution of substrates to the final films resistivity is shown figure 3 (samples a and b). The onset of resistivity goes from 90°K (on MgO) to 60°K on alumina. X-ray diffraction showed the 1:2:3 phase as well as some other unidentified peaks which might belong to a mixed oxide of yttrium, barium and aluminium. EDX revealed grains containing Ba and Al together. These results suggest that aluminium atoms do diffuse from the substrate into the film and explain the decrease in Tc(onset).

Solutions with various stoichiometries have been investigated to study the influence of composition on the properties of the final films. If the solution stochiometry is copper defficient (i.e, 1:2:2.9), $BaCuO_2$ and Y_2BaCuO_5 insulating phases are formed which reduce the Tc of the film to 29°K. If the solution contains excess copper (i.e, 1:2:3.1), an insulating phase of CuO will be formed; however its effect on Tc is of less importance (i.e, Tc reaches 50°K). The presence of CuO, generally in liquid phase, promotes the grain growth and increase the sintering rate of the samples. When a film containing excess copper is fired at 910°C for 1 hour and then

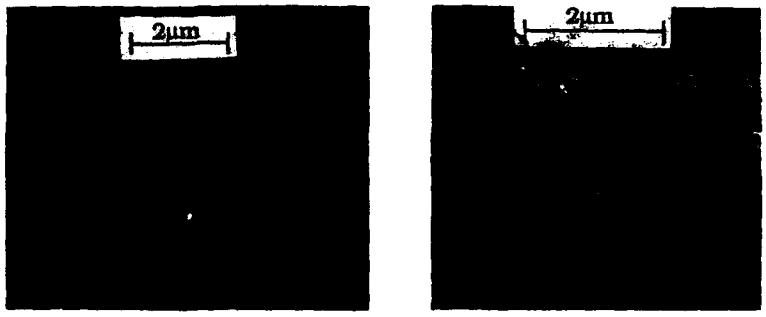
cooled slowly to room temperature without an annealing step, the film changes its semiconducting behavior (Figure.3: Samples a,b,c) to a conducting one (Figure 3: Sample d). The amount of CuO, detected in this film by X-ray diffraction, is apparently large enough to provide good densification but yet still small enough not to disturb the superconducting behavior of the film.

Figure 3: Superconducting transition for films



a) on MgO fired at 900°C for 12h
b) on alumina fired at 900°C for 12h
c) on MgO fired at 910°C for 1h an sintered at850°C
d) on MgO fired at 910°C for 1h without annealing at 450°C

Films produced, on MgO, by this "off stoichiometry process" are crack-free, with a thickness between 1 and 2μm and they have a Tc(R<10^{-3} Ω)=72°K. These films are composed mainly of the 1:2:3 phase and is highly oriented along the C-axis. The highly oriented texture is not visible under SEM investigation, as shown in Figure 4 [a]. This apparent contradiction between the two analysis techniques can be explained by the following hypothesis: the film contains two layers, a thin highly oriented layer underneath a thick randomly oriented one. The top, randomly oriented, layer is the only one visible under SEM and the thin highly oriented one is seen with the texture sensitive X-ray diffraction. The presence of these two layers is revealed by SEM investigation on a film scratched with diamond (Figure 4[b]). Critical current measurement were performed on a film deposited on a silver substrate and annealed at 910°C [15]. This investigation found a value of 10^4A/cm^2 in at 77°K. This high value of Jc indicates a well oriented structure which consequently agrees with the X-ray diffraction results.



(a) (b)

Figure 4: S.E.M micrograph of films on MgO fired at 910°C for 1h a) top-view and b) side-view of the scratched film

4 CONCLUSION

The process used is a simple dipping and pyrolysis of carboxilate solution on an appropriate substrate. By careful drying and pyrolysis, smooth crack-free films with a thickness of 1-2 µm were obtained. After appropriate firing, films are synthesized on MgO with a superconductive transition starting at 90°K and ending at 72°K (Tc, $R<10^{-3}\ \Omega$). This low Tc value could result from an imbalance stoichiometry in the precursor solutions which promotes the formation of insulating impurity phases. These films have a highly oriented crystallographic structure which results in high critical current value (Jc=13000 A/cm2 at 77°K). Films have been also synthesized on polycrystalline alumina with a superconducting transition from 60°K to 29°K. This decrease in the transition temperature is a result of the diffusion of aluminium into the film.

From this study, the stoichiometry of the precursors, temperature of firing, and time of firing, appear to be the predominant processing parameters. A careful study of their relative importance on the final characteristics of the films is needed to produce films with characteristic approaching those of physical deposition.

REFERENCES

[1] J.G. Bednorz, K.A. Müller, Condens. Matter 64 (1986) 189
[2] M.K.Wu, C.W.Chu, Physical Review Letters 58 (1987) 908
[3] M Kawai, T.Kawai, H.Masuhira, Mat. Res. Soc. proc. 99 (1988)
[4] R. L. Henry, H. Lessoff, J. of crystal growth 85 (1987) 615
[5] P.L.Villa, S.Zanella, V.Ottoboni, J. Less Comm. Met.150 (1989)
[6] C. E. Rice, R. B. Van Dover, G. J. Fisanick, Mat. Res. Soc. proc. 99 (1988)
[7] R.S.Liu, G.C.Lin, H.M.Sing, Y.C Chen, Mat. Res. Soc. proc. 99 (1988)
[8] P. Barboux, J. M. Tarascon, B. G. Bagley, L. H. Greene, G. W. Hull, B. W. Meagher, C.B. Eom, Mat. Res. Soc. proc. 121 (1989)
[9] A.H Hamdi, A.L.Micheli, R.C.Laugol J.V Mantese, Appl. Phys. lett. 51 (25) (1987)
[10] T.Kumagai, H.Yokota, K.Kawaguchi, Chem. Lett. 1987, 1645
[11] H.Nasu, S.Makida, T.Kato, Y.Ibara, Chem. Lett. 1987, 2403
[12] M.E.Gross, M.Hong, S.H.Liu, P.K.Gallagher, Mat. Res. Soc. proc. 99 (1988)
[13] T.Kumagai, H.Yokota, K.Kawaguchi, Chem. Lett. 1988, 551
[14] A.H Hamdi, A.L.Micheli, R.C.Laugol J.V Mantese, M.R.S. bulletin october 1989
[15] Dr C. Schüler private communication on November 15th

CHEMICAL PREPARATION OF SUPERCONDUCTING OXIDES USING CONVENTIONAL CHELATING AGENTS

Cyril Chiang and C. Y. Shei
Materials Research Laboratories, Industrial Technology Research Institute, Hsinchu, 31015, Taiwan, ROC.

ABSTRACT

Samples of $Bi_{1.4}Pb_{0.6}Sr_2Ca_2Cu_3O_y$ were prepared by sol-gel technique. The formation of polymeric chelate was made possible by oxalic acid in which metal cations are homogeneously distributed. The functional groups in the chelating agent determine the cation absorption rate that pH value is no more critical. XRD and SQUID showed that the compound has a nearly pure 2223 phase and T_c was measured at 110 K. The synthesis is reproducible and the process is amenable for scaling up.

1. INTRODUCTION

It is known that there are two Bi-Sr-Ca-Cu-O superconducting phases with critical temperature of 110 K (2223 phase) and 80 K (2212 phase).[1] Conventional solid state reaction of oxides with nominal composition of $Bi_2Sr_2Ca_2Cu_3O_y$ does not guarantee the formation of a single high-T_c phase. Takano *et al.* discovered that the partial substitution of Pb for Bi may stabilize the 2223 phase.[2] It was also revealed that additional Ca and Cu could accelerate the 2223 phase formation.[3]

Solid state reaction has slow kinetics because of the diffusion length. In order to prepare mainly high-T_c phase, the use of chemical precursors is essential in order to reduce the path between particles. The sol-gel technique generates ultrafine precursor powders permitting to lower the processing temperatures. Based on the formation of citrate complexes, the sol-gel process has been reported to prepare ceramic superconductors in the Y-Ba-Cu-O system.[4]

Sol-gel was not considered practical for the Bi-Sr-Ca-Cu-O system because of the low solubility of bismuth salt. Scientists reported that EDTA (ethylene-diamine-tetra-acetic acid) is capable of retaining bismuth cations in aqueous solution but the acidity has to be carefully normalized.[5] This paper describes a chelate of mixed cations, regardless of the bismuth, with a hydroxycarboxylic acid. The synthesis allows us to prepare pure 110 K phase without being required to monitor the pH in a small range.

In our study, sol is suppressed since bismuth cations are not completely complexed and the process is more likely a gelation step. Oxalic acid (HOOC-COOH) was used to chelate metal cations from corresponding metal nitrates. The exclusion of bismuth from the complexed precursor reduces the bismuth-loss during the sintering step, which consequently helps to form 110 K phase more accurately. The amount of the chelating agent has an impact on the organic decomposition, which determines a "clean" reaction. The molar ratio of oxalic acid to total nitrate anions from the metal salts was fixed at one half, in contrast to the claimed amount of two.[6] The following sections explain the advantages of the synthesis.

2. EXPERIMENTAL

The gel preparation was carried out with $Bi(NO_3)_3 \cdot 5H_2O$, $Pb(NO_3)_2$, $Sr(NO_3)_2$,

Mat. Res. Soc. Symp. Proc. Vol. 180. ©1990 Materials Research Society

$Ca(NO_3)_2 \cdot 4H_2O$, and $Cu(NO_3)_2 \cdot 3H_2O$. Based on 3 grams of copper nitrate, 5.1 grams of oxalic acid was added for the composition of $(Bi_{1.4}Pb_{0.6})Sr_2Ca_2Cu_3O_y$. After stirring for two hours, we titrated the solution with a 25% ammonium hydroxide solution from pH = 0.8 to pH = 5.6, 6.7 and 7.8, respectively. The solution was then placed in an 120°C oil bath for gelation. The gel color, reflecting the copper complex, increased along with the pH from light to deep blue. The gel was put into an open furnace for organic decomposition at 250°C/2 hrs and 300°C/1 hr. Calcination was done at 800°C for 12 hours in air. Powders obtained were then pelleted and air-sintered at 865°C for 54 hours.

The structure was determined by X-ray diffraction using a Ni-filtered Philips APD-1700 diffractometer (CuKα, λ = 1.5418 Å). A Quantum Design SQUID magnetometer was used to record magnetization curves in a field of 10 Oe between 5 K and 130 K. Differential Thermal Analysis (DTA) of calcined powder was carried out in air using a ULVAC 7000 thermoanalyzer. Particle morphology was monitored with a Hitachi scanning electron microscope (SEM) and a JEOL 2000FX transmission electron microscope (TEM) operating at 200 kV.

3. RESULTS AND DISCUSSION

It was suggested that the molar ratio of oxalic acid to total nitrate anion should be fixed at two.[6] Our results showed that too much chelating agent would destroy the BPSCCO 2223 stoichiometry to a poorly performed 80 K phase. We reduced the oxalic acid to only one half mole of the existing nitrate anions. Figure 1 depicts the resistivity of $Bi_{1.4}Pb_{0.6}Sr_2Ca_2Cu_3O_y$, which shows a sharp, clean decline regardless of the solution acidity. Zero resistance was reached at 111 K, 109 K, 110 K for pH = 5.6, 6.7, 7.8, respectively. Unlike the large 110 K resistivity transitions reported with insignificant amount of 2223 phase,[7-9] 110 K phase dominates in our XRD results (Figure 2). SQUID measurements confirmed the phase distribution (Figure 3). The calcined powder reveals the advantages of precursor synthesis. Figure 4 displays TEM photograph for the powders after complete organic decomposition at 800°C/12 hrs. Powders obtained are rod-like with particle size in the range of 0.2 μm. DTA result exhibits an evident endothermic peak around 865°C. This is important for the 110 K phase stabilization, by which the sintering condition was determined. Morphology of the sintered pellet samples are given in Figure 5.

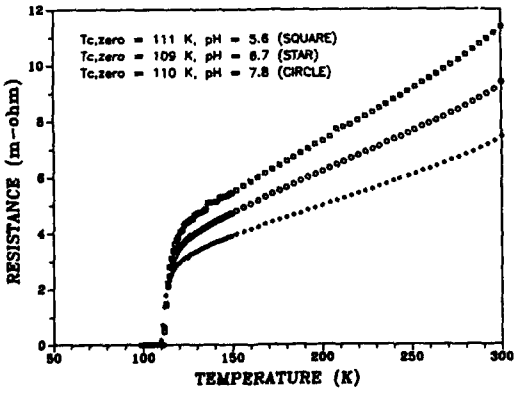


Fig. 1: Resitivity vs. temperature

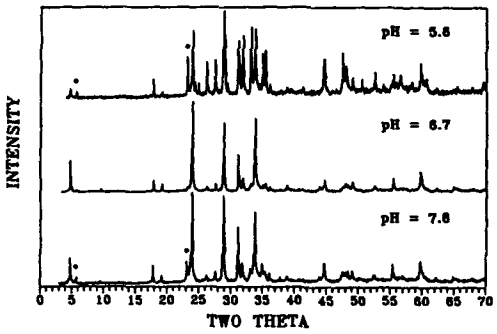


Fig. 2 (above): XRD at various pH values

Fig. 3 (below): SQUID measurements

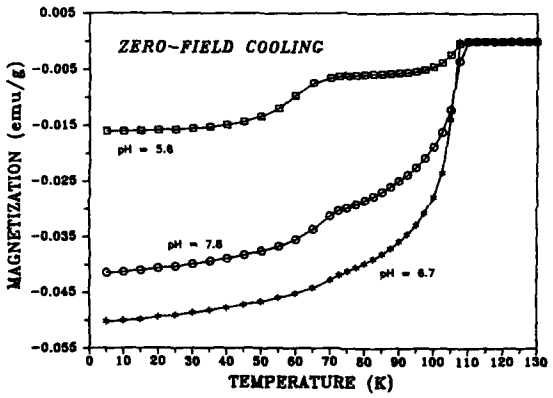




Fig. 4: Precursor TEM

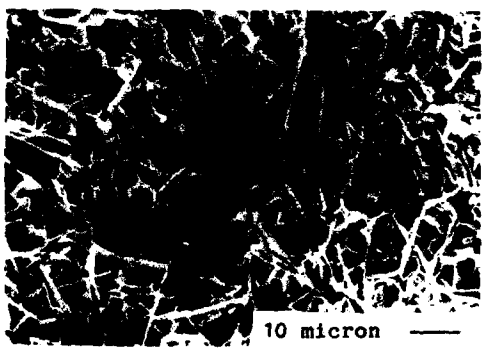


Fig. 5: SEM of final pellet

We have demonstrated that when the right amount of organic catalyst is used, the reaction becomes clean and under control. Since the bismuth cation cannot be well complexed, this work shows no significant reduction for sintering temperature. This has been overcome when the stoichiometry is enriched by Ca and Cu.[10,11] By the sol-gel technique, pure 110 K single phase can be prepared within 20 hours at a lower temperature. Details will be published elsewhere.

In conclusion, we have revised the novel sol-gel technique by more careful control of the carboxyl agent. Homogeneous precursor powders are highly reactive, ready for use, and requiring no more milling. With the problems encountered by other synthetic methods for Bi-Sr-Ca-Cu-O system, this study shows the possibility to obtain 110 K superconductive ceramics in large quantity via the most economical use of chemicals.

4. ACKNOWLEDGEMENT

This work was supported by the Ministry of Economic Affairs, Republic of China, under the contract number 33B1000 to the Industrial Technology Research Institute.

5. REFERENCES

1. H. Maeda, Y. Tanaka, M. Fukutomi, and T. Asano, Jpn. J. Appl. Phys., 27, L-209, (1988).
2. M. Takano, J. Takada, K. Oda, H. Kitaguchi, Y. Miura, Y. Ikeda, Y. Tomii, and H. Mazaki, Jpn. J. Appl. Phys., 27, L-1041, (1988).
3. A. Sumiyama, T. Yoshitomi, H. Endo, J. Tsuchiya, N. Nijima, M. Mizuno, and Y. Oguri, Jpn. J. Appl. Phys., 27, L-542, (1988).
4. C. -T. Chu, B. Dunn, J. Am. Ceram. Soc., 70, C-375, (1987).
5. J. Fransaer, J. R. Roos, L. Delaey, O. van der Biest, O. Arkens, and J. P. Celis, J. Appl. Phys., 65(8), 3277, (1989).
6. V. Slusarenko, K. R. Thampi, J. Kiwi, J. Solid State Chem., 79, 277, (1989).
7. M. Mizuno, H. Endo, J. Tsuchiya, N. Kijima, A. Sumiyama and Y. Oguri, Jpn. J. Appl. Phys., 27, L-1225, (1988).
8. K. Aota, H. Hattori, T. Hatano, K. Nakamura and K. Ogawa, Jpn. J. Appl. Phys., 28, L-2196, (1989).
9. Y. Hakuraku, K. Kittaka, S. Higo and T. Ogushi, Jpn. J. Appl. Phys., 28, L-67, (1989).
10. Y. T. Huang, C. Y. Shei, W. N. Wang, C. K. Chiang, W. H. Lee, submitted to *Physica C*, (1990).
11. Y. T. Huang, W. N. Wang, S. F. Wu, C. Y. Shei, W. -H. Hurng, W. H. Lee and P. T. Wu, submitted to J. Am. Cera. Soc., (1990).

SYNTHESIS OF SUPERCONDUCTING PEROVSKITE BY COPRECIPITATION OF HYDROXIDES

I. Valente-Campion, P. Barboux, L. Mazerolles, D. Michel, R. Morineau and J. Livage
Chimie de la Matière Condensée, Université P. et M. Curie, 4 Place Jussieu 75005 Paris, France

ABSTRACT

The synthesis of the superconducting perovskite $YBa_2Cu_3O_7$ using hydroxides as starting precursors has been investigated. Hydroxides are homogeneously coprecipitated from mixed alcohol-water solutions without loss of barium. Upon heat-treatment the perovskite phase rapidly forms around 750°C. However, it remains tetragonal even after long time annealing in oxygen ambient. This is related to an unusual microtwinning in the (ac) plane.

INTRODUCTION

The superconducting properties of the $YBa_2Cu_3O_7$ perovskite are very sensitive to the microstructure of ceramics[1]. Experience has shown that grain alignment is necessary to increase the superconducting links between the grains of the ceramics. A simple way to achieve this is the synthesis of textured films supported by a substrate that is commonly an oxide such as $SrTiO_3$, ZrO_2 or MgO. In order to obtain large critical currents both reaction with the substrate and shrinkage have to be avoided by lowering the reaction temperature.

This can be achieved by solution techniques through a better mixing of the starting reagents at a molecular level. Moreover, controlled precipitation or "sol-gel" techniques yield solutions whose rheological properties allow thin film deposition via spin-coating or dip-coating procedures[2]. However, most of these techniques use carbon containing chemical species as the starting precursors (acetates, carbonates...). Upon heat treatment a phase separation into CuO, Y_2O_3 and barium carbonate, $BaCO_3$, occurs. This latter is quite unreactive and slowly decomposes to react with other elements between 900-950°C, a temperature range where substrate reaction and particle growth simultaneously occur.

We report on the precipitation of hydroxides as a way to low temperature synthesis of textured films or ceramics. Precipitation of hydroxides may be simply done through addition of a base to an aqueous solution. Yttrium and copper hydroxides have a similar precipitation range(pH≈7) but the less polarizing Ba^{2+} cation requires a too high pH in order to obtain complete precipitation.

Mat. Res. Soc. Symp. Proc. Vol. 180. ©1990 Materials Research Society

EXPERIMENTAL

The synthesis procedure has already been discussed[2]. The three hydroxides are coprecipitated from the nitrates in a mixed alcohol-water solution by addition of NaOH 2N in ethanol. The precipitate is then filtered and washed two times with 200 ml of a 70% volume acetone and 30% water mixture. Samples are handled under argon ambient to avoid adsorption of CO_2 (leading to $BaCO_3$). After washing, the precipitate is dried at 120°C under vacuum. The resulting powders are pressed into pellets under a $12t/cm^2$ pressure before to be heated under oxygen flow for 12 hours at different temperatures ranging from 750°C to 950°C. Samples are then slowly cooled down to room temperature at a rate of 60°C/h.

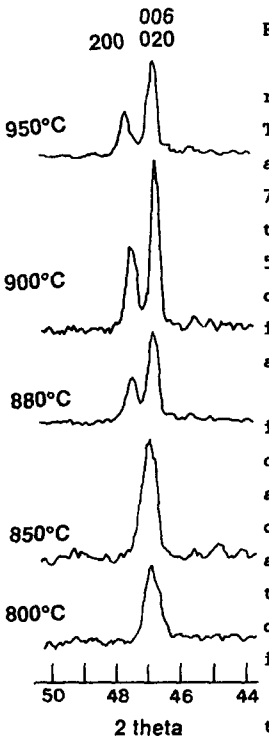


Figure 1: x-ray diffraction pattern for ceramics heat-treated at different temperatures.

RESULTS

For all the temperatures described here, the x-ray pattern corresponds to the pure triperovskite. This can even be achieved upon heating only 20 minutes at 850°C. However, for processing temperatures between 750°C and 850°C the resulting phases are apparently tetragonal even after longer oxygen annealings at 500°C. A tetragonal to orthorhombic transition is observed when the processing temperature is increased above 850° (Fig.1). Similar results have already been described[3].

Since the tetragonality of the $YBa_2Cu_3O_7$ compound is often related to a loss of oxygen we analyzed the oxidation state using iodometric titration. Results are shown in Figure 2a and 2b. Indeed, the tetragonal-orthorhombic transition that we observe is related to a low oxygen content of the phases of 6.65 ± 0.03 and the transition can be associated to a sudden increase of the oxygen composition to its common value of 6.93 in the $YBa_2Cu_3O_{6.93}$ superconducting material.

However, some questions remain since our tetragonal phase cannot recover oxygen. Moreover, Fig.2c shows the evolution of the a and b parameters with the oxygen contents of our phases as compared to the same parameters observed when oxygen is removed from a cristallized structure[4](Fig.2d). Note also that our tetragonal phases have an average oxidation state larger than 6.50

which is contrary to results observed elsewhere in well cristallized samples.

Fig. 3 shows a high resolution electron micrograph taken on a tetragonal phase heated at 800°C for 12 hours. We observe very small particles that are microdomains of twins, about 20 nm large. These twins are characteristic of stackings along the c axis that are perpendicular to each other. This can be observed on the diffraction pattern as well. Diffraction spots with a tripling of the cell (since $c^*=a^*/3$) along both perpendicular directions are clearly observed. They are thus related to twins in the (a,c) planes. Such a stacking fault may explain why a full recover of the oxygen content is not possible. Indeed, the oxygen conducting planes are suddenly interrupted by non equivalent sites. Upon heat treatment above 850°C these (a,c) plane twins are replaced by the usual twins in the (a,b) plane characteristic of the orthorhombic phase.

DISCUSSION

The use of hydroxide coprecipitation allows the synthesis of a pure superconducting phase at 750°C. However, even after oxygen annealing, the

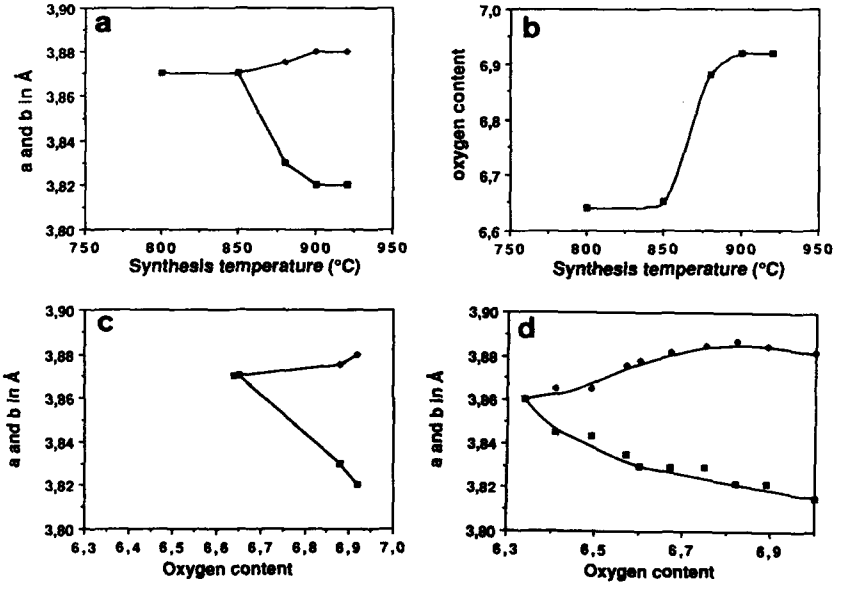


Figure 2: Analysis of $YBa_2Cu_3O_y$ ceramics from hydroxide precipitates.
a) cell parameters as a function of the synthesis temperature.
b) oxygen content y as a function of the synthesis temperature
c) a and b parameters as a function of the oxygen content
d) a and b parameters as a function of oxygen content for well cristallized phases. From Mc Kinnon et al.[4].

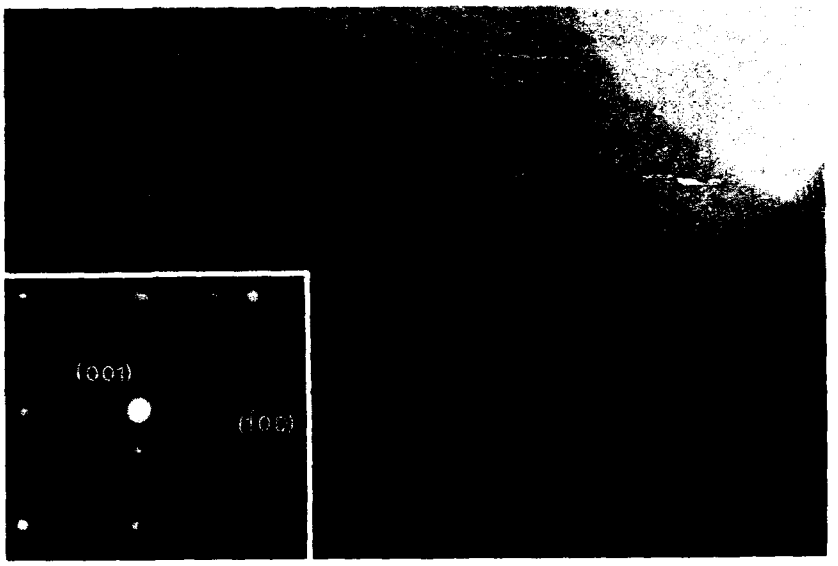


Figure 3: High resolution Electron Microscopy of $YBa_2Cu_3O_{6.65}$ obtained from a precipitate of hydroxide after 12 h at 800°C in oxygen ambient.

phase remains tetragonal with poor superconducting behavior. This can be attributed to a microtwinning in the (a,c) plane that blocks the oxygen stoichiometry at 6.65.

Such twins are usual in perovskite families and they relate to the cubic nature of the perovksite building blocks(ABO_3). During a very rapid synthesis at low temperature, the buildings blocks may stack on each other along the three possible directions. As a result, since the tetragonal phase is associated here to a cationic disorder better than to the usual oxygen disorder, higher temperatures are required to displace the cations and obtain the orthorhombic structure. This may be an additional difficulty in ceramic processing from solutions.

REFERENCES

1) D.W. Murphy, D.W. Johnson, S. Jin and R.E. Howard; Science 241 (1988) 922.
2) P. Barboux, I. Valente, J.M. Tarascon, S. Khan, F. Shokoohi, M. Henry, R. Morineau and B.G. Bagley, Mat. Res. Soc. Symp. Proc. Vol 156 (1989) 189.
3) A. Manthirham and J.B. Goodenough, Nature, 379 (1987) 701.
4) W.R. McKinnon, M.L. Post, L.S. Selwyn, G. Pleizier, J.M. Tarascon, P. Barboux, L.H. Greene and G.W. Hull, Phys. Rev. B 38 (1988) 6543.

SUPERCONDUCTING $YBa_2Cu_3O_{7-x}$ FIBERS FABRICATED BY THE SOL-GEL METHOD USING METAL ALKOXIDES

SHINGO KATAYAMA AND MASAHIRO SEKINE
Colloid Research Institute, 350-1 Ogura, Yahata-higashi-ku, Kitakyushu 805, Japan

ABSTRACT

Superconducting $YBa_2Cu_3O_{7-x}$ fibers were fabricated by the sol-gel method using modified metal alkoxides. To prepare precursors of a homogenous and viscous sol, Y and Cu alkoxides were modified with ethyl acetoacetate(EAA) and ethylenediamine(en), respectively. Their structures were determined by FT-IR and EXAFS. The sol prepared from modified alkoxides was spun into gel fibers by the spinning apparatus. They were subsequently fired to obtain superconducting fibers.

INTRODUCTION

The sol-gel method using metal alkoxides is of interest as means to fabricate superconducting oxide fibers because many ceramic and glass fibers have been produced successfully by this method. To fabricate $YBa_2Cu_3O_{7-x}$ fibers by this method, a homogeneous and viscous solution from metal alkoxides must be used for spinning. However, preparation of such a solution is difficult owing to the insolubility of Y and Cu alkoxides and high reactivity of Ba alkoxide with water. Although a viscous sol has been prepared by the hydrolysis of modified alkoxide[1], structures of modified alkoxides have yet to be determined.

In this paper, alkoxide precursors were designed for preparing a homogeneous and viscous sol through a Y-Ba-Cu complex alkoxide and the structures of alkoxide precursors were confirmed. The sol was continuously spun into gel fibers using a spinning apparatus and the fired fibers were characterized.

EXPERIMENTAL

1 mol of $Y(O\text{-}^iC_3H_7)_3$ was modified with 1 mol of EAA and 1 mol of $Cu(OCH_3)_2$ with 2 mol of ethylenediamine. Their structures were confirmed by FT-IR and EXAFS. To prepare a Y-Ba-Cu complex alkoxide, the modified Cu alkoxide in ethanol was partially hydrolyzed with equimolar water and mixed with Ba and Y alkoxides at a Y:Ba:Cu molar ratio of 1:2:3. Further hydrolysis was conducted at a H_2O/alkoxide molar ratio of 1 and the system was concentrated under reduced pressure to a viscous sol. This was spun into gel fibers using with a 12 hole-nozzle (diameter=160μm) spinning apparatus. The gel fibers were fired at 900°C for 1h in O_2 and characterized by SEM and XRD. Superconductivities were determined from AC susceptibility.

RESULTS AND DISCUSSION

$Y(O\text{-}^iC_3H_7)_3$ was modified with EAA to increase its solubility and reduce the reactivity of one of OR groups. The FT-IR spectrum of the modified Y alkoxide showed peaks at 1620 and 1515cm^{-1} which were assigned to C-O and C-C vibrations at the yttrium chelate link with EAA, respectively[2]. There are also

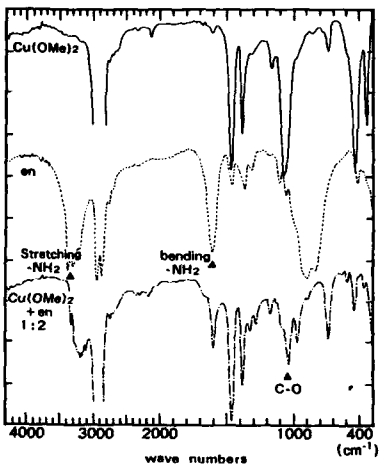


Fig.1 FT-IR sprectra of $Cu(OCH_3)_2$, ethylenediamine, and modified Cu alkoxide.

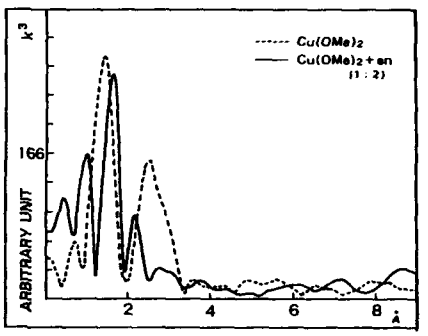


Fig.2 Fourier transforms of EXAFS spectra of $Cu(OCH_3)_2$ and modified Cu alkoxide.

peaks due to iso-propoxy groups. It is thus evident that the iso-propoxy group is partially substituted by EAA to from a chelate compound of $Y(O\text{-}^iC_3H_7)_2(EAA)$.

$Cu(OCH_3)_2$ was modified with ethylenediamine so as to make it soluble. Its structure was confirmed by FT-IR and EXAFS. The FT-IR spectra of $Cu(OCH_3)_2$, ethylenediamine, and modified Cu alkoxide are shown in Fig.1. The spectrum of ethylenediamine showed peaks of N-H stretching vibration between 3250 and 3400cm^{-1}, but these peaks in the modified Cu alkoxide shifted to a lower wave number where $Cu(OCH_3)_2$ had no peak, due to coordination of ethylenediamine with $Cu(OCH_3)_2$. The FT-IR spectrum of the modified Cu alkoxide also showed a peak at 1050cm^{-1} corresponding to C-O vibration of the methoxy groups.

Fourier transforms of the EXAFS spectra of $Cu(OCH_3)_2$ and modified Cu alkoxide are shown in Fig.2. $Cu(OCH_3)_2$ indicated two distinct peaks, located at the same position as the nearest O atoms around Cu of CuO and the other at the nearest Cu atoms of Cu neighbors owing to highly polymeric structure of $Cu(OCH_3)_2$[3]. The modified Cu alkoxide had only one peak corresponding to the nearest O or N atoms. The modified Cu alkoxide thus exists in a monomeric form of $Cu(OCH_3)_2(en)_2$ by coordination of ethylenediamine with $Cu(OCH_3)_2$, as in the case of Ti, Al, Zr, and Ta alkoxides[4].

$Ba(OC_2H_5)_2$ is soluble in ethanol, but precipitation occurs by hydrolysis in spite of the addition of alkylaminoalcohols[5] or β-diketones[6] often used to decrease alkoxide reactivity. Accordingly, $Ba(OC_2H_5)_2$ was reacted with partially hydrolyzed $Cu(OCH_3)_2(en)_2$ in the presence of the modified Y alkoxide. The possible reactions are as follows:

$$Cu(OCH_3)_2(en)_2 + H_2O \longrightarrow Cu(OCH_3)(en)_2(OH) + CH_3OH$$

$$Cu(OCH_3)(en)_2(OH) + M(OR)_n \longrightarrow (CH_3O)(en)_2Cu\text{-}O\text{-}M(OR)_{n-1} + ROH$$

where M=Y, Ba.

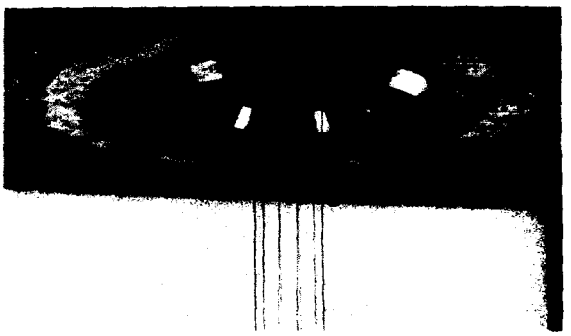
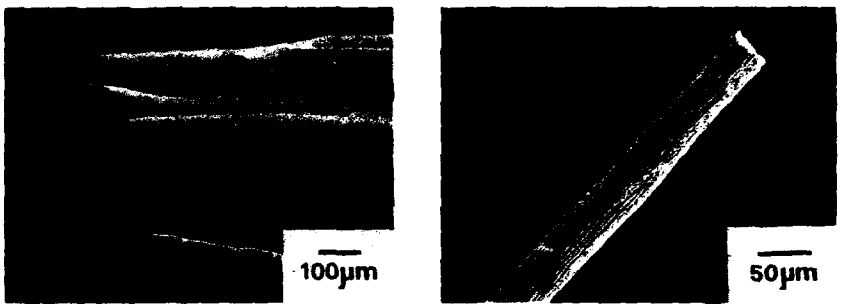


Fig.3 Photograph of gel fibers through 12 holes-nozzle (hole-diameter:160μm).



gel fibers fired fibers

Fig.4 SEM photographs of the gel fibers and fibers fired at 900°C for 1h in O_2.

The above Y-Ba-Cu complex alkoxide was hydrolyzed without precipitation. The formation of the Y-Ba-Cu complex alkoxide requires reactive alkoxy groups such as methoxy groups in the form of $Cu(OCH_3)_2(en)_2$ even after modification. Other modifiers such as 2-dimethylaminoethanol, also effective for increasing the solubility of $Cu(OCH_3)_2$ were not suitable owing to the very low reactivity of OR-substituted Cu alkoxide with water[7].

The hydrolyzed Y-Ba-Cu complex alkoxide was concentrated to a viscous sol which was subsequently spun easily into gel fibers as shown in Fig.3. SEM photographs of the gel fibers and fibers fired at 900°C for 1h in O_2 are shown in Fig.4. The gel fibers were about 100μm in diameter. The surface of the gel fibers had many wrinkles due to shrinkage during evaporation of the solvent after gelation of the surface. The fired fibers were about 50μm in diameter and a porous and polycrystal structure with a grain size of 0.5μm. Shrinkage of 50% occurred as a result of firing the fibers. XRD of the fired fibers mainly showed the $YBa_2Cu_3O_{7-x}$ phase, as indicated in Fig.5. The AC magnetic susceptibility of the fired fibers had a Tc onset = 65K as shown in Fig.6.

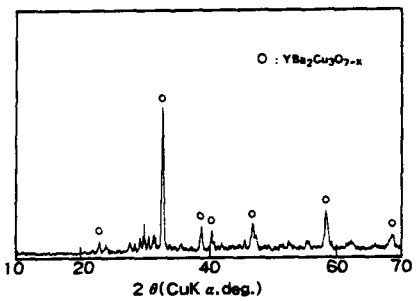


Fig.5 XRD of the fibers fired at 900°C for 1h in O_2.

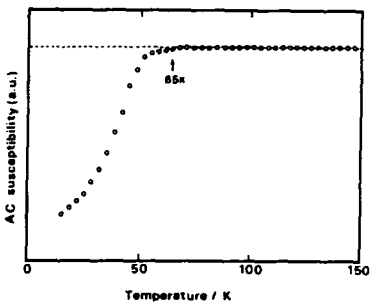


Fig.6 Temperature dependence of AC magnetic susceptibility of the fibers fired at 900°C for 1h in O_2.

CONCLUSIONS

$Y(O\text{-}^{i}C_3H_7)_3$ and $Cu(OCH_3)_2$ were modified by the formation of a chelate compound with EAA and ethylenediamine, respectively, to prepare the Y-Ba-Cu complex alkoxide as a starting material of a spinnable sol. The sol through this complex alkoxide was successfully spun into gel fibers by a spinning apparatus. The fired fibers showed superconductivity with Tc(onset)=65K.

ACKNOWLEDGMENTS

Financial support for this work was provided by the Japan Key Technology Center. The authors thank Dr. Y. Udagawa and Dr. K. Tohji at Institute for Molecular Science for conducting the EXAFS experiments, and also Mr. A. Noguchi for doing the spinning. The assistance of Miss A. Kamimura is gratefully acknowledged.

REFERENCES

1. H. Zheng, K. C. Chen, and J. D. Mackenzie, High-Temperature Superconductors II, edited by D. W. Capone II, W. H. Butler, B. Batlogg, and C. W. Chu(Mat. Res. Soc. Extended Abstracts, Reno, Nevada 1988), p.93.
2. R. K. Mehrotra and R. C. Mehrotra, Can. J. Chem. 39, 795(1961).
3. C. H. Brubaker, Jr. and M. Wicholas, J. Inorg. Nucl. Chem. 27, 59(1965).
4. M. S. Bains and D. C. Bradley, Can. J. Chem. 40, 2218(1962).
5. Y. Takahashi and H. Naganawa, Yogyo-Kyokai-shi 95(11), 1107(1987).
6. J. Livage, Better Ceramics Through Chemistry II, edited by C. J. Brinker, D. E. Clark, and D. R. Ulrich(Mater. Res. Soc. Proc. 73, Pittsburgh, PA 1987) p.717.
7. S. Katayama and M. Sekine, J. Mater. Res. (in press).

SOL-GEL PROCESSING OF THE $Tl_2Ca_1Ba_2Cu_2O_{8+x}$ HIGH Tc SUPERCONDUCTING PHASE

M. R. Teepe, D. S. Kenzer, G. A. Moore, and G. Kordas
Department of Materials Science and Engineering, Ceramics Division, and Science and Technology Center for Superconductivity, University of Illinois at Urbana-Champaign, 105 S. Goodwin, Urbana, IL 61801

Abstract

An alkoxide Sol-Gel system was developed to produce bulk powders of the $Tl_2Ca_1Ba_2Cu_2O_{8+x}$ high T_c superconducting phase. Methoxyethoxide and Cu(II) ethoxide precursors were used for the formation of homogeneous sols. Solubility of the Cu(II) ethoxide was aided by using a 2-methoxyethanol/methyl ethyl ketone/toluene solvent system. The sols were characterized by small angle x-ray scattering (SAXS) and TEM. Powders were produced by rotary evaporation followed by thermal treatment in a closed container with thallium metal present at 900 °C for various calcination times. Powders were characterized by x-ray diffraction, resistivity and magnetic susceptibility measurements, and chemical analysis. Samples exhibited transition onsets between 100 and 110K depending upon the processing conditions.

Introduction

Since the discovery [1-3] of superconductivity in the Tl-Ca-Ba-Cu-O system, much work has been done to determine the structure and properties of the superconducting phases in this system. These phases can be summarized as $Tl_mCa_{n-1}Ba_2Cu_nO_{m+2(n+1)}$ [4] with n=1, 2 and 3 and m=2 exhibiting T_c values of 90 K [1,2], 108 K [5], 125 K [5], respectively. The n-, m-, and T_c- values depend strongly on the synthesis conditions [5,6]. Typical preparation conditions involve thorough mixing of Tl_2O_3, CaO, BaO, and CuO in the desired ratios and firing at temperatures ranging from 880 to 950 °C in sealed containers [5-7]. An alternative preparation method has been reported [8] which utilizes single phase $CaBa_2CuO_4$ as the Ca and Ba source to avoid the use of the corrosive and hygroscopic CaO and BaO materials.

Previous work in this field has shown that superconducting powders and films can also be produced by the sol-gel technique . Using the spin or dip coating processes, for example, thin films can be produced which are uniform and highly oriented [9]. Using the sol-gel process for these types of materials may therefore prove to be quite useful for a variety of applications.

In this paper, we report a newly developed sol-gel route for the formation of the $Tl_2Ca_1Ba_2Cu_2O_{8+x}$ superconducting phase.

Experimental Procedure

Figure 1 outlines the procedure for sample preparation in the Tl-Ca-Ba-Cu system by the sol-gel method. This process begins with the solubilization of the individual metal components to form alkoxide precursors. For this process, Cu(II) ethoxide was used and synthesized as follows:

$$Cu(II)Cl_2 + 4Li(C_2H_5O) \text{ ------> } Cu(II)(C_2H_5O)_2 + 2LiCl + 2Li(C_2H_5O)$$

The formation of the undesirable copper chloride ethoxide was avoided by using excess lithium ethoxide.[10] The copper ethoxide was separated from solution by means of a pressurized filtration device utilizing a 5 μm PTFE membrane. Pure ethanol was forced through the resulting cake to remove residual lithium chloride and lithium ethoxide. Rinsing continued until no chloride was detected in the ethanol upon reaction with an aqueous silver nitrate solution. The copper ethoxide cake was then partially solubilized in an equal mixture of 2-

methoxyethanol/ methyl ethyl ketone (MEK)/ and Toluene by ultrasonication and continued mechanical stirring.

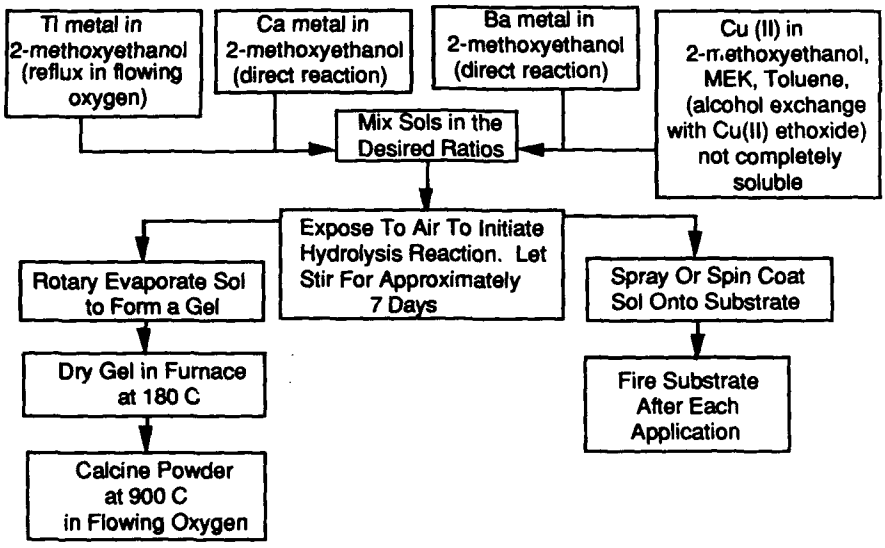


Figure 1. Flow chart of sample preparation in the Tl-Ca-Ba-Cu-O system by sol-gel methods.

Barium methoxyethoxide was produced by direct reaction of barium metal in 2-methoxyethanol to form a clear stable solution. This reaction is highly exothermic and was carried out in an inert argon atmosphere. Calcium methoxyethoxide was formed by direct reaction as well in an argon dry box. This produced an opaque purple solution which upon filtering through a disposable 0.5 μm filter became clear with a slight yellowish tint.

Synthesis of thallium methoxyethoxide was accomplished by two separate methods. The first method utilized 99.9999% pure thallium metal and was synthesized via the following series of reactions as was reported by Bradley in forming Thallium(I) ethoxide:[11]

$$2Tl + 1/2O_2 \text{ ----> } Tl_2O$$

$$Tl_2O + 2CH_3OC_2H_4OH \text{ ----> } 2Tl(CH_3OC_2H_4O) + H_2O$$

A bar of thallium metal was placed in a reflux of 2-methoxyethanol under flowing oxygen. A temperature of 120 °C was used to eliminate as much of the water as possible. This produced a clear yellow solution with a soft precipitate forming on the sides of the container. This precipitate is thought to be either a thallium methoxyethoxide gel formed by reaction of the alkoxide with residual water, or simply precipitated thallium methoxyethoxide due to limited solubility in the parent alcohol. The resulting solution was filtered with a 0.5 μm filter to remove any suspended particulates.

An alternative method of forming thallium methoxyethoxide was accomplished by refluxing thallium trioxide with 2-methoxyethanol in air. This produced a clear orange-yellow solution which was filtered to remove any unreacted powder particles. This alternative method was investigated in an attempt to form a Tl 3+ precursor.

Four component sols were produced by adding the thallium, calcium, and barium precursors in the desired ratios to the partially soluble copper mixture. A starting ratio of 2:2:2:3 was investigated. Stable green sols were obtained after exposing the solution to air for a

period of approximately six days. Exposure to the air enabled the alkoxide precursors to react with moisture in the atmosphere, thus producing a network of metal-oxygen bonds through a series of hydrolysis and condensation reactions. The average particle size of the stable sols was determined by placing a drop of solution on a carbon coated copper grid, allowing it to dry, and analyzing with TEM. The fractal dimension of a typical four component sol was also determined by using small angle x-ray scattering (SAXS) techniques.

Gel powders were produced from the final sols through a rotary evaporation process which strips away the solvent and leaves a gel powder with the desired metal ratios. Gels were dried at 180 °C for four hours prior to calcination to remove residual solvent groups. Due to the high volatility and toxicity of the thallium component, special firing procedures were required. Two alumina boats (1 x .5 x .125 in.) were used as a sample holder, one of which contained the powder while the other served as a cover. The boats were tied together tightly with thermocouple wire. In most runs, a 0.1 gram shot of thallium metal was placed in the sample holder to help prevent thallium loss in the sample. The sample was placed inside of a quartz tube with oxygen flow supplied through one end. The entire tube was then slowly inserted into a round ended quartz tube furnace set at 800 °C. A ramp rate of 20°C/min was used to heat the sample to 900 °C and held for varying times. The furnace was then cooled down to 800 °C at a rate of 20 °C/min and the sample tube was slowly taken out of the furnace.

X-ray diffraction was used to determine the phases present in the resulting powders. Magnetic susceptibility measurements were then performed on the powders with a Quantum Design SQUID device to determine the magnetic response, and the transition temperature. A conventional four point probe measurement was done on a pressed pellet using a 0.5 mA current source to further study the transition region. Chemical analysis (ICP) was also done to evaluate the thallium loss in the samples.

Results and Discussion

An inductively coupled plasma (ICP) technique was used on gels produced from each of the two types of thallium precursors to determine if processing conditions may have had any effect on the valence state of the thallium. The mass percent ratios for $Tl(OCH_2CH_2OCH_3)$ and $Tl(OCH_2CH_2OCH_3)_3$ were calculated as 73 Tl, 12.9 C, 2.53 H and 47.6 Tl, 25.2 C, 4.9 H, respectively. Experimental values for precursors produced from metal and oxide powder were 84.72 Tl, 4.28 C, .26 H and 87.95 Tl, 3.95 C, .07 H, respectively. These results suggest the formation of $Tl(OCH_2CH_2OCH_3)$ rather than the formation of $Tl(OCH_2CH_2OCH_3)_3$. Slight differences in calculated and observed values can be attributed to the possible formation of Tl-O-Tl bonding.

The typical particle size of a stable four component sol was determined using TEM. From this, the average particle size in solution was estimated at 50 nm. The shape of the particles was highly irregular as can usually be expected for polydisperse polymer networks. The fractal dimension of these particles as determined by SAXS techniques was found to be 1.8. In an oversimplified view, this indicates a hybrid particle (fractal) structure demonstrating 2 dimensional planar and linear growth. Such information can be useful when studying the structural development of the sol to gel transition. This development has a major effect on such characteristics as sol rheology, drying characteristics, and thermal decomposition and consolidation.[12] A 2-dimensional planar/linear structure was expected for this system due to the presence of divalent and monovalent metal cations. Trivalent cations generally constitute a structure which involves three dimensional cross-linking, thus giving a fractal dimension between 2 and 3.

Figure 2 shows x-ray data for a Tl-Ca-Ba-Cu gel powder with starting ratios of 2:2:2:3. Samples were fired at 900 °C for 30 min, 60 min, and 180 minutes with Tl metal present in the sample chamber. Each spectra shows strong evidence of the 2122 high T_c phase as determined from JCPDS. Samples fired for 30 and 60 minutes contain the least amount of impurity phases. Nearly every peak can be attributed to the 2122 phase. At 180 minutes, 2122 becomes less dominant as other phases begin to appear. Chemical analysis of each of the final powders showed an increase in thallium loss with firing time. After 60 minutes of calcination at 900 °C, a 10% Tl loss was observed. After 180 minutes, this value jumped to 50%. No change in Tl content was observed in the 30 minute sample. For comparison, another 30

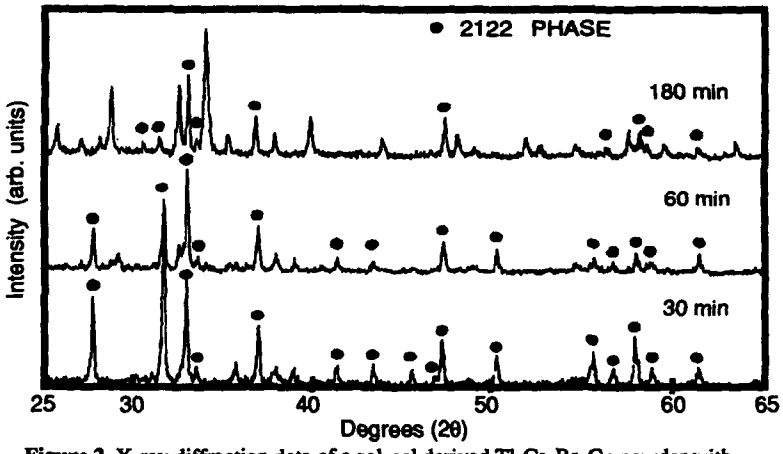


Figure 2. X-ray diffraction data of a sol-gel derived Tl-Ca-Ba-Cu powder with starting ratios of 2:2:2:3.

minute sample was prepared without the addition of extra thallium in the sample chamber. In this sample, 80% of the thallium was given off.

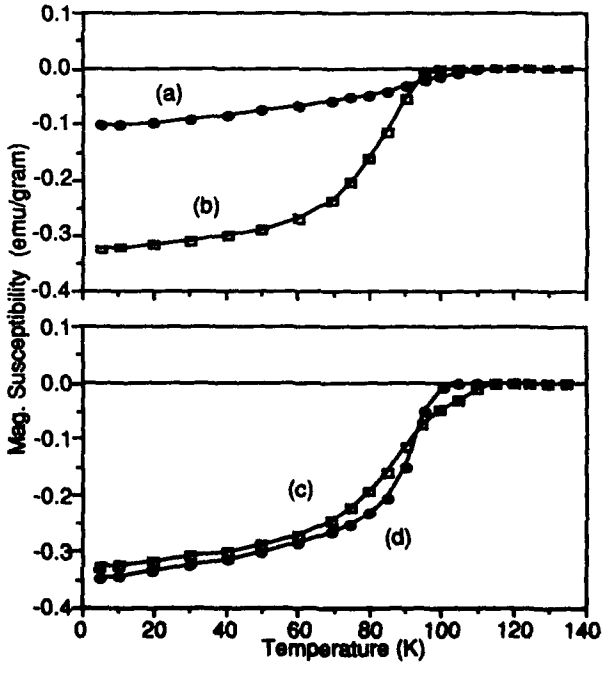


Figure 3. Susceptibility curves for samples with 2:2:2:3 initial ratios fired at 900°C: a,b) fired without and with Tl metal for 30 min, c,d) with Tl metal for 60 and 180 min.

Magnetic susceptibility measurements were performed on each of these samples to determine the effect of firing time and Tl concentration on the transition region. Figure 3 shows susceptibility curves for the 2:2:2:3 samples fired with and without Tl pressure for 30 minutes. A dramatic difference in the two responses is observed. A much larger response value was obtained for the sample fired with Tl metal present. As seen from the chemical ratios of the two final powders, a considerable Tl loss occurred in the powder from curve (a). This undoubtedly lead to a reduction in the percentage of superconducting phase in the overall sample leaving various oxides of the other three components. Although the response of curve (a) is much lower than (b), the transition temperature appears to be approximately 10 K higher than (b), giving it an initial drop-off at 110 K. ΔT_c is however much larger due to the additional presence of non superconducting phases.

The susceptibility curves for the samples fired for 60 and 180 minutes are also given in figure 3. Curve (d) has a drop-off beginning at 100 K which is even steeper than the 30 minute sample given as curve (b). This was quite unexpected because of the multiphase nature of the 180 minute sample as seen from the additional peaks in the x-ray pattern. A much broader transition region is normally observed for samples exhibiting multiphase behavior. Curve (c) differs from the 30 min sample as well even though the x-ray patterns are nearly identical. The transition begins at 110K which is normally expected for the 2122 phase and the transition region appears slightly broader.

The presence of secondary phases in these samples is likely since the ratios of the reactants is different than the stoichiometry of the final structure. Therefore, the broadness of these transitions is expected. Others have shown that for this system, the 2122 and 2223 high T_c phases are produced most readily from powders with ratios different from the final phase.[5,13,14] Therefore, unreacted oxide phases will necessarily form, reducing the percentage of superconducting phase. The transition regions for these materials are therefore expected to be broader than those normally observed for the YBCO system.

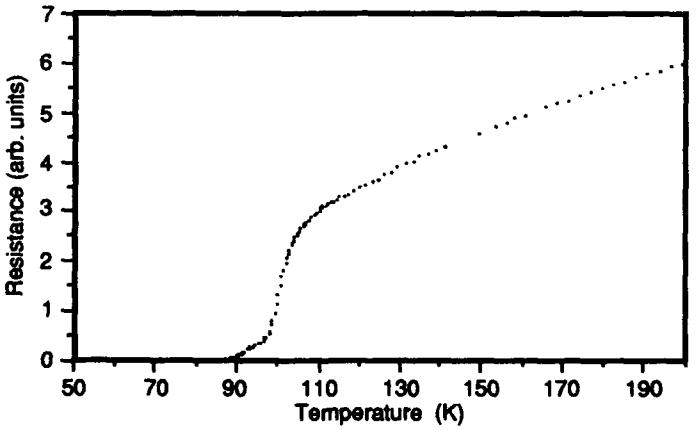


Figure 4. Resistivity vs. Temp curve for Tl-Ca-Ba-Cu pellet with 2:2:1:3 starting ratios fired at 900 °C.

Figure 4 shows a resistivity curve for a Tl-Ca-Ba-Cu pellet with 2:2:1:3 starting ratios. Here, a sharp transition is observed at 100 K followed by an additional leg which drops to zero resistance at 86 K. This leg is again due to the presence of residual non superconducting phases in the sample.

Conclusions

The formation of the $Tl_2Ca_1Ba_2Cu_2O_{8+x}$ high T_c phase was observed in bulk powders produced by sol-gel methods using metal alkoxides as precursors. An appropriate solvent system was established to produce stable four component sols with an average particle size of 50 nm. The fractal dimensions of these particles was found to be 1.8, suggesting a 2-dimensional/ linear network structure. A firing temperature of 900 °C was sufficient to produce powders dominant in the 2122 high T_c phase. Firing the samples with Tl metal present in the sample chamber proved an effective means of reducing the thallium loss in the samples. This loss was found to increase with calcination periods greater than 30 minutes. Susceptibility curves show transition temperatures as high as 110 K. However, zero resistance was observed at 86 K due to the presence of residual unidentified phases.

Acknowledgements

Funding for this project was provided by the NSF-funded Science and Technology Center for Superconductivity under Grant No. DMR-88-09854. Special thanks to B.M. Moon for his help and guidance.

References

1. Z. Z. Sheng, A. M. Hermann, and A. El Ali, Physical Review Letters, **60** [10], 937-940, (1988).
2. Z. Z. Sheng & A. M. Hermann, Nature, **332**, 55-58, (1988).
3. Z. Z. Sheng & A. M. Hermann, Nature, **332**, 138-139, (1988).
4. T. C. Huang, V. Y. Lee, R. Karimi, R. Beyers and S. S. P. Parkin, Mat. Res. Bull., **23**, 1307-1314, (1988).
5. S. S. P. Parking, V. Y. Lee, E. M. Engler, A. I. Nazzal, T. C. Huang, G. Gorman, R. Savoy and R. Beyers, Submitted to Physical Review Letters, March 11th, (1988).
6. C. C. Torardi, M. A. Subramanian, J. C. Calabrese, J. Gopalakrishnan, K. J. Morrissey, T. R. Askew, R. B. Flippen, U. Chowdhry, A. W. Sleight, Science, **240**, 631-633, (1988).
7. D. S. Ginley, B. Morosin, R. J. Baughman, E. L. Venturini, J. E. Schirber and J. F. Kwak, Accepted to J. Crystal Growth Special Ed on High Tc.
8. Nae-Lih Wu and Eli Ruckenstein, Materials Letters, **7**, number 5,6, 169-171, (1988).
9. S. A. Kramer, G. Kordas, J. McMillan, G. C. Hilton, and D. J. VanHarligen, Appl. Phys. Lett., **53**,[2], 156-158, (1989).
10. G. Moore, S. Kramer and G. Kordas, Materials Letters, **7**, number 12, 415-424, (1989).
11. D. C. Bradley, R. C. Mehrotra, and D. P. Gaur, Metal Alkoxides, Academic Press, (1978).
12. E. J. Pope and J. D. Mackenzie, Journal of Non-Crystalline Solids, **101**, 198-212, (1988).
13. R.M. Hazen, L.W. Finger, R.J. Angel, C.T. Prewitt, N.L. Ross, C.G. Hadidiacos, P.J. Heaney, D.R. Veblen, Z.Z. Sheng, A.El Ali, and A.M. Hermann, Physical Review Letters, **60**, 16, 1657-1660, (1988).
14. R.S. Liu, P.T. Wu, J.M. Liang, and L.J. Chen, preprint (1988).

PREPARATION OF SUPERCONDUCTING $YBa_2Cu_3O_{7-x}$ COMPOUNDS BY WATER EXTRACTION VARIANT OF SOL-GEL PROCESS

A. DEPTUŁA, W. ŁADA, T. OLCZAK, T. ŻOŁTOWSKI*, A. DI BARTOLOMEO**
* Institute of Nuclear Chemistry and Technology, Dept. of Structural Research, Warsaw, Poland
** ENEA, C.R.E Casaccia, Italy

ABSTRACT

The starting sols were prepared by addition of ammonium hydroxide to acidic solutions of Y-Ba-Cu acetates or by dissolving solid $BaCO_3$ or $CuCO_3 \cdot Cu(OH)_2 \cdot H_2O$ in acetates of the remaining components. The sols were then gelled to spherical particles with diameter below 50μm by extracting water with 2-ethyl-1-hexanol or to shard by evaporation of water. After thermal treatment of both powders amorphous and then crystalline $YBa_2Cu_3O_{7-x}$ were obtained. Formation of these compounds is strongly improved by aging the gel at 200°C. Green and sintered pellets exhibit excellent superconductivity properties.

INTRODUCTION

The classical sol-gel process was elaborated at Oak Ridge National Laboratory, USA [1,2] and used for the fabrication of uranium and thorium oxides microspheres for High Temperature Gas Cooled Reactors. In this process drops of concentrated metal hydroxide sol are formed in an organic solvent and water is extracted from the drops with this solvent. Since the discovery of superconductivity above 77K of the compound $YBa_2Cu_3O_{7-x}$[3] a large number of studies have been carried out on various sol-gel methods of the preparation of this compound. So far the water extraction sol-gel process has not been investigated presumably due to the lack of concentrated hydroxide sols for barium and copper [4]. Only yttrium forms sols of this type because of its ability to form polynuclear cations.

This work has been undertaken with two principal objectives: to obtain spherical particles of the gel with diameter below 50μm using other than hydroxide sols in the water extracting process and to determine conditions of their thermal decomposition to $YBa_2Cu_3O_{7-x}$ with conservation of the spherical shape. It should be noted that some attempts have been made to synthesize spherical or rounded $YBa_2Cu_3O_{7-x}$ powders but all of them were limited to preparation of very small (below 2μm) particles using e.g. freeze-drying technique [5], homogeneous precipitation [6] and aerosol decomposition [7,8,9]. However, the practical applications of spherical powders with higher particle sizes [4] seems to be more important, for example as free flowing feed for an automatic pellet press, for preparation of layers by plasma spraying technique and finally for low energy packing to a density of 60%TD in rods by vibration. This last possibility can facilitate production of wires of ceramic superconductors.

Mat. Res. Soc. Symp. Proc. Vol. 169. ©1990 Materials Research Society

EXPERIMENTAL

Mixtures of Y-Ba-Cu acetates as starting solutions were used in work [10]. In the present work instead of stoichiometric acetates ,acidic solutions were prepared by dissolving yttrium hydroxide (freshly precipitated from yttrium nitrate solution and washed by decantation) , $BaCO_3$ and $CuCO_3 \cdot Cu(OH)_2 \cdot H_2O$ in an excess of acetic acid. The compositions of these solutions are given in Table I.

For the sol preparation three methods were used: (A) mixing of the solutions indicated in Table 1; (B) addition of solid $BaCO_3$ to the solution of Y^{3+} and Cu^{2+}; (C) addition of solid $CuCO_3 \cdot Cu(OH)_2 \cdot H_2O$ to the solution of yttrium and barium. In the last case addition of some quantity of acetic acid (about 15% of the total amount) was necessary to ensure complete dissolution of the solids. These solutions were alcalized with NH_4OH to various pH values and gelled by : (WEV) evaporation of water as in [10] and (WEE) modified water extraction variant of the sol-gel process [4,11]. First, emulsion of the sol was formed in 2-ethyl-1-hexanol with an addition the surfactant SPAN-80 (EH). Drops of the emulsion were formed by introducing the sol (by means of vibrating capillaries) under the surface a vigorously stirred solvent-EH at 50°C. At the same time the dehydrated EH (4g H_2O/dm^3) in the amount of about 100 volumes per 1 volume of the sol was introduced to the reactor. A part of the water ,contained in the emulsion drops, was extracted to EH and the suspension of the gel particles in EH passed to sedimentation columns. The supernatant liquid (EH saturated up to 10-14 g H_2O/dm^3) was succed into a vacuum regeneration system and the water was evaporated at 70°C. The dehydrated EH was recycled. The gelled particles were periodically removed from the bottom of the sedimentation column and washed with petroleum benzin (35-80°C).

TABLE I. Composition of the starting solutions

Metallic cation	Metal (Me) concn. M	$\frac{CH_3COOC}{Me}$ molar ratio
Y^{3+}	0.33	10.9[x]
Ba^{2+}	1.09	4.9
Cu^{2+}	0.26	6.1

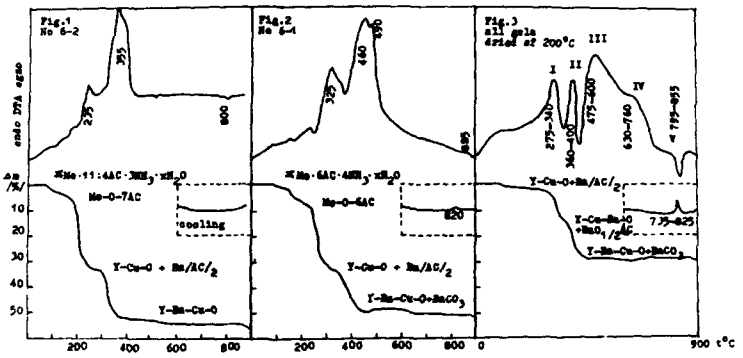
x in this solution nitrates and ammonia were present (0.45 and 0.03 mole, respectively, per 1M of yttrium).

The thermal decomposition (TG, DTA) of the gels was studied using a Hungarian MOM Derivatograph. X-ray diffraction measurements (using CoK-α radiation) were carried out with a Philips diffractometer PW1729 and SEM measurements with a Cambridge 250MK instrument.

Some calcined powders, after grinding in a hand mortar, were pressed (3 ton/cm^2) and sintered for 4h at 910°C. Superconductivity was demonstrated by observation of the levitation phenomenon of the pellets cooled in liquid nitrogen Electrical resistance measurements were carried out at various temperatures.

RESULTS AND DISCUSSION

The sols prepared by various techniques are characterized in Table II. As can be seen all the sols with pH values between



FIGS. 1, 2. 3. Thermal decomposition of the gels (see Table I).

TABLE II. Characterization of Y-Ba-Cu sols (concentration $\sum$ Me 0.31-0.38 M) and the gels prepared from them.

No	Techn. of prepn.	pH	Molar ratio AC / $\sum$ Me	Molar ratio NH_4OH / $\sum$ Me	Gellation technique and product
1	A	4.0	6.4	0	WEV, Cu^{2+} crystals
2	B	4.4	4.8	0	WEV, Cu^{2+} crystals
3	A	5.0	6.4	1.9	WEV, Cu^{2+} crystals
4	B	5.4	4.8	1.8	WEV, gel sh. *
5	A	5.6	6.5	3.6	" " "
6	B	5.6	4.8	1.8	
6-1 (in gel 100°C)			1.6	0.7	WEV, gel sh.
6-2 (in gel 20°C)			1.9	0.5	WEE, gel sp. *
7	C	5.6	4.0	1.5	WEV, gel sh.
8	A	6.0	6.4	3.2	" " "
9	B	6.0	5.1	2.3	" " "
10	C	6.0	4.0	1.8	" " "
11	A	7.0	6.5	3.9	" " "
12	B	7.0	5.0	3.1	" " "
13	C	7.0	4.0	1.8	" " "
14	A	8.0	6.4	5.0	" " "
15	B	8.0	5.0	4.3	" " "
16	C	8.0	4.0	3.7	" " "
in all gels WEV, dried at 200°C for 24h			0.66-0.76	0.004-0.03	

* sh. - shard ; sp. - spheres

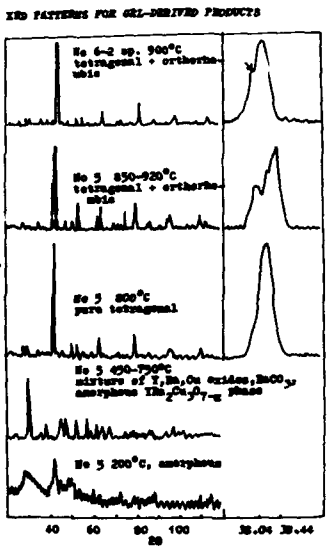


FIG. 4. XRD patterns for gel-derived products heated for 24h at the indicated temperatures (see Table II). The principal peak at 38°2θ is also shown separately.

5.4 and 8 can be successfully gelled in contrast to [10] where gelation was limited to pH 5.6-6. This can be explained by the fact that in the present work an excess of acetates was used, when in [10] only stoichiometric salts with molar ratio AC: $\sum$ Me=2.17 were used. This low molar ratio was not attained in all the sols presented in Table 2. Attempts to reduce it below 4 using technique "C" were unssuccesful , because of incomplete dissolution of $CuCO_3 Cu(OH)_2 H_2O$ in the starting Ba^{2+}-Y^{3+} solution.

The courses of the thermal decomposition of the gels are shown in Figs.1 and 2. The compositions of the gels prepared by water evaporation at 100°C (No 6-1) and water extraction (No 6-2) are similar. It seems that in the first step up to 200°C water and ammonia escape from the gel. Then in a very distinct exothermic process some weakly bonded (probably to Y^{3+} and/or Cu^{2+}) acetates are removed. The last part of acetates starts to decompose above 300°C. The molar ratio with respect to Ba^{2+} is 1.98-2.28 , which confirms the previous conclusion. Fig.3 shows thermal decomposition of all gels aged for 24h at 200°C. As can be seen the acetates are decomposed in two nearly equal steps with maximum exotherms denoted as I and II. It means that two molecules of acetates, bonded to Ba^{2+}, are successively decomposed. Some of them react with barium forming $BaCO_3$. The existance of this compound is confirmed by a very distinct endotherm near 800°C without weight changes. The presence of residual $BaCO_3$, indicated by the small endothermic dip at 830°C was also observed for the gels prepared using alkoxide[13] and citrate [14] precursors. Because in [12] this effect is attributed to reversible rhombic-hexagonal $BaCO_3$ transformation, in this work DTA curves during cooling were recorded. As can be seen in Fig.3 a small exothermic effect, shifted towards lower temperatures by 10-35°C, is observed. The quantity of $BaCO_3$ is much higher in the gels aged at 200°C than in the unaged (Fig. 1 and 2). All these informations suggest than under conditions of the thermal analysis (relatively high heating rate-10°C/min) not all carbonates are decomposed even at 950°C.

In Fig.3 also a large exothermic effect III without a weight change and IV (as a shoulder located on III) with a small increase of weight can be seen. From the XRD patterns shown in Fig.4 it can be seen that in this temperature range as well as during long annealing formation of crystalline $YBa_2Cu_3O_{7-x}$ does not take place. However the always present exotherms III and IV undoubtly indicate the reactions between the components of the sample, with some reoxidation effect. This last effect can be attributed to reoxidation of Cu^{1+} or even Cu, which can be formed by reduction of Cu^{2+} with organic components of the gels. The probable interpretation of these phenomenon seems to be the formation of some kind of amorphous cuprates. This process seems to be strongly activated when temperature aging is employed (lack of the III and IV effects in undried gels - Fig.1, weaker effects shifted to lower temperatures for gels preheated at 100°C-Fig.2).

Before the production of the gels in the form of spherical particles by the water extraction process, the sols were concentrated by evaporation of water to maximum 1.8 M $\sum$ Me. It was shown in the preliminary experiments that the EH changed its colour from honey yellow to blue. The analysis confirms that during the gellation the extraction of Cu^{2+} in the amount of



20°C 300°C 900°C

FIG.5 Microphotographs of spherical gel particles (No 6-2) calcined at indicated temperatures.



FIG.6. SEM micrograph of $YBa_2Cu_3O_{7-x}$ spheres (No 6-2) calcined for 24h at 900°C.



FIG.7 SEM micrograph of fracture surface of sintered $YBa_2Cu_3O_{7-x}$ pellets (TD 92%), prepared from powder No 5.

about 600 mg/dm^3 takes place. For this reason before the gelation experiments EH was saturated using normal gellation procedure for Y-Ba-Cu sols. Analysis of the product of routine runs (No 6-2) shows that the molar ratio of Y:Ba:Cu approaches to 1:2:3. Unfortunately the blue gel particles of diameters from several to several tens of microns (Fig.5) stick together during routine drying (also under vacuum at room temperature) to form a rigid cake. This phenomenon never observed for spherical gels of other elements [4] indicates very high reactivity of the studied gels. However by using a very slow heating rate(0.3°C/h) the spheres were dried to 300°C and then, without any special precautions, calcined for 24h at 900°C. The microspheres preserved spherical shapes(Fig.5 and 6). Spherical, dark brown, powders predominately consist of tetragonal phase of $YBa_2Cu_3O_{7-x}$ while sharp powders obtained by water evaporation methods and fired under the same conditions show nearly perfect orthorhombic structure (Fig.4). The high content of carbon in the spherical powder (3.6%) derived from surfactant or/and solvent probably retards the formation of the superconducting phase. The detrimental influence of carbon on superconducting properties of $YBa_2Cu_3O_{7-x}$ was observed in [15]. It seems that application of oxygen atmosphere during heating, as used nearly in all other works , can improve the properties of spherical powders.

Sintered pellets prepared from irregularly shaped powders have densities 80-92TD% , desirable microstructure (Fig.7) and show very good superconducting properties ,for example T_{c_o} =94K for the compact shown in Fig.7. It should be noted that the strong levitation effect , exhibited by the green compacts (62-78%TD), has never been observed before.

CONCLUSIONS

The water extraction variant of the sol-gel process together with special heat treatment can be applied to the preparation of spherical powders of $YBa_2Cu_3O_{7-x}$ compounds with diameters ranging from several to several tens of microns. The superconducting properties can be improved by heating in oxygen atmosphere. These treatment is not necessary if irregular powders are prepared from highly complexed and partially hydrolysed sols (pH 5.4-8) by evaporation of water. In that case the sintered pellets prepared from them exhibit very good superconducting properties (T_{Co} =94K). The transformation of the amorphous cuprates phase (formed at 475-760°C) to crystalline $YBa_2Cu_3O_{7-x}$ compounds is strongly improved by aging the gels at 200°C.

ACKNOWLEDGMENTS

The authors would like to thank Mrs. A.Będkowska, Mrs. B.Goszczyńska and Mr. H.Hahn for the assistance in the experiments. Thanks are due to Dr. B.Nazareno (ENEA) and Dr.H.Lewandowski for performing chemical analyses. The authors would also like to thank Mr.P.Szymański - the President of the PLUS Corporation Ltd., Warsaw,for sponsoring the participation of one of the authors of the present work in the MRS 1990 Meeting in San Francisco.

REFERENCES

1. J.P.McBride, ORNL Report No.TM-1980 (1967).
2. P.A.Haas, C.C.Haws, F.G.Kitts and A.D.Ryon, ORNL Report No.TM-1978 (1968).
3. M.K.Wu, J.R.Ashburn, C.J.Tong, P.H.Hor, R.L.Meng, L.Cao, Z.J.Zhang,Y.Q.Wang and C.W.Chu, Phys.Rev.Lett. 58,908 (1987).
4. A.Deptuła and C.Majani, Sol-gel Processes and Their Application, ENEA Report No.RT/TIB/86/25, ROMA, 1986.
5. R.Sanjines,K.Thampi and J.Kiwi,J.Am.Ceram.Soc.,71, C-512(1988).
6. P.M.Kayima and S.Qutubuddin, J.Mat.Sci.Lett. 8,171 (1989).
7. A.H.Carim,P.Doherty,T.T.Kodas and K.Ott,Matt.Lett.8,355 (1989).
8. K.Tsuchida,H.Tsudo and A.Kato,J.Mat.Sci.Lett.8,222 (1989).
9. P.Odier, R.Dubois, M.Gervais and A.Douy, Mat.Res.Bull. 24, 11 (1989).
10. H.Kozuka, T.Umeda, J.Jin, T.Monde and S.Saka, Bull.Inst. Chem.Res., 66, 80 (1988).
11. A.Deptuła, H,Hahn, J.Rebandel, W.Drozda and B.Kalinowski, Polish Patent No.83 484 (20 September, 1977).
12. Atlas of Thermoanalytical Curves, Edited by G.Liptay, Akademiai Kiado, Budapest 1971.
13. G.M.Moore, S.Kramer and G.Kordas, Matt.Lett. 12,415(1989).
14. H.K.Varama, K.P.Kumar, K.G.K.Warrier and A.D.Damodaran, J.Mat.Sci.Lett. 8, 1313 (1989).
15. P.Müller, M.Schubert, Ch.Rodig, G.Fuchs and K.Fischer, Appl.Phys.Lett. 55, 917 (1989).

METALLO-ORGANICS DERIVED TRACTABLE RESINS FOR YBCO SUPERCONDUCTING FIBER FABRICATION

K.C. Chen, A. Y. Chen and K. S. Mazdiyasni
General Atomics, PO Box 85608, San Diego, CA 92138-5608

ABSTRACT

Soluble resins were prepared by controlled hydrolysis of yttrium isopropoxide, barium isopropoxide and copper ethylhexanoate. The resins were converted to cohesive, viscous, fluid and precipitated states by the addition of different combinations of binary polar and non-polar organic solvents. Viscosity and spinnability of the resins were critically dependent on the solvent constituents. Continuous pre-ceramic fibers were spun from these resins and single phase $YBa_2Cu_3O_y$ superconducting fibers with T_c=91.5K and ΔT=1.5K have been obtained.

INTRODUCTION

The magnetic applications of a superconducting cable require high critical currents, strengths and modulus of the superconducting fibers. To meet these requirements, the fiber must have the following features: chemical stoichiometry, phase purity, high density, crystallographic orientation in the c direction, uniform fine microstructure and clean grain boundaries.

There are few known methods for fabricating superconducting fibers of 20-100 μm in diameter without an outer cladding or center wire as support. These methods include metal-alloy, powder-in-binder [1], powder in sol [2], sol-gel and metallo-organics [3-7]. In order to spin fibers directly from the metallo-organic derived resins, the resin not only has to meet the requirements for the final ceramic fiber, but must also have high viscosity, viscoelasticity, cohesiveness, green strength, low shrinkage and high oxide content. In this paper, we discuss the preparation of metallo-organic derived tractable resins that possess several key parameters of the aforementioned properties for continuous spinning of single phase $YBa_2Cu_3O_y$ fibers.

EXPERIMENTAL PROCEDURE

Yttrium isopropoxide/isopropanol solutions, barium isopropoxide/isopropanol solution and copper ethylhexanote/isopropanol stock solutions were prepared as described previously [8]. Solutions containing stoichiometric ($YBa_2Cu_3O_y$) amounts of required elements were prepared by pipetting the calculated volume from each stock solution into a 500 ml three-neck round bottom flask. First, barium isopropoxide and yttrium isopropoxide were mixed, and a clear yellowish solution was obtained. A green precipitate formed when copper ethylhexanoate solution was later introduced. This solution was refluxed gently in a dry nitrogen atmosphere for 2 hours. This precipitated solution was then hydrolyzed by adding a mixture of water/isopropanol, using 10 equivalents of water per mole of yttrium isopropoxide while the solution temperature was kept at 50-60°C. The greenish precipitate dissolved after adding water and a clear dark green solution formed. This solution was concentrated and initially dried in a rotary evaporator, was further dried in a vacuum oven and was then ground into powder for storage. Suitable viscosity could be achieved when the dried powder was dissolved with the proper amounts of several binary solvent mixtures, such as benzene-isopropanol, hexane-isopropanol, toluene-isopropanol and xylene-isopropanol. The fibers were then prepared by mechanical spinning from the cohesive mass.

RESULTS AND DISCUSSIONS

Behavior of the resin in different binary solvents

A number of processing parameters, including the amount of water added, temperature and time were critical to the formation of viscous resins. Low water ratios and low bath

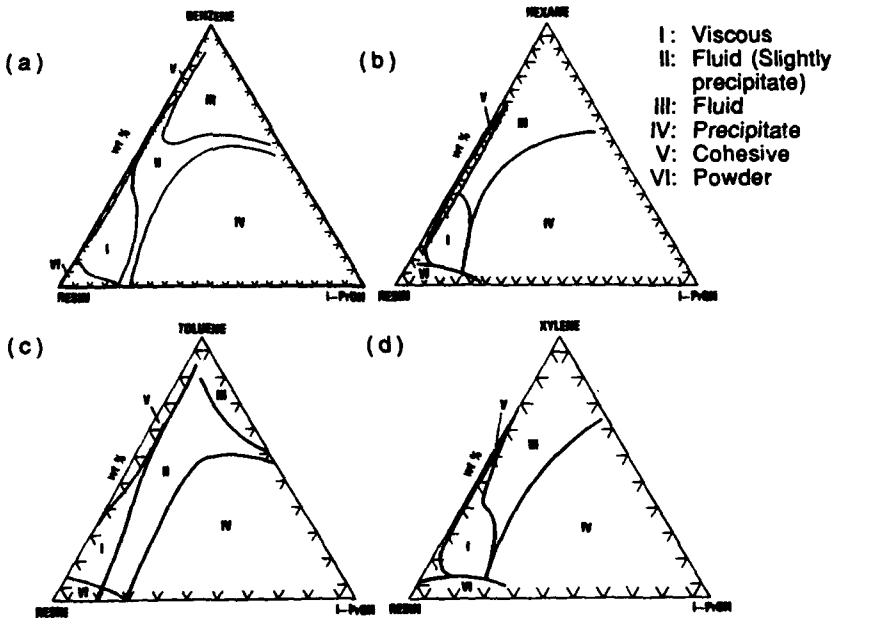


Figure 1. The characteristics of Y123 resins in binary solvent systems, (a) benzene-isopropanol; (b) hexane-isopropanol; (c) toluene-isopropanol and (d) xylene-isopropanol

temperatures prolonged the time needed for dissolving the green precipitate. Prolonged heating or refluxing after water addition caused precipitation in the solution that resulted in composition fluctuation within the resin.

The resins were stored in dry powder form that extended their shelf life and provided flexibility for processing. The dry resin powder was readily dissolved or "softened" by using proper ratios of benzene-isopropanol, hexane-isopropanol, toluene-isopropanol and xylene-isopropanol. The behaviors of the resin in these binary solutions are shown as a function of weight percentage in the ternary diagrams. (Figures 1 (a)-(d)). There are several regions of interest in these ternary diagrams.

In general, the viscosity of the resin solutions decreased with increasing amounts of either benzene or isopropanol in regions I, II, and III. In low benzene, low isopropanol region I, the resin became highly viscous and did not immediately flow when the glass vial was inverted. Fibers could be prepared by hand-drawing only within a small area in region I. Similar behavior was also observed in region I of the other systems. In regions II and III, the solutions instantaneously flowed when glass vials were tilted. Therefore, regions II and III were described as fluid regions in contrast to the non-flowing region I (viscous region). Region II had a very small amount of precipitation. The viscosity at the boundary between region I and III was approximately 10^6 mPa·s. Stable solutions were obtained throughout region III.

In region IV, which contained more isopropanol, massive precipitation occurred. The amount of the precipitation increased with increasing isopropanol. The resins were cohesive in region V and on the tie-line between resin and non-isopropanol solvents, except in hexane-isopropanol system. The resins did not stick to glass vials. This property enabled them to be molded or extruded into different shapes. The resin had a tendency to expel excess solvents that could co-exist as clear solution with the cohesive resin mass. The critical solvent contents for solvent separation were around 60-70 w% of benzene, toluene or xylene. In region VI, there was an insufficient amount of solvent to completely wet the resin. The transitions across the regional boundaries were gradual, but the transitions between the regions were reversible and could be done by solvent addition or removal. This reversibility greatly simplified the preparation of resins with optimal fiber spinnability.

Table 1. Characteristics of resins in benzene-isopropanol binary solvents.

Test Run	Resin constituents (wt%)			Resin Characteristics				
	C_6H_6	i-PrOH	Dry Resin	Cohesive	Surface Smoothness	Die Swell	Flexibility	Collapse
B1	26.8	0.0	73.1	yes	no	slight	some	no
B2	48.3	2.6	49.1	yes	yes	slight	yes	yes
B3	39.6	2.2	58.3	no	yes	large	yes	yes
B4	25.4	1.4	73.2	yes*	yes	large	yes	yes
B5	30.3	1.1	68.5	yes*	yes	no	yes	yes
B6	20.0	1.0	78.9	yes*	yes	large	yes	yes
B7	18.8	1.0	81.2	yes*	yes	no	yes	slight
B8	17.8	1.0	80.2	yes	yes	no	yes	no

* Slightly tenacious.

Spinning of precursor fibers

The viscosity of the resins was adjusted by mixing the dry resin powder with the required amounts of the solvents immediately before spinning. The resins could be dry-spun because of their cohesiveness, viscoelasticity and high viscosity. The elongational viscosity rapidly increased after extrusion from the nozzle as a result of solvent evaporation.

The viscosity of the viscous resins in the fiber drawing regions (regions I and V) was at least 10^6 mPa.s. Because of the cohesive property of the resins, the fiber retained the shape of the spinneret and readily wound onto the pick-up wheel. The viscoelasticity enabled the resin to be drawn to 1/10 to 1/3 of the opening of the nozzle. The viscosity, cohesiveness and viscoelasticity of the resin were very sensitive to the solvent constituents. Solvent contents in the resin also greatly influenced other fiber spinning properties, such as die-swelling, surface smoothness, flexibility, modes of fracture (brittle vs. ductile), collapsing and extrusion pressures. Table 1 gives the resin characteristics as a function of solvent contents in benzene-isopropanol systems. Figure 2 shows the effect of the solvent content on die-swelling and collapsing. With proper solvent composition, precursor fibers of 50-1000 μm in diameter were easily spun (Figure 3). Thin fibers were flexible and had sufficient green strength for handling.

Conversion of the resin into superconducting ceramic fibers

The dry resins and as-drawn fibers were X-ray amorphous. Calcination of the resin at 400-750°C resulted in mixed phases of Y_2CuO_5, $BaCO_3$ and CuO. $YBa_2Cu_3O_y$ phase appeared at 750°C. After 1 to 4 hours at 800°C, there were substantial amounts of $YBa_2Cu_3O_y$ with small amounts of Y_2BaCuO_5 and $BaCuO_2$ phases present. At 900°C for 1 to 8 hours, single phase $YBa_2Cu_3O_y$ was obtained. DTA run in dry nitrogen showed no low melting impurity phases at 950°C in these fibers [8]. Fibers having T_c =91.5K with ΔT=1.5K were obtained after heat treatment of 950°C for 15 hours followed by a 24-hour anneal at 400°C (Figure 4).

CONCLUSIONS

Suitable metallo-organic precursors were synthesized and processed to prepare tractable resins for YBCO fiber fabrication. These resins became cohesive, viscous, fluid or precipitated in several binary solvent systems. The spinnability of the resins was controlled by the amount of solvent constituents. Continuous precursor fibers were successfully spun from the resins. Superconducting fibers with T_c =91.5K and ΔT=1.5K were obtained.

ACKNOWLEDGEMENTS This research was supported by DARPA/ONR. The electrical properties were measured by Ms. Lisa Paulius and Dr. Patti Tsai of Physics Department, UCSD.

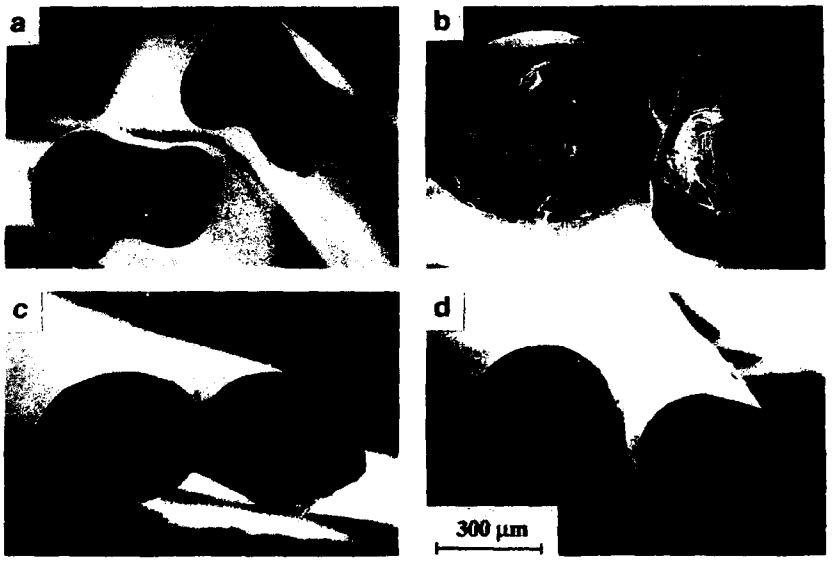


Figure 2. Precursor fibers morphology with different degrees of die-swelling and collapsing; (a) sample B5: no die-swelling, large collapsing; (b) sample B6: large die-swelling, medium collapsing; (c) sample B7: no die-swelling, medium collapsing and (d) sample B8: no die-swelling, no collapsing.



Figure 3. Continuous precursor fiber was prepared by dry-spinning of the resins.

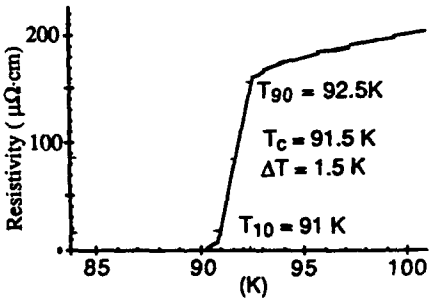


Figure 4. Resistivity of superconducting fiber calcined at 950°C for 15 hours and annealed at 400°C for 24 hours.

REFERENCES

1 T. Goto and M. Kada, J. Mater. Res. 3, 1292 (1988).
2. R. Enomoto et al., Japan. J. Appl. Phys. 28, L1207 (1989).
3. T. Umeda, H. Kozuka, and S. Sakka, Advanced Ceramic Materials 3, 520 (1988)
4. J. C. W. Chien et al, Phys. Rev B 38, 11-835 (1988).
5. H. Konishi, T. Takamura, H. Kaga and Katsuse, Japan. J. Appl. Phys. 28, L241 (1989).
6. F. Uchikawa and J. D. Mackenzie, J. Mater. Res. 4, 787 (1989).
7. M.W.Rupich, S. F. Cogan, B. Lagos and J. P. Hachey, Mater Res. Soc. Meeting, Fall 1989 Boston, MA, USA (to be published in MRS Proceeding).
8 K. C. Chen and K. S. Mazdiyasni, Mater. Res. Soc. Meeting, Fall 1989, Boston, MA. (to be published in MRS Proceeding).

PREPARATION OF Bi-Pb-Sr-Ca-Cu-O SUPERCONDUCTOR BY THERMAL DECOMPOSITION OF AN EDTA COLLOID

H.S.Koo*, C.K.Chiang*, Y.T.Huang* and G.C.Tu**
* Materials Research Laboratories, Industrial Technology Research Institute, Hsinchu, 31015, Taiwan, R.O.C.
** Institute of Materials Science and Engineering, National Chiao-Tung University, Hsinchu, 30049, Taiwan, R.O.C.

ABSTRACT

High-Tc superconducting Bi-Pb-Sr-Ca-Cu oxide with zero resistance temperature at above 100K has been synthesized via the use of ethylene-diamine-tetra-acetate(EDTA) colloid and corresponding metal nitrates. Remarkable sinterability of the precursor requires shorter time to achieve superconducting phases than conventional solid-state reactions. Superconducting properties were measured electrically and magnetically. The thermal decomposition, X-ray diffraction and microstructural characteristics of the precursor and the sintered samples were also discussed.

INTRODUCTION

Since the reports on the occurrence of the superconductivity at about 30K in the Ba-La-Cu-O[1] and 90K in the Y-Ba-Cu-O[2] systems, researchers are encouraged to investigate mechanism, higher-Tc superconductors and appropriate processing techniques for application interests. More recently, superconductivity at above 100K in the new Bi-Sr-Ca-Cu-O and Tl-Ba-Ca-Cu-O systems were discovered by Maeda *et al.*[3] and Sheng *et al.*[4], respectively. Although the highest-Tc superconductor is found in the Tl-based $Tl_2Ba_2Ca_2Cu_3O_y$[5], the Bi-based superconductors are still regarded as the most potential materials because of the stable moisture resistance and its nontoxic character.

At present, most superconducting oxides are prepared by solid state reaction through the mechanical/manual mixing of oxides and carbonates. Compare to chemical synthesis routes, this traditional way is difficult to achieve a precise control for powder characterizations such as homogeneity, particle size, particle distribution and morphology. The characteristics of the synthesized powder will impact the physical/mechanical properties of the final sintered products. The object of this search is to develope a chemical synthesis route for the preparation of Bi-Pb-Sr-Ca-Cu-O superconductors through the thermal decomposition of an EDTA colloid, in an attempt to have a better control over the final products.

EXPERIMENTAL

The initial step in our process was the preparation of a nitrates-ethylene glycol solution with stoichiometric metal molar ratio (Bi:Pb:Sr:Ca:Cu) = 1.68:0.32:1.75:1.85:2.80. Reagent-grade metal nitrates were individually dissolved in ethylene glycol and stirred to obtain a transparent light blue solution. Separately, ethylene-diamine-tetra-acetic acid was added to another ethylene glycol and the pH was adjusted to above 7.0 with ammonium hydroxide to dissolve the EDTA powder.

The metal nitrates-EDTA solution was prepared by mixing the nitrates-ethylene glycol solution and EDTA-ethylene glycol solution, which yielded a mixture in deep blue. The resulting solution was heated to vaporize the

Mat. Res. Soc. Symp. Proc. Vol. 180. ©1990 Materials Research Society

solvent for gelation. Product obtained was dried at 170-200°C for 5h and grinded into the precursor powder. The thermal decomposition mechanism of the precursor was investigated by the differential thermal analysis (DTA) and thermogravimetry (TGA). The structure of the crystal phases existed in the calcined and sintered samples were examined by a Philips 1700 APD X-ray diffractometer (XRD). The morphology of colloidal samples were observed by transmission and scanning electron microscopy (TEM/SEM). Finally, the superconducting characteristics of the sintered samples were measured electrically and magnetically.

RESULTS AND DISCUSSION

The DTA/TGA data of the dried precursor powder are given in Fig. 1 as a function of temperature, which indicates various temperature regions for thermal decomposition. The 2% weight drop during the temperature range of 100-250°C reflects the loss of water and adsorbed gases. A sharp weight loss, 15%, accompanied with an exothermic peak was seen aroung 300°C, which corresponds to the organic decomposition. On the other hand, a gradual weight loss in the temperature range of 300-500°C was also observed, and a very large exothermic peak took place in the vicinity of 400-500°C. They are contributed to the decomposition of the remaining EDTA and nitrates. Finally, two endothermic peaks occurred around 820°C and 840°C, which were considered the partial melting. Results are consistent with the XRD patterns of the precursor powders which were heat-treated at various temperature ranges[6].

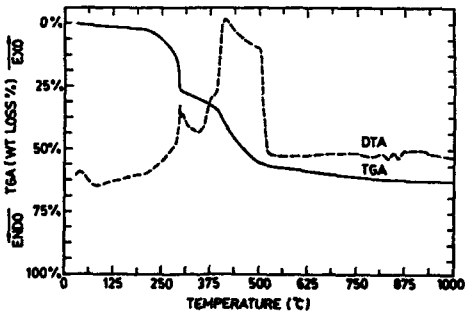


Fig. 1 The DTA/TGA data of the dried precursor powder.

Transmission electron micrographs of the as prepared colloid and the precursor powder calcined at 800°C are shown in Fig.2. A flocky structure of colloidal particles is observed in Fig.2(a) with a 10 nm particle size. Fig. 2(b) shows the grain morphology after calcination at 800°C for 10h. Grain size is between 0.1 μm to 0.2 μm with a platy mica-like shape.



Fig. 2 TEM photographs of the as prepared colloid(a)and the precursor powder calcined at 800°C for 10h(b).

There are three superconducting phases in the Bi-Sr-Ca-Cu-O system, namely $Bi_2Sr_2CuO_y$(2201,Tc=20K), $Bi_2Sr_2CaCu_2O_y$(2212,Tc=80K) and $Bi_2Sr_2Ca_2Cu_3O_y$(2223,Tc=110K)[7]. X-ray diffraction patterns are displayed in Fig. 3 for powders after 800°C/10h calcination (a) and after 850°C/60h sintering (b). The pattern for the calcined powder exhibits major $Bi_2Sr_2CaCu_2O_y$(2212) and minor Ca_2PbO_4 phases. In the sample sintered at 850°C for 60h, the XRD pattern depicts the coexistence of high-Tc(2223), low-Tc(2212) and Ca_2PbO_4. Recently, Huang *et al.*[8] reported that the optimal sintering conditions for $Bi_{1.7}Pb_{0.4}Sr_{1.6}Ca_{2.4}Cu_{3.6}O_y$ can achieve a nearly single high-Tc phase and the phase content increases with increasing sintering time. The microstructural morphologies of the samples sintered at 850°C for 20h(a) and 60h(b) are shown in Fig. 4. The size of plate-like grains, associated with the high-Tc phase[9], was observed to increase gradually against the sintering time. When the sintering temperature is raised up to 855°C, the severe melting phenomenon occurrs.

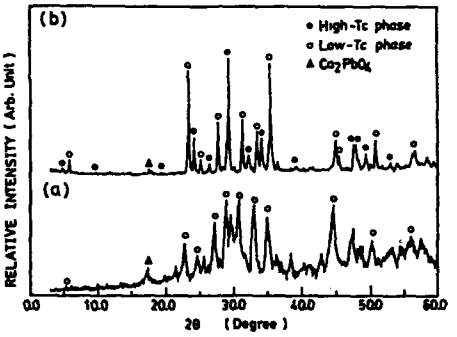


Fig. 3 XRD patterns for the precursor calcined at 800°C for 10h(a) and the sample sintered at 850°C for 60h(b).

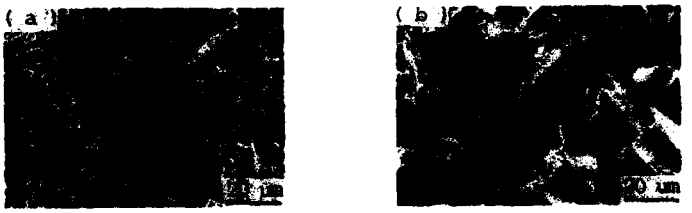


Fig. 4 SEM photograph of the samples sintered at 850°C for 20h(a) and 60h(b).

Relations between the electrical resistance and the temperature for the sample sintered at 850°C for 20h, 40h, 60h and 80h are shown in Fig. 5(a-d), respectively. A remarkable resistance drop around 110K was seen for each sample. Zero resistance temperatures increase when the sintering time is lengthened. The samples sintered at 850°C for 60h and 80h have zero resistance temperatures of 108K. Fig. 6 shows the temperature dependence of the magnetic susceptibility for the sample sintered at 850°C for 60h. The measurement was performed in the zero field cooling(ZFC, Shielding effect) and field cooling(FC, Meissner effect). The diamagnetism-onset temperature was about 110K and similar to the onset of the resistance drop. A step transition around 80K was also observed, this indicated that the sintered sample as shown in the XRD data is a multiphase and the volume fraction of perfect superconductivity was estimated to be about 20%.

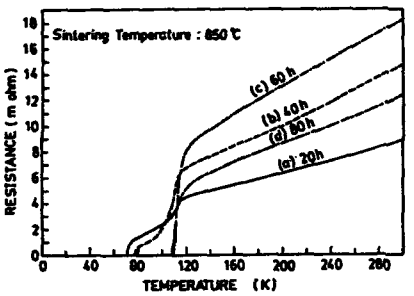


Fig. 5 Temperature dependence of the electric resistance for the samples sintered at 850°C for 20h(a), 40h(b), 60h(c) and 80h(d).

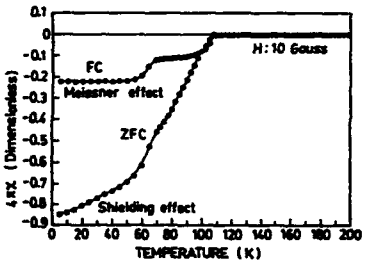


Fig. 6 Temperature dependence of the magnetic susceptibility for the sample sintered at 850°C for 60h.

CONCLUSIONS

A chemical route to prepare high-Tc superconducting Bi-Pb-Sr-Ca-Cu-oxide powder with particle size of 0.1-0.2 μm has been achieved by thermal decomposition of an EDTA colloid. XRD patterns revealed the coexistence of the high-Tc, low-Tc and Ca_2PbO_4 phases. The sample sintered at 850°C for 60h and 80h showed that the onset and zero resistance transition temperatures were 115K and 108K, respectively.

ACKNOWLEDGEMENT

We are grateful to Hsiao-Hsu Jen for performing the transmission electron microscopy experiment. This research is supported by the Ministry of Economic Affairs, Republic of China, under the contract No. 33B1000 to the Industrial Technology Research Institute.

REFERENCES

[1]. J.G. Bednorz and K.A. Muller, Z. Phys. B 64, 189 (1987).
[2]. M.K. Wu, J.R. Ashburn, C.J. Torng, P.H. Hor, R.L. Meng, L. Gao, Z.J. Huang, Y.Q. Wang and C.W. Chu, Phys. Rev. Lett. 58, 909 (1987).
[3]. H. Maeda, Y. Tanaka, M. Fukutomi and T. Asano, Jpn. J. Appl. Phys. 27, L209 (1988).
[4]. Z.Z. Sheng and A.M. Hermann, Nature 332, 55 (1988).
[5]. S.S.P. Parkin, V.Y. Lee, E.M. Engler, A.I. Nazzal, T.C. Huang, G. Gorman, R. Savoy and R. Beyers, Phys. Rev. Lett. 60, 2539 (1988).
[6]. H.S. Koo, C.K. Chiang, W.M. Horng and W.H. Lee, to be published.
[7]. J.M. Tarascon, W.R. McKinnon, P. Barboux, D.M. Hwang, B.G. Bagley, L.H. Greene, G.W. Hull, Y. LePage, N. Stoffel and M. Giroud, Phys. Rev. B 38, 8885 (1988).
[8]. Y.T. Huang, R.G. Liu, S.W. Lu, P.T. Wu and W.N. Wang, Appl. Phys. Lett. 56, 779 (1990).
[9]. N. Kijima, H. Endo, J. Tsuchiya, A. Sumiyama, M. Mizuno and Y. Oguri, Jpn. J. Appl. Phys. 27, L1852 (1988).

SOLUBLE AND VOLATILE PRECURSORS FOR THE PREPARATION OF SUPERCONDUCTING FILMS

NANCY N. SAUER, EDUARDO GARCIA, AND ROBERT R. RYAN
Isotope and Nuclear Chemistry Division, Los Alamos National Laboratory, Los Alamos, New Mexico 87545

ABSTRACT

Attempts to identify intermediates in an alkoxide-based solution route to films of the high temperature superconductor $YBa_2Cu_3O_7$ reported by Fahrenholtz et al.[1] have led to the isolation of the first molecular barium-copper cluster, $Ba_2Cu_2(OR)_4(acac)_4 \cdot 2$ HOR, R = $CH_2CH_2OCH_3$. The extension of this route to the preparation of the bismuth superconductors has necessitated the investigation of bismuth alkoxide chemistry. Two separate routes to bismuth alkoxides have been examined: the metathesis of the metal halides with NaOR, (R = t-butyl, and diisopropylphenoxide) and the alcoholysis of bismuth amides, $Bi(NR_2)_3$, [R = $N(SiMe_3)_2$] The alcoholysis preparation gives high yields of several alkoxides suitable as precursors to the high T_c materials. A monomeric bismuth phenoxide, which is targeted as a volatile precursor, and a bismuth t-butoxide cluster have been isolated and stucturally characterized. Solubility and volatility studies have also been undertaken.

INTRODUCTION

Thin films of the new high temperature superconductors, are needed for a range of technological applications. The primary goal of this work is the identification of compounds that are suitable for solution or vapor deposition of the ceramic superconductors. To achieve this end, we have focused our research on two areas: the isolation and characterization of intermediates from proven solution routes to superconducting materials, and the design and synthesis of discrete molecular precursors to the superconductors. While a large number of reports on solution routes to superconducting films have appeared in the literature, few describe attempts to isolate and characterize intermediates. Studies have shown that critical temperature (T_c) and the critical current (J_c) in the films are highly sensitive to processing conditions. Clearly, if solution techniques are to be of value as a source of these materials, better understanding and control of the chemistry occuring in the processes will be necessary. A natural extension of this work on solution intermediates and precursors is the identification of compounds suitable for precursors for chemical vapor deposition, (CVD).

RESULTS

This work was begun by examining a route reported by Fahrenholtz et al.[1] which uses a dimeric copper-acetylacetonate-alkoxide and barium and yttrium alkoxides as

Mat. Res. Soc. Symp. Proc. Vol. 180. ©1990 Materials Research Society

soluble precursors. Attempts were made to isolate intermediates at key stages of the precursor solution preparation. One result of these studies was the isolation and structural characterization of the alkoxide cluster $Ba_2Cu_2(acac)_4(OR)_4 \cdot 2$ HOR, R = $CH_2CH_2OCH_3$, from solutions in the first stage of the thin film preparation.[2] To our knowledge this cluster represents the first example of a discrete molecular barium-copper complex.

Preparation of Bismuth Alkoxides.

Two routes to bismuth alkoxides have been examined: metathesis of the metal halides, (chloride and iodide), and the alcoholysis of bismuth tris-trimethylsilylamide. In order to maximize the solubility and/or volatility of the product compounds, sterically demanding R groups such as t-butyl and substituted phenols were used to deter the formation or condensation of large metal alkoxide clusters.

Metathesis of commercially obtained anhydrous bismuth trichloride with lithium or sodium alkoxides gives alkoxide products of low solubility. Trace amounts of water in the commercially obtained chlorides results in the formation of condensed oxo-alkoxides, which cannot be readily separated from the halide salts formed as a side product. This low solubility renders these materials unsuitable for use as precursors. In an attempt to eliviate these problems, BiI_3 was choosen as the starting metal halide. Anhydrous BiI_3 can be prepared by the reaction of freshly cut bismuth metal with I_2 in THF at -20 °C, (rxn 1). Bright orange needles of $BiI_3 \cdot THF_x$ fall out of

$$Bi^\circ + 2/3\ I_2 \xrightarrow[-20\ ^\circ C]{THF} BiI_3 \cdot THF_x \qquad (1)$$

solution upon concentration, however the THF is only weakly coordinated, and is lost during filtration. A black powder of the anhydrous iodide results. Metathesis of this halide with potassium alkoxides would be expected to cleanly give the target alkoxides, and a highly insoluble precipitate of KI. In the reaction of BiI_3 with KO^tBu, the soluble metal alkoxide was isolated after removal of an insoluble canary yellow precipitate, (not KI) by filtration. Proton NMR of the colorless alkoxide showed only one alkoxide containing product. The yellow precipitate was identified as a mixture of K_2BiI_5 and K_3BiI_6, which form as a result of a side reaction between BiI_3 and KI. Similar chemistry was seen with several other potassium alkoxide salts. Consumption of the BiI_3 starting material in this reaction leads to unacceptably low yields (typically <30%) of the bismuth alkoxides, and an alternate synthesis was sought.

Alcoholysis of metal amides is an established route to metal alkoxides. The extremely soluble bismuth tris-trimethylsilylamide is prepared by metathesis (rxn 2), and can be separated from less soluble impurity salts by sublimation.

$$BiCl_3 + NaN(SiMe_3)_2 \longrightarrow Bi[N(SiMe_3)_2]_3 + NaCl \qquad (2)$$

This compound is believed to be a pyramidal monomer analogous to the structurally characterized $Bi[N(Ph)_2]_3$.[3] For a typical alcoholysis reaction, the amide is dissolved in a minimum of hexanes or benzene, and the dry alcohol added. The less soluble alkoxide forms and precipitates out of the hexane solution. Yields of the t-butoxide and diisopropylphenoxide (Dipp) obtained in this manner are >90%. Both can be recrystallized from hexanes or toluene at -40°C to give x-ray quality crystals. The $Bi(Dipp)_3$ was shown to be a monomer by single crystal x-ray diffraction.

The structure of the bismuth t-butoxide, *shown in Figure* 1, is much more complex. It is a tetramer, held together by two

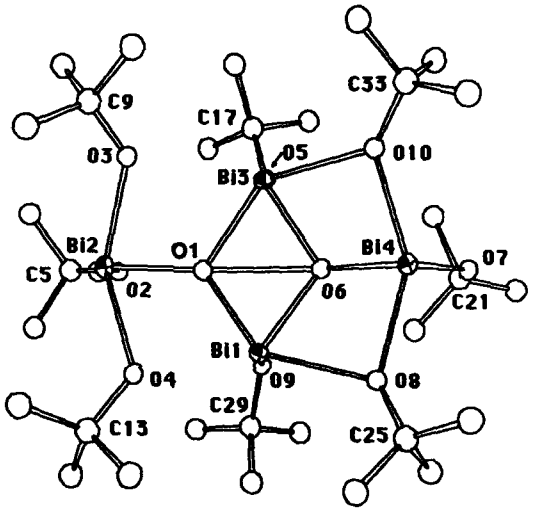


Figure 1

triply bridging oxo ligands. The four bismuth atoms are in a very nearly planar diamond shaped array. Two alkoxide ligands bridge over two faces of the Bi_4 diamond. This tetramer crystallizes in $P2_1/c$; a=12.372(2), b=19.833(2), c=22.182(2). A final R factor of 12.1% was obtained. We are currently attempting to isolate higher quality crystals for an additional x-ray structure analysis. Some pertinent distances and angles are given in Table 1.

Table I. Selected bond lengths and angles for $Bi_4O_2(OtBu)_7$.

Bi_3-O_1 = 2.[illegible](4) Å	Bi_1-O_1 = 2.10(4) Å	O_1-Bi_1-O_6 = 72(1)°
Bi_3-O_5 = 2.12(4) Å	Bi_2-O_1 = 2.09(4) Å	Bi_1-O_8-Bi_4 = 94(1)°
Bi_3-O_6 = 2.17(3) Å	Bi_4-O_6 = 2.11(3) Å	Bi_1-O_1-Bi_2 = 125(1)°
Bi_1-O_8 = 2.39(4) Å		O_{10}-Bi_4-O_8 = 145(1)°

This bismuth tetramer is fluctional in solution; one type of alkoxide is seen in the proton NMR down to - 50°C. Reactions where less than 1 eq. of t-butanol per alkoxide was used lead to

the formation of a product of incomplete alcholysis, $Bi_3(OtBu)_7(NSiMe_3)$. This compound, which has been structurally characterized, has a triply bridging alkoxide above one side of the Bi_3 triangle, and a triply bridging silyl imide on the other side, and is the first example of a bismuth imide.

Hydrolysis Studies

Hydrolysis studies were undertaken on both the t-butoxide and phenoxide compounds. Both materials were found to be highly moisture sensitive. Immediate precipitation of the hydrated metal oxides occurs upon the addition of even small amounts of distilled-deionized water (0.25 eq/OR) to NMR tubes containing the bismuth alkoxide. The hydrolysis of the t-butoxide compound appears to occur catalytically in the presence of small amounts of water. This compound was exhaustively hydrolyzed on a large scale. The resulting white powder dried, and fired at 850°C. Microprobe analysis of the resulting material showed that is was Bi_2O_3 of varying grain sizes, but free from carbon impurities. Proton NMR studies on $Bi(Dipp)_3$ showed that this material is less hydrolytically sensitive that the t-butoxide. No intermediate products of hydrolysis have been seen by the NMR for either of these alkoxides in these preliminary studies.

Volatility Studies.

The bismuth amide and phenoxide were examine for volitility. Both compounds sublimed under 150°C, and decomposed below 200°C. Under CVD conditions, the amide can be decomposed onto glass slides, however, silicon nitride may be formed. Oxygen plama deposition may be necessary to put down clean Bi_2O_3. While the $Bi(Dipp)_3$ seems to decompose more cleanly than the amide, partial discoloration of the solid Bi_2O_3 formed suggests that carboneceous impurities may also be present. Carbon impurity levels will be determined by nuclear reaction analysis.

REFERENCES

1. W. G. Fahrenholtz, G. M. Millar, D. A. Payne, American Ceramic Society Symp. Proc., "Ceramic Superconductors", May 1-5 1988.

2. N. N. Sauer, E. Garcia, K. V. Salazar, R. R. Ryan, J. A. Martin, J. Am. Chem. Soc., 112, 1524, (1989).

3. W. Clegg, N. A. Compton, R. J. Errington, N. C. Norman, N. Wishart, Polyhedron, 8, 1579, (1989).

KINETIC STUDY OF HIGH Tc Bi-Pb-Sr-Ca-Cu-O SYSTEM

W.-M. Hurng, Y. T. Huang, C. Y. Shei, C. Chiang, H. S. Koo, S. F. Wu and P. T. Wu

Materials Research Laboratories, Industrial Technology Research Institute, Chutung, Hsinchu, 31015, Taiwan, R. O. C.

ABSTRACT

By studying the Bi-Pb-Sr-Ca-Cu-O system, we have found that the sintering time to form high Tc Bi-Pb-Sr-Ca-Cu-O systems was quite different as the compositions of the starting materials varied. Especially, the ratio of Sr/Ca played an important role in determining the sintering time.

DTA study already showed that partial melting occurred during the reaction. The temperature of the partial melting was also related to the ratio of Sr/Ca. Our results supported the existence of a reactive liquid phase in sintering process.

INTRODUCTION

In the Bi-Sr-Ca-Cu-O system, two phases always coexisted; $Bi_2Sr_{2-x}Ca_{1+x}Cu_2O_y$ (Tc ≈ 84 K and denoted as 2212) and $Bi_2Sr_2Ca_2Cu_3O_y$ (Tc ≈ 110K and denoted as 2223) [1,2]. It is difficult to obtain a pure 2223 phase. A couple of methods were developed to yield the 2223 phase without the disturbance of 2212 including; varying the nominal compositions [3], using reduced oxygen atmosphere [4] and substituting part of the Bi with Pb [5]. Neverthaless, it always took more than sixty hours to complete sintering process [6]. We have found that the sintering time can be reduced down to twenty hours to form 2223 by varying the Sr/Ca ratio as Pb substitution is adopted and extra CuO added [7]. The real cause in shortening the sintering time was believed to be related to formation of a transient liquid phase during the 2223 formation process. In this paper, the thermal analysis of a series nominal compositions with different Sr/Ca ratio was conducted to reveal the influence in sintering time and liquid phase formation.

EXPERIMENTAL

A series of samples $Bi_{1.7}Pb_{0.4}Sr_{2-x}Ca_{2+x}Cu_{3.6}O_y$ (x = 0.0, 0.2, 0.4, 0.6, 0.8) were prepared by mixing and grinding stoichiometric Bi_2O_3, PbO, $SrCO_3$, $CaCO_3$ and CuO together. After calcined at 810°C in air for 30 hours with one intermediate grinding, the samples were pressed into disk like pellets. The sintering temperature was set within 840°C to 870°C (±0.5°C).

X-ray diffraction patterns were taken using a Phillips APD1700 diffractometer with Cu Kα radiation to identify calcined or sintered products and estimate the relative yields between the 2212 and 2223 phases. For ease of comparison, the (00$\underline{10}$) reflection of 2223 (occurred at 2θ = 23.9° and abbreviated as H(00$\underline{10}$)) and the neighboring (008) reflection of 2212 (appeared at 2θ = 23.1° and abbreviated as L(008)) were utilized to evaluate the relative yield between these two

Mat. Res. Soc. Symp. Proc. Vol. 180. ©1990 Materials Research Society

phases. Differential Thermal Analysis (DTA) study of the calcined samples was carried out using a ULVAC 7000 thermalanalyzer. The density of the pellets was also measured by using absolute ethanol as solvent.

RESULTS AND DISCUSSION

To accurately determine the optimal condition as x increased from 0.0 to 1.0, sintering temperature altered with the increment 2.5°C per sample from 840°C to 855°C except for x = 0.8. From 855°C to 870°C, the increment was set to 5°C per sample. Figure 1. shows the ratio of H(00$\underline{1}$0)/H(00$\underline{1}$0)+L(008) vs. various sintering temperature as sintering time was fixed to 20 hours. Apparently, the highest yield of 2223 in these samples could be obtained at 850°C with x equal to 0.4 or 0.6. Moreover, the optimal yield of 2223 was quite dependent on the x values. The dashed line in Fig. 1. indicated the optimal temperature forming 2223 shifted from 865°C down to 845°C as x varied from 0.0 to 0.8. That is, the increment of Ca depressed the optimal sintering temperature, but the highest yield of 2223 was observed when x was in the range 0.4 - 0.6 range.

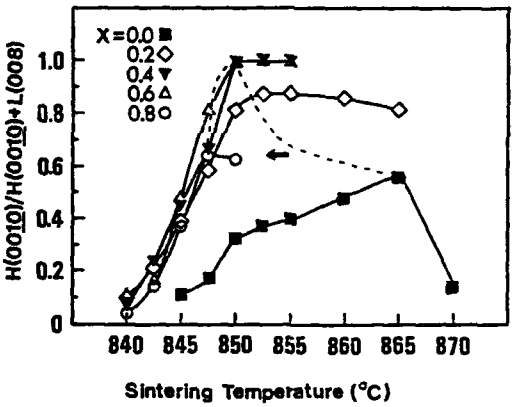


Fig. 1. The H(00$\underline{1}$0)/H(00$\underline{1}$0)+L(008) vs. sintering temperatures.

DTA was conducted in air to monitor the influence of different Sr/Ca ratio on the reactions. The DTA results are represented in Fig. 2. T_{onset} temperatures for the endothermic peaks were the same around 835°C while the T_{peak} temperatures were raised as x decreased. A close examination suggested the T_{peak} temperature were almost the same as optimal temperatures observed in Fig. 1. This could be explained if T_{onset} was a eutectic like temperature and T_{peak} corresponded to the formation temperature of 2223. The details of the peak analysis will be reported in another paper [8].

The formation mechanism of 2223 is quite complicated and is still not clear since it is composed of six elements. An intermediate or reactive liquid phase (this is called partial melting phenomenon) was proposed while Ca_2PbO_4 was reported to be the source of the liquid phase [9]. Our recent results confirmed the formation of liquid phase which should be

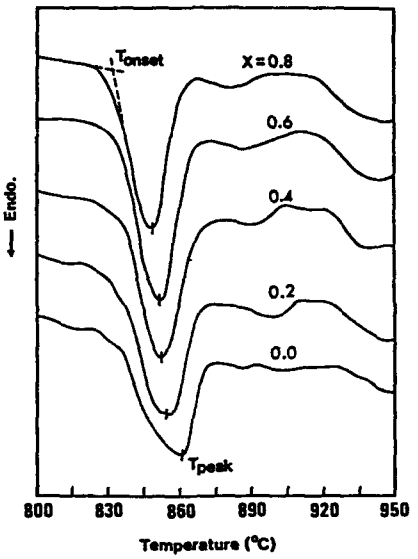


Fig. 2. DTA curves of 810°C/30h calcined $Bi_{1.7}Pb_{0.4}Sr_{2-x}Ca_{2+x}Cu_{3.6}O_y$ powders.

composed of at least three components - Ca_2PbO_4, 2212 and CuO [10]. The enhancement of the formation of 2223 by lowering Sr/Ca ratio provides additional evidence that Ca_2PbO_4 did participates in liquid phase formation. The density study of the sample pellets also supported the liquid phase aided mechanism. As displayed in Fig. 3, the density decreased down to the optimal temperature as Ca substitutent increased. This could be attributed to the more liquid phase presence as more Sr component replaced by Ca component.

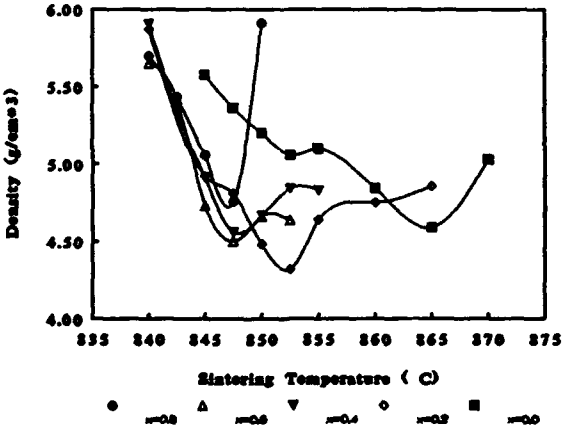


Fig. 3. Density of sintered pellets vs. sintering temperature.

The presence of the liquid phase not only acts as a flux to raise the contact frequency between different components but also reacts with the rest of components to form 2223. Therefore, there would be a optimal nominal composition to provide suitable amount liquid phase to form 2223. This is consistent with the results in Fig. 1. With x larger than 0.6, the yield of 2223 is lowered, although the grain growth did increase.

CONCLUSION

In this paper, the enhancement of formation of 2223 was demonstrated by varying Sr/Ca ratio. Also, the optimal sintering temperatures were consistent with the DTA results. This phenomenon supported the reactive liquid phase mechanism. The liquid phase or partial melting phenomena acted as a flux as well as reactants. Therefore, it is quite important to choose a suitable starting composition ($0.2 < x < 0.8$) and appropriate sintering temperature to form 2223.

ACKNOWLEDGEMENT

The present work was supported by the Ministry of Economic Affairs, The Republic of China, under contract no. 33B1000 to ITRI.

REFERENCE

1. C. Michel, M. Hervieu, M. M. Borel, A. Grandin, F. Deslanders, J. Provost and B. Reveau, Z. Phys. B 68, 421 (1987).
2. H. Maeda, Y. Tanaka, M. Fukutomi and T. Asano, Jpn. J. Appl. Phys. 27, L209 (1988).
3. U. Endo, S. Koyama and T. Kawai, Jpn. J. Appl. Phys. 28, L190 (1989).
4. U. Endo, S. Koyama and T. Kawai, Jpn. J. Appl. Phys. 27, L1476 (1988).
5. M. Takano, J. Takada, K. Oda, H. Kitaguchi, Y. Miura, Y. Ikeda, Y. Tomii and H. Mazaki, Jpn. J. Appl. Phys. 27, L1041 (1988).
6. N. Murayama, E. Sudo, M. Awano, K. Kani and Y. Torii Jpn. J. Appl. Phys. 27, L1629 (1988).
7. Y. T. Huang, W. N. Wang, R. G. Liu, S. W. Lu and P. T. Wu Appl. Phys. Lett. 56, 779 (1990).
8. Y. T. Huang, C. Y. Shei, W. N. Wang, C. K. Chiang and W. H. Lee, submitted to Physica C.
9. T. Uzumaki, K. Yamanaka, N. Kamehara and K. Niwa, Jpn. J. Appl. Phys. 28, L75 (1989).
10. Y. T. Huang, W. N. Wang, S. F. Wu, C. Y. Shei, W.-M. Hurng, W. H. Lee and P. T. Wu submitted to J. Am. Cera. Soc.

SOLUTION-DERIVED $YBA_2CU_3O_{7-\delta}$ THIN FILMS AND BARRIER LAYERS

G. E. Whitwell, J. H. Wandass, F. M. Cambria and M. F. Antezzo
Akzo Chemicals Inc., Akzo Research Laboratory Dobbs Ferry
Livingstone Ave., Dobbs Ferry, NY 10522

ABSTRACT

Hydrolyzed metal alkoxide solutions were spin-coated on Si substrates with subsequent thermal processing. Barrier layers of alkaline earth oxides, perovskites, Y_2O_3, ZrO_2 and others were produced. Characterization was performed via SEM, XRD, ESCA, Auger depth profiling and resistivity measurements. Barrier layer films were fairly smooth with some cracking and pitting present. Si migration was severe for alkaline earth thin films on Si wafers. Some perovskite films on Si showed formation of Ba-Si-O phases at the Si interface. Thin films of 1-2-3 on barrier layers of $SrTiO_3$ or ZrO_2 on Si showed Ba pileup at the Si interface and were not superconducting. 1-2-3 layers deposited on single crystal ZrO_2 were superconducting and showed onset temperatures of 90 K with zero resistance reached at about 55 K.

INTRODUCTION

Producing thin films for high T_c superconductor applications requires control of film stoichiometry, crystallinity, and substrate interactions. Some of the film forming techniques that have been reported to date are: evaporation [1], sputtering methods [2], and laser ablation [3]. These methods suffer from one or all of the following drawbacks: need for high vacuum conditions, differential sputtering rates, limitation to small areas, and line-of-sight access. Applications of high T_c materials such as antennas, magnetic shielding, waveguides, and printed circuit board traces would not be easily produced by the previous methods.

Spin coating/pyrolysis methods [4-6] have several advantages such as easy modification of stoichiometry and chemical composition, large and irregular sample handling via dipping or spraying, and inexpensive apparatus. Disadvantages include difficulties in producing the proper crystallite size and orientation, and achieving good film density and thickness. Spin coating of superconductor precursors in solution followed by pyrolysis has been used to produce high T_c thin films with acceptable onset temperatures [4-6], albeit broad transitions [4]. Lower than optimal film densities have been postulated as a reason for this.

This paper discusses the sol-gel synthesis of barrier layers and 1-2-3 thin films on Si and single crystal zirconia using hydrolyzed alkoxide solutions. These not only provide good viscosity and spinning characteristics, but the solution precursors are left in a hydrated ligand-associated state which facilitates pyrolysis. Since previous literature results have suggested that avoiding formation of interfacial Ba reaction products and Si migration on Si substrates is important [7-9], a variety of potential barrier layers on Si were synthesized. Synthesis of 1-2-3 superconductors on these barrier layers and substrates such as Si and single crystal ZrO_2 were also tried. The resulting thin film systems were analyzed by SEM for observation of morphology, XRD for crystallinity and phase identification, ESCA for near surface interface chemistry, Auger depth profiling for interface reactions and four-point probe resistivity measurements for verification of superconductivity.

Mat. Res. Soc. Symp. Proc. Vol. 180. ©1990 Materials Research Society

EXPERIMENTAL

Strontium and barium methoxypropoxides were both prepared by the same direct reaction [10] of the metals with 1-methoxy-2-propanol; details are given below for the strontium reaction. Strontium metal (70g) was treated with anhydrous 1-methoxy-2-propanol (974 ml) for 7 hours at room temperature and the resulting product was filtered. Yttrium methoxypropoxide was prepared by reaction of yttrium metal (2.0 g) with anhydrous 1-methoxy-2-propanol (75 ml) and $HgCl_2$ (40 mg). The solution was heated to 100° C for 24 hours, and the resultant product was filtered.

Copper aminoethoxide was prepared from copper(II) chloride and sodium aminoethoxide in ethanol. Freshly cleaned sodium metal (3.83g) was reacted with anhydrous ethanol (200 ml). A reagent solution was prepared from that solution (167 ml) and ethanolamine (9.05 ml). A portion (67 ml) of this solution was added to anhydrous $CuCl_2$ (4.0 g) in ethanol (75 ml). The solution was filtered and the solvent removed under vacuum. Titanium n-butoxide and zirconium n-butoxide-butanol complex were used as received.

Binary and ternary solutions of the metal alkoxides were prepared in 1-methoxy-2-propanol. The mixed alkoxide solutions were treated with 1 eq H_2O (5% in 1-methoxy-2-propanol) per each two alkoxide groups at room temperature. The hydrolysis solution was added over 20 mins with stirring, and the solution was further stirred for 2 hours.

Thin films were spun on 3" silicon wafers or 1" zirconia substrates. For systems containing alkaline earth metals, spinning was conducted in a nitrogen atmosphere. Typical spinning conditions were 2000 rpm for 30 secs which gave films of 25-100 nm thickness as determined by profilometry. Multilayered films of from 0.2 - 1 μm in thickness were made by multiple spinning depositions. An intermediate, partial cure was achieved by heating at 200° C for 5 min on a hot plate. Barrier layer firing was done over a period of 10 hours by heating in a water vapor-saturated N_2 atmosphere, holding at 750° C for two hours and then cooling to room temperature in an O_2 atmosphere. 1-2-3 firing was similar except that the peak temperature of 850° C was held for 15 minutes, and the total firing time was 20 hours.

Resistivity measurements were done using standard four-point probe techniques. Keithley model 181 nanovoltmeter and model 224 current source were used. An APD cryostat was used for cooling the samples. The cooling and measurement procedures were controlled by a PC/AT clone using in-house written routines.

Scanning electron microscopy was performed on an Amray 1830T digital SEM. Samples were sputter-coated with approximately 15 nm of gold before examination. X-ray diffraction data was collected on a Rigaku D/Max II powder diffractometer with Cu Kα radiation at 25 kV and 15 mA. Step size was 0.01°, with a counting time of 4 sec per step. Typical scan times were 4 - 7 hours. Samples were mounted flush with the sample holder surface with double sided tape and rotated during analysis. Several films were examined at the Rigaku/USA applications lab in Danvers, MA. The films were analyzed using Rigaku's thin film diffractometer with glancing angle geometry. The samples were held at an incidence angle of 1° while 2θ was scanned.

ESCA and Auger spectra were collected on several different instruments. These included a Phi 550 ESCA/SAM spectrometer, a VG ESCALAB 200A multi-technique instrument, and a VG 310D Auger spectrometer. Mg Kα radiation was used for XPS in all cases.

RESULTS AND DISCUSSION

Barrier Layers: A list of samples along with various analysis results is shown in Table I.

SEM examination of barrier layers on Si showed them to be fairly smooth, with some surface cracking and pitting present. Powder diffraction data were mostly inconclusive, probably due to the fact that the films were thin. A $BaZrO_3$ film on Si, examined by thin film XRD, was successfully identified. An additional phase was detected, near the Si substrate, when the incidence angle was increased to 2.5°. This phase could not be identified via XRD. Auger analysis suggests that this phase is Ba_2SiO_4, a reaction product of the Si substrate with the barrier layer.

The near surface interface chemistry of the alkaline earth-containing systems is dominated by the formation of stable carbonates. For BaO, CaO, and SrO, severe reaction and diffusion of Si into the thin film results in formation of the respective silicate. The CuO film showed significant $CuSiO_3$ formation. TiO_2, Al_2O_3, ZrO_2, Y_2O_3 and the Y_2O_3-stabilized ZrO_2 films showed sharply defined interfaces on Si with no evidence of reaction. However, the Y_2O_3, ZrO_2, and Al_2O_3 films showed subsurface C contamination which most likely results from inadequate pyrolysis.

All of the perovskite barrier layers except $SrTiO_3$ and Ba_2SiO_4 reacted with Si to form an oxidized Si-alkaline earth phase. For $BaAl_2O_4$, $BaTiO_3$, and $BaZrO_3$, Ba pileup occurred at the Si interface with formation of what is most likely Ba_2SiO_4. No evidence of Si migration into the thin film was observed. $SrTiO_3$ and Ba_2SiO_4 exhibited a sharp interface with no diffusion of metallic Si observed.

Table I: Analysis Results - Barrier Layer Systems

System	ESCA	Auger	XRD
BaO	$BaCO_3$, silicate	Si diffusion, Si ox, Ba_2SiO_4	$BaCO_3$
CaO	$CaCO_3$	Si diffusion, Si ox, CaO	ND/Si
SrO	$SrCO_3$, $SrSiO_3$	Si diffusion, Si ox	$SrSiO_3$
CuO	$CuSiO_3$	severe Si diffusion	CuO
TiO_2	TiO_2	sharp interface	ND
ZrO_2	ZrO_2, Si	subsurface C, no Si diffusion	ND
Al_2O_3	Al_2O_3	C "spike", no Si diffusion	ND/Si
Y_2O_3	Y_2O_3	C contamination, no Si diffusion	ND/Si
Y_2O_3 stab ZrO_2	Y_2O_3/ZrO_2	no Si diffusion	NA
Y_2O_3	Y_2O_3	C contamination, no Si diffusion	NA
$SrTiO_3$	$SrTiO_3$, $SrCO_3$	sharp interface, no Si diffusion	NA
$BaAl_2O_4$	$BaAl_2O_4$, $BaCO_3$	Ba pileup at interface, Ba_2SiO_4	$BaAl_2O_4$
$BaZrO_3$	$BaZrO_3$, $BaCO_3$	Ba pileup at interface, no Si	ND/Si
Ba_2SiO_4	$BaCO_3$, Ba_2SiO_4	sharp interface	SiO_2
$BaTiO_3$	$BaCO_3$, $BaTiO_3$	Ba pileup at interface	ND/Si
$SrZrO_3$	$SrCO_3$	Ba pileup at interface, Ba_2SiO_4	NA

* ND(/Si) = no crystalline phases detected (except Si substrate); NA = not analyzed

1-2-3 systems: A list of samples and analysis results for several 1-2-3 high T_c compositions is given in Table II.

Thin film XRD patterns of 1-2-3 films on Si showed the presence of $BaCO_3$ and CuO. The same film deposited on a ZrO_2 barrier layer on Si yielded a very strong 1-2-3 diffraction pattern with no other phases detected. Morphological examination of the 1-2-3/barrier layer/Si and 1-2-3/Si samples showed discontinuous films, with large gaps allowing the substrate to be visible. At higher magnifications, the 1-2-3/barrier layer/Si and 1-2-3/Si samples appeared to consist of submicron rounded nodules, giving the appearance of a melted phase. 1-2-3 films on single crystal ZrO_2 were less porous and more coherent with columnar crystallites and rounded nodules. Similar morphologies observed using TEM have been reported for 1-2-3 on oxidized Si using a ZrO_2 buffer layer [13]. This sample appears to be a transitional material with morphological traits of both the amorphous and crystalline 1-2-3 phases.

The 1-2-3/Si thin film reacted with the Si substrate to form Ba_2SiO_4 at the Si interface along with a Ba-depleted Cu-Y-O overlayer in agreement with previously reported results [9,11]. In some 1-2-3/Si samples, Si was observed at the surface perhaps due to cracking. Cheung et al [7] have postulated that the 1-2-3 phase initially reacts with Si to form Ba_2SiO_4, a 2-1-1 phase, and CuO with subsequent diffusion of Ba and Cu to continue the process. Although we do not directly observe the 2-1-1 phase or CuO, we believe that the formation of the Ba_2SiO_4 interface phase most likely proceeds by the pathway that they suggest. Since they observed no reaction products with 1-2-3 and Si up to 800° C, direct application of a spin-coated sol-gel film to Si should be possible if pyrolysis could be completed satisfactorily at temperatures lower than 800° C.

Table II: Analysis Results - 1-2-3 Systems

System	ESCA	Auger	XRD
Si	$BaCO_3$, Cu^{+2}	Ba pileup, Y-Cu Ba depleted/ Ba_2SiO_4/Si, Si migration	CuO, $BaCO_3$
$SrTiO_3$/Si	$BaCO_3$, no Si diffusion	Y-Cu Ba depleted/$SrTiO_3$/ Ba_2SiO_4/Si	NA
ZrO_2/Si	$BaCO_3$, Cu^{+2}	Y-Cu Ba depleted/ZrO_2/ Ba_2SiO_4/Si	1-2-3
Single crystal ZrO_2	$BaCO_3$, Cu^{+2}	uniform film, Cu depletion	1-2-3, ZrO_2

* NA = not analyzed

We observed three layers for 1-2-3 compositions spun on ZrO_2 or $SrTiO_3$ barrier layers/Si. The uppermost layer consisted of a Ba-depleted 1-2-3 composition. The next layer consisted of the barrier layer ($SrTiO_3$ or ZrO_2) while the third layer (closest to the Si interface) consisted of Ba_2SiO_4. The Ba diffusion observed in our systems seems to leave the barrier layers intact. Both of these samples were non-conductive at room temperature. Even though XRD detected 1-2-3 in the 1-2-3/ZrO_2/Si sample, the extensive cracking most likely limited conduction.

Cheung et al have observed replacement of Sr by Ba in $SrTiO_3$/1-2-3 systems along with formation of a Y-Ba-Cu-Ti phase, and Holloway et al [11] have seen similar results for 1-2-3 films on $SrTiO_3$/Si. For 1-2-3/ZrO_2 couples, Cheung et al observed inward diffusion of Ba towards the ZrO_2 particles along with $BaZrO_3$ formation. The ionic sizes of Ba^{+2} (0.135 nm) and Sr^{+2} (0.112 nm) are similar and Ba and Sr titanates have the same crystal structure allowing complete solid solution of these two materials. Thus Ba diffusion through the titanate barrier layers with subsequent formation of Ba_2SiO_4 seems plausible. On the other hand, the ionic radii of Ba^{+2} and Zr^{+4} (0.080 nm) are significantly different as are the crystal structures for ZrO_2 and $SrTiO_3$. This would tend to discourage intergranular diffusion of Ba and suggests that Ba diffusion around grain boundaries may be occurring. (Our barrier layers are relatively thin and show significant microcracking) Reaction of Ba in a 1-2-3 film with a Ca-stabilized ZrO_2 substrate to form $BaZrO_3$ has been reported [12], but direct diffusion of Ba through the ZrO_2 layer in our samples does not seem likely. No evidence of $BaZrO_3$ formation was observed for our 1-2-3/ZrO_2/Si sample. Si migration into either $SrTiO_3$ or ZrO_2 barrier layers or the overlying 1-2-3 layer was not observed.

A superconducting 1-2-3 layer was successfully deposited on single crystal ZrO_2. This film had a low room temperature resistance, and onset temperature of 90K and zero resistivity at about 55K. SEM examination of this sample revealed that the film had poor adhesion with significant cracking, most likely the result of mismatched thermal coefficients.

CONCLUSIONS

We have shown that thin films of a variety of materials may be successfully deposited by spinning hydrolyzed sol-gel precursors with subsequent pyrolysis on Si. Some of these thin films may have applications for use as barrier layers in high T_c thin film systems. In each instance, reaction thermodynamics will determine the predominant phases formed. For solution-deposited alkaline earth oxide thin films on Si, significant reaction with Si occurs to give silicates at 750° C. TiO_2, Al_2O_3, ZrO_2, Y_2O_3 and Y_2O_3-stabilized ZrO_2 thin films show good interfacial properties on Si. However, subsurface C must be eliminated. Smooth, relatively crack-free $SrTiO_3$ thin films on Si can be produced via this method. Ba-containing perovskite thin films show high reactivity on Si with formation of the respective silicate. Control of film cracking in these systems is important to increase adhesion and minimize potential diffusion processes.

1-2-3 films directly deposited on Si showed similar reactivity as reported previously in the literature. 1-2-3 thin films on $SrTiO_3$ or ZrO_2 barrier layers on Si showed formation of a three layer system: Y-Cu, Ba depleted/barrier layer/Ba_2SiO_4/Si interface. Microcracking in ZrO_2 barrier layers and compatible solid state structure for $SrTiO_3$ barrier layers is most likely responsible for enhanced Ba diffusion in these systems. A 1-2-3 superconducting thin film was successfully deposited on a single crystal zirconia substrate; however, there was severe cracking present.

ACKNOWLEDGMENTS

J.H.W. acknowledges VG Scientific, Ltd, in the UK for the use of ESCA/Auger equipment and personnel. F.M.C. acknowledges Rigaku/USA in Danvers, Massachusetts for the use of their thin film X-ray diffraction equipment.

REFERENCES

1. P. Chaudhari, R. H. Koch, R. B. Laibowitz, T. R. McGuire, R. J. Gambino, Phys. Rev. Lett. 58, 2684 (1987).
2. M. Wong, S. H. Liou, J. Kwo, B. A. Davidson, Appl. Phys. Lett. 51, 694, (1987).
3. J. Narayan, N. Biunno, R. Singh, O. W. Holland, O. Auciello, Appl. Phys. Lett. 52, 1845, (1988).
4. C. E. Rice, R. B. VanDover, G. J. Fisanick, Appl. Phys. Lett. 51, 1842, (1987).
5. M. E. Gross, M. Hong, S. H. Liou, P. K. Gallagher, J. Kwo, Appl. Phys. Lett. 52, 160, (1988).
6. Moore, G., Kramer, S., Kordas, G., Mater. Lett. 7(12), 415, (1989).
7. C. T. Cheung, E. Ruckenstein, J. Mater. Res. 4(1), 1, (1989)
8. T. Venkatesan, E. W. Chase, X. D. Wu, A. Inam, C. C. Chang, F. K. Shokoohi, Appl. Phys. Lett. 53(3), 243, (1988).
9. A. Mogro-Campero, B. D. Hunt, L. G. Turner, M. S. Burrell, W. E. Balz, Appl. Phys. Lett. 52, 584, (1988).
10. U. S. Patent 4,751,318, W. Summers and E. W. Burkhardt.
11. J. K. Truman, M. Leskela, C. H. Mueller, P. H. Holloway, preprint from 1988 AVS High Temperature Superconductor Topical Conference.
12. J. K. Grepstad, Ph. Niedermann, J. M. Triscone, L. Antognazza, M. G. Karkut, O. Fischer Physica C, 153-155, 1453, (1988).
13. A. Mogro-Campero, L. G. Turner, E. L. Hall, M. C. Burrell, Appl. Phys. Lett., 52(24), 2068, (1988).

PREPARATION, THERMAL PROCESSING BEHAVIOR AND CHARACTERIZATION OF POWDERED AND BULK $YBa_2Cu_3O_{7-x}$ FROM FREEZE DRIED NITRATE SOLUTIONS.

N. COPPA,* A. BURA,** J. W. SCHWEGLER,* R. E. SALOMON,* G. H. MYER,* and J. E. CROW**

*Center for Materials Research, Temple University, Philadelphia, PA 19122
**Center for Materials Research and Technology, Florida State University, Tallahassee, FL 32306-3016

ABSTRACT

Solutions of Y, Ba and Cu nitrate were spray-frozen. Very small particles consisting of atomic mixtures of these salts remained after the water was sublimed. These YBCO precursors were characterized and their behavior was studied in detail while they were thermally decomposed by a variety of techniques. Kilogram size batches are routine. The final YBCO products were obtained as powders and sintered bars. Sintered materials exhibited excellent phase purity (>99%) and super-conducting characteristics (Tc = 92 K), while powdered materials had secondary phases present. Some of these samples having high percentages of second phases exhibited sudden drops in resistivity to a few micro-ohms at 200 or 240 K followed by a zero resistance transition at 92 K. Coincident with this drop in resistance was a discontinuity in the magnetization.

I. INTRODUCTION

Freeze drying technology has been applied to the fabrication of ceramic materials.[1] and more recently it has been applied to the production of $YBa_2Cu_3O_{7-x}$ (YBCO).[2,3] Usually the starting components are dissolved in a liquid medium and quickly frozen; subsequently the medium is sublimed. A solution or liquid phase will allow the components to mix on an atomic scale and by quickly freezing the solution, the components are immobilized in this disordered state. Sublimation of the medium leaves behind the components trapped in a solid solution which for the most part has the mixing and disorder of the parent aqueous solution. The advantages of freeze drying techniques are several, for example, contaminants, from grinding surfaces used in the ceramic method, are eliminated since the mixing of the components is achieved by solution. Contamination from reaction vessel material is minimized since the reaction times and temperatures will be shorter and lower respectively. The production of extremely dilute homogeneously dispersed impurity doped materials are readily achieved, where this is virtually impossible using more conventional methods.

In this paper we give details for optimum powder preparation and discuss the mechanism of YBCO formation from nitrate precursors. The purpose and ultimate goal of this process is to produce a finely divided precursory material composed of yttrium, barium and copper nitrates which is mixed and remains mixed at the atomic scale. Such a precursor is subjected to a variety of thermal treatments depending on the desired form of the final product. Phase separation of the dissolved components is avoided by producing a fine aerosol dispersion of the solution and freezing it rapidly. Fine powders are produced as a result of combining the use of a small aerosol droplet and dilute parent solution.

Mat. Res. Soc. Symp. Proc. Vol. 180. ©1990 Materials Research Society

II. EXPERIMENTAL METHOD

Sample Preparation: Solutions were prepared from the oxides of yttrium and copper dissolved in nitric acid and barium nitrate and diluting to 0.03 M in yttrium using distilled deionized water. The pH of the solutions were between 2.20 to 2.80 and were filtered/degassed. An aerosol of the nitrate solution was produced using an ultrasonic spray nozzle (Sono Tek, 8700-120MS/PS-8S). The aerosol was frozen by allowing it to fall into stirred liquid nitrogen. The frozen aerosol was freeze-dried using a modified[4] commercial laboratory freeze dryer (FTS Systems, FD6-54A-O / TD-2A). Typically a rates of sublimation were 750 g d^{-1}. The freeze-dried product, referred to here the *precursor*, was dehydrated in a vacuum box furnace by slowly raising the temperature to 150 C. This material was denitrated by plunging it into a quartz lined tube furnace preheated to 600 C, under nitrogen and soaking at that temperature for 2 h. Denitrated powders were either directly heated from 600 to 900 C (1 C min^{-1}) under flowing nitrogen, or pressed pellets (1 kbar) and then heated to 900 C, (1 C min^{-1}). After a 2 h soak at 900 C the materials were cooled to 520 C (3 C m^{-1}), soaked for 2 h then cooled to room temperature at 4 C m^{-1}. The flowing gas was switched from nitrogen to oxygen at 525 C during the decent from 900 C.

Product Characterization: YBCO precursors and oxide products were analyzed by a variety of methods. XRD was used to determine the quantitative phase composition. Resistivity measurements were made to determine the transition temperature and the magnetization was measured to determine the superconducting volume fraction. Scanning electron micrographs (SEM) were obtained from some YBCO products.

Thermal Behavior Characterization: To elucidate the mechanism of product formation portions of YBCO precursor were heated to various temperatures for various lengths of time under oxygen. Samples were heated to 600, 700, 750, 800, 900 or 925 C for either 2, 8 and 24 h, under oxygen, and were analyzed using XRD. DSC, TGA and evolved gas analysis (EGA)[4] were used to identify the phase transformations and chemical reactions occurring during the thermal decomposition process. The heat of solution was determined using an apparatus described elsewhere,[4] to assess the extent of atomic mixing in the precursor material.

III. RESULTS

The freeze dried YBCO precursors consisted of a very light, fine, hydroscopic, pale blue, completely homogeneous (30x magnification) powder. The *as prepared* precursor appeared to *melt* or dissolve in the waters of hydration when heated to 102-108 C. XRD patterns of the precursor materials, have a high broad baseline which accounted for < 99% of the total scattering intensity. The heat of solution for the freeze dried nitrate precursor was in excess of 10 kcal mol^{-1}. Upon dehydrating the precursors described above, the appearance became pale green and the volume had been deceased by about one third. TGA thermograms and EGA analysis indicated that these materials behave in a manner identical to those of the non-dehydrated precursor except below 150 C where only slight weight losses were observed and, as indicated by DSC, no phases changes were observed. After 2 h at 600 C and a slow cool under N_2, the denitrated product appears homogeneous and black and were slightly agglomerated. SEM micrographs of denitrated materials reveal the existence of featureless agglomerates of 3-5 μm sized particles. XRD analysis of the denitrated materials indicates that

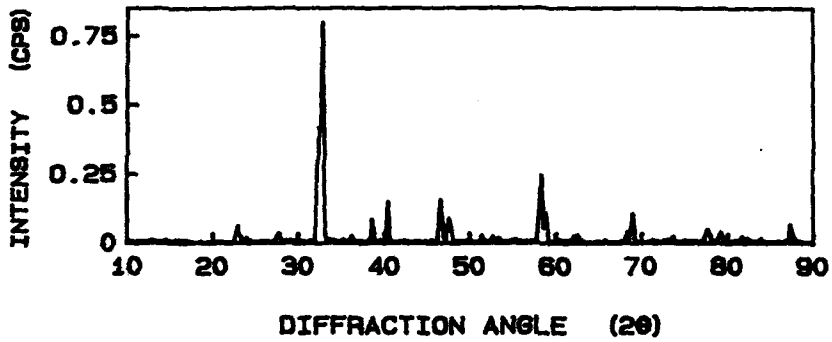


FIG. 1 XRD pattern after 900 C, 2 h, and 2 h oxygen anneal at 515 C. The orthorhombic splitting of the most intense peak for these materials is on an average 0.021 Å.

this material is almost exclusively composed of $Ba_2Cu_3O_{5+x}$ (023) and Y_2O_3 (100). No barium nitrate diffraction peaks were observed. After 2 h at 900 C under N_2 slow cool to 515 C for a 2 h anneal at under O_2, YBCO products formed appeared to consist of fine black powder; although, some sintering had occurred. Densities for compacted materials (1 kbar pressure), were 3.8 g ml^{-1} or ~70% theoretical density.

A typical XRD pattern from materials processed as powders, shown in FIG. 1, indicated that the scattering intensities originating from second phases were less than 1% of the total. Due to the low intensities and overlap of the diffraction peaks of the many possible secondary phases in the 25 - 30 2θ range, the identification of the secondary phases were difficult. But the most likely candidates were 211, 011 and possibly 023 characterized by the observed intensities at 3.055 and 3.025 Å. Materials which were processed as compacts exhibited higher purity (99% scattering intensity from 123). The orthorhombic splitting of the compacted materials was 0.026 Å. Unit cell calculations on the XRD patterns from these products give a = 3.8189, b = 3.8891 and c = 11.6738 Å for powders and a = 3.8193, b = 3.8856 and c = 11.6693 Å for the sintered compacts.

SEM micrographs obtained from powdered samples (FIG. 2) reveal agglomerates of 1-2 μm sized crystallites. Resistivity measurements on bars cut from sintered compacts typically show a pre-transition slope of 1.8×10^{-3} mΩ cm K^{-1}, where perfect metallic behavior for a material with identical room temperature resistivity would exhibit a slope of about 2.1×10^{-3} mΩ cm K^{-1}. $T_{c,0}$ was typically 90 K, while $T_{c,mid}$ and $T_{c,onset}$ were ≈ 94 (1.7×10^{-1} mΩ cm) and 98 K, respectively. Meissner volumes of 45% were measured on materials processed as sintered bars (using a density of 3.8 g ml^{-1}). In general Meissner volumes were very sensitive to the thermal processing and pressure used to prepare the compact.

Two samples which contained high amounts of secondary phases, exhibited a very high transition temperature (240 K) resistivity anomaly. At 240 K a sharp drop in resistance from 24 to about 2 mΩ cm was observed. The pretransition and post transition slopes were virtually flat as would be expected from impure samples. Following this drop in resistivity the material went superconducting at the normal transition temperature, (~90 K). This anomaly cannot be explained; however, other reports for this type of resistivity behavior have appeared in the



FIG. 2,SEM of a) YBCO product (see FIG. 1 for XRD) 160x, (bars = 10 μm), b) same material at 5000x (bars = 1 μm).

literature.[5-7] Coincident with the anomalous drop in resistivity at 240 K seen in two very phase-impure samples was a discontinuity in the magnetization.

IV. DISCUSSION

According to the models for freezing a 10 μm diameter spherical droplet aerosols of pure water will freeze in about 10^{-5} s or less.[4] As discussed in [4], the rate of freezing is sufficient to avoid solute phase separation. *Melting* was avoided by dehydrating the material as described above. By doing this, no melting occurred during further increases in temperature. The XRD patterns strongly indicate that the freeze dried YBCO precursor material lacks long range order while the high heat of solution indicates that the material lack short range order. These results are indicative of an atomic mixture.

By combining the measurements of TGA, DSC and EGA decomposition reactions can be distinguished from isogravametric phase transitions. Measurements such as these were necessary to determine the appropriate heat treatment schedules for the preparation of final products. The individual, weight-normalized, TGA decomposition curves for yttrium, barium and copper nitrates are superimposed into a TGA thermogram for the freeze dried precursor, (FIG. 3a). Copper nitrate apparently undergoes dehydration and denitration independent of the

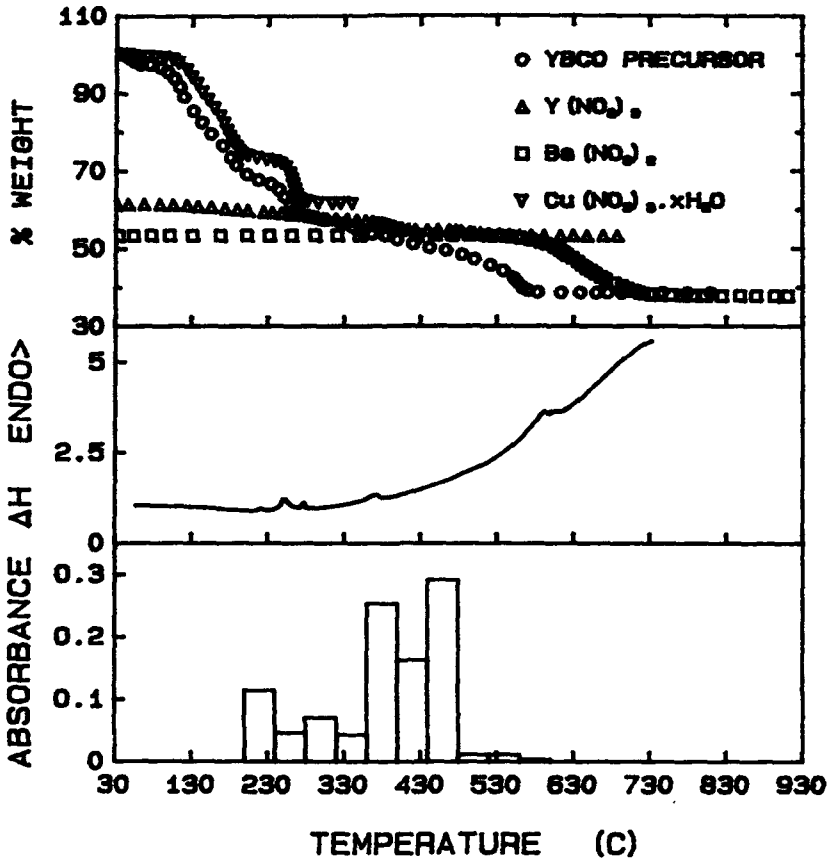


FIG. 3, a) Mole ratio normalized TGA of freeze dried precursor (o), $Cu(NO_3)_2 \cdot xH_2O$ (∇), $Y(NO_3)_3$ (Δ), and $Ba(NO_3)_2$ (□), b) DSC and c) EGA NO_2 absorbance of the same material measured as a function of temp.

other materials present. Thermograms (both TGA and DSC) of the precursors indicate that the thermal decomposition behavior of the precursors are unlike mechanical mixtures of the parent salts. As shown in FIG. 3, TGA indicated that the material had complete denitration had occurred by 600 C, while DSC (FIG. 1b), shows that isogravimetric phase transitions occur beyond this point. Nitrogen dioxide, which is a decomposition product of the nitrate ion, was most strongly detected by EGA in the range of 300 - 500 C (FIG. 3c) and by 600 C insignificant quantities were detected. It also appears that the yttrium and barium are decomposing simultaneously and decomposition is complete at a 600 C. XRD patterns obtained from the denitrated material do not indicate the presence of any barium nitrate. From these

data, it was apparent that barium nitrate, which normally decomposes in the 600 - 750 C temperature range, is decomposing at a much lower temperature. XRD patterns obtained from materials heated to 600 show the presence of 023 and 100 phases and no barium nitrate. As the temperature increases the ratio of 023 to 123 decreases.

A mechanism for the formation of YBCO from freeze dried nitrate precursor can be postulated. When the precursor material is plunged into the hot furnace, the decomposition of all the nitrates occur simultaneously. The atomic mixing of the reactants suggests that individual component molecules decompose in a environment of *unlike* components and in such a state are extremely reactive. Decomposition of barium nitrate, which in its pure form does not decompose until temperatures <600 C, is promoted at lower temperatures by the formation of a barium rich product with lower activity.[8] Barium nitrate apparently reacts with the highly reactive copper oxide forming a $Ba_2Cu_3O_{5+x}$ phase.[9] The most thermodynamically stable phase Y_2O_3, forms in isolation in an semi-amorphous state as indicated by the lack of intense diffraction intensities. As the temperature is increased towards 900 C, $Ba_2Cu_3O_{5+x}$ reacts with the amorphous Y_2O_3 to form YBCO. It is evident from the small crystallite size and the random distribution and orientation of crystallites in the product after 2 h at 925 C, that these processes are occurring at sites homogeneously distributed throughout the reaction milieu. These conclusions will be further justified in a forthcoming more comprehensive report.[10]

ACKNOWLEDGEMENT

This work was supported by DARPA/ONR contract #NOOO14-88--0587 and the Ben Franklin Partnership Program of the Commonwealth of Pennsylvania project #89S.5024R-3.

REFERENCES

1. For example see, K. F. Roehrig and T. R. Wright, J. Vac. Sci. Technol., 9(6), 1368, (1972).
2 M. Pham-Thi, R. Korman and A. Morell, Ind. Ceram. (Paris), 863, 197, (1989).
3. S. M. Johnson, M. I. Gussman and D. J. Rowcliffe, Adv. Ceram. Mater., 2(3B), 337, (1987).
4. N. Coppa, doctoral dissertation, Temple University, Philadelphia, (1990).
5. Ames High Tc Update, 3(19), (1989).
6. J. T. Chen, L. E. Wegner and C. J. McEwan, Phys. Rev. Lett., 58, 1972, (1987).
7. S. R. Ovshinski, R. t. Young, D. D. Allred, G. DeMaggio and G. A. Van der Leeden, Phys. Rev. Lett., 58, 2579, (1987).
8. P. Davies. personal communication, (1990).
9. J. G. Thompson, J. D. Fitz Gerald, R. L. Withers, P. J. Barlow and J. S. Anderson, Mat. Res. Bull., 24, 505 (1989).
10. N. Coppa, A. Bura, J. W. Schwegler, R. E. Salomon, G. H. Myer, and J. E. Crow, J. Mater. Res., to be submitted, (1990).

TEN MINUTE PREPARATION OF $YBa_2Cu_3O_{7-x}$ USING BARIUM HYDROXIDE

N. COPPA,* A. KEBEDE,* J. W. SCHWEGLER,* I. PEREZ,*
R. E. SALOMON,* G. H. MYER* AND J. E. CROW**
*Center for Materials Research, Temple University, Philadelphia PA 19122
**Center for Materials Research and Technology, Florida State University,
Tallahassee, FL 32306-3016

ABSTRACT

High quality bulk $YBa_2Cu_3O_{x-7}$ was synthesized by fusing stoichiometric amounts of yttrium and copper nitrates and barium hydroxide, in air, using an ordinary Bunsen burner. The starting materials go through a short-lived liquid phase yielding a solid black product which was subsequently heat treated, (900 C, 18-24 h, in air, followed by 500 C, 5 h., in O_2). These materials were greater than 99% phase pure with CuO as the only other phase and they exhibited a transition temperature of 92 K, a 15.5% perfect diamagnetic response (field cooled), 76% (zero field cooled). This synthesis represents an improvement over the much more labor and time intensive conventional methods in that it allows high quality materials of various compositions to be prepared quickly.

I. INTRODUCTION

The use of fused hydroxides for the synthesis of $YBa_2Cu_3O_{7-x}$ (YBCO) [1] and related materials[2] has been reported and those methods eliminated the need for multiple grinding/calcine cycles. However, these syntheses necessarily involved the use of water to remove the hydroxide which ultimately interfered with the direct synthesis of YBCO. It was also shown, in the case of YBCO, that the precise stoichiometry of the products was difficult to control.[3] In this paper, barium hydroxide is used as both flux and reactant. The liquid phases of barium hydroxide, described below, allow the products to mix in solution while the flux itself is consumed as a reactant. A YBCO product is directly formed, and the preparation time of bulk material is a very small fraction of any methods previously reported elsewhere. Although barium hydroxide had been used previously in the synthesis of YBCO,[4] it was used in that case as an alternative source of barium in the ceramic method. Here, the fact that barium hydroxide has two hydration states which differ greatly in their melting points is exploited. The low melting octahydrate (m.p. = 78 C[5]) acts as a solvent for the nitrates of copper and yttrium, while the higher melting anhydrous form (m.p. = 408 C[6]) serves as a medium and reactant which allows the mixing and subsequent reaction of the three metal ions. Complete decomposition and solid state reaction occur during subsequent thermal processing.

This method has an advantage over many existing methods in that the pre-calcine processing takes ten minutes; while others, for example, the ceramic,[7] coprecipitation,[8] sol-gel[9] or freeze-drying[10] methods, require investments of time on the order of hours or days. Calcine sintering, necessary to completely form the orthorhombic phase, takes an additional 18-24 hours which is also typical for the procedures mentioned above. In addition, this method, through the existence of an intermediate liquid phase, allows the homogeneous doping with minute amounts of impurities. The study of doped materials, such as these, are essential for the fundamental understanding of the superconducting properties these materials exhibit.[11]

Mat. Res. Soc. Symp. Proc. Vol. 180. ©1990 Materials Research Society

Many of the methods cited above are not easily adapted to accommodate homogeneous doping.

II. EXPERIMENTAL METHOD

All reagents were, as stated by the supplier (Johnson Matthey), 99.99% pure or better. Copper and yttrium nitrates were analyzed by TGA to determine the actual ratio of metal ion concentration. Barium hydroxide was determined to be anhydrous by TGA. YBCO was prepared by combining $Y(NO_3)_3 \cdot 6H_2O$, anhydrous $Ba(OH)_2$ and $Cu(NO_3)_2 \cdot 3H_2O$ in a mole ratio of 1:2:3 with 0.005 mol yttrium in a open ceramic crucible (Coors). They were first gently heated to allow uniform and complete melting of the reactants and then they were heated more intensely until the reactants underwent complete reaction as indicated by the formation of a black red-hot solid. The heat was applied, in air, from an ordinary Bunsen burner. For some samples, the temperature as a function of time was recorded from a thermocouple placed directly within the center of the reactants. Fusion and resolidification of the reaction milieu took no longer than three minutes although the sample was continuously heated for a total of ten minutes. The crucible was then cooled in air and the product removed. The product was either lightly crushed and processed as a powder or pressed into a pellet (12 x 3 mm, 1-3 kbar) and processed as follows in bulk. The crushed or pressed product was heated to 900 C in air for 4-24 h, cooled, and then heated to 500 C under a stream of oxygen for 5 hours. The material was cooled to room temperature while under oxygen.

Crucibles were cycled through the reaction procedure several times so that a residual coating was allowed to build up on the crucible walls; these crucibles were used to prepare samples for characterization.

The products formed at the end of the ten minute reaction and after the heat treatment were characterized by powder xray diffraction (XRD) and scanning electron microscopy (SEM). The calcined products were characterized by measuring the resistivity and magnetic susceptibility as a function of temperature, and by XRD. The unit cell parameters for the orthorhombic YBCO prepared by the above method was calculated from the XRD data using software by Appleman.[12] The resistivity (10-300 K) was measured using the standard four probe method on bars (1.5 x 1.5 x 10 mm) cut from sintered pellets. The Meissner volume was obtained by measuring the magnetic susceptibility χ, versus T, using a SQUID magnetometer (Quantum Designs) in a field of 1.00×10^{-2} T and cooled from above the superconducting transition temperature (field cooled). A measurement of the magnetic shielding was obtained by cooling the material to 4 K and measuring the magnetic susceptibility while raising the temperature through the transition temperature in a field as stated above.

III. RESULTS AND DISCUSSION

Octahydrated $Ba(OH)_2$ *melts* in the water of hydration at 78 C. In this process, the water comes from yttrium and copper nitrates which lose their water to the matrix of the reactants as they are heated. As heat was applied to the reaction mixture, a temperature plateau at about 165 C was observed where water and to a lesser extent NO_2 were evolved; the melt appeared blue-green and thickened toward the commencement of the temperature rise following this plateau. At about 450 C the reactants began to resemble a true, however short-lived, melt and concomitantly there was a more copious evolution of NO_2 with the

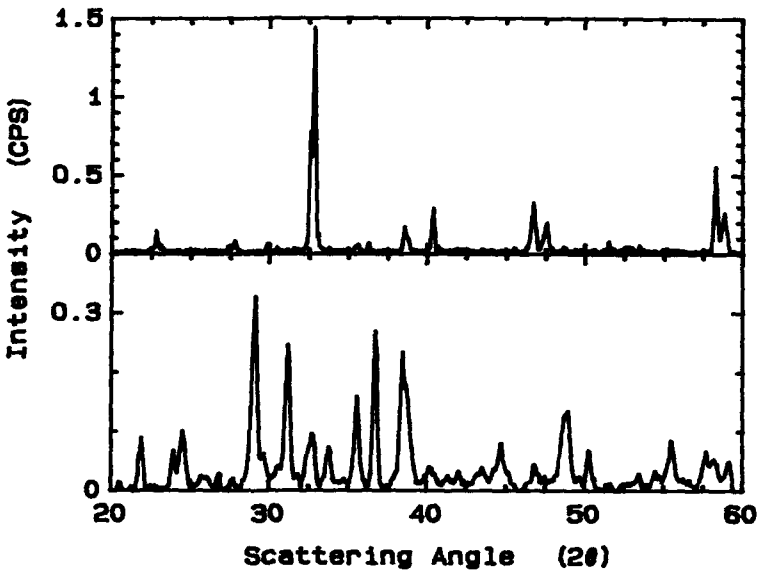


Fig. 1. a) X-ray powder diffraction intensity versus scattering angle (2θ) of the product precursors obtained after reacting the starting reagents for ten minutes. b) X-ray powder diffraction intensity versus scattering angle (2θ) of the orthorhombic superconducting phase. The diffraction pattern suggests a phase purity of ~99%, with the only identified impurity to be CuO.

simultaneous appearance of a black solid at the hottest regions of the crucible. The entire mass eventually solidified completely and the evolution of NO_2 ceased. The black products appeared granular and completely homogeneous when magnified 25x.

A typical XRD pattern is shown in FIG. 1a for the products after the ten minute reaction. Analysis of this pattern reveals that yttrium oxide and barium nitrate dominate the scattering intensity by contributing 26% and 35%, respectively; while $YBa_2Cu_3O_7$, CuO, $Ba(OH)_2$ and BaY_2O_4 contribute about 10% each. The line broadening seen in the pattern indicates the material to be largely composed of very small crystallites.[13] The presence of yttrium and copper oxides are not unexpected since the temperature of the reaction exceeds the nitrate decomposition temperatures. The presence of barium nitrate indicates that a true solution is achieved during the short lived liquid phase and its presence is not surprising since barium nitrate does not fully decompose until temperatures are in excess of 750 C. In addition, barium nitrate melts at 592 C and it may contribute to the mixing of the reactants; however, the quantities of barium nitrate present are insufficient to completely dissolve the reactants. There exist several accounts of the appearance of YBCO and related materials at temperatures in the 750 C region;[14] its presence here is most likely the product of the result of the direct reaction between highly reactive yttrium, barium and copper species, rather than the solid state reaction between crystallites. The mechanism for the formation of the YBCO

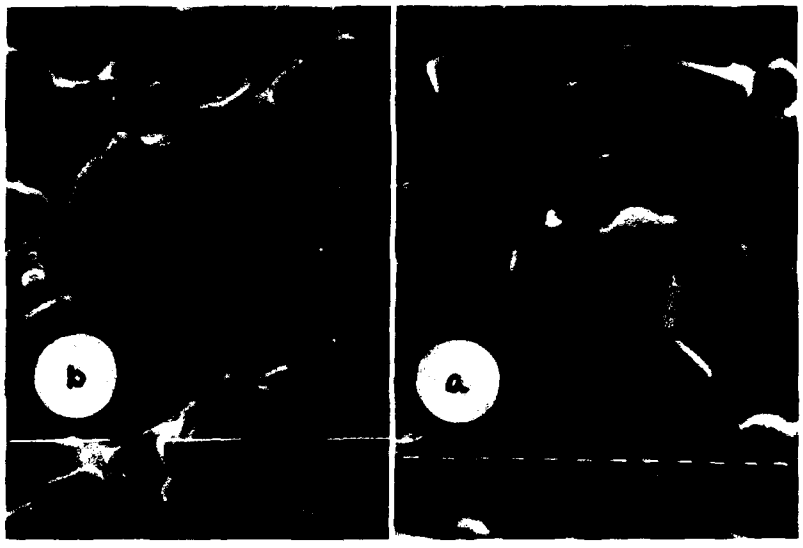


Fig. 2. SEM of YBCO after a) 24 h at 900 C, b) after 24 h 940 C.

component in the ten minute product may be related to the mechanisim of formation of similar materials synthesized by related methods.[2] There is no evidence of impurities from the crucible material in the XRD pattern, although some black material appeared to coat the crucible after several preparations. FIG. 2 is a SEM of the orthorhombic oxygenated phase obtained after 24 h at 900 and 940. As seen in this micrograph, the compacts are composed of crystallites on the order of 3 μm. Sintering at higher temperatures (940 C, 24 h), resulted in the growth of crystallites on the order of 30 μm. Analysis of the XRD pattern from the orthorhombic oxygenated phase, (FIG. 1b), indicates that the calcined product was greater than 99% pure orthorhombic YBCO with the only measurable impurity being CuO. There appeared in this pattern some diffraction intensities in the vicinity of 30 - 33 °2θ region; however, in attempting to identify them, only very poor and unreliable matches could be made to either $BaCuO_2$ or Y_2BaCuO_5. The lattice constants obtained from these measurements were a = 3.868, b = 3.810 and c = 11.679 Å, and are similar to those previously reported.[15] Analysis of the resistivity data show (FIG. 3a) zero resistivity was obtained at 91 K; the midpoint of the transition was 92 K with an onset of about 95 K. The magnetization measurements show a sharp superconducting transition at 91 K and a susceptibility extrapolated at 0 K of -1.23. The diamagnetic response, shown in FIG. 3b, was 15.5% that of a perfect diamagnet (X_{dia} = -1/4π emu/cm^3); however, in obtaining this value we assumed the density of the sintered material was 100% of the theoretical density and we neglected the demagnetization factor, which accounts for the geometry of the sample. Both of these assumptions tend to lower the value of the diamagnetic response. The magnetic shielding as measured by applying a field of 1.00 x 10^{-2} T to a sample cooled to 4 K and warmed through its transition temperature was

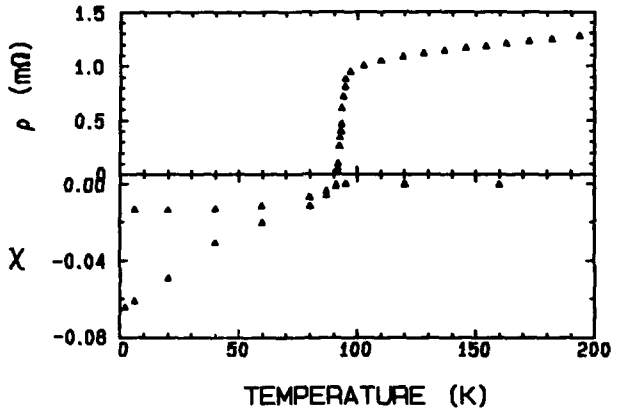


Fig. 3. a) The resistivity (mΩ-cm) versus temperature (K) shows Tc onset at 95 K, midpoint at 92 K and zero resistance at 91 K. b) Coincident with the resistivity transition is a drop in the magnetic susceptibility χ measured by cooling the sample in a field of 1.00×10^{-3} T. The sample exhibits 76% shielding when X is obtained while the sample was cooled in zero field.

76% perfect shielding. The high onset and sharpness of the transition temperature obtained from the resistivity measurements as well as the magnetization behavior are considered typical for samples prepared as sintered pellets.[16]

This synthesis is not without its limitations. Because the high temperature liquid state exists briefly before products begin to solidify, it is necessary that the sample be heated uniformly. In this manner, the reactants completely mix and the development of concentration gradients or phase separation is minimized. On the laboratory scale, where batch sizes are small and the applied heat is distributed throughout the reaction medium within the lifetime of the liquid phase, thorough mixing and phase homogeneity is not difficult to achieve. However, on a larger scale, uniform heating and complete fusion of the reactants will be more difficult. The appearance of solid products in hotter regions will affect the uniform distribution of heat and impair mixing of the reactants and consequently produce an inferior product. Other heating methods where the heat is evenly distributed throughout the entire batch will be required for scale up to large batch processing. While this synthesis may not immediately lend itself to mass production it does represent a valuable method for quickly preparing high quality laboratory-sized samples of various compositions.

In conclusion, these findings indicate that the method presented here can produce quality materials of various compositions whose physical properties are equivalent to those obtained by the much more labor and time intensive conventional methods.

ACKNOWLEDGEMENT

This work was supported by DARPA/ONR contract #NOOO14-88--0587 and the Ben Franklin Partnership Program of the Commonwealth of Pennsylvania project #89S.5024R-3.

REFERENCES

1. N. Coppa, D. Nichols, J. Schwegler, R. E. Salomon, G. H. Myer, J. E. Crow, J. Mat. Res., 4, 1307 (1989).
2. W. K. Ham, G. F. Holland, A. M. Stacey, J. Am. Chem. Soc., 110, 5214 (1988).
3. N. Coppa, doctoral dissertation, Temple University, Philadelphia PA, (1990).
4. J. S. Wallace, in *Ceramic Superconductors*, II, edited by M. F. Yan, (Am. Cer. Soc., Waterville, 1988), pp 243-251.
5. R. C. Weast, CRC *Handbook of Chemistry and Physics*, 66th ed., (CRC, Cleveland, OH 1985) p B76.
6. F. D. Rossini, D. D. Wagman, W. H. Evans, S. Levine, I. Jaffe, Natl. Bur. Std. (U. S. A.), Cir. 500, (1952).
7. C. N. R. Rao and J. Gopalakrishnan, *New Directions in Solid State Chemistry*, Cambridge, Chapter 3, (1989).
8. I. W. Chen, S Keating, C. Y. Keating, X. Wu, J. Xu, P. E. Reyes-Morel and T. Y. Tein, Adv. Ceram. Mater. 2[3B], 457, (1980).
9. J. M. Tarascon, L. H. Green, B. G. Bagley, W. R. McKinnon, P. Barboux and G. W. Hull, in *Novel Superconductivity*, edited by S. A. Wolf and V. Z. Kresin, (Plenum Press, New York, 1987), pp 705-724.
10. N. Coppa, A. Bura, J. W. Schwegler, R. E. Salomon, G. H. Myer and J. E. Crow, this publication.
11. See for example, M. B. Maple, L. E. DeLong, B. C. Sales, in *Handbook on the Physics and Chemistry of the Rare Earths*, edited by K. A. Gschneidnen, L. Eyring, (North-Holland, Amsterdam, 1978), Vol 1, p 797.
12. D. E. Appleman, H. T. Evans, Jr, *U. S. Geological Survey Computer Contribution 20*, U. S. National Technical Information Service Document PB2-16188, (1973).
13. R. C. Reynolds, in *Modern Powder Diffraction, Reviews in Mineralology*, D. L. Bish,, J. E. Post, (Mineralogical Soc. Amer., Washington D. C., 1989), Vol 20, p 145.
14. For example see, S. Sakka, MRS Int'l. Mtg. Adv. Mats., 6, 221 (1989).
15. W. Wong-Ng, H. F. McMurdie, B. Paretzkin, C. R. Hubbard, A. L. Dragoo, J. M. Stewart, Powder Diffract., 2, 106 (1987).
16. M. K. Wu, J. R. Ashburn, C. J. Torng, P. H. Hor, R. L. Meng, L. Gao, Z. J. Haung, Y. Q. Wang, C. C. Chu, Phys. Rev. Lett., 58, 908 (1987).

EVALUATION OF $YBa_2Cu_3O_{7-\delta}$ SOL-GEL DERIVED FILMS ON SAPPHIRE SUBSTRATES PRODUCED FROM DIFFERENT Cu(II) ALKOXIDE GROUPS.

D.S. Kenzer, M.R.Teepe, G.A. Moore, and G.Kordas
Science and Technology Center for Superconductivity, Materials Research Laboratory, Department of Materials Science and Engineering, Ceramics Division, University of Illinois at Urbana-Champaign, 105 S. Goodwin, Urbana, IL 61801

ABSTRACT

Yttrium methoxyethoxide, barium methoxyethoxide and various copper(II) alkoxide groups were used as precursors for the formation of $YBa_2Cu_3O_{7-\delta}$ stable sols in a 2-methoxyethanol / methyl ethyl ketone / toluene / diisopropyl ketone solvent system. Sol fractal dimensions were varied with the sol concentration and with the addition of pyridine. Strong correlation was found between the wettability and the fractal dimensions of the various precursors as determined by contact angle measurements. $YBa_2Cu_3O_{7-\delta}$ thin films were deposited on sapphire substrates using a dip-coating technique. The films were fired at 850 ^{o}C under flowing oxygen or an ozone/oxygen mixture. Although the ozone treatments helped in the formation of single $YBa_2Cu_3O_{7-\delta}$ phase, they contributed to extensive cracking in the films. The different copper(II) alkoxide precursors had little effect on final film microstructure.

INTRODUCTION

The formation of single phase $YBa_2Cu_3O_{7-\delta}$ superconducting thin films is of major importance to both device fabrication and research studies. $YBa_2Cu_3O_{7-\delta}$ thin films have been produced using vacuum deposition techniques such as sputtering [1,2], molecular beam epitaxy [3], and pulse laser deposition [4]. Sol-gel processing has also been used as an alternative for $YBa_2Cu_3O_{7-\delta}$ film deposition [5,6]. Sol-gel processing has several advantages that warrant a closer study of the technique. The sol-gel method allows for the processing of thin films which exhibit ultrafine structure, homogeneity, and alignment [5,6]. A wide range of microstructural modifications can be achieved through variation of sol-gel processing variables such as solvent concentrations, acidity/basicity of the system, water content and impurity distributions. Lower firing temperatures and shorter annealing times may also be achieved through the sol-gel technique.

In the present paper, we will evaluate the formation of $YBa_2Cu_3O_{7-\delta}$ thin films on sapphire substrates using different Cu(II)-alkoxides and firing conditions.

Mat. Res. Soc. Symp. Proc. Vol. 180. ©1990 Materials Research Society

EXPERIMENTAL PROCEDURE

Copper(II)-methoxide, Copper(II)-ethoxide and Copper(II)-1-propoxide were prepared from a copper chloride and lithium alkoxide exchange reaction:

$$Cu(II)Cl_2 + 8Li(OR) \rightarrow Cu(II)(OR)_2 + 2LiCl + 6Li(OR) \quad (1)$$

where R is a methyl, ethyl or 1-propyl group. The insoluble copper alkoxide was then separated from the other molecules by filtration and dispersed in a solvent system of 2-methoxyethanol / methyl ethyl ketone / toluene / diisopropyl ketone in ratios of 30/30/30/10 percent. Batches of Cu(II)-methoxide, Cu(II)-ethoxide, and Cu(II)-1-propoxide were formed in this fashion. Ba-methoxyethoxide and Y-methoxyethoxide were added to each system and stable $YBa_2Cu_3O_x$ sols were formed from each precursor system. Fractal dimensions of the three systems were measured using Small Angle X-ray Scattering (SAXS) techniques. Fractals were measured at various solvent concentrations and after the addition of pyridine for the three precursor systems. Contact angle measurements were taken to determine the wettability of various substrates by sols of different content and concentration. The sols were then either gelled to form fine powders or applied as thin films to sapphire substrates. Films were produced using a dip-coating technique at a dipping angle of 10^o. Polished single crystal (0001) sapphire substrates were used. Each green coat consisted of five dips in the sol followed by firing at 400^oC - 500^oC for 60 seconds. This produced a dry and uniform coating. After 7 - 25 dip coating applications, the layers were then fired at 850^oC for 2.5 minutes and slowly cooled to 450^oC. The substrate was annealed at 450^oC for 4-12 hours. All firing, drying and annealing procedures were done either under flowing oxygen or an oxygen / ozone (10%) mixture. X-ray diffraction (XRD) was performed on the films to determine phase formations. Scanning electron microscopy (SEM) techniques were used to evaluate adhesion, continuity and uniformity in the films.

RESULTS AND DISCUSSION

Figure 1 shows a SAXS plot of a $YBa_2Cu_3O_{7-\delta}$ sol derived from a Cu(II) 1-propoxide precursor system. This is a typical SAXS porod plot which shows a fractal dimension, D, of 2.47. Table 1 displays the variation of fractal dimension with concentration for a Cu(II) ethoxide derived $YBa_2Cu_3O_{7-\delta}$ sol. Trends in D of sols with a 10 wt% addition of pyridine (an organic base) can also be seen. These results indicate that the fractal dimension of the sol decreases with increasing concentration. The addition of pyridine to the sol has little effect on D at lower concentrations. However, at higher concentrations the addition of

pyridine causes the fractal dimension, D, to decrease to a more two dimensional-planar structure.

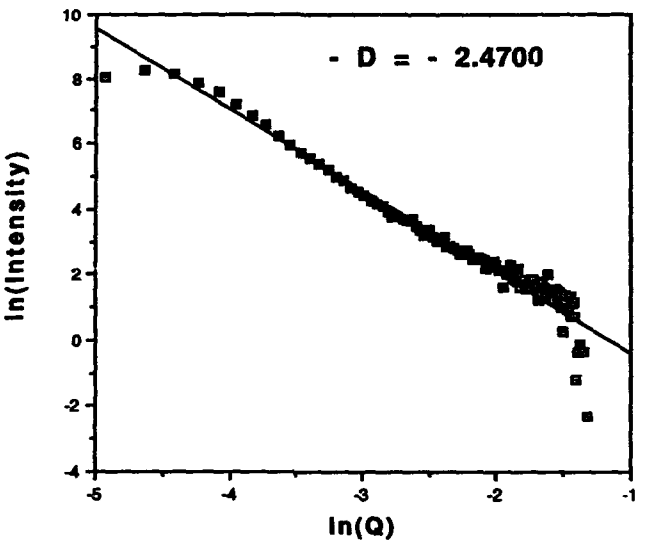


Figure 1. SAXS porod plot of $YBa_2Cu_3O_{7-\delta}$ sol derived from a Cu(II)-1-propanol precursor system.

Concentration(*molal*)	0.01	0.02	0.03	0.10
Cu(II)-ethoxide sol	2.39	2.24	2.18	2.19
+10% Pyridine	2.41	2.15	2.04	2.03

Table 1. Mass fractal dimensions determined from SAXS porod plots.

Table 2 summarizes the fractal dimensions of the different $YBa_2Cu_3O_{7-\delta}$ sols synthesized using different Cu(II)-alkoxide precursors. It appears that the fractal dimension is affected by the kind of the Cu(II)-alkoxide precursor used for sol formation. As the precursor alkoxide chain length increases, the fractal dimension decreases indicating that a more polymeric network is favored. The Cu(II)-1-propoxide precursor exhibits a flat two dimensional planar network at this concentration, while the Cu(II)-methoxide precursors has something between a planar and spherical network structure.

Table 3 shows contact angle measurements for three Cu(II) alkoxide precursors at different $YBa_2Cu_3O_{7-\delta}$ sol concentrations. Table 4 summarizes the

fractal dimension measurements versus contact angle for sols derived from Cu(II)-1-propoxide precursors. These measurements clearly suggest a relationship between contact angle (wettability) and fractal dimensions of the sols. A highly branched polymeric structure (table 2) exhibits a greater contact angle (table 3). Thus, it appears that as fractal dimension decreases the wettability increases. Similarly, the fractal dimension is affected by the concentration of the sols (table 1) which in return influences the wettability of the sols (table 4). In conclusion, the behavior of the sols on the substrate can be controlled through the variation of their fractal dimension which are determined by the sol chemistry. This allowed us to optimize the desired film quality on sapphire. Sol concentrations of 0.02 molal and higher were used since lower concentrations gave very high or complete wettability. The films were fired in either flowing (0.5 cu.ft./min) oxygen or a flowing mixture of 10% ozone / 90% oxygen.

Figure 2 shows a comparison between the XRD patterns of the ozone and non-ozone fired films.

TABLE 2	
PRECURSORS	D
Cu(II)-methoxide	2.51
Cu(II)-ethoxide	2.39
Cu(II)-1-propoxide	2.07

Table 2. Mass fractal dimensions of $YBa_2Cu_3O_{7-\delta}$ sols with concentration .01 molal synthesized by using different Cu(II)-alkoxide precursors .

CONCENTRATION	Cu(II)-METHOXIDE	Cu(II)-ETHOXIDE	Cu(II)-1-PROPOXIDE
0.3	8.5°	14°	21°
0.02	5.5°	6.5°	7°
0.01	2°	0°	0°

Table 3. Contact angle measurements taken on single crystal [100], polished sapphire substrates.

CONTACT ANGLE	D
21°	2.47
7°	2.22
0°	2.04

Table 4. Fractal dimension vs. contact angle for sols derived from Cu(II) 1-propoxide precursors

The films fired under ozone showed much stronger XRD patterns with sharp well defined peaks. The films fired under flowing oxygen exhibited weaker

patterns, in general, with more impurities. Each film fired under a slight ozone atmosphere was found to have virtually no impurities while some films fired under oxygen had a few impurity phases. These results lead one to believe that ozone treatments yield better films. SEM results showed little difference between the films produced from various precursors or between those of different concentrations. On the other hand, major variations in the films were obtained between films fired in ozone and those fired in oxygen. Figure 3 shows SEM micrographs of three .03 molal sol films fired on sapphire. A Cu(II)-1-propoxide precursor film fired in oxygen (3a), Cu(II)-methoxide precursor film fired in

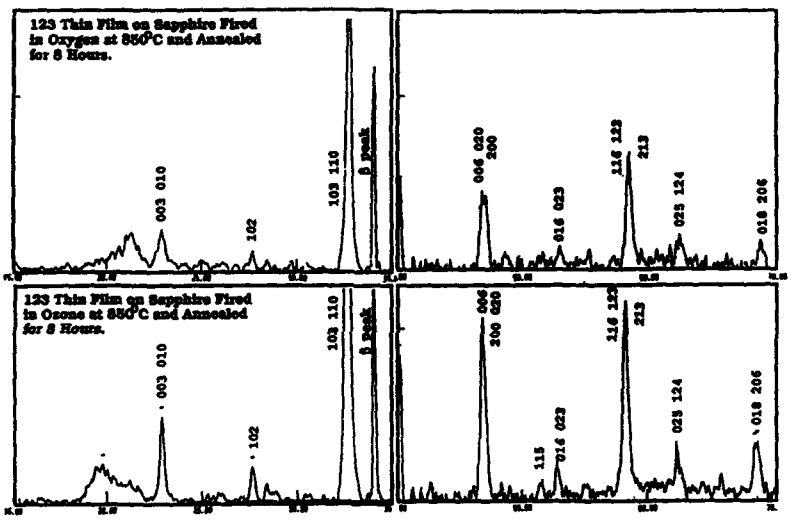


Figure 2. X-ray diffraction patterns of $YBa_2Cu_3O_{7-\delta}$ thin films on [100] single crystal sapphire substrates (substrate peak omitted) fired at 850 °C and annealed for 8 hours in oxygen (a) and 10% ozone / 90 % oxygen gas mixtures.

oxygen (3b) and a Cu(II)-1-propoxide film fired under ozone. Figure 3 reveals that the ozone treated films exhibited severe cracking. Films fired in oxygen showed less cracking.

Acknowledgements

This project was funded by the Science and Technology Center for Superconductivity under grant No. NSF-DMR-88-09854 and MRL grant under No. NSF-DMR 86-12860.

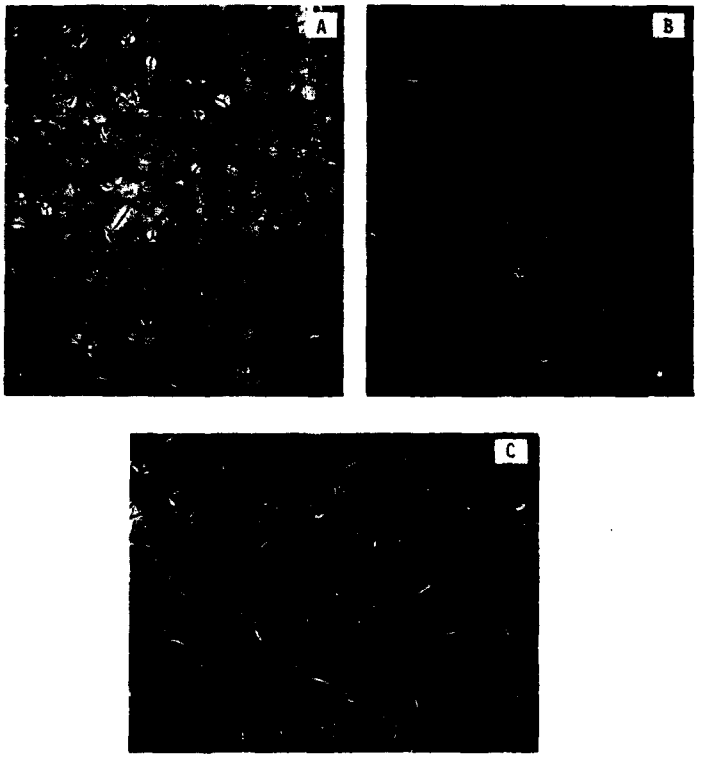


Figure 3. SEM micrographs of three 0.03 molal sol films fired on sapphire: A) Cu(II)-1-propoxide precursor fired in oxygen; B) Cu(II)-methoxide precursor fired in oxygen; and C) Cu(II)-1-propoxide precursor fired in ozone. The bars correspond to 20 μm.

REFERENCES

1. Y. Enomoto, T. Murakami, M. Suzuki, and K. Moriwaki, Jpn. J. Appl. Phys. 26(1987)1248
2. K. Char, A.D. Kent, A. Kapitulnik, M.R. Beasley, and T.H. Geballe, Appl. Phys. Lett., 51(1987)1370.
3. C. Webb, S.L. Weng, J.N. Eckstein, N.Missert, K. Char, D.G. Schlom, E.S. Hellman, M.R. Beasley, and J.S. Harris, Jr., Appl. Phys. Lett., 51(1987)1191.
4. D. Dijkamp, T. Venkatesan, X.D. Wu, S.A. Shaheen, N. Jisrawi, Y.H. Min-Lee, W.L. McLean, and M. Croft, Appl. Phys. Lett., B57(1988)167.
5. S.A. Kramer, G. Kordas, J. McMillan, G.C. Hilton, and D.J. Van Harlingen, Appl. Phys. Lett., 53(1988)156.
6. G. Moore, S. Kramer, and G. Kordas, Mat. Lett., 7(1989)415.

CHARACTERIZATION OF AMORPHOUS GEL TO SUPERCONDUCTING OXIDE CONVERSION FOR SOL-GEL PRODUCED $Y_1Ba_2Cu_3O_{7-x}$.

G.A. Moore, D. Kenzer, M. Teepe, and G. Kordas
Department of Material Science and Engineering, Ceramics Division, Materials Research Laboratory, and Science and Technology Center for Superconductivity, University of Illinois at Urbana-Champaign, 105 S. Goodwin, Urbana, IL 61801

ABSTRACT

Alkoxide sol-gel processing of $Y_1Ba_2Cu_3O_{7-x}$ was performed using copper(II) ethoxide, barium methoxyethoxide, and yttrium methoxyethoxide precursors in a methoxyethanol/methy ethyl ketone/toluene solvent system. In situ neutron diffraction experiments were performed on individual precursors and mixed component gels during heat treatment. Phase development and consumption was observed for both the calcination and annealing segments of the heat treatment. Formation of $Y_1Ba_2Cu_3O_{7-x}$ was observed as early as 700 °C. CuO, Cu_2O, BaCuO, YCu_2O_5, $BaCO_3$, $BaCO_4$, and $Y_1Ba_2Cu_3O_{7-x}$ were observed during the conversion/consolidation reactions to 850 °C.

INTRODUCTION

The processing of single phase $Y_1Ba_2Cu_3O_{7-x}$ superconducting powder and thin films is paramount to basic materials research studies as well as commercial product developments. Initially, single phase superconductors were produced by the solid state reactions of yttrium oxide, barium carbonate, and copper oxide powders [1]. A severe draw back of this process is the 950 °C processing temperature for several hours and then the annealing process in oxygen near 450 °C to yield the orthorhombic superconducting phase. The high calcination temperature usually results in extensive microstructural grain growth [2] and interaction of the superconducting film with the substrate [3, 4].

Sol-gel processing techniques offer an alternative to the traditional ceramic processing methods for superconductors. For example, Hirano et al. [6] has produced single phase $Y_1Ba_2Cu_3O_{7-x}$ superconducting powder at 750 °C using yttrium isopropoxide, barium isopropoxide, and copper(II) 2-ethoxyethoxide. Kramer et al. [7] has produced $Y_1Ba_2Cu_3O_{7-x}$ sol-gel superconductor powders using Y methoxyethoxide, Ba methoxyethoxide, and copper(II) ethoxide. Kramer et al. [8] has also demonstrated that epitaxial films can also be produced on $SrTiO_3$ via sol-gel routes. Therefore, the sol-gel technique can lead to high quality superconductors that can be used for physical property measurements as well as technological applications.

In the present paper, we discuss the conversion of our amorphous $Y_1Ba_2Cu_3$ gel to the corresponding superconducting oxide occurring through a complex structural development process which has been characterized using neutron diffraction. The chemical processing aspects of this $Y_1Ba_2Cu_3O_{7-x}$ system have been extensively described in a number of previous publications [8,9,10]. The

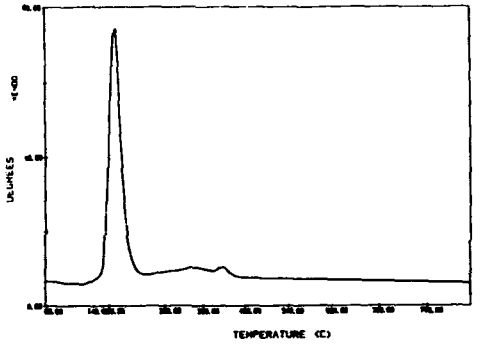
Mat. Res. Soc. Symp. Proc. Vol. 180. ©1990 Materials Research Society

neutron diffraction experiments were performed on the Special Environment and General purpose Powder Diffractometer, at the Intense Pulsed Neutron Source (IPNS) [11].

Results and Discussion

Figure 1a shows DTA results for the copper(II) methoxyethoxide precursor powder. This measurement reveals a large exothermic reaction between 200-270 °C and two smaller exothermic peaks between 350-450 °C. Based on this result, room temperature, 275 °C, 475 °C, and 675 °C were chosen as the temperatures for acquisition of neutron diffraction data for the copper(II) methoxyethoxide sample. These diffraction spectra for the copper(II) precursor pellets are shown in figure 1b. The room temperature data indicate the major constituent to be amorphous, with minor constituents being CuO, Cu_2O, and Cu metal. The presence of crystalline phases is attributed to the 120-200 °C temperature used during sample drying. The copper gel sample appears completely crystalline by 275 °C, with CuO being the sole copper constituent.

A



B

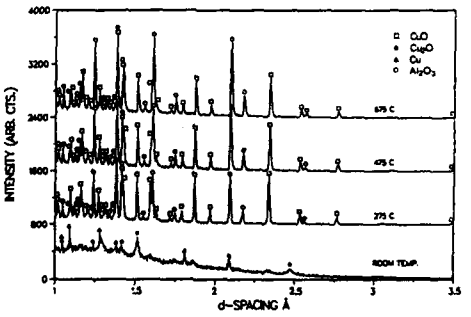


Figure 1. a) Differential thermal analysis of Copper(II) alkoxide.
b) Neutron diffraction patterns for Copper(II) alkoxide consolidation.

Thus, the large exothermic reaction observed just below 275 °C is attributed to the formation of CuO and the elimination of it's corresponding organic byproducts. Neither Cu metal or Cu_2O were observed in the 275 °C powder pattern. No

apparent crystallographic structure variation was observed in the 475 °C or 675 °C spectra indicating that the smaller exothermic reactions occurring between 350-450 °C were most likely due to a second stage of organic byproduct oxidation. Our single phase formation of CuO by 275 °C can be compared to work by Hirano et al, in which the presence of both Cu_2O and CuO were observed up to 475 °C as determined using x-ray diffraction techniques [12].

In addition to the copper-containing phases, the neutron diffraction patterns recorded above room temperature revealed the presence of Al_2O_3. As discussed previously, the sample pellets were positioned between two alumina dyes in the neutron beam. As a result of sample pellet shrinkage during the copper(II) precursor run, the upper alumina positioning cap entered the neutron beam. Thus, the spectra above room temperature showed the presence of alumina. However, this interference did not limit the identification of the copper oxide phases.

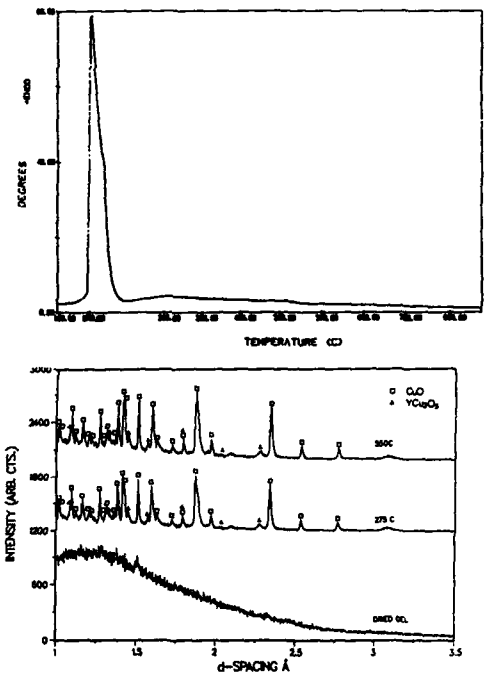
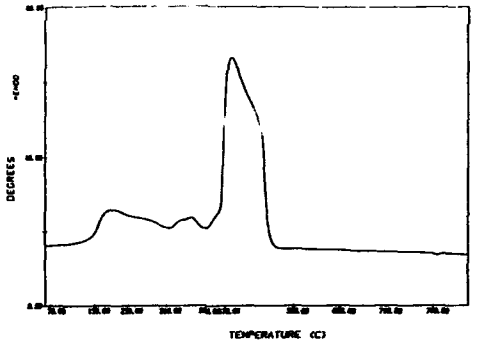


Figure 2. a) Differential thermal analysis of Y1Cu3 gel.
b) Neutron diffraction patterns for Y1Cu3 gel consolidation.

Figure 2a shows the DTA curve for the Y1Cu3 gel sample. The data indicate a sharp exothermic reaction below 275 °C followed by a gradual exothermic rise between 300 °C and 550 °C. Neutron diffraction data were therefore taken at room temperature, 275 °C, and 550 °C. The diffraction data are shown in figure 2 b.

A



B

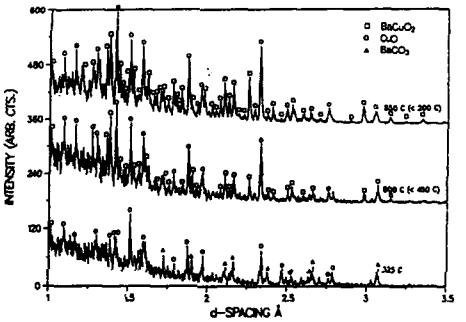


Figure 3. a) Differential thermal analysis of Ba_2Cu_3 gel.
b) Neutron diffraction patterns for Ba_2Cu_3 gel consolidation.

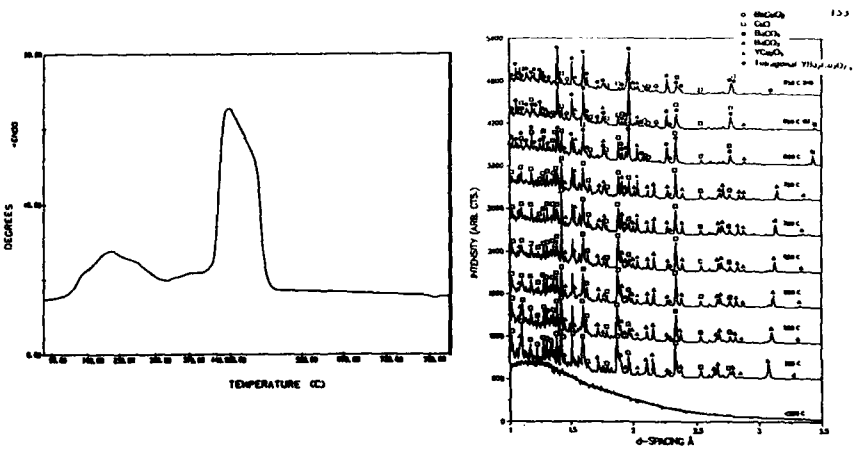
The data indicate CuO is the dominating phase in the 275 °C and 550 °C spectra and that YCu_2O_5 is a minor constituent. The presence of yttrium oxide was not observed in the patterns, indicating the direct formation of the yttrium copper oxide.

Figure 3a shows the DTA curve for Ba_2Cu_3 gel powder. The curve exhibits three exothermic peaks between 150 °C and 525 °C, and a small endothermic dip at 800 °C. The latter is reported to corresponded to a reversible $BaCO_3$ polymorphic transformation [13]. However, this data was not confirmed using diffraction techniques. We believe that for our system this transformation may yield $BaCO_4$, also a reversible transformation which when cooled returns to $BaCO_3$. Figure 3b shows neutron diffraction patterns of samples heat treated at 325, 800, and 850 °C. The first spectrum recorded at 325 °C shows CuO and $BaCO_3$ as the predominant

phases. The 800 °C and 850 °C sample spectra contained a large alumina contribution from the positioning cap. For these two samples additional neutron diffraction data were obtained after partially cooling the furnace and masking the portion of the neutron beam impinging the positioning cap.

The spectra representative of the 800 °C sample, recorded at 450 °C, indicates the presence $BaCuO_2$ and CuO. These phases were also detected in the 850 °C sample, recorded at 200 °C. In the 850 °C sample the $BaCuO_2$ phase is much more developed than in the 800 °C sample.

Figure 4a shows the DTA analysis of the $Y_1Ba_2Cu_3$ gel powder produced using Alfa Cu(II) ethoxide and processed using the methoxyethanol/ methyl ethyl ketone/ toluene The DTA curve shows two exothermic peaks at 200 °C and 500 °C. The $BaCO_3$ to $BaCO_4$ conversion endotherm occurred at 795 °C. This DTA measurement closely resembles that of the Ba_2Cu_3 gel. For example, the large exothermic peak between 400-500 °C appears to have similar intensities and widths in both plots, indicating that the barium and possibly copper constituent reactions are taking place. Figure 4b shows the neutron diffraction data of the $Y_1Ba_2Cu_3$ gel heat treated from 200-850 °C. From figure 4a it is observed that the $BaCO_3$ peaks do not change appreciably in intensity from 325-750 °C, but at 800 °C the phase has been completely replaced by $BaCO_4$. Thus, the $BaCO_3$ phase appears to be very inert up to the conversion temperature, approximately 790-800 °C. The Ba_2Cu_3 results indicate that two hours at 800 °C was sufficient to completely react the newly formed $BaCO_4$ with the copper oxide phases to form $BaCuO_3$. The presence of Ba_2CuO_3 has been observed by Wang et al. [14] at 950 °C in 2Ba:3Cu specimen



A B

Figure 4. a) Differential thermal analysis of $Y_1Ba_2Cu_3O_{7-x}$ gel.
b) Neutron diffraction for $Y_1Ba_2Cu_3O_{7-x}$ annealing treatments. prepared using the solid state method. Ba_2CuO_3 was not observed at any temperature in our Ba_2Cu_3 samples. From the room temperature acquired diffraction data shown in figure 4b, it is apparent that the $Y_1Ba_2Cu_3$ gel sample was

completely amorphous prior to heat treatment. The hump-like nature of the scattering intensity is representative of the under-moderated Maxwellian neutron distribution, characteristic of a pulsed spallation neutron source. The spectra appear quite complex due to the three component nature of the gel. However, with the aid of the previously discussed diffraction patterns, the data can be adequately interpreted. Two main phases were observed at 325 °C, CuO and $BaCO_3$, with a minor amount of YCu_2O_5 being present. Free Cu metal and Cu_2O were not observed at any temperature. The YCu_2O_5 peak intensities increased through the 750 °C acquisition, at which time the phase appeared to readily react with the other constituents to form tetragonal $Y_1Ba_2Cu_3O_{7-x}$. The $BaCO_3$ phase was very stable through the 750 °C acquisition, but at 800 °C had been converted to $BaCO_4$. The $BaCO_4$ was observed to readily react with CuO and YCu_2O_5 forming tetragonal $Y_1Ba_2Cu_3O_{7-x}$ and a small amount of $BaCuO_2$. After two hours at 850 °C only small traces of the $BaCO_4$ phase remained. Residual impurities after four hours at 850 °C were YCu_2O_5, CuO and $BaCuO_2$.

ACKNOWLEDGEMENTS:

Funding for this project was provided by NSF-DMR 86-12860. The work at Argonne was supported by U.S. Dept. of Energy, Div. of Basic Energy Sciences-Materials Sciences, under contract W-31-109ENG-38 and by the NSF-funded Science and Technology Center for Superconductivity under Grant No. DMR-88-09854.

References

1. M.K. Wu, J.R. Ashburn, C.J. Torng, P.H. Hor, R.L. Meng, L. Gao, Z.J. Huang, Y.Q. Wang, and C. W. Chu, Phys. Rev. Lett., 58, [9], 908-910, (1987).
2. K.E. Easterling, C.C. Sorrell, A.J. Bourdillon, S.X.Dou, G.J. Sioggett, and J.C. Macfarlane, Material Forum, 11, 30-42, (1988).
3. H. Koinuma, K. Fukuda, T. Hashimoto, and K. Fueki, Japanese J. of App. Physics, 27, [7], L1216-L1218, (1988).
4. C. T. Cheung and E. Ruckenstein, Mat. Lett., 7 [5,6] 172-177, (1988).
5. R. Roy, Science, 238, 1664-1669 (1987).
6. S. Hirano, T. Hayashi, M. Miura, and Hiroyuki Tomonaga, Bull. Chem. Soc. Jpn., 62, [3], 888-892, (1989).
7. S. Kramer, K. Wu, G. Kordas, Mat. Res. Soc. Symp. Proc., Vol. 99, 323-325, (1988).
8. S. A. Kramer, G. Kordas, J. McMillan, G. C. Hilton, and D.J. VanHarligen, Appl. Phys. Lett., 53, [2], 156-158, (1989).
9. S. Kramer, G. Moore, G. Kordas, P.A. Keifer, and C.T.G. Knight, Mat. Res. Soc. Symp. Proc, 121, 643-647, (1988).
10. G. Moore, S. Kramer, G. Kordas, Mat. lett., Vol. 7, 12, 415-423, (1989).
11. J. D. Jorgensen, J. Faber, JR., J. M. Carpernter, R. K. Crawford, J.R. Haumann, R.L. Hitterman, R. Kleb, G.E. Ostrowki, F.J. Rotaella, and T.G. Worltan, J.Appl. Cryst. 22, 321, (1989)
12. S Hirano, T. Hayashi, R H. Baney, M. Miura, H. Tomonaga, Chem. Letters, 665-668,(1988).
13. R. B. Fahim, M. I. Zaki, and G. A. M. Hussien, Powder Technologly, 33, 161-165, (1982)
14. A. Manthiram, J. S. Winnea, A. T Sui, H. Steinfink, and J. B. Goodenough, J. Am. Chem. Soc.,109, 6667-6669, (1987).

PART XII

Novel Processing I

ASPECTS OF CHEMISTRY AND CHEMICAL PROCESSING OF ORGANICALLY MODIFIED CERAMICS

HELMUT K. SCHMIDT
Fraunhofer-Institut für Silicatforchung, Neunerplatz 2, D-8700 Würzburg, Federal Republic of Germany
New address: Institut für Neue Materialien, Universität des Saarlandes, Gebäude 43, Im Stadtwald, D-6600 Saarbrücken, Federal Republic of Germany

ABSTRACT

For the synthesis of composites on a nano or molecular level, chemical or physical methods have to be used since mechanical procedures cannot be employed for these systems. If organics have to be included, low temperature processing has to be used for the synthesis of the inorganic component in order not to damage the organic component. Sol-gel techniques are an appropriate means to synthesize oxidic networks by soft chemistry, and various systems of organically modified ceramics (ORMOCERs) have been developed so far. It has been shown that the synthesis parameter can be used to tailor the material properties in a wide range. A review over the chemistry and chemical properties of ORMOCERs and several examples of material developments will be given.

INTRODUCTION

The aim of this paper is to point out special chemical aspects of organically modified ceramics of the ORMOCER type, mainly developed in the Fraunhofer-Institut für Silicatforschung in Würzburg, FRG. Due to the limited amount of space and with respect to the review, in several cases details were not reported here, but are foreseen for later publication or are found in the cited literature.

In numerous cases of materials application in technology one-component systems do not meet the complex practical requirements and, therefore, composites have to be used. The vast majority are so-called macroscopic composites like laminates or fiber reinforced materials. The lower limit of the component size in these cases is the μm range and is limited by mechanical processing (e.g. mixing, coating, blending). For coatings, layer thicknesses in the nano range can easily be achieved by deposition techniques and, as shown in [1], composites consisting of several hundreds of thin layers can be prepared by microwave assisted chemical vapor deposition. That means layered composites with one very small dimension can be obtained. Particulate phases, e.g. ceramic phases in ceramic matrices, are obtained by nucleation and crystallization processes at high temperatures. It is difficult to obtain very small grain sizes if one starts from conventional crystalline raw materials like oxides. Amorphous gels, however, can be transformed into ceramics with extremely small particle sizes [2]. If growth and agglomeration processes can be controlled

Mat. Res. Soc. Symp. Proc. Vol. 180. ©1990 Materials Research Society

particulate raw materials for ceramics in the nano range can be prepared [3]. In controlled sol-gel reactions, fine particles can be formed by a controlled growth mechanism in solution.

To obtain glasses or ceramics from gels or from ultrafine particles, the material has to be densified by heat treatment during a sintering process. The densification mechanism can either be a viscous flow, e.g. in glasses, as described in [4] or a diffusion controlled mechanisms, similar to sintering mechanisms of ceramics [5]. In ceramic multicomponent compositions, the diffusion paths can be extremely short if the particle size is small, leading to reduced crystallysation temperatures [6]. The high temperatures necessary for densification are a result of a molecular property of the inorganic units. They form a three-dimensional network since the number of bonds per unit, as a rule, is ≥ 3. Lower network connectivity numbers enhance densification as known from organic polymers. The organic modification in sols and gels should have the same effect. This idea was used for an improvement of the processing properties for fiber drawing from SiO_2 sols in [7]. In this case, a $\equiv SiOC_2H_5$ grouping represents the determining function. Other examples for chemical modifications are shown in [8]. In this case, the complexation of Al-alkoxides leads to ultrafine particles, suitable for fiber drawing or coating. In these examples, the organic modification is only used to overcome disadvantages of the three-dimensional crosslinking in processing steps before densification and afterwards the organics are burnt out. But if organics are carriers of special functions it might be of interest to keep them within the final product. In this case, hybrid materials with inorganic backbones and organic components are obtained and the organic component may act as a chemical or structural modification of the inorganic network. Therefore, the sol-gel process provides a means for the preparation of ultrafine dispersions for the inorganic phase and, in addition to this, organic groups can be included which enhance relaxation and densification of the network.

GENERAL ASPECTS OF ORGANIC MODIFICATION OF ORMOCERS

Various material syntheses by sol-gel techniques in combination with organic groups have already been described [9-14]. Different basic types of ORMOCER materials can be distinguished:

- organic groups act as non-reactive network modifiers, e.g. alkyl or aryl groups covalently bond to Si. There is a strong effect on Tg shown in fig. 1 (x, with phenyl groups as an example).

This type can be considered as a modified glass structure with organic groups as network modifiers instead of alkali ions. Curve (o) represents the case of a second type of structure:

- organic groups are linked together and can stabilize the "gel network" mechanically by forming flexible links.

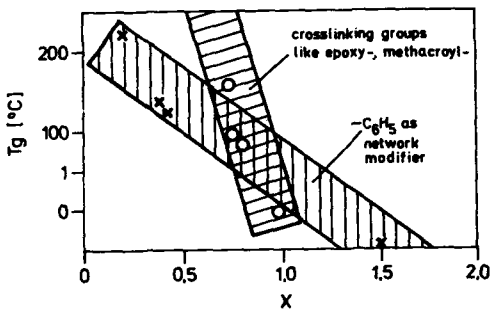


Fig. 1. Effect of organic groups on Tg in organically modified ceramics according to [10].

In this case, a steeper slope (o, fig. 1) results, as pointed out in [10]. No Tg can be determined if the ratio of network modifier carrying groups to network modifier-free groups becomes 0.7. Materials with r > 0.7 can be easily densified to bulks without cracking.

If one considers this behavior from the organic polymer point of view, it can be explained as a structure stabilizing effect of the inorganic components, too. Stabilized structures like this do not only show higher Tg, but show also special chemical properties like reduced diffusion for e.g. organic molecules. In fig. 2, the permeation rates P = S·D (S = solubility; D = diffusion coefficient) of coated and uncoated high density polyethylene (HDPE) are compared with a standard test gasoline fraction as permeate [15].

Another aspect of structural stabilization in combination with special properties is described in [16] in materials derived from $(CH_3O)_3Si-(CH_2)_3NH_2$. Hydrolysis and condensation results in transparent monolithic condensates stable up to 150 °C. Doping with $HClO_4$ or CF_3SO_3H leads to protonic solid state electrolytes with no change in conductivity by ageing time or temperature influences, indicating a high structural stability compared to organic polymers like polyethylene oxide. It is assumed that the inorganic backbone stabilizes structures according to fig. 3.

The proton transport can be explained by a chain motion mechanism, since the conductivity rises sharply at the glass transition temperature. Both findings, low permeation rates as well as stable conductivity behavior support the thesis of a structural stabilization effect of the inorganic backbone. From the ceramic point of view and according to fig. 1, the Tg values are substantially lowered compared to corresponding inorganic compositions (the inorganic backbone with the organics to be removed) and the densification behaviour should be affected, too.

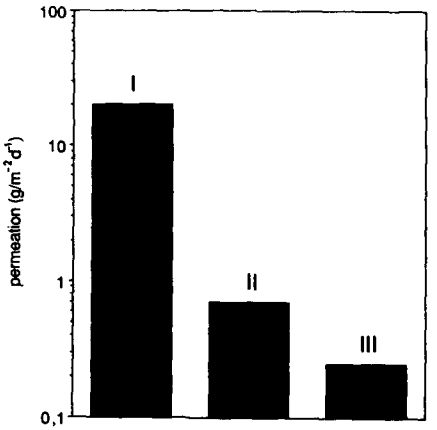


Fig. 2. Permeation of hydrocarbons through coated and uncoated HDPE. I = uncoated HDPE; II = coated with a polymer obtained from $Al(OBus)_3$:$(CH_3O)_3Si$-$(CH_2)_2OCOCH(CH_3)=CH_2$:$(C_2H_5O)_3Si$-$(CH_2)_2CH_3$:$(CH_3O)_3Si$-$(CH_2)_3NH_2$ = 20:50:30:4 (molar ratio) by hydrolysis and condensation and photocuring after coating with IRGACURE 184 (commercial photoinitiator from Ciba Geigy company); III = same polymer, but methacrylate grouping substituted by the epoxy grouping $(CH_3O)_3Si$-$(CH_2)_2OCH_2\overline{CH-CH_2O}$, thermally cured after coating at 90 °C. Coating thickness: 5 µm.
P: equilibrium rates after 50 hrs.

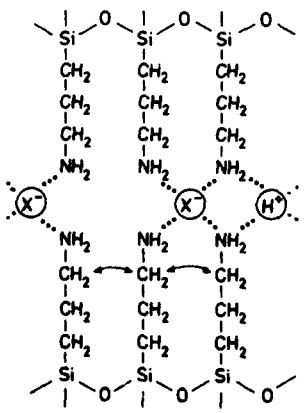


Fig. 3. Model of a proton conductive modified glass according to [17].

As shown in various examples [16,18], dense and crack-free bulk materials can be prepared very easily with ORMOCERs and especially by use of a two step process including organic polymerization (fig. 4). The advantage of the two step processing results from the separation of the sol-gel reaction (mainly controlled by H_2O and catalysts) from the organic polymerisation reaction (thermally activated or photoactivated). The organic crosslinking affects the chemical properties, too. Whereas structures with ≡Si-O-bonds as backbones and without polymeric crosslinking are sensitive to alkaline or hydrolytic attack, polymerized materials are chemically much more stable. This behavior can be used for pattern development by photolithography (fig. 5) [19]. Without stabilization by polymerization an ORMOCER film can be removed after drying at room temperature completely by diluted NaOH. By this, patterns can be developed after UV light exposure with appropriate masks.

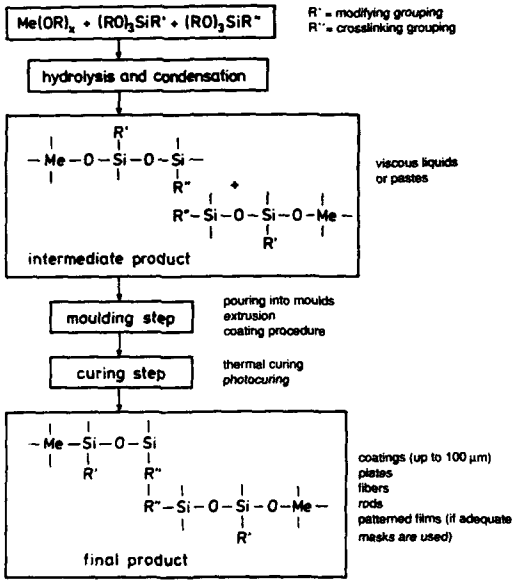
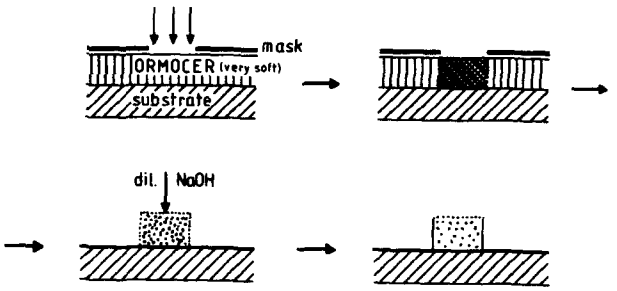


Fig. 4. Typical two step processing of organically crosslinked ORMOCERs; R': alkyl, aryl; R": vinyl, methacryl.

The sensitivity against NaOH decreases with increasing degree of organic polymerisation and can be affected by composition, too. If epoxy-free compositions are used and the methacrylate is substituted by vinyl, one can synthesize "silicates" extremely stable against alkaline attack, as shown in [20,21]. In additon to this, for example, coatings of the system $SiO_2/(C_6H_5)_2SiO/CH_3$-vinyl-SiO = 5:35:60 (molar ratio) show a low permittivity constant ε of about 2.7 (which does not change after wheathering due to a very low H_2O take up), and a high



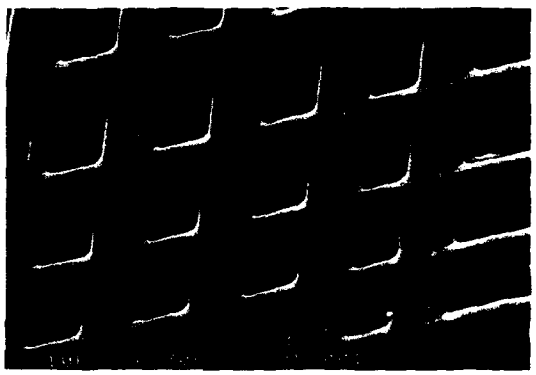


Fig. 5. Photolithography of ORMOCERs by polymerization stabilization.
a) ORMOCER composition:
$SiO_{3/2}(CH_2)_3OCOCH(CH_3)=CH_2$: 38.6)
$SiO_{3/2}(CH_2)_3OCH_2CHCH_2O$-: 38.6) molar ratios
$SiO_{3/2}CH=CH_2$: 18.9; SiO_2: 3.9)
Photoinitiator: IRGACURE 184 (Ciba Geigy)
b) Developed patterns; UV exposure by direct laser writing. chemical stability against concentrated bases, which is quite unusual for silica based materials. The material can be used for dielectric coatings.

In opposition to a high chemical stability, a high sensitivity for special compounds can be useful, too. As pointed out in the introduction, organofunctional groups can dominate the chemistry of ORMOCERs in a wide range. The use of aminogroups as charge carriers for solid state electrolytes already has been shown in fig. 3. They also can be used for complex formation for SO_2 [22]. In this case, secondary or tertiary amino groups react reversibly with gaseous SO_2 (1)

$$-CH_2-CH_2-\overset{R}{\underset{R}{N}} + SO_2 \rightleftharpoons -CH_2-CH_2-\overset{R}{\underset{R}{N}}\leftarrow SO_2 \qquad (1)$$

The complex formation is a function of the SO_2 partial pressure. The ORMOCER is dense, but SO2 can diffuse into the structure. The adsorption process can be monitored by IR as shown in fig. 6 but more efficently by other techniques. In fig. 7a and 7b the response of a coated piezo quartz and of an interdigitated capacitor is shown [23]. The frequency shift of the quartz is linear to the vapor pressure of SO_2. The capacitance device shows an extremely high sensitivity (<< 1 vpm SO_2)

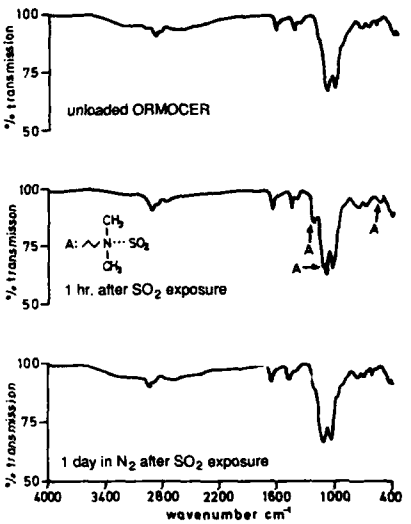


Fig. 6. Adsorption of SO_2 on a tertiary amine. The amine is covalently bond to a silane: $(CH_3CH_2)_2N(CH_2)_3Si(OR)_3$ and incorporated into the ORMOCER NND (34/1) according to [22].

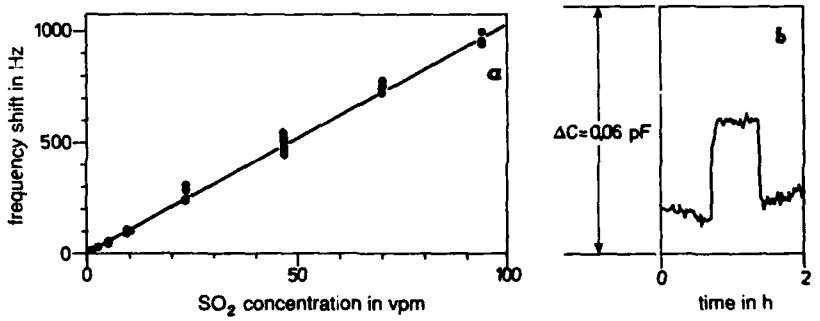


Fig. 7a-7b. a) Frequency shift of an ORMOCER coated piezo quartz as a function of the SO_2 partial pressure. b) Capacitance shift of an interdigitated capacitor coated with an ORMOCER by exposing 1 vpm SO_2 in N_2.

The examples described above demonstrate some special chemical properties of ORMOCERs. These properties are related to structural features and, in this connection, it seems to be of importance that the materials are of high homogeneity and no resolution of phases can be observed in the TEM (≈ 1 nm resolution). That does not necessarily mean that the homogeneity is on a molecular scale, but no correlation between the size of inorganic and organic domains could have been drawn so far.

CHEMICAL PROCESSING OF ORMOCERS

In the previous chapter mainly the question of chemical properties was discussed (on the basis of composition). But independent on composition, the properties are influenced by processing, too. In the following, several synthesis processes for different types of ORMOCERs and the influence on properties are described. As published elsewhere [9], a family of scratch resistant coatings was developed from an ORMOCER contact lens composition. The hardness of these materials was attributed to the inorganic backbone. These materials have to be prepared by a special condensation process according to [24] in order to obtain sufficent homogeneity. γ-glycidyloxipropyltrimethoxysilane (epoxy silane) was used as organic modifier, which is able to form a polyethylene oxide chain by polymerization. One disadvantage of these materials is their brittleness, which prevents their application on flexible substrates like rubber or thin foils to be bent with small curvature radii. The elongation limit of these coatings is in the range of about 1 - 2 %. The question arises, whether flexibility can be improved by reducing the concentration of inorganic units without loosing scratch resistance.

The simplest way to reduce the amount of inorganic backbone is the elimination of pure inorganic network formers and to start with the one-component system "epoxy silane". The synthesis process is described in details in [25]. For the hydrolysis of the epoxy silane two different concentrations of water were used: 1.5 mole H_2O/mole silane and 3.0 mole H_2O/mole silane. In fig. 8 the residual H_2O concentration after 10, 50 and 200 minutes hydrolysis at pH 9 after 16 hrs prehydrolysis at pH 5.5 is shown (at pH 5.5 only a small fraction of water is consumed).

The analysis of the epoxy groups shows that with 3.0 mole H2O the residual epoxy group content is remarkably lower. After pH 9 hydrolysis, ≈ 30 % of the epoxy groups are changed to glycol groups indicating that a part of H_2O is used for the epoxy ring opening instead of hydrolysation. With 1.5, almost no glycols are formed. This should have a serious effect on the epoxy crosslinking: For the 3.0 system, a weaker crosslinking and a more hydrophilic matrix is expected.

Coating experiments on metal and PET foils show significant differences. The 1.5 system shows after an amino-catalysed curing (= epoxy polymerization to PEO chains) a surprising flexibility compared to the 3.0 system, as indicated in fig. 9, which is attributed to the higher PEO chain content of this

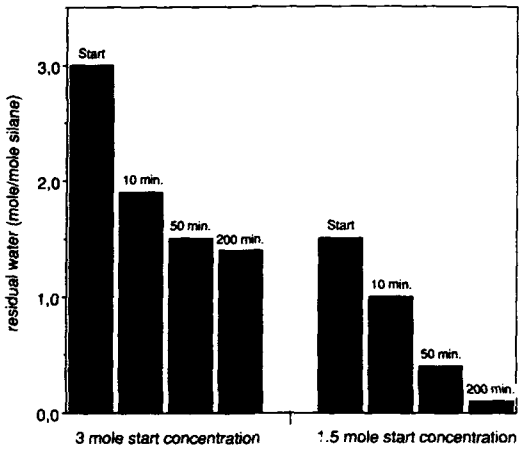


Fig. 8. Comparison of the hydrolysis kinetics of 3.0 and 1.5 mole H_2O concentration of the epoxysilane at pH 9; 16 hrs at pH 5.5.



Fig. 9. Differences in flexibility of the 1.5 and the 3.0 system.

chain content of this system. Humidity tests confirm the result: The 3.0 system shows crack formation after 14 days treatment at 40 °C in 100 % r.h. due to its higher water take up, whereas the 1.5 system remains unchanged. The results clearly show the strong impact of hydrolysis and condensation conditions on the material properties.

These materials can be easily employed as thick coatings (up to 50 µm) without cracking. Cracking in general occurs during the thermally induced condensation step by shrinkage due to the loss of H_2O (2) or closing of pores.

$$\equiv Si\text{-}OH + HO\text{-}Me\equiv \rightarrow \equiv Si\text{-}O\text{-}Me\equiv + H_2O\uparrow \qquad (2)$$

If no pores are present, shrinkage is only based on the loss of H_2O if the precursor is solvent-free and hydrolysis is complete. The elimination of ≡Si-OH groups should lead to an improvement of the shrinkage behavior. Therefore, in a

composition with 30 SiO_2 (from TEOS), 30 $C_6H_5SiO_{3/2}$ (from $C_6H_5Si(OEt)_3$) and $CH_2=C(CH_3)COO(CH_2)_3SiO_{3/2}$ (from the ethoxide), an average of 1.5 ≡Si-O bonds at the phenylsilane was substituted by F (fig. 10). This was carried out by introducing $C_6H_5SiF_3$, which hydrolyses to an average of 1.5 F during hydrolysis and condensation [26]. In fig. 11, the NIR spectra shows the dissappearance of the SiOH groups by the introduction of F.

Thermal treatment shows remarkable differences between the two systems. The fluorinated system (after photocuring the MMA groupings) undergoes a weight loss of only a few % between 100 and 280 °C with almost no shrinkage, whereas the non-fluorinated system loses already remarkable weight accompanied by crack formation in 10 µm thick coatings. Employed as coatings, the fuorinated materials can be used up to 250 °C without shrinkage

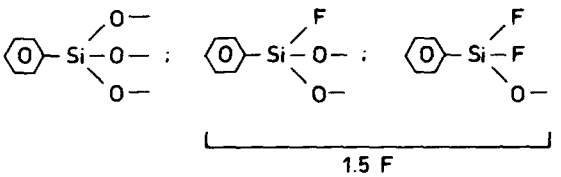


Fig. 10. Substitution of ≡Si-O- by ≡Si-F.

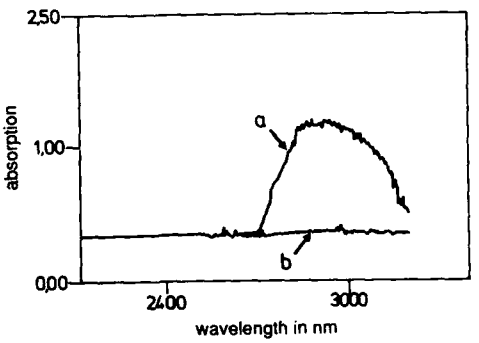


Fig. 11. NIR spectra of SiOH groups of the fluorine-free (a) and the fluorinated system (b).

and cracking. They are highly transparent and show a good scratch resistance, too. They are not effected by humidity in the wheathering test. The behavior can be explained by the lack of thermally activated condensation of SiOH groups in the flexible network.

Another interesting variation by chemistry can be used to incorporate metal oxides into polymers on a molecular or nano scale by complex formation. For example, $Zr(prop^1)_4$ complexed with methacrylic acid (MA) can be used for polymerizing the acid with olefins to form ZrO_2 containing polymers. The complex formation can be followed by IR (fig. 12), excess of MA (r/ZrO_2: MA > 2) leaves uncomplexed acid. Polycondensation and polymerization of the complexed $Zr(OR)_4$ with methacryloxysilane (1:9 molar ratio) leads to bulk materials with interesting mechanical properties [27]: Solid rods can be prepared with a bending strength up to 80 MPa. This can be interpreted by an internal reinforcement of the modified PMMA crosslinked ORMOCER.

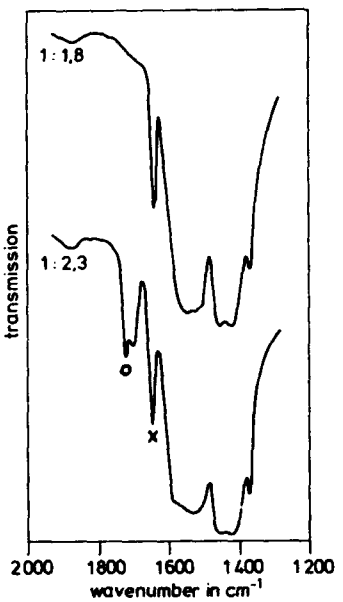


Fig. 12. Consumption of MA by complex formation with $Zr(prop^1)_4$; MA:Zr = 1:1.8 (upper curve) and 1:2.3 lower curve, molar ratios). x ≡ C=O vibration of complexes, o ≡ C=O vibration of the free acid.

CONCLUSIONS

Sol-gel chemistry in combination with organic modification can lead to new materials with interesting properties. Chemical properties can be changed in a wide range. But for the understanding of the properties, the understanding of the synthesis chemistry is necessary. This can be difficult, especially if multicomponent systems with differences in the reactivity of the different components occur. Investigations in many cases are only at its beginning but show already very hopeful results. The second point necessary to be investigated is the size effect of the inorganic-organic domains on the properties of the materials.

ACKNOWLEDGEMENT

The author wants to express his thank to the Staatsministerium für Wirtschaft und Verkehr of the State of Bavaria, the Bundesminister für Forschung und Technologie and several companies for the financial support of the work and to Dr. Arpac and Mr. Glaubitt for their helpful discussions.

REFERENCES

[1] Kersten, R. Th., In: Extended Abstracts of the Topical Meeting on Glasses for Optoelectronics, December 1, 1989, The Ceramic Society of Japan, Tokyo/Japan, 24.
[2] Sporn, D., Schmidt, H., In: Proceedings of the 1st European Ceramic Society Conference including Science of Ceramics 15, June 1989, North-Holland Physics Publishers, Amsterdam (in print).
[3] Aksay, I.A., Stangle, G.C , Sarikaya, M., In: Ceramic Powder Processing Science. Eds.: Hausner, H., Messing, G.L., Hirano, S.; Deutsche Keramische Gesellschaft 1989, 463.
[4] Scherer, G.W., J. Non-Cryst. Solids 100 (1988) 77.
[5] Scherer, G.W., J. Non-Cryst. Solids 121 (1990) 104.
[6] Mackenzie, D., Mat. Res. Soc. Symp. Proc. 32 (1984) 169.
[7] Sakka, S., In: Sol-Gel Technology for Thin Films, Fibers, Preforms, Electronics and Speciality Shapes. Ed.: Klein, L.C.; Noyes Publications, Park Ridge/New Jersey 1988, 140.
[8] Schmidt, H., Erzmetall 43 (1990) No. 2, 75.
[9] Schmidt, H., In: Proceedings Fourth International Confer. on Ultrastructure Processing of Ceramics, Glasses and Composites, February 1989, Tucson/USA. John Wiley and Sons, publishers (in print).
[10] Schmidt, H., Mat. Res. Soc. Symp. Proc. 171 (1990) 3.
[11] Schmidt, H., Popall, M., Rousseau, F., Poinsignon, C., Armand, M., In: Proceedings Second Internat. Symp. on Polymer Electrolytes, June 1989, Siena/Italy (in print).
[12] Wilkes, G.L., Brennan, A.B., Huang, H.-H., Rodrigues, D., Wang, B., Mat. Res. Soc. Symp. Proc. 171 (1990) 15
[13] Garrido, L., Ackerman, J.L., Mark, J.E., Mat. Res. Soc. Symp. Proc. 171 (1990) 65.
[14] Schaefer, D.W., Mark, J.E., McCarthy, D., Jian, L., Sun, C.-C., Farago, B., Mat. Res. Soc. Symp. Proc. 171 (1990) 57.
[15] Schottner, G., Oral presentation at 52nd Wilhelm-Else-Heraeus-Seminar, Bad Honnef/FRG, May 1989.
[16] Ravaine, D., Seminel, A., Charbouillot, Y., Vincens, M., J. Non-Cryst. Solids 82 (1986) 210.
[17] Charbouillot, Y., Ph.D. thesis. Institut National Polytechnique, Grenoble, 1987.
[18] Philipp, G., Schmidt, H., J. Non-Cryst. Solids 63 (1984) 283.
[19] Popall, M., Meyer, H., Presentation at VDI/VDE-TZ Seminar "Anwendung der laserinduzierten Metallabscheidung für Multi Chip Module", Berlin, March 21, 1990.
[20] Schmidt, H., Wolter, H., J. Non-Cryst. Solids 121 (1990) 428.
[21] Wolter, H., Schmidt, H., DVS-Berichte 129 (1990).

[22] Haas, K.H., Hutter, F., Schmidt, H., In: Proceedings Int. Conf. on Materials with Exceptional Properties, Expermat 87, Bordeaux, 1987.
[23] Annual Report 1989 of Fraunhofer-Institut für Silicatforschung, 131.
[24] Schmidt, H., Seiferling, B., Mat. Res. Soc. Symp. Proc. 73 (1986) 739.
[25] Naß, R., Arpac, E., Glaubitt, W., Schmidt, H., Non-Cryst. Solids 121 (1990) 370.
[26] Mutz, J.-L., Private Communication, to be published seperately.
[27] Naß, R., Arpac, E., Schmidt, H., In: Proceedings Third International Conf. on Ceramic Powder Processing Science, San Diego, February 1990, Amer. Cer. Soc. (in print).

ARYL-BRIDGED POLYSILSESQUIOXANES - NEW MICROPOROUS MATERIALS.

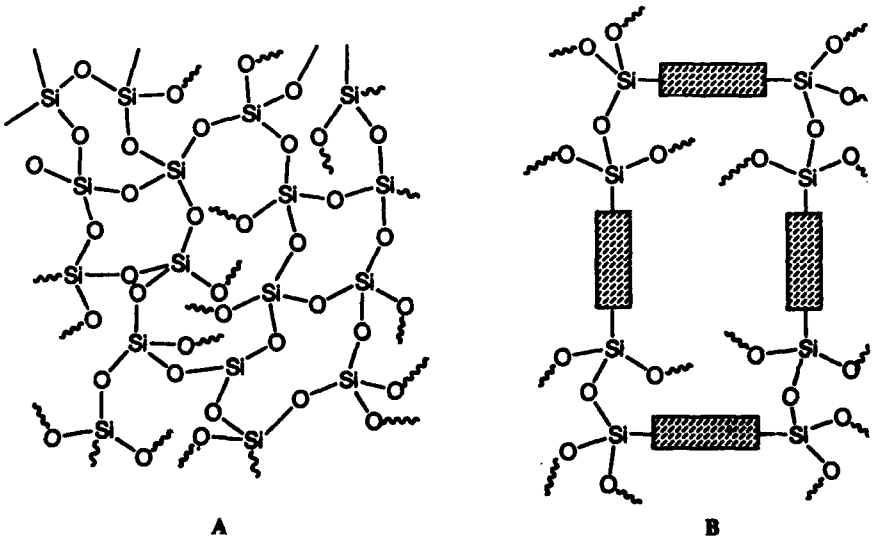
KENNETH J. SHEA,* OWEN WEBSTER**, AND DOUGLAS A. LOY*
*Department of Chemistry, University of California, Irvine, Irvine, California, 92717.
**Central Research & Development, E.I. duPont de Nemours & Company, Experimental Station, Wilmington, Delaware, 19898.

ABSTRACT

The first representatives of a new family of microporous, aryl-bridged polysilsesquioxanes have been prepared by sol-gel processing of bis-1,4-(triethoxysilyl)benzene **1a**, bis-4,4'-(triethoxysilyl)biphenyl **2a**, bis-4,4'-(triethoxysilyl)terphenyl **3a**, and bis-9,10-triethoxysilyl anthracene **4a**. The bis(trichlorosilyl) analogs of **1a** and **2a** (**1b** and **2b**, respectively) were also examined. The materials produced by hydrolysis and condensation of the monomers provide an opportunity to fully condense to a network with rigid-rod organic spacers interspaced at regular intervals in the silicate-like framework. The xerogels produced upon subsesquent processing of the gels have extremely high surface areas (256-1100 m^2/g; BET) with porosities confined to the micropore domain (< 200 nm). Solid state (CP MAS) ^{13}C and ^{29}Si NMR were used to evaluate the extent of hydrolysis and degree of condensation in the xerogels. The porosity and thermal stability of the aryl bridged polysilsesquioxanes may lead to applications as chromatographic absorbents. The transparent materials may also have optical applications arising from both the gels' high refractive indices and the covalent incorporation of ultraviolet chromophores.

INTRODUCTION

Synthetic silicates (Figure 1, A) prepared by sol-gel processing of alkoxysilanes (eq. 1) allow for the preparation of amorphous materials (xerogels) that are precursors to high purity glasses, ceramics, coatings, and fibers [1]. In a similar fashion, organically modified silicates can be prepared by condensing tetraethoxysilane (TEOS) with hydroxy terminated poly(dimethylsiloxanes) [2] or replacing an ethoxy substituent with an alkyl or aryl group (polysilsesquioxanes or T-resins) [3].



A B

Figure 1. Amorphous Silica (A) and Aryl-bridged Polysilsesquioxane (B).

Mat. Res. Soc. Symp. Proc. Vol. 180. ©1990 Materials Research Society

$$n\ Si(OEt)_4 + 2n\ H_2O \rightleftharpoons (SiO_2)_n + 4n\ EtOH \quad (1)$$

We report the preparation of a new class of microporous materials, aryl-bridged polysilsesquioxanes [4], through the sol-gel processing of bis(triethoxysilyl)aryl **1a-4a** and bis(trichlorosilyl)aryl **1b, 2b** monomers (Figure 2). These materials incorporate aryl groups in silsesquioxane networks with hexacoordinate connectivity (Figure 1, B). The xerogels would retain the useful optical properties of tricoordinate poly(arylsilsesquioxanes) in a more uniform, close packed network [7] The rigid aryl spacers [8] between the silicon atoms in the monomer may also provide control of the microarchitecture of the network, influencing properties such as microporosity. Such an effect has been proposed in layered metal aryl-bisphosphonates [9] and was anticipated but, as yet, not realized in related approaches using vinyl-functionalized spherosilicates [10], and carbon-based molecular level building blocks [11].

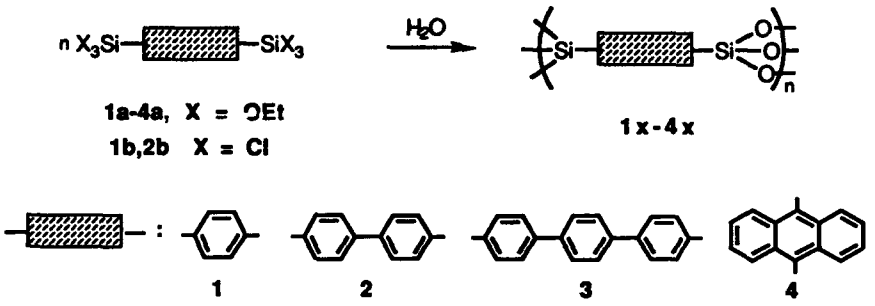


Figure 2. Hydrolysis/condensation of monomers 1-4.

EXPERIMENTAL

Monomers **1a** and **2a** were prepared by a Barbier-Grignard reaction of 1,4-dibromobenzene and 4,4'-dibromobiphenyl with TEOS (Figure 3) [12]. Monomers **3a** and **4a** could not be prepared by Grignard chemistry; lithium-halogen exchange followed by treatment with chlorotriethoxysilane afforded **3a** and **4a** in moderate yields [12]. Hexachloride derivatives **1b** and **2b** were prepared from **1a** and **2a**, respectively, by treatment with $SOCl_2$ in the presence of a catalytic amount of DMF.

The hexaethoxide monomers **1a-4a** were hydrolyzed/condensed under both acidic and basic conditions. In a typical acid-catalyzed polymerization, monomer **1a** (0.2-0.4 M in THF or EtOH) was mixed with 3 equiv H_2O and HCl (0.10 equiv) as catalyst. The solutions generally gel within several hours. Using the same concentrations of monomer and water, the base-catalyzed polymerization required weeks to reach gelation. To facilitate rapid gelation, an excess of H_2O (15 equiv) and NH_4OH (5.7 equiv) were used. Polymerization of the hexachloride monomers **1b** and **2b** (0.12M) were performed in THF with 3 equiv H_2O. The transparent gels were allowed to cure for 48 hours before drying.

The solvent could be removed from the gel to yield monoliths with little or no fractures by slow air drying (for months) or by immersing the gel in a sequence of solvents [13] with decreasing dielectric constant and then allowing them to air dry (2 days). Alternatively, monolithic xerogels (Figure 4) could be prepared from **1a** using formamide as a drying control chemical agent (DCCA) [14]. The xerogels were ground and dried under dynamic vacuum.

RESULTS AND DISCUSSION

The xerogels **1x** and **2x** were colorless, transparent solids. The xerogels **3a** and **4a** were transparent yellow and red solids due to the absorption characteristics of the terphenyl and anthracene spacers. The materials were thermally stable (DSC, TGA; N_2) to 500 °C. Scanning electron micrographs of both acid and base-catalyzed **1x** revealed smooth surfaces with glasslike fractures and no macropores. Transmission electron micrographs showed the composition more clearly (Figure 5). The amorphous characteristics bear striking resemblance to electron micrographs of condensed polymeric-type silica gels produced by acid catalyzed hydrolysis/condensation of TEOS [16]. These features are in constrast to colloidal gels, which consist of aggregates of discrete, dense particles [17].

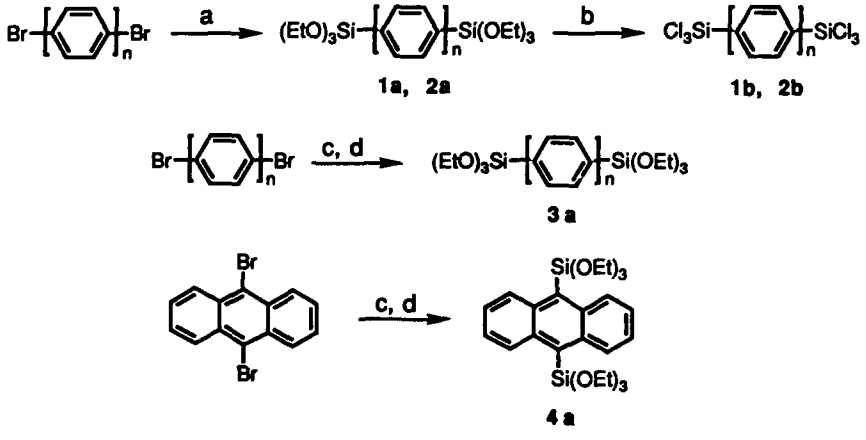


Figure 3. Conditions: (a) Mg^0, THF, TEOS, reflux for 3 days, n= 1,2; (b) $SOCl_2$, DMF catalysis, reflux for 5 days; (c) 4 equiv of t-buLi, Et_2O, -78 °C for 30 min, 25 °C for 3 h, n=3; (d) 2.5 equiv of chlorotriethoxysilane, -78 °C for 30 min, 25 °C for 4 h.



Figure 4. Dried transparent monoliths prepared by acid catalyzed hydrolysis/condensation (THF, H_2O, formamide, and HCL catalyst) of TEOS (right) and **1a** (left).

Pore analysis (N_2, BET) of **1x** and **2x** prepared by both acid and base-catalysis confirm the absence of macropores, but showed micropores with mean pore diameters at or below 2 nm. Argon adsorption/desorption (BET) studies of the base-prepared **1x** and **2x** found mean pore diameters of 0.8 nm and 0.6 nm, respectively; the pore diameters of these materials appears to be independent of the length of spacer. Porous **3x** has been prepared and the mean pore diameter will be determined in the near future. The materials **1x**, **2x**, and **4x** have extremely high surface areas (256-1150 m^2/g) [18].

Solid state ^{13}C and ^{29}Si NMR were the most useful tools for the characterization of these materials. ^{13}C NMR, in conjunction with FT-IR, was valuble for determining the extent of hydrolysis. The ^{13}C CP MAS NMR of **1x** clearly shows the aryl-carbon resonances at 135 ppm and the ethoxysilane resonances (minor) at 59 and 17 ppm. Interupted decoupling experiments were used to distinguish between mobile ethanol (and other adsorbed solvents) and those arising from bound ethoxysilanes [21]. Under the acidic polymerization conditions, the residual ethoxy residue ranged from approximately 19 to 0%. Under basic conditions, hydrolysis was complete- no residual bound ethoxy peaks are observed from the ethoxy precursors.

^{29}Si CP MAS NMR of **1x** (Figure 6) prepared under acidic hydrolysis conditions of **1a** followed by solvent replacement [14] and vacuum drying shows three resonances at -59, -68, and -76 ppm, respectively. The peaks correlate with the substructures $PhSi(OH)_2(OSi)$ (T_1^{Ph}), $PhSi(OH)(OSi)_2$ (T_2^{Ph}), and $PhSi(OSi)_3$ (T_3^{Ph}) [22, 23]. The silicon resonances were deconvoluted, and the areas, after correction for contact times, were integrated. Xerogels prepared by acid-catalyzed hydrolysis/condensation of **1a-4a** indicate the degree of condensation to be approximately 60-70%. Hydrolysis of the hexachlorides **1b** and **2b** gives rise to materials with approximately 70-75% condensation. Base-catalyzed hydrolysis/condensation produces materials with a higher degree of condensation (approximately 85%). Although quantitative conclusions regarding the calculated degree of condensation must be interpreted with caution [23c], the materials exhibit an extent of condensation similar to that found in pure silicate xerogels.

In conclusion, it is shown that organic spacers can be inserted at regular intervals into the Si-O-Si silicate structure. Sol-gel processing allows for the preparation of aryl-bridged polysilsesquioxanes, high surface area materials that have certain morphological properties in common with both silicates and simple poly(arylsilsesquioxanes), but with added opportunities for systematic modification.



Figure 5. Transmission electron micrograph of **1x** (THF, H_2O, HCl catalysis; bar = 100 nm).

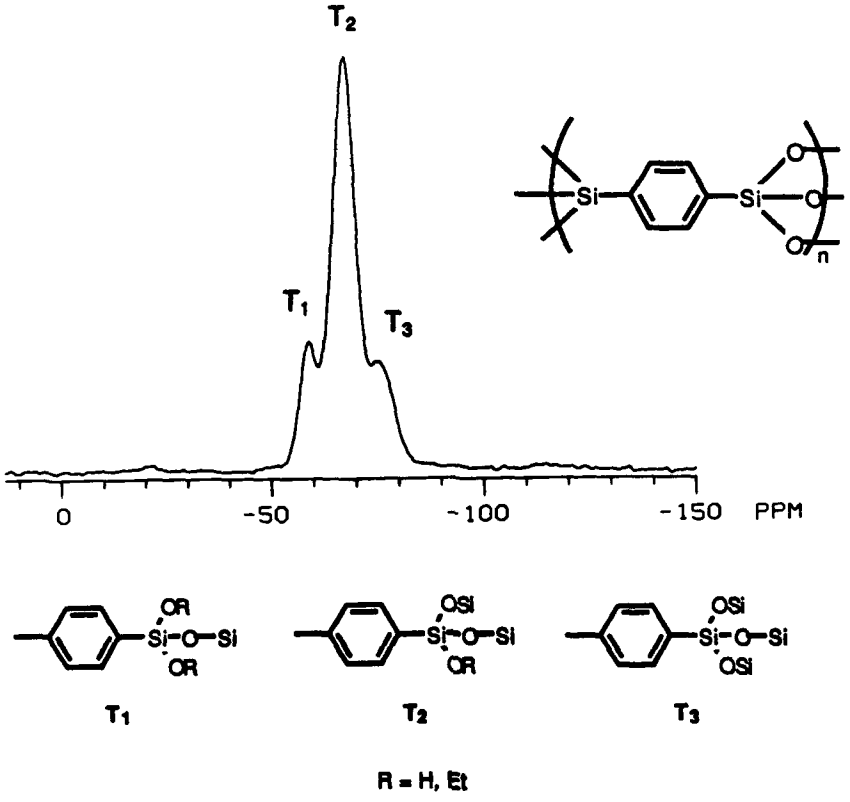


Figure 6. ^{29}Si CP MAS NMR spectrum of **1x** (prepared by acid catalysis, EtOH, H_2O) at 39.74 MHz. Experimental conditions: 8 μs 90° pulses, 5 μs cross polarization time, 25.65 ms acquisition time, 3.9 KHz spin speed, 1776 scans.

ACKNOWLEDGEMENT

We are grateful to Ron Farlee at du Pont and to James Frye, Chuck Bronnimann, and A. Jurkiewicz at the Colorado State University NMR Center for assistance in obtaining and interpreting the NMR data. We are also grateful to Fred Gentry for technical assistance and to Sue Fischer at the University of California, Irvine Electron Microscopy Facility for assistance in obtaing the electron micrographs. K.J.S. thanks duPont for an appointment as Visiting Research Scientist during which time this work was initiated.

REFERENCES AND NOTES

[1] L.C. Klein, Ed., Sol-Gel Technology for Thin Films, Fibers, Preforms, Electronics, and Speciality Shapes. (Noyes Publications: Park Ridge, NJ, 1988).
[2] H. Huang, B. Orler, and G.L. Wilkes, *Macromolecules*, **20**, 1322, (1987).
[3] H.K. Schmidt, "Inorganic and Organometallic Polymers." *ACS Symp. Ser.* **360**, 333, (1988).
[4] A coating incorporating **1a** [5], and a copolymer of **1b** and trichlorosilylbenzene and various dichlorosilane monomers [6] have been reported.
[5] Nippon Sheet Glass Co., Ltd. JP 59 11,374 [84 11,374], (1984); *Chem. Abstr.*, **100**, 193702 (1984).
[6] A.F. Moiseev, *Lakokra sochnye Materialy i ikh Primenenie* **5**, 14, (1965).
[7] Poly(arylsilsesquioxanes) are believed to be loosely interconnected cage oligosilsesquioxanes [8].
[8] J.F. Brown, Jr. *J. Am. Chem. Soc.* **87**, 4317, (1965).
[9] The phenyl, biphenyl, and terphenyl groups separate the silicon atoms with Si-aryl-Si distances of 0.67, 0.87, and 1.08 nm, respectively.
[10] M.B. Dines and P.M. DiGiacomo, *Inorg. Chem.* **20**, 92, (1981).
[11] P.A. Agaskar, *J. Am. Chem. Soc.* **111**, 6858, (1989).
[12] (a) P. Kaszynski and J. Michl, *J. Am. Chem. Soc.* **110**, 5225, (1988). (b) A.-D. Schulter, *Macromolecules* **21**, 1208, (1988).
[13] All new monomers satisfied chromatographic and spectroscopic (IR, ^{1}H and ^{13}C NMR, and high resolution mass spectrometry) criteria for purity and chemical composition.
[14] For sol-gels prepared in THF, the solvent series was tetrahydrofuran, methylene chloride, chloroform, diethyl ether, toluene, carbon tetrachloride, and 1,1,2-trichloro-1,2,2-trifluoroethane. This procedure minimized capillary stress during drying.
[15] L.L. Hench and D.R. Ulrich, Ultrastructure Processing of Ceramics, Glasses, and Composites. (Wiley, New York, *1985*) p 5.
[16] C.J. Brinker, W.D. Drotning, and G.W. Scherer, "Better Ceramics Through Chemistry," *Mater. Res. Soc. Symp. Proc.* **32**, 25, (1984).
[17] (a) C.J. Brinker, E.P. Roth, G.W. Scherer, and D.R. Tallant, *J. Non-Cryst. Solids* **71**,171, (1985). (b) G.W. Scherer, *J. Non-Cryst. Solids* **87**, 199, (1986). (c) C.J. Brinker and G.W. Scherer, *J. Non-Cryst. Solids* **70**, 301, (1985).
[18] Hydrolysis of trialkoxy- and trihaloaryl- or alkylsilanes typically results in nonporous resins or crystalline oligomers [19] The porosity and surface area of silica gels prepared by hydrolytic condensation of TEOS can vary widely. Recent values have ranged from 150 to 775 m^2/g [20].
[19] J.F. Brown, Jr., L.H. Vogt, and P.I. Prescott, *J. Am. Chem. Soc.* **86**, 1120, (1964). See, however: I.B. Slinyakova and L.I. Kurennaya, *Vysokomol. Soedin. Ser. B.* **14**, 889, (1972); *Chem. Abstr.* **78**, 136829V, (1973).
[20] (a) K.C. Chen, T. Tsuchiya, and J.D. Mackenzie, *J. Non-Cryst. Solids* **81**, 227, (1986). (b) K. Unger, *Angew. Chem., Int. Ed. Engl.* **11**, 267, (1972).
[21] G.E. Maceil, J.F. Haw, I.-S. Chuang, B.L. Hawkins, T.A. Early, D.R. McKay, and L. Petrakis, *J. Am. Chem. Soc.* **105**, 5529, (1983).
[22] R.K. Harris, J.D. Kennedy, and W. McFarlane, NMR and the Periodic Table, Edited by R.K. Harris *et al*, (Academic Press: London, 1978), Chapter 10, pp 309-340.
[23] (a) G.E. Maciel and D.W. Sindorf, *J. Am. Chem. Soc.* **102**, 7606, (1980). (b) E.T. Lippmaa, A.V. Samoson, V.V. Brei, and Y.I. Gorlov, *Dokl. Akad. Nauk. SSR* **259**, 403, (1981). (c) W.G. Klemperer, V.V. Mainz, and D.M. Millar, *Mater. Res. Soc. Symp. Proc.* **73**, 15, (1986). (d) G. Engelhardt, H. Janke, E. Lippmaa, and A. Samoson, *J. Organomet. Chem.* **210**, 295, (1981). (e) J.R. Fox, D.A. White, S.M. Oleff, R.D. Boyer, and P.A. Budinger, "Better Ceramics Through Chemistry," *Mater. Res. Soc. Symp. Proc.* **73**, 395, (1986).

RUBBERY ORMOSILS

Young J. Chung, Su-Jen Ting and John D. Mackenzie
Department of Materials Science and Engineering,
University of California, Los Angeles, CA 90024

ABSTRACT

A new technique which permits the successful preparation of ORMOSILS (Organically Modified Silicates) with rubbery elasticity has been developed. Common alkoxides were reacted with polydimethyl siloxane (PDMS) and the microstructures were carefully controlled. Large monoliths of the porous rubbery ORMOSILS have been prepared. Gelation process was studied by ^{29}Si liquid NMR spectroscopy. A structural model for rubber elasticity of ORMOSILS was proposed.

INTRODUCTION

Inorganic materials, such as glasses and ceramics, although they have high temperature stability, are brittle and not easily fabricated into large or complex shapes. Recently, oxide glasses and ceramics have been fabricated at relatively low temperatures by a new technology known as the "sol-gel" process [1,2]. Although the fabrication temperatures have been significantly lowered, the resulting materials, because they have all oxide bonds, are still brittle. Also, these materials tend to fracture during drying and heat-treatment because of the porosity of gels.

More recently, pure oxide gels have been modified by the incorporation of organic groups to improve the ductility . Some of these materials are known as ORMOSILS (Organically Modified Silicates)[3], and "Ceramers"[4]. ORMOSILS are less brittle and show less tendency to fracture, because some of the bonds are terminated by organic side groups.

Although ORMOSILS are less brittle than pure oxides, rubbery behavior of ORMOSILS has not been reported. In this paper, a new technique which permits the successful preparation of rubbery ORMOSILS will be discussed.

EXPERIMENTAL

Tetraethoxysilane (TEOS) was used as inorganic component and polydimethyl siloxane (PDMS) was used as the polymeric component. The appropriate amount of TEOS (Alfa Products) and silanol terminated PDMS oligomer with MW = 1700 (Petrach System) were mixed with organic solvents, distilled water and acid catalyst.

The solutions were reacted at elevated temperatures ($70^{o}C$ - $100^{o}C$) and cooled to room temperature. The solutions were cast into molds and sealed. After gelation, the wet gels were dried. Gelation time was measured by the tilt method.

Sample densities were measured by the Archimedes method. ^{29}Si liquid NMR spectroscopy was performed to study the reaction process. Solution samples were transferred, during the reaction, into the NMR sample tube and quenched immediately in liquid nitrogen. Frozen samples were melted just before the NMR spectroscopy was performed. ^{29}Si NMR spectra were recored on a AM 360 BRUKER spectrometer. A pluse width of 10μs was applied with a relaxation delay of 6s. TMS was used as a reference. The microstructure of the gel was studied by scanning electron microscopy (SEM). The mechanical

Mat. Res. Soc. Symp. Proc. Vol. 180. ©1990 Materials Research Society

properties were measured usi: n Istron Model 1122.

RESULTS AND DISCUSSION

There are several requirement for rubbery elasticity. Materials should have long flexible chain-like molecules. These long chains should be lightly cross-linked. Also, atoms or segments should be able to rotate to one another upon application of stress. For this rotation, "free volume" is needed. The control of the microstructure which in turn governs the rubbery behavior involves many interdependent factors (Figure 1). However, despite the complexity, successful results have been obtained in the present study.

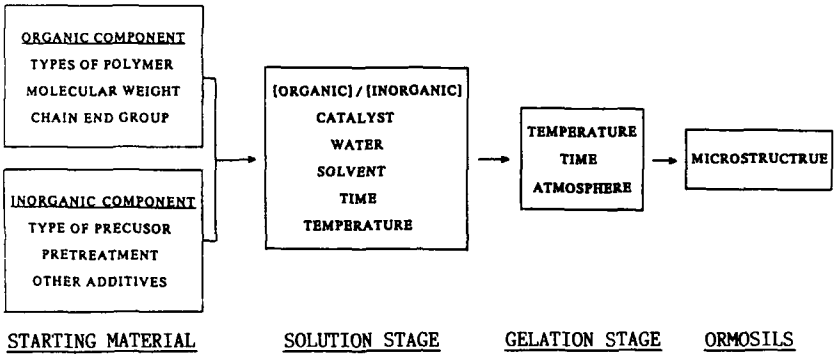


Fig. 1. Factors governing rubbery behavior of ORMOSILS.

The rubbery behavior of the ORMOSILS is shown in Figure 2. The compression - release cycles were performed 500 times and there was no change of the state of the ORMOSILS. The rubbery ORMOSILS prepared are shown in Figure 3. Large monolithic ORMOSILS with different shapes were successfully prepared without cracking. The bottom sample measured 19cm x 12cm x 1.3cm.

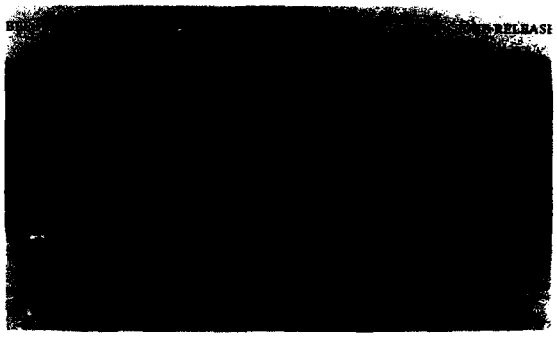


Figure 2. Rubbery behavior of ORMOSILS.



Fig. 3. ORMOSILS prepared.

The effects of concentration on the gelation time and bulk density of the ORMOSILS are shown in Figure 4 and Figure 5 respectively. Gelation time increased rapidly as the solvent content increased (Figure 4). Initially, bulk density decreased as the solvent content increased. Density, however, incresed again as the solvent content increased beyond a certain level (Figure 5).

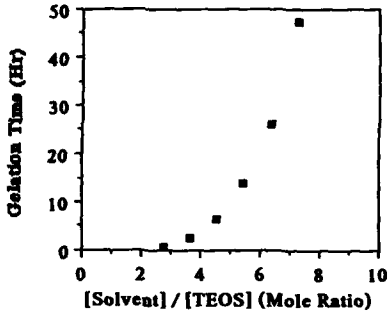


Fig 4. Effect of concentration on gelation time.

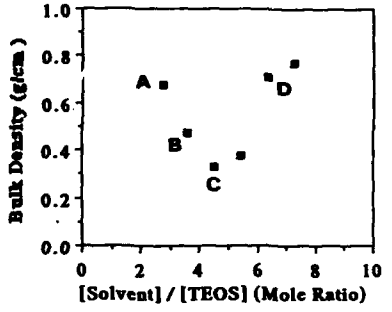


Fig. 5. Effect of concentration on bulk density of gel.

The microstructures of the corresponding gels discussed above (A, B,S,D of Figure 5) are shown in Figure 6. The changes of microstructure match to the bulk density changes. At high concentration, PDMS and TEOS can copolymerize easily due to high probability of mutual collision Figure 6-A). When concentration decreases, the probability of collision decreases and self condensation increases. The resulting microstructure consists of fine particles of silica gel surrounded by the porous copolymer matrix (Figure 6-B). This porous structure provided "free volume" needed for the rubbery elasticity. As the concentration decreased further, self condensation of TEOS

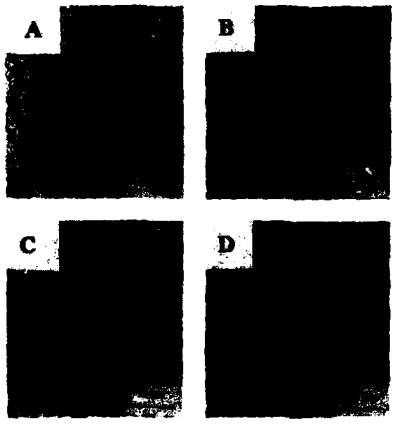


Fig 6. Effect of [Solvent]/[TEOS] on microstructure of gel
(A) 2.72 (B) 3.63
(C) 4.53 (D) 6.35

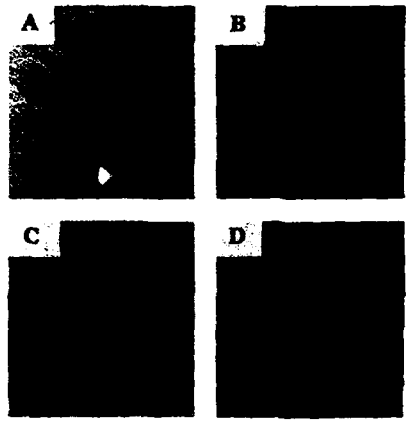


Fig 7. Effect of reaction time on microstructure of gel
(A) 30 min (B) 40 min
(C) 50 min (D) 60 min

became dominant resulting in the large spherical particles of silica gel surrounded by the layer of the copolymer (Figure 6-C). Even though the free volume increased due to the high porosity, these ORMOSILS are weak because of the small amount of copolymer available to provide rubbery elasticity. When the concentration is very low, the nucleus of the silica gel particle cannot grow rapidly. After gelation, the microstructure consists of fine particles surrounded by the copolymer matrix with small pores. The effects of concentration have been treated in detail for the TEOS system [7,8]. Also, the reaction time has a large effect on the gel microstructure (Figure 7). The self condensation of TEOS was enhanced by the pre-gelation treatment. As a result, microstructures of the gel are also influenced.

The results of the ^{29}Si NMR study are shown in Figure 8. In the solution without water/catalyst additions, M^{OH} (unit with Si atom in the hydroxyl terminated dimethyl siloxane), D (unit with Si atom in the dimethyl siloxane) and Q_0 (unit with Si atom in TEOS before any reaction) were present. As soon as water and acid were added at 20°C, M^{OH} and Q_0 unit disappeared and Q_2 (Si atom with two oxygen) and Q_3 (Si atom with three oxygen) units appeared due to the hydrolysis/condensation reaction.

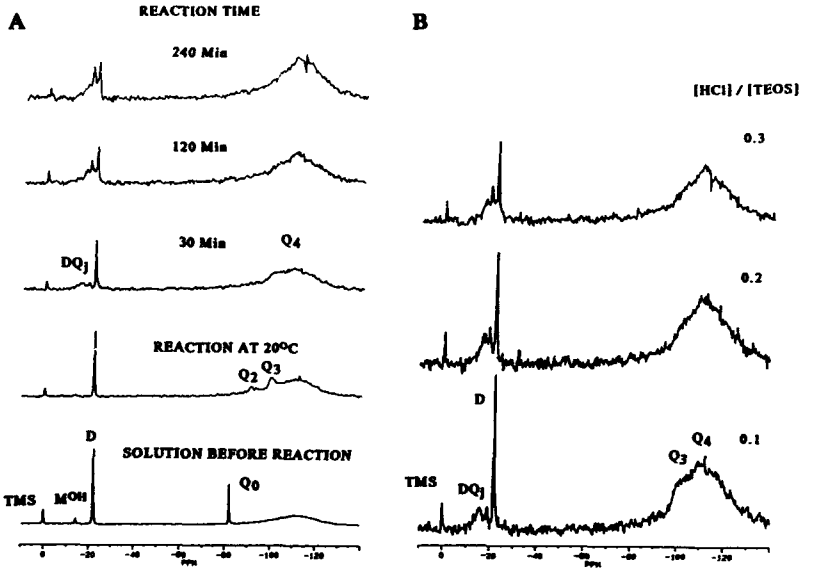


Fig. 8. Effects of reaction time (A) and catalyst (B) on gelation process.

As the reaction at elevated temperature proceeded, new DQ_j (unit with Si atom in the PDMS-TEOS copolymer) unit appeared and grew until gelation (Figure 8-A). As the acid content increased, copolymerization proceeded further. Also, hydrolysis and self condensation of TEOS increased (Figure 8-B). The resulting microstructures are shown in Figure 9. Similar microstructural changes due to the catalyst were reported for silica gel [8].

A structural model for rubbery elasticity is shown in Figure 10. ORMOSIL (A) has short chain length due to the high degree of copolymerization between PDMS and TEOS. The microstructure of ORMOSIL (B) consists of a matrix with medium chain length, fine silica gel particles and medium size pores. The microstructure of ORMOSIL (C) consists of large silica gel particles surrounded by a matrix with long chains and large pores. The ORMOSIL (B)

shows the best rubbery elasticity.

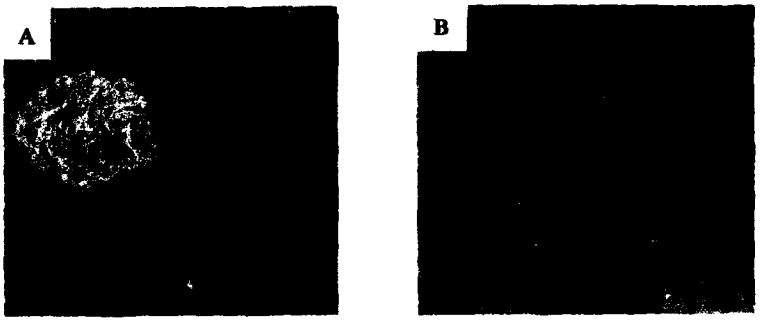


Fig. 9. Effect of catalyst content on gel microstructure.
[HCl]/[TEOS] : (A) 0.1 (B) 0.3

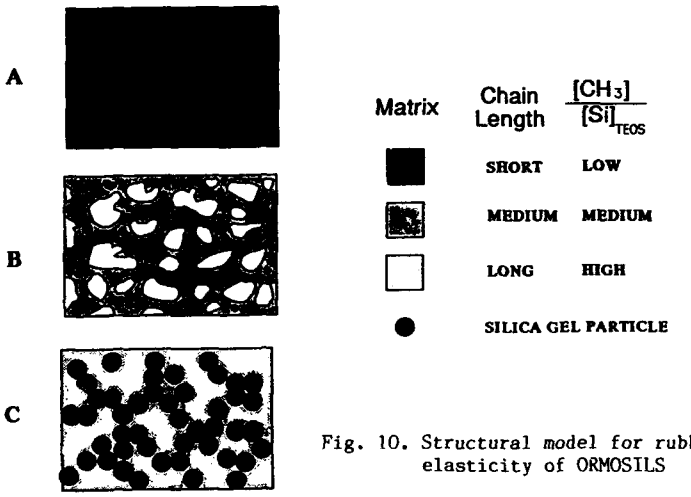


Fig. 10. Structural model for rubbery elasticity of ORMOSILS

Some comparision of the properties of RTV silicone rubber and ORMOSILS in this work are shown in Table I. Silicone rubber has very high molecular weight compared to the ORMOSILS. Also, silicone rubber has large elongation and high strength. However, silicone rubber has high organic content compared to the ORMOSILS.

SUMMARY

1. ORMOSILS with rubbery elasticity has been developed.
2. Large monoliths of porous rubbery ORMOSILS have been prepared.

Table I. Comparision of properties of silicone rubber and ORMOSILS.

	SILICON RUBER (RTV)	ORMOSILS (THIS WORK)
PDMS M.W.	26,000 - 200,000	1,700
$\frac{[CH_3]}{[Si]_{TMOS}}$	2,800 - 21,600	3.74
BULK DENSITY (g/cm^3)	1.1	0.57
OPEN POROSITY (%)	~ 0	52
ε (%)	400[a)]	68[b)]
σ (Mpa)	26 -33[a)]	12.5[b)]
E (Mpa)		2.6[b)]

a) TENSION

b) COMPRESSION

3. Gel microstructures were controlled by processing variables.
4. Gelation process was studied by ^{29}Si liquid NMR spectroscopy.
5. A structural model for rubbery elasticity of ORMOSILS was proposed.

ACKNOWLEDGEMENT

The authors are grateful to the Air Force Office of Scientific Research, Directorate of Chemical and Atmospheric Sciences, for support (Grant NO. AFSOR-88-0066) of this study.

REFERENCES

1. J. D. Mackenzie, J. Non-Cryst. Solids, 48, 1-10 (1982).
2. H. Dislich and P. Hinz, J. Non-Cryst. Solids, 48, 11-16 (1982).
3. H. Schmidt, J. Non-Cryst. Solids, 63, 283-292 (1984).
4. H. H. Huang and B. Orler and G. L. Wilkes, Polymer Bulletin, 14, 557-564 (1985).
5. J. E. Mark and C. C. Sun, Polymer Bulletin, 18, 259-264 (1987).
6. C. S. Parkhurst, W. F. Doyle, L. A. Silverman, S. Singh, M. P. Anderson, D. McClurg, G. E. Wnek and D. R. Uhlmann in Better Ceramics Through Chemistry II, edited by C. J. Brinker, D. E. Clark and D. R. Ulrich, (Mater. Res. Soc. Proc. 73, Palo Alto, CA, 1986) pp. 769-773.
7. B. E. Yoldas, J. Non-Cryst. Solids, 83, 375-390 (1986).
8. S. Sakka, H. Kozuka and S.H. Kim in Ultra Structure Processing of Advanced Ceramics, edited by J. D. Mackenzie and D. R. Ulrich (John Wiley & Sons, New York, 1986), pp. 159-171.

NON-LINEAR ORGANIC DYES IN POLYCERAM HOSTS

J.M. Boulton, J. Thompson, H.H. Fox, I. Gorodisher, G. Teowee, P.D. Calvert and D.R. Uhlmann
Department of Materials Science and Engineering,
University of Arizona, Tucson, AZ 85721.

ABSTRACT

Non-linear organic dyes, such as 2-methyl-4-nitroaniline (MNA) and p-nitroaniline (pNA), have been incorporated in Polyceram monoliths and thick films prepared by the hydrolysis and co-condensation of tetraethoxysilane and trimethoxysilylpropyl substituted polyethyleneimine. Strong second harmonic generation was observed.

1. INTRODUCTION

Sol-gel derived materials offer exciting potential as hosts for dye molecules [1,2]. For example, films containing laser dyes have been extensively studied [3-8], as well as materials incorporating dyes capable of hole burning [e.g., 9-11]. Organically modified silica gels containing spiropyranes show long-acting photochromic behavior [12]. Gels based on $EtSi(OEt)_3$ exhibit normal photochromic behavior (colorless to color), while Polycerams based on $Si(OMe)_4$ and poly(dimethylsiloxane) give reversed photochromism due to differences in cage properties.

Sol-gel derived materials have been investigated as hosts for non-linear organics. For example, composites of silica and poly(p-phenylenevinylene) gave promising third order waveguiding films [13]. Organic dyes, such as 2-methyl-4-nitroaniline (MNA) have high values of second harmonic generation, but a necessary criterion for second order generation is that the molecular environment must be non-centrosymmetric. There has been some investigation into the effect of enclosing MNA in a gel network, with either a host material of silica gel [14,15] or a silica gel-PMMA composite [15, 16]. The silica gel host was inadequate, since the acidic surface allowed for the oxidative decomposition of the MNA, changing from yellow to brown [15]. PMMA incorporation provided a method for sealing and coating the pores to protect the dye. The changed porosity reduced scattering effects as well. The electro-optical DC Kerr effect of the composite has been studied [16].

The present authors have been investigating the properties of organically modified oxides (Polycerams) [17,18]. These unique, hybrid materials offer many advantages over conventional alkoxide-derived gels. Advantages include the ability to tailor the chemical and physical properties and the ability to form thick films and monoliths relatively easily. The present paper reports the results of incorporating nitroanilines in these materials.

Mat. Res. Soc. Symp. Proc. Vol. 180. ©1990 Materials Research Society

2. EXPERIMENTAL

2.1 Preparation of Materials

Tetraethoxysilane (TEOS) and trimethoxysilylpropyl substituted polyethyleneimine (MPEI), (50 wgt. pct. in iso-propanol m.w. 1500-2000) were purchased from Petrarch (Bristol, PA). MNA and pNA were obtained from Aldrich Chemical Co. (Milwaukee, WI). All other reagents were reagent grade.

Sample preparation consisted of refluxing TEOS and H_2O (acidified to 0.15M HCl) in iso-propanol (IPA) at a H_2O:TEOS molar ratio of 2:1 for 15 mins. The reaction mixture was cooled, and PEI and organic dye were added. In all cases, the weight ratio of PEI solution to added IPA was 1:4. Solutions were passed through a 0.8 μm syringe filter and coated onto pre-cleaned glass slides by spin-coating at 1000 rpm for 10 sec. The coatings were dried in air for 5 mins. before coating again. Multiple coatings were applied to give the desired thickness. Thickness measurements were obtained using a Dektak 11A profilometer. The remaining solution was cast into poly(propylene) beakers and allowed to gel and dried slowly at room temperature. Films dried in air for 48 hours were investigated for second harmonic generation.

2.2 Investigation of Second Harmonic Generation

Second harmonic generation was investigated by the Maker fringe method [19], shown schematically in Fig. 1. The Nd/YAG laser was operated at 15 amps and 1500 Hz. Samples were first washed in IPA and then mounted on a computer controlled Oriel rotation stage and rotated through 360°. Filters, admitting only green light at 530-540 nm preceded the photomultiplier tube (Hammamatsu 1P28A), which converted the harmonic light to direct current. The signal was amplified (Stanford Instruments) and integrated (EGG 4100 boxcar integrator). A number of strong narrow peaks in intensity were observed as the sample was rotated. The maximum SHG intensity occurred when the beam hit the sample edge.

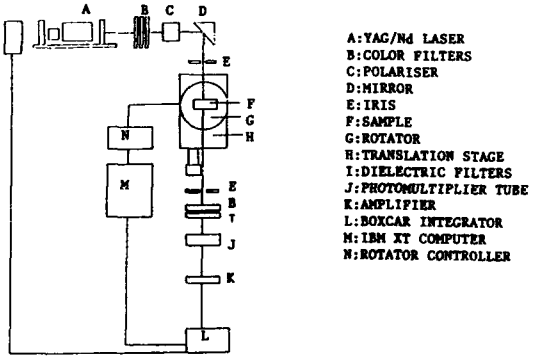


FIGURE 1. Schematic of the Maker Fringe SHG Experiment.

3. RESULTS AND DISCUSSION

Sol-gel derived organic-inorganic systems (Polycerams) are logical host materials for organic dyes. The organic component can act as a solvent phase in the network, increasing the solubility of the dye and also protecting the dye from acidic silica surfaces. The inorganic component of the Polyceram would improve the stability of the material by providing structural support and protecting the organic groups from inter-reaction. The poly(ethylene imine) coupled organic polymer system was selected in this case primarily because of the compatibility between the imine groups of the polymer and the amine groups of the dyes, both groups being basic in nature. Protonation of the amine group would be undesirable.

A further advantage is that the organic modification of the gel network minimizes the cracking problems associated with conventional alkoxide-derived gels. In this work, film thicknesses of about 30 μm were readily obtained and much thicker films could be formed. Additionally, under slow drying conditions monoliths could be prepared: a typical example of a 1 TEOS: 1 MPEI: 0.1 MNA (wgt. ratio) doped Polyceram is shown in Fig. 2.

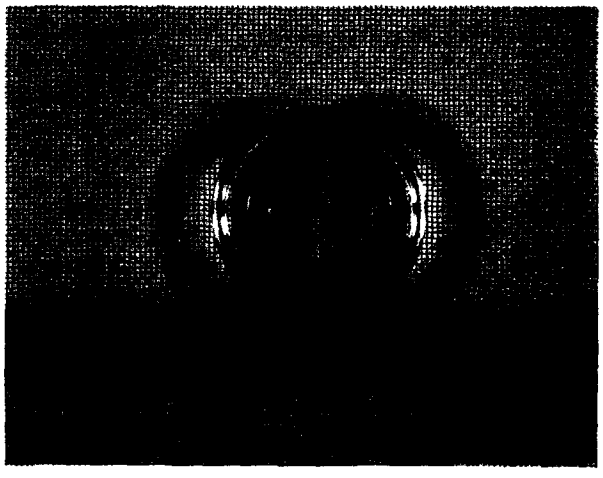


Figure 2. Monolithic 1 TEOS: 1 MPEI: 0.1 MNA Polyceram.

Initially, the effect of the TEOS: MPEI ratio on SHG was investigated. As can be seen in Table I, significant SHG signals were observed. By comparison, crystalline MNA powder (approx. 100μm thick) gave an SHG signal of around 1100 mV under these experimental conditions. All the coating compositions listed in Table I resulted in optically clear, crack-free, X-ray amorphous films.

TABLE I. Effect of TEOS: MPEI Wgt. Ratio on SHG (MNA: MPEI = 0.1)

TEOS: PEI	Thickness/Microns	Max. SHG Signal/mV
0	28.2	62.4
1	32.3	167
2	27.6	224
3	25.8	374

The intensity of the normalized SHG signal (SHG signal divided by thickness) is plotted in Fig. 3 vs. the TEOS: MPEI ratio at a constant MNA: MPEI ratio of 0.1. An increase in TEOS: MPEI ratio is seen to produce a dramatic increase in the SHG signal, despite the fact that since the MNA: MPEI ratio is constant, an increase in TEOS: PEI serves effectively to dilute the MNA. This suggests there is interaction between the silica surfaces in the Polyceram and the MNA molecules producing local orientation.

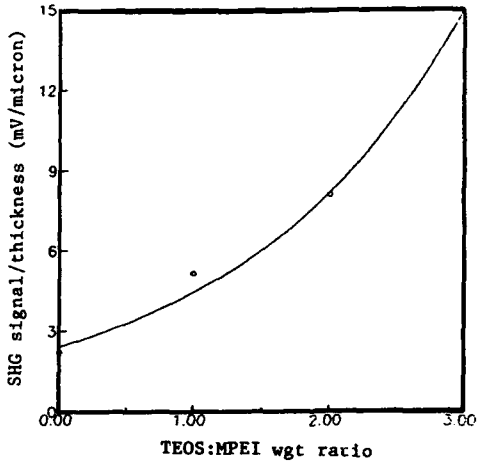


Figure 3. Effect of TEOS: MPEI ratio on normalized SHG signal (MNA:MPEI =0.1)

In the next stage of the investigation, the effect of the MNA: MPEI ratio on SHG was determined at a constant MNA: TEOS ratio of 2. SHG signals obtained from optically clear, crack-free and X-ray amorphous films are shown in Table II. Normalized SHG signals are shown in Figure 4.

TABLE II. Effect of MNA: MPEI Wgt. Ratio on SHG (TEOS: MPEI = 2)

MNA: PEI	Thickness/Microns	Max. SHG Signal/mV
0.1	27.6	224
0.15	26.1	390
0.2	27.6	660
0.24	31.0	953

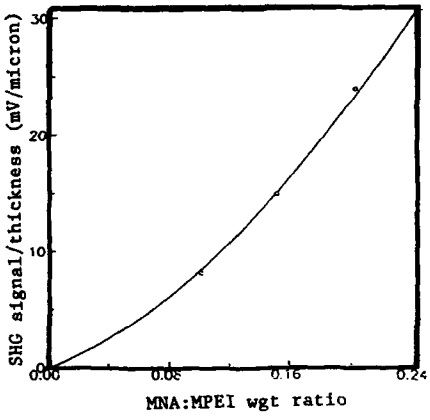


Figure 4. Effect of MNA: MPEI ratio on normalized SHG signal (TEOS:MPEI =0.2)

An increase in the MNA: MPEI ratio resulted in a linear increase in the normalized SHG signal. At higher MNA: MPEI ratios, substantial crystallization of the MNA occurred. An MNA: MPEI ratio of 0.28 resulted in an X-ray amorphous film. At the higher ratio of 0.284, substantial crystallization of MNA on the free surface of the film was observed; however, the characteristic MNA diffraction peaks could be removed by washing the film in IPA. Increasing the ratio to 0.3 resulted in substantial crystallization, both on the free surface and in the bulk.

The principal question arising from this work is whether the high SHG signals obtained from the clear films arose from the presence of microcrystalline MNA regions in the film, or whether alignment of the MNA molecules had occurred resulting in a non-centrosymmetric structure, or possibly both of these phenomena. As stated earlier, the results presented in Tables 1 and 2 were derived from optically clear, X-ray amorphous films. Investigation by cross-polarized optical microscopy

revealed small crystals at the film-glass slide interface; a typical micrograph is shown in Fig. 5.



Fig. 5. Optical Micrograph (Cross-Polarized) of 2 TEOS: 1 MPEI: 0.2 MNA film (bar=100μ)



Fig. 6. Optical Micrograph (Cross-Polarized) of heated 2 TEOS: 1 MPEI: 0.2 MNA (bar=100μm)

While crystalline MNA was present on the surface of the Polyceram films, the small size and number of crystals would not be expected to give rise to such strong SHG signals.

To elucidate further the basis of the observed second harmonic generation, a film with the composition 2 TEOS: 1 MPEI: 0.2 MNA was heated at 150C for 5 minutes, substantially higher than the melting point of MNA (131-133C). Heating resulted in substantial loss of the MNA due to its high volatility. Investigation of the heat-treated film showed the disappearance of the crystalline regions (see Figure 6). However, the sample still showed significant SHG; signals of approximately 287mV were obtained, which strongly suggests that MNA alignment had occurred in the film.

One final experiment was performed to confirm this finding: a 26μm film with the composition 2 TEOS: MPEI: 0.24 pNA was prepared. pNA undergoes centrosymmetric crystallization, whereas MNA undergoes non-centrosymmetric crystallization [20]. Therefore, when pNA crystallizes, the oppositely charged molecular ends align in the crystal, cancelling the net dipole moment and leading to zero quadratic hyperpolarizability, i.e., no SHG. The pNA-doped polyceram film showed a SHG signal of 547 mV, which is very strong evidence for molecular alignment in the sample.

4. CONCLUSION

Polycerams prepared from tetraethoxysilane and trimethoxysilylpropyl substituted polyethyleneimine have been shown to be excellent hosts for non-linear organic dyes. Strong SHG signals were obtained from both MNA and PNA, suggesting molecular alignment of the dye molecules in the samples.

ACKNOWLEDGMENTS

The authors gratefully acknowledge the financial support of the Air Force Office of Scientific Research.

REFERENCES

1. R. Reisfeld in Sol Gel Science and Technology, edited by M.A. Aegerter, M. Jafelicci Jr., D.F. Souza and E.D. Zanotto (World Scientific Publishing, Singapore, 1989), p. 323.
2. A. Makishima and T. Tani, J. Am. Ceram. Soc. 69, C-72 (1986).
3. Y. Kobayashi, Y. Imai and Y. Kurokawa, J. Mater. Sci. Lett. 7, 1148 (1988).
4. Y. Kobayashi, Y. Kurokawa, Y. Imai and S. Muto, J. Non-Cryst. Solids 105, 198 (1988).
5. M. Sasaki, Y. Kobayashi, S. Muto and Y. Kurokawa, J. Am. Ceram. Soc. 73, 453 (1990).
6. R. Reisfeld, R. Zusman, Y. Cohen and M. Eyal, Chem. Phys. Lett. 147, 142 (1988).
7. R. Reisfeld, M. Eyal and D. Brusilovsky, Chem. Phys. Lett. 153, 210 (1988).
8. D. Avnir, V.R. Kaufman and R. Reisfeld, J. Non-Cryst. Solids 74, 395 (1985).
9. T. Tani, A. Makishima, H. Namikawa and K. Awai, J. Appl. Phys. 58, 3559 (1985).
10. H. Tanaka, J. Takahashi, J. Tsuchiya, Y. Kobayashi and Y. Kurokawa, J. Non-Cryst. Solids 109, 164 (1989).
11. R. Locher, A. Renn and U.P. Wild, Chem. Phys. Lett. 138, 405 (1987).
12. D. Levy, S. Einhorn and D. Avnir, J. Non-Cryst. Solids 113, 137 (1989).
13. P.N. Prasad, presented at the 1989 Conference on Ultrastructure Processing, Tucson, AZ, 1989. Proceedings to be published by Wiley, 1990.

INORGANIC-ORGANIC COMPOSITES (ORMOCERs) AS STRUCTURED LAYERS FOR MICROELECTRONICS

MICHAEL POPALL*, HENNING MEYER*, HELMUT SCHMIDT**, JOCHEN SCHULZ*
*Fraunhofer-Institut für Silicatforschung, Neunerplatz 2, D-8700 Würzburg, F.R.G.
**Institut für Neue Materialien der Universität Saarbrücken, Im Stadtwald, Gebäude 43, D-6600 Saarbrücken, F.R.G.

ABSTRACT

Enhanced integration, faster signal transmission and reduced size of mounting devices in components for microelectronics requires new patternable materials. Inorganic-organic copolymers (ORMOCERs = ORganically MOdified CERamics), prepared by sol-gel techniques have been developed for interconnection technologies in microelectronics. Photopolymerization is enabled by unsaturated hydrocarbon or epoxide substituents and UV-sensitive initiators. Using a frequency doubled Argon-ion laser at 257 nm for direct laser writing, patterned layers with high edge quality have been realized. In combination with high breakthrough voltages, low permittivity constants and high bulk resistivities they open interesting aspects for very large system integration techniques (VLSI).

INTRODUCTION

The potential of new generations of ram and rom chips, especially processors, cannot be fully utilized without enhanced integration and multilayer technology [1]. Therefore microelectronics requires tailormade materials and new techniques for interconnection. Multilayer technology demands patternable dielectric materials with especially high electrical resistivity for high density of conducting paths, low permittivity constants for minimum signal deformation and good adhesion to substrate material and to active and passive components.

At the present state of the art dielectric materials like polyimide or polyimide/polyamide blends are well established [2]. For higher integration, however, the permittivity constant should be as low as possible, and water take up has to be minimized. As shown in [3], ORMOCERs could be synthesized with low ϵ values, good adhesion to substrates like aluminum, extremely low H_2O take up and curing temperatures as low as 280 °C. In [4] the possibility of the development of photolithographic patterns was investigated and it was shown, that ORMOCERs with polymerizable groups can be patterned. The objective of the present investigation was to develop ORMOCERs able to be patterned by direct laser writing techniques. This technique provides a flexible tool for microelectronic design. Therefore several types of ORMOCERs have been synthesized and tested for direct laser writing.

Mat. Res. Soc. Symp. Proc. Vol. 180. ©1990 Materials Research Society

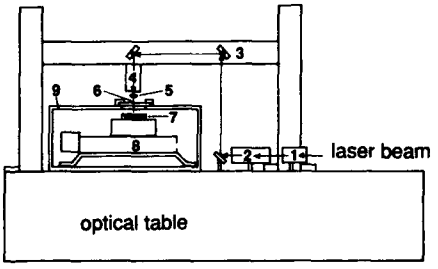
EXPERIMENTAL

Three compositions have been developed:
I: 0.45 mol 3-methacryloxypropyltrimethoxysilane, 0.30 mol phenyltrimethoxysilane, 0.25 mol aluminiumtri-sec.-butylate
II: 0.39 mol 3-(glycidoxypropyl)trimethoxysilane, 0.39 mol 3-methacryloxypropyltrimethoxysilane, 0.18 mol vinyltrimethoxysilane, 0.04 mol tetraethoxysilane.
III: 0.39 mol 3-(glycidoxypropyl)trimethoxysilane, 0.39 mol 3-methacryloxypropyltrimethoxysilane, 0.18 mol diphenylsilanediol, 0.04 mol tetraethoxysilane.

The components were mixed together without solvent and refluxed under air up to 6 hours. 50 % of the water necessary for a stoichiometric hydrolysis was added successively. The clear, viscous liquid was cooled to room temperature and stored in closed bottles.

For coatings, IRGACURE* 184 (photo initiator from Ciba Geigy) is added and the materials are applied onto the substrates (glass, silicon or thin film quality Al_2O_3) by spin coating and a coating thickness of 10 μm is obtained. Before photo curing, the coatings were dried at room temperature for 30 min. Photo curing can be carried out by UV radiation (1000 W high pressure mercury lamp) or by using a frequency doubled Ar ion laser (for patterning). After polymerization, the final curing has to take place at T > 120 °C for one hour. Patterned samples are developed before post baking with acetone/ultrasonic treatment. System II can be developed with 0.1 N NaOH within 10 seconds, too.

For laser writing a frequency doubled Ar ion laser yielding up to 100 mW at 257 nm was used.



1. electro optic modulator
2. polarizer
3. mirrors
4. Gallilei telescope
5. lens (fused silica)
6. window (fused silica)
7. target holder and target
8. motor driven stages
9. reactor

Figure 1: Scheme of the laser writing equipment

The set up is shown in fig. 1. The laser beam is directed towards the horizontal target via several mirrors. To achieve a minimum laser spot size the beam passes through a gallilean telescope expanding the beam by a factor of 2. A mechanical shutter or an electro optic modulator are used to turn the beam on and off by computer control. Finally the laser beam is focused by a quartz lens onto the target. The target itself is placed onto two motor driven stages providing the horizontal xy-movement. To adjust the focus on the target the lens position can be varied. The positioning system can be placed completely inside a vacuum vessel to operate under oxygene free conditions. To achieve the required flexibility in creating various patterns the positioning

system as well as the lens position are controlled by a computer. The resolution of the system is 100 nm at a maxium velocity of 20 mm/s.

For controlling focus diameter and profile the laser spot radius is measured using the scanning knife edge method [5]. A razor blade is placed on the target and while scanning the edge through the laser spot the intensity is monitored. The laser spot diameter is determined by differentiating the intensity profile. So far the smallest spot size thus obtained is 8 μm.

The kinematic viscosity of the ORMOCER lacquors has been measured by Ubbelohde method. Kinetic measurements have been performed by IR transmission spectroscopy of ORMOCER coated silicon wafers. Adhesion is tested by grid test (DIN 53151) combined with tape test. Shape and quality of the structures are documented by scanning electron microscopy and profilometric measurements. The thermochemical behaviour is investigated by DTA and TGA coupled with mass spectroscopy (TGA-MS) using a heating rate of 10 K/min. Dielectric strength is measured using an ORMOCER coated metal substrate and a metal brush as counter electrode. Permittivity constant and bulk resistivity are measured using a 10 KHz ac voltage. A humidity test was carried out according to DIN 50017, where ORMOCER coated substrates have been exposed to 100 % rel. humidity at 40 °C for 14 days. Subsequently the adhesion and the quality of the coating have been checked visually by polarized light microscopy.

RESULTS AND DISCUSSION

General material properties

For the applicability of coating systems, their viscosity and their shelf life is important. The kinematic viscosities of all three systems are in the range of $< 10^{-5}$ m^2/s after synthesis and it is possible to obtain coating thicknesses of about 10 μm with very good surface qualities. System I shows a sharp rise in viscosity after three days storage. The viscosity/storage time dependence for system II is given in fig. 2. System III has a shelf life around three months. That means that system II is the most suitable system for carrying out coating experiments from the same batch and therefore, this system was chosen for the majority of the laser writing experimental investigations.

The comparison of the adhesion of the three systems is given in table 1.

Table 1 Adhesion of the ORMOCER systems

Substrate material	system I	system II	system III
aluminumoxide ceramic	0-1	0-1 (200°C)	0-1 (260°C)
glass	0-1 (150°C)	3-4	1-2
silicon wafer	1-2	2-3	1-2

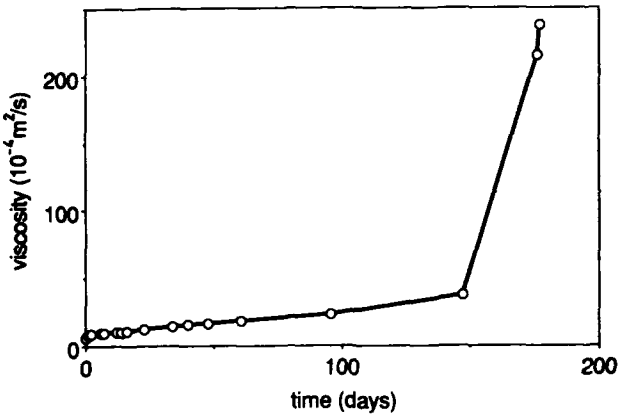


Figure 2: Time dependence of viscosity of system II.

In this test 0 corresponds to very good adhesion while 5 indicates no adhesion at all. Values in brackets indicate the temperature for the beginning of a reduced adhesion. All systems show very good adhesion to aluminumoxide ceramic. Only a poor adhesion to glass and silicon is found for system II. System III exhibits good adhesion on aluminumoxide ceramic even at high temperatures.

TGA-MS analysis shows the beginning of decomposition at T > 200 ° C for system II and T > 270 °C for system III. Thus system III fulfills the temperature requirements imposed by the soldering process.

All systems passed the humidity resistance test according to DIN 50017. Furthermore all systems are resistant to organic solvents like alcohols and acetone for at least a few minutes. Long time immersion of system III in acetone causes only a weight loss less than 0,5%.

The electrical properties have been determined for system II and III. They both show a bulk resistivity larger than $10^{14}\Omega\cdot$cm and low permittivity constants depending on sample preparation and curing history. The permittivity constants are varying between 3 and 6, but at the moment for both systems there cannot be given clear dependencies. The dielectric strengths for systems II an III are determined (100 V/μm for system II and 400 V/μm for system III).

UV-curing of ORMOCERs

The behavior was investigated for system I. It is similar to the polymerization of MMA. In fig. 3 the decay of the C = C bond concentration, measured by IR, of the methacryl groups of system I is shown. As one can see, about 20 % of the C = C bonds remain unreacted, probably due to the increa-

sing stiffness of the network due to polymerization. The effect on the long term stability of the olefinic residual groups has to be investigated.

For laser writing experiments, system II was coated onto glass, silicon and Al_2O_3 substrates. During the curing step at 120 °C, a substantial reduction of SiOH groups occurs, which could be followed by IR spectroscopy. A shrinkage of about 5 % by volume takes place.

The performance of the patterned layer depends on the material properties, the polymerization conditions (mainly

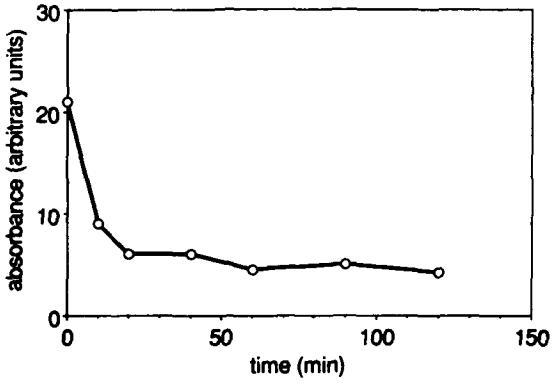


Figure 3: Time dependent absorbance of C_2= C vibration at 1630 cm^{-1} (Hg low pressure lamp, 3 mW/cm^2, 2 mass% IRGACURE® 184)

the laser parameters and the initiator) and the development conditions. Of special interest are parameters like laser beam intensity and initiator concentration. For laser polymerization radiation density, adsorption of the matrix, radiation time, quantum yield, radical yield and lifetime are the important parameters. It is extremely difficult to estimate these parameters in a laser scanning process, and furthermore, there is a high probability of uncontrolled polymerization by scattered light or reflected light from the substrate surface. Therefore it is necessary to control the width of the patterns as a function of processing parameters. In fig. 4, the dependence of width of the structure on laser beam intensity is shown. One can see a broadening of the width of the structure in rising the laser intensity. Increasing the initiator concentration at higher laser power causes more drastic broadening.

Fig. 5 shows the log dependence of the width on the initiator concentration for a laser intensity of 0.7 mW and 2.1 mW. The influence of the laser intensity on structure broadening seems to be lower compared to the initiator influence.

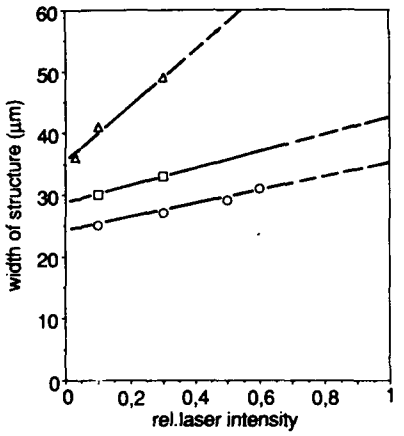


Figure 4: Dependence of width of structure on laser beam intensity
-o 0.05 mass% initiator
-□ 0.1 mass% initiator
-Δ 1.0 mass% initiator

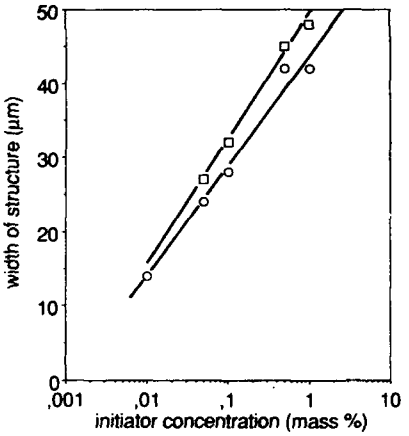


Figure 5: Dependence of width of structure on initiator concentrations
-o at 0.7 mW
-□ at 2.1 mW

An incomplete polymerization process will cause structures containing reaction time dependent concentrations of oligomers soluble in developing processing solvents. Eluation of these oligomers will cause a shrinkage of structure in height and width. This effect is severe at low initiator concentration as shown in fig. 6 (initiator concentration: 0.01 wt.%).

Fig. 7 verifies good structure quality at optimized processing conditions (system II, I_0 = 120 W/cm^2, stepping rate around 20 mm/s and [I] = 0,2 wt.%). The broadening of the structures from a laser spot size of 8 µm in diameter results in a width of 15 µm.



Figure 6: Patterned system II at initiator concentration of 0.01 wt.%.



Figure 7: Patterned system II at more optimized processing

CONCLUSIONS

ORMOCERs are patternable by UV-radiation and UV-sensitive initiators. A process to pattern ORMOCERs via laser direct writing could be established. First experiments show very interesting material data and good quality of structure. Further investigation of the correlations between system composition, exposure to UV-radiation for polymerization and etching process have to be carried out to optimize patternable ORMOCER layers for electronic applications.

ACKNOWLEDGEMENT

We wish to thank the Bundesministerium für Forschung und Technologie of the Federal Republic of Germany for their financial support. We also like to acknowledge the work of the technical staff members.

REFERENCES

[1] M. Terasawa, S. Minami and J. Rubin, Proceedings of ISHM Symposium on Microelectronics, 607 - 615 (1983).
C. A. Neugebauer and R. O. Carlson, IEEE Transactions on Components, Hybrids and Manufacturing Technology, 10 (2), 184 - 189 (1987).
Y. S. Lin, H.S. Cole in: Electronic Packaging Materials, Materials Science IV, eds. R. Jaccodine, K. A. Jackson, E. D. Lillie, R. C. Sundahl, MRS Vol. 154, Pittsburg 11 (1989).
[2] Plastics for Electronics, ed. M. T. Goosey, Elsevier Applied Science Publishers, London (1985).
[3] H. Schmidt and H. Wolter, Fifth International Workshop on Glasses and Ceramics from Gels, Rio de Janeiro (1989).
[4] H. Schmidt, M. Popall and J. Schulz in: Proceedings Second International Symposium on New Glass, The Association of New Glass Industries,Tokyo, 134 - 135 (1989).
D. B. Bailey, R. C. Daly, T. B. Brust and J. M. Pearson in: Polymers for Advanced Technologies, IUPAC International Symposium, ed.: Menachem Lewin, Jerusalem, 18 - 33 (1987).
[5] Y. Suzaki, A. Tachibana, Appl. Opt. 14, 2809 (1971).

RAPID THERMAL PROCESSING OF HIGH TEMPERATURE SUPERCONDUCTING FIBER

J.W. HALLORAN*, M.J. NEAL*, D.S.GINLEY**, E.L. VENTURINI**, J.F. KWAK**, R.J. BAUGHMAN**,M.A. MITCHELL**,B.MOROSIN**,S.N. BASU*** and T.E. MITCHELL***

*CPS Superconductor Corporation, Milford, MA 01757 **Sandia National Laboratories, Albuquerque, NM 87185 ***Los Alamos National Laboratories, Los Alamos, NM 87545

Abstract

We report on the rapid thermal processing (RTP) of $YBa_2Cu_3O_7$ (Y-123) fibers. Unsintered fibers are densified by RTP. We show that fibers which were originally semiconducting and tetragonal before RTP form normal twinned orthorhombic material after processing for 2-4 seconds above 1000°C with a 3 min. cool down in oxygen. They subsequently show T_c to 90K and magnetization indicative of substantially shielding. We present the effects of varying the RTP parameters on the morphology, phase, and superconducting properties of a number of tetragonal and orthorhombic Y-123 fibers.

Introduction

We have previously reported that Rapid Thermal Processing (RTP), using heat treatments as short as one second at temperatures around 1000°C, is an effective processing technique for high temperature superconductors [1,2]. RTP of $YBa_2Cu_3O_7$ (Y-123) fibers has produced material with $T_{c,r=0}$ of up to 90K and self field J_c to 1200 A/cm^2. RTP rapidly densifies unsintered material, creating a microstructure characteristic of the fiber composition, RTP temperature and time. Of particular interest is the fact that RTP annealed Y-123 is superconducting immediately after the RTP anneal, without requiring the 500°C oxygen anneal which is conventional for Y-123. Indeed, conventionally sintered Y-123 fibers, which are semiconducting in their as-sintered state, become superconducting after an RTP treatment, indicating that very rapid oxygenation occurs during RTP.

In this paper we discuss the development of the microstructure when sintering occurs by RTP and characterize the phenomenon of rapid oxygenation by examining superconducting properties of pre-sintered Y-123 after RTP treatment.

EXPERIMENTAL PROCEDURE

Fabrication of Fibers

Fibers were produced using a proprietary process in which Y-123 powders are compounded with a thermoplastic resin so they can be spun into continuous "green" fibers using a conventional textile fiber spinning machine. Most fibers used in this study had a green diameter of 125 microns. The powder was a phase pure Y-123 with 1.6 micron average particle diameter. Copper oxide-rich fibers were prepared with a 5 wt% admixture of CuO. Fibers which were RTP annealed in the unfired state had undergone a binder burnout in which the fibers were heated in air at 20°C/minute to 500°C, held for 10 minutes, then cooled to room temperature at 10°C/minute. This treatment removes most of the organic material, but does not allow any sintering of the Y-123. Pre-sintered fibers received a binder burnout and a 945°C/30 min sintering anneal in a continuous furnace, yielding a sintered density about 90% of theoretical.

Rapid Thermal Processing

Burned-out unsintered fibers and presintered fibers were RTP annealed in an ADDAX-AET model R-1000 rapid thermal annealer. The fibers were supported on a 4" Si wafer coated with 1 micron of silicon nitride. The system was equipped with two low mass thermocouples with one or both in direct contact with the fibers. Before during each run the system (100 cc chamber volume) was purged with high purity oxygen at 3 liters/sec. Typical run conditions (all under 1 atm. oxygen) were: i) a 10 second wait period, ii) 4 second ramp to peak temperature, iii) hold at peak temperature 1-4 seconds, iv) cooling ramp to 600°C

in 96 seconds, v) ramp to room temperature in 180 seconds. The programmed measured temperature agreed within 1%, except when below 300°C where the actual cooling rate lagged the program. The coated Si wafer was an effective substrate in cases reported here, with no apparent reaction with the fibers during the brief RTP anneal. At higher temperature, fibers reacted with the substrate.

Characterization

After RTP, specimens were characterized in the as-fired condition, with no oxygen anneal. Oxygen anneals, though not discussed here, did improve the superconducting properties in some cases. Fibers were examined by X-ray diffractometry had patterns indicative of well formed orthorhombic Y-123, although in some cases the lines were not as sharp as our best material. Precession photographs indicated no preferred orientation. The microstructures were characterized by optical microscopy, scanning electron microscopy, and transmission electron microscopy. Transport properties were determined with standard 4-probe techniques. Magnetization measurements down to 5K were performed in a SQUID magnetometer at 100 Oe, and AC susceptibility at 10 Oe was measured down to 75K.

RESULTS

Microstructure Development

Green Y-123 fibers sintered by RTP develop a sequence of microstructures depending upon time, temperature, and composition. It was generally observed that very rapid grain growth, suggestive of liquid phase formation, occurred in a narrow +/-25°C temperature window. Below the window there is local sintering of grains into dense patches, but no grain growth so the grain size remains 1-2 microns. As the window is approached, rapid grain growth creates distinctive blocky grains as large as 10 microns. At higher temperature, there is a profound change in grain morphology, creating locally oriented patches of elongated grains as large as 50 microns. Figure 1 is a series of SEM micrographs illustrating the evolution of microstructure with temperature and time for Y-123+5% CuO fibers. Figure 1A illustrates the fracture surface after a 1025°C/2 sec RTP anneal at, showing the blocky grain morphology. This microstructure is uniform throughout the cross-section of the fiber. A 4-sec RTP anneal at the same temperature creates the elongated grain structure shown in Figure 1B. Lower magnification views of this specimen, not shown here, show that the elongated grains form in circular patches with the grains radiating from a central nucleus. This suggests that recrystallization occurs by formation and growth of spherulites. The transition from blocky to spherulitic elongated grain morphology occurs more quickly at higher temperature. Figures 1C and 1D show blocky grains after a 1050°C/1 sec RTP anneal and elongated grains after a 1050°C/2 sec treatment. We find that similar microstructures develop in stoichiometric Y-123 fibers at about 25°C higher temperaturesl.

Both the blocky- and elongated-grain microstructures consist primarily of orthorhombic Y-123. This is confirmed by TEM of crushed fragments of fibers. Figure 2 is a bright field TEM of a fragment of a stoichiometric Y-123 fiber after an RTP anneal at 1025°C for 1 sec. The obvious twins indicate that the material is orthorhombic Y-123, a fact confirmed by electron diffraction.

Rapid Oxygenation

Green Y-123 fibers sintered by RTP are superconducting with zero resistance near 90K immediately after the rapid anneal [1]. We have also observed that Y-123 fibers pretreated with a conventional (eg., 925°C/30 min.) air sintering anneal to produce dense, largely tetragonal semiconducting fibers, can be rendered superconducting by RTP, suggesting that ultra-rapid oxygenation occurs in RTP. To investigate the rapid oxygenation effect, we prepared a series of stoichiometric Y-123 fibers by sintering fibers 30 minutes at 945°C in an atmosphere of flowing nitrogen. These N_2-sintered samples were semiconducting before RTP, but became superconducting after RTP treatment at 1000°C.

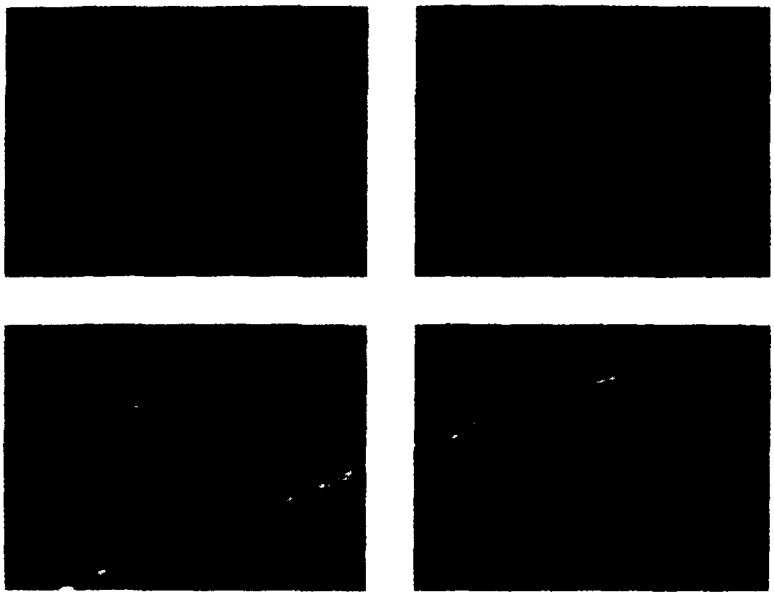


Figure 1 SEM Micrographs showing grain morphology in unsintered Y-123 + 5 wt% CuO wires, after RTP anneals of: A) 1025°C, 2 sec; B) 1025°C, 4 sec; C) 1050°C, 1 sec; D) 1050°C, 2 sec

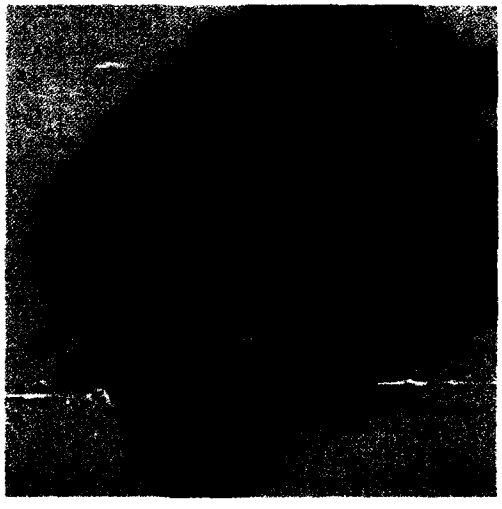


Figure 2 Transmission electron micrograph of twinned orthorhombic Y-123 from a stoichiometric Y-123 wire sintered by RTP at 1025°C

Figure 3, a plot of resistivity vs. temperature, illustrates that the N_2-sintered fibers had a resistivity above 2000 $\mu\Omega$-cm, with no hint of a resistive transition. A 1-second RTP treatment reduces the normal state resistivity below 300 $\mu\Omega$-cm, with a partial transition near 90K. After a 2-second RTP treatment, the specimen displays a broad transition with onset at 87K and zero resistance at 78K. The 4-second RTP treatment sharpens the transition, so that onset occurs at 92K with zero resistance at 87K.

Figure 4 shows the real and imaginary volume AC susceptibility down to 75K for the N_2-presintered fibers after 1000°C/1 sec RTP. No diamagnetism could be detected at 77K with this technique in the as-sintered specimen. The 2-second RTP sample has a small diamagnetic signal, reaching only -0.05 at 77K, while the 4-second sample has a diamagnetic susceptibility as high as -0.40 at 77K.

Table I displays the SQUID data for volume static susceptibility (diamagnetic shielding) in 100 Oe at 5K. Like other ceramic Y-123 samples, these RTP fibers have weak-link behavior, so in a 100 Oe field the grains are decoupled, allowing volume susceptibility to be estimated from the measured mass susceptibility. Completely superconducting grains would have a volume static susceptibility of $-1/4\pi$. We assume that the 5K data can be used as a rough indication of the extent of oxygenation of the Y-123. A more quantitative estimate would require corrections for the magnetic penetration depth and grain morphology. At 5K, the N_2 sintered sample had a measurable diamagnetic susceptibility, demonstrating that small fraction of orthorhombic phase exists after N_2 sintering. The susceptibilities of the 1000°C RTP samples cooled at the standard rate of 4°C/sec were similar when the dwell time was varied from 1 seconds to 4 seconds, indicating that little further oxygenation occurs after the first second. The peak temperature of the RTP treatment seems to be important, since heating to 850°C reduced the 5K susceptibility.

It runs counter to intuition to suggest that 1-4 second dwells at peak temperature causes oxygenation, since the equilibrium oxygen content at 1000°C is known to be in the non-superconducting tetragonal range. A more likely explanation would seem to be that the material oxygenates during the rapid cool. To test this, a series was run with constant dwell time, but cooling rates either twice as fast (8°C/sec) or twice as slow (2°C/sec) than the standard rate. This would have a decisive affect if the reoxygenation occurred during the rapid cool. The data of Table I, however, show that the volume susceptibility is not affected by the cooling rate. Thus we reach the surprising conclusion that RTP increases the oxygen stoichiometry at 1000° to levels high enough to create orthorhombic 90K material. The mechanism for this is unclear.

Transmission electron microscopy of the N_2 sintered Y-123 before RTP shows that most of the grains are tetragonal. A few grains are partially converted to orthorhombic, often with twins growing inward from the grain boundaries. This is consistent with partial reoxygenation by O^2 impurities, and is the origin of the small diamagnetic signal at 5K. Figure 5 is a series of bright field images from ion-milled foils. Figure 5A shows one of the more partially orthorhombic grains in the as-sintered material. The twins are poorly developed and a large number of (as yet uncharacterized) lattice defects are visible. The twins boundaries are not crisply defined, an indication of oxygen depletion. The 1000°C-1 sec. RTP reduces the population of tetragonal grains and improves the quality of the orthorhombic grains. Figure 5B shows "cleaner" twin boundaries and fewer lattice defects. After the 1000°C-2 sec. RTP, most of the microstructure is similar to Figure 5C, with minimal defects and the sharp twin boundaries which are a sign of high oxygen content.

Summary

Rapid thermal processing, involving 2-4 sec. around 1000°C with a 3 min. cool down in oxygen, forms the dense sintered fibers of orthorhombic Y-123. Green fibers are rapidly densified, displaying microstructures characterized by large grains with distinctive blocky or elongated morphology. Presintered Y-123 fibers do not undergo drastic microstructural change after RTP, but are

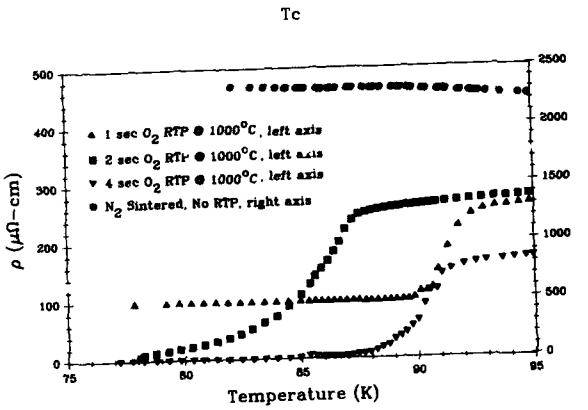


Figure 3 Resistivity vs. temperature for stoichiometric Y-123 fibers pre-sintered in nitrogen and RTP annealed in oxygen at 1000°C

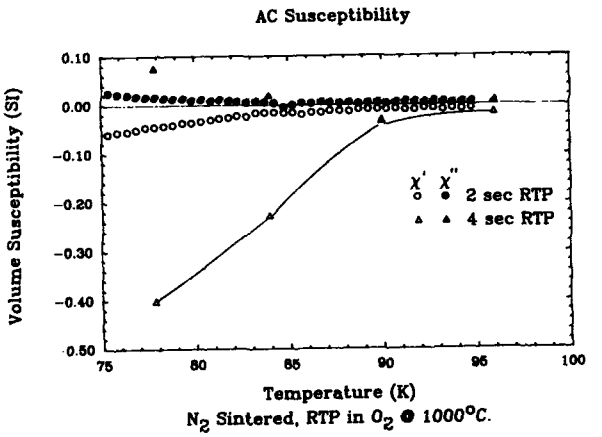


Figure 4 Real and imaginary AC susceptibility for stoichiometric Y-123 fibers pre-sintered in nitrogen and RTP annealed in oxygen at 1000°C

TABLE I

DIAMAGNETIC SHIELDING DATA AT 5K FOR NITROGEN-SINTERED Y-123

RTP PROCESS CONDITIONS	VOLUME SUSCEPTIBILITY AT 100 Oe
AS- SINTERED, NO RTP	-0.10/4π
1000°C - 2 sec hold - 2°C/sec cool	-0.21/4π
1000°C - 2 sec hold - 4°C/sec cool	-0.23/4π
1000°C - 2 sec hold - 8°C/sec cool	-0.24/4π
1000°C - 1 sec hold - 4°C/sec cool	-0.25/4π
1000°C - 4 sec hold - 4°C/sec cool	-0.26/4π
850°C - 2 sec hold - 4°C/sec cool	-0.15/4π

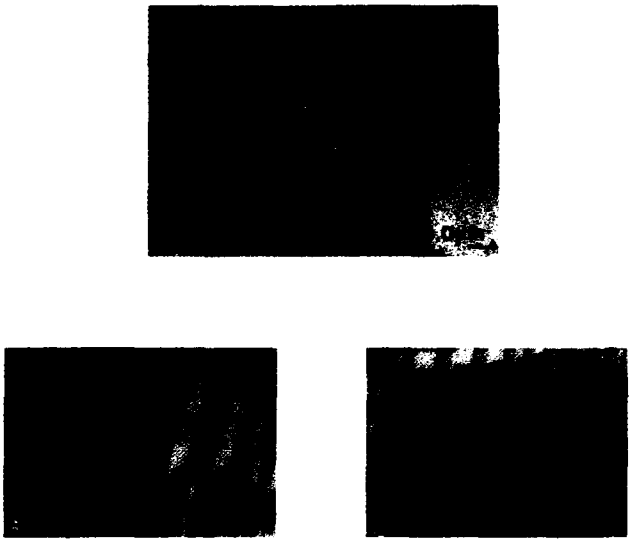


Figure 5 Bright field transmission electron micrographs of the nitrogen sintered series: A) as-sintered state, no RTP; (B) 1000°C/1 sec RTP; (C) 1000°C/2 sec RTP

rapidly oxygenated by the treatment. Presintered fibers,semiconducting and tetragonal before RTP, form twinned orthorhombic material after RTP with T_c to 90K and magnetization indicative of substantially shielding.

Experiments with RTP of tetragonal Y-123 fibers made by pre-sintering in N_2 show that re-oxygenation by RTP in oxygen occurs during the 1-4 second isothermal hold at 1000°C, rather than during the 3-minute cooling ramp. Twinned orthorhombic Y-123 grows predominantly from grain boundaries, suggesting grain boundary diffusion of oxygen during the RTP anneal.

Acknowledgements

The work at CPS Superconductor was supported by DARPA contract N00014-88-C-0512 and NASA-Lewis contract NAS-3-25876. The Los Alamos work was supported by the High Temperature Superconductor Pilot Center Cooperative Agreement CRDA-89-03. The work at Sandia was supported, in part, by the DOE Office of Basic Energy Sciences under contract No.DE-AC04-76DP00789.

References

1. D.S. Ginley, E.L. Venturini, J.F. Kwak, M. Mitchell, R. J. Baughman, J.W. Halloran, and M.J. Neal, Physics Review Letters (in press 1990)

2. D.S. Ginley, E.L. Venturini, J.F. Kwak, R. J. Baughman, R.J. Bourcier, M.A. Mitchell, B. Morosin, J.W. Halloran, M.J. Neal, and D.W. Capone, in High Temperature Superconductors: Fundamentals, Properties, and Novel Processing, ed. J. Narayan et al. Materials Research Society, Symposia Proceedings Volume 196 , (in press 1990)

PREPARATION OF POROUS OXIDE BEADS USING POLYMERIC BEADS TO CONTROL BEAD SIZE AND SHAPE

Anne B. Hardy, Wendell E. Rhine, and H. Kent Bowen
Ceramics Processing Research Laboratory, Massachusetts Institute of Technology, Cambridge, MA 02139

ABSTRACT

A method was developed for preparing silica gels by silicon alkoxide hydrolysis using water-swellable polymers to control the shape. A variety of polymer beads with different water absorbencies and different bead sizes were used. Silica beads in a wide range of sizes were prepared from polymer beads. The final bead size was dependent on the size and water absorbency of the beads, on the extent of reaction, and on the final density. It was shown that porosity could be formed in two regions. The silica beads contained pores of 3-4 nm that were attributed to the intrinsic gel structure. In addition, when large amounts of polymer were removed, additional porosity on the scale of 20-50 nm was formed. It was also shown that surface areas varied dramatically with calcining. For beads containing only small pores, surface areas varied from 400 m^2/g to less than 0.2 m^2/g as the calcining temperature was increased from 600°C to 1000°C. Beads containing porosity formed by removal of the polymer remained porous even after calcining at 1000°C.

INTRODUCTION

In ceramics applications, control of morphology is often of critical importance. Because ceramics are solids with high melting points, many of the processing approaches used to control morphology in metals or polymers are not feasible. In this paper a method is presented for controlling the shape and porosity of silica gels using water absorbable polymers as a template for the final gel shape. Silicon alkoxide (TEOS) was reacted with water absorbed in the beads to form a silica gel within the polymer. Previous research has shown that acidic water droplets in a water-in-oil emulsion react with TEOS and that the silica gelation appears to take place in the water phase [1]. This method incorporates the processing flexibility of polymers into the preparation of ceramics. Water absorbable polymers are available in a variety of shapes. Polymer beads were used because the regular shape simplified comparison between the original polymer and the silica beads and also because silica gels in spherical bead form are desirable for some applications.

Polymer fibers and other absorbent fibers have been used to prepare oxide fibers. In a typical formulation [2], cellulosic fibers such as Rayon imbibe an aqueous salt solution. The fibers are then heated to remove the polymer and convert the salt to the oxide. The oxide retains the shape of the original fiber. In addition to cellulose derivative fibers, a variety of novel fibers have been used including carbon fibers [3, 4] and intercalated graphite fibers [5]. Typically in these techniques absorption of the oxide precursor solution is relatively low, and when the precursor is converted to the oxide and the polymer is removed, the overall oxide yield is low. By contrast, in the technique presented here, by combining highly water absorbent polymers with silicon alkoxide hydrolysis, it was possible to obtain high oxide-to-polymer yields.

Mat. Res. Soc. Symp. Proc. Vol. 180. ©1990 Materials Research Society

EXPERIMENTAL PROCEDURE

Several water absorbing polymeric beads were used including Dowex® MSC-1 (Dow Chemical Co, Midland, MI), a series of crosslinked dextrans (Sephadex® G-25 and LH-60), and Sephasorb® (Pharmacia Biotechnology Products, Piscataway, NJ) and a superabsorbing polymer, Quat™ (supplied by Bernard Obenski and Co., Berwyn, PA). The Sephadex and Quat were preswelled in deionized water at various pHs. Hydrochloric acid was used as an acid catalyst (pH = 2-4), and either NaOH or NH_4OH was used as a base catalyst (pH = 10-12). The crosslinked dextrans were swelled for 1-3 h; the Quat was swelled for 5 min. Excess water was removed by filtering and then rinsing the beads with isoamyl alcohol. The Dowex beads contained 50 wt% water as received and were used without further swelling.

The water-swelled beads were transferred to a TEOS in hexane solution (TEOS:hexane ratio was either 1:1 or 1:2 by volume). Dowex beads were reacted for 5 h; Quat beads were reacted for 6-20 h. Reaction times for the crosslinked dextrans were dependent on the catalyst concentration and ranged from 12 h to 7 days. The reacted beads were recovered by filtering and rinsing with isopropanol to remove unreacted TEOS. They were dried at room temperature overnight before being heated to remove the polymer. A standard heating schedule was as follows: samples were heated at 2°C/min to 400°C with a 2 h isothermal hold

Table I. Some Properties of the Polymer Beads.

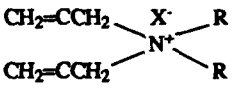
Polymer	Commercial Use	Physical Structure	Characteristics
Dowex MSC-1	ion exchange resin	sulfonized styrene divinylbenzene copolymer	rigid beads 300-850 μm
Sephadex Sephasorb	gel-filtration medium	crosslinked dextran	range of crosslinking particle size ranges: 10-23 μm 20-50 μm 40-120 μm
Quat	superabsorbent	quaternary ammonium compound monomer: 	lightly crosslinked 5-100 μm (dry)

Table II. Amount of Water Absorbed.

Polymer	Absorbency (g water/g dry polymer)
Dowex MSC-1	1.0
Sephadex LH-60	4-5
Sephadex G-25	1-2
Sephasorb	0.4
Quat	50-70

and were then heated at 5°C/min to the final temperature followed by a 2 h isothermal hold. Final temperatures ranged from 600°C to 1000°C. Bead morphology was observed by both optical microscopy and scanning electron microscopy (SEM) (Model S-530, Hitachi Ltd, Tokyo, Japan). Shrinkage of individual Quat beads after reaction was followed by optical microscopy using a hot stage attached to an optical microscope. Pore size distributions and densities were measured by mercury porosimetry (Autopore 9220, Micromeretics, Norcross, GA). Pore sizes were also measured by nitrogen adsorption (Quantasorb, Quantachrome, Syosset, NY) using 15 different nitrogen partial pressures. Surface areas were measured by the single point BET method.

RESULTS AND DISCUSSION

Preparation

Several different types of water-absorbing beads were used to provide a range of polymer types, bead sizes, and water absorbencies. Table I summarizes some of the physical properties of the polymers which were used. Measured absorbencies are reported in Table II and were found to vary by almost two orders of magnitude from the Sephasorb beads (0.4 g

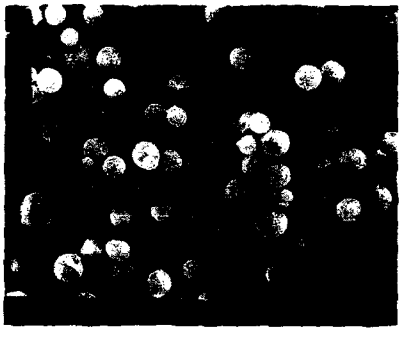


Fig. 1. Silica beads formed from Sephasorb (original bead diameter = 10-23

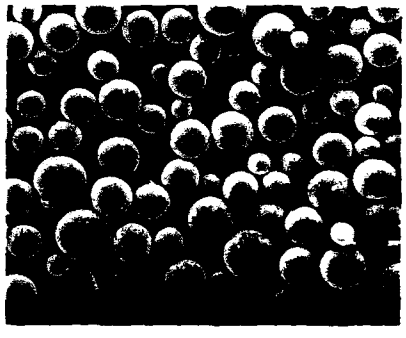


Fig. 2. Silica beads formed from Sephadex G-25 (original bead size = 20-50 μm).



Fig. 3. Silica beads formed from super-absorbing Quat.

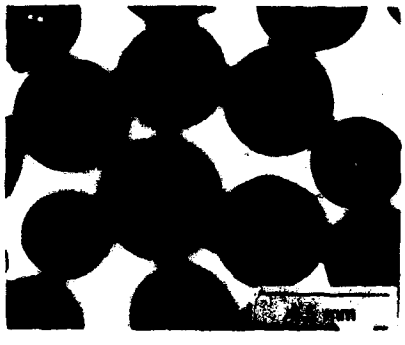


Fig. 4. Silica beads formed from Dowex MSC-1.

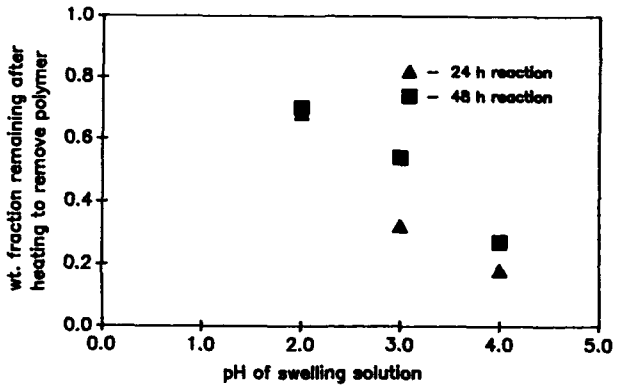


Fig. 5. Silica yield after polymer removal as a function of pH and reaction time.

water/g dry polymer) to the superabsorbing Quat beads which absorbed up to 70 g water/g dry polymer.

Figures 1-4 show some of the silica beads that were formed and illustrate that it was possible to produce silica beads in a wide range of sizes by using polymer beads with different sizes. The alkoxide reaction was catalyzed by the polymer for the Dowex and Quat polymers which have acidic groups in the polymer structure. For the crosslinked dextrans, both acid- and base-catalyzed hydrolysis was successfully used. Silica yields were very dependent on the pH of the absorbed water as shown in Figure 5. Weight losses (Table III) ranged from ~20 wt% for the Quat-derived silica beads to 70 wt% for the Dowex beads. Weight losses were attributed to the removal of polymer and unreacted water and the further conversion of unreacted hydroxyl groups and alkoxy groups to the oxide. After heating, the Dowex and crosslinked dextran products were white; the Quat products were either white or translucent. Silica to polymer ratios ranged from ~15-20 g oxide/g polymer for the Quat-derived silica to ~0.1 g oxide/g polymer for the Sephasorb-derived silica beads. Reaction times were limited because long reaction times caused beads to form hard agglomerates.

Quat-derived silica particles rapidly shrank 10-15% (linear shrinkage) while drying; the beads then shrank another 10% as they were heated. For the crosslinked dextran derived beads, the final bead size was compared to the initial (dry polymer) bead size using SEM micrographs. The final bead size was dependent on the initial absorbency and on the extent of reaction. Ratios of the final silica bead size to the initial polymer size ranged from ~0.5 (Sephasorb) to 1.5 (Sephadex LH-60).

Table III. Weight Losses and Oxide/Polymer Ratios for Different Silica Beads.

Polymer	Weight Loss (%)	Silica/Original Polymer (g/g)
Dowex MSC-1	70	0.2
Sephasorb (pH=2, 24 h)	90	0.1
Sephadex LH-60 (pH=4, 36 h)	--	8
Quat	20-25	15-20

Table IV. Surface Areas as a Function of Calcination Temperature.

Temperature (°C)	Dowex MSC-1 Surface Area (m^2/g)	Quat Surface Area (m^2/g)
uncalcined	0.6	400-450
600	250-300	410-450
800	180-230	160-250
1000	100-130	0.14-0.15

Presumably the reaction either began at the TEOS/water interface or some TEOS was transferred into the water phase (TEOS has a limited solubility in water [6]) where the reaction then began. Intermediate hydrolysis products were water soluble and further reacted within the water phase to form the hydrous oxide. As the reaction progressed, ethanol was produced which is preferentially soluble in the water phase [7]; the alcohol would increase the TEOS solubility in the water phase.

Bead Characteristics

Surface properties and pore sizes are important properties for many applications of silica gels (e.g, see [8, 9]). The surface area and pore sizes of silica beads prepared from Dowex and from Quat were measured to investigate how the pore structure was affected by removing different amounts of polymer. Dowex beads contained relatively little water (1 g/g dry polymer) and this was reflected in the product; the oxide-to-polymer ratio was low, indicating large amounts of polymer were removed on heating. Mercury porosimetry measurements showed that before removing the polymer, the bead had essentially no measurable porosity, which was reflected in the low surface areas for unheated beads (see Table IV). After removing the polymer, pores in the range of 20 to 50 nm formed and the surface areas increased substantially. Upon further heating to 1000°C, the surface area decreased but the pore size range remained about the same (see Fig. 6). The bead density after heating to 1000°C varied but was typically 0.8-0.9 g/cm^3. SEM micrographs (Fig. 7) show that the porosity appears to take the form of interstices between discrete particles (corpuscular type porosity [8]) rather than interconnected channels.

By contrast, beads formed from the Quat polymer and the Sephadex LH-60 polymers had very high surface areas before polymer removal (Table IV). After heating to 1000°C, the surface area corresponded to essentially nonporous, smooth-surface beads which indicated

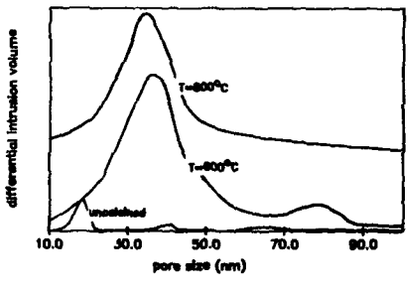


Fig. 6. Pore size for Dowex-derived silica beads as a function of calcination.



Fig. 7. Interior structure of broken silica bead (Dowex-derived).

most of the surface accessible porosity was removed. Mercury porosimetry measurements showed almost no measurable porosity (lower measurement limit was 5 nm). Nitrogen adsorption measurements showed sharp pore size distributions around 4-5 nm which are consistent with reported pore diameters for alkoxide-derived silica gels [10].

It was assumed in the Dowex-derived silica beads that the porosity measured by mercury porosimetry was dominated by pores created by the removal of polymer. However, for the Quat-derived silica it appeared that removal of the polymer had little effect on the porosity and that the porosity was intrinsic to the silica gel. The measured pore size and surface area for the Quat and Sephadex beads were within the range of porosity reported for other alkoxide-derived silica gels.

CONCLUSIONS

It was shown that water absorbed within polymer structures could be reacted with TEOS to form silica gels and that the gel retained the shape of the polymer. Silica beads were formed in a range of sizes from 5-10 μm up to ~0.5 mm depending on the size of the initial polymer bead. The oxide to polymer ratio was dependent on the absorbency of the polymer and the extent of reaction and ranged from ~0.1 g silica/g polymer to ~20 g silica/g polymer. It was possible to form pores in two size ranges. When large amounts of polymer were removed (e.g., Dowex MSC-1), 20-50 nm pores were formed, apparently due to the removal of polymer. These beads retained significant porosity on heating to 1000°C. When little polymer was removed (e.g., Quat), the pores were ~3-4 nm and were attributed to the intrinsic gel structure. Surface porosity could be eliminated by heating to 1000°C.

ACKNOWLEDGMENTS

The authors gratefully acknowledge the support of the Air Force Office of Scientific Research, contract number F49620-89C-0102DEF.

REFERENCES

1. A.B. Hardy, PhD Thesis, MIT, 1988.
2. B.H. Hamling, U.S. Patent No. 3,385,915 (1968).
3. R.J. Card, Adv. Cer. Mater. 3 (1), 29 (1986).
4. R.J. Card and M.P. O'Toole, J. Am. Ceram. Soc. 73 (3), 665 (1990).
5. B.W. McQuillan and G. Reynolds, in Ultrastructure Processing of Advanced Ceramics, edited by J.D. Mackenzie and D.R. Ulrich (J. Wiley and Sons, New York, 1988), pp. 739-745.
6. H. Pentinghaus, J. Non-Cryst. Sol. 63, 193 (1984).
7. A. Seidell, Solubility of Organic Compounds, Vol. 2, 3rd ed. (D. Van Nostrand Co. Inc., New York, 1941) p. 148.
8. K.K. Unger, Porous Silica, Its Properties and Use as Support in Column Liquid Chromatography (Elsevier Science Publishing Co. Inc., New York, 1979), p. 41.
9. R.K. Iler, The Chemistry of Silica, Solubility, Polymerization, Colloid and Surface Properties, and Biochemistry (J. Wiley and Sons, New York, 1979), pp. 578-599.
10. J.D. Mackenzie, in Ultrastructure Processing of Ceramics, Glasses, and Composites, edited by L.L. Hench and D.R. Ulrich (J. Wiley and Sons, New York, 1984).

PART XIII

Novel Processing II

NEW CHEMICAL ROUTES TO METAL NITRIDES

Wayne L. Gladfelter*, Jen-Wei Hwang*, John F. Evans*, Scott A. Hanson*, Klavs F. Jensen#, and Kwok-Lun Ho#
Department of *Chemistry, University of Minnesota, Minneapolis, Minnesota 55455 and Department of *Chemical Engineering, Massachusetts Institute of Technology 66-250, Cambridge, MA 02139

ABSTRACT

After a brief introduction on how the differing properties of H_2O and NH_3 may effect the strategies used to synthesize metal nitrides, an overview of our use of azides to produce aluminum nitride thin films will be presented. The effect of changing the nitrogen source to one which contains at least one N - C bond is to increase dramatically the carbon content of the films. Replacing the alkyl groups attached to the aluminum with hydride ligands removes the final carbon source and forms what appears to be a promising new class of precursors. This is demonstrated by the study of the reaction of Me_3NGaH_3 with NH_3 to produce the novel trimer, $[H_2GaNH_2]_3$. This fully characterized molecule converts at 150°C into gallium nitride. Surprisingly, it yields GaN having the sphalerite structure instead of the known wurtzite phase. A discussion of the reasons for this unusual route to a new crystalline phase of GaN is included.

INTRODUCTION

Just as water is the most common oxygen source in the preparation of oxide ceramics from molecular precursors, ammonia is the most frequently used nitrogen source for metal nitrides[1]. We would like to focus momentarily on some of the differences between these two compounds that have made the development of a nitrogen-based sol-gel process so difficult. The first difference is the much higher acidity of H_2O compared to NH_3. For removal of the first proton their respective pK_a values are 15.7 and 35. The high value for the pK_a of NH_3 places restrictions on the type of metal precursor that can be used in the reaction. Equilibrium constants for reaction of metal alkoxides with ammonia will be far less favorable. Some reactions will undoubtedly occur, but the general use of this process for complete ammonolysis is unlikely. More basic ligands such as dialkylamides (R_2N^-) should serve this purpose and examples of using these complexes for the preparation of nitrides from ammonia as well as oxides from water are known[2]. Reactive metal alkyls such as $AlMe_3$ have also

Mat. Res. Soc. Symp. Proc. Vol. 180. ©1990 Materials Research Society

been used to deprotonate NH_3, and in some cases the rates of the first and second eliminations of alkane differ enough to allow isolation of the product. Interrante and coworkers have found that the cyclic trimer, $[R_2AlNH_2]_3$ where R = Me, Et, *i*-Bu, and *t*-Bu, is formed at low temperatures from the reaction of AlR_3 and NH_3 and can be pyrolyzed to give AlN at relatively mild temperatures[3,4]. Less-reactive alkyls, such as those bound to silicon, are more reluctant to undergo this type of reaction; a feature that has allowed the synthesis of a variety of polysilazanes which are valuable as precursors to silicon nitride[5,6].

One of the most valuable features of the sol-gel process is that intermediate stages of polymerization lead to more or less controllable viscosities thereby aiding the processing for a wider variety of applications. Whereas oxygen is reasonably stable when bridging a minimun of two metals, nitrogen will require at least three in most systems. This preference will lead to much more extensive crosslinking in the polymeric network and in most cases formation of powders at an early stage in the reaction. Although this has been observed in many systems, there are exceptions that occur because of the kinetically slow second deprotonation. The preparation of polymers having formulas such as $(EtAlNH)_{0.76}(Et_2AlNH_2)_{0.24}(AlEt_3)_{0.018}$ by Tebbe and coworkers[7] is one such case. These polymers are stable and fusible at approx. 100°C allowing them to be extruded into fibers prior to pyrolysis to give AlN.

Most of our research has focused on the formation of metal nitride thin films by chemical vapor deposition[8-10]. In this paper we will first review our results using azides and various organonitrogen species as sources for nitrogen. This will be followed by a presentation of results showing the value of metal hydrides as sources for aluminum and gallium.

ALTERNATIVE SOURCES OF NITROGEN FOR ALUMINUM NITRIDE

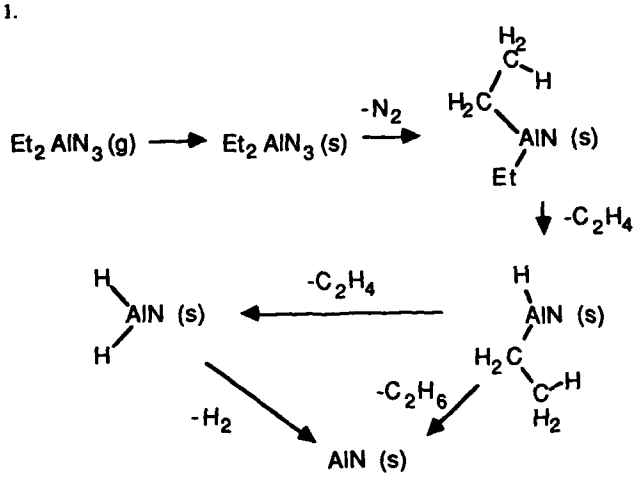
Azides. We have previously reported that azide (N_3^-) is effective at donating one nitrogen to a growing film[8-10]. Our most extensive work has involved the preparation of aluminum nitride films in the temperature range of 400 - 800°C. Studies of the overall growth kinetics of the compound, $[Et_2AlN_3]_3$, fit the following kinetic scheme[10].

$$[Et_2AlN_3]_3\ (gas) \underset{k_d}{\overset{k_a}{\rightleftharpoons}} [Et_2AlN_3]_3\ (surface) \xrightarrow{k_s} AlN + N_2 + H_2 + C_2H_4$$

The overall activation energy for the reaction that occurs on the surface (k_s) is 26.1 kcal/mol. Although k_s is a rate constant that includes several elementary

reactions, it agreed remarkably well with the results of the microscopic rate constants obtained from surface studies using temperature programmed reaction spectroscopy and related methods. Scheme 1 shows one of the possible scenarios for the mechanism of the reaction.

Scheme 1.



It is noteworthy that a paper describing the use of $[Et_2GaN_3]_3$ to prepare thin films of GaN has recently appeared[11].

Nitrogen Sources Containing N-C Bonds. Both azide (N_3) and amide (NH_2) are comparably effective as sources for nitrogen in the deposition of AlN. It was of interest to explore how much the variation in structure of the N-source would influence the AlN deposition, and we were particularly interested in determining the effect of incorporating a N-C bond into the precursor. The precursors studied included $[Me_2Al(NMe_2)]_2$[12], $[Me_2Al(Azir)]_3$ (Azir = aziridine)[13], Et_3AlNH_2(*t*-Bu)[14], and $\{Et_2Al[NH(t\text{-}Bu)]\}_2$[14]. All of these structures contain direct Al-N bonds, and with the exception of Et_3AlNH_2(t-Bu), all exist as cyclic four- or six-membered rings. The structures differ from the azide and amide precursors primarily due to the presence of the N-C bond. The substantial impact made by the presence of the N-C bond is highlighted in Table 1. All of these films contained large concentrations of carbon, and one contained only small amounts of nitrogen. In the case where the nitrogen source is the *t*-butylamine-triethylaluminum donor acceptor complex, the small concentrations

Table 1. Atomic Compositions of Thin Films Using XPS after Ar^+ sputtering.

Precursor[a]	Reactor	Temp. (°C)	%Al	%N	%C	%O
$[Et_2AlN_3]_3$	quartz	500	43	45	10	2
$[Et_2AlN_3]_3$	metal	480	44	45	10	1
$[Me_2AlN_3]_3$	quartz	500	43	44	11	2
$[Et_2Al(NH_2)]_3$	quartz	550	44	41	7	8
$[Me_2Al(NMe_2)]_2$	quartz	700	42	19	38	1
$[Me_2Al(Azir)]_3$	quartz	500	34	18	33	15
$[Et_2Al(NH\text{-}t\text{-}Bu)]_2$	quartz	700	44	36	15	4
$Et_3AlNH_2(t\text{-}Bu)$	quartz	500	30	2	5	63

a) azir = NCH_2CH_2; Me = CH_3; Et = CH_2CH_3; *t*-Bu = $C(CH_3)_3$

of N indicate that a facile Al-N cleavage is operative, e. g. simple dissociation of the donor-acceptor bond. The high oxygen content is due to oxidation of the poor quality aluminum films that result from this precursor. It should be noted that $[Me_2Al(NMe_2)]_2$, which also gave films with low N values, was the most stable of all the precursors examined. Even at oven temperatures of 450°C, this precursor would pass through the hot tube unchanged. The lower N content of the film may be the result of an Al-N bond cleavage process involving β-hydrogen elimination of the NMe_2 ligand. The intermediate case of $[Et_2Al(NH\text{-}t\text{-}Bu)]_2$ is interesting because it contains no β-hydrogens on the amido ligand. It is also related to $[Me_2Ga(As\text{-}t\text{-}Bu_2)]_2$ which was recently reported to give GaAs films[15]. The results show that most of the nitrogen is incorporated into the film; unfortunately, the carbon content is also high. The compound containing the 3-member, highly strained aziridine ring, $[Me_2Al(Azir)]_3$, gave results similar to those found for $[Me_2Al(NMe_2)]_2$.

A new development in this area involves the use of the trimethylsilyl (TMS) group bound to nitrogen. Because of the strong affinity of Si for halogens, reaction schemes using $[ClBNH]_3$ and $(TMS)_2NH$ have been successful at producing boron nitride[16].

METAL HYDRIDES AS SOURCES OF ALUMINUM AND GALLIUM

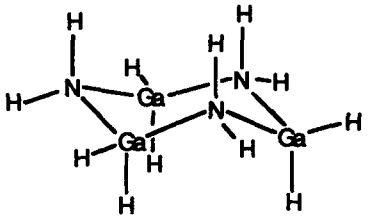
Aluminum Nitride. Despite the success of these organometallic precursors to form the nitrides at low temperatures, top quality films are difficult to grow because of the carbon left over from degradation of the organic ligand bound to the metal. One solution to the problem involves removing the carbon-containing substituent. Among the most promising replacements for the alkyl

group is the hydride ligand. Early studies of many of the main group metal hydrides was conducted by Wiberg[17], and he reported that the stepwise reaction of alane (AlH_3) with ammonia ultimately leads to AlN. Unfortunately this work contained no characterization of the final powders. Some more recent work has appeared making use of various donor-acceptor complexes of alane to form AlN by reaction with NH_3. Although details of the actual experiments differ Maya[18] and Ochi and coworkers[19] independently have converted $(Et_2O)AlH_3$ into powdered AlN. We have found that simply passing a stream of NH_3 over solid Me_3NAlH_3 at low temperature followed by pyrolysis at 400°C gives white to slightly gray powders of AlN. It is noteworthy that in the absence of NH_3 trimethlyamine alane is an excellent source of growing thin films of high quality aluminum at temperatures as low as 80°C[20].

Cubic Gallium Nitride. Like Me_3NAlH_3, Me_3NGaH_3 is a volatile white crystalline solid. We were interested to see if we could extend the use of metal hydrides to gallium and form GaN by the reaction between Me_3NGaH_3 and NH_3. As a III-V semiconductor having a band gap of 3.5 eV,[21] there is interest in using gallium nitride in various optoelectronic devices. The known syntheses of bulk powders of GaN involve reactions of various gallium sources (Ga_2O_3[22] Ga[23], or $[NH_4]_3[GaF_6]$[24]) with ammonia conducted at high temperatures (>900°C) and result exclusively in gallium nitride having a wurtzite (hexagonal) structure. Reports of epitaxial thin films of cubic gallium nitride grown by molecular beam epitaxy or organometallic vapor phase epitaxy on substrates such as GaAs[25], MgO[26], or cubic SiC[27] have appeared. We describe the synthesis and structure of the novel trimer, *cyclo*-trigallazane, and its reaction to give the first bulk samples of cubic GaN.

The only previous report of the reaction between $(Me_3N)GaH_3$ and NH_3 suggested the uncharacterized product was polymeric[28]. In our hands $[H_2GaNH_2]_3$ was prepared in 75% yield simply by passing gaseous NH_3 over solid $(Me_3N)GaH_3$ [29] at room temperature for 1 h. The less-than-quantitative yield results from losses of the volatile gallane starting material, and higher yields can be achieved by condensing liquid ammonia directly on $(Me_3N)GaH_3$. Even without further purification, elemental analysis of the white powder indicated the formula H_2GaNH_2, and the lack of measurable carbon confirmed the quantitative displacement of trimethylamine.[30] The highest mass peak observed using EI mass spectrometry (20 eV ionizing voltage) was 262 amu corresponding to the parent ion of the trimer minus one hydrogen. The extremely limited solubility of *cyclo*-trigallazane in all common organic solvents precluded us from obtaining a ^1H NMR spectrum. The infrared spectrum of the powder dispersed in *n*-undecane reveals ν_{N-H} vibrations at 3297 and 3247 cm^{-1}

and ν_{Ga-H} vibrations at 1890, 1865, and 1832 cm^{-1}. Careful sublimation yielded clear, colorless crystals which were shown by single crystal x-ray crystallography to consist of a six-membered rings in a chair conformation, 1, similar to that observed in $[H_2BNH_2]_3$.[31]



1

Thermogravimetric analysis (Figure 1) of *cyclo*-trigallazane shows an abrupt weight loss (typically 4.5 -5.5%) at 150°C. A smaller, more gradual weight loss occurs between 210 and 500°C. Mass spectral studies showed that the first weight loss was due to H_2 accompanied by a small amount of sublimation.

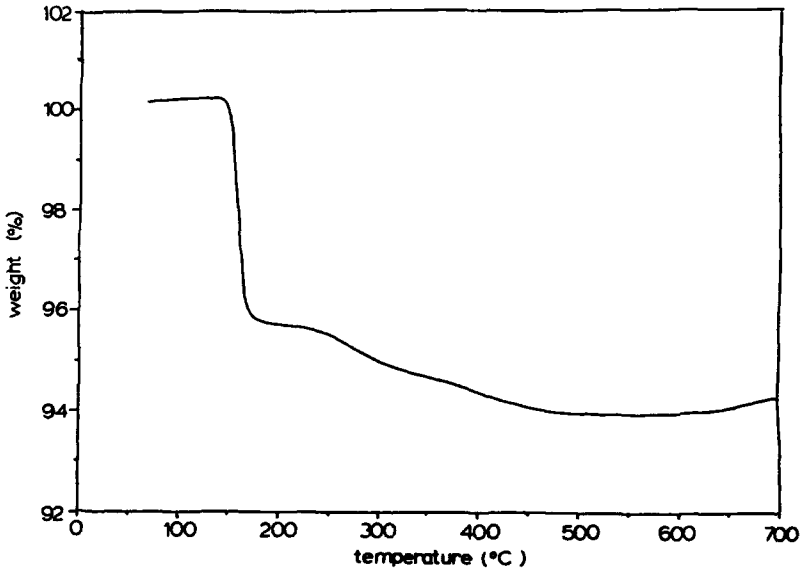


Figure 1. Thermogravimetric analysis of *cyclo*-trigallazane (12.41 mg) heated at 20°C/min in a ceramic pan under a flowing argon atmosphere.

The losses at higher temperatures involved H_2 only. Such a precipitous loss of hydrogen from *cyclo*-trigallazane could be facilitated by its crystal structure in

which the nearest intermolecular contact to each hydride ligand is a nitrogen-bound proton.

During the overall conversion, the white starting material is transformed to a dark gray solid. Figure 2 illustrates the x-ray powder diffraction patterns obtained after treating three separate samples of *cyclo*-trigallazane for 4 h under argon at the specified temperatures. Surprisingly, the onset of crystallinity is evident even in the sample treated at 180°C. Figure 2 also includes a graphical representation of the known diffraction pattern for hexagonal GaN. The notable absence in our patterns of several reflections of *h*-GaN [32] coupled with the similarity to the patterns of GaP and other cubic (sphalerite) structures[33] suggested that we had formed cubic GaN. Our calculated powder diffraction pattern for cubic GaN (a = 4.50 (2) Å) agrees well with the experimental results. The lattice constants of the various thin films of cubic GaN range from 4.52 to 4.55 Å. [25-27]

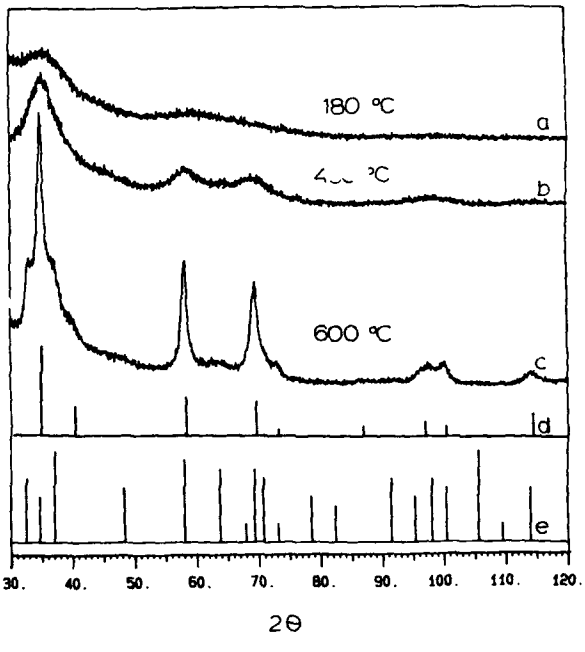


Figure 2. X-ray powder diffraction results. Patterns a, b, and c were obtained on powders heated for 4 h at the specified temperature under argon. In c, the shoulders on either side of the (111) reflection indicate the presence of a small amount of *h*-GaN. Patterns d and e are the calculated pattern for *c*-GaN and the experimental diffraction pattern for *h*-GaN, respectively.

Figure 3 shows a series of powder diffraction scans of *c*-GaN heated to 900°C for as long as 120 hours. Although quite slow the cubic form is converting to hexagonal GaN. Even after 120 hours, however, only 50% conversion has occurred.

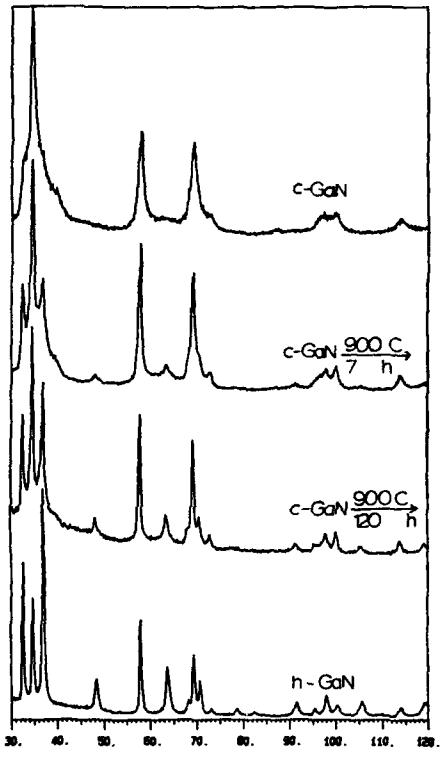


Figure 3. X-ray powder diffraction patterns showing the gradual conversion of *c*-GaN into *h*-GaN.

Why does the cubic phase of GaN form using gallazane? On the one hand this GaN synthesis is conducted at temperatures well below those typically used, perhaps in a temperature range where the cubic phase is thermodynamically favored. Alternatively the synthesis may well lead to a kinetically-trapped, metastable phase. To answer this question we attempted to repeat one of the early GaN preparations at 600°C. Gallium oxide (Ga_2O_3) was loaded onto a boat which was placed in a furnace operated at 600°C. Ammonia was passed over the oxide at atmospheric pressure for 22 hours (the original report used 900°C for 1

hour[22]). Only a very small amount of reaction took place, but the x-ray diffraction study (Figure 4) indicates that hexagonal GaN is formed. This strongly suggests that the pyrolysis of $[H_2GaNH_2]_3$ produces a metastable cubic GaN phase.

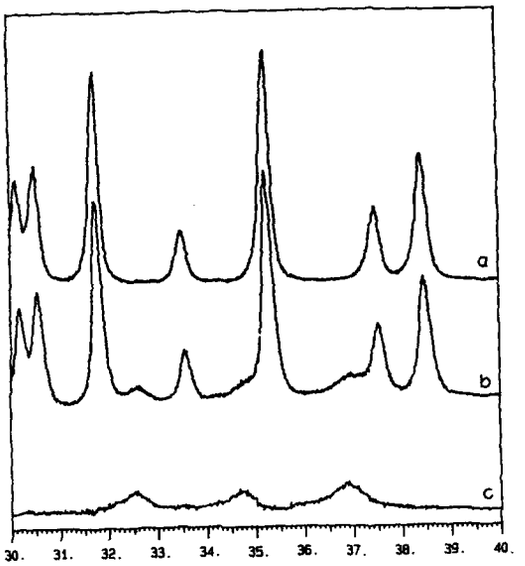


Figure 4. X-ray powder diffraction results showing the formation of *h*-GaN from the reaction of Ga_2O_3 with NH_3: a) pure Ga_2O_3, b) after reaction 22 hours at 600°C under NH_3 (1 atm), and c) pattern b - pattern a. The peaks at 32.6, 34.7 and 36.9° (2Θ) correspond in position and relative intensity to the (100), (111), (102) reflections of *h*-GaN.

Acknowledgement. This work was supported by a grant from the National Science Foundation (CHE-8711821).

References

1. N. N. Greenwood and A. Earnshaw, "Chemistry of the Elements", Pergamon: New York, p.479 (1984).

2. G. M. Brown and L. Maya, J. Am. Ceram. Soc., 71, 78 (1988).

3. L. V. Interrante, G. A. Sigel, M. Garbauskas, C. Hejna, and G. A. Slack, Inorg. Chem., 28, 252 (1989).

4. L. V. Interrante, L. E. Carpenter, C. Whitmarsh, W. Lee, and G. A. Slack, Mater. Res. Soc. Symp. Proc. 73, 986 (1986).

5. D. Seyferth, G. H. Wiseman, and C. Prud'homme, J. Am. Ceram. Soc., 66, C13 (1983).

6. K. A. Youngdahl, R. M. Laine, R. A. Kennish, T. R. Cronin, and G. G. A. Balavoine, Mater. Res. Soc. Symp. Proc. 121, 489 (1988).

7. R. T. Baker, J. D. Bolt, G. S. Reddy, D. C. Roe, R. H. Staley, F. N. Tebbe, A. J. Vega, Mater. Res. Soc. Symp. Proc. 121, 471 (1988).

8. W. L. Gladfelter, D. C. Boyd, J.-W. Hwang, R. T. Haasch, J. F. Evans, K.-L. Ho, and K. F. Jensen, Mater. Res. Soc. Symp. Proc. 131, 447 (1989).

9. D. C. Boyd, R. T. Haasch, D. R. Mantell, R. K. Schulze, J. F. Evans, and W. L. Gladfelter, Chem. Mater., 1, 119 (1989).

10. K. -L. Ho, K. F. Jensen, S. A. Hanson, J. F. Evans, D. C. Boyd, and W. L. Gladfelter, Mater. Res. Soc. Symp. Proc., in press.

11. J. Kouvetakis and D. B. Beach, Chem. Mater., 1, 476 (1989).

12. N. Davidson and H. C. Brown, J. Am. Chem. Soc., 64, 316 (1942).

13. J. L. Atwood and G. D. Stucky, J. Am. Chem. Soc., 92, 285 (1970).

14. K. Gosling, J. D. Smith, and D. H. W. Wharmby, J. Chem. Soc. (A), 1738 (1969).

15. A. H. Cowley, B. L. Benac, J. G. Ekerdt, R. A. Jones, K. B. Kidd, J. Y. Lee, and J. E. Miller, J. Am. Chem. Soc. 110, 6248 (1988).

16. C. K. Narula, R. Schaeffer, and R. T. Paine, J. Am. Chem. Soc., 109, 5556 (1987).

17. E. Wiberg and E. Amberger, "Hydrides of the Elements of the Main Groups I-IV", Elsevier: Amsterdam (1971).

18. L. Maya, Adv. Ceram. Mater., 1, 150 (1986).

19. A. Ochi, H. K. Bowen, and W. E. Rhine, Mater. Res. Soc. Symp. Proc. 121, 663 (1988).

20. W. L Gladfelter, D. C. Boyd, and K. F. Jensen, Chem. Mater., 1, 339 (1989).

21. M. Ilegems, R. Dingle, and R. A. Logan, J. Appl. Phys., 43, 3797 (1972).

22. R. C. Schoonmaker and C. E. Burton, Inorg. Synth. 7, 16 (1963).

23. W. C. Johnson, J. B. Parsons, and M. C. Crew, J. Phys. Chem., 36, 2651 (1932).

24. R. Juza and H. Z. Hahn, Anorg. Allgem. Chem., 244, 111 (1940).

25. M. Mizuta, S. Fujieda, Y. Matsumoto, and T. Kawamura, Jap. J. Appl. Phys., 25, L945 (1986).

26. R. C. Powell, G. A. Tomasch, Y. W. Kim, J. A. Thornton, and J. E. Greene, Abstracts of Papers, Fall Meeting, Boston, MA; Materials Research Society: Pittsburgh, PA, 1989; F7.2.

27. M. J. Paisley, Z. Sitar, J. B. Posthill, and R. F. Davis, J. Vac. Sci. Technol., A7, 701 (1989).

28. A. Storr, J. Chem. Soc. A, 2605 (1968).

29. D. F. Shriver and A. E. Shirk, Inorg. Synth., 17, 42 (1977).

30. Elem. Anal. Calcd.: Ga, 79.45; N, 15.96; H, 4.59; C, 0.00. Found: Ga, 79.70; N, 15.71; H, 4.46; C, 0.08 (Analitische Laboratorien in Engelskirchen, West Germany).

31. P. W. R. Corfield and S. G. Shore, J. Am. Chem. Soc., 95, 1480 (1973).

32. Powder Diffraction File, International Center for Diffraction Data, Swarthmore, PA, Card #2 - 1078.

33. Powder Diffraction File, International Center for Diffraction Data, Swarthmore, PA, Card #32 - 397.

BORON NITRIDE AND COMPOSITE AEROGELS FROM BORAZINE BASED POLYMERS

David A. Lindquist*, Douglas M. Smith**, Abhaya K. Datye**, Gregory P. Johnston**, Theodore T. Borek*, Riley Schaeffer*, and Robert T. Paine*, *Departments of Chemistry and Chemical Engineering, and **UNM/NSF Center for Micro-Engineered Ceramics, University of New Mexico, Albuquerque, NM 87131

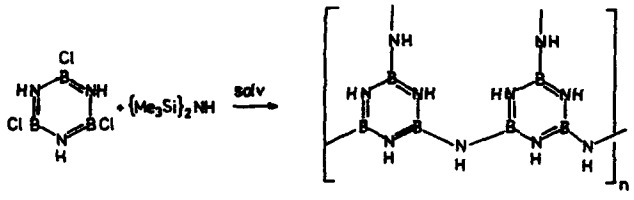
ABSTRACT

Poly(borazinylamines) have been processed in THF and toluene solvents and aerogel forms produced by supercritical drying methods. The polymer aerogels have been pyrolyzed and porous amorphous and crystalline BN monoliths have been produced. These have been characterized and effects of processing factors on surface area and pore structure are described.

INTRODUCTION

Oxide materials are commonly produced in dense forms; however, in recent years a number of oxides including *silica, boria, magnesia and titania have been* fashioned into unique, low density, porous bodies by using aerogel processing techniques[1-6]. Such porous oxides have potential applications as thermal barriers, catalysts supports, radiation detectors, membranes, adsorbents and composite matrices. For some applications it would be useful to have a porous non-oxide; however, very few attempts have been reported describing formation of porous non-oxide bodies. Sylwester and co-workers[7] have produced low density carbonized foams from a polyacrylonitrile polymer and Pekala and Kong[8] have produced carbonized aerogels from condensation of resorcinol and formaldehyde. Organic polymers[9] and carbosilane polymers[10] have also been supercritically sprayed and fine powders produced after pyrolysis.

Our group has recently reported the formation of a boron-nitrogen containing polymer based upon cross-linked borazine rings as shown in equation 1[11]. We have also briefly reported that this polymer forms a gel in some organic solvents and the solvent may be removed by supercritical CO_2(l) extraction. The resulting highly porous bodies may be thermally processed leaving stable, low density amorophous or crystalline boron nitride[12]. In the present report we outline more recent studies of processing variables in formation of boron-nitride aerogels.



(1)

EXPERIMENTAL

Poly(borazinylamine) was prepared as described previously[11] and wet gel monoliths (dimensions typically 2.5cm x 1.8cm) were formed from either tetrahydrofuran or toluene. Critical point extractions with CO_2(l) were performed as described previously[12] except as noted in the Results and Discussion. Pyrolysis chemistry was accomplished in controlled atmospheres (N_2,

NH_3) with use of standard tube furnaces. Surface area and pore structure analyses were performed by standard methods[12].

RESULTS AND DISCUSSION

1. Variation in Solvent Content

During the course of the initial BN aerogel preparations[12] THF was employed as the polymer gelation solvent, and it was qualitatively noted that the amount of solvent affected the integrity of the dry and thermally processed monoliths. In this study three gels were prepared with constant amounts of trichloroborazine (3.8 mmol) and hexamethyldisilazane (5.7 mmol) but different quantities of THF (3mL, 4mL and 7mL). The gels were formed at 25°C, solvent exchanged in CO_2(l) and supercritically dried. The monoliths were heated at 1200°C under NH_3 and the surface areas and pore volumes analyzed by N_2 adsorption and condensation. As shown in Figure 1, the pore volume was found to increase significantly with increasing amount of solvent while the surface area varied between `300-600 m^2/g.. This provides a guide to future studies of "pore tailoring".

2. Gel Shrinkage

The initial BN aerogel preparations revealed that the wet gels were subject to considerable shrinkage during CO_2 solvent exchange, supercritical drying, and pyrolysis.[12] This has been examined in greater detail for this study. For example, a wet gel plug (2.5cm x 1.8cm) prepared in 7mL THF from 3.81 mmol $(HNBCl)_3$ and 5.71 mmol hexamethyldisilazane was solvent exchanged and supercritically dried. The resulting plug had dimensions 1.5cm x 1cm. Assuming isotropic shrinkage this corresponds to a linear shrinkage of $\Delta L/L_o$=0.42. Treatment at 1200°C resulted in further shrinkage: plug dimensions 1.2cm x 0.65cm; $\Delta L/L_o$=0.58.

In order to test for solvent effects on shrinkage a potentially less interacting solvent was sought. Toluene provides relatively good solubility for the borazine monomer; therefore, it was employed to obtain gels similar to those prepared in THF. From 7 ml of toluene, after supercritical drying, a plug of dimensions 2.2cm x 1.4cm was obtained and after pyrolysis at 1200°C a plug of size 1.6cm x 1cm was achieved. These correspond to linear shrinkages of 0.17 and 0.40, respectively. Although the contraction is still high, it is apparent that the effect is less when toluene is utilized in the polymer preparation. We should note that the wet gel solvent content is sufficiently high such that a porosity of 0.98 would be obtained if no shrinkage occurred. Further studies of these solvent effects are in progress.

3. Surface Area and Pore Structure Variations

In the present study aerogels were prepared in toluene as described above and the surface area and pore volume were characterized. Data for aerogel plugs heated at 1200°C for 12 hours under NH_3, at 1550°C for 8 hours under N_2, and at 1600°C for 24 hours under N_2 are summarized in Figure 2. As found for aerogels prepared by using THF, the surface area and pore

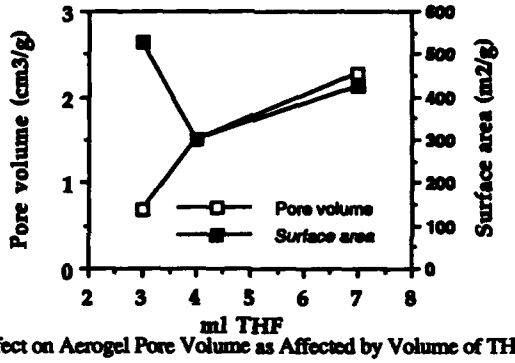


Figure 1. Effect on Aerogel Pore Volume as Affected by Volume of THF Solvent

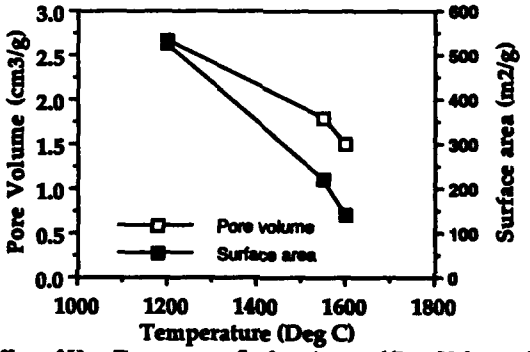


Figure 2. Effect of Heat Treatment on Surface Area and Pore Volume of Boron Nitride Aerogels.

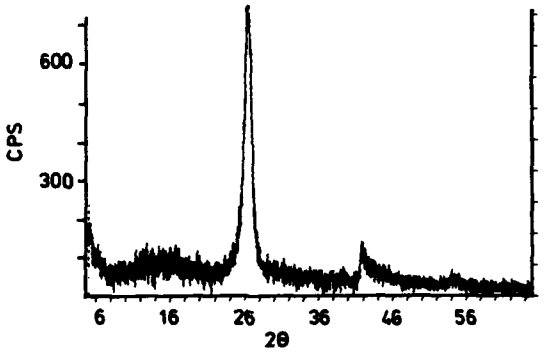


Figure 3. XRD Pattern for BN Aerogel Sample Prepared at 1650°C.

volume decrease with increasing temperature in the range 1200°C-1600°C. We have attributed this effect to micropore sintering followed by crystallization at increasing temperature, and indeed at 1600°C XRD analyses show evidence for hexagonal BN (Figure 3). A similar trend in decreasing surface area and pore volume was found for the aerogels prepared from THF although the absolute values at each temperature are greater for the aerogels prepared from toluene.

The crystallinity of the aerogels obtained from THF were studied further by processing a raw pellet at 1000°C for 12 hours under ammonia and then 1650°C (heating rate 30°C/min) for 8 hours under argon. Powder x-ray diffraction analysis showed the 002 reflection centered at 0.335 nm and the crystallite size was estimated at 10 nm from the Scherer relation. Nitrogen adsorption showed a surface area of 100 m^2/g, a pore volume of 1.21 cm^3/g and an average pore radius of 24 nm. TEM micrographs (Figure 4) reveal an approximately trimodal distribution of crystalline particles at 10nm, 50 nm and 600 nm. The smaller two crystallite sizes are grouped in clusters of approximately the same dimension as the 600 nm crystallites, and they appear to be sintering. Spotty diffraction patterns originating from the 600 nm crystallites suggest that they are single crystals, whereas the rings obtained from the small crystallites indicates their polycrystallinity. The large surface areas reported above can be largely attributed to the abundance of the smaller crystallites.

4. Preparation of Wet Gels in CO_2(l)

Given the solvent effects described above, it was of interest to determine if the polymerization and subsequent supercritical drying could be accomplished totally in the critical point solvent CO_2(l). Indeed, trichloro- borazine and hexamethyldisilazene were separately dissolved in CO_2(l) and the two solutions combined. After thorough mixing, the CO_2 was slowly released at the critical point. A white fluffy polymer was obtained rather than a monolithic gel. The polymer was pyrolyzed under NH_3 at 1200°C and amorphous BN was obtained. The surface area of the BN was 472 m^2/g and this is comparable with the surface area of materials obtained from organic solvent exchanged gels. However, the average pore radius, 2.5 nm, and pore volume of 0.60 cm^3/g are markedly smaller in the CO_2(l) derived samples. Micropore analysis indicates a micropore area of 97m^2/g and mesopore area of 375 m^2/g.

5. BN-SiC Composites

It is well known that fibers may be used to strengthen both dense and aerogel ceramic bodies. In an effort to improve the physical strength of the BN aerogels produced here we have added SiC whiskers to the gel mixture. Typically, 0.075g (30% w/w) of SiC whiskers (American Matrix) and a small quantity (<1%) of a commercial surfactant for nonaqueous solvents (Chevron OLOA-1200) were added to trichloroborazine (3.8 mmol) in 4mL of toluene. Hexamethyldisilazene (5.7 mmol) was added at -78°C and the mixture warmed to 25°C with periodic agitation. The resulting gel was aged for 2 days and the solvent exchanged and supercritically dried with CO_2(l). The porous gel was then heated under NH_3 for 12 hours at 1200°C. The resulting aerogel plug was qualitatively much stronger than aerogels without whisker reinforcement. The surface area and pore volume are essentially unchanged. Finally, optical microscopy show that the whiskers are uniformily distributed throughout the sample.

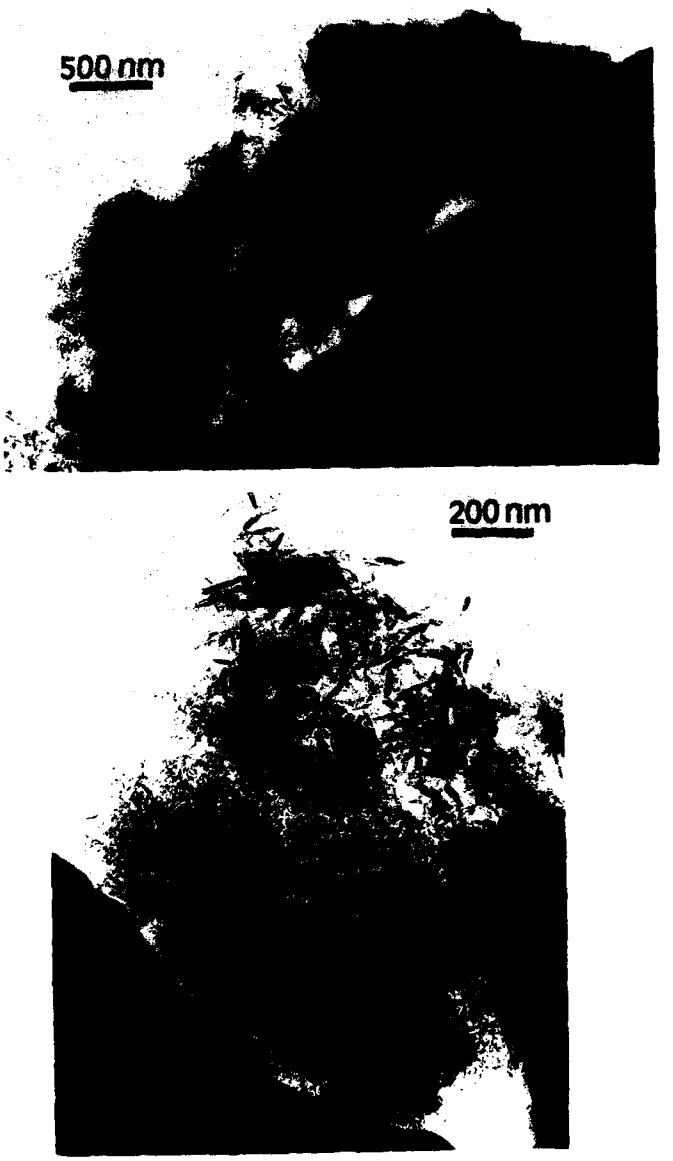


Figure 4 TEM for a BN Aerogel Sample Prepared at 1650°C

CONCLUSION

We have demonstrated that a poly-(borazinylamine) can be utilized to form low density, high surface area aerogel samples of amorphous or crystalline boron nitride. Aerogels prepared in toluene are more easily handled than those produced in THF and they typically have higher surface areas and pore volumes at any given temperature. We have also qualitatively observed that the aerogel body may be strengthened by inclusion of SiC whiskers and studies of applications for these ceramic composites is in progress.

Acknowledgement is made to the UNM/NSF Center for Micro-Engineered Ceramics for financial support. CMEC is supported by the National Science Foundation (CDR-8803512), the Los Alamos and Sandia National Laboratories, the New Mexico Research and Development Institute, and the ceramics industry.

REFERENCES

1. J. Fricke, "Aerogels - a Fascinating Class of High-Performance Porous Solids" P2 in Aerogels, J. Fricke, ed. Springer Progress in Physics, Vol 6, Springer, Heidelberg, 1986.

2. J. Fricke, "Aerogels - Highly Tenuous Solids with Fascinating Properties", J. Non-Cryst. Solids 100, 169-173 (1988).

3. D.W. Matson and R.D. Smith, "Supercritical Fluid Technologies for Ceramic Processing Applications" J. Am. Ceram. Soc. 72 [6] ,871- 881 (1989).

4. C.J. Brinker, K.J. Ward, K.D. Keefer, E. Holupka, P.J. Bray, and R.K. Pearson, "Synthesis and Structure of Borate Based Aerogels", p 57 in Aerogels, J. Fricke, ed., Springer Progress in Physics, Vol 6, Springer, Heidelberg, 1986.

5. S.J. Teichner, "Aerogels of Inorganic Oxides" p. 22 in Aerogels, J. Fricke, ed. Springer, Heidelberg, 1986.

6. J.N. Armor, and E.J. Carlson, "Variables in the Synthesis of Unusually High Pore Volume Aluminas" J. Mat. Sci. 22, 2549-2556 (1987).

7. A.P. Sylwester, J.H. Aubert, P.B. Rand, C. Arnold, and R.L. Clough, "Low Density Microcellular Carbonized Polyacrylonitrile (PAN) Foams", Polm. Mater. Sci. Eng., 57, 113-17, (1987).

8. R.W. Pekala, and F.M. Kong, "Resorcinol-Formaldehyde Aerogels and Their Carbonized Derivatives", Amer. Chem. Soc. Div. Polym. Chem. 30, 221-227, (1989).

9. J.H. Aubert, "Isotactic Polystrene Phase Diagrams and Physical Gelation" Macromolecules, 21, 3468-3473 (1988).

10. D.W. Matson, R.C. Petersen and R.D. Smith, "The Preparation of Polycarbosilane Powders and Fibers During Rapid Expansion of Supercritical Fluid Solutions" Mat. Lett. 4, 429-432 (1986).

11. C.K. Narula, R. Schaeffer and R.T. Paine, "Synthesis of Boron Nitride from Polyborazinylamine Precursors" J. Am. Chem. Soc. 109, 5556-5557 (1987).

12. D.A. Lindquist, T.T. Borek, S.J. Kramer, C.K. Narula, G.P.Johnston, R. Schaeffer, D.M. Smith and R.T. Paine, "Formation and Pore Structure of Boron Nitride Aerogels" Com. Amer. Ceram. Soc. 73, 757-60, (1990).

SPECTROSCOPIC CHARACTERIZATION OF A PRE-CERAMIC POLYMER FOR SiC/TiC SYSTEM.

FLORENCE BABONNEAU*, PATRICE BARRE* , JACQUES LIVAGE* AND MICHEL VERDAGUER**
* Laboratoire de Chimie de la Matière Condensée and ** Laboratoire de Chimie des Métaux de Transition, Université Pierre et Marie Curie, 4 place Jussieu, 75005 Paris, France.

ABSTRACT

Polytitanocarbosilane precursor for SiC/TiC ceramics was characterized by various spectroscopic techniques (^{29}Si and ^{13}C CP MAS NMR, Ti K-edge XANES and EXAFS) in order to follow how titanium ions are incorporated into the polycarbosilane-based polymer. This polymer has been fired in argon atmosphere, and the evolution of the local environments of Si and Ti atoms, during the pyrolysis process, have been followed using ^{29}Si MAS-NMR and Ti K-edge X-ray absorption : this study reveals the formation of Si-O bonds above 500°C, while Ti-C bonds clearly appear around 800°C. Above 1000°C, Si-O bonds are consumed by reaction with excess carbon and the system finally crystallizes into SiC/TiC mixture above 1200°C.

INTRODUCTION

The polymer route to non oxide ceramics has been greatly developped after the pioneering work of Yajima, who prepared SiC fibers from polycarbosilane (PC)[1]. This route offers a main advantage: fibers of refractory ceramics can easily been prepared. But other advantages have to be considered: soluble polymeric precursors can be chemically modified in order to get new systems with different properties. This point can be illustrated by the work of Yajima on polytitanocarbosilane[2]. By reacting a titanium alkoxide with polycarbosilane a new polymer is obtained that can be used to produce Si-Ti-C-O fibers with higher mechanical properties compared to the usual SiC fibers[3].

Several metallic atoms M such as Ti, Zr, Al or Nb, have been reacted with polycarbosilane, via a metallic alkoxide in order to get new polymeric precursors for Si-M-C-O systems. Spectroscopic characterizations of the precursors and of samples pyrolyzed in argon atmosphere have been undertaken with two main goals: (1) a better understanding of the reactions occuring during the preparation procedure between PC and the metallic alkoxide, (2) a study of the influence of M on the conversion process of the polymer into the final crystalline phases. This paper presents the spectroscopic study done on the Si-Ti-C-O system, mainly using ^{29}Si Magic Angle Spinning Solid State NMR (MAS NMR) and Ti K-edge X-ray absorption.

EXPERIMENTAL SECTION

The polytitanocarbosilane, PTC, was prepared by refluxing polycarbosilane (Dow Corning) with titanium n-butoxide (Fluka) in toluene for 2 hours under argon. The solvent was distilled and then the temperature was raised up to 300°C to complete the cross-linking procedure. Chemical analysis gives $SiC_{3.24}Ti_{0.19}H_{7.57}O_{1.16}$. The polymer was then fired under argon up to a given temperature with a heating rate of 10°C/min.

MAS-NMR spectra were recorded on MSL 300 (^{29}Si) and MSL 400 (^{29}Si CP and

Mat. Res. Soc. Symp. Proc. Vol. 180. ©1990 Materials Research Society

^{13}C CP) Bruker spectrometers. The Ti K-edge X-ray absorption spectra were recorded at room temperature, at LURE (Orsay, France) using the EXAFS III spectrometer with a Si 311 two crystals monochromator. Powdered samples were just put on adhesive tape while the liquid samples were introduced in 0.15 mm thick cells. A titanium metallic foil was used to calibrate the energy: the first maximum of the absorbance was taken as a reference at 4964.2 eV. The energy was scanned from 4950 to 5050 eV for XANES data and from 4760 to 5760 eV for EXAFS data. Data analysis have already been described[4].

RESULTS AND DISCUSSION

Characterization of the polytitanocarbosilane

The main interest of this study is to understand how the titanium atoms are retained in the PC based polymer. The presence of Si-O-Ti bonds formed from the reaction of the Ti-OR bonds with the Si-H groups of PC chains was postulated in several papers, especially from IR data [2,5]. Such a bridge is known to give a strong absorption band around 900 cm^{-1}.

The present study was started to characterize the local environment of Si and Ti atoms at various stages of the preparation procedure. After distillation of the solvent, the cross-linking procedure was stopped at 150°C, 200°C, 250°C and 290°C, when the final PTC is obtained.

^{29}Si and ^{13}C CP MAS NMR as well as infrared data have already been published [6]. The infrared spectra clearly show the consumption of the Si-H bonds during the cross linking and the presence of butoxy groups in the polymer. No evidence for any Si-O-Ti bonds was found, but PC presents a broad band in this frequency range. Figure 1 represents the ^{29}Si and ^{13}C CP MAS NMR of the samples heated up to 150°C and 290°C.

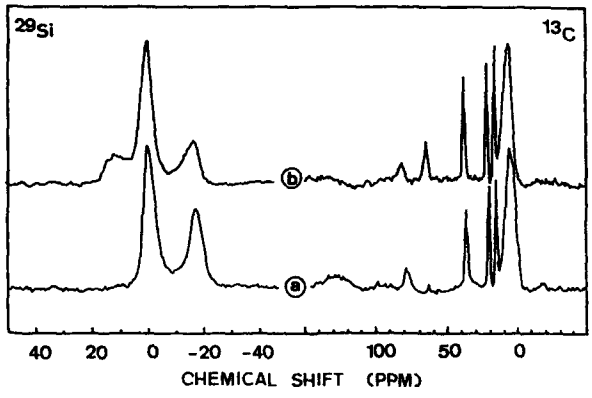


Figure 1 : ^{29}Si and ^{13}C CP MAS NMR of PTC samples prepared at 150°C, after evaporation of the solvent (a) and at 290°C after cross-linking (b).

At 150°C, the ^{29}Si NMR spectrum shows no difference with the spectrum of pure PC, with two peaks at -0.8 and -18.1 ppm corresponding to SiC_4 and SiC_3H units. At 200°C, the spectrum reveals a new signal around 10 ppm due to SiC_3O sites and a decrease of the peak due to SiC_3H

sites. Si-O bonds are formed during the cross-linking procedure with consumption of Si-H bonds.

At 150°C, the ^{13}C CP MAS-NMR spectrum shows a broad peak due to the C atoms of the PC chains around 5 ppm as well as peaks at 14.5, 19.6, 35.3 and 76.7 ppm due to C atoms of a butoxy chain. The chemical shift of X-O-$\underline{C}H_2$ groups is quite sensitive to the nature of X. A value of 76.7 ppm agrees with butoxy groups bonded to titanium atoms (74.4 ppm for $Ti(OBu^n)_4$). Above 200°C, a new peak appears at 62.2 ppm assigned to butoxy groups bonded to silicon atoms (63.0 ppm in $Si(OBu^n)_4$). The intensity of this peak increases with temperature while the one at 76.7 ppm is decreasing. At the same time, the solution turns blue: Ti^{4+} ions are reduced into Ti^{3+}. These experiments show evidence for the cleavage of Ti-OBu bonds and the formation of Si-OBu bonds.

The local environment of the Si atoms seems to be modified during the cross-linking stage and not during the reflux. Above 200°C, Si-O bonds are clearly formed, and seem closely related to the transposition of OR groups from the Ti atoms to the Si atoms.

Ti K-edge XANES (X-Ray Absorption Near Edge Structure) and EXAFS (Extended X-Ray Absorption Fine Structure) spectra of PTC, cross linked at 290°C, are compared to the spectra of pure $Ti(OBu^n)_4$ in Figure 2.

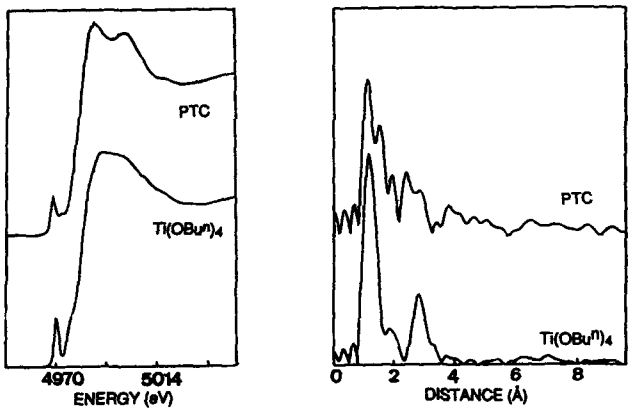


Figure 2 : Ti K-edge XANES spectra and k^3 Fourier transforms of the EXAFS spectra of $Ti(OBu^n)_4$ and PTC.

Titanium n-butoxide is known to be a trimer with Ti atoms in a 5 fold coordination [4]: the XANES spectrum presents one pre-edge peak at 4971.3 eV, and the EXAFS analysis gives two Ti-O distances (terminal OR groups at 1.85 Å and bridging OR groups at 2.08Å) and one Ti-Ti distance at 3.09Å. The local environment of Ti atoms in PTC is completely modified. The XANES spectrum shows a complex structure with two pre-peaks at 4968 and 4972 eV as well as two maxima at 4987 and 5000 eV. These features are quite similar to those found for TiO_2 anatase (a triplet at 4966, 4969 and 4971 eV and two maxima at 4984 and 5001 eV). A preliminary analysis of these EXAFS data shows a strong modification in the Ti-O distances

compared to the precursor $Ti(OBu^n)_4$: two distances around 1.95 and 2.10Å are present that could be assigned respectively to oxo and OR or OH brigdes. More surprising seems to be the presence of a very short Ti-O distance found around 1.50Å and a very long one around 2.65Å. The first one could be related to the presence of some titanyl bonds Ti=O, and the long distance to the presence of some solvent molecules, for example n-butanol. Some Ti-Ti distances around 3.06Å seem also to be present.

A description of the local environment of Ti atoms is not obvious from these first results and can only be speculated. It is nevertheless clear that Ti atoms are no more 5 coordinated, as in the precursor, but now 6 coordinated. A Ti-O distance of 1.95Å agrees with the presence of oxo bridges, such as in anatase (1.93 and 1.96Å), but the distribution of distances show a more complex environment.

This spectroscopic characterization cannot lead to a very precise description of the polytitanocarbosilane. However, it seems clear that no reaction occurs during the reflux procedure between PC and the titanium alkoxide. The titanium atoms are retained inside the polymer, certainly due to a slight hydrolysis of the moisture-sensitive alkoxide that leads to the formation of small oxide-based particles. During the cross-linking procedure, Ti-OR bonds are cleaved, leading to a reduction of Ti ions. OR groups react with Si-H bonds of the PC chains to form Si-OR bonds. At the end of the preparation procedure, Ti^{3+} ions are re-oxidized by reacting with air. The chemical reactions occurring during the preparation of this polymer are quite complex. However no chemical bonds between the PC chains and the Ti-containing particles seem to be formed.

Evolution of the local environments of Si and Ti atoms during the pyrolysis process

The pyrolysis of PTC under argon leads to the crystallization of SiC and TiC above 1200°C. Using an alkoxide as titanium precursor, it was interesting to understand how the TiC phase could be formed. Local environments of Si and Ti atoms were respectively characterized by ^{29}Si MAS-NMR and Ti K-edge X-ray absorption.

The local environment of Si atoms in the pyrolyzed PTC samples has already been studied by ^{29}Si MAS-NMR [7]. Above 500°C, new peaks appear around -30, -70 and -110 ppm, assigned to $SiC_{4-x}O_x$ units with x = 2, 3 and 4. Si-O bonds are formed up to 1000°C, and then disappear certainly by reaction with excess carbon present in the sample.

The local environment of Ti atoms in PTC pyrolyzed samples has been characterized by X-ray absorption spectroscopy (Figure 3). Below 700°C, the XANES spectra are characteristic of an octahedral environment for Ti atoms, close to the one found in TiO_2. At 840°C, the XANES spectra drastically change. The local symmetry remains octahedral, but the spectrum now presents two pre-edge peaks at 4964 and 4969 eV and two maxima at 4982 and 4995 eV. These values are close to those corresponding to crystalline TiC: pre-edge peaks at 4965, 4968 and 4970 eV and maxima at 4982 and 4994 eV. The energy shifts and the general shape of the edge structures are in agreement with a change from short Ti-O to longer Ti-C distances in an octahedral symmetry. Ti atoms are in a carbide environment. The EXAFS data are in complete agreement with this assumption. At 700°C, the Fourier transform shows a peak characteristic of

Ti-O distances. The peak is broader, compared to PTC, certainly because of an increasing disorder in the local environment of the Ti atoms. At 840°C, the Fourier transform is completely modified. The peak due to Ti-O distances is drastically reduced. The spectrum shows an intense peak around 3Å and three other peaks around 3.8, 5 and 5.8 Å, that seem to be the signature of the crystalline TiC phase. The very intense peak is due to the Ti-Ti distances (3.05Å in TiC). The intensity of these peaks are regularly increasing with the temperature revealing a growth of the crystallite size.

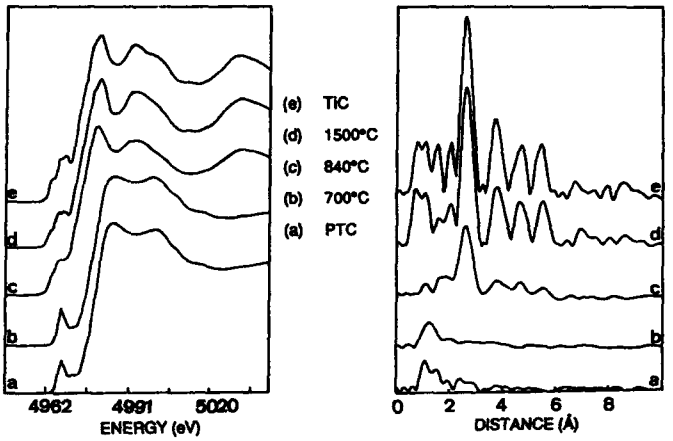


Figure 3: Ti K-edge XANES spectrum and k^3 Fourier transforms of EXAFS spectra of pyrolyzed PTC samples.

This spectroscopic study revealed interesting features concerning the conversion process of PTC into ceramics, and especially the formation of the TiC phase. In the precursor, the first neighbors are oxygen atoms, while Si atoms are mainly surrounded by carbon atoms. During a first step of pyrolysis that corresponds to the decomposition of the organic parts (T<800°C), both NMR and EXAFS experiments show a disordering of the local environments of Si and Ti atoms. Si-O bonds are formed, leading to $SiC_{4-x}O_x$ units. The formation of some Ti-C bonds at this stage can also be assumed with the presence of $TiO_{6-y}C_y$ units. At 840°C, the Ti atoms seem really to be in a carbide environment: the radial distribution function shows peaks up to 6Å that are the signature of TiC crystallites. Such structures at long distances unusual in EXAFS are clearly due to the foccussing effect allowed by the cubic structure of TiC and thus Ti-C-Ti alignments. XANES and EXAFS experiments show the formation of TiC particles at this temperature, while the crystallization of TiC only appears in the XRD pattern, at 1200°C. Above 1000°C, Si-O bonds are consumed via carbothermal reduction leading to the crystallization of SiC.

CONCLUSION

The polymer route appears quite attractive for the synthesis of new ceramics system. This process allows to tailor a large variety of new pre-ceramics precursors, especially to prepare multicomponent systems. However, to get a better control on the structure of the final ceramics, a detailed characterization of the precursor and of the conversion process seems absolutely necessary. Polytitanocarbosilane precursor for SiC-TiC system, has been studied in this paper. A spectroscopic investigation was undertaken using two powerful techniques to characterize local environments: ^{29}Si MAS-NMR and Ti K-edge X-ray absorption. Some interesting results were obtained concerning the environment of Ti atoms in the precursor and the formation of the titanium carbide phase.

The study performed on the precursor, does not show any chemical bond between the PC chains and the Ti-containing part. The presence of Si-O bonds was assigned to Si-O-Ti brigdes in previous works [2,5]. In fact, they seem closely related to the transposition of OR groups from Ti to Si atoms and thus to the formation of Si-OR bonds. Titanium atoms are certainly retained inside the polymer because of a partial hydrolysis of the alkoxide during the preparation, that lead to the formation of oxide based particles.

The affinity of Si atoms to form Si-O bonds, compared to Ti atoms to form Ti-O bonds, seems to play a key role in the conversion process. It certainly avoids the crystallization of TiO_2 at low temperature, and thus a carbothermal reduction of the oxide phase to form the carbide at high temperature. The most interesting feature comes from the EXAFS data that clearly show at 840°C structures due to long range ordering. Part of the Ti atoms are already in a crystalline TiC environment at this temperature even if the crystallization only appears in the XRD pattern at 1200°C. Above 1000°C, NMR spectra show the consumption of Si-O bonds, while EXAFS reveal a growth in the TiC crystallite size. Finally, at 1200°C, the XRD patterns present the diffraction peaks of SiC and TiC phases.

ACKNOWLEDGEMENTS

The authors would like to thank Dr G.D. Sorarù (Universty of Trento-Italy) for helpful discussions and Dr A. Michalowicz (LURE-Orsay-France) for his EXAFS analysis programms.

REFERENCES

[1] S. Yajima, K. Okamura, J. Hayashi, M. Omori, J. Am. Ceram. Soc. 59, 324 (1976)
[2] S. Yajima, T.Iwai, T. Yamamura, K. Okamura, Y. Hasegawa, J. Mater. Sci. 16, 1349 (1981)
[3] T. Yamamura, T. Ishikawa, M. Shibuya, T. Hisayuki, K. Okamura, J. Mater. Sci. 23, 2589 (1988)
[4] F. Babonneau, S. Doeuff, A. Léaustic, C. Sanchez, C. Cartier, M. Verdaguer, Inorg. Chem. 27, 3166 (1988).
[5] Y.C. Song, Y. Hasegawa, S.J. Yang, M. Sato J. Mater. Sci. 23, 1911 (1988)
[6] F. Babonneau, J. Livage, G.D. Sorarù, G. Carturan, J.D. Mackenzie New J. Chem. (in the press)
[7] F. Babonneau, G.D. Soraru, J.D. Mackenzie J. Mater. Sci. (in the press)

CHEMICAL REACTIONS DURING THE THERMAL PROCESSING OF BORAZENE POLYMERS

R. R. Rye*, T. T. Borek**, D. A. Lindquist**, and R. T. Paine**
*Sandia National Laboratories, Albuquerque, NM 87185
**Department of Chemistry, University of New Mexico, Albuquerque, NM

Abstract

A class of borazene polymers has been developed which consist of a two-dimensional array of six-membered borazene rings with the borons of adjacent borazene rings separated by -NH- groups. Pyrolysis of these polymers above ≈1000 C leads to crystalline graphite-like boron nitride (h-BN). The thermal chemistry of thin films of one polymer deposited on KOH etched Al has been examined by thermal decomposition mass spectroscopy (TDMS) and thermal gravimetric analysis (TGA), and the gas evolution chemistry is found to be essentially complete by temperatures of less than 400 C. All products desorb with the same temperature profile and the major desorbing species are NH_3 and N_2 consistent with a loss of excess nitrogen and hydrogen in the polymer, and HCl from decomposition of by-products of the synthesis step. Isotope labeling shows that complete exchange occurs below 400 C between the ring and amino bridge nitrogens. Since the formation of ordered crystalline h-BN films requires heating to temperatures of the order of 1000 C, whereas the gas evolution and ring opening chemistry is complete by roughly 400 C, it is concluded that gas evolution chemical processes are not rate limiting in BN ceramic production.

Introduction.

Soluble or fusible polymers offer benefits over powder processing and gas phase deposition schemes for the formation of ceramic materials, and they furnish a systematic framework with which to probe the mechanistic aspects of ceramic formation. In addition, polymers provide access to forms such as fibers, foams and some coatings not available from classical synthesis routes (1-3). Several groups have recently reported that preparations of polymers suitable for production of boron nitride (4-12) and polyborazinyl amines (5-7), prepared by cross-linking borazenes, are particularly useful. The polyborazinyl amine used here is schematically illustrated by the insert in Fig. 1.

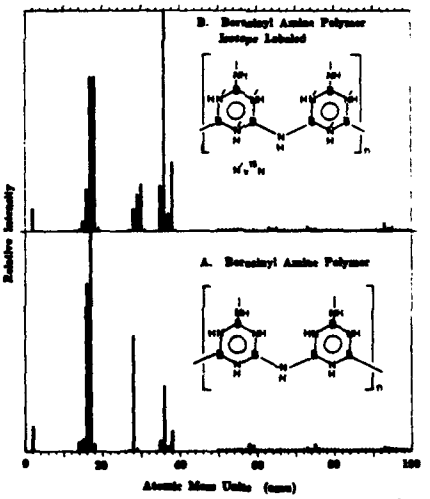


Figure 1. Mass spectra at the maximum decomposition rate. Spectrum A: borazene amine polymer. Spectrum B: ^{15}N labeled polymer.

In the present report thermal decomposition mass spectroscopy (TDMS), thermal gravimetric analysis (TGA) and X-ray photoelectron spectroscopy (XPS) are used to identify the major thermal decomposition

products produced from thin polyborazinyl amine coatings and to explore the pyrolysis mechanism. The pyrolysis chemistry is apparently complete below 400 C and this implies that the gas evolution processes are not rate limiting in the thermal conversion of borazene polymers to the graphite-like form of BN (noted here as h-BN).

Experimental.

The Al substrate (0.76 mm thick) was etched in hot KOH. XPS analysis of the Al substrate prior to polymer deposition showed it to be oxidized with O1s the dominant XPS peak. As described in the literature (13), samples were prepared by combination of trichloroborazene and hexamethyldisilazane (1:1.5 ratio) in diethyl ether at -78 C. The solution was warmed to 20 C, and transferred under dry nitrogen to a flat bottom vessel containing the substrates to be coated. After 12 hrs the coated substrates were removed and placed in a transfer tube. These samples are referred to as reacted samples.

The UHV system used for XPS and TDMS studies has been described previously (14) and will only be summarized here. It consists of an UHV system with a double-pass cylindrical-mirror analyzer (operated at 50 eV pass energy), a Mg/Al X-ray source for XPS, and a quadrupole mass spectrometer mounted in a separate snouted container for direct line-of-sight TDMS measurements. The quadrupole is computer controlled allowing collection of complete mass spectra at near the maximum scan rate. Individual samples are mounted on a transportable sample plug-in assembly containing a heater and thermocouple. The samples are clamped against the surface of the heater block with the thermocouple spot welded to the block. As a result the temperatures reported here are those of the heater block; the actual polymer temperatures are expected to be somewhat lower due to heat transfer limitations. Typical heating rates were roughly 0.9 C/sec. All sample loading and transfer steps were done in an Ar filled glove bag in order to minimize air exposure. Despite these precautions, XPS spectra always gave an appreciable O1s peak.

Thermal gravimetric analyses were performed on a Perkin-Elmer Model 3700 analyzer: sample sizes 5-20 mg, heating rate, 10 C min^{-1}, and argon flow rate 25 cc min^{-1}.

Results

XPS spectra show the complete absence of Al substrate peaks at approximately 75 and 119 eV. By using the peak intensities and the reported sensitivity factors (15), the N:B ratio is estimated as 1:1; the ratio expected from the polymer stoichiometry is 1.5. Also present are peaks from Si, Cl and C, probably from the trimethylsilyl chloride polymerization co-product. The only major change that occurs in the XPS spectra on heating is the complete loss of the Cl peaks.

Figure 1A contains representative mass spectra obtained near the maximum decomposition rate for reacted polymers on Al. The major products are in order: NH_3, identified from the mass 16 to 17 ratio; N_2, identified from the isolated mass 28 peak; and HCl, identified from the mass 36 to 38 ratio. Other possibilities for the fragment at 28 amu are CO or a BNH_x

species such as aminoborane ($H_2B\text{-}NH_2$), but the fragment at mass 12 is at least a factor of two too small for CO and the anticipated fragments around mass 28 are missing for species such as aminoborane (16). Unidentified, much less intense fragments are observed at higher mass.

Figure 1B is the same as 1A except that the nitrogens of the borazene ring have been labeled with ^{15}N and the amine bridge with ^{14}N. As is obvious from Fig. 1B the nitrogen containing products all show complete statistical mixing during pyrolysis. For example, the stoichiometry of the polymer would predict a value of 2/3 for the ratio $^{15}N/(^{15}N+^{14}N)$ while the ratio from the mass 28, 29 and 30 intensities is 0.62. If the contribution from CO to the mass 28 intensity is removed using the fragmentation masses at 12 amu for CO and 14 amu for N_2, the ratio becomes 0.71. Clearly there is complete exchange between the amine bridge and the borazene ring indicating very facile ring opening reactions.

The gas release process for these products can be more clearly seen from the TDMS spectra of the individual mass fragments. By recording mass spectra and the sample temperature as a function of time, the intensity variation of a single mass species as a function of temperature can be extracted. For an as reacted polymer film on Al, Fig. 2 contains the change in mass spectrometer ion signal for NH_3 (mass 17), N_2 (mass 28) and HCl (mass 36) from mass spectra such as in Fig. 1A. In this case the product distribution is $NH_3 > N_2 \approx HCl$, and all products are generated over the same temperature range (≈125 - 350 C) with some variation in the relative amounts of the two peaks. All other products appear at much lower intensity levels. While the use of ion currents instead of calibrated partial pressures is a source of possible error, this is not expected to change the relative product distributions. We estimate from the information given by UTI, Inc. on ionization efficiencies and multiplier gain for the model 100C Quadrupole mass analyzer that, relative to NH_3 (mass 17), the N_2 (mass 28) curve in Fig. 2 could be decreased by a factor of 1/2 and the HCl (mass 36) by a factor of 1/3.

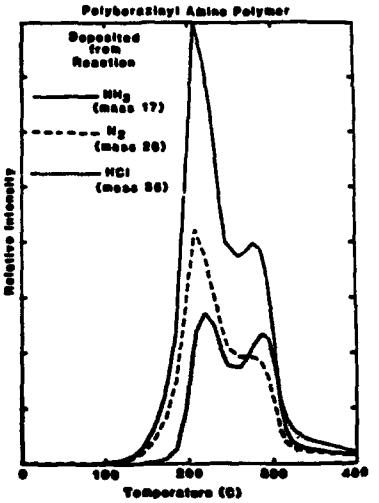


Figure 2. Thermal decomposition spectra for NH_3, N_2 and HCl.

Figure 3 contains the mass 17 TDMS spectrum from Fig. 2 directly compared to the TGA data for an as reacted polymer sample. The data are comparable in that both show two sharply differentiated decomposition steps at relatively low temperature. Furthermore, the TGA data show that the majority of the weight loss occurs below 350 C; nearly 90% of the total weight loss (52%) achieved by 1000 C occurs below 350 C while only 10%

occurs between 350 C and 1000 C. Thus, one can draw the same conclusions from both the TDMS and TGA data; gas evolution from pyrolysis of films directly deposited onto Al occurs in two distinct states at temperatures below approximately 400 C.

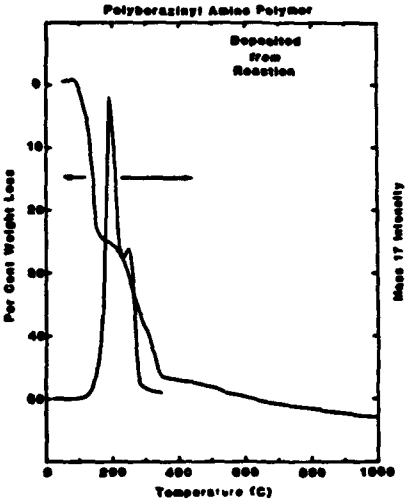


Figure 3. Comparison of NH_3 TDMS (Fig. 2) and TGA results.

Discussion

It has been demonstrated previously that the polyborazinyl amines form amorphous boron nitride upon pyrolysis at 900 C and crystalline h-BN at higher temperatures (12). It is of interest to determine how the cross-linked, nitrogen and hydrogen rich polymer is converted to the final solid state ceramic material. The present data clearly demonstrate that the majority of gas evolution and ring opening chemistry occurs in a low temperature range, 25 - 400 C.

The low temperature gaseous product release has important mechanistic implications. It can be concluded that the conversion of the polyborazinyl amine to h-BN is not limited by chemical steps (removal of excess nitrogen and hydrogen and ring opening) since the present data shows these to be mainly over by 400 C, a temperature at which crystalline h-BN is not identified (12). There is a small additional loss of hydrogen at high temperature, but this is unlikely to be a limiting factor in crystallization. Simple removal of "excess" nitrogen and hydrogen from the polymer would yield a material with the stoichiometry of BN but a greatly expanded volume without the continuous N-B-N bonding characteristic of the graphitic structure. Formation of crystalline h-BN would appear to require additional volume reduction steps in order to produce the extended napthalenic structure and not a biphenyl-like structure that would result from simple free radical coupling of hexagonal rings. With the chemical reaction steps occurring at such low temperatures, growth of crystalline h-BN requires a diffusion controlled volume reduction step. This diffusion step is clearly expected to be a high temperature, limiting process. If the solid phase diffusion step could be by-passed, for example, by step-by-step chemical addition from the gas phase of hexagonal rings to a nucleated h-BN, it should be possible to produce h-BN chemically at much lower temperatures.

Further conclusions cannot be drawn from present data. We currently have no direct information as to the chemical nature of the solid phase species at 400 C. The fact that both NH_3 and N_2 are observed means that the partially decomposed films at 400 C still contain an appreciable quantity of hydrogen (8-10); the slow release of this hydrogen at higher temperatures is probably the basis of the small additional weight loss that occurs between

400 C and 1000 C.

Summary.

Using a combination of thermal decomposition mass spectrometer, thermal gravimetric analysis and X-ray photoelectron spectroscopy we have investigated the pyrolysis of polyborazinyl amine polymers with the following conclusions:

1) All gaseous products form over the same temperature range below 400 C.

2) Decomposition products are NH_3, N_2 and HCl: NH_3 and N_2 from decomposition of the polymer and HCl from by-products of from incompletely reacted starting material.

3) Isotope labeling shows complete exchange occurs between bridging amine and ring nitrogens.

4) Conversion of the polyborazinyl amine polymer to h-BN probably involves deamination, ring opening reactions, and diffusion controlled volume reduction steps. Diffusion is the most likely thermal limiting step.

Acknowledgments.

This work was supported by the U. S. Department of Energy under Contract No. DE-AC04-76p00789, and the National Science Foundation (CHE-8503550).

References.

(1) R. W. Rice, Am. Ceram. Soc. Bull., 62, 889(1983).

(2) K. J. Wynne and R. W. Rice, Ann. Rev. Mater. Sci., 14, 297(1984).

(3) D. Seyferth, "Transformation of Organometallics into Common and Exotic Materials: Design and Activation", Laine, R. M. Ed, M. Nijhoff Publ., Dordrecht, 1988, p. 133.

(4) K. J. L. Paciorek, D. A. Harris and R. H. Kratzer, J. Polym. Sci. Polym. Chem. 24, 173(1986).

(5) K. J. L. Paciorek and R. H. Kratzer, Ceram. Eng. Sci. Proc., 9, 993 (1988).

(6) K. J. L. Paciorek, W. Krone-Schmidt, D. H. Harris, R. H. Kratzer, K. J. Wynne, ACS Symp. Ser., 360, 392(1988).

(7) M. G. L. Mirabelli, L. G. Sneddon, Inorg. Chem., 27, 3271(1988).

(8) A. T. Lynch, L. G. Sneddon, J. Amer. Chem. Soc., 109, 5867(1987).

(9) W. S. Rees and D. Seyferth, J. Amer. Ceram. Soc., 71, C194(1988).

(10) C. K. Narula, R. T. Paine and R. Schaeffer, Proc. Mat. Res. Soc., 73,

383(1986).

(11) C. K. Narula, R. T. Paine and R. Schaeffer, ACS Symp. Ser., 360, 378 (1988).

(12) C. K. Narula, R. Schaeffer, R. T. Paine, A. K. Datye and W. F. Hammetter, J. Am. Chem. Soc., 109, 5556(1987).

(13) R. R. Rye, T. T. Borek, D. L. Lindquest and R. T. Paine, J. Amer. Ceram. Soc., in press.

(14) R. R. Rye, Polymer Sci.: Part B: Polymer Physics, 26, 2133(1988).

(15) C. D. Wagner, W. M. Riggs, L. E. Davis, J. F. Moulder and G. E. Muitenberg, "Handbook of X-ray Photoelectron Spectroscopy", Perkin-Elmer, Corp, Eden Prairie, Minnesota, 1979.

(16) C. T. Kwon and H. A. McGee, Jr., Inorg. Chem., 9, 2458(1970).

(17) R. H. Toeniskoetter and F. R. Hall, Inorg. Chem., 2, 29(1963).

LASER DENSIFICATION OF SOL-GEL COATINGS

D.J. TAYLOR, B.D. FABES and M.G. STEINTHAL
University of Arizona, Department of Materials Science and Engineering, Tucson, Arizona 85721

ABSTRACT

Alkoxide-derived silica coatings were deposited on fused silica by dip coating. The samples were covered with a metal film to absorb the infrared radiation from an Nd:YAG laser. Coupling the laser power to the coating produced localized surface heating on the samples. By scanning the sample across the beam's path, channels in the coating were formed. The channels varied from 150 μm to 600 μm wide and from 200 Å to 1000 Å deep depending on the laser power and the translation speed. The size and shape of the channels also depended on the composition of the sol-gel coating. Optical microscopy showed that there were no cracks in either the substrate or in the coating on the micron scale. SEM revealed cracks on the nanometer scale in the laser fired coatings and no cracks in the unfired coatings. Ellipsometry showed that the index of refraction increased with increasing depth of the channels.

INTRODUCTION

Sol-gel methods can be used to make glass and ceramic materials of high purity, novel compositions, and novel microstructures. Sol-gel derived coatings offer outstanding opportunities because the attractive features offered by such processing can be obtained without many of the problems associated with the formation of bulk pieces [1]. In nearly all applications of sol-gel coatings, the control or elimination of porosity in the coating is key to obtaining the desired properties. Dense coatings are usually desired because they have a higher index of refraction, higher hardness, increased abrasion resistance, and other desirable properties. Unfortunately, the high temperatures (typically > 1000° C) required to densify the coatings often place severe restrictions on the choice of substrate material. In addition, unwanted diffusion between the substrate and the coating can occur during the firing process [2].

The goal of the present research is to densify highly refractory compositions on soft, less refractory substrates. We want to control densification not only normal to the substrate, but also in the plane of the coating. This type of process could open the door to many other applications, such as planar waveguides.

The main issue to be addressed is how to heat the coating sufficiently to densify it without melting or warping the substrate. The approach taken here is to densify the sol-gel derived coating with a laser. Hench reported using a CO_2 laser to form densified channels in bulk sol-gel samples [3]. The wavelength of the CO_2 laser (10.6 μm) would be absorbed by an oxide substrate if proper care were not taken. Hence, using a CO_2 laser to densify coatings might work if the power and modulation of the laser were closely controlled. However, it would be ideal to have a coating that absorbs at the wavelength

Mat. Res. Soc. Symp. Proc. Vol. 180. ©1990 Materials Research Society

of the laser and a substrate that does not. This might be accomplished by using an Nd:YAG laser (1.06 μm) and doping the coating to absorb at 1.06 μm, if the change in composition did not adversely affect the properties of the coating. Another approach might be to sputter a thin metal film onto the gel coating to absorb the laser power and provide localized heating at the surface of the coating. Here, we report on this latter approach.

There are likely to be many differences between densifying a sol-gel coating in a furnace versus with a laser. Two fundamental considerations would appear to be rapid burnout of organics and high thermal gradients. In a furnace, the organics can burn out on the order of several minutes. When the heating is done with a laser, burnout will probably have to occur in small fractions of a second due to the intense localized heating of the focussed laser beam. Therefore, the possibility of cracking and/or bloating of the film should be considered.

Unlike firing in a furnace, where the temperature of the sample is uniform, laser heating a coating would seem to produce high temperatures at the point (or line) of incidence, while the rest of the sample remains unchanged. Such thermal gradients could induce cracking in the coating and/or in the substrate. Here we report on initial experiments which were carried out to see if these issues present problems in densifying sol-gel derived coatings with an Nd:YAG laser.

EXPERIMENTAL PROCEDURE

The substrates used in these experiments were 25 x 38 x 1 mm fused silica slides. They were agitated in and scrubbed with a mild solution of glass soap and distilled water. The soapy water was washed off with distilled water, ethanol, and the substrates were dried with compressed air.

The coatings were made by dip coating the cleaned slides with an alkoxide solution. Tetraethoxysilane (TEOS) was mixed in a 1:4 ratio with ethanol. Both acid-catalyzed and base-catalyzed solutions were prepared. The acid-catalyzed solution contained a 2:1 mole ratio of water to TEOS. HCl was added to bring the solution pH to 2. The base-catalyzed solution contained a 2:1 mole ratio of water to TEOS. 12M NH_4OH was added to bring the solution pH to 11.

In order to form a uniform coating, the samples were extracted at a constant velocity of 4 mm/s. This extraction rate produced unfired coatings of about 1900 Å for the acid-catalyzed solution and 1500 Å for the base-catalyzed solution. Some of the samples were heat treated to 400° C prior to laser treatment to burn out the organics. A 400 Å layer of 60%Au-40%Pd was deposited onto each of the TEOS coatings by plasma sputtering using a 10 mA plasma in a 75 millitorr argon atmosphere.

After sputter coating, the samples were held individually in a mount on a computer-controlled translation table. The samples were translated across the laser beam at speeds between 1 and 12 mm/s using laser powers between 1 and 8 W in single mode operation. A power meter was placed behind the sample to monitor the laser's output before, during, and after each experiment.

After each experiment, the trace made by the laser was examined under the optical microscope to check for damage and cracking. The metal film was then washed off using aqua regia (3:1 $HCl:HNO_3$). Separate experiments showed that this treatment had no discernable affects on the sol-gel coatings. The depth, width, and shape of each laser trace was measured using a mechanical surface profilometer. SEM was used to examine the morphology of the coated samples. Ellipsometry was used to confirm the change in coating thickness and to determine the index of refraction of the coating.

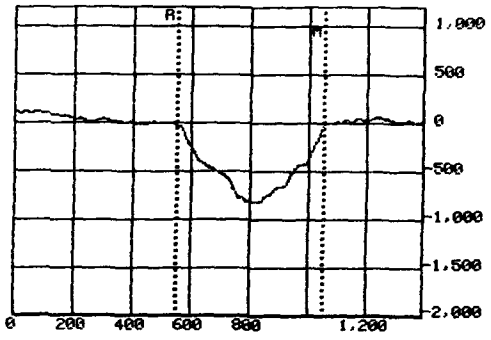


FIGURE 1: Surface profile of an acid catalyzed sol-gel coating that was laser heated at 8 watts with a 3 mm/s translation speed. (The depth of the channel is in angstroms, and the width is in microns.)

RESULTS AND DISCUSSION

It was observed that most of the metal film was removed from the surface of the coating by scanning the laser across the sample. The amount of the metal film remaining on the surface of the coating decreased as the power was increased or the scan speed was decreased. Under the optical microscope, neither the coating nor the substrate appeared cracked in any of the experiments. The profilometer traces showed that higher power, or slower scanning speeds, produced wider channels. Generally, as the power increased or the scanning speed decreased, the depth and width of the channels increased. A typical profilometer trace is shown in figure 1. The change in depth of the channel with laser power for both the acid-catalyzed and base-catalyzed coatings (figure 2a) was similar to the change in shrinkage with temperature for furnace firing (figure 2b).

At high laser powers, it is possible that the coatings were ablated. The surface profilometer showed depth of the channels, which does not necessarily mean an increased density of the laser heated coating. However, ellipsometry showed an increase in index of refraction with increased

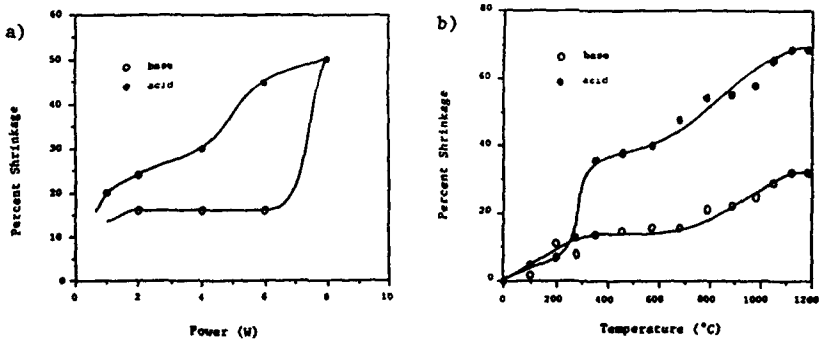


FIGURE 2: a) Shrinkage vs. laser power for acid catalyzed and base catalyzed TEOS solutions, and b) shrinkage vs. temperature for the same two solutions.

shrinkage. The index of refraction of the unfired gel was 1.424. A region of 25% shrinkage had an index of refraction of 1.431, and a region of 40% shrinkage had an index of 1.466. The amount of shrinkage that was measured with the ellipsometer closely agreed with that measured by the surface profilometer. The rise in index of refraction with increasing shrinkage of the coating indicates that the gel coating is densified and not simply ablated by the laser. The unusually high index of the laser treated material (1.466 vs. 1.456 for fused silica) indicates that carbon was probably trapped in the laser fired gel.

The morphology of the densified and undensified regions was examined using SEM, as shown in figure 3. The dark regions in figure 3a are the undensified areas, and the light strip is the laser densified channel. Figure 3b shows the morphology inside a laser heated channel. Figure 3c shows the morphology of the unfired coating at the same microscope parameters. While no cracks were seen at the micron level in the optical microscope, cracks were apparent in the laser fired regions on the nanometer scale. These small cracks may be due to weak bonding between the coating and the substrate at the time of laser firing, or could be due to the rapid burn out of the organics under laser irradiation.

CONCLUSION

We have shown that sol-gel derived coatings can be densified by coupling the radiation of a Nd:YAG laser into a thin metal surface film. At low laser power or high translation speeds, the laser had little affect on the coatings, especially the base-catalyzed coatings. However, increasing the laser power produced an increase in the amount of shrinkage. The power versus shrinkage data agreed with that of temperature versus shrinkage from firing the coatings in a furnace. Ellipsometry measurements showed an increase in index of refraction with increased shrinkage, indicating that the coatings were densified by the laser heating. It was also shown that the base-catalyzed solution required more power to densify than the acid-catalyzed solution. Although the method of laser firing is substantially different from furnace firing, the results appear to be quite similar.

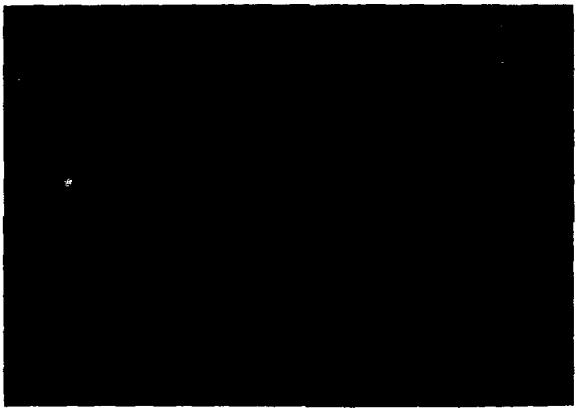
ACKNOWLEDGEMENTS

This work was funded by the Donnelly Corporation. Their support is greatly acknowledged. We would also like to thank Dave Klein, Gene Berry and Tian Hoe Lim for their contributions.

a)



b)



c)



FIGURE 3: SEM micrographs of a) a laser densified channel in a base-catalyzed TEOS solution, b) the surface morphology of the laser heated region, and c) the surface morphology of an unfired region in the coating.

REFERENCES

1. D.R. Uhlmann and G.P. Rajendran, in Ultrastructure Processing of Advanced Ceramics, edited by J.D. Mackenzie and D.R. Ulrich (John Wiley and Sons, 1988), p. 241.

2. B.D. Fabes and D.R. Uhlmann, in Innovations in Materials Processing Using Aqueous, Colloid and Surface Chemistry, edited by F.M. Doyle, S. Raghavan, P. Somasundaran and G.W. Warren (1988), p. 127.

3. L. Hench, from Fourth International Conference on Ultrastructure Processing of Ceramics, Glasses, and Composites, in Tucson, Arizona (Feb. 1989).

4. K.D. Keefer, in Mat. Res. Soc. Symp. Proc. 32 (Elsevier Science Publishers, New York, 1984), p. 15.

ELECTRODEPOSITION OF NANOMODULATED CERAMIC THIN FILMS

Jay A. Switzer*, Michael J. Shane, and Richard J. Phillips, University of Pittsburgh, Department of Materials Science and Engineering, Pittsburgh, PA 15261.
*Present Address, University of Missouri-Rolla, Department of Chemistry and Graduate Center for Materials Research, Rolla, MO 65401

ABSTRACT

Electrochemistry can be used for the atomic-level architecture of ceramic materials. In this report, ceramic superlattices based on the $Tl_xPb_yO_z/Tl_aPb_bO_c$ system were electrodeposited with individual layer thicknesses as thin as 3nm. The superlattices were deposited from a single aqueous solution at room temperature, and the layer thicknesses were galvanostatically controlled. Substitution of Tl_2O_3 into PbO_2 appears to stabilize a face-centered cubic structure with an average lattice parameter of 0.536nm. The lattice parameters for the $Tl_xPb_yO_z$ mixed oxides vary by less than 0.3% when the Pb/Tl ratio is varied from 0.84 to 7.3. Because the modulation wavelengths are of electron mean free path dimensions, this new class of degenerate semiconductor metal-oxide superlattices may show thickness-dependent quantum optical, electronic, or optoelectronic effects.

INTRODUCTION

We have recently demonstrated that it is possible to electrodeposit nanomodulated ceramic superlattices based on the $Tl_xPb_yO_z/Tl_aPb_bO_c$ system [1]. An idealized superlattice structure with square-wave modulation of composition and/or structure is shown below in Figure 1. The thicknesses of the A and B layers are not necessarily equal, as long as the structure is periodic.



Figure 1 Idealized superlattice structure with square-wave modulation of composition and/or structure.

Mat. Res. Soc. Symp. Proc. Vol. 180. ©1990 Materials Research Society

The idea of electrochemically depositing nanomodulated superlattices is not new, but it has not been applied previously to the deposition of nonmetallic materials. Several research groups have shown that compositionally modulated metallic alloys can be electrochemically deposited from a single plating bath by cycling either the potential or current [2-5]. The interest in nanomodulated metallic systems stems from their enhanced mechanical and magnetic properties [3,6].

We have chosen the $Tl_xPb_yO_z/Tl_aPb_bO_c$ system for our study for several reasons: (1) during our previous work on the electrochemical and photoelectrochemical deposition of thallium (III) oxide films we found that it was possible to deposit highly oriented films [7-9], (2) the deposition of PbO_2 [10,11] and $Pb_2Tl_2O_{5+\delta}$ [12,13] are well documented, (3) the anhydrous oxides deposit directly at room temperature and require no heat treatment, (4) there is a nearly isomorphous series of mixed thallium/lead oxides that should grow epitaxially, and (4) the device applications of these types of materials have not been studied previously.

We expect that these materials will prove to have very interesting optical and electrical properties. The end members of the series, PbO_2 and Tl_2O_3, are both degenerate n-type semiconductors. They have the high electrical conductivity of metals, with the optical properties of semiconductors. Because of their high majority carrier concentrations ($>10^{20}/cm^3$), they also have high reflectivity in the near-IR. Thallium (III) oxide, for instance, is a degenerate n-type semiconductor with a bandgap of 1.4eV and a room temperature resistivity of only 70 μohm-cm [14]. Lead (IV) oxide has a larger bandgap of approximately 1.8eV [10]. These materials are, therefore, the metal oxide analogs of semiconductors such as GaAs and AlGaAs, and they may function as multiple quantum wells when the modulation wavelength is in the nanometer range [15,16].

EXPERIMENTAL

Electrochemical depositions were performed using either a Princeton Applied Research (PAR) potentiostat/galvanostat, or a system consisting of a Stonehart BC 1200 potentiostat/galvanostat, PAR Model 175 universal programmer, and PAR Model 379 digital coulometer. Superlattices were deposited onto polycrystalline 430 stainless steel disks. The disks were housed in a PAR Model K105 flat specimen holder, so that only the front surface was exposed to the solution. The final polish on the stainless was 0.05μm alumina. Films were deposited from aqueous solutions of 0.005M TlNO, and 0.1M $Pb(NO_3)_2$ in 5M NaOH. The strong base is necessary to dissolve the $Pb(NO_3)_2$, which precipitates in 1M NaOH as PbO. The superlattices were deposited by galvanostatically pulsing between either 5mA or 1mA and a lower current such as 0.05mA. Each layer thickness was proportional to the product of current and time. Elemental analysis was done by EDS on a JEOL 35CF scanning electron microscope. The L lines of thallium and lead were used for the analysis because of the overlap of the K lines.

RESULTS AND DISCUSSION

Since Tl_2O_3 and PbO_2 can both be electrodeposited from alkaline solution, and there is considerable overlap of the deposition iV curves, it is possible to electrodeposit $Tl_xPb_yO_z$ films with compositions that are a function of applied potential or current [1]. We have carefully chosen the reactant concentrations so that it is possible to vary the Pb/Tl ratio over a wide range. Since the $TlNO_3$ concentration is only 0.005M, and the $Pb(NO_3)_2$ concentration is 0.1M, the deposition becomes mass-transport-limited in $[Tl^+]$ when the current is raised over about 1mA. The Pb/Tl ratio was varied from 0.84 to 7.3, when the current was increased from 0.05mA to 5.0mA (See Table I).

Table I Composition and values of the cubic lattice parameters for electrodeposited $Tl_xPb_yO_z$ films as a function of applied current (from Reference 1)

Applied Current (mA)	Measured Potential (V vs. SCE)	Pb/Tl mole ratio	Cubic Lattice Parameter (nm)
0.05	0.06	0.84	0.536
0.5	0.12	1.9	0.535
1.0	0.14	2.5	0.537
5.0	0.27	7.3	0.535

The X-ray diffraction patterns of the $Tl_xPb_yO_z$ films are very similar to the Tl_2O_3 pattern. An important difference between the patterns is that mixed-index reflections such as (211) are not observed for the mixed oxide, but they are present for Tl_2O_3. The systematic absence of mixed index reflections is consistent with an fcc structure. This is in agreement with the assignment of Sakai et al. [12], of electrodeposited $Pb_xTl_yO_z$, as an fcc fluorite-type structure with a cubic lattice parameter of 0.53331nm. For comparison, Tl_2O_3 has a bcc bixbyite structure with $a = 1.05434$nm, and PbO_2 has either an orthorhombic or tetragonal structure [17]. The lattice parameters that we measure for our mixed oxides vary by only 0.3% over the entire composition range listed in Table I. Hence, these oxides are ideal for the epitaxial growth of nanomodulated superlattices.

A modulated structure was prepared for SEM studies by alternately pulsing the electrode at 0.05mA for 8772 seconds and at 5.0mA for 88 seconds. The layers were intentionally made quite thick, so that they could be easily imaged in the SEM. Cross sections of a fractured film are shown in Figure 2 for two different magnifications. The lower magnification micrograph (top) shows the strong preferred

orientation of the film. We have previously reported similar columnar growth for electrodeposited thallium (III) oxide films. The higher magnification micrograph (bottom) clearly shows that the composition is modulated within each columnar grain.

Samples with much shorter modulation wavelengths and layer thicknesses were prepared by using shorter dwell times during the double-pulse galvanostatic deposition. The superlattices with modulation wavelengths in the nanometer range were characterized by X-ray diffraction. The periodicity of the superlattice manifests itself in two ways in the X-ray diffraction pattern. Bragg reflections are observed at low angles which correspond to the modulation wavelengths. These peaks at low angles would be observed even with a modulated amorphous material. At high angles the periodicity is seen as satellites around the main Bragg reflections for the material. The analysis of our superlattices was done at high angles. The modulation wavelength, Λ, can be calculated from Equation 1, where λ is the X-ray wavelength used, L is the order of the reflection, and θ is the diffraction angle. In Equation 1, L = 0 for the Bragg reflection, while the first satellite at low angle has the value L = -1, and the first satellite at higher angle has the value L = +1.

$$\Lambda = \frac{(L_1 - L_2)\,\lambda}{2\,(\sin\Theta_1 - \sin\Theta_2)} \qquad (1)$$

The modulation wavelengths for several superlattices are listed in Table II. The X-ray modulation wavelength, Λ_x was calculated from Faraday's law. For the Faraday's law calculation we used ρ = 10.353g/cm^3, n = 2, and M = 228g/mol. This is only an approximation since the density and formula weight varies somewhat with composition. We have found, however, that for all of the compositions in Table I, approximately 1.1 to 1.2μm of material are deposited per coulomb of anodic charge that is passed. There is remarkably good agreement between Λ_x and Λ_z in Table II considering the approximation used for Λ_x. Superlattice satellites were not observed for modulation wavelengths less than 5.9nm.

FUTURE WORK

The effect of quantum confinement on the optical and electrical properties of these material is unknown. Quantum confinement should produce thickness-dependent blue-shifting of the optical absorption spectra, and the development of excitonic features. We are presently studying the optical and electrical properties of these nanomodulated materials. Another important area of future research will be to study epitaxial growth in these systems by measuring nucleation and growth rate constants by transient potential-step experiments for varying degrees of lattice mismatch. These in situ studies should provide valuable information to architects of future superlattice structures.

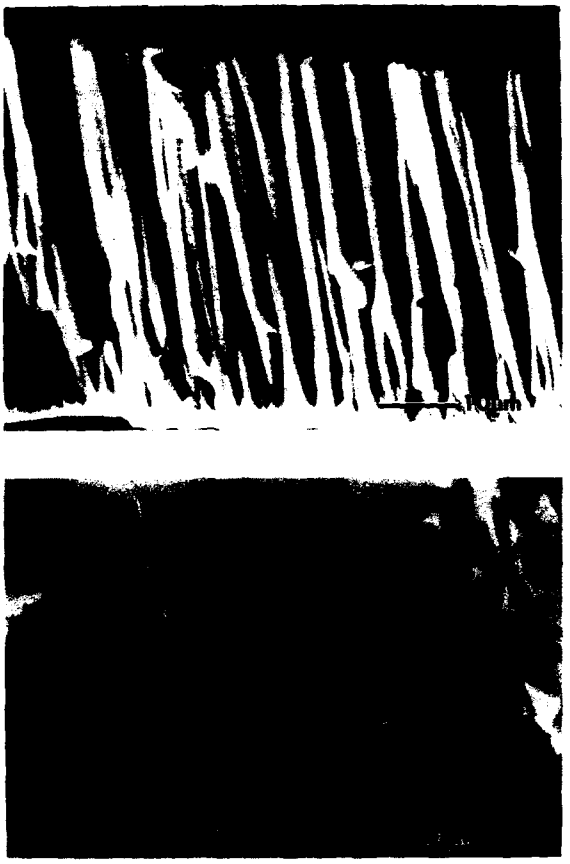


Figure 2 Scanning electron micrographs of modulated $Tl_xPb_yO_z/Tl_aPb_bO_t$ films. Micrographs are low (top) and higher (bottom) magnifications of a cross- sectional view of a fractured film. Film was deposited by cycling electrode between 0.05mA and 5mA in a solution of 0.005M $TlNO_3$ and 0.1M $Pb(NO_3)_2$ in 5M NaOH. Layer thicknesses are intentionally quite thick ($\sim 0.5\mu m$) so that SEM imaging is possible.

Table II Comparison of modulation wavelengths calculated from Faraday's law (Λ_f) and from X-ray satellite spacings (Λ_x) for ceramic superlattices deposited at various currents and dwell times. The electrode area ranged from 0.78 to 0.83cm^2.

i_a (mA)	t_a (s)	i_b (mA)	t_b (s)	Λ_f (nm)	Λ_x (nm)
0.05	40	5.0	0.4	5.9	5.9
0.05	50	5.0	0.5	7.4	7.4
0.05	60	5.0	0.6	8.3	8.0
0.05	70	5.0	0.7	9.7	9.9
0.05	80	5.0	0.8	11.5	11.6
0.05	90	5.0	0.9	12.3	12.9

ACKNOWLEDGEMENTS

One of the authors (J.A.S.) thanks Mitsubishi Corporation for financial support through a Mitsubishi Kasei faculty development award. We also thank Unocal Corporation for donation of all of the electrochemical instrumentation used in this research.

REFERENCES

1. J. A. Switzer, M. J. Shane, and R. J. Phillips, Science, 247, 444 (1990).
2. U. Cohen, F. B. Koch and R. Sard, J. Electrochem Soc., 130, 1987 (1983).
3. D. Tench and J. White, Metall. Trans. A, 15, 2039 (1984).
4. J. Yahalom et al., J. Mater. Res., 4, 755 (1989).
5. D. S. Lashmore and M. P. Daniel, J. Electrochem. Soc., 135, 1218 (1988).
6. L. H. Bennett et al., J. Magn. Magn. Mater., 67, 239 (1987).
7. R. J. Phillips, M. J. Shane, and J. A. Switzer, J. Mater. Res., 4, 923 (1989).

8. J. A. Switzer, Am. Ceram. Soc. Bull., 66, 1521 (1987).

9. J. A. Switzer, J. Electrochem. Soc., 133, 722 (1986).

10. W. Mindt, J. Electrochem. Soc., 116, 1076 (1969).

11. J. C. G. Thomas and D. W. Wabner, J. Electroanal. Chem., 135, 243 (1982).

12. M. Sakai, T. Sekine, and Y. Yamazaki, J. Electrochem Soc., 130, 1631 (1983).

13 W. Tillmetz and D. W. Wabner, Z. Naturforsch. Teil B39, 594 (1984).

14. V. N. Shukla and G. P. Wirtz, J. Am. Ceram. Soc., 60, 253 (1977).

15. C. R. Leavens and R. Taylor, Eds., "Interfaces, Quantum Wells, and Superlattices," (NATO Series B: Physics, vol. 179) (Plenum, New York, 1988).

16. E. E. Mandez and K. Von Klitzing, Eds., "Physics and Applications of Quantum Wells and Superlattices," (NATO Series B: Physics, vol. 170) (Plenum, New York, 1987).

17. P. T. Moseley, J. L. Hutchison, and M. A. M. Bourke, J. Electrochem. Soc., 129, 876 (1982).

THE CHEMICAL PROCESSING OF SILICATES FOR BIOLOGICAL APPLICATIONS - A REVIEW

L. L. HENCH* AND JUNE WILSON**
*Advanced Materials Research Center, University of Florida, One Progress Blvd., #14, Alachua, FL 32615
**Bioglass® Research Center, University of Florida, J413 J. Hillis Miller Health Center, Gainesville, FL 32610

ABSTRACT

A new application area for sol-gel processing biomaterials and implant devices, is presented. The concepts of bioactive fixation of implants is reviewed. Conventional processing methods for bioactive materials are compared with low temperature chemical processing. Advantages of sol-gel processing include new bioactive compositional ranges of ultraporous CaO-P_2O_5-SiO_2 biogel-glass powders. Clinical applications of bioactive implants are discussed.

INTRODUCTION

The scientific understanding of chemical processing of ceramics, glasses, and composites has matured [1,2] and several applications have reached commercialization. Sol-gel processing is now successfully used for films, powders, fibers, and even for as-cast net shape precision optical components [1,2]. This paper reviews a new application area for sol-gel processing; biomaterials or prosthetic (implant) devices. These new materials take advantage of the intermediate ultraporous state of gel processing. As summarized in Fig. 1, the thermal processing schedule used has six processing steps which lead to ultraporous matrices, without going to the seventh, full densification stage. Stabilization temperatures of pure silica components used for optics range from 650°C to 1000°C depending on pore size [2]. In contrast, the multicomponent biogel-glass systems are stabilized at lower temperatures of 400-600°C in order to avoid crystallization. As silica content of the biogel-glasses increases crystallization is suppressed and a broader range of stabilization treatments can be utilized (Fig. 1). In this paper the structural features of these porous gel systems and their potential applications are summarized. In addition, a brief review of the behavior of bioactive glass, glass-ceramic and ceramic implants is included to compare with the behavior of the new gel derived bioactive powders recently developed by Li et al. [3] and Whang et al [4].

Bioactive Ceramics

Until the seventies, when the reality of the term "bioactive" applied to implant materials entered the consciousness and the literature of the field acceptable implant materials were those considered inert. There are, of course, no such materials. All materials elicit a response when implanted in tissues. There are four main types of material/tissue response [5,6].

1) If a material is toxic, surrounding tissue dies.
2) If a material is not toxic but is resorbable the material is slowly replaced by tissues.
3) If the material is not toxic but is also inactive (formerly termed inert) the material is isolated by a thin, nonadherant fibrous capsule.

Mat. Res. Soc. Symp. Proc. Vol. 180. ©1990 Materials Research Society

4) If the material is not toxic but bioactive, it becomes attached to the adjacent tissue by an interfacial bond.

Examples of implant materials in the first category are understandably few but polymers stabilized with toxic materials have produced this effect. Degradable sutures and tricalcium phosphates are well known examples of the second, and medical grade silicone rubber, dense alumina ceramic, and stainless steel are widely used examples of the third group [5]. Examples of materials in the fourth category have been mainly ceramics which have been developed worldwide for use in hard tissue replacement [6,7] although recent publications have shown that certain co-polymers are bioactive [8] and certain ceramics are useful in both hard and soft tissue applications [9].

Bioactive ceramics have been prepared and tested in many different compositional ranges and forms. All contain calcium phosphates and all are able to form a bond with bone. Bioglass®, the original bioactive material [10], is a transparent glass which contains silica and oxides of sodium, calcium and phosphorus. Ceravital®, developed in Germany, is a glass-ceramic based on Bioglass® which contains, in addition small quantities of the oxides of potassium and magnesium [11]. A third glass-ceramic (developed in Kyoto, Japan) is named A/W glass-ceramic to indicate its apatite-wollastonite structure [12]. Another machineable bioactive material which comes from Jena in E. Germany contains apatite for bioactivity and fluorophlogopite for machinability and thus introduces fluoride and aluminosilicate to the composition [13].

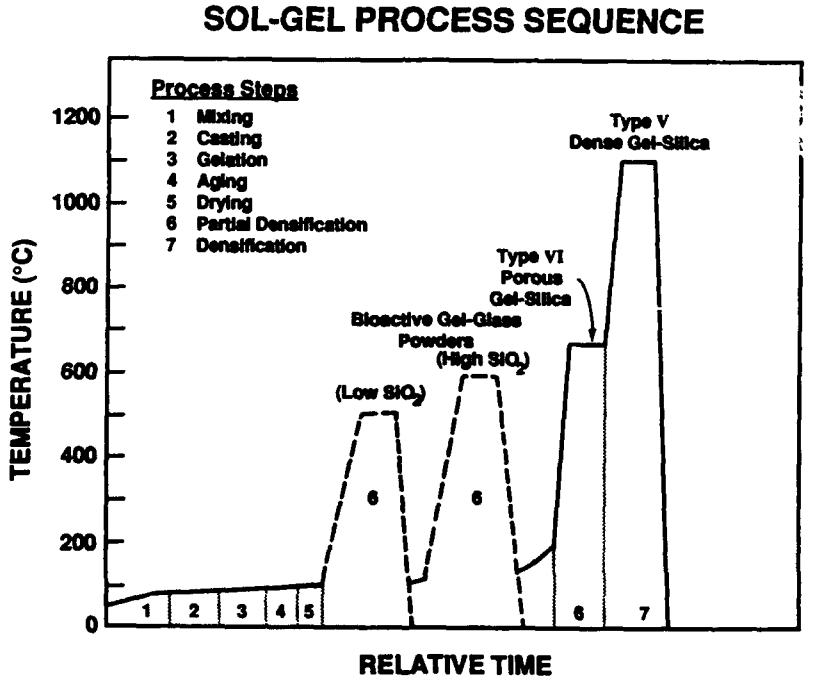


Fig. 1. Comparison of sol-gel processing schedules for Types V and VI gel-silica optics with bioactive gel-glasses.

Common to all of these glass and glass-ceramic materials is the delivery to the interface with bone calcium phosphate in the form of hydroxylapatite crystallites, which matches the natural host bone mineral. Inclusion of other elements may enhance other properties of the material but the essential requirement for bonding remains the hydroxylapatite crystallites. Silica and alkaline oxides affect the biochemistry of the interface as well as the chemistry of the materials and their fabricability and machinability.

As a consequence of the identification of the pivotal role of hydroxylapatite in bone bonding, a very large number of researchers have synthesized and optimized mineral hydroxylapatite as implantable materials [14-16]. These implants may be micro or macroporous and have been produced as solids and powders and, via a replanieform process, reproduce the elaborate structure of species of marine corals [17]. However, none of the hydroxylapatite materials contains silica, which is a vital component of the materials being discussed herein.

However the calcium phosphate is presented or accumulated at the tissue interface, the presence of mixed hydroxy carbonate apatite as crystallites is the essential first step in the development of the bonded interface. These crystallites nucleate and bond to interfacial metabolites in the tissues, such as mucopolysaccharides, glycoproteins and collagen. The rate at which these reactions occur and the time needed for the bonded interface to mature and acquire sufficient strength to function varies with the composition of the material, as does the eventual thickness of the bonded area across which stress must be transferred [18].

The presence of calcium phosphate is essential to bioactivity, the nucleation within the glass which converts a glass to a glass-ceramic does not affect bioactivity, although effects on long term stability may occur depending on the proportion of glassy to crystal phase in the glass-ceramic. Multivalent cations are known to affect bioactivity adversely, especially Al^{+3}, Zr^{4+} and Ta^{5+} which affect the glass structure as well as the intercellular mineralization mechanisms in cells [11,19]. The inclusion of relatively high concentrations of Al^{3+} in the machineable bioactive material from Jena [13] is possible only because the cells in the tissue are protected from the ions which are bound tightly in the phlogopite phase.

The compositional effects which control bioactivity appear to be a complex interdependence of physico chemical and biological factors that depend on interfacial cationic and anionic concentration kinetics and solubility limits. By changing these kinetic reactions the rate at which hard tissue forms at an implant's interface can be altered and measured. The index of bioactivity of a material is defined as the inverse of the time required for more than 50% of the interface to be bonded [18].

$$I_B = 100/t_{0.5bb}$$

The 50% bonding criterion is selected since the interface between implant and bone is irregular. The essential contact between implant surface and the cells which colonize it, osteoblasts, chondroblasts and fibroblasts, varies with the fit of the implant and the preparation of the implant site. All bioactive implant materials require an incubation period before bonding occurs and the *in vivo* I_B value for different materials varies over a very wide range, as shown in Ref. 18. The compositional limit of bioactivity for soda-lime-phosphate-silica systems with constant 6% wt% P_2O_5 is shown in Figure 2 [5]. Inside the boundary marked A are all of the bioactive glasses and glass-ceramics currently studied. The data presented in Ref. 18 indicate that there are Iso - I_B contours within the bioactivity boundary. Comparative data from the literature and extrapolation based on relative reaction kinetics suggest that the *in vivo iso* I_B *contours are as shown* in Fig. 2. There is a sharp decrease in I_B as the ratio of SiO_2 to (Na_2O + CaO) approaches the boundary.

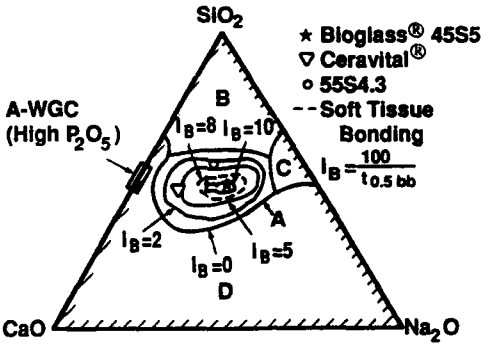


Fig. 2. Compositional dependence of tissue bonding. All compositions in the center have a constant 6 weight % P_2O_5.

Addition of very small amounts of multivalent cations have been shown to reduce bioactivity [11] thus, even minimal contamination of compositions close to the I_B boundary can eliminate bioactivity. Attempts to develop bioactive coatings on high strength substrates, in order to avoid the mechanical weakness of bioactive glasses, are compromised by this contamination effect.

Within Zone A in Fig. 2 a smaller zone within which soft tissue bonding can occur has now been identified. Compositions within this zone have only been identified for Bioglass® materials with very high bioactivity. Compositions which do not bond to soft tissue, Ceravital® and A/W glass-ceramics, are outside this area. The interaction of glass-ceramics, such as these are, with soft tissue is complicated by the occurrence of preferential dissolution of the glassy phase when in contact with cellular enzymes and other products of the cells found in connective tissue. This causes a roughening of the materials surface and eventual disintegration of the crystalline phase which then prolongs and increases the cellular interaction [11]. Use of bone pate at the interface with soft tissue has been promoted to protect such materials from the tissue [20].

Applications of Bioactive Ceramics

The ability of bioactive materials to bond to hard tissues was first seen as a potential solution to the problems associated with loosening of orthopaedic devices, such as hip and knee prostheses. Although the concept of bioactive bonding as a replacement for bone cement has been proven many times in many animal species the development of devices in which chemical rather than mechanical fixation is used, is still in process. In orthopaedic applications hydroxylapatite has been used to improve mechanical fixation but not yet to substitute for it.

Successful application of bioactive materials as space-filling implants after tumor resection has taken place in Kyoto, Japan and in Dresden, Germany [7]. In dental surgery bioactive materials have been used in many applications, in alveolar ridge maintenance [21] and ridge augmentation [16] and as coatings on loadbearing implants [5,22]. As powders they have been used to treat the bone loss which occurs in periodontal disease [7]. Bioactive materials can be used to make anchors for orthodontic treatment which allow teeth to be moved in situations where no suitable anchor teeth are available [23]. Bioactive materials as powders have proven effective as pulp capping agents in animal studies.

The ability of Bioglass® to coat metal has been used to coat electrodes which are immobilized in the mastoid bone as an essential component of cochlear prostheses used to treat profound deafness. Treatment of conductive deafness has been more successful since the development of middle ear prostheses made from bioactive materials [7,20,24].

The identification and application of the soft tissue bond to certain Bioglass® compositions has widened the field in which these materials may be used clinically. The middle ear device must attach to the remains of the stapes, which forms the critical interface with the oval window and fluids of the inner ear. A bone bond is essential at that junction. The other end of the device must attach to the soft tissue of the eardrum so that the vibrations received by the outer ear may be transmitted across the implant. Unfortunately, the interaction of materials which do not bond to soft tissues, (that is those made from inert materials or bioactive materials outside the dashed region E in Fig. 2) usually results in extrusion, due to interfacial movement. The extrusion through the eardrum destroys the eardrum itself and replacement with another prosthesis is made more difficult. With soft tissue bonding the bonded interface has no interfacial movement and extrusion does not occur. It has also been shown clinically that this bond can be made with a grafted, that is repaired, eardrum [24].

Another area in which interfaces with soft and bony tissue are normally present is the maxillofacial area. After trauma or surgery as well as for cosmetic reasons space filling materials with bony hardness are needed which must be immobilized in hard and soft tissues. Comparison of Bioglass® implants with all other available materials showed that they were superior to those made from bone or porous inert materials which are presently available [25].

Processing of Bioactive Ceramics

Many alternative methods of processing of bioactive ceramics have been developed, as summarized in Table I. Most of these methods involve high temperatures and tend to be specific for an individual material. Often multiple process steps are required. Consequently, there is considerable potential for use of chemically based processing to improve the preparation of presently developed bioactive ceramics. There is also the exciting possibility of achieving new bioactive ceramics by use of low temperature chemical processing.

Potential Advantages of Chemical Processing of Biomaterials

Many of the advantages of sol-gel processing observed for porous optical matrices are also relevant for implant applications. They divide into three general areas: 1) Net Shape Casting, 2) Molecular Chemistry Processing, and 3) Control of Ultrastructural Porosity. The features of these areas applicable to biomaterials are summarized in Table II.

At present only a very few features listed in Table II have been demonstrated for bioceramics. However, the incentive certainly exists to explore these potential advantages. As one example, a composite of Bioglass® powders and a resorbable polymer is being tested for use in controlling urinary incontinence [26]. The rheology of the composite, which must be injected through a fine needle, is very important and spherical powders are advantageous. Sol-gel processing offers a much easier and less expensive route to producing spherical bioactive powders than does a high temperature molten glass shot tower.

Table I

PRESENT METHODS for PROCESSING BIOACTIVE MATERIALS

Melting, Casting to Shape
Bioglass

Melting, Casting, Ceraming, Machining to Shape
Ceravital

Melting,Fritting, Mixing, Hot Pressing to Shape
A/W Glass-Ceramic

Melting,Fritting, Grinding,Sieving
Bioactive Glass Powders

Solution-Precipitation, Grinding, Calcination
TriCalciumPhosphate,ALCAP Powders

Solution-Ppt, Grinding, Pressing to Shape, Sintering
Hydroxyapatite

Flame Spray Coating
Bioglass on Metal

Glaze Coating
Bioglass on Alumina

Enamel Coating
Bioactive Glass on Metal

Plasma Spray Coating
Hydroxyapatite on Metal

Melt Impregnation of Sintered Metal Fibers
Stainless Steel or Titanium Fiber Reinforced Bioglass

Hot Pressed Glass-Ceramic with Metal Powders
Ceravital and Titanium

Hot Pressed Glass-Ceramic with Transformation Toughened Zirconia Powders
Zirconia Modified A/W Glass-Ceramic

Bioactive Powders with Polymers
Hydroxyapatite with Collagen
Hydroxyapatite with BMP

Table II

POTENTIAL ADVANTAGES OF THE SOL-GEL PROCESS FOR BIOMATERIALS

Net Shape/Surface Casting of Devices

Production of Small Devices

Production of Small Quantities

Surface Replication of Morphological Fixation Features

Casting of Internal Structures

Molecular Chemistry Processing
Additional Composition Ranges

Higher Purity

Greater Homogeneity

Fewer Defects

Controlled Powder Sizes w/o Grinding and Sieving

Powder Shape Control

Controlled Ultrastructural Porosity
Enhanced Bioactivity

Controlled Chemical Doping

Controlled Surface Hydration States

Controlled Surface Oxidation States

Impregnation with Second Phases

Lower Densification Temperatures

Laser Assisted Densification

Coating of Polymers

Coating of Metals

Coating of Ceramics

Bioactive Gel-Glasses

Recent developments by Whang et al. [4] show that it is possible to make four component Na_2O-CaO-P_2O_5-SiO_2 bioactive gel-glass powders using sol-gel processing methods. The thermal schedule used for stabilization and densification of these low SiO_2 compositions is summarized in Fig. 1.

As discussed above, the principal criterion for bioactivity is development of a hydroxylapatite (HA) layer on the material when exposed to a physiological solution. The more rapid the development of the HA layer, the higher is the I_b value. Infrared reflection spectroscopy can determine the formation of the HA layer. Figure 3A compares Na_2O-CaO-P_2O_5-SiO_2 melt-derived Bioglass® FTIR spectra before and after reaction to a simulated physiological solution. The IR peaks characteristic of HA are present after reaction at 37°C for 4 days. See Kim et al. [27] for a detailed discussion of peak assignments of HA layers grown on bioactive glasses. Figure 3B, from Whang et al, compares a 52S9.1 bioactive Na_2O-CaO-P_2O_5-SiO_2 gel-glass before and after reaction in simulated physiological solution (tris-buffer solution) for 4 days after 37°C. The P-O stretching vibrations characteristic of a HA surface layer are present. The sharpness of the peaks indicates that the HA has crystallized. These results show that sol-gel processing can produce bioactive materials that form HA layers.

Studies of Li et al [3] have shown that it is possible to produce gel-glasses that are bioactive with only CaO-P_2O_5-SiO_2 in the composition. Figure 3C compares the FTIR spectra of one of these bioactive gel-glasses before and after reaction at 37°C in a simulated physiological solution. The rate of HA film formation is so rapid after only 4 hours the surface of the particles is completely covered with HA. X-ray diffraction confirms the formation of hydroxyapatite crystallization for the powders [3].

In addition to the increased rate of HA film formation, the sol-gel processing of the CaO-P_2O_5-SiO_2 glass powders increases the compositional range of bioactivity by a significant amount. The new compositional field of bioactivity is illustrated in Fig. 4 on a four component Na_2O-CaO-P_2O_5-SiO_2 diagram. Bioactive gel-glasses can contain as much as 90 mole % SiO_2 with 4 mole % P_2O_5 and 6 mole % CaO and still show formation of a HA layer within 7 days reaction of 37°C. The previous composition limit of bioactivity was established at 60%, as shown in Fig. 2. Thus, the important potential advantage of low temperature solution processing of yielding new compositions, Table II, has been realized. The mechanism proposed for the enhanced bioactivity and the larger compositional region of bioactivity is the heterogeneous nucleation of HA on the very small pores of the sol-gel derived gel-glasses [3]. Consequently, the ability to produce and control a residual pore network in the bioactive materials is as important in biological applications as it is in optical applications.

Implications

It has been established for many years that a critical concentration of biologically fixed silicon is essential for the mineralization of bone [28]. Experiments have shown that there is an enrichment of silicon ahead of the calcium-phosphate mineralization front during ossification. However, the mechanisms of biological fixation of silicon, the metabolic pathways for silicon fixation, and the role of silicon in the cellular or acellular processes of mineralization are still not understood. There is also growing evidence that the loss of biological silicon from arterial walls is associated with the accumulation of plaque and the onset of atherosclerosis [29]. The mechanisms are still uncertain.

The successful development of gel-glasses that contain as much as 90 mole % SiO_2 and still form HA layers indicates that the presence of silanol condensation reactions in an aqueous environment may be catalytic in the

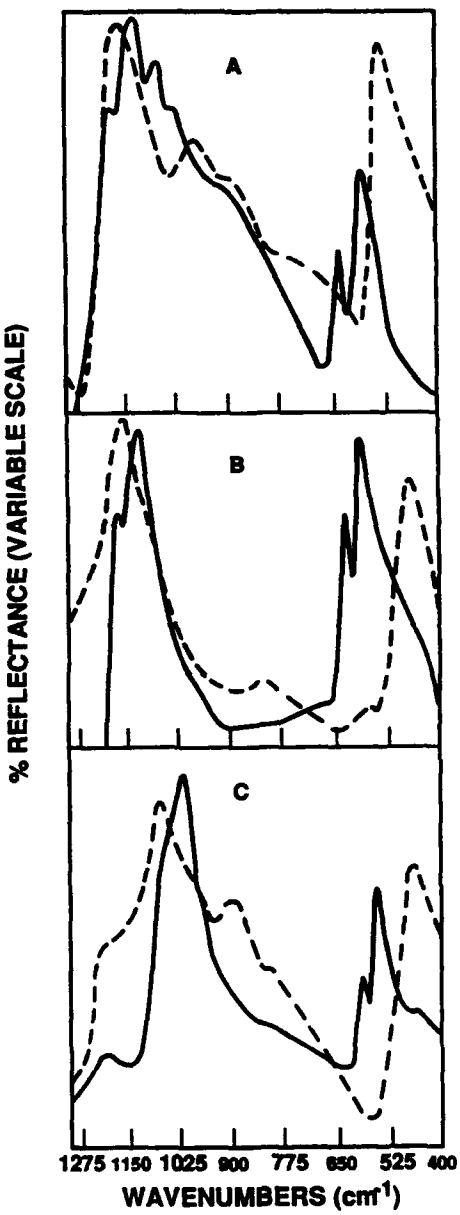
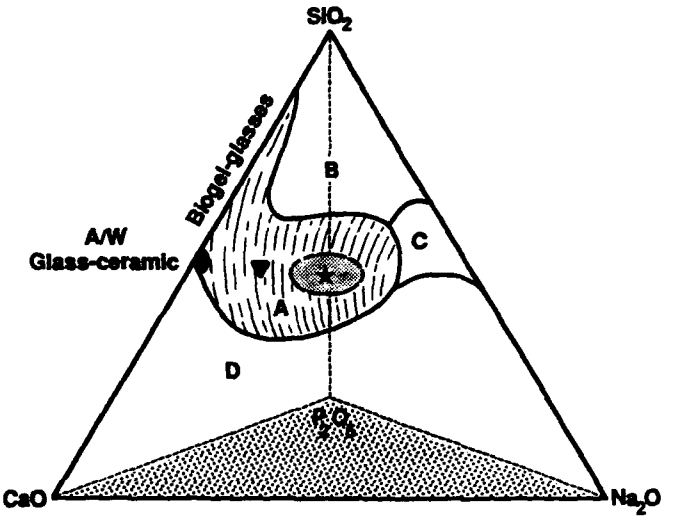


Fig. 3. Comparison of FTIR spectra before (dashed lines) and after (full lines) exposure to simulated physiological solution. (A) Melt derived 45S5 Bioglass® (Ha layer developed after 4 days reaction); (B) Sol-gel derived 52S9.1 Bioglass® (HA layer developed after 4 days reaction); (C) 55 mole % SiO_2-41 mole % CaO-4 mole % P_2P_5 Biogel-glass (HA layer developed after 4 hours reaction).



Bioactive Bonding Boundaries

A Bonding at 30 days or less
B Non bonding, reactivity is too low
C Non bonding, reactivity is too high
D Non bonding, non glass-forming

★ Bioglass ® 45S5
▼ Ceravital ®

– – – Soft Tissue Bonding

Fig. 4. Compositional dependence of bioactivity of Na_2O-CaO-$P_2O_5$$SiO_2$ implants.

nucleation and crystallization of hydroxylapatites from amorphous calcium phosphate solutions. The seminal paper on bioactive bone bonding [10] showed that a melt-derived 45S5 Bioglass® surface acted as a heterogeneous catalyst for HA formation. However, it has been assumed for many years since that early work that the critical step was the alkali-proton ion exchange leading to a localized increase in hydroxyl concentrations that accelerated the calcium phosphate precipitation and crystallization. The recent discovery [3] that alkali-free microporous CaO-P_2O_5-SiO_2 gel-glasses have even more rapid rates of HA formation suggest that the exothermic condensation of surface silanols may be involved in nucleating HA crystallites. If this can be proven in subsequent experiments it may provide the basis for an understanding of the role of biologically fixed silicon in *in vivo* mineralization and prevention of the loss of biologically fixed silicon and consequent prevention of atherosclerosis.

Acknowledgements

The authors are grateful for the financial support of the Air Force Office of Scientific Research under contract #F49620-88-C-0073, and the Division of Sponsored Research, University of Florida.

References

1. C. J. Brinker and G. W. Scherer, Sol-Gel Science (Academic Press, New York, 1989).

2. L. L. Hench and J. K. West, Chem. Rev. 90, 33-72 (1990).

3. R. Li, A. E. Clark and L. L. Hench, "Bioactive Glass Powders by Sol-Gel Processing," Trans. SFB Vol. XIII (1990)

4. C. M. Whang, A. E. Clark and L. L. Hench, "Preparation and Characterization of Bioactive Glasses by the Sol-Gel Process," J. Biomaterials (submitted).

5. L. L. Hench and E. C. Ethridge, Biomaterials: An Interfacial Approach, (Academic Press, New York, 1982).

6. L. L. Hench and J. Wilson, Science 226, 630 (1984).

7. T. Yamamuro, L. L. Hench, and J. Wilson, Handbook of Bioactive Ceramics, Vol I: Bioactive Glasses and Glass-Ceramics; Vol II: Calcium-Phosphate Ceramics, (CRC Press, Boca Raton, FL. 1990)

8. D. Bakker, C. A. van Blatterswijk, S. C. Hesseling, W. F. Daems, and J. J. Grote, J. Biomed. Maters. Res. 24, 277 (1990).

9. J. Wilson, G. Pigott, F. J. Schoen, and L. L. Hench, J. Biomed. Mater. Res. 15, 805 (1981).

10. L. L. Hench, R. J. Splinter, W. C. Allen, and Greenlee, Jr., J. Biomed. Res. Symp. No. 2. Interscience, N.Y., (1972) p. 117.

11. V. Gross, R. Kinne, H. J. Schmitz, and V. Strunz, CRC Critical Reviews in Biocompatibility 4, 2 (1981).

12. T. Nakamura, T. Yamumuro, S. Higashi, T. Kokubo, and S. Ito, J. Biomed. Mater. Res. 19, 685 (1985).

13. W. Hohland, W. Vogel, K. Naumann, and J. Gummel, J. Biomed. Mater. Res. 19, 303 (1985).

14. K. de Groot, Bioceramics of Calcium-Phosphate (CRC Press, Boca Raton, FL., 1983).

15. M. Jarcho Clin. Orthop. Relat. Res. 157, 259 (1981).

16. R. Z. Le Geros, Adv. Dent. Res. 2, 164-180 (1988).

17. E. W. White, J. N. Webber, D. M. Roy, E. L. Owen, R. T. Chiroff, and R. A. White, J. Biomed. Mater. Res. Symp. 6, 23-27 (1975).

18. L. L. Hench, in Bioceramics: Materials Characteristics Versus In-Vivo Behavior, Vol 523, edited by P. Ducheye and J. Lemons (Annals N.Y. Acad. Sci. 1988) p. 54.

19. V. Gross and V. Strunz, J. Biomed. Mater. Res. 19, 251 (1985).

20. R. Reck, S. Storkel, and A. Meyer, in Bioceramics: Materials Characteristics Versus In-Vivo Behavior, Vol. 523, edited by P. Ducheyne and J. Lemons (Annals NY Acad. Sci. 1988) p. 100.

21. H. R. Stanley, M. B. Hall, F. Colaizzi, and A. E. Clark, J. Prosth. Dent. 58 (5), 607-613 (1987).

22. R. V. McKinney, Jr. and J. Lemons, The Dental Implant, (PSG Publishing Co., Littleton, Mass, 1985),.

23. J. B. Gray, M. E. Steen, G. J. King and A. E. Clark, Am. J. Orthodontics 83 (4), 311 (1983).

24. G. E. Merwin, Annals of Otorhinolaryngology 95 (1), 78-82 (1986).

25. J. Wilson and G. E. Merwin, J. Biomed. Maters. Res. 22 (A2), 159 (1988).

26. M. Ramer, June Wilson, R.D. Walker and A. E. Clark, Trans. Society for Biomaterials, Charleston, SC, Vol. XIII (1990).

27. C. Y. Kim, A. E. Clark, and L. L. Hench, J. Non-Crystalline Solids 113, 195 (1989).

28. Silicon Biochemistry, CIBA Foundation Symposium #121 (John Wiley and Sons, New York, 1986).

29. L. L. Hench and G. Orcel, J. Non-Crystalline Solids 82, 1-10 (1986).

PART XIV

Late Papers Accepted

MAGNETIC RESONANCE AS A STRUCTURAL PROBE OF A URANIUM (VI) SOL-GEL PROCESS

Charles M. King*, R. Bruce King**, A. Ronald Garber***, Major C. Thompson* and Bruce R. Buchanan*
*Westinghouse Savannah River Company, Aiken, SC **Department of Chemistry, University of Georgia, Athens, GA ***Department of Chemistry, University of South Carolina, Columbia, SC

ABSTRACT

Nuclear Magnetic Resonance (NMR) investigations on the Oak Ridge National Laboratory process for sol-gel synthesis of microspherical nuclear fuel (UO_2), has been extremely useful in sorting out the chemical mechanism in the sol-gel steps. ^{13}C, ^{15}N, and ^{1}H NMR studies on the HMTA gelation agent (hexamethylenetetramine, $C_6H_{12}N_4$) has revealed near quantitative stability of this adamantane-like compound in the sol-gel process, contrary to its historical role as an ammonia source for gelation from the worldwide technical literature. ^{17}O NMR of uranyl (UO_2^{++}) hydrolysis fragments produced in colloidal sols has revealed the selective formation of a uranyl trimer, $[(UO_2)_3\ (\mu_3\text{-}O)(\mu_2\text{-}OH)_3]^+$, induced by basic hydrolysis with the HMTA gelation agent. Spectroscopic results will be presented to illustrate that trimer condensation occurs during sol-gel processing leading to layered polyanionic hydrous uranium oxides in which $HMTAH^+$ is occluded as an "intercalation" cation. Subsequent sol-gel processing of microspheres by ammonia washing results in in-situ ion exchange and formation of a layered hydrous ammonium uranate with a proposed structural formula of $(NH_4)_2\ [(UO_2)_8\ O_4\ (OH)_{10}] \cdot 8H_2O$. This compound is the precursor to sintered UO_2 ceramic fuel.

INTRODUCTION

Beginning in the late 1950s, sol-gel processes were developed for the preparation of nuclear reactor fuels of U, Th, and Pu in the form of microspheres required for high-temperature, gas-cooled reactors. These fuels are commonly coated with pyrolytic carbon or other ceramics to serve as "pressure vessels" to contain fission products. The sol-gel processes for nuclear fuel were developed at Oak Ridge National Laboratory (ORNL) [1-3] and were based on the gelation of colloidal sols by "internal" gelation methods previously developed for nuclear fuel synthesis in the Netherlands [4]. In this process, hexamethylene tetramine (HMTA) is mixed at about 0°C, in the presence of urea, with a uranyl nitrate solution causing hydrolysis of the uranyl cation to a hydrous uranium oxide network. HMTA functions as a weak base for hydrolysis and is also assumed to decompose to ammonia and formaldehyde. Ammonia is assumed to be produced in-situ or "internally" during the gelation process and is assumed to be the key component causing gelation of the hydrous uranium oxide. All of these steps are conducted in equipment (i.e., cannulae) to form spherical drops [5] which are converted to gelatinous microspheres by suspension in a hot organic liquid (i.e., trichloroethylene). The hydrous uranium oxide in microspherical form is eventually converted to ceramic UO_2 by sintering.

EXPERIMENTAL

The rate of hydrolysis of HMTA was monitored by ^{13}C NMR and ion chromatography as a function of pH, temperature, urea and uranyl concentration. ^{15}N and ^{1}H NMR were utilized to provide structural information on hydrolysis products. Uranyl gels were prepared by methods published by the ORNL [1, 2]. ^{17}O NMR was utilized to monitor the hydrolysis fragments of the uranyl cation with ^{17}O exchange with labeled water induced by photolysis. The details of ^{17}O labeling and NMR results are described in a companion publication [6]. NMR spectra were obtained on Bruker instrumentation (^{1}H, ^{13}C:AM300; ^{17}O, ^{15}N:AM500) in the Chemistry Department at the University of South Carolina. Chemical shifts are reported

Mat. Res. Soc. Symp. Proc. Vol. 180. ©1990 Materials Research Society

relative to TMS for ^{1}H and ^{13}C spectra and relative to ^{17}O water referenced to an external D_2O/H_2O standard. Concentrated (1.0 to 3.9M) aqueous stock solutions of uranyl nitrate and uranyl chloride were prepared in water enriched to 5 to 10% ^{17}O from the 0.037% natural abundance using commercial 28% ^{17}O water from ICON Services, Inc. (Summit, New Jersey). NMR peak areas were obtained by spectral integration, and were calibrated by reference to a set of standard HMTA solutions. NMR temperature control was obtained via heat input from a variable temperature controller in 10-20°C incremental steps from ambient to permit equilibration. Calibration was obtained using the proton spectra of ethylene glycol in DMSO-d^6 and correlating the difference ($\Delta\upsilon$) in chemical shift of the methylene and alcohol resonances with $T^{o}K = 466 - 1.694\ \Delta\upsilon$, based on Bruker procedures.

Conditions of chemical composition, pH and temperature for gelation studies were obtained from the work of Collins et. al. [2] of ORNL, who very thoroughly demonstrated conditions for gelation of uranyl compositions in the temperature range of 62-92°C. Collins, et. al., demonstrated in detail that variable pH is observed in gel synthesis but pH never decreased below 3.0 under a wide variety of UO_2^{++}/HMTA/Urea compositions. The pH generally varied from 3.4 to 5.2 during gelation with extremes of 3.0 to 6.0 from the Collins, et. al., work. This range is very important in quantifying HMTA stability to hydrolysis during gelation. Gelation induction periods were generally found to be $\leq$1 minute, and, in many cases, on the order of seconds [2]. Temperature extremes in pilot scale gelation columns at the WSRC never exceeded 85°C and this temperature was chosen as the upper limit for HMTA and uranyl hydrolysis/gelation studies.

Fourier Transform Infrared spectra (FTIR) were recorded with a Nicolet 20-DX Fourier Transform Interferometer after preparation of dried gels and solids in a potassium bromide matrix compressed to 10,000 psig. X-Ray powder diffraction (XRPD) patterns were recorded on a Siemans Diffrac-500 X-Ray Diffractometer using CuKα radiation and a scintillation detector. Uranium samples were handled in a completely contained Siemans apparatus. X-Ray diffraction patterns of experimental samples were compared to reference patterns using the International Centre for Diffraction Data (Swarthmore, Pa.) Joint Committee on Powder Diffraction Standards (JCPDS) files for graphic pattern evaluation including phase identification and "d" spacing.

RESULTS AND DISCUSSION

^{1}H and ^{13}C NMR of HMTA Solutions and Gels

The proton NMR spectra of HMTA for a uranium gel-forming system was first reported by Soviet workers in the Russian Journal of Inorganic Chemistry [11] for the uranyl (VI). nitrate/HMTA/urea/water system. The Soviet workers report "the formation of a gel probably proceeds via hydrolysis of uranyl ions with the subsequent formation throughout the solution of a hydrogen bonded skeleton through hydroxyl bridges". Uranyl hydrolysis occurred due to the increase in solution pH resulting from HMTA protonation. The Soviets also reported no evidence for the formation of ammonia or formaldehyde due to HMTA decomposition during uranyl gel synthesis by ^{1}H NMR monitoring. Our results are consistent with Soviet [11] and British [10] reports. ^{13}C NMR was found to be very instructive of structural modifications during hydrolysis and gelation. Figure 1a is the ^{13}C NMR of a 3M HMTA solution at pH 8.9 and 75°C. The nonprotonated form exhibits a single resonance at 75.6 ppm—confirming thechemical and magnetic equivalence of the six methylene carbon atoms of the adamantane-like structure (inset). Area integration of the signal over one hour showed no change (±1%) and no new resonances—implying complete stability. The ^{13}C NMR spectrum was monitored as a function of pH, time, temperature, urea, and uranium concentration to test for hydrolytic instability under gelation conditions. Some observations are also presented in Figure 1 to illustrate the trends. At 85°C and pH 3.2, three new resonances appear at 46.4, 73.6, and 83.4 ppm and increase with time (stack spectra) in an approximate ratio of 1/2/3. HMTA is converting slowly to a highly symmetric new product whose carbon framework is similar to HMTA. The weak 46.4 ppm resonance is consistent in chemical shift with a carbon adjacent

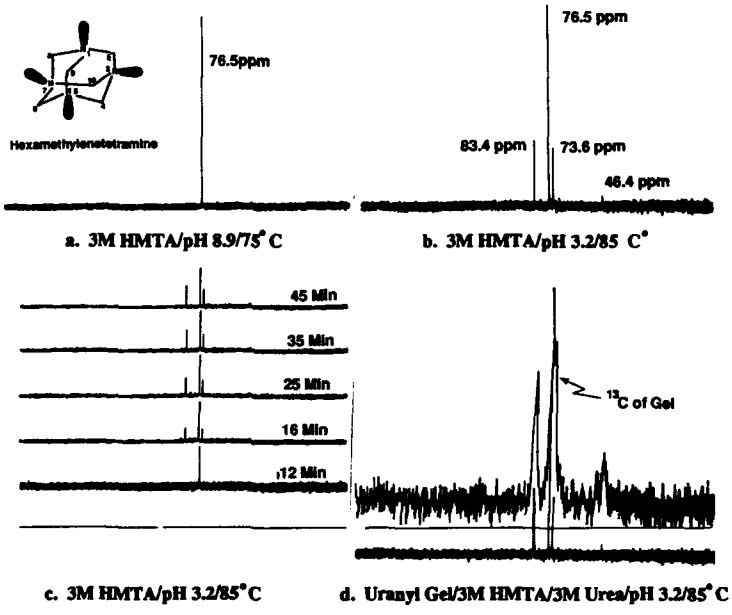


Figure 1. ^{13}C NMR of 3M HMTA solutions and gel

to a primary amine (i.e., CH_2 - NH_2) and the latter resonances reflect a carbon environment similar in structure to HMTA. The ^{13}C NMR of a uranyl gel structure containing urea and HMTA is significantly broadened due to increased gel viscosity but the same pattern is discernable. The sol-to-gel transition can be observed in a magnetic field. Formaldehyde or polyoxy methylene oligomer resonances of aqueous formaldehyde polymers, expected at ~90 ppm [12], were never observed in the pH range of 2.0 to 8.9 even at high gelation temperatures. This was confirmed by recording the ^{13}C NMR spectrum of 30% aqueous formaldehyde which clearly showed a distinct but very complex pattern in the low field (~90 ppm) region [14]. Integration of the observed HMTA ^{13}C resonances was recorded with time [14]. The half-life for HMTA decomposition by hydrolysis is ~70 minutes at 85°C, pH 3.2 and is independent of the presence of urea and uranium (zero order). The reaction or residence time for sol-gel synthesis of microspherical particles is is known to be ≤3 minutes based upon ORNL experience [1, 2]. Clearly, HMTA under these conditions is nearly quantitatively stable based upon NMR signal integration.

^{17}O NMR of Uranyl Hydrolysis Fragments Under Gelation Conditions

^{17}O NMR was utilized to monitor uranyl speciation under sol-gel conditions [6]. Specifically, in the ORNL flowsheet, "Acid Deficient Uranyl Nitrate" (ADUN) is prepared as the "sol" and pH adjustment with HMTA is conducted to prepare the feed for the gelation step under microsphere forming conditions. The composition of ADUN has not been elucidated. Prior ^{17}O NMR work by Japanese [15] and Soviet [16] researchers had illustrated the utility of ^{17}O NMR in characterization of uranyl hydrolysis products as a function of pH, temperature, and ligand complexation by monitoring the ^{17}O resonance of the axial uranyl oxygen. This prior work was used to assist in making assignments of uranyl hydrolysis oligomers based upon chemical shift measurements and dynamic modification of observed resonances as a function of pH adjustment. ^{17}O has a spin of 5/2 and an associated nuclear quadrapole moment [7] which may induce line broadening, particularly in viscous gels. Figure 2a illustrates the ^{17}O NMR resonances of the axial uranyl oxygens for synthetic ADUN compositions induced by extraction of the counter ion by tri-n-decyl amine in xylene—a known method for synthesis of

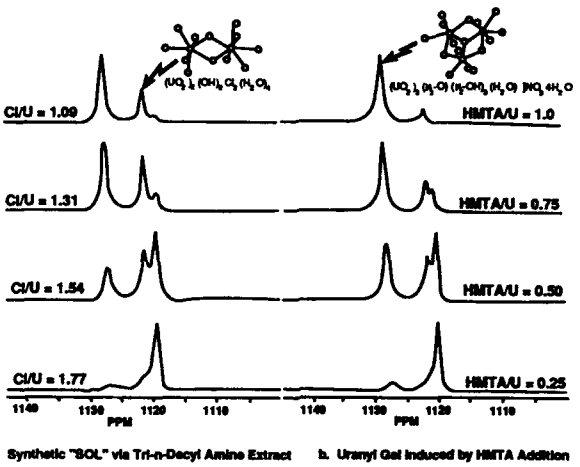


Figure 2. ^{17}O NMR of UO_2^{++} hydrolysis fragments in the axial oxygen region

a colloidal sol [1-6]. The spectra clearly show the monomer, UO_2OH^+; the dimer $(UO_2)_2(OH)_2^{++}$, and the trimer, $(UO_2)_3(OH)_5^+$, at approximately 1119.4, 1121.2, and 1127.7 ppm respectively [6, 15]. When a tertiary amine base, such as HMTA, is used to induce hydrolysis (Figure 2b) the spectra are similar but greatly modified with preferential formation of trimer (95%) in the presence of the gelation agent. These results also provide a clue for the role of the urea in the ORNL flowsheet. Urea complexes, probably by oxygen lone pair donation via the carbonyl functionality, to the equatorial coordination sphere of the uranyl oligomers [17]. This was observed as minor downfield shifts of all the resonances, as reported by Japanese workers [15, 17], due to increasing base strength of the equatorial ligands of the uranyl ion. Urea promotes solution stability of the uranyl hydrolysis fragments and prevents premature precipitation of the "sol" oligomers upon addition of a base—such as HMTA. Hence, urea and HMTA are both integral in the preparation of a stable uranyl gel. Urea promotes colloidal uranyl oligomer stability by ligand coordination and prevents premature uranium precipitation. HMTA provides the pH adjustment necessary for a gel network to form, induces uranyl trimer formation, and probably promotes the formation of a stable gel network by intra-molecular and inter-molecular hydrogen bonding.

A schematic of the proposed molecular complex of the uranyl trimer, urea, and HMTA is shown in Figure 3. Each uranyl group is in pentagonal bipyramidal coordination [18-21] with the equatorial coordination number satisfied by urea or water complexation as a ligand (L). The triad of uranyl groups is stabilized by a μ_3-oxo bridge [19-21] and μ_2-OH bridging [18]. Intra-molecular hydrogen bonding with HMTA occurs via hydroxyl bridges with proton donation to a lone pair nitrogen of HMTA. The other nitrogen lone pairs can participate in inter-molecular hydrogen bonding establishing a gel network. Further support for this representation was found by observation of the Fourier Transform Infrared Spectra (FTIR) of HMTA in the gel structure (Figure 4). HMTA exists in the gel structure as $HMTAH^+$ characterized by the splitting of degenerate C-N vibrations (1030 cm^{-1}) due to nitrogen protonation and distortion of the cage structure [13] causing a change of molecular symmetry from T_d to C_{3v}. In addition, a complex pattern around 2500 cm^{-1} is characteristic of the quaternary ammonium species. This gel form was further substantiated by FTIR comparison with the simple hydrochloride salt of HMTA (HMTA · HCl) [30].

The Structure of the Hydrous Uranium Oxide Precursors to Sintered UO_2

In the ORNL flowsheet, gelatinous microspheres are washed with 0.5M NH_4OH, which is assumed to leach impurities such as urea, formaldehyde and nitrate. The resulting pH increase

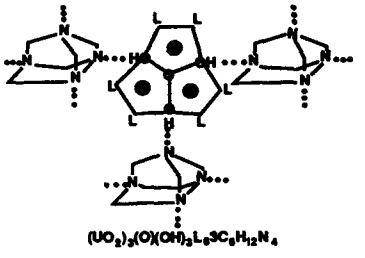


Figure 3. Uranyl trimer complex with urea as equitorial ligand and HMTA in hydrogen bonding

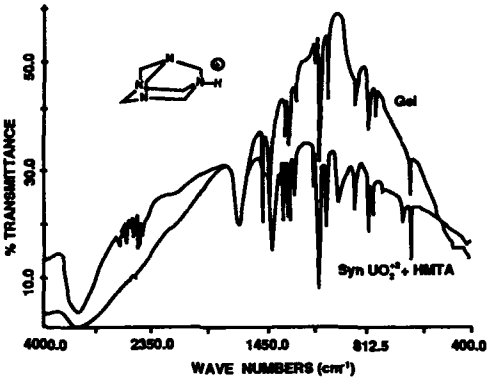
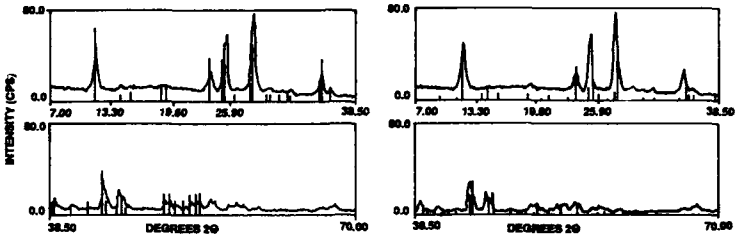


Figure 4. Fourier transform infared spectrum (FTIR) of HMTAH+ in a uranyl gel

also causes additional uranyl trimer condensation to hydrous uranium oxide polymers. The nature of the polymer in the post-washed gel formed in the internal gelation process has been studied by Lloyd, et. al., [22] under various chemical conditions and was found to be consistent with a complex composition of $UO_3 \cdot 2H_2O$, $4\ UO_3 \cdot NH_3 \cdot 7H_2O$ and $2UO_3 \cdot NH_3, \cdot 3H_2O$ based upon X-ray diffraction analysis. Our results compliment the Lloyd, et.al., interpretation and provide additional insight on the structure of the hydrous uranium oxide polymer and the mechanism of the washing step.

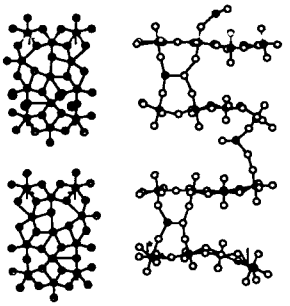
The ammonia washing treatment has been shown to be an ion exchange step in which the occluded HMTA molecule in protonated form ($HMTAH^+$) is exchanged for the ammonium cation. At the same time, further condensation of the uranyl trimer occurs to polyanionic hydrous uranium oxide in a layered configuration. $HMTAH^+$ and/or NH_4^+ are incorporated as "intercalation" cations to balance the negative charge of the hydrous uranium oxide layer. This was confirmed by XRPD and FTIR measurements on uranyl gels and synthetic compositions. In addition, a very interesting structural analogue in the uranium mineral family [23] has been extremely useful in providing a structural interpretation of the hydrous uranium oxide network.

Figure 5a is an XRPD pattern of a synthetic sample from ammonia treatment of a uranyl solution at pH 4.5. The yellow crystalline compound had an approximate stoichiometry of $4\ UO_3 \cdot NH_3 \cdot 7\ H_2O$ and is in good agreement with the literature pattern of Garner [24]. XRPD on washed gel samples gave broader, more amorphous, patterns but were similar to Figure 5a. The Garner composition was classified in the orthorombic system as a layered structure with a 002 or basal reflection of 7.55 Å, the distance between the layers, but the atomic arrangements were undefined. Recently, complete crystal structures of a series of hydrous uranium oxide minerals were published by workers from the University of Maryland and the Smithsonian Institute [23]. A XRPD pattern comparison with our synthetic ammonium, gel-like, derivative is shown in Figure 5b for the natural mineral Billietite ($BaO \cdot 6\ UO_3 \cdot 11\ H_2O$), whose atomic arrangements (Figure 5c) are shown from the Pagoaga, et. a1., work. Billietite is a naturally occurring barium-containing hydrous uranium oxidepolymer in which the uranyl moity is retained in μ_3-oxo bridging in an oxygen layer and the barium cations maintain the layer dimensions (7.50 Å) along with interstitial water in hydrogen bonding. Hence, barium is the "intercalation" cation between hydrous uranium oxide layers. Billietite contains quasi-linear $(UO_2)^{+2}$ groups coordinated by five oxygen atoms to form a pentagonal bipyramid of $[(UO_2)O_2(OH)_3]$. This polyhedron shares

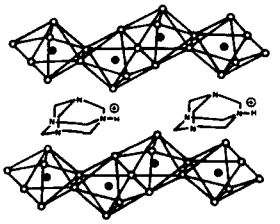


a. Gel-like synthetic ammonium derivative versus $4UO_3 \cdot NH_3 \cdot 7H_2O$

b. Billietite ($BaO \cdot 6UO_3 \cdot 11H_2O$) versus synthetic $4UO_3 \cdot NH_3 \cdot 7H_2O$



c. The structure of billietite showing layer pattern and barium intercalation



d. Proposed HMTA+ intercalate of hydrous uranium oxide

Figure 5. X-ray powder diffraction patterns (XRPD) of hydrous uranium oxide polymers

pentagonal edges to form sheets of $[(UO_2)_6O_4(OH)_6]_n^{-2n}$, which are parallel and are bonded together by intercalation barium cations and water molecules.

The Pagoaga, et.al., work [23] confirms the predictions of Evans [25] that hydrous uranium oxides would show mainly pentagonal coordination around the uranyl ion–allowing the equatorial oxygen atoms to remain in a plane orthogonal to the uranyl species without crowding. The uranium-oxygen sheet found in the uranyl oxide hydrate minerals is similar in structure to the sheets in α and β-U_3O_8[17]. In α-U_3O_8, each of the quasi-uranyl ions is coordinated to five oxygen atoms in the uranyl equatorial plane—a pentagonal bipyramidal array. In β-U_3O_8, two of the quasi-uranyl ions are equatorially five coordinate, but one uranyl ion is only four coordinate equatorially and hence exhibits tetragonal bipyramid or "distorted" octahedral symmetry. Billietite is similar to the α–U_3O_8 structure but is distorted towards β-U_3O_8 with coordination around two uranyl ions in the uranium-oxygen sheet being almost fourfold [23]. U_3O_8 is also a significant structure and composition in nuclear fuel synthesis.

It is instructive to note that the uranyl equatorial coordination number of five, and the oxygen/hydroxy bridging framework of the uranyl trimer of Aberg [19] and the uranyl tetramer of Aberg [20] and Perrin, et.al., [21] exhibit the pentagonal bipyramidal configurations and oxygen bonding patterns of the infinite chain hydrous uranium oxide minerals [23]. It is our contention that the uranyl trimer, as observed by ^{17}O NMR, is in fact the precursor to condensation of an infinite chain polymer of uranium—induced by basic hydrolysis with $HMTAH^+$ or NH_4^+. The remarkable agreement between synthetic and natural mineral patterns, (Figure 5b), both in "d" spacing and intensities, provides additional structural information. For a series of natural uranium minerals, including Billietite, structural formulae have been calculated from empirical formulae and x-ray patterns [30]. We have proposed a structural formula for the synthetic ammonium derivative to be: $(NH_4)_2[(UO_2)_8O_4(OH)_{10}] \cdot 8H_2O$, a layered hydrous uranium oxide with ammonium ions as intercalation cations. The intercalation of ammonium and alkyl-ammonium cations ($HMTAH^+$) (Figure 5d)

proved to be a general phenomenon of hydrous uranium oxide condensation. Seven alkyl ammonium derivatives have been prepared and shown to be isostructural by XRPD and solid state ^{17}O NMR. The intercalation cations can be observed and structurally characterized by FTIR and TGA/Mass Spectroscopy [30]. The basal or layer dimension is controlled by the size of the intercalation cation, similar to the known intercalates of hydrogen uranyl phosphate [26]. All are precursors to ceramic nuclear fuel (UO_2) and exhibit ion exchange properties. Structural characterization and properties will be described in future publications [27-31].

CONCLUSIONS

HMTA is stable in the internal gelation process for urania microsphere synthesis as the protonated cation and plays a structural role in gel formation, probably through hydrogen bonding. The colloidal "sol" was shown to be a mixture of uranyl oligomers. The uranyl trimer is predominant in the "gel" structure with urea in the uranium equatorial coordination sphere and $HMTAH^+$ promoting uranyl trimer formation and the gel network. The trimer condenses to a layered hydrous uranium oxide polymer in which ammonium or $HMTAH^+$ cations stabilize the layer configuration as "intercalation" cations. A structural concept of the layered configuration was obtained from natural uranium mineral analogues. The layered network serves as the structural precursor to ceramic nuclear fuel (UO_2).

ACKNOWLEDGEMENTS

This work was conducted under Contract No. DE-AC09-76SR00001 with the U.S. Department of Energy. The authors gratefully acknowledge the assistance of Prof. Andrew Streitwieser of the University of California/Berkeley Department of Chemistry on ^1H and ^{13}C NMR interpretation, Dr. John M. Read of the E. I. du Pont de Nemours & Co. Medical Products Department on initial guidance on NMR measurements, and Dr. Jack Collins of ORNL on useful literature and process insight. Coworkers of the WSRC included Mrs. Nancy Gregory, Mrs. Arlene Ray and Mr. Joel Livingston (Radiochemistry), Mrs. Joyce L. Hunter (XRPD), Mrs. Marti Finney (SEM) and Mr. Dan Steedly (TEM). Their tireless effort is gratefully acknowledged. The authors also thank Dr. M. Katherine Pagoaga of the NIST (Boulder, CO) for helpful discussions, literature and approval to use Hydrous Uranium Oxide structural data.

REFERENCES

1. P. A. Hass, J. M. Begovich, A. D. Ryon and J. S. Vavruska, *I & EC Product Research and Development* 19, 459 (1980).
2. J. L. Collins, M. H. Lloyd, and R. L. Fellows, *Radiochem. Acta* 42, 121 (1987).
3. P. A. Haas, *Chemical Engineering Progress*, 44 April (1989).
4. J. B. W. Kanji, A. J. Noothout, and O. Votocek, "The KEMA U(VI) Process for the Production of UO_2 Microspheres", 185 in *Sol-Gel Processes for Fuel Fabrication*, IAEA-161, International Atomic Energy Agency, Vienna, 1974.
5. V. N. Vaidya, S. K. Mukerjee, J. K. Joshi, R. V. Kamat, and D. D. Sood, *Journal of Nuclear Materials* 148, 324 (1987).
6. R. Bruce King, C. M. King and A. R. Garber, "Oxygen-17 NMR Studies of Uranium (VI) Hydrolysis and Gelation". In the *Proceedings of Better Ceramics through Chemistry IV, Materials Research Society*, San Francisco, CA. April 16-21, 1990.
7. W. G. Klemperer, Angew. *Chem. Int. Ed. Engl.* 17, 246 (1978).
8. P. A. Schaffer, Jr., *J. Amer. Chem. Soc.*, 69, 1557 (1947).
9. H. Tada, *Journal American Chemical Society* 82, 225 (1960).
10. P. Golding, A. P. Cooney, and M. R. Crampton, *Journal Chemical Society, Perkin Trans. II*, 835 (1986).
11. A. A. Vashman, I. S. Pronin, T. V. Brylkina, and V. M. Makarov, *Russ J. of Inorg. Chem.*, 24 (10), 1515 (1979) (English).
12. S. Narasimhan and A. S. Kumar, *Indian Journal of Chemistry* 24B, 568 (1985).
13. T. C. W. Mak, W. K. Li, and W. H. Yip, *Acta Cryst.* C39, 134 (1983).

14. C. M. King, M. C. Thompson, A. R. Garber, and A. Streitwieser, Jr. "Studies on the Mechanism of Hydrolysis of [1, 3, 5, 7] Tetra-aza adamantane", *Journal American Chemical Society* (to be submitted); "NMR Studies on the Role of Gelation Agents in a U(VI) Sol-Gel Process" *Better Ceramics through Chemistry Symposium*; Materials Research Society Proceedings, San Francisco, CA, April 16-21, 1990.
15. W. S. Jung, H. Tomiyasu, and H. Fukutomi, *Chem. Comm.*, 372 (1987).
16. V. A. Shcherbakov and L. G. Mashirov, *Soviet Radiochemistry* 26, 666 (1984) (English).
17. W. S. Jung, H. Tomiyasu, and H. Fukutomi, *Bulletin Chem. Soc. Japan* 58, 938 (1985).
18. M. Aberg, *Acta Chem. Scand.* 23, 791 (1969).
19. M. Aberg, *Acta Chem. Scand.* A32, 101 (1978).
20. M. Aberg, *Acta Chem. Scand.* A30, 507 (1976).
21. A. Perrin and J. Y. le Marouille, *Acta Cryst.*, B33, 2477 (1977).
22. M. H. Lloyd, K. Bischoff, K. Peng, H. U. Nissen, and R. Wessicken, *Journal Inorganic and Nuclear Chemistry* 38, 1141 (1976).
23. M. K. Pagoaga, D. E. Appleman, and J. E. Stewart, *American Minerologist*, 72, 1230 (1987).
24. W. Garner, *Journal Inorganic and Nuclear Chemistry* 21, 380 (1960).
25. H. T. Evans, *Science* 141, 154 (1963).
26. R. Pozas-Tormo, L. Moreno-Real, M. Martinez-Lara, and S. Bruque-Gamez, *Can. Journal Chemistry* 64, 30 (1986).
27. C. M. King, M. C. Thompson, and V. Van Brunt, "New Precursors to Ceramic Nuclear Fuel: Polycyclic Polyamine Polyuranates", *J. Nuclear Materials* (to be submitted).
28. C. M. King, R. B. King, P. Ellis, and J. A. Edwards, "Solid State ^{17}O NMR of Hydrous Uranium Oxide Alkyl Amine Intercalation Compounds", *Journal American Chemical Society* (to be submitted).
29. C. M. King, M. C. Thompson, R. B. King, B. R. Buchanan, and A. R. Jurgenson, "Structural Characterization of New Intercalation Compounds of Hydrous Uranium Oxide", *Inorganic Chemistry* (to be submitted).
30. M. C. Thompson, C. M. King, and R. B. King, "Spectroscopic Probes of the Structure of Hydrous Uranium Oxide Precursors to UO_2 Ceramic Fuel", *Better Ceramics through Chemistry IV*; Materials Research Society Proceedings, San Francisco, CA, April 16-21, 1990.
31. C. M. King, "New Insights Into U(VI) Sol-Gel Processing", Tutorial Lecture on Novel Ceramic Processing, Nuclear Div. of the Amer. Ceramic Society, *J. Amer. Ceramic Society* 69 (3), 548 (1990).

OXYGEN-17 NMR STUDIES OF URANIUM (VI) HYDROLYSIS AND GELATION

R. BRUCE KING*, CHARLES M. KING**, AND A. RONALD GARBER***
*Department of Chemistry, University of Georgia, Athens, Georgia 30602
**Westinghouse Savannah River Company, Savannah River Site, Aiken, South Carolina, 29802 ***Department of Chemistry, University of South Carolina, Columbia, South Carolina 29201

ABSTRACT

Hydrolysis and gelation processes in uranyl solutions are observed using the strong sharp uranyl oxygen-17 resonance.

INTRODUCTION

The hydrolysis and subsequent gelation of uranyl ion is of both fundamental and practical interest. From a fundamental point of view the uranyl and other actinyl ions are unusual in having inert strong multiple bonds to the axial oxygen atoms and labile weak bonds to the equatorial ligands. From a practical point of view the hydrolysis and subsequent gelation of uranyl ion is important in connection with the manufacture of UO_2 microspheres for nuclear fuel applications [1].

This paper describes our efforts to follow the hydrolysis and gelation of uranyl derivatives by using oxygen-17 NMR spectroscopy of the axial oxygens as a probe. The oxygen-17 resonance of the axial uranyl oxygens, which was first observed by Rabideau [2], is very narrow and thus very easy to observe relative to other types of resonances of the quadrupolar oxygen-17 nucleus. In addition the position of the oxygen resonance in uranyl derivatives is very sensitive to the equatorial ligands [3] and even to isotopic substitution of the opposite uranyl oxygen atom [4]. Furthermore the kinetic inertness of the axial uranyl oxygen to oxygen exchange [5] allows distinct resonances for different types of uranyl groups to be observed in mixtures of uranyl species rather than a single uranyl resonance at an average chemical shift for the components of the mixture.

EXPERIMENTAL

Oxygen-17 NMR spectra were obtained at 11.7T (67.8 MHz) on a Bruker AM-500 at the Chemistry Department of the University of South Carolina. Data were acquired at a sweep width of 125 kHz following excitation by a 6.2 msec pulse (~66°). Each scan consisted of 65,536 (64K) data points. Minimum relaxation delays were used giving a 0.262 sec recycle time. The resulting FID's were zero filled to 128K before transformation yielding a digital resolution of 1.9 Hz/point. The spectra in the Figures are the sum of 4096 individual scans. Chemical shifts are reported relative to H_2O and were referenced to an external D_2O/H_2O standard. All samples were run in 5 mm NMR tubes and spectra were acquired at ambient temperature. Concentrated (1.8 to 3.9 M) aqueous stock solutions of uranyl chloride and uranyl nitrate were enriched photolytically [5] to 5 to 10% oxygen-17 using commercial 28% enriched oxygen-17 water purchased from Icon Services, Inc. (Summit, New Jersey).

RESULTS

Figure 1 shows the oxygen-17 NMR spectra in the uranyl region obtained by the hydrolysis of uranyl chloride by the addition of 10% aqueous Me_4NOH in 0.25 OH^-/UO_2^{2+} increments. The final spectra clearly show the monomer, the dimer $(UO_2)_2(OH)_2^{2+}$, and the trimer $(UO_2)_3(OH)_5^+$ at approximately 1119.4, 1121.2, and 1127.7 ppm, respectively. These assignments are consistent with the increases and decreases in peak intensities upon additions of successive increments of base. Similar spectra were obtained in an analogous hydrolysis of uranyl chloride using extraction with increments of a 0.5 M solution of tri-n-decylamine in xylene as the base [6]. Analogous hydrolysis experiments using uranyl nitrate

Mat. Res. Soc. Symp. Proc. Vol. 180. ©1990 Materials Research Society

rather than uranyl chloride resulted in the production of less trimer and led to broader resonances indicating a significant dependence of the course of hydrolysis on the counteranion.

A question of interest is whether this hydrolysis pattern would be modified if a base was selected to promote gelation. In this connection hexamethylenetetramine, $(CH_2)_6N_4$ (HMTA), was selected as a base in view of its role as a gelation agent in the internal gelation process for the production of UO_2 microspheres [1]. Figure 2 shows the oxygen-17 NMR in the uranyl region obtained by hydrolysis of uranyl chloride by the incremental addition of aqueous HMTA. The hydrolysis pathway using HMTA (Figure 2) is seen to differ markedly from that using Me_4NOH (Figure 1) or amine extraction by leading selectively to production of trimer at HMTA/UO_2^{2+} ratios above 0.6. If the hydrolysis of uranyl chloride is carried out by adding increments of an equimolar HMTA/urea mixture, thus more closely approximating the conditions of the internal gelation process [1], a series of uranyl oxygen-17 NMR spectra essential identical to that in Figure 2 is obtained indicating that addition of urea in such quantities does not have a significant effect on the uranyl hydrolysis by HMTA. If the hydrolysis of uranyl chloride with an equimolar HMTA/urea mixture was carried out to a base/UO_2^{2+} ratio of 1/1 and the resulting NMR sample is allowed to stand overnight at ambient temperature, the solution became a gel. The oxygen-17 NMR spectrum of the gel was essentially identical to that of the same sample before gelation indicating that no significant change had taken place during the gelation process.

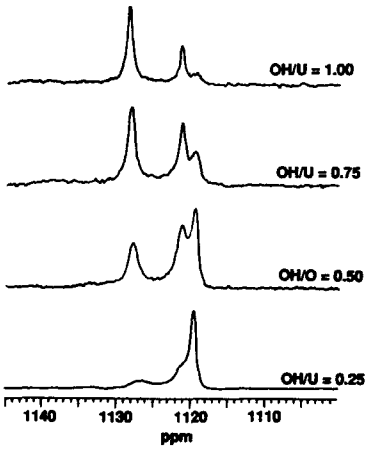


Figure 1. Oxygen-17 NMR spectra in the uranyl region of solutions obtained from the hydrolysis of 0.9M UO_2Cl_2 by addition of increments of 10% aqueous tetramethylammonium hydroxide

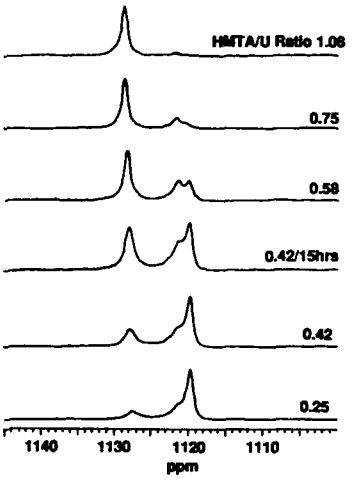


Figure 2. Oxygen-17 NMR spectra in the uranyl region of solutions obtained from the hydrolysis of 0.9M UO_2Cl_2 by addition of increments of 3M aqueous HMTA. This experiment was interrupted overnight when the HMTA/UO_2 ratio was 0.42.

Gelation of a uranyl system was also studied in a strongly alkaline medium making use of the reported [7] appreciable solubility of actinyl salts in aqueous Me_4NOH. Photolysis of an approximately 0.1 M yellow solution of uranyl nitrate in 10% aqueous Me_4NOH ($OH^-/UO_2^{2+} \approx 9$) caused gelation. The oxygen-17 NMR spectrum of this gel exhibited a sharp resonance at 1114.4 ppm indicating directly for the first time the stability of the uranyl ion in strongly alkaline media in accord with reported [8] potentiometric and spectrometric studies.

DISCUSSION

The ability to follow the hydrolysis of uranyl salts by observation of the sharp uranyl oxygen-17 resonance provides a clear indication of the dependence of uranyl hydrolysis on the counteranion (nitrate versus chloride) but not on the means of introducing hydroxide into the solution (Me_4NOH versus R_3N extraction). In addition, two different pathways for gelation are suggested. In the first pathway the uranyl hydrolysis is conducted with a base (HMTA in these studies) which preferentially forms trimeric $(UO_2)_3$ (μ_3-O) units which can then condense into the polymeric $UO_2O_{6/3}$ layers of a gel based on the hexagonal structure of α-$UO_2(OH)_2$ [9]. In the second gelation pathway a uranyl derivative is treated with excess hydroxide in the absence of a metal or hydrogen-bonding ammonium cations which form insoluble solids uranates. Consensation of the resulting solution of soluble $UO_2(OH)_n^{2-n}$ anions can then lead to a similar polymer $UO_2O_{4/2}$ or $UO_2O_{6/3}$ structure of a gel.

ACKNOWLEDGEMENTS

The authors would like to acknowledge the support of NSF grant CHE-8904942 which facilitated the purchase of the AM-500 NMR spectrometer at the University of South Carolina. This work was prepared in connection with work done under Contract No. DE-AC09-76SR00001 with the U.S. Department of Energy. The authors gratefully acknowlege the assistance of Mrs. Helga Cohen of the Chemistry Department of the University of South Carolina in acquiring some of the NMR spectra.

REFERENCES

1. J. L. Collins, M. H. Lloyd, and R. L. Fellows, Radiochem. Acta 42, 121 (1987).

2. S. W. Rabideau, J. Phys. Chem. 71, 2747 (1967).

3. W. S. Jung, H. Tomiyasu, and H. Fukutomi, Bull. Chem. Soc. Japan 58, 938 (1985).

4. W. S. Jung, Y. Ikeda, H. Tomiyasu, and H. Fukutomi, Bull. Chem. Soc. Japan 57, 2317 (1984).

5. G. Gordon and H. Taube, J. Inorg. Nucl. Chem. 16, 272 (1961).

6. I. L. Jenkins and J. Robson, Nature 194, 864 (1962).

7. D. Cohen and S. Fried, Inorg. Nucl. Chem. Lett. 5, 1653 (1969).

8. C. Musikas, Radiochem. Radioanal. Lett. 11, 307 (1972).

9. J. C. Taylor, Acta Cryst. B27, 1088 (1971).

MECHANICAL PROPERTIES OF SILICA ALCOGELS AND AEROGELS.

T. WOIGNIER, J. PHALIPPOU, H. HDACH, L.S.M.V., Université de Montpellier II, 34095 Montpellier Cedex 05, France; and G.W. SCHERER, E.I. DuPont de Nemours & Co, Central R & D Department, P.O. Box 80356, Wilmington, DE 19880-0356.

ABSTRACT

The mechanical properties of silica gels (alcogels and aerogels) are measured by three point bending. The elastic moduli (E,G) and the fracture strength (σ) are investigated as functions of the concentration of silicon precursor, the catalysing conditions, and the aging time.

Elastic moduli and strength follow scaling laws as a function of the bulk density of the solid. The scaling exponents are discussed in terms of percolation theory.

The evolution of the mechanical properties is also followed during the steps of the gel to glass transformation :

- hypercritical drying
- oxidation of the organic groups
- densification heat treatment

At each step of the process the increases of the elastic moduli and σ are related to the gel structure. During the hypercritical drying flexible "dead ends" in the network can condense and form new links. The connectivity is also enhanced by the removal of the organic groups creating siloxane bonds. Finally densification leads to a material having mechanical properties identical to those of conventional vitreous silica.

I - INTRODUCTION

One of the most important problem studied during this last decade in the sol-gel-glass process is the synthesis of bulk monolithic dry gels. Cracks can appear during syneresis, which expels liquid from pores and creates stresses in the network. The tendency of the gel to crack during drying is attributed to the capillary forces generated in the fragile structure of the gel. Knowledge of the mechanical properties of the alcogel is thus necessary to predict the cracking of the material.

Silica aerogel, which is obtained by hypercritical drying (HCD) of the alcogel, is a good candidate as precursor of pure silica glass. This solid material is extremely porous and brittle but only a few studies mention measurements of the strength of a such material. Studies have been performed either on alcogels [1-4] or on aerogels [5-8]. The shear modulus G and the modulus of rupture σ of the alcogel increase during aging [2-4] ; in aerogels, Young's modulus E [5-8] and σ [8] show a power-law dependence on the bulk density.

In this work we want to focus our experiments on :

- the modification of the mechanical properties G, E and σ induced by HCD.
- the influence of the experimental conditions, such as concentration of tetramethoxysilane, pH of the hydrolyzing solution, and aging at near ambient temperature on E, G and σ for both alcogels and resulting aerogels. All of these parameters induce structural changes,
- the evolution of the mechanical properties during the heat treatments leading to the aerogel-glass transformation.

II - EXPERIMENTAL PROCEDURE

The alcogels are prepared by hydrolysis and polycondensation reactions of tetramethoxysilane (TMOS). The TMOS is dissolved in various amounts of methanol thereby adjusting the oxide content of the sol (and the final bulk density of the aerogels). The solutions are hydrolyzed under neutral, basic (NH_4OH, 5.10^{-2} N) or acidic (HNO_3, 10^{-4} N) conditions and aged at 65°C for up to two weeks.

The alcogels are transformed into aerogels by hypercritical evacuation of the solvent. In an autoclave, the alcogel is treated at a temperature and a pressure higher

than the critical point of the solvent in the pores. Then, the solvent is vented from the autoclave. This procedure allows the monolithicity of the gel network to be preserved. For several samples the hypercritical heat treatment is not followed by the evacuation of the superfluid, so the solvent reimpregnates the gel during cooling. The interest of this procedure is to prepare material full of solvent for which the solid network has undergone the same heat treatment as for classical aerogel.

The densification of the aerogels is obtained by a heat treatment at a temperature of 1050°C. Depending on the duration of the heat treatment the density of the material may become as high as that of the vitreous silica. A preliminary heat treatment in the temperature range 250-500°C is necessary to oxidize the residual organic groups.

The bulk density of the aerogels is determined by weighing samples of known dimensions. The bulk density of the solid network of the alcogel is calculated from the bulk density of the aerogel and the shrinkage measured after the autoclave treatment. This shrinkage was observed to be isotropic within experimental accuracy.

The elastic moduli and the modulus of rupture of the samples were measured by the 3 point bending technique using an Instron testing machine with a 2000 g load cell; the precision of the measurement was 1 g. The experiments were performed on parallelepipedic samples with a thickness of about 1 cm (measured on each sample) and a span of 7 cm; the cross-head speed is 0.5 mm/min. Similar values of the elastic moduli were found on loading and unloading. Crosshead speeds ranging from 0.05 to 5 mm/min were used; they lead to the same elastic values. It was established that the buoyancy force acting on the moving upper part of the equipment plays a minor role on the elastic values. The reported σ values are averages of results for at least 3 measurements.

The Small Angle Neutron Scattering (SANS) experiments were performed on the PACE Spectrometer at the Léon Brillouin CEA - CNRS laboratory in Saclay, France. Scattering vectors q ranging from 0.0018 to 0.3 $Å^{-1}$ were explored ($q = 4\pi \sin\theta/\lambda$, 2θ is scattering angle). A standard analysis of data including detector efficiency correction, background substraction and relative amplitude calibration allows a determination of the density-density correlation function in the length scale from 3 to 500 Å.

III - RESULTS

All the materials studied show mechanical behaviour characteristic of a brittle material. The load displacement data are linear, indicating purely elastic behaviour and the appearance of the fracture surface of aerogel is identical to that of glass.

In analyzing the results, it must be recognized that the beam bending test gives two different kinds of elastic modulus when the sample is an aerogel or an alcogel. For aerogels the test yields the Young's modulus which is classical for solid samples. However, for the alcogels the situation is more complicated because of the presence of liquid. Scherer [3] has shown that, due to the low permeability of the gel, the liquid cannot escape during the course of the moulus measurement. The volume of the bar is unchanged by the deformation which means that the network is in a state of pure shear, providing a measurement of the shear modulus of the network. Thus to compare data measured on aerogel and alcogel the shear modulus of aerogel is calculated from the E determination with the following relation :

$$G = \frac{E}{2(1+n)}$$

where the Poisson's ratio n has been previously measured close to 0.2 by Brillouin Scattering [6,10]. This value is in agreement with another determination obtained by sound velocity propagation [9].

III - a) Alcogel-aerogel transformation

It is generally accepted that HCD is gentle compared to classical drying and preserves the fragile network of the solid part of the alcogel. It is clear that the shrinkage of the xerogel is larger than that of the aerogel, which macroscopically looks like an alcogel without solvent. However, during HCD a shrinkage 2 to 25 linear percent occurs, depending on the aging time, the concentration, and the catalysis conditions [11] . Textural and structural variation during HCD have also been observed [12-14]. Thus, we can expect a modification of the stiffness and the strength of the solid network.

Figure 1 shows the evolution of the elastic and rupture moduli for a set of gels with different silica concentrations. As expected, E, G and σ increase with % TMOS over almost two orders of magnitude. What is more interesting is the increase at each concentration of G and σ by a factor 20 after HCD. However, it is obvious that the mechanical properties depend on the load-bearing fraction of gel. It has been shown [11] that HCD induces a shrinkage of the material and thus an increase of the volume fraction of solids (bulk density) in the gel.

In Figure 2 the mechanical properties have been plotted as functions of the bulk density of the solid network. Nevertheless, G and σ of the aerogels are around a factor of 5 higher than for the alcogel set. The known effect of HCD on the structure of the gel is a methoxylation reaction which replaces the OH surface by methoxy groups [14,15]. However this reaction cannot explain the increase of the mechanical properties and rather would induce a weakening of the network if siloxane bonds were broken by the methoxylation [15]. The increase of G and σ must be related to new siloxane bonds created between "dead ends" in the alcogel (i.e. branches of the network linked at only a few points to the spanning cluster). These dead ends contribute to the mass of the network but not to its stiffness (and strength). During HCD, these dead ends covered with SiOH groups come into contact and new siloxane bonds are formed. This condensation reaction between SiOH groups must take place in the temperature range 25°C - 200°C before the methoxylation reaction. The consequences of HCD (condensation reactions, shrinkage and mechanical evolution) are comparable to those of a long aging.

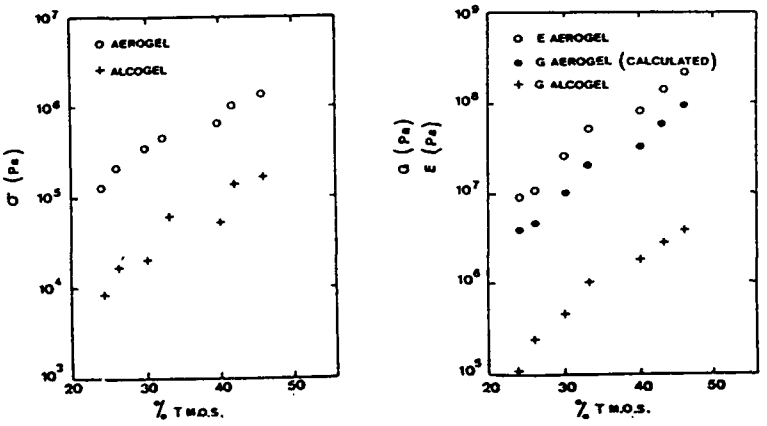
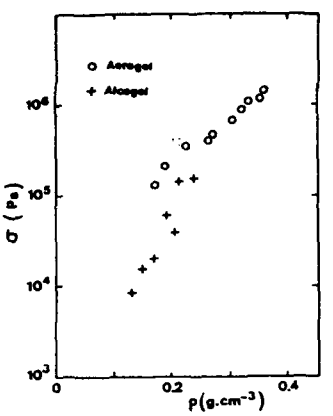


Figure 1 : Evolution of E, G, σ, as a function of the TMOS concentration



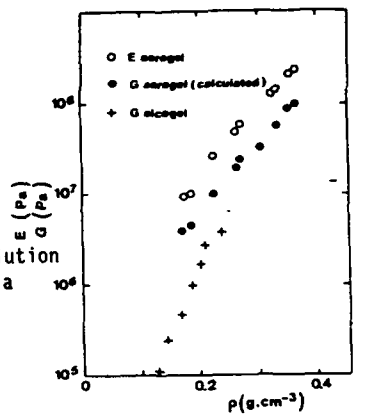
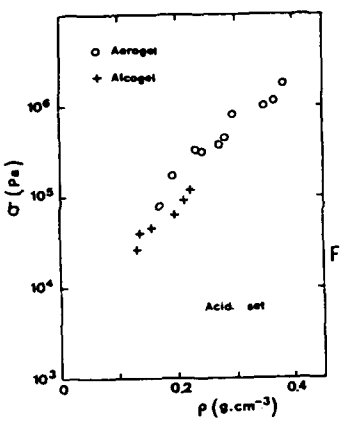


Figure 2 : Evolution of E, G, σ as a function of ρ (Neutral set)



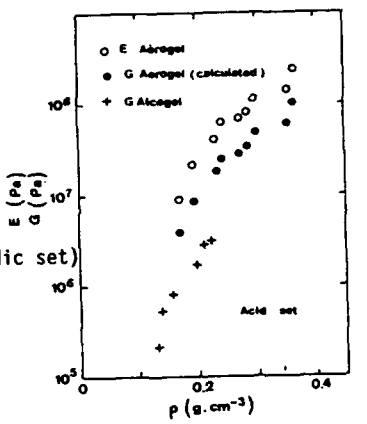
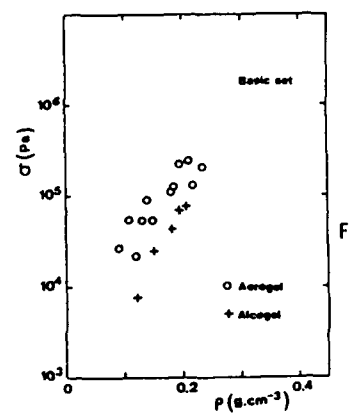


Figure 3 : (Acidic set)



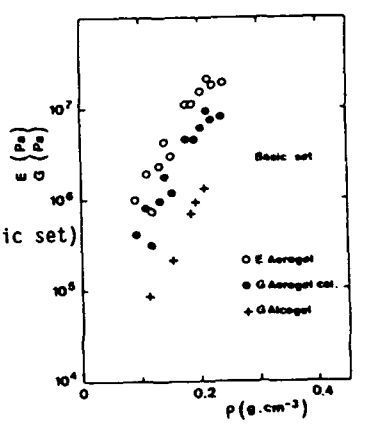


Figure 4 : (Basic set)

III-b) Influence of the catalyzing medium.

As shown in figures 3 and 4 the elastic and rupture moduli of basic and acidic sets of material follow the same evolution as that observed for the neutral set. For the reasons previously explained, the results are plotted as a function of the bulk density.

In the case of the acidic set we can invoke a process identical to that described for the neutral sets. Acid-catalyzed silica gel is expected to consist of relatively flexible polymeric chains [16]. The flexibility of the chains allows motion, contacts and condensation of SiOH between chains. This process increases the connectivity of the network.

What is more surprising is the strengthening observed for the basic set during HCD. Gels made in basic conditions consist of a network of particles or dense clusters [16] and exhibit little shrinkage during aging or HCD [11]. The branched parts are more widely spaced than in the neutral and acidic sets. We could assume that a large increase of the reticulation by condensation of SiOH is possible without shrinkage of these network. Another explanation seems more realistic : the relatively high solubility of silica permits dissolution - reprecipitation and transfer of material to the neck between particles. These reactions are favoured at high temperature in the autoclave We propose that the strengthening of the basic set during HCD is not due

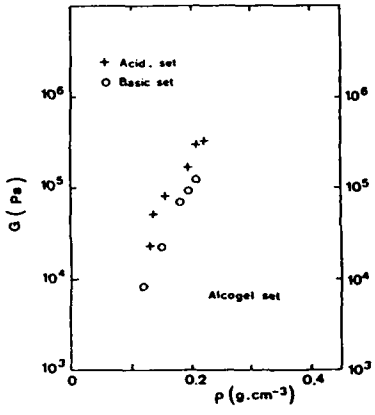


Figure 5 : Comparison between acidic and basic sets.

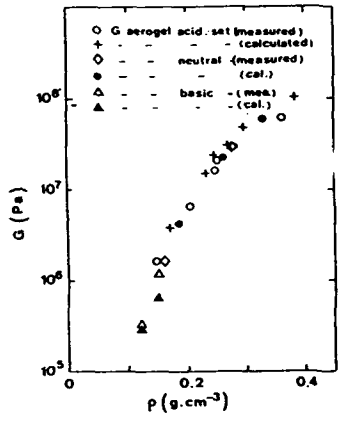


Figure 6 : Comparison between measured and calculated G values.

to an increase of the reticulation in the network but rather to the growth of the necks between "particles".

Now, if we compare the mechanical properties of the alcogels obtained from the acidic and the basic hydrolysis we observe a result previously shown for aerogels [8]. The basic system shows G values slightly lower than the acidic alcogels (Figure 5). This result can be related to the smaller connectivity of the basic network compared to that of the acidic one. The difference in the structure is reflected in the lower fractal dimension, as we will see later.

It has been supposed above that Poisson's ratio for the different gels is close to 0.2. This value of n was obtained by the measurement of the transverse and longitudinal sound velocities of neutral [6,10] and basic [9] aerogels. The G values of aerogels measured with the liquid inside the pores ("reimpregnated aerogel") are plotted in Figure 6. The measured and calculated values of G are shown to be in close agreement for the different kinds of material.

III-c) Influence of the aging time.

It is well known that silica alcogels shrink during aging [18]. It has also been shown that the shear modulus and the modulus of rupture of an alcogel increase during aging [2,3,19]. The increase is around one decade for σ and 2 decades for G in the case of alcogels made in acidic conditions [3] and less than a factor 5 [19] for gels made according a two-step procedure, described by Brinker et al. [16] with the second step performed under basic conditions.

It is not obvious however that the effect of aging performed at near ambient temperature would be preserved after the severe thermal treatment experienced by the gel during supercritical drying. Figure 7 shows the evolution of σ and E of aerogels after aging over a two week period. For the aerogels aging prior to HCD increases E and σ by only a factor 4 over the two week period, compared to the factor 10 or 100 for the alcogels. That means that aerogels retain some memory of the aging in their alcogel state. In fact the increase of the mechanical properties is associated with a residual shrinkage observed in the aerogel.

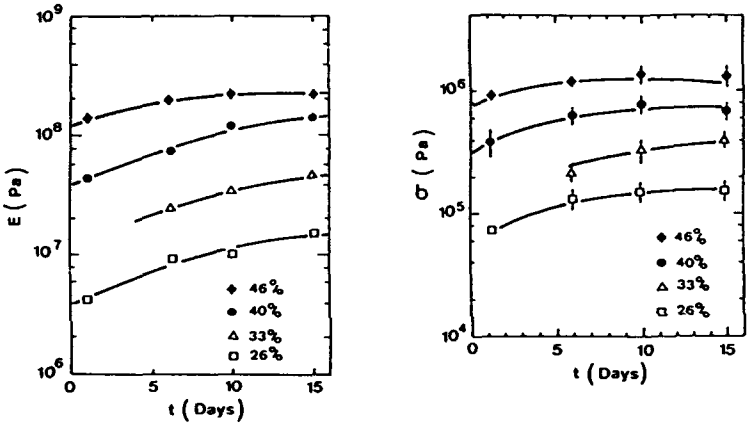


Figure 7 Influence of aging time

III-d) Aerogel - glass transformation

Since the pioneering work of J. Phalippou and coworkers [20] aerogels can be transformed into pure silica glass by simple heat treatments. Two kinds of transformation happen during the aerogel-glass transformation :

- Structural transformation by an oxidation heat treatment in the range 250°C-500°C which replaces the $O\text{-}CH_3$ residual groups by hydroxyls.
- Textural transformation by the elimination of the pore volume in a temperature range higher than 900°C.

On Figures 9 and 10 are plotted the E and σ values after the oxidizing heat treatment for a neutral set of aerogels (Figure 8) and during the densification (Figure 9). After the oxidation heat treatment there is no significant change in the bulk density, but Young's modulus increases by a factor of two. The transformation of $SiOCH_3$ into silanol and siloxane bonds increases the connectivity of the network and its stiffness. Strength data show greater scatter. In fact σ depends on the connectivity but is also related to the existence of flaws in the material. During densification the aerogel hardens strongly and E and σ increase continuously (about 3 decades) due to the large decrease of the porosity. Finally the mechanical properties of the fully dense material are identical to those of the silica glass.

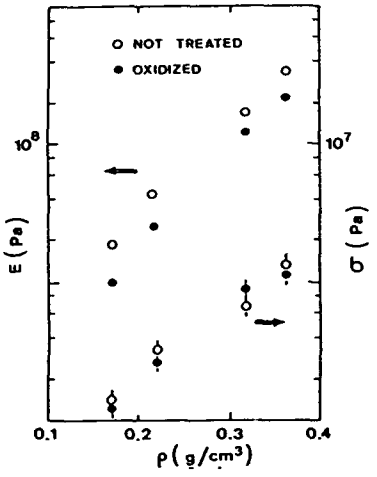


Figure 8 : Influence of the oxidation heat-treatment.

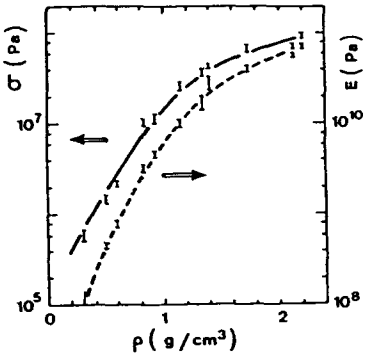


Figure 9 : Influence of the densification heat-treatment.

IV - DISCUSSION

IV - A) Percolation - gelation analogy

It has been proposed that an analogy could exist between a gel and a percolation cluster [21]. As a consequence the mechanical behaviour of a gel would agree with the prediction of the percolation theory.

This theory treats the random occupation of sites by entities (or the creation of bonds) on a fixed lattice, leading to the appearance of a coherent network at the percolation threshold. In this theory, physical properties such as viscosity, conductivity or mechanical properties are expected to scale as

$$\text{Phys. Prop.} \propto (P - P_C)^A$$

here P is the probability for a site to be occupied (or a bond to be created), P_C is the percolation threshold (defined as the value of P above which an infinite cluster exists), and A is the critical exponent characteristic of the physical property.

Experimental studies on gels or polymers [22-25] have been analyzed with this analogy. The most important difficulty deals with the choice of the physical variable which can replace the unknown mathematical variable $(P-P_C)$. Various variables such as concentration of monomer [23,25] or time [22,24] were proposed, assuming implicitly a proportionality between the variables and the P scale. It has been proposed that for silica aerogels a good approximation is to identify P with ρ and to let $\rho_C = 0$ [5] (since a network can form with an arbitrarily small solids content).

The log-log plot in Figures 10 demonstrates a power law dependence of E [5,6,8,11] and σ [8] for the set of aerogels. Identical results have been found for organic aerogels [26]. On the assumption that $P - P_C \propto \rho$ we find that the critical exponent of the elastic constant τ is equal to 3.7 which is in excellent agreement with the analytical work and simulations on a discrete lattice [27,28].

While the behaviour of the elastic constant of the percolating object has been the focus of a number of theoretical investigations, very little attention has been paid to the fracture properties of such solids [29,30]. Also a power law dependence of the

strength is predicted and Ray et al. [31] have proposed a lower bound for the scaling exponent t:

$$\sigma \propto (P - P_C)^t$$

$$t \geq \frac{1}{2}(\tau + (D - D_B)\nu)$$

τ is the elasticity exponent, D the dimensionality of space, D_B the fractal dimension of the percolative backbone (the set of sites which carry the stress) and ν the correlation length exponent. Inserting the values τ = 3.7 [27,28] D = 3, D_B = 2 [32], ν = 0.8 [21] we find that $t \geq 2.5$ which is in a good agreement with our experimental result t = 2.6.

These results would suggest that the aerogel structure is a percolative medium. This conclusion is not so clear after a thorough analysis. The comparison between the experimental determination and the percolation exponents is based on the assumption that ρ is equivalent to $P - P_C$. This hypothesis assumes implicitly that all the occupied sites (monomers having reacted) belong to the infinite cluster (gel network). In fact in the straightforward gelation percolation analogy [21], the physical properties of the gelifying solution (such as number of macromolecules, degree of polymerization and gel fraction) scale with the percolation parameter $P - P_C$ and with critical exponents. The gel fraction (and thus the bulk density) is associated with the percolation probability $\mathcal{P}(P)$ (the probability for a site to belong to the infinite cluster) and scales with the exponent β :

$$\rho \propto \mathcal{P}(p) \propto (P - P_C)^\beta$$

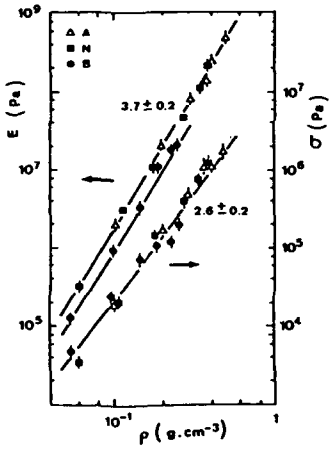


Figure 10 : Power-law dependence of E and σ on ρ in neutral aerogels.

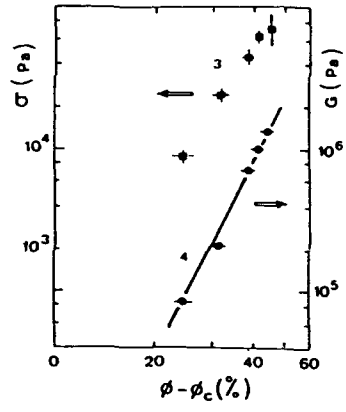


Figure 11 : Power-law dependence of G and σ on monomer concentration for basic aerogels

The experimentally determined values would not be directly τ or t but τ/β and t/β. Using a β value equal to 0.4 (the theoretical prediction [33] in a 3 dimension model), we find τ and t respectively equal to 1.5 and 1.05, far from the predicted exponents. The value 0.4 for β takes into account the fact that in a percolation model a part of the occupied sites belong to finite clusters and do not participate in the infinite

backbone. The ambiguity of the simple analogy is that in the course of the autoclave treatment, diffusion in the sol allows the microclusters to stick to the infinite cluster and one expects a larger β value tending towards 1. In any case, either t and τ, or β would be different from the prediction of the percolation gelation analogy and an identification of the aerogel structure with the infinite cluster of percolation can only be an approximation.

We have shown that the shrinkage during HCD is detrimental for the analysis in terms of the gelation - percolation analogy. It increases the mechanical integrity, modifies the bulk density, and leads to ambiguous conclusions for the β exponent. To avoid the problem of the shrinkage, the gelation-percolation analogy can be tried on the alcogel sets.

The gelation process is compared to a site-bond percolation model with two probabilities :

1) the probability of bond formation P_b is a function of H_2O concentration, catalyst, duration and temperature of the polymerization reaction.

2) The probability of occupied sites P_s is proportional to the concentration of monomers in the solution.

The completion of the gelation reaction could transform the site-bond percolation model into a simple site percolation process where the P_s scale is replaced by the monomer concentration ϕ.

Gels prepared in basic conditions offer the most appropriate test of this idea because :

1) the polycondensation reaction in basic condition favours the formation of bonds.

2) the syneresis phenomenon is very weak and almost no shrinkage is observed [11].

Figure 11 shows the log log plot of G and σ as a function of the monomer concentration $\phi - \phi_c$. The value of ϕ_c has been estimated experimentally in the range 0 - 2%, which corresponds to the critical concentration to obtain a gel. With this assumption we find the exponent $\tau = 4$. The t value is around 3 but a precise determination is difficult because of the scatter of the data. These exponents could be in a rough agreement with the percolation predictions.

Thus, the initial choice for the physical variable which is thought to correspond to $P - P_c$ is highly important since the different choices drawn from the literature lead to contradictory conclusions. This result points out the difficulty of finding the "correct" physical variable to describe a supposedly percolating system. Another difficulty is that the critical exponents are expected to apply near the percolation threshold, and in our case we are not in the vicinity of the gel point.

The analysis in terms of the percolation theory can also be discussed considering the structure of the material and the comparison between the fractal dimensions D_f. Thus, the fractal dimension of the percolation infinite cluster is 2.5 although D_f is around 1.7 for alcogels in basic catalysis [34] and 2.2 in neutral conditions [35]. Such D_f values suggest that the gelation under basic conditions corresponds to a Diffusion Limited Cluster-Cluster Aggregation (D_f = 1.8) [36,37] and for the acidic and neutral sets to a Reaction Limited Cluster-Cluster Aggregation (D_f = 2.1) [36,37]. The percolation theory could only give a qualitative description for the last stage of the gelation when the clusters became nearly immobile, so that further bonding involves a percolative process with the sites being filled by the clusters.

IV-B) Relation between mechanical properties and structure.

In section III, the evolution of the mechanical properties has been explained by the transformation of the gel structure induced by HCD, catalyst, aging or heat treatment. Now we will quantify the structural evolution by means of the fractal description.

Fractal geometry constitutes a novel base for describing the disordered and porous structures of the gel network and scattering techniques (SANS, SAXS, Light)

are efficient tools to measure the fractal characteristics (fractal dimension D_f and fractal range) of such material. The SANS data obtained for different aerogels are shown in Figure 12. For each sample three regions can be reconized on the wave vector dependent scattering curves S(q). At large q (Porod region) the experiment senses the particles surfaces and gives information on the roughness (surface fractal dimension) of the beads. In the intermediate regime S(q) is dependent on the fractal dimension of the network, while at very small q (Guinier region) the material becomes homogeneous. The position of the two crossover points between the Porod and the fractal regimes and between the fractal and the Guinier regimes are related respectively to a^{-1} and ξ^{-1} where a is a radius of gyration of the structural units and ξ corresponds to the size of the fractal cluster.

It must be noted that the analysis of the SANS data can only give precise information on the structure in the fractal range. However, the structural transformations pointed out in the fractal range are the signature of an overall evolution of the gel network. For example, during the autoclave treatment no shrinkage and no variation of D_f are noted for the basic set. The fractal dimensions measured on alcogels [35] and aerogels [38] of the same concentration are close to 1.7. On the other hand the macroscopic shrinkage observed for the A and N sets is related to the modification of the fine structure, indicated by the increase of D_f from 2.2 [35] to 2.4 [38]. This variation of D_f (of about 0.2) indicates densification of the structure. The fractal dimension describes the mass distribution but if one needs information on the connectivity, one must define the "spreading dimension" d [39] :

$$m(L) \propto L^d$$

m(L) is all the mass visited on a walk of length L, whatever is the path. d depends only on the manner the masses are connected. However, there exists a relation between d and D_f : $d = D_f/\lambda$ where λ, the exponent of the tortuosity, (or fractal dimension of the minimum path) defines the circumparambulations necessary fo go from one point to another. For a percolation cluster, $\lambda = 1.34$; [40] for DLCCA, $\lambda = 1.25$ [41]. Since λ is expected to decrease or to be constant during HCD an increase of D_f signifies increased connectivity in the gel network and can explain the strengthening of the material.

An identical conclusion can be drawn for the influence of the catalyst, between the basic sets and the acidic set. Base catalyzed materials are composed of large and generally smooth particles, (a = 12 Å) [38]. They are fractal over a smaller range of q and their D_f value is low compared to the neutral or acidic set (Figure 12). If we consider the spatial arrangement of the different networks, N and A materials can be described as highly branched polymers where the chains are formed by small and rough particles. B materials are a random assembly of larger particles with a lower connectivity. However, the increases of G, E and σ between B sets and A or N sets is less than during the alcogel-aerogel transformation (a factor about 2 instead of 5), although the increase of D_f is larger (about 0.4 instead of 0.2). Other parameters than the spatial arrangment, such as the size of the necks between particles, can play an important role.

During the aerogel to glass transformation two kinds of structural development are observed.

1) Surface microporosity forming the fractal roughness is removed during the oxidation heat treatment. The fractal dimension of the surface falls from 2 to 2 [8]. The elimination of the organic compounds and the formation of new siloxane bonds is accompanied by a diffusional process causing little densifcation, and the increase of E is apparently due to the growth of the necks between particles.

2) After the heat treatment carried out at higher temperature (> 1000°C) the solid network shrinks by a viscous flow process. The considerable densification eliminates the fractal structure. Figure 13 shows that at a bulk density 0.7 a fractal description is meaningless. The large increase of E and σ is then related to the strong increase of the fraction of solid and of the necks.

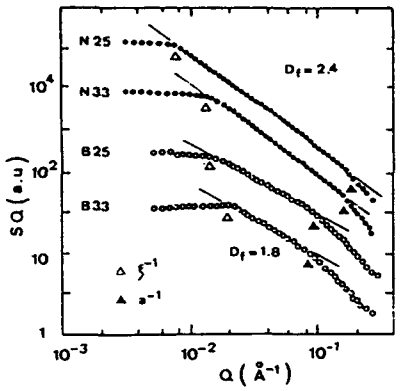


Figure 12 : SANS data for neutral aerogels. The solid triangles and the open triangles indicate the position of $1/a$ and $1/\xi$ respectivly.

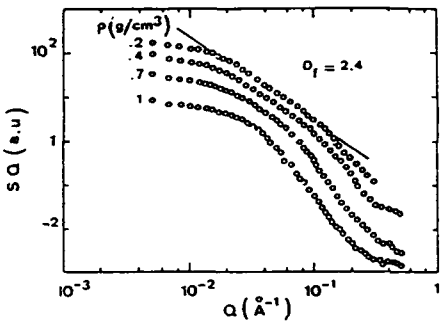


Figure 13 : SANS data for densified neutral aerogels.

REFERENCES

1 - M.J. MURTAGH, E.K. GRAHAM, C.G. PANTANO. J. Amer. Ceram. Soc. 69(11), 775 (1986).

2 - J. DUMAS, S. BAZA, S. SERUGHETTI. J. Mater. Sci. Lett. 5, 478 (1986).

3 - G.W. SCHERER, S.A. PARDENEK, R.M. SWIATEK. J. Non-Cryst. Solids 107, 14 (1988).

4 - G.W. SCHERER. J. Non-Cryst. Solids, 109, 183 (1989).

5 - M. GRONAUER, A. KADUR, J. FRICKE. Aerogels (Springer-Verlag), Proceeding in Physics 6, 167 (1986).

6 - T. WOIGNIER, J. PELOUS, R. VACHER, E. COURTENS. J. Non-Cryst. Solids, 95-96, 1197 (1989).

7 - T. CALEMCZUK, A.M. DE GOER, B. SALCE, T. MAYNARD, A. ZAREMBOVITCH. Europhys. Lett, 3, 1205 (1987).

8 - T. WOIGNIER, J. PHALIPPOU. Rev. Phys. Appliquée, 24(C4), 179 (1989).

9 - J. GROSS, G. REICHENAUER, J. FRICKE. J. Phys D, 21, 1447 (1988).

10 - J. PELOUS, T. WOIGNIER. Unpublished results.

11 - H. HDACH, T. WOIGNIER, J. PHALIPPOU, G.W. SCHERER. J. Non-Cryst. Solids, 121, 202 (1990).

12 - J.F. QUINSON, J. DUMAS, J. SERUGHETTI. J. Phys., 46(C8), 467 (1985).

13 - D.W. SCHAEFFER, C.J. BRINKER, J.P. WILCOSON, D.Q. WU, J.C. PHILLIPS, B. CHU. in "Better ceramics though chemistry III" edited by C.J. Brinker, D.E. Clark, D.R. Ulrich. (Mat. Res. Soc. Symp. Proc. 121, Pittsburgh, PA, (1988), p 691.

14 - R.K. ILER. The Chemistry of Silica, Wiley Interscience, New-York, (1979), p 689.

15 - G. MERTENS, J.J. FRIPIAT. J. Coll. Inter. Sci. 42(2), 169 (1973).

16 - C.J. BRINKER, K.D. KEEFER, D.W. SCHAEFFER, R.A. ASSINK, B.D. KAY, C.S. ASHLEY. J. Non-Cryst. Solids, 63, 45 (1984).

17 - T. WOIGNIER, J. PHALIPPOU, R. VACHER. J. Mater. Res., 4(3), 688 (1989).

18 - G.W. SCHERER. J. Non-Cryst. Solids, 108, 28 (1989).

19 - G.W. SCHERER. J. Non-Cryst. Solids, 109, 183 (1989).

20 - M. PRASSAS, J. PHALIPPOU, J. ZARZYCKI. Glastechnisch. Ber. 56K, 542 (1983).

J. PHALIPPOU, T. WOIGNIER. Ultrastructure Processing of Ceramics Glasses and Composites. L.L. Hench, D.R. Ulrich ed, Wiley Intens. Pub. 70 (1983).

J. PHALIPPOU, T. WOIGNIER, M. PRASSAS. Rev. Phys. Appliquée, 24(C4), 47 (1989).

21 - D. STAUFFER. J. Chem. Soc. Faraday., 72, 1354 (1972).

22 - B. GAUTHIER-MANUEL, E. GUYON. J. Phys. Lett. France, 41, L-503 (1980).

23 - M. TOKITA, R. NIKI, K. NIKICHI. J. Phys. Soc. Jpn, 53, 480 (1984).

24 - M. ADAM, M. DELSANTI, D. DURAND, G. HILD, J.P. MUNCH. Pure Appl. Chem., 53, 1489 (1981).

25 - M. TOKITA, R. NIKI, J. NIKICHI. J. Chem. Phys., 83, 2583 (1985).

26 - R.W. PEKALA, F.M. KONG. Rev. Phys. Appliquée, 24(C4), 179 (1989).

27 - S. FENG, P.N. SEN. Rev. Phys. Lett., 52, 216 (1984).

28 - Y. KANTOR, I. WEBMAN. Phys. Rev. Lett., 52, 1891 (1984).

29 - K. SIERADZKI, R. LI. Rev. Letters, 56, 2509 (1986).

30 - D. SORNETTE. Physical Review B, 36, 8847 (1987).

31 - P. RAY, B.K. CHAKRABARTI. Preprint.

32 - S. KIRKPATRICK. in III Condensed Mater, R. Ballina, R. Maynard, G. Toulouse., eds, North-Holland (1979).

33 - J.W. ESSAM. Rep. Prog. Phys. 43, 904 (1980).

34 - P. LOURDIN, J. APPEL, J. PELOUS, T. WOIGNIER, R. VACHER. Rev. Phys. Appliquée, C4(24), 197 (1989).

35 - R. WINTER, D.W. HUA, P. THIYAGARAJAN, J. JONAS. J. Non-Cryst. Solids, 108, 137 (1989).

36 - M. KOLB, R. BOTET, J. JULLIEN. Phys. Rev. Lett., 51, 1123 (1983).

37 - P. MEAKIN. Phys. Rev. Lett., 51, 1119 (1983).

38 - R. VACHER, T. WOIGNIER, J. PHALIPPOU, J. PELOUS, E. COURTENS. J. Non-Cryst. Solids., 106, 161 (1988).

R. VACHER, T. WOIGNIER, J. PELOUS, E. COURTENS. Phys. Rev. B, 37(11), 6500 (1988).

39 - S. HAVLIN, R. NOSSAL. J. Phys. 1, 17, L427 (1984).

40 - H.J. HERRMANN, H.E. STANLEY. J. Phys. A : Math. Gen., 21, L829 (1988).

41 - P. MEAKIN. I. MAJID, S. HAVLIN, H.E. STANLEY. J. Phys. A : Math. Gen. 17, L975 (1984).

Author Index

Ackerson, Bruce J., 159
Aegerter, Michel A., 429
Ahmad, I., 401
Aksay, Ilhan A., 167, 625
Allard, Lawrence F., 807
Alviso, C.T., 791
Amal, R., 299
Amini, Mostafa M., 675
Anast, M., 453
Andrist, A. Harry, 779
Antezzo, M.F., 929
Aoki, S.I., 485
Arai, D., 569
Ashley, C.S., 247, 413
Assink, Roger A., 21

Babonneau, Florence, 815, 1035
Baes, Jr., C.F., 85
Bailey, Joseph K., 153, 759
Banash, Mark A., 727
Barbe, Christophe, 883
Barboux, P., 893
Barre, Patrice, 1035
Barrie, J.D., 347
Bartlett, J.R., 191
Basaran, Osman A., 853
Basu, S.N., 1003
Baughman, R.J., 1003
Beelen, Theo P.M., 273
Beier, Wolfram, 467
Bein, Thomas, 595
Bell, J.M., 453
Belleville, Philippe, 289
Belot, V., 3
Ben-Nissan, B., 453
Berglund, Kris A., 733, 801
Berthet, P., 541
Bhandarkar, Suhas, 637
Bleier, Alan, 185
Bogush, Gregory H., 131, 491
Boilot, J.P., 211, 305
Borek, Theodore T., 807, 1029, 1041
Bose, Arijit, 637
Boulton, J.M., 277, 407, 645, 773, 987
Bowen, H. Kent, 1009
Breval, Else, 217
Brice, V.T., 269
Brinker, C. Jeffrey, 229, 235, 247, 413, 433, 491, 575, 583, 595
Brion, D., 365
Bu, Xin Y., 779
Buchanan, Bruce R., 1075
Bura, A., 935
Burford, R.R., 767
Burkhardt, E.W., 767
Byers, Charles H., 853

Cagle, P.C., 29
Caldwell, J. Brian, 727
Calvert, Paul D., 619, 987
Cambria, Frank M., 837, 929
Campaniello, J., 541
Campostrini, R., 351
Carturan, G., 351
Chaput, F., 211, 305
Che, Tessie M., 329, 727
Chen, A.Y., 913
Chen, K.C., 663, 913
Chia, Taipau, 819
Chiang, Cyril K., 889, 917, 925
Chiba, T., 611
Choi, S.C., 485
Chow, M.K., 131
Chu, C-J., 457
Chung, Young J., 981
Cima, Michael J., 697, 877
Clark, D.E., 401
Clark, T.J., 329
Coffman, Phillip R., 709
Cogliati, G., 329
Conroy, Paula, 779
Coppa, N., 935, 941
Corriu, R., 3
Crow, J.E., 935, 941
Cruse, Richard W., 727
Cullen, J., 453
Cunningham, M.P., 387

Dal Maschio, R., 351
Dale, G.W., 371
Daran, Jean-Claude, 73
Datye, Abhaya K., 807, 1029
Dauger, A., 305
Davis, Pamela J., 235
Davis, T.L., 377
de Geyer, A., 305
Deatcher, J.H., 767
Deptula, A., 907
deVilliers, D., 453
DeVore, Lauri J., 473
Devreux, F., 211, 305
Dey, Sandwip K., 709
Dhingra, S., 825
Di Bartolomeo, A., 907
Di Maggio, Rosa, 481
Dire', S., 351
Doughty, Daniel H., 583

Dulebohn, Joel I., 733
Dunn, B., 747
Dunuwila, Dilum, 801

Earl, W.L., 229
Eichorst, Dennis J., 669
Emblem, H.G., 277
Epperson, E., 117
Evans, John F., 1017
Evans, William J., 39

Fabes, B.D., 605, 1047
Fahrenholtz, W.G., 229
Fathi, Z., 401
Fattman, George F., 283
Floch, Herve, 397
Fosmoe II, Albert G., 843
Fox, H.H., 371, 407, 773, 987
Frye, Gregory C., 433, 583
Fuqua, P.D., 747

Gagliardi, Charles D., 801
Gallo, T.A., 269
Garber, A. Ronald, 1075, 1083
Garcia, Eduardo, 921
Garino, Terry J., 497
Garvey, Garry J., 223
Gerenza, Deborah A., 283
Getman, T., 457
Giannelis, E.P., 383, 425, 685
Ginley, D.S., 1003
Gladfelter, Wayne L., 1017
Glisenti, Antonella, 811
Goodbrake, C.J., 97
Gorodisher, I., 987
Graham, Alan L., 173
Granozzi, Gaetano, 811
Gudgel, T., 407
Guerin, C., 3
Guglielmi, M., 329
Gulliver, E.A., 61
Gunnison, K.E., 625

Hain, Jr., John H., 39
Hallock, Robert B., 877
Halloran, J.W., 1003
Hampden-Smith, M.J., 61
Hanson, Scott A., 1017
Hardy, Anne B., 1009
Harrington, R.O., 461
Harris, Michael T., 853
Hashimoto, T., 861
Hawthorne, M.F., 457
Hayashi, Kazutaka, 717
Hebert, V., 365
Hench, Larry L., 819, 843, 1061
Henner, B., 3
Herman, H., 831
Hietala, S.L., 229, 433
Hietala, V.M., 433
Hill, J.R., 97
Hilliard, Janice, 583
Hirashima, H., 611
Ho, Kwok-Lun, 1017
Ho, S.F., 533
Hoang, G., 15
Holmes-Farley, S. Randall, 439
Hopkins, B., 325
Hoppe, Martin L., 865
Hrubesh, Lawrence W., 309, 315, 321
Hsieh, C.K., 819
Huang, Y.T., 917, 925
Hubert-Pfalzgraf, Liliane G., 73, 393, 397
Huffman, J.C., 61
Huling, Jeffrey C., 515
Hurd, Alan J., 229, 433, 575
Hurng, W.-M., 925
Hurwitz, Frances I., 779
Hwang, Jen-Wei, 1017

Iwasaki, Mitsunobu, 717

Jagota, S., 547
Janusson, H., 421
Jensen, Klavs F., 1017
Johnson, P.F., 341, 355
Johnston, G., 453
Johnston, Gregory P., 1029
Jolivet, Jean Pierre, 289
Jolly, M.S., 877
Jones, K., 277
Jones, L.C., 61
Jones, S.L., 123
Jutson, J.A., 123

Kaae, J.L., 461
Kalish, R., 703
Kanatzidis, M.G., 825
Kaner, R.B., 747
Katayama, Shingo, 873, 897
Kawaguchi, T., 569
Kay, Bruce D., 21
Kebede, A., 941
Keddie, J.L., 383, 425
Kennish, Richard A., 865
Kenzer, D.S., 901, 947, 953
Khairulla, Farida, 527
Kim, G.H., 625
Kim, Seong Il, 167
King, Charles M., 1075, 1083
King, R. Bruce, 1075, 1083
Klein, D.L., 605
Klein, L.C., 533
Klemperer, W.G., 29
Knobbe, E.T., 747
Koinuma, H., 861
Kong, P., 849
Koo, H.S., 917, 925

Kopylov, Nonna A., 541
Kordas, G., 901, 947, 953
Koussa, A., 407
Kwak, J.F., 1003

Lada, W., 907
Laine, Richard M., 865
Lakeman, C.D.E., 335
Lapham, D., 117
Leclercq, D., 3
Lecomte, A., 211
LeMay, J.D., 321
Lenahan, P.M., 247, 413
Lessard, Ronald B., 733
Li, Xiaoming, 341, 355
Limatta, E., 457
Lindquist, David A., 1029, 1041
Livage, Jacques, 289, 893, 1035
Look, J-L., 131
Loy, Douglas A., 975
Lu, Z.P., 857

Mackenzie, John D., 457, 663, 815, 981
Macosko, C.W., 555
Majors, P.D., 491
Mark, James E., 445
Martin, James E., 199
Martin, Stephen J., 583
Masnovi, John, 779
Massiani, Marie-Cecile, 393
Matsumoto, Roger L.K., 797
Matsuzaki, K., 569
Mattes, B.R., 747
Mazdiyasni, K.S., 913
Mazerolles, L., 893
McCormick, Alon, 263
Meakin, Paul, 141
Mecartney, Martha L., 153, 555, 759
Mehrotra, V., 685
Melpolder, S.M., 387
Meshishnek, M.J., 347
Mesmer, R.E., 85
Messing, Gary L., 515
Meyer, Henning, 995
Michel, D., 893
Milius, D.L., 625
Millar, C.E., 421
Miller, Doug, 779
Milne, S.J., 421
Mininni, Robert M., 283, 727
Mitchell, M.A., 1003
Mitchell, T.E., 1003
Moller, Karin, 595
Mondy, Lisa A., 173
Montgomery, F.C., 461
Moore, G.A., 901, 947, 953
Morineau, R., 893
Moriya, N., 703
Morosin, B., 1003
Morris, T.A., 159
Muratake, R., 611
Mutin, H., 3
Myer, G.H., 935, 941

Nagai, T., 861
Nagase, T., 759
Napier, D.G., 117
Nazar, L.F., 117
Neal, M.J., 1003
Neilson, G.F., 773
Nikles, Randall E., 283, 727
Nishida, F., 747
Nocera, Daniel G., 733
Norman, C., 123

Odler, Ivan, 467
Ohsaki, Hisashi, 429
Olczak, T., 907
Or, T.W., 849
Osborne, Nora R., 473

Paquio, S.P., 461
Paine, Robert T., 807, 1029, 1041
Papiernik, Renee, 393
Parraud, Stephen, 397
Parvizi-Majidi, A., 547
Payne, D.A., 79, 335, 485, 669
Pekala, Richard W., 321, 785, 791
Perez, I., 941
Petuskey, William T., 709
Pfender, E., 849, 857
Phalippou, J., 1087
Phillips, Richard J., 1053
Phule, Pradeep P., 527
Poco, John F., 315
Poncelet, Olivier, 73
Popall, Michael, 995
Potember, Richard S., 753
Pozarnsky, G.A., 759
Prasad, Paras N., 741

Qin, Chaobin, 819
Quarles, C.A., 325
Qui, Xiaomei, 807

Rabinovich, E.M., 541
Ramamurthi, S.D., 79
Raper, J.A., 299
Ray, D. Jean, 865
Raymond, L.J., 605
Reed, S.T., 413
Reese, Mary, 263
Revcolevschi, A., 541
Rexer, P.O., 877
Rheingold, A.L., 61

Rhine, Wendell E., 697, 877, 1009
Ribot, F., 47
Ricco, Antonio J., 583
Richardson, R.M., 123
Riman, Richard E., 293
Ring, Terry A., 883
Roncone, R.L., 377
Ruben, George C., 785
Rummens, Kees P.J., 273
Russell, M.W., 685
Ryan, Robert R., 921
Rye, R.R., 1041

Sacks, Michael D., 675
Salomon, R.E., 935, 941
Sanchez, C., 47
Sanchez, Jorge, 263
Sarikaya, M., 625
Sauer, Nancy N., 921
Sawaoka, A.B., 861
Scardi, Paolo, 481
Schaeffer, Riley, 1029
Scherer, George W., 503, 1087
Schilling, Christopher H., 167
Schmidt, Helmut K., 961, 995
Schulz, Jochen, 995
Schwartz, Robert W., 335
Schwegler, J.W., 935, 941
Scott, Timothy C., 853
Scozzafava, Mary Rose, 697
Scriven, L.E., 555
Sekine, Masahiro, 873, 897
Septe, Bernard, 393
Shacham-Diamand, Y., 703
Shaffer, G.R., 413
Shane, Michael J., 1053
Shanefield, Daniel J., 293
Sharma, R., 387
Shea, Kenneth J., 975
Shei, C.Y., 889, 925
Sherif, Fawzy G., 831
Shichiri, Takaki, 429
Shih, Wan Y., 167
Shih, Wei-Heng, 167
Shiraishi, T., 861
Shyu, Lieh-Jiun, 837
Siedle, A.R., 97
Simmons, C.A., 29
Simms, B.L., 269
Skarjune, R.P., 97
Smith, Bruce E., 223
Smith, Douglas M., 229, 235, 433, 491, 1029
Soraru, Gian D., 351, 811, 815
Soskey, Paul R., 283
Speck, Kenneth R., 753
Spiccia, L., 453
Stachowicz, L., 849
Steinthal, M.G., 1047
Streckert, H.H., 461
Switzer, Jay A., 1053

Takagi, Y., 861
Taneda, N., 569
Taylor, D.J., 1047
Teepe, M.R., 901, 947, 953
Teowee, G., 407, 645, 987
Thompson, J., 987
Thompson, Major C., 1075
Tillotson, Thomas M., 309, 315, 321
Ting, Su-Jen, 457, 981
Toledano, P., 47
Tomasi, Andrea, 481
Tronc, Elisabeth, 289
Tsurita, Y., 361
Tu, G.C., 917

Uhlmann, D.R., 407, 645, 773, 987

Valente-Campion, I., 893
van Santen, Rutger A., 273
Van Vlierberge, Béatrice, 733
Venturini, E.L., 1003
Verdaguer, Michel, 1035
Vilminot, S., 365
Vioux, A., 3

Wada, K., 361
Waite, T.D., 299
Walden, Barbara L., 217
Wall, D.R., 461
Wallace, S., 255
Wandass, J.H., 929
Wang, Jiun-Fang, 293
Wang, Q., 3
Wang, Shuhong, 445
Warden, Victor N., 727
Wark, T.A., 61
Warren, W.L., 247, 413
Watkins, I., 453
Watson, J., 15
Webster, Owen, 975
Weisenbach, L., 377
Weller-Brophy, Laura A., 371, 377
West, A.W., 387
West, B.O., 453
West, J.K., 255
Westmoreland, C. Gary, 185
White, William B., 217
Whitwell, G.E., 929
Wijnen, Peter W.J.G., 273
Wilcoxon, Jess, 199
Wilson, June, 1061
Woignier, T., 1087
Wood, T.E., 97
Woolfrey, J.L., 191

Wu, P.T., 925
Wu, S.F., 925

Xu, Ping, 445

Yaacob, Iskandar, 637
Yamane, Masayuki, 717
Yamashita, T., 611
Yanagida, H., 485
Yanyo, Lynn C., 439
Yasrebi, M., 625
Yasum ri, Atsuo, 717
Yoshimoto, M., 861
Youngdahl, Kay A., 865
Yu, Jeong-a, 733

Zelinski, Brian J.J., 371, 377, 645
Zerda, T.W., 15, 325
Zhang, Zhi-Fan, 865
Żółtowski, T., 907
Zukoski, C.F., 131

Subject Index

2-(2-ethoxyethoxy)ethoxide, 697
2-methyl-4-nitroaniline, 987

acetylacetone, 485
aerogels, 217, 309, 315
  alumino-silicate, 305
  and nitride synthesis, 1028
  comparison to xerogels, 329
  organic, 321, 785, 791
  silica, 321, 785
aggregation
  colloidal, 141
  mechanisms, 131, 273
  iron oxide, 299
alkoxides
  bismuth, 921
  calcium-bismuth, 873
  carboxylate complexes, 801
  lead and niobium, 393
  modification with propionic acid, 365
  strontium-bismuth, 873
alumina-silica gels, 229, 433
  aerogels, 305
  matrix for composites, 547
aluminum
  chlorohydrate, 277
  nitride, 709, 853, 1017
  oxycarbide, 811
aragonite, 619, 625
aryl-bridged
  polysilsesquioxanes, 975
azides, 1017

barium
  aluminate, 365
  hydroxide, 941
  titanate, 453, 645
  zirconate, 527
base catalysis, 3
Bi-Pb-Sr-Ca-Cu-O, 889, 917, 925
Bi-Sr-Ca-Cu-O, 873, 889
bimetallic alkoxides, 669, 675
bioactive fixation, 1061
biomaterials, 1061
biomimetic materials, 619, 625, 637, 685
bismuth amides, 921
borazene amine polymers, 1041
boron nitride, 807, 1028, 1041

calcium aluminate, 365
$CaO-P_2O_5-SiO_2$ biogels, 1061
carboxylates, 865, 883
carboxylic acids, 801, 877
centrifugation, 167
ceramers, 407, 439, 767, 773, 961, 975, 981
  acyl-group-containing polymeric titania, 801
  adhesion, 995
  as patternable dielectrics, 995
  photonic applications, 741, 747, 987
  rubbery ORMOSILS, 981
  UV-curing, 995
ceramic superlattices, 1053
chalcogenides, 825
chemical sensors, 583
chromatographic absorbents, 975
coatings
  boron nitride, 807
  for building materials, 467
  inhomogeneities in, 605
  on
    fibers, 461
    metals, 473, 481
composites, 185, 421, 445
  biomimetic processing, 625
  BN/SiC, 1028
  ceramer, 961
  densification, 503
  in situ crystallization, 547
  nonlinear optical applications, 741, 747
concentrated dispersions
  consolidation, 167
  rheology, 173
  shear affects on structure, 159
condensation
  base catalyzed system, 263
  kinetics, 21
  silicon alkoxides, 211
conjugated polymers, 747
counter-flow liquid injection plasma synthesis, 849
cracking of thin films, 497
cryo-TEM, 153, 759
crystallization
  controlled by seeding, 515
  lithium niobate, 669
  pyrolyzed polysilazanes, 797
  PZT films, 663
  SiC-mullite composite, 547
  silica-titania waveguides, 377
  SiO_2-SnO_2 composites, 351
  $SiO_2-ZrO_2-Na_2O$ glasses, 361

crystallization (continued)
transition metal oxide coatings, 611
versus densification, 503
zirconium silicate gels, 347, 355

defect structures in silica, 247
densification, 335, 377
inclusion effects on, 503
laser, 819, 1047
thin films, 425, 611
dimethylaminoalane, 709
dip coating, 575, 753
DLVO theory, 191
drying, 235
thin films, 497

EDTA colloid, 917
electrical dispersion reactor, 853
electrodeposition, 1053
electronic properties
aluminum silicate thin films, 433
dielectric(s), 527, 703
properties of ceramers, 407, 995
electroactive polymers, 685
ferroelectric thin films, 645
niobate, 401, 669, 675
$PbTiO_3$ fibers, 485
thin films, 413, 453
electrophoretic mobility, 293
ellipsometry, 371, 377, 383, 387, 433, 605, 1047
in situ imaging of dip coating, 575
emulsion precipitation, 831, 837
epoxysilane, 961
ESR spectroscopy, 247
etching
silica films, 605
spin-on-glasses, 703
ethylenediamine, 897
ethylsilane, 779
EXAFS spectroscopy, 595, 873, 897, 1035

ferrites, 637
ferroelectrics, 645
fibers, 421, 457, 485, 555, 569
coatings on, 461
superconducting, 865, 897, 913, 1003
fractal(s)
aerogels, 211
alumina sol-gels, 117
alumino-silicate aerogels, 305
and particle aggregation, deposition, segregation, 141, 273, 299
structure, 199, 217
time, 199, 685
$YBa_2Cu_3O_7$ sols, 947
freeze drying, 935

galium nitride, 1017
gel-ceramic transition, 335, 341, 347, 355
gelation
effects of trioxane on, 341
fractal structure, 199
gradient index glass (see GRIN glass)
GRIN glass, 727, 717

hybrid gels, 515
hydrogenosiliconates, 3
hydrolysis
aluminum salt solutions, 97
bismuth alkoxides, 921
effects on thin film cracking, 497
emulsion, 831, 837
epoxysilane, 961
in presence of water-soluble polymers, 1009
ions in aqueous solution, 85
kinetics, 21
lead titanium alkoxides, 335
modified yttrium alkoxides, 73
TEOS and TMOS, 15, 309
hydroxides, 85
superconductors, 893, 941
hydroxyapatite, 619
hypercritical drying, 321
hypervalent silicon species, 3

implants, 1061
intercalation, 685
interdigitated capacitor, 961
interferometry, 727
intravesicular precipitation, 637
ion
exchange materials, 595
implantation effects, 703
IR spectroscopy, 255, 393, 611, 669, 703, 897

kinetics
effects of trioxane on gelation, 341

kinetics (continued)
  growth of silica
    aggregates, 273
    spheres, 445, 491
  TEOS and TMOS, 21

lanthanide ions, 733
laser
  damage, 397
  densification, 819, 1047
  direct writing, 995
lead titanate, 335, 421, 485, 645
light harvesting centers, 733
lithium
  niobate, 669
  silicate gels, 533
luminescence, 733

mechanical properties
  aerogels, 321
  alumina coated fibers, 461
  silica
    fibers, 569
    films, 605
  SiO_2-SnO_2 composites, 351
melamine-formaldehyde, 791
mixed metal oxides, 61, 289
molecular orbital theory, 255
Monte-Carlo simulations
  aggregation, deposition and segregation, 141
mullite, 515

N_2 adsorption studies, 29
nanostructures, 637, 685, 1053
neutron diffraction, 953
NMR spectroscopy, 223, 263, 309, 315, 491
  aged and dried gels, 235
  alumina sol-gels, 117
  bismuth alkoxides, 921
  ceramers, 981
  imaging of concentrated suspensions, 173
  lead
    and niobium alkoxides, 393
    titanate gels, 79
  niobates, 675
  organoaluminum precursor, 709
  polycarbosilane precursors, 815
  polysilsesquioxanes, 975
  pre-ceramic polymers for SiC/TiC, 1035
  silica aerogel, 211
  superconductors, 873
nonlinear optics, 741, 747
nucleophilic activation, 3

octamethyl orthosilicate, 29
optical
  interference filters, 383
  GRIN glass, 717, 727
  niobates, 669, 675
  niobium and tantalum oxide films, 397, 611
  nonlinear materials, 741, 747, 987
  sensors, 733
  switches, 753
  thin films, 645
  V_2O_5 films and gels, 611
  waveguides, 371, 377
  windows, transpiration cooled, 843
organometallic decomposition, 883
ORMOCERs (see ceramers)
ORMOSILs (see ceramers)
oxalic acid, 1009
oxidation resistance, boron nitride, 807
oxo-alkoxides, 47
oxometalate-glass composites, 595

p-nitroaniline, 987
perovskites, 645, 663, 893, 929
photochemical polymerization, 779
photolithography, 961
photonics, 741, 987
plasma synthesis, 831, 849, 857
PMMA particles, concentrated solutions, 159
polyaniline, 747
poly(borazinylamines), 1028
polycarbosilanes, 779, 811, 815
polycerams (see ceramers)
polymerization
  alkenylsilanes, 779
  melamine with formaldehyde, 791
  photochemical, 779
  zirconyl chloride, 123
polynuclear species, 85
polyselenide complexes, 825
polysilanes, 779
polysilazanes, 797
polytitanocarbosilane, 1035
pore structure, 235, 1028
  and positronium decay, 325
  closed porosity, 433
  porous glasses, 361
  size distribution via SAW, 583
positronium decay, 325
potassium niobate, 675

precipitation
  carboxylic acids, 877, 883
  emulsion, 831, 837
  hydroxides, 893
  magnetic particles in vesicles, 637
  silica in polymer matrix, 445
  uniform particles, 131
pressure filtration, 167
pyrochlore, 645, 663
pyrolysis
  precursors
    boron nitride, 1041
    carbide, 797, 811, 815

Raman spectroscopy
  defect bands, 247
  lithium niobate, 669
  pre-resonant, 801
  silica
    and silicophosphate aerogels, 217
    -titania gels, 329
  TEOS and TMOS, 15
refractive index profile, 717, 727
rheology
  base catalyzed gels, 223
  concentrated suspensions, 159, 173
  sol-gel transition, 283
  solutions for fiber and film formation, 555
  stability transitions in alpha-alumina, 185
  vanadia gels, 759
Rutherford backscattering spectroscopy, 383, 425, 453

SANS, 47, 305
SAXS, 123, 273, 901, 947
second harmonic generation, 741, 987
seeding of gels, 515
selenides, 825
self-similarity, 305
semiconductor-to-metal transition, 753
shear
  effects on concentrated dispersions, 159
  flow in alpha-Al_2O_3, 185
shrinkage, 497
  effects of inclusions, 503
SiC/TiC, 1035
silica(-)
  beads, 1009
  monodisperse colloidal particles, 153
  titania
    aerogels, alcogels, 329
    interference filters, 383
    thin films, 387
    waveguides, 371, 377
  type VI, 843
silicon
  carbide, 797, 811, 815, 1035
  nitride, 293, 797
silsesquioxanes, 767, 975
$SiO_2ZrO_2Na_2O$, 361
sol-gel
  processing
    aging and drying, 235, 497
    alumina gels, 97
    base catalysis, 223, 263, 269
    biomimetic, 619, 625, 637
    carboxylic acid effects, 365
    chemistry of alkoxide precursors, 47
    colloidal suspensions, 167
    dip coating, 575
    electrical dispersion reactor, 853
    electrodeposition, 1053
    emulsion precipitation, 831, 837
    extrusion of gels, 421, 865
    freeze drying, 935
    gel infiltration technique, 533
    heteropolymetallic alkoxides, 39
    laser densification, 819
    low surface area gels, 229
    microwave, 401
    organic catalysts, 269
    organically modified ceramics, 377, 407, 439, 767, 773, 961, 975, 981, 995
    $PbTiO_3$ gels, 79
    plasma, 831, 849, 857
    polymerization, 29
    rapid thermal processing, 1003
    resins, 913
    solvent effects, 277
    superconducting material, 697, 865, 877, 883, 889, 893, 897, 901, 907, 913, 917, 921, 925, 935, 941, 947, 953, 1003
    Synroc B, 191
    trioxane effects on gelation, 341
    water extraction, 907
  transition, 223, 283, 341

solid state electrolytes, 961
sols
  copper and copper-barium yttrium, 697
  niobium and tantalum, 397
  superconductors, 901, 907, 947
  vanadia, 759
  zirconium silicate, 541
spin-on-glass, 703
spinel, 289, 849
structure
  alumina
    from aqueous solution, 97
    via NMR and SANS, 117
  bismuth alkoxides, 39, 921
  Ce, Ti, Nb metal alkoxide precursors, 47
  concentrated dispersions, 159, 173
  copper alkoxide, 39
  lead and niobium alkoxides, 393
  lithium niobate, 669
  modified copper alkoxide, 873
  organoaluminum precursors, 709
  partially condensed silica, 309
  pre-ceramic polymers for SiC/TiC, 1035
  SiO_2 gel-films, 429
  tin oxide compounds, 61
superconductors, 697, 889, 917, 925
  barrier layers, 929
  carboxylates, 865, 883
  carboxylic acids, 877
  fibers, 865, 877, 897
  films, 873, 883
  fractal dimensions, 947
  freeze drying, 935
  from soluble resins, 913
  hydroxides, 893, 941
  neutron diffraction, 953
  precursors, 39, 921
  rapid thermal processing, 1003
  Tl-Ca-Ba-Cu-O, 901
  water extraction, 907
surface
  acoustic wave, 433, 583
  area, 229, 1028
    evolution during sphere growth, 491
    low surface area films, 433
    SAW measurements of, 583
  charge, 293
  hydroxyls, 255, 325
synthesis
  bismuth and copper alkoxides, 39
  carbides, 811, 815
  chalcogenides, 825
  GRIN materials, 727
  heterometallic alkoxides, 393
  iron oxides, oxyhydroxides, 289
  low density silica aerogel, 315
  multicomponent ceramic (Synroc B), 191
  organoaluminum precursors, 709
  porous mixed oxide supports, 361
  superconductor precursors, 873, 921
  TiC precursors, 457
  tin alkoxide, low temperature, 61

TEM
  alumina coatings, 461
  boron nitride films, 807
  cryo-genic, 153, 759
  electron diffraction of SiO_2 films, 429
  hybrid gels, 515
  platinum-carbon replication technique, 785
  silica, 217, 445, 605
    aerogels, 785
  silicophosphate, 217
  SiO_2-TiO_2 thin films, 387
  superconductors, 893, 901
thermal control paints, 347
thin films
  anisotropic, 439
  barrier layers, 929
  boron nitride, 807
  cracking, 497
  densification of TiO_2, 425
  dip coating, 575
  electronic properties, 413
  ferroelectric, 645
  inhomogeneities in, 605
  luminescent, 733
  nanomodulated, by electrodeposition, 1053
  niobium and tantalum oxide, 397
  nitrides, 807, 1017
  on Nicalon fibers, 461
  organo-titania, 801
  oxometalate-glass composite, 595
  protective, 467, 473, 481

thin films (continued)
rheology of solutions for, 555
SiO_2-TiO_2, 377, 383, 387
superconducting, 873, 883, 947
TiC, 457
titania colloidal particles, 153
titanium carbide, 811, 815, 1035
Tl-Ca-Ba-Cu-O, 897
TlPbO, 1053
transpiration cooled windows, 843
triple DC torch plasma reactor, 857

vanadium dioxide, 753, 759
vinylsilane, 779

water
extraction, 907
swellable polymers, 1009
waveguides, 371, 377

XANES spectroscopy, 1035
xerogels, 29, 123
comparison to aerogels, 329
polysilsesquioxane, 975
type VI silica, 843
XPS spectroscopy, 533, 811
x-ray
heterometallic alkoxides, 393
niobates, 669, 675
PZT films, 663
radiography of concentrated suspensions, 173
silica-titania gels, 329
SiO_2-SnO_2 composites, 351
superconductors, 889, 893, 901, 907
transition metal oxide coatings, 611
ZrO_2-SiO_2 gels, 341, 355, 541

$YBa_2Cu_2O_7$, 697
$YBa_2Cu_3O_7$, 865, 877, 883, 897, 907, 913, 929, 935, 941, 947, 953, 1003
yttrium alkoxide, modification with acetylacetone, 73

zeta potential, 185
zirconia, 481, 831, 837
zirconium
carbide, 815
silicate, 347, 355, 541

MATERIALS RESEARCH SOCIETY SYMPOSIUM PROCEEDINGS

ISSN 0272 - 9172

Volume 1—Laser and Electron-Beam Solid Interactions and Materials Processing, J. F. Gibbons, L. D. Hess, T. W. Sigmon, 1981, ISBN 0-444-00595-1

Volume 2—Defects in Semiconductors, J. Narayan, T. Y. Tan, 1981, ISBN 0-444-00596-X

Volume 3—Nuclear and Electron Resonance Spectroscopies Applied to Materials Science, E. N. Kaufmann, G. K. Shenoy, 1981, ISBN 0-444-00597-8

Volume 4—Laser and Electron-Beam Interactions with Solids, B. R. Appleton, G. K. Celler, 1982, ISBN 0-444-00693-1

Volume 5—Grain Boundaries in Semiconductors, H. J. Leamy, G. E. Pike, C. H. Seager, 1982, ISBN 0-444-00697-4

Volume 6—Scientific Basis for Nuclear Waste Management IV, S. V. Topp, 1982, ISBN 0-444-00699-0

Volume 7—Metastable Materials Formation by Ion Implantation, S. T. Picraux, W. J. Choyke, 1982, ISBN 0-444-00692-3

Volume 8—Rapidly Solidified Amorphous and Crystalline Alloys, B. H. Kear, B. C. Giessen, M. Cohen, 1982, ISBN 0-444-00698-2

Volume 9—Materials Processing in the Reduced Gravity Environment of Space, G. E. Rindone, 1982, ISBN 0-444-00691-5

Volume 10—Thin Films and Interfaces, P. S. Ho, K.-N. Tu, 1982, ISBN 0-444-00774-1

Volume 11—Scientific Basis for Nuclear Waste Management V, W. Lutze, 1982, ISBN 0-444-00725-3

Volume 12—In Situ Composites IV, F. D. Lemkey, H. E. Cline, M. McLean, 1982, ISBN 0-444-00726-1

Volume 13—Laser-Solid Interactions and Transient Thermal Processing of Materials, J. Narayan, W. L. Brown, R. A. Lemons, 1983, ISBN 0-444-00788-1

Volume 14—Defects in Semiconductors II, S. Mahajan, J. W. Corbett, 1983, ISBN 0-444-00812-8

Volume 15—Scientific Basis for Nuclear Waste Management VI, D. G. Brookins, 1983, ISBN 0-444-00780-6

Volume 16—Nuclear Radiation Detector Materials, E. E. Haller, H. W. Kraner, W. A. Higinbotham, 1983, ISBN 0-444-00787-3

Volume 17—Laser Diagnostics and Photochemical Processing for Semiconductor Devices, R. M. Osgood, S. R. J. Brueck, H. R. Schlossberg, 1983, ISBN 0-444-00782-2

Volume 18—Interfaces and Contacts, R. Ludeke, K. Rose, 1983, ISBN 0-444-00820-9

Volume 19—Alloy Phase Diagrams, L. H. Bennett, T. B. Massalski, B. C. Giessen, 1983, ISBN 0-444-00809-8

Volume 20—Intercalated Graphite, M. S. Dresselhaus, G. Dresselhaus, J. E. Fischer, M. J. Moran, 1983, ISBN 0-444-00781-4

Volume 21—Phase Transformations in Solids, T. Tsakalakos, 1984, ISBN 0-444-00901-9

Volume 22—High Pressure in Science and Technology, C. Homan, R. K. MacCrone, E. Whalley, 1984, ISBN 0-444-00932-9 (3 part set)

Volume 23—Energy Beam-Solid Interactions and Transient Thermal Processing, J. C. C. Fan, N. M. Johnson, 1984, ISBN 0-444-00903-5

Volume 24—Defect Properties and Processing of High-Technology Nonmetallic Materials, J. H. Crawford, Jr., Y. Chen, W. A. Sibley, 1984, ISBN 0-444-00904-3

Volume 25—Thin Films and Interfaces II, J. E. E. Baglin, D. R. Campbell, W. K. Chu, 1984, ISBN 0-444-00905-1

MATERIALS RESEARCH SOCIETY SYMPOSIUM PROCEEDINGS

Volume 26—Scientific Basis for Nuclear Waste Management VII, G. L. McVay, 1984, ISBN 0-444-00906-X

Volume 27—Ion Implantation and Ion Beam Processing of Materials, G. K. Hubler, O. W. Holland, C. R. Clayton, C. W. White, 1984, ISBN 0-444-00869-1

Volume 28—Rapidly Solidified Metastable Materials, B. H. Kear, B. C. Giessen, 1984, ISBN 0-444-00935-3

Volume 29—Laser-Controlled Chemical Processing of Surfaces, A. W. Johnson, D. J. Ehrlich, H. R. Schlossberg, 1984, ISBN 0-444-00894-2

Volume 30—Plasma Processing and Synthesis of Materials, J. Szekely, D. Apelian, 1984, ISBN 0-444-00895-0

Volume 31—Electron Microscopy of Materials, W. Krakow, D. A. Smith, L. W. Hobbs, 1984, ISBN 0-444-00898-7

Volume 32—Better Ceramics Through Chemistry, C. J. Brinker, D. E. Clark, D. R. Ulrich, 1984, ISBN 0-444-00898-5

Volume 33—Comparison of Thin Film Transistor and SOI Technologies, H. W. Lam, M. J. Thompson, 1984, ISBN 0-444-00899-3

Volume 34—Physical Metallurgy of Cast Iron, H. Fredriksson, M. Hillerts, 1985, ISBN 0-444-00938-8

Volume 35—Energy Beam-Solid Interactions and Transient Thermal Processing/1984, D. K. Biegelsen, G. A. Rozgonyi, C. V. Shank, 1985, ISBN 0-931837-00-6

Volume 36—Impurity Diffusion and Gettering in Silicon, R. B. Fair, C. W. Pearce, J. Washburn, 1985, ISBN 0-931837-01-4

Volume 37—Layered Structures, Epitaxy, and Interfaces, J. M. Gibson, L. R. Dawson, 1985, ISBN 0-931837-02-2

Volume 38—Plasma Synthesis and Etching of Electronic Materials, R. P. H. Chang, B. Abeles, 1985, ISBN 0-931837-03-0

Volume 39—High-Temperature Ordered Intermetallic Alloys, C. C. Koch, C. T. Liu, N. S. Stoloff, 1985, ISBN 0-931837-04-9

Volume 40—Electronic Packaging Materials Science, E. A. Giess, K.-N. Tu, D. R. Uhlmann, 1985, ISBN 0-931837-05-7

Volume 41—Advanced Photon and Particle Techniques for the Characterization of Defects in Solids, J. B. Roberto, R. W. Carpenter, M. C. Wittels, 1985, ISBN 0-931837-06-5

Volume 42—Very High Strength Cement-Based Materials, J. F. Young, 1985, ISBN 0-931837-07-3

Volume 43—Fly Ash and Coal Conversion By-Products: Characterization, Utilization, and Disposal I, G. J. McCarthy, R. J. Lauf, 1985, ISBN 0-931837-08-1

Volume 44—Scientific Basis for Nuclear Waste Management VIII, C. M. Jantzen, J. A. Stone, R. C. Ewing, 1985, ISBN 0-931837-09-X

Volume 45—Ion Beam Processes in Advanced Electronic Materials and Device Technology, B. R. Appleton, F. H. Eisen, T. W. Sigmon, 1985, ISBN 0-931837-10-3

Volume 46—Microscopic Identification of Electronic Defects in Semiconductors, N. M. Johnson, S. G. Bishop, G. D. Watkins, 1985, ISBN 0-931837-11-1

Volume 47—Thin Films: The Relationship of Structure to Properties, C. R. Aita, K. S. SreeHarsha, 1985, ISBN 0-931837-12-X

Volume 48—Applied Materials Characterization, W. Katz, P. Williams, 1985, ISBN 0-931837-13-8

Volume 49—Materials Issues in Applications of Amorphous Silicon Technology, D. Adler, A. Madan, M. J. Thompson, 1985, ISBN 0-931837-14-6

MATERIALS RESEARCH SOCIETY SYMPOSIUM PROCEEDINGS

Volume 50—*Scientific Basis for Nuclear Waste Management IX*, L. O. Werme, 1986, ISBN 0-931837-15-4

Volume 51—Beam-Solid Interactions and Phase Transformations, H. Kurz, G. L. Olson, J. M. Poate, 1986, ISBN 0-931837-16-2

Volume 52—Rapid Thermal Processing, T. O. Sedgwick, T. E. Seidel, B.-Y. Tsaur, 1986, ISBN 0-931837-17-0

Volume 53—Semiconductor-on-Insulator and Thin Film Transistor Technology, A. Chiang. M. W. Geis, L. Pfeiffer, 1986, ISBN 0-931837-18-9

Volume 54—Thin Films—Interfaces and Phenomena, R. J. Nemanich, P. S. Ho, S. S. Lau, 1986, ISBN 0-931837-19-7

Volume 55—Biomedical Materials, J. M. Williams, M. F. Nichols, W. Zingg, 1986, ISBN 0-931837-20-0

Volume 56—Layered Structures and Epitaxy, J. M. Gibson, G. C. Osbourn, R. M. Tromp, 1986, ISBN 0-931837-21-9

Volume 57—Phase Transitions in Condensed Systems—Experiments and Theory, G. S. Cargill III, F. Spaepen, K.-N. Tu, 1987, ISBN 0-931837-22-7

Volume 58—Rapidly Solidified Alloys and Their Mechanical and Magnetic Properties, B. C. Giessen, D. E. Polk, A. I. Taub, 1986, ISBN 0-931837-23-5

Volume 59—Oxygen, Carbon, Hydrogen, and Nitrogen in Crystalline Silicon, J. C. Mikkelsen, Jr., S. J. Pearton, J. W. Corbett, S. J. Pennycook, 1986, ISBN 0-931837-24-3

Volume 60—Defect Properties and Processing of High-Technology Nonmetallic Materials, Y. Chen, W. D. Kingery, R. J. Stokes, 1986, ISBN 0-931837-25-1

Volume 61—Defects in Glasses, F. L. Galeener, D. L. Griscom, M. J. Weber, 1986, ISBN 0-931837-26-X

Volume 62—Materials Problem Solving with the Transmission Electron Microscope, L. W. Hobbs, K. H. Westmacott, D. B. Williams, 1986, ISBN 0-931837-27-8

Volume 63—Computer-Based Microscopic Description of the Structure and Properties of Materials, J. Broughton, W. Krakow, S. T. Pantelides, 1986, ISBN 0-931837-28-6

Volume 64—Cement-Based Composites: Strain Rate Effects on Fracture, S. Mindess, S. P. Shah, 1986, ISBN 0-931837-29-4

Volume 65—Fly Ash and Coal Conversion By-Products: Characterization, Utilization and Disposal II, G. J. McCarthy, F. P. Glasser, D. M. Roy, 1986, ISBN 0-931837-30-8

Volume 66—Frontiers in Materials Education, L. W. Hobbs, G. L. Liedl, 1986, ISBN 0-931837-31-6

Volume 67—Heteroepitaxy on Silicon, J. C. C. Fan, J. M. Poate, 1986, ISBN 0-931837-33-2

Volume 68—Plasma Processing, J. W. Coburn, R. A. Gottscho, D. W. Hess, 1986, ISBN 0-931837-34-0

Volume 69—Materials Characterization, N. W. Cheung, M.-A. Nicolet, 1986, ISBN 0-931837-35-9

Volume 70—Materials Issues in Amorphous-Semiconductor Technology, D. Adler, Y. Hamakawa, A. Madan, 1986, ISBN 0-931837-36-7

Volume 71—Materials Issues in Silicon Integrated Circuit Processing, M. Wittmer, J. Stimmell, M. Strathman, 1986, ISBN 0-931837-37-5

Volume 72—Electronic Packaging Materials Science II, K. A. Jackson, R. C. Pohanka, D. R. Uhlmann, D. R. Ulrich, 1986, ISBN 0-931837-38-3

Volume 73—Better Ceramics Through Chemistry II, C. J. Brinker, D. E. Clark, D. R. Ulrich, 1986, ISBN 0-931837-39-1

Volume 74—Beam-Solid Interactions and Transient Processes, M. O. Thompson, S. T. Picraux, J. S. Williams, 1987, ISBN 0-931837-40-5

MATERIALS RESEARCH SOCIETY SYMPOSIUM PROCEEDINGS

Volume 75—Photon, Beam and Plasma Stimulated Chemical Processes at Surfaces, V. M. Donnelly, I. P. Herman, M. Hirose, 1987, ISBN 0-931837-41-3

Volume 76—Science and Technology of Microfabrication, R. E. Howard, E. L. Hu, S. Namba, S. Pang, 1987, ISBN 0-931837-42-1

Volume 77—Interfaces, Superlattices, and Thin Films, J. D. Dow, I. K. Schuller, 1987, ISBN 0-931837-56-1

Volume 78—Advances in Structural Ceramics, P. F. Becher, M. V. Swain, S. Sōmiya, 1987, ISBN 0-931837-43-X

Volume 79—Scattering, Deformation and Fracture in Polymers, G. D. Wignall, B. Crist, T. P. Russell, E. L. Thomas, 1987, ISBN 0-931837-44-8

Volume 80—Science and Technology of Rapidly Quenched Alloys, M. Tenhover, W. L. Johnson, L. E. Tanner, 1987, ISBN 0-931837-45-6

Volume 81—High-Temperature Ordered Intermetallic Alloys, II, N. S. Stoloff, C. C. Koch, C. T. Liu, O. Izumi, 1987, ISBN 0-931837-46-4

Volume 82—Characterization of Defects in Materials, R. W. Siegel, J. R. Weertman, R. Sinclair, 1987, ISBN 0-931837-47-2

Volume 83—Physical and Chemical Properties of Thin Metal Overlayers and Alloy Surfaces, D. M. Zehner, D. W. Goodman, 1987, ISBN 0-931837-48-0

Volume 84—Scientific Basis for Nuclear Waste Management X, J. K. Bates, W. B. Seefeldt, 1987, ISBN 0-931837-49-9

Volume 85—Microstructural Development During the Hydration of Cement, L. Struble, P. Brown, 1987, ISBN 0-931837-50-2

Volume 86—Fly Ash and Coal Conversion By-Products Characterization, Utilization and Disposal III, G. J. McCarthy, F. P. Glasser, D. M. Roy, S. Diamond, 1987, ISBN 0-931837-51-0

Volume 87—Materials Processing in the Reduced Gravity Environment of Space, R. H. Doremus, P. C. Nordine, 1987, ISBN 0-931837-52-9

Volume 88—Optical Fiber Materials and Properties, S. R. Nagel, J. W. Fleming, G. Sigel, D. A. Thompson, 1987, ISBN 0-931837-53-7

Volume 89—Diluted Magnetic (Semimagnetic) Semiconductors, R. L. Aggarwal, J. K. Furdyna, S. von Molnar, 1987, ISBN 0-931837-54-5

Volume 90—Materials for Infrared Detectors and Sources, R. F. C. Farrow, J. F. Schetzina, J. T. Cheung, 1987, ISBN 0-931837-55-3

Volume 91—Heteroepitaxy on Silicon II, J. C. C. Fan, J. M. Phillips, B.-Y. Tsaur, 1987, ISBN 0-931837-58-8

Volume 92—Rapid Thermal Processing of Electronic Materials, S. R. Wilson, R. A. Powell, D. E. Davies, 1987, ISBN 0-931837-59-6

Volume 93—Materials Modification and Growth Using Ion Beams, U. Gibson, A. E. White, P. P. Pronko, 1987, ISBN 0-931837-60-X

Volume 94—Initial Stages of Epitaxial Growth, R. Hull, J. M. Gibson, David A. Smith, 1987, ISBN 0-931837-61-8

Volume 95—Amorphous Silicon Semiconductors—Pure and Hydrogenated, A. Madan, M. Thompson, D. Adler, Y. Hamakawa, 1987, ISBN 0-931837-62-6

Volume 96—Permanent Magnet Materials, S. G. Sankar, J. F. Herbst, N. C. Koon, 1987, ISBN 0-931837-63-4

Volume 97—Novel Refractory Semiconductors, D. Emin, T. Aselage, C. Wood, 1987, ISBN 0-931837-64-2

Volume 98—Plasma Processing and Synthesis of Materials, D. Apelian, J. Szekely, 1987, ISBN 0-931837-65-0

MATERIALS RESEARCH SOCIETY SYMPOSIUM PROCEEDINGS

Volume 99—High-Temperature Superconductors, M. B. Brodsky, R. C. Dynes, K. Kitazawa, H. L. Tuller, 1988, ISBN 0-931837-67-7

Volume 100—Fundamentals of Beam-Solid Interactions and Transient Thermal Processing, M. J. Aziz, L. E. Rehn, B. Stritzker, 1988, ISBN 0-931837-68-5

Volume 101—Laser and Particle-Beam Chemical Processing for Microelectronics, D.J. Ehrlich, G.S. Higashi, M.M. Oprysko, 1988, ISBN 0-931837-69-3

Volume 102—Epitaxy of Semiconductor Layered Structures, R. T. Tung, L. R. Dawson, R. L. Gunshor, 1988, ISBN 0-931837-70-7

Volume 103—Multilayers: Synthesis, Properties, and Nonelectronic Applications, T. W. Barbee Jr., F. Spaepen, L. Greer, 1988, ISBN 0-931837-71-5

Volume 104—Defects in Electronic Materials, M. Stavola, S. J. Pearton, G. Davies, 1988, ISBN 0-931837-72-3

Volume 105—SiO_2 and Its Interfaces, G. Lucovsky, S. T. Pantelides, 1988, ISBN 0-931837-73-1

Volume 106—Polysilicon Films and Interfaces, C.Y. Wong, C.V. Thompson, K-N. Tu, 1988, ISBN 0-931837-74-X

Volume 107—Silicon-on-Insulator and Buried Metals in Semiconductors, J. C. Sturm, C. K. Chen, L. Pfeiffer, P. L. F. Hemment, 1988, ISBN 0-931837-75-8

Volume 108—Electronic Packaging Materials Science II, R. C. Sundahl, R. Jaccodine, K. A. Jackson, 1988, ISBN 0-931837-76-6

Volume 109—Nonlinear Optical Properties of Polymers, A. J. Heeger, J. Orenstein, D. R. Ulrich, 1988, ISBN 0-931837-77-4

Volume 110—Biomedical Materials and Devices, J. S. Hanker, B. L. Giammara, 1988, ISBN 0-931837-78-2

Volume 111—Microstructure and Properties of Catalysts, M. M. J. Treacy, J. M. Thomas, J. M. White, 1988, ISBN 0-931837-79-0

Volume 112—Scientific Basis for Nuclear Waste Management XI, M. J. Apted, R. E. Westerman, 1988, ISBN 0-931837-80-4

Volume 113—Fly Ash and Coal Conversion By-Products: Characterization, Utilization, and Disposal IV, G. J. McCarthy, D. M. Roy, F. P. Glasser, R. T. Hemmings, 1988, ISBN 0-931837-81-2

Volume 114—Bonding in Cementitious Composites, S. Mindess, S. P. Shah, 1988, ISBN 0-931837-82-0

Volume 115—Specimen Preparation for Transmission Electron Microscopy of Materials, J. C. Bravman, R. Anderson, M. L. McDonald, 1988, ISBN 0-931837-83-9

Volume 116—Heteroepitaxy on Silicon: Fundamentals, Structures,and Devices, H.K. Choi, H. Ishiwara, R. Hull, R.J. Nemanich, 1988, ISBN: 0-931837-86-3

Volume 117—Process Diagnostics: Materials, Combustion, Fusion, K. Hays, A.C. Eckbreth, G.A. Campbell, 1988, ISBN: 0-931837-87-1

Volume 118—Amorphous Silicon Technology, A. Madan, M.J. Thompson, P.C. Taylor, P.G. LeComber, Y. Hamakawa, 1988, ISBN: 0-931837-88-X

Volume 119—Adhesion in Solids, D.M. Mattox, C. Batich, J.E.E. Baglin, R.J. Gottschall, 1988, ISBN: 0-931837-89-8

Volume 120—High-Temperature/High-Performance Composites, F.D. Lemkey, A.G. Evans, S.G. Fishman, J.R. Strife, 1988, ISBN: 0-931837-90-1

Volume 121—Better Ceramics Through Chemistry III, C.J. Brinker, D.E. Clark, D.R. Ulrich, 1988, ISBN: 0-931837-91-X

Volume 122—Interfacial Structure, Properties, and Design, M.H. Yoo, W.A.T. Clark, C.L. Briant, 1988, ISBN: 0-931837-92-8

MATERIALS RESEARCH SOCIETY SYMPOSIUM PROCEEDINGS

Volume 123—Materials Issues in Art and Archaeology, E.V. Sayre, P. Vandiver, J. Druzik, C. Stevenson, 1988, ISBN: 0-931837-93-6

Volume 124—Microwave-Processing of Materials, M.H. Brooks, I.J. Chabinsky, W.H. Sutton, 1988, ISBN: 0-931837-94-4

Volume 125—Materials Stability and Environmental Degradation, A. Barkatt, L.R. Smith, E. Verink, 1988, ISBN: 0-931837-95-2

Volume 126—Advanced Surface Processes for Optoelectronics, S. Bernasek, T. Venkatesan, H. Temkin, 1988, ISBN: 0-931837-96-0

Volume 127—Scientific Basis for Nuclear Waste Management XII, W. Lutze, R.C. Ewing, 1989, ISBN: 0-931837-97-9

Volume 128—Processing and Characterization of Materials Using Ion Beams, L.E. Rehn, J. Greene, F.A. Smidt, 1989, ISBN: 1-55899-001-1

Volume 129—Laser and Particle-Beam Modification of Chemical Processes on Surfaces, A.W. Johnson, G.L. Loper, T.W. Sigmon, 1989, ISBN: 1-55899-002-X

Volume 130—Thin Films: Stresses and Mechanical Properties, J.C. Bravman, W.D. Nix, D.M. Barnett, D.A. Smith, 1989, ISBN: 1-55899-003-8

Volume 131—Chemical Perspectives of Microelectronic Materials, M.E. Gross, J. Jasinski, J.T. Yates, Jr., 1989, ISBN: 1-55899-004-6

Volume 132—Multicomponent Ultrafine Microstructures, L.E. McCandlish, B.H. Kear, D.E. Polk, and R.W. Siegel, 1989, ISBN: 1-55899-005-4

Volume 133—High Temperature Ordered Intermetallic Alloys III, C.T. Liu, A.I. Taub, N.S. Stoloff, C.C. Koch, 1989, ISBN: 1-55899-006-2

Volume 134—The Materials Science and Engineering of Rigid-Rod Polymers, W.W. Adams, R.K. Eby, D.E. McLemore, 1989, ISBN: 1-55899-007-0

Volume 135—Solid State Ionics, G. Nazri, R.A. Huggins, D.F. Shriver, 1989 ISBN: 1-55899-008-9

Volume 136—Fly Ash and Coal Conversion By-Products: Characterization, Utilization and Disposal V, R.T. Hemmings, E.E. Berry, G.J. McCarthy, F.P. Glasser, 1989, ISBN: 1-55899-009-7

Volume 137—Pore Structure and Permeability of Cementitious Materials, L.R. Roberts, J.P. Skalny, 1989, ISBN: 1-55899-010-0

Volume 138—Characterization of the Structure and Chemistry of Defects in Materials, B.C. Larson, M. Ruhle, D.N. Seidman, 1989, ISBN: 1-55899-011-9

Volume 139—High Resolution Microscopy of Materials, W. Krakow, F.A. Ponce, D.J. Smith, 1989, ISBN: 1-55899-012-7

Volume 140—New Materials Approaches to Tribology: Theory and Applications, L.E. Pope, L. Fehrenbacher, W.O. Winer, 1989, ISBN: 1-55899-013-5

Volume 141—Atomic Scale Calculations in Materials Science, J. Tersoff, D. Vanderbilt, V. Vitek, 1989, ISBN: 1-55899-014-3

Volume 142—Nondestructive Monitoring of Materials Properties, J. Holbrook, J. Bussiere, 1989, ISBN: 1-55899-015-1

Volume 143—Synchrotron Radiation in Materials Research, R. Clarke, J. Gland, J.H. Weaver, 1989, ISBN: 1-55899-016-X

Volume 144—Advances in Materials, Processing and Devices in III-V Compound Semiconductors, D.K. Sadana, L. Eastman, R. Dupuis, 1989, ISBN: 1-55899-017-8

Volume 145—III-V Heterostructures for Electronic/Photonic Devices, C.W. Tu, V.D. Mattera, A.C. Gossard, 1989, ISBN: 1-55899-018-6

Volume 146—Rapid Thermal Annealing/Chemical Vapor Deposition and Integrated Processing, D. Hodul, J. Gelpey, M.L. Green, T.E. Seidel, 1989, ISBN: 1-55899-019-4

MATERIALS RESEARCH SOCIETY SYMPOSIUM PROCEEDINGS

Volume 147—Ion Beam Processing of Advanced Electronic Materials, N.W. Cheung, A.D. Marwick, J.B. Roberto, 1989, ISBN: 1-55899-020-8

Volume 148—Chemistry and Defects in Semiconductor Heterostructures, M. Kawabe, T.D. Sands, E.R. Weber, R.S. Williams, 1989, ISBN: 1-55899-021-6

Volume 149—Amorphous Silicon Technology-1989, A. Madan, M.J. Thompson, P.C. Taylor, Y. Hamakawa, P.G. LeComber, 1989, ISBN: 1-55899-022-4

Volume 150—Materials for Magneto-Optic Data Storage, C.J. Robinson, T. Suzuki, C.M. Falco, 1989, ISBN: 1-55899-023-2

Volume 151—Growth, Characterization and Properties of Ultrathin Magnetic Films and Multilayers, B.T. Jonker, J.P. Heremans, E.E. Marinero, 1989, ISBN: 1-55899-024-0

Volume 152—Optical Materials: Processing and Science, D.B. Poker, C. Ortiz, 1989, ISBN: 1-55899-025-9

Volume 153—Interfaces Between Polymers, Metals, and Ceramics, B.M. DeKoven, A.J. Gellman, R. Rosenberg, 1989, ISBN: 1-55899-026-7

Volume 154—Electronic Packaging Materials Science IV, R. Jaccodine, K.A. Jackson, E.D. Lillie, R.C. Sundahl, 1989, ISBN: 1-55899-027-5

Volume 155—Processing Science of Advanced Ceramics, I.A. Aksay, G.L. McVay, D.R. Ulrich, 1989, ISBN: 1-55899-028-3

Volume 156—High Temperature Superconductors: Relationships Between Properties, Structure, and Solid-State Chemistry, J.R. Jorgensen, K. Kitazawa, J.M. Tarascon, M.S. Thompson, J.B. Torrance, 1989, ISBN: 1-55899-029

Recent Materials Research Society Proceedings listed in the front.

MATERIALS RESEARCH SOCIETY CONFERENCE PROCEEDINGS

Tungsten and Other Refractory Metals for VLSI Applications, Robert S. Blewer, 1986; ISSN 0886-7860; ISBN 0-931837-32-4

Tungsten and Other Refractory Metals for VLSI Applications II, Eliot K. Broadbent, 1987; ISSN 0886-7860; ISBN 0-931837-66-9

Ternary and Multinary Compounds, Satyen K. Deb, Alex Zunger, 1987; ISBN 0-931837-57-X

Tungsten and Other Refractory Metals for VLSI Applications III, Victor A. Wells, 1988, ISSN 0886-7860; ISBN 0-931837-84-7

Atomic and Molecular Processing of Electronic and Ceramic Materials: Preparation, Characterization and Properties, Ilhan A. Aksay, Gary L. McVay, Thomas G. Stoebe, J.F. Wager, 1988; ISBN 0-931837-85-5

Materials Futures: Strategies and Opportunities, R. Byron Pipes, U.S. Organizing Committee, Rune Lagneborg, Swedish Organizing Committee, 1988: ISBN 1-55899-000-3

Tungsten and Other Refractory Metals for VLSI Applications IV, Robert S. Blewer, Carol M. McConica, 1989; ISSN 0886-7860; ISBN 0-931837-98-7

Tungsten and Other Advanced Metals for VLSI/ULSI Applications V, S. Simon Wong, Seijiro Furukawa, 1990; ISSN 1048-0854; ISBN 1-55899-086-2

High Energy and Heavy Ion Beams in Materials Analysis, Joseph R. Tesmer, Carl J. Maggiore, Michael Nastasi, J. Charles Barbour, James W. Mayer, 1990; ISBN 1-55899-091-7

Physical Metallurgy of Cast Iron IV, Goro Ohira, Takaji Kusakawa, Eisuke Niyama, 1990; ISBN 1-55899-090-9

MATERIALS RESEARCH SOCIETY MONOGRAPH

Atom Probe Microanalysis: Principles and Applications to Materials Problems, M.K. Miller, G.D.W. Smith, 1989; ISBN 0-931837-99-5

MATERIALS RESEARCH SOCIETY INTERNATIONAL SYMPOSIUM PROCEEDINGS

International Meeting on Advanced Materials
Sunshine City, Ikebukuro, Tokyo, Japan
May 30-June 3, 1988

Executive Editors
Masao Doyama, Shigeyuki Sōmiya, Robert P.H. Chang

Volume 1—Ionic Polymers/Ordered Polymers for High Performance Materials/Biomaterials, Senior Editors: Norio Ise, Eishun Tsuchida/Shohei Inoue, Minoru Matsuda/Hideki Aoki, Yohji Imai, Ishi Miura, 1989, ISBN: 1-55899-030-5

Volume 2—Hydrogen Absorbing Materials/Catalytic Materials, Senior Editors: Shuitiro Ono, Yasuo Sasaki, Seijirau Suda/Yoshihiko Moro-oka, 1989, ISBN: 1-55899-031-3

Volume 3—Powder Preparation/Rapid Quenching, Senior Editors: Kazuo Akashi, Yoshiharu Ozaki, Tohoru Takeda,/Akihisa Inoue, Tsuyoshi Masumoto, Takeyuki Suzuki, 1989, ISBN: 1-55899-032-1

Volume 4—Composites/Corrosion-Coating of Advanced Materials, Senior Editors: Shiushichi Kimura, Akira Kobayashi, Sokichi Umekawa/Kazuyoshi Nii, Yasutoshi Saito, Masahiro Yoshimura, 1989, ISBN: 1-55899-033-X

Volume 5—Structural Ceramics/Fracture Mechanics, Senior Editors: Yoshiteru Hamano, Osami Kamigaito/Teruo Kishi, Mototsugu Sakai, 1989, ISBN: 1-55899-034-8

Volume 6—Superconductivity, Senior Editors: Koichi Kitazawa, Kyoji Tachikawa, 1989, ISBN: 1-55899-035-6

Volume 7—Superplasticity, Senior Editors: Masaru Kobayashi, Fumihiro Wakai, 1989, ISBN: 1-55899-036-4

Volume 8—Metal-Ceramic Joints, Senior Editors: Nobuya Iwamoto, Tadatomo Suga, 1989, ISBN: 1-55899-037-2

Volume 9—Shape Memory Materials, Senior Editors: Kazuhiro Otsuka, Ken'ichi Shimizu, 1989, ISBN: 1-55899-038-0

Volume 10—Multilayers, Senior Editors: Ryoichi Yamamoto, Tomeji Ohno, 1989, ISBN: 1-55899-039-9

Volume 11—Microstructure-Property Relationships in Magnetic Materials, Senior Editors: Motofumi Homma, Yasuo Imaoka, Masuo Okada, 1989, ISBN: 1-55899-040-2

Volume 12—Photoresponsive Materials, Senior Editor: Shigeo Tazuke, 1989, ISBN: 1-55899-041-0

Volume 13—Advanced Cements and Chemically Bonded Ceramics, Senior Editors: Masaki Daimon, Shigeyuki Sōmiya, Giichi Sudoh, Kunihiro Takemoto, 1989, ISBN: 1-55899-042-9

Volume 14—Biosensors, Senior Editor: Isao Karube, 1989, ISBN: 1-55899-043-7

JSAP-MRS INTERNATIONAL CONFERENCE ON ELECTRONIC MATERIALS

Shigaku-Kaikan, Tokyo, Japan
June 13-15, 1988

Proceedings of First International Conference on Electronic Materials, Editors: Takuo Sugano, Robert P.H. Chang, Hiroshi Kamimura, Izuo Hayashi, Takeshi Kamiya, 1989, ISBN: 1-55899-044-5